Title: The Belle II Physics Book

Author: Henryk Czyż, E. Kou, P. Urquijo, W. Altmannshofer, F. Beaujean, G. Bell i in.

Citation style: Czyż Henryk, Kou E., Urquijo P., Altmannshofer W., Beaujean F., Bell G. i in. (2019). The Belle II Physics Book. "Progress of Theoretical and Experimental Physics" Vol. 2019, iss. 12 (2019), art. no 4329, doi 10.1093/ptep/ptz106

PTEP

Prog. Theor. Exp. Phys. **2019**, 123C01 (654 pages)
DOI: 10.1093/ptep/ptz106

The Belle II Physics Book

E. Kou[75,*,§,†], P. Urquijo[145,‡,†], W. Altmannshofer[135,§], F. Beaujean[79,§], G. Bell[122,§], M. Beneke[114,§], I. I. Bigi[148,§], F. Bishara[150,16,§], M. Blanke[49,51,§], C. Bobeth[113,114,§], M. Bona[152,§], N. Brambilla[114,§], V. M. Braun[50,§], J. Brod[112,135,§], A. J. Buras[115,§], H. Y. Cheng[43,§], C. W. Chiang[92,§], M. Ciuchini[59,§], G. Colangelo[128,§], A. Crivellin[102,§], H. Czyz[156,29,§], A. Datta[146,§], F. De Fazio[53,§], T. Deppisch[51,§], M. J. Dolan[145,§], J. Evans[135,§], S. Fajfer[109,141,§], T. Feldmann[122,§], S. Godfrey[7,§], M. Gronau[62,§], Y. Grossman[15,§], F. K. Guo[45,134,§], U. Haisch[150,11,§], C. Hanhart[21,§], S. Hashimoto[30,26,§], S. Hirose[89,§], J. Hisano[89,90,§], L. Hofer[127,§], M. Hoferichter[168,§], W. S. Hou[92,§], T. Huber[122,§], T. Hurth[63,§], S. Jaeger[159,§], S. Jahn[83,§], M. Jamin[126,§], J. Jones[104,§], M. Jung[113,§], A. L. Kagan[135,§], F. Kahlhoefer[1,§], J. F. Kamenik[109,141,§], T. Kaneko[30,26,§], Y. Kiyo[64,§], A. Kokulu[114,140,§], N. Kosnik[109,141,§], A. S. Kronfeld[20,§], Z. Ligeti[19,§], H. Logan[7,§], C. D. Lu[41,§], V. Lubicz[153,§], F. Mahmoudi[142,§], K. Maltman[173,§], S. Mishima[30,§], M. Misiak[166,§], K. Moats[7,§], B. Moussallam[74,§], A. Nefediev[39,88,77,§], U. Nierste[51,§], D. Nomura[30,§], N. Offen[50,§], S. L. Olsen[133,§], E. Passemar[37,118,§], A. Paul[16,31,§], G. Paz[170,§], A. A. Petrov[170,§], A. Pich[164,§], A. D. Polosa[58,§], J. Pradler[40,§], S. Prelovsek[109,141,50,§], M. Procura[123,§], G. Ricciardi[54,§], D. J. Robinson[132,19,§], P. Roig[9,§], J. Rosiek[166,§], S. Schacht[60,15,§], K. Schmidt-Hoberg[16,§], J. Schwichtenberg[51,§], S. R. Sharpe[167,§], J. Shigemitsu[117,§], D. Shih[105,§], N. Shimizu[162,§], Y. Shimizu[69,§], L. Silvestrini[58,§], S. Simula[59,§], C. Smith[76,§], P. Stoffer[131,§], D. Straub[113,§], F. J. Tackmann[16,§], M. Tanaka[98,§], A. Tayduganov[112,§], G. Tetlalmatzi-Xolocotzi[95,§], T. Teubner[140,§], A. Vairo[114,§], D. van Dyk[114,§], J. Virto[82,114,§], Z. Was[93,§], R. Watanabe[147,§], I. Watson [155,§], S. Westhoff[139,§], J. Zupan[135,§], R. Zwicky[136,§], F. Abudinén[83,‡], I. Adachi[30,26,‡], K. Adamczyk[93,‡], P. Ahlburg[129,‡], H. Aihara[162,‡], A. Aloisio[54,‡], L. Andricek[84,‡], N. Anh Ky[44,‡], M. Arndt[129,‡], D. M. Asner[5,‡], H. Atmacan[158,‡], T. Aushev[87,‡], V. Aushev[110,‡], R. Ayad[161,‡], T. Aziz[111,‡], S. Baehr[48,‡], S. Bahinipati[33,‡], P. Bambade[75,‡], Y. Ban[103,‡], M. Barrett[170,‡], J. Baudot[47,‡], P. Behera[36,‡], K. Belous[38,‡], M. Bender[78,‡], J. Bennett[8,‡], M. Berger[40,‡], E. Bernieri[59,‡], F. U. Bernlochner[48,‡], M. Bessner[138,‡], D. Besson[88,‡], S. Bettarini[57,‡], V. Bhardwaj[32,‡], B. Bhuyan[34,‡], T. Bilka[10,‡], S. Bilmis[86,‡], S. Bilokin[47,‡], G. Bonvicini[170,‡], A. Bozek[93,‡], M. Bračko[144,109,‡], P. Branchini[59,‡], N. Braun[48,‡], R. A. Briere[8,‡], T. E. Browder[138,‡], L. Burmistrov[75,‡], S. Bussino[59,‡], L. Cao[48,‡], G. Caria[145,‡], G. Casarosa[57,‡], C. Cecchi[56,‡], D. Červenkov[10,‡], M.-C. Chang[22,‡], P. Chang[92,‡], R. Cheaib[146,‡], V. Chekelian[83,‡], Y. Chen[154,‡], B. G. Cheon[28,‡], K. Chilikin[77,‡], K. Cho[70,‡], J. Choi[14,‡], S.-K. Choi[27,‡], S. Choudhury[35,‡], D. Cinabro[170,‡], L. M. Cremaldi[146,‡], D. Cuesta[47,‡], S. Cunliffe[16,‡], N. Dash[33,‡], E. de la Cruz Burelo[9,‡], E. de Lucia[52,‡], G. De Nardo[54,‡], M. De Nuccio[16,‡], G. De Pietro[59,‡], A. De Yta Hernandez[9,‡], B. Deschamps[129,‡], M. Destefanis[60,‡], S. Dey[116,‡], F. Di Capua[54,‡], S. Di Carlo[75,‡], J. Dingfelder[129,‡], Z. Doležal[10,‡], I. Domínguez Jiménez[125,‡], T. V. Dong[30,26,‡], D. Dossett[145,‡], S. Duell[129,‡], S. Eidelman[6,96,77,‡],

[†]Editor.
[‡]Belle II Collaborator.
[§]Theory or external contributing author.

Funded by SCOAP[3]

D. Epifanov[6,96,‡], J. E. Fast[100,‡], T. Ferber[16,‡], S. Fiore[18,‡], A. Fodor[85,‡], F. Forti[57,‡], A. Frey[24,‡], O. Frost[16,‡], B. G. Fulsom[100,‡], M. Gabriel[83,‡], N. Gabyshev[6,96,‡], E. Ganiev[61,‡], X. Gao[3,‡], B. Gao[23,‡], R. Garg[101,‡], A. Garmash[6,96,‡], V. Gaur[169,‡], A. Gaz[90,‡], T. Geßler[65,‡], U. Gebauer[24,‡], M. Gelb[48,‡], A. Gellrich[16,‡], D. Getzkow[65,‡], R. Giordano[54,‡], A. Giri[35,‡], A. Glazov[16,‡], B. Gobbo[61,‡], R. Godang[157,‡], O. Gogota[110,‡], P. Goldenzweig[48,‡], B. Golob[141,109,‡], W. Gradl[63,‡], E. Graziani[59,‡], M. Greco[60,‡], D. Greenwald[114,‡], S. Gribanov[6,96,‡], Y. Guan[17,‡], E. Guido[60,‡], A. Guo[41,‡], S. Halder[111,‡], K. Hara[30,26,‡], O. Hartbrich[138,‡], T. Hauth[48,‡], K. Hayasaka[94,‡], H. Hayashii[91,‡], C. Hearty[130,‡], I. Heredia De La Cruz[9,‡], M. Hernandez Villanueva[9,‡], A. Hershenhorn[130,‡], T. Higuchi[66,‡], M. Hoek[63,‡], S. Hollitt[124,‡], N. T. Hong Van[44,‡], C.-L. Hsu[160,‡], Y. Hu[41,‡], K. Huang[92,‡], T. Iijima[89,90,‡], K. Inami[90,‡], G. Inguglia[40,‡], A. Ishikawa[119,‡], R. Itoh[30,26,‡], Y. Iwasaki[30,‡], M. Iwasaki[97,‡], P. Jackson[124,‡], W. W. Jacobs[37,‡], I. Jaegle[137,‡], H. B. Jeon[73,‡], X. Ji[41,‡], S. Jia[3,‡], Y. Jin[162,‡], C. Joo[66,‡], M. Künzel[16,‡], I. Kadenko[110,‡], J. Kahn[78,‡], H. Kakuno[121,‡], A. B. Kaliyar[36,‡], J. Kandra[10,‡], K. H. Kang[73,‡], Y. Kato[90,‡], T. Kawasaki[68,‡], C. Ketter[138,‡], M. Khasmidatul[143,‡], H. Kichimi[30,‡], J. B. Kim[71,‡], K. T. Kim[71,‡], H. J. Kim[73,‡], D. Y. Kim[108,‡], K. Kim[172,‡], Y. Kim[172,‡], T. D. Kimmel[169,‡], H. Kindo[30,26,‡], K. Kinoshita[135,‡], T. Konno[68,‡], A. Korobov[6,96,‡], S. Korpar[144,109,‡], D. Kotchetkov[138,‡], R. Kowalewski[165,‡], P. Križan[141,109,‡], R. Kroeger[146,‡], J.-F. Krohn[145,‡], P. Krokovny[6,96,‡], W. Kuehn[65,‡], T. Kuhr[78,‡], R. Kulasiri[67,‡], M. Kumar[81,‡], R. Kumar[101,‡], T. Kumita[121,‡], A. Kuzmin[6,96,‡], Y.-J. Kwon[172,‡], S. Lacaprara[55,‡], Y.-T. Lai[30,‡], K. Lalwani[81,‡], J. S. Lange[65,‡], S. C. Lee[73,‡], J. Y. Lee[106,‡], P. Leitl[83,‡], D. Levit[114,‡], S. Levonian[16,‡], S. Li[3,‡], L. K. Li[41,‡], Y. Li[41,‡], Y. B. Li[103,‡], Q. Li[103,‡], L. Li Gioi[83,‡], J. Libby[36,‡], Z. Liptak[138,‡], D. Liventsev[169,‡], S. Longo[165,‡], A. Loos[158,‡], G. Lopez Castro[9,‡], M. Lubej[109,‡], T. Lueck[57,‡], F. Luetticke[129,‡], T. Luo[23,‡], F. Müller[16,‡], Th. Müller[48,‡], C. MacQueen[145,‡], Y. Maeda[90,‡], M. Maggiora[60,‡], S. Maity[33,‡], E. Manoni[56,‡], S. Marcello[60,‡], C. Marinas[129,‡], M. Martinez Hernandez[4,‡], A. Martini[59,‡], D. Matvienko[6,96,77,‡], J. A. McKenna[130,‡], F. Meier[160,‡], M. Merola[54,‡], F. Metzner[48,‡], C. Miller[165,‡], K. Miyabayashi[91,‡], H. Miyake[30,26,‡], H. Miyata[94,‡], R. Mizuk[77,88,87,‡], G. B. Mohanty[111,163,‡], H. K. Moon[71,‡], T. Moon[106,‡], A. Morda[55,‡], T. Morii[66,‡], M. Mrvar[109,‡], G. Muroyama[90,‡], R. Mussa[60,‡], I. Nakamura[30,26,‡], T. Nakano[99,‡], M. Nakao[30,26,‡], H. Nakayama[30,26,‡], H. Nakazawa[92,‡], T. Nanut[109,‡], M. Naruki[72,‡], K. J. Nath[34,‡], M. Nayak[116,‡], N. Nellikunnummel[151,‡], D. Neverov[90,‡], C. Niebuhr[16,‡], J. Ninkovic[84,‡], S. Nishida[30,26,‡], K. Nishimura[138,‡], M. Nouxman[143,‡], G. Nowak[93,‡], K. Ogawa[94,‡], Y. Onishchuk[110,‡], H. Ono[94,‡], Y. Onuki[162,‡], P. Pakhlov[77,88,‡], G. Pakhlova[87,‡], B. Pal[5,‡], E. Paoloni[57,‡], H. Park[73,‡], C.-S. Park[172,‡], B. Paschen[129,‡], A. Passeri[59,‡], S. Paul[114,‡], T. K. Pedlar[80,‡], M. Perelló[46,‡], I. M. Peruzzi[52,‡], R. Pestotnik[109,‡], L. E. Piilonen[169,‡], L. Podesta Lerma[125,‡], V. Popov[87,‡], K. Prasanth[111,‡], E. Prencipe[21,‡], M. Prim[48,‡], M. V. Purohit[158,‡], A. Rabusov[114,‡], R. Rasheed[47,‡], S. Reiter[65,‡], M. Remnev[6,96,‡], P. K. Resmi[36,‡], I. Ripp-Baudot[47,‡], M. Ritter[78,‡], M. Ritzert[139,‡], G. Rizzo[57,‡], L. Rizzuto[141,109,‡], S. H. Robertson[85,‡], D. Rodriguez Perez[125,‡], J. M. Roney[165,‡], C. Rosenfeld[158,‡], A. Rostomyan[16,‡], N. Rout[36,‡], S. Rummel[78,‡], G. Russo[54,‡], D. Sahoo[111,‡], Y. Sakai[30,26,‡], M. Salehi[143,78,‡], D. A. Sanders[146,‡], S. Sandilya[135,‡], A. Sangal[135,‡], L. Santelj[47,‡], J. Sasaki[162,‡], Y. Sato[30,‡], V. Savinov[151,‡], B. Scavino[63,‡], M. Schram[100,‡], H. Schreeck[24,‡], J. Schueler[138,‡], C. Schwanda[40,‡], A. J. Schwartz[135,‡], R. M. Seddon[85,‡], Y. Seino[94,‡], K. Senyo[171,‡], O. Seon[90,‡], I. S. Seong[138,‡], M. E. Sevior[145,‡], C. Sfienti[63,‡], M. Shapkin[38,‡], C. P. Shen[3,‡], M. Shimomura[91,‡], J.-G. Shiu[92,‡], B. Shwartz[6,96,‡], A. Sibidanov[165,‡], F. Simon[83,113,‡], J. B. Singh[101,‡], R. Sinha[42,‡], S. Skambraks[83,‡], K. Smith[145,‡], R. J. Sobie[165,‡], A. Soffer[116,‡], A. Sokolov[38,‡], E. Solovieva[77,87,‡], B. Spruck[63,‡], S. Stanič[149,‡], M. Starič[109,‡], N. Starinsky[147,‡], U. Stolzenberg[24,‡], Z. Stottler[169,‡], R. Stroili[55,‡], J. F. Strube[100,‡], J. Stypula[93,‡], M. Sumihama[25,‡],

K. Sumisawa[30,26,‡], T. Sumiyoshi[121,‡], D. Summers[146,‡], W. Sutcliffe[48,‡], S. Y. Suzuki[30,26,‡], M. Tabata[13,‡], M. Takahashi[16,‡], M. Takizawa[107,‡], U. Tamponi[60,‡], J. Tan[145,‡], S. Tanaka[30,26,‡], K. Tanida[2,‡], N. Taniguchi[30,‡], Y. Tao[137,‡], P. Taras[147,‡], G. Tejeda Munoz[4,‡], F. Tenchini[16,‡], U. Tippawan[12,‡], E. Torassa[55,‡], K. Trabelsi[30,26,‡], T. Tsuboyama[30,26,‡], M. Uchida[120,‡], S. Uehara[30,26,‡], T. Uglov[77,87,‡], Y. Unno[28,‡], S. Uno[30,26,‡], Y. Ushiroda[30,26,162,‡], Y. Usov[6,96,‡], S. E. Vahsen[138,‡], R. van Tonder[48,‡], G. Varner[138,‡], K. E. Varvell[160,‡], A. Vinokurova[6,96,‡], L. Vitale[61,‡], M. Vos[46,‡], A. Vossen[17,‡], E. Waheed[145,‡], H. Wakeling[85,‡], K. Wan[162,‡], M.-Z. Wang[92,‡], X. L. Wang[23,‡], B. Wang[135,‡], A. Warburton[85,‡], J. Webb[145,‡], S. Wehle[16,‡], C. Wessel[129,‡], J. Wiechczynski[93,‡], P. Wieduwilt[24,‡], E. Won[71,‡], Q. Xu[41,‡], X. Xu[41,‡], B. D. Yabsley[160,‡], S. Yamada[30,‡], H. Yamamoto[119,‡], W. Yan[3,‡], W. Yan[154,‡], S. B. Yang[71,‡], H. Ye[16,‡], I. Yeo[70,‡], J. H. Yin[41,‡], M. Yonenaga[121,‡], T. Yoshinobu[94,‡], W. Yuan[55,‡], C. Z. Yuan[41,‡], Y. Yusa[94,‡], S. Zakharov[77,87,‡], L. Zani[57,‡], M. Zeyrek[86,‡], J. Zhang[41,‡], Y. Zhang[23,‡], Y. Zhang[154,‡], X. Zhou[3,‡], V. Zhukova[77,‡], V. Zhulanov[6,96,‡], and A. Zupanc[141,109,‡]

[1]*RWTH, Aachen University, D-52056 Aachen, Germany*
[2]*Advanced Science Research Center, Japan Atomic Energy Agency, Naka 319-1195, Japan*
[3]*Beihang University, Beijing 100191, China*
[4]*Benemerita Universidad Autonoma de Puebla, Puebla 72570, Mexico*
[5]*Brookhaven National Laboratory, Upton, New York 11973, USA*
[6]*Budker Institute of Nuclear Physics SB RAS, Novosibirsk 630090, Russian Federation*
[7]*Ottawa-Carleton Institute of Physics, Department of Physics, Carleton University, Ontario K1S 5B6, Canada*
[8]*Carnegie Mellon University, Pittsburgh, Pennsylvania 15213, USA*
[9]*Centro de Investigacion y de Estudios Avanzados del Instituto Politecnico Nacional, Mexico City 07360, Mexico*
[10]*Faculty of Mathematics and Physics, Charles University, 121 16 Prague, Czech Republic*
[11]*CERN, Theoretical Physics Department, CH-1211 Geneva 23, Switzerland*
[12]*Chiang Mai University, Chiang Mai 50202, Thailand*
[13]*Chiba University, Chiba 263-8522, Japan*
[14]*Chonnam National University, Kwangju 660-701, South Korea*
[15]*Department of Physics, LEPP, Cornell University, Ithaca, NY 14853, USA*
[16]*Deutsches Elektronen–Synchrotron, 22607 Hamburg, Germany*
[17]*Duke University, Durham, North Carolina 27708, USA*
[18]*ENEA Casaccia, I-00123 Roma, Italy*
[19]*Ernest Orlando Lawrence Berkeley National Laboratory, University of California, Berkeley, CA 94720, USA*
[20]*Theoretical Physics Department, Fermi National Accelerator Laboratory, Batavia, IL 60510, USA*
[21]*Forschungszentrum Jülich, 52425 Jülich, Germany*
[22]*Department of Physics, Fu Jen Catholic University, Taipei 24205, Taiwan*
[23]*Key Laboratory of Nuclear Physics and Ion-beam Application (MOE) and Institute of Modern Physics, Fudan University, Shanghai 200443, China*
[24]*II. Physikalisches Institut, Georg-August-Universität Göttingen, 37073 Göttingen, Germany*
[25]*Gifu University, Gifu 501-1193, Japan*
[26]*The Graduate University for Advanced Studies (SOKENDAI), Hayama 240-0193, Japan*
[27]*Gyeongsang National University, Chinju 660-701, South Korea*
[28]*Hanyang University, Seoul 133-791, South Korea*
[29]*Helmholtz-Institute 55128 Mainz, Germany*
[30]*High Energy Accelerator Research Organization (KEK), Tsukuba 305-0801, Japan*
[31]*Institut für Physik, Humboldt-Universität zu Berlin, D-12489 Berlin, Germany*
[32]*Indian Institute of Science Education and Research Mohali, SAS Nagar, 140306, India*
[33]*Indian Institute of Technology Bhubaneswar, Satya Nagar 751007, India*
[34]*Indian Institute of Technology Guwahati, Assam 781039, India*
[35]*Indian Institute of Technology Hyderabad, Telangana 502285, India*
[36]*Indian Institute of Technology Madras, Chennai 600036, India*
[37]*Indiana University, Bloomington, Indiana 47408, USA*

[38]*Institute for High Energy Physics, Protvino 142281, Russian Federation*
[39]*Institute for Theoretical and Experimental Physics, B. Cheremushkinskaya 25, 117218 Moscow, Russia*
[40]*Institute of High Energy Physics, Vienna 1050, Austria*
[41]*Institute of High Energy Physics, Chinese Academy of Sciences, Beijing 100049, China*
[42]*Institute of Mathematical Sciences, Chennai 600113, India*
[43]*Institute of Physics, Academia Sinica Taipei, Taiwan 115, Republic of China*
[44]*Institute of Physics, VAST, Hanoi, Vietnam*
[45] *Institute of Theoretical Physics, Chinese Academy of Sciences, Beijing 100190, China*
[46]*Instituto de Fisica Corpuscular, Paterna 46980, Spain*
[47]*Institut Pluridisciplinaire Hubert Curien, Strasbourg 67037, France*
[48]*Institut für Experimentelle Teilchenphysik, Karlsruhe Institute of Technology, 76131 Karlsruhe, Germany*
[49]*Institut für Kernphysik, Karlsruhe Institute of Technology, Hermann-von-Helmholtz-Platz 1, D-76344 Eggenstein-Leopoldshafen, Germany*
[50]*Institut für Theoretische Physik, Universität Regensburg, D-93040 Regensburg, Germany*
[51]*Institut für Theoretische Teilchenphysik, Karlsruhe Institute of Technology, Wolfgang-Gaede-Str. 1, D-76131 Karlsruhe, Germany*
[52]*INFN Laboratori Nazionali di Frascati, I-00044 Frascati, Italy*
[53]*INFN Sezione di Bari, Via Orabona 4, I-70126 Bari, Italy*
[54]*INFN Sezione di Napoli and Dipartimento di Scienze Fisiche, Università di Napoli Federico II, I-80126 Napoli, Italy*
[55]*INFN Sezione di Padova and Dipartimento di Fisica, Università di Padova, I-35131 Padova, Italy*
[56]*INFN Sezione di Perugia and Dipartimento di Fisica, Università di Perugia, I-06123 Perugia, Italy*
[57]*INFN Sezione di Pisa and Dipartimento di Fisica, Università di Pisa, I-56127 Pisa, Italy*
[58]*INFN Sezione di Roma and Università di Roma "La Sapienza", I-00185 Roma, Italy*
[59]*INFN Sezione di Roma Tre and Università di Roma Tre, I-00146 Roma, Italy*
[60]*INFN Sezione di Torino and Dipartimento di Fisica, Università di Torino, I-10125 Torino, Italy*
[61]*INFN Sezione di Trieste and Dipartimento di Fisica, Università di Trieste, I-34127 Trieste, Italy*
[62]*Physics Department, Technion, Israel Institute of Technology, 32000 Haifa, Israel*
[63]*Johannes Gutenberg-Universität Mainz, Institut für Kernphysik, D-55099 Mainz, Germany*
[64]*Department of Physics, Juntendo University, Inzai, Chiba 270-1695, Japan*
[65]*Justus-Liebig-Universität Gießen, 35392 Gießen, Germany*
[66]*Kavli Institute for the Physics and Mathematics of the Universe (WPI), University of Tokyo, Kashiwa 277-8583, Japan*
[67]*Kennesaw State University, Kennesaw, Georgia 30144, USA*
[68]*Kitasato University, Tokyo 108-0072, Japan*
[69]*Kogakuin University, 2665-1 Nakano, Hachioji, Tokyo 192-0015, Japan*
[70]*Korea Institute of Science and Technology Information, Daejeon 305-806, South Korea*
[71]*Korea University, Seoul 136-713, South Korea*
[72]*Kyoto University, Kyoto 606-8502, Japan*
[73]*Kyungpook National University, Daegu 702-701, South Korea*
[74]*L'institut de physique nucléaire d'Orsay, IN2P3/CNRS et Université Paris-Sud 11, Centre Scientifique d'Orsay, F-91898 Orsay Cedex, France*
[75]*Laboratoire de l'Accélérateur Linéaire, IN2P3/CNRS et Université Paris-Sud 11, Centre Scientifique d'Orsay, F-91898 Orsay Cedex, France*
[76]*Laboratoire de Physique Subatomique et Cosmologie, IN2P3/CNRS et Université Grenoble Alpes, 38000 Grenoble, France*
[77]*P.N. Lebedev Physical Institute of the Russian Academy of Sciences, Moscow 119991, Russian Federation*
[78]*Ludwig Maximilians University, 80539 Munich, Germany*
[79]*Excellence Cluster Universe, Ludwig Maximilians University, 80539 Munich, Germany*
[80]*Luther College, Decorah, Iowa 52101, USA*
[81]*Malaviya National Institute of Technology Jaipur, Jaipur 302017, India*
[82]*Center for Theoretical Physics, Massachusetts Institute of Technology, Cambridge, MA 02139, USA*
[83]*Max-Planck-Institut für Physik, 80805 München, Germany*
[84]*Semiconductor Laboratory of the Max Planck Society, Max-Planck-Institut für Physik, 81739 München, Germany*
[85]*McGill University, Montréal, Québec, H3A 2T8, Canada*

[86]*Middle East Technical University, 06531 Ankara, Turkey*
[87]*Moscow Institute of Physics and Technology, Moscow Region 141700, Russian Federation*
[88]*Moscow Physical Engineering Institute, Moscow 115409, Russian Federation*
[89]*Kobayashi-Maskawa Institute, Nagoya University, Nagoya 464-8602, Japan*
[90]*Graduate School of Science, Nagoya University, Nagoya 464-8602, Japan*
[91]*Nara Women's University, Nara 630-8506, Japan*
[92]*Department of Physics, National Taiwan University, Taipei 10617, Taiwan*
[93]*H. Niewodniczanski Institute of Nuclear Physics, Krakow 31-342, Poland*
[94]*Niigata University, Niigata 950-2181, Japan*
[95]*Nikhef, Science Park 105, NL-1098 XG Amsterdam, Netherlands*
[96]*Novosibirsk State University, Novosibirsk 630090, Russian Federation*
[97]*Osaka City University, Osaka 558-8585, Japan*
[98]*Department of Physics, Graduate School of Science, Osaka University, Toyonaka, Osaka 560-0043, Japan*
[99]*Research Center for Nuclear Physics, Osaka University, Osaka 567-0047, Japan*
[100]*Pacific Northwest National Laboratory, Richland, Washington 99352, USA*
[101]*Panjab University, Chandigarh 160014, India*
[102]*Paul Scherrer Institut, CH-5232 Villigen PSI, Switzerland*
[103]*Peking University, Beijing 100871, China*
[104]*Seccion Fisica, Departamento de Ciencias, Pontificia Universidad Catolica del Peru, Apartado 1761, Lima, Peru*
[105]*NHETC, Rutgers University, Piscataway, NJ 08854 USA*
[106]*Seoul National University, Seoul 151-742, South Korea*
[107]*Showa Pharmaceutical University, Tokyo 194-8543, Japan*
[108]*Soongsil University, Seoul 156-743, South Korea*
[109]*J. Stefan Institute, 1000 Ljubljana, Slovenia*
[110]*Taras Shevchenko National University of Kyiv, Kiev, Ukraine*
[111]*Tata Institute of Fundamental Research, Mumbai 400005, India*
[112]*Technische Universität Dortmund, Fakultät Physik, Otto-Hahn-Str. 4, D-44227 Dortmund, Germany*
[113]*Excellence Cluster Universe, Technische Universität München, 85748 Garching, Germany*
[114]*Department of Physics, Technische Universität München, 85748 Garching, Germany*
[115]*Institute for Advanced Study, Technische Universität München, Lichtenbergstr. 2a,D-85748 Garching*
[116]*Tel Aviv University, School of Physics and Astronomy, Tel Aviv, 69978, Israel*
[117]*The Ohio State University, Department of Physics, Columbus, OH 43210, USA*
[118]*Theory Center, Thomas Jefferson National Accelerator Facility, Newport News, VA 23606, USA*
[119]*Department of Physics, Tohoku University, Sendai 980-8578, Japan*
[120]*Tokyo Institute of Technology, Tokyo 152-8550, Japan*
[121]*Tokyo Metropolitan University, Tokyo 192-0397, Japan*
[122]*Theoretische Physik 1, Naturwissenschaftlich-Technische Fakultät, Universität Siegen, D-57068 Siegen, Germany*
[123]*Fakultät für Physik, Universität Wien, Boltzmanngasse 5, Vienna 1090, Austria*
[124]*Department of Physics, University of Adelaide, Adelaide, South Australia 5005, Australia*
[125]*Universidad Autonoma de Sinaloa, Sinaloa 80000, Mexico*
[126]*IFAE, Autonomous University of Barcelona, Spain*
[127]*Departament de Fisica Quántica i Astrofisica (FQA), Institut de Ciéncies del Cosmos (ICCUB), Universitat de Barcelona (UB), Spain*
[128]*Albert Einstein Center for Fundamental Physics, Institute for Theoretical Physics, University of Bern, Sidlerstrasse 5, 3012 Bern, Switzerland*
[129]*University of Bonn, 53115 Bonn, Germany*
[130]*University of British Columbia, Vancouver, British Columbia, V6T 1Z1, Canada*
[131]*Department of Physics, University of California at San Diego, 9500 Gilman Drive, La Jolla, CA 92093-0319, USA*
[132]*Santa Cruz Institute for Particle Physics and Department of Physics, University of Calfornia at Santa Cruz, Santa Cruz CA 95064, USA*
[133]*University of the Chinese Academy of Science, Beijing, 100049, People's Republic of China*
[134]*School of Physical Sciences, University of Chinese Academy of Sciences, Beijing 100049, China*
[135]*University of Cincinnati, Cincinnati, Ohio 45221, USA*

[136]*Higgs Centre For Theoretical Physics, School of Physics and Astronomy, University of Edinburgh, Edinburgh EH9 3JZ, Scotland*
[137]*University of Florida, Gainesville, Florida 32611, USA*
[138]*University of Hawaii, Honolulu, Hawaii 96822, USA*
[139]*University of Heidelberg, 68131 Mannheim, Germany*
[140]*Department of Mathematical Sciences, University of Liverpool, Liverpool L69 3BX, UK*
[141]*Faculty of Mathematics and Physics, University of Ljubljana, 1000 Ljubljana, Slovenia*
[142]*Université Lyon 1, ENS de Lyon, CNRS, Centre de Recherche Astrophysique de Lyon UMR5574, F-69230 Saint-Genis-Laval, France*
[143]*University of Malaya, 50603 Kuala Lumpur, Malaysia*
[144]*University of Maribor, 2000 Maribor, Slovenia*
[145]*School of Physics, The University of Melbourne, Victoria 3010, Australia*
[146]*University of Mississippi, University, Mississippi 38677, USA*
[147]*Université de Montréal, Physique des Particules, Montréal, Québec, H3C 3J7, Canada*
[148]*Department of Physics, University of Notre Dame du Lac Notre Dame, IN 46556, USA*
[149]*University of Nova Gorica, 5000 Nova Gorica, Slovenia*
[150]*Rudolf Peierls Centre for Theoretical Physics, University of Oxford, OX1 3NP Oxford, UK*
[151]*University of Pittsburgh, Pittsburgh, Pennsylvania 15260, USA*
[152]*Queen Mary University of London, School of Physics and Astronomy, Mile End Road, London E1 4NS, UK*
[153]*Dipartimento di Matematica e Fisica, Università di Roma Tre, Via della Vasca Navale 84, I-00146 Roma, Italy*
[154]*University of Science and Technology of China, Hefei 230026, China*
[155]*University of Seoul, 130-743 Seoul, South Korea*
[156]*Institute of Physics, University of Silesia, PL-41500 Chorzow, Poland*
[157]*University of South Alabama, Mobile, Alabama 36688, USA*
[158]*University of South Carolina, Columbia, South Carolina 29208, USA*
[159]*Department of Physics and Astronomy, University of Sussex, Falmer, Brighton BN1 9QH, UK*
[160]*School of Physics, University of Sydney, New South Wales 2006, Australia*
[161]*Department of Physics, Faculty of Science, University of Tabuk, Tabuk 71451, Saudi Arabia*
[162]*Department of Physics, University of Tokyo, Tokyo 113-0033, Japan*
[163]*Utkal University, Bhubaneswar 751004, India*
[164]*IFIC, University of Valencia - CSIC, Spain*
[165]*University of Victoria, Victoria, British Columbia, V8W 3P6, Canada*
[166]*Institute of Theoretical Physics, Faculty of Physics, University of Warsaw, 02-093 Warsaw, Poland*
[167]*Physics Department, University of Washington, Seattle WA 98195, USA*
[168]*Institute for Nuclear Theory, University of Washington, Seattle, WA 98195-1550, USA*
[169]*Virginia Polytechnic Institute and State University, Blacksburg, Virginia 24061, USA*
[170]*Wayne State University, Detroit, Michigan 48202, USA*
[171]*Yamagata University, Yamagata 990-8560, Japan*
[172]*Yonsei University, Seoul 120-749, South Korea*
[173]*Department of Mathematics and Statistics, York University, Toronto, Ontario M3J 1P3, Canada*
*E-mail: kou@lal.in2p3.fr

Received October 26, 2018; Accepted November 11, 2018; Published December 23, 2019

Subject Index C50

1. Preface

The Belle II Theory Interface Platform (B2TiP) was created as a physics prospects working group of the Belle II collaboration in June 2014. It offered a platform where theorists and experimentalists could work together to elucidate the potential impacts of the Belle II program, which includes a wide scope of physics topics: B physics, charm, τ, quarkonium physics, electroweak precision measurements, and dark sector searches. It is composed of nine working groups (WGs), which

are coordinated by teams of theory and experiment conveners: WG1, Semileptonic and leptonic B Decays; WG2, Radiative and Electroweak Penguins; WG3, ϕ_1 and ϕ_2 (Time-Dependent CP Violation) Measurements; WG4, ϕ_3 Measurement; WG5, Charmless Hadronic B Decay; WG6, Charm; WG7, Quarkonium(-like); WG8, τ and Low-Multiplicity Processes; WG9, New Physics. We organized workshops twice a year from 2014 until 2016, which moved from KEK in Japan to Europe and the Americas, gathering experts in the respective fields for discussions with Belle II members.

One of the goals for B2TiP was to propose so-called "golden and silver channels": we asked each working group to choose, among numerous possible measurements, those that would have the highest potential impact and to focus on them for the writeup. Theorists scrutinized the role of those measurements in terms of understanding the theory behind them, and estimated the theoretical uncertainties now achievable as well as prospects for the future. For flavor physics, having tight control of hadronic uncertainties is one of the most crucial aspects in the field, and this is considered an important criterion in determining the golden or silver channels. Experimentalists, on the other hand, investigated the expected improvements with data from Belle II. For the channels where the errors are dominated by statistical uncertainties, or where systematic errors are reducible, the errors can decrease rapidly as more data becomes available. The impact of the upgraded performance from Belle II is a crucial element in reducing the uncertainties: we therefore include the latest available studies of the detector efficiency using Monte Carlo simulated events. We list the golden and silver channel table in the introductory chapter, as a guide for the chapters that follow.

This book is not a collection of reports based on talks given at the workshops. The working group conveners endeavored to construct a coherent document that can be used by Belle II collaborators, and others in the field of flavor physics, as a reference. Two books of a similar type have been produced in the past: *The BaBar Book* [1] and *The Physics of the B Factories* [2]. In order to avoid too much repetition with respect to those references, we refer to them wherever possible for introductory material.

We would like to thank the section editors and contributing authors for the many stimulating discussions and their tremendous efforts in bringing the book together.

1.1. Working groups

The Belle II Theory Interface Platform working groups and convenors were assigned as follows.

Leptonic and Semileptonic B Decays
Experiment: G. De Nardo (Naples), A. Zupanc (IJS)
Theory: F. Tackmann (DESY), A. Kronfeld (FNAL, *LQCD*), R. Watanabe (Montreal)

Radiative and Electroweak Penguin B Decays
Experiment: A. Ishikawa (Tohoku), J. Yamaoka (PNNL)
Theory: U. Haisch (Oxford), T. Feldmann (Siegen)

Time-Dependent CP Violation of B Mesons
Experiment: A. Gaz (Nagoya), L. Li Gioi (MPI Munich)
Theory: S. Mishima (Rome/KEK), J. Zupan (Cincinnati)

Determination of the Unitarity Triangle Angle ϕ_3
Experiment: J. Libby (IIT Madras)
Theory: Y. Grossman (Cornell), M. Blanke (CERN)

Hadronic *B* Decays and Direct CP Violation
Experiment: P. Goldenzweig (KIT)
Theory: M. Beneke (TUM), C-W. Chiang (NCU)

Charm Flavor and Spectroscopy
Experiment: G. Casarosa (Pisa), A. Schwartz (Cincinnati)
Theory: A. Petrov (Wayne), A. Kagan (Cincinnati)

Quarkonium(-like) Physics
Experiment: B. Fulsom (PNNL), R. Mizuk (ITEP), R. Mussa (Torino), C-P. Shen (Beihang)
Theory: N. Brambilla (TUM), C. Hanhart (Juelich), Y. Kiyo (Juntendo), A. Polosa (Rome), S. Prelovsek (Ljubljana, *LQCD*)

Tau Decays and Low-Multiplicity Physics
Experiment: K. Hayasaka (Nagoya), T. Ferber (DESY)
Theory: E. Passemar (Indiana), J. Hisano (Nagoya)

New Physics and Global Analyses
Experiment: F. Bernlochner (Bonn), R. Itoh (KEK)
Theory: J. Kamenik (Ljubljana), U. Nierste (KIT), L. Silvestrini (Rome)

Further direct contributors to the chapters are given in the chapter headers.

1.2. Committees

The B2TiP workshop and book organizing committee is comprised of

- Emi Kou (LAL)
- Phillip Urquijo (Melbourne)

An international advisory committee assisted in steering the coordination of the workshops and report.

- Marco Ciuchini (Rome)
- Tim Gershon (Warwick)
- Bostjan Golob (IJS)
- Shoji Hashimoto (KEK)
- Francois Le Diberder (LAL)
- Zoltan Ligeti (LBNL)
- Thomas Mannel (Siegen)
- Hitoshi Murayama (IPMU)
- Matthias Neubert (Mainz)
- Junko Shigemitsu (Ohio)

The Belle II experiment ex officio is comprised of

- Francesco Forti (Pisa)
- Thomas Browder (Hawaii)
- Yoshihide Sakai (KEK)

1.3. Workshops

This report is the culmination of a two-year workshop series held to develop the physics program for Belle II. The schedule for the workshops was as follows.

KEK	Kickoff meeting	16th–17th June 2014
KEK	Joint KEK-FF / First B2TiP workshop	30th–31st October 2014
Krakow	Second B2TiP workshop	27th–28th April 2015
KEK	Joint KEK-FF / Third B2TiP workshop	28th–29th October 2015
Pittsburgh	Fourth B2TiP workshop	23rd–25th May 2016
Munich	Fifth B2TiP workshop and editorial meeting	15th–17th November 2016

Contents PAGE

2. Introduction

Section authors: P. Urquijo, E. Kou

2.1. Introduction

The primary physics goals of Belle II, as a next-generation flavor factory, are to search for new physics (NP) in the flavor sector at the intensity frontier, and to improve the precision of measurements of Standard Model (SM) parameters. The SuperKEKB facility is designed to collide electrons and positrons at center-of-mass energies in the regions of the Υ resonances. Most of the data will be collected at the $\Upsilon(4S)$ resonance, which is just above the threshold for B-meson pair production where no fragmentation particles are produced. The accelerator is designed with asymmetric beam energies to provide a boost to the center-of-mass system and thereby allow for time-dependent charge–parity (CP) symmetry violation measurements. The boost is slightly less than at KEKB, which is advantageous for analyses with neutrinos in the final state that require good detector hermeticity, although it requires better vertex reconstruction resolution. SuperKEKB has a design luminosity of $8 \times 10^{35}\ \mathrm{cm}^{-2}\ \mathrm{s}^{-1}$, about 40 times larger that of KEKB's recorded peak and 80 times KEKB's design luminosity. This luminosity will produce a total of 5×10^{10} b, c, and τ pairs over a period of eight years. The first collision data-taking run was undertaken in 2018, used primarily for accelerator and detector commissioning.

The SM is, at the current level of experimental precision and at the energies reached so far, the best-tested theory of nature at a fundamental level. Despite its tremendous success in describing the fundamental particles and their interactions, excluding gravity, it does not provide answers to many fundamental questions. The SM does not explain why there should be only three generations of elementary fermions and why there is an observed hierarchy in the fermion masses. The origin of mass of fundamental particles is explained within the SM by spontaneous electroweak symmetry breaking, resulting in the Higgs boson. However, it is not clear whether the Higgs boson can account for neutrino masses. It is also not yet clear whether there is a only single SM Higgs boson or whether there may be a more elaborate Higgs sector with other Higgs-like particles, as in supersymmetry or other NP models. At the cosmological scale, there is the unresolved problem with the matter–antimatter asymmetry in the universe. While the violation of CP symmetry is a necessary condition for the evolution of a matter-dominated universe, the observed CP violation within the quark sector that originates from the complex phase of the Cabibbo–Kobayashi–Maskawa (CKM) matrix is many orders of magnitude too small to explain the dominance of matter in the universe. Hence, there must exist undiscovered sources of the CP asymmetry. Furthermore, the elements of the CKM matrix exhibit a roughly diagonal hierarchy, even though the SM does not require this. This may indicate the presence of a new mechanism, such as a flavor symmetry, that exists unbroken at a higher energy scale. Considering the open questions that remain unanswered in the SM, it is fair to conclude that the present theory is an extremely successful but phenomenological description of subatomic processes at energy scales up to $\mathcal{O}(1\ \mathrm{TeV})$. Many new physics scenarios have been proposed to explain these shortcomings of the SM, where new particles and new processes arise.

Experiments in high-energy physics are designed to address the above questions through searches of NP using complementary approaches. At the energy frontier, the Large Hadron Collider (LHC) experiments are able to discover new particles produced in proton–proton collisions at a center-of-mass energy of up to 14 TeV. Sensitivity to the direct production of a specific new particle depends on the cross section and on the size of the data sample. At the intensity frontier, signatures of new

particles or processes can be observed through measurements of suppressed flavor physics reactions or from deviations from SM predictions. An observed discrepancy can be interpreted in terms of NP models. This is the approach of Belle II.

The sensitivity of Belle II to NP depends on the strength of the flavor-violating couplings of the NP. The mass reach for new particle/process effects can be as high as $\mathcal{O}(100\,\text{TeV})$ if the couplings are not as suppressed as in the SM [3]. In the past, measurements of processes' quantum corrections have given access to high-mass-scale physics before accelerators were available to directly probe these scales. Belle II and SuperKEKB will exploit our strengths at the intensity frontier by moving beyond simple observation of an NP effect to its detailed characterization through over-constraining measurements in several related flavor physics reactions.

2.2. New physics search strategy after the B factories and LHC run I and run II first data

The LHC experiments ATLAS, CMS, and LHCb have been operating extremely well since its commencement in 2009 and are rapidly changing the scene of particle physics. Needless to say, the discovery of the Higgs boson in 2012 was the most significant event in particle physics in recent years. Its mass, 125 GeV, and its production and decay patterns being SM-like not only provides a confirmation of the SM but also puts very strong constraints on the Higgs sector of various new physics models (especially those that contain more than one neutral Higgs). The 125 GeV Higgs has excluded a large parameter space of minimal supersymmetric (SUSY) models, from which we expected some signals in Belle II observables. The mass constraints on direct searches for new particles are also advancing. For example, the lower mass bounds of the new gauge bosons, $m_{Z',W'}$, within the sequential model (i.e. SM-like) has been pushed up to $\sim$3 TeV and the vector-like fermion masses now exceed $\sim$800 GeV. Since new physics effects in Belle II observables are roughly proportional to the inverse of the mass of these particles (with powers of 2, 3, 4, etc. depending on the observable), the chance of observing a signal from such generic models is diminishing. However, it is important to note that such minimal or generic models are often quite unnatural from the theoretical point of view since we need to impose a very high degree of symmetry (i.e. to mimic the SM) to realize them. New physics models that we search for in Belle II are those that include more specific flavor couplings, for which indirect searches can push the new physics scale much higher than the direct search programs. Hints of new physics in previous and ongoing experiments may provide us with some indication of the kind of new flavor phenomena that we should look for.

An important flavor coupling structure to examine for new physics is $b \to s$ transitions, which have been a focus of both theory and experiment in recent years. Since the start of the B factory experiments precise CP violation measurements in the B_d system have been done using tree-level $b \to c\bar{c}s$ transitions (such as the golden mode $B \to J/\psi K^0_S$ final state), and as time went by, the B factories started observing CP violation through the loop induced $b \to s$ transitions, such as the $B \to \phi K^0_S$ or $B \to \eta' K^0_S$ processes (the first observation in 2003 had shown a small tension as well). The $b \to s\bar{q}q$ transition is induced by gluon penguin diagrams. In the SM, CP violation in $b \to s$ transitions is expected to be very small. Thus, any significant observation of CP violation can be interpreted a signal beyond the SM. This is a new area of research in B physics as the precision is still very far from the measurements using the tree-level processes and there is a lot room for new physics contributions. It is worth mentioning that a small tension has also been observed in another type of CP violation, direct CP violation, in $B \to K\pi$ decays, which also occurs in part due to penguin $b \to s\bar{q}q$ transitions. The LHCb experiment is in the right position to tackle this question from a different direction, by measuring the parameters of $B_s - \overline{B}_s$ mixing, which occurs due to another type

of loop diagram, the $b \to s$ box process. So far, the LHCb results for this observable are consistent with the SM. However, since 2013, LHCb has started observing a few very interesting deviations from the SM in the other $b \to s$ transitions such as the $B \to K^* \mu^+ \mu^-$ angular distribution and the ratio of rates of $B \to K^{(*)} e^+ e^-$ to $B \to K^{(*)} \mu^+ \mu^-$ (so-called $R(K^{(*)})$). Those excesses are said to be reaching the 4–5 σ level. The very specific appearances of these anomalies were not predicted and they are opening a new trend in particle physics: new particles with very distinct flavor couplings in the $b \to s$ transition as well as a possible lepton universality violation.

Another important hint of new physics was in the measurement of the branching ratio of $B \to \tau \nu$, which in 2006 had shown a deviation from SM expectation (in particular $|V_{ub}|$ measured from other channels). There is now some tension between measurements by Belle and BaBar of this rate. This is a tree-level annihilation $b \to u$ transition and the final state includes at least two neutrinos so it is experimentally quite challenging; so far the B factories have reconstructed only a few hundred events. As $B \to \tau \nu$ is particularly sensitive to the charged Higgs that in general couples more strongly to heavier particles, this result is somehow natural from the new physics point of view. Even more intriguingly, other anomalies were reported in similar channels, $B \to D* \tau \nu$ and $B \to D \tau \nu$, by the BaBar, Belle, and LHCb collaborations. The tension with the SM is now reaching the $\sim 4\,\sigma$ level. These results may be indicating that tau leptons have a unique sensitivity to new physics. As mentioned above, the identification of the decay modes involving tau leptons is challenging, but they will become readily accessible at Belle II. Thus, the flavor structure with distinguished tau lepton coupling will be tested at Belle II at a higher precision.

2.3. Flavor physics questions to be addressed by Belle II

Further study of the quark sector is necessary to reveal NP at high mass scales, even beyond the direct reach of the LHC, that may manifest in flavor observables. There are several important questions that can only be addressed by further studies of flavor physics, as described below. Belle II will access a large number of new observables to test for NP in flavor transitions in the quark and lepton sectors.

- *Are there new CP-violating phases in the quark sector?* The amount of CP violation in the SM quark sector is orders of magnitude too small to explain the baryon–antibaryon asymmetry. New insights will come from examining the difference between B^0 and $\bar{B}^0$ decay rates, namely via measurements of time-dependent CP violation in penguin transitions of $b \to s$ and $b \to d$ quarks, such as $B \to \phi K^0$ and $B \to \eta' K^0$. CP violation in charm mixing, which is negligible in the SM, will also provide information on new phenomena in the up-type quark sector. Another key area will be to understand the mechanisms that produced the large amounts of CP violation in the time-integrated rates of charmless hadronic B decays, such as $B \to K\pi$ and $B \to K\pi\pi$, observed by the B factories and LHCb.
- *Does nature have multiple Higgs bosons?* Many extensions to the SM, such as two-Higgs-doublet models, predict charged Higgs bosons in addition to a neutral SM-like Higgs. The charged Higgs will be searched for in flavor transitions to τ leptons, including $B \to \tau \nu$ and $B \to D^{(*)} \tau \nu$. Deviations from the SM have been observed in the latter with significance greater than 3 σ. Extended Higgs mechanisms can also introduce extra sources of CP violation.
- *Does nature have a left–right symmetry, and are there flavor-changing neutral currents beyond the SM?* Approaches include measurements of time-dependent CP violation in $B \to K^{*0}(\to K^0_S \pi^0)\gamma$, triple-product CP violation asymmetries in $B \to VV$ decays, and semileptonic decays $B \to V \ell \nu$, $V = D^*, \rho$. It is of great interest to measure $b \to s \nu \bar{\nu}$ transitions such as $B \to$

$K^{(*)}\nu\bar{\nu}$, part of a class of decays with large missing energy. It is also important to improve flavor-changing neutral current (FCNC) measurements of $b \to d$, $b \to s$, and $c \to u$ transitions. It is crucial to measure forward–backward asymmetries as a function of the q^2 of the dilepton, $A_{\rm FB}(q^2)$, in inclusive $b \to s\ell^+\ell^-$ decays and in charged weak interactions.

- *Are there sources of lepton flavor violation (LFV) beyond the SM?* Neutrino experiments have found large mixing involving τ neutrinos, raising the question: are there flavor-changing processes such as $\tau \to \mu\gamma$ visible at the 10^{-8} level? LFV in charged lepton decay at such rates is a key prediction in many neutrino mass generation mechanisms and other models of physics beyond the SM. The expected sensitivities to τ decays will be unrivalled due to correlated production with minimal collision background. Belle II will analyze τ leptons for LF and CP violation, and measurements of the electric dipole moment and $(g-2)$ of the τ.

It is also worth noting that Belle II will measure the current array of CKM observables, the matrix elements and their phases, with unprecedented precision.

2.4. Non-flavor program physics case

Belle II will be able to address fundamental questions not directly related to flavor physics, leveraging the clean environment of e^+e^- collisions, and the large data set. Two of the driving questions are as follows.

- *Is there a dark sector of particle physics at the same mass scale as ordinary matter?* Belle II has unique sensitivity to dark matter via missing energy decays. While most searches for new physics at Belle II are indirect, there are models that predict new particles at the MeV to GeV scale, including weakly and non-weakly interacting massive particles that couple to the SM via new gauge symmetries. These models often predict a rich sector of hidden particles that include dark matter candidates and gauge bosons. Belle II is implementing new trigger strategies, such as a single photon trigger, to capture these elusive events.
- *What is the nature of the strong force in binding hadrons?* With B factories and hadron colliders having discovered a large number of states that were not predicted by the conventional meson interpretation, changing our understanding of QCD in the low-energy regime, study of quarkonia is high on the agenda at Belle II. New particles can be produced near resonance, achievable by adjusting the machine energy, or by initial state radiation, which effectively provides a continuum of center-of-mass energies. Belle II has near hermetic coverage and good detection capabilities for all neutral and charged particles, and can play a central role in these analyses.

2.5. Advantages of SuperKEKB and Belle II

There are many experimental reasons that make SuperKEKB and Belle II perfectly suited to address these puzzles in particle physics.

- Running on the $\Upsilon(4S)$ resonance produces a very clean sample of $B^0\bar{B}^0$ pairs in a quantum-correlated 1^{--} state. The low background environment allows for reconstruction of final states containing photons from decays of π^0, $\rho^\pm$, η, η', etc. Neutral $K^0_{\rm L}$ mesons are also efficiently reconstructed.
- Detection of the decay products of one B allows the flavor of the other B to be tagged.
- Flavor production asymmetry is zero, while the detector hermeticity and azimuthal asymmetry make charged asymmetries in reconstruction very small.

- Due to low track multiplicities and detector occupancy, the B, D, and τ reconstruction efficiency is high and the trigger bias is very low. This reduces correction and systematic uncertainties in many types of measurements, e.g. Dalitz plot analyses.
- With asymmetric beam energies the Lorentz boost of the e^+e^- system is large enough that B or D mesons travel an appreciable distance before decaying, allowing precision measurements of lifetimes, mixing parameters, and CP violation.
- Since the absolute delivered luminosity is measured with Bhabha scattering, the experiment is able to measure absolute branching fractions.
- Since the initial state is known, "missing mass" analyses can be performed to infer the existence of new particles via energy/momentum conservation rather than reconstructing their final states. By fully reconstructing a B or D decay in a hadronic or semileptonic final state, rare decays with neutrinos can be observed or measured with minimal model dependence.
- In addition to producing large samples of B and D decays, an e^+e^- machine produces large samples of τ leptons allowing for measurements of rare τ decays and searches for lepton flavor and lepton number violation τ decays in a very low background environment.
- The high output rate and relatively low background environment allows for highly efficient triggers of low multiplicity and dark sector signatures.
- The precisely known interaction center-of-mass energy and excellent detector hermeticity are key for searches for bottomonium transitions using recoil techniques.
- Production of resonances through initial state radiation processes allows for clean and complete probes of the charmonium sector through a continuum of production energies.

The legacy of the B factories laid the groundwork for many areas that will be further exploited at SuperKEKB. Their results provided a theoretically clean measurement of the unitarity triangle (UT) angle ϕ_1. After the accumulation of $\sim$1 ab^{-1} of data, it proved to be a precise calibration for NP. To check the consistency of the SM, Belle measured the other two angles of the UT, ϕ_2 and ϕ_3. The results for the sides and angles of the UT are consistent. However, NP contributions of the order of 10% of the size of the SM amplitude are still allowed. In parallel to fixing the weak interaction parameters of the UT, Belle also completed a decade of studies and publications on rare decays and quantum chromodynamics (QCD). Belle II builds on this experience, shifting focus to NP exploration beyond the SM.

2.6. Overview of SuperKEKB

The target luminosity of SuperKEKB is a factor of 40 greater than the recorded peak of KEKB, requiring a substantial upgrade to the accelerator complex [4]. The essential elements in the increase of the luminosity are a reduction in the beam size at the collision point by a factor of 20, from about 1 μm to 50 nm, and an increase in the currents by a factor of 2 compared to the KEKB values (Table 1). This is known as a "nano-beam" scheme, and was invented by P. Raimondi for the Italian super B factory [5]. Compared to KEKB, the two beams collide at an even larger angle of 83 mrad (22 mrad in KEKB). A somewhat lower beam energy asymmetry of 7 GeV (electrons) and 4 GeV (positrons), instead of 8 GeV and 3.5 GeV, was chosen to reduce the beam losses due to Touschek scattering in the lower energy beam. This is expected to reduce the spatial separation between B mesons, studied in time-dependent CP violation measurements, but leads to slight improvements in solid angle acceptance for missing energy decays.

Table 1. SuperKEKB: design parameters of the low-energy (LER) and high-energy (HER) accelerator rings [4].

	LER (e^+)	HER (e^-)	
Energy	4.000	7.007	GeV
Half crossing angle	41.5		mrad
Horizontal emittance	3.2	4.6	nm
Emittance ratio	0.27	0.25	%
Beta functions at IP (x / y)	32 / 0.27	25 / 0.30	mm
Beam currents	3.6	2.6	A
Beam–beam parameter	0.0881	0.0807	
Luminosity	8×10^{35}		$\mathrm{cm^{-2}\,s^{-1}}$

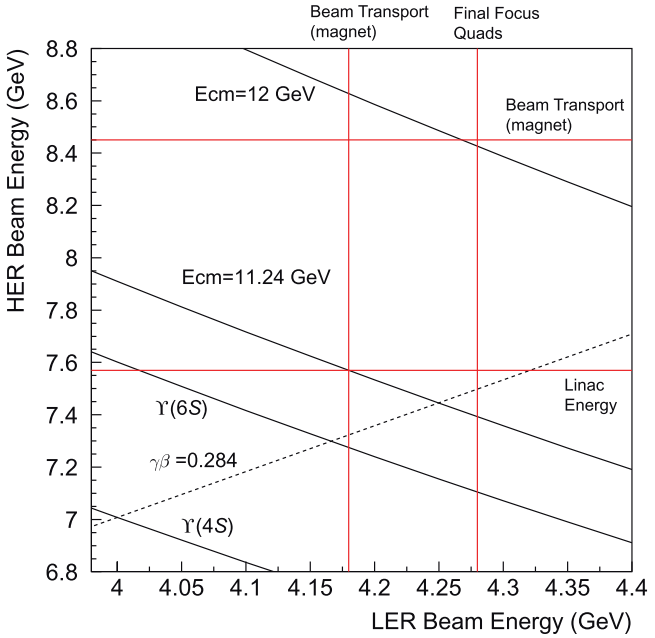

Fig. 1. Beam energies required to achieve center-of-mass energies for $\Upsilon(4S)$, $\Upsilon(6S)$, 11.24 GeV, and 12 GeV. The horizontal axis is the LER beam energy and the vertical axis is the HER beam energy.

The modifications to the accelerator complex include: a new electron injection gun, a new target for positron production, and a new additional damping ring for the positron beam. The upgrade of the accelerator also includes a redesign of the lattices of the low-energy and high-energy rings, replacing short dipoles with longer ones (in the low-energy ring), installing TiN-coated beam pipes with ante-chambers, modifications to the RF system, and a completely redesigned interaction region.

Figure 1 shows the flexibility in the allowed beam energies of the LER and HER respectively. The range of beam energies covers the $\Upsilon(1S)$ and $\Upsilon(6S)$ resonance states for physics operation. The maximum achievable center-of-mass energy is 11.24 GeV at SuperKEKB due to the limited power of the injector linac, but even if this limit could be circumvented the beam transport limit (due magnet strength) would only allow an increase to about 12 GeV. With beam energies much lower than $\Upsilon(1S)$, for example near the τ production threshold, the current lattice design is not sufficient.

Table 2. Existing e^+e^- datasets collected near Υ resonances.

Exp.	Scans / Off-res.	$\Upsilon(5S)$ 10876 MeV		$\Upsilon(4S)$ 10580 MeV		$\Upsilon(3S)$ 10355 MeV		$\Upsilon(2S)$ 10023 MeV		$\Upsilon(1S)$ 9460 MeV	
	fb^{-1}	fb^{-1}	10^6	fb^{-1}	10^6	fb^{-1}	10^6	fb^{-1}	10^6	fb^{-1}	10^6
CLEO	17.1	0.4	0.1	16	17.1	1.2	5	1.2	10	1.2	21
BaBar	54	R_b scan		433	471	30	122	14	99	—	
Belle	100	121	36	711	772	3	12	25	158	6	102

2.7. Data-taking overview

The SuperKEKB accelerator will have the capacity to deliver e^+e^- collisions in the center-of-mass energy range from just below the $\Upsilon(1S)$ (9.46 GeV) to just above the $\Upsilon(6S)$ (11.24 GeV). While the vast majority of the data will be taken at $\Upsilon(4S)$, a program of data-taking at other center-of-mass energies will be undertaken as was done at Belle. The existing B factory datasets are given in Table 2.

There are a multitude of physics topics unique to the physics program of Belle II, with rare decays and CP asymmetries in B decays at the forefront. The program provides simultaneous studies of a wide range of areas in b-quark, c-quark, τ-lepton, two-photon, quarkonium and exotic physics. The latter two topics have come to the fore in recent times, particularly concerning puzzles in our understanding of QCD in describing four-quark and five-quark states, and the searches for a dark sector. Open questions will be addressed with extended run periods at $\Upsilon(1S)$, $\Upsilon(2S)$, $\Upsilon(3S)$, $\Upsilon(5S)$, near the $\Upsilon(6S)$, and fine energy scans in intermediate regions. Measurements at $\Upsilon(5S)$ also offer useful insights into B_s decays.

Data-taking at SuperKEKB will be performed in two main phases.

- In the first collision data-taking phase (called "phase 2," as "phase 1" denoted the accelerator commissioning phase in 2016 without the final focus and Belle II detector), commencing February 2018 and running until July 2018, SuperKEKB and the interaction region was commissioned before the installation of the sensitive silicon inner detectors. The peak luminosity delivered by SuperKEKB reached $0.5 \times 10^{34}\,cm^{-2}\,s^{-1}$, and a dataset of order $0.5\,fb^{-1}$ was collected at the $\Upsilon(4S)$ resonance. This small dataset may be used for searches of dark sectors that were previously limited by a lack of efficient triggers.
- The second collision phase will see the full detector and will allow for the full flavor program to commence, expected to start in early 2019. The expected projected peak instantaneous and integrated luminosities at SuperKEKB through to 2025 are shown in Fig. 2. The full data-taking program for samples at the different center-of-mass energies is under development, and the subject of many working group chapters. It is clear that well-motivated studies with non-$\Upsilon(4S)$ data-taking could have substantial statistical gains even in early data-taking. The physics program at $\Upsilon(4S)$ is covered in most chapters of this book, while the program at $\Upsilon(5S)$ is covered over several chapters: B_s decays are covered in the semileptonic B and hadronic B chapters, while bottomonium is covered in the quarkonium chapter.

2.8. Overview of this book

Belle II detector, simulation, reconstruction, algorithms In the first few chapters we cover the detector design, detector simulation, beam induced background, particle reconstruction, and analysis

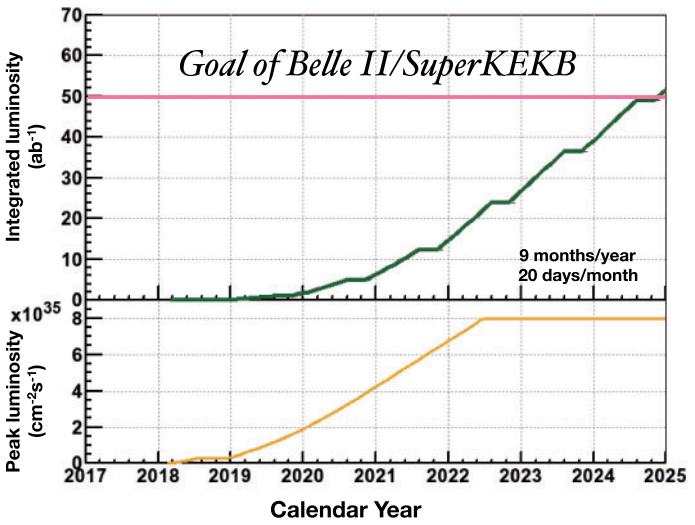

Fig. 2. The projected peak instantaneous and integrated luminosities at SuperKEKB through to 2025 assuming nine months operation per year.

algorithms of Belle II. The performance of Belle II for particle reconstruction and robustness against a higher beam background is shown, which are critical in assessing the reach of the experiment. New algorithms for flavor tagging, B full reconstruction, and vertex reconstruction are also presented.

Theory Fundamentals of flavor interactions and strong interaction dynamics are presented. A recap of the CKM picture and effective Hamiltonians for flavor interactions is provided, followed by a detailed assessment of the prospects of lattice QCD calculations over the coming decade. Finally, we provide a primer on resonances, relevant for many hadronic decay analyses at Belle II.

Semileptonic and leptonic B decays This chapter presents the prospects for leptonic and semileptonic B decays to electron, muon, and tau leptons, summarized in Tables 3 and 4. There is significant interest in the sensitivity to lepton flavor universality violating (LFUV) new phenomena, such as a charged Higgs-like coupling to tau leptons, where Belle II can make substantial advances. The chapter also details the experimental and theoretical advances for precision measurements of the CKM matrix elements, $|V_{ub}|$ and $|V_{cb}|$. Full simulation studies of Belle II in $B \to \pi \ell \nu$ and $B \to \tau \nu$ are presented. It is expected that $5\,\sigma$ discovery level measurements of $B \to \tau \nu$ and $B \to \mu \nu$ are possible with less than $5\,\text{ab}^{-1}$ at SM branching fractions.

Radiative and electroweak penguin B decays The prospects for FCNC B decays to radiative and rare dilepton final states are presented, summarized in Tables 5 and 6. There are several clear strengths of the Belle II program: the use of full B reconstruction allows for precise studies of missing energy decays such as $B \to K^{(*)} \nu \bar{\nu}$ which should be accessible with the Belle II dataset, improved particle identification detectors will be used for precision studies of $b \to d\gamma$ transitions, inclusive transitions will be studied through various techniques, and LFUV will be studied thanks to the low radiation length in the tracking volume allowing for precise reconstruction of electrons, muons, and tau leptons.

Table 3. Expected errors on several selected observables in leptonic and semileptonic B decays.

Observables	Belle	Belle II	
	(2017)	5 ab^{-1}	50 ab^{-1}
$\|V_{cb}\|$ incl.	$42.2 \cdot 10^{-3} \cdot (1 \pm 1.8\%)$	1.2%	—
$\|V_{cb}\|$ excl.	$39.0 \cdot 10^{-3} \cdot (1 \pm 3.0\%_{\text{ex.}} \pm 1.4\%_{\text{th.}})$	1.8%	1.4%
$\|V_{ub}\|$ incl.	$4.47 \cdot 10^{-3} \cdot (1 \pm 6.0\%_{\text{ex.}} \pm 2.5\%_{\text{th.}})$	3.4%	3.0%
$\|V_{ub}\|$ excl. (WA)	$3.65 \cdot 10^{-3} \cdot (1 \pm 2.5\%_{\text{ex.}} \pm 3.0\%_{\text{th.}})$	2.4%	1.2%
$\mathcal{B}(B \to \tau\nu)$ [10^{-6}]	$91 \cdot (1 \pm 24\%)$	9%	4%
$\mathcal{B}(B \to \mu\nu)$ [10^{-6}]	< 1.7	20%	7%
$R(B \to D\tau\nu)$ (Had. tag)	$0.374 \cdot (1 \pm 16.5\%)$	6%	3%
$R(B \to D^*\tau\nu)$ (Had. tag)	$0.296 \cdot (1 \pm 7.4\%)$	3%	2%

Table 4. Belle II golden/silver observables for the pure leptonic and semi-leptonic B decays. The theory column indicates robustness against the theory uncertainties. The discovery column shows the integrated luminosity at which the discovery of new physics is possible. The vs. LHCb/BESIII and Belle columns show the originality and the competitiveness against those experiments. The anomaly column indicates whether there is an existing hint of new physics, and the NP column shows whether the observable is sensitive to new physics models.

	Process	Observable	Theory	Sys. dom. (Discovery) [ab^{-1}]	vs. LHCb	vs. Belle	Anomaly	NP
●	$B \to \pi\ell\nu_\ell$	$\|V_{ub}\|$	★★★	10–20	★★★	★★★	★★	★
●	$B \to X_u\ell\nu_\ell$	$\|V_{ub}\|$	★★	2–10	★★★	★★	★★★	★
●	$B \to \tau\nu$	Br	★★★	>50 (2)	★★★	★★★	★	★★★
●	$B \to \mu\nu$	Br	★★★	>50 (5)	★★★	★★★	★	★★★
●	$B \to D^{(*)}\ell\nu_\ell$	$\|V_{cb}\|$	★★★	1–10	★★★	★★	★★	★
●	$B \to X_c\ell\nu_\ell$	$\|V_{cb}\|$	★★★	1–5	★★★	★★	★★	★★
●	$B \to D^{(*)}\tau\nu_\tau$	$R(D^{(*)})$	★★★	5–10	★★	★★★	★★★	★★★
●	$B \to D^{(*)}\tau\nu_\tau$	P_τ	★★★	15–20	★★★	★★★	★★	★★★
●	$B \to D^{**}\ell\nu_\ell$	Br	★	—	★★	★★★	★★	—

Time-dependent CP violation in B decays The prospects for time-dependent CP violation of B mesons and the determination of the CKM angles ϕ_1 and ϕ_2 are presented in this chapter, and are summarized in Tables 7 and 8. Sensitivity studies based on Belle II simulation for ϕ_1 measurement with the penguin-dominated modes, $B \to \phi K^0_S, \eta' K^0_S, \pi^0 K^0_S$, are performed. The theoretical progress on *penguin pollution* for high-precision measurement of ϕ_1 with tree-level processes is discussed. A Belle II sensitivity study on the challenging $B \to \pi^0\pi^0$ time-dependent CP asymmetry measurement for ϕ_2 determination is performed. The subsequent ϕ_2 measurement will rely on isospin relations: theoretical estimates of the isospin-breaking effects on the ϕ_2 determination are reviewed.

Measurement of the UT angle ϕ_3 The prospects for measuring the CKM UT angle ϕ_3 with tree-level measurements of $B \to D^{(*)}K^{(*)}$ decays are presented in this chapter, and are summarized in Tables 9 and 10. It is expected that Belle II will ultimately reach a precision of 1°–2° on this angle through use of a variety of channels and extraction techniques.

Table 5. Expected errors on several selected observables in radiative and electroweak penguin B decays. Note that $50\,\text{ab}^{-1}$ projections for B_s decays are not provided as we do not expect to collect such a large $\Upsilon(5S)$ dataset.

Observables	Belle	Belle II	
	(2017)	$5\,\text{ab}^{-1}$	$50\,\text{ab}^{-1}$
$\mathcal{B}(B \to K^{*+}\nu\overline{\nu})$	$< 40 \times 10^{-6}$	25%	9%
$\mathcal{B}(B \to K^{+}\nu\overline{\nu})$	$< 19 \times 10^{-6}$	30%	11%
$A_{\text{CP}}(B \to X_{s+d}\gamma)$ $[10^{-2}]$	$2.2 \pm 4.0 \pm 0.8$	1.5	0.5
$S(B \to K^0_S\pi^0\gamma)$	$-0.10 \pm 0.31 \pm 0.07$	0.11	0.035
$S(B \to \rho\gamma)$	$-0.83 \pm 0.65 \pm 0.18$	0.23	0.07
$A_{\text{FB}}(B \to X_s\ell^+\ell^-)$ $(1 < q^2 < 3.5\,\text{GeV}^2/c^4)$	26%	10%	3%
$\text{Br}(B \to K^+\mu^+\mu^-)/\text{Br}(B \to K^+e^+e^-)$ $(1 < q^2 < 6\,\text{GeV}^2/c^4)$	28%	11%	4%
$\text{Br}(B \to K^{*+}(892)\mu^+\mu^-)/$ $\text{Br}(B \to K^{*+}(892)e^+e^-)$ $(1 < q^2 < 6\,\text{GeV}^2/c^4)$	24%	9%	3%
$\mathcal{B}(B_s \to \gamma\gamma)$	$< 8.7 \times 10^{-6}$	23%	—
$\mathcal{B}(B_s \to \tau\tau)$ $[10^{-3}]$	—	< 0.8	—

Table 6. Belle II golden/silver observables for the radiative and the electroweak penguin B decays. See the caption of Table 4 for more details. The precision limit of the $B \to X_s\gamma$ measurement is estimated simply by estimating the point where the statistical uncertainties dominate. The systematic uncertainties may be further reduced by adding more data.

Process	Observable	Theory	Sys. dom. (Discovery) $[\text{ab}^{-1}]$	vs. LHCb	vs. Belle	Anomaly	NP
$B \to K^{(*)}\nu\nu$	Br, F_{L}	★★★	>50	★★★	★★★	★	★★
$B \to X_{s+d}\gamma$	A_{CP}	★★★	>50	★★★	★★★	★	★★
$B \to X_d\gamma$	A_{CP}	★★	>50	★★★	★★★	—	★★
$B \to K^0_S\pi^0\gamma$	$S_{K^0_S\pi^0\gamma}$	★★	>50	★★	★★★	★	★★★
$B \to \rho\gamma$	$S_{\rho\gamma}$	★★	>50	★★★	★★★	—	★★★
$B \to X_s\ell^+\ell^-$	Br	★★★	>50	★★★	★★	★★	★★★
$B \to X_s\ell^+\ell^-$	R_{X_s}	★★★	>50	★★★	★★★	★★	★★★
$B \to K^{(*)}e^+e^-$	$R(K^{(*)})$	★★★	>50	★★	★★★	★★★	★★★
$B \to X_s\gamma$	Br	★★	1–5	★★★	★	★	★★
$B_{d,(s)} \to \gamma\gamma$	Br, A_{CP}	★★	>50	★★	★★	—	★★
$B \to K^*e^+e^-$	P'_5	★★	>50	★★★	★★	★★★	★★★
$B \to K\tau\ell$	Br	★★★	>50	★★	★★★	★★	★★★

Hadronic B decays This chapter presents the prospects for charmless hadronic B decays and direct CP violation, as summarized in Tables 9 and 11. The theoretical computation of the branching ratio and CP asymmetry of the $B \to PP$, PV, VV (P and V denote pseudoscalar and vector mesons, respectively) processes using QCD and SU(3) symmetry is reviewed. The theoretical prediction is

Table 7. Expected errors on several selected observables related to the measurement of time-dependent CP violation in B decays and the measurement of the UT angles ϕ_1 and ϕ_2.

Observables	Belle	Belle II	
	(2017)	5 ab^{-1}	50 ab^{-1}
$\sin 2\phi_1(B \to J/\psi K^0)$	$0.667 \pm 0.023 \pm 0.012$	0.012	0.005
$S(B \to \phi K^0)$	$0.90^{+0.09}_{-0.19}$	0.048	0.020
$S(B \to \eta' K^0)$	$0.68 \pm 0.07 \pm 0.03$	0.032	0.015
$S(B \to J/\psi \pi^0)$	$-0.65 \pm 0.21 \pm 0.05$	0.079	0.025
ϕ_2 [°]	85 ± 4 (Belle+BaBar)	2	0.6
$S(B \to \pi^+\pi^-)$	$-0.64 \pm 0.08 \pm 0.03$	0.04	0.01
$\mathrm{Br}(B \to \pi^0\pi^0)$	$(5.04 \pm 0.21 \pm 0.18) \times 10^{-6}$	0.13	0.04
$S(B \to K^0\pi^0)$	-0.11 ± 0.17	0.09	0.03

Table 8. Belle II golden/silver observables on the measurement of time-dependent CP violation in B decays and the measurement of the UT angles ϕ_1 and ϕ_2. See the caption of Table 4 for more details.

	Process	Observable	Theory	Sys. dom. (Discovery) [ab^{-1}]	vs. LHCb	vs. Belle	Anomaly	NP
●	$B \to J/\psi K^0_S$	ϕ_1	★★★	5–10	★★	★★	★	★
●	$B \to \phi K^0_S$	ϕ_1	★★	>50	★★	★★★	★	★★★
●	$B \to \eta' K^0_S$	ϕ_1	★★	>50	★★	★★★	★	★★★
●	$B \to \rho^\pm \rho^0$	ϕ_2	★★★	>50	★	★★★	★	★
●	$B \to J/\psi \pi^0$	ϕ_1	★★★	>50	★	★★★	—	—
●	$B \to \pi^0\pi^0$	ϕ_2	★★	>50	★★★	★★★	★★	★★
●	$B \to \pi^0 K^0_S$	S_{CP}	★★	>50	★★★	★★★	★★	★★

Table 9. Expected errors on several selected hadronic B decay observables, including direct CP violation.

Observables	Belle	Belle II	
	(2017)	5 ab^{-1}	50 ab^{-1}
ϕ_3 GGSZ	68 ± 13	4.7	1.5
$\mathcal{A}_{CP}(B \to K^0\pi^0)$ [%]	$-0.05 \pm 0.14 \pm 0.05$	0.07	0.04
$\mathcal{I}(B \to K\pi)$ [%]	0.27 ± 0.14	0.07	0.03
$\mathcal{I}(B \to K\rho)$ [%]	-0.44 ± 0.49	0.25	0.06

partially data driven and each decay mode plays a different role in reducing the theoretical uncertainties. The phenomenology of the angular analysis of three-body final states for new physics searches is also reviewed. Experimental measurement for these channels will be reduced significantly at Belle II, since those are currently dominated by statistical or reducible systematical errors.

Charm physics This chapter presents the prospects for charm meson physics, as summarized in Tables 12 and 13. Charm is a large area of opportunity for Belle II, covering CP violation, FCNC,

Table 10. Belle II golden/silver observables for ϕ_3 measurements. The GLW method utilizes the CP-eigenstate final states and the ADS method the final states K^+X^- ($X^- = \pi^-, \pi^-\pi^0, \pi^-\pi^-, \pi^+$). The GGSZ method utilizes the self-conjugate multi-body final states $K^0_S h^+ h^-$, and the GLS method the $K^0_S K^+\pi^-$ final state.

Process	Observable	Theory	Sys. dom. (Discovery) [ab^{-1}]	vs. LHCb	vs. Belle	Anomaly	NP
GGSZ	ϕ_3	★★★	>50	★★	★★★	★	★★
GLW	ϕ_3	★★★	>50	★★	★★★	★	★★
ADS	ϕ_3	★★	>50	★★	★★★	★	★★★
Time-dependent	$\phi_3 - \phi_2$	★★	—	★★	★★	★	★

Table 11. Belle II golden/silver observables for hadronic B decay measurements.

Process	Observable	Theory	Sys. dom. (Discovery) [ab^{-1}]	vs. LHCb	vs. Belle	Anomaly	NP
$B \to \pi^0 K^0$	$A_{CP}, I_{K\pi}$	★★	>50	★★★	★★★	★★★	★★
$B \to \rho K$	$A_{CP}, I_{K\rho}$	★	>50	★★	★★★	—	★★
$B \to \ell\nu\gamma$	λ_B	★★	>50(10)	★★★	★★★	★	★★
$B \to \rho K^*$	f_L	★★	>50	★★	★★	—	★★★
$B \to K^+K^-/\pi^+\pi^-$	Br, A_{CP}	★★	>50	★	★★★	★★	★★
$B \to K\pi\pi, KKK$	A_{CP}	★★	>50	★★	★	★★★	★
$B_s \to K^0\overline{K}^0$	Lifetime	★	>5	★★	★★★	—	★★

Table 12. Expected errors on several selected charm physics observables.

Observables	Belle	Belle II	
	(2017)	5 ab^{-1}	50 ab^{-1}
$x(D^0 \to K^0_S\pi^+\pi^-)$ [10^{-2}]	$0.56 \pm 0.19 \pm {}^{0.07}_{0.13}$	0.16	0.11
$y(D^0 \to K^0_S\pi^+\pi^-)$ [10^{-2}]	$0.30 \pm 0.15 \pm {}^{0.05}_{0.08}$	0.10	0.05
$\lvert q/p\rvert(D^0 \to K^0_S\pi^+\pi^-)$	$0.90 \pm {}^{0.16}_{0.15} \pm {}^{0.08}_{0.06}$	0.12	0.07
$A_{CP}(D^+ \to \pi^+\pi^0)$ [10^{-2}]	$2.3 \pm 1.2 \pm 0.2$	0.54	0.17
$A_{CP}(D^0 \to \pi^0\pi^0)$ [10^{-2}]	$-0.03 \pm 0.64 \pm 0.10$	0.28	0.09
$A_{CP}(D^0 \to K^0_S\pi^0)$ [10^{-2}]	$-0.21 \pm 0.16 \pm 0.09$	0.08	0.02
$A_{CP}(D^0 \to K^0_S K^0_S)$ [10^{-2}]	$0.02 \pm 1.53 \pm 0.17$	0.66	0.23
$A_{CP}(D^0 \to \phi\gamma)$ [10^{-2}]	$-9.4 \pm 6.6 \pm 0.1$	± 3.0	± 1.0
f_{D_s}	2.5%	1.1%	0.3%

tree level, and missing energy decay transition measurements. Novel techniques for tagging in CP violation measurements are shown.

Quarkonium This chapter presents the prospects for quarkonium(-like) physics, providing a detailed theoretical overview of perturbative QCD computation and lattice QCD; models for unconventional states (tetraquark, hybrid mesons, and hadronic molecule) are also presented. At Belle II,

Table 13. Belle II golden/silver observables for charm physics.

Process	Observable	Theory	Sys. dom. (Discovery) [ab^{-1}]	vs. LHCb/BESIII	vs. Belle	Anomaly	NP
$D^0 \to K_s\pi^+\pi^-$	$x, y, \lvert q/p\rvert$	⋆⋆⋆	20	⋆⋆	⋆⋆⋆	—	⋆⋆
$D^0 \to K^0_S K^0_S$	A_{CP}	⋆⋆	>50	⋆⋆⋆	⋆⋆⋆	⋆	⋆
$D^0 \to \pi^0\pi^0$	A_{CP}	⋆⋆⋆	>50	⋆⋆⋆	⋆⋆	⋆	⋆
$D^+ \to \pi^+\pi^0$	A_{CP}	⋆⋆	>50	⋆⋆⋆	⋆⋆	⋆	⋆⋆
$D_s \to \ell^+\nu$	f_{D_s}	⋆⋆⋆	1–5	⋆⋆⋆	⋆	—	⋆⋆
$D^0 \to V\gamma$	A_{CP}	⋆	>50	⋆⋆	⋆⋆	⋆⋆	⋆⋆
$D^0 \to \gamma\gamma$	Br	⋆	>50	⋆⋆	⋆⋆	⋆⋆	⋆⋆
$D^0 \to \nu\bar{\nu}$	Br	⋆⋆⋆	>50	⋆⋆⋆	⋆⋆	⋆⋆⋆	⋆⋆⋆
$D \to \ell^+\nu$	f_D	⋆⋆⋆	1–5	⋆	⋆	—	⋆⋆

Table 14. Expected limits on several selected τ LFV searches.

Observables	Belle	Belle II	
	(2014)	5 ab^{-1}	50 ab^{-1}
Br($\tau \to \mu\gamma$) [10^{-9}]	< 45	< 15	< 5
Br($\tau \to e\gamma$) [10^{-9}]	< 120	< 39	< 12
Br($\tau \to \mu\mu\mu$) [10^{-9}]	< 21	< 3	< 0.3
Br($\tau \to eee$) [10^{-9}]	< 27	< 4	< 0.4
Br($\tau \to eKK$) [10^{-9}]	< 33	< 6	< 0.6
Br($\tau \to \mu\pi^0$) [10^{-9}]	< 120	< 34	< 11
$\lvert\Im(\eta_s)\rvert(\tau \to K^0_S\pi\nu)$	0.026	0.010	0.003

charmonium(-like) states can be produced from B decays, initial state radiation, two-photon collisions, and double charmonium production, which allow for detailed studies of the nature of any observed states. The motivations for dedicated non-$\Upsilon(4S)$ runs are detailed: to provide us with a deeper understanding of bottomonium(-like) states. Light Higgs and lepton universality violation searches using decays of $\Upsilon(1S, 2S, 3S)$ are also reviewed.

Tau and low-multiplicity physics The prospects for tau and low-multiplicity physics are presented in this chaper, and are summarized in Tables 14 and 15. The measurement of the lepton flavor-violating τ decays will be improved by orders of magnitude by Belle II experiments. The sensitivity of different decay channels to theoretical models are discussed by using the effective couplings. CP violation in τ decay is possible in the measurement of both the cross section difference in $\tau^\pm$ and various angular observables at Belle II. Improved measurement of the e^+e^- hadronic cross section as well as hadron production from two-photon collisions at Belle II and the impact on the theoretical prediction of the muon anomalous magnetic moment $g-2$ are also discussed.

Beyond the standard model and global fit analyses The beyond standard model chapter describes new physics models that can be observed in flavor transitions, specifically those testable at Belle II. A variety of theoretical models are discussed, along with the best decay modes to observe effects from those models.

Table 15. Belle II golden/silver observables for τ physics and low multiplicity.

Process	Observable	Theory	Sys. dom. (Discovery) [ab^{-1}]	vs. LHCb/BESIII	vs. Belle	Anomaly	NP
$\tau \to \mu\gamma$	Br	⋆⋆⋆	>50	⋆⋆⋆	⋆⋆⋆	⋆	⋆⋆⋆
$\tau \to \ell\ell\ell$	Br	⋆⋆⋆	>50	⋆⋆⋆	⋆⋆⋆	⋆	⋆⋆⋆
$\tau \to K^0_S \pi \nu$	$\lvert\Im(\eta_s)\rvert$	⋆⋆⋆	>50	⋆⋆⋆	⋆⋆⋆	⋆⋆	⋆⋆
$e^+e^- \to \gamma A'(\to \text{invisible})$	σ	⋆⋆⋆	>50	⋆⋆⋆	⋆⋆⋆	⋆	⋆⋆⋆
$e^+e^- \to \gamma A'(\to \ell^+\ell^-)$	σ	⋆⋆⋆	>50	⋆⋆⋆	⋆⋆⋆	⋆	⋆⋆⋆
$e^+e^- \to \gamma a'(\to \gamma^+\gamma^-)$	σ	⋆⋆⋆	>50	⋆⋆⋆	⋆⋆⋆	⋆	⋆⋆⋆
$\Upsilon(1S) \to$ invisible	⋆⋆⋆	Br	>50	⋆⋆⋆	⋆⋆⋆	⋆	⋆⋆⋆
$\chi_{b0}(1P) \to \tau\tau$	⋆⋆⋆	Br	>50	⋆⋆⋆	⋆⋆⋆	⋆	⋆⋆⋆
π form factor	$g-2$	⋆⋆	—	⋆⋆⋆	⋆⋆	⋆⋆	⋆⋆⋆
ISR $e^+e^- \to \pi\pi$ g-2	$g-2$	⋆⋆	—	⋆⋆⋆	⋆⋆⋆	⋆⋆	⋆⋆⋆

In the global fit chapter, we provide prospects for Belle II in global fit analyses of the CKM unitarity triangle, based on studies by the CKMFitter and UTFit groups. Global analyses of tree and FCNC B decays are performed in effective operator approaches using projected constraints from Belle II on inclusive and exclusive decays.

2.9. The Belle II golden flavor channels

A summary of the expected sensitivities for key flavor observables at selected integrated luminosities is given in Table 16, which indicates modes where LHCb will be in close competition with Belle II.

LHCb will have high-statistics samples of all b and c hadrons, which are particularly sensitive to modes to all charged particle final states. Belle II will be particularly sensitive to B and $D_{(s)}$ measurements where the final states contain neutrinos, multiple photons, π^0 mesons, or neutral kaons. The e^+e^- program of Belle II also includes extensive scope for studies of τ leptons and a number of other non-flavor-physics topics (not shown in this table).

3. Belle II detector

Section authors: B. Fulsom, P. Križan, P. Urquijo, C. H. Li

3.1. Introduction

The tool for discoveries at the new-generation (super) B factory will be the Belle II detector (Fig. 3). While the new detector clearly fits the same shell as its predecessor, the superconducting solenoid magnet with the iron return yoke, all components are either new or considerably upgraded [6].

Compared to Belle, the Belle II detector will be taking data at an accelerator with a 40 times higher luminosity, and thus has to be able to operate at 40 times higher event rates, as well as with background rates higher by a factor of 10 to 20 [6]. To maintain the excellent performance of the spectrometer, the critical issue will be to mitigate the effects of higher background levels, which lead to an increase in occupancy and radiation damage, as well as to fake hits and pile-up noise in the electromagnetic calorimeter, and to neutron-induced hits in the muon detection system. Higher event rates also require modifications to the trigger scheme, data acquisition system (DAQ), and computing with respect to the precursor experiment. The trigger and DAQ have also been adapted to support a broader low-multiplicity (dark sector) physics analysis program. In addition, improved

Table 16. Expected errors on several selected flavor observables with an integrated luminosity of 50 ab^{-1} of Belle II data. Errors given in % represent relative errors. In the final column we denote where LHCb is expected to reach a highly competitive level of precision: if one experiment is expected to be slightly more accurate we list it first.

Observables	Exp. theor. accuracy	Exp. experim. uncertainty	Facility (2025)
UT angles and sides			
ϕ_1 [°]	***	0.4	Belle II
ϕ_2 [°]	**	1.0	Belle II
ϕ_3 [°]	***	1.0	LHCb/Belle II
$\|V_{cb}\|$ incl.	***	1%	Belle II
$\|V_{cb}\|$ excl.	***	1.5%	Belle II
$\|V_{ub}\|$ incl.	**	3%	Belle II
$\|V_{ub}\|$ excl.	**	2%	Belle II/LHCb
CP violation			
$S(B \to \phi K^0)$	***	0.02	Belle II
$S(B \to \eta' K^0)$	***	0.01	Belle II
$\mathcal{A}(B \to K^0\pi^0)$ [10^{-2}]	***	4	Belle II
$\mathcal{A}(B \to K^+\pi^-)$ [10^{-2}]	***	0.20	LHCb/Belle II
(Semi-)leptonic			
$\mathcal{B}(B \to \tau\nu)$ [10^{-6}]	**	3%	Belle II
$\mathcal{B}(B \to \mu\nu)$ [10^{-6}]	**	7%	Belle II
$R(B \to D\tau\nu)$	***	3%	Belle II
$R(B \to D^*\tau\nu)$	***	2%	Belle II/LHCb
Radiative and EW penguins			
$\mathcal{B}(B \to X_s\gamma)$	**	4%	Belle II
$A_{CP}(B \to X_{s,d}\gamma)$ [10^{-2}]	***	0.005	Belle II
$S(B \to K^0_S\pi^0\gamma)$	***	0.03	Belle II
$S(B \to \rho\gamma)$	**	0.07	Belle II
$\mathcal{B}(B_s \to \gamma\gamma)$ [10^{-6}]	**	0.3	Belle II
$\mathcal{B}(B \to K^*\nu\overline{\nu})$ [10^{-6}]	***	15%	Belle II
$R(B \to K^*\ell\ell)$	***	0.03	Belle II/LHCb
Charm			
$\mathcal{B}(D_s \to \mu\nu)$	***	0.9%	Belle II
$\mathcal{B}(D_s \to \tau\nu)$	***	2%	Belle II
$A_{CP}(D^0 \to K^0_S\pi^0)$ [10^{-2}]	**	0.03	Belle II
$\|q/p\|(D^0 \to K^0_S\pi^+\pi^-)$	***	0.03	Belle II
$A_{CP}(D^+ \to \pi^+\pi^0)$ [10^{-2}]	**	0.17	Belle II
Tau			
$\tau \to \mu\gamma$ [10^{-10}]	***	< 50	Belle II
$\tau \to e\gamma$ [10^{-10}]	***	< 100	Belle II
$\tau \to \mu\mu\mu$ [10^{-10}]	***	< 3	Belle II/LHCb

hadron identification is needed, and a hermeticity at least as good as the original Belle detector is required.

The requirements for a B factory detector can be summarized as follows. The apparatus should meet the following criteria:

- excellent vertex resolution ($\sim$50 μm)
- very high reconstruction efficiencies for charged particles with momenta down to a few hundred MeV/c, and improved efficiency for charged particles with momenta down to 50 MeV/c

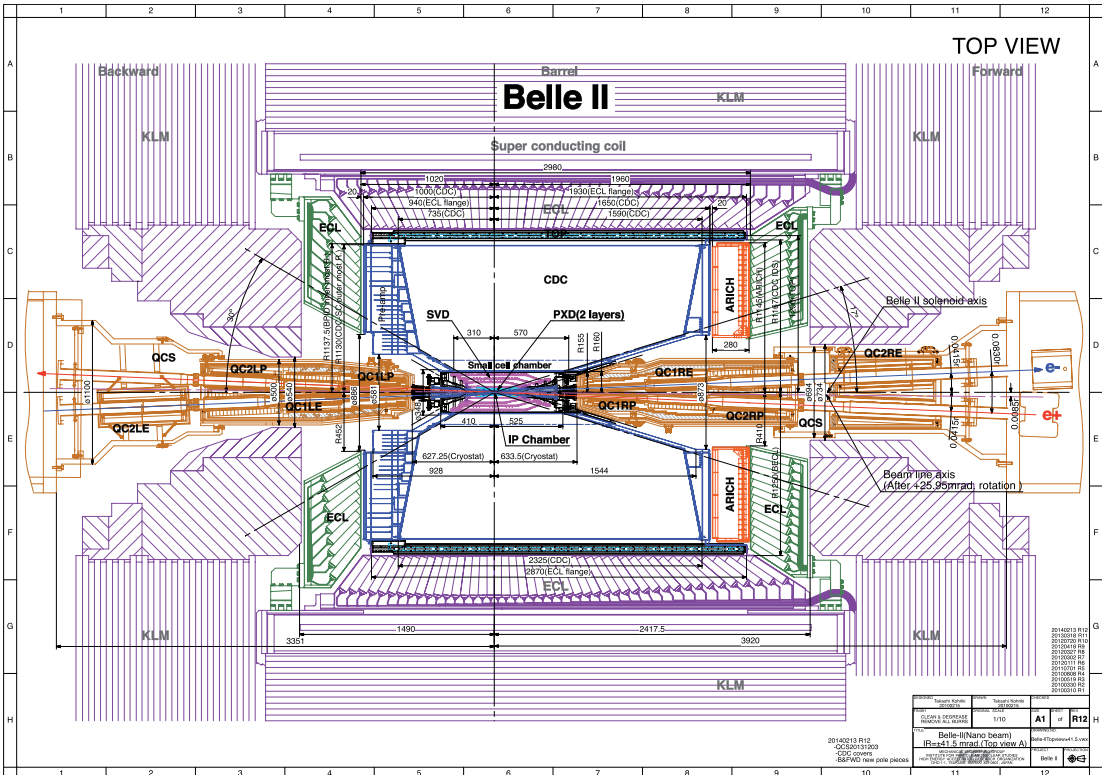

Fig. 3. Belle II top view.

- very good momentum resolution over the whole kinematic range of the experiment, i.e. up to ∼8 GeV/c
- precise measurements of photon energy and direction from a few tens of MeV to ∼8 GeV, and efficient detection from 30 MeV onwards
- highly efficient particle identification system to separate pions, kaons, protons, electrons, and muons over the full kinematic range of the experiment
- cover (almost) the full solid angle
- fast and efficient trigger system, as well as a data acquisition system capable of storing large quantities of data.

The design choices of the Belle II experiment are summarized in Table 17, and are discussed in some detail below. A full discussion can be found in the Technical Design Report (TDR) [6].

The expected Belle II detector performance of some of the critical components, including the track reconstruction efficiency and particle identification capabilities, are discussed in Sect. 5.

3.2. Vertex detector (VXD)

The new vertex detector is comprised of two devices, the silicon pixel detector (PXD) and the silicon vertex detector (SVD), with a total of six layers (Fig. 4) around a 10 mm radius Be beam pipe. The first layers at $r = 14$ mm and $r = 22$ mm will use pixelated sensors of the DEPFET type [7,8]. The remaining four layers at radii of 39 mm, 80 mm, 104 mm, and 135 mm will be equipped with double-sided silicon strip sensors. In comparison, in Belle the outermost vertex detector layer was at a radius of 88 mm. Table 17 lists the sensor strip pitch sizes.

Table 17. Summary of the detector components.

Purpose	Name	Component	Configuration	Readout channels	θ coverage
Beam pipe	Beryllium		Cylindrical, inner radius 10 mm, 10 μm Au, 0.6 mm Be, 1 mm paraffin, 0.4 mm Be		
Tracking	PXD	Silicon pixel (DEPFET)	Sensor size: 15 × (L1 136, L2 170) mm^2, pixel size: 50 × (L1a 50, L1b 60, L2a 75, L2b 85) μm^2; two layers at radii: 14, 22 mm	10 M	[17°; 150°]
	SVD	Silicon strip	Rectangular and trapezoidal, strip pitch: 50(p)/160(n)–75(p)/240(n) μm, with one floating intermediate strip; four layers at radii: 39, 80, 104, 135 mm	224 k	[17°; 150°]
	CDC	Drift chamber with He–C_2H_6 gas	14 336 wires in 56 layers, inner radius 160 mm, outer radius 1130 mm	14 k	[17°; 150°]
Particle ID	TOP	RICH with quartz radiator	16 segments in ϕ at $r \approx 120$ cm, 275 cm long, 2 cm-thick quartz bars with 4 × 4-channel MCP PMTs	8 k	[31°; 128°]
	ARICH	RICH with aerogel radiator	2 × 2 cm-thick focusing radiators with different n, HAPD photodetectors	78 k	[14°; 30°]
Calorimetry	ECL	CsI(Tl)	Barrel: $r = 125$–162 cm, endcap: $z = -102$–$+196$ cm	6624 (barrel), 1152 (FWD), 960 (BWD)	[12.4°; 31.4°], [32.2°; 128.7°], [130.7°; 155.1°]
Muon ID	KLM	barrel: RPCs and scintillator strips	2 layers with scintillator strips and 12 layers with 2 RPCs	θ 16 k, ϕ 16 k	[40°; 129°]
	KLM	endcap: scintillator strips	12 layers of (7–10)×40 mm^2 strips	17 k	[25°; 40°], [129°; 155°]

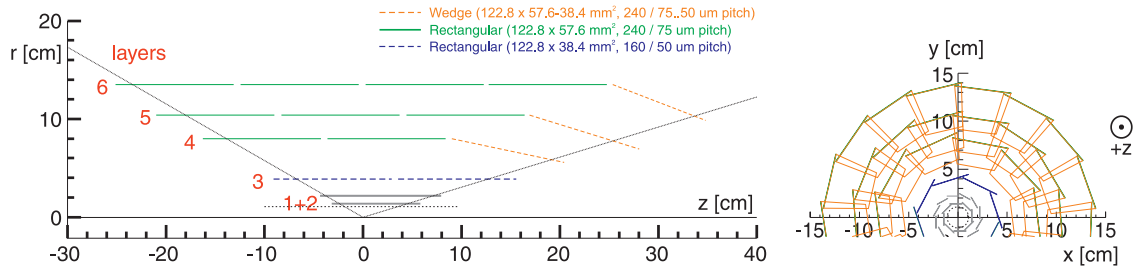

Fig. 4. A schematic view of the Belle II vertex detector with a Be beam pipe, two pixelated layers, and four layers with silicon strip sensors.

Compared to the Belle vertex detector, the beam pipe and the first two detector layers are closer to the interaction point, and the outermost layer is at a considerably larger radius. As a result, significant improvement is expected with respect to Belle in the vertex resolution, as well as in the reconstruction efficiency for $K^0_S \to \pi^+\pi^-$ decays with hits in the vertex detector [6].

3.3. Central drift chamber (CDC)

One of the core instruments of the Belle II spectrometer is the central tracking device, a large-volume drift chamber with small drift cells. Compared to Belle, it extends to a larger radius (1130 mm compared to 880 mm) due to the upgrade to a much thinner particle identification (PID) device in the barrel region. To be able to operate at high event rates with increased background levels, the chamber has smaller drift cells than the one used in Belle. In total, the CDC contains 14 336 sense wires arranged in 56 layers, either in "axial" orientation (aligned with the solenoidal magnetic field) or "stereo" (skewed with respect to the axial wires). By combining information from the axial and stereo layers it is possible to reconstruct a full three-dimensional (3D) helix track. The chamber gas is comprised of a He–C_2H_6 50:50 mixture with an average drift velocity of 3.3 cm μs^{-1} and a maximum drift time of about 350 ns for a 17 mm cell size.

The drift chamber is by now fully constructed and installed in the Belle II detector and has been commissioned with cosmic rays (Fig. 5).

3.4. Particle identification system (TOP and ARICH)

For particle identification in the barrel region, a time-of-propagation (TOP) counter is used [9, 10]. This is a special kind of Cherenkov detector where the two-dimensional information of a Cherenkov ring image is given by the time of arrival and impact position of Cherenkov photons at the photodetector at one end of a 2.6 m quartz bar (Fig. 6). Each detector module (16 in total) consists of a 45 cm wide and 2 cm thick quartz bar with a small expansion volume (about 10 cm long) at the sensor end of the bar. The expansion wedge introduces some additional pinhole imaging, relaxes slightly the precision timing requirements, and reduces the hit occupancy at the photodetector [10]. At the exit window of the wedge, two rows of sixteen fast multi-anode photon detectors are mounted. The TOP counter requires photo-sensors with a single-photon time resolution of about 100 ps, which can be achieved with a 16-channel microchannel plate (MCP) photomultiplier tube (PMT) [10,11] specially developed for this purpose. For the precision timing required in this type of counter, custom-made waveform sampling readout electronics are used [12]. Note that for this identification method the starting (particle production) time has to be known with a precision of about 50 ps; this is indeed challenging, but was already achieved for the time-of-flight (TOF) counter of Belle [13].

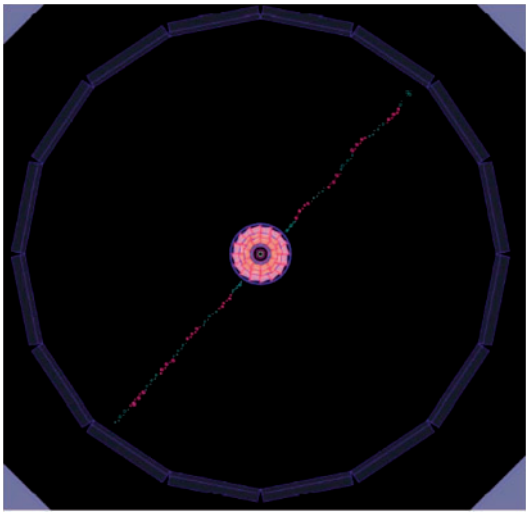

Fig. 5. A cosmic muon as recorded by the Belle II CDC.

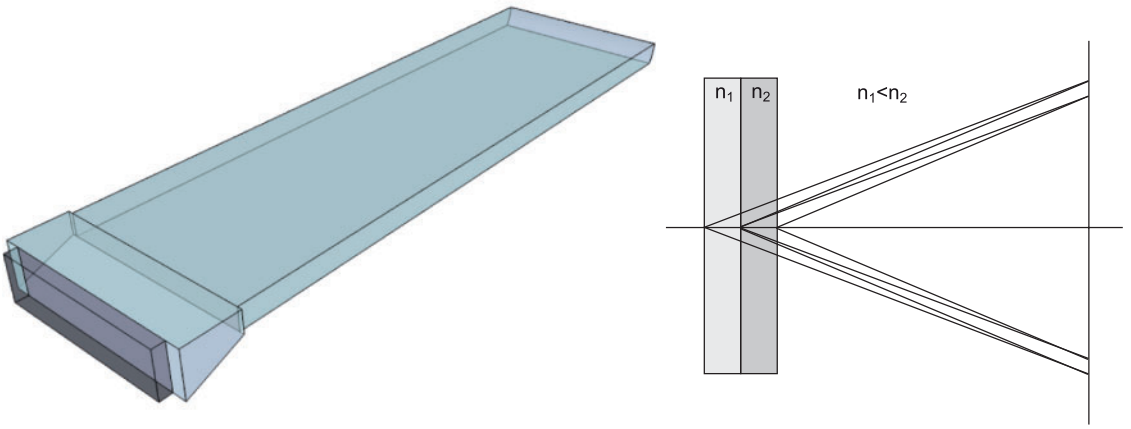

Fig. 6. Belle II PID systems. (Left) One of the modules of the TOP counter. (Right) Principle of operation of the proximity focusing Cherenkov ring imaging detector with a non-homogeneous aerogel radiator in the focusing configuration.

In the forward endcap region, ARICH, a proximity focusing Cherenkov ring imaging detector with aerogel as Cherenkov radiator will be employed to identify charged particles. The design requirements include a low momentum threshold for pions and good separation of pions and kaons from 0.4 GeV/c up to about 4 GeV/c.

A key parameter of the RICH, the number of detected Cherenkov photons, is increased by a novel method (Fig. 6). Two 2 cm-thick layers of aerogel with different refractive indices ($n = 1.045$ upstream, $n = 1.055$ downstream) are used to increase the yield without degrading the Cherenkov angle resolution [14,15]. As the single-photon-sensitive high-granularity sensor, a hybrid avalanche photon detector (HAPD) is used, developed in a joint effort with Hamamatsu [16,17]. In this 73×73 mm^2 sensor with 144 channels, photo-electrons are accelerated over a potential difference of 8 kV, and are detected in avalanche photodiodes (APD). Sensor production was optimized (thicknesses of p and p+ layers, additional intermediate electrode) following radiation tolerance tests [17] with

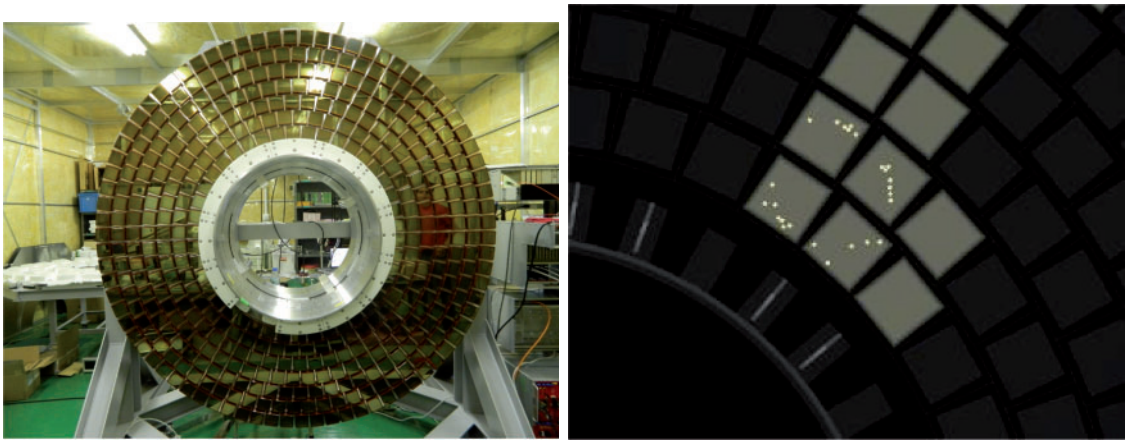

Fig. 7. ARICH detector. (Left) Photon detector plane with HAPD sensors. (Right) A ring produced by a cosmic muon.

neutrons and gamma rays. All 16 modules of the TOP counter have been installed, and are being commissioned. The ARICH detector is fully installed; all photo-sensor modules (HAPD light sensors and readout electronics boards) have by now been installed and are being commissioned. With a partially equipped detector, the first Cherenkov rings observed are shown in Fig. 7.

3.5. Electromagnetic calorimeter (ECL)

The electromagnetic calorimeter is used to detect gamma rays as well as to identify electrons, i.e. separate electrons from hadrons, in particular pions. It is a highly segmented array of thallium-doped caesium iodide CsI(Tl) crystals assembled in a projective geometry (Fig. 3). All three detector regions, the barrel as well as the forward and backward endcaps, are instrumented with a total of 8736 crystals, covering about 90% of the solid angle in the centre-of-mass system. The CsI(Tl) crystals, preamplifiers, and support structures have been reused from Belle, whereas the readout electronics and reconstruction software have been upgraded. In the Belle experiment, the energy resolution observed with the same calorimeter was $\sigma_E/E = 4\%$ at 100 MeV, 1.6% at 8 GeV, and the angular resolution was 13 mrad (3 mrad) at low (high) energies; π^0 mass resolution was 4.5 MeV/c^2 [2]; in the absence of background a very similar performance would also be expected for Belle II.

In the presence of considerably elevated background levels as compared to the operation in Belle, the relatively long decay time of scintillations in CsI(Tl) crystals will considerably increase the overlapping of pulses from neighboring (background) events. To mitigate the resulting large pile-up noise, scintillator photo-sensors were equipped with wave-form-sampling readout electronics. In the forward region of the detector, close to the beam pipe, much higher background rates are expected, such that even with the new wave-form-sampling electronics the pile-up noise will degrade the performance. Some further degradation could come from a reduction of the light yield due to radiation damage, although this effect seems to be less significant than originally anticipated [18]. As a possible solution for this region of the spectrometer, a replacement of CsI(Tl) with considerably faster and radiation tolerant pure CsI is being studied [19].

3.6. K_L muon detector (KLM)

The K_L^0 and muon detector (KLM) consists of an alternating sandwich of 4.7 cm-thick iron plates and active detector elements located outside the superconducting solenoid. The iron plates serve as the magnetic flux return for the solenoid. They also provide 3.9 interaction lengths or more of material, beyond the 0.8 interaction lengths of the calorimeter, in which K_L^0 mesons can shower hadronically.

The Belle KLM, based on glass-electrode resistive plate chambers (RPC), has demonstrated good performance during the entire data-taking period of the Belle experiment. Contrary to Belle, in some Belle II KLM detector areas (both endcaps and the innermost layers in the barrel region) large background rates are expected due to neutrons that are mainly produced in electromagnetic showers from background reactions (e.g. radiative Bhabha scattering). The long dead time of the RPCs during the recovery of the electric field after a discharge significantly reduces the detection efficiency under such background fluxes. The resulting fake muon identification probability would become so high in the endcap region of the spectrometer and in the two inner layers of the barrel that such a counter would be useless [6]. To mitigate this problem, the RPCs have been replaced by layers of scintillator strips with wavelength-shifting fibers, read out by silicon photomultipliers (SiPMs, Geiger mode operated APDs) as light sensors [20]. Note that the high neutron background will also cause damage the SiPMs, and will therefore considerably increase the dark count rate in the light sensor; irradiation tests have shown, however, that such a detector system can be reliably operated by appropriately setting the discrimination threshold.

3.7. Trigger system

The trigger system of Belle II has a non-trivial role to identify events of interest during data-taking. The scope of physics analysis topics that require dedicated triggers will be broad at Belle II. These triggers must work efficiently in the presence of the much higher background rates expected from SuperKEKB, and satisfy the limitations of the DAQ. A well-designed trigger system unlocks a broad variety of topics not probed in the previous generation *B* factories. Excellent examples of triggers for new phenomena include the single-photon trigger for dark sector searches, and the two- and three-photon triggers for axion-like particle searches.

The dominant beam background sources are discussed in detail in the next chapter; they are the Touschek effect, beam–gas scattering, synchrotron radiation, the radiative Bhabha process, the two-photon process, and beam–beam effects. The rates of these background processes are correlated with multiple factors, e.g. beam size, beam current, luminosity, accelerator status, vacuum conditions, and so on.

Most of these processes are characterized by the presence of fewer than two charged particle tracks in CDC, accompanied by one or two clusters in the ECL. These topologies are similar to those of primary collision events to low-multiplicity production modes, and are therefore a large problem for such physics studies.

The flagship measurements for Belle II in *B* and *D* flavor physics are expected to be highly robust to trigger implementation, where events will be easily identified from the presence of at least three tracks in the CDC trigger and a large deposition of energy in the ECL. Similarly to Belle, the trigger for most *B* decays will be close to 100% efficient for events that are reconstructed by offline algorithms.

The long list of new low-multiplicity and dark sector triggers under development at Belle II will increase the physics scope but present a large challenge to the DAQ system. In addition to *B* physics, Belle II is also an excellent basis for the study of many other important topics, e.g. τ physics, dark

sector searches, two-photon physics, and precision measurements for low-multiplicity and initial-state radiation (ISR) processes. Precision measurements of luminosity from low-multiplicity events are also important inputs to precision flavor physics measurements. The low-multiplicity topology of these processes is, however, similar to the background processes mentioned above, leading to low purity, and must be tackled using online algorithms.

The Belle II trigger system is composed of two levels: a hardware-based low-level trigger (L1) and a software-based high-level trigger (HLT). The key design features of each level are described below.

The nominal L1 trigger has a latency of 5 μs, and a maximum trigger output rate of 30 kHz, limited by the read-in rate of the DAQ. To cope with the high event rate and background level at Belle II, a series of upgrades have been implemented at L1. The key areas of improvement involve the implementation of firmware-based reconstruction algorithms and trigger logic.

- *Tracking* Novel 3D tracking algorithms (based on 3D fitting and multi-layer perceptron (MLP) respectively) have been developed to provide the vertex position in the direction of the beam line (z-axis). This is used to suppress beam background that does not originate from the interaction point. At Belle, only 2D information was derived in the L1 trigger. The 3D track information allows matching of the CDC track with associated ECL clusters, and therefore improves particle identification at the trigger level.
- *Calorimeter* The high-rate background from radiative Bhabha scattering, which had a cross section of of 74 nb in the CDC acceptance, will be reduced with improved online reconstruction techniques. Bhabha vetoes in the B factories tended to remove a substantial fraction of interesting low-multiplicity processes. To better suppress Bhabha events, 3D Bhabha logic has been developed in the ECL trigger which uses 3D ECL clustering information.
- *Global reconstruction* The trigger information from each sub-detector trigger is combined using FPGA-based global reconstruction logic (GRL) to perform low-level particle and event reconstruction, e.g. matching between tracks found in the CDC and clusters found by the ECL trigger. The GRL is one of the key new components of the Belle-II L1, and will be critical for controlling rates at high luminosity.
- *Trigger menu* Belle II will have a new trigger menu, or set of trigger lines, to satisfy a variety of physics analysis targets. Hadronic processes, e.g. B decays and continuum, will be triggered with high efficiency by requiring that there are at least three tracks in CDC. Low-multiplicity processes are easily mimicked by radiative Bhabha or beam background events, and are therefore difficult to efficiently trigger on.
- *Trigger conditions* The trigger menu will be designed for specific periods of data-taking at varying collision centre-of-mass energies and instantaneous luminosity. It will be tuned to take into account varying background flux as a function of the polar angle of the detector. The regions of the detector close to the beam pipe suffer high beam-induced background. Background from the beam gas is more prevalent at the beginning of data-taking due to the beam vacuum conditions at startup. Background processes with scattering rates proportional to the luminosity, e.g. Bhabha, will be more prevalent as luminosity rises.
- *Dark sector trigger* Dark matter searches are a big challenge for the trigger; they can be characterized by the presence of only one energetic photon in the final state. Bhabha and $e^+e^- \to \gamma\gamma$ are the dominant background in the endcaps and at high luminosity. Consequently, loose triggers are applied for the photon in the barrel of the ECL, and tight conditions are applied

in the endcaps. Some trigger lines may eventually need to be prescaled, but this will be decided later. These triggers are detailed further in the dark sector physics section.

As a key component of the DAQ, the HLT must reduce online event rates to 10 kHz for offline storage, and it must identify track regions of interest for PXD readout to reduce data flux. The HLT reconstructs the event with offline reconstruction algorithms, allowing access to full-granularity event reconstruction using all detectors except for the PXD.

- *Architecture* The HLT will first suppress the event rate to 15 kHz using information from the CDC track-finding and ECL reconstruction, which have been optimized for fast online operation. Only events passing this first step are considered for full event reconstruction. This step typically rejects residual beam background not found by the L1 trigger. The event rate is further reduced to 10 kHz by using full reconstruction information.
- *Trigger menu* A robust trigger menu for the HLT is in development. As with L1, Bhabha scattering is a dominant background.
- *CPU farm* To process at a nominal 30 kHz, a total of 6000 CPU cores are employed. This is the required rate for nominal instantaneous luminosity.

3.8. Detector commissioning phases

The Belle II experiment is scheduled to begin its first "physics" run in 2019. As a prelude to this, two commissioning periods known as "Phase 1" (February–June 2016) and "Phase 2" (February–July 2018) were scheduled where a collection of detectors, known as BEAST 2 (Beam Exorcism for A Stable Belle II Experiment) were deployed for measuring background rates and operating conditions. During Phase 1 the solenoid was not active, and no collisions took place. However, for Phase 2 all subsystems except for the full vertex detectors were employed, for colliding beams to produce useful physics and calibration events.

Given the expected luminosity profile, it will likely take until at least mid-2019 for Belle II to collect an $\Upsilon(4S)$ dataset large enough to equal that of the B factory experiments. Data collected at different centre-of-mass energies is a consideration to ensure Belle II accesses unique datasets from early in its program.

During Phase 2, Belle II will contain only one octant of the PXD and SVD, consisting of two and four ladders, respectively. They will be placed in the $+x$ direction, which is expected to have the highest beam background radiation. The final focusing magnets, QCSL and QCSR, will be installed such that, combined with the Belle II solenoid, the final magnetic field configuration will be present for charged particle track reconstruction. An exact copy of the final physics run beam pipe with final geometry and composition will be installed (the exception is the gold foil thickness, which will be 6.6 μm instead of the nominal 10 μm in order to measure synchrotron radiation). Most of the BEAST 2 commissioning detectors will not be included in the Belle II DAQ, and are used solely for beam background characterization. All of the outer detector elements will be present and operational in Phase 2: CDC, TOP, ARICH, ECL, and KLM.

The main aim of Phase 2 is to commission the SuperKEKB accelerator to a point where integrating the full VXD is deemed safe. The majority of time will be spent in achieving this aim. The nominal operating energy is 7 GeV on 4 GeV (the centre-of-mass energy at $\Upsilon(4S)$), but the machine should be capable of operating anywhere in the range from $\Upsilon(2S)$ (at 10.02 GeV) up to 11.25 GeV. The beam energy spread is expected to be fairly close to the nominal value of approximately 5 MeV, even during this stage. The goal is to reach an instantaneous luminosity of approximately 1×10^{34} cm^{-2} s^{-1}, and

to measure the luminosity dependence of the leading background processes. The first few months of Phase 2 will be devoted to machine commissioning goals, BEAST background studies, and ramp-up of the instantaneous luminosity to reach its target. If these tasks are accomplished in a timely manner, the remainder can be used for physics data collection.

The lack of VXD elements is expected to have the largest impact on physics during Phase 2. Due to the missing VXD, track reconstruction in Phase 2 is entirely dependent on the CDC, and therefore tracks must be able to reach this detector and produce sufficient hits in order to be reconstructed. This leads to efficiency losses at low p_T due to acceptance. These effects are seen with momenta below 1 GeV/c and become most pronounced below 150 MeV/c, with almost no sensitivity to tracks with $p_T < 75$ MeV in Phase 2. Losses are approximately uniform in the azimuthal angle ϕ, except in the $\phi = 0$ direction where PXD and SVD elements will be partially installed. Efficiency in the polar angle is roughly constant except at the CDC edge and SVD wedge regions. Therefore, analyses requiring these tracks (e.g. soft pions in $\Upsilon(3S) \to \pi^+\pi^-\Upsilon(2S)$ decays, detecting all tracks in an event) will be affected. Studies of photon efficiency indicate that no appreciable difference is expected in performance between Phases 2 and 3. The full ECL will be present and operational during both phases. Even though the VXD will be absent, the BEAST 2 components contribute a nearly equivalent amount of material. This has been reduced as much as possible to avoid affecting performance for physics and commissioning. As a result, analyses relying on photon detection are expected to be as effective in Phase 2 as in Phase 3.

The physics potential for these phases will be discussed further in the WG7 quarkonium(-like) physics and WG8 tau decay and low-multiplicity physics chapters.

4. Belle II simulation

Section authors: T. Ferber, D. Kim, H. Nakayama, M. Ritter, M. Staric

4.1. Introduction

This chapter describes the simulation tools used in the studies presented in this report. This includes a brief review of the main event generators, the detector simulation, and an overview of the expected beam backgrounds. Some analyses require very specific event generators whose description is given in the respective subsections. The reference cross sections for various physics processes are also provided.

All simulations start with at least one event generator that simulates the primary physics process, followed by a detailed detector simulation. Some studies include the effects of beam background, which is simulated in specific background simulations and added to the physics event simulation.

The studies presented, and the performance reported, throughout this report use different versions of the Belle II software, `basf2`. This software is under active development and the performance (e.g. resolution, efficiency, background tolerance) typically improves with each software revision. Most of the studies make use of centrally produced MC campaigns: MC5 is based on release-00-05-03, MC6 and MC7 are based on release-00-07-02, and MC8 is based on release-00-08-00. The latest `basf2` version used in the publication is release-00-09-01, which is referenced in some performance outlooks.

4.2. Cross sections

Cross sections for the most important physics processes are given in Table 18 at the default beam energy. In addition to the normalization values, a rough estimate for observable cross sections within

Table 18. Total production cross section from various physics processes from collisions at $\sqrt{s} = 10.58$ GeV. $W_{\ell\ell}$ is the minimum invariant secondary fermion pair mass.

Physics process	Cross section [nb]	Selection criteria	Reference
$\Upsilon(4S)$	1.110 ± 0.008	—	[2]
$u\bar{u}(\gamma)$	1.61	—	KKMC
$d\bar{d}(\gamma)$	0.40	—	KKMC
$s\bar{s}(\gamma)$	0.38	—	KKMC
$c\bar{c}(\gamma)$	1.30	—	KKMC
$e^+e^-(\gamma)$	300 ± 3 (MC stat.)	$10^\circ < \theta_e^* < 170^\circ$, $E_e^* > 0.15$ GeV	BABAYAGA.NLO
$e^+e^-(\gamma)$	74.4	$p_e > 0.5$ GeV/c and e in ECL	—
$\gamma\gamma(\gamma)$	4.99 ± 0.05 (MC stat.)	$10^\circ < \theta_\gamma^* < 170^\circ$, $E_\gamma^* > 0.15$ GeV	BABAYAGA.NLO
$\gamma\gamma(\gamma)$	3.30	$E_\gamma > 0.5$ GeV in ECL	—
$\mu^+\mu^-(\gamma)$	1.148	—	KKMC
$\mu^+\mu^-(\gamma)$	0.831	$p_\mu > 0.5$ GeV/c in CDC	—
$\mu^+\mu^-\gamma(\gamma)$	0.242	$p_\mu > 0.5$ GeV in CDC, $\geq 1\ \gamma$ ($E_\gamma > 0.5$ GeV) in ECL	—
$\tau^+\tau^-(\gamma)$	0.919	—	KKMC
$\nu\bar{\nu}(\gamma)$	0.25×10^{-3}	—	KKMC
$e^+e^-e^+e^-$	39.7 ± 0.1 (MC stat.)	$W_{\ell\ell} > 0.5$ GeV/c^2	AAFH
$e^+e^-\mu^+\mu^-$	18.9 ± 0.1 (MC stat.)	$W_{\ell\ell} > 0.5$ GeV/c^2	AAFH

acceptance and some typical generator-level selection criteria are given by the indented values. The selection criteria (if any) for the nonindented cross section values correspond to typical event generator selections.

4.3. Generators

Most studies in this report are based on three main event generators. EvtGen 1.3 [21] is used to model the decays of B and D mesons into exclusive final states. PYTHIA 8.2 [22] is used for inclusive decay final states and for the continuum production of light quark pairs. τ pair production is generated using KKMC 4.15 [23,24] with the decays handled by TAUOLA [25]. In addition, the large-cross-section quantum electrodynamic (QED) background processes $e^+e^- \to e^+e^-(\gamma)$ and $e^+e^- \to \gamma\gamma(\gamma)$ are simulated using BABAYAGA.NLO [26–30], and $e^+e^- \to e^+e^-e^+e^-$ and $e^+e^-\mu^+\mu^-$ are simulated using AAFH[1] [31–33].

All event generators use the same beam parameters, such as the mean beam energies and the vertex position, which are provided by a central database. The default beam energies are $E_{\rm HER} = 7.004$ GeV and $E_{\rm LER} = 4.002$ GeV. The effect of beam energy smearing is included in EvtGen and BABAYAGA.NLO only. The smearing is modeled as single Gaussian for the HER and LER beams individually, with widths of $\sigma_{\rm HER} = 5.13$ MeV and $\sigma_{\rm LER} = 2.375$ MeV, respectively. The default vertex position is the detector center $(0, 0, 0)$. The vertex smearing covariance matrix is calculated from the horizontal (x) and vertical (y) beam size at the IP, with the bunch lengths (z) of the LER ($\sigma_x = 10.2\ \mu$m, $\sigma_y = 0.059\ \mu$m, $\sigma_z = 5$ mm) and HER ($\sigma_x = 7.75\ \mu$m, $\sigma_y = 0.059\ \mu$m, $\sigma_z = 6$ mm). The beam angles with respect to the z-axis are $\theta_{\rm HER} = 0.0415$ and $\theta_{\rm LER} = -0.0415$. Normally distributed bunch densities are assumed for the calculation, and the probability density

[1] This generator is sometimes also called BDK or DIAG36.

Table 19. PYTHIA 8.2 parameters with changed values for Belle II.

Parameter name	Default	Belle II
StringFlav:etaSup	0.60	0.27
StringFragmentation:stopMass	1.0	0.3
StringZ:aLund	0.68	0.32
StringZ:bLund	0.98	0.62
StringZ:rFactC	1.32	1.0

functions for the two bunches are multiplied to get a resulting beam spot. Vertex position smearing is included for all generators.

EvtGen is an event generator originally developed for BaBar and CLEO. It accounts for cascade decays involving multiple vertices and spin configurations. Input data for each decay process is passed to the code as a complex amplitude. In cases where a number of complex amplitudes are invoked for the same process, these are added before the decay probabilities are calculated and consequently the interference terms, which are of significant importance in many B-physics studies, are included. EvtGen is controlled by means of a fairly complete decay table (DECAY.DEC), which lists all possible decay processes, their branching ratios, and the model (amplitude) to be used to decay them. Belle II currently uses the simplified default EvtGen decay file for generic B events, which lacks some improvements that were included in the Belle or BaBar decay files. Since EvtGen only handles exclusive final states, PYTHIA 8.2 is used to produce final states not included in the decay file. Double counting is avoided by rejecting decays produced by PYTHIA 8.2 that are already included in the decay file. PHOTOS is used to simulate final state radiation correction in decays [34]. Up to MC8, EvtGen is also used to simulate $u\bar{u}$, $d\bar{d}$, $s\bar{s}$, and $c\bar{c}$ continuum events that are fragmented into final states using PYTHIA 8.2. Unlike at Belle, the continuum light quark production in EvtGen does not include initial state radiation. Starting with release-00-09-01, continuum events are produced using KKMC and PYTHIA 8.2 and include ISR.

In general, it is not straightforward to translate the Belle fragmentation settings to Belle II since the PYTHIA version has been changed from PYTHIA 6 to PYTHIA 8.2, and not all PYTHIA 6 parameters have PYTHIA 8.2 equivalents and vice versa. All currently used nondefault PYTHIA 8.2 parameters are listed in Table 19 and were chosen to approximate the settings used in Belle. It is planned to tune the PYTHIA 8.2 parameters that control the fragmentation process of light (uds) and charm quarks for Belle II based on Belle data before the start of Belle II phase 3 data-taking. The parameters will be tuned separately with and without the ones responsible for excited meson production.

KKMC is the default generator to simulate the two-fermion final states $e^+e^- \to \mu^+\mu^-(\gamma)$ and $e^+e^- \to \tau^+\tau^-(\gamma)$. The currently implemented version is based on the Belle implementation of KKMC4.19, including a modified interface for tau decays. KKMC generates multi-photon initial-state radiation (ISR), final-state radiation (FSR), and the interference of initial- and final-state radiation (IFI). These QED corrections are complete next-to-leading order (NLO) for ISR, IFI, and FSR, and almost complete next-to-next-to-leading order (NNLO) for ISR and FSR within the framework of exclusive coherent exponentiation based on Yennie–Frautschi–Suura exclusive exponentiation. τ decays are handled by TAUOLA-exp-11-10-2005, taking into account spin polarization effects and transverse spin correlations in τ decays. The hadronic currents for $\tau \to 4\pi$ are taken from CMD-2, all others from CLEO. Electroweak corrections within KKMC are implemented using the

DIZET6.21 library of the ZFITTER project [35,36]. The DIZET6.21 routine REPI for the calculation of the time-like real part of the electromagnetic coupling $\alpha_{\rm QED}(s)$ has been replaced as described in Ref. [37]. The electroweak corrections are complete one-loop with some higher-order extensions. The theoretical precision of the generator for lepton pairs is stated to be better than 0.5% for both cross section and inclusive differential distributions within the detector acceptance for beam energies at and above $\Upsilon(4S)$, including uncertainties due to vacuum polarization [37].

BABAYAGA.NLO is the default generator to simulate large-angle (above about 5° in the CM frame) $e^+e^- \to e^+e^-(\gamma)$ (Bhabha) and $e^+e^- \to \gamma\gamma(\gamma)$ final states. BABAYAGA.NLO generates multi-photon ISR, FSR, and IFI based on the matching of exact NLO corrections with a parton shower algorithm. Z exchange and γ–Z interference are included at the Born level. Narrow resonances and vacuum polarization corrections are included, but no other electroweak corrections. The theoretical precision of the generator is stated to be about 0.1% for both cross section and inclusive differential distributions within the detector acceptance.

The non-radiative four-fermion final states $e^+e^- \to e^+e^-e^+e^-$ and $e^+e^- \to e^+e^-\mu^+\mu^-$ are simulated using AAFH. AAFH includes all leading-order (LO) QED diagrams and their interference, but no higher-order QED corrections, no weak corrections, and no Z–exchange. The LO calculation is exact and includes final-state mass kinematics. The LO divergency of the process is controlled using a selection criterion on the minimum invariant secondary fermion pair mass, typically with $W_{\ell\ell} > 0.5\,{\rm GeV}/c^2$.

4.4. Beam-induced background

We begin by giving an overview of the five main beam background sources at SuperKEKB. We include luminosity-dependent backgrounds such as radiative Bhabha scattering and production of two-photon events.

4.4.1. Touschek scattering

The first background source is the Touschek effect, which is enhanced at SuperKEKB due to the nano-beam scheme. The Touschek effect is an intra-bunch scattering process, where Coulomb scattering of two particles in the same beam bunch changes the particles' energies to deviate from the nominal energy of the bunch. One particle ends up with an energy higher than nominal, the other with lower energy than nominal.

The Touschek scattering probability is calculated using Bruck's formula, as described in Ref. [4]. The total scattering rate, integrated around the ring, is proportional to the number of filled bunches and the second power of the bunch current, and inversely proportional to the beam size and the third power of the beam energy. Simple extrapolation based on beam size predicts that the Touschek background at SuperKEKB will be a factor of ∼20 higher than at KEKB.

Touschek-scattered particles are subsequently lost at the beam pipe inner wall after they propagate further around the ring. If the loss position is close to the detector, the resulting shower might reach the detector. To mitigate Touschek background, we utilize horizontal and vertical movable collimators and metal shields. The collimators, located at different positions around the ring, stop particles that deviate from nominal trajectories and prevent them from reaching Belle II. While we had horizontal collimation only from the inner side of the beams at KEKB, Touschek background can be reduced effectively by collimating the beam horizontally from both the inner and outer side. The horizontal collimators located just before the interaction region play an important role in minimizing the beam loss rate inside the detector. The nearest LER collimator is only 18 m upstream of the interaction point.

In phase 3 there will also be heavy-metal shields in the VXD volume and on the superconducting final focus cryostat, to prevent shower particles from entering the Belle II acceptance.

4.4.2. Beam–gas scattering

The second beam background source is the so-called beam–gas scattering, i.e. scattering of beam particles by residual gas molecules in the beam pipe. This can occur via two processes: Coulomb scattering, which changes the direction of the beam particle, and bremsstrahlung scattering, which decreases the energy of the beam particles. The rate of beam–gas scattering is proportional to the beam current and to the vacuum pressure in the beam pipe. At SuperKEKB, the beam currents will be approximately twice as high as at KEKB, while the vacuum level, except for the interaction region, will be similar to that at KEKB.

The rate of beam–gas bremsstrahlung losses in the detector is well suppressed by horizontal collimators and is negligible compared to the Touschek loss rate in the detector. However, the beam–gas Coulomb scattering rate is expected to be a factor of $\sim$100 higher than at KEKB, because the SuperKEKB beam pipe radius inside the detector is smaller, and the maximum vertical beta function is larger. Beam–gas-scattered particles are lost by hitting the beam pipe inner wall while they propagate around the ring, just like Touschek-scattered particles.

The countermeasures used for Touschek background, movable collimators and heavy-metal shields, are also effective at reducing beam–gas background. In particular, vertical collimators are essential for reducing Coulomb scattering backgrounds. However, potential transverse mode coupling (TMC) instabilities caused by vertical collimators should be carefully examined, since the vertical beta function is larger than the horizontal beta function. Therefore, the collimator width must satisfy two conditions at the same time:

- narrow enough to avoid beam loss in the detector
- wide enough to avoid TMC instability.

The only way to achieve this is to use vertical collimators with $\sim$2 mm width in locations where the vertical beta function is relatively small. This is different from horizontal collimators, which are installed where the horizontal beta function is large.

4.4.3. Synchrotron radiation

The third background source is synchrotron radiation (SR) emitted from the beam. Since the SR power is proportional to the beam energy squared and magnetic field strength squared, the HER beam is the main source of this type of background. The energy spectrum of SR photons ranges from a few keV to tens of keV.

During early running of KEKB, the inner layer of the Belle SVD was severely damaged by X-rays with $E \approx 2$ keV from the HER. To absorb SR photons before they reach the Belle II inner detectors (PXD/SVD), the inner surface of the beryllium beam pipe is coated with a gold layer. The shape of the IR beam pipe is designed to avoid direct SR hits at the detector. Ridge structures on the inner surface of incoming pipes prevent scattered photons from reaching the interaction point.

4.4.4. Radiative Bhabha process

The fourth background source is radiative Bhabha scattering. Photons produce by the radiative Bhabha process propagate along the beam axis direction and interact with the iron of the magnets. In

these interactions there is a very large production rate of neutrons via the photo-nuclear resonance mechanism.

Such neutrons are the main background source for the outermost Belle II detector, the K_L and muon detector (KLM), situated in the return yoke of the experiment's solenoid magnet. The rate of neutron production by radiative Bhabha events is proportional to the luminosity, which is 40 times higher at SuperKEKB than at KEKB. Additional neutron shielding in the accelerator tunnel is required to stop these neutrons.

Both the electron and positron energy decrease after radiative Bhabha scattering. KEKB employed shared QCS magnets for the incoming and outgoing beams, and as a result the scattered particles were over-bent by the QCS magnets. The particles then hit the wall of the magnets and electromagnetic showers were generated.

In SuperKEKB we use two separate quadrupole magnets and both orbits for incoming and outgoing beams are centered in the Q-magnets. We therefore expect the radiative Bhabha background due to over-bent electrons and positrons to be small, and only the small fraction with very large energy loss (ΔE) is lost inside the detector. However, since the design luminosity of SuperKEKB is 40 times higher than that of KEKB, the rate of those large-ΔE particles is still not negligible and will be comparable to Touschek and beam–gas background after installation of collimators. The transverse kick from the solenoid field due to a finite crossing angle is the crucial and inevitable cause of these beam losses. The intrinsic angular beam divergence at the IP, angular diffusion by the radiative Bhabha process, and leak fields from the other rings' Q-magnets also play a role, but are less crucial than the solenoid kick.

In addition, radiative Bhabha losses within $|s| < 65$ cm of the IP are particularly dangerous because we cannot put enough shielding material in that region to prevent showers from entering the acceptance region. The cryostat is located at $|s| > 65$ cm.

4.4.5. Two-photon process

The fifth beam background results from very-low-momentum electron–positron pairs produced via the two-photon process $ee \to eeee$. Such pairs can spiral around the solenoid field lines and leave multiple hits in the inner Belle II detectors.

In addition to the emitted pairs, primary particles which lose large amounts of energy or scatter with large angles can be lost inside the detector, in the same way as explained in the radiative Bhabha section. Losses within $|s| < 65$ cm from the IP are also dangerous.

4.4.6. Simulated samples

According to beam background simulation provided by the accelerator group, the most important sources are radiative Bhabha scattering, Touschek scattering, and beam–gas interactions. These backgrounds are simulated with dedicated accelerator group software called `SAD` [38], which is not part of `basf2`.

`SAD` simulates the transportation of particles through the accelerator. If a particle leaves the nominal beam trajectory and collides with the beam pipe or collimator in the Belle II experimental region, its position and momentum vector are saved to a file. The files normally correspond to 1 μs of running the accelerator at the nominal SuperKEKB luminosity. The data from `SAD` simulation are then passed to the `Geant4` simulation software [39,40] within `basf2` to produce background samples of a given

Table 20. Beam background types (12th background campaign).

Type	Source	Rate [MHz]
Radiative Bhabha	HER	1320
Radiative Bhabha	LER	1294
Radiative Bhabha (wide angle)	HER	40
Radiative Bhabha (wide angle)	LER	85
Touschek scattering	HER	31
Touschek scattering	LER	83
Beam–gas interactions	HER	1
Beam–gas interactions	LER	156
Two-photon QED	—	206

type.[2] The samples are saved in the standard `basf2` ROOT format [41]. The events in these files correspond to the interaction of a single beam particle in the material of the interaction region and consist of simulated hits (SimHits) of all detector components. The equivalent accelerator running time and the background type are also saved within the files.

The two-photon QED background has been studied for the inner tracking detectors but is not yet included in the default background mixing. It is generated within `basf2` using the generator `AAFH` (see Sect. 4.3) followed by `Geant4` simulation, and the output is saved in the same file format. The earlier versions of the simulation library did not have an adequate description of the magnetic field, so only PXD and SVD SimHits were included in the output files. Later, with improvements to the magnetic field description, SimHits for the outer detectors will also be included in the output. Other backgrounds like synchrotron radiation and gammas from radiative Bhabha scattering events are less intense and are currently not included in the background mixing.

The background types are listed in Table 20. The rates of events are calculated from the number of events in the sample and the equivalent accelerator running time.

Background mixing The simulated background samples are used to add background to the simulated events. Adding background to simulated events is done by adding SimHits; digitization is done after that. Possible pile-up of hits is therefore inherently included. The average number of background events of a given type to be added to a single simulated event is determined from the rate R of a particular background sample and the time window Δt in which the background is mixed:

$$\bar{N} = sR\Delta t, \tag{1}$$

where s is an optional scaling factor. The number of background events added to a particular simulated event is then generated according to a Poisson distribution with mean $\bar{N}$. To simulate contributions from a different bunch, the background events are shifted in time randomly within the time window. This means that all SimHits of a given background event are shifted by the same time and therefore the correlations between detector components are preserved. The discrete bunch nature is, however, neglected because of sufficiently small bunch spacing.

The size of the time window depends on the detector component. It ranges from 100 ns (TOP) to 26 μs (ECL). To reduce CPU time we chose a time window of $[-1.0, 0.8]$ μs, which fits most

[2] The set of physics models used for the `Geant4` simulation of the background events is different from the one used for physics events. This is to reproduce the behavior of neutrons more precisely.

Table 21. Number of digitized hits per event for beam-induced background (12th background campaign) and for generic $B\overline{B}$ events without background. For PXD and SVD, clusters are counted instead of digits. The numbers in parentheses are without two-photon QED background.

Component	Background	Generic $B\overline{B}$
PXD	10000 (580)	23
SVD	284 (134)	108
CDC	654	810
TOP	150	205
ARICH	191	188
ECL	3470	510
BKLM	484	33
EKLM	142	34

detector components, except PXD and ECL; these two have time windows of $[-17.6, 8.5]\,\mu$s and $[-10.0, 10.0]\,\mu$s, respectively. Additional background samples are used for mixing the background outside the default time window in these two cases.

Table 21 shows a comparison of the number of digitized hits (clusters for PXD and SVD) per event from beam-induced background with those from generic $B\overline{B}$ events.

Background overlay When experimental data becomes available we will use a different method. Instead of using simulated beam background, the background overlay method will add background measured by random trigger. The background overlay is therefore done by adding the measured background event to the simulated one using digitized hits. Possible pile-up of hits must be taken into account with dedicated methods. These methods can model the pile-up only approximately since the measured background includes only the hits above the detection threshold.

A framework for background overlay has been designed to unify the method for all detector components. It consists of two `basf2` modules and a base class for digitized hits (or clusters of hits). The first module, which must run in a single process mode, reads the data from a standard `basf2` ROOT background file, and the second module, which can run in a multi-process mode, performs the overlay. Each class for digitized hits must implement two base class methods: the one that returns the unique channel identifier of the hit and the one that implements the pile-up method, which is usually detector specific. The first method is used to identify channels where background hits are added to the existing simulated hit. If this happens, the second method is called. The return value then signals whether the pile-up criterion was fulfilled. If not, the background hit is added to the collection of simulated hits.

4.5. Detector simulation

The `basf2` simulation package is based on the `Geant4` software [39,40] version number 10.1.2.[3] There are two methods to supply the primary event to `Geant4`: one can use the particle gun class, which is part of the `Geant4` package, or one can employ specific generator software. For the latter case, the particles created by the generator package are sent to `Geant4` for simulation via the interface implemented in the `basf2` simulation package. Most of the decay processes of particles are described by the generator software. Short-lived particles such as K^0_S are usually decayed by

[3] `Geant4` version 10.1.2 was included in `basf2` release 00–06–00 of December 2015. Before that, version 9.6.2 was used.

`Geant4`. Exchange bosons and initial particles such as e^- and e^+ are not passed to `Geant4`. During the simulation, `Geant4` transports each primary particle step by step inside the detector and creates secondary particles. Digitization of hit information in the sensitive volume of the detectors is handled by separate `basf2` modules, rather than using software objects incorporated into `Geant4` [6]. The result from the `Geant4` simulation is sent to a persistent data storage (DataStore) to be used by other `basf2` modules.

To simulate propagation of particles in the detector, the physics processes of the interactions between the particles and the detector materials must be specified. These physics models can either be supplied by users or selected from the physics lists provided by the Geant4 group. We use the recommended physics list of the Geant4 group for high-energy physics experiments, `FTFP_BERT` [42].[4] The FTFP and BERT acronyms stand for hadronic shower models at different energies: the Fritiof quark–gluon string model at high energy, and the Bertini intra-nuclear cascade model at low energy. The transition area between the two models depends on each particle type, but is typically from 4 to 5 GeV (see Ref. [42, Sect. 3] and Refs. [43–46]). `FTFP_BERT` contains all the standard electromagnetic processes provided by the Geant4 group [47].

For the production threshold for secondary particles inside the detector material, we use the default level set by the `Geant4` software [48].

4.6. Magnetic field in `basf2`

Uncertainties in magnetic fields will affect Belle II analyses in several ways. The magnetic field is an input to the reconstruction of charged tracks. To obtain the optimal resolution of the charged track momentum, the magnetic field must be understood precisely. The reconstruction efficiencies of particles depend on the accuracy of the magnetic field information. Differences between the magnetic field used for the detector simulation and the one used for collision datasets may result in systematic bias. Differences between the magnetic field used for the offline reconstruction and the true magnetic field may create a systematic bias as well.

Inside the Belle II detector there are two sources of magnetic fields: the detector solenoid and the final focus system (QCS). The detector solenoid, which is comprised of an iron yoke and a superconducting solenoid, creates a uniform magnetic field of 1.5 T at the center of the detector [6]. The iron yoke is interlaced with the KLM detector. The QCS is an extension of the SuperKEKB collider, whose purpose is to focus the incoming e^+ and e^- beams at the collision point [49]. The main components of the QCS are eight superconducting quadrupole magnets. In addition, there are secondary superconducting magnets used for correction and compensation. On the surface, the magnetic fields generated by all the components of the QCS can be added linearly and used for simulation. However, due to the ferromagnetic yokes and shields around the main quadrupole magnets, nonlinear characteristics are introduced in the magnetic field [49].

The `Opera3D/TOSCA` software [50] was used to produce precision models of the magnetic field. The resulting 3D magnetic field map was incorporated into `basf2` in April 2016,[5] replacing the constant field of 1.5 T as the default map for simulation and reconstruction (see Fig. 8). Note that earlier analysis results are based on the constant field map. Detailed studies are being conducted to improve the precision of the 3D magnetic field map. In situ measurements of the Belle II magnetic field

[4] Included in `basf2` release 00–04–00 since May 2014.
[5] In `basf2` release 00–07–00.

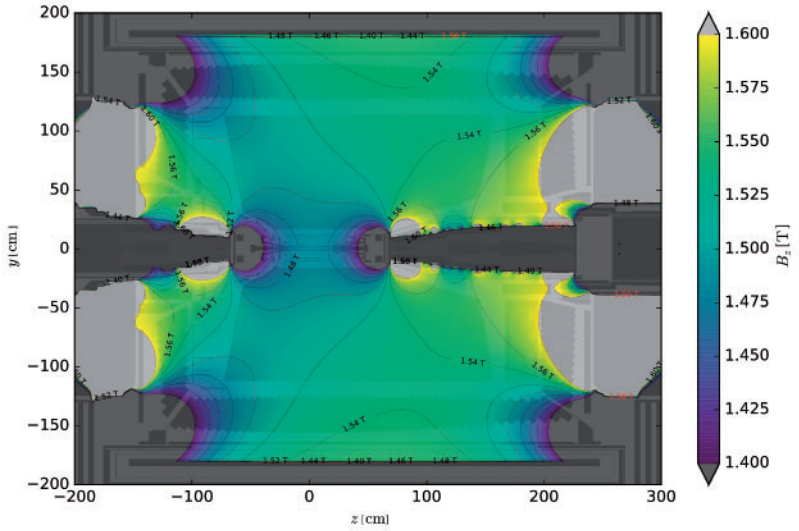

Fig. 8. The z component of the 3D magnetic field map as used in `basf2` release version 00–07–00.

were carried out in September 2015 to provide references for the model. More in situ measurements and further analysis are planned to improve the precision of the field map to 0.1%.

5. Reconstruction software

Section authors: F. Abudinen, J. Bennett, T. Bilka, G. Casarosa, T. Ferber, J.-F. Krohn, C. MacQueen, L. Piilonen, L. Santelj, M. Staric

5.1. Introduction

The Belle II detector will build upon the success of the first-generation B factories to establish a strong physics program. While many components of the Belle II detector are based on the design of the Belle detector, many improvements have been made in order to maintain similar performance in a much higher-background environment. Significant efforts have also been made in improving the reconstruction software to this end. The reconstruction algorithms and their performance characteristics are summarized in this chapter.

5.2. Software overview

Online and offline data handling is performed by the Belle II analysis software framework (`basf2`). The framework is designed to allow independent processing blocks called modules to perform relatively small tasks, which are executed linearly within a defined path. The configuration of modules for a specific purpose is defined using steering files. Modules communicate by passing information to and from a common object store, which also keeps track of relationships between objects in each event.

Given the enormous data output rate at Belle II, a robust and efficient framework for data analysis is vital. Datasets will be processed in several phases, with reduction and enhancement occuring in each phase. The raw data is reconstructed to provide physical quantities from detector information like track hits and calorimeter clusters. This information can then be used to construct high-level objects such as charged tracks. The hit- and cell-level information is then discarded and the event size is reduced by a factor of approximately 40. The reduced information, including the high-level

objects, is then used to determine particle-level information such as four-momentum and event shape variables.

As this book contains projections and preliminary studies based on samples produced in several different MC campaigns, the performance of the reconstruction algorithms is sometimes given for multiple software releases. Unless otherwise noted, the performance plots and reconstruction algorithms described in this chapter are based on `basf2` release-00-05-03, which was used in the fifth MC campaign (MC5). Performance characterization is also given for more recent `basf2` software libraries, including release-00-07-00, release-00-07-02, and release-00-08-00, which were used in the sixth (MC6), seventh (MC7), and eighth (MC8) MC campaigns, respectively.

5.3. Tracking

The main task of the tracking is the reconstruction of charged particles originating from the primary and secondary decay vertices. Simply speaking, it consists of (1) identifying the VXD and CDC hits due to ionization of a given charged particle in a sea of background hits from other particles, machine background, or detector noise, and (2) obtaining the trajectory from a fit to the hit positions. Most of the tracks originate from inside the beam pipe, except for the charged decay products of the long-lived V^0-like particles (K^0_S, Λ, and converted photons) that are created outside the beam pipe. The tracking algorithms must identify the two oppositely charged decay products of K^0_S, Λ, and photons decaying inside the tracking volume and pair them. In Sect. 5.3.1 we describe the steps of charged particle reconstruction, while in Sect. 5.3.2 more information specific to V^0-like particle reconstruction is provided.

Reconstructed particle trajectories are also used for the alignment of the detector. An optimally aligned detector is crucial to perform high-precision unbiased measurements of flavor quantities with time dependence. The details of alignment are explained in Sect. 5.3.3.

Finally, run-dependent knowledge of the spatial distribution of primary interactions (beam spot) can be used as a powerful constraint when fitting decay chains. The beam spot can be inferred from the reconstruction of $e^+e^- \to \mu^+\mu^-$ events. This is foreseen but is not yet implemented.

5.3.1. Charged particle reconstruction

The tracking software provides the analyst with lists of charged particle trajectories that have been fitted with an associated mass hypothesis. At the analysis level, a track is represented by $\{\vec{p}, \vec{x}\}$, where $\vec{x}$ is the point of closest approach to the origin of the coordinate system, and $\vec{p}$ is the particle momentum in $\vec{x}$. The detector hits associated to the track are not propagated after tracking, in order to reduce the size of the analysis files (mDST). Additional information is also preserved for the analyst, e.g. the number of hits in each detector layer of the VXD and CDC that has been used to fit the track. This is important for selecting high-quality tracks in analysis.

Charged particle reconstruction can be divided in two main parts:

- *track finding*, where detector hits belonging to a single track are collected together into a track candidate, and
- *track fitting*, where the track trajectory is determined by fitting the track candidate.

In the following we report the details of these reconstruction steps.

Track finding Track finding consists of applying pattern recognition algorithms to determine track candidates. The features of the detector hits in the CDC and the VXD are different, therefore dedicated pattern recognition algorithms for each detector have been developed.

The VXD track finder algorithm is based on the cellular automaton (CA) model [51,52]. The large number of combinatorial track candidates in this approach is reduced by applying filters of increasing sophistication. First, track segments are built, connecting pairs of hits in adjacent layers. They are the core units of the CA, known as cells. In this approach only compatible hits are combined into cells by consulting a lookup table, called the sector map, which is created by simulating a large number of tracks in the VXD. The second stage consists of determining whether cells that share a hit are neighbors passing a set of geometrical requirements. As in the first stage, the selection criteria are obtained from the sector map. This process is iterated and the track candidates are then identified as threads of neighboring cells. In order to obtain a set of non-overlapping track candidates, a Hopfield network using a quality indicator is employed. The sector maps may vary according to the momentum of the particle, therefore it is possible to run the track finder multiple times by using sector maps for different momentum regions.

Two complementary algorithms for CDC track finding are employed: a global and a local track finder. The global track finder uses all hits at the same time by applying a Hough transformation [53] to the hit positions and looking for intersections in the Legendre space using a quad tree search. It is fast and highly efficient for high-p_t tracks originating from the origin, and can treat cases with missing hits. The local track finder searches for segments and tracks using a cellular automaton and the neighborhood relations between hits. The track finder is robust against energy losses and tracks that do not originate from the IP. The combination of these two track finders results in excellent reconstruction efficiency.

The track candidates from the VXD and the CDC are then merged according to the distance between the VXD and CDC track candidates extrapolated to the CDC outer wall. In the future we foresee cross-detector searches, for example the extrapolation of CDC track candidates toward the VXD detector planes in order to add VXD hits to CDC track candidates, and vice versa, from the VXD to the CDC.

Track fitting A track propagating in a vacuum in a constant magnetic field moves along a helix described by five parameters, defined at a point $\vec{P}$ of the trajectory. In Belle II the point $\vec{P}$ is identified with the perigee, the point of closest approach to the origin in the r–ϕ plane. The five parameters employed in the Belle II tracking software are the following:

- d_0: the signed distance of the perigee from the origin in the transverse plane. The sign depends on the direction of the angular momentum of the track at the perigee with respect to the magnetic field.
- z_0: the longitudinal signed distance of the perigee from the origin.
- ϕ_0: the angle between the transverse momentum at the perigee and the x axis.
- $\tan\lambda$: the tangent of the angle between the momentum at the perigee and the transverse plane.
- ω: the curvature, where the sign corresponds to the charge of the track.

The trajectories of tracks in Belle II are not ideal helices, as the charged particles interact with both passive and active detector material inside the tracking volume, losing a fraction of their energy and undergoing multiple scattering. In addition, the magnetic field provided by the superconducting

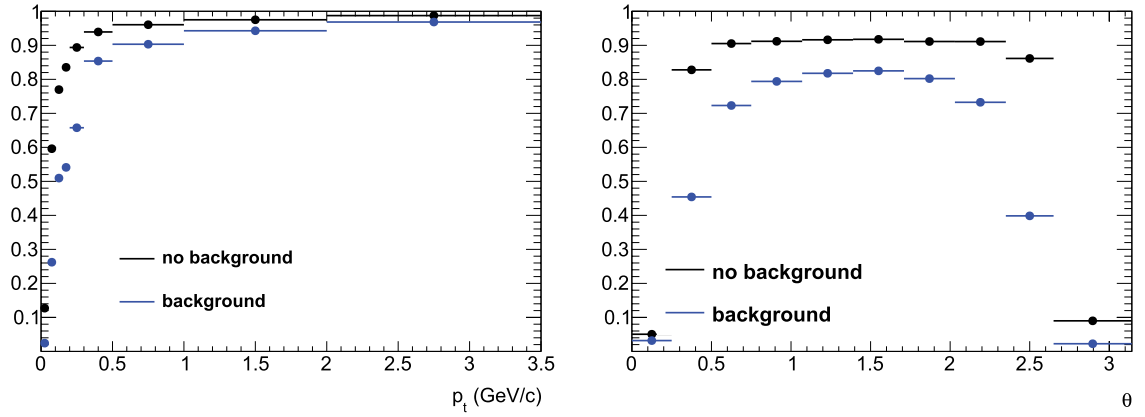

Fig. 9. Tracking efficiency as a function of transverse momentum (left) and polar angle (right) evaluated on $\Upsilon(4S)$ events.

solenoid is not constant in space. These effects are all taken into account in the tracking algorithms, in particular in the track fitting and track extrapolation stages. In order to correctly treat the interaction of particles with matter, a hypothesis on the mass of the particle must be made. The version of the software used for sensitivity studies shown in this book only supports the pion mass hypothesis. However, we have implemented the functionality to account for different mass hypotheses (electron, muon, pion, kaon, or proton) depending on the momentum of the track. For example, high-energy pions and kaons have very similar interactions with matter, therefore a single mass hypothesis is sufficient at momenta above 1 GeV/c, whereas different mass hypotheses yield better resolution below that threshold.

The main track fitting algorithm used in our reconstruction is the deterministic annealing filter (DAF) [54]. The DAF is based on a standard track fitting algorithm, the Kalman filter (KF) [55]. The latter is equivalent to a least squares method, where it takes into account the interactions with the material but has no means of dealing with false hit assignments or incorrect assumptions about wire passage. Both DAF and KF are implemented in the `GENFIT` package [56,57]. To deal with these shortcomings, Belle II uses a DAF in which the points are weighted according to their residual to the smoothed track and hits with large residuals are suppressed with an annealing procedure.

Combined performance The tracking efficiency for charged particle reconstruction is reported in Fig. 9 as a function of the transverse momentum and the polar angle, with and without beam-induced background. The efficiency is defined as the ratio between the number of fitted tracks and the number of generated charged primary particles. The efficiency at low transverse momentum in the presence of beam induce background is lower than ideal. There are ongoing improvements to the algorithms that are being incorporated into the tracking software as the experiment evolves, to mitigate the impact of such background. The efficiency of a more recent version of tracking algorithms is reported below.

In Fig. 10 we show the fitted impact parameter pull distributions. The core Gaussian shows very little bias and is within the nominal width for both parameters. A small fraction of events, below 10%, show a positively biased pull distribution and a width a factor of two larger.

The average particle boost $\langle\beta\gamma\rangle$ for B mesons produced at the predecessor collider KEKB was about 0.425. Here, $\beta = v/c$ is the ratio between the velocity of the particle v and the speed of

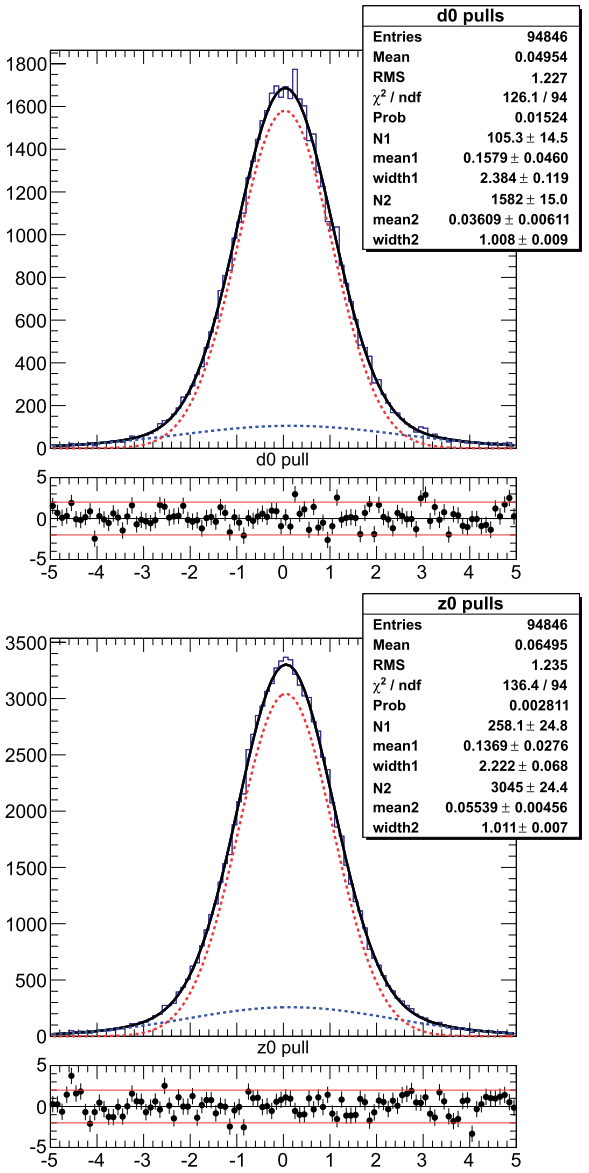

Fig. 10. Distribution of the transverse (left) and longitudinal (right) impact parameter pulls fitted with the sum of two Gaussians, evaluated on $e + e^- \to \Upsilon(4S)$ events.

light c, and γ is the Lorentz factor. Due to the lower boost at SuperKEKB ($\langle\beta\gamma\rangle \approx 0.284$), we need more precise track reconstruction than achieved by the predecessor experiment Belle to reach a comparable resolution in the measurement of the decay time of primary particles (Sect. 6.2.3). In Fig. 11 we show the resolutions of the transverse d_0 and the longitudinal z_0 impact parameters as functions of the pseudo-momenta $p\beta\sin(\theta)^{3/2}$ and $p\beta\sin(\theta)^{5/2}$. The pseudo-momenta are chosen to take into account the effect of multiple scattering of charged particles [58]. A precision of about 10 μm on both impact parameters is expected for high-momentum tracks matching the expectations in the Technical Design Report [6]. Figure 11 shows that on both track impact parameters we improve the resolution by almost a factor of two with respect to Belle.

Improvements in tracking efficiency In this section we report on the efficiency of the VXD and the CDC standalone pattern recognition. The VXD pattern recognition algorithm has been redesigned

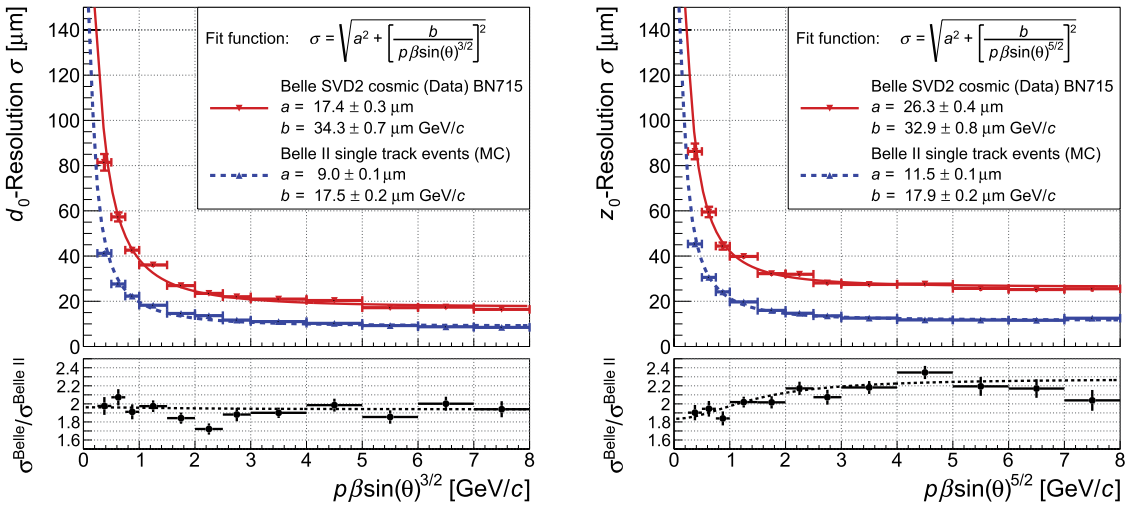

Fig. 11. Resolution of the transverse d_0 (left) and longitudinal z_0 (right) impact parameters. The results for MC events with a single muon track using the Belle II tracking algorithm are compared with the results for Belle cosmic events [58]. The resolution in each bin is estimated using the σ value of a single Gaussian function fitted in a region containing 90% of the data around the mean value of the distributions.

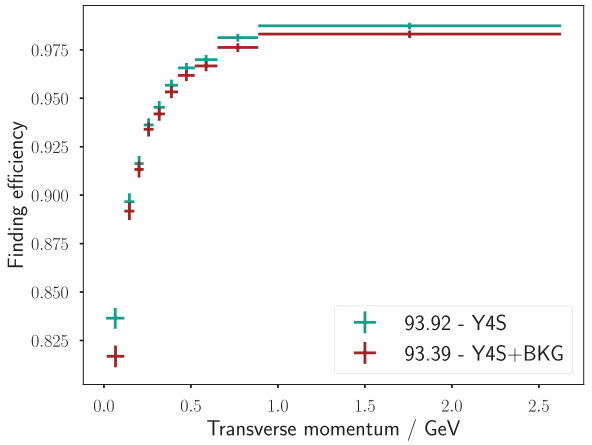

Fig. 12. SVD-only pattern recognition efficiency versus transverse momentum, for $e^+e^- \to \Upsilon(4S)$ events with and without beam-induced background.

and reimplemented since the majority of the physics MC studies were performed for this book. As an example, we show in the left plot of Fig. 12 the track finding efficiency using only SVD hits. The overall efficiency is higher, and the degradation of the performance due to background is much less pronounced than earlier versions of the tracking algorithms.

5.3.2. V^0-like particle reconstruction

Long-lived neutral particles that decay into two charged particles at some distance away from the interaction point are reconstructed using a dedicated algorithm. This V^0 reconstruction takes place after the reconstruction of charged particles and is intended to avoid extrapolation through material on the analysis level, where the actual V^0 selection takes place. This is in accordance with the design goal of removing dependence of analysis-level information on knowledge of the detector material.

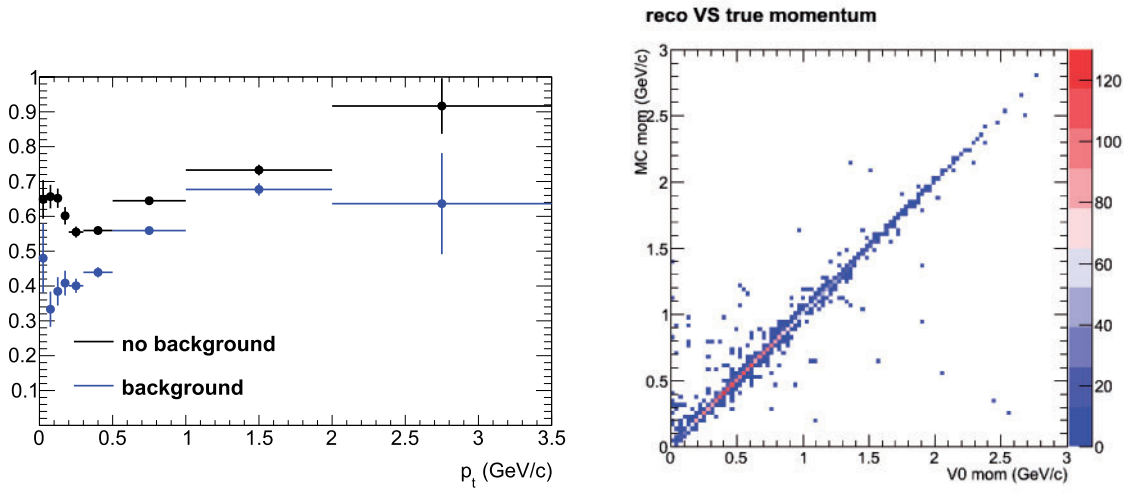

Fig. 13. (Left) The $K^0_S \to \pi^+ \pi^-$ reconstruction efficiency as a function of transverse momentum. (Right) A 2D histogram of the generated versus reconstructed K^0_S momentum.

The goal of V^0 reconstruction is to keep good V^0 candidates originating from outside the beam pipe, as well as those from inside the beam pipe whose reconstructed mass is close to the mass of the mother particle. Unlikely track combinations may be suppressed by restricting the χ^2 from the vertex fit or the radius of the V^0 vertex.

The V^0 reconstruction algorithm pairs all oppositely charged tracks and extrapolates each track to the innermost hit of either track. If the extrapolation fails, the combination is rejected. Studies show that this restriction has no effect on efficiency. Each accepted combination is processed by the vertex reconstruction package `RAVE` [59]. If the vertex fit fails, the combination is rejected. Each surviving combination is then subject to selection criteria that depend on the vertex fit χ^2 (less than 50) and, for vertices inside the beam pipe (a vertex radius less than 1 cm), the mass window (within 30 MeV/c^2 of the nominal V^0 mass).

The V^0 algorithm will be used to reconstruct $K^0_S \to \pi\pi$, Λ, and photon conversions. Figure 13 shows the efficiency of K^0_S reconstruction efficiency as a function of transverse momentum, with and without beam background effects.

5.3.3. Alignment

To reach the design performance of the detector, various calibration constants must be determined. For the VXD, many of these constants describe the position and orientation of the silicon sensors. This calibration is commonly referred to as alignment. To determine the alignment constants, a so-called global approach using the `Millepede II` tool [60,61] has been chosen for use at Belle II. The alignment is computed through minimization of track-to-hit residuals by means of a linear least squares method. Because `Millepede` fits all track and alignment parameters simultaneously, all correlations are kept in the solution. It is therefore desirable to determine as many constants as possible simultaneously. For this reason, the CDC is also integrated into the procedure and its alignment and some calibration constants can be determined together with the VXD alignment. Investigation of the possibility to integrate other sub-detectors into the procedure is ongoing, e.g. the alignment of the muon system.

Track parameterization Reconstructed tracks and decays, as well as cosmic muons, can be used as input to the alignment procedure. All such tracks are first refitted by the "general broken lines" algorithm (GBL) [62], which is integrated into the `GENFIT` toolkit [63] and `basf2`. `GENFIT` is a generic track fitting toolkit for high-energy physics experiments. It allows for the generic treatment of measurements of various types and dimensions (planar 1D or 2D measurements, wire hits, etc.) and offers all the capabilities required for track extrapolation in detector material and inhomogeneous magnetic fields. The GBL parameterization carefully treats multiple scattering effects, adding additional fit parameters (kink angles) to an initial reference trajectory derived from the result of the standard reconstruction output. The additional degrees of freedom are removed by constraining the variance of multiple scattering angles from the moments of the radiation length distribution along the reference particle's trajectory. Tracks are locally parameterized using five or four parameters at each measurement plane depending on the presence or absence of a magnetic field, respectively. For the drift chamber, a virtual measurement plane is constructed by means of the `GENFIT` formalism. Combined particle candidates, composed of multiple particle tracks constrained to originate from a common vertex, can be an input of the alignment as well. Optionally, a beam constraint can be added for decays originating from the primary interaction point, such as di-muon events. In a similar manner, two-body decays with an invariant mass constraint (for example) can be introduced in the procedure.

Alignment parameterization In the VXD, the sensors are parameterized as planes with six rigid-body alignment parameters: for the 212 sensors, we have 1276 parameters. Sensor deformations or additional calibrations of the Lorentz angle in the magnetic field can be included in the procedure as well. For the treatment of correlated movements of sensors, a hierarchy of alignment objects can be defined. This allows for the treatment of time dependence of the larger structures, which is different to internal sensor alignments during simultaneous minimization.

For the CDC, the alignment of the layers and larger structures, e.g. end plates, is considered. The x–t relation as well as channel timing offsets or time walk corrections can be calibrated. For the muon system, the modules are treated as rigid planar bodies in the initial stage.

Beam and vertex constraints rely on the estimation of the primary vertex position (based on beam spot parameters), and corrections to it can be determined during the simultaneous minimization. Only the position of the primary vertex is calibrated. The covariance matrix of the primary beam spot is an input to the procedure and is calibrated via other means.

Alignment workflow `Millepede II` is integrated into the common calibration framework, which makes use of dedicated `basf2` modules to collect samples and run calibration algorithms. During the collection step for alignment, reconstructed tracks are refitted using the nominal detector positions corrected with previously determined alignment constants. Each detector interfaces with this procedure via a special class representing the local-to-global transformation. This class also provides the derivatives of local residuals with respect to its assigned calibration parameters. Various track samples (primary decays, background, cosmic rays, etc.) from different operating conditions (cosmics without magnetic field) are under investigation.

Ultimately, some constants may be determined in a time-dependent way, especially those affecting many measurements, such as the positions of large structures, while keeping the procedure computationally manageable. The procedure as a whole can also be applied locally, for example only for the PXD alignment or to determine the relative alignment of the PXD and SVD. If such corrections

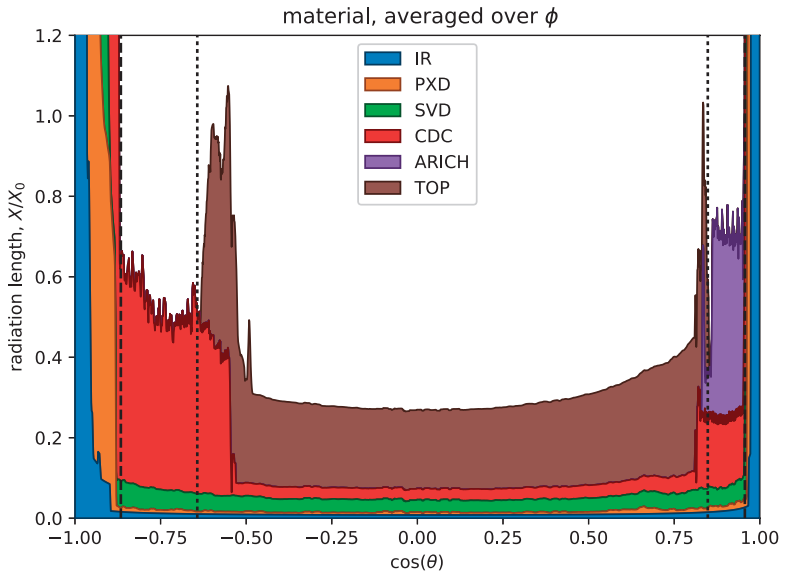

Fig. 14. The number of EM radiation lengths (or thickness) X/X_0 in front of the calorimeter as a function of $\cos\theta$, averaged over ϕ.

are determined online, they will serve as initial values for the global procedure when enough data and track samples are accumulated.

5.4. Calorimeter reconstruction

The electromagnetic calorimeter is used to reconstruct the energy and position of depositions from neutral and charged particles with the best possible resolution and efficiency. While the energy and position reconstruction is primarily needed for photons and neutral hadrons, it may also aid the electron and charged hadron reconstruction in regions without, or with only limited, tracking coverage. The sum of all reconstructed showers is used to constrain the missing energy in decays involving neutrinos. A special case is the reconstruction of highly energetic $\pi^0 \to \gamma\gamma$ decays where the two photon showers overlap or merge.

The second task of the calorimeter is particle identification for electrons, muons, charged hadrons, neutral hadrons, and photons based on shower shape variables and tracks matched to clusters.

A critical aspect of calorimeter cluster reconstruction and electron reconstruction is the material budget in front of the calorimeter. In Belle II the number of radiation lengths (or thickness) X/X_0 is approximately 0.3 in the barrel and higher in the endcaps and in regions with service material. The material budget is depicted in Fig. 14.

The clustering used up to release-00-07-02 is an incomplete adaptation of the Belle clustering code which was developed for a low-background environment. It starts from an initial list of crystals with energy deposits above some threshold, nominally 0.5 MeV, which is about twice the expected level from electronics noise. To obtain some robustness against high beam backgrounds, the energy threshold was raised as a function of crystal polar angle to between 1.28 MeV (barrel) and 2.5 MeV (outer endcap rings). A cluster starts with a seed crystal with at least 10 MeV that is a local energy maximum amongst its nearest-neighbor crystals. A nearest neighbor touches either the side or the corner of the crystal and a local maximum is a crystal whose energy exceeds that of its next neighbors. All crystals from the initial list that are nearest or next-to-nearest neighbors of the seed crystal are

added to the cluster. In the barrel, the size of a cluster is thus limited to a square arrangement of 5×5 crystals. If clusters share crystals after this step, their energies are split according to the ratio of the energy of each cluster to the sum of the energies of all crystals in the overlapping clusters. This energy splitting does not provide the correct position nor the correct weighted list of crystals for subsequent shower shape calculations. The centroid $\vec{x}$ of each cluster is calculated by using linear weights of all crystals in a cluster,

$$\vec{x} = \frac{\sum_i E_i \vec{x}_i}{\sum_i E_i}, \tag{2}$$

where E_i is the energy of the ith crystal and x_i is the geometric center of the ith crystal. It should be noted that this position reconstruction is known to be biased towards the crystal center of the highest-energy crystal in the shower. The cluster energy is reconstructed as the linear sum over all included crystals. The peak position of the reconstructed photon energy is corrected to the true value in a subsequent step as a function of reconstructed polar angle and energy. The cluster time t_{cluster} is the time of the highest energetic crystal in a cluster with respect to the collision time. In order to reduce out-of-time beam backgrounds, clusters with $|t_{\text{cluster}}| < 125$ ns are rejected. Clusters are matched with tracks using a `Geant`-based extrapolation routine. A cluster that contains a crystal hit that is consistent with an extrapolated track is matched to that track.

The described calorimeter reconstruction does not perform optimally in a high-background environment and has various shortcomings, e.g. biased position reconstruction, simplistic track matching, and oversimplified cluster splitting. The average dose caused by various background sources as a function of the polar angle θ in the ECL is shown in Fig. 15. Several improvements have been introduced to the ECL reconstruction with release-00-08-00. The new cluster algorithm reconstructs connected regions (CR) starting with single crystals with an energy of at least 10.0 MeV as seeds, as before. Surrounding crystals are added if their energy is above 0.5 MeV. This procedure is continued if the added crystal energy is at least 1.5 MeV. If two CRs share a crystal, they are merged. The optimal CR contains all deposited energy for a particle and merges CRs from different particles only if different particles deposit energy in the shared crystals. Each CR is then split into one or more clusters as follows:

Each crystal in a CR that is a local energy maximum amongst its nearest neighboring crystals serves as seed for one cluster. Iteratively, all crystals of the CR are assigned to each local maximum using shared weights that are normalized to unity per crystal. The weight per crystal is given by

$$w_i = \frac{E_i e^{(-Cd_i)}}{\sum_k E_k e^{(-Cd_k)}}, \tag{3}$$

where $C = 0.7$ is a constant determined from MC, d_i is the distance between the ith crystal and the cluster centroid, and the denominator sums over all crystals, k, in the cluster. This weight is motivated by the lateral distribution of an electromagnetic shower, which decreases exponentially from the cluster center. The centroid $\vec{x}$ of each cluster is then calculated by using logarithmic weights of all crystals,

$$\vec{x} = \frac{\sum_i w_i' \vec{x}_i}{\sum_i w_i'}, \tag{4}$$

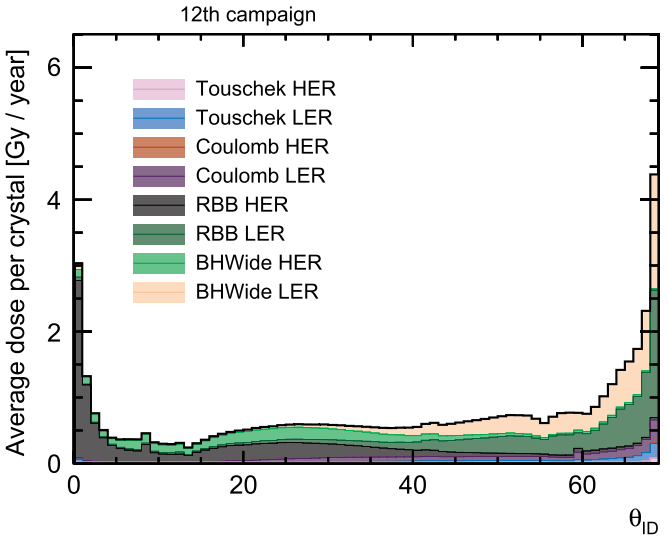

Fig. 15. Average dose per crystal as function of ECL θ-ring. $\theta_{\rm ID} = 0$ corresponds to the most forward crystals, and $\theta_{\rm ID} = 68$ corresponds to the most backward crystals.

where $w_i' = 4.0 + \log(w_i \times E_i/E_{\rm all})$, and $E_{\rm all}$ is the sum of all weighted crystals with weights $w_i > 0$. Only crystals with $w_i' > 0$ are included in the calculation of $\vec{x}$. This procedure is iterated until the average centroid positions of all clusters in the CR are stable within 1 mm.

The cluster energy E is reconstructed by summing the n crystals with highest weighted crystal energies $E = \sum_n w_i \times E_i$ of up to 21 nearest neighbors. The number of crystals, n, depends on the background levels per event and an energy estimation based on the sum of the eight nearest neighbors. The reconstructed peak photon energy is corrected to the true value as a function of reconstructed polar angle, azimuthal angle, energy, and expected background level. The cluster time resolution is determined to contain 99% of all signal clusters based on MC. Showers below 50 MeV with a reconstructed time above this value are not stored.

A comparison of the photon energy resolution obtained using the clustering code of release-00-05-03 (MC5) and release-00-08-00 for different background levels is shown in Fig. 16. The new reconstruction offers a significantly improved energy resolution at low energies. The photon reconstruction efficiency is shown in Fig. 17. The new ECL reconstruction can be extended to reconstruct multiple hypotheses based on the particle type that created the shower, and additional shower shape variables are available. In addition, the dedicated reconstruction of merged π^0 mesons, where the two photons cannot be separated into two different clusters, will be performed. Track matching will be based on the likelihood of the nearest track to a cluster using the covariance matrix of the track fit.

5.5. Charged particle identification

Effective and efficient charged particle identification (PID) is vital to the physics goals of the Belle II experiment. Good PID information is necessary to isolate hadronic final states, reduce backgrounds, and enable flavor-tagging techniques. The Belle II detector, described in Sect. 3, contains an upgraded PID system, including a time-of-propagation (TOP) counter in the barrel region of the detector and a proximity-focusing aerogel ring-imaging Cherenkov (ARICH) detector in the forward endcap region, to provide information on charged particles over the full kinematic range. The information from these detector systems is combined with that from specific ionization (dE/dx) measurements

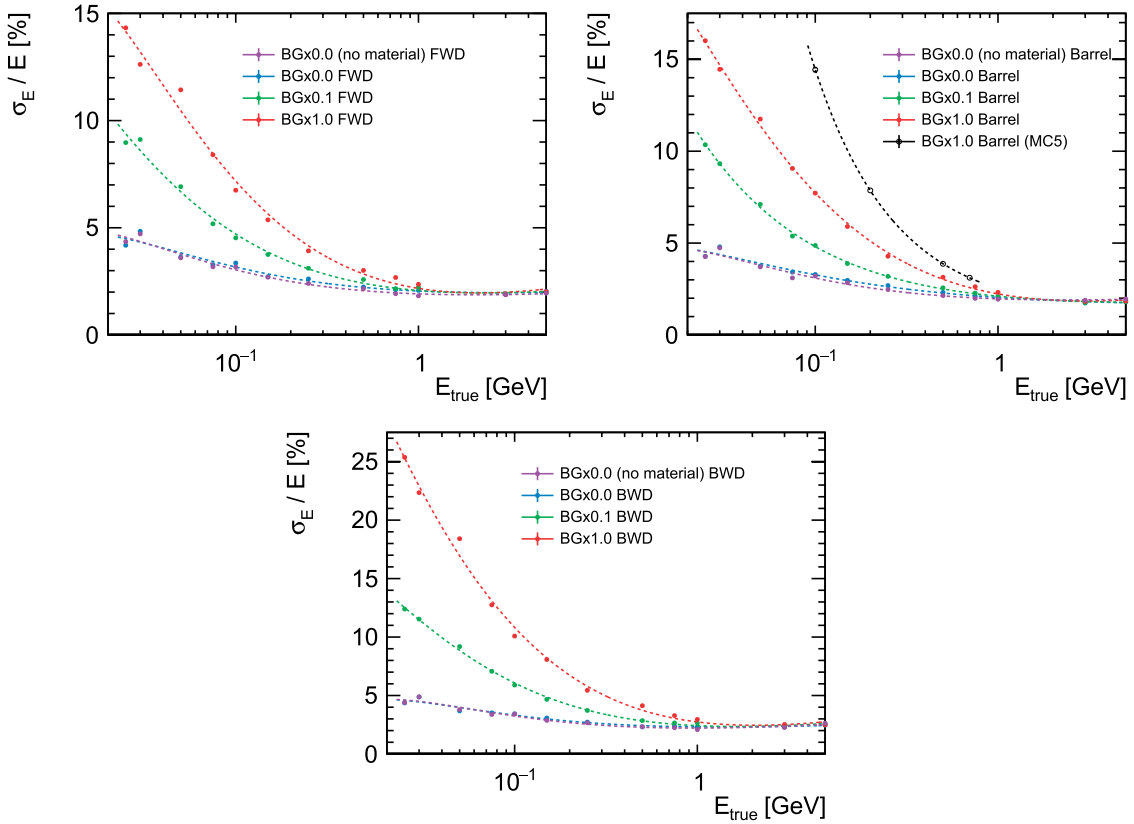

Fig. 16. Photon energy resolution as a function of true photon energy for the FWD endcap (a), barrel (b), and BWD endcap (c) regions. Note the different y-axis ranges of the plots. A smooth curve has been fitted to the points to guide the eye. An older implementation of the ECL reconstruction software (used in MC5) is also plotted in (b).

from the SVD and CDC to act as the primary sources of information for charged hadron PID. In a similar way, the ECL provides the primary information for use in electron identification, and the KLM does so for muon identification. Charged hadron and lepton PID are described in more detail in the following sections.

Charged particle identification at Belle II relies on likelihood-based selectors. Information from each PID system is analyzed independently to determine a likelihood for each charged particle hypothesis. These likelihoods may then be used to construct a combined likelihood ratio. Analysis-specific criteria may be used to construct prior probabilities. When combined with the likelihoods, the priors allow for the construction of the probability for a charged track to have a particular identity. This provides the optimal PID performance, but comes at the cost of requiring analysis-specific optimization. The uncertainty on the selection efficiency cannot be predetermined using this method.

The likelihood selectors rely on likelihood ratios constructed in the following way. First, the PID log likelihoods from each detector are summed to create a combined PID likelihood for each of six long-lived charged particle hypotheses: electron, muon, pion, kaon, proton, and deuteron. Next, the difference in log likelihood between two particle hypotheses is used to construct a PID value $L(\alpha : \beta)$ according to

$$\mathcal{L}(\alpha : \beta) = \frac{1}{1 + e^{\ln \mathcal{L}_\alpha - \ln \mathcal{L}_\beta}} = \frac{\prod_{\text{det}} \mathcal{L}(\alpha)}{\prod_{\text{det}} \mathcal{L}_\alpha + \prod_{\text{det}} \mathcal{L}_\beta}, \tag{5}$$

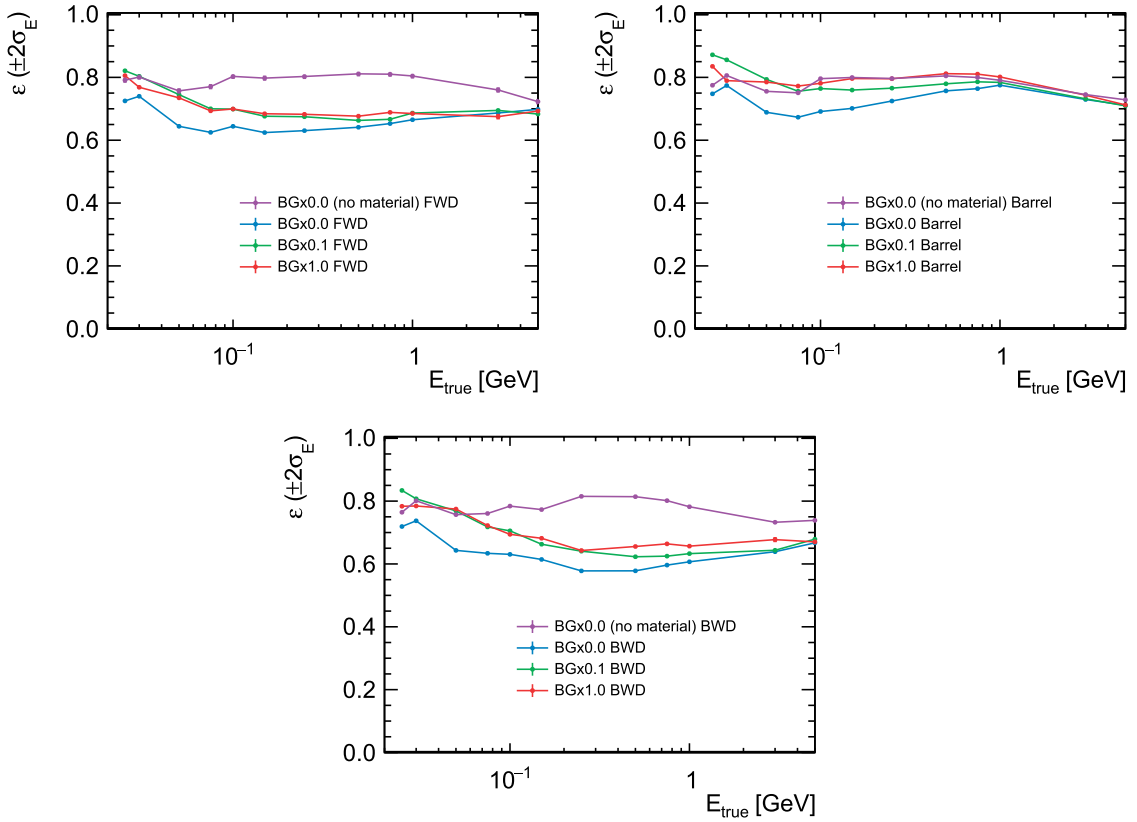

Fig. 17. ECL reconstruction efficiency for single photons for different background levels, with and without material in front of the ECL, for the FWD endcap (a), barrel (b), and BWD endcap (c) regions. The points are connected by straight lines to guide the eye.

where α and β represent two different particle types and the product is over the active detectors for the PID type of interest. The value $\mathcal{L}(\alpha : \beta)$ is greater than 0.5 for a charged track that more closely resembles a particle of type α than one of type β and is less than 0.5 otherwise. More details on the PID types are given in the following sections.

The performance plots included in this section were generated from inclusive samples of 10^6 $c\bar{c}$ events generated during the fifth and sixth MC campaigns. These samples were reconstructed with release-00-05-03 and release-00-07-00 of the Belle II software, respectively.

5.5.1. dE/dx measurements

The ionization energy loss, dE/dx, of a particle traveling through the Belle II detector is determined from measurements in the VXD and CDC. It is expected that the dE/dx measurement should depend only on the particle velocity, β, or equivalently $\beta\gamma = p/m$. Thorough calibration is required to avoid systematic effects that break this dependence. The $\beta\gamma$ universality of the dE/dx response for pions and kaons at Belle II is displayed in Fig. 18. In general, the dE/dx information provides better discrimination power for particle momenta below about 1 GeV/c (Fig. 19).

Determination of likelihoods The VXD and CDC detectors make independent dE/dx measurements and require different calibration procedures. At the time this document is written, the dE/dx reconstruction algorithms in both subsystems construct likelihood values using information from

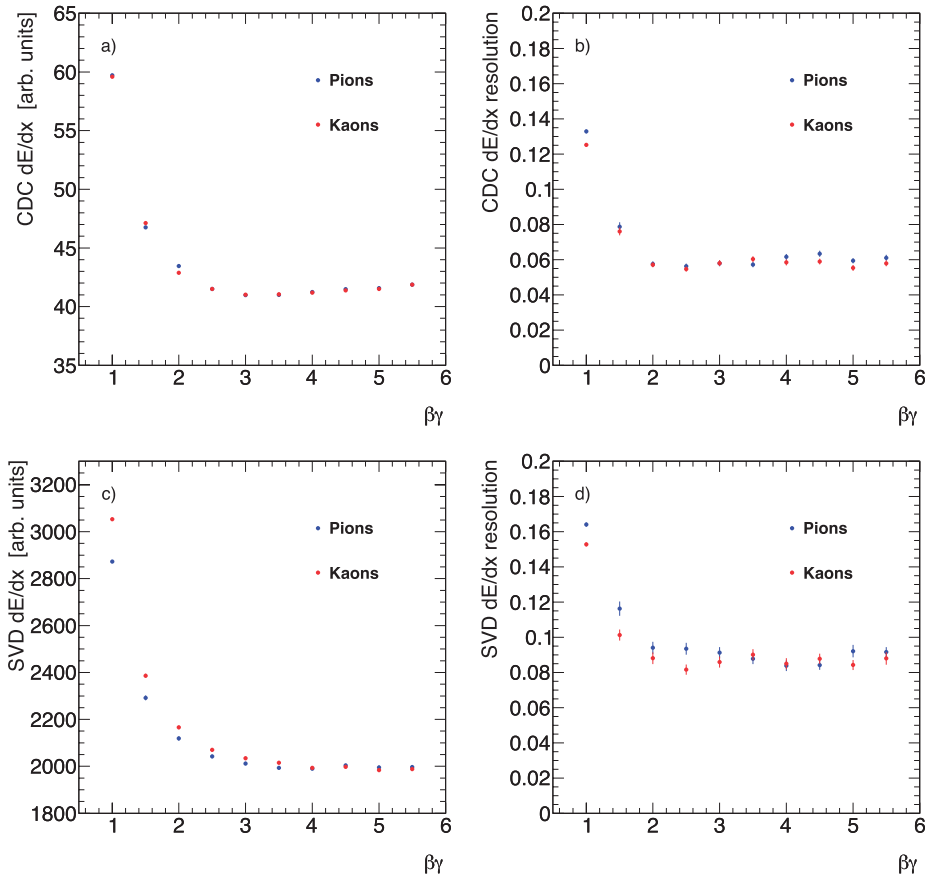

Fig. 18. Truncated dE/dx means (a,c) and resolutions (b,d) for pion and kaon samples generated at specific values of $\beta\gamma$. The residual non-universality in the SVD is due to the fact that the measured momentum at the IP is different than the momentum in each SVD layer.

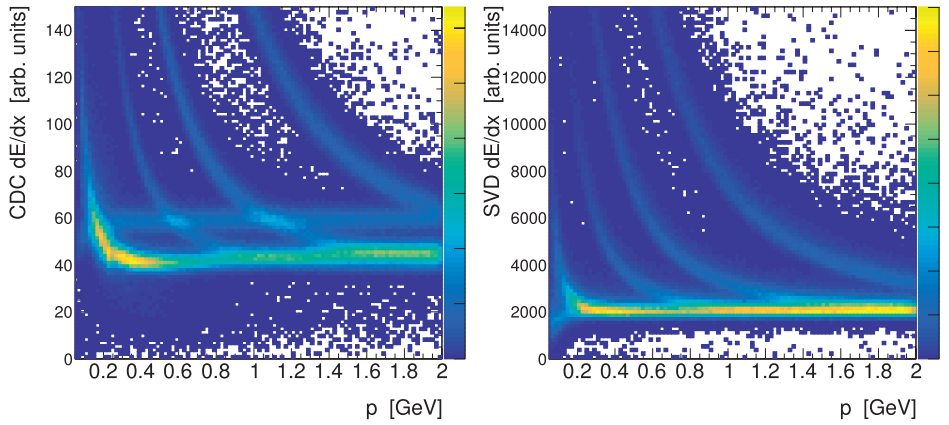

Fig. 19. Truncated dE/dx means as a function of momentum for the CDC (left) and SVD (right). Distinct bands are evident for the various particle species below about 1 GeV/c.

individual hits. A likelihood value is determined for each particle hypothesis, including pion, kaon, proton, muon, electron, and deuteron, using a lookup table constructed from large MC samples. To reduce the effect of non-Gaussian tails, the lowest 5% and highest 25% dE/dx measurements of each track are not used in the likelihood determination.

Future versions of the software will use a parameterization of the truncated mean and resolution to determine dE/dx PID discriminators. A χ variable is determined by comparing the measured dE/dx truncated mean to a predicted value and resolution. The predicted values are calculated from a parameterization of dE/dx as a function of $\beta\gamma$. The predicted resolutions depend on the dE/dx measurement, the number of hits on the track, and the polar angle of the track. After determining the parameterization for the predicted means and resolutions, a χ value is determined according to

$$\chi_h = \frac{I_{\text{meas}} - I_{\text{pred},h}}{\sigma_{\text{pred},h}}, \tag{6}$$

where h is the particle type, I is the dE/dx truncated mean, and σ is the resolution for the given particle type. As the distributions of this χ variable are approximately Gaussian, it may be converted to a likelihood and combined with the output of other PID systems. The performance of such an algorithm is generally similar to the current method, but will enable better charaterization of the resolution.

Performance Defining the signal efficiency as the fraction of events relative to the generated quantity that have a likelihood of being identified as the true particle type greater than that of being identified as another particle type (e.g. $L_K > L_\pi$), the average kaon efficiency from dE/dx in the SVD below 700 MeV/c is about 96%. The comparable value in the CDC is nearly identical. The fraction of pions misidentified as kaons under the same criteria is about 3.1% in the SVD and about 1.1% in the CDC. Combining the information from these two detectors yields an average kaon efficiency of about 99.5% below 700 MeV/c, with a fake rate of about 0.2%.

5.5.2. Charged hadron identification

Particle identification for charged hadrons, which in this context include pions, kaons, protons, and deuterons, $\{\pi, K, p, d\}$, depends primarily on likelihood information from the CDC, TOP, and ARICH detectors. These detectors also contribute to the particle identification of charged leptons, $\{e, \mu\}$. The methods to construct the likelihoods for each of these detector systems are briefly described here.

TOP likelihoods The TOP counter is a novel type of PID device that combines time-of-flight measurements with the Cherenkov ring imaging technique [9]. The dominant contribution to the resolution of this detector is the dispersion of light while propagating in the quartz bar. This effect is mitigated by focusing the Cherenkov light onto the photon detector with a spherical mirror and measuring the coordinates of the photon impact position. To further improve the resolution, an expansion prism is added at the bar exit window.

The TOP counter consists of sixteen 2.7 m-long modules positioned in the space between the CDC and the ECL and covers the polar angles from 32° to 120°. The gaps between the modules account for about 5% of the uncovered area.

An extended likelihood method is used to determine log likelihoods for the six long-lived charged particle types. The extended log likelihood probability for a given charged particle hypothesis h is defined as

$$\ln \mathcal{L}_h = \sum_{i=1}^{N} \ln\left(\frac{S_h(x_i, y_i, t_i) + B(x_i, y_i, t_i)}{N_e}\right) + \ln P_N(N_e), \tag{7}$$

where $S_h(x,y,t)$ is the signal distribution for the hypothesis, h, $B(x,y,t)$ is the distribution of background, and $N_e = N_h + N_B$ is the expected number of detected photons, being the sum of the expected number of signal photons N_h for hypothesis h and the expected number of background photons, N_B. The channel coordinates are given by x and y, and the integration is performed over the full range t of the time-of-arrival measurement. The second term in Eq. 7 is the Poisson probability to obtain N photons if the mean is N_e.

The normalizations of $S_h(x,y,t)$ and $B(x,y,t)$ are:

$$\sum_{j=1}^{n_{\rm ch}} \int_0^{t_m} S_h(x_j,y_j,t)dt = N_h, \tag{8}$$

$$\sum_{j=1}^{n_{\rm ch}} \int_0^{t_m} B(x_j,y_j,t)dt = N_B, \tag{9}$$

where the sum runs over all channels $n_{\rm ch}$ of the photon detector array.

The ring image of the TOP counter is a complicated pattern, which, besides the Cherenkov angle, also depends on the particle impact position and the angles with respect to the quartz bar. The distribution for a particular detection channel j can be parameterized as a sum of Gaussian distributions,

$$S_h(x_j,y_j,t) = \sum_{k=1}^{m_j} n_{kj} g(t - t_{kj}; \sigma_{kj}), \tag{10}$$

where n_{kj} is the number of photons in the kth peak of channel j; t_{kj} is the position and σ_{kj} the width of the peak, and $g(t - t_{kj}; \sigma_{kj})$ is the normalized Gaussian distribution; and m_j counts the number of peaks in channel j for $t < t_m$.

The quantities n_{kj}, t_{kj}, and σ_{kj} are functions of the Cherenkov angle $\theta_{\rm c}$, the photon emission point (x_0, y_0, z_0) given by the particle impact position, the particle impact angles (θ, ϕ), and the unfolded channel coordinate $x_D^{kj} = ka \pm x_j$, where k represents the number of internal reflections at the side walls and a the width of the quartz bar. Using the above input data it is possible to solve for the unknown Cherenkov azimuthal angle $\phi_{\rm c}^{kj}$ and thus determine the photon directional vector [10,64].

Once the photon direction is known, t_{kj} is obtained by ray-tracing. The number of photons in the peak is calculated with

$$n_{kj} = N_0 \ell \sin^2\theta_{\rm c} \frac{\Delta\phi_{\rm c}^{kj}}{2\pi}, \tag{11}$$

where N_0 is the figure of merit of the Cherenkov counter, ℓ is the length of the particle trajectory in the quartz bar, and $\Delta\phi_{\rm c}^{kj}$ is the range of the Cherenkov azimuthal angle covered by the measuring channel j. The peak width σ_{kj} is obtained by summing in quadrature the following contributions:

- photon emission point spread (parallax error),
  $\sigma_\ell = dt_{kj}/d\lambda \cdot \ell/\sqrt{12}$, where λ is the running parameter of the particle trajectory inside the quartz bar ($0 \le \lambda \le \ell$);
- multiple scattering of the particle in the quartz,
  $\sigma_{\rm scat} = dt_{kj}/d\theta_{\rm c} \cdot \theta_0(\ell/2)$, where $\theta_0(\ell/2)$ is calculated with the well-known multiple scattering approximation [65];

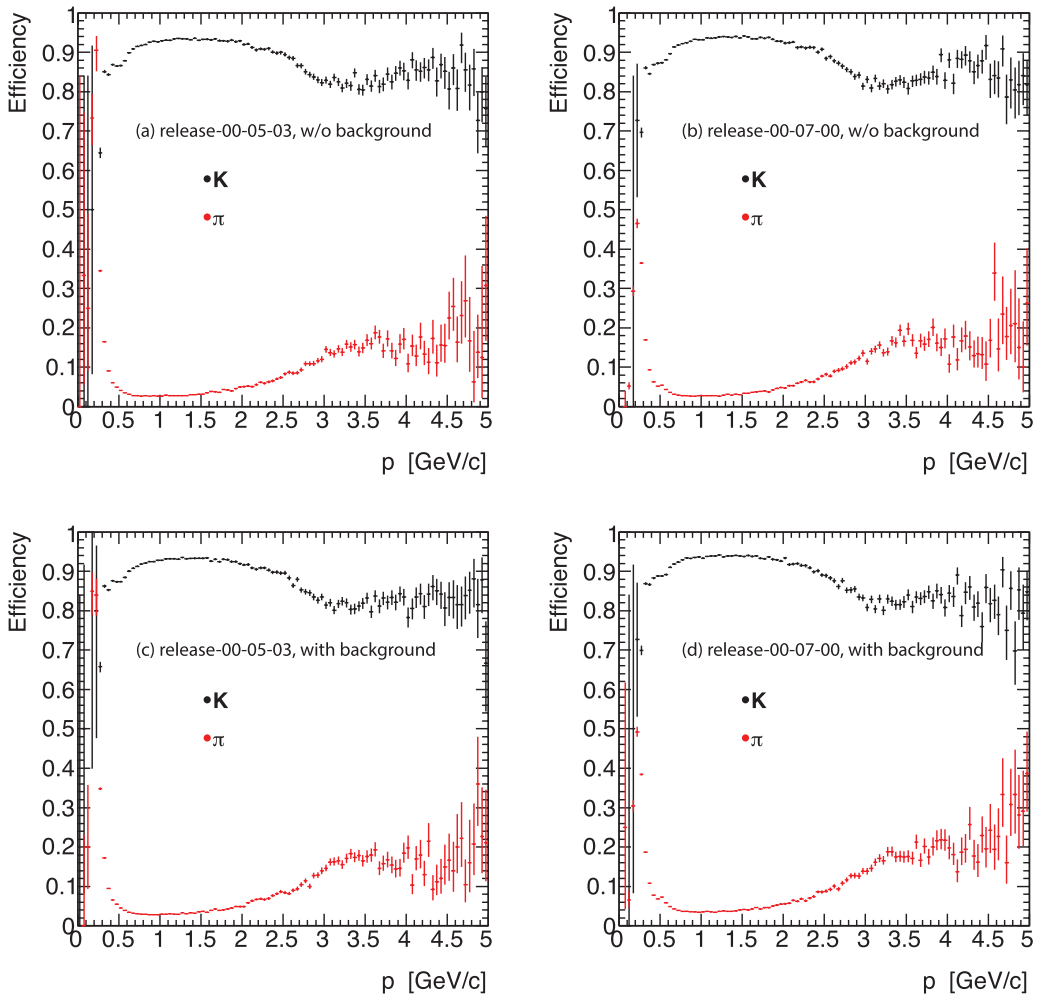

Fig. 20. TOP counter kaon identification efficiency (black markers) and pion fake rate (red markers) as a function of momentum for $\ln \mathcal{L}_K > \ln \mathcal{L}_\pi$, obtained with an MC simulation without beam background (a,b) and with beam background (c,d). The performance using release-00-05-03 is given in (a) and (c), while that for release-00-07-00 is given in (b) and (d). Only tracks that fall within the TOP acceptance are considered.

- dispersion (chromatic error),
  $\sigma_{\rm disp} = dt_{kj}/de\sigma_e$, where σ_e is the r.m.s. of the energy distribution of detected photons in the channel;
- channel size,
  $\sigma_{\rm ch} = dt_{kj}/dx_D \cdot \Delta x_j/\sqrt{12}$, where Δx_j is the channel width;
- and the transit time spread of the photon detector, $\sigma_{\rm TTS}$.

The derivatives $dt_{kj}/d\lambda$, $dt_{kj}/d\theta_{\rm c}$, dt_{kj}/de, and dt_{kj}/dx_D are calculated numerically according to the method described in detail in Refs. [10,64].

Identification and misidentification efficiencies have been studied with MC simulations. Using $e^+e^- \to c\bar{c}$ samples, we obtain the performance shown in Fig. 20. The efficiency is defined as the proportion of tracks that are properly identified according to the generated information for all tracks that fall within the TOP acceptance. In the momentum region below 2 GeV/c, the efficiency of identifying a kaon is about 94% with a probability of approximately 4% of being misidentified as a pion. Above 2 GeV/c the performance slowly decreases and gives about 85% efficiency with a 15%

fake rate at 3 GeV/c. Figure 20 also shows that when the nominal beam background is included, the performance of the counter is not appreciably degraded. Other interesting studies are discussed in Ref. [66]. Discrimination of multiple charged particle hypotheses is possible with the TOP.

ARICH likelihoods In the Belle II detector, PID in the forward endcap is achieved with the aerogel ring imaging Cherenkov counter (ARICH). The ARICH covers the polar angle range from 17° to 35°. Reconstructed tracks from the CDC are extrapolated to the ARICH detector volume and a likelihood function is constructed for each of the six different particle type hypotheses for tracks that pass through the aerogel layer. The likelihood function is based on a comparison of the observed spatial distribution of Cherenkov photons on the photodetector plane with the expected distribution for the given track parameters (position and momentum vector on the aerogel plane) for a given particle type.

The ARICH likelihood functions are constructed based on the method described in Refs. [67,68]. For each of the particle type hypotheses, h, a likelihood function is calculated as $\mathcal{L}_h = \prod_i p_i^h$, where i runs over all pixels of the detector and p_i^h is the probability for pixel i to record the observed number of hits (1 or 0) assuming particle type h. As p_i^h is a Poisson distribution, one can show that $\mathcal{L}_h$ can be rewritten as $\ln \mathcal{L} = -N + \sum_i (n_i + \ln(1 - e^{-n_i}))$, where N is the expected total number of hits, n_i is the expected (calculated) average number of hits on pixel i, and the sum runs only over the pixels that were hit in an event.[6]

The expected average number of hits on pixel i, n_i, is obtained as the sum of contributions from signal and background hits, $n_i = n_i^{\mathrm{s}} + n_i^{\mathrm{b}}$, where the signal contribution is divided into contributions from the first and second aerogel layers, $n_i^{\mathrm{s}} = n_i^{\mathrm{s},1} + n_i^{\mathrm{s},2}$. The contribution of each aerogel layer (r) is calculated as

$$n_i^{\mathrm{s},r} = \epsilon_{\mathrm{det}} N^{\mathrm{s},r} \int_{\Omega_i} \frac{1}{2\pi} G(\theta, \theta_h^r, \sigma_h^r) d\theta d\phi, \tag{12}$$

where ϵ_{det} is the photon detection efficiency and $N^{\mathrm{s},r}$ is the number of photons emitted from aerogel layer r (theoretically calculated). The integral gives the probability for a Cherenkov photon being emitted by particle type h from aerogel layer r into the solid angle covered by pixel i (θ and ϕ are the polar and azimuthal angles with respect to the track direction). A Gaussian function G with a mean at the expected Cherenkov angle (θ_h^r) and width σ_h^r (due to uncertainty in photon emission position) for a track of particle type h is used to describe the Cherenkov angle distribution (i.e. θ). To obtain the number of photons emitted from the aerogel layer ($N^{\mathrm{s},r}$) a general expression is used for the Cherenkov photon yield, where the track path length in the aerogel, Rayleigh scattering, and the photon loss on the edges of aerogel tiles are taken into account. A constant (pixel-independent) value is assumed for the background contribution n_i^{b}, set to correctly describe the observed distribution.

The expected total number of hits, N, is obtained as $\epsilon_{\mathrm{det}}\epsilon_{\mathrm{acc}}(N^{\mathrm{s},1} + N^{\mathrm{s},2})$, where ϵ_{acc} is the geometrical acceptance correction factor (i.e. what fraction of the Cherenkov ring falls on the photosensitive surface). The acceptance correction factor is calculated using a simple ray-tracing simulation in which 200 rays, uniformly distributed in ϕ and at the expected Cherenkov angle θ_h^r, are propagated from the mean emission point in the aerogel to the detector plane. The number of track lines that hit the photosensitive surface is used to determine the correction factor.

[6] For brevity the index h is omitted, but note that N and n_i depend on h.

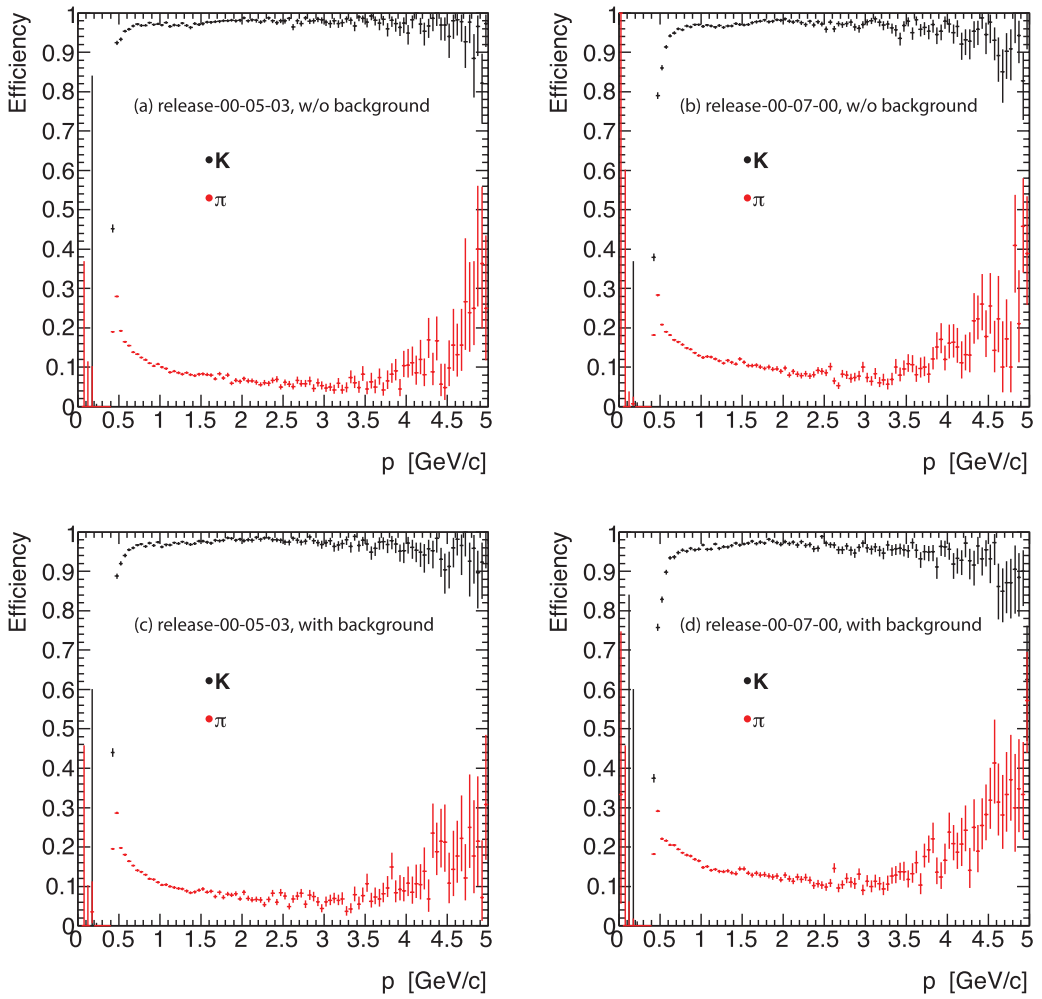

Fig. 21. ARICH kaon identification efficiency (black markers) and pion fake rate (red markers) as a function of momentum for $\ln \mathcal{L}_K > \ln \mathcal{L}_\pi$, obtained with an MC simulation without beam background (a,b) and with beam background (c,d). The performance using release-00-05-03 is given in (a) and (c), while that for release-00-07-00 is given in (b) and (d). Only tracks that fall within the ARICH acceptance are considered.

The above procedure is carried out for all six particle hypotheses. The log likelihood difference, $\ln \mathcal{L}_{h_1} - \ln \mathcal{L}_{h_2}$, is used to distinguish h_1 and h_2 particle types. On average about 12 signal photons are detected per saturated track (i.e. with $\theta_{\text{Cherenkov}} = \theta^{\text{max}}_{\text{Cherenkov}}$). The PID performance is mainly degraded by tracks with poor track information (position and direction on the aerogel plane), which result either from poor reconstruction or rescattering in the CDC aluminum endplate, and by tracks that produce a very low number of photons. The latter are mainly tracks that pass through the gap between two adjacent aerogel tiles, or tracks producing a Cherenkov ring that largely misses the photosensitive area.

The PID performance of the ARICH detector for K/π separation is depicted in Fig. 21.

5.5.3. Muon identification

Muon identification (MuID) in the KLM uses the differences in longitudinal penetration depth and transverse scattering of the extrapolated track. The MuID reconstruction module in the tracking package of `basf2` proceeds in two steps: (1) track extrapolation using the muon hypothesis;

(2) likelihood extraction for each of six particle hypotheses: muon, pion, kaon, proton, deuteron, and electron.

The six likelihoods that are assigned to a given track are stored as unnormalized log likelihood values and normalized likelihood values in the MuID data object. In the post-reconstruction analysis, the log likelihood differences may be used to select or reject the muon hypothesis for a given track.

The KLM geometry exhibits several features: the barrel has 15 detector layers with no iron before the innermost layer; the forward (backward) endcap has 14 (12) detector layers with iron before the innermost layer. The iron plates are about 4.7 cm thick and are separated by detector-filled 4.4 cm gaps. The KLM has less iron and detector coverage in the forward and backward overlap regions since the endcaps' outer radius is about 310 cm; there may be as few as eight detector layers for some polar angles. Thus, the separation power between muons and non-muons is weaker here.

Track extrapolation Each charged track that is reconstructed in the tracking detectors (CDC, SVD, and PXD) is extrapolated outward using `GEANT4E` [39], starting at the last hit on the reconstructed track in the CDC, assuming the muon hypothesis. During this extrapolation, `GEANT4E` reduces the track's momentum by the mean integrated specific ionization (dE/dx) energy loss in the intervening material and inflates the elements of the phase-space covariance matrix due to (elastic) multiple scattering and fluctuations in dE/dx. Particles are assumed to not decay during this extrapolation.

Extrapolation through the non-KLM sections by `GEANT4E` does not consider actual hits in any of the sensitive elements. In contrast, extrapolation through the KLM uses each matching hit in a Kalman-filtering adjustment of the track parameters and covariance matrix [69].

The extrapolation proceeds step by step through the detector geometry, starting at the outermost point on the reconstructed track's trajectory (usually in the CDC) and with the reconstructed track's phase-space coordinates and covariance matrix. Upon crossing a KLM detector layer, the nearest two-dimensional hit—if any—in that layer is considered for association with the track. If the hit is within about $3\,\sigma$ in either of the two local coordinate directions (where σ is the sum in quadrature of the extrapolation's position uncertainty and the hit-measurement uncertainty) then it is declared a matching hit and the Kalman filter uses it to adjust the track properties before the next step in the extrapolation. At the same time, the Kalman filter's fit quality (χ^2) is accumulated for the track. A given 2D hit may be associated with more than one track. The hit-matching algorithm begins with the inner layers and moves outward such that a given KLM detector layer is examined at most once for a given track. The extrapolation ends when the kinetic energy falls below a user-defined threshold (nominally 2 MeV) or the track curls inward to a cylindrical radius below 40 cm or escapes from the KLM.

Determination of likelihoods If the track reached the KLM, it is classified according to how and where the extrapolation ended (stopped in or exited from the barrel or the endcap). The likelihood of having the matched-hit range and transverse-scattering χ^2 distribution (based on the distance between the measured and extrapolated tracks) is obtained from pre-calculated probability density functions (PDFs). There are separate PDFs for each charged particle hypothesis and charge, and for each extrapolation outcome.

The longitudinal profile PDF value $\mathcal{P}_{\mathrm{L}}(\vec{x}; O, \ell, H)$ for extrapolation-ending outcome O and outermost layer ℓ and for particle hypothesis $H \in \{\mu^{\pm}, \pi^{\pm}, K^{\pm}, e^{\pm}, p, \bar{p}, d, \bar{d}\}$ is sampled according to the measurement vector $\vec{x}$ given by (a) the pattern of all KLM layers touched during the extrapolation—not just the outermost such layer—and (b) the pattern of matched hits in the touched layers. Note

that the momentum and direction are not included in the measurement vector; the outermost extrapolation layer ℓ is a proxy for these. The extrapolation outcome O accounts for the KLM geometry by classifying a track as stopping in or exiting (1) the barrel only, (2) the forward endcap only, (3) the backward endcap only, (4) the overlap region between the forward barrel and endcap, and (5) the overlap region between the backward barrel and endcap.

The transverse scattering probability density function $\mathcal{P}_{\mathrm{T}}(\chi^2, n; D, H)$ for KLM region D (barrel-only, endcap-only, or overlap) and particle hypothesis H is sampled according to the measurements of χ^2 from the Kalman filter and the number $n \in \{2, 4, \ldots, 36\}$ of degrees of freedom—twice the count of matching-hit layers since there are two independent measurements per layer. The muon hypothesis PDF is very close to the ideal χ^2 distribution for the given number of degrees of freedom while the non-muon hypothesis PDFs are considerably broader for low degrees of freedom—the most likely scenario for a true non-muon.

For each track, the likelihood for a given particle hypothesis is the product of the corresponding longitudinal-profile and transverse-scattering PDF values:

$$\mathcal{L}(H; O, \ell, D, \vec{x}, \chi^2, n) = \mathcal{P}_{\mathrm{L}}(\vec{x}; O, \ell, H) \cdot \mathcal{P}_{\mathrm{T}}(\chi^2, n; D, H). \tag{13}$$

The natural logarithm of this value is stored in the MuID data object. Then, the six likelihood values are normalized by dividing by their sum and stored in the MuID data object.

Presently, significance levels, $\mathcal{S}$, are not available. Such values might be used, for example, to remove tracks that are not consistent with *any* hypothesis by requiring $\mathcal{S} > \mathcal{S}_{\mathrm{min}}$. This feature will be added in a future release.

Muon efficiency and pion fake rate The log likelihood difference

$$\Delta \equiv \ln(\mathcal{L}(\mu^+; O, \ell, D, \vec{x}, \chi^2, n)) - \ln(\mathcal{L}(\pi^+; O, \ell, D, \vec{x}, \chi^2, n)) \tag{14}$$

is the most powerful discriminator between the competing hypotheses. The requirement $\Delta > \Delta_{\mathrm{min}}$ for a user-selected Δ_{min} provides the best signal efficiency for the selected background rejection.

Log likelihood differences for true muons and pions are shown in Fig. 22 as a function of the track momentum. Clearly, choosing a momentum-independent threshold on Δ_{min} that is non-zero (and positive) will reject low-momentum muons. Similar behavior is seen when choosing a criterion that is independent of the polar or azimuthal angles since the log likelihood differences are softer in the uninstrumented azimuthal cracks between sectors and in the barrel–endcap overlap regions where the KLM is thinner (with only around eight detector and iron layers).

Muon efficiency and pion fake rate are shown in Fig. 23 as functions of momentum, polar angle, and azimuthal angle for three values of the log likelihood difference threshold. The black curves exhibit the behavior for the nominal cut of $\Delta > 0$: the muon efficiency is 90%–98% for momenta above 1.0 GeV/c while the pion fake rate is 2.5%–6%; the muon efficiency is flat at 96% in θ while the pion fake rate is 2%–6%; the muon efficiency is 92%–98% in ϕ (with dips at each octant boundary and at the solenoid cryostat chimney) while the pion fake rate is roughly flat at 3.5% (or 4% at the chimney). The red curves exhibit more pronounced differences as a function of p, θ, and ϕ for the much tighter cut of $\Delta > 20$, where muon efficiency is sacrificed somewhat—and unevenly in each of these variables—for much better purity.

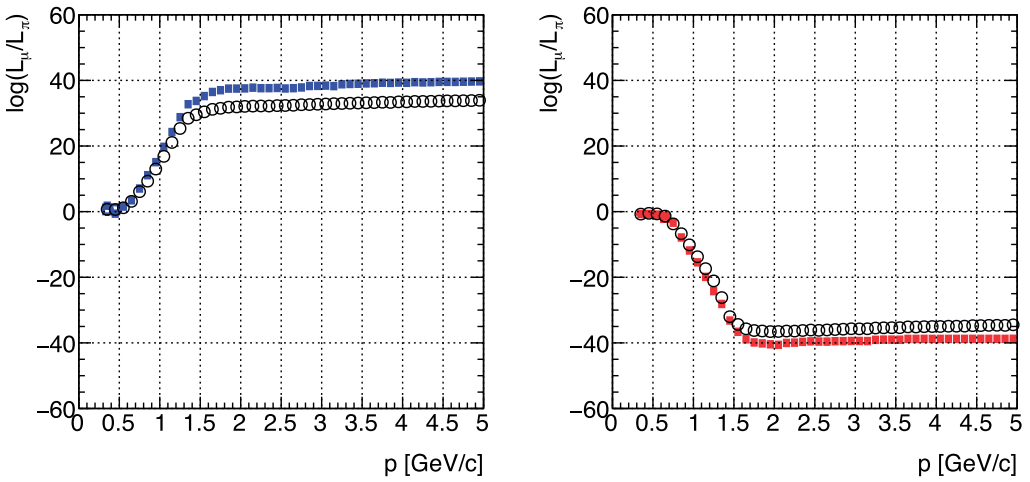

Fig. 22. Log likelihood difference between muon and pion hypotheses for true muons (left) and true pions (right) as a function of the track momentum in GeV/c. In each bin, the open circle (box) represents the mean (median) of the distribution at a given momentum. The mean (or median) deviates increasingly from zero with rising momentum (i.e. with increasing number of crossed KLM layers) and then saturates at about ± 40 for exiting tracks.

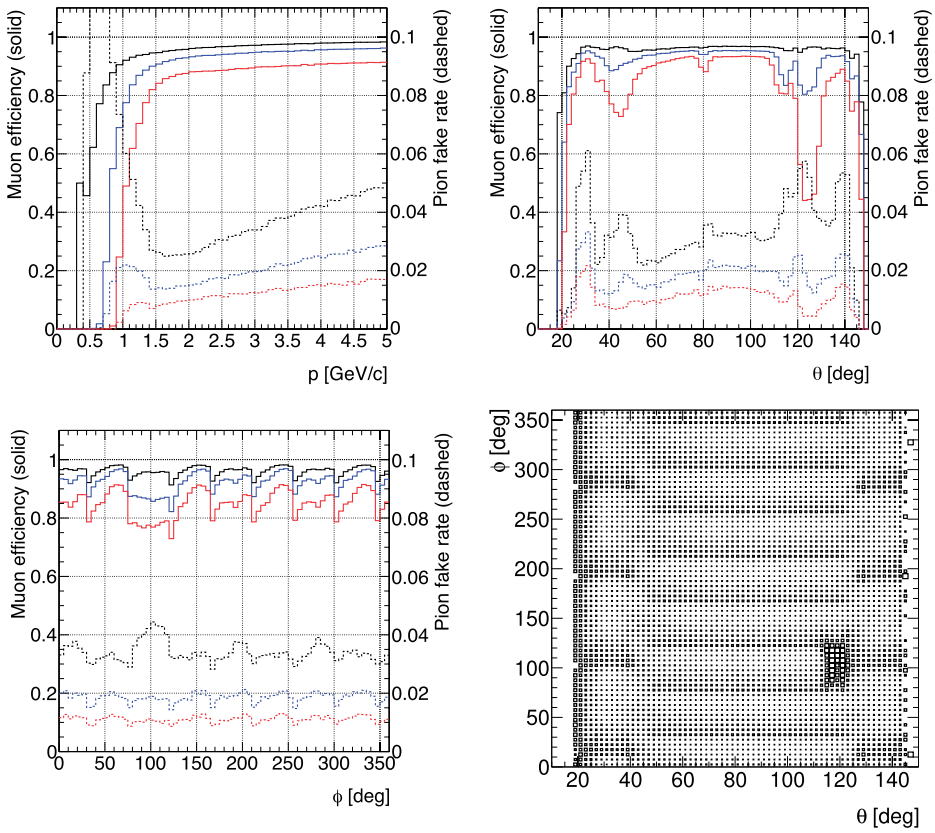

Fig. 23. Muon efficiency (solid, left-axis scale) and pion fake rate (dashed, right-axis scale) for three values of the log likelihood difference cut—$\Delta_{\mathrm{min}} = 0$ (black), 10 (blue), and 20 (red)—as a function of momentum (top left), polar angle (top right), and azimuthal angle (bottom left). Muon inefficiency as a function of ϕ vs. θ (bottom right), illustrating the geometric inefficiencies at the sector boundaries (eight horizontal enhancements in the barrel; four horizontal enhancements in each endcap) and in the vicinity of the solenoid chimney.

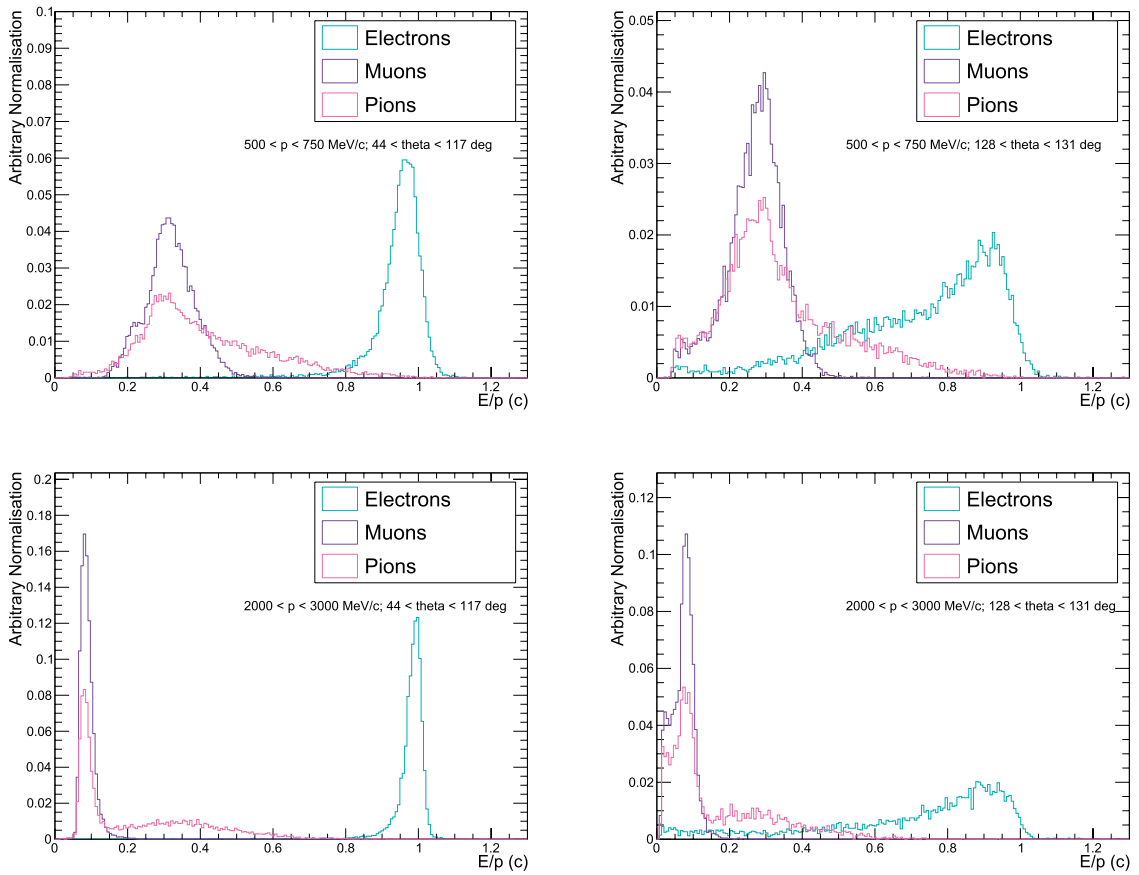

Fig. 24. The E/p distributions for two momentum ranges (500 MeV/c $< p <$ 750 MeV/c and 2000 MeV/c $< p <$ 3000 MeV/c) and two polar angle ranges ($44° < \theta < 117°$ and $128° < \theta < 131°$). This is an excellent discriminator for EID when $p > 1$ GeV/c and in the barrel region. However, for low-momentum particles and particles near the crack region, the separation is less distinct.

5.5.4. Electron identification

Global electron identification (EID) combines individual likelihoods from the ECL, dE/dx measurements taken from the SVD and CDC, and Cherenkov PID information from the TOP and ARICH. The E/p value, however, is the primary feature for separating electrons from other charged particles (muons and pions), where E is the energy measured in the ECL and p is the absolute track momentum. The E/p distributions for electrons, muons, and pions are shown in Fig. 24 for a variety of momentum ranges. For $p \geq 1$ GeV/c there is sufficient distinction between electrons and other charged particles in this distribution, making it a useful parameter for a fit-based likelihood profile for EID.

The ECL electron ID module is responsible for using momentum- and polar-angle-dependent PDF fit parameters to find the best fit to the E/p distribution. It then derives a fit-based electron log likelihood. This log likelihood can then be combined with EID log likelihoods from other subdetectors to create the combined global EID log likelihood used in analyses. The E/p distribution is fit using a Gaussian convoluted with a crystal ball (CB) function in bins of track momentum and polar angle of the ECL shower associated with the electron.

Separation between electrons and muons is quite good for sufficiently energetic particles (i.e. muons with $p > 0.3$ GeV/c which are able to reach the KLM). Separation between electrons and

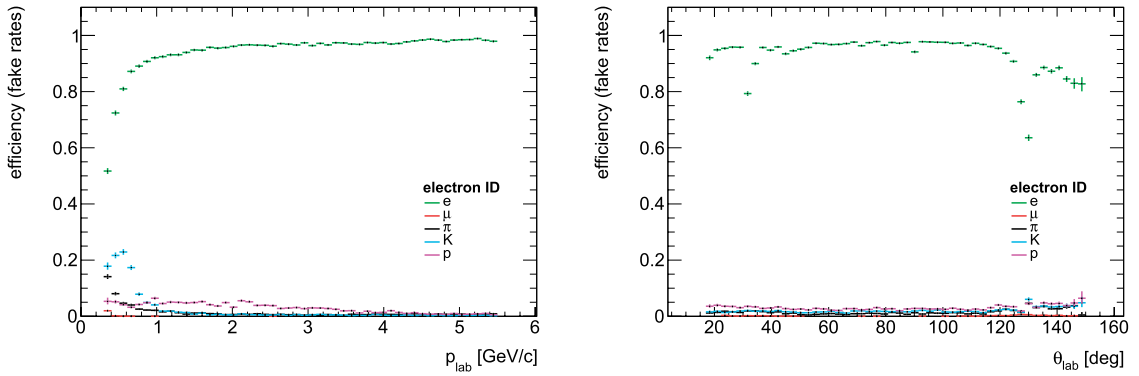

Fig. 25. ECL-only EID efficiency as a function of momentum (left) and as a function of polar angle (right).

pions, however, is much more difficult. This is particularly true for low-momentum particles where, as is seen in Fig. 24, the E/p distributions for differing particle types are very similar. The difficulty in distinguishing electrons from pions is further exemplified in Fig. 25, which shows the electron efficiency for true electrons and true pions as a function of momentum. We see a high electron efficiency and low pion misidentification for momenta $1 \leq p \leq 3\,\mathrm{GeV}/c$. At low momentum, the electron efficiency drastically drops off as the radius of curvature of a low-momentum electron in the presence of the magnetic field is very small. Therefore, for low-momentum electrons, the particle often fails to reach the ECL.

A useful quantity for charged PID is the delta log likelihood value, defined as $\Delta = \ln(\mathcal{L}_e) - \ln(\mathcal{L}_\pi)$, where $\mathcal{L}_e$ is the global electron likelihood and $\mathcal{L}_\pi$ is the global pion likelihood. For true electrons this quantity takes on positive values, while for true pions it takes on negative values. Moreover, we can represent the separation between electrons and pions by considering receiver operating characteristic (ROC) curves of electron efficiency against pion fake rate for various momentum ranges, calculated using the delta log likelihood distributions for true electrons and true pions. Figure 26 shows that the separation between electrons and pions becomes more ambiguous at lower momenta. More sophisticated electron ID algorithms will be considered for Belle II analyses, based on Zernike moments (image moments using Zernike polynomials as basis functions) of lateral shower shapes, longitudinal shower information, track–cluster matching, and corrections for bremsstrahlung.

5.5.5. Combined PID performance

The performance of Belle II PID is estimated using inclusive $e^+e^- \to c\bar{c}$ MC samples. Minimal track quality restrictions are applied. Using the generated information, a sample of each particle type is constructed. The PID efficiency for a sample of particles of type α (π, K, p, e, μ) is determined by taking the ratio of events that have $L(\alpha : \beta) > 0.5$ to the total sample size, for a given β (π, K, p, e, μ). For example, the K/π selection efficiency is given by the fraction of a sample of true kaon tracks that have $L(K : \pi) > 0.5$. In a similar fashion, the pion fake rate is the fraction of a sample of true pion tracks that have $L(K : \pi) > 0.5$. The selection efficiency for various pairs of particle types are given in Figs. 27 and 28. The slight difference in PID performance between the two releases is primarily due to errors in the dE/dx PDFs in release-00-05-03. The performance for release-00-07-00 is a more accurate estimate.

In addition to the efficiency plots, Figs. 29 and 30 show ROC plots for K/π and π/K separation in release-00-05-03 and release-00-07-00, respectively. These plots use kaon and pion samples from

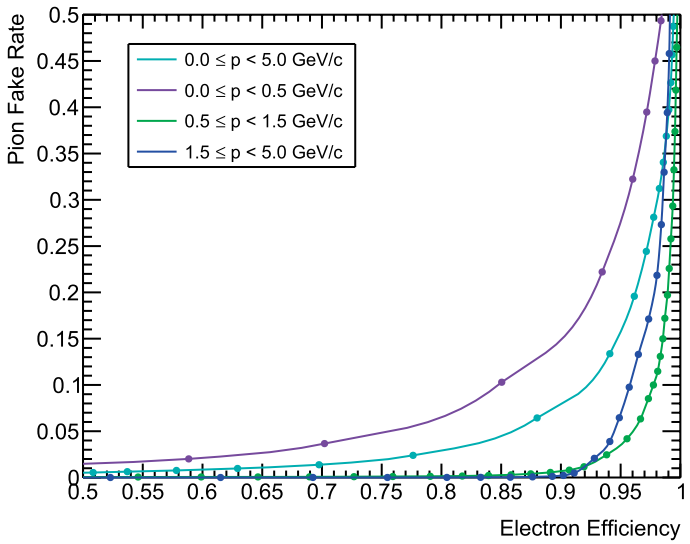

Fig. 26. Electron efficiency against pion fake rate as calculated using the delta log likelihood. This is shown for all particles, low-momentum particles, mid-momentum particles, and high-momentum particles.

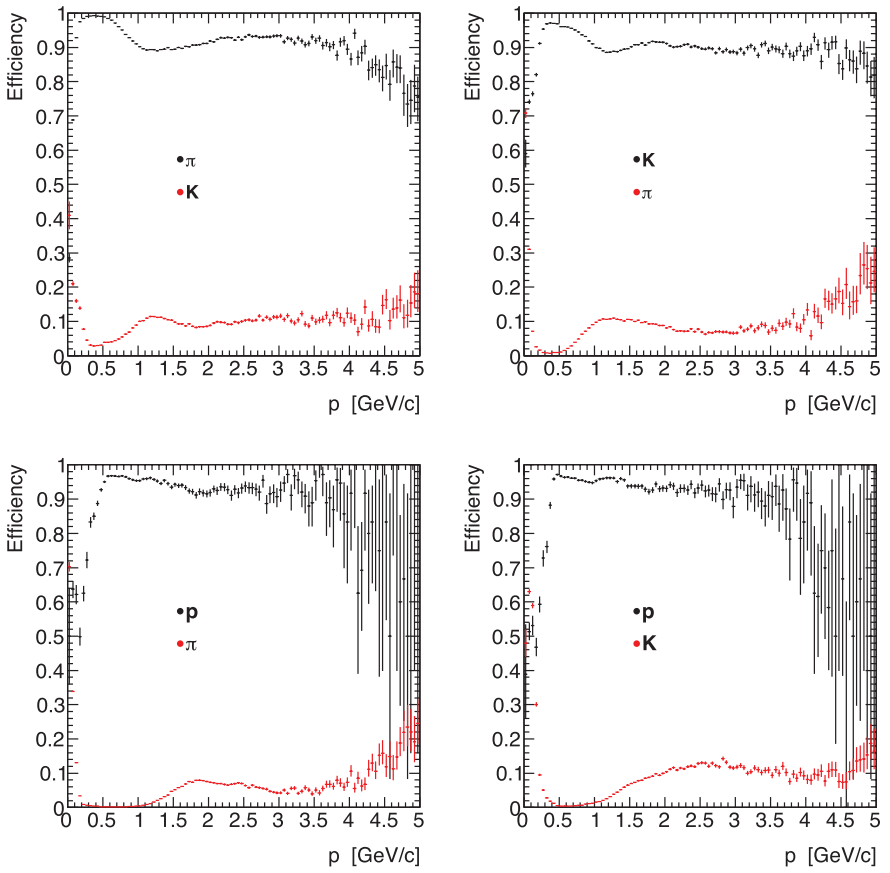

Fig. 27. Charged particle identification selection efficiency for various pairs of particle types as a function of momentum in release-00-05-03. The black markers show the selection efficiency as determined from an inclusive MC sample without beam backgrounds, while the red markers show the fake rate. Only tracks that fall within the acceptance of at least one of the PID detectors or the CDC are considered.

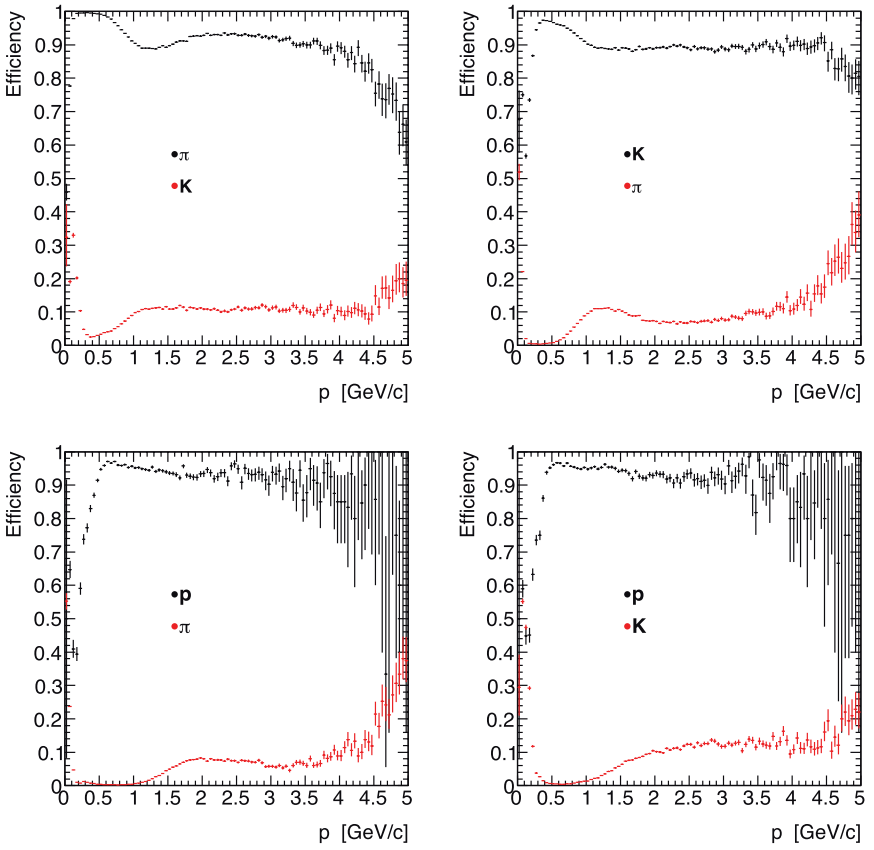

Fig. 28. Charged particle identification selection efficiency for various pairs of particle types as a function of momentum in release-00-07-00. The black markers show the selection efficiency as determined from an inclusive MC sample without beam backgrounds, while the red markers show the fake rate. Only tracks that fall within the acceptance of at least one of the PID detectors or the CDC are considered.

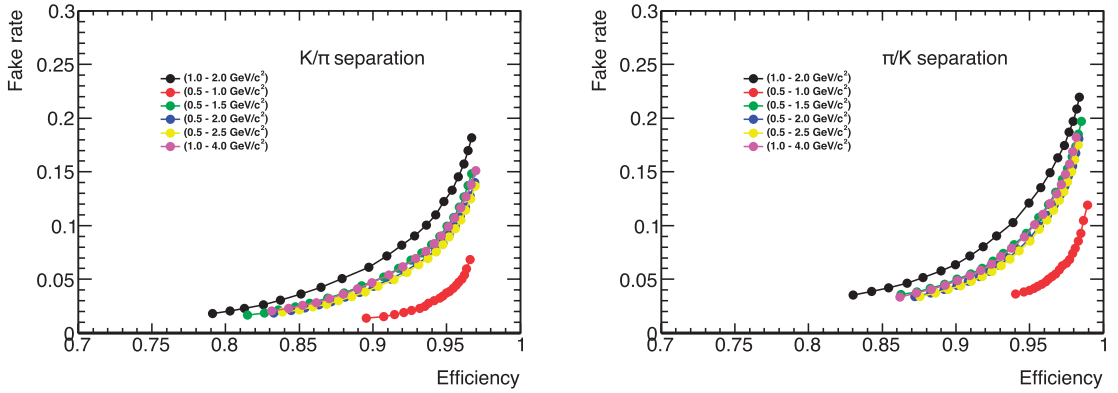

Fig. 29. Fake rates versus efficiencies for K/π (left) and π/K (right) separation in release-00-05-03. The colored lines show the ROC curves for different momentum regions. The markers represent different cuts on the likelihood ratio.

D^* decays to $D^0\pi$ in $\Upsilon(4S)$ MC, where the D^0 decays to $K\pi$. In this way, a relatively clean sample of each particle type can be obtained with minimal selection criteria and without truth information.

The kaon efficiency and pion fake rates using only dE/dx, TOP, and ARICH information respectively is given in Fig. 31. For each sub-detector we show the performance in their respective solid angle acceptance regions.

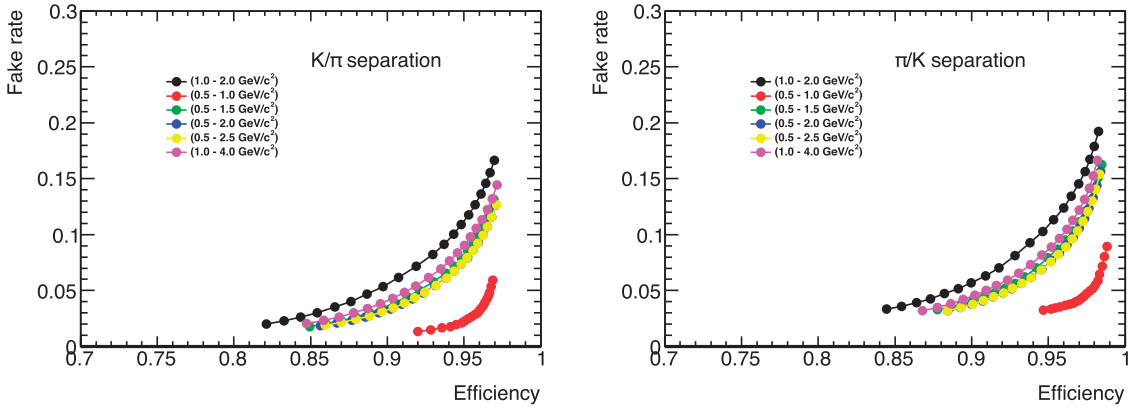

Fig. 30. Fake rates versus efficiencies for K/π (left) and π/K (right) separation in release-00-07-00. The colored lines show the ROC curves for different momentum regions. The markers represent different cuts on the likelihood ratio.

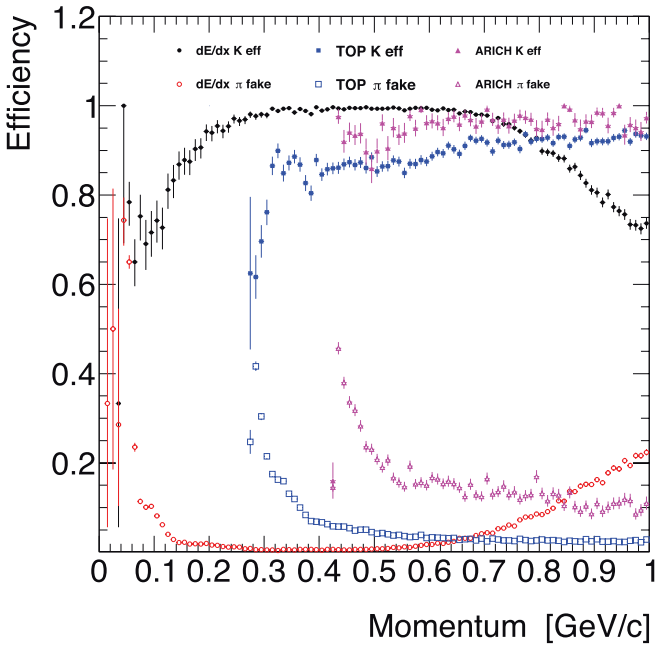

Fig. 31. Kaon detection efficiency and pion fake rate for low-momentum tracks from release-00-05-03. The performance is determined using only those tracks that are within the acceptance of the detector of interest. That is, the denominator for the efficiency is different for each detector.

5.6. Neutral particle identification

5.6.1. Photon and π^0 identification

The identification of photons in the ECL is based on parameters that describe the shower shape of ECL clusters not matched to a reconstructed track. The identification relies on the fact that electromagnetic showers caused by an incident photon are cylindrically symmetric in the lateral direction and the energy deposition decreases exponentially with the distance from the incident axis.

The ECL reconstruction up to release-00-07-02 provides only the energy ratio of the nearest 3×3 to the nearest 5×5 crystals around a local maximum, which is close to unity for true photons. The main background for photon cluster reconstruction comes from neutral or charged hadron interactions. These interactions create asymmetric shower shapes and often result in more than one ECL cluster that is not matched to a charged track, hadronic splitoffs, which yield a large number of fake photon candidates if not identified. The minimal energy of an ECL cluster for physics studies in the presence of nominal backgrounds is 100 MeV in the forward endcap, 90 MeV in the barrel, and 160 MeV in the backward endcap for the original ECL reconstruction. Starting with release-00-08-00, the ECL reconstruction provides additional shower shape variables and the improved clustering algorithm allows lowering of the energy threshold to about 25 MeV. Photon likelihoods based on kinematics, shower shapes, and timing information can be used in the future to provide particle lists of different efficiency and purity.

The reconstruction of π^0 mesons in the decay mode $\pi^0 \to \gamma\gamma$ is based on the combination of two photon candidates. For π^0 energies below about 1 GeV, the angular separation between the two photons is usually large enough to produce two non-overlapping ECL clusters. For π^0 energies above about 1 GeV but below about 2.5 GeV, the ECL clusters from the two photons overlap but can still be reconstructed as two separate photon candidates in the ECL. The π^0 energy can be directly reconstructed from the photon four-momenta. The π^0 energy resolution is improved by performing a mass-constrained fit of the two photon candidates to the nominal π^0 mass. Multivariate classifiers can be used to provide higher-purity π^0 particle lists. A low photon energy threshold is mandatory to obtain a high π^0 efficiency for generic B decays: a 50 MeV threshold for both photons results in a π^0 efficiency of 76%, 30 MeV in 93%, and 20 MeV in 98%.

For π^0 energies above about 2.5 GeV, e.g. from $B \to \pi^0\pi^0$, the two photon-induced showers often do not have separate local maxima any more and are reconstructed as one photon candidate. The π^0 energy can be deferred from the shower's second-moment shape variable.

5.6.2. K_L^0 identification

The identification of K_L^0 mesons is based on information collected by the KLM and ECL detectors. The detector material of the KLM provides > 3.9 hadronic interaction lengths (λ_0) and the ECL provides $\sim 0.8\lambda_0$. Multivariate methods are used to classify ECL clusters and KLM clusters according to their probability of originating from a K_L^0. Classifiers are constructed from stochastically gradient-boosted decision trees (BDT), implemented as described in Ref. [70]. The classification is performed separately for the KLM and ECL in the reconstruction package of `basf2`. The classifiers are trained on a K_L^0 target in $\Upsilon(4S)$ events and their output is normalized to $x \in (0, 1)$. In general, K_L^0 mesons are not easy to classify as their signal in the detector is not mutually different from other more common neutral particles such as neutrons, π^0, and photons (in the ECL). The largest contributions to the background are from neutrons and photons originating from beam interactions with detector or beam pipe material, followed by neutral particles from the primary interaction. However, the classifiers still outperform the K_L^0 identification algorithms of Belle by a factor of ~ 2, assuming generic events without preselection.

Variables used in the classifications The classifiers are fed with all the information that is available, including cluster shapes, kinematic variables, and information gained from other detectors and algorithms. There is no single variable that provides significant separation power alone. The three most important variables that have the best proven separation in the KLM are as follows:

- Distance to the next track: neutral clusters are not likely to have a nearby track.
- Cluster timing: fake clusters from beam background are likely not to be in time with the primary collision.
- Number of innermost layers hit: hadronic clusters are likely to have a wider radius than electromagnetic clusters.

In total, 19 variables are used for this classifier.

In the ECL the most significant variables are as follows:

- Distance to the next track: neutral clusters should only rarely have a track close by.
- Energy in the central 9 crystals divided by the energy in the outer 21: the shape depends on whether it is a hadronic or electromagnetic cluster.
- Total energy deposition in the cluster: each K_L^0 deposits very little energy in the clusters, typically in the < 50 MeV range.

For this classifier, a total of 38 variables including shower shapes, ECL cluster Zernike polynomials, and kinematic variables were investigated.

Performance of the classifiers The classifier performance is evaluated on $\Upsilon(4S) \to \bar{B}B$ events. The background rejection versus efficiency behavior of the classifiers is depicted in Fig. 32. Fake rates and efficiencies of the classifications depend on the chosen working point (threshold). The optimal threshold value depends on the desired performance and the type or size of the background. The fake rates and efficiencies for the arbitrary threshold are depicted in Fig. 33. In general, the K_L^0 classification performance depends on the background level and composition, the magnetic field map, and the tracking performance.

6. Physics analysis software

Section authors: F. Abudinen, L. Li Gioi, P. Goldenzweig, T. Keck, F. Tenchini, D. Weyland, A. Zupanc.

6.1. Introduction

The physics analysis software of Belle II makes use of the available data to perform efficient, reproducible measurements of physical quantities of interest, minimizing both statistical and systematic uncertainties. The analysis software contains commonly used analysis tools allowing easy, efficient, and accurate data analysis. Here we focus on novel innovations on vertex fitting, $q\bar{q}$ continuum suppression, flavor tagging, and full B reconstruction algorithms for missing energy analyses. For each of these algorithms we provide the respective expected performance at Belle II, and in some cases make comparisons to Belle.

6.2. Vertex reconstruction

Vertex reconstruction is the procedure by which the parameters of a decay vertex or interaction vertex are determined from the reconstructed parameters of the outgoing particles. It deals both with finding (pattern recognition) and with fitting the interaction vertices. It extracts the vertex position and recalculates the momentum and the invariant mass of the decaying particle, using the modified daughters' momenta after the vertex reconstruction. The decay length of an unstable particle inside a decay chain or the decay time difference, Δt, between the two B mesons from an $\Upsilon(4S)$ decay can also be computed using a vertex fitter.

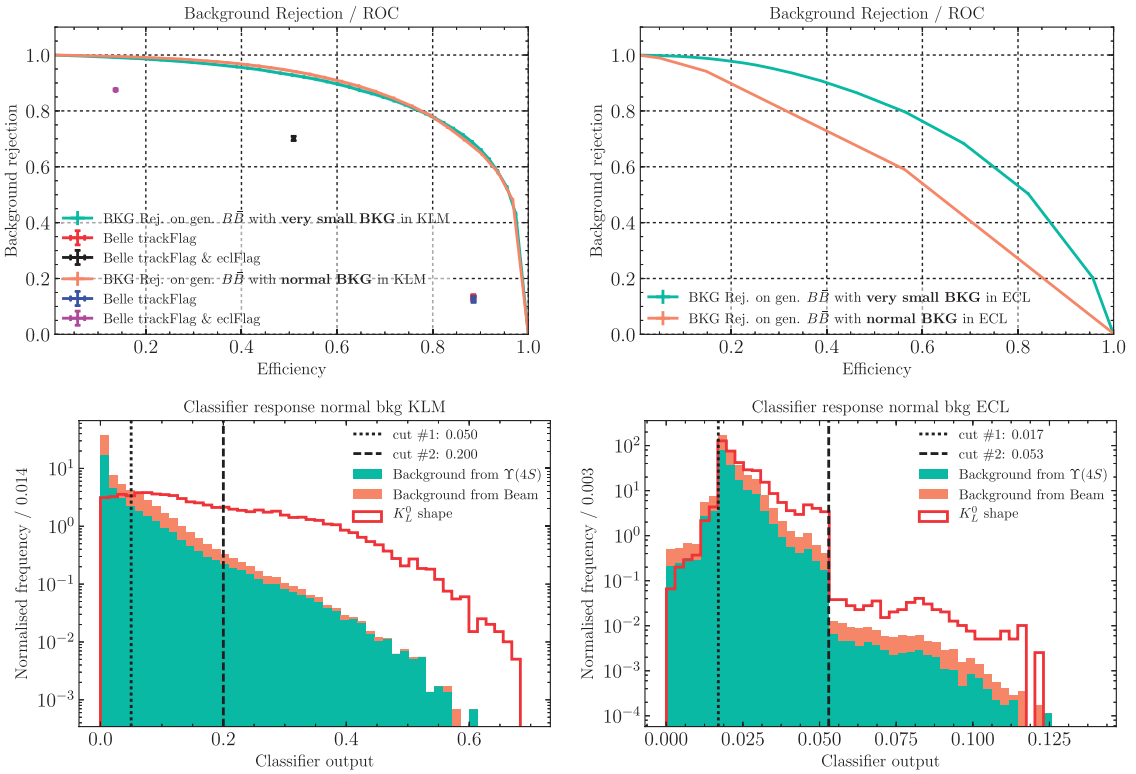

Fig. 32. (a) Efficiency–background rejection behavior of the K_L^0 KLM classifiers for nominal (orange) and small (green) background levels. For each background level, a classifier was trained and tested. The expected performance using the deprecated Belle algorithms for small and nominal background levels are depicted as data points. (b) Efficiency–background rejection behavior of the ECL classifiers for different levels of beam background. (c) Output distribution of the KLM classifier. (d) Output distribution of the ECL classifier. The vertical lines (cuts) displayed in the classifier outputs will be used for performance evaluation in Fig. 33.

6.2.1. Vertex-finding algorithms

The Belle II experiment has deployed three implementations of a vertex fit: `KFitter`, developed for the Belle experiment, `RAVE` [59], a standalone package originating from the CMS vertex-fitting libraries, and `TreeFitter` [71], initially conceived by the BaBar collaboration. We use both `KFitter` and `RAVE` for kinematic fits and `RAVE` for geometric fits. `TreeFitter` is used for fitting entire decay chains.

Kinematic fits Kinematic fitting uses the known properties of a specific decay chain to improve the measurements of the process. Lagrangian multipliers are used in order to impose the kinematic constraints to the fit. Given the measurements $\mathbf{q} = (q_1, \ldots, q_n)$ with a covariance matrix V and kinematic constraints $\mathbf{h}(\mathbf{q})$, the function to be minimized in terms of the most suitable vertex is

$$\chi^2 = (\mathbf{q} - \bar{\mathbf{q}})^{\mathrm{T}} V^{-1} (\mathbf{q} - \bar{\mathbf{q}}) + 2\lambda^{\mathrm{T}} (\mathbf{D}\boldsymbol{\delta}\mathbf{y} + \mathbf{h}(\mathbf{q})), \tag{15}$$

where λ is the Lagrange multiplier, $\mathbf{h}(\bar{\mathbf{q}}) = 0$, and $\mathbf{D} = \partial\mathbf{h}/\partial\mathbf{y}$. Here, $\bar{\mathbf{q}}$ represents the improved measurements, $\mathbf{D}$ is the kinematic constraint at the starting value, and $\boldsymbol{\delta}\mathbf{y}$ is the difference between the improved measurement and the starting value.

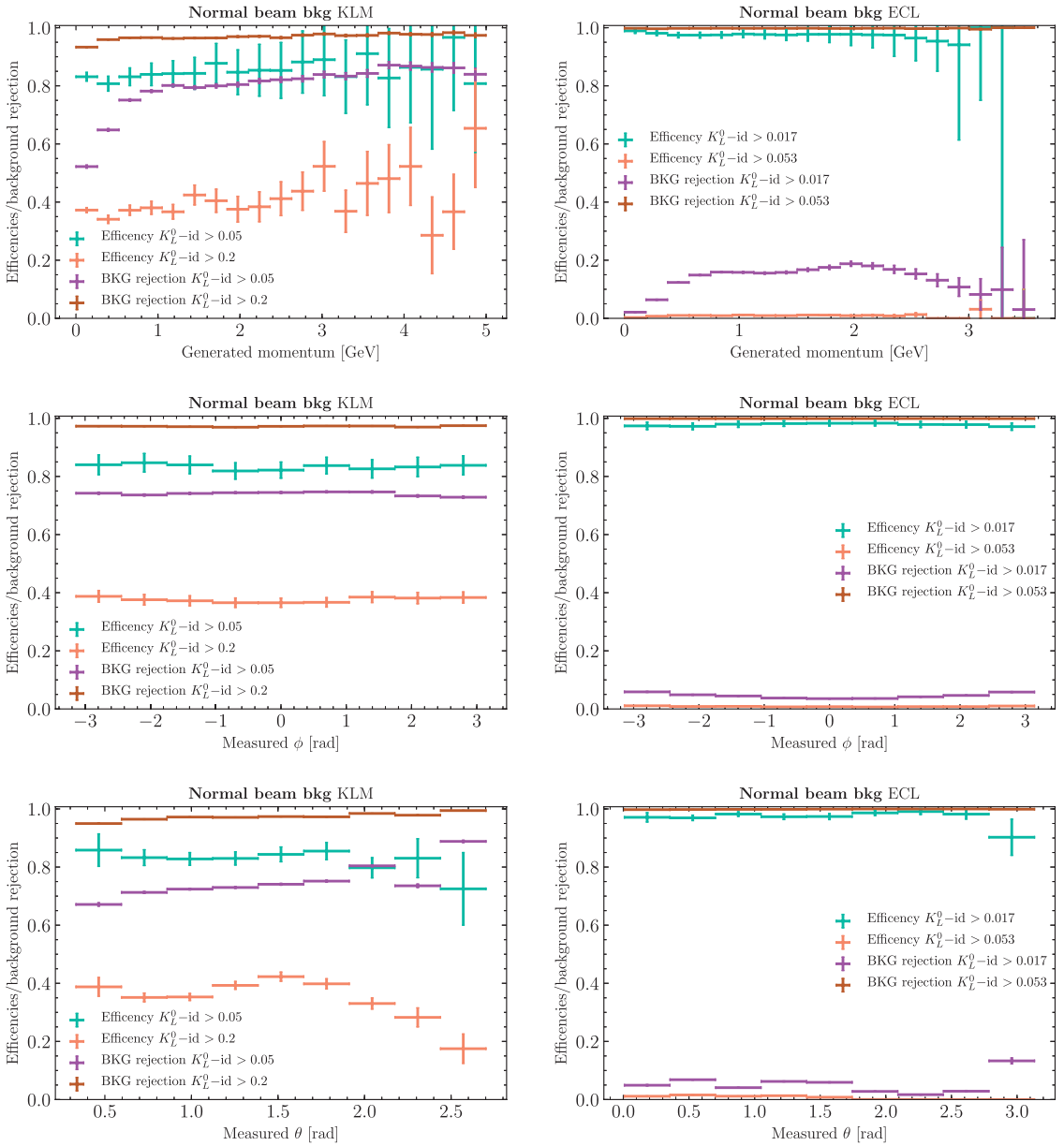

Fig. 33. K_L^0 classification performance in KLM (left column) and ECL (right column): background rejection and efficiencies are depicted for arbitrary thresholds on the classifier output, measured in bins of generated momentum (first row), ϕ (second row), and θ (last row). The classifiers used were trained and evaluated on nominal beam background levels. The choice of the thresholds is depicted in Fig. 32.

Adaptive vertex fit The RAVE libraries [59,72] introduce the concept of soft assignment: a track is associated to a specific vertex with an assignment probability or weight w_i [72]:

$$w_i(\chi_i^2) = \frac{e^{-\chi_i^2/2T}}{e^{-\chi_i^2/2T} + e^{-\sigma_{\text{cut}}^2/2T}}, \tag{16}$$

where χ_i^2 is the square of the standardized residual, σ_{cut} is defined as the standardized residual for which $w_i = 0.5$, and the temperature parameter T defines the softness of the weight function.

The fitter is then implemented as an iterated, reweighted Kalman filter [69]: in every iteration new track weights are computed and the vertex is estimated using these weights. This weight can be

interpreted as a track-to-vertex assignment probability. Instead of minimizing the least squares sum, as is expected from a Kalman fitting method, the algorithm minimizes the weighted least squares sum. In order to avoid falling prematurely into local minima, a deterministic annealing schedule is introduced; in each iteration step the temperature parameter is lowered [72]:

$$T_i = 1 + r \cdot (T_{i-1} - 1), \tag{17}$$

where T_i is the temperature parameter T at iteration i and r denotes the annealing ratio. For convergence, $0 < r < 1$ is needed.

Decay chain fitting The typical approach when reconstructing a decay chain is to start fitting final state particles, building the tree from the bottom up until the head of the decay is reached. This approach is generally valid, but may not always be optimal.

The `TreeFitter` module implements an alternate approach [71] where the decay tree is parameterized and fitted globally. This allows for the sharing of information across the tree, improving vertices that would otherwise be badly resolved or even impossible to fit without additional conditions such as mass constraints. This approach is especially useful to succesfully fit decay channels that are rich in neutral or missing particles, and also provides the analyst with the full decay covariance matrix, which is beneficial for error treatment in time-dependent Dalitz analyses.

Since the whole tree is parameterized, a naive χ^2 minimization would naturally involve the inversion of large matrices, making the fit computationally very expensive. This problem is solved by applying the constraints to the fit individually using a Kalman gain formalism, which reduces execution times to a manageable level. The computational speed of `TreeFitter` then becomes comparable to `KFitter` when fitting individual vertices, and scales roughly quadratically with the complexity of the decay. When fitting a typical-sized decay tree, execution times are comparable to `RAVE`.

6.2.2. *Decay vertex*

Decay vertex positions are usually determined using kinematic vertex fits. As a benchmark for testing the Belle II vertex reconstruction performance, we use the decay vertex of the J/ψ in the $B^0 \to J/\psi K^0_S$ decay mode. Figure 34 shows the fit residuals of the z component of the fitted J/ψ vertex position. A resolution of 26 μm is obtained. The same vertex fit performed using Belle MC returns a resolution of 46 μm, which is almost twice as large. The improvement seen is consistent with the expected improvement in the impact parameter resolution (Sect. 5.3.1) due to the Belle II PXD.

6.2.3. *Tag-side B vertex fitting*

To be sensitive to time-dependent CP-violating effects, the vertex resolution must be sufficient to resolve the oscillations of neutral B mesons. The measurement of the distance between their decay vertices uses the relation

$$\Delta t \equiv t_{\text{rec}} - t_{\text{tag}} = \Delta l / \beta\gamma c, \tag{18}$$

where t_{rec} (t_{tag}) is the decay time of the fully reconstructed (tag) B meson and Δl is the distance between the two B decay vertices in the boost direction. The largest contribution to the Δt resolution

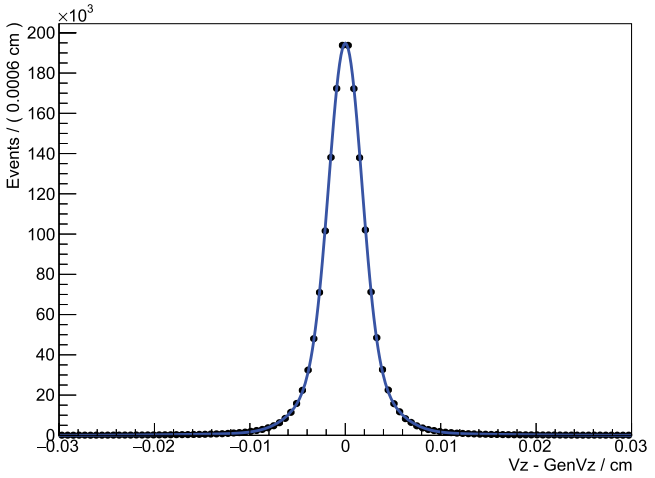

Fig. 34. $J/\psi \to \mu^+\mu^-$ vertex fit residuals: resolution = 26 μm. The fit is performed using the sum of three Gaussian functions. The values of the shift and resolution are defined as the weighted averages of the mean values and the standard deviations of the three functions.

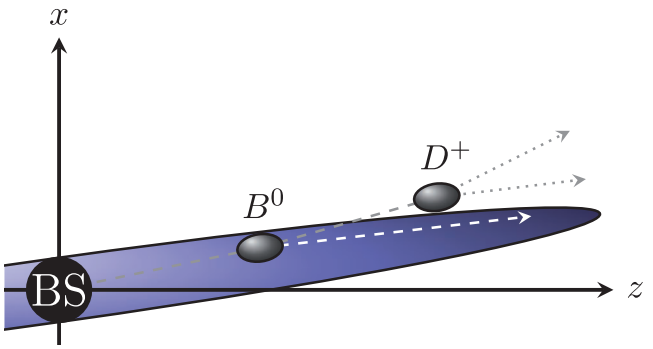

Fig. 35. Schematic representation of the tag B vertex fit. The B meson will have a higher vertex fit probability than the D meson originating from the B. BS denotes the beam spot.

comes from the tag B vertex fit. In the decay tree of a B meson we can divide the tracks into three groups: tracks originating from the B decay, including the ones coming from decay vertices indistinguishable from the B (e.g. μ^+ and μ^- in $B^0 \to [J/\psi \to \mu^+\mu^-]K^0_S$); tracks originating from D mesons; and tracks originating from K^0_S decays. We fit the tag-side B using the `RAVE` adaptive vertex fit algorithm. This takes as input all tracks with at least one hit in the PXD that are not used for the signal-side B candidate, except from the tracks attributed to K^0_S candidates. In the case of a non-converging fit, tracks that do not have associated PXD hits are also used.

To reduce the weight of the tracks originating from D mesons, we constrain the fit to a region defined by an ellipsoid around the boost direction (Fig. 35), where the B is more likely to decay rather than D mesons that carry more transverse momentum. This constraint acts as a weight in the final χ^2.In the case of a non-converging fit, the constraint is redefined, enlarging its size in the boost direction, becoming virtually equivalent to a cylinder.

We obtain, for the tag-side vertex fit of correctly reconstructed B mesons, a bias of 6 μm and a resolution of 53 μm, independent of the signal B decay mode. The total efficiency is 96%, constant as a function of Δt. Figure 36 (left) shows the residuals of the tag B vertex fit of fully reconstructed $B^0 \to [J/\psi \to \mu^+\mu^-][K^0_S \to \pi^+\pi^-]$.

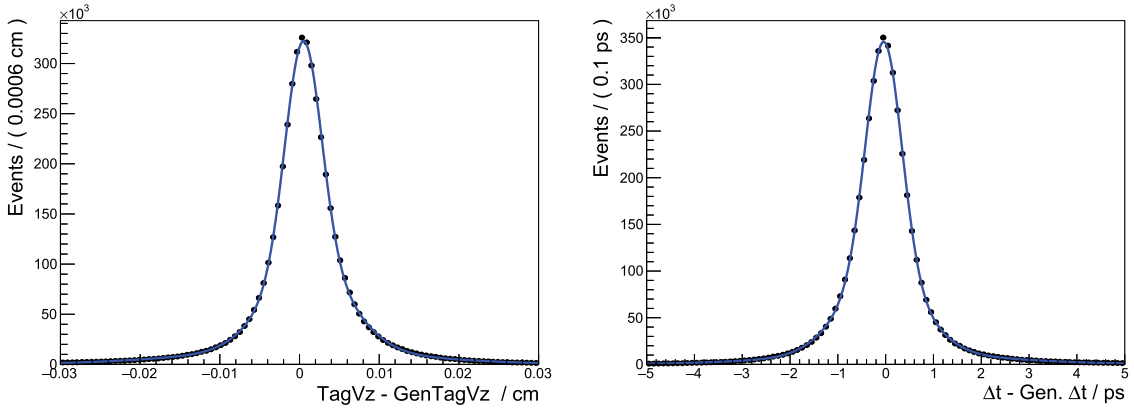

Fig. 36. The tag-side vertex fit residuals (left), with bias = 6 μm and resolution = 53 μm, and the Δt residuals (right), with bias = -0.03 ps, resolution = 0.77 ps, for the fully reconstructed $B^0 \to [J/\psi \to \mu^+\mu^-][K^0_S \to \pi^+\pi^-]$. Both fits are performed using the sum of three Gaussian functions.

The sensitivity to the time-dependent CP-violating parameters of Eq. (296) in Sect. 10.1 strongly depends on the resolution of the Δt measurement, Eq. (18). The lower boost of SuperKEKB, with respect to KEKB, produces an average distance between the two B mesons of about 130 μm, 35% compared to 200 μm at KEKB. This makes it more difficult to resolve the decay vertices of the two B mesons and it is one of the main motivations for the development of the Belle II PXD. The new hardware, together with the new vertex reconstruction algorithms, provide an improvement in the vertex resolution of both B mesons. This translates to a Δt resolution of 0.77 ps and a bias of -0.03 ps, which provides superior separation capability compared to Belle (resolution = 0.92 ps, bias = 0.2 ps), exceeding the design requirements. Figure 36 (right) shows the Δt residuals of $B^0 \to [J/\psi \to \mu^+\mu^-][K^0_S \to \pi^+\pi^-]$.

6.3. Composite particle reconstruction

In the Belle II experiment, short-lived particles decaying at or near the interaction point (such as B mesons or charm hadrons) cannot be measured directly by the sub-detectors, but instead must be reconstructed from the four-momenta of their long-lived decay products. Discriminating variables sensitive to composite particle properties can be subsequently built from final state information in order to perform background separation. A few such quantities are discussed in this section.

6.3.1. Invariant mass resolution

One of the simplest ways to reduce background, in particular that of the combinatorial kind, is to introduce selection criteria based on the invariant mass of intermediate particles in the decay chain.

The relative mass resolution achievable by Belle II can be estimated by performing a vertex fit of multiple resonances (J/ψ, $\psi(2S)$, $\Upsilon(1S)$, and $\Upsilon(2S)$) decaying into a di-muon state, as shown in Fig. 37. This takes advantage of the common kinematics shared by the final states. True muons from MC are selected from well-reconstructed tracks originating from the interaction region.

The resulting mass resolution is summarized as a function of mass in Fig. 38. The projected resolution is $\sim$0.2% for charmonium and $\lesssim$ 0.3% for bottomonium resonances, with a 30% improvement compared to Belle. This largely originates from the improved transverse momentum, p_T, resolution provided by the Belle II CDC.

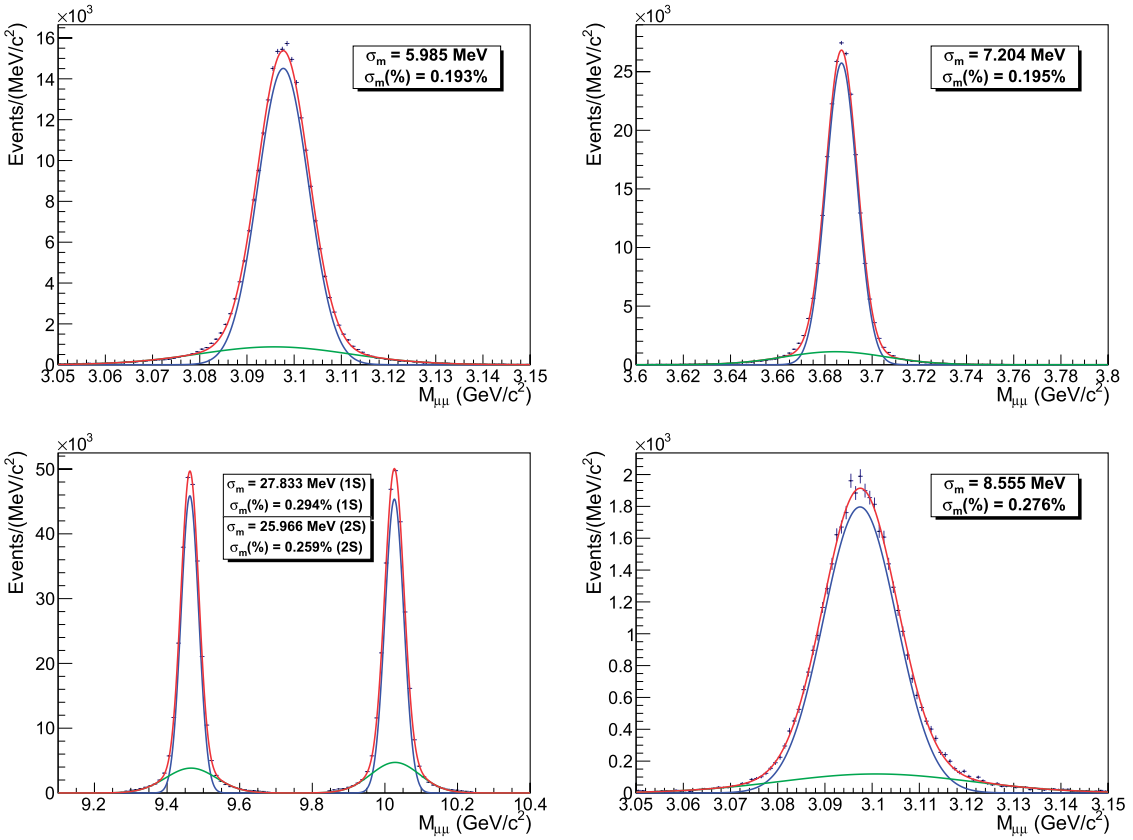

Fig. 37. Mass vertex fit residuals for di-muon resonances in Belle II: J/ψ (top left), $\psi(2S)$ (top right), $\Upsilon(1S/2S)$ (bottom left); and Belle: J/ψ (bottom right). The fit is performed using the sum of two Gaussian functions.

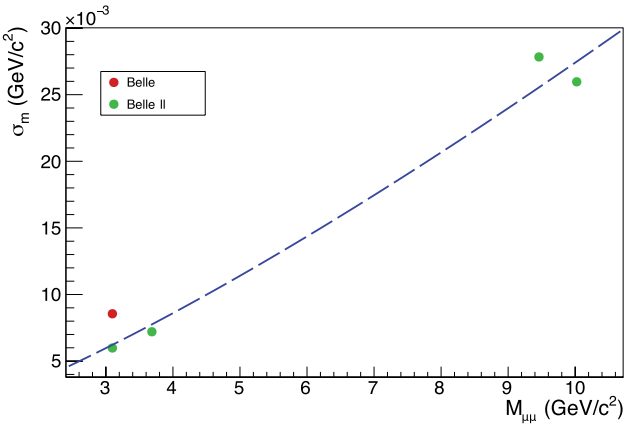

Fig. 38. Mass resolution as a function of resonant mass for Belle II (green) and Belle (red) MC. An empirical power-law curve is fitted through the points.

6.3.2. Beam-constrained fits

When performing vertex reconstruction, knowledge of the production vertex can be used as an additional constraint to improve the fit resolution if the vertex is not well constrained. One example is the $D^{*+} \to D^0\pi^+$ decay, where the low-momentum pion track is very sensitive to multiple

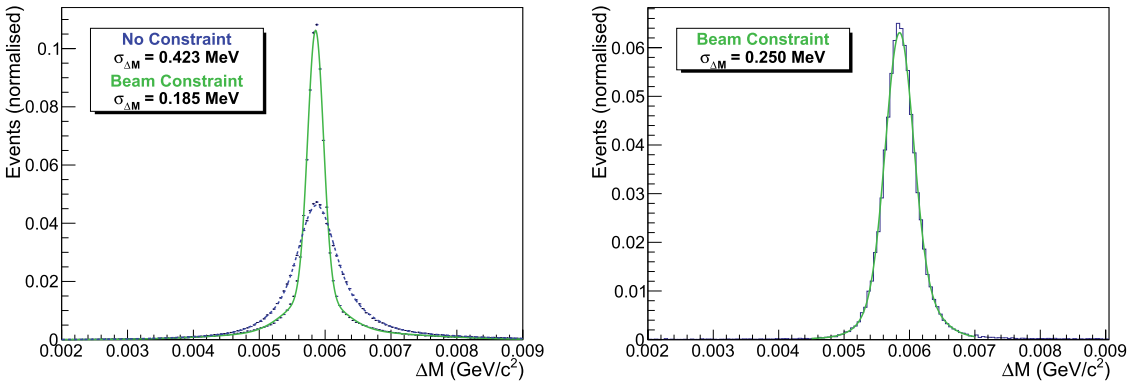

Fig. 39. Mass difference resolution for $D^{*+} \to [D^0 \to K^+\pi^-]\pi^+$ simulated events in Belle II (left) and Belle (right). The distribution for unconstrained vertices is shown in blue while those with beam spot constraints are in shown in green.

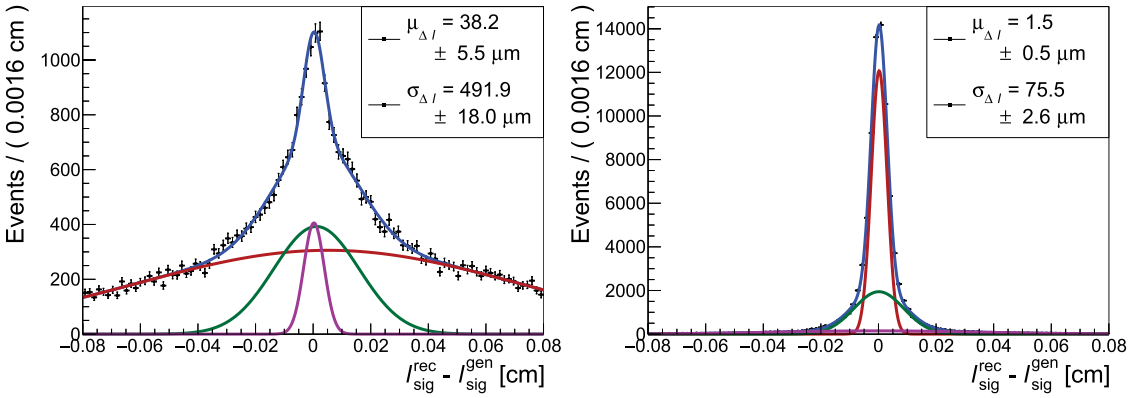

Fig. 40. B^0 vertex resolution in the boost direction of $B^0 \to \pi^0\pi^0$ with one of the two π^0 mesons decaying via the Dalitz channel $\pi^0 \to e^+e^-\gamma$ for the unconstrained fit (left), and `IPTube`-constrained fit (right).

scattering, while the D^0 vertex fit only provides a directional constraint. Requiring the D^{*+} to originate from the beam spot substantially improves the vertex resolution.

We test the impact of this constraint by using the $D^{*+} \to [D^0 \to K^-\pi^+]\pi^+$ decay. The mass difference resolution is pictured in Fig. 39 with and without the beam constraint applied; the fit resolution is significantly improved. A comparison to a beam-constrained Belle fit of the same decay is provided, where the achievable mass resolution shows a 27% improvement.

In time-dependent analyses, good vertex resolution in the boost direction is key for the measurement of CP parameters. Performing the vertex fit with a constraint parallel to the boost direction can improve the vertex resolution in all cases where the direction of the momentum cannot be precisely extracted from the track fit results. This type of fit is also needed when only one (pseudo-)track is available for the determination of the vertex. The `RAVE` fitter defines the `IPTube` constraint as an ellipsoid with a very long axis in the direction of the boost with the size of the beam spot in the orthogonal directions. Figure 40 shows the results of the B^0 vertex resolution in the boost direction of $B^0 \to \pi^0\pi^0$ with one of the two π^0 mesons decaying via the Dalitz channel $\pi^0 \to e^+e^-\gamma$. An improvement of 85% in the vertex resolution is observed when using the `IPTube` constraint.

6.3.3. *Beam-constrained observables*

Rather than using the B invariant mass, e^+e^- B factories provide an additional energy- and mass-like constraint that can be used for background separation. B mesons produced at the $\Upsilon(4S)$ resonance have well-defined kinematics which are constrained by the mass of the $\Upsilon(4S)$ and by the properties of the beam.

The reconstructed invariant mass of the single B system must be equal to the nominal B meson mass m_B, while the total energy should be equal to the beam energy when reconstructed in the rest frame, $E^*_{\rm beam} = \sqrt{s}/2$. Two new variables can be defined using these constraints: the energy difference ΔE and the beam-energy-constrained mass $M_{\rm bc}$. ΔE is defined as

$$\Delta E = E^*_B - E^*_{\rm beam} = (2p^\mu_B p^\mu_{\rm boost} - s)/2\sqrt{s}, \tag{19}$$

where p^μ_B and $p^\mu_{\rm boost}$ are the four-momenta of the B meson and the e^+e^- system, respectively. The beam-energy-constrained mass is constructed by substituting the B energy with the beam energy in the invariant mass calculation:

$$M_{\rm bc} = \sqrt{E^{*2}_{\rm beam} - \mathbf{p}^{*2}_B}. \tag{20}$$

For a correctly reconstructed B meson decay, the true values would be $\Delta E = 0$ and $M_{\rm bc} = m_B$. Figure 41 shows the distribution of these observables for two sample decay channels, $B^+ \to [D^0 \to K^-\pi^+]\pi^+$ and $B^+ \to [D^0 \to K^-\pi^+\pi^0]\pi^+$, for both Belle and Belle II MC. As we can see, the performance in channels such as $D^0 \to K^-\pi^+$ is comparable between the two experiments. On the other hand, modes with neutral pions such as $D^0 \to K^-\pi^+\pi^0$ show a significant improvement in the latest versions of the Belle II software, owing to lower bias on the photon position determination (see Sect. 5.4). The improvement on the distribution core is ∼20% on $M_{\rm bc}$ and ∼50% on ΔE for this particular channel. Improvements in neutral particle reconstruction directly affect reconstruction in modes where they are present.

6.4. *Continuum suppression*

The dominant source of combinatorial background in B physics analyses at Belle II comes from $e^+e^- \to q\bar{q}$ ($q = u, d, s, c$) events, where random combinations of particles in the final state may mimic the kinematic signatures of the signal. These events are referred to as "continuum background." In charmless B decay ($b \to u, s$) channels, combinatorial background from continuum events is often the dominant source of background. Continuum suppression is also important in controlling potential systematic uncertainties in precision measurements of charm $b \to c$ decay modes.

The *Physics of the B Factories* book provides a comprehensive review of the variables and methods employed by the Belle and BaBar collaborations to suppress continuum background [2]. While the definitions of many of the variables used in Belle II are identical to those in Belle, the implementation often differs. For example, in Belle II we introduce deep-learning techniques that use detector-level (DL) information as input for classification. In the following subsections we first briefly review the traditional, engineered variables (E) used in continuum suppression in both Belle and Belle II, as described in Ref. [2]. We then introduce the DL variables, and compare the performance of various configurations of input variables and classifier algorithms (hereby referred to as classifiers), namely

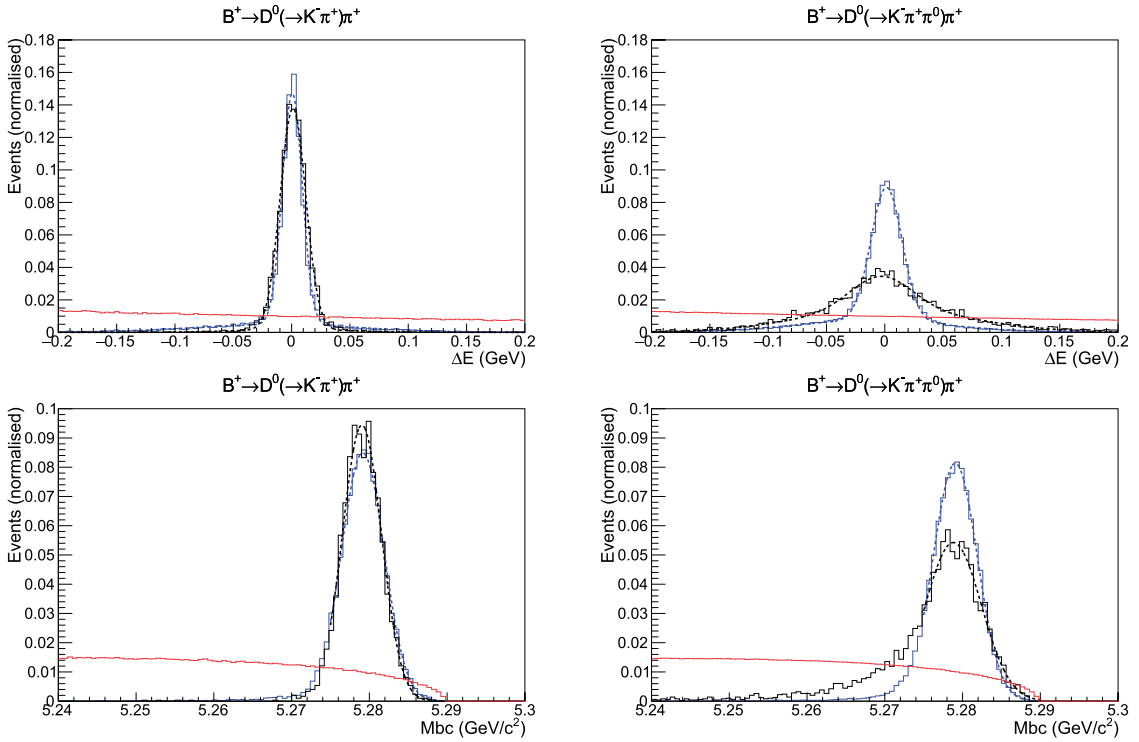

Fig. 41. ΔE and $M_{\rm bc}$ distributions for $B^+ \to [D^0 \to K^-\pi^+(\pi^0)]\pi^+$ simulated events in Belle II (blue) in comparison with Belle (black). The red curve shows the distribution for continuum background. Beam background is included in the simulation.

boosted decision trees (BDTs) and deep neural networks (DNNs).[7] All results are obtained using MC simulated $B^0 \to K^0_S\pi^0$ events for signal and MC simulated continuum events for background.

6.4.1. Engineered variables

B meson direction Using the angle θ_B between the reconstructed momentum of the B candidate (computed in the $\Upsilon(4S)$ reference frame) and the beam axis, the variable $|\cos\theta_B|$ allows one to discriminate between signal B decays and the B candidates from continuum background. The spin-1 $\Upsilon(4S)$ decaying into two spin-0 B mesons results in a $\sin^2\theta_B$ angular distribution with respect to the beam axis; in contrast, for $e^+e^- \to f\bar{f}$ events the spin-1/2 fermions $f\bar{f}$ and the two resulting jet-like structures are distributed according to a $1 + \cos^2\theta_B$ distribution.

Thrust For a collection of N momenta $\vec{p}_i$ $(i = 1, \ldots, N)$, the thrust axis $\vec{T}$ is defined as the unit vector along which their total projection is maximal. The thrust scalar T (or thrust) is defined as

$$T = \frac{\sum_{i=1}^{N} |\vec{T} \cdot \vec{p}_i|}{\sum_{i=1}^{N} |\vec{p}_i|}. \tag{21}$$

The thrust of both the B (T_B) and the rest of the event (ROE) ($T_{\rm ROE}$) provide discrimination between signal and continuum background.

[7] For a comprehensive study, see Ref. [73].

Thrust angles A useful related variable is $|\cos\theta_{\rm T}|$, where $\theta_{\rm T}$ is the angle between the thrust axis of the momenta of the B candidate decay's final state particles (all evaluated in the $\Upsilon(4S)$ rest frame) and the thrust axis of the ROE. For a $B\bar{B}$ event, both B mesons are produced almost at rest in the $\Upsilon(4S)$ rest frame, so their decay particles are isotropically distributed and their thrust axes are randomly distributed. Therefore, $|\cos\theta_{\rm T}|$ follows a uniform distribution in the range $[0, 1]$. In contrast, for $q\bar{q}$ events, the momenta of particles follow the direction of the jet-like structures in the event, and as a consequence the thrusts of both the B candidate and the ROE are strongly directional and collimated, yielding a $|\cos\theta_{\rm T}|$ distribution strongly peaked at large values.

Another thrust-related variable is $\theta_{\rm T,B}$, the angle between the thrust axis of the B decay particles and the beam axis; for $B\bar{B}$ events $|\cos\theta_{\rm T,B}|$ is uniformly distributed, while for continuum events the thrust of particle momenta from the B candidate tends to follow a $1+\cos^2\theta_{\rm T,B}$ distribution followed by the jet-like structures.

CLEO cones The CLEO collaboration introduced variables based on the sum of the absolute values of the momenta of all particles within angular sectors around the thrust axis in intervals of 10°, resulting in nine concentric cones [74]. The cone in the direction of the thrust axis is merged with the respective cone in the opposite direction. There are two options for constructing the CLEO cones in Belle II: they can be calculated from all final state particles in the event, or from only ROE particles.

Fox–Wolfram moments For a collection of N particles with momenta p_i, the lth-order Fox–Wolfram moment H_l [75] is defined as

$$H_l = \sum_{i,j}^{N} |p_i|\,|p_j|\,P_l\left(\cos\theta_{i,j}\right), \tag{22}$$

where $\theta_{i,j}$ is the angle between p_i and p_j, and P_l is the lth-order Legendre polynomial. In the limit of vanishing particle masses $H_0 = 1$, which is why the normalized ratio $R_l = H_l/H_0$ is often used, so that for events with two strongly collimated jet-like structures, R_l takes values close to zero (one) for odd (even) values of l. These sharp signatures provide convenient discrimination between events with different topologies. The variable R_2 is a strongly discriminating variable, commonly used in B physics analyses.

Modified Fox–Wolfram moments The Belle collaboration developed the modified Fox–Wolfram moments H_{xl}^{so} and H_l^{oo} ($l \in [0, 4]$), where all reconstructed particles in an event are divided into two categories: B candidate daughters (denoted as s) and particles from the ROE (denoted as o). The H_{xl}^{so} moments are decomposed into an additional three categories (denoted as x) depending on whether the particle is charged ($x = c$), neutral ($x = n$), or missing ($x = m$). Additionally, for H_{xl}^{so}, the missing momentum of an event is treated as an additional particle. For even l,

$$H_{xl}^{so} = \sum_{i}\sum_{jx} |p_{jx}| P_l(\cos\theta_{i,jx}), \tag{23}$$

where i runs over the B daughters, jx runs over the ROE in the category x, p_{jx} is the momentum of particle jx, and $P_l(\cos\theta_{i,jx})$ is the lth-order Legendre polynomial of the cosine of the angle between

particles i and jx. For odd l, we have $H^{so}_{nl} = H^{so}_{ml} = 0$ and

$$H^{so}_{cl} = \sum_i \sum_{jx} Q_i Q_{jx} |p_{jx}| P_l(\cos\theta_{i,jx}), \tag{24}$$

where Q_i and Q_{jx} are the charges of particles i and jx, respectively. There are a total of 11 H^{so}_{xl} moments: two for $l = 1, 3$ and nine (3×3) for $l = 0, 2, 4$.

The definitions of the five H^{oo}_l moments are as follows:

$$H^{oo}_l = \begin{cases} \sum_j \sum_k |p_j||p_k| P_l(\cos\theta_{j,k}) & (l \text{ even}), \\ \sum_j \sum_k Q_j Q_k |p_j||p_k| P_l(\cos\theta_{j,k}) & (l \text{ odd}), \end{cases}$$

where j and k run over the ROE and the other variables are the same as in Eq. (24). The H^{so}_{xl} and H^{oo}_l moments are normalized to $H^{\max}_0$ and $\left(H^{\max}_0\right)^2$, respectively, where $H^{\max}_0 = 2\left(E^*_{\text{beam}} - \Delta E\right)$, to not depend on ΔE.

There are two options for constructing the modified Fox–Wolfram moments: they can be calculated from the B primary daughters, or from the final state particles from the B decay. However, the latter is rarely employed due to potential biases introduced with the method.

Missing mass and transverse energy The missing mass squared is defined as

$$M^2_{\text{miss}} = \left(E_{\Upsilon(4S)} - \sum_{n=1}^{N_t} E_n\right)^2 - \sum_{n=1}^{N_t} |p_n|^2, \tag{25}$$

where $E_{\Upsilon(4S)}$ is the energy of $\Upsilon(4S)$, E_n and p_n are the energy and momentum of the reconstructed particle n respectively, and N_t is the total number of reconstructed final state particles. The transverse energy is the scalar sum of the transverse momentum of each particle $\sum_{n=1}^{N_t} |(P_T)_n|$.

Vertex separation of B and $\overline{B}$ Due to the relatively long lifetime of B mesons with respect to strongly decaying lighter mesons, they have a longer average flight distance due to the boost between the $\Upsilon(4S)$ and the laboratory systems. The quantity $\Delta z = z_{B_{\text{sig}}} - z_{B_{\text{tag}}}$ (the distance in the beam direction between the B vertex, $z_{B_{\text{sig}}}$, and the vertex from the ROE, $z_{B_{\text{tag}}}$) has a broader distribution for $B\bar{B}$ events than for continuum events, and can be used to suppress continuum in analyses.

Flavor tagging The flavor tagging algorithm (Sect. 6.5) returns the flavor of the tagged meson, q ($= \pm 1$), along with a flavor-tagging quality factor, r, which ranges from zero for no flavor discrimination to one for unambiguous flavor assignment. For signal events, q is usually consistent with the flavor opposite to that of the signal B, while it is random for continuum events.

6.4.2. Detector-level variables

In contrast to the engineered variables, which represent the whole event, the detector-level variables are built on a track and calorimeter cluster basis. Twelve variables are used for tracks and ten for calorimeter clusters. In addition to these variables, the classifier also contains information relating to the charge and to whether or not the cluster or track belong to the ROE.

Momentum (clusters and tracks) The momentum variables include the magnitude p, the azimuth angle ϕ, and the cosine of the polar angle $\cos\theta$, as well as their uncertainties. Instead of using the center-of-mass system, the z-axis is also rotated to the thrust axis of the B candidate. This rotated coordinate system is inspired by the CLEO cones and is called the thrust frame.

Calorimeter cluster-specific variables There are four variables: number of hits, timing, E9E21, and region. The number of hits of the cluster is employed as well as its timing, which is used to tell if the cluster occurred at the same time as the event. E9E21 is the ratio of the energy between the inner 9 and outer 21 cells of a calorimeter cluster. The region here refers to the ECL region in which the cluster was detected (forward, barrel, or backward).

Track-specific variables The track-specific variables include particle probabilities for kaons, electrons, muons, and protons. The χ^2 probability of the track fit is used, as well as the number of CDC hits.

Vertex variables (V) The use of vertex variables (available for tracks) adds discriminating power, but can create unwanted correlations between the classifier output and Δz. Due to these correlations, the vertex variables cannot be used in every analysis and are therefore treated separately. When used, they are calculated in the same thrust frame as the momentum variables.

6.4.3. Variable sets

Three different input variable sets are used for comparison. The engineered (E) variables are the variables used in the traditional approach and therefore serve as the baseline set containing 30 variables. In the second set, the variables are complemented by the detector-level variables without vertex information (E+DL), resulting in 470 variables. The vertex variables are added in the last set (E+DL+V) for a total of 530 variables.

6.4.4. Hyper parameters

Selecting the optimal hyper parameters is crucial to a classifier. To evaluate different hyper parameter sets, typically a figure of merit based on statistical uncertainty is needed.

6.4.5. Comparison between traditional and deep-learning methods

The comparison is done with two classifiers, each trained on three different variable sets. The first approach, BDT (E), uses the FastBDT algorithm trained on the engineered continuum suppression variables often used at Belle II [70]. Therefore, it serves as the baseline. For the deep neural networks we use `TensorFlow`.[8]

We introduce a metric to compare classifiers relative to the baseline BDT (E), RB(98), the relative amount of background remaining after a 98% signal efficiency criterion. The amount of background remaining after this criterion is calculated relative to the amount of background of the baseline procedure. As an example, an RB(98) of 60% means that the user can expect only 60% of the background compared to the baseline classifier, losing 2% of signal in both cases.

The training time is chosen as the last metric for comparison. This should only serve as an approximation, as training time is hardware dependent and BDTs and DNNs are trained on different hardware.

[8] Comparisons with relational networks and adversarial networks can be found in Ref. [73].

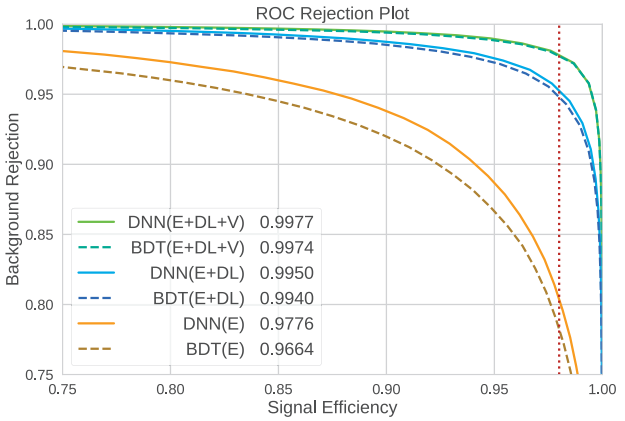

Fig. 42. ROC curve of the BDTs and DNNs for each variable set. Each training is performed five times and the best result is used for this plot. The corresponding AUC score is listed in the legend. The 98% signal efficiency cut used for Table 22 is shown in red.

Table 22. The relative amount of background on a 98% signal efficiency cut (RB(98)) and the time needed for training for each classifier shown in Fig. 42. As a baseline, the traditional approach BDT based on the first variable set is chosen.

Classifier	RB(98) (%)	Training time (hr:min)
DNN (E+DL+V)	9.81	1:01
BDT (E+DL+V)	10.12	26:26
DNN (E+DL)	21.65	0:33
BDT (E+DL)	23.24	25:42
DNN (E)	90.35	0:54
BDT (E)	100	1:39

(GPUs were used for the training of the DNNs to speed up the training, while only CPU-based training is possible for BDTs.)

6.4.6. Performance

The ROC curves and their area-under-the-curve (AUC) scores are shown in Fig. 42. With each additional variable set, the classification result significantly improves, though aside from the first variable set E, there are only small differences between BDTs and DNNs.

The RB(98) scores and the training times are shown in Table 22. The RB(98) scores further confirm the large increase in classification capability using the new variable sets. With the variable set E+DL, the amount of background is only around 20% relative to the amount from the BDT (E) approach. When including the vertex variables the background is reduced by an additional factor of two, and is only 10% of the amount remaining in the BDT (E) approach. The largest difference between DNNs and BDTs are in the training times.

The discriminating variables described above are combined into a continuum suppression discriminant C_{CS} using any of the methods described above. In the majority of analyses, a loose threshold is initially applied to C_{CS} to reject continuum events with minimal loss of signal, and the remaining

events are transformed to a new observable,

$$C'_{\rm CS} = \log\left(\frac{C_{\rm CS} - {\rm cut}}{1 - C_{\rm CS}}\right), \tag{26}$$

which has a Gaussian-like shape that can be described analytically by a single or double Gaussian function.

It should be noted that, given the large number of input parameters in the most advanced configurations of the classifiers, correlations can be very high both between the input parameters and between the classifier itself and signal observables. The depth and complexity of the continuum suppression classifiers employed in analyses will need to be chosen judiciously and their application will be analysis dependent. Adversarial network approaches to penalize approaches for high correlations to signal observables may be considered in the future.

6.5. Flavor tagger

Flavor tagging is required for measurements of B meson mixing and for measurements of CP violation, where the decay of a neutral B meson ($B^0_{\rm sig}$) is fully reconstructed and the flavor of the accompanying B^0 meson ($B^0_{\rm tag}$) has to be determined. The task of the flavor tagger is to determine the flavor of $B^0_{\rm tag}$ at the time of its decay. At the $\Upsilon(4S)$ resonance, B meson pairs are produced in isolation, i.e. without additional particles. Therefore, reconstructed tracks and neutral ECL and KLM clusters remaining after the full reconstruction of $B^0_{\rm sig}$ can be assumed to a good approximation to belong to the decay of $B_{\rm tag}$.

B mesons exhibit a large number of possible decay channels. Many of them provide unambiguous flavor signatures through flavor-specific final states. Flavor signatures correspond to signed characteristics of the decay products that are correlated with the charge sign of the b quark in the B meson. Because of the wide range of possible decay channels it is not feasible to fully reconstruct a large fraction of flavor-specific $B_{\rm tag}$ decays. Instead of a full reconstruction, the flavor tagger applies inclusive techniques based on multivariate methods to maximally exploit the information provided by the different flavor-specific signatures in flavor-specific decays.

The Belle II flavor tagger has been developed by adopting several useful concepts from previous algorithms used by the Belle and the BaBar collaborations [2].

6.5.1. Definitions

Given a total number of events N, the efficiency ε is defined as the fraction of events to which the flavor tagging algorithm can assign a flavor tag, i.e.

$$\varepsilon = \frac{N^{\rm tag}}{N}, \tag{27}$$

where $N^{\rm tag}$ is the number of tagged events. The fraction of wrong identifications over the number of tagged events is denoted by w. Thus, the number of tagged B^0 and $\bar{B}^0$ events is given by

$$\begin{aligned} N^{\rm tag}_{B^0} &= \varepsilon(1-w)N_{B^0} + \varepsilon w N_{\bar{B}^0}, \\ N^{\rm tag}_{\bar{B}^0} &= \varepsilon(1-w)N_{\bar{B}^0} + \varepsilon w N_{B^0}, \end{aligned} \tag{28}$$

where N_{B^0} and $N_{\bar{B}^0}$ are the true number of B^0 and $\bar{B}^0$ mesons on the tag side, respectively. The observed CP violation asymmetry is then

$$a_{\rm CP}^{\rm obs} = \frac{N_{B^0}^{\rm tag} - N_{\bar{B}^0}^{\rm tag}}{N_{B^0}^{\rm tag} + N_{\bar{B}^0}^{\rm tag}} = (1-2w)\cdot\frac{N_{B^0} - N_{\bar{B}^0}}{N_{B^0} + N_{\bar{B}^0}} = (1-2w)\cdot a_{\rm CP}, \tag{29}$$

where $a_{\rm CP}$ corresponds to the CP violation asymmetry measured in CP violation analyses (Eq. (296), in Sect. 10.1). To reduce systematic uncertainties, the value of w should be precisely measured. The size of the observed CP asymmetry is proportional to $|1-2w|$, i.e. the CP asymmetry becomes "diluted" due to the wrong tag fraction. The so-called dilution factor is defined as

$$r \equiv |1-2w|, \tag{30}$$

where $r = 0$ means no flavor information ($w = 0.5$) and $r = 1$ corresponds to an unambiguous tag ($w = 0, 1$). The statistical uncertainty of $a_{\rm CP}$ is

$$\delta a_{\rm CP} = \frac{\delta a_{\rm CP}^{\rm obs}}{1-2w}. \tag{31}$$

Assuming that $a_{\rm CP}^{\rm obs}$ is small, i.e. $N_{B^0}^{\rm tag} \approx N_{\bar{B}^0}^{\rm tag}$, one obtains for the statistical uncertainty of $a_{\rm CP}^{\rm obs}$

$$\delta a_{\rm CP}^{\rm obs} \overset{N_{B^0}^{\rm tag} \approx N_{\bar{B}^0}^{\rm tag}}{=} \frac{1}{\sqrt{N^{\rm tag}}}. \tag{32}$$

Thus, one finds that

$$\delta a_{\rm CP} = \frac{1}{\sqrt{N^{\rm tag}}(1-2w)}. \tag{33}$$

The effective tagging efficiency $\varepsilon_{\rm eff}$ of a flavor tagging algorithm is defined such that the statistical uncertainty on the measured asymmetry $a_{\rm CP}$ is related to the effective number of tagged events $N^{\rm eff}$ by $1/\sqrt{N^{\rm eff}} = 1/\sqrt{\varepsilon_{\rm eff}\cdot N}$. Comparing this with Eq. (33), one obtains

$$\varepsilon_{\rm eff} = \frac{N^{\rm tag}}{N}\cdot(1-2w)^2 = \varepsilon\cdot r^2. \tag{34}$$

The maximization of the effective efficiency results in minimization of the statistical uncertainty. In general, the scaling of $\delta a_{\rm CP}$ with $\varepsilon_{\rm eff}$ is only approximate. For a likelihood-based analysis, the expected statistical uncertainty of an estimated CP or mixing asymmetry can be obtained with a maximum-likelihood estimator (Sect. 10.1).

Up to now, w and ε have been considered to be equal for $q = +1$ (-1). However, a slight difference can arise as a result of charge-asymmetric detector performance. To take this effect into account, one redefines

$$\varepsilon = \frac{\varepsilon_{B^0} + \varepsilon_{\bar{B}^0}}{2}, \qquad w = \frac{w_{B^0} + w_{\bar{B}^0}}{2}, \tag{35}$$

and introduces the differences

$$\Delta\varepsilon = \varepsilon_{B^0} - \varepsilon_{\bar{B}^0}, \qquad \Delta w = w_{B^0} - w_{\bar{B}^0}, \tag{36}$$

where the index corresponds to the true flavor, e.g. w_{B^0} is the fraction of true B^0 mesons that were wrongly classified as $\bar{B}^0$.

Table 23. Tagging categories and their targets (left) with some characteristic examples of the considered decay modes (right). "P*" stands for momentum in the center-of-mass frame and $l^{\pm}$ for charged leptons (μ or e).

Categories	Targets for $\overline{B}^0$	Underlying decay modes
Electron	e^-	$\overline{B}^0 \to D^{*+}\ \overline{\nu}_\ell\ \ell^-$
Intermediate Electron	e^+	$\quad\hookrightarrow D^0\ \pi^+$
Muon	μ^-	$\quad\quad\hookrightarrow X\ K^-$
Intermediate Muon	μ^+	
Kinetic Lepton	l^-	$\overline{B}^0 \to D^+\ \pi^-\ (K^-)$
Intermediate Kinetic Lepton	l^+	$\quad\hookrightarrow K^0\ \nu_\ell\ \ell^+$
Kaon	K^-	
Kaon–Pion	K^-, π^+	$\overline{B}^0 \to \Lambda_c^+\ X^-$
Slow Pion	π^+	$\quad\hookrightarrow \Lambda\ \pi^+$
Maximum P*	l^-, π^-	$\quad\quad\hookrightarrow p\ \pi^-$
Fast–Slow Correlated (FSC)	l^-, π^+	
Fast Hadron	π^-, K^-	
Lambda	Λ	

6.5.2. *Tagging categories*

The flavor tagger is based on flavor-specific decay modes with relatively high branching fractions ($\gtrsim 2\%$). Each decay mode exhibits a particular decay topology and provides a flavor-specific signature. Some additional signatures are obtained by combining similar or complementary decay modes. Within a so-called category, a particular flavor signature is considered separately. The current flavor tagger is based on 13 categories, which are presented in Table 23.

The decay modes are characterized by flavor-specific final state particles. These particles are treated as targets since their charges are correlated with the flavor of B_{tag}. In order to extract these flavor-specific signatures, the targets have to be identified among all available particle candidates. To accomplish this task, discriminating variables are calculated for each particle candidate. An overview of the discriminating variables for each category is presented in Table 24.

Leptons Primary and secondary leptons from B decays are used as target particles for different categories. In the first case, the leptons stem from $\overline{B}^0 \to X\, l^- \bar{\nu}_l$ decays via $b \to c(u)\, l^- \bar{\nu}_l$. A negatively (positively) charged primary lepton unambiguously tags a $\overline{B}^0$ (B^0) meson. Primary electrons and muons are the targets of the Electron and Muon categories, respectively. Both are considered as targets in the Kinetic Lepton category.

Secondary leptons that are produced through the cascade decay of charmed mesons and baryons of the type $\overline{B}^0 \to X_c \left[\to l^+ \nu_l X_{s(d)}\right] X$ via transitions $b \to c \to s\,(d)\, l^+ \nu_l$ can be used to tag the flavor of the B meson. In this case the charge–flavor correspondence is reversed, i.e. a positively (negatively) charged secondary lepton tags a $\overline{B}^0$ (B^0) meson. Since their momentum spectrum is much softer (lower) in comparison with the primary leptons, secondary leptons are referred to as intermediate leptons. Intermediate electrons and intermediate muons are the targets of the Intermediate Electron and Intermediate Muon categories, respectively. Both are considered as targets in the Intermediate Kinetic Lepton category.

In order to distinguish primary and secondary leptons from all other candidates, kinematic and particle identification variables (PID), such as the electron and muon likelihoods $\mathcal{L}_e$ and $\mathcal{L}_\mu$ (Sect. 5.5), are used as discriminating variables. Within the kinematic variables, the momentum variables, such as the absolute momentum p^* and the transverse momentum p_{T}^* in the $\Upsilon(4S)$ center-of-mass frame as

Table 24. Discriminating input variables for each category. For some of the categories the p-value of the track fit is taken into account. For the Lambda category, the p-value of the reconstructed Λ decay vertex is used. All variables are calculated for each considered particle candidate.

Categories	Discriminating input variables
Electron Int. Electron	$\mathcal{L}_e$, p^*, p_t^*, p, p_t, $\cos\theta$, d_0, $\lvert\boldsymbol{x}\rvert$, M_{rec}^2, E_{90}^W, p_{miss}^*, $\cos\theta_{\mathrm{miss}}^*$, $\cos\theta_T^*$, p-value
Muon Int. Muon	$\mathcal{L}_\mu$, p^*, p_t^*, p, p_t, $\cos\theta$, d_0, $\lvert\boldsymbol{x}\rvert$, M_{rec}^2, E_{90}^W, p_{miss}^*, $\cos\theta_{\mathrm{miss}}^*$, $\cos\theta_T^*$, p-value
Kin. Lepton Int. Kin. Lepton	$\mathcal{L}_e$, $\mathcal{L}_\mu$, p^*, p_t^*, p, p_t, $\cos\theta$, d_0, $\lvert\boldsymbol{x}\rvert$, M_{rec}^2, E_{90}^W, p_{miss}^*, $\cos\theta_{\mathrm{miss}}^*$, $\cos\theta_T^*$, p-value
Kaon	$\mathcal{L}_K$, p^*, p_t^*, p, p_t, $\cos\theta$, d_0, $\lvert\boldsymbol{x}\rvert$, $n_{K_S^0}$, $\sum p_t^2$, M_{rec}^2, E_{90}^W, p_{miss}^*, $\cos\theta_{\mathrm{miss}}^*$, $\cos\theta_T^*$, χ^2
Slow Pion Fast Hadron	$\mathcal{L}_\pi$, $\mathcal{L}_e$, $\mathcal{L}_K$, p^*, p_t^*, p, p_t, $\cos\theta$, d_0, $\lvert\boldsymbol{x}\rvert$, $n_{K_S^0}$, $\sum p_t^2$, M_{rec}^2, E_{90}^W, p_{miss}^*, $\cos\theta_{\mathrm{miss}}^*$, $\cos\theta_T^*$, p-value
Kaon–Pion	$\mathcal{L}_K$, y_{Kaon}, y_{SlowPion}, $\cos\theta_{K\pi}^*$, $q_K \cdot q_\pi$
Maximum P*	p^*, p_t^*, p, p_t, d_0, $\lvert\boldsymbol{x}\rvert$, $\cos\theta_T^*$
FSC	$\mathcal{L}_{K\mathrm{Slow}}$, p_{Slow}^*, p_{Fast}^*, $\cos\theta_{\mathrm{T,\,Slow}}^*$, $\cos\theta_{\mathrm{T,\,Fast}}^*$, $\cos\theta_{\mathrm{SlowFast}}^*$, $q_{\mathrm{Slow}} \cdot q_{\mathrm{Fast}}$
Lambda	$\mathcal{L}_p$, $\mathcal{L}_\pi$, p_Λ^*, p_Λ, p_p^*, p_p, p_π^*, p_π, q_Λ, M_Λ, $n_{K_S^0}$, $\cos\theta_{\boldsymbol{x}_\Lambda \boldsymbol{p}_\Lambda}$, $\lvert\boldsymbol{x}_\Lambda\rvert$, σ_Λ^{zz}, p-value

well as the absolute momentum p and the transverse momentum p_t in the laboratory frame, have the highest discrimination power, especially for primary leptons. Intermediate leptons are more difficult to distinguish from other candidates because of their softer momentum spectrum. Additionally, the cosine of the polar angle of the momentum in the laboratory frame, $\cos\theta$, is considered.

Direct leptons are produced at the B_{tag}^0 decay vertex and therefore have small impact parameters.

Further separation power is obtained from additional variables calculated in the $\Upsilon(4S)$ center-of-mass frame, assuming that B_{tag} is produced at rest:

- M_{rec}^2, the squared invariant mass of the recoiling system X, where the four-momentum is defined by

$$p_X^\mu = \sum_{i \neq l} p_i^\mu, \tag{37}$$

  the index i running over all charged and neutral candidates and l corresponding to the index of the lepton candidate. Therefore,

$$M_{\mathrm{rec}}^2 = m_X^2 = g_{\mu,\nu} p_X^\mu p_X^\nu. \tag{38}$$

- p_{miss}^*, the absolute value of the missing momentum $\boldsymbol{p}_{\mathrm{miss}}^*$, which is defined by

$$\boldsymbol{p}_{\mathrm{miss}}^* = \boldsymbol{p}_{B^0}^* - \boldsymbol{p}_X^* - \boldsymbol{p}_l^*. \tag{39}$$

  Taking into account that the B^0 meson is produced at rest in the $\Upsilon(4S)$ frame, i.e. $\boldsymbol{p}_{B^0}^* \approx \boldsymbol{0}$, one obtains

$$\boldsymbol{p}_{\mathrm{miss}}^* \approx -\left(\boldsymbol{p}_X^* + \boldsymbol{p}_l^*\right). \tag{40}$$

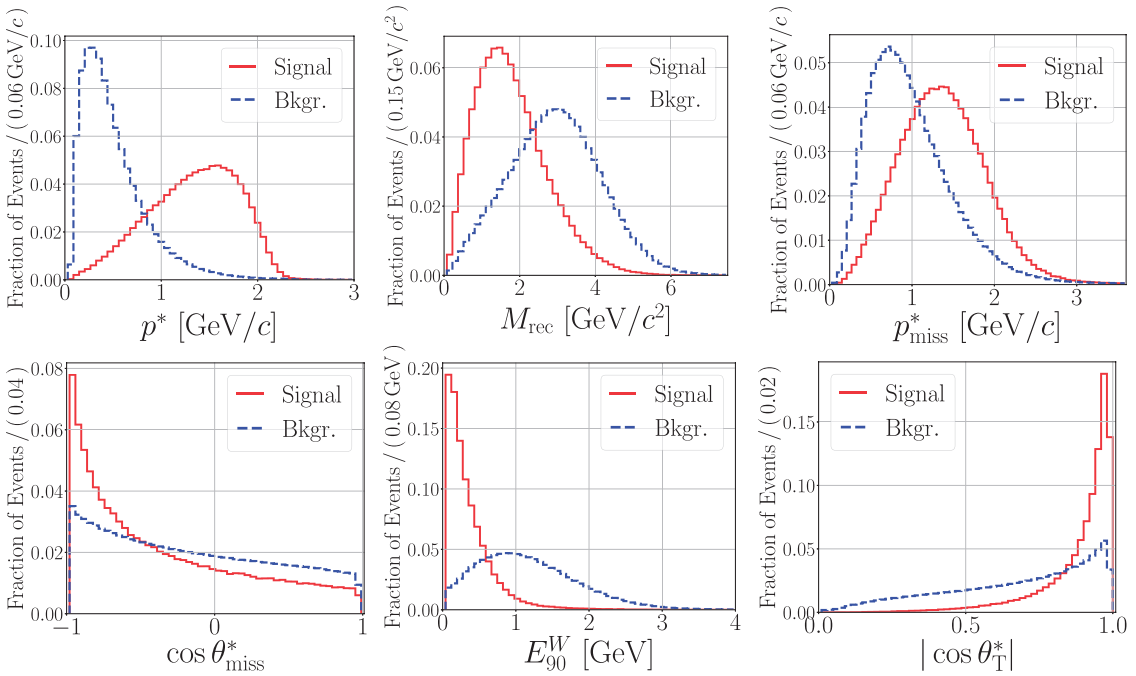

Fig. 43. Distributions of p^*, $M_{\rm rec}$, $p^*_{\rm miss}$, $\cos\theta^*_{\rm miss}$, E^W_{90}, and $\cos\theta^*_{\rm T}$ for the Kinetic Lepton category. Target muons and electrons are called signal, while all other particles are called background.

- $\cos\theta^*_{\rm miss}$, the cosine of the angle between the momentum $\boldsymbol{p}^*_l$ of the lepton candidate and the missing momentum $\boldsymbol{p}^*_{\rm miss}$.
- E^W_{90}, the energy in the hemisphere defined by the direction of the momentum transfer (virtual $W^\pm$) in the B meson decay. The momentum of the virtual $W^\pm$ is given by

$$\boldsymbol{p}^*_W = \boldsymbol{p}^*_l + \boldsymbol{p}^*_\nu \approx \boldsymbol{p}^*_l + \boldsymbol{p}^*_{\rm miss} = -\boldsymbol{p}^*_X, \tag{41}$$

  where the momentum $\boldsymbol{p}_\nu$ of the neutrino is estimated using the missing momentum $\boldsymbol{p}^*_{\rm miss}$. The sum of energies for E^W_{90} extends over all charged and neutral candidates in the recoiling system X that are in the same hemisphere with respect to the $W^\pm$:

$$E^W_{90} = \sum_{i\in X, \boldsymbol{p}^*_i\cdot\boldsymbol{p}^*_W>0} E_i. \tag{42}$$

- $\cos\theta^*_{\rm T}$, the cosine of the angle between the lepton candidate's momentum $\boldsymbol{p}^*_l$ and the thrust axis of the $B^0_{\rm tag}$ in the $\Upsilon(4S)$ center-of-mass frame [Eq. (21)].

Figure 43 shows example distributions of discriminating input variables for the Kinetic Lepton category (all the distributions and correlation plots can be found in Ref. [76]).

Kaons Kaons are produced predominantly through decays of charmed mesons via $b \to c \to s$ transitions, $\bar{B}^0 \to D\left[\to K^- X\right] X$. Kaons stemming from such decays, and from decays of charmed baryons via $b \to c \to s$ transitions, tag a $\bar{B}^0$ (B^0) if they are negatively (positively) charged, and are referred to as "right sign" kaons.

The Kaon category has the highest flavor discrimination power due to the large inclusive branching fraction $\mathcal{B}\left(B^\pm/B^0 \to K^\pm\right) = (78.9 \pm 2.5)\%$ [77] and the fact that the fraction of right sign kaons

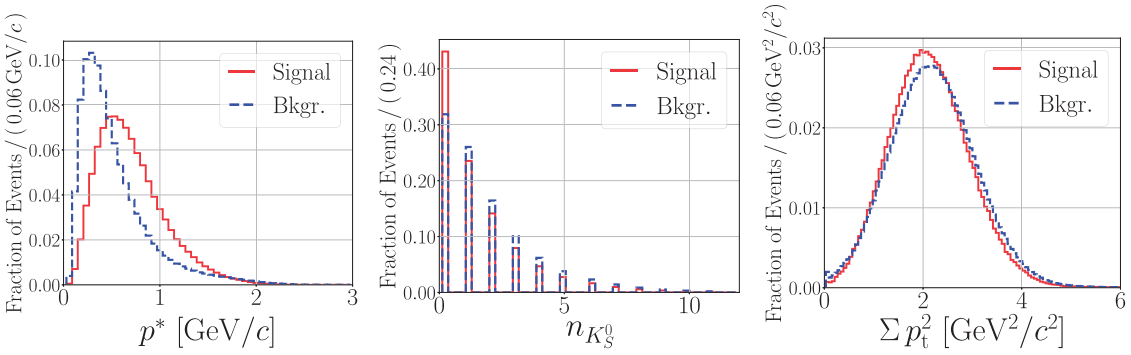

Fig. 44. Distributions of p^*, $n_{K^0_S}$, and $\sum p_t^2$ for the Kaon category. Target kaons are called signal, while all other particles are called background.

$\mathcal{B}\left(B^\pm/B^0 \to K^+\right) = (66 \pm 5)\%$ is higher than the fraction of wrong sign kaons $\mathcal{B}\left(B^\pm/B^0 \to K^-\right) = (13 \pm 4)\%$ [77]. For example, kaons produced through $\bar{b} \to W^+ \left[\to c\bar{s}/c\bar{d}\right] X$ with $c \to s \to K^-$.

In addition to the momentum variables (p^*, p_t^*, p, p_t, and $\cos\theta$) and the impact parameters (d_0 and $|\boldsymbol{x}|$), the following discriminating variables are used to identify target kaons:

- $\mathcal{L}_K$, the PID kaon likelihood (Sect. 5.5).
- $n_{K^0_S}$, the number of reconstructed K^0_S on the tag side. A charged kaon produced through $b \to c\bar{c}s/c\bar{c}d$ transitions or through hadronization of $s\bar{s}$ out of the vacuum is usually accompanied by one or more K^0_S.
- $\sum p_t^2$, the sum of the squared transverse momentum of all tracks on the tag side in the laboratory frame. A high value of this quantity indicates a higher probability that the kaon candidate was produced through $b \to W^- c \left[\to s \to K^-\right]$. Lower values indicate a production through $b \to XW^- \left[\to \bar{c}s/\bar{c}d\right]$, $\bar{c} \to \bar{s} \to K^+$ which corresponds to a wrong sign kaon.
- M^2_{rec}, E^W_{90}, p^*_{miss}, $\cos\theta^*_{\text{miss}}$, and $\cos\theta^*_T$, the variables in the $\Upsilon(4S)$ frame which distinguish the lepton background.

Figure 44 shows example distributions of discriminating input variables for the Kaon category.

Slow pions Primary and secondary pions are considered as target particles for several categories. The charge of secondary pions from $\bar{B}^0 \to XD^{*+} \left[\to D^0\pi^+\right]$ decays provide tagging information. Due to their soft (lower mean) momenta they are referred to as slow pions and considered as targets in the Slow Pion category. The Slow Pion category uses all the variables applied within the Kaon category, in order to distinguish the background from kaons and leptons. Additionally, the pion and the electron PID likelihoods $\mathcal{L}_\pi$ and $\mathcal{L}_e$ of each particle candidate are considered. The latter helps to distinguish the background from electrons created either through photon conversions or through $\pi^0 \to e^+e^-\gamma$ Dalitz decays.

The variable $\cos\theta^*_T$ has considerable separation power. Slow pions are produced together with the D^0 nearly at rest in the D^{*+} frame. Therefore, the flight direction of the target slow pions is close to the direction of the D^0 decay products and opposite to the other B^0_{tag} decay products. Low-momentum background tracks can be distinguished by correlating the direction of the candidate and the direction of the remaining tracks from the B^0_{tag} decay, which corresponds to a good approximation to the B^0_{tag} thrust axis.

Figure 45 shows example distributions of discriminating input variables for the Slow Pion category.

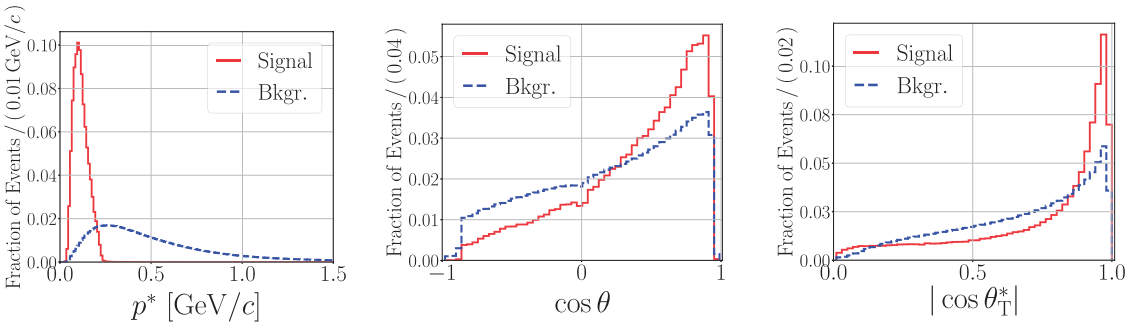

Fig. 45. Distributions of p^*, $\cos\theta$, and $\cos\theta^*_{\rm T}$ for the Slow Pion category. Target slow pions are called signal, while all other particles are called background.

Fast hadrons The targets of the Fast Hadron category are kaons and pions from the W boson in $b \to c(u)W^-$ decays and from "one-prong" decays of primary tauons, i.e. $\bar{B}^0 \to \tau^- \left[\to \pi^-(K^-)\nu_\tau\right] \bar{\nu}_\tau X$. The category also considers as targets those kaons and pions that are produced through intermediate resonances, which decay via strong processes conserving the flavor information, e.g. $\bar{B}^0 \to K^{*-} \left[\to K^-\pi^0\right] X$ or $\bar{B}^0 \to \tau^- \left[\to \rho^- \left[\to \pi^-\pi^0\right] \nu_\tau\right] \bar{\nu}_\tau X$. The target kaons and pions are referred to as fast hadrons because of their hard (higher mean) momentum spectrum. A negatively (positively) charged fast hadron indicates a $\bar{B}^0$ (B^0) meson. The Fast Hadron category uses the same set of variables applied within the Slow Pion category.

Correlation between kaons and slow pions (Kaon–Pion) If an event contains both a target kaon and a target slow pion, e.g. a $\bar{B}^0 \to XD^{*+} \left[\to D^0 \left[\to K^- X\right] \pi^+\right]$ decay, the flavor tagging information from the individual categories is improved by exploiting the correlations between both targets.

The following variables are considered:

- $\mathcal{L}_K$, the PID kaon likelihood.
- $y_{\rm Kaon}$, the probability of being a target kaon obtained from the individual Kaon category.
- $y_{\rm SlowPion}$, the probability of being a target slow pion obtained from the individual Slow Pion category.
- $\cos\theta^*_{K\pi}$, the cosine of the angle between the kaon and the slow pion momentum in the $\Upsilon(4S)$ frame. If both targets are present, they are emitted in approximately the same direction in the $\Upsilon(4S)$ frame.
- $q_K \cdot q_\pi$, the charge product of the kaon and the slow pion candidates. A right sign kaon and the corresponding slow pion are produced with opposite charges in agreement with their individual flavor–charge correspondence.

High-momentum particles (Maximum P)* Hadrons and leptons from the W boson in $b \to c(u)W^-$ are characterized by a very hard momentum spectrum. An inclusive tag can be performed by selecting the track with the highest momentum in the $\Upsilon(4S)$ frame and using its charge as a flavor tag. A negatively (positively) charged fast particle indicates a $\bar{B}^0$ (B^0) meson. The purpose is to recover flavor tagging information from primary particles that may not have been selected either as a primary lepton or as a fast hadron. The discriminating variables are the momentum variables (p^*, $p^*_{\rm t}$, p, $p_{\rm t}$, and $\cos\theta$), the impact parameters (d_0 and $|\boldsymbol{x}|$), and $\cos\theta^*_{\rm T}$.

Correlation between fast and slow particles (FSC) Events of the kind $\bar{B}^0 \to D^{*+}W^-$ contain both a target slow pion and a high-momentum primary particle originating from the W boson. In that case, additional flavor tagging information can be gained by using the correlations between the slow pion and the high-momentum particle.

The $W^\pm$ and the D^{*+} are produced back-to-back in the $B^0_{\rm tag}$ center-of-mass frame. Therefore, the angle between the track of the target fast particle and the target slow pion is expected to be very large. Useful discriminating variables are:

- $\mathcal{L}_{K\,\rm Slow}$, the PID kaon likelihood of the slow pion candidate.
- $p^*_{\rm Slow}$, the momentum of the slow pion candidate in the $\Upsilon(4S)$ frame.
- $p^*_{\rm Fast}$, the momentum of the high-momentum candidate in the $\Upsilon(4S)$ frame.
- $\cos\theta^*_{\rm T,\,Slow}$, the cosine of the angle between the thrust axis and the slow pion candidate in the $\Upsilon(4S)$ frame.
- $\cos\theta^*_{\rm T,\,Fast}$, the cosine of the angle between the thrust axis and the high-momentum candidate in the $\Upsilon(4S)$ frame.
- $\cos\theta^*_{\rm SlowFast}$, the cosine of the angle between the slow and the high-momentum candidates in the $\Upsilon(4S)$ frame.
- $q_{\rm Slow}\cdot q_{\rm Fast}$, the charge product of the slow pion and the high-momentum candidates. In agreement with their individual flavor–charge correspondence, the targets have to be produced with opposite charges.

Lambda baryons Additional flavor tagging information can be obtained by considering the flavor of Λ baryons, since they are likely to contain an s quark from the cascade transition $b \to c \to s$. The presence of a Λ ($\bar{\Lambda}$) baryon indicates a $\bar{B}^0$ (B^0). Although the fraction of events containing a target Λ is rather small, they provide relatively clean flavor tagging information. The Λ candidates are obtained by reconstructing $\Lambda \to p\pi^-$ ($\bar{\Lambda} \to \bar{p}\pi^+$) decays through combinations of proton and pion candidates on the tag side. In addition to the momentum variables of the reconstructed Λ, proton, and pion used for the reconstruction, the following discriminating variables are used:

- $\mathcal{L}_p$, $\mathcal{L}_\pi$, the PID likelihoods of the proton and the pion.
- q_Λ, the flavor of the Λ baryon.
- M_Λ, the reconstructed mass of the Λ.
- $n_{K^0_{\rm S}}$, the number of reconstructed $K^0_{\rm S}$ on the tag side.
- $\cos\theta_{\boldsymbol{x}_\Lambda,\boldsymbol{p}_\Lambda}$, the cosine of the angle between the Λ momentum $\boldsymbol{p}_\Lambda$ and the direction from the IP to the reconstructed Λ vertex $\boldsymbol{x}_\Lambda$ in the laboratory frame.
- $|\boldsymbol{x}_\Lambda|$, the distance between the Λ vertex and the IP.
- σ^{zz}_Λ, the error of the Λ vertex fit in the z direction.

A summary of the discriminating variables for each category is presented in Table 24.

6.5.3. Algorithm

The Belle II flavor tagger is a modular algorithm based on multivariate methods which provide a flavor tag q for the $B^0_{\rm tag}$ meson together with the corresponding flavor dilution factor r. It does so by analyzing the tracks and the neutral clusters that remain after $B^0_{\rm sig}$ reconstruction. The output $y \in [-1, 1]$ of the flavor tagger is equivalent to $y = q \cdot r$, where $y = -1$ (1) corresponds to a perfectly tagged $\bar{B}^0$ (B^0).

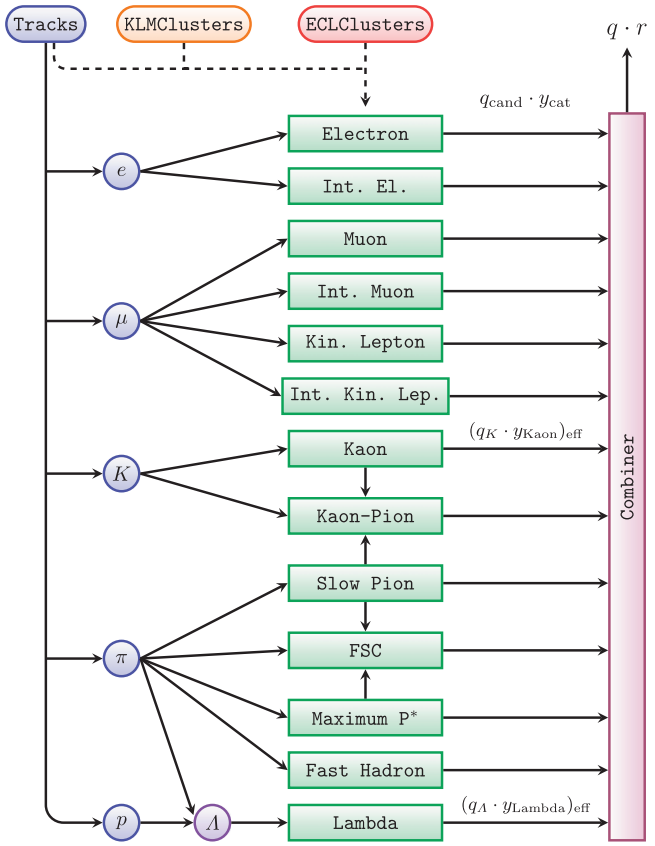

Fig. 46. Schematic overview of the flavor tagger. Reconstructed tracks are available for five different mass hypotheses. Each green box corresponds to a category. The charge q_{cand} and the probability y_{cat} are explained in the text. The values $(q_{\mathrm{cand}} \cdot y_{\mathrm{cat}})_{\mathrm{eff}}$ are defined in Eq. (43).

The flavor of B^0_{tag} results from a combination of the 13 flavor signatures discussed in the previous subsections. Each of these signatures corresponds to the output of a single category which can be understood as an individual "sub-tagger." A schematic overview of the information flow in the algorithm is presented in Fig. 46. The algorithm of the flavor tagger is a two-level process comprised of event and combiner levels. The event-level process is performed within each individual category. On this level, a multivariate method assigns to each particle candidate a probability y_{cat}, which is the probability of being the target of the corresponding category providing the correct flavor tag. The particle candidates correspond to the tracks that remain from the reconstruction of the signal B_{sig} meson. Since each track is fitted with five different mass hypotheses (e, μ, K, π, and p), each category considers the mass hypotheses belonging to its own targets. To determine y_{cat}, the event-level multivariate methods are given the discriminating variables of the corresponding category. In some calculations all reconstructed tracks and all neutral ECL and KLM clusters that remain after the full B^0_{sig} reconstruction are taken into account.Within each category, the particle candidates are ranked according to the values of y_{cat}. The candidate with the highest y_{cat} is selected as the target. The exception is the Maximum P* category, where the target is the candidate with the largest momentum in the $\Upsilon(4S)$ frame.

The procedure within each single category is illustrated in Fig. 47. The combiner level is the last step in the process. It corresponds to a multivariate method that takes 13 input values and gives $y = q \cdot r$ as the output. Each input value is the product $q_{\mathrm{cand}} \cdot y_{\mathrm{cat}}$ of each category, where the charge

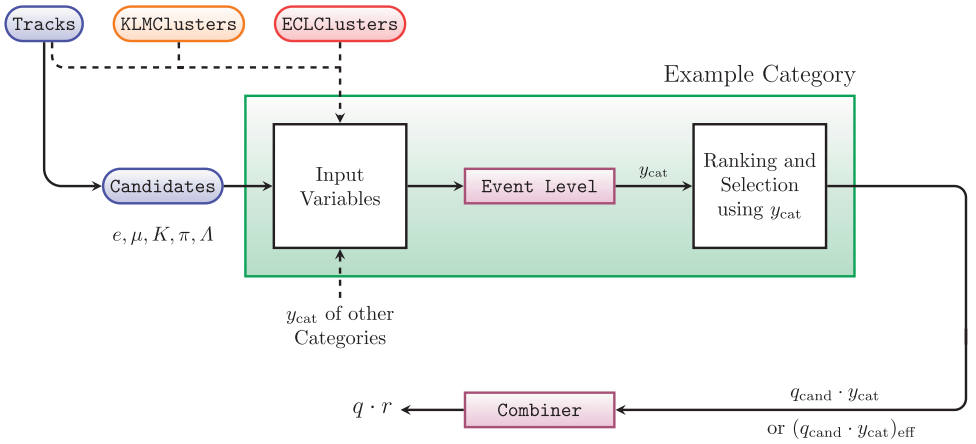

Fig. 47. Procedure for each single category (green box). The candidates correspond to the reconstructed tracks for a specific mass hypothesis. The input variables are presented in Table 24; some of them consider all reconstructed tracks and all neutral ECL and KLM clusters on the tag side. The magenta boxes represent multivariate methods; y_{cat} is the output of the event level. The output of the combiner is equivalent to the product $q \cdot r$.

q_{cand} and the probability y_{cat} correspond to the particle candidate selected as target. For two special cases, the Kaon and the Lambda categories, the input value is the effective product

$$(q_{\text{cand}} \cdot y_{\text{cat}})_{\text{eff}} = \frac{\prod_i \left(1 + (q_{\text{cand}} \cdot y_{\text{cat}})_i\right) - \prod_i \left(1 - (q_{\text{cand}} \cdot y_{\text{cat}})_i\right)}{\prod_i \left(1 + (q_{\text{cand}} \cdot y_{\text{cat}})_i\right) + \prod_i \left(1 - (q_{\text{cand}} \cdot y_{\text{cat}})_i\right)}, \tag{43}$$

where the products extend over the three particles with the highest y_{cat} probability. For the Lambda category, q_{cand} corresponds to the B^0 flavor tagged by the Λ candidate, i.e. $q_\Lambda = -1(+1)$ for $\Lambda(\bar{\Lambda})$.

The multivariate method chosen for the event and the combiner levels is a fast boosted decision tree (FBDT) [70]. For the combiner level, an independent multivariate method, a multi-layer perceptron (MLP) [78,79], is employed to cross-check the result of the FBDT.

The flavor tagger is trained using two statistically independent MC samples, one for the event level and one for the combiner level, to avoid bias from a possible statistical correlation. At each training step, one half of the sample is used as the training sample and the other half as a test and validation sample. The event level is trained first and each category is trained independently. The FBDT and the MLP combiners are trained afterwards.

6.5.4. Performance

The performance of the Belle II flavor tagger has been evaluated using Belle II MC, as well as using Belle MC and Belle collision data. The MC events used for training and testing correspond to $B^0\bar{B}^0$ pairs in which one meson (B^0_{sig}) decays to $J/\psi\, K^0_S$ while B^0_{tag} decays to any possible final state according to the known branching fractions [77]. Only events where the decay channel $B^0_{\text{sig}} \to J/\psi \left[\to \mu^+\mu^-\right] K^0_S \left[\to \pi^+\pi^-\right]$ could be fully reconstructed and correctly matched with the MC decay chain are selected for training and testing. After the selection, the size of the Belle II and the Belle training samples is approximately 2×1.3 and 2×1 million MC events, respectively, and the size of the Belle II and the Belle testing samples is approximately 2.6 and 2 million MC events, respectively.

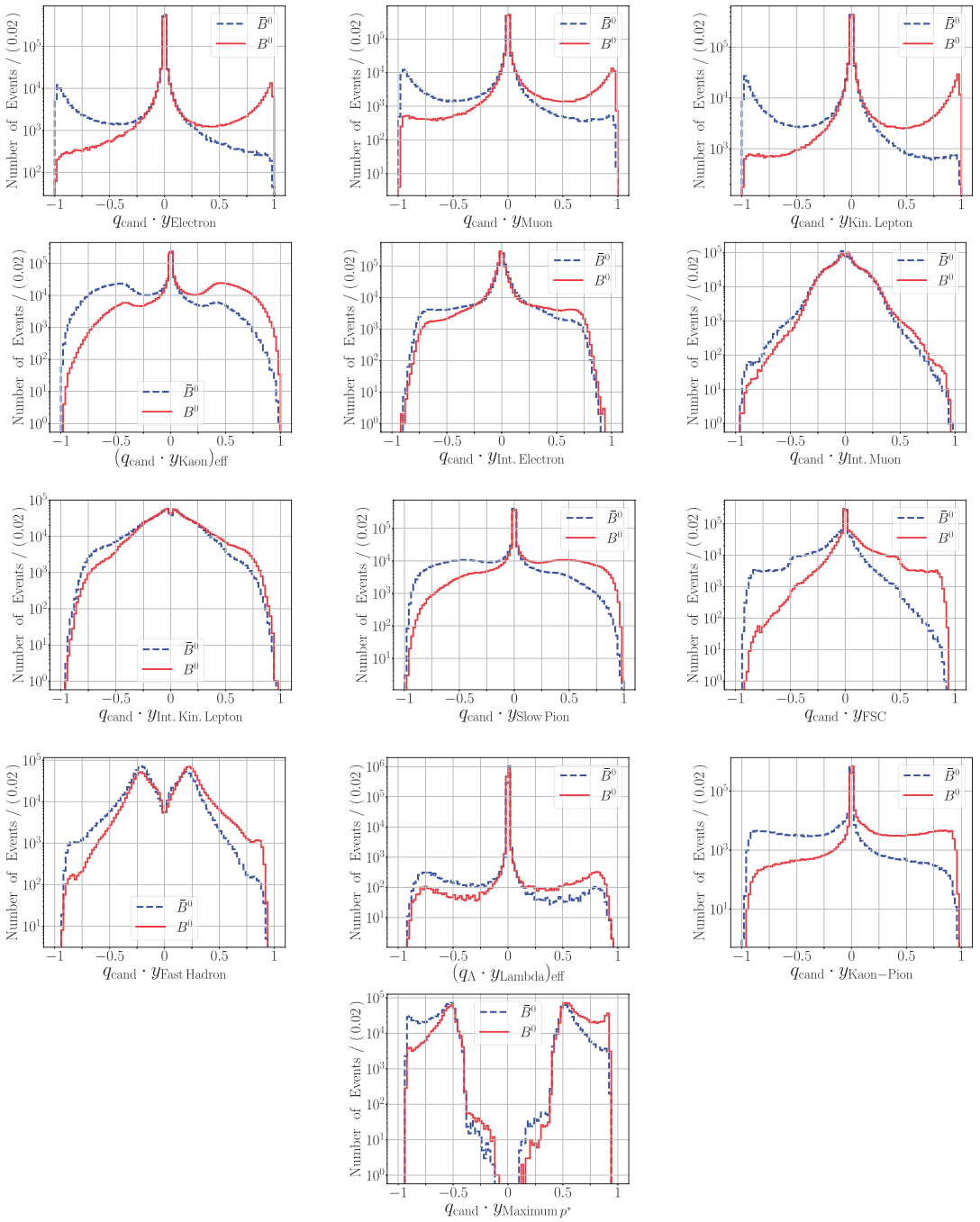

Fig. 48. Combiner input distributions for all categories.

The test with Belle collision data is performed on a set of $B^0\bar{B}^0$ pairs, where the same decay channel $B^0_{\rm sig} \to J/\psi\,[\to \mu^+\mu^-]\,K^0_S\,[\to \pi^+\pi^-]$ is reconstructed on the signal side. The signal selection is performed following previous Belle analyses [80] using the full Belle data sample which corresponds to 711 fb^{-1}. The obtained signal yield is 8508 events.

The distributions of the 13 combiner input values, which are derived from the outputs, $y_{\rm cat}$, of the individual categories, are presented in Fig. 48. The large peaks at zero are due to cases where the target provides no flavor information. In general, a value close to zero indicates that the probability

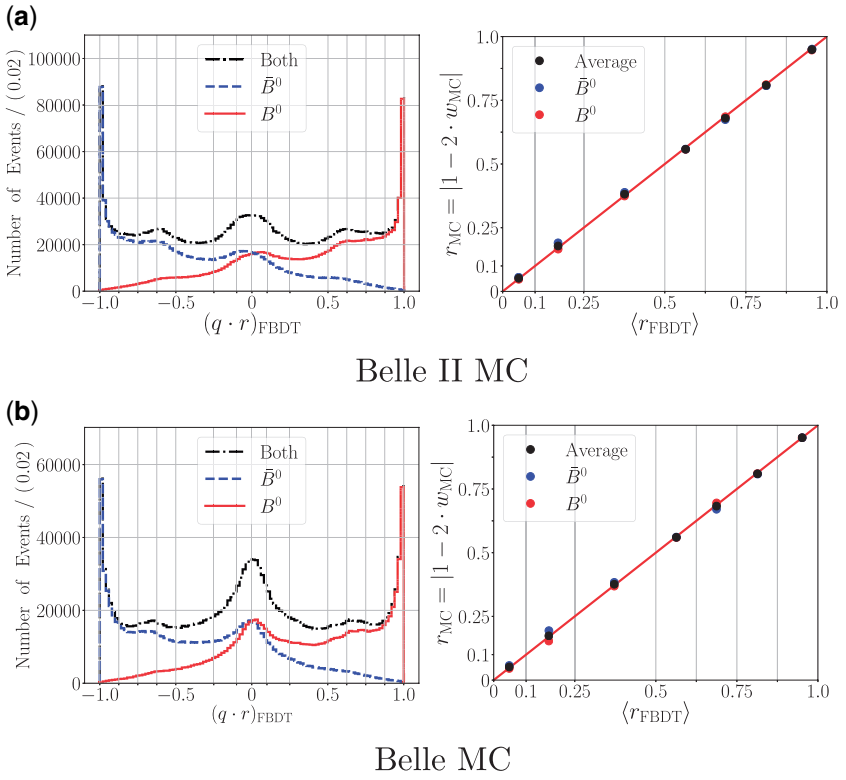

Fig. 49. Results of the FBDT combiner using (a) Belle II MC and (b) Belle MC. Left: Distributions of the output $q \cdot r$. Right: Correlations between the dilution $r_{\mathrm{MC}} = 1 - 2w_{\mathrm{MC}}$ taken from MC truth and the mean absolute value of the combiner output $r = |q \cdot r|$ in each r bin. The errors on both axes are not visible due to their small size. The red diagonal line is a guideline and the vertical gray lines correspond to the limits of the r bins.

of finding a certain flavor-specific signature within the B^0_{tag} final state is very low. A value closer to ± 1 indicates a more reliable flavor tag.

The output $y = q \cdot r$, which corresponds to the product of tagged flavor q and the dilution factor r, can be found in Fig. 49 (left) for the FBDT combiner on MC. Figure 49 (right) also shows a linearity check between the true dilution r_{MC} determined using MC information and the mean $\langle r \rangle$ of the dilution provided by the combiners. The dilution determined using MC information corresponds to $r_{\mathrm{MC}} = 1 - 2w_{\mathrm{MC}}$, where the wrong tag fraction w_{MC} is determined by comparing the MC truth with the combiner output, i.e. an event is wrongly tagged if $q_{\mathrm{MC}} \neq q = \mathrm{sgn}(q \cdot r)$. The mean dilution $\langle r \rangle$ of the combiner output is simply the mean of $|q \cdot r|$ for each r bin. Figure 49 (right) shows the results of the linearity check for events where B_{tag} is a B^0, for events where B_{tag} is a $\bar{B}^0$, and on average.

The results using Belle data and Belle MC are shown together in Fig. 50 by superimposing the normalized $q \cdot r$ output distributions. Within the uncertainties, the shapes of the normalized $q \cdot r$ distributions for Belle data and Belle MC show good agreement.

At Belle II, differences between the performance for B^0 and for $\bar{B}^0$ can occur due to CP asymmetries on the tag side. Due to the initial entanglement of the neutral B meson pair at the $\Upsilon(4S)$, CP asymmetries on the signal-side B-meson decay cause CP asymmetries on the tag side. These result in different decay vertex distributions for B^0 and for $\bar{B}^0$, causing different impact parameter distributions for positively and for negatively charged target particles. Thus, if the MC events used to train the flavor

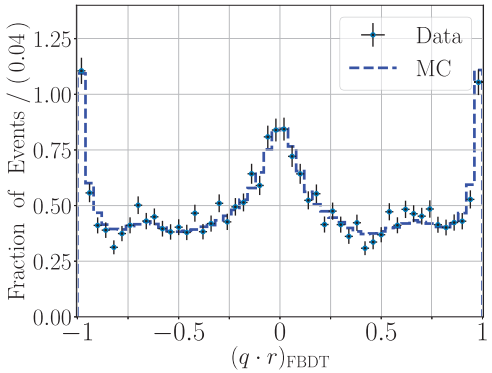

Fig. 50. Normalized $q \cdot r$ distributions on Belle data and on Belle MC.

tagger are generated with CP violation on the signal side, the flavor tagger learns the corresponding CP asymmetry on the tag side to artificially distinguish between B^0 and $\bar{B}^0$. Belle II is sensitive to CP asymmetries on the tag side due to the novel small size of the interaction region (about 20 times smaller than at Belle in the beam direction). To avoid the flavor tagger learning these asymmetries, it must be trained with MC events generated without built-in CP violation [76]. Another possible cause for differences between B^0 and $\bar{B}^0$ are asymmetries in the detector performance for positively and negatively charged particles.

The effective efficiency $\varepsilon_{\mathrm{eff}}$ is defined by sorting the tagged events into bins of the dilution factor, r, adopting the same binning applied by the Belle experiment [81]. The expression for the effective efficiency in Eq. (34) becomes

$$\varepsilon_{\mathrm{eff}} = \varepsilon \sum_i \frac{n_i}{N_{\mathrm{tag}}} \langle r \rangle_i^2 = \sum_i \frac{n_i}{N} \langle r \rangle_i^2 = \sum_i \varepsilon_i \langle r \rangle_i^2, \quad \text{using} \quad \varepsilon_i = \frac{n_i}{N}, \tag{44}$$

where the sum extends over all r bins, and the tagging efficiency corresponds to $\varepsilon = \frac{N_{\mathrm{tag}}}{N}$, where N_{tag} is the number of tagged events. The measured value of ε on Belle data is 99.8%, which is equal to the previous value measured by Belle using the Belle flavor tagger [81] and is consistent with the value of 99.9% obtained using the Belle II flavor tagger on Belle MC and on Belle II MC.

For each individual category, an effective efficiency can be calculated if the corresponding combiner input value $q_{\mathrm{cand}} \cdot y_{\mathrm{cat}}$ is taken as a single flavor tag, i.e. if each category is considered as a "sub-tagger." These effective efficiencies are presented in Table 25. The Lepton, the Kaon, and the Pion categories provide relatively clean flavor signatures and relatively high branching fractions.

In general, the fraction w can be extracted from the combiner output $y = q \cdot r$ through

$$w = \frac{1 - |y|}{2} \tag{45}$$

if the dilution $r = |y|$ provided by the combiner is linear with respect to the true dilution $r_{\mathrm{MC}} = 1 - 2w_{\mathrm{MC}}$, determined using MC information. This linearity has been verified for Belle II and for Belle MC in Fig. 49 (right).

Table 26 lists the global performance quantities of the flavor tagger on MC for both combiner-level multivariate methods. The FBDT combiner achieves a total effective efficiency $\varepsilon_{\mathrm{eff}}$ of $(36.67 \pm 0.05)\%$ on Belle II MC and $(34.26 \pm 0.03)\%$ on Belle MC. The performance of the flavor tagger on Belle data is presented in Table 27. The FBDT combiner achieves a total effective efficiency of $(33.6 \pm 0.5)\%$ on Belle data.

Table 25. Performance of individual categories for the flavor tagging algorithm. All values are given as a percentage considering only statistical uncertainties.

	Belle II MC		Belle MC	
Categories	$\varepsilon_{\text{eff}} \pm \delta\varepsilon_{\text{eff}}$	$\Delta\varepsilon_{\text{eff}} \pm \delta\Delta\varepsilon_{\text{eff}}$	$\varepsilon_{\text{eff}} \pm \delta\varepsilon_{\text{eff}}$	$\Delta\varepsilon_{\text{eff}} \pm \delta\Delta\varepsilon_{\text{eff}}$
Electron	5.53 ± 0.01	0.20 ± 0.02	5.80 ± 0.01	-0.04 ± 0.03
Int. Electron	1.51 ± 0.01	-0.18 ± 0.01	0.74 ± 0.01	0.00 ± 0.01
Muon	5.51 ± 0.01	0.22 ± 0.02	5.74 ± 0.01	0.08 ± 0.03
Int. Muon	0.40 ± 0.01	-0.03 ± 0.01	0.33 ± 0.01	0.00 ± 0.01
Kin. Lepton	11.36 ± 0.02	0.31 ± 0.03	11.70 ± 0.02	0.08 ± 0.04
Int. Kin. Lepton	1.41 ± 0.01	-0.10 ± 0.01	0.56 ± 0.01	0.00 ± 0.01
Kaon	22.41 ± 0.02	-0.84 ± 0.04	19.28 ± 0.02	-0.29 ± 0.04
Kaon–Pion	14.85 ± 0.01	-0.25 ± 0.03	15.15 ± 0.02	-0.26 ± 0.04
Slow Pion	10.16 ± 0.01	0.07 ± 0.02	9.27 ± 0.01	-0.05 ± 0.03
FSC	14.16 ± 0.02	-0.13 ± 0.03	11.54 ± 0.01	-0.11 ± 0.03
Maximum P*	13.05 ± 0.01	1.36 ± 0.03	11.96 ± 0.02	0.05 ± 0.03
Fast Hadron	4.61 ± 0.01	1.14 ± 0.01	1.54 ± 0.01	-0.04 ± 0.01
Lambda	2.77 ± 0.01	0.79 ± 0.01	1.53 ± 0.01	0.24 ± 0.01

Table 26. Performance of FBDT combiner on MC. All values are given as a percentage considering only statistical uncertainties.

r interval	ε_i	$\Delta\varepsilon_i$	$w_i \pm \delta w_i$	$\Delta w_i \pm \delta\Delta w_i$	$\varepsilon_{\text{eff},i} \pm \delta\varepsilon_{\text{eff},i}$	$\Delta\varepsilon_{\text{eff},i} \pm \delta\Delta\varepsilon_{\text{eff},i}$
FBDT combiner on Belle II MC						
0.000–0.100	12.0	−0.28	47.42 ± 0.09	0.41 ± 0.18	0.0320 ± 0.0022	-0.0110 ± 0.0044
0.100–0.250	14.3	0.07	41.09 ± 0.08	1.23 ± 0.16	0.4537 ± 0.0082	-0.1234 ± 0.0163
0.250–0.500	19.9	0.12	30.92 ± 0.06	0.72 ± 0.13	2.8961 ± 0.0196	-0.2012 ± 0.0392
0.500–0.625	11.9	0.06	22.10 ± 0.07	0.05 ± 0.15	3.7022 ± 0.0205	0.0040 ± 0.0410
0.625–0.750	12.0	0.14	16.01 ± 0.06	-0.57 ± 0.13	5.5576 ± 0.0231	0.2529 ± 0.0462
0.750–0.875	11.6	0.21	9.54 ± 0.05	-0.25 ± 0.11	7.5934 ± 0.0236	0.2267 ± 0.0473
0.875–1.000	18.3	−0.32	2.55 ± 0.02	0.19 ± 0.05	16.4389 ± 0.0265	-0.4199 ± 0.0529
Total				$\varepsilon_{\text{eff}} = \sum_i \varepsilon_i \cdot \langle 1 - 2w_i \rangle^2 = 36.67 \pm 0.05$		$\Delta\varepsilon_{\text{eff}} = -0.27 \pm 0.10$
FBDT combiner on Belle MC						
0.000–0.100	15.4	0.06	47.61 ± 0.09	0.59 ± 0.18	0.0354 ± 0.0001	0.0002 ± 0.0002
0.100–0.250	16.1	0.01	41.50 ± 0.09	2.03 ± 0.17	0.4667 ± 0.0009	-0.0011 ± 0.0017
0.250–0.500	20.0	−0.16	31.41 ± 0.07	0.74 ± 0.15	2.7591 ± 0.0042	-0.0410 ± 0.0085
0.500–0.625	9.9	0.01	21.83 ± 0.09	0.08 ± 0.18	3.1384 ± 0.0067	0.0101 ± 0.0134
0.625–0.750	10.4	0.14	15.64 ± 0.08	-1.24 ± 0.16	4.9015 ± 0.0102	0.1380 ± 0.0203
0.750–0.875	10.3	0.04	9.32 ± 0.06	-0.10 ± 0.13	6.7843 ± 0.0141	0.0418 ± 0.0283
0.875–1.000	17.9	−0.13	2.43 ± 0.03	0.01 ± 0.05	16.1464 ± 0.0244	-0.2362 ± 0.0487
Total				$\varepsilon_{\text{eff}} = \sum_i \varepsilon_i \cdot \langle 1 - 2w_i \rangle^2 = 34.26 \pm 0.03$		$\Delta\varepsilon_{\text{eff}} = -0.09 \pm 0.06$

6.5.5. Novel aspects of the Belle II flavor tagger

The major improvements in the Belle II flavor tagger with respect to the Belle flavor tagger consist of the inclusion of three complementary flavor signatures corresponding to the Kaon–Pion, the FSC, and the Maximum P* categories; the consideration of fast kaons as targets in the Fast Hadron category (Belle used only fast pions); the use of more tagging variables within each category; and the employment of robust FBDT and MLP multivariate methods. The Belle flavor tagger is based on multidimensional lookup tables and considers 10 flavor signatures, which correspond to those used by the Belle II flavor tagger apart from the three complementary signatures mentioned above. The flavor

Table 27. Performance of the Belle II flavor tagger on Belle data. All values are given in percent considering only statistical uncertainties.

r interval	ε_i	$w_i \pm \delta w_i$	$\varepsilon_{\mathrm{eff},i} \pm \delta\varepsilon_{\mathrm{eff},i}$
FBDT Combiner			
0.000–0.100	15.19	47.64 ± 0.04	0.034 ± 0.001
0.100–0.250	16.53	41.50 ± 0.06	0.477 ± 0.013
0.250–0.500	20.28	31.39 ± 0.09	2.803 ± 0.066
0.500–0.625	10.04	21.74 ± 0.06	3.204 ± 0.105
0.625–0.750	11.07	15.63 ± 0.06	5.222 ± 0.162
0.750–0.875	10.34	9.40 ± 0.06	6.807 ± 0.218
0.875–1.000	16.38	2.33 ± 0.05	14.863 ± 0.366
Total		$\varepsilon_{\mathrm{eff}} = \sum_i \varepsilon_i \cdot \langle 1 - 2w_i \rangle^2 = 33.6 \pm 0.5$	

signatures used by the Belle flavor tagger are sorted into four categories (Lepton, Kaon, Slow Pion, and Lambda). In comparison, the Belle II flavor tagger considers 13 flavor signatures. Furthermore, in the Fast Hadron category, fast pions and fast kaons are considered together. In the Belle approach, each particle candidate could be used only once as a candidate within a certain category according to a specific classification criterion, while in the Belle II flavor tagger each particle candidate is used as a candidate within all categories (disregarding the Lambda category).

In comparison with the previous Belle flavor tagger, which reached an effective efficiency of $(30.1 \pm 0.4)\%$ on Belle data [2], the Belle II flavor tagger reaches an effective efficiency of $(33.6 \pm 0.5)\%$ on Belle data. An additional increase of about 3% in effective efficiency is observed with the Belle II flavor tagger on Belle II MC, which is due to the improved track reconstruction and the improved PID performance at Belle II.

6.6. Full event interpretation

6.6.1. Introduction

Measurements of decays including neutrinos, in particular rare decays, suffer from missing kinematic information. The full event interpretation [82] (FEI) algorithm partially recovers this information by reconstructing one of the B mesons from the decay of the $\Upsilon(4S)$ meson. Information from the reconstructed B meson together with the precisely known initial state infers kinematic and flavor constraints on the remaining B meson, which is considered for a subsequent signal analysis. The two mesons are denoted the tag-side B_{tag} and the signal-side B_{sig}, respectively, as illustrated in Figure 51.

FEI is an essential component in a wide range of analyses, including the measurement of the CKM matrix element $|V_{ub}|$ through the semileptonic decay $b \to u\ell\nu$, the search for a charged Higgs effect in $B \to D\tau\nu$, and the precise measurement of the branching fraction of $B \to \tau\nu$.

Belle employed a similar algorithm for tag-side B meson reconstruction called full reconstruction (FR) [83]. As further developments, FEI includes best candidate selections and more decay modes, and provides more automation.

6.6.2. Algorithm

The basic idea of FEI is to reconstruct, in a hierarchical manner, individual particle decay channels that occur in the decay chain of the B meson. For each unique decay channel of a particle, a multivariate classifier (MVC) is trained using simulated events.

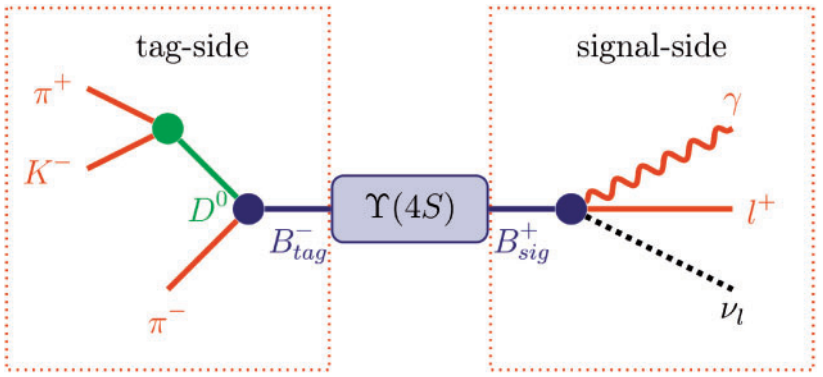

Fig. 51. Diagram showing the use of FEI in a search for the decay $B^+ \to l^+\nu_l\gamma$. The FEI algorithm is used to reconstruct the tag-side B meson, $B^-_{\rm tag}$, which in this case decays as $B^-_{\rm tag} \to (D^0 \to \pi^+K^-)\pi^-$. Meanwhile, the signal-side B meson, $B^-_{\rm signal}$, decays to $l^+\nu_l\gamma$.

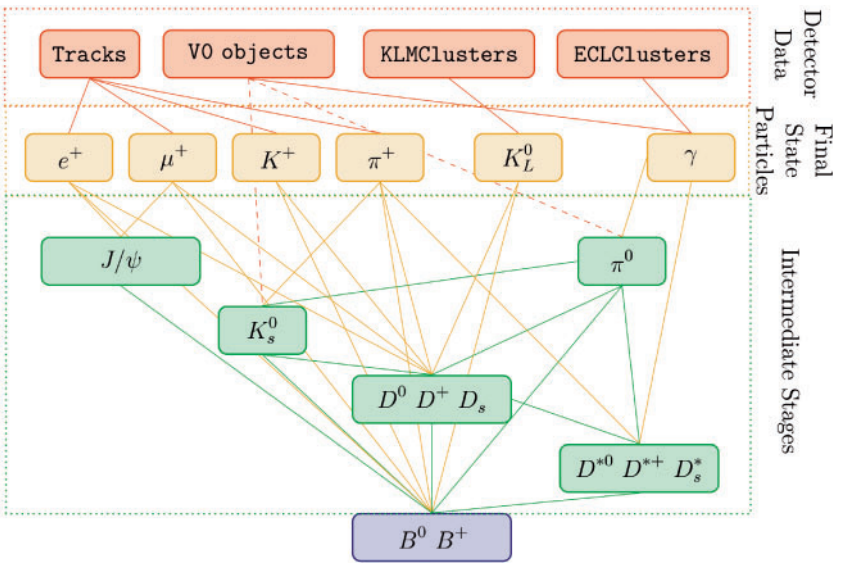

Fig. 52. Hierarchy of the full event interpretation algorithm.

The algorithm starts by selecting final-state particle candidates, which include electrons, muons, pions, $K^0_{\rm L}$ mesons, and photons, and training an MVC for each of these using detector information. Building on this, intermediate particle candidates, which include J/ψ , π^0, D, and D^* mesons, are reconstructed and an MVC is trained for each reconstructed decay channel. Finally, the B candidates are reconstructed and the corresponding classifiers are trained. The hierarchical structure of FEI is shown in Fig. 52, and a full list of decay modes reconstructed by the algorithm is given in Table 28.

An important aspect of FEI is that the MVC of a given particle utilizes as an input the MVC outputs of any daughters in addition to kinematic information (e.g. daughter four-momenta, vertex fit information). The MVC for a candidate, in effect, combines all the information about a candidate into a single value, the signal probability. Consequently, candidates from different decay channels can be treated equally in the following reconstruction steps. For instance, FEI reconstructs 15 decay channels of the D^0. Afterwards, the generated D^0 candidates are used to reconstruct D^{*0} in two decay channels. All the information about the specific D^0 decay channel of the candidate is encoded in its signal probability, which is available to the D^{*0} classifiers. Thereby, the hierarchical approach

Table 28. B^+, B^0, and D decay modes included in FEI. The modes listed in the lower part of the table were not considered in the Belle FR.

B^+ modes	B^0 modes	D^+, D^{*+}, D_s^+ modes	D^0,D^{*0} modes
$B^+ \to \bar{D}^0\pi^+$	$B^0 \to D^-\pi^+$	$D^+ \to K^-\pi^+\pi^+$	$D^0 \to K^-\pi^+$
$B^+ \to \bar{D}^0\pi^+\pi^0$	$B^0 \to D^-\pi^+\pi^0$	$D^+ \to K^-\pi^+\pi^+\pi^0$	$D^0 \to K^-\pi^+\pi^0$
$B^+ \to \bar{D}^0\pi^+\pi^0\pi^0$	$B^0 \to D^-\pi^+\pi^+\pi^-$	$D^+ \to K^-K^+\pi^+$	$D^0 \to K^-\pi^+\pi^+\pi^-$
$B^+ \to \bar{D}^0\pi^+\pi^+\pi^-$	$B^0 \to D_s^+D^-$	$D^+ \to K^-K^+\pi^+\pi^0$	$D^0 \to \pi^-\pi^+$
$B^+ \to D_s^+\bar{D}^0$	$B^0 \to D^{*-}\pi^+$	$D^+ \to K_S^0\pi^+$	$D^0 \to \pi^-\pi^+\pi^0$
$B^+ \to \bar{D}^{*0}\pi^+$	$B^0 \to D^{*-}\pi^+\pi^0$	$D^+ \to K_S^0\pi^+\pi^0$	$D^0 \to K_S^0\pi^0$
$B^+ \to \bar{D}^{*0}\pi^+\pi^0$	$B^0 \to D^{*-}\pi^+\pi^+\pi^-$	$D^+ \to K_S^0\pi^+\pi^+\pi^-$	$D^0 \to K_S^0\pi^+\pi^-$
$B^+ \to \bar{D}^{*0}\pi^+\pi^+\pi^-$	$B^0 \to D^{*-}\pi^+\pi^+\pi^-\pi^0$	$D^{*+} \to D^0\pi^+$	$D^0 \to K_S^0\pi^+\pi^-\pi^0$
$B^+ \to \bar{D}^{*0}\pi^+\pi^+\pi^-\pi^0$	$B^0 \to D_s^{*+}D^-$	$D^{*+} \to D^+\pi^0$	$D^0 \to K^-K^+$
$B^+ \to D_s^{*+}\bar{D}^0$	$B^0 \to D_s^+D^{*-}$	$D_s^+ \to K^+K_S^0$	$D^0 \to K^-K^+K_S^0$
$B^+ \to D_s^+\bar{D}^{*0}$	$B^0 \to D_s^{*+}D^{*-}$	$D_s^+ \to K^+\pi^+\pi^-$	$D^{*0} \to D^0\pi^0$
$B^+ \to \bar{D}^0K^+$	$B^0 \to J/\psi\, K_S^0$	$D_s^+ \to K^+K^-\pi^+$	$D^{*0} \to D^0\gamma$
$B^+ \to D^-\pi^+\pi^+$	$B^0 \to J/\psi\, K^+\pi^+$	$D_s^+ \to K^+K^-\pi^+\pi^0$	
$B^+ \to J/\psi\, K^+$	$B^0 \to J/\psi\, K_S^0\pi^+\pi^-$	$D_s^+ \to K^+K_S^0\pi^+\pi^-$	
$B^+ \to J/\psi\, K^+\pi^+\pi^-$		$D_s^+ \to K^-K_S^0\pi^+\pi^+$	
$B^+ \to J/\psi\, K^+\pi^0$		$D_s^+ \to K^+K^-\pi^+\pi^+\pi^-$	
		$D_s^+ \to \pi^+\pi^+\pi^-$	
		$D_s^{*+} \to D_s^+\pi^0$	
$B^+ \to D^-\pi^+\pi^+\pi^0$	$B^0 \to D^-\pi^+\pi^0\pi^0$	$D^+ \to \pi^+\pi^0$	$D^0 \to K^-\pi^+\pi^0\pi^0$
$B^+ \to \bar{D}^0\pi^+\pi^+\pi^-\pi^0$	$B^0 \to D^-\pi^+\pi^+\pi^-\pi^0$	$D^+ \to \pi^+\pi^+\pi^-$	$D^0 \to K^-\pi^+\pi^+\pi^-\pi^0$
$B^+ \to \bar{D}^0D^+$	$B^0 \to \bar{D}^0\pi^+\pi^-$	$D^+ \to \pi^+\pi^+\pi^-\pi^0$	$D^0 \to \pi^-\pi^+\pi^+\pi^-$
$B^+ \to \bar{D}^0D^+K_S^0$	$B^0 \to D^-D^0K^+$	$D^+ \to K^+K_S^0K_S^0$	$D^0 \to \pi^-\pi^+\pi^0\pi^0$
$B^+ \to \bar{D}^{*0}D^+K_S^0$	$B^0 \to D^-D^{*0}K^+$	$D^{*+} \to D^+\gamma$	$D^0 \to K^-K^+\pi^0$
$B^+ \to \bar{D}^0D^{*+}K_S^0$	$B^0 \to D^{*-}D^0K^+$	$D_s^+ \to K_S^0\pi^+$	
$B^+ \to \bar{D}^{*0}D^{*+}K_S^0$	$B^0 \to D^{*-}D^{*0}K^+$	$D_s^+ \to K_S^0\pi^+\pi^0$	
$B^+ \to \bar{D}^0D^0K^+$	$B^0 \to D^-D^+K_S^0$	$D_s^{*+} \to D_s^+\pi^0$	
$B^+ \to \bar{D}^{*0}D^0K^+$	$B^0 \to D^{*-}D^+K_S^0$		
$B^+ \to \bar{D}^0D^{*0}K^+$	$B^0 \to D^-D^{*+}K_S^0$		
$B^+ \to \bar{D}^{*0}D^{*0}K^+$	$B^0 \to D^{*-}D^{*+}K_S^0$		
$B^+ \to \bar{D}^{*0}\pi^+\pi^0\pi^0$	$B^0 \to D^{*-}\pi^+\pi^0\pi^0$		

reconstructs $2 \times 15 = 30$ exclusive decay channels and provides a signal probability for each candidate that makes use of all available information.

It is computationally infeasible to handle all possible B meson candidates from all possible particle candidates. The FEI algorithm handles this issue of combinatorics by applying pre- and post-selections on each particle candidate. The pre-selection is performed before computationally demanding tasks such as vertex fits or application of MVCs, and consists of a basic selection to remove wrongly reconstructed candidates and a best candidate selection. For the best candidate selection, the candidates are ranked according to a discriminating variable and only the n highest ranked candidates are accepted, where n depends on the particle species and is usually is between 10 and 20. The post-candidate selection makes a tighter selection on the signal probability of the candidate itself and hence uses all available information about the candidate. In addition, it includes a best candidate selection accepting the m (usually in the range 10–20) highest ranked candidates according to signal probability.

6.6.3. Hadronic, semileptonic and inclusive tagging

There are three distinct tag-side reconstruction methods in common use: hadronic, semileptonic, and inclusive tag-side reconstruction.

- Hadronic tagging solely uses hadronic decay channels for B reconstruction. Hence, the kinematics of the reconstructed candidates are well known and the tagged sample is pure. The method is typically low in efficiency, at the order of 0.1%.
- Semileptonic tagging uses semileptonic B decays. Due to the high branching fraction of semileptonic decays this approach usually has a higher tagging efficiency. This method suffers from missing kinematic information due to the neutrino in the final state of the decay. Hence, the sample is not as pure as in the hadronic case.
- Inclusive tagging combines the four-momenta of all particles in the rest of the event of the signal-side B candidate. The achieved tagging efficiency is usually one order of magnitude above the hadronic and semileptonic tagging approaches. However, the decay topology is not explicitly reconstructed, and the method suffers from high background.

FEI combines the first two methods, hadronic and semileptonic tag-side reconstruction, into a single algorithm.

6.6.4. Training modes

FEI is trained on MC and subsequently applied to collision data. There are three different types of events one has to consider in the training and application of FEI:

- $B\bar{B}$ events: $\Upsilon(4S) \to B\bar{B}$ for charged and neutral $B\bar{B}$ pairs.
- Continuum events: $e^+e^- \to c\bar{c}, s\bar{s}, d\bar{d}, u\bar{u}$.
- Signal events: $e^+e^- \to \Upsilon(4S) \to B\bar{B}$, where one B decays generically and the other decays in a signal channel such as $B^+ \to \tau^+\nu$.

The final classifier output for the B_{tag} mesons is used to separate signal from background. The dominant background is typically from $B\bar{B}$ events. In the study presented here, continuum suppression criteria are not applied and the FEI algorithm is trained solely using simulated $B\bar{B}$ events.

6.6.5. Performance estimates

The performance of FEI can quantified by the tag-side efficiency, which is defined as the number of correctly reconstructed tag-side B mesons divided by the total number of $\Upsilon(4S)$ events. While, in MC, events correctly reconstructed events can be determined using MC matching, in data a maximum likelihood fit in a discriminating variable must be used to distinguish correctly reconstructed tag-side B mesons. Another important performance estimate of FEI is the purity, which is defined as the number of correctly reconstructed tag-side B mesons divided by the number of events in which a tag-side B meson is reconstructed. Tighter selections on the signal probability of the tag-side B meson increase purity with the trade-off of a lower tag-side efficiency. The maximal achievable tag-side efficiency is particularly important as it is directly related to maximal achievable signal efficiency for a given measurement.

The maximum tag-side efficiency of FEI as estimated on Belle and Belle II MC is compared with that of the predecessor FR algorithm in Table 29. We observe much higher efficiency with the Belle II algorithm in Belle MC for both hadronic and semileptonic channels, particularly for loose selection.

Table 29. Tag-side efficiency defined as the number of correctly reconstructed tag-side B mesons divided by the total number of $\Upsilon(4S)$ events. Belle II has much higher beam background, which can affect the total efficiency.

Tag	FR, Belle	FEI, Belle MC	FEI, Belle II MC
Hadronic B^+	0.28 %	0.49 %	0.61 %
Semileptonic B^+	0.67 %	1.42 %	1.45 %
Hadronic B^0	0.18 %	0.33%	0.34 %
Semileptonic B^0	0.63 %	1.33%	1.25 %

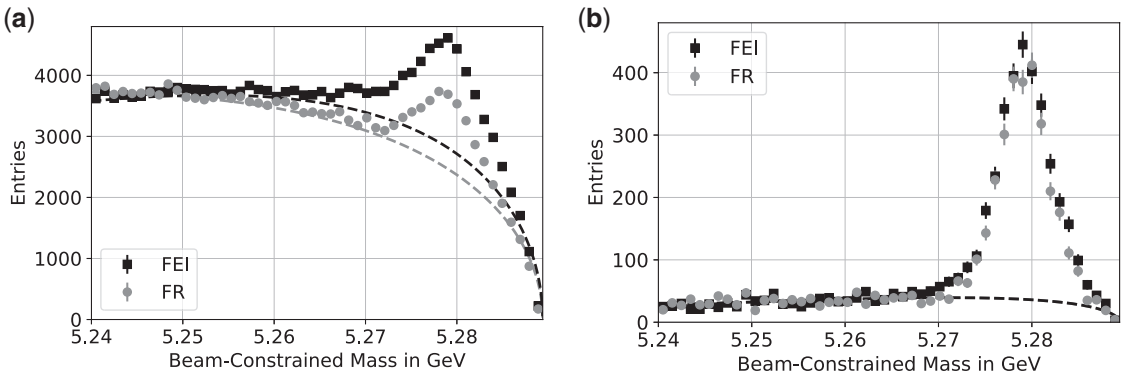

Beam-energy constrained mass of charged hadronic tag candidates with a loose threshold on the classifier output.

Beam-energy constrained mass of charged hadronic tag candidates with a tight threshold on the classifier output.

Fig. 53. Performance of B candidate reconstruction in hadronic decay modes with the FEI and FR algorithms on Belle data.

This is largely attributable to the newly added modes in FEI, which are less clean than those used commonly with FR. Figure 53 shows a comparison between the beam-energy-constrained mass distributions of FEI and FR with Belle data for tight and loose selections on the signal probability. We observe a much higher efficiency with the Belle II algorithm for purities below 50% (75%) for charged (neutral) B_{tag} reconstruction. This is most likely due to the newly added modes in FEI, which are less clean than those used commonly with FR. This, additionally, results in the algorithm having a much higher maximum tag-side efficiency, as shown in Table 29.

Figure 54 shows the tag-side efficiency against purity for B^+ and B^0 tag-side candidates in Belle II MC. The points correspond to the scan of the tag-side B meson signal probability starting from 0.01 with steps of 0.04. We find that beam-induced background has a large effect and reduces the achievable tag-side efficiency for a given purity.

6.6.6. Calibration

There can be substantial differences between the tag-side reconstruction efficiency in data and simulation given the large number of decay modes considered by FEI, the large number of MVCs, and the reliance on simulation to train FEI. An important systematic error in analyses using full B reconstruction methods is the FEI efficiency calibration, which directly affects absolute branching

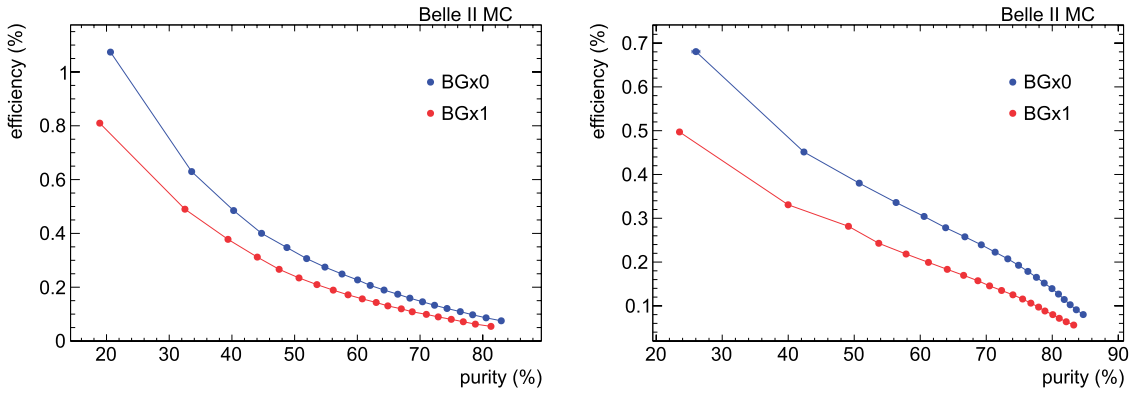

Fig. 54. Efficiency versus purity of charged B (left) and neutral B (right) candidates reconstructed with FEI in hadronic modes. Two beam-induced background scenarios are compared: zero background (BGx0) and nominal background (BGx1).

fraction measurements. In the case of semileptonic B decay measurements, it has become the dominant systematic uncertainty and hence is a limiting factor in precision measurements at Belle II. Several techniques for calibration have been used at Belle:

- $B \to D^{(*)}\ell\nu$ *calibration*. Events are double tagged, where the signal side is reconstructed in a known semileptonic decay mode, in bins of the tag quality variables. This has been used in $B \to X_u\ell\nu$ analyses. The systematic errors were approximately 4.5%, shared between statistical (1.5%), reconstruction (2.7%), and branching fraction uncertainties (3%) [84]. The detection uncertainties are mostly based on data-driven techniques, while the branching fractions are more difficult to improve in the future.
- $B \to X\ell\nu$ *calibration*. Events are also double tagged, but here the signal side selected only via the presence of a charged lepton originating from a semileptonic B decay. This has been used in precision exclusive $B \to D^{(*)}\ell\nu$ decay analyses [85]. The technique is systematics-limited but higher precision than the $B \to D^{(*)}\ell\nu$ calibration approach.
- *Control mode calibration*. An analysis sideband region is chosen that is enhanced in a well-known decay mode, and calibrated accordingly. This technique has been used by rare decay analyses where it is useful to calibrate tag efficiencies with topologies similar to the signal process.

7. Theory overview

Section authors: C. Hanhart, S. Hashimoto, T. Kaneko, E. Kou, A.S. Kronfeld, U. Nierste, S. Prelovsek, S.R. Sharpe, J. Shigemitsu, S. Simula

7.1. Introduction

The source of flavor violation in the SM is the Yukawa interaction between fermions and the Higgs doublet,

$$\Phi = \begin{pmatrix} \phi^+ \\ v + \frac{H+i\chi}{\sqrt{2}} \end{pmatrix}. \tag{46}$$

Here, H is the field of the physical Higgs fields, $v = 174$ GeV is the vacuum expectation value (vev), and ϕ^+ and χ are the pseudo-Goldstone fields related to longitudinally polarized W^+ and Z bosons.

The quark Yukawa Lagrangian is

$$\mathcal{L}^q_{\rm Yuk} = -\,\overline{Q}_j\, Y^d_{jk}\, \Phi\, d'_{Rk} \;-\; \overline{Q}_j\, Y^u_{jk}\, \epsilon\, \Phi^* u'_{Rk} + \text{h.c.}, \tag{47}$$

where $j,k = 1,2,3$ label the generation (repeated indices are summed over) and

$$\epsilon = \begin{pmatrix} 0 & 1 \\ -1 & 0 \end{pmatrix}.$$

The right-handed quark fields u'_{Rk}, d'_{Rk} are singlets of the electroweak gauge group SU(2), while the left-handed quarks form SU(2) doublets:

$$Q_j = \begin{pmatrix} u'_{Lj} \\ d'_{Lj} \end{pmatrix}.$$

The arbitrary complex 3×3 Yukawa matrices $Y^{u,d}$ give rise to the two quark mass matrices $M^{u,d} = Y^{u,d} v$. To diagonalize these matrices we perform unitary rotations of the fields $u'_{L,Rk}$, $d'_{L,Rk}$ (called "weak eigenstates") to a new basis of "mass eigenstates": $u'_{L,Rj} = S^u_{L,Rjk}\, u_{L,Rk}$, $d'_{L,Rj} = S^d_{L,Rjk}\, d_{L,Rk}$.

The unprimed fields correspond to the physical particles, and where convenient we write $u_R = u_{R1}$, $c_R = u_{R2}$, and $t_R = u_{R3}$, with analogous notation for the left-handed and down-type quark fields. The piece of $\mathcal{L}^q_{\rm Yuk}$ containing the—now diagonal—mass matrices reads:

$$\begin{aligned} \mathcal{L}_m &= -\,m_{u_j}\left[\bar{u}_{Lj} u_{Rj} + \bar{u}_{Rj} u_{Lj}\right] - m_{d_j}\left[\bar{d}_{Lj} d_{Rj} + \bar{d}_{Rj} d_{Lj}\right] \\ &\equiv -\sum_{q=u,d,s,c,b,t} m_q\, \overline{q} q. \end{aligned}$$

Here, $m_{u,\ldots t}$ are the quark masses and we have introduced the usual four-component Dirac field $q \equiv q_L + q_R$ (recalling $\overline{q}_R q_R = \overline{q}_L q_L = 0$). The four unitary matrices $S^{u,d}_{L,R}$ drop out everywhere with one important exception: the Cabibbo–Kobayashi–Maskawa (CKM) matrix,

$$V = S^{u\dagger}_L S^d_L, \tag{48}$$

appears in the couplings of the W boson to quarks:

$$\mathcal{L}^q_W = \frac{g}{\sqrt{2}}\left[V_{jk}\, \bar{u}_{Lj}\, \gamma^\mu d_{Lk}\, W^+_\mu + V^*_{jk}\, \bar{d}_{Lk}\, \gamma^\mu u_{Lj}\, W^-_\mu\right]. \tag{49}$$

CKM elements are commonly labeled with the quark flavors, so that, e.g., $V_{cb} \equiv V_{u_2 d_3} \equiv V_{23}$. $\mathcal{L}^q_W$ violates the discrete symmetries parity (P), time reversal (T), and charge conjugation (C). The parity transformation $\vec{x} \to -\vec{x}$ exchanges the left-handed quark fields in the Lagrangian of Eq. (49) with their right-handed counterparts. Since the W boson does not couple at all to right-handed quarks, P violation in the SM is maximal. The same is true for C violation, because C maps left-handed fermion fields onto right-handed anti-fermion fields. However, the combination of the two transformations, CP, does not change the chirality of the fermion fields in Eq. (49):

$$\bar{u}_{Lj}\, \gamma^\mu d_{Lk}\, W^+_\mu \quad \overset{\rm CP}{\longleftrightarrow} \quad \bar{d}_{Lk}\, \gamma^\mu u_{Lj}\, W^-_\mu. \tag{50}$$

Apparently $\mathcal{L}^q_W$ conserves CP if V_{jk} is real. However, $\text{Im}\, V_{jk} \neq 0$ does not imply that CP is violated: if we can make V_{jk} real by multiplying the quark fields with unphysical phase factors, $d_k \to d_k \exp(i\phi_{d_k})$ and $u_j \to u_j \exp(i\phi_{u_j})$, CP is conserved as well. You can easily check that this

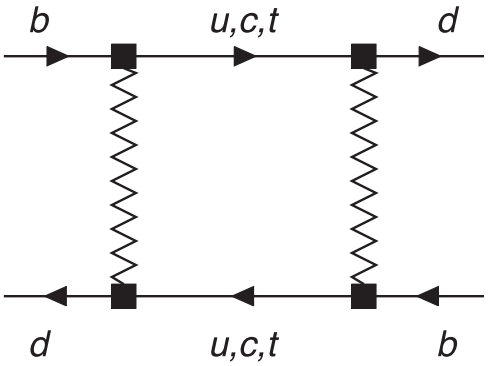

Fig. 55. Box diagram for $B^0_d - \overline{B}^0_d$ mixing.

rephasing of the quark fields changes V_{jk} in Eq. (49) to $V_{jk}\exp(i\phi_{d_k} - i\phi_{u_j})$. In a world with just two fermion generations it is always possible to render V_{jk} real. Kobayashi and Maskawa realized that this is no longer true once you add a third generation, and thereby correctly identified the dominant mechanism of CP violation in flavor-changing transitions [86]. A unitary 3×3 matrix involves six complex phases, five of which can be removed by the rephasing transformation described above. The remaining phase is a physical, CP-violating parameter, the Kobayashi–Maskawa (KM) phase $\delta_{\rm KM}$.

Flavor-changing transitions among fermions with the same electric charge are called flavor-changing neutral current (FCNC) processes. The unitarity of the matrices $S^{u,d}_{L,Rjk}$ and the CKM matrix V in Eq. (48) leads to a dramatic suppression of FCNC transitions, which is referred to as the Glashow–Iliopoulos–Maiani (GIM) mechanism. The tree-level GIM mechanism renders the couplings of the neutral gauge bosons (Z, photon γ, gluon g) flavor-diagonal. We exemplify this for Z coupling to right-handed down-type quarks here:

$$\begin{aligned} Z^\mu\, \bar{d}'_{Rj}\gamma_\mu d'_{Rj} &= Z^\mu\, \bar{d}_{Rk} S^{d\dagger}_{Rkj}\gamma_\mu S^d_{Rjl} d_{Rl} \\ &= Z^\mu\, \bar{d}'_{Rk}\gamma_\mu d_{Rk}. \end{aligned}$$

In the last step the unitarity relation $S^{d\dagger}_{Rkj}S^d_{Rjl} = \delta_{kl}$ has been used. Historically, the aim to understand the suppression of the FCNC process $s \to d\mu^+\mu^-$ led Glashow, Iliopoulos, and Maiani to postulate the existence of a fourth quark, charm, to build an SU(2) doublet $Q_2 = (c_L, s_L)^{\rm T}$ in analogy to $Q_1 = (u_L, d_L)^{\rm T}$. The GIM mechanism only works if the gauge interactions treat all fermion generations on the same footing, so that the described unitary rotations are meaningful. While FCNC processes are forbidden at tree level, they nevertheless occur through loop diagrams. Figures 55 and 56 show two prominent examples, the $B^0_d - \overline{B}^0_d$ mixing box and the gluon penguin diagrams.

The GIM mechanism also affects such loop-induced FCNC transitions. The diagrams of Figs. 55 and 56 involve contributions from different quarks on the internal lines, namely u, c, and t. These contributions differ from each other only by the CKM elements accompanying the W couplings and by the masses of the virtual up-type quarks, e.g. for the penguin amplitude of Fig. 56 we may write

$$\mathcal{A} = \sum_{q=u,c,t} V^*_{qb}V_{qd}\, f\left(\frac{m_q^2}{M_W^2}\right), \tag{51}$$

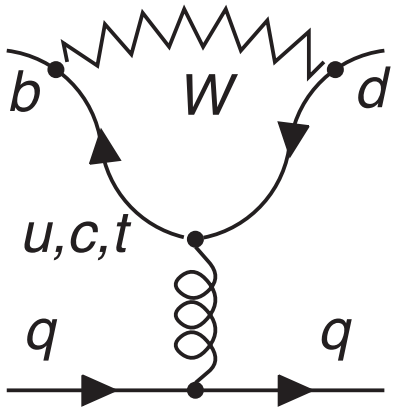

Fig. 56. Penguin diagram for the decay $b \to dq\bar{q}$ with the curly line representing a gluon. For $q = u$ or $q = c$ there is also a tree diagram.

where M_W is the mass of the W boson. Now, CKM unitarity implies that $V_{cb}^* V_{cd} = -V_{tb}^* V_{td} - V_{ub}^* V_{ud}$, and we may eliminate $V_{cb}^* V_{cd}$ from Eq. (51):

$$\mathcal{A} = \; V_{tb}^* V_{td} \left[f\left(\frac{m_t^2}{M_W^2}\right) - f\left(\frac{m_c^2}{M_W^2}\right) \right] + V_{ub}^* V_{ud} \left[f\left(\frac{m_u^2}{M_W^2}\right) - f\left(\frac{m_c^2}{M_W^2}\right) \right]. \tag{52}$$

We observe that the terms in square brackets vanish if the two masses involved are equal. Nowadays this feature is usually meant when people refer to the GIM mechanism. Since $m_c - m_u \ll M_W$, the second term in Eq. (52) is GIM suppressed. We realize that the large value of m_t makes the first term unsuppressed. Historically, the unexpectedly large $B_d^0 - \overline{B}_d^0$ mixing observed in 1987 at the ARGUS detector at DESY was the first hint of a heavy top quark. The situation is different in charm physics. Here, the quarks on the internal line are d, s, and b, and moreover the diagrams with virtual t come with the tiny CKM factor $V_{cb}^* V_{ub}$. Thus the SM predictions for FCNC transitions of charm quarks are tiny.

In summary, flavor physics probes the Yukawa sector of the SM. Theories going beyond the SM (BSM models) may contain a larger Higgs sector with new Yukawa couplings or may involve flavor-violating parameters which are unrelated to Higgs–fermion couplings. FCNC transitions are suppressed by a loop factor and small CKM elements. In a large class of FCNC observables (including all FCNC charm transitions and FCNC decays of charged leptons) there is an additional GIM suppression. These features make FCNC transitions very sensitive to new physics, with the power to probe virtual effects of particles with masses above 100 TeV (and the actual sensitivity depending on the considered model). To date, flavor physics is the only field in which CP violation has been observed. The SM accommodates CP violation in flavor-changing transitions through a single parameter, the KM phase in the CKM matrix.

7.2. CKM matrix and unitarity triangle

The CKM matrix is the 3×3 unitary matrix

$$\mathbf{V} = \begin{pmatrix} V_{ud} & V_{us} & V_{ub} \\ V_{cd} & V_{cs} & V_{cb} \\ V_{td} & V_{ts} & V_{tb} \end{pmatrix}, \quad \mathbf{V}\mathbf{V}^\dagger = 1, \tag{53}$$

which can be parameterized by four free parameters. The flavor physics program at Belle II, just like at its predecessors, will have the ability to over-constrain these parameters and the potential to discover significant deviations from SM expectations.

The standard choice of the CKM matrix is obtained as the product of three rotation matrices ordered as [87,88]

$$\mathbf{V} = \begin{pmatrix} c_{12}c_{13} & s_{12}c_{13} & s_{13}e^{-i\delta} \\ -s_{12}c_{23} - c_{12}s_{23}s_{13}e^{i\delta} & c_{12}c_{23} - s_{12}s_{23}s_{13}e^{i\delta} & s_{23}c_{13} \\ s_{12}s_{23} - c_{12}c_{23}s_{13}e^{i\delta} & -c_{12}s_{23} - s_{12}c_{23}s_{13}e^{i\delta} & c_{23}c_{13} \end{pmatrix}, \tag{54}$$

where $c_{ij} = \cos\theta_{ij}$, $s_{ij} = \sin\theta_{ij}$, and δ is the CP-violating phase. With experimental knowledge of the hierarchy $|V_{ub}|^2 \ll |V_{cb}|^2 \ll |V_{us}|^2$, an expansion was introduced [89]. By defining [90]

$$s_{12} \equiv \lambda, \quad s_{23} \equiv A\lambda^2, \quad s_{13}e^{-i\delta} = A\lambda^3(\rho - i\eta), \tag{55}$$

where $\lambda \simeq 0.22$, we can rewrite the CKM matrix in terms of the four new parameters A, λ, ρ, and η:

$$\mathbf{V} = \begin{pmatrix} 1 - \frac{1}{2}\lambda^2 & \lambda & A\sqrt{\rho^2+\eta^2}e^{-i\delta}\lambda^3 \\ -\lambda & 1 - \frac{1}{2}\lambda^2 & A\lambda^2 \\ A(1 - \sqrt{\rho^2+\eta^2}e^{i\delta})\lambda^3 & -A\lambda^2 & 1 \end{pmatrix} + \mathcal{O}(\lambda^4), \tag{56}$$

which is, up to $\mathcal{O}(\lambda^4)$, equivalent to the Wolfenstein parameterization [89]. Notice that the definition in Eq. (55) implies that the unitarity condition can be written in terms of A, λ, ρ, and η at all orders of λ.

The unitarity condition of the CKM matrix leads to nine independent equations. The one most relevant to B physics is

$$V_{ud}^* V_{ub} + V_{cd}^* V_{cb} + V_{td}^* V_{tb} = 0. \tag{57}$$

In order to form the *unitarity triangle* (UT), we divide this equation by $V_{cd}V_{cb}^*$,[9]

$$1 + \frac{V_{ud}^* V_{ub}}{V_{cd}V_{cb}^*} + \frac{V_{td}^* V_{tb}}{V_{cd}V_{cb}^*} = 0, \tag{58}$$

and then introduce new parameters [91]:

$$\bar{\rho} + i\bar{\eta} \equiv -\frac{V_{ud}V_{ub}^*}{V_{cd}V_{cb}^*}, \qquad 1 - (\bar{\rho} + i\bar{\eta}) \equiv -\frac{V_{td}V_{tb}^*}{V_{cd}V_{cb}^*}, \tag{59}$$

which are related to ρ and η in Eq. (55) as[10]

$$\rho + i\eta = \frac{\sqrt{1 - A^2\lambda^4}(\bar{\rho} + i\bar{\eta})}{\sqrt{1-\lambda^2}[1 - A^2\lambda^4(\bar{\rho} + i\bar{\eta})]}. \tag{60}$$

[9] Note that $V_{cd}V_{cb}^* = -A\lambda^3 + \mathcal{O}(\lambda^7)$, but in practice we often assume that $V_{cd}V_{cb}^*$ is real and $|V_{cd}V_{cb}^*| = A\lambda^3$.

[10] Note that the definition of $\bar{\rho}$ and $\bar{\eta}$ in Eq. (59) and the relation in Eq.(60) are to all orders in λ. The $\bar{\rho}, \bar{\eta}$ here are equivalent to those in Ref. [90] up to $\mathcal{O}(\lambda^4)$.

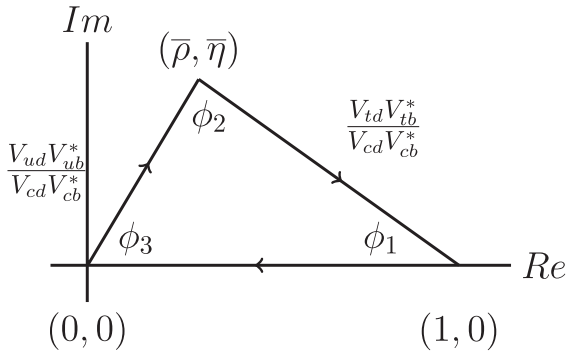

Fig. 57. The unitarity triangle.

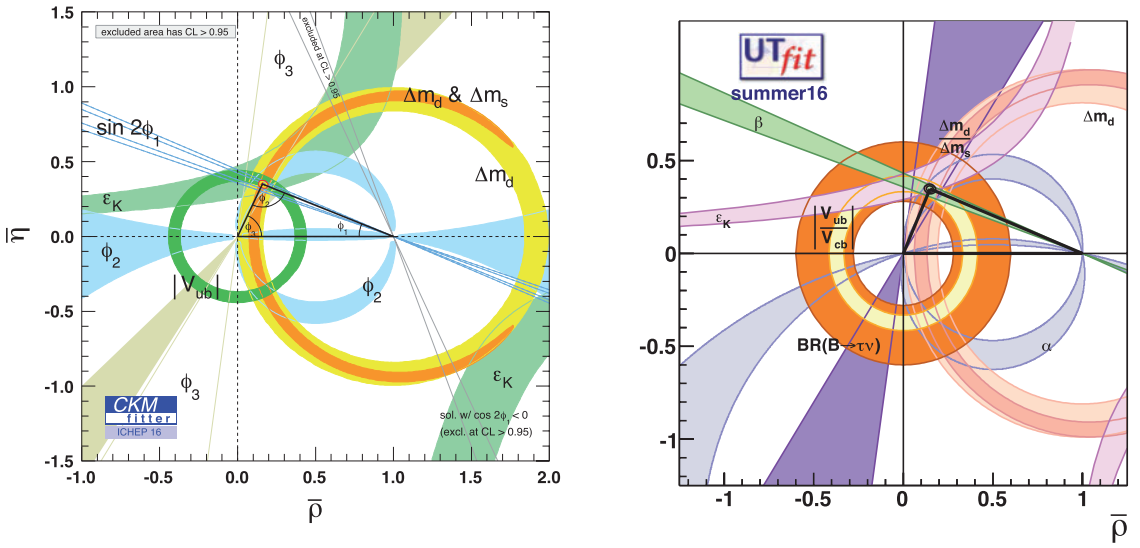

Fig. 58. The current situation for the unitarity triangle constraints using `CKMfitter` (left) and `UTfit` (right).

The UT is then obtained by drawing Eq. (58) on the $\bar{\rho}$–$\bar{\eta}$ plane (see Fig. 57). The three angles are defined as

$$\phi_1 \equiv \arg\left[-\frac{V_{cd}V_{cb}^*}{V_{td}V_{tb}^*}\right], \quad \phi_2 \equiv \arg\left[-\frac{V_{td}V_{tb}^*}{V_{ud}V_{ub}^*}\right], \quad \phi_3 \equiv \arg\left[-\frac{V_{ud}V_{ub}^*}{V_{cd}V_{cb}^*}\right]. \tag{61}$$

These angles are also known as $\phi_1 = \beta$, $\phi_2 = \alpha$, and $\phi_3 = \gamma$.

The latest results of the global fit to UT parameters are shown in Fig. 58. Two sides of the triangle are determined from measurements of decay rates $|V_{ub}|/|V_{cb}|$ and mixing $\Delta M_d/\Delta M_s$. These constraints, as well those coming from indirect CP violation measurements in kaons, ϵ_K, depend strongly on the hadronic parameter inputs. The theoretical computations of these parameters will be reviewed in the next subsection. We emphasize that improvements in lattice QCD computations become crucial for a more precise determination of the sides of the triangle.

The bound from the $|V_{ub}|/|V_{cb}|$ constraint shown in these figures is obtained through combinations of various measurements. However, as reviewed in Chapter 8, there are tensions between V_{ub} determinations with exclusive and inclusive semi-leptonic $b \to ul\nu$ decays in addition to a hint of a deviation from the SM in the tauonic pure-leptonic $B \to \tau\nu$ decay. New physics contributions can be different for these three types of processes (see Chapter 17) and improved Belle II measurements will

provide us with a more detailed picture. We note in passing that the V_{us} element, which determines the λ parameter, also shows some disagreement between its determination by the exclusive K decays and the inclusive τ decay. The latter can be studied at Belle II, which can help to improve the V_{us} determination (see Chapter 15).

The angles ϕ_1, ϕ_2 are determined from measurements of time-dependent CP asymmetries, as detailed in Chapter 10. The angle ϕ_1 has been measured from the interference between B_d oscillation with $b \to c\bar{c}s$ decays, and was an outstanding success of the BaBar and Belle collaborations. Contrary to the other oscillation parameter, ΔM_d, most of the hadronic uncertainties cancel out in this CP-violating observable and it therefore provides a very clean and precise determination of ϕ_1. B_d oscillation arises from an FCNC $b\bar{d}$–$\bar{b}d$ coupling, which is induced by the W boson box diagram in the SM, as shown in the previous section. Various new physics models predict extra contributions to the $b\bar{d}$–$\bar{b}d$ coupling, via either tree or loop diagrams. For either process, we should keep in mind that there is correlation between new physics contributions to ϕ_1 measured in $b \to c\bar{c}s$ decays and those to ΔM_d, since both come from the $b\bar{d}$–$\bar{b}d$ coupling. Currently there is reasonable agreement between the average value of $|V_{ub}|$ and ϕ_1. If we take, for example, the $|V_{ub}|$ value derived from inclusive semi-leptonic decays or $B \to \tau\nu$, there is a tension. Belle II will clarify this situation.

The angle ϕ_2 is measured from interference between the $b \to ud\bar{u}$ tree and the $b \to dq\bar{q}$ penguin ($q = u, d$) process, with the decays such as $B \to \pi\pi, \pi\rho, \rho\rho$. In minimal models, new physics contributions to the $b \to dq\bar{q}$ penguin loop diagram and $b\bar{d}$–$\bar{b}d$ diagram can be strongly correlated, while there are many new physics models which contribute to only one of them. The experimental error on ϕ_2 is still very large, and more precise measurements by Belle II have the potential to reveal a deviation from the other UT fit inputs.

The third angle, ϕ_3, is measured via the CP asymmetry which occurs due to the interference between different tree-level diagrams (see Chapter 11). Decay modes of the type $B \to D^{(*)}K^{(*)}$ and $B \to D^{(*)}\pi$, where the D meson decays to a variety of final states, can be used to obtain a very precise determination of ϕ_3. The theoretical uncertainty, which comes from the loop diagrams, can be kept very well under control. The measurement of ϕ_3 is highly statistics limited, and will be greatly improved in the era of Belle II. If ϕ_3 turns out to be inconsistent with the other UT constraints, there is a possibility of new physics contributing to tree-level $B \to D^{(*)}K^{(*)}(\pi)$ processes. On the other hand new physics contributions could be in the other measurements, especially those in loop-induced observables (see Chapter 11 for more details).

In summary, there is excellent potential at Belle II to discover new physics through precision tests of the unitarity triangle. In order to clarify the significance of the agreement or deviation, global fits may be necessary. A more detailed discussion on this aspect can be found in Chapter 18.

7.3. Effective Hamiltonian

Flavor-changing amplitudes involve widely separated mass scales, ranging from $\Lambda_{\rm QCD} \approx 350\,\text{MeV}$ over $\overline{m}_c \approx 1.25\,\text{GeV}$ and $\overline{m}_b \approx 4.3\,\text{GeV}$ to $M_W = 80.4\,\text{GeV}$ and $\overline{m}_t \approx 165\,\text{GeV}$. The QCD coupling $\alpha_s = g_s^2/(4\pi)$ changes dramatically over this range of energies. While we can use perturbation theory (i.e. calculate Feynman diagrams with quarks and gluons) for QCD effects associated with scales of $\overline{m}_b$ and above, this is not possible for the dynamics associated with the energy scale $\Lambda_{\rm QCD}$ related to genuine non-perturbative effects like the confinement of quarks and gluons into colorless hadrons. In a given calculation, we must separate the physics of the different scales to apply different calculation methods to the different energy regimes.

To this end an important theoretical tool is the effective weak Hamiltonian. For the description of the decay of b-flavored hadrons we need the $|\Delta B| = 1$ Hamiltonian $H^{|\Delta B|=1}$. Here, B denotes the beauty quantum number which changes by one unit if the b or $\bar{b}$ decays into lighter quarks. $H^{|\Delta B|=1}$ is constructed in a way that reproduces the decay amplitudes of the full SM up to corrections of order m_b^2/M_W^2. An important feature of the effective theory described by $H^{|\Delta B|=1}$ is the absence of W and top-quark fields. To find the interaction vertices of $H^{|\Delta B|=1}$ one contracts the lines with heavy W and t lines in the SM Feynman diagrams to a point. For instance, to lowest order in QCD the W-mediated decay $b \to c\bar{u}d$ is described by the effective operator $Q_2^{c\bar{u}d} = \bar{d}_L^\alpha \gamma_\mu u_L^\alpha \, \bar{c}_L^\beta \gamma^\mu b_L^\beta$, where α and β are color indices. Beyond leading order in α_s we can exchange a gluon between the b–c and u–d quark lines. To accomodate this in $H^{|\Delta B|=1}$ we need another operator, $Q_1^{c\bar{u}d} = \bar{d}_L^\alpha \gamma_\mu u_L^\beta \, \bar{c}_L^\beta \gamma^\mu b_L^\alpha$. The piece of $H^{|\Delta B|=1}$ responsible for $b \to c\bar{u}d$ decays is

$$H^{b\to c\bar{u}d} = \frac{4G_\mathrm{F}}{\sqrt{2}} V_{cb} V_{ud}^* \sum_{j=1,2} C_j Q_j^{c\bar{u}d}. \tag{62}$$

Here, the Fermi constant G_F and the CKM elements are factored out by convention. The Wilson coefficients C_j are the coupling constants of the effective operators Q_j. These coefficients contain the full short-distance information of the theory, i.e. the full dependence on the heavy masses M_W and m_t. The C_j can be calculated in perturbation theory; the order of α_s is referred to as "LO" (leading order), "NLO" (next-to-leading order), and so on. The calculation involves two steps.

First, a given decay amplitude is calculated in the SM and compared to the same amplitude calculated with the effective Hamiltonian (matching calculation). Requiring both results to be the same up to terms of m_{bq}^2/M_W^2 then fixes C_j at a chosen renormalization scale, the matching scale μ_W. This scale must be chosen of the order of the heavy masses M_W and m_t to ensure that the perturbative calculation makes sense (i.e. that corrections decrease with the order of α_s). A physical process does not depend on the numerical value of μ_W, and the μ_W dependence of a given amplitude decreases order by order in α_s.

Secondly, one calculates the C_j at a low-energy scale μ_b, where μ_b is of the order of m_b, which sets the energy scale for decays of b-flavored hadrons. This second step is called renormalization group evolution. The result can be written as

$$\vec{C}(\mu_b) = U(\mu_b, \mu_W)\vec{C}(\mu_w), \tag{63}$$

where

$$\vec{C}(\mu) \equiv \begin{pmatrix} C_1(\mu) \\ C_2(\mu) \end{pmatrix}. \tag{64}$$

As for the matching calculation, we can use established perturbative methods to determine the evolution matrix $U(\mu_b, \mu_W)$.

We now apply this framework to a given physical process, taking $B^- \to D^0\pi^-$ as an example. The decay amplitude reads

$$\langle D^0\pi^-|H^{b\to c\bar{u}d}|B^-\rangle = \frac{G_\mathrm{F}}{\sqrt{2}} V_{cb} V_{ud}^* \times \sum_{j=1,2} C_j(\mu_b) \langle D^0\pi^-|Q_j^{c\bar{u}d}(\mu_b)|B^-\rangle.$$

An important feature of the effective Hamiltonian is the independence of the Wilson coefficients from the actual physical process. If we study other $b \to c\bar{u}d$ modes such as $\overline{B}^0 \to D^+\pi^-$ or

$\Lambda_b \to \Lambda_c \pi -$, we will encounter the same coefficients C_j, with all process dependence residing in the hadronic matrix elements of the operators $Q_{1,2}$. The calculation of the hadronic matrix elements from first principles is difficult. In our example we can express $\langle D^0 \pi^- | Q_{1,2}^{c\bar{u}ud}(\mu_b) | B^- \rangle$ in terms of the $B \to D$ form factor and the pion decay constant in certain limits of QCD (considering either an infinite number N_c of colors or an infinitely heavy b quark). The corrections to these limits are not calculable with present techniques. It is often possible to relate different hadronic matrix elements to each other by using symmetries of QCD like flavor SU(3). This approximate symmetry connects matrix elements which are related by unitary rotations of the three light quark fields u, d, s. Flavor SU(3) would be an exact symmetry if these quarks had the same mass. The SU(2) subgroup related to unitary rotations of $(u, d)^{\mathrm{T}}$ corresponds to isospin symmetry and holds with an accuracy of 2% or better. Most importantly, QCD respects the CP symmetry. In our example this entails $\langle D^0 \pi^- | Q_j^{c\bar{u}ud}(\mu_b) | B^- \rangle = \langle \overline{D}^0 \pi^+ | Q_j^{c\bar{u}ud\,\dagger}(\mu_b) | B^+ \rangle$. The CP symmetry of QCD is a key feature allowing us to eliminate all hadronic matrix elements from the CP asymmetries in several "golden modes." The full $|\Delta B| = 1$ Hamiltonian needed to describe SM physics is

$$H^{|\Delta B|=1} = H^{b\to c\bar{u}ud} + H^{b\to u\bar{c}d} + H^{b\to c\bar{u}s} + H^{b\to u\bar{c}s} + H^{b\to s} + H^{b\to d}. \tag{65}$$

Here, terms describing the tree-level semi-leptonic decays $b \to q\ell\overline{\nu}$, $q = u, c$, $\ell = e, \mu, \tau$ are omitted, as the effective Hamiltonian picture is not really needed to describe these decays. (The relevant Wilson coefficients are equal to 1 at all scales.) The last two terms in Eq. (65) are the most interesting pieces of $H^{|\Delta B|=1}$. Most of the physics described in this report involves $H^{b\to s}$ or $H^{b\to d}$.

7.4. Remarks about Resonances

Section author: C. Hanhart

7.4.1. Introduction

A detailed understanding of the concept of resonances and the non-perturbative interactions of QCD at low and intermediate energies will be crucial for a theoretically controlled analysis of various Belle II data. To see this, observe, e.g., that they not only shape the Dalitz plots of heavy meson decays—and therefore need to be controlled quantitatively, e.g. for an effective hunt for CP violation within and beyond the SM in these observables (for a recent discussion see Refs. [92,93])—but also are interesting for their own sake: as of today, we do not even understand what kinds of hadrons (= bound systems of quarks and gluons) do exist in nature. While Belle played a crucial role in establishing the existence of hadrons beyond the most simple quark–antiquark structure with the discovery of the charged charmonium-like states $Z_b(10610)$ and $Z_b(10650)$ in 2013, as of today we understand neither the structure of those states nor under what conditions they are produced—for details, refer to the chapter on quarkonia.

Therefore, to lift the last mysteries of the SM and beyond in the years to come, high-precision data analyzed with sophisticated theoretical tools are needed. In particular, the simple Breit–Wigner description that parameterizes the invariant matrix element $\mathcal{M}$ for some reaction in a given partial wave as

$$\mathcal{M}_{ab} = -\sum_r \frac{g_a^r g_b^r}{s - s_r}, \tag{66}$$

with $s_r = (M_r - i\Gamma_r/2)^2$, appears to be justified only under very special conditions, as explained below. In this section the concept of resonances (as well as other singularities of the scattering matrix) is introduced and possible parameterizations thereof are explained.

7.4.2. What is a resonance?

In a particle physics experiment, transition rates are in general measured between defined in and out states. Theoretically, e.g., transitions from the states A, B to some multi-body final state are described by the so-called S-matrix (see, e.g., Ref. [94, Chapter 4]),

$$_{\text{out}}\langle \mathbf{p_1 p_2} \ldots | \mathbf{k_A k_B} \rangle_{\text{in}} \equiv \langle \mathbf{p_1 p_2} \ldots | S | \mathbf{k_A k_B} \rangle, \tag{67}$$

where the particles in both the initial and final states are characterized by their three-momenta—all other possibly relevant quantum numbers like spin, charge, etc. are not shown explicitly to keep the notation simple. While the "in" and "out" states that appear on the left are defined at some large negative and positive time, respectively, the states on the right may be defined at any common reference time. As a consequence of the conservation of probability, the S-matrix is a unitary operator: $S^\dagger S = \mathbb{1}$. It describes the full scattering process, including the piece where the two initial particles pass by without any interaction. It is useful to separate the interesting, interacting part from the full S-matrix via

$$\langle \mathbf{p_1 p_2} \ldots | S - \mathbb{1} | \mathbf{k_A k_B} \rangle = (2\pi)^4 \delta^{(4)} \left(k_A + k_B - \sum p_f \right) i\mathcal{M}(k_A, k_B \to p_f), \tag{68}$$

where $\mathcal{M}$ denotes the invariant matrix element. Particles manifest their existence as poles of the S-matrix or, equivalently, as poles of $\mathcal{M}$. Thus, one needs to map out the singularities of the scattering matrix in order get access to the particle content of a given reaction. In general it is assumed that the S-matrix is analytic up to the following:

- *Branch points*: On the one hand these occur at each threshold for a kinematically allowed process (e.g. at the $\bar{K}K$ threshold in the $\pi\pi$ scattering amplitude); these are called right-hand cuts. On the other hand there might also be left-hand cuts, which occur when reactions in the crossed channel become possible. Those are often located in the unphysical regime for the reaction studied but can still influence significantly, e.g., the energy dependence of a reaction. When a reaction goes via an intermediate state formed by one or more unstable states, branch points can also be located inside the complex plane of the unphysical sheet [95].
- *Bound states*: These appear as poles on the physical sheet and are only allowed to occur on the real s-axis below the lowest threshold. Narrow unstable states which correspond to poles on the physical sheet for not the lowest threshold behave very similarly in many aspects. Classic examples in this context are the $f_0(980)$ located on the physical sheet for the $\bar{K}K$ channel which also couples to the much lighter $\pi\pi$ channel,[11] and $D_{s0}(2317)$ and $D_{s1}^*(2460)$ located on the physical sheet for the KD and KD^* channels, respectively, but decaying via isospin violation into $D_s\pi$ and $D_s^*\pi$, respectively.
- *Virtual states*: As bound states, these appear on the real s-axis below the lowest threshold; however, they appear on the unphysical sheet. Probably the most famous example of this kind of S-matrix singularity is the pole in S-wave proton–proton or neutron–neutron scattering (as

[11] For a detailed discussion on this aspect of the $f_0(980)$, see Refs. [96,97].

well as the isovector part of proton–neutron scattering). The corresponding pole is located within about 1 MeV of the threshold, giving rise to a scattering length of about 20 fm. However, in contrast to the isoscalar channel, where the deuteron appears as a bound state, in the isovector channel the interaction is too weak to form a bound state. There is also evidence that the $X(3872)$ is a virtual state [98].

- *Resonances*: These appear as poles on an unphysical sheet close to the physical one.

For a discussion of the analytic structure of the S-matrix with a focus on scattering experiments, see Ref. [95] and references therein. In what follows the focus will be on the physics of resonances and how to parameterize them. For a detailed discussion on the subject we refer to the resonance review in the *Review of Particle Physics* by the Particle Data Group [88].

7.4.3. A comment on Breit–Wigner functions

A pole in the S-matrix, and thus any resonance, is uniquely characterized by its pole position and its residues. Thus, a parameterization of the kind given in Eq. (66) appears natural, and one may identify the couplings g_a with the residues res_a^r.[12] This expression is nothing but a sum over Breit–Wigner functions, which is not only commonly used in very many experimental analyses but also in recent theoretical works—see, e.g., Ref. [99]. This kind of parameterization in general allows for a high-quality description of data (as long as enough terms are included in the sum). However, it should be used with care for it may introduce various uncontrollable systematic uncertainties into the analysis, as detailed below.

First of all, Breit–Wigner functions with a constant width violate analyticity, since the analyticity of the S-matrix leads to the Schwarz reflection principle, $S(s^*) = S^*(s)$. Therefore, a pole at $s = s_0$ is necessarily accompanied by a pole at $s = s_0^*$. As illustrated in Fig. 59, for narrow, isolated resonances it is only the pole in the lower half-plane of the unphysical sheet that is relevant near the resonance peak, and it is this pole that it is accounted for by the Breit–Wigner function in the vicinity of the pole. However, at the threshold clearly both poles are equally distant and thus equally relevant. Thus, as soon as amplitudes are to be described over a larger energy range, the relevant cuts need to be included properly, e.g. by the well-known Flatte parametrization [100] or variants thereof. However, there are resonances where even this modification is not sufficient. An example is the $f_0(500)$ or σ meson, which has a line shape that deviates significantly even from that of a Breit–Wigner with an energy-dependent width [101]. In these cases more sophisticated forms need to be used. We return to this point below.

Second, a sum of Breit–Wigners necessarily violates unitarity. To see this we focus on elastic two-body scattering. Then it is straightforward to derive, from the unitarity of the S-matrix,

$$\mathcal{M} - \mathcal{M}^* = 2i\sigma\mathcal{M}^*\mathcal{M}, \tag{69}$$

where σ denotes the two-body phase space. Furthermore, if we assume that

$$\mathcal{M} = -\frac{(\text{res}^{(1)})^2}{s - M_1^2 + iM_1\Gamma_1} - \frac{(\text{res}^{(2)})^2}{s - M_2^2 + iM_2\Gamma_2}, \tag{70}$$

[12] For simplicity we do not discuss possible angular distributions of the decay particles here, which may be included in a straightforward way. See, e.g., Ref. [88].

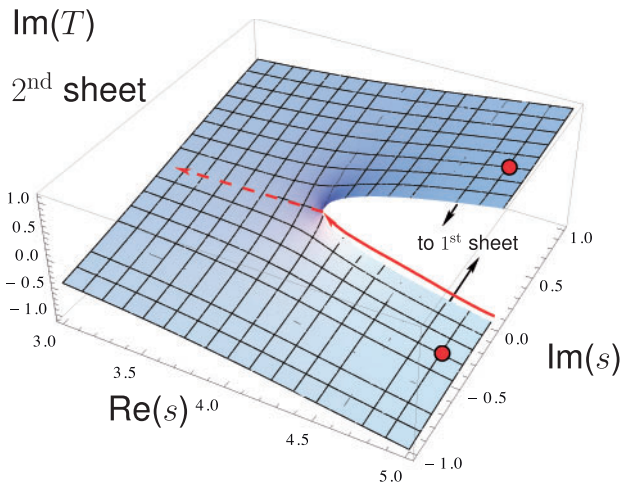

Fig. 59. Sketch of the imaginary part of the scattering amplitude on the unphysical sheet of the complex s-plane close to the opening of a threshold. The red solid line shows the physical axis, located on the physical sheet very close to the lower part of sheet. The red dots show the possible location of the resonance poles.

we get

$$\mathrm{Im}(\mathcal{M})-\sigma|\mathcal{M}|^2 = \frac{(\mathrm{res}^{(1)})^2(\Gamma_1 M_1-\sigma(\mathrm{res}^{(1)})^2)}{(s-M_1^2)^2+M_1^2\Gamma_1^2} + \frac{(\mathrm{res}^{(2)})^2(\Gamma_2 M_2-\sigma(\mathrm{res}^{(2)})^2)}{(s-M_2^2)^2+M_2^2\Gamma_2^2} + \mathrm{Re}\left(\frac{2\sigma(\mathrm{res}^{(1)}\mathrm{res}^{(2)})^2}{(s-M_1^2+iM_1\Gamma_1)(s-M_2^2-iM_1\Gamma_2)}\right).$$

Unitarity requires this expression to vanish. While the first two terms might be removed by choosing $\Gamma_i M_i = \sigma \mathrm{res}^{(\mathrm{i})2}$, which is the unitarity condition for a single resonance,[13] it does not appear possible to remove the interference term shown in the last line of Eq. (71) with constant residues. Thus, using Eq. (66) for a single partial wave amplitude with two (or more) resonances is justified only if $M_1 - M_2 \gg (M_1\Gamma_1 + M_2\Gamma_2)/(M_1 + M_2)$. Since the production rate of the individual resonances depends on the source term, the resonance parameters extracted using Eq. (66) necessarily become reaction dependent.

Most experiments in particle physics are not scattering but production experiments. For these, the unitarity relation reads

$$\left[\mathcal{A}_a - \mathcal{A}_a^*\right] = 2i\sum_c \mathcal{M}_{ca}^*\sigma_c\mathcal{A}_c. \tag{71}$$

Since $\mathcal{A}$ and $\mathcal{M}$ have identical poles, this relation can also not be fulfilled by a simple Breit–Wigner ansatz. Moreover, a channel- and energy-dependent production mechanism might distort the line shape of a particular resonance significantly, such that any fit with a symmetric function (as a Breit–Wigner) will deliver channel-dependent parameters. For example, if one fits the two-pion invariant mass distribution of $\eta \to \pi\pi\gamma$ (most recently measured at KLOE [102]) with a Breit–Wigner amplitude, one can get a decent fit, although with quite a low mass parameter for the ρ meson. What is often done in analyses to cure this is to add to the ρ Breit–Wigner distribution a contact term, which

[13] This implies that the residue is real—a condition already used to write Eq. (71).

is then interpreted as a non-resonant contribution. However, this also violates unitarity, for then the phase of the scattering amplitude, in the example above assumed to be given by the ρ amplitude, deviates from the phase of the production amplitude, in conflict with the Watson theorem [103].[14] Note that the logic presented is not in conflict with the presence of a particle production at tree level: as soon as the final state interaction (e.g. in from for a resonant rescattering) is taken into account for this term, the tree-level term gets canceled. This is discussed within a resonance model in Ref. [104] and in more general terms in Ref. [105].

The only sensible way to account for non-constant production operators is via multiplying the ρ distribution with, e.g., a polynomial; for the case of $\eta \to \pi\pi\gamma$, this is discussed in detail in Ref. [106]. This may be improved further by the inclusion of the leading left-hand singularity induced by the a_2 meson in the crossed channel [107]. An even more striking energy dependence of the production mechanism can be induced by triangle singularities. This is demonstrated in the examples of $\eta(1405)$ and $\eta(1475)$ in Ref. [108], where both signals are explained by a single pole accompanied by a triangle singularity (for a recent discussion of triangle singularities, see Ref. [109]).[15]

7.4.4. How to do better

One way to improve is to construct coupled-channel models consistent with the fundamental principles, especially multi-channel unitarity. This approach is developed best for meson–baryon scattering as discussed in Ref. [112]. For the particular case of the very near threshold states $Z_b(10610)$ and $Z_b(10650)$, the coupled channel equations are solved analytically in Refs. [113,114].

Alternatively, one may use the unitarity relation presented in Eq. (71) as the basis for a dispersion-theoretical approach. In the single-channel case there is a straightforward analytic solution, the Omnès function, for the production amplitude in terms of the scattering phase shift $\delta(s)$ in the corresponding channel [115]:

$$\mathcal{A}(s) = P(s)\Omega(s), \tag{72}$$

with

$$\Omega(s) = \exp\left(\frac{s}{\pi}\int \frac{ds'\,\delta(s')}{s'(s'-s-i\epsilon)}\right), \tag{73}$$

where the presence of the polynomial $P(s)$ acknowledges the fact that the unitarity relation of Eq. (71) only fixes the amplitude up to a function that does not have a right-hand discontinuity. For the $\pi\pi$ P-waves, where the phase shifts show a prominent resonant structure driven by the ρ meson, the resulting Omnès function resembles a pronounced ρ peak—see the left panel of Fig. 60. Note that the two pion phase shifts are known very well due to sophisticated analyses based on Roy equations and variants thereof [116,117]. An illustrative example showing that using the Omnès solutions is not only theoretically more sound than using Breit–Wigner functions but also beneficial in data analyses is presented in Ref. [118], where recent data on $\overline{B}^0_{d/s} \to J/\psi\pi\pi$ by the LHCb collaboration [119,120]

[14] The Watson theorem may be read off from Eq. (71) immediately: In the single-channel case the left-hand side denotes $2i$ times the imaginary part of $\mathcal{A}$, which is purely imaginary. Accordingly, the phase of $\mathcal{A}$ needs to match the phase of $\mathcal{M}$.

[15] Triangle singularities can also enhance transition amplitudes in certain kinematic regimes, as discussed in Ref. [110].

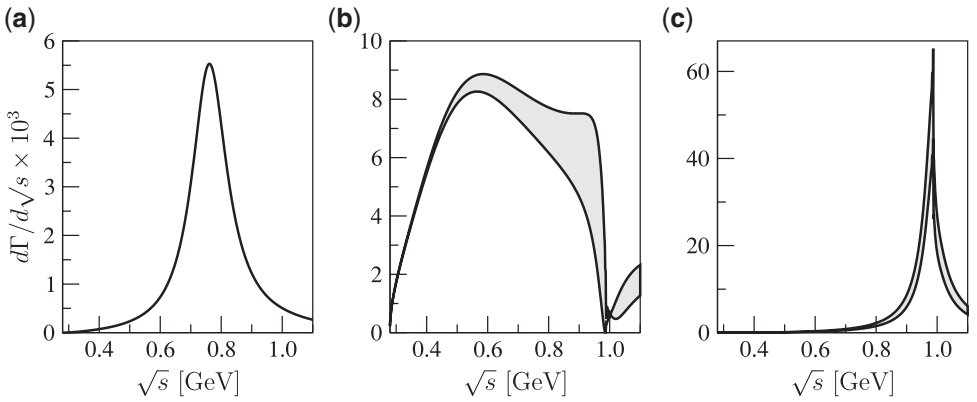

Fig. 60. The predicted signals individually for the currents (a) $\bar{q}\gamma^\alpha q$, (b) $(\bar{u}u + \bar{d}d)/2$, and (c) $\bar{s}s$ calculated for the kinematics relevant for the transition $\tau \to \mu\pi\pi$. In all cases the effective coupling constant is set to $1\,\mathrm{GeV}^{-2}$. For the uncertainty, the bands reflect the uncertainty in the form factor normalization. The figure is adapted from Ref. [111].

are studied. For example, for pion invariant energies up to 1 GeV the $\bar{B}^0$ decays can be described equally well with only three free parameters as compared to the LHCb Breit–Wigner fit that required 14 parameters to analyze the same energy region.

As soon as the first relevant inelasticity enters, the above solution no longer applies. Then possible strategies are to match the low-energy Omnès solution to a resonance description of the N/D type at higher energies [105], or to solve the corresponding coupled channel problem [121]. In the isovector–vector channel ($\pi\pi$ P-wave) the first inelasticity formally enters at the four-pion threshold, however, in reality this channel provides a visible inelasticity only well above 1 GeV [122]. The situation is different in the scalar–isoscalar channel, since the $\pi\pi$ system couples strongly to $\bar{K}K$. Chiral perturbation theory allows one to fix the value of the light quark part of the pion scalar form factor at $s = 0$ to sufficient accuracy; however, the normalization of the strangeness pion scalar form factor is not that well known. Figure 60 shows the results obtained for the modulus of the pion vector form factor and the non-strange and strange scalar form factors in panels (a), (b), and (c), respectively, here shown as predicted for the BSM process $\tau \to \mu\pi\pi$ in Ref. [111]. The sensitivity due to the uncertainty in the strange form factor normalization is illustrated by the uncertainty bands. The strange form factor exhibits a peak around 1 GeV, which is produced by the $f_0(980)$ resonance. On the contrary, in the pion scalar non-strange form factor the σ or $f_0(500)$ meson appears as a broad bump (notice the non-Breit–Wigner shape) around 500 MeV and the $f_0(980)$ appears as a dip rather than a peak. The very different line shapes of the different form factors shown in Fig. 60 can be exploited to disentangle different BSM source terms. The ideas of Ref. [111] were generalized in Refs. [123,124].

So far we have discussed two hadron interactions only and largely ignored left-hand cut contributions. The formalism can be extended by means of the Khuri–Treiman equations [125] to also include crossed-channel singularities as well as three-body dynamics [126–132], but discussing this goes beyond the scope of this presentation.

7.5. Lattice QCD

7.5.1. Introduction

The intensity frontier probes new physics through quantum loop effects by a strict comparison between precise theoretical predictions and experimental measurements. For many quantities, the

accuracy of the comparison is currently limited by the theoretical uncertainties from the hadronic matrix elements describing non-perturbative QCD effects in the underlying processes. Moreover, as the heavy-flavor factories accumulate high-statistics data, many new quarkonium and exotic states have been observed. Non-perturbative dynamics of QCD is also essential in understanding their nature, including the spectra, quantum numbers, and decay properties. Lattice QCD is a powerful method to study non-perturbative aspects of QCD with controlled and systematically improvable accuracy. It is expected to play a key role in the success of the SuperKEKB / Belle II experiment by providing timely theoretical inputs with commensurate uncertainties.

Lattice QCD is a regularization of QCD on a discrete Euclidean space-time lattice. On a finite-volume lattice, the path integral is reduced to a finite-dimensional integral and can be numerically evaluated by a Monte Carlo sampling of gauge field configurations on a computer. This numerical simulation does not rely on the perturbative expansion, and enables us to non-perturbatively study QCD.

In principle, uncertainties due to the lattice formulation and numerical simulation can be systematically reduced by a large-scale simulation; namely, by generating many configurations on a fine and large lattice. While such a realistic simulation is computationally intensive, continuous development of powerful computers and simulation techniques has led to increasingly precise and wide applications of lattice QCD. These include physics of the QCD vacuum, hadron spectrum and structure, QCD at finite temperature and density, *ab initio* nuclear physics, and simulations of theories beyond QCD.

For instance, the energy of a hadron stable under QCD can be calculated from the asymptotic behavior of a two-point function,

$$\langle \mathcal{O}_H(t)\mathcal{O}_H^\dagger(0)\rangle \to \frac{|Z_H|^2}{2E_H} e^{-E_H t} \qquad (t\to\infty), \tag{74}$$

towards the large temporal separation t. Here, $\mathcal{O}_H$ is an interpolating field of the hadron, and $Z_H = \langle 0|\mathcal{O}_H|H\rangle$ represents the overlap of $\mathcal{O}_H$ with the physical state $|H\rangle$. The low-lying hadron spectrum calculated in this way is in impressive agreement with experiment [133]. The permille-level neutron–proton mass splitting has also been reproduced by taking account of the mass difference of up and down quarks as well as the electromagnetic (EM) corrections [134,135].

Precise study of flavor physics has been one of the most important applications of lattice QCD from its early stages. When a process has at most one hadron stable under QCD both in the initial and final states, the relevant hadronic matrix element can be straightforwardly extracted from the correlation function. For leptonic decays, for instance, the overlap factor in Eq. (74) gives $\langle 0|A_\mu|H\rangle$ by using the axial current as $\mathcal{O}_H$. The matrix element $\langle H'|O_{\rm int}|H\rangle$ for the semi-leptonic decays and neutral meson mixings can be obtained from the three-point function

$$\langle \mathcal{O}_{H'}(t')\mathcal{O}_{\rm int}(t)\mathcal{O}_H^\dagger(0)\rangle \to \frac{Z_{H'}Z_H^*}{4E_{H'}E_H}\langle H'|O_{\rm int}|H\rangle e^{-E_{H'}(t'-t)-E_H t} \quad (t,t'-t\to\infty), \tag{75}$$

where $\mathcal{O}_{\rm int}$ represents the interaction operator. Recent realistic simulations can accurately calculate these two- and three-point functions, and we refer to the relevant matrix elements as "gold-plated." A main thrust of recent lattice efforts is improving the accuracy of the gold-plated quantities. We summarize the current status in Sect. 7.5.2, and make forecasts for the future precision in Sect. 7.5.5.

We have to take account of the final state interaction to study hadronic decays. In this case, however, the amplitudes of the correlation functions are not directly related to the hadronic matrix elements,

as we discuss in Sect. 7.5.3. A theoretical framework for studying hadronic decays is under active development, and is being applied to the quarkonium and exotic states, which generally lie above thresholds (Sect. 7.5.4).

7.5.2. (Semi-)leptonic decays and mixing

The hadronic matrix element for the leptonic decay is parameterized by using the decay constant

$$\langle 0|A_\mu|B_{(s)}(p)\rangle = p_\mu f_{B_{(s)}}, \tag{76}$$

and vector and scalar form factors for the $B \to \pi \ell \nu$ and $D\ell\nu$ semileptonic decays,

$$\langle H(p')|V_\mu|B_{(s)}(p)\rangle = \left(p + p' - \frac{M_B^2 - M_H^2}{q^2} q\right)_\mu f_+(q^2) + \frac{M_B^2 - M_H^2}{q^2} q_\mu f_0(q^2), \tag{77}$$

where $q^2 = (p' - p)^2$ is the momentum transfer. The $B_{(s)}$ meson mixing matrix element is written by using the bag parameter as

$$\langle \bar{B}^0_{(s)}|\mathcal{O}_1|B^0_{(s)}\rangle = \frac{8}{3} f^2_{B_{(s)}} M^2_{B_{(s)}} B_{B_{(s)}}, \tag{78}$$

where $\mathcal{O}_1 = \left[\bar{b}\gamma_\mu(1-\gamma_5)q\right]\left[\bar{b}\gamma_\mu(1-\gamma_5)q\right]$ and $q = d$ (s) for B (B_s). Precise knowledge of these gold-plated quantities is essential in the search for new physics at Belle II. Their accuracy can be straightforwardly improved by a large-scale simulation accumulating high statistics on a fine and large lattice at the physical point, where quark masses are set to their physical values.

Such a realistic simulation is computationally very demanding, because the simulation cost quite rapidly increases as we approach the continuum limit and decrease the up and down quark masses to the physical point. Previous lattice simulations have often employed unphysically heavy up and down quarks, and extrapolated their results to the physical point. This procedure is referred to as the chiral extrapolation. However, thanks to recent advances in computer power and improvements in simulation algorithms, gauge field ensembles including the effects of dynamical up, down, strange, and even charm quarks are becoming available near and at the physical point.

Typical lattice spacings are larger than or comparable to the Compton wavelengths of the bottom quarks m_b^{-1}. The control of discretization errors arising from bottom valence quarks is therefore an essential issue in the current and future precision study of B physics. We note that the lattice action is not unique: it can be improved to have reduced discretization errors by, for instance, adding irrelevant operators. Heavy quark actions on the lattice have been developed based on the heavy quark effective theory, non-relativistic QCD, and the so-called Fermilab formalism [136–138] to directly simulate m_b at the currently available lattice spacings and to describe the discretization errors of simulation results. Another good strategy is to compute suitable ratios of physical observables by using a relativistic lattice action, and interpolate them between available heavy quark masses and their known static limit [139].

As discussed in Chapter 8 in detail, the gold-plated quantities are now being calculated with fully controlled errors. The $B_{(s)}$ meson decay constants have been calculated with an accuracy of a few percent, and confirmed by several independent calculations with different actions [140]. The accuracies of the state-of-the-art studies of the $B \to \pi \ell \nu$ [141–143], $B \to D^{(*)} \ell \nu$ [144–147] decays and the $B_{(s)}$ mixing [148–151] are approaching the same level, although the number of such precision computations is rather limited.

Over the next decade we expect more independent calculations with even better accuracies by simulating the physical point on finer lattices. In Sect. 7.5.5 we make forecasts for the future lattice precision that are used in this report to discuss the interplay between precise lattice calculations and Belle II measurements in the search for new physics.

So far, the B meson matrix elements have usually been calculated in the isospin limit without EM corrections. As the precision approaches the percent level, control of the isospin corrections becomes increasingly important and is actively being pursued [152]. Recently, a method has been proposed to compute the EM effects in hadronic processes where infrared divergences are present [153]. The isospin corrections to the leptonic decay rates $\Gamma(\pi, K \to \ell\nu)$ have been successfully calculated [154]. We note that this method is applicable to heavy meson (semi-)leptonic decays.

The scope of the precision lattice calculation is expanding to other gold-plated processes. For instance, $B_s \to K\ell\nu$ provides an independent determination of $|V_{ub}|$, and $B \to K(\pi)ll$ mediated by FCNC is sensitive to new physics. Simulation techniques for $B \to \pi\ell\nu$ can be straightforwardly applied to these decays, and results with similar accuracies are becoming available [141,155–159].

Baryon decays also provide independent determinations of the CKM matrix elements and constraints on new physics, but with systematics different from meson decays. The first lattice calculations for the $\Lambda_b \to p\ell\nu$, $\Lambda_c\ell\nu$, and $\Lambda\ell\ell$ decays have been reported in Refs. [160–162]. However, baryons are known to be more challenging in controlling the chiral extrapolation and finite-volume effects. These issues can be addressed in the relatively short term by more realistic and/or independent calculations.

The gold-plated quantities are important inputs to determine relevant CKM matrix elements from given exclusive decays. As is well known, however, there is a long-standing tension between the exclusive and inclusive decays in $|V_{ub}|$ and $|V_{cb}|$ [88]. Although the analysis of the inclusive decay rate employs the heavy quark expansion (HQE) and hence has very different theory systematics from those for the exclusive decays, lattice QCD can contribute to the inclusive determinations as well. In the HQE, the expansion coefficients encode non-perturbative hadronic dynamics. Lattice calculation of the coefficients has been pursued for more than 20 years [163–169]. Another interesting future direction is to extract the inclusive decay rate on the lattice [170,171]. In this approach, the relevant structure functions are accessible through the scattering matrix element of two weak currents between single $B_{(s)}$ meson states $\langle B_{(s)}|T\{J_\mu^\dagger J_\nu\}|B_{(s)}\rangle$, which is gold-plated. While the numerical calculation of the relevant four-point functions is challenging, encouraging results for the $B_s \to X_c\ell\nu$ decay have been obtained in Ref. [170].

7.5.3. Hadronic decays

There are, however, many interesting observables that are not gold-plated. These involve final states with more than one strongly interacting particle, e.g. $K \to \pi\pi$, $D \to \pi\pi$, and $B \to DK$ decay amplitudes, or require the calculation of long-distance contributions, e.g. D^0–$\bar{D}^0$ mixing. To calculate these using lattice QCD requires new methods beyond those needed for gold-plated observables, and also requires, in general, significantly more computational resources. Such quantities lie at the frontier of present lattice efforts; some have been calculated with controlled errors, others are close to being controlled, while for others the required theoretical formalism does not yet exist.

We first discuss the issues that arise when calculating decay amplitudes. The key theoretical issue is that lattice calculations perforce are done in a finite spatial volume V, so that the multi-particle states, e.g. $|DK\rangle_V$, differ from the infinite-volume out-states, $|DK\rangle_{\text{out}}$, that are needed to define decay amplitudes. Thus, while a lattice calculation can, in principle, calculate matrix elements such

as $\langle B|H_W|DK\rangle_V$ (with H_W the effective weak Hamiltonian), these differ in an essential way from the desired amplitudes, e.g. $\langle B|H_W|DK\rangle_{\rm out}$. One difference is that the desired amplitude is complex (due to final state interactions) while the finite-volume amplitude is real.[16] A more significant difference is that multi-particle states such as $|DK\rangle_V$ contain a mixture of all the particle combinations that are accessible via strong interactions at the energy of the initial particle. For the DK state with energy M_B, these combinations include $DK\pi\pi$, D^*K^*, and many other possibilities. These "contaminations" are not small, but rather are $\mathcal{O}(1)$ effects.

An additional, more practical, issue is that one must use a finite-volume DK state that has the same energy as the initial B. This is therefore a highly excited state compared to the ground state in which the D and K are at rest (assuming that the total momentum vanishes). The signal for the ground state will dominate over that for the excited state by a factor of $e^{(M_B-M_D-M_K)\tau}$, where τ is the Euclidean time. This problem can be overcome in principle by using appropriate operators to couple to the DK system, tuned to avoid couplings to lighter states. In this regard, it is encouraging that there have in recent years been tremendous advances in the methodology for extracting excited state energies, for example in Refs. [173,174].

While these issues are challenging, substantial progress has been made, particularly in the case of $K \to \pi\pi$ decays. This is based on seminal work by Lüscher relating the spectrum of two-particle finite-volume states below the inelastic threshold to the elastic phase shift [175,176], and subsequent work by Lellouch and Lüscher showing how to relate the finite-volume matrix elements described above to the physical amplitudes [177].

This formalism has been successfully implemented in recent work by the RBC/UKQCD collaboration. They finesse the issue of excited states using tuned boundary conditions so that the lightest state is the desired one. They have a fully controlled result for the $\Delta I = 3/2$ $K \to \pi\pi$ amplitude [178], and a result at a single lattice spacing for the $\Delta I = 1/2$ amplitude [179]. Fully controlled results for the latter are expected soon. They have also determined the imaginary parts of these amplitudes, albeit with larger errors, and thus can provide the SM prediction for the direct CP violation parameter $\mathrm{Re}\left[\epsilon'/\epsilon\right]$ [179]. A slight tension with the experimental value [88] is of great phenomenological interest [179–181].

Subsequent to the work of Lüscher and Lellouch, the theoretical framework for studying two-particle systems in lattice QCD has been generalized to a moving frame, to non-identical particles with arbitrary spin, and to multiple two-particle channels [182–187]. These extensions have been applied successfully in lattice studies of resonance physics (see Sect. 7.5.4). They are, however, not yet sufficient to allow lattice simulations to study D or B decays, because of the prevalence of states containing three or more particles. Producing the required generalization is an active area of research, with significant progress made for three particles [188–191], but further developments are needed for a general theory. It is not unreasonable to hope that such a theory will be available in three to five years.

We close this subsection by commenting briefly on prospects for lattice calculations of D^0–$\bar{D}^0$ mixing amplitudes. The short-distance contributions require gold-plated calculations and are under good control [192,193]. However, the mixing is dominated by long-distance contributions from many intermediate states, and for these a new methodology is needed. Significant progress has been made on the analogous, although simpler, case of K^0–$\bar{K}^0$ mixing [194]. Here a new technique has been developed involving the insertion of two factors of H_W integrated over their relative time

[16] This is related to the Maiani–Testa no-go theorem [172].

separation, and first results indicate that the method works. The extension to D^0 mesons faces two major challenges: the need to control many exponentially growing intermediate states with sufficient accuracy, and the need to make a finite-volume correction. The latter will require the completion of the multi-particle formalism discussed above.

7.5.4. Quarkonium and exotic states

High-statistics data of the e^+e^- collision at B factories brought about rich outcomes for the spectroscopy of hadrons containing heavy quarks. One of the most interesting is the discovery of the exotic hadrons. Chapter 14 considers lattice studies of interesting quarkonium-like states, while a brief summary of the status is given here.

Lattice QCD is a powerful method for studying heavy hadron spectroscopy from first principles: it can study properties of experimentally observed states, and can also provide valuable reference spectra for yet-unobserved states.

Quarkonium spectra below open flavor thresholds are gold-plated, and recent precise lattice calculations show good agreement with experiment. The main remaining uncertainty for these comes from the omission of $\bar{c}c$ or $\bar{b}b$ disconnected diagrams; these remain a great challenge as they lead to intermediate states with multiple light hadrons.

Until recently, all quarkonium(-like) states above thresholds were treated as stable under the strong interaction; the most extensive excited and hybrid charmonium spectrum with this approach has been obtained in Ref. [195]. This unphysical assumption is now being removed by the developments described below.

Many interesting hadrons, and in particular all candidates for the exotic hadrons, lie near or above thresholds. The properties of such unstable particles are not gold-plated and are encoded in their scattering and transition amplitudes. Among those, lattice can most easily treat hadrons that lie above only one two-particle threshold $M_{H_1}+M_{H_2}$, or lie slightly below it; such cases are (unfortunately) rare in Nature. The most rigorous way to extract the scattering matrix $S(E)$ for elastic H_1H_2 scattering is based on Lüscher's formalism, discussed in Sect. 7.5.3. One determines energies of H_1H_2 eigenstates E from a lattice simulation in a finite volume. This gives the infinite-volume scattering matrix $S(E)$ at that energy via Lüscher's relation [196]. This leads to $S(E)$ only for specific values of E since the spectrum in a finite volume is discrete. A hadronic resonance $R \to H_1H_2$ is inferred from the pole of $S(E)$ on the unphysical Riemann sheet. Likewise, the bound state is inferred from a pole on the real axis below threshold, as discussed in Sect. 7.4.1.

This approach has been extensively verified on elastic resonances like ρ and K^*, where it leads to masses and widths close to the experimental values. In the quarkonium sector, for instance, the mass and width of the vector charmonium $\psi(3770)$ were extracted by considering $D\bar{D}$ scattering [197]. An experimentally established charmonium-like state $X(3872)$ seems not to fit into the simple quark model, but its existence is theoretically confirmed from lattice QCD [198,199]. It is found as a pole in $D\bar{D}^*$ scattering just below threshold. For $X(5568)$, as reported by the D0 collaboration [200], a lattice simulation of the relevant $B_s\pi^+$ scattering [201] does not find any evidence in accordance with the recent LHCb measurement [202].

The radiative and weak transitions $\langle H_2|J^\mu|H_1\rangle$ for $H_{1,2}$ that are strongly stable are gold-plated. Considerably more challenging are transitions where the initial or final hadrons are strongly decaying resonances. The general strategy to treat those was proposed, for example, in Ref. [203]. This has been employed only for the $\langle\rho|J^\mu_{em}|\pi\rangle$ transition [204,205], which in practice implied the determination of the $\pi\pi \to \pi\gamma$ amplitude and its evaluation at the ρ meson pole.

Most of the interesting and exotic hadrons actually lie above two or more thresholds, i.e. they can decay to several two-hadron final states. The rigorous way to address this problem is via a generalized Lüscher formalism [189]. Each energy of the lattice eigenstate E leads to one equation with several unknown $S^{ij}(E)$. The direct extraction of $S^{ij}(E)$ becomes practically impossible. The Hadron Spectrum Collaboration managed to extract 2×2 [206] and 3×3 [174] scattering matrices by parameterizing $S^{ij}(E)$ as a function of E using a certain number of parameters. The S-matrix was continued to the complex plane: its poles on the unphysical Riemann sheet indicate the masses and widths of the resonances, while poles on the real axis indicate the bound states. This challenging strategy was applied only for "non-exotic" channels when the scattering particles did not carry spin. Most of the exotic hadrons have $J = 1$ and involve scattering of particles with spin, which brings additional complications.

One can expect rigorous results in the next five years for hadrons that can decay via a few (two or three) two-hadron final states. That applies, for example, to $Z_c^+(3900)$, while $Z_c^+(4430)$ and Z_b^+ lie above many more two-hadron thresholds and it is difficult to envisage rigorous progress along these lines there. Many interesting hadrons can also strongly decay to three-hadron final states, which presents an even greater challenge. A theoretical framework to address those is being constructed [189–191], but no QCD simulations have employed it so far.

Another possibility to extract $S(E)$ is the HALQCD approach [207], which starts by determining the two-hadron Bethe–Salpeter wave function and two-hadron potential from lattice QCD. The scattering matrix $S(E)$ is then obtained using the Schrödinger equation for the given two-hadron potential. This approach has not been verified on conventional resonances yet. Recently the HALQCD collaboration employed the coupled-channel version of this approach to determine the 3×3 matrix $S(E)$ relevant for the $Z_c(3900)$ channel [208].

The Born–Oppenheimer approach may be applied for systems with heavy quarks Q, where the static heavy-quark sources are surrounded by light degrees of freedom. The potential $V(r)$ is calculated as a function of the distance r between a static pair $Q(0)Q(r)$ or $Q(0)\bar{Q}(r)$ in the presence of the light degrees of freedom. The potential $V(r)$ is used in the Schrödinger equation to search for bound states and resonances. This has been considered for low-lying bottomonia, quenched hybrids [209], $BB^{(*)}$, and recently also for closed-bottom $B\bar{B}^{(*)}$ [210]. Many interesting Born–Oppenheimer potentials [211] remain to be explored.

7.5.5. Current lattice inputs and forecasts for future precision

In this subsection we summarize the current lattice inputs and make forecasts for the future lattice precision that are used in this report to discuss the Belle II sensitivity to new physics.

Assumptions for forecasts We provide the following five types of lattice inputs:

- *Current:* As the current lattice input, we quote the world average by the Flavor Lattice Averaging Group (FLAG) in Ref. [140], where available. Note that Table 30 lists the updated average for the decay constants and mixing parameters by including the recent precise results in Refs. [151,212]. For details we refer readers to the web update of the FLAG review at http://itpwiki.unibe.ch/flag.[17]

[17] The latest review quotes $B_B = 1.30(0.10)$ and $B_{B_s}/B_B = 1.032(38)$, which have slightly larger uncertainty than those in Table 30 due to a change in estimating the correlation among different calculations.

Table 30. Lattice inputs for decay constants $f_{B_{(s)}}$ and bag parameters $B_{B_{(s)}}$ in the SM. The current average of $f_{B_{(s)}}$ for $N_f = 2+1$ and $2+1+1$ are obtained from Refs. [150,213–216] and Refs. [212,217], respectively. The average of $B_{B_{(s)}}$ is obtained from Refs. [148,150,151]. $f_{B_{(s)}}\sqrt{B_{B_{(s)}}}$ is in units of MeV.

N_f	Input	f_B [MeV]	f_{B_s} [MeV]	f_{B_s}/f_B
2+1+1	Current	188(3)	227(4)	1.203(0.007)
	5 yr w/o EM	188(1.5)	227(2.0)	1.203(0.0035)
	5 yr with EM	188(2.4)	227(3.0)	1.203(0.013)
	10 yr w/o EM	188(0.60)	227(0.80)	1.203(0.0014)
	10 yr with EM	188(2.0)	227(2.4)	1.203(0.012)
2+1	Current	192.0(4.3)	228.4(3.7)	1.201(0.016)
	5 yr w/o EM	192.0(2.2)	228.4(1.9)	1.201(0.0080)
	5 yr with EM	192.0(2.9)	228.4(2.9)	1.201(0.014)
	10 yr w/o EM	192.0(0.86)	228.4(0.74)	1.201(0.0032)
	10 yr with EM	192.0(2.1)	228.4(2.4)	1.201(0.012)
N_f	Input	$f_B\sqrt{B_B}$	$f_{B_s}\sqrt{B_{B_s}}$	ξ
2+1	Current	225(9)	274(8)	1.206(0.017)
	5 yr w/o EM	225(4.5)	274(4.0)	1.206(0.0085)
	5 yr with EM	225(5.0)	274(4.8)	1.206(0.015)
	10 yr w/o EM	225(1.8)	274(1.6)	1.206(0.0034)
	10 yr with EM	225(2.9)	274(3.2)	1.206(0.013)
N_f	Input	B_B	B_{B_s}	B_{B_s}/B_B
2+1	Current	1.30(0.09)	1.35(0.06)	1.032(0.036)
	5 yr w/o EM	1.30(0.045)	1.35(0.030)	1.032(0.018)
	5 yr with EM	1.30(0.047)	1.35(0.033)	1.032(0.021)
	10 yr w/o EM	1.30(0.018)	1.35(0.012)	1.032(0.0072)
	10 yr with EM	1.30(0.022)	1.35(0.018)	1.032(0.013)

- *5 yr w/o EM:* We assume a factor of two reduction in the lattice QCD uncertainty in the next five years, and that the uncertainty of the EM correction is negligible (e.g. for processes insensitive to the EM correction).
- *5 yr with EM:* The lattice QCD uncertainty is reduced by a factor of two, but we add in quadrature 1% uncertainty from the EM correction.[18]
- *10 yr w/o EM:* We assume a factor of five reduction of the lattice QCD uncertainty in the next ten years. It is also assumed that the EM correction will be under control and its uncertainty is negligible.
- *10 yr with EM:* We assume lattice QCD uncertainties are reduced by a factor of five, but add in quadrature 1% uncertainty from the EM correction.

Note that recent precision lattice calculations are starting to provide their estimate of the QED uncertainty. The entries for 5 yr with EM and 10 yr with EM suggest that the control of this uncertainty will become increasingly important in the future.

Leptonic decays and $B_{(s)}$ meson mixing The hadronic matrix elements for the $B_{(s)}$ meson leptonic decays and mixing are parameterized by using the decay constants $f_{B_{(s)}}$ and bag parameters $B_{B_{(s)}}$ as

[18] For the $B \to D^*$ form factor in Table 38, we assume the 0.5% uncertainty estimated in Ref. [144].

in Eqs. (76) and (78). These gold-plated quantities have been calculated in $N_f = 2+1$ QCD, which includes degenerate up and down sea quarks as well as strange sea quarks. Results with dynamical charm quarks are also available for $f_{B_{(s)}}$. Table 30 summarizes the current lattice inputs and the forecasts. We note that there are several definitions for the bag parameters in the literature. Here, as in the lattice papers, the same definitions as for kaons are used (see, e.g., Ref. [151] and references therein).

In the SM, only the matrix element in Eq. (78) contributes to the mass difference $\Delta M_{(s)}$ between the $B_{(s)}$ meson mass eigenstates. Beyond the SM, however, $\Delta M_{(s)}$ receives contributions from an additional four operators:

$$\mathcal{O}_2 = \bar{b}^a(1-\gamma_5)q^a\bar{b}^b(1-\gamma_5)q^b, \quad \mathcal{O}_3 = \bar{b}^a(1-\gamma_5)q^b\bar{b}^b(1-\gamma_5)q^a,$$
$$\mathcal{O}_4 = \bar{b}^a(1-\gamma_5)q^a\bar{b}^b(1+\gamma_5)q^b, \quad \mathcal{O}_5 = \bar{b}^a(1-\gamma_5)q^b\bar{b}^b(1+\gamma_5)q^a,$$

where a and b denote color indices, and $q = d$ (s) for B (B_s). Their matrix elements can be parameterized as

$$\langle \bar{B}^0_{(s)}|\mathcal{O}_i|B^0_{(s)}\rangle = c_i\left\{\left(\frac{M_{B_{(s)}}}{m_b+m_q}\right)^2 + d_i\right\} f^2_{B_{(s)}} M^2_{B_{(s)}} B_{B_{(s)}},$$

with

$$(c_2,d_2) = (-5/3,0), \quad (c_3,d_3) = (1/3,0), \quad (c_4,d_4) = (2,1/6), \quad (c_5,d_5) = (2/3,3/2).$$

These bag parameters have been calculated in Ref. [149] ($N_f = 2$, namely only with dynamical up and down quarks) and Ref. [151] ($N_f = 2+1$). As seen in Table 31, however, there is a tension in $B^{(5)}_{B_{(s)}}$ between $N_f = 2$ and $2+1$, the cause of which has to be understood in the future. We use results for $N_f = 2+1$ to make the forecast.

Semi-leptonic decays The $B_{(s)} \to H\ell\nu$ semi-leptonic decays have been studied in $N_f = 2+1$ QCD. If the daughter meson H is pseudoscalar, only the weak vector current contributes due to parity symmetry, and the matrix element in Eq. (77) is parameterized by the vector and scalar form factors, which depend on the momentum transfer q^2. In Ref. [140], FLAG fitted available lattice data into a model-independent parameterization of the q^2 dependence proposed by Bourrely, Caprini, and Lellouch [218]:

$$f_+(q^2) = \frac{1}{B_+(q^2)} \sum_{n=0}^{N_+-1} a^+_n \left\{ z^n - (-1)^{n-N_+}\frac{n}{N_+} z^{N_+}\right\}, \tag{79}$$

$$f_0(q^2) = \frac{1}{B_0(q^2)} \sum_{n=0}^{N_0-1} a^0_n z^n. \tag{80}$$

The Blaschke factor $B_{+(0)}$ is chosen as $B_{+(0)}(q^2) = 1 - q^2/M_{\mathrm{pole},+(0)}$, if there exists a lowest resonance in the vector (scalar) channel with mass $M_{\mathrm{pole},+(0)}$ below the threshold $\sqrt{t_+} = M_{B_{(s)}} + M_H$. For $B \to \pi\ell\nu$, this factor is set to $B_0(q^2) = 1$. The expansion parameter z is defined as

$$z(q^2,t_0) = \frac{\sqrt{t_+ - q^2} - \sqrt{t_+ - t_0}}{\sqrt{t_+ - q^2} + \sqrt{t_+ - t_0}}, \tag{81}$$

Table 31. Lattice inputs for bag parameters beyond the SM from $N_f = 2$ [149] and $2+1$ [151] QCD. $f_{B_{(s)}}\sqrt{B^{\{(2),\ldots,(5)\}}_{B_{(s)}}}$ is in units of MeV.

N_f	Input	$f_B\sqrt{B_B^{(2)}}$	$f_B\sqrt{B_B^{(3)}}$	$f_B\sqrt{B_B^{(4)}}$	$f_B\sqrt{B_B^{(5)}}$
2+1	Current	169(8)	200(19)	197(7)	190(9)
	5 yr w/o EM	169(4.0)	200(9.5)	197(3.5)	190(4.5)
	5 yr with EM	169(4.3)	200(9.7)	197(4.0)	190(4.9)
	10 yr w/o EM	169(1.6)	200(3.8)	197(1.4)	190(1.8)
	10 yr with EM	169(2.3)	200(4.3)	197(2.4)	190(2.6)
2	Current	160(8)	177(17)	185(9)	229(14)
N_f	Input	$f_{B_s}\sqrt{B_{B_s}^{(2)}}$	$f_{B_s}\sqrt{B_{B_s}^{(3)}}$	$f_{B_s}\sqrt{B_{B_s}^{(4)}}$	$f_{B_s}\sqrt{B_{B_s}^{(5)}}$
2+1	Current	205(7)	240(16)	231(7)	222(8)
	5 yr w/o EM	205(3.5)	240(8.0)	231(3.5)	222(4.0)
	5 yr with EM	205(4.1)	240(8.4)	231(4.2)	222(4.6)
	10 yr w/o EM	205(1.4)	240(3.2)	231(1.4)	222(1.6)
	10 yr with EM	205(2.5)	240(4.0)	231(2.7)	222(2.7)
2	Current	195(7)	215(17)	220(9)	285(14)
N_f	Input	$B_B^{(2)}$	$B_B^{(3)}$	$B_B^{(4)}$	$B_B^{(5)}$
2+1	Current	0.76(0.08)	1.07(0.22)	1.04(0.09)	0.96(0.10)
	5 yr w/o EM	0.76(0.040)	1.07(0.11)	1.04(0.045)	0.96(0.050)
	5 yr with EM	0.76(0.041)	1.07(0.11)	1.04(0.046)	0.96(0.051)
	10 yr w/o EM	0.76(0.016)	1.07(0.044)	1.04(0.018)	0.96(0.020)
	10 yr with EM	0.76(0.018)	1.07(0.045)	1.04(0.021)	0.96(0.022)
2	Current	0.72(0.03)	0.88(0.13)	0.95(0.05)	1.47(0.12)
N_f	Input	$B_{B_s}^{(2)}$	$B_{B_s}^{(3)}$	$B_{B_s}^{(4)}$	$B_{B_s}^{(5)}$
2+1	Current	0.81(0.06)	1.10(0.16)	1.02(0.07)	0.94(0.07)
	5 yr w/o EM	0.81(0.030)	1.10(0.080)	1.02(0.035)	0.94(0.035)
	5 yr with EM	0.81(0.031)	1.10(0.081)	1.02(0.036)	0.94(0.036)
	10 yr w/o EM	0.81(0.012)	1.10(0.032)	1.02(0.014)	0.94(0.014)
	10 yr with EM	0.81(0.014)	1.10(0.034)	1.02(0.017)	0.94(0.017)
2	Current	0.73(0.03)	0.89(0.12)	0.93(0.04)	1.57(0.11)

where $t_0 = (M_{B_{(s)}} + M_H)(\sqrt{M_{B_{(s)}}} - \sqrt{M_H})^2$. The FLAG analysis employed $N_+ = N_0 = 3$. The expansion coefficients $a^+_{\{0,1,2\}}$ and $a^0_{\{0,1\}}$ are fit parameters, whereas a^0_2 is expressed in terms of all remaining coefficients to impose the kinematical constraint $f_+(0) = f_0(0)$.

In this report we quote the current inputs for the coefficients $a_n^{\{+,0\}}$ and their correlation matrix, and make forecasts for $a_n^{\{+,0\}}$. Those for the $B \to \pi\ell\nu$ and $B_s \to K\ell\nu$ decays are summarized in Tables 32–35.

Due to imperfect knowledge of the resonance spectrum, the Blaschke factors are set to $B_{\{+,0\}} = 1$ for the $B \to D\ell\nu$ decay. We list the lattice inputs in Tables 36 and 37. Results for the ratio $R_D = \mathrm{Br}(B \to D\tau\nu)/\mathrm{Br}(B \to D\ell\nu)$ are available in Refs. [145,146]. Their average is $R(D) = 0.300(8)$.

The $B \to D^*\ell\nu$ decay rate receives contributions both from the weak vector and axial vector currents. However, modern lattice calculation [144] focuses on the zero recoil point, where the matrix element reduces to a single form factor $\mathcal{F}$ from the axial current,

$$\langle D^*|A_\mu|B\rangle = i\sqrt{4M_B M_{D^*}}\epsilon_\mu \mathcal{F}. \tag{82}$$

Table 32. Current input for $B \to \pi \ell \nu$ obtained from Refs. [141,143].

a_n^i	Current	Correlation matrix				
a_0^+	0.404(13)	1	0.404	0.118	0.327	0.344
a_1^+	−0.68(13)	0.404	1	0.741	0.310	0.900
a_2^+	−0.86(61)	0.118	0.741	1	0.363	0.886
a_0^0	0.490(21)	0.327	0.310	0.363	1	0.233
a_1^0	−1.61(16)	0.344	0.900	0.886	0.233	1

Table 33. Forecasts for $B \to \pi \ell \nu$.

Forecast	a_0^+	a_1^+	a_2^+	a_0^0	a_1^0
5 yr w/o EM	0.404(0.0065)	−0.68(0.065)	−0.86(0.31)	0.490(0.011)	−1.61(0.080)
5 yr with EM	0.404(0.0077)	−0.68(0.065)	−0.86(0.31)	0.490(0.012)	−1.61(0.082)
10 yr w/o EM	0.404(0.0026)	−0.68(0.026)	−0.86(0.12)	0.490(0.0042)	−1.61(0.032)
10 yr with EM	0.404(0.0048)	−0.68(0.027)	−0.86(0.12)	0.490(0.0065)	−1.61(0.036)

Table 34. Current input for $B_s \to K \ell \nu$ obtained from Refs. [141,155].

a_n^i	Current	Correlation matrix				
a_0^+	0.360(14)	1	0.098	−0.216	0.730	0.345
a_1^+	−0.828(83)	0.098	1	0.459	0.365	0.839
a_2^+	1.11(55)	−0.216	0.459	1	0.263	0.6526
a_0^0	0.233(10)	0.730	0.365	0.263	1	0.506
a_1^0	0.197(81)	0.345	0.839	0.652	0.506	1

Table 35. Forecasts for $B_s \to K \ell \nu$.

Forecast	a_0^+	a_1^+	a_2^+	a_0^0	a_1^0
5 yr w/o EM	0.360(0.0070)	−0.828(0.042)	1.11(0.28)	0.233(0.0050)	0.197(0.041)
5 yr with EM	0.360(0.0079)	−0.828(0.042)	1.11(0.28)	0.233(0.0055)	0.197(0.041)
10 yr w/o EM	0.360(0.0028)	−0.828(0.017)	1.11(0.11)	0.233(0.0020)	0.197(0.016)
10 yr with EM	0.360(0.0046)	−0.828(0.019)	1.11(0.11)	0.233(0.0031)	0.197(0.016)

Table 36. Current input for $B \to D \ell \nu$ obtained from Refs. [145,146].

a_n^i	Current	Correlation matrix				
a_0^+	0.909(14)	1	0.737	0.594	0.976	0.777
a_1^+	−7.11(65)	0.737	1	0.940	0.797	0.992
a_2^+	66 (11)	0.594	0.940	1	0.666	0.938
a_0^0	0.794(12)	0.976	0.797	0.666	1	0.818
a_1^0	−2.45(65)	0.777	0.992	0.938	0.818	1

Here, ϵ represents the polarization of D^*. The current input and forecasts are summarized in Table 38, where we assume 0.5% uncertainty of the EM correction estimated in Ref. [144].

The $\Lambda_b \to p \ell \nu$ and $\Lambda_b \to \Lambda_c \ell \nu$ decays provide an independent determination of $|V_{ub}|/|V_{cb}|$. So far, only one modern, unquenched calculation exists for the relevant form factors [161], leading to

Table 37. Forecasts for $B \to D\ell\nu$.

Forecast	a_0^+	a_1^+	a_2^+	a_0^0	a_1^0
5 yr w/o EM	0.909(0.0070)	−7.11(0.33)	66(5.5)	0.794(0.0060)	−2.45(0.33)
5 yr with EM	0.909(0.011)	−7.11(0.33)	66(5.5)	0.794(0.010)	−2.45(0.33)
10 yr w/o EM	0.909(0.0028)	−7.11(0.13)	66(2.2)	0.794(0.0024)	−2.45(0.13)
10 yr with EM	0.909(0.0095)	−7.11(0.15)	66(2.3)	0.794(0.0083)	−2.45(0.13)

Table 38. Lattice inputs for $B \to D^*\ell\nu$ from Ref. [144].

Input	Current	5 yr w/o EM	5 yr with EM	10 yr w/o EM	10 yr with EM
$\mathcal{F}$	0.906(0.013)	0.906(0.0065)	0.906(0.0079)	0.906(0.0026)	0.906(0.0052)

$|V_{ub}|/|V_{cb}| = 0.083(0.004)_{\rm ex}(0.004)_{\rm lat}$. As mentioned in Sect. 7.5.2, baryons are more challenging in controlling the chiral extrapolation and finite-volume effects. While these systematics have to be checked by independent calculations, these issues can be addressed in the relatively short term.

8. Leptonic and semi-leptonic *B* decays

Editors: A. S. Kronfeld, G. De Nardo, F. J. Tackmann, R. Watanabe, A. Zupanc
Additional section writers: F. Bernlochner, M. Gelb, P. Goldenzweig, S. Hirose, Z. Ligeti, M. Merola, F. Metzner, G. Ricciardi, Y. Sato, C. Schwanda, M. Tanaka, P. Urquijo

8.1. Introduction

In this chapter we consider leptonic and semi-leptonic B meson decays that proceed in the SM via first-order weak interactions and are mediated by the W boson. B meson decays involving electrons and muons are expected to be dominated by the tree-level W boson decays and any new physics contributions are expected to be highly suppressed with respect to the SM. Semi-leptonic decays involving light leptons therefore provide an excellent laboratory for measurement of the magnitudes of the CKM matrix elements V_{cb} and V_{ub}. These are fundamental parameters of the SM and have to be determined experimentally. The magnitude of V_{cb} normalizes the unitarity triangle, and the ratio of the magnitudes of V_{ub} and V_{cb} determines the side opposite to the angle ϕ_1 (β). Thus, they play a central role in tests of the CKM sector of the SM, and complement the measurements of CP asymmetries in B decays. Leptonic and semi-leptonic decays involving the heavier τ lepton provide additional information on SM processes and can also be sensitive to non-SM contributions such as charged Higgs bosons.

The rest of the chapter is structured as follows. In this introduction we briefly present an overview of the experimental techniques used in studies of B decay modes involving neutrinos or missing energy. Then, in Sect. 8.2 we establish notation for the matrix elements appearing in leptonic and semi-leptonic B decays. In the remainder of the chapter we present the Belle II prospects for measuring various observables in purely leptonic B meson decays (Sect. 8.3), leptonic decays radiating a hard (high-energy) photon (Sect. 8.4), favored and suppressed semi-tauonic decays (Sect. 8.5), exclusive favored and suppressed semi-leptonic decays (Sect. 8.6), and inclusive favored and suppressed semi-leptonic decays (Sect. 8.7), and discuss their potential to uncover new physics. The Belle II prospects are partly based on studies performed on simulated Belle II and Belle MC samples, and partly on estimates obtained by projecting existing results from Belle and Babar, taking into account

improvements in the detector and software algorithms. The beam-induced background (see Sect. 4) is expected to be much higher in Belle II compared to Belle or BaBar, which represents a more challenging environment for studies of decays with missing energy. One of the major goals of all the studies performed on Belle II MC samples that are presented in the rest of the chapter is to show that we can successfully and effectively suppress the much higher beam-induced background with the improved capabilities of the upgraded Belle II detector (see Chapter 3).

Experimental techniques Semi-leptonic and leptonic decays have at least one neutrino in the final state, which escapes the detector undetected, and limits the use of kinematic constraints to reject background that are constructed from the measured momenta and energies of the visible decay products (e.g. the beam-energy-constrained mass $M_{\rm bc}$, Eq. (185), and the energy difference ΔE, Eq. (186)). Semi-leptonic and leptonic decays or other B meson decays with missing energy can be measured at the B factories due to the unique experimental conditions: the known production process of $B\overline{B}$ pairs and the fact that the detector encloses the interaction region almost hermetically. These two properties allow us to infer the four-momenta of undetected particles, such as neutrinos, from the measured momenta and energies of all the other particles produced in the e^+e^- collision (except for the neutrino) and imposing energy-momentum conservation. Such a measurement technique is commonly referred to as an untagged measurement. In the case where both the signal B meson (denoted as $B_{\rm sig}$) and the other B meson (denoted as the tag $B_{\rm tag}$ meson) are reconstructed in the event, two powerful constraints can be constructed and exploited to suppress the background or to identify signal decays:

- The missing mass squared is defined as

$$M^2_{\rm miss} = (p_{e^+e^-} - p_{B_{\rm sig}} - p_{B_{\rm tag}})^2, \tag{83}$$

  where $p_{e^+e^-}$ is the known four-momentum of the colliding beams, and $p_{B_{\rm sig}}$ and $p_{B_{\rm tag}}$ are the measured four-momenta of the reconstructed signal and tag B mesons, respectively. In the case of semi-leptonic decay of the signal B meson, such as $B \to \pi \ell \nu$ or $B \to D \ell \nu$, only one neutrino is missing and hence $M^2_{\rm miss} = m^2_\nu$ peaks at zero. Note that in this section ℓ typically denotes e or μ.
- The extra energy in the calorimeter, $E_{\rm extra}$, is defined as the sum of the energy deposits in the calorimeter that cannot be directly associated with the reconstructed daughters of $B_{\rm tag}$ or $B_{\rm sig}$. For signal events, $E_{\rm extra}$ (or $E_{\rm ECL}$) must be either zero or a small value arising from beam background hits and detector noise, since neutrinos do not interact in the calorimeter. On the other hand, most background events (whether B decays or $q\bar{q}$ continuum) are distributed toward higher $E_{\rm extra}$ due to the contribution from additional clusters, produced by unassigned tracks and neutrals from mis-reconstructed tag and/or signal B mesons.

Measurements of leptonic and semi-leptonic decays have in the past been performed using three different experimental techniques, differing only in the way that the tag B meson in the event is reconstructed. In untagged analyses, the missing energy and momentum of the whole event are used to determine the four-momentum of the missing neutrino from the signal (semi-)leptonic decay as described above. Measurements where the tag B meson is reconstructed in well-defined decays are commonly denoted as tagged measurements. Semi-leptonic tagging involves partial reconstruction of a $B_{\rm tag} \to D^{(*)} \ell \nu_\ell$ decay as the tagging mode. In this case, two neutrinos are present in the

event and the four-momentum of the $B_{\rm sig}$ cannot be fully constrained. In full reconstruction tagging, a hadronically decaying $B_{\rm tag}$ meson is reconstructed, against which the signal decay recoils. The improvements to the detector acceptance, efficiency of particle detection, and the tag B meson reconstruction efficiency expected in Belle II have a large impact on the physics potential. The slightly reduced beam energy asymmetry at Super KEKB compared to KEKB leads to a small increase in solid angle coverage. Improved particle identification and $K^0_{\rm S}$ reconstruction efficiency improves separation between $b \to u$ and $b \to c \to s$ transitions. Dedicated low-momentum tracking algorithms will improve tagging efficiencies and identification of events that have slow pions from D^* decays. The latter is also very important for $b \to c$ background rejection in inclusive $b \to u\ell\nu$ analyses. See Sect. 6.6 for more details on tag B meson reconstruction and expected performance at Belle II.

8.2. Matrix elements of electroweak currents

Author: A. S. Kronfeld (th.)

As hadronic matrix elements in exclusive leptonic and semi-leptonic decays are used in Chapter 9, as well as here, it is convenient to standardize the notation by collecting the necessary formulae in one place. To keep the notation general, we write the definitions of decay constants and form factors using B mesons in the initial state decaying to either pseudoscalar mesons ($P = D, \pi, K$) or vector mesons ($V = D^*, \rho, K^*$) in the final state. The CKM elements for the tree-level decays will be abbreviated V_{qb}, where $q = c, u$.

8.2.1. Leptonic decays $B^+ \to \ell^+\nu$ and $B^0 \to \ell^+\ell^-$

At leading order in the electroweak interaction, the amplitude for the leptonic decay contains a hadronic factor,

$$\langle 0|A^\mu|B(p)\rangle = ip^\mu f_B, \tag{84}$$

where A^μ is an axial-vector current (for the charged current, $A^\mu = \bar{b}\gamma^\mu\gamma^5 u$), and the decay constant f_B is a useful parameterization, because the only Lorentz structure available is the B meson four-momentum p^μ. By conservation of angular momentum, the only other non-vanishing matrix element for $B \to$ no-hadrons is

$$\langle 0|P|B(p)\rangle = -i\frac{M_B^2}{m_b + m_u} f_B, \tag{85}$$

where P is the pseudoscalar density (here $P = \bar{b}\gamma^5 u$), M_B is the B meson mass, and m_b and m_u are renormalized quark masses.[19] The decay constant f_B is the same in Eqs. (84) and (85) owing to the partial conservation of the axial-vector current (PCAC), $\partial \cdot A = i(m_b + m_u)P$, which holds when A^μ, P, and the masses are renormalized consistently. These considerations apply amplitudes both to the charged current decay $B^+ \to \ell^+\nu_\ell$ and to the flavor-changing neutral current (FCNC) decay $B^0_{(s)} \to \ell^+\ell^-$. In each formula in this section, M_B and f_B are the mass and decay constant of the $B^\pm$, B^0, or B_s meson, as the case may be. Feynman diagrams of SM and beyond SM leptonic B^+ decays are shown in Fig. 61.

[19] We use lower-case m for masses of elementary particles (quarks and leptons) and upper case M for hadron masses.

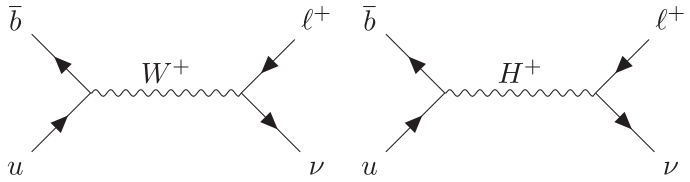

Fig. 61. Feynman diagrams of purely leptonic B^+ decays, mediated by a charged weak boson (left) or a charged Higgs as predicted in new physics models (right).

The partial width for either decay (assuming axial contributions only) is

$$\Gamma(B \to \ell_1 \ell_2) = \frac{M_B}{4\pi} |G|^2 f_B^2 \zeta_{12} \frac{\lambda_{12}^{1/2}}{M_B^2}, \tag{86}$$

where G contains couplings and (for FCNCs) loop factors, m_1 and m_2 are the lepton masses, and

$$\lambda_{12} = (M_B^2 - m_1^2 - m_2^2)^2 - 4m_1^2 m_2^2, \tag{87}$$

$$\zeta_{12} = m_1^2 + m_2^2 - \frac{(m_1^2 - m_2^2)^2}{M_B^2}. \tag{88}$$

These formulas do not hold when the final-state leptons' masses differ unless the interaction boils down to $V \pm A$. In a general setting, $|G|^2 \zeta_{12}$ must be replaced with a more complicated expression. Processes such as $B^0 \to \mu^\pm \tau^\mp$ have unmeasurably small rates in the SM, so the general formula is not important.

In the SM, one finds

$$G = \frac{G_F}{\sqrt{2}} V_{ub} \quad (m_{\nu_\ell} \to 0), \qquad \text{charged-current decay } B^+ \to \ell^+ \nu_\ell, \tag{89}$$

$$G = \frac{G_F^2 m_W^2}{\pi^2} V_{tb}^* V_{tq} C_A, \qquad \text{FCNC decay } B_{(s)}^0 \to \ell^+ \ell^-,\ q \in \{d, s\}, \tag{90}$$

where G_F is the Fermi constant, V is the CKM matrix, m_W is the W boson mass, and C_A is the Wilson coefficient obtained from integrating out the massive W, Z, and top quark. Reference [219] contains results for C_A including QED corrections.

The factor of the lepton mass in the leptonic decay amplitude arises because the lepton has to flip its spin to conserve angular momentum. This helicity suppression (for $\ell = e, \mu$) does not apply to the radiative leptonic decay $B^+ \to \ell^+ \nu_\ell \gamma$. This feature is relevant for $D_{(s)}^+ \to \mu^+ \nu_\mu(\gamma)$ and important for $B^+ \to \mu^+ \nu_\mu(\gamma)$ [220]. (For the $D_{(s)}$ decay, Ref. [221] estimates a 1% effect for the photon cuts used in existing measurements.) Once measurements of the $B^+ \to \mu^+ \nu_\mu$ branching fraction are made with a precision of a few percent, theorists should revisit the radiative corrections; for light mesons these issues are under control [222]. As discussed in Sect. 8.4.1, when the photon is hard, $E_\gamma \sim \frac{1}{2} M_B$, these decays can be used to extract information about B meson structure and non-leptonic decays [223].

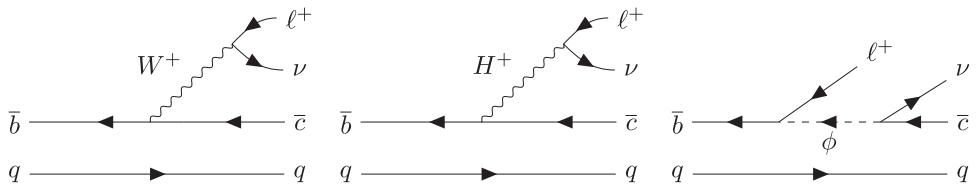

Fig. 62. Feynman diagrams of semi-leptonic B decays, mediated by a charged weak boson (left) and mediators predicted in new physics models: a charged Higgs (middle), and a leptoquark (right).

8.2.2. Semi-leptonic decay to a pseudoscalar meson

The amplitudes for the semi-leptonic decays $B^0 \to P^-\ell^+\nu_\ell$ and $B^+ \to P^0\ell^+\nu_\ell$, at leading order in the electroweak interaction, contain the hadronic factor

$$\langle P(k)|V^\mu|B(p)\rangle = \left(p^\mu + k^\mu - \frac{M_B^2 - M_P^2}{q^2}q^\mu\right)f_+(q^2) + \frac{M_B^2 - M_P^2}{q^2}\,q^\mu f_0(q^2), \tag{91}$$

where V^μ is the vector part of the weak current ($V^\mu = \bar{b}\gamma^\mu u$ for $B \to \pi$ and $B_s \to K$, and $V^\mu = \bar{b}\gamma^\mu c$ for $B \to D$ and $B_s \to D_s$). Two four-vectors appear in this process, and hence two form factors, which are functions of q^2 (where $q = p - k$). The vector (scalar) form factor f_+ (f_0) arises when the $\ell\nu_\ell$ system has $J^P = 1^-$ (0^+). At $q^2 = 0, f_0(0) = f_+(0)$.

Beyond the SM, scalar and tensor currents can mediate these decays. Such contributions to the decay amplitude entail the scalar and tensor form factors

$$\langle P(k)|S|B(p)\rangle = \frac{M_B^2 - M_P^2}{m_b - m_q}f_0(q^2), \tag{92}$$

$$\langle P(k)|T^{\mu\nu}|B(p)\rangle = \frac{2}{M_B + M_P}\left(p^\mu k^\nu - p^\nu k^\mu\right)f_T(q^2), \tag{93}$$

where S and $T^{\mu\nu}$ are scalar and tensor currents (here $S = \bar{b}q$, $T^{\mu\nu} = \bar{b}i\sigma^{\mu\nu}q$, $q = c, u$). The scalar form factor in Eq. (92) is the same as that in Eq. (91), owing to the partial conservation of the vector current (PCVC), $i\partial \cdot V = (m_b - m_q)S$. Feynman diagrams of SM and beyond SM semi-leptonic B decays are shown in Fig. 62.

The doubly differential partial width for $B \to P\ell^\pm\nu_\ell$ (assuming no scalar or tensor current) is [224]

$$\frac{d^2\Gamma}{dq^2\,d\cos\theta_\ell} = C_q|\eta_{\rm EW}|^2\frac{G_{\rm F}^2|V_{qb}|^2}{(2\pi)^3}\frac{\lambda^{1/2}}{8M_B^3}\frac{\lambda_{12}^{1/2}}{q^2}\left[\left(q^2 - m_1^2 - m_2^2 - \frac{\lambda_{12}}{q^2}\cos^2\theta\right)\frac{\lambda}{q^2}|f_+|^2 + \right. \tag{94}$$

$$\left. + \zeta_{12}\frac{(M_B^2 - M_P^2)^2}{q^2}|f_0|^2 \mp 2(m_1^2 - m_2^2)(M_B^2 - M_P^2)\frac{\lambda^{1/2}}{q^2}\frac{\lambda_{12}^{1/2}}{q^2}\cos\theta\,\Re\left(f_+f_0^*\right)\right],$$

where $C_q = 1/2$ for π^0 and 1 otherwise,[20] $\eta_{\rm EW}$ is an electroweak correction discussed below, λ_{12} and ζ_{12} are obtained from Eqs. (87) and (88) by substituting $M_B^2 \to q^2$, and

$$\lambda = (M_B^2 + M_P^2 - q^2)^2 - 4M_B^2M_P^2, \tag{95}$$

$$\cos\theta = 4\lambda^{-1/2}\left(1 - \frac{m_\ell^2}{q^2}\right)^{-1}\left(\frac{p_B \cdot q\,p_\ell \cdot q}{q^2} - p_B \cdot p_\ell\right), \tag{96}$$

[20] This factor stems from the fact that a $b \to u$ current produces only the $\bar{u}u$ component of the π^0.

the last being the angle in the center of mass of the $\ell\ell$ system between the B meson and lepton 1 with charge ± 1. Quantities such as λ, λ_{12} are sometimes known as the Källén functions.

Integrating over $\cos\theta$,

$$\frac{d\Gamma}{dq^2} = C_q |\eta_{\rm EW}|^2 \frac{G_{\rm F}^2 |V_{qb}|^2}{(2\pi)^3} \frac{\lambda^{1/2}}{4M_B^3} \frac{\lambda_{12}^{1/2}}{q^2} \left\{ \lambda \beta_{12} |f_+|^2 + \zeta_{12} \frac{(M_B^2 - M_P^2)^2}{q^2} |f_0|^2 \right\}, \tag{97}$$

where

$$\beta_{12} = 1 - \frac{m_1^2 + m_2^2}{q^2} - \frac{\lambda_{12}}{(q^2)^2}. \tag{98}$$

For a massless neutrino,

$$\beta_{\ell 0} = \left(1 - \frac{m_\ell^2}{q^2}\right)\left(\frac{2}{3} + \frac{m_\ell^2}{3q^2}\right), \tag{99}$$

$$\zeta_{\ell 0} = m_\ell^2 \left(1 - \frac{m_\ell^2}{q^2}\right), \tag{100}$$

$$\frac{\lambda_{\ell 0}^{1/2}}{q^2} = \left(1 - \frac{m_\ell^2}{q^2}\right). \tag{101}$$

The kinematic factors for $\ell^+\ell^-$ are obtained by setting $m_2 = m_1 = m_\ell$:

$$\beta_{\ell\ell} = \frac{2}{3}\left(1 - \frac{m_\ell^2}{q^2}\right), \tag{102}$$

$$\zeta_{\ell\ell} = 2m_\ell^2, \tag{103}$$

$$\frac{\lambda_{\ell\ell}^{1/2}}{q^2} = \left(1 - \frac{4m_\ell^2}{q^2}\right)^{1/2}. \tag{104}$$

These formulas hold for a V–A lepton current; in general, the pattern of lepton masses and couplings is more complicated. Of course, any measurable signal with lepton flavor violation, i.e. $m_1 \neq m_2$, is a major discovery whatever the V and A couplings are.

When the scalar and tensor currents contribute (beyond the SM), the expression for $d\Gamma/dq^2$ becomes very complicated. See Ref. [225] or the arXiv version of Ref. [226] for the full formula (written for $D \to K\ell\nu$ decay). See also Ref. [227].

The decay amplitude has two interesting corrections. In Eq. (94), $\eta_{\rm EW}$ denotes the leading logarithmic contribution of two-loop electroweak diagrams,

$$\eta_{\rm EW} = 1 + \frac{\alpha}{\pi}\left[\ln\frac{M_W}{\mu} + \tan^2\theta_W \frac{M_W^2}{M_Z^2 - M_W^2} \ln\frac{M_Z}{M_W}\right], \tag{105}$$

where μ is a scale separating this contribution and contributions that depend on hadron structure. In the leading-logarithmic approximation the same hadronic matrix elements arise, so the correction is multiplicative; in this context it is reasonable to set $\mu = M_B$. In Eqs. (94), (97), and (117) (below), $G_{\rm F}$ is defined via the muon lifetime. Second, final states with two charged particles have a Coulomb

attraction that increases the rate. For a discussion, see Refs. [228,229]. More theoretical work may be needed, but it is clear that experimental results must be reported separately for $B^0 \to P^- \ell^+ \nu$ and $B^+ \to P^0 \ell^+ \nu$.

8.2.3. Semi-leptonic decay to a vector meson

Last, let us consider the amplitude for the semi-leptonic decay $B^+ \to V^0 \ell^+ \nu_\ell$ at leading order in the electroweak interaction. Now there are three four-vectors in the process, so the decomposition of the amplitude into form factors reads ($\varepsilon^{0123} = +1$)

$$\langle V(k,\epsilon^{(V)})|V^\mu|B(p)\rangle = i\bar{\epsilon}^{(V)}_\rho \frac{2\varepsilon^{\mu\rho}{}_{\sigma\tau} p^\sigma k^\tau}{M_B + M_V} V(q^2), \tag{106}$$

$$\begin{aligned}\langle V(k,\epsilon^{(V)})|A^\mu|B(p)\rangle = \bar{\epsilon}^{(V)}_\rho \Bigg[& 2M_V \frac{q^\rho q^\mu}{q^2} A_0(q^2) + (M_B + M_V)\left(g^{\rho\mu} - \frac{q^\rho (p+k)^\mu}{M_B^2 - M_V^2}\right) A_1(q^2) \\ & + 2M_V q^\rho \left(\frac{(p+k)^\mu}{M_B^2 - M_V^2} - \frac{q^\mu}{q^2}\right) A_3(q^2)\Bigg],\end{aligned} \tag{107}$$

with the same vector current, V^μ, as above and the axial current $A^\mu = \bar{b}\gamma^\mu\gamma^5 u$ or $\bar{b}\gamma^\mu\gamma^5 c$. Here, $\bar{\epsilon}^{(V)}$ denotes the polarization vector of the final state. Note that $M_B^2 - M_V^2 = q \cdot (p+k)$. Sometimes A_3 is eliminated in favor of a form factor A_2 via $2M_V A_3 = (M_B + M_V)A_1 - (M_B - M_V)A_2$. At $q^2 = 0$, $A_0(0) = A_3(0)$.

It is more useful to decompose the amplitude according to the helicity of the virtual W [224]. There are several notations for form factors in the literature. Whatever one chooses on the right-hand side of Eqs. (106) and (107), it is straightforward to relate the matrix elements to the helicity amplitudes.

Being off shell, the W has four polarizations: scalar (spin 0), longitudinal, and two transverse (the last three spin 1). In the frame with the B at rest and the V flying out along the $+z$ axis, the polarization vectors, respectively, are ($q^0 = M_B - E_V$, $E_V = p \cdot k / M_B$)

$$\epsilon^{(W)}_s = \frac{1}{\sqrt{q^2}}\left(q^0, 0, 0, -|\boldsymbol{k}|\right) = \frac{q}{\sqrt{q^2}}, \tag{108}$$

$$\epsilon^{(W)}_0 = \frac{1}{\sqrt{q^2}}\left(|\boldsymbol{k}|, 0, 0, -q^0\right), \tag{109}$$

$$\epsilon^{(W)}_\pm = \frac{1}{\sqrt{2}}(0, \pm 1, -i, 0), \tag{110}$$

where $\boldsymbol{k}$ is the three-momentum of the final-state vector meson in the rest frame of the B. The subscript s denotes the $J = 0$ partial wave (for historical reasons), and 0 and $\pm$ denote the J_z component of the $J = 1$ partial wave. Similarly,

$$\epsilon^{(V)}_0 = \frac{1}{M_V}(|\boldsymbol{k}|, 0, 0, E_V), \tag{111}$$

$$\epsilon^{(V)}_\pm = \frac{1}{\sqrt{2}}(0, \mp 1, -i, 0) \tag{112}$$

provide the polarization vectors for the final-state vector meson. In Eqs. (106) and (107), a bar on a polarization vector denotes complex conjugation in Minkowski space, and complex conjugation of only the spatial components in Euclidean space (useful in lattice QCD).

The helicity amplitudes $H_a = \langle V(k,\epsilon^{(V)})|\bar{\epsilon}_a^{(W)} \cdot (V-A)|B(p)\rangle$ are then

$$H_s(q^2) = -\frac{\lambda^{1/2}}{\sqrt{q^2}} A_0(q^2), \tag{113}$$

$$H_0(q^2) = -\frac{\sqrt{q^2}(M_B^2 + 3M_V^2 - q^2)}{2M_V(M_B - M_V)} A_1(q^2) - \frac{\lambda}{(M_B^2 - M_V^2)\sqrt{q^2}} A_3(q^2), \tag{114}$$

$$H_\pm(q^2) = -(M_B + M_V)A_1(q^2) \pm \frac{\lambda^{1/2}}{M_B + M_V} V(q^2), \tag{115}$$

where the Källén function λ is the same as before, except with M_V instead of M_P. In H_s and H_0, the final-state vector meson has $J_z = 0$; in $H_\pm$, it has $J_z = \pm 1$. Note that in lattice QCD, it is most straightforward to compute A_1, V, and two more linear combinations of A_0, A_1, and A_3. The full amplitude is then proportional to

$$\sum_{ab} g^{ab} L_a H_b = L_s H_s - L_0 H_0 - L_+ H_+ - L_- H_-, \qquad a \in \{s, 0, +, -\}, \tag{116}$$

with lepton helicity amplitudes $L_a = \bar{u}(\nu)\gamma \cdot \epsilon_a^{(W)}(1-\gamma_5)v(\ell)$.

The triple differential rate (in q^2, $\cos\theta$, and ϕ, which is the angle between the decay planes of B and V) for the semi-leptonic decay $B^+ \to V^0 \ell^+ \nu_\ell$ can be found in Refs. [224]. Integrating over all angles,

$$\frac{d\Gamma}{dq^2} = C_q |\eta_{\rm EW}|^2 \frac{G_{\rm F}^2 |V_{qb}|^2}{(2\pi)^3} \frac{\lambda^{1/2}}{4M_B^3} \frac{\lambda_{12}^{1/2}}{q^2} \left\{ q^2 \beta_{12} \left[|H_+|^2 + |H_-|^2 + |H_0|^2 \right] + \zeta_{12} |H_s|^2 \right\}, \tag{117}$$

where $C_q = 1/2$ for ρ^0 and 1 otherwise, λ_{12} and ζ_{12} are obtained from Eqs. (87) and (88) by substituting $M_B^2 \to q^2$, and

$$\beta_{12} = 1 - \frac{m_1^2 + m_2^2}{q^2} - \frac{\lambda_{12}}{(q^2)^2}. \tag{118}$$

Note that the differential rate for the semi-leptonic decay $B^+ \to P^0 \ell^+ \nu_\ell$ is the same after dropping the $H_\pm$ terms.[21] These formulas again hold for a V–A lepton current; in general, the pattern of lepton masses and couplings is more complicated.

Beyond the SM, the pseudoscalar and tensor currents can mediate these decays, in addition to the SM vector and axial-vector currents. The matrix element for the pseudoscalar follows in analogy to Eq. (85):

$$\langle V(k,\epsilon^{(V)})|P|B(p)\rangle = \frac{2M_V}{m_b + m_q} \bar{\epsilon}^{(V)} \cdot q A_0(q^2) = \frac{\lambda^{1/2}}{m_b + m_q} A_0(q^2), \tag{119}$$

[21] In $B \to P\ell\nu$, $H_0(q^2) = (\lambda/q^2)^{1/2} f_+(q^2)$ and $H_s = [(M_B^2 - M_P^2)/\sqrt{q^2}] f_0(q^2)$.

with the last equality holding only in the polarization, namely $\epsilon^{(V)} = \epsilon_0^{(V)}$, with a non-zero amplitude. The tensor current has the matrix element

$$\langle V(k,\epsilon^{(V)})|T^{\mu\nu}|B(p)\rangle = i\varepsilon^{\mu\nu}{}_{\sigma\tau}\bar{\epsilon}_\rho^{(V)}\left\{g^{\rho\sigma}(p+k)^\tau T_1(q^2) - g^{\rho\sigma}q^\tau\frac{M_B^2-M_V^2}{q^2}\left[T_1(q^2)-T_2(q^2)\right]\right.$$
$$\left. + q^\rho\frac{(p+k)^\sigma q^\tau}{q^2}\left[T_1(q^2)-T_2(q^2)-\frac{q^2}{M_B^2-M_V^2}T_3(q^2)\right]\right\}. \tag{120}$$

In penguin amplitudes, the combinations $q_\nu T^{\mu\nu}$ and $\varepsilon^{\mu\nu\alpha\beta}q_\nu T_{\alpha\beta}$ appear, leading straightforwardly to additional terms in the helicity amplitudes. See also Ref. [227].

The discussion of electroweak and Coulomb correction in the paragraph with Eq. (105) applies here too.

8.3. *Leptonic B decays*

Authors: G. De Nardo (exp.), M. Merola (exp.), R. Watanabe (th.)

The branching fraction of $B^+ \to \ell^+\nu$, $\mathcal{B}_\ell$, is proportional to the mass squared of the charged lepton, cf. Eqs. (86) and (88). Hence, B_τ, B_μ, and B_e are hierarchical in the respective lepton mass in the absence of new physics. We take $|V_{ub}| = (3.55 \pm 0.12) \times 10^{-3}$, determined from exclusive semi-leptonic B decays by HFLAV [230], and $f_B = (186 \pm 4)$ MeV from Ref. [217], which is the only entry in the 2016 FLAG [140] average with four active flavors.[22] The predicted values for the SM are then found to be

$$B_\tau = (7.7 \pm 0.6) \times 10^{-5},\ \ B_\mu = (3.5 \pm 0.3) \times 10^{-7},\ \ B_e = (8.1 \pm 0.6) \times 10^{-12}. \tag{121}$$

This class of decays is of interest not only to test the SM but also search for new physics at Belle II.

Past measurements of $\mathcal{B}(B \to \tau\nu_\tau)$ by Belle and BaBar were performed with two independent approaches to reconstruct $B_{\rm tag}$: using semi-leptonic and hadronic decays [232–236]. At present, no single experiment finds a significance greater than $5\,\sigma$. Combining the measurements by Belle and BaBar, the world average is given as $(1.06 \pm 0.19) \times 10^{-4}$ [230], which has over $5\,\sigma$ significance. This is consistent with the prediction ($B_\tau = (7.7 \pm 0.6) \times 10^{-5}$) at $2\,\sigma$.

The light leptonic modes $B \to \ell\nu_\ell$ for $\ell = e, \mu$ are two-body decays, which implies that the charged lepton momentum in the rest frame of $B_{\rm sig}$ is $m_B/2$. Thus, this unique two-body decay topology can be exploited in search analyses. The light leptonic modes have not yet been observed [237,238]. The upper limit on B_μ is then summarized as $< 1 \times 10^{-6}$ at 90% CL, whereas that on B_e is also given as $< 0.98 \times 10^{-6}$ [77].

The above summary shows that the present branching fraction measurement of $B^+ \to \tau^+\nu_\tau$ and upper limit of $B^+ \to \mu^+\nu_\mu$ are already close to their SM predictions. We expect that these processes will eventually be observed with more than $5\,\sigma$ significance at SuperKEKB/Belle II. The decay $B^+ \to e^+\nu_e$ can be observed only if new physics greatly enhances its decay rate.

In the absence of new physics, purely leptonic decays can provide direct determinations of $|V_{ub}|$ with relatively small theoretical uncertainty. Since discrepancies amongst the $|V_{ub}|$ determinations

[22] FLAG will update its averages in 2018. For decay constants, the most significant new result is $f_B = 189.4 \pm 1.4$ MeV from Ref. [231].

from exclusive and inclusive processes are long-standing, leptonic decays can provide important orthogonal information, as in the determination of $|V_{cd}|$ and $|V_{cs}|$.

The presence of new physics with different chiral structure would primarily be observed through modifications to $B^+ \to \ell^+ \nu_\ell$ rates. Namely, we can describe the branching fraction as

$$\mathcal{B}(B^+ \to \ell^+ \nu_\ell)_{\rm NP} = \mathcal{B}(B^+ \to \ell^+ \nu_\ell)_{\rm SM} \times \left|1 + r^\ell_{\rm NP}\right|^2 \tag{122}$$

for the new physics model. Comparing the current data and the SM reference values shown above, we can see the present constraints as

$$\left|1 + r^\tau_{\rm NP}\right| = 1.17 \pm 0.12\,, \quad \left|1 + r^\mu_{\rm NP}\right| < 1.7\ (90\%\ {\rm CL})\,, \quad \left|1 + r^e_{\rm NP}\right| < 348\ (90\%\ {\rm CL})\,. \tag{123}$$

Theoretical uncertainties are not taken into account in the latter two results as they are considered negligible.

8.3.1. $B \to \tau \nu_\tau$

Belle II full simulation study The study presented here aims at estimating the precision of Belle II on the measurement of the branching fraction of $B \to \tau \nu_\tau$ with 1, 5, and 50 ab^{-1} of data respectively. The analysis is performed on the MC5 Belle II production (see Sect. 4) corresponding to 1 ab^{-1} of generic $B^+B^-/B^0\overline{B}^0$, $u\overline{u}$, $d\overline{d}$, $s\overline{s}$, $c\overline{c}$ background processes and 100×10^6 signal events. In these samples the expected machine background (see Sect. 4) is superimposed with the simulated primary collision events.

The analysis strategy is to use a hadronic tag method through the full event interpretation (FEI) algorithm (Sect. 6.6). It makes use of thousands of B meson decay modes and builds up a multivariate discriminant to assign to each B candidate (tag) a probability of correct reconstruction. In order to reject mis-reconstructed $B_{\rm tag}$ candidates, a criterion is placed on the FEI discriminant corresponding to purities of 49% and 93% for correctly reconstructed B mesons in the background and signal samples, respectively. In the case that multiple candidates are reconstructed in the event, the one with the highest FEI discriminant value is chosen. The purity of the samples is evaluated after continuum background rejection by means of a fit to the $M_{\rm bc}$ distribution. The $M_{\rm bc}$ distribution is modeled with an Argus function for the combinatorial background plus a crystal ball function for the correctly reconstructed B candidates. The number of events under the crystal ball is then counted above an $M_{\rm bc}$ threshold of 5.275 GeV/c^2.

After the reconstruction of the $B_{\rm tag}$ side, the presence of only one additional track in the event is required, consistent with a one-prong τ decay. Particle identification (PID) criteria are applied to select four τ decay modes: $\mu\nu\overline{\nu}$, $e\nu\overline{\nu}$, $\pi\nu$, and $\rho\nu$. The PID criteria are based on likelihood ratios, described in detail in Sect. 5.5. Candidate charged ρ mesons are required to originate from $\pi\pi^0$ pairs in the mass window $0.625 < m_{\pi\pi^0} < 0.925$ GeV/c^2; in turn, the π^0 candidates are reconstructed by pairing two neutral clusters and applying an invariant mass window on the $\gamma\gamma$ pair of $0.12 < m_{\gamma\gamma} < 0.16$ GeV/c^2. Mis-reconstructed $B_{\rm tag}$ candidates are suppressed at this stage applying the following selection criteria: $5.275 < M_{\rm bc} < 5.290$ GeV/c^2 and $-0.20 < \Delta E < 0.04$ GeV.

Due to the high level of machine background in Belle II (due to the smaller beam size of SuperKEKB) a dedicated study has been performed on MC simulated events to optimally select the photon candidates from e^+e^- collisions (from now on called "physics" photons) and reject beam-induced background photon candidates (from now on called "background" photons). Several cluster-related discriminating variables have been exploited for this purpose, among which the most

important are the cluster energy, the cluster timing, and the ratio between the energy deposited in a 3×3 and in 5×5 square of crystals around the center of the cluster, E9/E25. (Note that E9/E21 will be used in future Belle II physics analyses). Physics photon candidates are required to satisfy a minimum energy threshold since they have a harder energy spectrum than background photons. Beam-induced photon production is not correlated with bunch crossings, and so the cluster time distribution shows a uniform distribution for background photons and a peak near the bunch crossing time for physics photons. A tight time window is selected corresponding to a 90%–95% efficiency for physics photons. Physics photon candidates are expected to have a relatively narrow E9/E25 distribution consistent with a single photon, while beam-induced photon showers exhibit a larger spread of energy deposits. As background photons are expected to have a large impact on the forward region of the detector, different selection criteria are imposed for the forward, barrel, and backward detector regions. These photon candidates are used in π^0 reconstruction and for determining the remaining energy deposition in the calorimeter from physics photons, denoted $E_{\rm ECL}$.

In order to reduce contamination from continuum background events (mainly $e^+e^- \to q\bar{q}$), several topological variables (Sect. 6.4) have been considered: normalized second Fox–Wolfram moments, $\cos\theta_{\rm thrust}$, CLEO cones, and Kakuno super Fox–Wolfram (KSFW) moments, exploiting the different topology of events with spherical symmetry as B^+B^- over events with back-to-back symmetry, as $\ell^+\ell^-$ and, to a lesser extent, $q\bar{q}$. Keeping only the variables that are weakly correlated with $E_{\rm ECL}$, two multivariate discriminants using boosted decision trees (BDTs) have been trained on continuum background and signal $B \to \tau\nu_\tau$ events in the signal window $5.27 < M_{\rm bc} < 5.29$ GeV/c^2 and $E_{\rm ECL} < 0.3$ GeV, using the `TMVA` toolkit [239]. Leptonic and hadronic τ decay modes are trained separately, since the latter are most affected by continuum background. Continuum events are rejected by placing a threshold on the BDT discriminant at the maximum point in the figure of merit (FOM) $S/\sqrt{S+B}$, where S and B are the numbers of signal and background events, respectively. The thresholds are found to be ${\rm BDT}_{\rm had} > 0.2$ corresponding to 99% continuum rejection and 47% signal efficiency, and ${\rm BDT}_{\rm lep} > 0.04$, corresponding to 93% continuum rejection and 65% signal efficiency. Figure 63 shows the BDT discriminant output for signal and background events, separated by hadronic and leptonic modes.

A characteristic feature of $B \to \tau\nu_\tau$ decays is the presence of two or three neutrinos in the final state. This property can be used in the analysis by requiring that a significant amount of missing energy and momentum is present for leptonic channels, $M^2_{\rm miss} > 12\,({\rm GeV}/c^2)^2$, and less for the hadronic channels, $M^2_{\rm miss} < 12\,({\rm GeV}/c^2)^2$. In addition, the reconstructed momentum of the π and ρ on the signal side in the CMS frame is required to satisfy $p^*_{\rm sig} > 1.6$ GeV/c. The thresholds listed for $M_{\rm miss}$ and $p^*_{\rm sig}$ have been chosen based on FOM optimization. It should be noted that Belle used $M_{\rm miss}$ in the signal yield fit; however, we have taken a simplified one-dimensional fit approach for this sensitivity study.

In Fig. 64(a) the $E_{\rm ECL}$ distribution is shown after applying all selection criteria. A comparison of the signal $E_{\rm ECL}$ distribution of this analysis with the one obtained by the Belle Collaboration measurement with a hadronic tag [234] is also shown, in Fig. 64(b). The extra energy resolution at Belle II is slightly better than Belle despite the increased beam background levels. The one-sided 68th percentile of the $E_{\rm ECL}$ distribution is found to be 0.22 GeV for Belle II and 0.28 GeV for Belle.

The signal efficiencies and expected signal and background yields in two $E_{\rm ECL}$ windows are reported in Table 39 for this analysis and compared to the Belle MC from hadronic tag measurement [234].

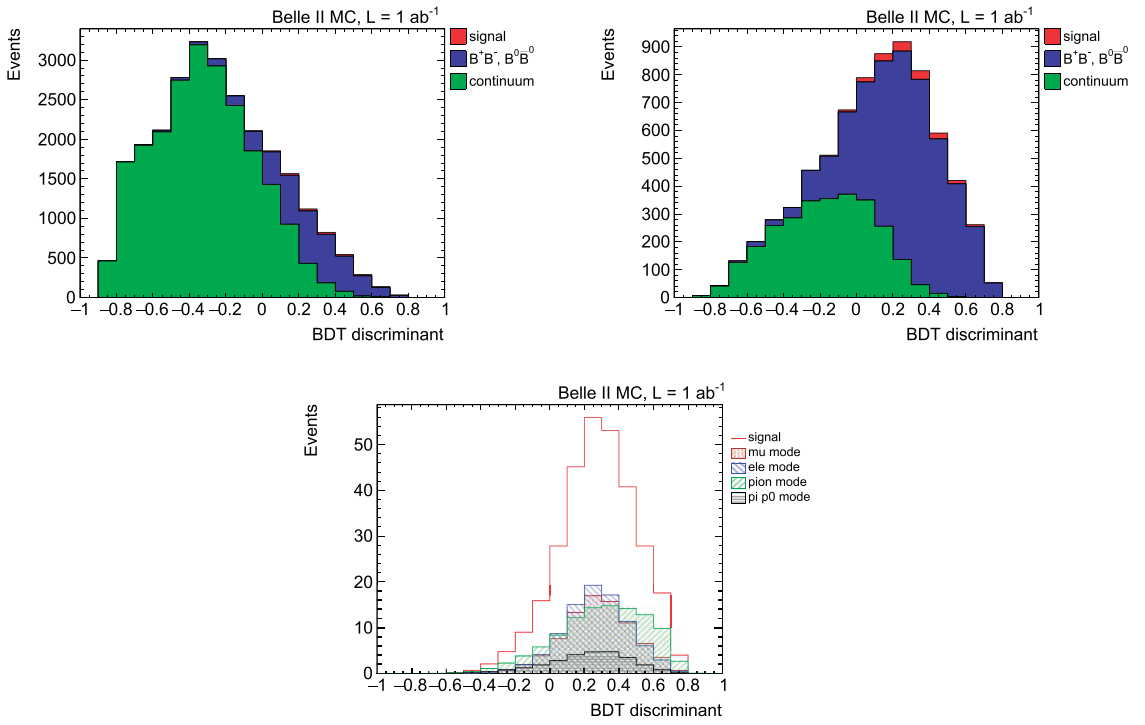

Fig. 63. Top left and right: BDT discriminant distributions for the $B \to \tau\nu_\tau$ analysis, depicting the signal (red), $B\bar{B}$ background (blue), and continuum events (green), in the hadronic (left) and leptonic (right) τ decay channels. Bottom: BDT discriminant distribution for signal events, showing separately the contribution of the four decay modes. The events are normalized to an integrated luminosity of 1 ab^{-1}.

In order to estimate the expected precision of the $B \to \tau\nu_\tau$ branching fraction measurement, a toy MC study has been performed generating a high-statistics sample of pseudo-experiments. For each experiment, a pseudo-dataset has been generated according to the signal and background MC expectations, and a binned maximum likelihood fit is performed using a two-component parameterized function where the $E_{\rm ECL}$ distributions for signal and background events are taken from simulation. Figure 64(c) shows an illustrative plot of the fit to one pseudo-dataset.

Assuming a branching fraction of 0.82×10^{-4} (December 2016 result from the CKMfitter group [91]), the mean uncertainty is found to be ∼29% with 1 ab^{-1} of equivalent integrated luminosity. A large number of pseudo-experiments have been generated to estimate the expected significance of the branching fraction measurement, according to the following procedure: a likelihood ratio test statistic Q has been defined and evaluated on pseudo-datasets sampled from signal-plus-background (S+B) and background-only $E_{\rm ECL}$ distributions. Then the p-value of the background null hypothesis is evaluated as the ratio between the number of pseudo-experiments which give a value of Q lower than the expected test statistics (for an S+B hypothesis), and the total number of pseudo-experiments. The calculation led to a p-value in the background-only hypothesis of 3.8×10^{-4}, corresponding to a statistical significance of $3.4\,\sigma$.

Systematic uncertainties Based on Belle measurements [234], the main sources of systematic uncertainties are the signal and background $E_{\rm ECL}$ PDFs, the uncertainty on the relative contributions from B decays that peak near zero $E_{\rm ECL}$ (i.e. peaking background), the tagging efficiency, and the $K^0_{\rm L}$ veto efficiency, followed by the minor uncertainties due to the number of $B\bar{B}$ pairs, the signal

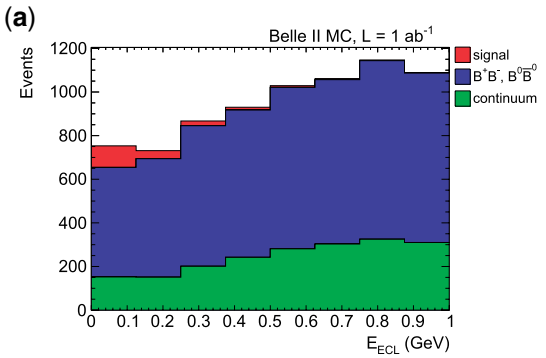

$E_{\rm ECL}$ distribution for signal (red), $B\overline{B}$ background (blue) and continuum (green). The events are normalised to an integrated luminosity of 1 ab^{-1}

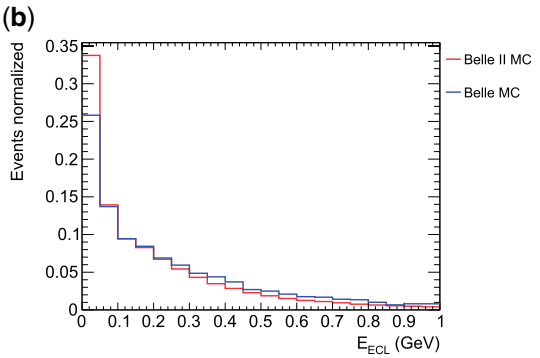

Comparison of signal $E_{\rm ECL}$ distribution for this analysis (red) and the Belle measurement with hadronic tag (blue).

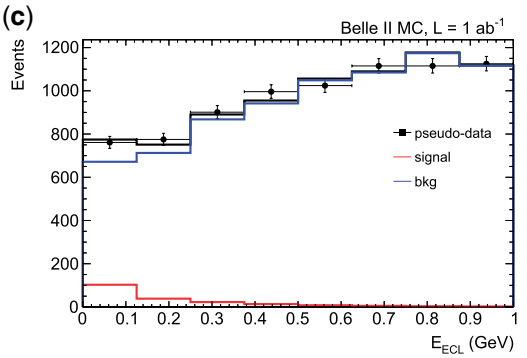

Maximum likelihood fit to pseudo-data $E_{\rm ECL}$ distribution sampled from simulation. The red and blue histograms represent the signal and background fit functions (templates from simulation). The events correspond to an integrated luminosity of 1 ab^{-1}.

Fig. 64. $E_{\rm ECL}$ distributions for signal and background in the analysis of $B \to \tau\nu$.

Table 39. Expected Belle II yields of signal and background events in 1 ab^{-1} for two different $E_{\rm ECL}$ windows, compared to Belle MC.

$E_{\rm ECL}$		< 1 GeV	< 0.25 GeV
Belle II	Background yield	7420	1348
	Signal yield	188	136
	Signal efficiency (10^{-3})	2.2	1.6
Belle	Background yield	2160	365
	Signal yield	97	60
	Signal efficiency (10^{-3})	1.2	0.7

efficiency (PID efficiency, τ branching fractions, π^0 efficiency, and tracking efficiency), and MC sample sizes used for background PDFs.

The uncertainties on PDFs and tagging efficiency are limited by the statistical precision in the $B \to D^{*0}\ell\nu$ control sample on data, and so are expected to scale with luminosity similarly to the statistical uncertainty. The uncertainty due to the modeling of the peaking background components, typically due to an undetected $K^0_{\rm L}$, is estimated by varying the branching fractions of the contributing

Table 40. Yields of expected signal and background events in the $B \to \tau\nu_\tau$ study for two different $E_{\rm ECL}$ windows, with and without beam background, with a dataset of $L = 1\,{\rm ab}^{-1}$.

$E_{\rm ECL}$		< 1 GeV	< 0.25 GeV
Without background	Background yield	12835	2062
	Signal yield	332	238
	Signal efficiency (‰)	3.8	2.7
With background	Background yield	7420	1348
	Signal yield	188	136
	Signal efficiency (‰)	2.2	1.6

decays within the experimental uncertainties. This will be a major concern in Belle II analyses. We expect to reach a systematic uncertainty of better than 3% from this contribution. The uncertainty on the $K^0_{\rm L}$ veto efficiency is obtained from control samples in data, comparing yields of $\phi \to K^0_{\rm L}K^0_{\rm S}$ to $\phi \to K^-K^+$ in a $D^0 \to \phi K^0_{\rm S}$ sample. Such calibrations were found to be very large in Belle, where data and MC efficiencies differed by approximately 40%. The discrepancy is attributable to the inaccuracy in modeling hadronic interactions in the KLM. `GEANT4`, which Belle II will use instead of `GEANT3` as in Belle, may provide more accurate simulation, but given that the calibration is large it may be difficult to improve the systematic uncertainty to better than 2% on the $B \to \tau\nu_\tau$ branching fraction.

The uncertainty on the signal efficiency is expected to scale with luminosity, as in the case of the statistical uncertainty. The uncertainties due to the τ branching fractions ($> 0.6\%$) are not expected to improve substantially. Finally, the uncertainty on the number of $B\bar{B}$ pairs is expected to be limited to about 1%.

The expected systematic uncertainty on the $B \to \tau\nu_\tau$ branching fraction with an integrated luminosity of $1\,{\rm ab}^{-1}$ is calculated to be 13%, based on a scaling of the uncertainties of the Belle measurement with a hadronic tag [234].

Anticipating the results detailed in Table 41, the luminosity needed to reach a $5\,\sigma$ discovery of $B \to \tau\nu_\tau$ including statistic and systematic uncertainties is about $2.6\,{\rm ab}^{-1}$.

Beam background In order to estimate the impact of machine background on the branching fraction measurement, the analysis is repeated on an MC5 Belle II production where no machine background is superimposed on physics events. Continuum background suppression and the signal-side selection have been reoptimized for this configuration and the statistical evaluation with toy MC is performed as above. The results are shown in Table 40, compared to the case including the expected machine background, and in Fig. 65. The higher selection efficiency in the absence of beam background is due to higher B tag reconstruction efficiency (see Fig. 66) and that, in order to maximize the FOM, a looser selection is applied on the signal side. It may also be due to a greater abundance of fake tracks in the presence of beam background, which must be further studied at Belle II. For a more general discussion of the FEI tagging performance, refer to Sect. 6.6. The mean uncertainty on the $B \to \tau\nu_\tau$ branching fraction is found to be $\sim$20% with $1\,{\rm ab}^{-1}$ of equivalent integrated luminosity, corresponding to a statistical significance of approximately $5\,\sigma$.

Summary Table 41 summarizes the results and projections of the uncertainties on the branching fraction measurement with 1, 5, and $50\,{\rm ab}^{-1}$ datasets, using hadronic and semi-leptonic tagging

Table 41. Expected uncertainties on the $B \to \tau \nu_\tau$ branching fraction for different luminosity scenarios with hadronic and semi-leptonic tag methods.

	Integrated luminosity (ab^{-1})	1	5	50
Hadronic tag	Statistical uncertainty (%)	29	13	4
	Systematic uncertainty (%)	13	7	5
	Total uncertainty (%)	32	15	6
Semileptonic tag	Statistical uncertainty (%)	19	8	3
	Systematic uncertainty (%)	18	9	5
	Total uncertainty (%)	26	12	5

Table 42. The results of searches for the decay $B \to \mu \nu_\mu$.

Experiment	Upper limit (90% CL)	Comment
Belle [241]	2.7×10^{-6}	Fully reconstructed hadronic tag, 711 fb^{-1}
Belle [242]	1.1×10^{-6}	Untagged analysis, 711 fb^{-1}
BaBar [238]	1.0×10^{-6}	Untagged analysis, 468×10^6 $B\bar{B}$ pairs

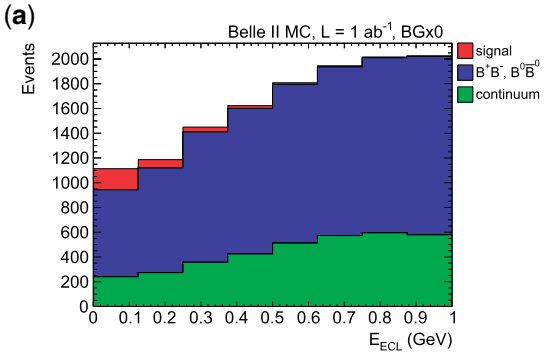

$E_{\rm ECL}$ distribution for signal (red), $B\overline{B}$ background (blue) and continuum (green) events.

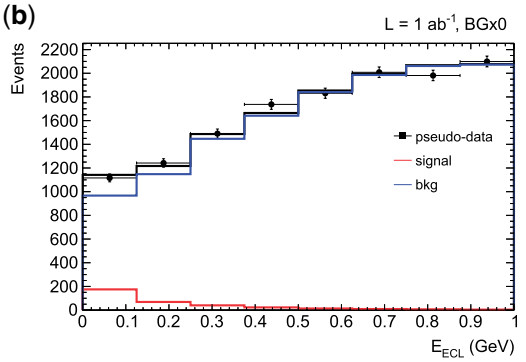

Maximum likelihood fit to pseudo-data $E_{\rm ECL}$ distribution sampled from simulation. The red and blue histograms represent the signal and background fit functions.

Fig. 65. $E_{\rm ECL}$ distributions for the $B \to \tau \nu_\tau$ study without machine background. The events correspond to an integrated luminosity of 1 ab^{-1}.

respectively. These approaches are statistically independent. The projections of measurements using semi-leptonic tags are based entirely on Belle measurements [240], since no dedicated studies have been performed with Belle II simulation.

8.3.2. $B \to \mu \nu_\mu$

There have been several searches for the $B \to \mu \nu_\mu$ decay to date; the most recent ones [238,241,242] are summarized in Table 42. The most stringent limits to date are set by untagged searches.

Table 43 shows the expected branching fractions and event yields in the full Belle dataset as well as expected Belle II milestones using the value of $|V_{ub}| \times 10^3 = 3.55 \pm 0.12$ from the 2016 HFLAV report [230] and $f_B = 186 \pm 4$ MeV from Ref. [217], which is the only entry in the 2016 FLAG average [140].[22] The process $B^\pm \to \mu^\pm \nu_\mu$ may be observed with $3\,\sigma$ significance with around

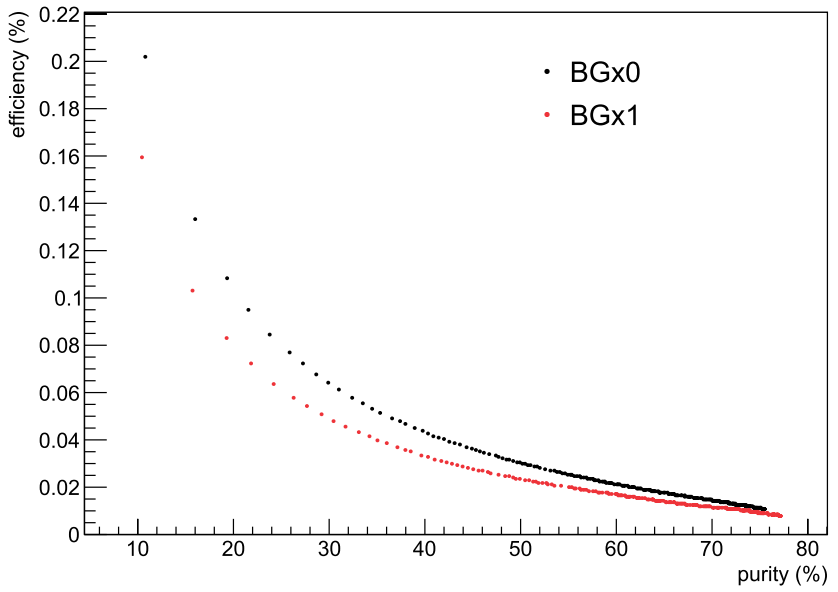

Fig. 66. B tag ROC curves with (BGx1) and without (BGx0) nominal beam background in the $B \to \tau \nu_\tau$ study. The points correspond to a scan of the FEI discriminant output. The efficiency is evaluated as the ratio between the B tag reconstructed candidates (i.e. passing the FEI discriminant cut) and the total generated candidates, and the purity as the ratio between the correctly reconstructed B tags and the total reconstructed candidates. The curves are evaluated on B^+B^- events requiring the presence of only one track and PID quality criteria on the signal side.

Table 43. The branching fractions for leptonic B decays in the SM calculations, and the respective event yields with the full Belle data sample and the expected Belle II datasets.

ℓ	$\mathcal{B}_{\rm SM}$	711 fb^{-1}	5 ab^{-1}	50 ab^{-1}
τ	$(7.71 \pm 0.62) \times 10^{-5}$	$61\,200 \pm 5000$	$430\,000 \pm 35\,000$	$4\,300\,000 \pm 350\,000$
μ	$(3.46 \pm 0.28) \times 10^{-7}$	275 ± 23	1930 ± 160	$19\,300 \pm 1600$
e	$(0.811 \pm 0.065) \times 10^{-11}$	0.0064 ± 0.0005	0.0453 ± 0.0037	0.453 ± 0.037

2 ab^{-1}, whereas the $B^\pm \to e^\pm \nu_e$ process is not measurable even with the Belle II dataset, and only an upper limit is expected for SM-like scenarios.

The clean environment of an e^+e^- machine, where only one $B\bar{B}$ pair is expected in an event, allows for two main search approaches: *untagged* and *full reconstruction*. The latter leads to very good purity at the cost of very low efficiency. In the untagged analysis the products of the signal decay are selected first and the rest of the event (RoE) is used to build various shape parameters that discriminate B meson decays from other hadronic modes. The efficiency of the untagged method can be rather high.

A 2014 Belle study [241] searched for the $B \to \mu \nu_\mu$ process using one fully reconstructed B meson as a tag. In the signal B meson rest frame the momentum of the μ is monochromatic due to two-body decay kinematics, with good momentum resolution of $\sim$14 MeV/c that separates the signal from other B decays. This analysis demonstrated the drawback of the method: extremely low signal selection efficiency of $\sim 10^{-3}$ which leads to the result shown in Table 42, and only $\sim$21 signal events with the full Belle II integrated luminosity are expected.

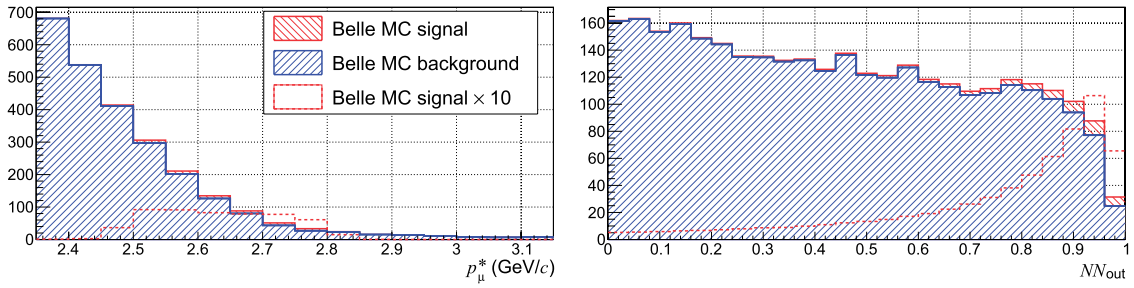

Fig. 67. The distributions of the muon momentum p^*_μ in the center of mass and the neural net output variable $NN_{\rm out}$ in the signal-enhanced region $2.6\,{\rm GeV}/c < p^*_\mu < 2.85\,{\rm GeV}/c$, and $NN_{\rm out} > 0.84$, respectively, based on Belle MC and equivalent to the full Belle dataset of 711 fb^{-1}.

The most recent untagged analysis of $B \to \mu\nu_\mu$ with Belle data has much higher signal selection efficiency of 39% but suffers from much higher background. It can be used to anticipate results with the Belle II dataset. To separate signal from background events a simple neural network has been developed and trained using various event kinematic parameters. The projections of the muon momentum p^*_μ in the center-of-mass frame and the neural net output variable for the full Belle dataset in the signal-enhanced region are shown in Fig. 67. For $2.6\,{\rm GeV}/c < p^*_\mu < 2.85\,{\rm GeV}/c$ and $NN_{\rm out} > 0.84$ the figure of merit is ${\rm FOM}_{\rm Belle} = N_{\rm sig}/\sqrt{N_{\rm sig}+N_{\rm bkg}} = 31.5/\sqrt{31.5+300} \approx 1.73$ and can be scaled to the full Belle II expected dataset as ${\rm FOM}_{\rm BelleII} = {\rm FOM}_{\rm Belle} \times \sqrt{50\,{\rm ab}^{-1}/0.711\,{\rm ab}^{-1}} \approx 14.5$. We therefore expect approximately 7% statistical precision on the branching fraction. Naively, to reach $5\,\sigma$ significance Belle II should collect approximately $6\,{\rm ab}^{-1}$. With a much larger dataset at Belle II, the systematic uncertainties will be as good as or better than the statistical uncertainty in this channel.

8.3.3. Sensitivity to new physics

In the following, we will consider the scenario that new physics only measurably affects the tau mode, that is, $r^\mu_{\rm NP} = r^e_{\rm NP} = 0$. The dominant sources of theoretical uncertainty in $B^+ \to \ell^+\nu_\ell$ are f_B and $|V_{ub}|$; therefore, to mitigate them we can form ratios to light leptonic modes defined as

$$R_{\rm ps} = \frac{\tau_{B^0}}{\tau_{B^+}} \frac{\mathcal{B}(B^+ \to \tau^+\nu_\tau)}{\mathcal{B}(B^0 \to \pi^-\ell^+\nu_\ell)}, \qquad R_{\rm pl} = \frac{\mathcal{B}(B^+ \to \tau^+\nu_\tau)}{\mathcal{B}(B^+ \to \mu^+\nu_\mu)}. \tag{124}$$

Experimentally, $R_{\rm ps}$ has the advantage that $B^0 \to \pi^-\ell^+\nu_\ell$ is experimentally well known, whereas $R_{\rm pl}$ is not yet measured. On the theoretical side, $R_{\rm ps}$ contains theoretical uncertainties from f_B/f_+, while $R_{\rm pl}$ has a very precise theoretical prediction in the SM.

Predictions for these ratios are calculated in Ref. [243] and are as follows:

$$R^{\rm NP}_{\rm ps} = (0.539 \pm 0.043)\left|1 + r^\tau_{\rm NP}\right|^2, \tag{125}$$

$$R^{\rm NP}_{\rm pl} = \frac{m_\tau^2}{m_\mu^2} \frac{(1 - m_\tau^2/m_B^2)^2}{(1 - m_\mu^2/m_B^2)^2}\left|1 + r^\tau_{\rm NP}\right|^2 \simeq 222.37\left|1 + r^\tau_{\rm NP}\right|^2. \tag{126}$$

The current experimental constraints on $B^+ \to \tau^+\nu_\tau$ [77] and $B^0 \to \pi^-\ell^+\nu_\ell$ [230] result in $R^{\rm exp}_{\rm ps} = 0.73 \pm 0.14$. This is compared with Eq. (125) to find the following constraint on $r^\tau_{\rm NP}$:

$$\left|1 + r^\tau_{\rm NP}\right| = 1.16 \pm 0.11. \tag{127}$$

Table 44. Expected 95% CL limits on $r^{\tau}_{\rm NP}$ from $R_{\rm ps}$ and $R_{\rm pl}$ at Belle II with 5 ab^{-1} and 50 ab^{-1} of accumulated data. The new physics contribution is assumed to be real and no larger than the SM contribution ($|r^{\tau}_{\rm NP}| < 1$).

Luminosity	$R_{\rm ps}$	$R_{\rm pl}$
5 ab^{-1}	$[-0.22, 0.20]$	$[-0.42, 0.29]$
50 ab^{-1}	$[-0.11, 0.12]$	$[-0.12, 0.11]$

We find that $R_{\rm ps}$ provides a slightly tighter bound than the direct branching fraction measurement. The present experimental uncertainty in $R^{\rm exp}_{\rm ps}$ of 0.14 is expected to improve substantially, as discussed in Sect. 8.3.1. The purely muonic mode has only upper limits on $\mathcal{B}(B^+ \to \mu^+\nu_\mu)$. The upper limit is approaching the SM prediction, and we expect that the muonic mode will be precisely measured at Belle II. Therefore, $R_{\rm pl}$ may also play an important role for new physics searches in $B^+ \to \tau^+\nu_\tau$. The following study discusses the future sensitivities of $R_{\rm ps}$ and $R_{\rm pl}$ to new physics contributions, $r^{\tau}_{\rm NP}$, with 5 ab^{-1} and 50 ab^{-1} of Belle II data.

To determine the sensitivity to new physics through $r^{\tau}_{\rm NP}$, we assume that experimental central values of the ratios are at the SM expectation and that the new physics contributions are no greater than the SM contributions ($|r^{\tau}_{\rm NP}| < 1$) unless otherwise stated. The expected experimental errors on $R_{\rm ps}$ and $R_{\rm pl}$ are then determined by taking the Belle II estimates of $B \to \tau\nu_\tau$, $B \to \mu\nu_\mu$, and $B \to \pi\ell\nu_\ell$ with luminosities of 5 ab^{-1} and 50 ab^{-1}:

$$R^{5\,{\rm ab}^{-1}}_{\rm ps} = 0.54 \pm 0.11, \qquad R^{50\,{\rm ab}^{-1}}_{\rm ps} = 0.54 \pm 0.04, \tag{128}$$

$$R^{5\,{\rm ab}^{-1}}_{\rm pl} = 222 \pm 76, \qquad R^{50\,{\rm ab}^{-1}}_{\rm pl} = 222 \pm 26. \tag{129}$$

With the use of the above expected constraints, the 95% CL expected limits on $r^{\tau}_{\rm NP}$ are given in Table 44. A new physics contribution to $B \to \tau\nu_\tau$ with $r^{\tau}_{\rm NP} \gtrsim O(0.1)$ can be tested at 95% CL. The observable $R_{\rm pl}$ has low sensitivity at 5 ab^{-1}, but with 50 ab^{-1} it will be comparable with $R_{\rm ps}$. Further improvements in the sensitivity of $R_{\rm pl}$ may be achieved through more direct measurements.

8.4. Radiative leptonic

8.4.1. $B^+ \to \ell^+\nu_\ell\gamma$

Authors: F. Metzner, M. Gelb, P. Goldenzweig (Exp.)

The radiative leptonic decay $B^+ \to \ell^+\nu_\ell\gamma$ yields important information for the theoretical predictions of non-leptonic B meson decays into light meson pairs. The emission of the photon probes the first inverse moment λ_B of the light-cone distribution amplitude (LCDA) of the B meson. This parameter is a vital input to QCD factorization schemes for the non-perturbative calculation of non-leptonic B meson decays [244,245] (see Sect. 12.3.2). The importance of $B^+ \to \ell^+\nu_\ell\gamma$ decays in the empirical determination of the parameter λ_B can be found in Refs. [223,246], where detailed theoretical calculations of the decay are presented.

The partial branching ratio $\Delta\mathcal{B}$ is given by the integral of the differential decay width over the photon energies relevant for the considered selection, multiplied by the lifetime of the B meson τ_B:

$$\Delta\mathcal{B}(B^+ \to \ell^+\nu_\ell\gamma) = \tau_B \int_{\rm Selection} dE_\gamma \, \frac{d\Gamma}{dE_\gamma}, \tag{130}$$

where photon energies below 1 GeV are considered as unsafe since the factorization approach for the calculation of the form factors requires the condition $2E_\gamma \sim m_b$. Thus, only photons with energies

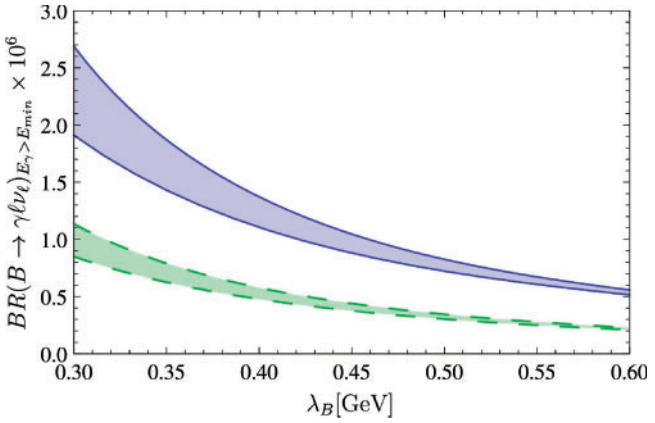

Fig. 68. Dependence of the theoretical prediction for the partial branching fraction $\Delta\mathcal{B}(B^+ \to \ell^+\nu_\ell\gamma)$ on the value of the QCD factorization parameter λ_B for two signal photon selection criteria: the threshold with lower theoretical uncertainties $E_\gamma > 1.7$ GeV (lower, dashed), and the threshold $E_\gamma > 1.0$ GeV which yields a significantly higher efficiency [246].

Table 45. Expected signal yields determined with Belle MC for the new analysis using the signal-specific FEI in `basf2` (N_{New}). The values are compared to the expected yields in the published Belle analysis ($N_{\text{Published}}$) [247]. Both MC studies assume a partial branching fraction of $\Delta\mathcal{B}(B^+ \to \ell^+\nu_\ell\gamma) = 5.0 \times 10^{-6}$, to enable a comparison of the expected yields with the different analysis frameworks.

	$B^+ \to e^+\nu_e\gamma$	$B^+ \to \mu^+\nu_\mu\gamma$	Combined
N_{New}	24.8	25.7	50.5
$N_{\text{Published}}$	8.0	8.7	16.5

above this threshold were considered in the most recent Belle analysis [247]. The theoretical relation between the value of λ_B and the respective partial branching ratio for two selection criteria for the signal photon energy is shown in Fig. 68.

Belle obtained limits of $\Delta\mathcal{B}(B^+ \to \ell^+\nu_\ell\gamma) < 3.5 \times 10^{-6}$ and $\lambda_B > 238$ MeV (90% CL) for photons above 1 GeV with the full $\Upsilon(4S)$ dataset of 711 fb^{-1} [247] (see Ref. [248] for an updated Belle result). In preparation for Belle II, a new analysis has been prepared with Belle MC in the `basf2` framework, where the signal-specific FEI is employed (Sect. 6.6). To enable a comparison of the two analysis methods, the expected yield (determined from MC with a partial branching fraction of $\Delta\mathcal{B}(B^+ \to \ell^+\nu_\ell\gamma) = 5.0 \times 10^{-6}$) for both methods is displayed in Table 45. The new tagging algorithm results in three times the expected signal yield with the same dataset. The yield is extracted from a simultaneous fit to the squared missing mass distributions of the electron and muon channels. The results for the improved analysis are shown in Fig. 69.

Further constraints on the energy of the neutrino would enable the experimental examination of the difference between the axial and vector form factor, and thus the impact of the power-suppressed contributions to the decay width [223]. However, the selection required for this study—the neutrino has to receive the majority of the B meson's energy—reduces the statistics significantly, rendering it unfeasible with the Belle dataset. However, with the large Belle II dataset, this aspect of the decay will also be addressed.

In addition, a toy MC study is used to estimate the expected statistical error with 5 ab^{-1} and 50 ab^{-1} of Belle II data. The statistical errors are expected to be significantly reduced with the increased dataset. The results can be found in Table 46.

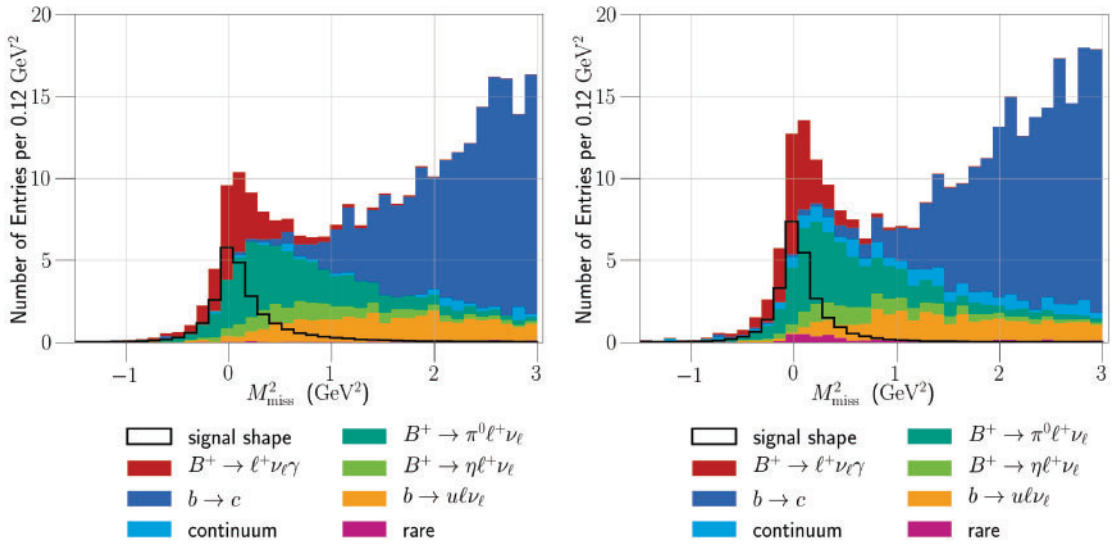

Fig. 69. The Belle MC squared missing mass distribution for $B^+ \to e^+\nu_e\gamma$ (left) and $B^+ \to \mu^+\nu_\mu\gamma$ (right) of the new analysis using the signal-specific FEI in `basf2`. The signal yield ($N_{\rm New}$) is reported in Table 45.

Table 46. Expected statistical error in 10^{-6} for Belle and Belle II for a simulated partial branching fraction of $\Delta\mathcal{B}(B^+ \to \ell^+\nu_\ell\gamma) = 5.0 \times 10^{-6}$.

Belle new analysis	Belle II 5 ab^{-1}	Belle II 50 ab^{-1}
$+1.48$	$+0.56$	$+0.18$
-1.39	-0.53	-0.17

8.5. Semi-tauonic decays

8.5.1. $B \to D^{(*)}\tau\nu$

Authors: S. Hirose, Y. Sato (exp.), M. Tanaka (th.), R. Watanabe (th.)

The decays $B \to D^{(*)}\tau\nu$ are described at the quark level as $b \to c\tau\nu$ tree-level transitions that proceed in the SM through the exchange of a virtual W boson. The ratios, defined as

$$R_{D^{(*)}} = \frac{\mathrm{Br}(B \to D^{(*)}\tau\nu_\tau)}{\mathrm{Br}(B \to D^{(*)}\ell\nu_\ell)}, \tag{131}$$

are useful observables to test for new physics as theoretical uncertainties in form factors and $|V_{cb}|$ largely cancel out. First measured by Belle [249], these ratios have since been more precisely measured by BaBar [250], Belle [251], and LHCb [252]. The combination of these measurements shows a tendency towards larger values than SM expectation with a deviation of nearly $4\,\sigma$. A better understanding of these anomalous results is a high priority at Belle II, because the discrepancy could be due to NP contributions. In addition to $R(D^{(*)})$, measurements of the polarizations of the τ lepton and the D^* meson respectively are also good probes for the NP. They are defined by

$$P_\tau(D^{(*)}) = \frac{\Gamma^+ - \Gamma^-}{\Gamma^+ + \Gamma^-}, \tag{132}$$

$$P_{D^*} = \frac{\Gamma_{\rm L}}{\Gamma_{\rm L} + \Gamma_{\rm T}}, \tag{133}$$

where $\Gamma^{+(-)}$ and $\Gamma_{\rm L(T)}$ are the decay rate with the τ helicity $+1/2$ $(-1/2)$ and that with the longitudinally (transversely) polarized D^*, respectively. In the future, Belle II should also be able to perform precise differential measurements in q^2, and will measure the decay angles, θ_ℓ, θ_V, χ, as was done for $B \to D^{(*)}\ell\nu$ decays at Belle and BaBar (see Sect. 8.6.1). It will be challenging to reconstruct θ_ℓ and χ in the τ channels due to the presence of at least two neutrinos, but there will be some experimental sensitivity.

SM predictions Processes of the type $B \to D^{(*)}\tau\nu$ have a rich phenomenology that can be used to probe the nature of any NP contributions. For example, differential distributions, such as the momentum transfer to the lepton pair $q^2 = (p_\tau + p_\nu)^2 = (p_B - p_{D^{(*)}})^2$ can be modified in the presence of a charged Higgs. Form factors of $B \to D^{(*)}$ transitions and the CKM matrix element magnitude $|V_{cb}|$ are extracted through measurements of $B \to D^{(*)}\ell\nu$ for $\ell = e, \mu$. The differential decay rates are described in Sects. 8.2.2 and 8.2.3, and the form factors $f_+(q^2)$ for $B \to D$ and $V(q^2)$, $A_i(q^2)$ for $B \to D^*$ can be determined from experimental data combined with results from lattice QCD. (For notation, see Eqs. (91), (106), and (107).) The differential decay rates of $B \to D^{(*)}\tau\nu$ decays contain additional form factors, $f_0(q^2)$ and $A_0(q^2)$, from terms proportional to m_τ^2. These additional form factors can also be computed with lattice QCD. At present there are lattice QCD results for $f_+(q^2)$ and $f_0(q^2)$ [145,146], while calculations of the q^2 dependence of the $B \to D^*$ form factors are underway [253].

Various SM predictions for $R_D^{(*)}$ have been calculated [145,146,250,254–261]. In addition to the lattice QCD study, heavy quark effective theory (HQET) and QCD sum rules have been applied to evaluate the form factors. For example, in Refs. [259,261] theoretical inputs from lattice and QCD sum rules are combined to be fitted to the experimental data of $B \to D^{(*)}\ell\nu$, up to $\mathcal{O}(\Lambda_{\rm QCD}/M_Q)$ and $\mathcal{O}(\alpha_s)$ corrections to the form factors in HQET (a higher-order contribution of $\mathcal{O}(\Lambda_{\rm QCD}^2/M_Q^2)$ could be important [262]). Another approach, based on the Boyd–Grinstein–Lebed parameterization [258, 260], has also been considered. Taking into account all recent SM predictions, HFLAV presently (2018 value) quotes:

$$R_D^{\rm SM} = 0.299 \pm 0.003, \tag{134}$$

$$R_{D^*}^{\rm SM} = 0.258 \pm 0.005. \tag{135}$$

At present, the τ and D^* polarizations have been estimated in the SM as follows: $P_\tau(D) = 0.34 \pm 0.03$ [263] (0.325 ± 0.009 [255]), $P_\tau(D^*) = -0.47 \pm 0.04$ [260] (-0.497 ± 0.013 [264]), and $P_{D^*} = 0.46 \pm 0.04$ [265], where the values in parentheses are older estimations with only the leading-order contributions of the HQET expansion.

Experimental data The strategy of $R_{D^{(*)}}$ measurements is to evaluate the ratio of the efficiency-corrected yields of $B \to D^{(*)}\tau\nu_\tau$ and $B \to D^{(*)}\ell\nu_\ell$ events. The experimental approach for measuring $B \to D^{(*)}\tau\nu_\tau$ decays is similar to that used for $B \to \tau\nu_\tau$, owing to the presence of two or more neutrinos in the final state. Three different methods are used: hadronic tag, semi-leptonic tag, and untagged (or inclusive tag). The experimental methods in the B factory experiments are summarized in Table 47.

Table 47. Summary of experimental measurements of semi-tauonic B decays.

Experiment	Tag method	τ^- decays	Observables	Fit variables
Belle [249]	Untagged	$e^-\nu_\tau\bar{\nu}_e, \pi\nu_\tau$	$\mathcal{B}(\bar{B}^0 \to D^{*+}\tau^-\bar{\nu}_\tau)$	$M_{\rm bc}^{\rm tag}$
Belle [266]	Untagged	$\ell^-\nu_\tau\bar{\nu}_\ell, \pi\nu_\tau$	$\mathcal{B}(B^- \to D^{(*)0}\tau^-\bar{\nu}_\tau)$	$M_{\rm bc}^{\rm tag}$ and p_{D^0}
Belle [251]	Hadronic	$\ell^-\nu_\tau\bar{\nu}_\ell$	R_D, R_{D^*}, q^2, $\lvert p_\ell^*\rvert$	$M_{\rm miss}^2$ and $\mathcal{O}_{NB}$
Belle [267]	Semi-leptonic	$\ell^-\nu_\tau\bar{\nu}_\ell$	R_{D^*}, $\lvert p_\ell^*\rvert$ $\lvert p_{D^*}^*\rvert$	$E_{\rm ECL}$ and $\mathcal{O}_{NB}$
Belle [268]	Hadronic	$h^-\nu_\tau$	R_{D^*}, $P_\tau(D^*)$	$E_{\rm ECL}$ and $\cos\theta_{\rm hel}$
Belle [269]	Semi-leptonic	$\ell^-\nu_\tau\bar{\nu}_\ell$	R_D, R_{D^*}	$E_{\rm ECL}$ and $\mathcal{O}_{BDT}$
BaBar [250,270]	Hadronic	$\ell^-\nu_\tau\bar{\nu}_\ell$	R_D, R_{D^*}, q^2	$M_{\rm miss}^2$ and p_ℓ
LHCb [252]	—	$\ell^-\nu_\tau\bar{\nu}_\ell$	E_μ^*, $m_{\rm miss}^2$, q^2	
LHCb [271]	—	$h^-h^+h^-\nu_\tau$	q^2, t_τ, $\mathcal{O}_B DT$	

In the untagged method, the most important variable to extract signal events is the beam-energy-constrained mass of the tag B meson, $M_{\rm bc}^{\rm tag}$. In the Belle analysis of $B \to D^{(*)}\tau\nu_\tau$ with a hadronic tag, the most important variables are related to the missing momentum such as $M_{\rm miss}^2$ and the extra energy in the calorimeter, $E_{\rm ECL}$. The $M_{\rm miss}^2$ distribution is used to separate $B \to D^{(*)}\tau\nu_\tau$ signals from $B \to D^{(*)}\ell\nu_\ell$. In the higher $M_{\rm miss}^2$ region, where most of the $B \to D^{(*)}\tau\nu_\tau$ signal is present, a fit to a multivariate classifier is performed, based on several input variables such as $E_{\rm ECL}$ and the lepton momentum, p_ℓ. In the BaBar analysis, p_ℓ is used for the fit as well as $M_{\rm miss}^2$; $E_{\rm ECL}$ is used only for background suppression prior to the final fit.

In the analyses with a semi-leptonic tag, $E_{\rm ECL}$ is used to separate $B^0 \to D^*\tau\nu_\tau$ and $B^0 \to D^*\ell\nu_\ell$ from other background, and a multivariate classifier is formed using the signal-side $\cos\theta_{B-D^*\ell}$, $m_{\rm miss}^2$, and $E_{\rm visible}$. Ultimately, two-dimensional binned fit approaches are used to determine the signal yields of the signal and normalization modes.

In the above analyses, leptonic τ decay modes were chosen to achieve better background rejection. The most important background in these studies originates from $B \to D^{**}\ell\nu_\ell$, where the D^{**} mesons are excited charmed mesons higher than the $D^*(2010)$. If we fail to reconstruct particles (mainly π^0s) from D^{**} in the $B \to D^{**}\ell\nu_\ell$ decay, such events can mimic the signal, and so the identification of $B \to D^{**}\ell\nu_\ell$ background is critical. We have limited knowledge of the branching fractions to $B \to D^{**}\ell\nu_\ell$ and the D^{**} decay itself, which needs to be addressed at Belle II.

In the most recently published Belle analysis of $B \to D^*\tau\nu_\tau$ [272], hadronic τ decay modes ($\tau^- \to h^-\nu_\tau$ $h^- = \pi^-$, ρ^-) have been used, which are statistically independent from the other measurements and can be determined with useful precision. The main background originates from hadronic B decays, $B \to D^*\pi^+X$, where X consists of one or more unreconstructed π^0, η, γ, or pairs of charged particles. Large uncertainties in the branching fractions of the exclusive hadronic B decay modes may introduce a sizeable systematic uncertainty. Nevertheless, it is advantageous that $B \to D^*\tau\nu_\tau$ is measured with a different composition of systematic uncertainties with respect to all other measurements using $\tau^- \to \ell^-\bar{\nu}_\ell\nu_\tau$. To extract the signal yields, a similar approach to the previous hadronic tag analysis with $\tau^- \to \ell^-\bar{\nu}_\ell\nu_\tau$ has been employed; $M_{\rm miss}^2$ and $E_{\rm ECL}$ are used for the determination of the $B \to D^*\ell\nu_\ell$ and $B \to D^*\tau\nu_\tau$ yields, respectively. Another advantage of this analysis is the capability to measure $P_\tau(D^*)$ using the kinematics of two-body τ decays. $P_\tau(D^*)$ is measured using the distribution of $\cos\theta_{\rm hel}$, the cosine of the angle between the momentum of the τ-daughter meson and the direction opposite the momentum of the $\tau\nu_\tau$ system.

Table 48. Results of $R_{D^{(*)}}$ measurements by BaBar, Belle, and LHCb. The correlation column lists the linear R_D–R_{D^*} statistical, systematic, and total correlations respectively. The averages are taken from the 2018 HFLAV combination [230]. The analysis method and the τ decay are indicated: Had for the hadronic tag, SL for the semi-leptonic tag, ℓ^- for $\tau^- \to \ell^- \bar{\nu}_\ell \nu_\tau$, and h^- for $\tau^- \to h^- \nu_\tau$.

	R_D	R_{D^*}	Correlation
BaBar (Had, ℓ^-)	$0.440 \pm 0.058 \pm 0.042$	$0.332 \pm 0.024 \pm 0.018$	$-0.45/-0.07/-0.27$
Belle (Had, ℓ^-)	$0.375 \pm 0.064 \pm 0.026$	$0.293 \pm 0.038 \pm 0.015$	$-0.56/-0.11/-0.49$
Belle (SL, ℓ^-)	$0.307 \pm 0.037 \pm 0.016$	$0.283 \pm 0.018 \pm 0.014$	$-0.53/-0.51/-0.51$
LHCb (ℓ^-)	N/A	$0.336 \pm 0.027 \pm 0.030$	N/A
LHCb (h^-)	N/A	$0.291 \pm 0.019 \pm 0.029$	N/A
Belle (Had, h^-)	N/A	$0.270 \pm 0.035^{+0.028}_{-0.025}$	N/A
Average	$0.340 \pm 0.027 \pm 0.013$	$0.295 \pm 0.011 \pm 0.008$	-0.38
		$P_\tau(D^*)$	
Belle (Had, h^-)		$-0.38 \pm 0.51^{+0.21}_{-0.16}$	

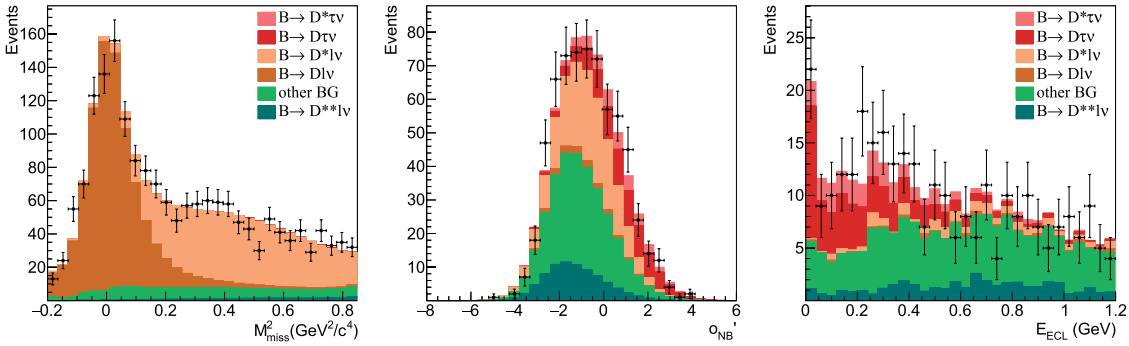

Fig. 70. Fit projections and data points with statistical uncertainties for the $B \to D\tau\nu_\tau$ mode in the Belle hadronic tag analysis with $\tau^- \to \ell^- \bar{\nu}_\ell \nu_\tau$ [251]. The left, center, and right panels show the distributions of $M^2_{\rm miss}$, $\mathcal{O}'_{NB}$ ($M^2_{\rm miss} > 0.85\,{\rm GeV}^2/c^4$) and $E_{\rm ECL}$ ($M^2_{\rm miss} > 2.0\,{\rm GeV}^2/c^4$), respectively.

The current experimental results for R_D, R_{D^*}, and $P_\tau(D^*)$ are summarized in Table 48. Typical figures for the $B \to D\tau\nu_\tau$ mode in the hadronic tag analysis with $\tau^- \to \ell^- \bar{\nu}_\ell \nu_\tau$ are shown in Fig. 70. In addition to Belle and BaBar, LHCb has also demonstrated its capability to measure R_{D^*} at the Large Hadron Collider. The world-average $R_{D^{(*)}}$ shows about $4\,\sigma$ deviation from the SM predictions. The result of $P_\tau(D^*)$ is consistent with the SM prediction and excludes $P_\tau(D^*) > +0.5$ at 90% confidence level. NP effects can be thoroughly probed in kinematic distributions as well as the total branching fraction. So far, only the measured q^2 spectrum and the momenta of the D^* and the charged lepton have been compared to NP scenarios. The spectra are generally consistent with SM predictions, although they are highly statistics limited at this stage.

Table 49 shows the composition of the systematic uncertainties in each recent Belle measurement of $R_{D^{(*)}}$. Currently, the dominant source of systematic uncertainty is the limited MC sample size, which affects the estimations of reconstruction efficiency, the understanding of the cross-feed components, and the description of the PDFs used in the fit. These uncertainties are clearly reducible using larger MC sample sizes.

Apart from MC sample size, a significant systematic uncertainty arises from branching fractions of the decays of $B \to D^{**}\ell\nu_\ell$ and D^{**} for the analyses with $\tau^- \to \ell^- \bar{\nu}_\ell \nu_\tau$, and hadronic B decays for the analysis with $\tau^- \to h^- \nu_\tau$. Belle and BaBar take different approaches to determine the yields

Table 49. Composition of the systematic uncertainty in each Belle analysis. Relative uncertainties in percent are shown. The analysis method and the τ decay mode are indicated in parentheses; their meaning is explained in the caption of Table 48.

Source	Belle (Had, ℓ^-) R_D	Belle (Had, ℓ^-) R_{D^*}	Belle (SL, ℓ^-) R_{D^*}	Belle (Had, h^-) R_{D^*}
MC statistics	4.4%	3.6%	2.5%	$^{+4.0}_{-2.9}$%
$B \to D^{**}\ell\nu_\ell$	4.4%	3.4%	$^{+1.0}_{-1.7}$%	2.3%
Hadronic B	0.1%	0.1%	1.1%	$^{+7.3}_{-6.5}$%
Other sources	3.4%	1.6%	$^{+1.8}_{-1.4}$%	5.0%
Total	7.1%	5.2%	$^{+3.4}_{-3.5}$%	$^{+10.0}_{-9.0}$%

of $B \to D^{**}\ell\nu_\ell$. In the BaBar analysis, the yield of the $B \to D^{**}\ell\nu_\ell$ background is constrained with control samples in which an additional neutral pion is required with respect to the nominal event selection. This approach assumed that the D^{**} branching ratio is saturated by $D^{**} \to D^{(*)}\pi$ modes (i.e. single pion transitions), which is not the case and may have caused some bias, although a corresponding systematic uncertainty was applied. On the other hand, in the Belle analyses the yield of the $B \to D^{**}\ell\nu_\ell$ background, where D^{**} decays to a variety of allowed modes, is floated in the fit for the signal sample. For precision measurements at Belle II, dedicated measurements of $B \to D^{**}\ell\nu_\ell$ and hadronic B decays with a large data sample are essential. Other non-negligible systematic uncertainties arise from the form factors of $B \to D^{(*)}\ell/\tau\nu$ decays, background from $B \to X_c D^{(*)}$, and large cross-feed from $B \to D^*\ell/\tau\nu$ to $B \to D\ell/\tau\nu$. Ultimately, Belle II must also constrain $B \to D^{**}\tau\nu_\tau$ through dedicated measurements.

Theoretical interpretation: model independent In the presence of NP, semi-tauonic ($B \to D^{(*)}\tau\nu_\tau$) decays can be described by the most general effective Lagrangian of $b \to c\tau\bar{\nu}$:

$$-\mathcal{L}_{\text{eff}} = 2\sqrt{2}G_F V_{cb}\big[(1+C_{V_1})\mathcal{O}_{V_1} + C_{V_2}\mathcal{O}_{V_2} + C_{S_1}\mathcal{O}_{S_1} + C_{S_2}\mathcal{O}_{S_2} + C_T\mathcal{O}_T\big], \tag{136}$$

where the four-fermion operators are defined as

$$\mathcal{O}_{V_1} = \bar{c}_L\gamma^\mu b_L\,\bar{\tau}_L\gamma_\mu\nu_L, \tag{137}$$

$$\mathcal{O}_{V_2} = \bar{c}_R\gamma^\mu b_R\,\bar{\tau}_L\gamma_\mu\nu_L, \tag{138}$$

$$\mathcal{O}_{S_1} = \bar{c}_L b_R\,\bar{\tau}_R\nu_L, \tag{139}$$

$$\mathcal{O}_{S_2} = \bar{c}_R b_L\,\bar{\tau}_R\nu_L, \tag{140}$$

$$\mathcal{O}_T = \bar{c}_R\sigma^{\mu\nu}b_L\,\bar{\tau}_R\sigma_{\mu\nu}\nu_L, \tag{141}$$

and the C_X terms ($X = V_{1,2}, S_{1,2}, T$) denote the Wilson coefficients of the operators, $\mathcal{O}_X$, which represent possible NP contributions. The SM condition requires that $C_X = 0$ for all X types.

Here we will consider NP scenarios where only one C_X at a time is non-zero. In addition, two scenarios of non-vanishing $C_{S_2} = \pm 7.8 C_T$, predicted by the S_1^{LQ} or R_2^{LQ} leptoquark model [225,273], are considered. The BaBar study in Ref. [250] showed that the anomalous values of the ratios are unlikely to be explained by a type II 2HDM charged Higgs, corresponding to the S_1 scenario ($C_{S_1} \neq 0$) above (of course, it also disfavors the SM). Their study showed that the acceptance and the measured shapes of the kinematic distributions are affected by the existence of NP effects: most notably the presence of a charged Higgs influences the q^2 spectrum in $B \to D\tau\nu$.

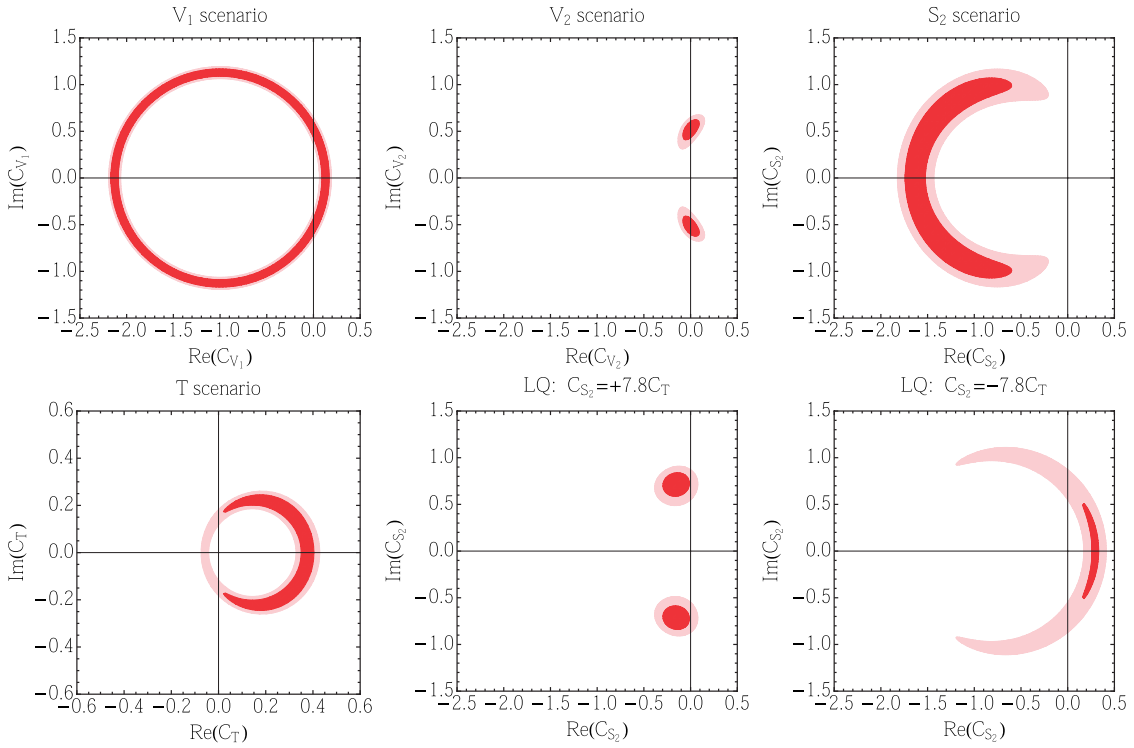

Fig. 71. Current constraints on NP scenarios based on measurements from Belle, Babar, and LHCb. The (light) red regions are allowed at 68% (95%) CL. The "V_i scenario" means that $C_{V_i} \neq 0$ and all other $C_X = 0$.

Constraints on the other scenarios, based on a rough estimate, comparing the existing R_D and R_{D^*} measurements in Table 48, are presented in Fig. 71. In each scenario, shaded regions in (light) red are allowed at 68% (95%) CL. The allowed regions are well away from the SM points in all cases ($C_X = 0$), implying that current experimental data favors a large contribution from NP.

Theoretical interpretation: model dependent Semi-tauonic B decays are mediated by tree-level processes in the SM, and the current experimental values differ quite significantly from the SM predictions (at the level of 20% for the V_1 scenario, as can be seen in Fig. 71). BSM physics close to the weak scale is required in order to explain the deviations from the SM if the NP is perturbative. There are two classes of models which can give the desired effects at tree level: (i) models with an extended Higgs sector providing a charged scalar, and (ii) models with leptoquarks. Dedicated analyses of constraints on these models are described in Sect. 18.3.1, with projections for future constraints expected at Belle II. Here, phenomenological aspects of models relevant for R_D and R_{D^*} are briefly reviewed.

Due to the heavy τ lepton in the final state, tauonic B decays are sensitive to charged Higgs bosons, which contribute to the scalar effective operators ($\mathcal{O}_{S_{1,2}}$) [274–278]. A simultaneous explanation of R_D and R_{D^*} is only possible for the S_2 scenario with a sizeable contribution ($C_{S_2} \sim -1.5$). The 2HDM of type II generates a dominant contribution to $\mathcal{O}_{S_1}$ (for large tan β). It can neither explain R_D and R_{D^*} simultaneously [250] nor R_{D^*} alone without violating bounds from other flavor observables [279]. Other 2HDMs such as I, X (leptospecific), Y (flipped), and aligned type also cannot accommodate the $R_{D^{(*)}}$ anomaly within other flavor constraints. A comprehensive study of flavor constraints for the 2HDMs with natural flavor conservation is given in Refs. [280–282]. The 2HDM of type III is

Table 50. Expected precision for $R_{D^{(*)}}$ and $P_\tau(D^*)$ at Belle II, given as the relative uncertainty for $R_{D^{(*)}}$ and absolute for $P_\tau(D^*)$. The values given are the statistical and systematic errors respectively.

	$5\,\text{ab}^{-1}$	$50\,\text{ab}^{-1}$
R_D	$(\pm 6.0 \pm 3.9)\%$	$(\pm 2.0 \pm 2.5)\%$
R_{D^*}	$(\pm 3.0 \pm 2.5)\%$	$(\pm 1.0 \pm 2.0)\%$
$P_\tau(D^*)$	$\pm 0.18 \pm 0.08$	$\pm 0.06 \pm 0.04$

still capable of explaining the data, because a charged Higgs contribution to $\mathcal{O}_{S_2}$ can be sizeable if the coupling of the third-generation quark doublet to a right-handed c quark is large [283–285].

The current results for $R_{D^{(*)}}$ are $R_D^{\text{exp}}/R_D^{\text{SM}} \approx R_{D^*}^{\text{exp}}/R_{D^*}^{\text{SM}}$ within uncertainty. Such a relation is naturally given in scenarios that contain a non-zero contribution to $\mathcal{O}_{V_1}$, i.e. a left-handed current. A straightforward realization of the left-handed current is given by a W' boson implemented in a new SU(2)_L gauge group. This class of model can also address the R_K anomaly (lepton flavor non-universality in $B \to K\ell^+\ell^-$), as well as $R_{D^{(*)}}$; see Refs. [286–290]. Some types of leptoquark model can also induce $\mathcal{O}_{V_1}$ [225,288,291–295] and explain R_K and $R_{D^{(*)}}$ at the same time [288,289].

Future prospects Based on the existing results from Belle and the expected statistical and experimental improvements at Belle II, we provide estimates of the precision on $R_{D^{(*)}}$ and $P_\tau(D^*)$ in Table 50 for two integrated luminosities. In Fig. 72, the expected precisions at Belle II are compared to the current results and SM expectations. They will be comparable to the current theoretical uncertainty. Furthermore, precise polarization measurements, $P_\tau(D^*)$, and decay differentials will provide further discrimination of NP scenarios (see, e.g., Refs. [227,263] for a detailed discussion). In the estimates for $P_\tau(D^*)$, we take the pessimistic scenario that no improvement to the systematic uncertainty arising from hadronic B decays with three or more π^0, η, and γ can be achieved. However, although challenging, our understanding of these modes should be improved by future measurements at Belle II and hence the systematic uncertainty will be further reduced. As shown in Fig. 70, the Belle analyses of $B \to D^{(*)}\tau\nu_\tau$ largely rely on the E_ECL shape to discriminate between signal and background events. One possible challenge at Belle II is therefore to understand the effects from the large beam-induced background on E_ECL. From studies of $B \to \tau\nu$, shown earlier in this section, E_ECL should be a robust observable.

With the Belle II dataset, NP scenarios can be precisely tested with q^2 and other distributions of kinematic observables. Figure 73 demonstrates the statistical precision of the q^2 measurement with $50\,\text{ab}^{-1}$ data based on a toy MC study with hadron-tag-based analysis. A quantitative estimation of the future sensitivity to a search for NP in $\bar{B} \to D^{(*)}\tau\bar{\nu}$ is shown in Fig. 74 [296]: it shows the regions of C_X that are probed by the ratios (red) and the q^2 distributions (blue) at Belle II with $5\,\text{ab}^{-1}$ (dashed lines) and $50\,\text{ab}^{-1}$ (solid lines) respectively, at 95% CL. One finds that the distributions are very sensitive to all NP scenarios, including those with new scalar or tensor mediators. NP contributions that enter in C_X can be described as

$$C_X \approx \frac{1}{2\sqrt{2}G_\text{F}V_{cb}}\frac{gg'}{M_\text{NP}^2}, \tag{142}$$

where g and g' denote the couplings of new heavy particles to quarks and leptons respectively (at the NP mass scale M_NP). Assuming couplings of $g, g' \sim 1$, one finds that the Belle II NP mass scale reach, $M_\text{NP} \sim (2\sqrt{2}G_\text{F}V_{cb}C_X)^{-1/2}$, is about 5–10 TeV/c^2.

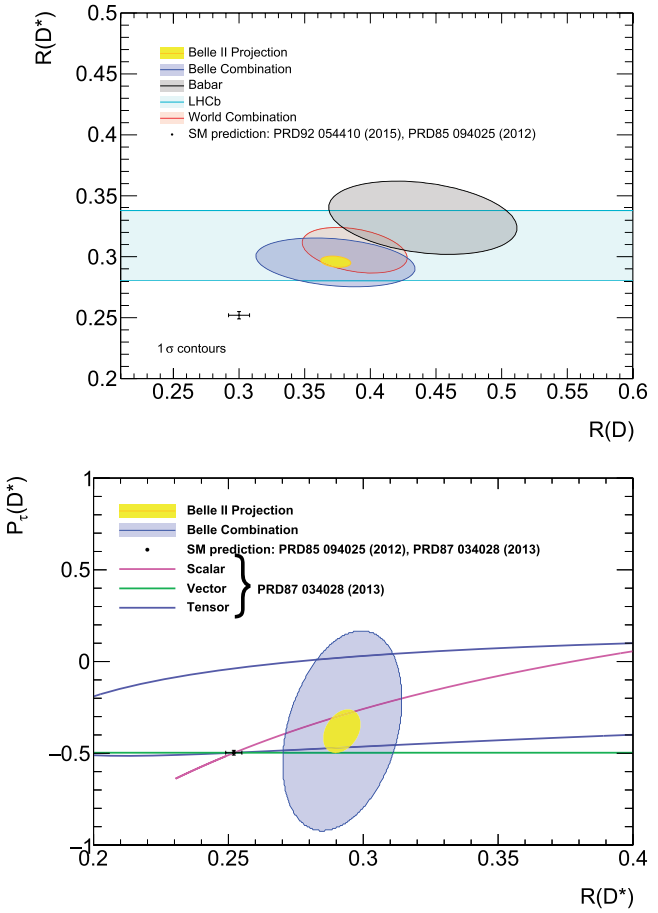

Fig. 72. Expected Belle II constraints on the R_D vs. R_{D^*} plane (left) and the R_{D^*} vs. $P_\tau(D^*)$ plane (right) compared to existing experimental constraints from Belle. The SM predictions are indicated by the black points with theoretical error bars. In the right panel, the NP scenarios "Scalar," "Vector," and "Tensor" assume contributions from the operators $\mathcal{O}_{S_1}$, $\mathcal{O}_{V_1}$, and O_T, respectively.

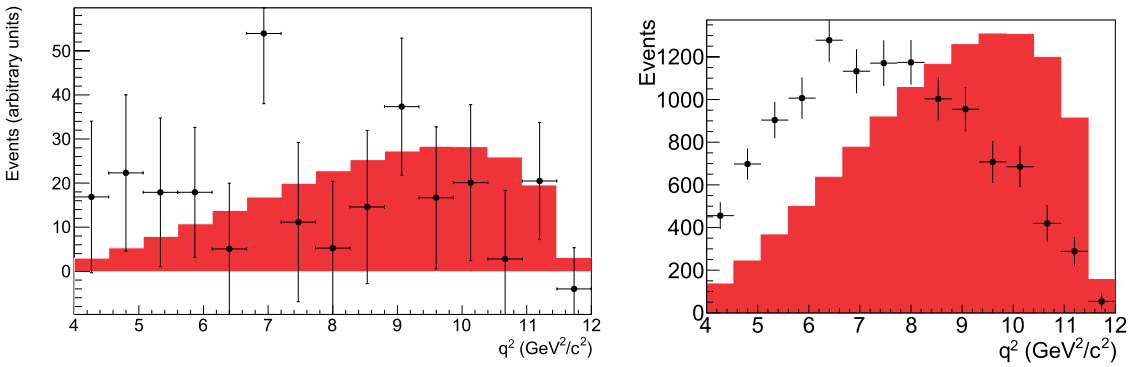

Fig. 73. Left: The $B \to D\tau\nu$ q^2 distribution in the hadronic tag analysis and $\tau^- \to \ell^-\bar{\nu}_\ell\nu_\tau$ with the full Belle data sample [251]. Right: The projection to the 50 ab^{-1} Belle II dataset. In both panels, the solid histograms show the predicted distribution shape with the 2HDM of type II at $\tan\beta/m_{H^\pm} = 0.5\,(\mathrm{GeV}/c^2)^{-1}$. In the right panel, pseudo-data are shown based on the SM hypothesis.

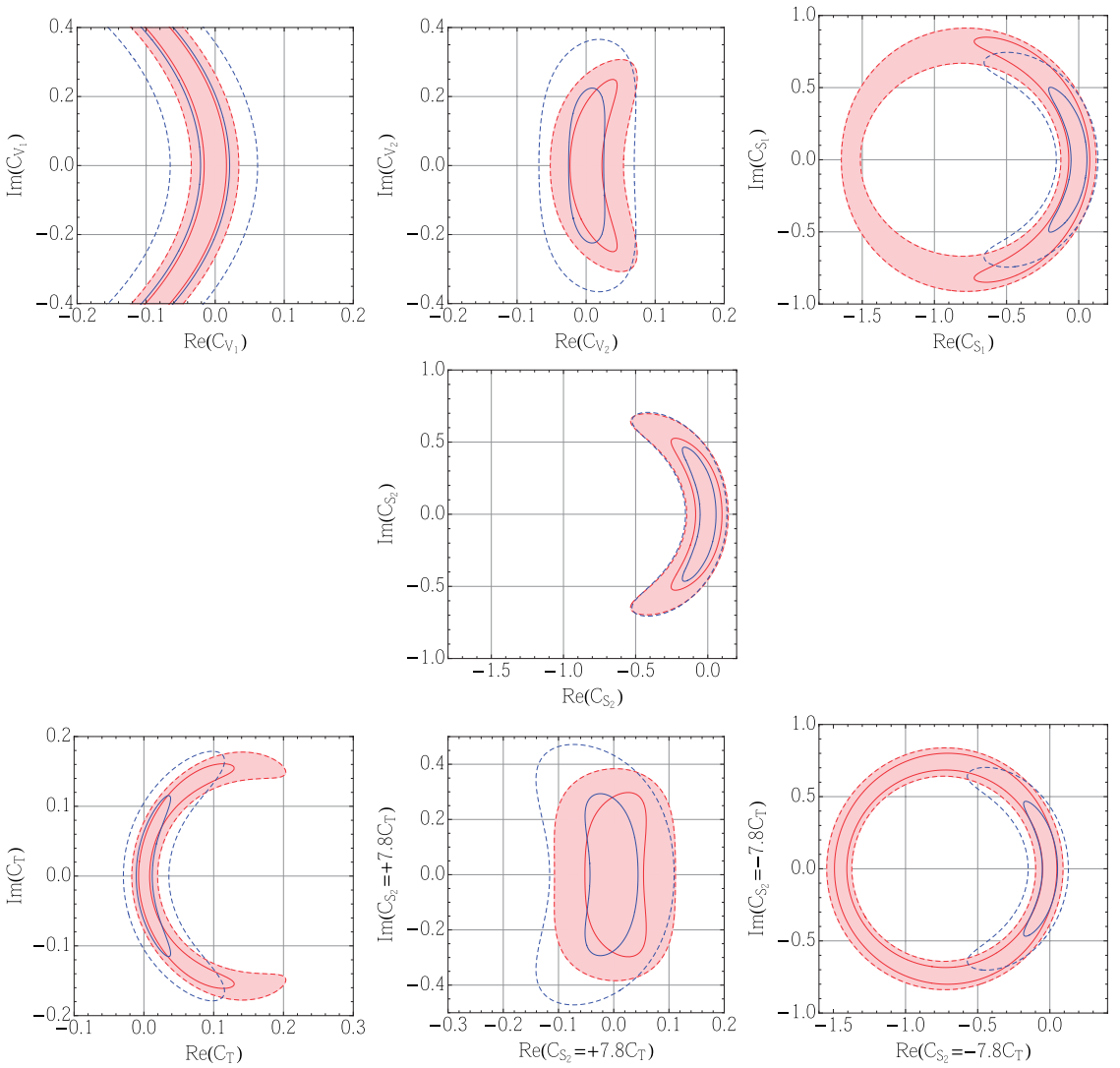

Fig. 74. Expected sensitivity of Belle II to constrain NP coefficients, C_X, at 95% CL. The regions inside the boundaries in red and blue can be probed at Belle II by measurement of the ratios and the distributions, respectively, with 5 ab^{-1} (dashed lines) and 50 ab^{-1} (solid lines).

8.5.2. $B \to \pi\tau\nu$

Authors: R. Watanabe (th.), F. Bernlochner (exp.)

It is natural to expect that any NP contributions in $b \to c\tau\nu$ may also show up in $b \to u\tau\nu$ processes. A limit on the branching fraction of $B \to \pi\tau\nu$ has been determined by the Belle collaboration in Ref. [297]. They observed no significant signal and obtained the 90% CL upper limit as $\mathcal{B}(B \to \pi\tau\nu) < 2.5 \times 10^{-4}$. The measured branching fraction obtained was $\mathcal{B}(B \to \pi\tau\nu) = (1.52 \pm 0.72 \pm 0.13) \times 10^{-4}$, where the first error (along with the central value) is statistical and the second is systematic.

Evaluations of the form factors for the $B \to \pi$ transition have been performed using QCD predictions and experimental data. In the recent lattice studies of Refs. [143,159] the authors have computed the vector and tensor amplitudes for $B \to \pi$. In their studies, the form factors are parameterized in the model-independent Bourelly–Caprini–Lellouch (BCL) expansion approach [143,159],

defined as

$$f_0(q^2) = \sum_{n=0}^{N_z-1} b_n^0 z^n, \tag{143}$$

$$f_j(q^2) = \frac{1}{1 - q^2/M_{B^*}^2} \sum_{n=0}^{N_z-1} b_n^j \left[z^n - (-1)^{n-N_z} \frac{n}{N_z} z^{N_z} \right] \tag{144}$$

for polarizations $j = +$ and T, where $M_{B^*} = 5.325\,\text{GeV}$, $b_n^{0,+,T}$ are expansion parameters, and $N_z(= 4)$ is the expansion order.

The analytical variable z is defined as

$$z \equiv z(q^2) = \frac{\sqrt{t_+ - q^2} - \sqrt{t_+ - t_0}}{\sqrt{t_+ - q^2} + \sqrt{t_+ - t_0}}, \tag{145}$$

where $t_0 = (M_B + M_\pi)(\sqrt{M_B} - \sqrt{M_\pi})^2$ and $t_+ = (M_B + M_\pi)^2$. The expansion parameters have been determined in fits to lattice simulations and experimental data on light leptonic modes $B \to \pi \ell \nu_\ell$ [84,298–300]. The scalar form factor, present in τ modes, has been obtained in lattice QCD via the vector matrix element; cf. Eqs. (91) and (92).

We consider the ratio of branching fractions to test for NP contributions:

$$R_\pi \equiv \frac{\mathcal{B}(B \to \pi \tau \nu_\tau)}{\mathcal{B}(B \to \pi \ell \nu_\ell)} \equiv \frac{\mathcal{B}_\tau}{\mathcal{B}_\ell}, \tag{146}$$

where $|V_{ub}|$ cancels out. Possible NP scenarios can be described by

$$-\mathcal{L}_{\text{eff}} = 2\sqrt{2} G_{\text{F}} V_{ub} \big[(1 + C_{V_1}) \mathcal{O}_{V_1} + C_{V_2} \mathcal{O}_{V_2} + C_{S_1} \mathcal{O}_{S_1} + C_{S_2} \mathcal{O}_{S_2} + C_T \mathcal{O}_T \big], \tag{147}$$

similarly to the $b \to c$ case above, where C_X (for $X = V_{1,2}, S_{1,2}$, and T) indicates an NP contribution in terms of the Wilson coefficient of $\mathcal{O}_X$ normalized by $2\sqrt{2} G_{\text{F}} V_{ub}$. The differential branching fractions for each tau helicity, $\lambda_\tau = \mp 1/2$, are then written as [243]

$$\frac{d\mathcal{B}_\tau^-}{dq^2} = N_B \big| (1 + C_{V_1} + C_{V_2}) \sqrt{q^2} H_{V,+} + 4 C_T m_\tau H_T \big|^2, \tag{148}$$

$$\begin{aligned} \frac{d\mathcal{B}_\tau^+}{dq^2} = \frac{N_B}{2} \big[& \big| (1 + C_{V_1} + C_{V_2}) m_\tau H_{V,+} + 4 C_T \sqrt{q^2} H_T \big|^2 \\ & + 3 \big| (1 + C_{V_1} + C_{V_2}) m_\tau H_{V,0} + (C_{S_1} + C_{S_2}) \sqrt{q^2} H_S \big|^2 \big], \end{aligned} \tag{149}$$

with

$$N_B = \frac{\tau_B G_{\text{F}}^2 V_{ub}^2}{192 \pi^3 M_B^3} \sqrt{Q_+ Q_-} \left(1 - \frac{m_\tau^2}{q^2} \right)^2, \tag{150}$$

where $Q_\pm = (M_B \pm M_\pi)^2 - q^2$ and the quantities H contain the hadron transition form factors. The differential branching fractions for $B \to \pi \ell \nu_\ell$ are given by

$$\frac{d\mathcal{B}_\ell^-}{dq^2} = \left. \frac{d\mathcal{B}_\tau^-}{dq^2} \right|_{m_\tau \to 0,\, C_X = 0}, \qquad \frac{d\mathcal{B}_\ell^+}{dq^2} = 0. \tag{151}$$

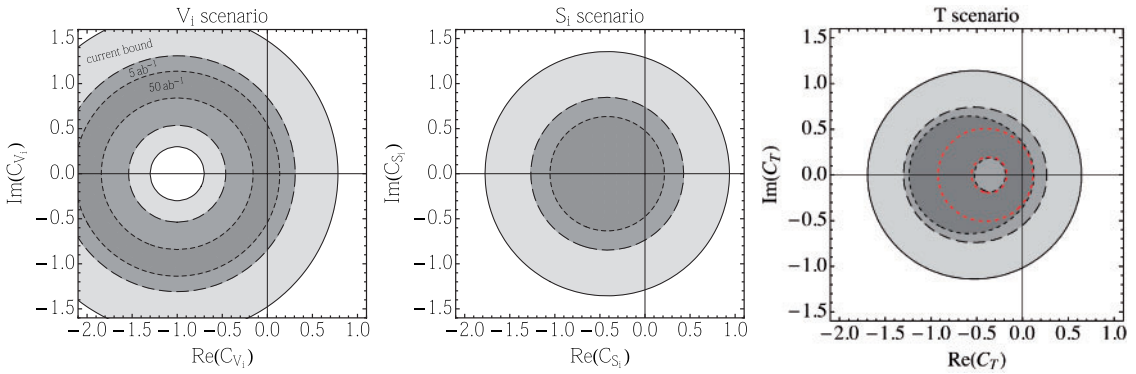

Fig. 75. Allowed regions for V_1, V_2, S_1, S_2, and T scenarios based on the measurement of R_π. The light gray region is allowed from the measurement of R_π by the Belle experiment at 95% CL. The V_1 and V_2 (S_1 and S_2) scenarios have the same region since their contributions are identical. The dark (darker) gray regions with black dashed curves denote a possible reach of 95% CL constraint expected at the Belle II, when $\mathcal{L} = 5\,\text{ab}^{-1}$ ($50\,\text{ab}^{-1}$) data is accumulated. For these results, the theoretical uncertainties given in Refs. [143,159] are taken into account. The thick dashed red lines for the tensor case show the exclusion limit when the theoretical uncertainty is reduced by a factor of two.

Finally, R_π is given as

$$R_\pi = \frac{\int_{m_\tau^2}^{q^2_{\text{max}}} (d\mathcal{B}_\tau^+ + d\mathcal{B}_\tau^-)/dq^2}{\int_0^{q^2_{\text{max}}} d\mathcal{B}_\ell^-/dq^2}, \tag{152}$$

where $q^2_{\text{max}} = (M_B - M_\pi)^2$.

Given the above formula and input for $b_n^{0,+}$, the SM predicts $R_\pi^{\text{SM}} = 0.641 \pm 0.016$, whereas the experimental data suggests $R_\pi^{\text{exp.}} \approx 1.05 \pm 0.51$ by using $\mathcal{B}(B \to \pi \ell \bar{\nu}_\ell) = (1.45 \pm 0.05) \times 10^{-4}$ [77]. Thus, at present the experimental result is consistent with the SM prediction given the large uncertainty. We can place loose bounds on NP scenarios from R_π. In Fig. 75, the constraints on C_{V_1}, C_{V_2}, C_{S_1}, C_{S_2}, and C_T are shown, where it is assumed that the NP contribution comes from only one effective operator $\mathcal{O}_X$ for $X = V_1, V_2, S_1, S_2$, or T. As can be seen, the current data has already constrained NP contributions to be roughly $|C_X| \lesssim O(1)$, which implies that a contribution larger than that of the SM ($2\sqrt{2}G_F V_{ub}$) is disfavored.

A key reason for measuring $B \to \pi\tau\nu$ is that the tensor-type interaction of NP that affects $b \to u\tau\nu$ cannot be constrained from $B \to \tau\nu$. The current results for b_n^T for the tensor form factor still have large uncertainties [159]. Nevertheless, the constraint on C_T is comparable to the other NP scenarios. Improvements in the evaluation of the tensor form factor will be significant for the future measurement of this process at Belle II.

The following study determined the future sensitivity of R_π to NP scenarios with $5\,\text{ab}^{-1}$ and $50\,\text{ab}^{-1}$ of Belle II data, based on Ref. [243]. To estimate exclusion limits on the Wilson coefficient C_X, it is assumed that the experimental central value is identical to the SM prediction and the expected experimental errors at $5\,\text{ab}^{-1}$ and $50\,\text{ab}^{-1}$ are extrapolated from the Belle measurement [297]. The expected constraints from Belle II are therefore

$$R_\pi^{5\,\text{ab}^{-1}} = 0.64 \pm 0.23, \tag{153}$$

$$R_\pi^{50\,\text{ab}^{-1}} = 0.64 \pm 0.09. \tag{154}$$

The above values are compared with each NP scenario to determine constraints on C_X, as shown in Fig. 75. Focusing on the vicinity of the origin of C_X, we see that $|C_X| \gtrsim O(0.1)$ can be tested by the R_π measurement for vector and tensor scenarios. A large negative contribution to $C_{V_i} \sim -2$, for example, will always be allowed within the uncertainty. For the tensor case, we expect to constrain $|C_T| \lesssim 1$, which can be improved if the theoretical uncertainties are addressed. In the figure, a scenario where the theoretical uncertainty is reduced by half is also presented, indicating improved sensitivity to tensor interactions. As for the scalar scenarios, $B \to \tau\nu$ has better sensitivity than $B \to \pi\tau\nu$ due to the chiral enhancement of the pseudoscalar contribution in the purely leptonic decay.

8.5.3. $B \to X_c\tau\nu$

Authors: F. Bernlochner (exp.), J. Hasenbusch (exp.), Z. Ligeti (th.)

Introduction The anomalously large rates of $B \to D^{(*)}\tau\nu$ measured by BaBar, Belle, and LHCb demand additional, independent measurements of $b \to c\tau\nu$ transitions. The measurement of inclusive $B \to X_c\tau\bar{\nu}$ decays could provide such additional information. This rate has not been directly measured, except for the related Large Electron–Positron (LEP) accelerator measurements usually quoted as the average rate of an admixture of b-flavored hadrons to decay semi-leptonically to $\tau + X$ [88]:

$$\mathcal{B}(b \to X\tau^+\nu) = (2.41 \pm 0.23)\%. \tag{155}$$

The LEP analyses selected large missing energy events in the hemisphere opposite to a b-tagged jet, so the measurements constrain a linear combination of $b \to X\tau\bar{\nu}$, $\tau\bar{\nu}$, $X\nu\bar{\nu}$, and $X\tau\bar{\tau}$ [301,302], of which, in the SM, the $X_c\tau\bar{\nu}$ rate dominates. The approaches for modeling semi-leptonic B decays were inconsistent in the LEP measurements. ALEPH, for example, claims the most precise constraint by far on $R(X_c)$ yet does not explicitly quote any uncertainty for the $B \to D^{**}\ell\nu$ background. The LEP result in Eq. (155) is nevertheless in good agreement with the SM, as a more recent update of the SM prediction for $R(X_c)$ yields [293]

$$R(X_c) = 0.223 \pm 0.004, \tag{156}$$

which, combined with the world average, $\mathcal{B}(B^- \to X_c e\bar{\nu}) = (10.92 \pm 0.16)\%$ [230,303], yields [293]

$$\mathcal{B}(B^- \to X_c\tau\bar{\nu}) = (2.42 \pm 0.05)\%. \tag{157}$$

The above prediction does not include $O(1/m_b^3)$ and $O(\alpha_s^2)$ effects, which turn out to be quite sizeable. More recent publications have evaluated these effects: see, for example, Ref. [304], which gives $R(X_c) = 0.212 \pm 0.003$, and Ref. [305], which gives $R(X_c) = 0.214 \pm 0.004$. This prediction is nevertheless precise, thus the inclusive measurement can provide information complementary to the exclusive channels.

There is a tension between the exclusive and inclusive measurements [293], as the isospin-constrained fit for the sum of branching ratios [250]

$$\mathcal{B}(\bar{B} \to D^*\tau\bar{\nu}) + \mathcal{B}(\bar{B} \to D\tau\bar{\nu}) = (2.78 \pm 0.25)\%, \tag{158}$$

is above the inclusive measured rate. This tension is further exacerbated by the 0.15% SM prediction for the branching fractions to the four $D^{**}\tau\bar{\nu}$ modes [306]. Measuring the inclusive rate should be feasible. Uncertainties of the individual $\bar{B} \to D^{(*)}\tau\bar{\nu}$ branching ratios are expected to be reduced to about 3% with Belle II data.

Theoretical results Here, we briefly discuss the SM predictions (following Ref. [293]) for differential distributions in inclusive $B \to X_c\tau\bar{\nu}$ decays, including $1/m_b^2$ and α_s corrections. These results can improve the sensitivity of $b \to c\tau\bar{\nu}$ related observables to BSM physics. The inclusive $B \to X_c\tau\bar{\nu}$ decay rates can be computed independent of the model in an operator product expansion (OPE) just like for $B \to X_c\ell\bar{\nu}$; see Sect. 8.7. The perturbative and non-perturbative corrections can be systematically incorporated, and are modest if one measures the total inclusive rate without substantial phase space cuts. We outline here how these corrections become large near endpoint regions of these spectra. The triple differential $B \to X\tau\bar{\nu}$ distribution has long been known, including the leading non-perturbative corrections of order $1/m_b^2$ [307–309]. Until recently [310], the theoretical predictions were not available using a well-defined short-distance quark mass scheme.

One often uses the dimensionless kinematic variables

$$\hat{q}^2 = \frac{q^2}{m_b^2}, \quad v\cdot\hat{q} = \frac{v\cdot q}{m_b}, \quad y = \frac{2E_\tau}{m_b}, \quad x = \frac{2E_\nu}{m_b}, \tag{159}$$

where $q = p_\tau + p_\nu$ is the dilepton momentum, $v = p/M_B$ is the four-velocity of the B meson, and $E_{\tau,\nu}$ are the τ, ν energies in the B rest frame. The mass ratios

$$\rho_\tau = m_\tau^2/m_b^2, \qquad \rho = m_c^2/m_b^2 \tag{160}$$

are also needed.

The triple differential decay rate in the B rest frame is

$$\begin{aligned}\frac{1}{\Gamma_0}\frac{d\Gamma}{d\hat{q}^2\,dy\,dv\cdot\hat{q}} &= 24\,\theta\big[(2v\cdot\hat{q}-y_+)y_+ - \hat{q}^2\big]\,\theta\big[\hat{q}^2-(2v\cdot\hat{q}-y_-)y_-\big]\\ &\quad\times\Big\{2(\hat{q}^2-\rho_\tau)\hat{W}_1 + \big[y(2v\cdot\hat{q}-y)-\hat{q}^2+\rho_\tau\big]\hat{W}_2\\ &\qquad + 2\big[\hat{q}^2(y-v\cdot\hat{q})-\rho_\tau v\cdot\hat{q}\big]\hat{W}_3\\ &\qquad + \rho_\tau(\hat{q}^2-\rho_\tau)\,\hat{W}_4 + 2\rho_\tau(2v\cdot\hat{q}-y)\,\hat{W}_5\Big\},\end{aligned} \tag{161}$$

where

$$\Gamma_0 = |V_{cb}|^2 G_F^2 \frac{m_b^5}{192\pi^3} \tag{162}$$

is the tree-level free-quark decay rate. The $\hat{W}_i$ are the structure functions of the hadronic tensor [307, 311], which in the local OPE of $\Lambda_{\rm QCD}^2/m_b^2$ contain Dirac δ, δ', and δ'' functions of $(1+\hat{q}^2-2v\cdot\hat{q}-\rho)$. The key kinematical difference between zero and non-zero lepton mass arises from the fact that

$$y_\pm = \frac{1}{2}\big(y \pm \sqrt{y^2-4\rho_\tau}\big), \tag{163}$$

which enters the phase space boundaries in Eq. (161), simplifies in the $m_\tau \to 0$ limit: $y_+ \to y$ and $y_- \to 0$ (in general, $y_+y_- = \rho_\tau$). In the massive lepton case, the appearance of the second

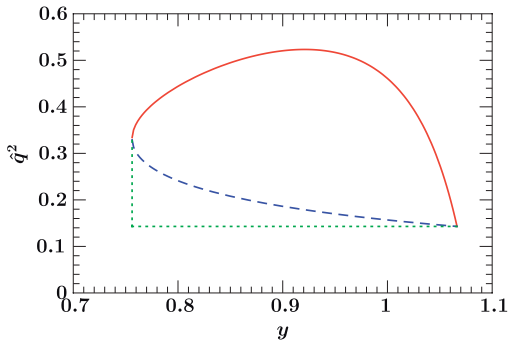

Fig. 76. The $b \to c\tau\bar{\nu}$ Dalitz plot for free quark decay. The solid orange boundary comes from the first θ function in Eq. (161), the dashed blue boundary from the second one [310].

non-trivial Heaviside θ function in Eq. (161) sets a lower limit on $\hat{q}^2$. For fixed $\hat{q}^2$ and $v \cdot \hat{q}$,

$$\hat{q}_- + x_\tau \hat{q}_+ \le y \le \hat{q}_+ + x_\tau \hat{q}_-, \tag{164}$$

where $\hat{q}_\pm = v \cdot \hat{q} \pm \sqrt{(v \cdot \hat{q})^2 - \hat{q}^2}$. At the parton level, $v \cdot \hat{q} = (1 + \hat{q}^2 - \rho)/2$ gives the partonic phase space in the $\hat{q}^2$–y plane at tree level. The limits on $\hat{q}^2$ for fixed y are

$$y_-\Big(1 - \frac{\rho}{1 - y_-}\Big) \le \hat{q}^2 \le y_+\Big(1 - \frac{\rho}{1 - y_+}\Big). \tag{165}$$

This is illustrated in Fig. 76, where $\rho = (1.3/4.7)^2$ and $\rho_\tau = (1.777/4.7)^2$ were used. Beyond tree level, the lower limit of the $\hat{q}^2$ integration and the lower limit of y integration for $\hat{q}^2 < \hat{q}_0^2 = \sqrt{\rho_\tau}\big[1 - \rho/(1 - \sqrt{\rho_\tau})\big]$ is replaced by $\hat{q}^2 > \rho_\tau$ and $y > 2\sqrt{\rho_\tau}$.

Integrating over $\hat{q}^2$, the limits on y are

$$2\sqrt{\rho}_\tau < y < 1 + \rho_\tau - \rho. \tag{166}$$

Integrating over y, the limits of $\hat{q}^2$ are

$$\rho_\tau < \hat{q}^2 < (1 - \sqrt{\rho})^2. \tag{167}$$

These are the partonic phase space limits which enter the OPE calculation, while the physical phase space limits are determined by the hadron masses.

Besides the total rate, the q^2 and E_τ spectra have been studied in detail [310]. The OPE breaks down for large values of E_τ. Similar to $B \to X_s\gamma$ and $B \to X_u l\bar{\nu}$ (see Sect. 8.7), the terms in the OPE that are enhanced near the endpoint can be resummed into a non-perturbative shape function. The shape function expansion can be rendered valid away from the endpoint region as well, such that it smoothly recovers the local OPE result [312–314]. One obtains, at leading order [310],

$$\begin{aligned}\frac{1}{\Gamma_0}\frac{d\Gamma}{dy} = 2\sqrt{y^2 - 4\rho_\tau} \int d\hat{\omega} m_b F(m_b\hat{\omega} + m_B - m_b) \\ \times \theta(y - 2\rho_\tau)\theta(1 - R_\omega)(1 - R_\omega)^2 \Big\{ y\rho \frac{1 - R_\omega}{R_\omega} \\ + (1 + 2R_\omega)\big[y - \hat{\omega}y_- - 2\rho_\tau\big](2 - y - \hat{\omega})\Big\},\end{aligned} \tag{168}$$

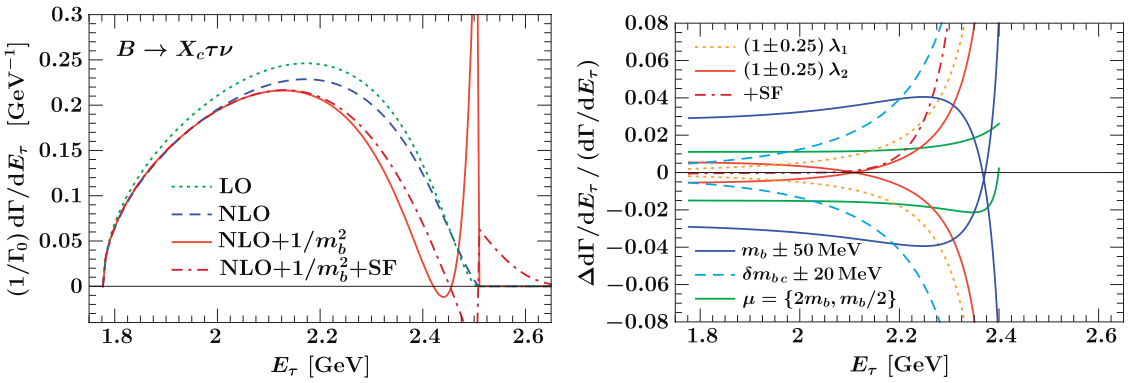

Fig. 77. The OPE predictions for $d\Gamma/dE_\tau$ in $B \to X_c \tau \bar{\nu}$ [310]. Left: The dotted green curve shows the free-quark decay result, the dashed blue curve includes $\mathcal{O}(\alpha_s)$ corrections, and the solid orange curve includes both α_s and $1/m_b^2$ corrections. The dot-dashed dark red curve combines $\mathcal{O}(\alpha_s, 1/m_b^2)$ with the leading shape function. Right: The solid blue curve shows the fractional uncertainty due to the variation of m_b^{1S} by $\pm 50\,\mathrm{MeV}/c^2$, the dashed light blue curves show that of δm_{bc} by $\pm 20\,\mathrm{MeV}/c^2$, the solid green curves show the μ variation between $m_b/2$ and $2m_b$, and the solid red (dotted light orange) curves show the variation of λ_2 (λ_1) by $\pm 25\%$. The dot-dashed dark red curve shows the correction from the leading shape function.

where $\Gamma_0 = |V_{cb}|^2 G_F^2 m_b^5/(192\pi^3)$ is the tree-level free-quark decay rate, $R_\omega = \rho/[(1-y_+-\hat{\omega})(1-y_-)]$, and $F(k)$ is the leading-order universal shape function. The endpoint region of the E_τ spectrum is given by $1 - y_+ \sim \Lambda_{\rm QCD}/m_b$. For smaller values of E_τ, the usual local OPE is reliable.

The order-$1/m_b^2$ corrections reduce the $B \to X_c \tau \bar{\nu}$ rate by about 7%–8%, concentrated mainly at higher values of $\hat{q}^2$, dominated by the terms proportional to λ_2. As for large values of E_τ, the OPE also breaks down for large values of $\hat{q}^2$. Near maximal $\hat{q}^2$, the λ_2 terms behave as $(\hat{q}^2_{\rm max} - \hat{q}^2)^{-1/2}$, and the differential rate becomes negative. This breakdown of the OPE occurs because the hadronic final state gets constrained to the lightest few hadronic resonances, which are not calculable in the OPE. Thus, integration over some range of $\Delta\hat{q}^2$ is necessary near maximal $\hat{q}^2$ to obtain a reliable result.

Restoring the dimensions of the variables, the phase space limits are

$$m_\tau < E_\tau < \frac{m_b^2 - m_c^2 + m_\tau^2}{2m_b}, \qquad m_\tau^2 < q^2 < (m_b - m_c)^2. \tag{169}$$

One can see, using $m_{b,c} = m_{B,D} - \bar{\Lambda} + \mathcal{O}(\Lambda^2_{\rm QCD}/m^2_{b,c})$, that the difference of the upper limit of q^2 at the parton level, $(m_b - m_c)^2$, and at the hadronic level, $(m_B - m_D)^2$, is suppressed by $\Lambda^2_{\rm QCD}$. However, the lepton energy endpoint receives an $\mathcal{O}(\Lambda_{\rm QCD})$ correction, although numerically only about 100 MeV (it is ~300 MeV for $B \to X_u e \bar{\nu}$).

Writing $m_c = m_b^{1S} - \delta m_{bc}$, and treating $\delta m_{bc} = m_b - m_c$ as an independent parameter is practical, as it is well constrained by measured $B \to X_c \ell \bar{\nu}$ spectra, and is the dominant source of formally $\mathcal{O}(\lambda_1/m_c^2)$ corrections [315]. We use a conservative $\pm 20\,\mathrm{MeV}/c^2$ uncertainty on δm_{bc}. We also use $\lambda_1 = -0.3\,\mathrm{GeV}^2$ and $\lambda_2 = 0.12\,\mathrm{GeV}^2$, and vary both by 25% to account for uncertainties and higher-order effects.

Figure 77 shows the predictions for $d\Gamma/dE_\tau$ in the $1S$ mass scheme for the b quark. The $1/m_b^2$ corrections are negligible at low values of E_τ (and q^2), while their effects become important for larger values. The peculiar shape of $d\Gamma/dE_\tau$ including the $\mathcal{O}(1/m_b^2)$ terms is due to the fact that near the endpoint both the λ_1 and λ_2 terms are large, and the λ_1 term changes sign. The dot-dashed (dark red) curve combines the $\mathcal{O}(\alpha_s)$ and $\mathcal{O}(1/m_b^2)$ corrections with the tree-level leading shape function

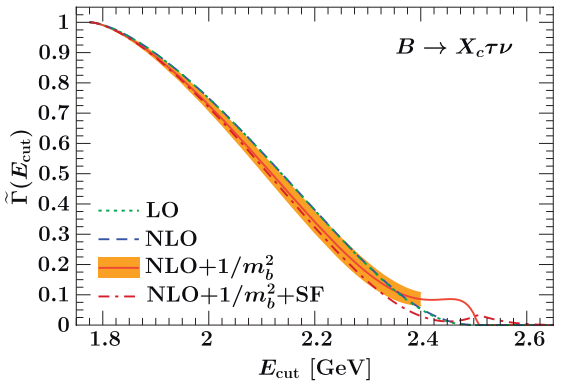

Fig. 78. Fraction of events above a given τ energy threshold $d\Gamma/dE_\tau$. The shaded band shows the total uncertainty.

result in Eq. (168). For this, the fit result from Ref. [316] was used (and for consistency also m_b^{1S}, with a conservative $\pm 50\,\mathrm{MeV}/c^2$ uncertainty).

The right panel of Fig. 77 shows the fractional uncertainties from varying the parameters. The variations from $m_b = (4.71 \pm 0.05)\,\mathrm{GeV}/c^2$ keeping $\delta m_{bc} = 3.4\,\mathrm{GeV}/c^2$ fixed and $\delta m_{bc} = \pm 20\,\mathrm{MeV}/c^2$ dominate at low and high values, respectively. Variations on the renormalization scale, μ, between $m_b/2$ and $2m_b$, the coefficients of λ_2 and λ_1, and relative corrections due to shape function effects are shown.

Since the spectrum cannot be calculated reliably near maximal E_τ, Fig. 78 shows the rate above a cut, normalized to the total rate, $\widetilde{\Gamma}(E_{\rm cut}) = (1/\Gamma)\int_{E_{\rm cut}} d\Gamma/dE_\tau$, at different orders in the OPE. The $\mathcal{O}(\alpha_s)$ corrections have a negligible effect on these distributions since they affect the shapes very mildly. The yellow band shows the total uncertainty obtained by adding all uncertainties in quadrature. The dot-dashed (dark red) curve shows the effect of including the leading shape function.

Experimental challenges The analysis of $B \to X\tau\nu$ at the B factories is a tremendous challenge, even at Belle II. Here we discuss the main experimental considerations.

To study $B \to X\tau\nu$, tagged samples are a big advantage, particularly tags that are fully reconstructed in hadronic decay modes. Furthermore, it is useful to restrict the analysis to $\tau \to \ell\nu\nu$ modes, as the background level is lower than the hadronic modes. An important discriminant is the lepton momentum in the rest frame of the decaying B meson, which can be determined from the kinematics of the hadronic tag. The lepton momentum is lower for $B \to X\tau\nu$ signal events compared to $B \to X\ell\nu$ events as the latter produces higher-energy prompt (decay daughters of the B) leptons and thus separates this background very well. However, background from hadronic B decays, producing secondary leptons ($B \to D \to \ell$) or hadrons faking leptons, will contribute with similar momenta to the signal.

Other important properties of the signal are the three undetectable neutrinos in the decay, which carry away momentum and energy. From the known initial e^+e^- state kinematics and under the assumption that the tag side decayed in a hadronic decay mode, the missing energy and momentum can be derived. Most of the relevant background contributions are expected to have less missing momentum and energy than the signal decay, which is typically probed using the missing mass squared $m^2_{\rm miss}$ observable. All major background contributions peak at zero missing mass as they decay with a single neutrino, while the signal resides in the tail regions. Combined, the lepton

momentum and missing mass squared can provide a powerful two-dimensional discriminant. This is a high-statistics analysis with an overwhelmingly high background level. Thus, even small deviations between data and MC cannot be treated as statistical fluctuations and need to be well understood. This leads directly to the challenges and needs of this analysis.

The analysis relies heavily on the modeling of signal and background semi-leptonic B decay processes, particularly at low lepton momentum. Mismodeling of the inclusive semi-leptonic B decay spectrum can significantly bias the result, demanding accurate form factors for all semi-leptonic decay contributions and accurate composition of the X_c components. The biggest challenge is to describe the poorly measured high-mass excited charm state modes, which can behave similarly to the signal. However, even the well-known $B \to D^* \ell \nu$ decay is a source of uncertainty since it is the largest individual contribution to the lepton momentum spectrum.

The modeling of secondary leptons must also be accurate. Secondary leptons that arise through upper vertex cascade transitions ($B \to D \to \ell$) will have similar momenta to the signal and therefore pose a challenge. Furthermore, hadronic B decays where hadrons fake leptons may contribute through a diverse set of decay chains of hadronic B decays. Such hadronic decays are typically not well constrained. Further work must be done to reduce the hadron fakes by improving lepton identification separation power at low momentum regions.

The analysis is sensitive to the accuracy of detector modeling. This leads to slight efficiency differences that become significant in tails of missing mass distributions.

Belle II should consider strategies to isolate $B \to D^{**} \tau \nu$ decay modes by first reconstructing a D or D^* and looking for an additional M_X component. It will be challenging due to the lower rates of these modes, and the lower efficiency of explicitly reconstructing the charm mesons.

8.6. Exclusive semi-leptonic

8.6.1. $B \to D^{(*)} \ell \nu$

Authors: A. S. Kronfeld (th.), C. Schwanda (exp.)

Experimental status The decays $B \to D^* \ell \nu$ and $B \to D \ell \nu$ are currently the preferred modes for determining the CKM element magnitude $|V_{cb}|$ using exclusive decays. The experiments measure the differential decay rate of $B \to D^{(*)} \ell \nu$ as a function of the recoil variable q^2 or, equivalently, $w = (M_B^2 + M_{D^{(*)}}^2 - q^2)/2M_B M_{D^{(*)}}$. The formulas for differential decay rates in q^2 (and $\cos\theta$, which is an angle between the hadrons and the charged lepton) are given in Sect. 8.2.

The experimental analyses have to date used a simplifying parameterization of the form factors from Caprini, Lellouch, and Neubert (CLN) [317]. For the form factor, $f_+(q^2)$, and $A_1(q^2)$, this parameterization reads[23]

$$A_1(q^2) = A_1(q^2_{\max})\big[1 - 8\rho^2_{D^*} z + (53\rho^2_{D^*} - 15)z^2 - (231\rho^2_{D^*} - 91)z^3\big], \tag{170}$$

$$f_+(q^2) = f_+(q^2_{\max})\big[1 - 8\rho^2_{D} z + (51\rho^2_{D} - 10)z^2 - (252\rho^2_{D} - 84)z^3\big], \tag{171}$$

where

$$z = \frac{\sqrt{w+1} - \sqrt{2}}{\sqrt{w+1} + \sqrt{2}} \tag{172}$$

[23] The literature on heavy-to-heavy transitions often introduces notation for quantities proportional to A_1 and f_+.

Table 51. Measurements of $\eta_{\rm EW}\mathcal{F}(1)|V_{cb}|$ and of $\rho^2_{D^*}$ in the CLN parameterization of the form factor [317].

Experiment	$\eta_{\rm EW}\mathcal{F}(1)\lvert V_{cb}\rvert\,[10^{-3}]$	$\rho^2_{D^*}$
BaBar [318]	$34.4 \pm 0.3_{\rm stat} \pm 1.1_{\rm syst}$	$1.191 \pm 0.048_{\rm stat} \pm 0.028_{\rm syst}$
BaBar [319]	$35.9 \pm 0.2_{\rm stat} \pm 1.2_{\rm syst}$	$1.22 \pm 0.02_{\rm stat} \pm 0.07_{\rm syst}$
Belle [320]	$35.1 \pm 0.2_{\rm stat} \pm 0.6_{\rm syst}$	$1.106 \pm 0.031_{\rm stat} \pm 0.007_{\rm syst}$

Table 52. Measurements of $\eta_{\rm EW}\mathcal{G}(1)|V_{cb}|$ and of ρ^2_D in the CLN parameterization of the form factor [317].

Experiment	$\eta_{\rm EW}\mathcal{G}(1)\lvert V_{cb}\rvert\,[10^{-3}]$	ρ^2_D
BaBar [319]	$43.1 \pm 0.8_{\rm stat} \pm 2.3_{\rm syst}$	$1.20 \pm 0.04_{\rm stat} \pm 0.07_{\rm syst}$
BaBar [321]	$43.0 \pm 1.9_{\rm stat} \pm 1.4_{\rm syst}$	$1.20 \pm 0.09_{\rm stat} \pm 0.04_{\rm syst}$
Belle [85]	42.29 ± 1.37	1.09 ± 0.05

and $q^2_{\rm max} = (M_B - M_{D^{(*)}})^2$ corresponds to $w = 1$ and $z = 0$. The CLN parameterization for the other form factors (or, equivalently, helicity amplitudes) for $B \to D^*$ are given by

$$R_1(w) = R_1(1) - 0.12(w-1) + 0.05(w-1)^2, \tag{173}$$

$$R_2(w) = R_2(1) + 0.11(w-1) - 0.06(w-1)^2, \tag{174}$$

for certain form-factor ratios. It is important to bear in mind that the numerical coefficients in Eqs. (170), (171), (173), and (174) are estimates with (omitted) uncertainties. Before using CLN in future work, the coefficients would have to be reevaluated with modern inputs and their uncertainty propagated. It is advisable, however, to move to a model-independent parameterization; see below.

Tables 51 and 52 summarize the most significant measurements of $B \to D^*\ell\nu$ and $B \to D\ell\nu$. They report $\eta_{\rm EW}\mathcal{F}(1)|V_{cb}|$, $\rho^2_{D^*}$, $\eta_{\rm EW}\mathcal{G}(1)|V_{cb}|$, and ρ^2_D, where $\mathcal{F}(1) \propto A_1(q^2_{\rm max})$, $\mathcal{G}(1) \propto f_+(q^2_{\rm max})$. Due to the cleanliness of the $D^{*+} \to D^0\pi^+$, $D^0 \to K^-\pi^+$ signal, untagged analyses of $B \to D^*\ell\nu$ yield the most precise results on $\Upsilon(4S)$ datasets of order $1\,{\rm ab}^{-1}$. The systematic uncertainty in $\eta_{\rm EW}\mathcal{F}(1)|V_{cb}|$ is five times larger than the statistical one, with leading systematics arising from tracking, lepton, and hadron identification efficiencies. Background uncertainties are not a leading source of uncertainty. For $B \to D\ell\nu$, however, background is a major concern. On B factory datasets the most precise analyses used hadronic tagging and a large number of reconstructed D modes. In the most precise analysis [85], statistical and systematic uncertainty are of similar size, with the leading source of systematic uncertainty being the hadronic tag calibration. This can be controlled further at Belle II if high-purity tag side decay modes are used.

The Heavy Flavor Averaging Group (HFLAV) has performed a fit to these measurements [230] and obtained, for $D^*\ell\nu$,

$$\eta_{\rm EW}\mathcal{F}(1)|V_{cb}| = (35.61 \pm 0.43) \times 10^{-3}, \tag{175}$$

$$\rho^2_{D^*} = 1.205 \pm 0.026, \tag{176}$$

and for $D\ell\nu$,

$$\eta_{\rm EW}\mathcal{G}(1)|V_{cb}| = (41.57 \pm 1.00) \times 10^{-3}, \tag{177}$$

$$\rho^2_D = 1.128 \pm 0.033. \tag{178}$$

To convert these results into measurements of $|V_{cb}|$, theory input for the form factor normalization at zero recoil ($w = 1$) is needed. Using the most recent lattice QCD calculations from the Fermilab Lattice and MILC collaborations [144,145] for $\mathcal{F}(1)$ and $\mathcal{G}(1)$, HFLAV obtained

$$|V_{cb}|_{D^*\ell\nu} = (39.05 \pm 0.47_{\rm exp} \pm 0.58_{\rm th}) \times 10^{-3}, \tag{179}$$

$$|V_{cb}|_{D\ell\nu} = (39.18 \pm 0.94_{\rm exp} \pm 0.36_{\rm th}) \times 10^{-3}. \tag{180}$$

There is good consistency between $|V_{cb}|$ determined from $B \to D^*\ell\nu$ and $B \to D\ell\nu$ decays, but the exclusive measurement is at odds with the inclusive determination of $|V_{cb}|$ (Sect. 8.7) by approximately $3\,\sigma$ ($3.2\,\sigma$ for $|V_{cb}|$ from $B \to D^*\ell\nu$ and $2.4\,\sigma$ for $|V_{cb}|$ from $B \to D\ell\nu$), which clearly calls for further studies at Belle II.

As discussed in Sect. 8.5, lattice QCD already provides the full kinematic dependence of the $B \to D\ell\nu$ form factors [145,146,257], and corresponding work for $B \to D^*\ell\nu$ is underway [253]. Instead of CLN, these studies use the parameterization of Boyd, Grinstein, and Lebed (BGL) [322], which uses the same variable z but with no assumptions on the coefficients, apart from mild constraints stemming from unitarity in quantum mechanics.

There are indications that a change from CLN to BGL might shed light on the inclusive/exclusive discrepancy. Note that reporting only the CLN parameters, instead of the form factors bin by bin, impedes a simultaneous fit with lattice QCD data at $w > 1$. This is especially problematic for $B \to D\ell\nu$ where the experimental rate approaches zero at zero recoil with $\lambda^{3/2}$ instead of $\lambda^{1/2}$; cf. Eqs. (97) and (117). In Ref. [85], it was shown that the change from CLN to BGL together with the inclusion of lattice QCD results at $w > 1$ shifts $\eta_{\rm EW}|V_{cb}|$ from $(40.12 \pm 1.34) \times 10^{-3}$ to $(41.10 \pm 1.14) \times 10^{-3}$, i.e. towards the inclusive result. See also Refs. [145,146,257] for similar results. Furthermore, Ref. [323] presented a reanalysis of the preliminary Belle data of Ref. [324] and found that a change from CLN to BGL changes the fit result for $|V_{cb}|$ from $(38.2 \pm 1.5) \times 10^{-3}$ to $(41.7 \pm 2.0) \times 10^{-3}$, again compatible with $|V_{cb}|$ inclusive measurements. An investigation of unitarity bounds on the form factor parameters was performed in Ref. [260]. The recent untagged analysis of Belle [320] finds compatible results for the CLN and BGL parameterizations: $|V_{cb}|({\rm CLN}) = (38.4 \pm 0.9) \times 10^{-3}$, and $|V_{cb}|({\rm BGL}) = (38.3 \pm 1.0) \times 10^{-3}$.

Opportunities at Belle II The goal of Belle II for exclusive $|V_{cb}|$ is to see whether fits to lattice QCD and experimental results from the full kinematics agree in shape and, if so, obtain a robust determination. With current $\Upsilon(4S)$ datasets of order $1\,{\rm ab}^{-1}$, the limitation has been systematic uncertainties. Unless the detector performance is better understood at Belle II, the experimental uncertainties cannot be reduced. This is feasible, but requires careful examination of tracking efficiencies and particle identification. Recently, a tagged analysis of $B \to D^*\ell\nu$ using the full Belle dataset has become available, although its results are still preliminary [324]. Here, the experimental uncertainty in $|V_{cb}|$ is 3.5% compared to 2.9% in Ref. [325]. It should be noted that the main systematic uncertainty in the latter paper was on tracking efficiencies, which has since been improved threefold at Belle. In any case, the tagged analysis of $B \to D^*\ell\nu$ is approaching the precision of untagged measurements while still being limited systematically, due to the calibration of the hadronic tag. In summary, a reduction of systematic uncertainties at Belle II, namely of the hadronic tag calibration for tagged measurements, is required to improve current measurements of $|V_{cb}|$ exclusive. Belle II analyses of $B \to D^{(*)}\ell\nu$ can emphatically address the discrepancy between $|V_{cb}|$ inclusive and exclusive.

These modes can be precisely probed for new physics currents that may modify angular distributions or introduce phenomena such as lepton flavor universality violation [262]. Dedicated studies by experiment are yet to be performed, despite the rich offering of experimental information in these high-rate, high-purity decay modes. Crucially, Belle II must report results of measurements in parameterization-independent ways, i.e. by providing unfolded spectra or similar.

8.6.2. $B \to D^{**}\ell\nu$

Author: G. Ricciardi (th.)

The study of semi-leptonic decays to excited charm modes was an ongoing challenge in the B factories, yet knowledge of their contribution to the total decay width is a limiting uncertainty in $|V_{cb}|$ and semi-tauonic B decays.

The orbitally excited charm states $D_1(2420)$ and $D_2^*(2460)$ have relatively narrow widths, about 20–30 MeV/c^2, and have been observed and studied by a number of experiments (see Ref. [326] for the most recent study). The other two states, $D_0^*(2400)$ and $D_1'(2430)$, are more difficult to detect due to their large widths, about 200–400 MeV/c^2 [327–331]. The theoretical expectation is that the states with large width should correspond to $j^l = 1/2^+$ states, which decay as $D_{0,1}^* \to D^{(*)}\pi$ through S waves by conservation of parity and angular momentum. Similarly, the states with small width should correspond to $j^l = 3/2^+$ states, since $D_2^* \to D^{(*)}\pi$ and $D_1 \to D^*\pi$ decay through D waves. Decays such as $D_1 \to D^*\pi$ may occur through both D and S waves, but the latter are disfavored by heavy quark symmetry.

The spectroscopic identification of heavier states is less clear. In 2010 Babar observed candidates for the radial excitations of the D^0, D^{*0}, and D^{*+}, as well as the $L = 2$ excited states of the D^0 and D^+ [332]. Resonances in the 2.4–2.8 GeV/c^2 region of hadronic masses have also been identified at LHCb [333–336].

Most calculations, using sum rules [337,338], quark models [339–342], OPE [343,344] (but not constituent quark models [345]), indicate that the narrow width states should dominate over the broad D^{**} states. This is in contrast to experimental results: a tension known as the "1/2 vs. 3/2" puzzle. One possible weakness common to these theoretical approaches is that they are derived in the heavy quark limit and corrections might be large. For instance, it is expected that $1/m_c$ corrections induce a significant mixing between D_1 amd D_1', which could soften the 1/2 vs. 3/2 puzzle at least for the 1^+ states [346]. However, no real conclusion can be drawn until more data on the masses, widths, and absolute branching ratios of the orbitally excited D meson states become available. The other puzzle is that the sum of the measured semi-leptonic exclusive rates with a $D^{(*)}$ in the decay chain is less than the inclusive one (the "gap" problem) [331,347]. Decays into $D^{(*)}$ make up ∼70% of the total inclusive $B \to X_c l\bar{\nu}$ rate and decays into $D^{(*)}\pi$ make up another ∼15%, leaving a gap of about 15%. In 2014 the full Babar dataset was used to improve the precision on decays involving $D^{(*)}\pi\,\ell\,\nu$ and to search for decays of the type $D^{(*)}\pi\,\pi\ell\,\nu$. Preliminary results assign about 0.7% to $D^{(*)}\pi\,\pi\ell\,\nu$, reducing the significance of the gap from $7\,\sigma$ to $3\,\sigma$ [348].

The theoretical description of $B \to D^{**}\ell\nu$ channels has been investigated in Ref. [306]. Lattice QCD studies are in progress with realistic charm mass, while preliminary results on $\bar{B} \to D^{**}\ell\nu$ form factors are available [349–351].

Belle II must precisely isolate all four orbitally excited modes and characterize their sub-decay modes as accurately as possible to ultimately constrain and measure the branching ratios. Form factors must be determined in all modes through precise differential measurements. Complementary

information on the decay rates of orbitally excited modes should be extracted from hadronic B decays and include multi-pion and other light quark meson transitions.

8.6.3. $B \to \pi \ell \nu$

Authors: A. S. Kronfeld (th.), M. Lubej (exp.), A. Zupanc (exp.)

The aim for Belle II is to reach 1%-level determinations of $|V_{ub}|$ through a variety of experimental and theoretical approaches. In the case of $B \to \pi \ell \nu$, the challenge is that the experimental branching fraction measurements are most precise at low q^2, whereas the lattice QCD form factors are best determined at high q^2. Interpolating the results will rely on constraining form factor parameterizations. To obtain the best possible $|V_{ub}|$, the numerical lattice QCD form factor data must be extended to the full kinematic range, while the experimental measurement is expected to greatly improve with improved statistical power. An order of magnitude more data will allow precise tests of these lattice QCD predictions for the q^2 dependence. If the q^2 shapes of experiment and lattice QCD agree, it is straightforward to fit the relative normalization to obtain $|V_{ub}|$.

Measurements of decay rates of exclusive $B \to X_u \ell \nu_\ell$ decays, where X_u denotes a light meson containing a u quark, such as π, ρ, ω, $\eta^{(\prime)}$, etc., and ℓ an electron or muon, have in the past been performed using three different experimental techniques that differ only in the way the tag B meson in the event is reconstructed: tagged hadronic, tagged semi-leptonic, or untagged. In the rest of this subsection we present results of sensitivity studies on the determination of $|V_{ub}|$ through exclusive $B \to \pi \ell^+ \nu_\ell$ decays using the untagged and hadronic tagged reconstruction techniques of the $B_{\rm tag}$ performed with the Belle II MC5 sample.

Untagged measurement To reconstruct signal B candidates, good pion and lepton candidates are selected based on the responses of particle identification sub-detectors and by requiring that their momenta in the laboratory system exceeds 1 GeV/c. Improved K/π separation in Belle II allows for better $b \to c \to s$ rejection than in Belle or BaBar. The two charged daughter particles are required to originate from the same vertex. Under the assumption that the neutrino is the only missing particle, the cosine of the angle between the inferred direction of the reconstructed B and that of the $Y = \pi \ell$ system is

$$\cos\theta_{BY} = \frac{2E_B^* E_Y^* - M_B^2 - M_Y^2}{2p_B^* p_Y^*}, \tag{181}$$

where E^* and p^* are energy and three-momentum magnitude in the CMS system of the B and Y, respectively. The energy and momentum magnitude of the B meson are given by energy–momentum conservation and can be calculated as $E_B^* = E_{CMS}/2$ and $p_B^* = \sqrt{E_B^{*2} - M_B^2}$. Correctly reconstructed candidates should strictly populate the interval $|\cos\theta_{B,Y}| \leq 1$, although due to the detector resolution a small fraction of signal is reconstructed outside this interval. Background processes usually have more than one missing particle and therefore the angle is not constrained between -1 and 1. Due to detector resolution effects, we require $-1.2 < \cos\theta_{BY} < 1.1$ to ensure high efficiency.

The Belle II detector geometry hermetically covers a large portion of the full solid angle (approximately 90%), so we assume all remaining tracks and clusters in the rest of the event (ROE) originate from the tag $B_{\rm tag}$ meson. This $B_{\rm tag}$ candidate is not reconstructed in the same way as in tagged

analyses, but rather just by adding the four-momenta of the remaining tracks and clusters as

$$\mathrm{p}_{\mathrm{ROE}} = \sum_i (E_i, \boldsymbol{p}_i) + \sum_j \left(\sqrt{m_j^2 + p_j^2}, \boldsymbol{p}_j \right), \tag{182}$$

where the i and j indices run over all clusters and tracks not used in the reconstruction of the signal side, respectively. The mass hypothesis of track j, m_j, is determined based on the response of the PID sub-detectors. We take it to be the one with the highest posterior probability.

The missing four-momentum of the event is given as

$$\mathrm{p}_{\mathrm{miss}} = (E_{\mathrm{miss}}, \boldsymbol{p}_{\mathrm{miss}}) = \mathrm{p}_{e^+e^-} - \mathrm{p}_Y - \mathrm{p}_{\mathrm{ROE}}, \tag{183}$$

where $\mathrm{p}_{e^+e^-} = (E_{e^+e^-}, \boldsymbol{p}_{e^+e^-})$ denotes the four-momentum of the colliding beam particles. For correctly reconstructed candidates and only one missing neutrino, $\mathrm{p}_{\mathrm{miss}}$ should be equal to p_ν, with $\mathrm{p}_{\mathrm{miss}}^2 = m_\nu^2 = 0$. Due to resolution effects, the signal distribution peaks at zero with a non-zero spread.

With the neutrino momentum determined, we can attempt to correct the Y momentum to obtain the momentum of the signal B meson as

$$\mathrm{p}_B = \mathrm{p}_Y + (p_{\mathrm{miss}}, \boldsymbol{p}_{\mathrm{miss}}) = (E_B, \boldsymbol{p}_B), \tag{184}$$

where we have substituted the missing energy E_{miss} with the missing momentum magnitude p_{miss} due to better energy resolution.

With the B meson four-momentum we can calculate the B meson specific variables: M_{bc}, the beam-energy-constrained mass, and ΔE, the beam energy difference, defined in the laboratory frame as

$$M_{\mathrm{bc}} = \sqrt{\frac{(s/2 + \boldsymbol{p}_B \cdot \boldsymbol{p}_{e^+e^-})^2}{E_{e^+e^-}^2} - p_B^2}, \tag{185}$$

$$\Delta E = \frac{\mathrm{p}_B \cdot \mathrm{p}_{e^+e^-} - s/2}{\sqrt{s}}, \tag{186}$$

where $\sqrt{s}$ is the CMS energy.

The momentum transferred from the B meson to the leptonic part is calculated as $q^2 = (\mathrm{p}_B - \mathrm{p}_\pi)^2$. The q^2 resolution function is shown in Fig. 81. The resolution can be even further improved (reducing the root mean square of the resolution by around 20%) by taking into account the fact that the B momentum is kinematically constrained to lie on a cone around the Y pseudo-particle's momentum, and taking the weighted average over four possible configurations of the direction of the B meson.

It is not optimal to sum over all remaining calorimeter clusters and charged tracks in the event as indicated in Eq. (182) due to extra tracks and extra clusters from back-splashes, beam-background-induced interactions, and secondary interactions of primary particles produced in e^+e^- collisions. To select good tracks and reject those produced in secondary interactions of primary particles with the detector material, we train a boosted decision tree (BDT) using the following input: impact parameters in radial (d_0) and z directions (z_0) and their uncertainties, the track momentum p, cosine of the polar angle of the track ($\cos\theta$), number of hits in the vertex detector, track fit p-value, and the distance to the nearest cluster at the calorimeter radius. To reject beam-background-induced energy deposits in the calorimeter and back-splashes we train another BDT with the following input: energy deposited in a 3×3 block over that in a 5×5 block of calorimeter crystals, E_9/E_{25},

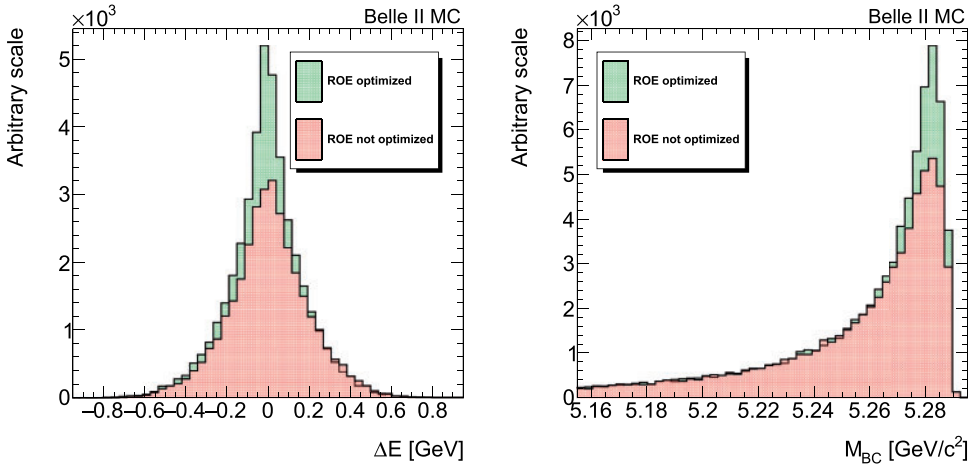

Fig. 79. The distributions of ΔE and $M_{\rm bc}$ for the untagged $B \to \pi \ell \nu$ analysis, with and without ROE optimization.

cosine of the polar angle of the cluster, $\cos\theta$, cluster timing, cluster energy, number of hits in the calorimeter, probability of the cluster coming from a π^0 particle, and distance to the nearest track hit at the calorimeter radius. As mentioned before, improper summation of tracks and clusters leads to degraded B candidate distributions, as shown in Fig. 79. To optimize the ROE selection based on an MVA output discriminant we use the criteria that maximize the signal purity in the ΔE signal region.

There are three major sources of background: quark continuum ($e^+e^- \to q\overline{q}$, $q = u,d,s,c$), Cabibbo-favored processes ($B \to X_c \ell \nu$), and other Cabibbo-suppressed processes other than $B \to \pi \ell \nu$ ($B \to X_u \ell \nu$). Suppressing each type of background requires separate treatment. Continuum events represent the easiest background category to suppress, since the event shape of continuum events is more jet-like, whereas $B\overline{B}$ events have a more isotropic event shape. For this background type we train four different BDT classifiers (defined in Sect. 6.4): (i) CLEO cones (event topology), (ii) Kakuno super Fox–Wolfram moments (event topology), (iii) output from (i) and (ii) with additional thrust-axis variables, and (iv) output from (iii) with additional B meson selection variables.

Additional B meson selection variables include the pion identification probability, the lepton helicity angle $\cos\theta_\ell$, the missing momentum polar angle $\theta_{\rm miss}$, the difference between the flight distances of the B mesons dz, the angle between the Y pseudo-particle and the z axis $\cos\theta_{BY}$, and an improved version of the $m^2_{\rm miss}$ variable, $m^2_{\rm miss}/2E_{\rm miss}$, where its resolution does not decrease with $E_{\rm miss}$. Each input variable was checked for its correlation with q^2, and all variables with a significant correlation were discarded. The optimal BDT output selection requirement is determined by maximizing a statistical power figure of merit. To suppress $b \to u\ell\nu_\ell$ background, we train another BDT. The final sample composition, after all selection criteria are applied, is shown in Fig. 80. The q^2-averaged signal efficiency is found to be around 20%. We identify signal candidates by performing a two-dimensional fit to $M_{\rm bc}$ and ΔE. The sample is then split into 13 bins of q^2 from 0 to $q^2_{\rm max} = 26.4\,{\rm GeV}^2/c^2$. We define the fit region as $M_{\rm bc} > 5.095\,{\rm GeV}/c^2$ and $|\Delta E| < 0.95\,{\rm GeV}$, and perform fits to extract the raw signal yield in each q^2 bin.

Tagged measurement In the tagged measurement we first require that the tag B meson is fully reconstructed in one of many potential hadronic decay modes. After finding a good $B_{\rm tag}$ candidate,

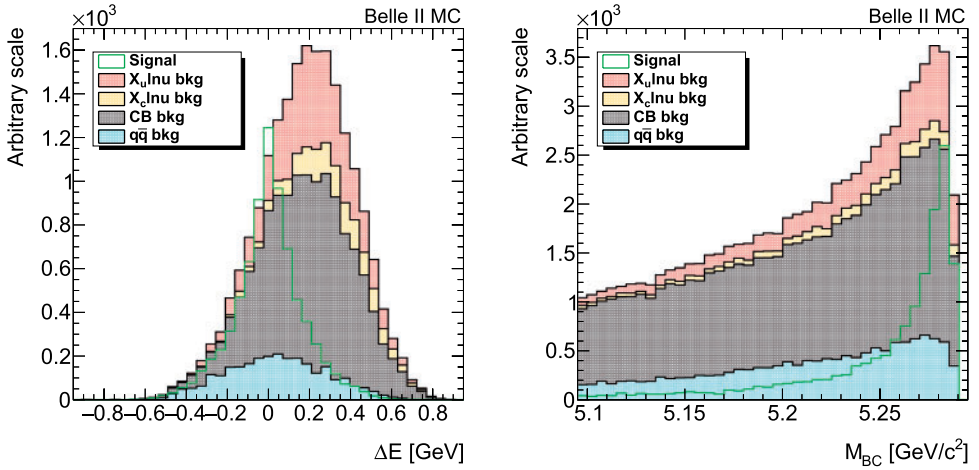

Fig. 80. The distributions of $M_{\rm bc}$ (with $|\Delta E| < 0.15\,\text{GeV}$) and ΔE (with $M_{\rm bc} > 5.27\,\text{GeV}/c^2$) with signal and background components for the full q^2 range. The signal is shown separately and set to the expected yield.

we require that the rest of the event is consistent with the signature of the signal decay; it contains only two additional oppositely charged tracks, one being consistent with the pion and one with the lepton hypothesis based on particle identification sub-detectors. The lepton charge must be consistent with the flavor of the decaying B. As in the case of the $B^+ \to \tau^+\nu_\tau$ study, we use $B_{\rm tag}$ candidates provided by the FEI algorithm (see Sect. 6.6) with a signal probability exceeding 0.1%. In the case of multiple $B_{\rm tag}B_{\rm sig}$ candidates we keep the combination with the $B_{\rm tag}$ candidate that has the highest signal probability. Since we measure the four-momentum of the tag B meson, we can infer the signal B meson four-momentum, the missing four-momentum of the neutrino produced in the signal decay, and the momentum transfer to the lepton system squared, q^2, as

$$\mathrm{p}_{B_{\rm sig}} = \mathrm{p}_{\Upsilon(4S)} - \mathrm{p}_{B_{\rm tag}}, \tag{187}$$

$$\mathrm{p}_{\rm miss} = \mathrm{p}_\nu = \mathrm{p}_{\Upsilon(4S)} - \mathrm{p}_{B_{\rm tag}} - \mathrm{p}_\pi - \mathrm{p}_\ell, \tag{188}$$

$$q^2 = (\mathrm{p}_\ell + \mathrm{p}_\nu)^2 = (\mathrm{p}_{B_{\rm sig}} - \mathrm{p}_\pi)^2 = (\mathrm{p}_{\Upsilon(4S)} - \mathrm{p}_{B_{\rm tag}} - \mathrm{p}_\pi)^2, \tag{189}$$

where we take the tag B meson four-momentum in the $\Upsilon(4S)$ frame to be

$$\mathrm{p}_{B_{\rm tag}} = (E_{\rm CMS}/2, \boldsymbol{p}_{B_{\rm tag}}). \tag{190}$$

The precise measurement of the momentum of the tag B meson results in an improved measurement of q^2 compared to the untagged measurement, as shown in Fig. 81. The overall reconstruction efficiency is found to be 0.55% in the MC sample, which is considerably above the reconstruction efficiency (0.3%) of the tagged measurement reported by Belle [84].

The signal is extracted from the missing mass squared distribution ($M^2_{\rm miss} = \mathrm{p}^2_{\rm miss}$), where the signal is expected to be located in a narrow peak near zero, while background from other $b \to u\ell\nu$ transitions populates a wider region towards higher missing mass, due to extra missing particles in the decay, as shown in Fig. 82. These processes can be further suppressed by requiring that there is little energy deposited in the calorimeter that cannot be associated to the decay products of the signal nor to the tag B. Alternatively, the signal can be extracted by performing a two-dimensional fit to $M^2_{\rm miss}$ and $E_{\rm extra}$ (see Fig. 83).

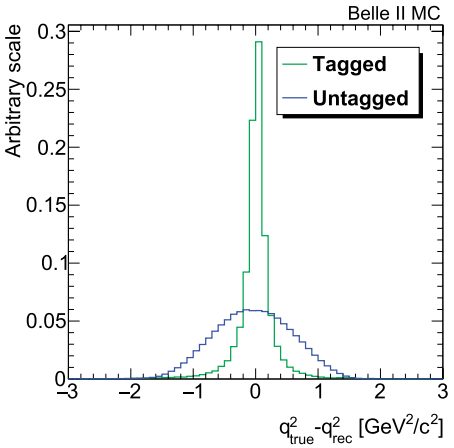

Fig. 81. Resolution of q^2 from untagged and tagged measurement of $B^0 \to \pi^- \ell^+ \nu_\ell$ decays.

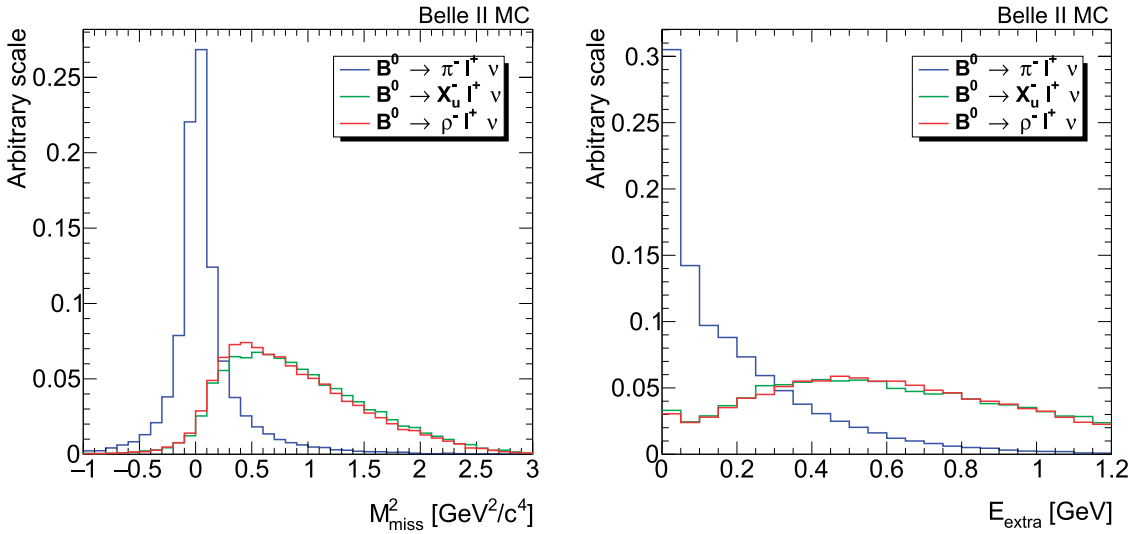

Fig. 82. The $M^2_{\rm miss} = {\rm p}^2_{\rm miss}$ (left) and $E_{\rm extra}$ (right) distributions of tagged $B^0 \to \pi^- \ell^+ \nu_\ell$ candidates as obtained from events containing signal $B^0 \to \pi^- \ell^+ \nu_\ell$ decays, and background $B^0 \to \rho^- \ell^+ \nu_\ell$ and $B^0 \to X_u^- \ell^+ \nu_\ell$ decays.

Systematic uncertainties A full breakdown of the systematic uncertainties of the tagged and untagged measurements is given in Table 53. In the tagged method, most systematic uncertainties are determined from purely data-driven techniques. Systematics due to background modeling from $B \to X_c \ell \nu$ and $B \to X_u \ell \nu$ (cross-feed) are reasonably small due to the high purity of the method. The untagged method suffers from low purity, which makes it more difficult to isolate signal from poorly understood cross-feed background. Although the quoted model uncertainties are already small, totaling less than 2% on the branching fraction, it would require far more detailed studies of the full $B \to X_u \ell \nu$ rate across q^2 to reliably reduce them further. The remaining irreducible uncertainty is derived from the normalization to the number of B mesons produced, shared between the Belle $N(B\overline{B})$ measurement and the production fraction f_{00}/f_{+-}. Although these are systematics-limited quantities, they can be improved with better experimental detection systematics and more orthogonal measurements. A conservative limit of 1% is assigned.

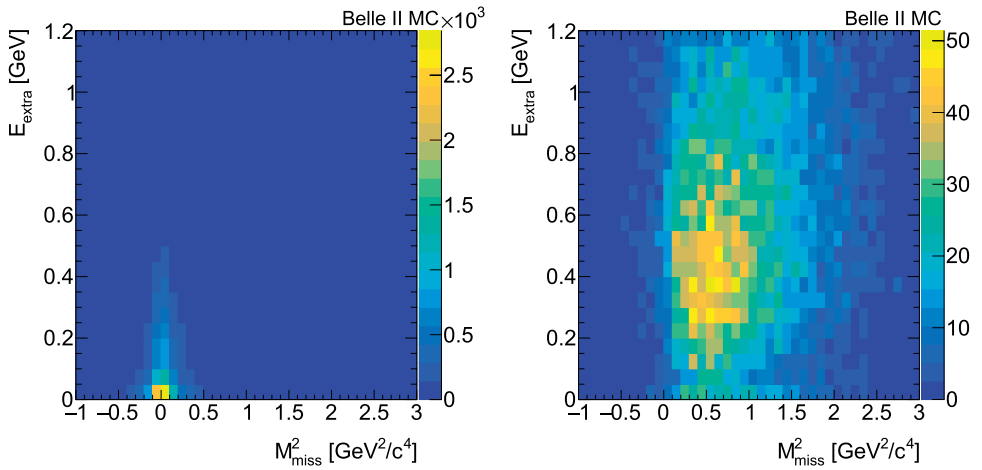

Fig. 83. The 2D $M^2_{\rm miss}$ and $E_{\rm extra}$ distribution of tagged $B^0 \to \pi^-\ell^+\nu_\ell$ candidates as obtained from events containing signal (left) and background $B^0 \to \rho^-\ell^+\nu_\ell$ decays (right).

Table 53. Summary of systematic uncertainties on the branching fractions of $B^0 \to \pi^-\ell^+\nu_\ell$ decays in hadronic tagged and untagged Belle analyses with 711 fb^{-1} [84] and 605 fb^{-1} [299] data samples, respectively. The estimated precision limit for some sources of systematic uncertainties is given in parentheses.

Source	Error (limit) [%]	
	Tagged	Untagged
Tracking efficiency	0.4	2.0
Pion identification	—	1.3
Lepton identification	1.0	2.4
Kaon veto	0.9	—
Continuum description	1.0	1.8
Tag calibration and $N_{B\bar{B}}$	4.5 (2.0)	2.0 (1.0)
$X_u\ell\nu$ cross-feed	0.9	0.5 (0.5)
$X_c\ell\nu$ background	—	0.2 (0.2)
Form factor shapes	1.1	1.0 (1.0)
Form factor background	—	0.4 (0.4)
Total	5.0	4.5
(reducible, irreducible)	(4.6, 2.0)	(4.2, 1.6)

8.6.4. $B_s \to K\ell\nu$

The decay $B^0_s \to K^-\ell^+\nu_\ell$ proceeds at the tree level in the SM via the flavor-changing charged-current $b \to u$ transition. The only difference between this decay and the $B \to \pi\ell\nu$ decays is in the spectator quark: a strange quark in $B^0_s \to K^-\ell^+\nu_\ell$ and a down (up) quark in $B_{d(u)} \to \pi^{-(0)}\ell\nu_\ell$ decays. Recently, several groups have performed lattice QCD calculations of the form factors in $B^0_s \to K^-\ell^+\nu_\ell$ decays [141,155]. Thus, precise measurements of the rate and q^2 dependence will provide an independent way to determine $|V_{ub}|$.

As can be seen from the SM predicted differential decay rate for $B^0_s \to K^-\ell^+\nu_\ell$ and $B \to \pi\ell\nu$ decays by the RBC and UKQCD collaborations [141] in Fig. 84, the predictions for $B^0_s \to K^-\ell^+\nu_\ell$ are more precise than those made for $B \to \pi\ell\nu$ decays. The decay $B^0_s \to K^-\ell^+\nu_\ell$ has not yet been measured, but it will be possible to measure it using data from an $\Upsilon(5S)$ run at Belle II.

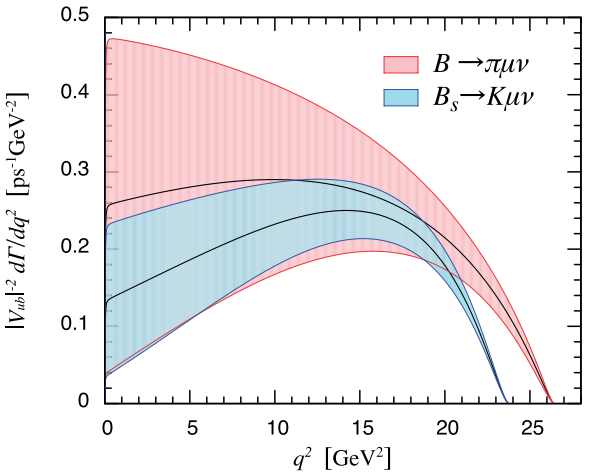

Fig. 84. Standard model predictions for the differential decay rate divided by $|V_{ub}|^2$ for $B_s^0 \to K^-\mu^+\nu_\mu$ and $B^0 \to \pi^-\mu^+\nu_\mu$ decays from Ref. [141].

The number of $B_s^{(*)}\overline{B}_s^{(*)}$ pairs produced in e^+e^- collisions at CMS energies near the $\Upsilon(5S)$ resonance is more than an order of magnitude lower than the number of $B\overline{B}$ pairs produced near the $\Upsilon(4S)$ center-of-mass energy ($E_{\rm CM}$) per ab^{-1}. The reason is due to the lower cross section for $b\bar{b}$ production at $E_{\rm CM}(\Upsilon(5S))$ (approximately 0.3 nb) and the low probability for $b\bar{b}$ to hadronize to $B_s^{(*)}\overline{B}_s^{(*)}$ pairs (about 20%). A data sample collected at $E_{\rm CM}(\Upsilon(5S))$ corresponding to 1 ab^{-1} would contain only around 60 million $B_s^{(*)}\overline{B}_s^{(*)}$ pairs, which makes the measurement of $B_s^0 \to K^-\ell^+\nu_\ell$ much more challenging due to a degraded signal-to-noise ratio and the high rate of $B_{u/d} \to X_c\ell\nu$ and $B_{u/d} \to X_u\ell\nu$ background. The untagged measurement approach is best suited for the study of $B_s^0 \to K^-\ell^+\nu_\ell$ decays.

The untagged measurement strategy described here follows the strategy described earlier for $B^0 \to \pi^-\ell^+\nu_\ell$ decays. The major difference with respect to the $B^0 \to \pi^-\ell^+\nu_\ell$ study is in the simulated sample. Here, we used Belle's simulated sample of $e^+e^- \to \Upsilon(5S) \to B_s^{(*)}\overline{B}_s^{(*)}, B^{(*)}\overline{B}^{(*)}, B^{(*)}\overline{B}^{(*)}\pi$, $B\overline{B}\pi\pi$, and $e^+e^- \to q\bar{q}$, as such samples were not yet available for Belle II at the time of writing. The Belle experiment's simulated samples, corresponding to a data sample of around 720 fb^{-1}, were converted to Belle II's data format and analyzed with the Belle II analysis software.

The reconstruction efficiency for signal $B_s^0 \to K^-\ell^+\nu_\ell$ decays is found to be 9.2%, while the background suppression rate for other processes is similar to that reported by previous $B^0 \to \pi^-\ell^+\nu_\ell$ untagged studies. The efficiencies for background $B_s^{(*)}\overline{B}_s^{(*)}$, $B\overline{B}X$, and $q\bar{q}$ events are found to be 1.9×10^{-4}, 3.2×10^{-4}, and 2.5×10^{-6}, respectively. The $M_{\rm bc}$ and ΔE distributions for accepted events are shown in Fig. 85. Fits to the $M_{\rm bc}$ and ΔE distributions in six bins of q^2 yields in total 2196 ± 165 signal events (setting $\mathcal{B}(B_s^0 \to K^-\ell^+\nu_\ell) = 1.5 \times 10^{-4}$ in the simulation), indicating that measurement of the decay rate can reach 5%–10% precision at Belle II with a 1 ab^{-1} data sample collected at $E_{\rm CM}(\Upsilon(5S))$.

8.6.5. $|V_{ub}|$ extraction

The value of $|V_{ub}|$ and its expected precision are extracted via a simultaneous fit to simulated data and lattice QCD predictions. Both inputs were used to construct a $\chi^2 = \chi^2_{\rm data} + \chi^2_{\rm QCD}$ function that was minimized. The fits of all three modes for $\mathcal{L} = 5$ ab^{-1} of simulated data are shown in Fig. 86. The values of $\sigma_{V_{ub}}$ for all three modes and projections to various values of integrated luminosity are

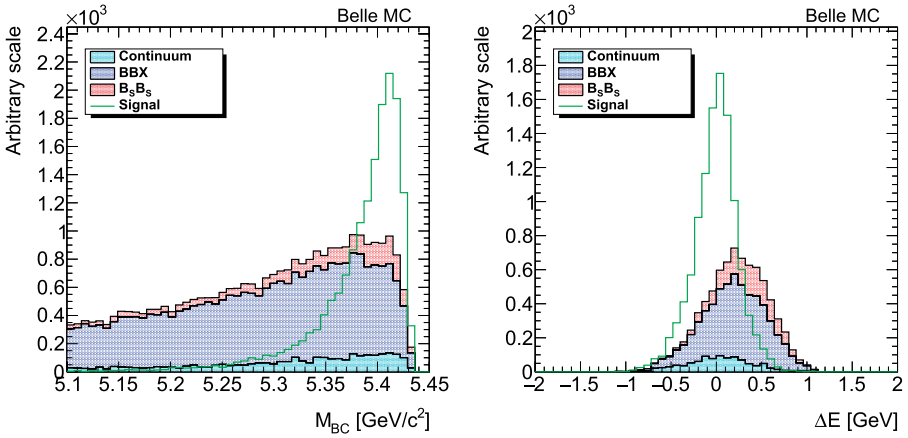

Fig. 85. $M_{\rm bc}$ and ΔE distributions of the $B_s \to K\ell\nu$ analysis over the full q^2 range, with signal and background components depicted separately and with arbitrary normalization. The signal component is not to scale with the background.

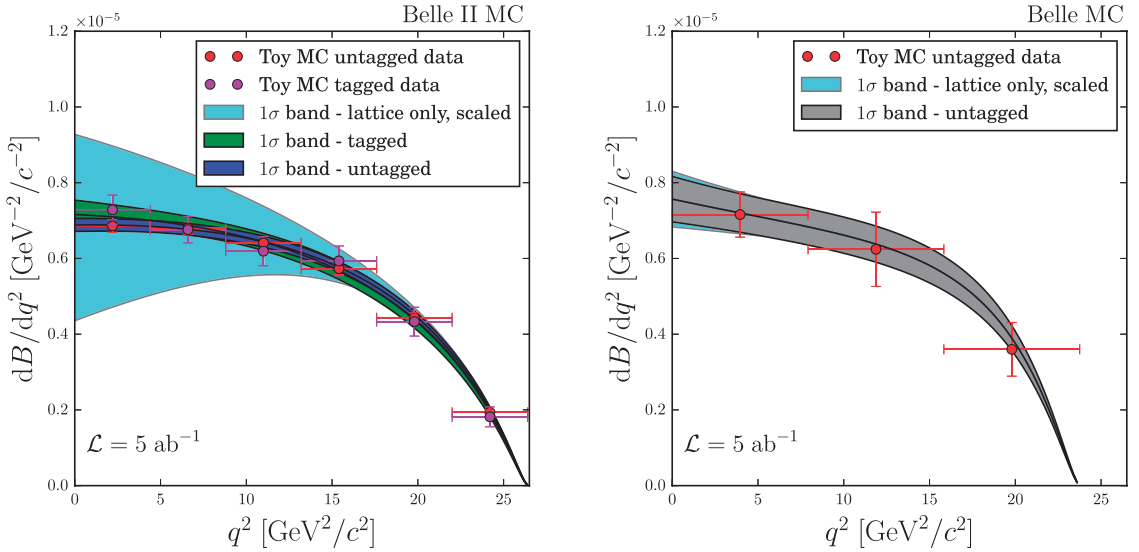

Fig. 86. Model-independent BCL fits ($N_{\rm par} = 3 + 1$) for $B \to \pi\ell\nu$ tagged and untagged (left) and $B_s \to K\ell\nu$ untagged (right) with 5 ab^{-1} data samples, and lattice QCD error forecasts in five years (w/EM).

shown in Tables 54 and 55. Lattice QCD uncertainties also have a large impact on the precision of $|V_{ub}|$, so efforts to reduce the lattice QCD uncertainties are expected in the future (see Sect. 7.5). Projections of $\sigma_{V_{ub}}$ for various cases of lattice QCD forecasts can be seen in Fig. 87.

8.7. Inclusive semi-leptonic

Authors: G. Ricciardi (th.), F. J. Tackmann (th.), P. Urquijo (exp.)

8.7.1. Overview

In inclusive semi-leptonic $B \to X\ell\nu$ decays one considers the sum over all possible kinematically allowed hadronic final states X. In the theoretical description the optical theorem then allows one to replace the sum over hadronic final states with a sum over partonic final states, which eliminates

Table 54. Projections of $|V_{ub}|$ uncertainties at various Belle II luminosities for $B \to \pi \ell \nu$ tagged (T) and untagged (UT) modes. All uncertainties are in %. Lattice QCD error forecasts were taken into account according to Sect. 7.5. The error in the second right-most column corresponds to forecasts with uncertainties due to EM corrections (Sect. 7), and the final column corresponds to forecasts without uncertainties due to EM corrections.

$\mathcal{L}$ [ab^{-1}]	Tag	$\sigma_{\mathcal{B}}$ (stat, sys)	$\sigma_{\text{QCD}}^{\text{forecast}}$	$\sigma_{V_{ub}}$ (EM)	$\sigma_{V_{ub}}$ (no EM)
1	T	3.6, 4.4	Current	6.2	—
	UT	1.3, 3.6		3.6	3.6
5	T	1.6, 2.7	In 5 yr	3.2	3.0
	UT	0.6, 2.2		2.1	1.9
10	T	1.2, 2.4	In 5 yr	2.7	2.6
	UT	0.4, 1.9		1.9	1.7
50	T	0.5, 2.1	In 10 yr	1.7	1.4
	UT	0.2, 1.7		1.3	1.0

Table 55. Projections of $|V_{ub}|$ uncertainties at various Belle II luminosities for the $B_s \to K \ell \nu$ untagged mode. All uncertainties are in %. Lattice QCD error forecasts were taken into account according to Sect. 7.5.

$\mathcal{L}$ [ab^{-1}]	$\sigma_{\mathcal{B}}$ (stat, sys)	$\sigma_{\text{QCD}}^{\text{forecast}}$	$\sigma_{V_{ub}}$ (EM)	$\sigma_{V_{ub}}$ (no EM)
1	6.5, 3.6	Current	6.5	
5	2.9, 2.2	In 5 yr	4.7	4.5

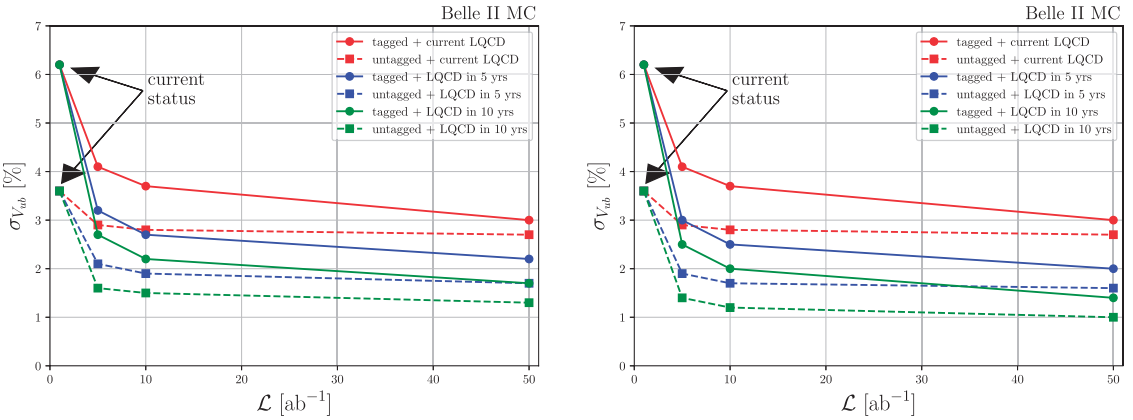

Fig. 87. Projections of the $|V_{ub}|$ uncertainty for various luminosity values and lattice QCD error forecasts for $B \to \pi \ell \nu$ tagged and untagged modes: (left) using lattice forecasts with EM corrections; (right) without these corrections.

any long-distance sensitivity to the final state. The short-distance QCD corrections, which appear at the typical scale $\mu \sim m_b$ of the decay, can be computed in perturbation theory.

The remaining long-distance corrections are related to the initial B meson. They can be expanded in the heavy quark expansion (HQE) in powers of $\Lambda_{\text{QCD}}/m_b \sim 0.1$, where Λ_{QCD} is a typical hadronic scale of order $M_B - m_b \sim 0.5$ GeV. This expansion systematically expresses the decay rate in terms of non-perturbative parameters that describe the universal properties of the B meson.

The non-perturbative parameters affect the differential decay rates from which $|V_{cb}|$ and $|V_{ub}|$ are extracted. Their dominant effect is on the shapes of the distributions, while $|V_{cb}|$ and $|V_{ub}|$ only enter

through the overall normalization. Hence, the strategy for a precise determination of $|V_{cb}|$ and $|V_{ub}|$ is to fit them together with the relevant non-perturbative parameters, as well as the b quark mass, from the experimental measurements.

The present inclusive $|V_{cb}|$ and $|V_{ub}|$ determinations are theoretically limited by imprecise knowledge of the required non-perturbative parameters. Hence, a key goal for Belle II will be to reduce this systematic limitation, in conjunction with theoretical improvements, by exploiting the large dataset to obtain precise and detailed measurements of differential distributions, ultimately mapping out the complete triple differential decay rate in p_ℓ, m_X^2, and q^2. In the case of $|V_{cb}|$, this effort will be focused on extending the scope of existing moment measurements. For $|V_{ub}|$, spectral information will be compared to theory for the first time in global analyses.

8.7.2. Inclusive $|V_{cb}|$ from $B \to X_c \ell \nu$

The perturbative calculations of the $B \to X_c \ell \nu$ differential decay rates are well established. The current global fits for $|V_{cb}|$ are performed to the measured moments of the lepton energy, E_ℓ, and hadronic mass, m_X^2 (with various minimum energy thresholds on the lepton) [230]. The most recent HFLAV global fit (in the kinetic scheme) extracts $|V_{cb}|$ together with the local OPE parameters appearing at $1/m_b^2$ and $1/m_b^3$ as well as the quark masses, yielding $|V_{cb}| = (42.19 \pm 0.78) \times 10^{-3}$.

The total uncertainty of about 2% is limited by the theoretical uncertainties, dominated by perturbative and power correction uncertainties. The fit is also very sensitive to the precise treatment of the theory uncertainty correlations in the predictions for the different moments [352]. The HFLAV fit uses theory predictions up to NNLO, while the $1/m_b^2$ and higher corrections are included at tree level. The complete power corrections up to $O(\alpha_s \times 1/m_b^2)$ are known, and including them in the global fit [353] leads to $|V_{cb}| = (42.19 \pm 0.78) \times 10^{-3}$. A similar result in Ref. [354] using external information on m_b finds $|V_{cb}| = (42.00 \pm 0.65) \times 10^{-3}$. The effect of the $1/m_b^4$ and $1/m_b^5$ corrections in the global fit have also been estimated [354] by constraining the large number of new parameters with the so-called lowest-lying state approximation (LLSA) [354–356]. They are found to have a minor effect, giving $|V_{cb}| = (42.11 \pm 0.74) \times 10^{-3}$. Further theoretical improvements are feasible through the calculation of the $O(\alpha_s \times 1/m_b^3)$ corrections and eventually the $O(\alpha_s^3)$ corrections.

Although the current global $|V_{cb}|$ fit is theoretically limited, more precise measurements of inclusive $B \to X_c \ell \nu$ at Belle II will be very valuable to scrutinize the inclusive $|V_{cb}|$ determinations, and help to resolve the tension between the inclusive and exclusive determinations. In particular, precise measurements of hadronic mass moments directly in bins of E_ℓ instead of a lower cut on E_ℓ would be useful to avoid unnecessary large statistical correlations in the measurements. Precise measurements of the E_ℓ spectrum, including the kinematic endpoint, should be performed, which will provide valuable insight into the eventual breakdown of the local OPE description. It may also be possible to obtain non-trivial constraints on the shape functions that are of primary relevance for inclusive $|V_{ub}|$ determinations [312]. In addition, measurements of other single differential spectra, such as the hadronic energy, E_X, neutrino energy, E_ν, and q^2 spectra will be useful to provide complementary kinematic information.

$B_s \to X_c \ell \nu$ from $\Upsilon(5S)$ data Both inclusive and semi-inclusive measurements of $B_s \to X_c \ell \nu$ have been performed by experiments to date. This class of measurements is not typically used for the extraction of $|V_{cb}|$ but rather the determination of B_s production rates at B factories and hadron colliders. A precise measurement of the B_s production fraction at $\Upsilon(5S)$ will allow measurements of the absolute branching fractions of channels that are used as normalization modes at LHCb. It is

also an important background to any future measurements of charmless semi-leptonic B_s decays at Belle II. Measurements of inclusive and semi-inclusive rates at Belle II would be based on data taken near the $\Upsilon(5S)$ resonance. Due to the relatively small values of the B_s production fraction, $f_s \approx 0.2$, and $\sigma(\Upsilon(5S)) \approx 0.3$ nb, these analyses suffer from a larger background than those of B mesons at the $\Upsilon(4S)$ resonance.

The inclusive semi-leptonic branching fraction of $B_s \to X\ell\nu$ decays was measured by BaBar and Belle [357,358] and found to be in agreement with the expectations from SU(3) flavor symmetry [359,360], which is also interesting to test more precisely. Such tests are crucial for understanding branching fraction predictions for B_s decays. Semi-inclusive analyses of $B_s \to D_s^- X\ell^+\nu$ and $B_s \to D_s^{*-} X\ell^+\nu$ decays and measurements of their branching fractions have been performed by the D0 [361], LHCb [362], and Belle experiments [363]. Belle also reported the first measurement of the semi-inclusive branching fractions $\mathcal{B}(B_s \to D_s X\ell\nu)$ and $\mathcal{B}(B_s \to D_s^* X\ell\nu)$ using its entire 121 fb^{-1} $\Upsilon(5S)$ dataset.

These measurements were limited by production rate uncertainties. In Belle II, B_s tagging methods on data samples in excess of 1 ab^{-1} will circumvent B_s normalization limitations and mitigate background from B mesons. With a sample of about 5 ab^{-1} we should expect to reach a statistical precision of 2% and systematic precision of about 4% using a hadronic tag. Other methods may be of greater use with smaller data sets, such as a D_s and/or lepton tag, but ultimately the hadronic tag is most effective in accurate absolute branching ratio measurements.

8.7.3. Inclusive $|V_{ub}|$

The current $|V_{ub}|$ measurements from BaBar, Belle, and CLEO generally exhibit tension with exclusive and CKM global fit determinations. The inclusive values vary depending on the kinematic fiducial region, which may be due to differences in theory treatment in these regions, or to experimental signal and background modeling imperfections. Above all, the goal for the measurement of $|V_{ub}|$ from inclusive $B \to X_u\ell\nu$ decays is to understand the persistent tension between exclusive and inclusive determinations. The large dataset at Belle II must be exploited to constrain the dominant sources of uncertainties, namely non-perturbative parameters in decay modeling, and final state hadronization effects.

Theoretical overview The theoretical description of inclusive $B \to X_u\ell\nu$ decays is based on the same underlying principles that are used for inclusive $B \to X_c\ell\nu$ decays. The total $B \to X_u\ell\nu$ rate can in principle be calculated in an OPE in terms of local operators, which has a similar structure as for the total $B \to X_c\ell\nu$ rate, with non-perturbative corrections first appearing at $O(1/m_b^2)$.

However, the primary challenge for the inclusive $|V_{ub}|$ determination is the overwhelming background from $B \to X_c\ell\nu$. As a result, the dominant experimental sensitivity to $B \to X_u\ell\nu$ and $|V_{ub}|$ is in the region of phase space where the $B \to X_c\ell\nu$ background is kinematically forbidden, namely the region where the hadronic X_u system has invariant mass $m_X \leq M_D$. Due to the much larger $B \to X_c\ell\nu$ rate, the residual background from mis-reconstructed $B \to X_c\ell\nu$ decays is still important in this region.

In this phase space region, non-perturbative corrections are kinematically enhanced, and as a result the non-perturbative dynamics of the decaying b quark inside the B meson becomes an $O(1)$ effect.

In addition to the lepton energy, E_ℓ, the decay kinematics can be described with the hadronic variables

$$p_X^+ = E_X - |\vec{p}_X|, \qquad p_X^- = E_X + |\vec{p}_X|, \tag{191}$$

where E_X and $\vec{p}_X$ are the energy and momentum of the hadronic system in the B meson rest frame. In terms of these, the total hadronic and leptonic invariant masses are given by

$$m_X^2 = p_X^+ p_X^-, \qquad q^2 = (M_B - p_X^+)(M_B - p_X^-). \tag{192}$$

The differential decay rate is given by

$$\frac{d^3\Gamma}{dp_X^+\, dp_X^-\, dE_\ell} = \frac{G_F^2 |V_{ub}|^2}{192\pi^3} \int dk\, C(E_\ell, p_X^-, p_X^+, k)\, F(k) + O\Big(\frac{\Lambda_{\rm QCD}}{m_b}\Big). \tag{193}$$

The photon energy spectrum in the inclusive rare decay $B \to X_s\gamma$ plays an important role in determinations of $|V_{ub}|$, as it is given in terms of the same leading shape function appearing in Eq. (193),

$$\frac{d\Gamma}{dE_\gamma} = |C_7^{\rm incl}|^2 |V_{tb} V_{ts}^*|^2 m_b^2 \int dk\, C(E_\gamma, k)\, F(k) + O\Big(\frac{\Lambda_{\rm QCD}}{m_b}\Big). \tag{194}$$

The "shape function" $F(k)$ is a non-perturbative function that describes the momentum distribution of the b quark in the B meson [364,365]. For $p_X^+ \sim k \sim \Lambda_{\rm QCD}$, which includes the endpoint region of the lepton energy spectrum as well as a large portion of the small-m_X region, the full shape of the non-perturbative component of $F(k)$ is necessary to obtain an accurate description of the differential decay rate. An essential property is that $F(k)$ is normalized to unity, such that it only affects the shape of the decay rate but not the normalization.

In addition to $F(k)$, several additional sub-leading shape functions appear at $O(\Lambda_{\rm QCD}/m_b)$ [366], and an even larger number of unknown shape functions appear at $O(\alpha_s \Lambda_{\rm QCD}/m_b)$ [367]. The differential decay rate contains three underlying hadronic structure functions, so there are effectively three independent combinations entering the description of $B \to X_u \ell\nu$.

For $p_X^+ \gg k \sim \Lambda_{\rm QCD}$, only the first few moments of $F(k)$ are needed, which recovers the expansion in terms of local OPE parameters. In practice, the experimental measurements can lie anywhere between these two kinematic regimes, which makes it important to have a consistent description across phase space.

The coefficient $C(E_\ell, p_X^-, p_X^+, k)$ in Eq. (193) describes the partonic quark decay $b \to u\ell\nu$ and can be computed in QCD perturbation theory. It is known up to NNLO. In the $b \to u$ sensitive region, $p_X^+ \ll p_X^-$, it also contains Sudakov double logarithms, $\ln^2(p_X^+/p_X^-)$, which can be resummed up to NNLL.

The unknown form of the shape function is a dominant systematic limitation in the inclusive $|V_{ub}|$ determination. An important parametric uncertainty is due to m_b. While the total decay rate scales as m_b^5, in the shape function region the dependence can be much stronger. A substantial part of the m_b dependence is entangled with $F(k)$ and enters indirectly via its first moment, which makes consistent treatment of $F(k)$ important.

For highly inclusive analyses the local OPE applies and the shape function becomes irrelevant, but the experimental analyses depend crucially on the signal modeling. References [368–371] have

Table 56. Status of inclusive $|V_{ub}|$ determinations from HFLAV [230].

	$(\lvert V_{ub}\rvert \times 10^3)$			
Measurement	BLNP [369–371]	GGOU [368]	DGE [373]	ADFR [374–376]
HFLAV 2016	$4.44 \pm 0.15^{+0.21}_{-0.22}$	$4.52 \pm 0.16^{+0.15}_{-0.16}$	$4.52 \pm 0.15^{+0.11}_{-0.14}$	$4.08 \pm 0.13^{+0.18}_{-0.12}$
Belle $p^*_\ell > 1$ GeV/c [377]	$4.50 \pm 0.27^{+0.20}_{-0.22}$	$4.62 \pm 0.28^{+0.13}_{-0.13}$	$4.62 \pm 0.28^{+0.09}_{-0.10}$	$4.50 \pm 0.30^{+0.20}_{-0.20}$
BaBar $p^*_\ell > 1$ GeV/c [378]	$4.33 \pm 0.24^{+0.19}_{-0.21}$	$4.45 \pm 0.24^{+0.12}_{-0.13}$	$4.44 \pm 0.24^{+0.09}_{-0.10}$	$4.33 \pm 0.24^{+0.19}_{-0.19}$
CLEO $2.1 < E_e < 2.6$ GeV [379]	$4.22 \pm 0.49^{+0.29}_{-0.34}$	$3.86 \pm 0.45^{+0.25}_{-0.27}$	$4.23 \pm 0.49^{+0.22}_{-0.31}$	$3.42 \pm 0.40^{+0.17}_{-0.17}$
Belle $1.9 < E_e < 2.6$ GeV [380]	$4.93 \pm 0.46^{+0.26}_{-0.29}$	$4.82 \pm 0.45^{+0.23}_{-0.23}$	$4.95 \pm 0.46^{+0.16}_{-0.21}$	$4.48 \pm 0.42^{+0.20}_{-0.20}$
BaBar $2.0 < E_e < 2.6$ GeV [381]	$4.51 \pm 0.12^{+0.41}_{-0.34}$	$3.92 \pm 0.10^{+0.23}_{-0.29}$	$3.81 \pm 0.10^{+0.18}_{-0.16}$	—

attempted to estimate the uncertainty stemming from the functional form of the shape function(s). They consistently found relatively small errors, and more advanced analyses [372] have ended up with only slightly larger uncertainties, at the level of a few percent. While we certainly need to understand the shape function(s), we also need to validate the existing theory frameworks on experimental data and the best way to do this is to measure kinematic distributions.

Measurements Existing inclusive $|V_{ub}|$ determinations are typically based on measurements of partial branching fractions in various fiducial kinematic regions. These regions have been chosen to balance between experimental statistical uncertainties and theoretical uncertainties, and to probe for inconsistencies in predictions of non-perturbative effects. Several theoretical approaches have been used to translate the measurements into $|V_{ub}|$, which differ in their treatment of perturbative corrections and the parametrization of non-perturbative effects, in particular in the shape function region. These are BLNP (Bosch, Lange, Neubert, Paz) [369–371], GGOU (Gambino, Giordano, Ossola, Uraltsev) [368], DGE (dressed gluon exponentiation by Andersen and Gardi) [373], and ADFR (Aglietti, Di Lodovico, Ferrera, Ricciardi) [374–376]. The former two use non-perturbative model functions to parameterize the shape functions, where the model parameters are adjusted to obtain the correct first non-perturbative moments such that the local OPE result is reproduced outside the shape function region. The latter two use perturbative models for the shape function. A detailed review can be found in Ref. [2].

Selected results are summarized in Table 56 with the HFLAV average [230]. Currently the most precise $|V_{ub}|$ determinations by both BaBar and Belle appear to come from the most inclusive measurements, which use 467 and 657 million $B\bar{B}$ pairs, respectively. These analyses rely on hadronic tagging, which provides flavor and kinematic information for inclusive reconstruction of the signal side. The signal is reconstructed by identifying a charged lepton then summing all tracks and neutral clusters in the event to form a hadron candidate. Selection criteria include charged and neutral kaon vetoes (events with $K^\pm$, K_S, but not K_L on the signal side are rejected), vetoes for events that contain slow pions likely to have originated from D^{*+} decays, and requirements for small missing mass. The signal yields are determined from simultaneous fits of the $b \to u$ signal and the dominant $b \to c$ background in the two-dimensional hadron mass m_X–q^2 distribution. The only explicit phase space

Table 57. Systematic errors (in percent) on the branching fractions for $B \to X_u \ell \nu$ in the hadron tagged sample, with 605 fb^{-1} of Belle data. The precision limit for some systematics is given in brackets.

Source	Error on $\mathcal{B}$ (irreducible limit)
$\mathcal{B}(D^{(*)}\ell\nu)$	1.2 (0.6)
Form factors ($D^{(*)}\ell\nu$)	1.2 (0.6)
Form factors and $\mathcal{B}(D^{(**)}\ell\nu)$	0.2
$B \to X_u \ell \nu$(SF)	3.6 (1.8)
$B \to X_u \ell \nu (g \to s\bar{s})$	1.5
$\mathcal{B}(B \to \pi/\rho/\omega \ell \nu)$	2.3
$\mathcal{B}(B \to \eta^{(\prime)} \ell \nu)$	3.2
$\mathcal{B}(B \to X_u \ell \nu)$ unmeasured/fragmentation	2.9 (1.5)
Continuum and combinatorial	1.8
Secondaries, fakes, and fit	1.0
PID and reconstruction	3.1
BDT/normalization	3.1 (2.0)
Total	8.1
(Total reducible)	7.4
(Total irreducible)	3.2

restriction on the extracted $B \to X_u \ell \nu$ branching ratio is the lower threshold on the lepton momentum, $E_\ell > E_{\rm min}$, with $E_{\rm min}$ as low as 0.8 GeV. However, these analyses do have many selection criteria that induce non-trivial dependence of the efficiency on decay dynamics. Therefore the fit and the detection efficiency both require knowledge of the $b \to u$ signal model, and since the sensitivity to $b \to u$ comes from the shape function region, this leads to direct dependence on the theoretical decay model. Direct sensitivity to the underlying theory model used in MC was studied in a recent BaBar analysis of the lepton energy spectrum [381]. A breakdown of the systematic uncertainties in the most recent Belle analysis is shown in Table 57, broken into reducible and irreducible components.

Normalization for $|V_{ub}|$ may reach a precision limitation due to calibration of the tagging method, although it can be measured as a ratio with $B \to X_c \ell \nu$ which will cancel some uncertainties. Systematics related to reconstruction efficiencies, fake leptons, and continuum are data driven and expected to improve with a larger dataset. Belle II's hadron tag is expected to perform better than that used in the previously published Belle inclusive analysis with about 3–4 times better efficiency.

A large fraction of the residual background is due to $B \to X_c \ell \nu$ events where the charm meson decays to a $K^0_{\rm L}$. It is difficult to reconstruct $K^0_{\rm L}$ mesons and model their hadronic interactions with the KLM and ECL. If precise measurements and reliable calibration of $K^0_{\rm L}$ identification can be performed in Belle II using high-rate control modes, it would greatly aid in purifying this analysis in the high-M_X region. Very few analyses to date have attempted to veto on the presence of $K^0_{\rm L}$ in the signal due to the large differences between data and MC simulation in hadronic interactions. Belle II should also look into vetoes of slow π^0 mesons from D^{*0} decays, and exploit improved low-momentum tracking for more efficient slow π^+ reconstruction.

Decay modeling and fragmentation Systematic uncertainties and biases introduced through model dependence are a very important consideration for Belle II measurements of this channel. Measurements must improve modeling, and improve robustness to fluctuations in modeling choices.

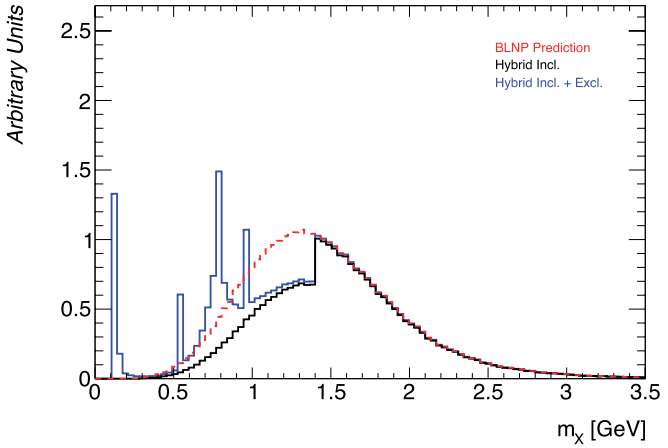

Fig. 88. Modeling of the $B \to X_u \ell \nu$ decay hadronic invariant mass, based on the BLNP [369–371] inclusive prediction (dashed red line) as well as the inclusive (solid black line) and inclusive plus exclusive cocktail (solid blue line) used commonly in MC simulations.

Table 58. The relative proportion of each $B \to X_s \gamma$ mode in the range $1.15\,\mathrm{GeV}/c^2 < M_{X_s} < 2.8\,\mathrm{GeV}/c^2$ in the data and default MC. The striking difference between default PYTHIA MC and data multiplicity must be addressed directly in inclusive $b \to u \ell \nu$ measurements.

Mode	Data	Default MC
$K\pi$ without π^0	4.2 ± 0.4	10.3
$K\pi$ with π^0	2.1 ± 0.2	5.4
$K2\pi$ without π^0	14.5 ± 0.5	12.9
$K2\pi$ with π^0	24.0 ± 0.7	15.2
$K3\pi$ without π^0	8.3 ± 0.8	5.9
$K3\pi$ with π^0	16.1 ± 1.8	15.7
$K4\pi$	11.1 ± 2.8	12.3
$K2\pi^0$	14.4 ± 3.5	14.4
$K\eta$	3.2 ± 0.8	4.9
$3K$	2.0 ± 0.3	3.0

$B \to X_u \ell \nu$ modeling is performed via an admixture of exclusive and inclusive contributions, as depicted in Fig. 88. Typically the exclusive component is comprised of well-measured contributions, such as $X_u = \pi, \rho, \eta, \omega$, but this is only around 20% of the total rate. The remainder is left to be modeled by an inclusive generator. Further measurements of the specific hadronic contributions to the semi-leptonic decay width are crucial.

Another effect not yet effectively addressed in previous $B \to X_u \ell \nu$ analyses is the fragmentation of the X_u system. Studies in recent Belle exclusive $B \to X_u \ell \nu$ and a semi-exclusive $B \to X_s \gamma$ analyses demonstrate that the nominal light quark fragmentation is different to that found in data. Both found that the probability for low-multiplicity final states to be produced is overestimated by PYTHIA (JETSET), as shown in Table 58. This can substantially affect reconstruction efficiencies and PDF shapes for branching fraction fits. To further constrain this effect, inclusive analyses will need to allow for a degree of freedom in hadron multiplicity, similar to the semi-exclusive approach pioneered in $B \to X_s \gamma$. Strange–anti-strange production, i.e. $B \to K\bar{K}\ell\nu$, is not constrained by experiment and yet kaon vetoes are commonly used in inclusive analyses. Such channels must be measured to reduce bias, as listed in Table 57.

The large dataset at Belle II will allow for differential measurements in kinematic observables, such as M_X^2, q^2, and p_ℓ, separately for both charged and neutral B decays. This provides important information to constrain uncertainties on shape functions, weak annihilation, and signal modeling. The inclusive analyses performed to date provide insufficient information to rule out any of the theoretical frameworks used in the extraction of $|V_{ub}|$, and hence new and better shape information is critical.

Model-independent measurements To take advantage of future theory improvements, measurements at Belle II should be performed and reported as independently of theoretical assumptions as possible. This will require measurements of differential spectra that fully characterize the transitions as in exclusive decays, e.g. q^2, θ_ℓ, m_X^2, p_ℓ. Such measurements have not been performed accurately by the B factories to date.

One of the quoted HFLAV averages is $|V_{ub}| = 4.62 \pm 0.20 \pm 0.29$ [230], which is obtained using the alternative BLL (Bauer, Ligeti, and Luke) [382] approach based on performing a local OPE calculation at large q^2, and is hence limited to measurements that use a cut in the m_X–q^2 plane. Weak annihilation contributions, which are concentrated at maximal q^2, seem to be strongly constrained by semi-leptonic charm decays [383–385]. Nevertheless, they remain a source of theoretical uncertainty that is hard to quantify here. Hence, precise separate measurements of charged and neutral B meson decays to constrain these contributions are well motivated at Belle II, as are direct searches for weak annihilation effects at high q^2.

Key inputs to these extractions are the values of the HQE parameters: the b quark mass, m_b, and the Fermi motion quantity, μ_π^2. These quantities are typically obtained from fits to moments in $B \to X_c \ell \nu$ inclusive decays, with additional constraints from either QCD calculations for m_c in the kinetic scheme, or from $B \to X_s \gamma$ inclusive decays. They can also be extracted from the heavy-quark-mass dependence of meson masses containing heavy and light quark pairs, computed in lattice QCD [167,169,386,387]. Measurement of the HQE parameters is limited by experimental precision and can be improved with dedicated analyses at Belle II with a larger dataset and smaller experimental systematic uncertainties.

$|V_{ub}|$ global fit Due to the intrinsic trade-off between experimental and theoretical cleanliness, there is no simple prescription for an optimal region of phase space in which to measure the partial branching fraction. Instead, the most precise and reliable inclusive $|V_{ub}|$ determination should exploit all available experimental and theoretical information. This is accomplished with a global fit to the full spectrum information to simultaneously extract the overall normalizations ($|V_{ub}|$ for $B \to X_u \ell \nu$ and $|C_7^{\rm incl}|$ for $B \to X_s \gamma$) together with the required parameters such as m_b and the leading (and eventually sub-leading) non-perturbative shape functions $F(k)$. In this way one minimizes the uncertainties and makes maximal use of all available data, and the fit automatically "chooses" the most sensitive region given the experimental and theoretical uncertainties.

Compared to the global $|V_{cb}|$ fit, a global $|V_{ub}|$ fit is more involved, since the non-perturbative quantities to be fitted are now continuous functions rather than a few numbers. For this reason it will be important to combine both $B \to X_u \ell \nu$ and $B \to X_s \gamma$ data and constraints on the shape function moments from the non-perturbative parameters extracted from $B \to X_c \ell \nu$.

Experimentally, this requires the precise measurement of as many independent differential spectra as possible to maximize the available shape information, which will be key to constraining sub-leading corrections. Interesting possibilities would be double differential measurements in

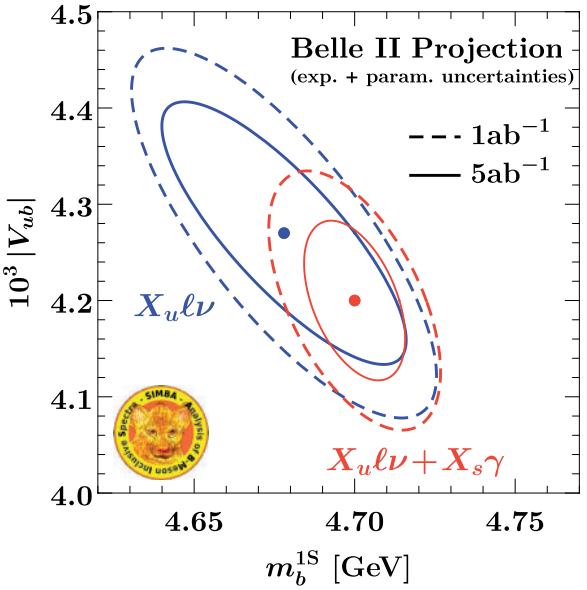

Fig. 89. Projections for a global $|V_{ub}|$ fit at Belle II with 1 ab^{-1} and 5 ab^{-1}. No theory uncertainties are included in the fit, which can be expected to be of similar size to the experimental ones.

E_ℓ and m_X, but also in other variables such as p_X^+, q^2, E_X, or E_ν. Ultimately one should aim to measure the full spectra of each of these quantities as precisely as possible. The separation of charged and neutral B mesons will also be important to understand effects such as weak annihilation.

Theoretically, the central ingredient for a global $|V_{ub}|$ fit is a model-independent treatment of the shape function, as was first proposed in Ref. [314]. More recently, artificial neural networks have been used to provide a very flexible and essentially model-independent parameterization of the shape function [372]. The important requirement is that it must be possible within the global fit to let the form of $F(k)$ as well as its uncertainties be characterized solely by the uncertainties in the included experimental measurements, such that any intrinsic limitations from model-dependent assumptions are avoided.

Using this approach, a global fit to all available $B \to X_s\gamma$ measurements extracting $|C_7^{\rm incl}|$ along with $F(k)$ has been performed in Ref. [316], demonstrating the feasibility of this approach.

Projections for a global fit using two projected single differential spectra in m_X and E_ℓ for $B \to X_u\ell\nu$ and an E_γ spectrum in $B \to X_s\gamma$ from Belle II at 1 ab^{-1} and 5 ab^{-1} are shown in Fig. 89. Projections with even higher integrated luminosity are hard to obtain, because they will require improvements in the experimental systematics.

The achievable precision will strongly depend on the precision and number of available spectra. The projected fit uncertainties at 1 ab^{-1} (5 ab^{-1}) are about 4.5% (3%) for the fit to $B \to X_u\ell\nu$ only and 3% (2%) for the combined fit to $B \to X_s\gamma$ and $B \to X_u\ell\nu$. These fit uncertainties already include the dominant parametric uncertainties from m_b and $F(k)$, and are constrained in the fit by the data. These projections do not include sub-leading shape function effects, which are expected to become relevant at this level of precision, but can also be constrained by measurements. Such effects were discussed and evaluated in Ref. [372]. In general, one can expect that Belle II data can and should be exploited to reduce the current theoretical uncertainties.

Table 59. Expected uncertainties in $|V_{ub}|$ measurements, given in percent, with the Belle full data sample, 5 ab^{-1} and 50 ab^{-1} Belle II data. Note that the statistical uncertainty quoted for exclusive $|V_{ub}|$ is that of the branching fraction; however, a fit to the spectrum information is typically used to determine $|V_{ub}|$. While we expect to eventually perform a $|V_{ub}|$ measurement with $B \to \mu\nu$, we do not list an estimate for total precision: there is no clearly established signal with the B factory data, and the searches suffered significant systematic uncertainties making it difficult to perform a reliable projection. We use the lattice QCD projected precision for the future data sets. The systematic error is reported as (reducible, irreducible).

	Statistical	Systematic	Total exp.	Theory	Total
$\|V_{ub}\|$ exclusive (had. tagged)					
711 fb^{-1}	3.0	(2.3, 1.0)	3.8	7.0	8.0
5 ab^{-1}	1.1	(0.9, 1.0)	1.8	1.7	3.2
50 ab^{-1}	0.4	(0.3, 1.0)	1.2	0.9	1.7
$\|V_{ub}\|$ exclusive (untagged)					
605 fb^{-1}	1.4	(2.1, 0.8)	2.7	7.0	7.5
5 ab^{-1}	1.0	(0.8, 0.8)	1.2	1.7	2.1
50 ab^{-1}	0.3	(0.3, 0.8)	0.9	0.9	1.3
$\|V_{ub}\|$ inclusive					
605 fb^{-1} (old B tag)	4.5	(3.7, 1.6)	6.0	2.5–4.5	6.5–7.5
5 ab^{-1}	1.1	(1.3, 1.6)	2.3	2.5–4.5	3.4–5.1
50 ab^{-1}	0.4	(0.4, 1.6)	1.7	2.5–4.5	3.0–4.8
$\|V_{ub}\|$ $B \to \tau\nu$ (had. tagged)					
711 fb^{-1}	18.0	(7.1, 2.2)	19.5	2.5	19.6
5 ab^{-1}	6.5	(2.7, 2.2)	7.3	1.5	7.5
50 ab^{-1}	2.1	(0.8, 2.2)	3.1	1.0	3.2
$\|V_{ub}\|$ $B \to \tau\nu$ (SL tagged)					
711 fb^{-1}	11.3	(10.4, 1.9)	15.4	2.5	15.6
5 ab^{-1}	4.2	(4.4, 1.9)	6.1	1.5	6.3
50 ab^{-1}	1.3	(2.3, 1.9)	2.6	1.0	2.8

A summary of projections for inclusive $|V_{ub}|$ is given in Table 59, in addition to the determinations based on exclusive and leptonic decay described earlier. Large ranges on the theoretical uncertainty of the inclusive method are due to variations in results from the contributing theory groups.

8.8. Conclusions

Belle II will have a lot to say on leptonic and semi-leptonic B meson decays. Precise measurements of the CKM matrix element magnitudes are crucial for pinning down the allowed level of CP violation in the SM, but much work must be done to resolve inconsistencies in approaches for both $|V_{ub}|$ and $|V_{cb}|$. Prospects are particularly good for improvements to $|V_{ub}|$, on inclusive and exclusive approaches, owing to more data and better particle reconstruction performance at Belle II. Highly significant anomalies in semi-tauonic modes should be confirmed or refuted after only 5 ab^{-1} of data. This will only be achievable if substantial effort is made to measure and carefully characterize the $B \to D^{**}\ell\nu$ background. Differential spectra will be measured with great precision, to probe possible new physics models. Measurements of leptonic B decays are yet to be seen with $5\,\sigma$ significance in either the tau or muon modes by a single experiment. The former is achievable with approximately 2 ab^{-1} at Belle II, and the latter is achievable with about 5 ab^{-1} (assuming the SM branching ratio). Many new opportunities for new physics searches will be opened up with more data.

9. Radiative and electroweak penguin B decays

Editors: T. Feldmann, U. Haisch, A. Ishikawa and J. Yamaoka
Additional section writers: W. Altmannshofer, G. Bell, C. Bobeth, S. Cunliffe, T. Huber, J. Kamenik, A. Kokulu, E. Kou, E. Manoni, M. Misiak, G. Paz, C. Smith, D. Straub, J. Virto, S. Wehle, and R. Zwicky

9.1. Introduction

Flavor-changing neutral current $b \to s$ and $b \to d$ processes continue to be of great importance to precision flavor physics. The FCNC processes proceed to lowest order via one-loop diagrams (called penguin or box diagrams) in the SM. Since new physics particles may enter the loop diagrams or even mediate FCNCs at tree level, the $b \to s$ and $b \to d$ transitions are sensitive to physics beyond the SM. Since final states involving photons or lepton pairs are both theoretically and experimentally clean, radiative and electroweak (EW) penguin B decays are an ideal place to search for new physics. The Belle II physics program in this area will focus on processes such as the inclusive $B \to X_{s,d}\gamma$ and $B \to X_{s,d}\ell^+\ell^-$ channels, as well as rare decays involving photons or neutrinos like $B_{d,s} \to \gamma\gamma$, $B \to K^{(*)}\nu\bar{\nu}$, $B_{d,s} \to \tau^+\tau^-$, and $B \to K^{(*)}\tau^+\tau^-$. Fully inclusive measurements of the $b \to s, d\,\gamma$ and $b \to s, d\,\ell^+\ell^-$ transitions are very difficult at LHCb, as is the detection of B meson decays into final states containing photon pairs, neutrinos, or taus. As a result, Belle II is the only experiment that can provide detailed information on the latter FCNC processes in the near future.

A second important physics goal of Belle II in the area of radiative and EW penguin B decays will be to provide independent tests of the anomalies recently uncovered by the LHCb and Belle experiments in the angular analysis of $B \to K^*\ell^+\ell^-$ [388–390] as well as in the determination of $R_K = \mathrm{Br}(B^+ \to K^+\mu^+\mu^-)/\mathrm{Br}(B^+ \to K^+e^+e^-)$ [391] and $R_{K^*} = \mathrm{Br}(B^0 \to K^{*0}\mu^+\mu^-)/\mathrm{Br}(B^0 \to K^{*0}e^+e^-)$ [392]. Some of these measurements have also been performed by ATLAS and CMS, although with less sensitivity [393–395]. In order to shed further light on the possible origin of the existing flavor anomalies, additional independent measurements are needed. Given that the reconstruction efficiency for electrons is comparable to that for muons thanks to the excellent electromagnetic calorimeter, the Belle II experiment is the natural place to perform such measurements.

In this section we discuss the theoretical basics and the Belle II sensitivity to the aforementioned decay modes. The chapter is organized as follows. In Sect. 9.1.1 the theoretical framework is provided, namely the effective Hamiltonian as well as a brief overview of the hadronic effects relevant to the radiative and the EW penguin decays. In Sect. 9.2, the inclusive and exclusive radiative decays, $b \to s\gamma$ and $b \to d\gamma$, are discussed. It becomes apparent in this section that at Belle II separation of $B \to \rho\gamma$ from $B \to K^*\gamma$ becomes more accurate due to the improved particle identification. In Sect. 9.3, double-radiative decays are examined. A first observation of $B \to \gamma\gamma$ decay may be possible during the early data-taking of Belle II. In Sect. 9.4 the inclusive and exclusive EW penguin decays, $b \to s\ell^+\ell^-$ decays, are reviewed. The Belle II experiment can play an important role to test the anomalies observed by LHCb in the angular observable of $B \to K^*\mu^+\mu^-$. Furthermore, Belle II will have access to the $B \to K^*e^+e^-$ channel with nearly the same sensitivity as $B \to K^*\mu^+\mu^-$, which will provide crucial additional information. The interplay of the inclusive and exclusive $B \to K^*\ell^+\ell^-$ and $B \to X_s\ell^+\ell^-$ decays is also stressed. In Sect. 9.5, decay channels which involve missing energy such as $B \to K^{(*)}\nu\bar{\nu}$ and $B_{d,s} \to \nu\bar{\nu}$ are discussed. An early discovery of $B \to K^{(*)}\nu\bar{\nu}$ is possible at Belle II. Possible dark matter interpretations of the missing energy signatures are also briefly analyzed.

9.1.1. Theoretical basics

Contributing authors: T. Feldmann and U. Haisch

Effective Hamiltonian After decoupling the top quark, the Higgs boson, and the EW gauge bosons, flavor-changing weak interactions relevant for the $b \to q\gamma$ transitions with $q = d, s$ can be described in the SM by the following effective Hamiltonian (see, e.g., Refs. [396,397]):

$$\mathcal{H}_{\rm eff}^{\rm SM} = -\frac{4G_{\rm F}}{\sqrt{2}}\,\lambda_t^{(q)}\left[\sum_{i=1}^{8} C_i\,Q_i + \kappa_q \sum_{i=1}^{2} C_i\,(Q_i - Q_i^u)\right]. \tag{195}$$

Here, $G_{\rm F}$ is the Fermi constant and we have defined $\kappa_q = \lambda_u^{(q)}/\lambda_t^{(q)} = (V_{uq}^* V_{ub})/(V_{tq}^* V_{tb})$. The crucial difference between the transitions with d quarks and s quarks in the final state stems from the distinct CKM hierarchy

$$\begin{aligned}
\lambda_u^{(s)} : \lambda_c^{(s)} : \lambda_t^{(s)} &= \mathcal{O}(\lambda^4 : \lambda^2 : \lambda^2),\\
\lambda_u^{(d)} : \lambda_c^{(d)} : \lambda_t^{(d)} &= \mathcal{O}(\lambda^3 : \lambda^3 : \lambda^3),
\end{aligned} \tag{196}$$

with the Wolfenstein parameter $\lambda \approx 0.225$ governing the sizes of the branching ratios and the respective hierarchies of different decay topologies.

Expressions for the current–current ($Q_{1,2}$), four-quark (Q_{3-6}), photonic dipole (Q_7), and gluonic dipole (Q_8) operators can be found, for instance, in Ref. [397]. We quote here the most important ones:

$$\begin{aligned}
Q_1 &= (\bar{q}_L\gamma_\mu T^a c_L)(\bar{c}_L\gamma^\mu T^a b_L),\\
Q_2 &= (\bar{q}_L\gamma_\mu c_L)(\bar{c}_L\gamma^\mu b_L),\\
Q_7 &= \frac{e}{16\pi^2}\,m_b(\bar{q}_L\sigma^{\mu\nu} b_R)F_{\mu\nu},\\
Q_8 &= \frac{g_s}{16\pi^2}\,m_b(\bar{q}_L\sigma^{\mu\nu} T^a b_R)G^a_{\mu\nu},
\end{aligned} \tag{197}$$

where e and g_s are the electromagnetic and strong coupling, $F_{\mu\nu}$ and $G^a_{\mu\nu}$ the $\mathrm{U}(1)_{\rm em}$ and $\mathrm{SU}(3)_c$ field strength tensors, T^a are color generators, and the indices L, R denote the chirality of the quark fields. The operators $Q^u_{1,2}$ appearing in Eq. (195) are obtained from $Q_{1,2}$ by replacing the c quark fields by u-quark.

The Wilson coefficients C_i in Eq. (195) contain the short-distance (SD) dynamics, i.e. physics from high energies, and can thus be calculated in perturbation theory. In the SM, they are first evaluated at the scale $\mu_w = \mathcal{O}(m_W)$ and then evolved down to $\mu_b = \mathcal{O}(m_b)$ using the renormalization group equations (RGEs) in the effective theory. At present, all the low-energy Wilson coefficients $C_i(\mu_b)$ relevant for $b \to q\gamma$ are known to NNLO in QCD, and include a resummation of logarithmically enhanced effects of $\mathcal{O}(\alpha_s^2)$ contributions [398].

In the case of the rare decays into two charged leptons, $b \to q\ell^+\ell^-$ with $\ell = e, \mu, \tau$, the SM operator basis in Eq. (195) has to be extended by two additional operators,

$$\begin{aligned}
Q_9 &= \frac{e}{16\pi^2}(\bar{q}_L\gamma_\mu b_L)(\bar{\ell}\gamma^\mu \ell),\\
Q_{10} &= \frac{e}{16\pi^2}(\bar{q}_L\gamma_\mu b_L)(\bar{\ell}\gamma^\mu\gamma_5 \ell),
\end{aligned} \tag{198}$$

while for the $b \to q\nu\bar{\nu}$ transitions only the single operator

$$Q_L^\ell = (\bar{q}_L \gamma_\mu b_L)(\bar{\nu}_{\ell L} \gamma^\mu \nu_{\ell L}) \tag{199}$$

is relevant. Also, in the case of the $b \to q\ell^+\ell^-$ modes the relevant low-energy Wilson coefficients $C_i(\mu_b)$ are known to NNLO accuracy within the SM [399–401], while in the case of $b \to q\nu\bar{\nu}$ only the NLO corrections are fully known [402,403].[24]

The effect of physics beyond the SM (BSM) to radiative and rare $b \to q$ transitions can enter Eq. (195) in essentially two ways: (i) through modified values for the high-scale Wilson coefficients C_i not necessarily aligned with the flavor coefficients $\lambda_t^{(q)}$, and/or (ii) through additional operators with different chirality and/or flavor structures compared to the SM.

Hadronic effects As it stands, the effective Hamiltonian in Eq. (195) only describes the weak decays at the parton level. The physics associated with long-distance (LD) dynamics requires evaluating hadronic matrix elements

$$\langle X_{d,s}\gamma\ (\ell^+\ell^-)|Q_i|B\rangle \tag{200}$$

of the operators Q_i, which contain non-perturbative QCD effects. A particular subtlety arises from the fact that in case of purely hadronic operators, the final state can also be generated by (real or virtual) photon radiation from internal lines during the hadronic transition. The theoretical description of hadronic corrections to the partonic decay crucially depends on the way these transitions are probed in terms of one or the other hadronic observable. In all cases one exploits the fact that the mass m_b of the decaying b quark is significantly larger than the typical hadronic scale set by (multiples of) the fundamental QCD scale $\Lambda_{\rm QCD} = \mathcal{O}(200\,{\rm MeV})$.

For fully inclusive observables, the heavy quark expansion (HQE) is equivalent to a local operator product expansion (OPE) [311,407] by which total decay rates can be expressed in terms of forward B meson matrix elements of local operators. Here, the partonic decay represents the leading term in a simultaneous expansion in powers of $\Lambda_{\rm QCD}/m_b$ and $\alpha_s(m_b)$. The OPE breaks down when one tries to calculate differential inclusive decay distributions near phase-space boundaries. A twist expansion involving forward matrix elements of non-local light cone operators (so-called shape functions) is then required to properly account for non-perturbative effects [364,365,408]. It was generally believed that all non-local operators reduce to local ones when the differential decay distributions are integrated over the entire phase space, but it was shown in Refs. [409,410] for $B \to X_s\gamma$ that this is not always the case. These non-local power corrections can be expressed in terms of soft functions or sub-leading shape functions. At present our knowledge of these functions is limited to their asymptotic behavior as well as constraints on their moments. In consequence, the precise impact of non-local power corrections is difficult to estimate in practice.

In the case of exclusive decay observables, B meson decays involving no energetic light hadrons can be described in heavy quark effective theory (HQET). At first approximation, the relevant hadronic quantities are given by $B \to X$ transition form factors, which can be obtained with reasonable accuracy from lattice QCD simulations; see Ref. [411] and references therein. In recent years,

[24] The smallness of NNLO effects in $B_s \to \mu^+\mu^-$ [404] suggests that in the case of $b \to q\nu\bar{\nu}$ such contributions should also have a very limited phenomenological impact. NLO EW effects similar to those studied in Refs. [405,406] are instead more relevant.

various lattice results have become available, e.g. $B \to \pi$ form factors [143,159], $B \to K$ form factors [158,412], and $B \to K^*$ and $B_s \to \phi$ form factors [413,414]. The lattice simulations are performed for high momentum transfer, $q^2 \geq 14\,\text{GeV}^2$, i.e. small hadronic recoil. Predictions for smaller values of the invariant mass q^2 of the lepton pair are then obtained by employing well-motivated extrapolations.

In many cases (notably for $B \to V\gamma$ decays), however, we are interested in situations where the energy transfer E_{recoil} to light hadrons in the final state is large, of the order of $m_b/2$. In these cases the systematic heavy-mass expansion leads to the concept of QCD (improved) factorization (QCDF) (cf. Refs. [415,416]). The predictive power of QCDF is limited by hadronic uncertainties related to the transition form factors and the light cone distribution amplitudes for the leading Fock states in the involved hadrons, as well as by power corrections in Λ_{QCD}/m_b. Form factors at large hadronic recoil can, for instance, be calculated with QCD light cone sum rules (LCSRs); for a review, see, e.g., Refs. [417,418]. Recent LCSR estimates include twist-three radiative and twist-four tree-level contributions, but have an accuracy of not better than 10%, which implies an uncertainty of at least 20% on the level of branching ratios (see, for instance, Ref. [419] for a recent discussion). More troublesome is the issue of power corrections. A naive dimensional estimate indicates that such contributions should be of the order of $\Lambda_{\text{QCD}}/E_{\text{recoil}}$, but the exact number is hard to quantify.

9.2. Inclusive and exclusive radiative penguin decays

9.2.1. Inclusive $B \to X_q\gamma$ decays

Contributing authors: M. Misiak and G. Paz

Experimental status The inclusive $B \to X_q\gamma$ decays provide important constraints on the masses and interactions of many possible BSM scenarios such as models with extended Higgs sectors or SUSY theories. Measurements of their CP-averaged and isospin-averaged branching ratios by BaBar [420–423] and Belle [424,425] led to the following combined results:

$$\text{Br}^{\text{exp}}_{s\gamma} = (3.27 \pm 0.14) \cdot 10^{-4}, \tag{201}$$

$$\text{Br}^{\text{exp}}_{d\gamma} = (1.41 \pm 0.57) \cdot 10^{-5}. \tag{202}$$

These are in perfect agreement with the corresponding SM predictions [426,427]:

$$\text{Br}^{\text{SM}}_{s\gamma} = (3.36 \pm 0.23) \cdot 10^{-4}, \tag{203}$$

$$\text{Br}^{\text{SM}}_{d\gamma} = \left(1.73^{+0.12}_{-0.22}\right) \cdot 10^{-5}. \tag{204}$$

The results in Eqs. (201)–(204) correspond to the photon energy cut $E_\gamma > E_0 = 1.6\,\text{GeV}$ in the decaying meson rest frame. The measurements have been performed at $E_0 \in [1.7, 2.0]\,\text{GeV}$ for $\text{Br}_{s\gamma}$, and at $E_0 \approx 2.24\,\text{GeV}$ for $\text{Br}_{d\gamma}$. Next, extrapolations down to $E_\gamma > E_0 = 1.6\,\text{GeV}$ were applied. Such extrapolations are unavoidable because the experimental background subtraction errors grow rapidly with decreasing E_0, while the theoretical non-perturbative uncertainties grow with increasing E_0.

In the average for $\text{Br}^{\text{exp}}_{s\gamma}$ given in Eq. (201), only the measurements at $E_0 = 1.9\,\text{GeV}$ have been chosen as an input, and the extrapolation factors from Ref. [428] have been used. The question as to whether uncertainties in these factors have been properly estimated awaits a devoted study [316,429, 430], especially in view of the upcoming more precise measurements at Belle II. The extrapolation

necessary for $\mathrm{Br}_{d\gamma}^{\mathrm{exp}}$ in Eq. (202) was performed in Ref. [431], following the method of Ref. [428]. In this case, the precision is much less of an issue given the large uncertainties in the original experimental result [421].

Basic formulas Theoretical calculations of $\mathrm{Br}_{q\gamma}$ within and beyond the SM are based on the equality

$$\Gamma(\bar{B} \to X_q\gamma) = \Gamma(b \to X_q^p\gamma) + \delta\Gamma_{\text{non-per}}, \tag{205}$$

where $\Gamma(b \to X_q^p\gamma)$ stands for the perturbative b quark decay rate with only charmless partons in the final state X_s^p (strangeness $= -1$) or X_d^p (strangeness $= 0$). As long as the photon energy cut E_0 is large (i.e. $E_0 \gtrsim 1\,\mathrm{GeV}$) but not too close to the endpoint $E_{\max} \approx 2.56\,\mathrm{GeV}$ (i.e. $E_{\max} - E_0 \gtrsim \Lambda_{\mathrm{QCD}}$), the non-perturbative effects accounted for by $\delta\Gamma_{\text{non-per}}$ remain under control, and constitute a correction at the few percent level [410,432]. However, to discuss their size in a meaningful manner, one needs to get rid of $m_{b,\mathrm{pole}}^5$ from the leading perturbative contribution $\Gamma(b \to X_q^p\gamma)$, as on-shell masses of quarks are ill-defined. For this purpose, a normalization to the semi-leptonic decay rate can be used. The SM results quoted in Eqs. (203) and (204) have been derived from the formula [433]

$$\mathrm{Br}_{q\gamma} = \mathrm{Br}_{c\ell\nu}\,\xi_q\,\frac{6\alpha}{\pi\,C}\Big[P_q(E_0) + N_q(E_0)\Big], \tag{206}$$

where $\xi_q = |V_{tq}^* V_{tb}/V_{cb}|^2$ is the relevant CKM factor, $\alpha = \alpha(0)$ is the electromagnetic coupling constant renormalized at $q^2 = 0$, $\mathrm{Br}_{c\ell\nu}$ stands for the CP-averaged and isospin-averaged branching ratio of the semi-leptonic $\bar{B} \to X_c\ell\bar{\nu}$ decay, and C represents the so-called semi-leptonic phase space factor

$$C = \left|\frac{V_{ub}}{V_{cb}}\right|^2 \frac{\Gamma(\bar{B} \to X_c\ell\bar{\nu})}{\Gamma(\bar{B} \to X_u\ell\bar{\nu})}. \tag{207}$$

The function $P_q(E_0)$ is defined by the ratio

$$\frac{\Gamma(b \to X_q^p\gamma) + \Gamma(\bar{b} \to X_{\bar{q}}^p\gamma)}{|V_{cb}/V_{ub}|^2\,\Gamma(b \to X_u^p e\bar{\nu})} = \xi_q\frac{6\alpha}{\pi}P_q(E_0). \tag{208}$$

In the $q = s$ case, the non-perturbative effects accounted for by $N_s(1.6\,\mathrm{GeV})$ in Eq. (206) enhance the central value of $\mathrm{Br}_{s\gamma}^{\mathrm{SM}}$ by around 3% [434], while the corresponding uncertainty amounts to about $\pm 5\%$ [410]. In the $q = d$ case, one encounters additional sources of uncertain hadronic effects that originate from the CKM-unsuppressed $b \to du\bar{u}\gamma$ transitions [432]. We shall come back to the issue of non-perturbative corrections after discussing the dominant perturbative term $P_q(E_0)$.

Theoretical calculations of $P_s(E_0)$ For $b \to s\gamma$, the CKM element ratio κ_s in Eq. (195) is small, changing $\mathrm{Br}_{s\gamma}^{\mathrm{SM}}$ by less than 0.3%. Barring this effect and the higher-order EW ones, $P_s(E_0)$ is given within the SM by

$$P_s(E_0) = \sum_{i,j=1}^{8} C_i^{\mathrm{eff}}(\mu_b)C_j^{\mathrm{eff}}(\mu_b)\,K_{ij}, \tag{209}$$

where $C_i^{\rm eff}$ are certain linear combinations of the Wilson coefficients C_i (cf. Ref. [426]). They differ from C_i only for $i = 7, 8$, and are fixed by the requirement that the leading-order (LO) $b \to s\gamma$ and $b \to sg$ amplitudes are proportional to $C_7^{\rm eff}$ and $C_8^{\rm eff}$.

To match the experimental precision, the symmetric matrix K_{ij} needs to be determined up to $\mathcal{O}(\alpha_s^2)$ in its perturbative expansion,

$$K_{ij} = \sum_{n=0}^{\infty} \left(\frac{\alpha_s(\mu_b)}{4\pi} \right)^n K_{ij}^{(n)}. \tag{210}$$

The quantities $K_{ij}^{(0)}$ and $K_{ij}^{(1)}$ are already known in a practically complete manner, with the latest contributions coming from Refs. [435,436]. As far as $K_{ij}^{(2)}$ are concerned, it is sufficient to restrict to the operators listed in Eq. (197) because the remaining ones are negligible at the NNLO level due to their small Wilson coefficients and other suppression factors. Currently complete NNLO expressions are available for $K_{77}^{(2)}$ [437–439] and $K_{78}^{(2)}$ [440,441] only. For $K_{ij}^{(2)}$ with $i,j \in \{1,2,8\}$, the two-body final state contributions are known in a complete manner, while the three-body and four-body contributions have been evaluated [442–444] in the Brodsky–Lepage–Mackenzie (BLM) [445] approximation.

It remains to discuss $K_{17}^{(2)}$ and $K_{27}^{(2)}$. The BLM approximations for these quantities have been established for some time [442,446]. The same is true for effects due to non-vanishing quark masses in loops on the gluon lines [447]. However, the generic non-BLM parts of $K_{17}^{(2)}$ and $K_{27}^{(2)}$ have been found so far only in two limiting cases for the c quark mass, namely $m_c \gg m_b/2$ [448,449] and $m_c = 0$ [426]. An interpolation between these two limits was performed in Ref. [426], leading to the conclusion that the considered non-BLM corrections are sizeable, enhancing $\mathrm{Br}_{s\gamma}^{\rm SM}$ by about 5%.

An uncertainty of $\pm 3\%$ due to the interpolation in m_c was included in the error budget of Eq. (203). It was added in quadrature to the other three uncertainties of $\mathrm{Br}_{s\gamma}^{\rm SM}$: non-perturbative ($\pm 5\%$), higher-order ($\pm 3\%$), and parametric ($\pm 2\%$). Future improvements in the accuracy of the perturbative calculations of $P_s(E_0)$ will require determining $K_{17}^{(2)}$ and $K_{27}^{(2)}$ for the physical value of m_c without any interpolation. A first step in this direction has been made in Ref. [450]. One should also investigate whether the quoted size of the non-perturbative uncertainties can be reduced by combining lattice inputs with measurements of observables like the CP and/or the isospin asymmetry (IA) in $B \to X_s\gamma$ (cf. the discussion after Eq. (215)). Improving both the uncertainty due to the interpolation in m_c and the non-perturbative errors by a factor of 2, the total uncertainty of $\mathrm{Br}_{s\gamma}^{\rm SM}$ would be reduced from around 7% to about 4%. Whether such theoretical improvements are possible in the near future remains to be seen.

The case of $\mathrm{Br}_{d\gamma}^{\rm SM}$ Extending the NNLO calculation to the case of $\mathrm{Br}_{d\gamma}^{\rm SM}$, one needs to take into account that, contrary to κ_s, the ratio κ_d is not numerically small. The global CKM fit in Ref. [451] implies that

$$\kappa_d = \left(0.007^{+0.015}_{-0.011}\right) + i\left(-0.404^{+0.012}_{-0.014}\right). \tag{211}$$

Due to the small value of $\mathrm{Re}\,\kappa_d$, terms proportional to $|\kappa_d|^2$ turn out to give the dominant κ_d effects in the CP-averaged $\mathrm{Br}_{d\gamma}^{\rm SM}$. In such terms, perturbative two-body and three-body final state contributions arise only at $\mathcal{O}(\alpha_s^2)$ and $\mathcal{O}(\alpha_s)$, respectively. They vanish for $m_c = m_u$, which implies that they

are suppressed by $m_c^2/m_b^2 \approx 0.1$. As a result, the main κ_d effect comes from four-body final states, namely from the $b \to du\bar{u}\gamma$ mode that appears already at tree level.

One way to calculate these contributions consists in evaluating the $b \to du\bar{u}\gamma$ diagrams including a common light quark mass m_q inside the collinear logarithms [444], and then to vary m_b/m_q between $10 \sim m_B/m_K$ and $50 \sim m_B/m_\pi$ to estimate the uncertainty. Such an approach leads to an effect of 2% to 11% on $\mathrm{Br}_{d\gamma}$. A more involved analysis with the help of fragmentation functions gives an almost identical range [432]. As a result, the SM prediction for $\mathrm{Br}_{d\gamma}$ in Eq. (204) is essentially insensitive to which of the two methods is used. The central value in that equation corresponds to the first method with $m_b/m_q = 50$.

Non-perturbative effects in $B \to X_q\gamma$ In discussing the non-perturbative effects in $B \to X_q\gamma$, one has to distinguish contributions from the interference of Q_7 with itself, and contributions from other operators. It is convenient to express the quantity $N_s(E_0)$ that was defined in Eq. (206) in terms of the Wilson coefficients; by analogy with Eq. (209),

$$N_s(E_0) = \sum_{i,j=1}^{8} C_i^{\mathrm{eff}}(\mu_b) C_j^{\mathrm{eff}}(\mu_b)\, S_{ij}. \tag{212}$$

For E_0 far from the endpoint region, S_{77} is parameterized by matrix elements of higher-dimensional local operators. These matrix elements are universal in the sense that they also contribute to semi-leptonic B decays. In consequence, one finds that

$$S_{77} = \sum_{n=2}^{\infty} \frac{1}{m_b^n} \sum_k c_{k,n} \langle O_{k,n} \rangle. \tag{213}$$

The $\langle O_{k,n} \rangle$ matrix elements scale as Λ_{QCD}^n, which implies that the power corrections start at power $\Lambda_{\mathrm{QCD}}^2/m_b^2$. The coefficients $c_{k,2}$ were calculated up to $\mathcal{O}(\alpha_s)$ in Refs. [452,453]. Their $\mathcal{O}(\alpha_s^0)$ parts [454,455] turn out to vanish due to accidental cancelation of corrections of this order to the radiative and semi-leptonic $B \to X_u \ell \bar{\nu}$ decays. The quantity S_{77} affects the SM prediction for $\mathrm{Br}_{s\gamma}$ in Eq. (203) by only around -0.3%, which includes the effect of the $\mathcal{O}(\alpha_s^0)$ coefficients $c_{k,3}$ [456]. The coefficients $c_{k,4}$ and $c_{k,5}$ have also been calculated at $\mathcal{O}(\alpha_s^0)$ [355], but the corresponding matrix elements are poorly constrained, and the resulting small correction has been neglected in Eq. (203).

In the endpoint region, the (Q_7, Q_7) interference part of the photon energy spectrum is described by the following symbolic factorization formula:

$$\frac{d\Gamma_{77}}{dE_\gamma} \sim H \cdot J \otimes S + \frac{1}{m_b} \sum_i H \cdot J \otimes s_i + \frac{1}{m_b} \sum_i H \cdot j_i \otimes S + \mathcal{O}\left(\frac{\Lambda_{\mathrm{QCD}}^2}{m_b^2}\right). \tag{214}$$

The hard functions H and jet functions J, j_i are calculable in perturbation theory. The shape functions S and s_i are non-perturbative and given in terms of non-local matrix elements. At the leading power, there is only a single shape function S. It is universal in the sense that it also appears for the endpoint region of semi-leptonic B decays [364,365,408]. The sub-leading shape functions s_i also contribute to the endpoint region of semi-leptonic B decays, but in a different linear combination. For the first term in Eq. (214), H [438] and J [457] are known up to $\mathcal{O}(\alpha_s^2)$. For the second term, H and J are known explicitly at $\mathcal{O}(\alpha_s^0)$ only [367,371,458] (see also Ref. [366]). For the third term, H is known at $\mathcal{O}(\alpha_s^0)$ and j_i at $\mathcal{O}(\alpha_s)$ [459]. As one integrates over the photon energy in

Eq. (214), the shape functions reduce to local operators and one obtains Eq. (213). Measurements of the $B \to X_s\gamma$ photon spectrum are being used in calculations that are necessary to extract $|V_{ub}|$ from $B \to X_u\ell\bar{\nu}$ [364,369,430,460,461]. These computations currently do not include uncertainties stemming from the resolved photon contributions (see below).

Non-perturbative effects from other pairs of operators are more complicated. Apart from the "direct" photon contribution arising from diagrams in which the photon couples directly to the weak vertex, there are also "resolved" photon contributions in which the photon couples to light partons. For example, Q_8 gives rise to the process $b \to sg \to s\bar{q}q\gamma$, and Q_2 leads to the process $b \to s\bar{c}c \to sg\gamma$. Such effects have been discussed in the literature [409,434,462–467] but were only studied systematically in Ref. [410]. Taking them into account, the photon spectrum in the endpoint region can be factorized symbolically as [410]

$$\frac{d\Gamma}{dE_\gamma} \sim H \cdot J \otimes S + H \cdot J \otimes s \otimes \bar{J} + H \cdot J \otimes s \otimes \bar{J} \otimes \bar{J}. \tag{215}$$

The first term in Eq. (215) is the direct photon contribution, similar to Eq. (214), while the terms in the second line correspond to the resolved photon contributions that start at order $\Lambda_{\rm QCD}/m_b$. The jet functions $\bar{J}$ are perturbative. The soft functions s are non-perturbative and, unlike the shape functions, they contain non-localities in two light cone directions.

In the integrated rate, the resolved photon contributions lead to $\Gamma \sim \bar{J} \otimes h$, where h are non-local matrix elements. At power $\Lambda_{\rm QCD}/m_b$, the only non-vanishing contributions to the integrated rate arise from S_{27}, S_{78}, and S_{88}. Conservative modeling gives a total of around 5% non-perturbative uncertainty in $\mathrm{Br}^{\rm SM}_{s\gamma}$ from the resolved photon contributions at $E_0 = 1.6\,\mathrm{GeV}$. Direct photon contributions to S_{ij} are smaller, and can be included in the 5% uncertainty estimate.

The resolved photon contributions are more important in the case of the CP asymmetry

$$A_{\rm CP} = \frac{\Gamma(\bar{B} \to X_s\gamma) - \Gamma(B \to X_{\bar{s}}\gamma)}{\Gamma(\bar{B} \to X_s\gamma) + \Gamma(B \to X_{\bar{s}}\gamma)}. \tag{216}$$

As shown in Ref. [468], they dominate over perturbative effects [469–472]. Within the SM, one obtains the prediction

$$A^{\rm SM}_{\rm CP} \in [-0.6, 2.8]\%, \tag{217}$$

while including perturbative effects alone would lead to an asymmetry of around 0.5%. Resolved photon contributions also imply that the difference between the CP asymmetries for charged and neutral B mesons are sensitive to new physics effects [468]. To linear order in the new physics contributions to the Wilson coefficients C_7 and C_8, and assuming that the dominant current–current contribution C_2 remains SM-like, one finds for the additive new physics contribution to $A_{\rm CP}$ the following approximate expression:

$$A^{\rm NP}_{\rm CP} \approx 0.05\,\mathrm{Re}\left(C^{\rm NP}_7\right) - 0.47\,\mathrm{Im}\left(C^{\rm NP}_7\right) + 0.24\,\mathrm{Im}\left(C^{\rm NP}_8\right). \tag{218}$$

This result implies that $A_{\rm CP}$ is a sensitive probe of new physics that leads to CP-violating contributions to the dipole operators Q_7 and Q_8. Such effects are only weakly constrained by the $B \to X_s\gamma$ branching ratio.

Currently, the main source of uncertainty in $\mathrm{Br}^{\rm SM}_{s\gamma}$ are the resolved photon contributions. The extraction of HQET parameters from $B \to X_c\ell\bar{\nu}$, as done in Ref. [354], can help to better control

the S_{27} contribution. By better measuring the IA in $B \to X_s\gamma$ defined as

$$\Delta_{0+} = \frac{\Gamma(B^0 \to X_s\gamma) - \Gamma(B^+ \to X_s\gamma)}{\Gamma(B^0 \to X_s\gamma) + \Gamma(B^+ \to X_s\gamma)}, \tag{219}$$

one can furthermore hope to pin down the S_{78} contributions, since these quantities are directly related [410,473]. Employing the so-called vacuum-insertion approximation (VIA) to estimate the relevant hadronic matrix element leads to the following SM prediction:

$$\Delta_{0+}^{\rm SM} \in [0.1, 7.4]\%, \tag{220}$$

where one should keep in mind that the VIA is a very rough approximation. Rather than comparing the SM prediction in Eq. (220) to future precise measurements of Δ_{0+} to look for new physics, it thus seems more advantagous to exploit the relation

$$\frac{N_s^{78}(E_0)}{P_s(E_0)} = -\frac{\Delta_{0+}}{3} \tag{221}$$

to experimentally constrain the size of the non-perturbative contribution $N_s^{78}(E_0)$ (or equivalent S_{78}) introduced in Eq. (206). New Belle II measurements of Δ_{0+} can therefore help to reduce the non-perturbative uncertainties in the SM prediction for $B \to X_s\gamma$, in particular if these measurements remain consistent with zero.

9.2.2. Measurements of $B \to X_s\gamma$

Contributing author: A. Ishikawa

There are two methods to reconstruct $B \to X_q\gamma$ decays. They will be referred to as the sum-of-exclusive method and the fully inclusive method. In the sum-of-exclusive method, the hadronic system is reconstructed from many exclusive decays containing a kaon, such as $Kn\pi$, $K\eta m\pi$, or $3Km\pi$, where $n \geq 1$ and $m \geq 0$. Hadronic candidates are then combined with a hard photon to reconstruct B meson candidates. In the fully inclusive method, the other B meson is usually tagged to improve the S/B ratio. One can require a fully reconstructed hadronic final state (hadronic tag), a fully reconstructed semi-leptonic decay (semi-leptonic tag), or only an energetic lepton (leptonic tag) from the B meson decay.

The prompt photons are selected as isolated clusters in the ECL that are not matched to any charged tracks. The polar angle of the photon direction must be within the barrel ECL region. The cluster shape is required to be consistent with an electromagnetic shower. In order to reduce contaminations from asymmetric $\pi^0/\eta \to \gamma\gamma$ decays, the photon candidate is paired with all other photons in the event. When the pair is consistent with π^0 or η, the prompt photon candidate is discarded. In the case of Belle, the signal yields for $E_\gamma > 1.9\,\text{GeV}$ with $711\,\text{fb}^{-1}$ are $13\,359 \pm 169$ for sum-of-exclusive and 8945 ± 240 for fully inclusive with lepton tagging. The errors are statistical only.

The two reconstruction methods have their own pros and cons, and provide access to different observables, as summarized in Table 60. Only the sum-of-exclusive method can specify that the transition was $b \to s$ (or $b \to d$), whereas the fully inclusive method can only ever measure the sum of $b \to s$ and $b \to d$ transitions. Reconstructing the other B meson decay determines the charges of the b quark and/or the spectator quark (d or u) in the signal B meson, which is required to measure direct CP and/or isospin violation.

The branching ratio of $B \to X_s\gamma$ was measured by BaBar [420,422,423,474], Belle [424,475], and CLEO [476]. The uncertainties of the measured branching ratios are systematically dominated.

Table 60. Observables accessible in $B \to X_q\gamma$ and the corresponding reconstruction methods. S/B: signal to background ratio; q: whether the spectator quark may be specified; p_B: whether the momentum of the signal B meson is measured.

Reconstruction	Tagging	Efficiency	S/B	q	p_B	A_{CP}	Δ_{0+}	ΔA_{CP}
Sum-of-exclusive	None	High	Moderate	s or d	Yes	Yes	Yes	Yes
Fully inclusive	Hadronic B	Very low	Very good	s and d	Yes	Yes	Yes	Yes
	Semi-leptonic B	Very low	Very good	s and d	No	Yes	Yes	Yes
	Leptonic	Moderate	Good	s and d	No	Yes	No	No
	None	Very high	Very bad	s and d	No	No	No	No

Given the expected large Belle II data sample, a reduction of systematic uncertainties is of utmost importance. For instance, at Belle, the dominant source of systematic uncertainties in the inclusive analysis with lepton tagging arises from neutral hadrons faking photons. Dedicated studies of the cluster shape in the calorimeter, which were not performed at Belle, allow us to constrain the contribution of the fake photons, or even reduce their contribution. At Belle II, it should be possible to reduce this uncertainty from 3.7% to 1.9% by these studies. A conservative estimate suggests that the total systematic uncertainty with a photon energy threshold of 1.9 GeV can be reduced from 5.3% to 3.2%.

So far, all measurements have required a photon energy threshold in the range of $[1.7, 2.0]$ GeV, extrapolating to the photon energy threshold of 1.6 GeV assuming a theoretical model. At Belle II, the branching ratio with a photon energy threshold of 1.6 GeV is directly measurable, removing the need to perform the extrapolation and in turn the corresponding source of systematic uncertainties. Lowering the photon energy threshold leads, however, to an increase in the size of the systematic uncertainty due to hadronic backgrounds. Thus, several energy thresholds will need to be considered in the future experimental analyses to better control this systematic uncertainty.

The photon spectrum in the B meson rest frame can be directly measured with a fully inclusive analysis with hadronic tagging, since the momentum of the B meson is known. Note that unfolding of the Doppler effect due to a finite B meson momentum in the $\Upsilon(4S)$ rest frame is needed in the case that a fully inclusive analysis with lepton tagging is performed. The hadronic tagging provides a straightforward approach to measure the moments of the photon energy spectrum. The uncertainty on the branching ratio measured with hadronic tagging is expected to be dominated by statistics at Belle due to the limited number of tagged B mesons. In view of the large dataset at Belle II, systematic uncertainties will instead dominate. In fact, as in the case of lepton tagging, the dominant source of systematic uncertainty arises from mis-reconstruction of neutral hadrons as photons. As a result the uncertainties of the branching ratio measurements with hadronic tagging will be comparable and strongly correlated with the uncertainty in the lepton tagging analysis.

The branching ratio measurement with the sum-of-exclusive method has different systematics compared to the fully inclusive analysis. The dominant sources of systematic uncertainties will be due to fragmentation and missing decay modes. Given the large dataset it should, however, be possible to reduce the latter source of uncertainty by including additional decay modes, but even then the accuracy of the branching ratio measurement via the sum-of-exclusive method is expected to be slightly lower than the uncertainty provided by fully inclusive analyses.

As already mentioned around Eq. (219), measurements of the isospin asymmetry Δ_{0+} could be useful to reduce the theoretical uncertainties of the branching ratio of $B \to X_q\gamma$. It

has been found in Refs. [409,473] that if a more precise measurement of Δ_{0+} turns out to stay near zero, that would help to significantly reduce the theoretical uncertainty. The BaBar collaboration measured $\Delta_{0+}(B \to X_s\gamma) = (-0.6 \pm 5.8 \pm 0.9 \pm 2.4)\%$ with the sum-of-exclusive method [477] and $\Delta_{0+}(B \to X_{s+d}\gamma) = (-6 \pm 15 \pm 7)\%$ with the fully inclusive method [420] with partial datasets of $81.9\,\text{fb}^{-1}$ and $210\,\text{fb}^{-1}$, respectively. Recently, Belle also measured $\Delta_{0+}(B \to X_s\gamma) = (-0.48 \pm 1.49 \pm 0.97 \pm 1.15)\%$ with the sum-of-exclusive method using a full data sample of $711\,\text{fb}^{-1}$ [478]. In the measurements, the first error is statistical, the second is systematic, and the third is due to the production ratio of B^+B^- and $B^0\bar{B}^0$ from $\Upsilon(4S)$ decay (f_{+-}/f_{00}). At Belle II, both the sum-of-exclusive method and the fully inclusive method with hadronic tagging can be performed. As an example, the sum-of-exclusive method can reduce the experimental uncertainty in Δ_{0+} down to 0.6% with $50\,\text{ab}^{-1}$ of data (see Table 61).

The dominant uncertainty of $\Delta_{0+}(B \to X_s\gamma)$ at Belle II will be of systematic origin and related to the ratio f_{+-}/f_{00}. The most promising method to measure f_{+-}/f_{00} without assuming isospin invariance in hadronic B decays is the use of double semi-leptonic decays, $\bar{B} \to D^*\ell^-\bar{\nu}$, as has been done by BaBar [479]. Belle II measurements of $\Delta_{0+}(B \to X_{s+d}\gamma)$ will instead be statistically limited.

Direct CP violation in $B \to X_{s+d}\gamma$ has also been measured in an inclusive analysis with lepton tagging. Belle has measured this quantity with the full dataset and the result is dominated by statistics, $A_{\text{CP}}(B \to X_{s+d}\gamma) = (1.6 \pm 3.9 \pm 0.9)\%$ for $E_\gamma > 2.1\,\text{GeV}$ [480]. At Belle II with $50\,\text{ab}^{-1}$ the statistical uncertainty will amount to 0.5%. The dominant source of systematic uncertainty from the asymmetry of the background can be assessed using increased data in background regions (so-called sidebands). A conservative estimate shows that a systematic uncertainty of 0.4% is reachable.

Both the sum-of-exclusive reconstruction and the fully inclusive reconstruction with hadronic tagging can determine the flavor and isospin of the parent in $B \to X_q\gamma$ decays. Such a separation is needed in order to study the direct CP violation and the difference of direct CP violation between the charged and neutral B mesons $\Delta A_{\text{CP}}(B \to X_q\gamma) = A_{\text{CP}}(B^+ \to X_q^+\gamma) - A_{\text{CP}}(B^0 \to X_q^0\gamma)$. Given that $\Delta A_{\text{CP}}(B \to X_s\gamma) \propto \text{Im}\,(C_8/C_7)$ [468], measurements of $\Delta A_{\text{CP}}(B \to X_s\gamma)$ provide sensitive probes of new physics.

As stated earlier, the theoretical uncertainty of the CP asymmetry in Eq. (216) is dominated by the contribution from resolved photons [468]. Precise measurement of A_{CP} hence allows us to constrain the size of non-local power corrections. The existing measurements of A_{CP} by BaBar and Belle with $429\,\text{fb}^{-1}$ and $711\,\text{fb}^{-1}$ use the sum-of-exclusive method and find $(+1.7 \pm 1.9 \pm 1.0)\%$ [481] and $(+1.71 \pm 1.26 \pm 0.21)\%$ [478], respectively. BaBar and Belle also measured $\Delta A_{\text{CP}} = (+5.0 \pm 3.9 \pm 1.5)\%$ for $E_\gamma > 2.1\,\text{GeV}$ [481] and $\Delta A_{\text{CP}} = (+3.69 \pm 2.65 \pm 0.76)\%$ for $E_\gamma > 1.9\,\text{GeV}$ [478], respectively.

Belle II can measure both A_{CP} and ΔA_{CP}, yet with a much larger dataset. A reduction of the systematic uncertainties is therefore crucial at Belle II. The systematic uncertainty due to the detector asymmetry can be reduced, in part due to the statistics of the larger data sample, since it is in practice determined from control samples or sideband events. The bias from the asymmetry due to peaking background can be expressed as the product of the number of peaking background events and the difference of A_{CP} between signal and peaking background. BaBar conservatively took all of the $B\bar{B}$ background events as contributing to the latter uncertainty. At Belle II it should be possible to obtain a more realistic estimate, since the CP asymmetries of both charged and neutral $B \to X_s\gamma$ decays and the dominant peaking backgrounds can be measured precisely. As a result, the achievable

accuracy of the measurement of $\Delta A_{\rm CP}$ is determined by the statistical uncertainty, for which a precision of 0.3% is expected. BaBar and Belle usually assumed that direct CP violation does not depend on the specific X_s decay mode, while Belle II can also test this assumption with its large dataset.

Belle II will also perform a measurement of $\Delta A_{\rm CP}(B \to X_{s+d}\gamma)$ using the fully inclusive reconstruction with hadronic tagging. With 711 fb^{-1}, about 300 ± 27 signal events are expected at Belle with the neutral B fraction of 52%, which corresponds to a 16% precision on $\Delta A_{\rm CP}$. At Belle II, the statistical uncertainty is still dominant even after including a factor of two improvement in the hadronic tagging efficiency.

9.2.3. Measurement of $B \to X_d\gamma$

Contributing author: A. Ishikawa

In contrast to $B \to X_s\gamma$, the inclusive $B \to X_d\gamma$ decay is experimentally largely unexplored. In consequence, Belle II is in the near future the only place to study the various $B \to X_d\gamma$ observables.

Since a fully inclusive analysis is impossible in the presence of the large $B \to X_s\gamma$ background, a measurement of $B \to X_d\gamma$ has to rely on the sum-of-exclusive method. BaBar, in Refs. [421], has managed to reconstruct $7X_d$ decay modes, 2π, 3π, and 4π modes with at most one neutral pion and $\pi^{\pm}\eta\,(\to \gamma\gamma)$ mode, and applied a hadronic mass cut of 2.0 GeV. At Belle II the statistical uncertainties will at some point be smaller than the systematic ones, and the increase in luminosity can be exploited to achieve a better understanding of the hadronic spectrum as well as the fragmentation of the X_d system, including missing modes to reduce the systematic uncertainties as done by the B factories in the sum-of-exclusive measurement of $B \to X_s\gamma$. In fact, the dominant systematic uncertainty from missing modes can be reduced to 10% by adding reconstructed decay modes, such as final states having five pions, two π^0, two kaons, and an η plus multiple pions or an η' plus multiple pions, as well as by applying a looser hadronic mass cut. The second and third largest uncertainties are of statistical origin (6%) and the systematic uncertainty due to fragmentation (5%). The total uncertainty on $\mathrm{Br}_{d\gamma}$ is expected to be around 14% with 50 ab^{-1} of integrated luminosity.

The observables $\Delta_{0+}(B \to X_d\gamma)$, $A_{\rm CP}(B \to X_d\gamma)$, and $\Delta A_{\rm CP}(B \to X_d\gamma)$ have up to now not been measured. In the asymmetries, large parts of the systematic uncertainties cancel out and the corresponding measurements will therefore be statistically limited at Belle II. With 50 ab^{-1} of data, the precision on $\Delta_{0+}(B \to X_d\gamma)$ can be estimated to be about 14%. The accuracy of $A_{\rm CP}$ is expected to be slightly worse than that of Δ_{0+} since flavor tagging of the other B^0 meson is needed for flavor non-eigenstate $B^0 \to X^0_{d\bar{d}}\gamma$ decays. By taking into account an effective flavor tagging efficiency of 30% and using the product of the mixing probability in the $B^0\bar{B}^0$ system, $\chi_d = 0.1875$, the anticipated precision of $A_{\rm CP}(B \to X_d\gamma)$ is 5%. The quoted uncertainty is dominated by the statistical uncertainty on $A_{\rm CP}(B^+ \to X^+_{u\bar{d}}\gamma)$, while the accuracy of a future $\Delta A_{\rm CP}$ measurement is dominated by the statistical uncertainty on $A_{\rm CP}(B^0 \to X^0_{d\bar{d}}\gamma)$ and amounts to roughly 11%.

A summary of the Belle II sensitivities for the various $B \to X_d\gamma$ channels is shown in Table 61.

9.2.4. Exclusive $b \to q\gamma$ decays

Contributing authors: E. Kou and R. Zwicky

Table 61. Sensitivities of observables for the radiative inclusive B decay. A photon energy threshold of $E_\gamma > 1.9\,\text{GeV}$ ($E_\gamma > 2.0\,\text{GeV}$) is assumed for the $B \to X_s\gamma$ ($B \to X_d\gamma$) analysis. Some sensitivities at Belle are extrapolated to $0.71\,\text{ab}^{-1}$. In the case of the branching ratios the quoted uncertainties are relative ones, while for Δ_{0+}, A_{CP}, and ΔA_{CP} they are absolute numbers.

Observables	Belle $0.71\,\text{ab}^{-1}$	Belle II $5\,\text{ab}^{-1}$	Belle II $50\,\text{ab}^{-1}$
$\text{Br}(B \to X_s\gamma)^{\text{lep-tag}}_{\text{inc}}$	5.3%	3.9%	3.2%
$\text{Br}(B \to X_s\gamma)^{\text{had-tag}}_{\text{inc}}$	13%	7.0%	4.2%
$\text{Br}(B \to X_s\gamma)_{\text{sum-of-ex}}$	10.5%	7.3%	5.7%
$\Delta_{0+}(B \to X_s\gamma)_{\text{sum-of-ex}}$	2.1%	0.81%	0.63%
$\Delta_{0+}(B \to X_{s+d}\gamma)^{\text{had-tag}}_{\text{inc}}$	9.0%	2.6%	0.85%
$A_{CP}(B \to X_s\gamma)_{\text{sum-of-ex}}$	1.3%	0.52%	0.19%
$A_{CP}(B^0 \to X^0_s\gamma)_{\text{sum-of-ex}}$	1.8%	0.72%	0.26%
$A_{CP}(B^+ \to X^+_s\gamma)_{\text{sum-of-ex}}$	1.8%	0.69%	0.25%
$A_{CP}(B \to X_{s+d}\gamma)^{\text{lep-tag}}_{\text{inc}}$	4.0%	1.5%	0.48%
$A_{CP}(B \to X_{s+d}\gamma)^{\text{had-tag}}_{\text{inc}}$	8.0%	2.2%	0.70%
$\Delta A_{CP}(B \to X_s\gamma)_{\text{sum-of-ex}}$	2.5%	0.98%	0.30%
$\Delta A_{CP}(B \to X_{s+d}\gamma)^{\text{had-tag}}_{\text{inc}}$	16%	4.3%	1.3%
$\text{Br}(B \to X_d\gamma)_{\text{sum-of-ex}}$	30%	20%	14%
$\Delta_{0+}(B \to X_d\gamma)_{\text{sum-of-ex}}$	30%	11%	3.6%
$A_{CP}(B^+ \to X^+_{u\bar{d}}\gamma)_{\text{sum-of-ex}}$	42%	16%	5.1%
$A_{CP}(B^0 \to X^0_{d\bar{d}}\gamma)_{\text{sum-of-ex}}$	84%	32%	10%
$A_{CP}(B \to X_d\gamma)_{\text{sum-of-ex}}$	38%	14%	4.6%
$\Delta A_{CP}(B \to X_d\gamma)_{\text{sum-of-ex}}$	93%	36%	11%

Preliminaries Radiative decays into light vector mesons $B_{(q,s)} \to V\gamma$ with $V = K^*, \rho, \omega, \phi$, represent prototypes of FCNC transitions. Promising candidates are $B_{(q,s)} \to (K^*, \phi)\gamma$ for $b \to s$ transitions and $B_{(q,s)} \to (\rho/\omega, \bar{K}^*)\gamma$ for $b \to d$ transitions.

To first approximation, only the matrix elements of the photonic dipole operator Q_7 in Eq. (197) enter, which are described by hadronic transition form factors for the $b \to q$ tensor currents. The remaining operators describe LD physics contributions from internal emission of the photon during the hadronic transition, and thus generically involve strong-interaction phases. There are three basic LD topologies. One originating from the gluonic dipole operator Q_8 and two from four-quark operators Q_{1-6}, referred to as weak annihilation (WA) and quark loop (QL) topologies in the following (see, e.g., Ref. [482, Sect. 2] for the relevant Feynman diagrams). The WA topology is only relevant if the valence quarks in the initial B and light vector meson matches the flavor structure of the respective four-quark operator in Eq. (195). In the QL topology two quarks from the four-quark operators with the same flavor are contracted to a closed loop from which the external photon and/or additional gluons can be radiated.

In QCDF the LD processes have been shown to factorize at LO in Λ_{QCD}/m_b and $\mathcal{O}(\alpha_s)$ [482–484]. An LCSR computation for the contribution of Q_8 at leading twist has been performed in Ref. [485], where a discussion of the relation to QCDF can also be found. WA has been computed in the LCSR approach in Refs. [486–488]. The computation of QL in LCSR is involved, and a hybrid treatment

of QCDF and LCSR has been presented in Ref. [488]. LD c quark loop contributions are a topic in their own right and will be discussed in more detail later on.

Unlike their semi-leptonic counterparts $B_{(q,s)} \to V\ell^+\ell^-$, to be discussed in Sect. 9.4.3, $B_{(q,s)} \to V\gamma$ decays do not lend themselves to a rich angular analysis. Instead, they are described by two helicity amplitudes corresponding to the two possible photon polarizations. Schematically, one has

$$H_\mp \propto \lambda_t^{(d,s)} \left\{ \begin{matrix} m_b \\ m_{(d,s)} \end{matrix} \right\} C_7\,(1+\delta_{\rm fac})\,T_1(0) + \sum_{U=u,c} \lambda_U^{(d,s)}\, L_\mp^U(0), \tag{222}$$

where $T_1(0)$ is the relevant $B \to V$ transition form factor, $\delta_{\rm fac}$ denotes factorizable QCD corrections, and $L_\mp^U$ stands for the previously discussed LD contributions (including the Wilson coefficients of the hadronic operators).

While in the SM the polarization of the photon is predominantly left-handed, leading to the hierarchy $H_- \gg H_+$, in models beyond the SM with right-handed currents this does not necessarily have to be the case. In fact, LHCb reported recently the first direct observation (with $5.2\,\sigma$ significance) that the photon is not unpolarized in $b \to s\gamma$ through a measurement of angular correlations in $B^\pm \to K^\pm\pi^\mp\pi^\pm\gamma$ [489]. This raises the question by how much Belle II can improve on this and future LHCb measurements. Concerning the sensitivity of the photon polarization to new physics, one should compare the prospects that exclusive $b \to s\gamma$ measurements have to those that arise from $B \to K^*\ell^+\ell^-$. Relevant articles in this context are, for instance,, Refs. [490–493].

The branching ratios for $B \to V\gamma$ decays are proportional to $|H_+|^2 + |H_-|^2$, where the form factor $T_1(0)$ in Eq. (222) provides a major part of the theoretical uncertainties. Numerically, they are estimated to be of $\mathcal{O}(4 \cdot 10^{-5})$ for the $b \to s$ transitions, while those for the $b \to d$ transitions are further suppressed by a factor of $\lambda^2 \approx 0.05$. In contrast, WA turns out to be sizeable for the $b \to d\gamma$ modes [494] as a result of the CKM hierarchies in Eq. (196).

Observables Because of the rather large hadronic uncertainties of more than 20%, the branching ratios $B \to V\gamma$ are not considered to be the most promising candidates for discovering BSM physics. On the other hand, since the uncertainties of individual modes are strongly correlated, considering ratios of branching ratios such as $R_{K^*\gamma/\phi\gamma} = {\rm Br}(B \to K^*\gamma)/{\rm Br}(B_s \to \phi\gamma)$ is advantageous from both theoretical and experimental points of view. The SM prediction for this ratio reads [488][25]

$$R^{\rm SM}_{K^*\gamma/\phi\gamma} = 0.78 \pm 0.18, \tag{223}$$

while the LHCb collaboration measured $R^{\rm exp}_{K^*\gamma/\phi\gamma} = 1.23 \pm 0.12$ [495,496]. The observed deviation of $2\,\sigma$ cannot be regarded as statistically significant, but it would be interesting to understand whether there can be a correlation to the discrepancies observed by LHCb in $B \to K^*\mu^+\mu^-$ and $B_s \to \phi\mu^+\mu^-$ (see, e.g., Refs. [388,389,497–499]). Another ratio of interest is $R_{\rho\gamma/K^*\gamma}$, which has been used for the first determinations of $|V_{td}/V_{ts}|$ [482,484,500]. After the precision measurements of B_s–$\bar{B}_s$ mixing, the extractions of $|V_{td}/V_{ts}|$ via $R_{\rho\gamma/K^*\gamma}$ are no longer competitive, however.

[25] The quoted theory uncertainty is improvable as correlations have only partially been taken into account in Ref. [488].

Other observables sensitive to BSM contributions to Eq. (195) are the IAs, and the direct and indirect CP asymmetries. The IAs can be defined as

$$a_I^{\bar{0}-} = \frac{c_V^2\,\Gamma(\bar{B}^0 \to \bar{V}^0\gamma) - \Gamma(B^- \to V^-\gamma)}{c_V^2\,\Gamma(\bar{B}^0 \to \bar{V}^0\gamma) + \Gamma(B^- \to V^-\gamma)}, \tag{224}$$

where $c_{\rho^0} = \sqrt{2}$ and $c_{K^{*0}} = 1$ are isospin symmetry factors. The IAs are essentially driven by two effects, both of them involving LD physics: (i) photon emission from the spectator quark which probes the different charge factors for u quarks and d quarks, and (ii) matrix elements of isotriplet combinations of hadronic operators in the effective Hamiltonian of Eq. (195). In order to accumulate more statistics one can define CP-averaged IAs through $\bar{a}_I = (a_I^{\bar{0}-} + a_I^{0+})/2$. Subtleties concerning the CP averaging of the IAs are discussed in Ref. [488].

Early analyses of the IAs in the framework of QCDF can be found in Refs. [482,484,501]. It turns out that the dominant SM contribution to Eq. (224) for $B \to K^*\gamma$ arises as a sub-leading effect in the HQE and involves the Wilson coefficients of Q_{1-6}. Compared to this, the effect of Q_8 is numerically suppressed, but in QCDF suffers from endpoint divergences of convolution integrals, which leads to rather large uncertainties. The problem of endpoint divergences can be avoided by determining the relevant matrix elements directly in the LCSR approach, which has been performed for the contributions of Q_8 in Ref. [485] and for the QL topologies in Ref. [488].

For exclusive $b \to d\gamma$ transitions the situation is somewhat different because the current–current operators $Q_{1,2}^u$ enter with unsuppressed CKM factors $\lambda_u^{(d)}$. Their relatively large annihilation contribution thus interferes with the naively factorizing contribution from the electromagnetic operator Q_7 proportional to $\lambda_t^{(d)}$. The resulting strong dependence of the IA of $B \to \rho\gamma$ on $\cos\phi_2$ was noted in Refs. [482,484], where approximate formulas can be found.

The most up-to-date theoretical predictions for the IAs are [488]

$$\bar{a}_I^{\rm SM}(K^*\gamma) = (4.9 \pm 2.6)\,\%, \qquad \bar{a}_I^{\rm SM}(\rho\gamma) = (5.2 \pm 2.8)\,\%. \tag{225}$$

Notice that the former prediction is consistent with the HFLAV average $\bar{a}_I^{\rm exp}(K^*\gamma) = (6.3 \pm 1.7)\%$ [230], whereas the latter is in slight tension with $\bar{a}_I^{\rm exp}(\rho\gamma) = (30^{-13}_{+16})\%$, albeit with considerable uncertainty. Notice that HFLAV uses the definition $\Delta_{\rho\gamma} = -2\bar{a}_I(\rho\gamma)/\,(1 + \bar{a}_I(\rho\gamma))$ instead of $\bar{a}_I(\rho\gamma)$. The closeness of the two values in Eq. (225) is a consequence of the CKM angle ϕ_2 being roughly 90°, which suppresses the abovementioned interference term. This can be exploited to define the observable [488]

$$1 - \delta_{a_I} = \frac{\bar{a}_I(\rho\gamma)}{\bar{a}_I(K^*\gamma)} \sqrt{\frac{\bar{\Gamma}(B \to \rho\gamma)}{\bar{\Gamma}(B \to K^*\gamma)}}\left|\frac{V_{ts}}{V_{td}}\right|, \tag{226}$$

where δ_{a_I} is close to zero, and the quantity $(1 - \delta_{a_I})^{\rm SM} = 0.90 \pm 0.11$ shows a reduced uncertainty with respect to the individual CP-averaged IAs introduced in Eq. (225). The experimental average $\delta_{a_I}^{\rm exp} = -4.0 \pm 3.5$ [488] can be improved at Belle II through more statistics as well as taking into account experimental correlations. The sensitivity of Eq. (226) to BSM physics has been studied in Ref. [488] in a model-independent fashion.

At Belle II, one can study the time-dependent CP asymmetries [502]

$$A_{\rm CP}(t) = \frac{\Gamma(\bar{B} \to f\gamma) - \Gamma(B \to f\gamma)}{\Gamma(\bar{B} \to f\gamma) + \Gamma(B \to f\gamma)} = \frac{S_{f\gamma}\sin(\Delta m_q t) - C_{f\gamma}\cos(\Delta m_q t)}{\cosh\left(\frac{\Delta\Gamma_q t}{2}\right) - H_{f\gamma}\sinh\left(\frac{\Delta\Gamma_q t}{2}\right)}, \tag{227}$$

where f ought to be a CP eigenstate as otherwise the effect washes out. Note that the width difference $\Delta\Gamma_q$ can be safely neglected for B_d, but this is not the case for B_s. This feature leads to the new observables $H_{f\gamma}$ [503]. The mixing-induced asymmetries $S_{f\gamma}$ arise from the interference between $B(\bar{B}) \to f\gamma$ and $B(\bar{B}) \to \bar{B}(B) \to f\gamma$ amplitudes and read

$$S_{V\gamma} = \frac{2\,\xi_V \mathrm{Im}\left[\frac{q}{p}\left(\bar{H}_+ H_+^* + \bar{H}_- H_-^*\right)\right]}{|H_+|^2 + |H_-|^2 + |\bar{H}_+|^2 + |\bar{H}_-|^2}, \tag{228}$$

where ξ_V is the CP eigenvalue of V, p and q relate the physical and flavor eigenstates, $H_\pm$ were defined in Eq. (222), and $\bar{H}_\pm$ are the corresponding amplitudes of the conjugate decay. At Belle II, one can expect a significant improvement in the determination of $A_{\mathrm{CP}}(t)$ in the channels such as $f = K_S^0\pi^0, \pi^+\pi^-$ mediated by K^* and ρ resonances, which will be discussed in some more detail.

Before embarking on the discussion of LD contributions, we first give predictions for Eq. (228) including SD effects only. Using $q/p \approx e^{-2i\phi_1}$, one obtains

$$S^{\mathrm{SM,SD}}_{K^*(K_S^0\pi^0)\gamma} = -2\,\frac{m_s}{m_b}\,\sin 2\phi_1, \qquad S^{\mathrm{SM,SD}}_{\rho^0(\pi^+\pi^-)\gamma} = 0. \tag{229}$$

Numerically, $S^{\mathrm{SM,SD}}_{K^*(K_S^0\pi^0)\gamma} = \mathcal{O}(-3\%)$, while the quantity $S^{\mathrm{SM,SD}}_{\rho^0(\pi^+\pi^-)\gamma}$ vanishes because the CP-odd oscillation phase ϕ_1 cancels exactly against the phase from the helicity amplitude. Examples of BSM models which can induce sizeable right-handed currents consistent with the constraint from $\mathrm{Br}(B \to X_s\gamma)$ include left–right symmetric models [502,504,505] and a SUSY SU(5) grand unified theory with right-handed neutrinos [505]. A model-independent study can be found in Ref. [490]. In the presence of a right-handed magnetic penguin operator Q_7', one obtains, for instance,

$$S^{\mathrm{SD}}_{K^*(K_S^0\pi^0)\gamma} \approx \frac{\mathrm{Im}\left[e^{-2i\phi_1}\left(C_7^* C_7' + C_7 C_7'^*\right)\right]}{|C_7|^2 + |C_7'|^2}. \tag{230}$$

LD QCD contributions denoted by L_U in Eq. (222) modify the predictions in Eq. (229) and arise first at $\mathcal{O}(\Lambda_{\mathrm{QCD}}/m_b)$. The dominant corrections are expected to stem from c quark loops [506], because such effects are due to the current–current operators $Q_{1,2}$ in Eq. (195) that have large Wilson coefficients. By using the corresponding contribution of the inclusive decays, it has been concluded in the latter work that the LD contamination in Eq. (229) could be as large as 10%. By performing a kinematic decomposition it can, however, be shown that $H_- \gg H_+$ holds at leading twist for any local transition operator [485,507]. The hierarchy of helicity amplitudes can therefore only be broken by higher-twist effects, and one such contribution comes from gluon exchange between the c quark loop and the vector meson. An explicit evaluation of the LD corrections due to c quark loops [494,503,508] yields a correction of $\mathcal{O}(1\%)$, which is considerably smaller than the inclusive calculation would suggest (see also Ref. [509]).[26] Further evidence for the smallness of LD c quark effects arises from the fact that the corrections to the helicity hierarchy are of $\mathcal{O}(m_V^2/m_b^2)$. This indicates that the hierarchy is more badly broken by excited (i.e. heavier) vector meson states. Vertex

[26] It was recently proposed in Ref. [510] that the LD contributions entering H_+ can be controlled by considering both the $B \to V(1^-)\gamma$ and the $B \to A(1^+)\gamma$ decay with V and A nearly degenerate states, such as the ρ and the a_1 meson. By taking the sum $S_{B\to\rho\gamma} + S_{B\to a_1\gamma}$, one measures the LD contributions entering H_+, whereas the difference can measure the new physics contribution with considerably improved precision depending on calculable ratios of LD effects. These methods also extend to the low-q^2 region of $B \to V\ell^+\ell^-$, with particular promise for the electron channels.

corrections are treated in QCDF [482,483] and automatically obey $H_- \gg H_+$. The evaluation of the vertex corrections beyond factorization is challenging and remains a future task. Including both SD and LD contributions, the quantities in Eq. (229) turn into [494,511]

$$S^{\rm SM}_{K^*(K^0_S\pi^0)\gamma} = (-2.3 \pm 1.6)\%, \qquad S^{\rm SM}_{\rho^0(\pi^+\pi^-)\gamma} = (0.2 \pm 1.6)\%. \tag{231}$$

The photon polarization is one of the most challenging measurements in B physics today, and various modes have been proposed to further improve the precision—see Ref. [490] for more details. LHCb has already applied many of the proposed methods and Belle II should be able to further extend these studies. For instance, at Belle II it should be possible to expand the recent LHCb analysis [489] of angular correlations in $B^\pm \to K^\pm\pi^\mp\pi^\pm\gamma$ [512,513] by including the neutral modes as well as performing a Dalitz analysis [514]. The angular analysis of $B \to K^* e^+ e^-$ has been performed by LHCb [515] at very low q^2 where the photonic dipole operator Q_7 and its chirality-flipped partner Q'_7 dominate. A similar analysis should be possible at Belle II and, furthermore, the use of the angular distribution of the converted photon from $B \to K^*\gamma$ is under discussion [516].

The direct CP asymmetries $C_{f\gamma}$ require weak CP-odd and strong CP-even phase differences of two amplitudes and are therefore by default sensitive to CP-odd phases beyond the SM. CP-even phases instead originate from LD QCD effects. In the SM the direct CP asymmetry for $b \to s\gamma$ is small, since there is no CP-odd phase at $\mathcal{O}(\lambda^3)$. These observables can thus serve as null tests. As an example we quote $C^{\rm SM}_{\phi(\to KK)\gamma} = (0.5 \pm 0.5)\,\%$ from Ref. [503]. For the $b \to d\gamma$ modes, on the other hand, the t quark loop diagram induces a sizeable CP-odd phase. For example, in Ref. [517] a direct CP asymmetry of 15% is predicted for $B_d \to \pi^+\pi^-\gamma$ within the SM.

9.2.5. Measurement of $B \to V\gamma$ decays

Contributing author: A. Ishikawa

The $b \to s\gamma$ transition was first observed by CLEO via $B \to K^*\gamma$ in 1993 [518]. Two decades later this decay is still important in the search for new physics. The three most important observables in this channel are the photon polarization, the isospin, and the CP asymmetries.

The K^* mesons are reconstructed from any of the $K^-\pi^0$, $K^0_S\pi^-$, $K^-\pi^+$, and $K^0_S\pi^0$ decays. The B meson candidate is reconstructed by combining the K^* candidate and a hard photon reconstructed from an electromagnetic cluster in the ECL which is not associated with any charged tracks in the tracking system. Exclusive modes are much cleaner than the fully inclusive mode thanks to requirements imposed on the difference in energy, ΔE, and the beam-constrained mass, $M_{\rm bc}$. The $K^-\pi^0$, $K^0_S\pi^-$, and $K^-\pi^+$ modes are flavor eigenstates which can be used for measurements of $A_{\rm CP}$m while $K^0_S\pi^0$ with flavor tagging of the other B meson can be used to measure the time-dependent CP asymmetry of Eq. (227) which is sensitive to the polarization of the final state photon.[27]

At Belle II with 5 ab^{-1} of data the measurement of $\bar{a}_I(K^*\gamma)$ may already be systematically limited. The dominant uncertainty is due to f_{+-}/f_{00} and amounts to 0.5%. Notice that this uncertainty is smaller by a factor of five than that of the most up-to-date SM prediction in Eq. (225). Measurements of the direct CP asymmetries will instead still be statistically limited. The corresponding uncertainties are estimated to be 0.2% and 0.3% for $A_{\rm CP}(B^0 \to K^{*0}\gamma)$ and $A_{\rm CP}(B^+ \to K^{*+}\gamma)$, respectively, which constitutes a factor of eight improvement compared to the Belle result [523]. Notice that the

[27] At Belle, the time-dependent CP asymmetries were measured with $B \to K^*(K^0_S\pi^0)\gamma$ [519], $B \to K^0_S\eta\gamma$ [520], $B \to K^0_S\pi^+\pi^-\gamma$ [521], and $B \to K^0_S\phi\gamma$ [522].

theoretical uncertainty of the corresponding SM prediction $A_{CP}^{SM}(B^0 \to K^{*0}\gamma) = (0.3 \pm 0.1)\%$ [493] is smaller than the statistical uncertainty reachable at Belle II. A precision measurement of $A_{CP}(B^0 \to K^{*0}\gamma)$ is nevertheless an important goal since it will allow us to set stringent constraints on the imaginary part of the Wilson coefficient of Q_7 [493,524], which otherwise is difficult to bound. Like A_{CP}, the measurement of ΔA_{CP} will also be statistically limited at Belle II and the projected uncertainty amounts to 0.4% with 50 ab^{-1} of luminosity.

The $b \to d\gamma$ process was first observed in 2006 [525] by Belle through the exclusive $B \to \rho\gamma$ and $B^0 \to \omega^0\gamma$ decays. All the branching ratios, isospin asymmetries, direct and time-dependent CP asymmetries have been measured subsequently [526–528], but the achieved precision is not high enough to set stringent limits on new physics. This lack in precision is unfortunate since the measured value of $\bar{a}_I(\rho\gamma)$ shows a slight tension with the SM prediction, a fact that has already been mentioned in the context of Eq. (225). Thanks to the good PID system and the large integrated luminosity to be recorded at Belle II, precise measurement of $B \to (\rho, \omega)\gamma$ will be possible for the first time, which is crucial in view of the aforementioned tension.

The ρ and ω mesons are reconstructed from two-pion and three-pion final states. Hard photon candidates are combined with the light mesons to form B meson candidates. A dominant continuum background can be suppressed by a multivariate analysis with event shape variables. The large $b \to s\gamma$ background which peaks in ΔE and M_{bc} can be significantly suppressed by the new PID system, using the iTOP for the barrel region and the ARICH for the forward endcap region.

Assuming that that the current central experimental value of $\bar{a}_I(\rho\gamma)$ is confirmed, Belle II can observe a $5\,\sigma$ deviation from the SM prediction already with 6 ab^{-1}. With 50 ab^{-1} of data the statistical uncertainty (1.7%) will dominate the measurement, with the largest systematic uncertainties arising from f_{+-}/f_{00} (0.5%) and background modeling (0.5%). In total, a precision of 1.9% on $\bar{a}_I(\rho\gamma)$ will be achievable at Belle II, which compares favorably with the current theoretical SM uncertainty of 2.8% as quoted in Eq. (225).

The CP asymmetries in the case of charged and neutral B mesons are measured in different ways. The mode $B^+ \to \rho^+\gamma$ is self-flavor tagging thus allowing for a straightforward measurement of the direct CP asymmetry. In contrast, $B^0 \to \rho^0\gamma$ is not a flavor eigenstate, yet a time-dependent measurement with flavor tagging will allow extraction of both A_{CP} and the S parameter. With 50 ab^{-1} of data one can expect to reach a precision of 3.0%, 3.8%, and 6.4% for $A_{CP}(B^+ \to \rho^+\gamma)$, $A_{CP}(B^0 \to \rho^0\gamma)$, and $S_{\rho^0\gamma}$, respectively.

The magnitude of the ratio V_{td}/V_{ts} of CKM matrix elements can be extracted by measuring appropriate ratios of branching ratios such as $\mathrm{Br}(B \to (\rho, \omega)\gamma)/\mathrm{Br}(B^0 \to K^*\gamma)$ [494]. However, already with 1 ab^{-1} of integrated luminosity the resulting uncertainty will be dominated by the theoretical uncertainties.

Radiative B_s^0 decays can be also studied at the $\Upsilon(5S)$ resonance. The Belle measurement of the branching ratio of $B_s^0 \to \phi\gamma$ [529] is limited by the uncertainty on the B_s^0 production ($f_s\sigma_{b\bar{b}}$) at the $\Upsilon(5S)$ resonance, which amounts to about 17%. The current precision of the world average of f_s is dominated by the Belle measurement of the inclusive $B_s^0 \to D_{(s)}X$ decay [530] that uses 1.9 fb^{-1} of data at the $\Upsilon(5S)$ resonance. This measurement can be improved at Belle II with a few different approaches, namely the dilepton method, exclusive decays in B_s^0 tagged and untagged events, as well as inclusive B_s decays. Assuming that 4% precision on f_s is achieved at Belle II, the sensitivity of $\mathrm{Br}(B_s^0 \to \phi\gamma)$ will be 6.5%, which is still dominated by the uncertainty on $f_s\sigma_{b\bar{b}}$.

The $B_s^0 \to K^{*0}\gamma$ decay mode has not been searched for yet. The reconstruction of this decay is almost the same as for $B^0 \to K^{*0}\gamma$ and thus straightforward to perform. The $b \to s$ counterpart,

Table 62. Sensitivities of observables for radiative exclusive B decays. We assume that 5 ab^{-1} of data will be taken on the $\Upsilon(5S)$ resonance by Belle II. Some numbers at Belle are extrapolated to 0.71 ab^{-1} (0.12 ab^{-1}) for the $B_{u,d}$ (B_s) decay. As in Table 61, the quoted uncertainties depend on the observable, and are either relative or absolute ones.

Observables	Belle 0.71 ab^{-1} (0.12 ab^{-1})	Belle II 5 ab^{-1}	Belle II 50 ab^{-1}
$\Delta_{0+}(B \to K^*\gamma)$	2.0%	0.70%	0.53%
$A_{CP}(B^0 \to K^{*0}\gamma)$	1.7%	0.58%	0.21%
$A_{CP}(B^+ \to K^{*+}\gamma)$	2.4%	0.81%	0.29%
$\Delta A_{CP}(B \to K^*\gamma)$	2.9%	0.98%	0.36%
$S_{K^{*0}\gamma}$	0.29	0.090	0.030
$\mathrm{Br}(B^0 \to \rho^0\gamma)$	24%	7.6%	4.5%
$\mathrm{Br}(B^+ \to \rho^+\gamma)$	30%	9.6%	5.0%
$\mathrm{Br}(B^0 \to \omega\gamma)$	50%	14%	5.8%
$\Delta_{0+}(B \to \rho\gamma)$	18%	5.4%	1.9%
$A_{CP}(B^0 \to \rho^0\gamma)$	44%	12%	3.8%
$A_{CP}(B^+ \to \rho^+\gamma)$	30%	9.6%	3.0%
$A_{CP}(B^0 \to \omega\gamma)$	91%	23%	7.7%
$\Delta A_{CP}(B \to \rho\gamma)$	53%	16%	4.8%
$S_{\rho^0\gamma}$	0.63	0.19	0.064
$\lvert V_{td}/V_{ts}\rvert_{\rho/K^*}$	12%	8.2%	7.6%
$\mathrm{Br}(B_s^0 \to \phi\gamma)$	23%	6.5%	—
$\mathrm{Br}(B^0 \to K^{*0}\gamma)/\mathrm{Br}(B_s^0 \to \phi\gamma)$	23%	6.7%	—
$\mathrm{Br}(B_s^0 \to K^{*0}\gamma)$	—	15%	—
$A_{CP}(B_s^0 \to K^{*0}\gamma)$	—	15%	—
$\mathrm{Br}(B_s^0 \to K^{*0}\gamma)/\mathrm{Br}(B_s^0 \to \phi\gamma)$	—	15%	—
$\mathrm{Br}(B_s^0 \to K^{*0}\gamma)/\mathrm{Br}(B^0 \to K^{*0}\gamma)$	—	15%	—

i.e. $B_s^0 \to \phi\gamma$, serves as a peaking background, which can, however, be eliminated by studying the invariant mass of the hadronic system under a kaon mass assumption as well as using the good PID information of Belle II. Other possible peaking backgrounds from $B_s^0 \to K^{*0}\pi^0/\eta$ with asymmetric decays of π^0/η are also not yet measured. These can be suppressed by a π^0/η veto and by examining the helicity angle distribution of the K^{*0}. The $B_s^0 \to K^{*0}\gamma$ decay can be observed at Belle II with an integrated luminosity of 3.5 ab^{-1}, and the achievable precision on the branching ratio can be expected to be 15% with 5 ab^{-1}. The ratios of the branching ratios and the direct CP asymmetries can also be measured with the same precision.

A summary of the Belle II sensitivities for the various exclusive $B \to V\gamma$ channels is provided in Table 62.

9.2.6. Importance of PID for $b \to d\gamma$

Contributing author: S. Cunliffe

In both the inclusive and exclusive transition analyses, PID information plays an important role. Specifically, PID is necessary to reduce the problematic background originating from misidentified kaons from $B \to X_s\gamma$ processes. To give a relevant example, consider the case of $B^0 \to K^{*0}\gamma$ followed by $K^{*0} \to K^+\pi^-$. The latter decay rate is roughly a factor of 30 larger than the dominant $b \to d\gamma$ process, i.e. $B^0 \to \rho^0\gamma$ with $\rho^0 \to \pi^+\pi^-$, meaning that a good PID is necessary to be able to separate signal from background.

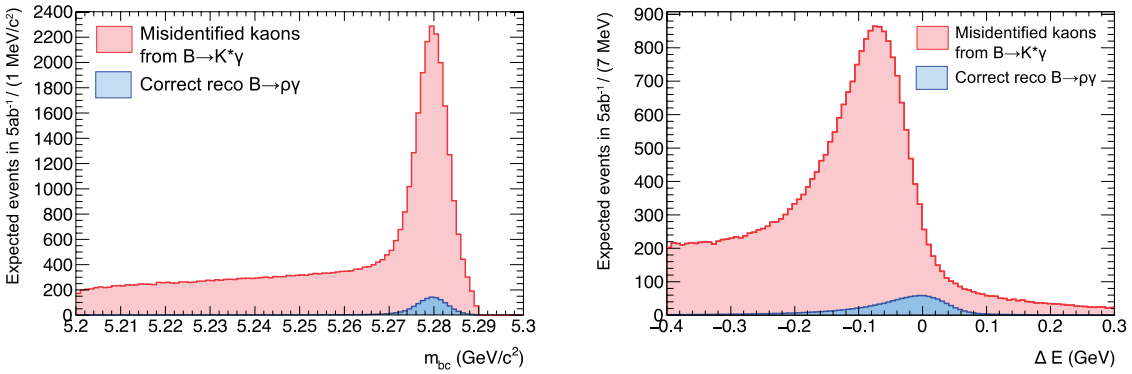

Fig. 90. Distributions of $M_{\rm bc}$ and ΔE for correctly identified $B^0 \to \rho^0\gamma$ signal events (blue) overlaid with misidentified $B \to K^*\gamma$ where the kaon from the K^{*0} decay is mis-reconstructed as a pion (red). With no PID selection cut the background swamps the signal.

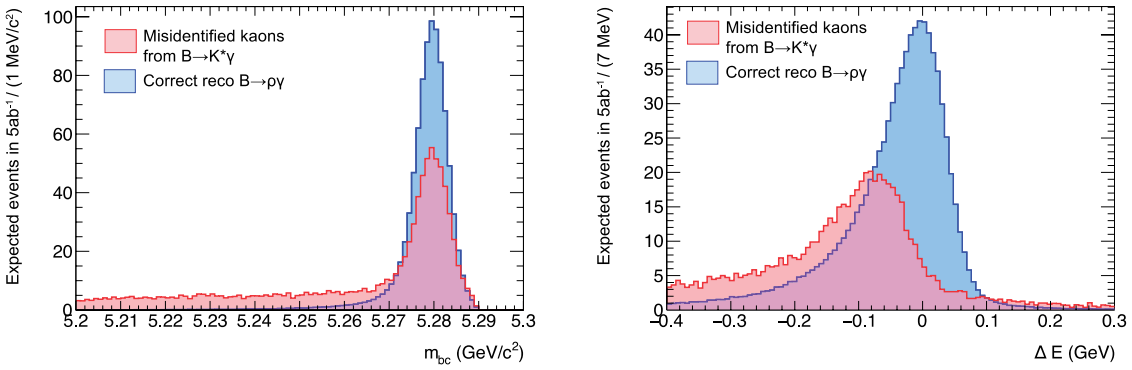

Fig. 91. As Fig. 90 but employing PID information. Distributions of $M_{\rm bc}$ and ΔE for correctly identified $B^0 \to \rho^0\gamma$ signal events (blue) overlaid with misidentified $B \to K^*\gamma$ where the kaon from the K^{*0} decay is mis-reconstructed as a pion (red). After a simple optimization of PID selection, the background is reduced significantly.

A study based on the full Belle II simulation is performed to quantify the performance of the PID system. Samples of 1 million events of both $B^0 \to \rho^0\gamma$ and $B^0 \to K^{*0}\gamma$ are generated. After performing a full detector reconstruction, a simple preselection criterion is applied to both samples. An optimization for a cut on the pion probability (defined in Sect. 5.5) is performed to maximize the figure of merit, $S/\sqrt{S+B}$. Here, S is the number of correctly identified $B^0 \to \rho^0\gamma$ events, and B is the number of $B^0 \to K^{*0}\gamma$ where the kaon track was mis-reconstructed as a pion. Both S and B are scaled to the expected number of events in 5 ab^{-1} of data. The value of the optimal selection cut is found to give a figure of merit well above 10.

Figures 90 and 91 show overlaid distributions of the beam-constrained mass, $M_{\rm bc}$, and energy difference, ΔE, for both samples before and after the selection cut at the optimal point. The importance of PID is evident from the two figures.

The above study is repeated using a simulation of the Belle detector in order to compare to the associated Belle PID performance. The Belle optimization is performed for the analogous PID likelihood variables described in [2, Sect. 5.1.2]. The Belle II PID system is found to provide an improvement in the figure of merit by approximately 30%.

9.3. Double radiative decays

Contributing authors: C. Bobeth and A. Kokulu

9.3.1. $B_q \to \gamma\gamma$ decays

In the SM, the branching ratios of the $B_q \to \gamma\gamma$ decays scale as the involved CKM elements $|V_{td}|^2$ and $|V_{ts}|^2$, predicting an enhancement of the $B_s \to \gamma\gamma$ decay over the $B_d \to \gamma\gamma$ decay by a factor of $|V_{ts}/V_{td}|^2 \approx 20$. Using the full dataset at $\Upsilon(5S)$ [529], Belle obtained the 90% CL upper limit

$$\mathrm{Br}(B_s \to \gamma\gamma)_{\mathrm{exp}} < 3.1 \cdot 10^{-6} \tag{232}$$

on the branching ratio of $B_s \to \gamma\gamma$. The searches for $B_d \to \gamma\gamma$ at $\Upsilon(4S)$ resulted instead in the 90% CL upper limits

$$\mathrm{Br}(B_d \to \gamma\gamma)_{\mathrm{exp}} < \begin{cases} 3.2 \cdot 10^{-7}, \\ 6.2 \cdot 10^{-7} \end{cases} \tag{233}$$

from the full dataset of BaBar [531], and a partial dataset of 104 fb^{-1} of Belle [532] out of the available 711 fb^{-1}. The corresponding SM predictions are given by [533]

$$\begin{aligned} \mathrm{Br}(B_s \to \gamma\gamma)_{\mathrm{SM}} &\in [0.5, 3.7] \cdot 10^{-6}, \\ \mathrm{Br}(B_d \to \gamma\gamma)_{\mathrm{SM}} &\in [1.0, 9.8] \cdot 10^{-8}, \end{aligned} \tag{234}$$

and are either close to or only an order of magnitude below the bounds in Eqs. (232) and (233). The above comparison shows that Belle II will be able to discover $B_d \to \gamma\gamma$ with the anticipated 50 times larger dataset at $\Upsilon(4S)$. Furthermore, an appropriately large $\Upsilon(5S)$ dataset could provide an observation of $B_s \to \gamma\gamma$.

From a theoretical point of view, double radiative $B_q \to \gamma\gamma$ decays are complementary to the corresponding radiative inclusive $B \to X_q\gamma$ decay. They depend on the same Wilson coefficient C_7 of the photonic dipole operator in Eq. (197), but the contribution of four-quark operators in $B_q \to \gamma\gamma$ is different compared to $B \to X_q\gamma$. This feature provides a complementary test of the Wilson coefficient C_7 which plays an important role in many BSM models.

As will be explained in more detail below, the main source of theoretical uncertainty in the QCDF approach arises due to the first negative moment, λ_B, of the B meson distribution amplitude. This hadronic parameter can be determined from the radiative leptonic decay $B \to \ell\bar{\nu}\gamma$ [223,246]. For the definition and a detailed discussion of the phenomenological impact on two-body hadronic decays, see Sect. 8.

The amplitude of the $\bar{B} \to \gamma(k_1, \epsilon_1)\,\gamma(k_2, \epsilon_2)$ decays—hereafter B stands for both B_q—has the general structure

$$\mathcal{A} = A_+ \left[2(k_1 \cdot \epsilon_2)(k_2 \cdot \epsilon_1) - m_B^2(\epsilon_1 \cdot \epsilon_2)\right] - A_- \, 2i\varepsilon_{\mu\nu\alpha\beta} k_1^\mu k_2^\mu \epsilon_1^\alpha \epsilon_2^\beta. \tag{235}$$

The CP properties of the corresponding two-photon final states are indicated by the subscripts $\pm$ on the amplitudes $A_\pm$. The parallel spin polarization of the photons is described by A_+, whereas the perpendicular one is encoded in A_-.

The decay rate is obtained after summation over photon polarizations:

$$\Gamma(\bar{B} \to \gamma\gamma) = \frac{m_B^3}{16\pi}\left(|A_+|^2 + |A_-|^2\right). \tag{236}$$

In the absence of methods to tag the flavor of the initial B meson, the CP-averaged branching ratio must be considered instead,

$$\overline{\mathrm{Br}}_{\gamma\gamma} = \frac{\tau_B}{2}\left[\Gamma(\bar{B} \to \gamma\gamma) + \Gamma(B \to \gamma\gamma)\right], \tag{237}$$

where $\Gamma(B \to \gamma\gamma)$ is determined from Eq. (236) using the amplitudes $\bar{A}_\pm$ of the CP-conjugated decay $B \to \gamma\gamma$. Further, for the case of untagged B_s decays the sizeable decay width leads to rapid mixing and requires a time-integration [534] in order to obtain the experimentally measured CP-averaged and time-integrated branching ratio

$$\langle\overline{\mathrm{Br}}_{\gamma\gamma}\rangle = \frac{1 + y_s A_{\Delta\Gamma}}{1 - y_s^2}\,\overline{\mathrm{Br}}_{\gamma\gamma}. \tag{238}$$

This depends on $y_s = \Delta\Gamma_s/(2\Gamma_s) = 0.075 \pm 0.012$, where $\Gamma_s = 1/\tau_{B_s}$, the inverse of the lifetime, the CP-averaged branching ratio in Eq. (237) at time $t = 0$, and the mass–eigenstate rate asymmetry $A_{\Delta\Gamma}$ in $B \to \gamma\gamma$. The latter quantity can in principle be determined in an untagged but time-dependent analysis via a measurement of the effective lifetime [534]. Notice that the prefactor appearing on the right-hand side of Eq. (238) amounts to around $[0.9, 1.1]$ if $A_{\Delta\Gamma}$ is varied in its physically allowed range of $[-1, 1]$. Given the sizeable uncertainties quoted in Eq. (234), one can hence simply use $\langle\overline{\mathrm{Br}}_{\gamma\gamma}\rangle = \overline{\mathrm{Br}}_{\gamma\gamma}$ when comparing to future Belle II data.

Direct CP violation can be tested by a tagged measurement of

$$\begin{aligned} r_{\mathrm{CP}} &= \frac{|\mathcal{A}|^2 - |\bar{\mathcal{A}}|^2}{|\mathcal{A}|^2 + |\bar{\mathcal{A}}|^2}, \\ r_{\mathrm{CP}}^{\pm} &= \frac{|A_\pm|^2 - |\bar{A}_\pm|^2}{|A_\pm|^2 + |\bar{A}_\pm|^2}, \end{aligned} \tag{239}$$

where extractions of $r_{\mathrm{CP}}^{\pm}$ also require the determination of the photon polarizations.

A systematic analysis of these decays in the heavy quark limit $m_b \gg \Lambda_{\mathrm{QCD}}$ was first given in Ref. [533]. In this limit, the hadronic matrix elements of operators Q_i of the effective Hamiltonian in Eq. (195) factorize:

$$\langle\gamma\gamma|Q_i|\bar{B}\rangle = f_B \int_0^1 d\omega\, T_i^{\mu\nu}(\omega)\phi_B^+(\omega)\epsilon_{1\mu}\epsilon_{2\nu}. \tag{240}$$

The $T_i^{\mu\nu}$ are perturbatively calculable SD functions, whereas the non-perturbative effects are contained in the B meson decay constant f_B and the leading light cone distribution amplitude (LCDA) of the B meson in HQET, denoted as ϕ_B^+. The latter depend on the light cone momentum ω of the spectator quark inside the B meson. Within the QCD factorization setup [533], only the first negative moment,

$$\frac{1}{\lambda_B} = \int_0^1 d\omega\, \frac{\phi_B^+(\omega)}{\omega}, \tag{241}$$

of the LCDA of the B meson appears.

The leading-power contribution arises from the emission of a hard photon from the B meson spectator quark for the matrix element of the photonic dipole operator Q_7,

$$A_\pm = \frac{G_F}{\sqrt{2}}\frac{\alpha}{3\pi} f_B \sum_{p=u,c} \lambda_p^{(q)} A_\pm^p,$$
$$A_\pm^p = -C_7^{\rm eff}\,\frac{m_B}{\lambda_B}, \tag{242}$$

where $C_7^{\rm eff}$ is the effective coupling of this operator at the low-energy scale μ_b. At this order in the power expansion one has $(r_{\rm CP}^\pm)_{\rm SM} = 0$. Furthermore, since $\overline{\rm Br}_{\gamma\gamma} \propto (f_B/\lambda_B)^2$, and given the accuracy of lattice predictions for f_B, in the case of the branching ratios the main theoretical uncertainty comes from λ_B.

At the sub-leading order in the power expansion there are two types of contributions to the matrix element of Q_7: (i) higher-twist contributions, and (ii) the one-particle-reducible (1PR) diagram where the photon is emitted from the b quark line. Both corrections naively represent a correction of $\mathcal{O}(\Lambda_{\rm QCD}/m_b) = \mathcal{O}(10\%)$ and have so far been neglected in the theoretical predictions. One-particle-irreducible (1PI) contributions of the four-quark operators in the effective Hamiltonian of Eq. (195) also arise at $\mathcal{O}(\Lambda_{\rm QCD}/m_b)$. The corresponding matrix elements were shown to factorize in the heavy quark limit to NLO in QCD, leading to $\langle\gamma\gamma|Q_i|\bar{B}\rangle = f_B T_i^{\mu\nu}\epsilon_{1\mu}\epsilon_{2\nu}$, independent of ω. Numerically the largest contributions stem from the current–current operators $Q_{1,2}^p$. They give an additional contribution to the coefficient A_-^p appearing in Eq. (242). One obtains

$$A_-^p = -C_7^{\rm eff}\,\frac{m_B}{\lambda_B} - \frac{2}{3}\left(C_1^p + N_c C_2^p\right) g(z_p), \tag{243}$$

where $C_{1,2}^p$ are the Wilson coefficients of $Q_{1,2}^p$ at the scale μ_b and $N_c = 3$. The function $g(z_p)$ with $z_p = m_p^2/m_b^2$ develops an imaginary part only for $p = c$ when setting m_u to zero, which provides the leading contribution to $r_{\rm CP}^-$. The quantity $r_{\rm CP}^+$, on the other hand, still remains zero. The QCD penguin operators Q_{3-6} contribute equally to the u quark and c quark sectors, and their overall effect is very small [535]. Feynman graphs that depict all the relevant contributions can be found in Sects. 3 and 4 of Ref. [533].

Including all relevant effects, the CP asymmetries have been estimated as [533,536,537]

$$(r_{\rm CP})_{\rm SM}^s \approx 0.5\%, \qquad (r_{\rm CP}^-)_{\rm SM}^s \approx 0.4\%,$$
$$(r_{\rm CP})_{\rm SM}^d \approx -5\%, \qquad (r_{\rm CP}^-)_{\rm SM}^d \approx -10\% \tag{244}$$

within the SM, while $(r_{\rm CP}^+)_{\rm SM}^{s,d} \approx 0\%$. Notice that the predictions for B_d are larger than those for B_s as a result of the CKM hierarchies in Eq. (196).

The dependence of the branching ratios on λ_B cancels almost completely in their ratio, leading to

$$\frac{{\rm Br}(B_s \to \gamma\gamma)_{\rm SM}}{{\rm Br}(B_d \to \gamma\gamma)_{\rm SM}} \approx \left|\frac{V_{ts}}{V_{td}}\right|^2 \frac{\tau_{B_s} f_{B_s}^2 m_{B_s}^3}{\tau_{B_d} f_{B_d}^2 m_{B_d}^3}. \tag{245}$$

Compared to λ_B, other parametric uncertainties due to the CKM elements and f_B are currently subdominant. Higher-order radiative QCD effects are estimated via factorization-scale variation to be of $\mathcal{O}(30\%)$, and sub-leading power corrections are expected to be of $\mathcal{O}(10\%)$ [533].

In BSM models, the $B_q \to \gamma\gamma$ decays can receive two types of non-standard contributions:

(i) Modifications of the Wilson coefficient C_7, which will also leave an imprint in $B \to X_q\gamma$.
(ii) Modifications of the 1PI contributions due to four-fermion operators $b \to qf\bar{f}$, where f stands for the five possible light quarks or the three charged leptons.

The first type has been studied in various models such as the two-Higgs doublet model of type II (2HDM-II) [538,539], the minimal supersymmetric SM (MSSM) [540], and universal extra dimensions [541]. However, due to strong constraints on C_7 from $B \to X_q\gamma$, large modifications of $\mathrm{Br}(B_q \to \gamma\gamma)$ are by now already excluded.

The complementarity of $B_q \to \gamma\gamma$ therefore comes mainly from the second type of modifications due to non-standard four-fermion operators $b \to qf\bar{f}$ with vectorial and scalar Dirac structures, which contribute differently to $B_q \to \gamma\gamma$ and $B \to X_q\gamma$ [537], turning it into an interesting probe of such effects. Experimentally least constrained are the $b \to s\tau^+\tau^-$ operators, which have been studied model-independently in Ref. [537]. Currently, large deviations from $(r_{\mathrm{CP}})^s_{\mathrm{SM}}$ are still allowed. The rate might be enhanced up to a factor of order two, depending also on the exact value of λ_B, which determines the relative size of the four-fermion operators versus the contribution of Q_7. Such effects arise for example in SUSY with broken R parity [542] or leptoquark scenarios [537].

9.3.2. Searches for $B_q \to \gamma\gamma$

Contributing author: A. Ishikawa

Since the final states do not have charged particles, the $B_s \to \gamma\gamma$ and $B_d \to \gamma\gamma$ decays have so far only been searched for at e^+e^- colliders [529,531,532]. The obtained upper limits in Eqs. (232) and (233) are several times larger than the corresponding SM predictions of Eq. (234). Given its large dataset, Belle II will be able to observe the $B_q \to \gamma\gamma$ decays and perform new physics searches through precise measurements of these unique transitions.

The reconstruction of $B_q \to \gamma\gamma$ decays is straightforward. Two isolated clusters in the calorimeter, whose shower shapes are consistent with an electromagnetic shower, are combined to reconstruct the B meson candidates. The B meson is identified through the ΔE and M_{bc} distributions. Since the calorimeter is about 16 radiation lengths, the ΔE distribution has a longer tail to lower ΔE values due to shower leakage. The dominant backgrounds are off-timing Bhabha events on top of hadronic events and continuum events with initial state radiation. The former can be reduced by requiring tight timing constraints on ECL and trigger hits (which is the default in the Belle II reconstruction), while the latter can be suppressed by the use of event shape variables.

Assuming that $\mathrm{Br}(B_d \to \gamma\gamma) = 3.1 \cdot 10^{-8}$, the decay should be observed with an integrated luminosity of $12\,\mathrm{ab}^{-1}$ and the relative uncertainty on the branching ratio is expected to be about 10% with $50\,\mathrm{ab}^{-1}$ of data. The given uncertainty is statistically dominated. After an observation, the direct CP violation can be measured using flavor tagging. With $50\,\mathrm{ab}^{-1}$ it should be possible to measure $A_{\mathrm{CP}}(B_d \to \gamma\gamma)$ with a precision of about 25%.

The data-taking strategy at $\Upsilon(5S)$ is not determined yet. If we make the standard assumption of this document that $5\,\mathrm{ab}^{-1}$ data will be accumulated, the data sample will contain about $2.9 \cdot 10^8$ $B_s^{(*)0}\bar{B}_s^{(*)0}$ pairs. The precision of $\mathrm{Br}(B_s^0 \to \gamma\gamma)$ with $5\,\mathrm{ab}^{-1}$ will be 23%, which is a bit larger to claim an observation. To observe the $B_s \to \gamma\gamma$ decay, $7\,\mathrm{ab}^{-1}$ of integrated luminosity are needed. There is no reason not to add another few ab^{-1} of data for observation, which takes a few months. Since flavor tagging of B_s mesons is difficult due to fast B_s–$\bar{B}_s$ oscillations and worse proper-time

Table 63. Belle II sensitivities for the $B_{d,s} \to \gamma\gamma$ modes. We assume that 5 ab^{-1} of data will be taken on the $\Upsilon(5S)$ resonance at Belle II. Some numbers at Belle are extrapolated to 0.71 ab^{-1} (0.12 ab^{-1}) for the B_d (B_s) decay. The given branching ratio and asymmetry uncertainties are relative and absolute uncertainties, respectively.

Observables	Belle 0.71 ab^{-1} (0.12 ab^{-1})	Belle II 5 ab^{-1}	Belle II 50 ab^{-1}
$\mathrm{Br}(B_d \to \gamma\gamma)$	$< 740\%$	30%	9.6%
$A_{\mathrm{CP}}(B_d \to \gamma\gamma)$	—	78%	25%
$\mathrm{Br}(B_s \to \gamma\gamma)$	$< 250\%$	23%	—

resolution compared to the B_d case, a measurement of the direct CP asymmetry of $B_s \to \gamma\gamma$ seems very difficult. An exception could be provided by CP tagging of the other B_s meson in the $\Upsilon(5S) \to B_s^0 \bar{B}_s^0$ or $\Upsilon(5S) \to B_s^{*0} \bar{B}_s^{*0}$ processes. Further studies of the CP tagging efficiency using full event interpretation are needed to clarify this issue.

The Belle II sensitivities for the $B_{d,s} \to \gamma\gamma$ modes are summarized in Table 63.

9.3.3. $B \to X_s\gamma\gamma$ decay

Contributing authors: C. Bobeth and A. Kokulu

Compared to $B \to X_s\gamma$, the double radiative process $B \to X_s\gamma\gamma$ is suppressed by an additional factor of $\alpha/(4\pi)$, which leads to the naive expectation $\mathrm{Br}(B \to X_s\gamma\gamma)_{\mathrm{SM}} = \mathcal{O}(10^{-7})$. Given its small branching ratio it is unsurprising that the mode $B \to X_s\gamma\gamma$ has not been observed so far.

Even though it is very rare compared to the single radiative $B \to X_s\gamma$ decay, the double radiative process has some features that make it worthwhile studying at Belle II. These features are:

(i) In contrast to $B \to X_s\gamma$, the current–current operators $Q_{1,2}$ contribute to $B \to X_s\gamma\gamma$ via 1PI diagrams already at LO. As a result, measurements of the double radiative decay mode would allow us to put bounds on these 1PI corrections.

(ii) For $B \to X_s\gamma\gamma$ one can study more complicated distributions such as $d^2\Gamma/(dE_1 dE_2)$, where $E_{1,2}$ are the final state photon energies, or a forward–backward asymmetry (A_{FB}) that can provide additional sensitivity to BSM physics.

In order to exploit these features in a clean way, SM predictions beyond the LO are needed. A first step towards achieving NLO accuracy has been made in Refs. [543,544] by the calculation of the (Q_7, Q_7) interference contribution to the differential distributions at $\mathcal{O}(\alpha_s)$. In the latter works it has been shown that the NLO corrections associated to (Q_7, Q_7) are large and can amount to a relative change of around $\pm 50\%$ compared to the corresponding LO predictions [545–548]. Further progress towards $B \to X_s\gamma\gamma$ at NLO was made recently in Ref. [549] by providing the (Q_8, Q_8) self-interference contribution. Although these corrections should be suppressed relative to those from (Q_7, Q_7) by $\left|C_8^{\mathrm{eff}} Q_d / C_7^{\mathrm{eff}}\right|^2 \approx 3\%$, the appearance of collinear logarithms $\ln(m_s/m_b)$ could upset this naive expectation. One important outcome of Ref. [549] is that the logarithmically enhanced contributions stay small in the full phase space, and as a result the (Q_8, Q_8) interference represents only a sub-leading NLO correction. The NLO calculation of the numerically important (Q_7, Q_7) interference contribution has very recently been extended to the case of a non-zero s quark mass [550].

Including all known perturbative corrections, the state-of-the-art SM prediction reads [550]

$$\mathrm{Br}(B \to X_s\gamma\gamma)_{\mathrm{SM}}^{c=0.02} = (0.9 \pm 0.3) \cdot 10^{-7}, \tag{246}$$

where c represents a cut on the phase space (for details, see Ref. [550]) which guarantees that the two photons are not soft and also not parallel to each other. The quoted uncertainty is dominated by the error due to scale variations $\mu_b \in [m_b/2, 2m_b]$. Since scale ambiguities represent the largest theoretical uncertainty at present, a more reliable SM prediction can only be achieved by calculating further NLO corrections, such as the $(Q_{1,2}, Q_7)$ interference term. We add that LD resonant [547] and spectator quark [551] effects are small and have therefore not been included in Eq. (246).

The inclusive $B \to X_s\gamma\gamma$ decay has also been examined in extensions of the SM. Predictions for $\mathrm{Br}(B \to X_s\gamma\gamma)$ and A_{FB} have been obtained in 2HDMs [546,548] and in the framework of R-parity-violating SUSY [542]. In all cases it has been found that $\mathcal{O}(1)$ effects in $B \to X_s\gamma\gamma$ can arise in the models under consideration.

Experimentally, the inclusive $B \to X_s\gamma\gamma$ can be studied by the sum of the exclusive method, i.e. measuring $B \to (K, K^*, \ldots)\gamma\gamma$ decays. The challenge of this measurement is to eliminate the background of $\gamma\gamma$ originating from various resonances. The $B^\pm \to K^\pm h \to K^\pm\gamma\gamma$ decay was studied by the Belle Collaboration [552] in 2006, where the resonance contributions from $h = (\eta, \eta', \eta_c, \eta_c(2S), \chi_{c0}, \chi_{c2}, J/\psi, X(3872))$ were measured. The largest contributions came from $\mathrm{Br}(B^\pm \to K^\pm\eta \to K^\pm\gamma\gamma) = (0.87^{+0.16+0.10}_{-0.15-0.07}) \times 10^{-6}$ and $\mathrm{Br}(B^\pm \to K^\pm\eta' \to K^\pm\gamma\gamma) = (1.40^{+0.16+0.15}_{-0.15-0.12}) \times 10^{-6}$, while the branching ratios for the other channels were typically less than $\mathcal{O}(10^{-7})$. As the branching ratio measurements of $B^\pm \to K^\pm h$ as well as $h \to \gamma\gamma$ have been significantly improved since 2006, and will be further improved in the future, we must be able to estimate these background contributions at a high accuracy. Further investigation is needed in order to quantify the sensitivity to the new physics in this channel, while we see great potential at Belle II.

9.4. Inclusive and exclusive $b \to s\ell^+\ell^-$ decays

9.4.1. Inclusive $B \to X_q\ell^+\ell^-$ decay

Contributing authors: G. Bell and T. Huber

Inclusive $B \to X_q\ell^+\ell^-$ decays provide information on the quark flavor sector that is complementary to inclusive $b \to q\gamma$ and exclusive $b \to q\ell^+\ell^-$ transitions. In contrast to $B \to X_q\gamma$, an angular analysis of the decay products entails a richer dependence on the SD Wilson coefficients. Compared to exclusive $b \to q\ell^+\ell^-$ decays, on the other hand, hadronic uncertainties are under better theoretical control for the inclusive modes. Measurements of the $B \to X_q\ell^+\ell^-$ decay distributions at Belle II will thus complement the LHCb studies of the exclusive $b \to q\ell^+\ell^-$ transitions, thereby providing important cross checks of the deviations found by LHCb and Belle in $B \to K^*\mu^+\mu^-$ and related modes [389–391,553].

The two main kinematic variables in inclusive $B \to X_s\ell^+\ell^-$ decays are the dilepton invariant mass squared $m^2_{\ell\ell} = q^2$ and $z = \cos\theta$, where θ is the angle between the three-momenta of the positively charged lepton ℓ^+ and the initial B meson in the dilepton center-of-mass frame. In terms of these variables, the double differential decay width takes the form of a second-order polynomial in z [554],

$$\frac{d^2\Gamma}{dq^2\,dz} = \frac{3}{8}\Big[(1+z^2)H_T(q^2) + 2zH_A(q^2) + 2(1-z^2)H_L(q^2)\Big]. \tag{247}$$

The functions H_T, H_A, and H_L represent three independent observables. H_A is up to a rational factor equivalent to the forward–backward asymmetry [555], while the q^2 spectrum is given by the sum of

H_T and H_L:

$$\frac{dA_{\rm FB}}{dq^2} = \int_{-1}^{+1} dz\, \frac{d^2\Gamma}{dq^2 dz}\, {\rm sgn}(z) = \frac{3}{4} H_A(q^2),$$
$$\frac{d\Gamma}{dq^2} = \int_{-1}^{+1} dz\, \frac{d^2\Gamma}{dq^2 dz} = H_T(q^2) + H_L(q^2). \tag{248}$$

The observables mainly depend on the Wilson coefficients C_7, C_9, and C_{10}. Taking only these three coefficients into account and suppressing a common prefactor $G_{\rm F}^2 m_b^5 \left|V_{ts}^* V_{tb}\right|^2 / (48\pi^3)$, one has (with $\hat{s} = q^2/m_b^2$)

$$H_T(q^2) = 2\hat{s}\left(1-\hat{s}\right)^2 \left[\left|C_9 + \frac{2}{\hat{s}} C_7\right|^2 + |C_{10}|^2\right],$$
$$H_L(q^2) = (1-\hat{s})^2 \left[\left|C_9 + 2\, C_7\right|^2 + |C_{10}|^2\right],$$
$$H_A(q^2) = -4\hat{s}\left(1-\hat{s}\right)^2 \ {\rm Re}\left[C_{10}\left(C_9 + \frac{2}{\hat{s}} C_7\right)\right]. \tag{249}$$

The dilepton invariant mass spectrum is dominated by charmonium resonances (J/ψ, $\psi(2S)$, etc.), which are usually removed by kinematic cuts. This leads to the so-called perturbative dilepton invariant mass regions: the low-q^2 region for $q^2 \in [1,6]\,{\rm GeV}^2$ and the high-q^2 region for $q^2 > 14.4\,{\rm GeV}^2$. Within these regions, one expects that the theoretical uncertainties can be controlled to around 10%.

In the low-q^2 region, the observables can be computed within a local OPE in the heavy quark limit. The perturbative calculation is well advanced and higher-order QCD [399,556–564] and EW [564–567] corrections are available to NNLO and NLO, respectively. The leading power corrections of order $\Lambda_{\rm QCD}^2/m_b^2$ [455,568–570], $\Lambda_{\rm QCD}^3/m_b^3$ [571,572], and $\Lambda_{\rm QCD}^2/m_c^2$ [434] are also known. The latter can be considered as parts of the resolved photon contributions [573].

In the high-q^2 region, on the other hand, the heavy mass expansion breaks down at the endpoint of the q^2 spectrum. For the integrated high-q^2 spectrum, however, there exists an effective expansion in inverse powers of $m_b^{\rm eff} = m_b\left(1-\sqrt{\hat{s}_{\rm min}}\right)$ instead of m_b. This expansion converges less rapidly, and the convergence behavior depends on the value of the q^2 cut, $\hat{s}_{\rm min} = q^2_{\rm min}/m_b^2$ [562].

The differential decay width is, furthermore, affected by QED corrections, which lead to two major modifications. First, the electron and muon channels get different contributions of the form $\ln(m_b^2/m_\ell^2)$, which stem from collinear photon emissions. Second, the simple z dependence of the double differential decay distribution in Eq. (247) gets modified and becomes a complicated function of z [567]. In the presence of QED radiation, the observables in Eq. (249) are therefore defined by taking appropriate projections of the double differential rate [567]. In order to compare theoretical predictions with experimental data, it is important that the experimental analyses use the same prescriptions.

The theoretical uncertainties can be further reduced by normalizing the observables to the inclusive semi-leptonic $B \to X_c \ell \bar{\nu}$ decay rate. The SM predictions for the $B \to X_s \mu^+ \mu^-$ observables then

become

$$\begin{aligned} H_T[1,6]_{\mu\mu} &= (4.03 \pm 0.28) \cdot 10^{-7}, \\ H_L[1,6]_{\mu\mu} &= (1.21 \pm 0.07) \cdot 10^{-6}, \\ H_A[1,6]_{\mu\mu} &= (-0.42 \pm 0.16) \cdot 10^{-7}, \\ \text{Br}[1,6]_{\mu\mu} &= (1.62 \pm 0.09) \cdot 10^{-6}, \\ \text{Br}[>14.4]_{\mu\mu} &= (2.53 \pm 0.70) \cdot 10^{-7}. \end{aligned} \tag{250}$$

Here, the notation $O[q_0^2, q_1^2]$ with $O = H_T, H_L, H_A, \text{Br}$ means that the relevant observable has been integrated over $q^2 \in [q_0^2, q_1^2]$. The complete list of theory predictions can be found in Ref. [567]. To tame the large uncertainty in the high-q^2 branching ratio, which mainly stems from poorly known parameters in the power corrections, a normalization to the semi-leptonic $B \to X_u \ell \bar{\nu}$ rate with the same cut in q^2 was proposed [572]:

$$\mathcal{R}(s_0) = \frac{\displaystyle\int_{\hat{s}_0}^1 d\hat{s}\, \frac{d\Gamma_{B\to X_s \ell^+\ell^-}}{d\hat{s}}}{\displaystyle\int_{\hat{s}_0}^1 d\hat{s}\, \frac{d\Gamma_{B\to X_u \ell \bar{\nu}}}{d\hat{s}}}. \tag{251}$$

Employing this normalization results in

$$\mathcal{R}(14.4)_{\mu\mu} = (2.62 \pm 0.30) \cdot 10^{-3}. \tag{252}$$

Unfortunately, the achieved precision cannot yet be exploited, because the BaBar [574,575] and Belle [576–578] measurements suffer from sizeable experimental uncertainties in the ballpark of 30% (cf. Eq. (253)). Furthermore, all measurements performed at the B factories are based on a sum over exclusive final states, which makes a direct comparison to the theoretical predictions non-trivial.

Belle II can significantly improve upon this situation, and with its two orders of magnitude larger data sample it might for the first time be possible to perform a complete angular analysis of $B \to X_s \ell^+ \ell^-$ decays. In the beginning, Belle II will still have to rely on the sum-over-exclusive method, but a fully inclusive analysis based on the recoil technique may be feasible in the long term.

The prospects for future improvements on the experimental side call for refinements of the SM predictions. Some of the important questions to be addressed are:

(i) In the absence of a fully inclusive analysis, one has to revisit the theoretical issues that arise from semi-inclusive analyses. In particular, a cut on the hadronic invariant mass $M_{X_s} \lesssim 1.8\,\text{GeV}$ affects the low-q^2 region and induces additional theoretical uncertainties. The theoretical description in this "shape function region" is similar to $B \to X_u \ell \nu$ and $B \to X_s \gamma$ decays [579,580]. An analysis of the effects from sub-leading shape functions was presented in Ref. [581], and a prediction for the position of the zero of the forward–backward asymmetry in the presence of the M_{X_s} cut was given in Ref. [582]. Similar studies for other observables. as well as a detailed analysis of the impact of the M_{X_s} cut on the extraction of the Wilson coefficients, are yet to be performed.

(ii) Similar to inclusive $B \to X_s \gamma$ decays (see Sect. 9.2.1), a systematic analysis of hadronic non-local power corrections includes resolved contributions in which the virtual photon couples to light partons instead of connecting directly to the effective weak interaction vertex. These

contributions stay non-local even when the hadronic mass cut is released and therefore represent an irreducible uncertainty independent of the cut. A first analysis that quantifies this uncertainty can be found in Ref. [573].

(iii) To estimate the impact of the charmonium resonances on the low-q^2 and high-q^2 regions, one may attempt to model the resonance structure explicitly. The most commonly used implementation via the Krüger–Sehgal approach [583] uses dispersion relations for the electromagnetic vacuum polarization. The model is based on the assumption that the $c\bar{c}$ loop and the $b \to s$ transition factorize, which is not justified on theoretical grounds. Since LHCb measurements of $B^+ \to K^+\mu^+\mu^-$ indeed suggest that non-factorizable corrections substantially modify the interference, theoretical investigations that go beyond the Krüger–Sehgal approach seem to be required.

(iv) The ratio $R_{X_s} = \mathrm{Br}_{\mu\mu}/\mathrm{Br}_{ee}$, in analogy to the quantity $R_{K^{(*)}}$ in the exclusive modes, is among the "golden modes" proposed for the early Belle II run. A measurement of R_{X_s} will shed light on possible hints for lepton flavor non-universality recently observed by LHCb [391,392]. Given the expected Belle II precision, a careful reanalysis of photon radiation will become important since collinear QED corrections represent the leading source of lepton flavor universality breaking in the SM. As the size of these contributions is sensitive to the imposed experimental cuts, a close interaction between experiment and theory is needed.

(v) The latest analyses of $B \to X_d\ell^+\ell^-$ decays date back more than 10 years [584,585]. An update with a decomposition into angular observables, including higher-order QCD and QED bremsstrahlung corrections, appears to be timely. Due to the different hierarchy of CKM elements, one expects larger CP-violating effects in $b \to d\ell^+\ell^-$ than in $b \to s\ell^+\ell^-$ transitions.

The experimental data can be used to constrain new physics effects in a model-independent fashion, i.e by constraining the Wilson coefficients (see Sect. 9.4.5 for further details). For the case of C_9 and C_{10}, the current situation as well as the potential impact of future Belle II measurements is illustrated in Fig. 92 [554,567]. From the figure it is evident that the new physics potential of $B \to X_s\ell^+\ell^-$ decays has not yet been fully exploited. Furthermore, right-handed currents—which have been extensively studied in exclusive transitions—were not included in the latest theory studies, and the synergy and complementarity of inclusive and exclusive $b \to s\ell^+\ell^-$ analyses is yet to be explored. To this end, detailed Monte Carlo (MC) studies could be used in conjunction with realistic theory predictions to estimate how much statistics is needed at Belle II to reach or exceed the sensitivity of the LHCb measurements on the exclusive modes. Such analyses could build on the studies [554,567].

9.4.2. Measurement of $B \to X_s\ell^+\ell^-$

Contributing author: A. Ishikawa

All existing measurements of the inclusive $B \to X_s\ell^+\ell^-$ mode have employed the sum-of-exclusive method [574–578] in which the hadronic system X_s is reconstructed from $Kn\pi$ final states with $n \leq 4$, allowing for at most one neutral pion. The X_s system is combined with the dielectron or dimuon pair to reconstruct the B meson. The B meson is identified by its ΔE and M_{bc} distributions. Since the decay does not contain hard photons, the ΔE resolution is much better than that in $B \to X_s\gamma$. This allows one to adopt a tight ΔE selection which, compared to the $B \to X_s\gamma$ analysis, suppresses the likelihood of multiple candidates in a single event and the self cross-feed. A hadronic mass selection is applied to reduce combinatorial backgrounds, i.e. $M_{X_s} < 1.8\,\mathrm{GeV}$ at BaBar [575] and $M_{X_s} < 2.1\,\mathrm{GeV}$ [576] or $M_{X_s} < 2.0\,\mathrm{GeV}$ [577,578] at Belle. For the low-q^2 and high-q^2 regions,

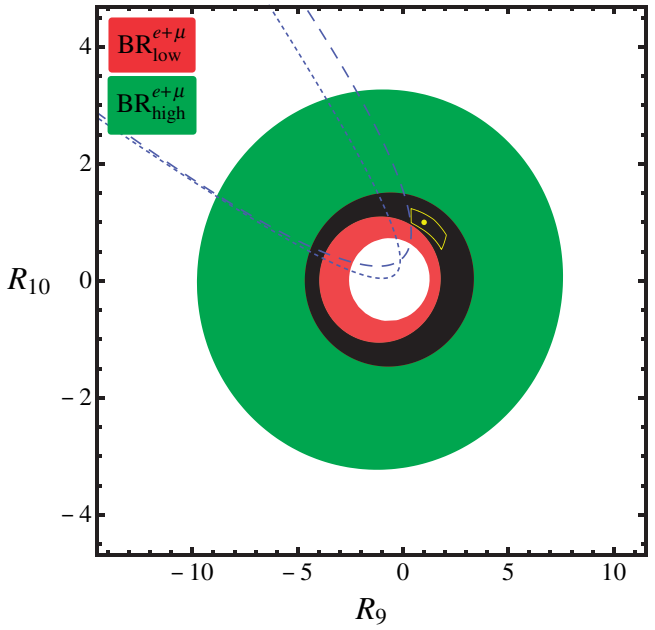

Fig. 92. Constraints at 95% CL on the Wilson coefficient ratios $R_{9,10} = C_{9,10}/C^{\mathrm{SM}}_{9,10}$. Shown are the branching ratio constraints at low-q^2 (red) and high-q^2 (green), together with their overlap (black). The region outside the dashed parabola-shaped regions is allowed by the Belle measurement of the forward–backward asymmetry. The yellow dot is the SM point and the yellow contour is the future Belle II reach, assuming the central values of $R_{9,10}$ are unity as in the SM. See Ref. [567] for further details.

the weighted averages of the experimental results read [567]

$$\begin{aligned} \mathrm{Br}[1,6]^{\mathrm{exp}}_{\ell\ell} &= (1.58 \pm 0.37) \cdot 10^{-6}, \\ \mathrm{Br}[>14.4]^{\mathrm{exp}}_{\ell\ell} &= (4.8 \pm 1.0) \cdot 10^{-7}, \end{aligned} \tag{253}$$

respectively. Notice that, compared to the theory prediction in Eq. (250), the measurement of $\mathrm{Br}[1,6]_{\ell\ell}$ has an uncertainty that is larger by around a factor of four. In addition, Belle presented a measurement of the forward–backward asymmetry [578] and BaBar a measurement of the CP asymmetry [575].

Our study of the prospects of the $B \to X_s \ell^+ \ell^-$ measurements at Belle II are based on a cut of $M_{X_s} < 2.0\,\mathrm{GeV}$, but we emphasize that this selection can be loosened in order to better understand the X_s spectrum and to reduce theoretical uncertainties. There are three dominant backgrounds. The first one is associated to $c\bar{c}$ continuum events in which both charm quarks decay semi-leptonically, the second one arises from $B\bar{B}$ events with two leptons either from semi-leptonic B or D decays, and the third one is due to $B \to J/\psi\,(\psi(2S))X_s$ backgrounds. The semi-leptonic backgrounds can be suppressed by missing energy information and vertex quality requirement, while the $B \to J/\psi\,(\psi(2S))X_s$ backgrounds can be eliminated by applying appropriate cuts on the invariant mass of the dilepton system.

The partial branching ratios in the low-q^2 and high-q^2 regions are under good theoretical control (see Eqs. (250) and (252)) and thus precise measurements of the dilepton spectra will allow constraints on the Wilson coefficients C_9 and C_{10}. We define the following q^2 regions: $[1.0, 3.5]\,\mathrm{GeV}^2$ (low1), $[3.5, 6.0]\,\mathrm{GeV}^2$ (low2), and $>14.4\,\mathrm{GeV}^2$ (high). Given the large data sample expected at Belle II, the reduction of systematic uncertainties is crucial. Thanks to the large branching fractions of the

$B \to K^{(*)}\ell^+\ell^-$ modes and the good ΔE resolution compared to $B \to X_s\gamma$, missing mode and fragmentation uncertainties can be reduced by adding additional reconstructed decays, such as three-kaon modes, that were not included in earlier studies. In the high- (low-) q^2 region, these uncertainties are expected to be as small as 1% (as large as 4%) due to the lower (higher) multiplicity of X_s decays, while K^*–X_s transition uncertainty could be as large as 2% (as small as 1%) due to the larger (smaller) fraction of K^*. With 50 ab^{-1} of data we expect total uncertainties of 6.6%, 6.4%, and 4.7% for the partial branching ratios in the low1, low2, and high regions as defined above.

Belle II measurements of the forward–backward asymmetry $A_{\rm FB}$ in $B \to X_s\ell^+\ell^-$ are expected to provide the most stringent limits on the Wilson coefficients C_9 and C_{10}. Since large parts of the theoretical and experimental systematic uncertainties cancel out in $A_{\rm FB}$, the corresponding measurements will be statistically limited. The expected uncertainties on $A_{\rm FB}$ in the low1, low2, and high regions are 3.1%, 2.6%, and 2.4%, respectively, assuming the SM.

A helicity decomposition of $B \to X_s\ell^+\ell^-$ provides the three observables H_i defined in Eq. (247). While H_A and the combination $H_T + H_L$ have been measured (cf. Eq. (248)), independent measurements of H_T and H_L have not been performed by BaBar and Belle, but will be possible at Belle II. As for measurements of the branching ratios, the experimental determinations of the coefficients H_i will not be systematically limited until 10 ab^{-1} have been collected. Considering normalized observables might help to reduce the systematic uncertainties.

Measurement of the CP asymmetries in $B \to X_s\ell^+\ell^-$ can be used to search for new sources of CP violation. Not only the rate asymmetry, but also the CP asymmetry of angular distributions, such as forward–backward CP asymmetry ($A_{\rm FB}^{\rm CP}$) are useful [586]. Since the denominator of $A_{\rm FB}^{\rm CP}$ can be zero if $A_{\rm FB}$ for $\bar{B}$ and B are zero or have opposite sign, we consider the difference of $A_{\rm FB}$ between $\bar{B}$ and B mesons defined as $\Delta_{\rm CP}(A_{\rm FB}) = A_{\rm FB}^{\bar{B}} - A_{\rm FB}^{B}$. Since most of systematic uncertainties cancel out by taking the ratio, the dominant uncertainty is statistical.

Tests of lepton flavor universality can also be performed by measuring R_{X_s}. The Belle II detector has certainly a good resolution for the e^+e^- mode and the R_{X_s} measurement is promising. We can expect a performance similar to those of the exclusive channel (i.e. the $R_{K^{(*)}}$ measurement), which will be discussed in Sect. 9.4.4.

A summary of the Belle II sensitivities for the various $B \to X_s\ell^+\ell^-$ observables is provided in Table 64.

9.4.3. Exclusive $B \to K^{(*)}\ell^+\ell^-$ decays

Contributing authors: W. Altmannshofer, U. Haisch, and D. Straub

The $\bar{B} \to \bar{K}^*(\to \bar{K}\pi)\,\ell^+\ell^-$ transition

$$\frac{d^4\Gamma}{dq^2\, d\cos\theta_\ell\, d\cos\theta_K\, d\phi} = \frac{9}{32\pi} I(q^2, \theta_\ell, \theta_K, \phi) \tag{254}$$

is completely described in terms of 12 angular coefficient functions I_j [587–589], namely

$$\begin{aligned} I(q^2, \theta_\ell, \theta_K, \phi) = {} & I_1^s \sin^2\theta_K + I_1^c \cos^2\theta_K + (I_2^s \sin^2\theta_K + I_2^c \cos^2\theta_K)\cos 2\theta_\ell \\ & + I_3 \sin^2\theta_K \sin^2\theta_\ell \cos 2\phi + I_4 \sin 2\theta_K \sin 2\theta_\ell \cos\phi \\ & + I_5 \sin 2\theta_K \sin\theta_\ell \cos\phi + (I_6^s \sin^2\theta_K + I_6^c \cos^2\theta_K)\cos\theta_\ell \\ & + I_7 \sin 2\theta_K \sin\theta_\ell \sin\phi + I_8 \sin 2\theta_K \sin 2\theta_\ell \sin\phi \\ & + I_9 \sin^2\theta_K \sin^2\theta_\ell \sin 2\phi. \end{aligned} \tag{255}$$

Table 64. The Belle II sensitivities for the inclusive $B \to X_s \ell^+ \ell^-$ observables corresponding to an invariant mass cut of $M_{X_s} < 2.0\,\text{GeV}$. The given sensitivities are relative or absolute uncertainties depending on the quantity under consideration.

Observables	Belle $0.71\,\text{ab}^{-1}$	Belle II $5\,\text{ab}^{-1}$	Belle II $50\,\text{ab}^{-1}$
$\text{Br}(B \to X_s \ell^+ \ell^-)$ ($[1.0, 3.5]\,\text{GeV}^2$)	29%	13%	6.6%
$\text{Br}(B \to X_s \ell^+ \ell^-)$ ($[3.5, 6.0]\,\text{GeV}^2$)	24%	11%	6.4%
$\text{Br}(B \to X_s \ell^+ \ell^-)$ ($>14.4\,\text{GeV}^2$)	23%	10%	4.7%
$A_{\text{CP}}(B \to X_s \ell^+ \ell^-)$ ($[1.0, 3.5]\,\text{GeV}^2$)	26%	9.7%	3.1%
$A_{\text{CP}}(B \to X_s \ell^+ \ell^-)$ ($[3.5, 6.0]\,\text{GeV}^2$)	21%	7.9%	2.6%
$A_{\text{CP}}(B \to X_s \ell^+ \ell^-)$ ($>14.4\,\text{GeV}^2$)	21%	8.1%	2.6%
$A_{\text{FB}}(B \to X_s \ell^+ \ell^-)$ ($[1.0, 3.5]\,\text{GeV}^2$)	26%	9.7%	3.1%
$A_{\text{FB}}(B \to X_s \ell^+ \ell^-)$ ($[3.5, 6.0]\,\text{GeV}^2$)	21%	7.9%	2.6%
$A_{\text{FB}}(B \to X_s \ell^+ \ell^-)$ ($>14.4\,\text{GeV}^2$)	19%	7.3%	2.4%
$\Delta_{\text{CP}}(A_{\text{FB}})$ ($[1.0, 3.5]\,\text{GeV}^2$)	52%	19%	6.1%
$\Delta_{\text{CP}}(A_{\text{FB}})$ ($[3.5, 6.0]\,\text{GeV}^2$)	42%	16%	5.2%
$\Delta_{\text{CP}}(A_{\text{FB}})$ ($>14.4\,\text{GeV}^2$)	38%	15%	4.8%

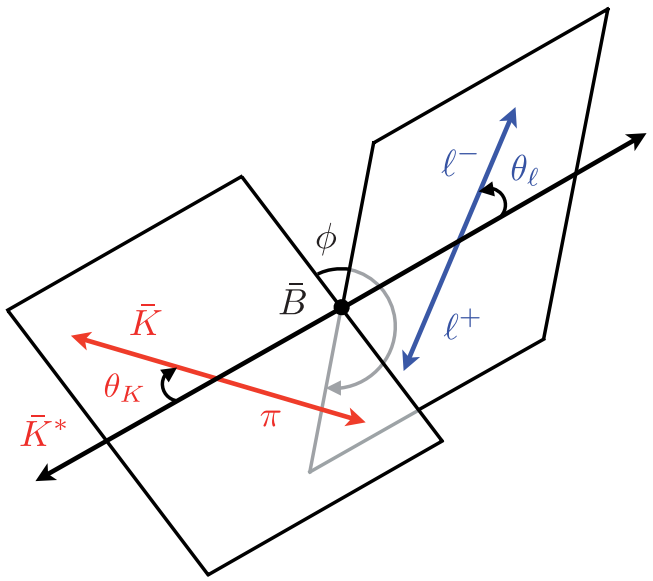

Fig. 93. Angular conventions used in the description of the $\bar{B} \to \bar{K}^* (\to \bar{K}\pi)\, \ell^+ \ell^-$ decay.

The adopted angular conventions are illustrated in Fig. 93 and follow Ref. [388] (see also Ref. [589]). The angle θ_ℓ is the angle between the direction of the ℓ^- in the dilepton rest frame and the direction of the dilepton in the $\bar{B}$ rest frame. The angle θ_K is the angle between the direction of the kaon in the $\bar{K}^*$ rest frame and the direction of the $\bar{K}^*$ in the $\bar{B}$ rest frame. The angle ϕ is the angle between the plane containing the dilepton pair and the plane containing the kaon and pion from the $\bar{K}^*$.

The decay distribution for the CP-conjugate mode $B \to K^* (\to K\pi) \ell^+ \ell^-$ is given by a formula analogous to Eq. (254) with different angular functions, which we call $\bar{I}_j$. Note that for this decay, θ_ℓ is the angle between the direction of the ℓ^+ in the dilepton rest frame and the direction of the dilepton in the B rest frame, while θ_K is the angle between the direction of the kaon in the K^* rest frame and the direction of the K^* in the B rest frame. As a result, the functions $\bar{I}_j$ can be obtained by

the replacements

$$I^{(a)}_{1,2,3,4,5,6} \to \bar{I}^{(a)}_{1,2,3,4,5,6}, \qquad I^{(a)}_{7,8,9} \to -\bar{I}^{(a)}_{7,8,9}, \tag{256}$$

with $a = s, c$. These quantities which encode the angular distribution of the exclusive decay can be expressed in terms of helicity (or transversity) amplitudes that depend on the dilepton invariant mass squared, the Wilson coefficients $C_7, C_9, C_{10}, C_S, C_P$ and their chirality-flipped counterparts as well as the $B \to K^*$ form factors that arise from the matrix elements $\langle K^*|Q_i|B\rangle$. The situation is much simpler for the $B \to K\ell^+\ell^-$ decay, which gives rise to only three observables, namely the branching ratio, the forward–backward asymmetry $A_{\rm FB}$, and the flat term F_H [590].

The self-tagging nature of the $\bar{B} \to \bar{K}^*(\to \bar{K}\pi)\,\ell^+\ell^-$ decay means that it is possible to determine both CP-averaged and CP-asymmetric quantities that depend on the coefficients [588]

$$S_j = \left(I_j + \bar{I}_j\right) \Big/ \frac{d\Gamma}{dq^2}, \qquad A_j = \left(I_j - \bar{I}_j\right) \Big/ \frac{d\Gamma}{dq^2}, \tag{257}$$

respectively. The two most measured angular observables are the forward–backward asymmetry and the K^* longitudinal polarization fraction:

$$A_{\rm FB} = \frac{3}{4}S_{6s} + \frac{3}{8}S_{6c}, \qquad F_{\rm L} = -S_{2c}. \tag{258}$$

By exploiting symmetry relations it is also possible to construct CP-averaged observables that are largely insensitive to form factor uncertainties [591–593]. These are

$$P_1 = \frac{S_3}{2S_{2s}}, \qquad P_2 = \frac{S_{6s}}{8S_{2s}}, \qquad P_3 = -\frac{S_9}{4S_{2s}}, \tag{259}$$

as well as

$$\begin{aligned} P'_4 &= \frac{S_4}{2\sqrt{-S_{2s}S_{2c}}}, \qquad P'_5 = \frac{S_5}{2\sqrt{-S_{2s}S_{2c}}}, \\ P'_6 &= \frac{S_7}{2\sqrt{-S_{2s}S_{2c}}}, \qquad P'_8 = \frac{S_8}{2\sqrt{-S_{2s}S_{2c}}}. \end{aligned} \tag{260}$$

The above definitions of the coefficients S_j and the observables P_i and P'_i correspond to those used by LHCb [389]. Analog CP-violating observables $P_i^{\rm CP}$ and $P_i'^{\rm CP}$ can be defined by simply replacing the coefficient S_j in the numerator of P_i and P'_i by the corresponding coefficient A_j. Notice that the observables P_1 and P_2 are commonly also called $A_T^{(2)} = P_1$ [594], $A_T^{(\rm Re)} = 2P_2$, and $A_T^{(\rm Im)} = -2P_3$ [595].

In order to illustrate the importance of Belle II measurements of the observables defined in Eqs. (258)–(260), we consider the two cases P_1 and P'_5. At small dilepton masses the angular variable P_1 is sensitive to the photon polarization. In fact, in the heavy-quark and large-energy limit, and ignoring α_s and m_s/m_b suppressed effects, one finds

$$A_T^{(2)} \approx \frac{2{\rm Re}\left(C_7 C'^*_7\right)}{|C_7|^2 + |C'_7|^2}, \qquad A_T^{(\rm Im)} \approx \frac{2{\rm Im}\left(C_7 C'^*_7\right)}{|C_7|^2 + |C'_7|^2}. \tag{261}$$

To maximize the sensitivity to the virtual photon it is necessary to go to very small q^2, which is only possible in the case of the decay $B \to K^* e^+ e^-$. Precision measurements of P_1 and P_3 in the dielectron channel are thus essential for probing possible BSM effects related to the right-handed

magnetic penguin operator Q_7' [491,507,596]. Consequently, decays like $B \to K^* e^+ e^-$ emerge as highly relevant for the Belle II program.

The angular observable P_5' is instead a sensitive probe of the semi-leptonic operators Q_9 and Q_{10} and their interference with Q_7. In the same approximation that led to Eq. (261), one obtains the expression

$$P_5' \approx \frac{\mathrm{Re}\big(C_{10}^* C_{9,\perp} + C_{9,\|}^* C_{10}\big)}{\sqrt{\big(|C_{9,\perp}|^2 + |C_{10}|^2\big)\,\big(|C_{9,\|}|^2 + |C_{10}|^2\big)}} \tag{262}$$

if only contributions from SM operators are included. Here,

$$C_{9,\perp} = C_9^{\mathrm{eff}}(q^2) + \frac{2m_b m_B}{q^2}\, C_7^{\mathrm{eff}}, \qquad C_{9,\|} = C_9^{\mathrm{eff}}(q^2) + \frac{2m_b}{m_B}\, C_7^{\mathrm{eff}}. \tag{263}$$

Importantly, the above results for P_1 and P_5' are correct only in the infinite heavy-quark limit. While in the case of Eq. (261) the leading-power corrections are formally of $\mathcal{O}(\Lambda_{\mathrm{QCD}}^2/m_b^2)$, in the case of Eq. (262) a rather complex structure of $\Lambda_{\mathrm{QCD}}/m_b$ terms arises (see Ref. [491] for details). Since at present the relevant power corrections can only be modeled, assumption-free extractions of C_9 and C_{10} as well as their chirality-flipped partners from measurements of P_5' and other angular observables are not possible.

Additional information on C_9, C_{10}, C_9', and C_{10}' can fortunately be gleaned from the lepton flavor universality ratios

$$R_H[q_0^2, q_1^2] = \frac{\displaystyle\int_{q_0^2}^{q_1^2} dq^2\, \frac{d\Gamma(B \to H\mu^+\mu^-)}{dq^2}}{\displaystyle\int_{q_0^2}^{q_1^2} dq^2\, \frac{d\Gamma(B \to He^+e^-)}{dq^2}}, \tag{264}$$

with $H = K, K^*$. The SM predictions for these ratios are 1 with high precision. Phase space effects are small and can be taken into account. Theoretical uncertainties from CKM factors as well as from form factors and other hadronic effects cancel in the ratio. Corrections due to collinear photon emissions have been studied recently and appear to be well described by existing Monte Carlo tools [597]. Any deviation in R_H from the SM prediction exceeding the few percent level would thus be a sign of new physics.

Including only the dominant linear BSM contributions from interference with the SM, the ratios R_K and R_{K^*} can be approximated by [598]

$$R_K[1,6] \approx 1 + \Delta_+, \qquad R_{K^*}[1,6] \approx 1 + \Delta_+ - p\,(\Delta_+ - \Delta_-)\,, \tag{265}$$

with

$$\Delta_\pm = \frac{2}{\big|C_9^{\mathrm{SM}}\big|^2 + \big|C_{10}^{\mathrm{SM}}\big|^2} \left\{ \sum_{i=9,10} \mathrm{Re}\left[C_i^{\mathrm{SM}}\left(C_i^{\mathrm{NP}\,\mu} \pm C_i'^{\,\mu}\right)\right] - (\mu \to e) \right\}, \tag{266}$$

where $p \approx 0.86$ is the so-called polarization fraction of the K^* meson [590,598]. The labels "SM" and "NP" denote the SM and new physics contributions, respectively, and the index μ or e indicates

the flavor content of the corresponding operator. Under the assumption that new physics modifies the dimuon channels only and that the relevant corrections are real, one obtains numerically

$$\begin{aligned} R_K[1,6] &\approx 1 + 0.24\big(C_{LL}^{\mathrm{NP}\,\mu} + C_{RL}^{\mu}\big), \\ R_{K^*}[1,6] &\approx 1 + 0.24\big(C_{LL}^{\mathrm{NP}\,\mu} - C_{RL}^{\mu}\big) + 0.07\, C_{RL}^{\mu}, \end{aligned} \tag{267}$$

where we have introduced the chiral Wilson coefficients

$$C_{LL}^{\mathrm{NP}\,\ell} = C_9^{\mathrm{NP}\,\ell} - C_{10}^{\mathrm{NP}\,\ell}, \qquad C_{RL}^{\ell} = C_9^{\prime\ell} - C_{10}^{\prime\ell}. \tag{268}$$

From Eq. (267) one observes that R_K only probes the combination $C_{LL}^{\mathrm{NP}\,\ell} + C_{RL}^{\ell}$ of Wilson coefficients, while R_{K^*} is mostly sensitive to $C_{LL}^{\mathrm{NP}\,\ell} - C_{RL}^{\ell}$. The observables R_K and R_{K^*} thus provide complementary information as they constrain different chirality structures of possible lepton flavor universality violating new physics in rare B decays. Notice furthermore that measurements of lepton flavor universality double ratios such as $R_K/R_{K^*} \approx 1 + 0.41\, C_{RL}^{\mu}$ directly probe right-handed currents in a theoretically clean way [598].

Belle II will also be able to perform lepton flavor universality tests using angular observables. Suitable variables include differences of angular observables in $B \to K^*\mu^+\mu^-$ and $B \to K^*e^+e^-$ [599,600], for instance $\Delta_{A_{\mathrm{FB}}} = A_{\mathrm{FB}}(B \to K^*\mu^+\mu^-) - A_{\mathrm{FB}}(B \to K^*e^+e^-)$ or $Q_i = P_i^{\mu} - P_i^{e}$. The differences in angular observables are predicted to be zero in the SM with high accuracy. Non-zero values would therefore again be an indication of new physics.

The recent LHCb measurements of $R_K[1,6] = 0.745^{+0.090}_{-0.074} \pm 0.036$ [391] and $R_{K^*}[1.1,6] = 0.69^{+0.11}_{-0.07} \pm 0.05$ [392] deviate by $2.6\,\sigma$ and $2.4\,\sigma$ from their SM values. Previous measurements from BaBar [601] and Belle [602] have considerably larger uncertainties and are compatible with both the SM prediction and the LHCb results. New physics that only modifies the $b \to s\mu^+\mu^-$ transition but leaves $b \to se^+e^-$ unaffected can explain the deviations seen in the lepton flavor universality ratios R_K and R_{K^*} and simultaneously address other B physics anomalies, like the discrepancy in P_5' [389] and the too-low $B_s \to \phi\mu^+\mu^-$ branching ratio [499]. Independent validations of the deviations observed in P_5', R_K, and R_{K^*} are needed to build a solid case for new physics. In the near future, Belle II is the only experiment that can perform such cross checks.

9.4.4. Measurements of $B \to K^{(*)}\ell^+\ell^-$

Contributing authors: A. Ishikawa and S. Wehle

The $b \to s\ell^+\ell^-$ transition was first observed in 2001 by Belle in the $B \to K\ell^+\ell^-$ channel [603]. Two years later, in 2003, Belle observed the $B \to K^*\ell^+\ell^-$ mode [604]. These observations opened the door for new physics searches via EW penguin B decays. The branching ratio and forward–backward asymmetry as a function of q^2 in $B \to K^{(*)}\ell^+\ell^-$ are important observables. A first measurement of the forward–backward asymmetry was also done by Belle in 2006 [605]. By now, several experiments have measured them [393,394,602,606–609]. Due to the spin structure of the K^* meson, a full angular analysis of $B \to K^*\ell^+\ell^-$ with optimized observables is a very powerful way to search for new physics. These optimized angular observables are less sensitive to form factor uncertainties that plague the theory calculations.

$B \to K^*\mu^+\mu^-$ channel In 2013, the LHCb collaboration announced the observation of a tension in the optimized observable P_5' with 1 fb^{-1} of data [610]. This tension was confirmed two years later when LHCb presented their $B \to K^*\mu^+\mu^-$ angular analysis based on the full LHC Run I dataset of

$3\,\text{fb}^{-1}$ [389]. Belle has recently also reported the results of an angular analysis with its full dataset using both charged and neutral B mesons decaying to $K^*e^+e^-$ and $K^*\mu^+\mu^-$ [390]. The Belle results are consistent with the angular analyses by LHCb, which considered alone show a $3.3\,\sigma$ discrepancy from the SM [611].

The observed deviations make further independent measurements of the angular distributions in $B \to K^*\mu^+\mu^-$ mandatory. Our extrapolations for Belle II are based on the systematic uncertainties obtained at Belle. For example, the difference between simulation and data was estimated directly from $B \to J/\psi K^*$ decays as measured by Belle. Since at Belle II the mis-modeling in the simulation will be improved, such an approach should lead to conservative projections. The uncertainty due to peaking backgrounds can be reduced by including the individual components in the fitted model. The individual components, which may be small, are more reliably modeled in a larger dataset. The uncertainty that is associated to the efficiency modeling can be reduced by adding correlation between q^2 and the helicity angle $\cos\theta_\ell$ in the efficiency function. We find that with $2.8\,\text{ab}^{-1}$ of Belle II data, the uncertainty on P_5' in the $q^2 \in [4,6]\,\text{GeV}^2$ bin using both muon and electron modes will be comparable to the $3.0\,\text{fb}^{-1}$ LHCb result [389] that uses the muon mode only. A naive extrapolation then leads to the conclusion that Belle II with $50\,\text{ab}^{-1}$ of data can reach accuracies of the optimized observables slightly higher than LHCb on a comparable time scale, i.e. with an integrated luminosity of approximately $22\,\text{fb}^{-1}$. We add that at Belle II the iTOP and ARICH might be able to identify low-momentum muons, which may increase the available data in the low-q^2 region. Our projections do not include such possible improvements.

$B \to K^*e^+e^-$ channel As mentioned before, an angular analysis of $B \to K^*e^+e^-$ at very low q^2 is a sensitive probe of the photon polarization [491,507,595,596]. In fact, angular observables such as P_1 and P_3^{CP} or $A_T^{(2)}$ and A_T^{Im} are functions of different combinations of real and imaginary parts of C_7 and C_7', and hence together with $S_{K^*\gamma}$ and $\text{Br}(B \to X_s\gamma)$ form a basis of clean observables that allow us to completely determine the contributions to Q_7 and Q_7' from experiment.

LHCb has measured the angular observables using $3\,\text{fb}^{-1}$ of data [515]. They reconstructed 124 signal events for the q^2 range $[0.002, 1.12]\,\text{GeV}^2$, where the lower bound is limited by angular resolution on $\tilde{\phi}$, where $\tilde{\phi} = \phi + \phi$ if $\phi < 0$. At Belle II, the resolution in $\tilde{\phi}$ is better than at LHCb, and the reconstruction efficiency of the electron mode is higher than that of the muon mode at low q^2. These features will allow for precise Belle II measurement of $B \to K^*e^+e^-$ in the low-q^2 region. With $50\,\text{fb}^{-1}$ of data, the sensitivities of $A_{\text{T}}^{(2)}$ and $A_{\text{T}}^{(\text{Im})}$ will be 0.066 and 0.064, respectively. The quoted uncertainties are dominated by statistical errors.

Belle II will not only be able to perform measurements of $B \to K^*e^+e^-$ in the low-q^2 region, but also has a unique sensitivity to the high-q^2 region. As mentioned earlier, Belle has already measured the angular function of $B \to K^*e^+e^-$ in the high-q^2 region [390], which provides important additional information to help understand the LHCb anomaly in the $B \to K^*\mu^+\mu^-$ channel. From this study, it is expected that approximately the same sensitivity to the $B \to K^*\mu^+\mu^-$ and $B \to K^*e^+e^-$ channels can be achieved at Belle II. This is possible since, in contrast to LHCb where radiative photon recovery is difficult, the reconstruction efficiency for electrons is comparable to that for muons at Belle II thanks to the better electromagnetic calorimeter.

Test of lepton flavor universality As mentioned above, we can expect a very high sensitivity to both muon and electron modes at Belle II. By taking the ratio between these two modes, almost all systematic uncertainties cancel out. In consequence, all the ratios R_K, R_{K^*}, and R_{X_s} can be measured

Table 65. The Belle II sensitivities for the observables in the low-q^2 region of the $B \to K^* \ell^+ \ell^-$ decay. Some numbers at Belle are extrapolated to 0.71 ab^{-1}.

Observables	Belle 0.71 ab^{-1}	Belle II 5 ab^{-1}	Belle II 50 ab^{-1}
$A_T^{(2)}$ ($[0.002, 1.12]\,\text{GeV}^2$)	—	0.21	0.066
A_T^{Im} ($[0.002, 1.12]\,\text{GeV}^2$)	—	0.20	0.064

precisely. At present, LHCb has measured R_K and R_{K^*} only in the low-q^2 region, while Belle II will have access to both the low-q^2 and high-q^2 regions. The dominant source of uncertainty is due to the imperfect lepton identification, which is expected to lead to a relative error of 0.4%. Given the smallness of this uncertainty, the Belle II measurements of R_K, R_{K^*}, and R_{X_s} will all be statistically limited. It thus follows that with 20 ab^{-1} of data, Belle II should be able to confirm the R_K anomaly observed by LHCb with a significance of $5\,\sigma$, if it is indeed due to new physics. We add that measurements of the observables $Q_{4,5} = P'^{\mu}_{4,5} - P'^{e}_{4,5}$ [600], which have recently been performed by Belle for the first time [390], are also statistically limited at Belle II.

The Belle II sensitivities for the $B \to K^{(*)} \ell^+ \ell^-$ channels are summarized in Table 65 (observables in the low-q^2 region), Table 66 (angular observables for different bins), and Table 67 (observables to test lepton flavor universality).

9.4.5. Interplay of future inclusive and exclusive $b \to s\ell^+\ell^-$ measurements

Contributing authors: T. Huber, A. Ishikawa, and J. Virto

In the following we will study the phenomenological impact that future Belle II measurements of the branching ratio and forward–backward asymmetry in $B \to X_s \ell^+ \ell^-$ with 50 ab^{-1} of integrated luminosity may have. We consider three q^2 bins, namely $[1, 3.5]\,\text{GeV}^2$, $[3.5, 6]\,\text{GeV}^2$, and $>14.4\,\text{GeV}^2$, and derive model-independent constraints on the Wilson coefficients of the operators Q_9 and Q_{10} introduced in Eq. (198). In particular, we will ask the following question: if the true values of the new physics contributions are C_9^{NP} and C_{10}^{NP}, respectively, with what significance will Belle II be able to exclude the SM?

This question is answered by the contours shown in Fig. 94, which have been obtained from a χ^2 fit based on the theory predictions of Ref. [567], but including an extra 5% uncertainty to account for non-perturbative effects [573]. Consider, for example, a point in the C_9^{NP}–C_{10}^{NP} plane which resides on the contour labeled "5." If this point represents the true values of the new physics contributions then a fit including only the measurements $\text{Br}(B \to X_s \ell^+ \ell^-)$ and $A_{\text{FB}}(B \to X_s \ell^+ \ell^-)$ will result in a pull of the SM with respect to the best-fit point by $5\,\sigma$. The figure thus allows us to determine the significance with which future Belle II measurements of $B \to X_s \ell^+ \ell^-$ can exclude the SM, depending on the true values of the Wilson coefficients C_9 and C_{10}.

For comparison, the $1\,\sigma$, $2\,\sigma$, and $3\,\sigma$ regions in the C_9^{NP}–C_{10}^{NP} plane that are obtained from the global analysis [612] are also shown in Fig. 94 as red contours. One can see that Belle II would exclude the SM by more than $5\,\sigma$ if the central value $C_9^{\text{NP}} = -1$ preferred by the global fit turns out to be correct. Notice that since the underlying hadronic uncertainties in the inclusive mode are independent of those that enter exclusive transitions, precision measurements of the $B \to X_s \ell^+ \ell^-$ channel provide important complementary information in the context of global fits. This shows that Belle II can play a decisive role in the search for new physics via $b \to s\ell^+\ell^-$ transitions.

Table 66. The Belle II sensitivities of the angular observables in $B \to K^* \ell^+ \ell^-$. Some numbers at Belle are extrapolated to 0.71 ab^{-1}.

Observables	Belle 0.71 ab^{-1}	Belle II 5 ab^{-1}	Belle II 50 ab^{-1}
$F_{\rm L}$ ($[1.0, 2.5]\,{\rm GeV}^2$)	0.19	0.063	0.025
$F_{\rm L}$ ($[2.5, 4.0]\,{\rm GeV}^2$)	0.17	0.057	0.022
$F_{\rm L}$ ($[4.0, 6.0]\,{\rm GeV}^2$)	0.14	0.046	0.018
$F_{\rm L}$ ($>14.2\,{\rm GeV}^2$)	0.088	0.027	0.009
P_1 ($[1.0, 2.5]\,{\rm GeV}^2$)	0.59	0.24	0.078
P_1 ($[2.5, 4.0]\,{\rm GeV}^2$)	0.53	0.21	0.071
P_1 ($[4.0, 6.0]\,{\rm GeV}^2$)	0.43	0.17	0.057
P_1 ($>14.2\,{\rm GeV}^2$)	0.33	0.12	0.040
P_2 ($[1.0, 2.5]\,{\rm GeV}^2$)	0.32	0.12	0.040
P_2 ($[2.5, 4.0]\,{\rm GeV}^2$)	0.30	0.11	0.036
P_2 ($[4.0, 6.0]\,{\rm GeV}^2$)	0.24	0.090	0.029
P_2 ($>14.2\,{\rm GeV}^2$)	0.086	0.034	0.011
P_3 ($[1.0, 2.5]\,{\rm GeV}^2$)	0.32	0.12	0.040
P_3 ($[2.5, 4.0]\,{\rm GeV}^2$)	0.30	0.11	0.036
P_3 ($[4.0, 6.0]\,{\rm GeV}^2$)	0.24	0.090	0.029
P_3 ($>14.2\,{\rm GeV}^2$)	0.18	0.068	0.022
P_4' ($[1.0, 2.5]\,{\rm GeV}^2$)	0.50	0.18	0.056
P_4' ($[2.5, 4.0]\,{\rm GeV}^2$)	0.45	0.15	0.049
P_4' ($[4.0, 6.0]\,{\rm GeV}^2$)	0.34	0.12	0.040
P_4' ($>14.2\,{\rm GeV}^2$)	0.26	0.099	0.032
P_5' ($[1.0, 2.5]\,{\rm GeV}^2$)	0.47	0.17	0.054
P_5' ($[2.5, 4.0]\,{\rm GeV}^2$)	0.42	0.15	0.049
P_5' ($[4.0, 6.0]\,{\rm GeV}^2$)	0.34	0.12	0.040
P_5' ($>14.2\,{\rm GeV}^2$)	0.23	0.088	0.027
P_6' ($[1.0, 2.5]\,{\rm GeV}^2$)	0.50	0.17	0.054
P_6' ($[2.5, 4.0]\,{\rm GeV}^2$)	0.45	0.15	0.049
P_6' ($[4.0, 6.0]\,{\rm GeV}^2$)	0.36	0.12	0.040
P_6' ($>14.2\,{\rm GeV}^2$)	0.27	0.10	0.032
P_8' ($[1.0, 2.5]\,{\rm GeV}^2$)	0.51	0.19	0.061
P_8' ($[2.5, 4.0]\,{\rm GeV}^2$)	0.47	0.17	0.056
P_8' ($[4.0, 6.0]\,{\rm GeV}^2$)	0.38	0.14	0.045
P_8' ($>14.2\,{\rm GeV}^2$)	0.27	0.10	0.032

9.5. Missing energy channels: $B \to K^{(*)} \nu\bar{\nu}$ and $B_q \to \nu\bar{\nu}$

9.5.1. $B \to K^{(*)} \nu\bar{\nu}$ transitions

Contributing author: D. Straub

The $B \to K^{(*)} \nu\bar{\nu}$ decays provide clean testing grounds for new dynamics modifying the $b \to s$ transition [613–615]. Unlike in other B meson decays, factorization of hadronic and leptonic currents is exact in the case of $B \to K^{(*)} \nu\bar{\nu}$ because the neutrinos are electrically neutral. Given the small perturbative and parametric uncertainties, measurements of the $B \to K^{(*)} \nu\bar{\nu}$ decay rates would hence in principle allow extraction of the $B \to K^{(*)}$ form factors to high accuracy.

Closely related to the $B \to K^{(*)} \nu\bar{\nu}$ modes are the B decays that lead to an exotic final state X, since the missing energy signature is the same. Studies of such signals are very interesting in the dark matter context and may allow us to illuminate the structure of the couplings between the dark and SM sectors [616].

Table 67. The Belle II sensitivities to $B \to K^{(*)}\ell^+\ell^-$ observables that allow testinf of lepton flavor universality. Some numbers at Belle are extrapolated to 0.71 ab^{-1}.

Observables	Belle 0.71 ab^{-1}	Belle II 5 ab^{-1}	Belle II 50 ab^{-1}
R_K ([1.0, 6.0] GeV^2)	28%	11%	3.6%
R_K (>14.4 GeV^2)	30%	12%	3.6%
R_{K^*} ([1.0, 6.0] GeV^2)	26%	10%	3.2%
R_{K^*} (>14.4 GeV^2)	24%	9.2%	2.8%
R_{X_s} ([1.0, 6.0] GeV^2)	32%	12%	4.0%
R_{X_s} (>14.4 GeV^2)	28%	11%	3.4%
Q_{F_L} ([1.0, 2.5] GeV^2)	0.38	0.12	0.050
Q_{F_L} ([2.5, 4.0] GeV^2)	0.34	0.12	0.044
Q_{F_L} ([4.0, 6.0] GeV^2)	0.28	0.092	0.036
Q_{F_L} (>14.2 GeV^2)	0.18	0.054	0.018
Q_1 ([1.0, 2.5] GeV^2)	1.2	0.48	0.15
Q_1 ([2.5, 4.0] GeV^2)	1.0	0.42	0.14
Q_1 ([4.0, 6.0] GeV^2)	0.86	0.34	0.11
Q_1 (>14.2 GeV^2)	0.66	0.24	0.080
Q_2 ([1.0, 2.5] GeV^2)	0.64	0.24	0.080
Q_2 ([2.5, 4.0] GeV^2)	0.60	0.22	0.072
Q_2 ([4.0, 6.0] GeV^2)	0.48	0.18	0.058
Q_2 (>14.2 GeV^2)	0.17	0.068	0.022
Q_3 ([1.0, 2.5] GeV^2)	0.64	0.24	0.080
Q_3 ([2.5, 4.0] GeV^2)	0.60	0.22	0.072
Q_3 ([4.0, 6.0] GeV^2)	0.48	0.18	0.058
Q_3 (>14.2 GeV^2)	0.36	0.14	0.044
Q_4 ([1.0, 2.5] GeV^2)	1.0	0.36	0.11
Q_4 ([2.5, 4.0] GeV^2)	0.90	0.30	0.10
Q_4 ([4.0, 6.0] GeV^2)	0.68	0.24	0.080
Q_4 (>14.2 GeV^2)	0.52	0.20	0.064
Q_5 ([1.0, 2.5] GeV^2)	0.94	0.34	0.11
Q_5 ([2.5, 4.0] GeV^2)	0.84	0.30	0.10
Q_5 ([4.0, 6.0] GeV^2)	0.68	0.24	0.080
Q_5 (>14.2 GeV^2)	0.46	0.18	0.054
Q_6 ([1.0, 2.5] GeV^2)	1.0	0.34	0.11
Q_6 ([2.5, 4.0] GeV^2)	0.90	0.30	0.10
Q_6 ([4.0, 6.0] GeV^2)	0.72	0.24	0.080
Q_6 (>14.2 GeV^2)	0.54	0.20	0.064
Q_8 ([1.0, 2.5] GeV^2)	1.0	0.38	0.12
Q_8 ([2.5, 4.0] GeV^2)	0.94	0.34	0.11
Q_8 ([4.0, 6.0] GeV^2)	0.76	0.28	0.090
Q_8 (>14.2 GeV^2)	0.54	0.20	0.064

$B \to K^{(*)}\nu\bar{\nu}$ in the SM Due to the exact factorization, the precision of the SM prediction for the branching ratios of $B \to K^{(*)}\nu\bar{\nu}$ is mainly limited by the $B \to K^{(*)}$ form factors and by the knowledge of the relevant CKM elements. The relevant Wilson coefficient is known in the SM, including NLO QCD and NLO EW correction to a precision of better than 2% [402,403,405]. Concerning the form factors, combined fits using results from LCSRs at low q^2 and lattice QCD at high q^2 can improve the theoretical predictions.

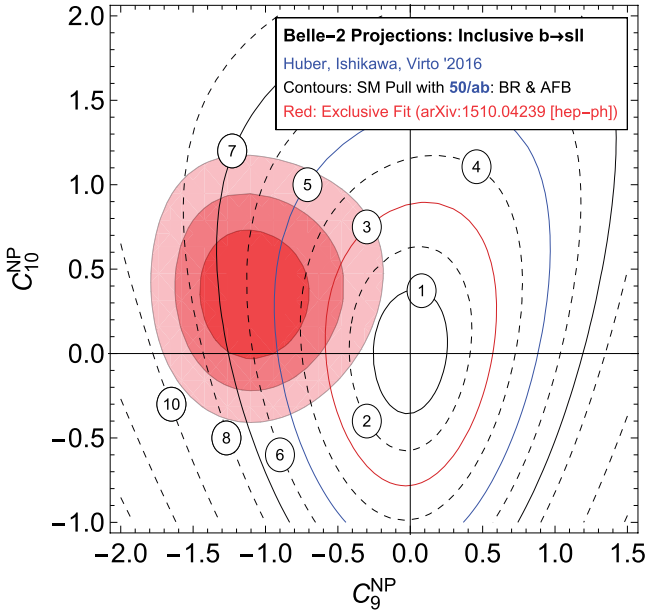

Fig. 94. Exclusion contours in the $C_9^{\rm NP}$–$C_{10}^{\rm NP}$ plane resulting from future inclusive $b \to s\ell^+\ell^-$ measurements at Belle II. For comparison, the constraints on $C_9^{\rm NP}$ and $C_{10}^{\rm NP}$ following the global fit presented in Ref. [612] are also shown.

Using $|\lambda_t^{(s)}| = (4.06 \pm 0.16) \cdot 10^{-2}$ for the relevant CKM elements, obtained using unitarity and an average of inclusive and exclusive tree-level determinations of $|V_{cb}|$, as well as a combined fit to LCSR [419] and lattice QCD [617] results for the $B \to K^*$ form factors, one obtains the following SM prediction for the $B \to K^*\nu\bar{\nu}$ branching ratio [618]:

$$\mathrm{Br}(B \to K^*\nu\bar{\nu})_{\rm SM} = (9.6 \pm 0.9) \cdot 10^{-6}. \tag{269}$$

An angular analysis of the angle spanned by the B meson and the K^+ meson resulting from the $K^* \to K^+\pi^-$ decay gives access to an additional observable, the K^* longitudinal polarization fraction $F_{\rm L}$, which is sensitive to right-handed currents [614]. The corresponding SM prediction is $F_{\rm L}^{\rm SM} = 0.47 \pm 0.03$ [613]. Even with the low number of events expected, it can been shown that such an analysis is quite possible at Belle II (details can be found below in the corresponding experimental section).

The $B \to K$ form factors are known to an even better precision from lattice QCD. Extrapolating the lattice result to the full q^2 range, one arrives at [618]

$$\mathrm{Br}(B^+ \to K^+\nu\bar{\nu})_{\rm SM} = (4.6 \pm 0.5) \cdot 10^{-6}. \tag{270}$$

Since the isospin asymmetry vanishes for both decays (except for a presumably negligible difference in the charged and neutral form factors), the B^0 vs. B^+ branching ratios can be trivially obtained by rescaling with the appropriate lifetimes—once the tree-level $B^+ \to \tau^+\nu$ ($\tau^+ \to K^+\bar{\nu}$) contribution is properly taken into account [615].

BSM physics in $B \to K^{(*)}\nu\bar{\nu}$ Within the SM, the $B \to K^{(*)}\nu\bar{\nu}$ decays are mediated by the effective operator in Eq. (199), which involves a sum over the three neutrino flavors $\ell = e, \mu, \tau$. In BSM scenarios, there can be a left-handed operator for each neutrino flavor as well as a right-handed

one of the form

$$Q_R^\ell = (\bar{s}_R \gamma_\mu b_R)(\bar{\nu}_{\ell L} \gamma^\mu \nu_{\ell L}). \tag{271}$$

In total there can therefore be six different operators.

The two branching ratios give access to two combinations of the six Wilson coefficients, namely

$$\begin{aligned} \frac{\mathrm{Br}(B \to K \nu\bar{\nu})}{\mathrm{Br}(B \to K \nu\bar{\nu})_{\mathrm{SM}}} &= \frac{1}{3} \sum_\ell (1 - 2\,\eta_\ell)\, \epsilon_\ell^2, \\ \frac{\mathrm{Br}(B \to K^* \nu\bar{\nu})}{\mathrm{Br}(B \to K^* \nu\bar{\nu})_{\mathrm{SM}}} &= \frac{1}{3} \sum_\ell \left(1 + \kappa_\eta \eta_\ell\right) \epsilon_\ell^2, \end{aligned} \tag{272}$$

where κ_η is a ratio of binned form factors [613] and

$$\epsilon_\ell = \frac{\sqrt{|C_L^\ell|^2 + |C_R^\ell|^2}}{|C_L^{\mathrm{SM}}|}, \qquad \eta_\ell = \frac{-\mathrm{Re}\left(C_L^\ell C_R^{\ell *}\right)}{|C_L^\ell|^2 + |C_R^\ell|^2}. \tag{273}$$

While in principle no general constraint on the size of BSM effects in $B \to K^{(*)} \nu\bar{\nu}$ decays can be derived from other processes, in practice in many models there is a relation between semi-leptonic decays with neutrinos and the ones with charged leptons in the final state. This is because $\mathrm{SU}(2)_L$ gauge symmetry relates left-handed neutrinos and charged leptons. This relation can be most conveniently studied in the SM effective field theory (SMEFT) [619,620], based on an OPE in powers of the inverse new physics scale. The relevant dimension-six operators are

$$\begin{aligned} Q_{Hq}^{(1)} &= (\bar{q}_L \gamma_\mu q_L) H^\dagger i \overleftrightarrow{D}^\mu H, \\ Q_{Hq}^{(3)} &= (\bar{q}_L \gamma_\mu \tau^a q_L) H^\dagger i \overleftrightarrow{D}^\mu \tau^a H, \\ Q_{Hd} &= (\bar{d}_R \gamma_\mu d_R) H^\dagger i \overleftrightarrow{D}^\mu H, \\ Q_{ql}^{(1)} &= (\bar{q}_L \gamma_\mu q_L)(\bar{l}_L \gamma^\mu l_L), \\ Q_{ql}^{(3)} &= (\bar{q}_L \gamma_\mu \tau^a q_L)(\bar{l}_L \gamma^\mu \tau^a l_L), \\ Q_{dl} &= (\bar{d}_R \gamma_\mu d_R)(\bar{l}_L \gamma^\mu l_L), \end{aligned} \tag{274}$$

where H denotes the Higgs doublet field, while q_L and l_L are the quark and lepton doublets, respectively, and we have suppressed flavor indices. The generators of $\mathrm{SU}(2)_L$ are denoted by τ^a. The SMEFT Wilson coefficients can be matched onto the low-energy Wilson coefficients $C_{L,R}^\ell$, and those relevant for $b \to s\ell^+\ell^-$ transitions are as follows [613,621,622]:

$$\begin{aligned} C_L &\propto C_{ql}^{(1)} - C_{ql}^{(3)} + C_Z, \\ C_R &\propto C_{dl} + C_Z', \\ C_9 &\propto C_{qe} + C_{ql}^{(1)} + C_{ql}^{(3)} - \zeta\, C_Z, \\ C_9' &\propto C_{de} + C_{dl} - \zeta\, C_Z', \\ C_{10} &\propto C_{qe} - C_{ql}^{(1)} - C_{ql}^{(3)} + C_Z, \\ C_{10}' &\propto C_{de} - C_{dl} + C_Z', \end{aligned} \tag{275}$$

where

$$C_Z = \frac{1}{2}\left(C_{Hq}^{(1)} + C_{Hq}^{(3)}\right), \qquad C_Z' = \frac{1}{2} C_{Hd}, \tag{276}$$

and $\zeta = 1 - 4s_{\rm w}^2 \approx 0.08$ is the accidentally small vector coupling of the Z boson to charged leptons, with $s_{\rm w}$ the sine of the weak mixing angle. While in full generality these relations are not very useful due to the larger number of operators in the SMEFT, they become useful in models where only a subset of the SMEFT operators are generated. For instance, in models with an additional SU(2)$_L$-singlet neutral heavy gauge boson (Z'), one has $C_{ql}^{(3)} = 0$. If in addition Z–Z' mixing is small, one obtains the prediction

$$C_L = \frac{C_9 - C_{10}}{2}, \qquad C_R = \frac{C_9' - C_{10}'}{2}. \tag{277}$$

In the opposite limit of a new physics model where only the coefficients C_Z and C_Z' are generated, one obtains

$$C_L = C_{10}, \qquad C_9 = -\zeta\, C_{10}, \tag{278}$$

and

$$C_R = C_{10}', \qquad C_9' = -\zeta\, C_{10}'. \tag{279}$$

In both cases, the existing data on $b \to s\ell^+\ell^-$ transitions limit the size of possible BSM effects in $B \to K^{(*)}\nu\bar{\nu}$. However, in models where new physics enters in the pattern $C_{ql}^{(1)} = -C_{ql}^{(3)}$, larger modifications are possible without any constraint from $b \to s\ell^+\ell^-$ processes. Indeed, such a pattern is realized in a particular leptoquark model [613] up to loop effects [294]. Finally, we stress that the constraints from $b \to s\ell^+\ell^-$ processes can be weakened by the contributions of additional operators not relevant in $b \to s\nu\bar{\nu}$, like dipole operators or operators involving right-handed leptons.

In the discussion after Eq. (274) we have so far neglected lepton flavor. In fact, in the $B \to K^{(*)}\nu\bar{\nu}$ decays all three neutrino flavors contribute and cannot be distinguished experimentally. In $b \to s\ell^+\ell^-$ transitions, on the other hand, the most precise measurements have been done with muons, and the modes with electrons in the final state are less strongly constrained. Finally, $b \to s\tau^+\tau^-$ decays have not been observed at all to date due to the difficulty posed by the identification of tau leptons. This highlights another important feature of the $B \to K^{(*)}\nu\bar{\nu}$ decays: if new physics couples mostly to the third generation of leptons (and lepton neutrinos), it could cause large enhancements of the $B \to K^{(*)}\nu\bar{\nu}$ branching ratios without strongly affecting $b \to se^+e^-$ or $b \to s\mu^+\mu^-$ decays. Such a dominant coupling to third-generation lepton flavor has recently been put forward to explain various anomalies in B physics [287,623] (cf. the related discussion in Sect. 9.6).

Related $b \to q\nu\bar{\nu}$ decays The processes $B_s \to \phi\nu\bar{\nu}$ or $B_s \to \eta^{(\prime)}\nu\bar{\nu}$ are based on the same quark-level transition as $B \to K^{(*)}\nu\bar{\nu}$ and only differ in their form factors. In addition, there are also exclusive decays based on the $b \to d\nu\bar{\nu}$ transition, e.g. $B \to \rho\nu\bar{\nu}$, $B \to \omega\nu\bar{\nu}$, or $B \to \pi\nu\bar{\nu}$. In the SM, the SD contribution to these decay rates are parametrically suppressed by $|V_{td}/V_{ts}|^2 \approx 0.05$ with respect to the $b \to s\nu\bar{\nu}$ modes, and are thus challenging to detect. Further, charged modes are

polluted by the large Cabibbo-allowed tree-level contribution $B^+ \to \tau^+\nu\,(\tau^+ \to (\pi,\rho)^+\bar{\nu})$. Still, order-of-magnitude enhancements of these modes relative to the SM expectations are not excluded in a model-independent fashion.

9.5.2. Measurements of $B \to K^{(*)}\nu\bar{\nu}$

Contributing authors: A. Ishikawa, E. Manoni, and D. Straub

Searches for the $B \to K^{(*)}\nu\bar{\nu}$ charged and neutral channels have been performed by both BaBar and Belle using hadronic tagging [624,625] and semi-leptonic tagging [626,627]. The resulting upper limits at 90% CL are a factor of two to five above the SM predictions [613] for the K^+, K^{*+}, and K^{*0} channels. Even if new physics does not contribute to the $b \to s\nu\bar{\nu}$ transitions, Belle II will be able to observe the $B \to K^{(*)}\nu\bar{\nu}$ decays.

We have estimated the sensitivities of $B \to K^+\nu\bar{\nu}$, $B \to K^{*0}\nu\bar{\nu}$, and $B \to K^{*+}\nu\bar{\nu}$ by combining the hadronic tagging and semi-leptonic tagging analyses. The three decay modes will be observed with about 10 ab^{-1} of data, and with 50 ab^{-1} the sensitivities on the branching ratio will be about 10%. Once the K^* modes are observed, measurements of the differential branching ratio and K^* polarization are important subjects. We performed toy studies and found that it should be possible to measure $F_{\rm L}$ with an uncertainty of 0.11 when the input $F_{\rm L}$ value is 0.47 as predicted in the SM [613].

In order to evaluate the impact of machine background on the $B \to K^{(*)}\nu\bar{\nu}$ searches, we have studied signal and generic MC samples (from the MC5 central campaign, described in Sect. 4), in two configuration: physics events superimposed on the nominal machine background ("BGx1" configuration), and physics events without machine background ("BGx0" configuration). We considered the $B^\pm \to K^{*\pm}\nu\bar{\nu}$ channel with $K^{*\pm}$ reconstructed in the $K^\pm\pi^0$ final state.

The generic MC samples used consist of a mixture of B^+B^-, $B^0\bar{B}^0$, $u\bar{u}$, $d\bar{d}$, $c\bar{c}$, and $s\bar{s}$ corresponding to 1 ab^{-1} of data. About 1 million signal MC events with $K^{*\pm}$ decaying to both $K^\pm\pi^0$ and $K^0_{\rm S}\pi^\pm$ have also been generated. The signal signature in the recoil of a B reconstructed in hadronic final states is searched for. To do that we used the official FEI algorithm (see Sect. 6.6) with ad hoc refinements on particle identification and cluster cleaning, as done for the $B \to \tau\nu$ analysis documented in Sect. 8.3.

We select $\Upsilon(4S)$ candidates in which the $B_{\rm tag}$ probability given by the FEI is higher than 0.5%. Moreover, no extra tracks (tracks not associated to the signal B meson nor to the tag-side B meson) should be reconstructed. We select the best $\Upsilon(4S)$ candidate in the event according to the highest $B_{\rm tag}$ signal probablity and the smallest difference between the reconstructed K^* mass and the Particle Data Group (PDG) value.

Once the best $B\bar{B}$ pair is selected, we exploit variables related to the $B_{\rm tag}$ kinematics ($M_{\rm bc}$ and ΔE variables) in order to remove mis-reconstructed candidates. Both requirements suppress events in which the $B_{\rm tag}$s originate from a wrong combination of charged and neutral particles, both in $B\bar{B}$ and $q\bar{q}$ events.

The continuum events can be further reduced by considering event shape variables such as R_2, i.e. the normalized second Fox–Wolfram moment. The goodness of the strange mesons reconstructed in the signal side is checked through a selection requirement on the difference between the reconstructed mass and the PDG value. Properties of the missing energy in the signal side are also exploited. We define the missing four-momentum in the center-of-mass (CM) frame as the difference of the $\Upsilon(4S)$ four-momentum and the sum of the $B_{\rm tag}$ and K^* four-momenta. Since no extra tracks are allowed, the missing momentum is related to actual neutrinos, extra-neutrals, and particles escaping the detector acceptance. One of the most powerful selection variables of the analysis is the sum of the missing

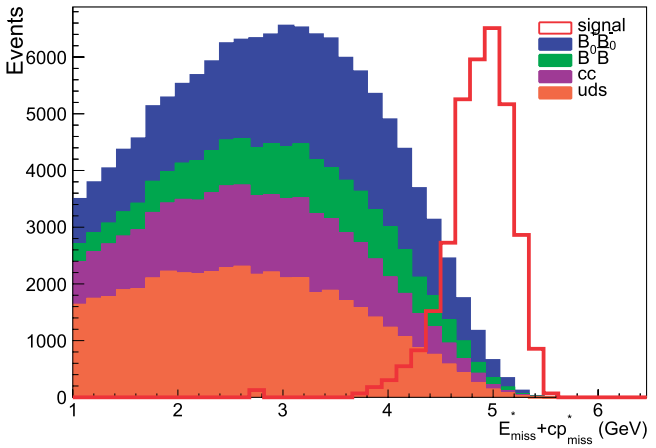

Fig. 95. Distribution of $E^*_{\rm miss} + cp^*_{\rm miss}$ for the signal (red) and for the generic MC samples (see legend) in the case of the $K^{*+} \to K^+\pi^0$ channel. The results shown correspond to the "BGx1" configuration after all the selection criteria have been applied except the ones on $E^*_{\rm miss} + cp^*_{\rm miss}$ and $E_{\rm ECL}$. The number of generic MC events corresponds to an integrated luminosity of 1 ab^{-1}, while the signal normalization is arbitrary.

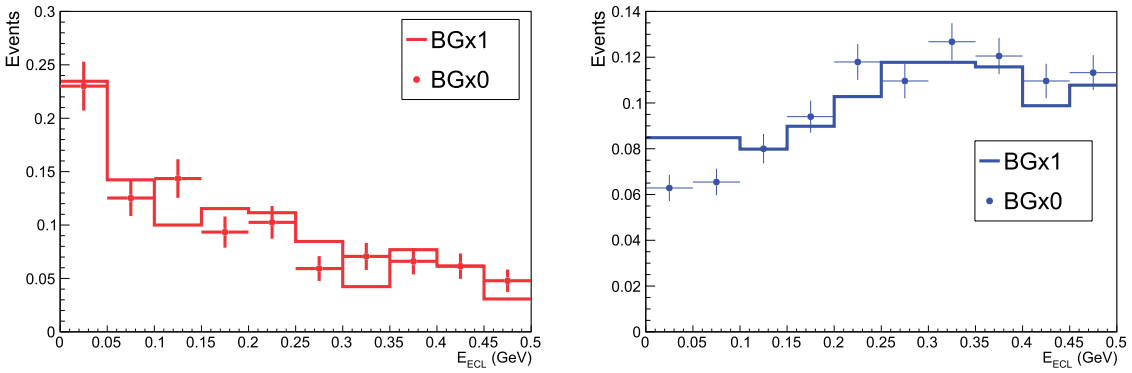

Fig. 96. Distribution of $E_{\rm ECL}$ normalized to unitary area for the "BGx0" (dots) and "BGx1" (line) configurations in the case of the $K^{*+} \to K^+\pi^0$ channel after applying all selection criteria. Left: signal MC sample. Right: charged B^+B^- sample.

energy and of the modulus of the missing three-momentum in the CM frame ($E^*_{\rm miss} + cp^*_{\rm miss}$), which is required to be greater than 4.5 GeV.

Figure 95 shows the $E^*_{\rm miss} + cp^*_{\rm miss}$ distributions for the $K^{*+} \to K^+\pi^0$ channel, for signal and generic MC samples in the "BGx1" configuration. The quantity $E^*_{\rm miss} + cp^*_{\rm miss}$ is much less correlated to the $\nu\bar{\nu}$ invariant mass than $E^*_{\rm miss}$ or $p^*_{\rm miss}$ alone, making it suitable for a model-independent analysis. A signal region in the extra-neutral energy deposited in the calorimeter ($E_{\rm ECL}$) is also defined, requiring $E_{\rm ECL} < 0.5$ GeV. The distributions for signal MC and the dominant source of background surviving the selection, namely charged $B\bar{B}$ decays, are shown in Fig. 96 in both "BGx1" and "BGx0" configurations.

In Table 68 a comparison of the selection performance considering the two machine background configurations are reported. Clearly, both efficiency and background contamination is higher for the "BGx0" case. This is because the selection at reconstruction level has been optimized using the "BGx1" sample, and also for the "BGx0" configuration we have used FEI training performed

Table 68. Number of generic events ($N_{\rm bkg}$), signal selection efficiency (ε), signal significance ($N_{\rm sig}/\sqrt{N_{\rm bkg}}$, with arbitrary normalization of the signal), and expected upper limit (UL) at 90% CL extracted with a Bayesian approach, for zero and nominal background configurations. The MC5 campaign with 1 ab^{-1} of data is used. The uncertainties reported and those used in the UL estimation are statistical only.

	Background $\times 0$	Background $\times 1$
$N_{\rm bkg}$	6415 ± 80	3678 ± 61
ε (10^{-4})	10.3 ± 0.3	5.38 ± 0.23
$N_{\rm sig}/\sqrt{N_{\rm bkg}}$	0.16	0.15
UL (10^{-4})	2.6	3.8

on the sample with machine background superimposed. The overall signal significance is higher in the background-free sample, as expected. From this study we can conclude that, with the machine background campaign used in the MC5 production cycle, the detector performance and reconstruction algorithms are robust against machine background. This has been tested on a K^{*+} final state with both a neutral particle and charged tracks. In this respect, the analysis of final states with $K^{*+} \to K^0_S(\pi^+\pi^-)\pi^+$ and $K^{*0} \to K^+\pi^-$, reconstructed with track only, should give similar or better results.

The above study (Figs. 95 and 96 and Table 68) was performed only for testing the robustness of the analysis against beam background, which will become one of the major obstacles for physics as the luminosity increases. In order to obtain the ultimate sensitivity achievable at Belle II we will need to impose more optimized selection criteria and to consider more realistic efficiency and systematic effects, which is beyond the scope of this book. For now, we can extrapolate the Belle sensitivity to Belle II by reducing the statistical errors by the increase in integrated luminosity (see Table 69). We can see that Belle II should be able to observe $B \to K^{(*)}\nu\bar{\nu}$ decays with approximately 5 ab^{-1} of data by combining the charged and neutral B decay modes. The expected sensitivity of the branching ratios for $B \to K^{(*)}\nu\bar{\nu}$ with 50 ab^{-1} are of the order of 10%, and thus comparable to the theoretical uncertainties of the SM predictions. A toy MC simulation of the extraction of the longitudinal polarization fraction $F_{\rm L}$ of the K^* has been performed and the sensitivity reaches 0.08 for both charged and neutral B decays. The corresponding uncertainty on the SM prediction is 0.03.

Figure 97 shows the constraints on the new physics contributions to the Wilson coefficients $C_L^{\rm NP}$ and C_R normalized to the SM value of C_L, assuming them to be real and independent of the neutrino flavor. The gray areas indicate the 90% CL excluded regions from the first-generation B factories, which rule out large enhancements of the Wilson coefficients with respect to the SM expectations. They also rule out a band where $C_L^{\rm NP} + C_R \approx -C_L^{\rm SM}$. In this region the branching ratio of $B \to K^+\nu\bar{\nu}$, which is only sensitive to the sum $C_L + C_R$, is close to zero and the combination of the BaBar and Belle searches already rules out a vanishing branching ratio at 90% CL. The colored bands show the regions allowed at 68% CL by the Belle II measurements with full statistics, assuming the sensitivities quoted in Table 69 and the SM central values for both $F_{\rm L}$ and the branching ratios. The green band refers to the $B^+ \to K^+\nu\bar{\nu}$ measurement. For $B \to K^*\nu\bar{\nu}$, two bands are shown. The purple one accounts for constraints from the branching ratio only, while the orange one shows the constraint obtained by combining both the branching ratio and $F_{\rm L}$. As can be seen, a large portion of the currently allowed parameter space will be excluded with the full Belle II statistics.

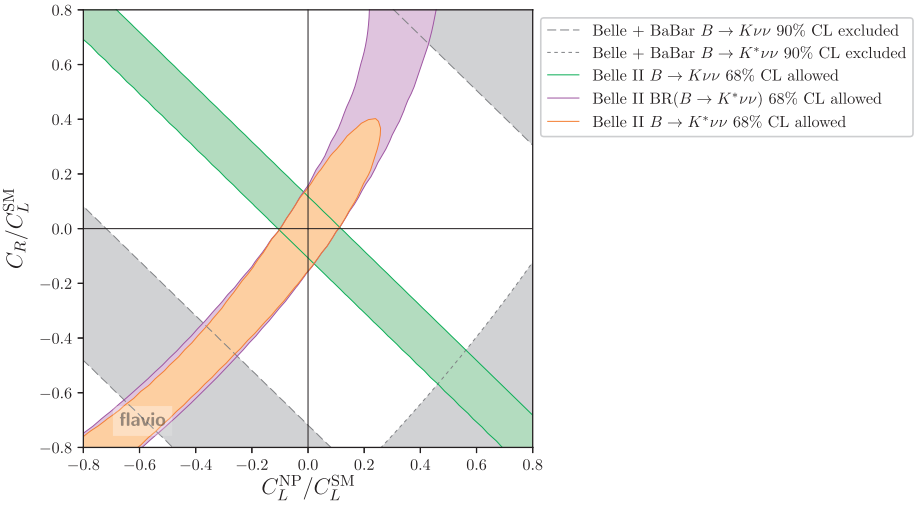

Fig. 97. Constraint on new physics contributions to the Wilson coefficients $C_L^{\rm NP}$ and C_R normalized to the SM value of C_L, assuming them to be real and independent of the neutrino flavor. The dashed (dotted) lines show 90% CL excluded regions from upper limits on Br($B \to K^{(*)}\nu\bar{\nu}$) at Belle and Babar; the green (purple) band represents the 68% CL allowed region from expected measurements of Br($B \to K^{(*)}\nu\bar{\nu}$) at Belle II; and the orange band gives the 68% CL allowed region from expected measurements of $F_{\rm L}(K^*)$ and the branching ratio in $B \to K^*\nu\bar{\nu}$ at Belle II.

Table 69. Sensitivities to the modes involving neutrinos in the final states. We assume that 5 ab^{-1} of data will be taken on the $\Upsilon(5S)$ resonance at Belle II. Some numbers at Belle are extrapolated to 0.71 ab^{-1} (0.12 ab^{-1}) for the $B_{u,d}$ (B_s) decay.

Observables	Belle 0.71 ab^{-1} (0.12 ab^{-1})	Belle II 5 ab^{-1}	Belle II 50 ab^{-1}
Br($B^+ \to K^+\nu\bar{\nu}$)	$< 450\%$	30%	11%
Br($B^0 \to K^{*0}\nu\bar{\nu}$)	$< 180\%$	26%	9.6%
Br($B^+ \to K^{*+}\nu\bar{\nu}$)	$< 420\%$	25%	9.3%
$F_{\rm L}(B^0 \to K^{*0}\nu\bar{\nu})$	—	—	0.079
$F_{\rm L}(B^+ \to K^{*+}\nu\bar{\nu})$	—	—	0.077
Br($B^0 \to \nu\bar{\nu}$) $\times 10^6$	< 14	< 5.0	< 1.5
Br($B_s \to \nu\bar{\nu}$) $\times 10^5$	< 9.7	< 1.1	—

9.5.3. Experimental search for $B_q \to \nu\bar{\nu}$ or invisible final states

Contributing author: A. Ishikawa

The $B_d \to \nu\bar{\nu}$ decay and B_d meson decays to invisible final states were searched for by BaBar with semi-leptonic tagging [628] and by Belle using hadronic tagging [629]. The resulting 90% CL upper limits on the branching ratios are $1.7 \cdot 10^{-5}$ and $1.3 \cdot 10^{-4}$, respectively. The $B_s \to \nu\bar{\nu}$ decay has not yet been searched for. These decays are helicity suppressed by the neutrino mass, so that the SM expectation is exactly zero (see Ref. [630] for predictions taking into account the neutrino masses).

Since there are no charged tracks or photons in the final states, only the tag-side B mesons can be used for the searches. The Belle analysis used an old hadronic tagging without a hierarchical reconstruction method [631], which can increase the tagging efficiency by a factor of two. Another factor of two improvement can be obtained by introducing the FEI. Requirements on event shape variables using multivariate techniques to suppress continuum and $\tau^+\tau^-$ backgrounds are promising

to improve the sensitivity further. In combination, an improvement by a factor of five on the efficiency of the hadronic tagging analysis is expected at Belle II. Such an improvement is still not sufficient to beat the semi-leptonic tagging analysis, which is expected to provide upper limits on the branching ratios that are three times better than those following from hadronic tagging. By combining hadronic and semi-leptonic tagging, Belle II is expected to set an upper limit on $\mathrm{Br}(B_d \to \nu\bar{\nu})$ of $1.5 \cdot 10^{-6}$ with $50\,\mathrm{ab}^{-1}$ of integrated luminosity.

The hadronic B_s tagging efficiency using a hierarchical reconstruction method gives an efficiency that is twice as good as that for B_d. The semi-leptonic tagging has not been tried yet, however it is expected that the tagging efficiency is smaller than that for B_d, since the dominant semi-leptonic decay $B_d^0 \to D^{*-}\ell^+\nu$ is clean due to the small mass splitting of D^{*-} and $\bar{D}^0\pi^-$. We conservatively assume that the semi-leptonic B_s tagging is three times worse than that for B_d. By combining the hadronic and semi-leptonic tagging, it is expected that an upper limit on $\mathrm{Br}(B_s \to \nu\bar{\nu})$ of $1.1 \cdot 10^{-5}$ can be set with the full dataset of $5\,\mathrm{ab}^{-1}$ collected at $\Upsilon(5S)$.

A summary of the Belle II sensitivities for the modes with neutrinos in the final states is presented in Table 69.

9.5.4. Interpreting missing energy signals as non-standard invisible states

Contributing author: C. Smith

The successes of the SM do not rule out the presence of new light particles. Indeed, if they are sufficiently weakly interacting with SM particles, they could have evaded direct detection until now. One could think, for example, of the extreme situation in which a unique new particle, fully neutral under the whole SM gauge group, is added to the SM. Our only window to discover such a particle would be its gravitational interactions, and there would be no hope of an earth-based discovery in the foreseeable future. In a more realistic setting, though, new neutral light particles would be accompanied by new dynamics at some scale. Presumably, this new dynamics would also affect the SM, and would thus indirectly couple the visible and hidden sectors.

There are many examples of such BSM models. The most well-known example is the axion [632–635], introduced to cure the strong CP problem of the SM. More crucially, there are now very strong indications that the universe is filled with dark matter, so there should be at least one new electrically neutral colorless particle, possibly lighter than the EW scale. Once that door is open, it is not such a drastic step to imagine a whole dark sector, i.e. a set of darkly interacting dark particles only loosely connected to our own visible sector. For a recent review, including further physical motivations from string theory or extra-dimensional settings, see, for instance, Ref. [636].

Experimental searches New light states could show up as missing energy in some process $A \to BX_{\mathrm{dark}}$, with A and B some SM particle states and X_{dark} representing one or more dark particles. Because of their very weak couplings, high luminosity is crucial to have any hope of discovery, and except in some special circumstances colliders cannot compete with low-energy experiments yet.

Several B decay modes offer unique windows for the search of new dark states with masses up to a few GeV. Specifically, the most promising processes are

$$\begin{aligned} B &\to X_{\mathrm{dark}}, \\ B &\to (\pi, \rho) X_{\mathrm{dark}}, \\ B &\to (K, K^*) X_{\mathrm{dark}}, \end{aligned} \tag{280}$$

with $X_{\rm dark}$ made of at least two dark particles for the first mode, but possibly only one for the others. This also includes situations in which the dark particle is not stable but has cascade decays in the hidden sector, e.g. $X_{\rm dark} \to Y_{\rm dark} Y_{\rm dark}$.

In this context, the SM decays with $X_{\rm SM} = \nu\bar{\nu}$ act as an irreducible background. The relevant branching ratios are smaller than about 10^{-9} for the fully invisible mode, and 10^{-5} for those with π, ρ, K, or K^*. It is important to stress, though, that the kinematics may be different. The differential rate $d\Gamma/dq_X^2$, with q_X^2 the missing invariant mass, depends on the nature of $X_{\rm dark}$ and may strongly deviate from that with $X_{\rm SM}$. This is obvious if $X_{\rm dark}$ is a single particle, in which case $d\Gamma/dq_X^2$ would show a peak at $q_X^2 = m_X^2$, or when $X_{\rm dark}$ is made of two states Y with $m_Y^2 \gg 0$ since $d\Gamma/dq_{YY}^2$ would vanish below $q_{YY}^2 = 4m_Y^2$. More generally, $d\Gamma/dq^2$ strongly depends on the Dirac structure(s) involved in the effective couplings of the dark states to the SM quark current $b \to q$, and thereby on whether these states are scalar, fermion, or vector particles.

This caveat concerning the differential rate must be kept in mind when reinterpreting the bounds on the branching ratios for $B \to (\pi, \rho, K, K^*)\nu\bar{\nu}$ as bounds on the production of new light states. Not only are those limits obtained from measurements over a fraction of the phase space, but the SM differential rate is explicitly assumed in the extrapolation. To be consistent, it is thus compulsory to use the same cuts on the produced meson momentum as in the experimental analysis. In this respect, it should be remarked that some recent experimental results [624] do perform differential analyses over the whole q^2 range. Those are the data most suitable for looking for new light states.

Finally, it should be mentioned that these modes also indirectly constrain other observables. For example, since the branching ratios $\mathrm{Br}(B^+ \to K^{*+} J/\psi) = (0.143 \pm 0.008)\%$ or $\mathrm{Br}(B^+ \to \rho^+ \bar{D}) = (1.34 \pm 0.18)\%$ [77] are significantly larger than those for the decays with missing energy in Eq. (280), the latter modes indirectly bound $J/\psi \to X_{\rm dark}$ or $\bar{D} \to X_{\rm dark}$ whenever $m_{J/\psi}^2$ or m_D^2 falls within the missing invariant mass window of the experimental search. This method has been used, and is the best available for charmonium, but remains to be applied for charmed mesons. It is not so promising for $K_{\rm L,S} \to X_{\rm dark}$ because the B decay branching ratios involving kaons are not much enhanced compared to those with a neutrino pair, and because the reach on $B(K \to X_{\rm dark})$ would in any case be very far from the 10^{-10} achievable for the golden mode $B(K \to \pi X_{\rm dark})$.

Theoretical classification and expectations To organize the search for new light states as model-independently as possible, the strategy is to construct the equivalent of the SMEFT operator basis [619,620,637] once the SM particle content is extended, and then constrain all the operators involving the new state(s). This program is more involved than it seems. Clearly, the leading operators one has to consider, the so-called portals, strongly depend on generic assumptions on the nature of the new state. For example, its spin has to be specified, as well as whether it carries a dark charge and needs to be produced in pairs.

Importantly, the dimension of the leading effective operators depend on these assumptions, and we refer to Refs. [616,638] for a complete list of leading interactions of the SM fields with a dark scalar, spin 1/2 or 3/2 fermion, or vector boson. For each type of new particle, we separate the case in which it is neutral or charged under some dark symmetry, and then further distinguish the overall leading operators to those involving the quark currents. Indeed, from the point of view of flavor physics, whether the dark states couple dominantly to Higgs or gauge bosons, hence are flavor-blind, or when they couple to quarks and leptons, whether they are able to directly induce the flavor transition is crucial. Even if it is not favorable from a dimensionality point of view to couple $X_{\rm dark}$ directly to quarks, failure to do so means that the flavor transition must still proceed through the SM

weak interaction, and ends up suppressed by G_F and CKM factors. From these considerations, three classes of scenarios for a generic effective coupling of $X_{\rm dark}$ to quarks can be identified. We refer to Ref. [616] for the full classification of the effective operators, and here only illustrate these three classes for the case of the production of a dark fermion pair.

First, consider the SM contributions which constitute the irreducible background for BSM production of dark states. This can be embodied into the generic dimension-six effective operators

$$\mathcal{H}_{\rm eff} = \sum_{q=s,d} \frac{c^{bq}}{\Lambda^2}\, \bar{b}\Gamma q\, \bar{\nu}\Gamma \nu, \tag{281}$$

where Γ represents all possible Dirac structures and c^{bq} denote the Wilson coefficients. We recall that in the SM one has $\Lambda \approx m_W$, $c^{bs}_{\rm SM} \approx \alpha_w/(4\pi)\,\lambda$, and $c^{bd}_{\rm SM} \approx \alpha_w/(4\pi)\,\lambda^3$, with $\alpha_w = g^2/(4\pi)$ the $\mathrm{SU}(2)_L$ coupling constant.

For the first scenario, imagine that the production of a dark fermion pair proceeds through the flavor-changing operator $\bar{Q}^I \gamma_\mu Q^J \bar{\psi}\gamma^\mu\psi$, where Q is a left-handed quark doublet and I, J denote flavor indices. The BSM rate will be of the order of the SM $b \to q\nu\bar{\nu}$ rate when

$$\frac{c^{bq}_{\rm dark}}{\Lambda^2} \simeq G_F\, \frac{\alpha_w}{4\pi}\, \lambda_t^{(q)}. \tag{282}$$

Provided the Wilson coefficient $c^{bq}_{\rm dark}$ is $\mathcal{O}(1)$, the reach in Λ is rather high, i.e. about 40 TeV (20 TeV) for $b \to d$ ($b \to s$) transitions.

On the contrary, for the second scenario, imagine that the leading coupling is flavor-blind, say $H^\dagger \overleftrightarrow{D}_\mu H \bar{\psi}\gamma^\mu\psi \supset v^2 \bar{\psi}\gamma_\mu\psi Z^\mu$, with $v \approx 246\,\mathrm{GeV}$ the Higgs vacuum expectation value. Then, the production of new states is driven by the SM Z penguin. As a result, the relation in Eq. (282) takes the form

$$c^{HH}_{\rm dark}\, \frac{v^2}{\Lambda^2}\, G_F\, \frac{\alpha_w}{4\pi} \lambda_t^{(q)} \simeq G_F\, \frac{\alpha_w}{4\pi}\, \lambda_t^{(q)}. \tag{283}$$

In this case, the reach in Λ is around the EW scale at best, i.e. when $c^{HH}_{\rm dark} = \mathcal{O}(1)$, and is in general not competitive with other searches using EW precision observables, invisible Higgs boson decay, or other flavor-blind searches. Note that even very low-energy probes are sensitive to $v^2\bar{\psi}\gamma_\mu\psi Z^\mu$, since the Z boson couples to all SM fermions. A similar conclusion is valid for all the flavor-blind operators, even when those arise at a much lower order and appear superficially less suppressed by the new physics scale Λ than those involving quark fields.

Between these two extreme situations there is a third scenario. If the dark state couples dominantly to top-quark pairs, then all the flavor-blind low-energy searches would be inefficient, while high-energy collider searches relying for example on the associated production of a top quark and a dark state would not be competitive yet. In this case, the FCNC processes still represent our best window, even if the reach in the BSM scale Λ would not be much higher than the EW scale.

9.6. Tauonic EW penguin modes

Contributing authors: W. Altmannshofer and J. Kamenik

B meson decays to $\tau^+\tau^-$ final states are experimentally largely uncharted territory. While a few bounds like $\mathrm{Br}\left(B_d \to \tau^+\tau^-\right) < 1.3 \cdot 10^{-3}$ [639] and $\mathrm{Br}\left(B^+ \to K^+\tau^+\tau^-\right) < 2.25 \cdot 10^{-3}$ [640] do exist, they are all orders of magnitude away from the corresponding SM predictions. In view

of the fact that measurements of $\tau^+\tau^-$ final states remain a big challenge at LHCb, and that it is unclear whether a sensitivity beyond $\mathcal{O}(10^{-3})$ can be reached [641], Belle II might be the only next-generation machine that allows the exploration of these modes in some depth.

9.6.1. $b \to q\tau^+\tau^-$ and lepton flavor violating modes with taus

Purely tauonic modes The most recent SM predictions for the branching ratios of the purely leptonic $B_s \to \tau^+\tau^-$ and $B_d \to \tau^+\tau^-$ decays include NNLO QCD corrections and NLO EW corrections [219,404,406]. They are given by

$$\begin{aligned} \mathrm{Br}(B_s \to \tau^+\tau^-)_{\mathrm{SM}} &= (7.73 \pm 0.49) \cdot 10^{-7}, \\ \mathrm{Br}(B_d \to \tau^+\tau^-)_{\mathrm{SM}} &= (2.22 \pm 0.19) \cdot 10^{-8}. \end{aligned} \tag{284}$$

These SM predictions refer to the average time-integrated branching ratios. The uncertainties are dominated by CKM elements and the B meson decay constants f_{B_q}. The input parameters used are collected in Ref. [219].

Semi-tauonic modes Predictions for exclusive semi-leptonic decays depend on form factors. In the semi-tauonic decays the dilepton invariant mass, q^2, is restricted to the range from $4m_\tau^2 \approx 12.6\,\mathrm{GeV}^2$ to $(m_B - m_H)^2$, where $H = \pi, K, K^*, \ldots$ To avoid contributions from the resonant decay through the narrow $\psi(2S)$ charmonium resonance, $B \to H\psi(2S)$ with $\psi(2S) \to \tau^+\tau^-$, SM predictions are typically restricted to a ditau invariant mass $q^2 > 15\,\mathrm{GeV}^2$. In this kinematic regime, lattice computations are expected to provide reliable results for the form factors (see the discussion in Sect. 9.1.1).

Combining the uncertainties from the relevant CKM elements and form factors leads to SM predictions for the branching ratios of the semi-tauonic decays with an accuracy of around 10% to 15%. The presence of broad charmonium resonances above the open charm threshold is a source of additional uncertainty. Possible effects of the broad resonances are typically taken into account by assigning an additional error of a few percent following Ref. [642] (or possibly more [643] when the $B \to K\ell^+\ell^-$ LHCb data [644] is considered), which is subdominant compared to the CKM and form factor uncertainties.

SM predictions for the decay $B \to \pi\tau^+\tau^-$ have been presented in Refs. [159,645] using form factors from the Fermilab/MILC collaboration [143,159]. Results are given for the branching ratios and the "flat term" in the angular distributions (cf. Refs. [590,645] for the definition of the latter observable)

$$\begin{aligned} \mathrm{Br}(B^+ \to \pi^+\tau^+\tau^-)_{\mathrm{SM}} &= (4.29 \pm 0.39) \cdot 10^{-9}, \\ \mathrm{Br}(B^0 \to \pi^0\tau^+\tau^-)_{\mathrm{SM}} &= (1.99 \pm 0.18) \cdot 10^{-9}, \\ F_H(B \to \pi\tau^+\tau^-)_{\mathrm{SM}} &= 0.80 \pm 0.02\,, \end{aligned} \tag{285}$$

where the prediction for $F_H(B \to \pi\tau^+\tau^-)_{\mathrm{SM}}$ holds for both B^+ and B^0, and all errors quoted in Refs. [159,645] have been added in quadrature to obtain the final uncertainties. The above predictions correspond to a ditau invariant mass squared $q^2 \in [15, 22]\,\mathrm{GeV}^2$. Predictions for additional q^2 bins are available in Refs. [159,645]. The dominant uncertainties in the branching ratios come from the $B \to \pi$ form factors and the CKM input. Those uncertainties cancel to a large extent in the flat term.

Also, for the $B \to K\tau^+\tau^-$ decays, SM predictions have been given in Ref. [645] using recent lattice determination of the $B \to K$ form factors from the Fermilab/MILC collaboration [158]. The SM predictions for the branching ratios and the flat terms read

$$\begin{aligned} \mathrm{Br}(B^+ \to K^+\tau^+\tau^-)_{\mathrm{SM}} &= (1.22 \pm 0.10) \cdot 10^{-7}, \\ \mathrm{Br}(B^0 \to K^0\tau^+\tau^-)_{\mathrm{SM}} &= (1.13 \pm 0.09) \cdot 10^{-7}, \\ F_H(B \to K\tau^+\tau^-)_{\mathrm{SM}} &= 0.87 \pm 0.02, \end{aligned} \tag{286}$$

where we added all uncertainties quoted in Ref. [645] in quadrature. As in the case of the $B \to \pi\tau^+\tau^-$, the value of $F_H(B \to K\tau^+\tau^-)_{\mathrm{SM}}$ applies to the charged and neutral channel and the above predictions refer to the q^2 range $[15, 22]\,\mathrm{GeV}^2$. Predictions for additional q^2 bins can be found in Ref. [645]. Again, the dominant source of uncertainty in the branching ratio arises from the $B \to K$ form factors and from the CKM elements, while in the flat terms these errors largely cancel.

The SM predictions for the $B \to K^*\tau^+\tau^-$ branching ratios read [618]

$$\begin{aligned} \mathrm{Br}(B^+ \to K^{*+}\tau^+\tau^-)_{\mathrm{SM}} &= (0.99 \pm 0.12) \cdot 10^{-7}, \\ \mathrm{Br}(B^0 \to K^{*0}\tau^+\tau^-)_{\mathrm{SM}} &= (0.91 \pm 0.11) \cdot 10^{-7}, \end{aligned} \tag{287}$$

where the ditau q^2 ranges from $15\,\mathrm{GeV}^2$ to the kinematic endpoint around $19.2\,\mathrm{GeV}^2$. The $B \to K^*$ form factors used are based on a combined fit of lattice and LCSR results [419].

The SM prediction for the $B_s \to \phi\tau^+\tau^-$ branching ratio is given by [618]

$$\mathrm{Br}(B_s \to \phi\tau^+\tau^-)_{\mathrm{SM}} = (0.73 \pm 0.09) \cdot 10^{-7}, \tag{288}$$

where the ditau invariant mass ranges from $15\,\mathrm{GeV}^2$ to the kinematic endpoint at roughly $18.9\,\mathrm{GeV}^2$. The $B_s \to \phi$ form factors used are based on a combined fit of lattice and LCSR results [419].

Lepton flavor universality ratios with taus We define the lepton flavor universality ratios, in analogy to Eq. (264) as

$$R_H^{\ell\ell'}[q_0^2, q_1^2] = \frac{\int_{q_0^2}^{q_1^2} dq^2 d\mathrm{Br}(B \to H\ell^+\ell^-)/dq^2}{\int_{q_0^2}^{q_1^2} dq^2 d\mathrm{Br}(B \to H\ell'^+\ell'^-)/dq^2}.$$

In these ratios uncertainties from CKM elements drop out. Also, form factor uncertainties cancel almost exactly in ratios involving electrons and muons, while in ratios with taus, these uncertainties get reduced.

The SM predictions from Ref. [645] read

$$\begin{aligned} (R_\pi^{\mu\tau})_{\mathrm{SM}} &= 1.18 \pm 0.06, \\ (R_K^{\mu\tau})_{\mathrm{SM}} &= 0.87 \pm 0.02 \end{aligned} \tag{289}$$

for the $q^2 \in [15, 22]\,\mathrm{GeV}^2$ bin. For the $B \to K^*$ decays we find [618]

$$(R_{K^*}^{\mu\tau})_{\mathrm{SM}} = 2.44 \pm 0.09, \tag{290}$$

where $q^2 \in [15, 19.2]\,\mathrm{GeV}^2$. Within the quoted uncertainties, the results in Eqs. (289) and (290) apply to both charged and neutral decays.

Probing BSM physics Since the $b \to q\tau^+\tau^-$ decays involve third-generation fermions in the final state, one can envisage new physics scenarios—such as models with extended Higgs or gauge sectors, or scenarios with leptoquarks—that give rise to effects in the $\tau^+\tau^-$ modes, while leaving the e^+e^- and/or $\mu^+\mu^-$ channels unaltered. In a model-independent approach, tau-specific new physics in rare B meson decays can be described by an effective Hamiltonian that contains, besides the operators Q_7, Q_9, Q_{10} introduced in Eqs. (197) and (198), their chirality-flipped partners Q'_7, Q'_9, Q'_{10} as well as

$$\begin{aligned} Q_S &= (\bar{q}_L b_R)(\bar{\tau}_R \tau_L), \\ Q'_S &= (\bar{q}_R b_L)(\bar{\tau}_L \tau_R). \end{aligned} \tag{291}$$

To constrain all possible $\tau^+\tau^-$ operators, one should try to measure/bound both purely leptonic and semi-leptonic modes, since they have different blind directions in parameter space [537,646]. In this respect it is also interesting to note that $b \to s\nu\bar{\nu}$ decays can constrain the operator combinations containing a left-handed tau current $Q_9 - Q_{10}$ and $Q'_9 - Q'_{10}$, due to $\mathrm{SU}(2)_L$ invariance. On the other hand, $b \to s\nu\bar{\nu}$ is blind to the orthogonal directions $Q_9 + Q_{10}$ and $Q'_9 + Q'_{10}$ that contain right-handed tau currents.

Many BSM models can lead to modifications in the $b \to q\tau^+\tau^-$ channels. Interestingly, several models that address the LHCb anomalies in the $b \to s\mu^+\mu^-$ sector [389,391,497–499,610,647] or the evidence of lepton flavor universality violation in $B \to D^{(*)}\ell\nu$ decays [250–252,267,268,270,272] predict characteristic deviations in $b \to s\tau^+\tau^-$ transitions from the SM predictions.

The model proposed in Ref. [648] contains a Z' boson, associated to the gauge symmetry of muon number minus tau number, $L_\mu - L_\tau$. Given the current anomalies in the $b \to s\mu^+\mu^-$ sector, the model predicts a suppression of all semi-leptonic $b \to s\mu^+\mu^-$ decays by about 20% [599]. The $L_\mu - L_\tau$ symmetry implies that all semi-leptonic $b \to s\tau^+\tau^-$ decays are instead enhanced. Translating the predictions for $b \to s\mu^+\mu^-$ transitions found in the minimal flavor violation (MFV) scenario of Ref. [599] to the tau sector using Ref. [618], we find

$$\begin{aligned} \mathrm{Br}(B^+ \to K^+\tau^+\tau^-)_{L_\mu - L_\tau} &= (1.46 \pm 0.13) \cdot 10^{-7}, \\ \mathrm{Br}(B^0 \to K^0\tau^+\tau^-)_{L_\mu - L_\tau} &= (1.35 \pm 0.12) \cdot 10^{-7}, \\ \mathrm{Br}(B^+ \to K^{*+}\tau^+\tau^-)_{L_\mu - L_\tau} &= (1.53 \pm 0.23) \cdot 10^{-7}, \\ \mathrm{Br}(B^0 \to K^{*0}\tau^+\tau^-)_{L_\mu - L_\tau} &= (1.40 \pm 0.21) \cdot 10^{-7}, \end{aligned} \tag{292}$$

where the $K^{+,0}$ branching ratios refer to the q^2 region $q^2 \in [15, 22]\,\mathrm{GeV}^2$, while the K^* rates correspond to $q^2 \in [15, 19.2]\,\mathrm{GeV}^2$. The $B_s \to \tau^+\tau^-$ decay remains SM-like in the $L_\mu - L_\tau$ framework.

In the scenarios discussed in Refs. [286,287,623], the current B physics anomalies are addressed by BSM physics in the form of left-handed currents involving mainly the third generation. In these scenarios the $b \to s\tau^+\tau^-$ decays can in principle be enhanced by an order of magnitude compared to the SM predictions. Left-handed (LH) currents imply a strong correlation between $b \to s\tau^+\tau^-$ and $b \to s\nu\bar{\nu}$ decays; see also the discussion in Sect. 9.5.1. Using the current upper bound on $\mathrm{Br}(B^+ \to K^+\nu\bar{\nu}) < 1.6 \cdot 10^{-7}$ [624], one finds the following maximal values for the tauonic

branching ratios [618]:

$$\begin{aligned}
\mathrm{Br}(B^+ \to K^+\tau^+\tau^-)_{\mathrm{LH}} &< 24.5 \cdot 10^{-7},\\
\mathrm{Br}(B^0 \to K^0\tau^+\tau^-)_{\mathrm{LH}} &< 22.5 \cdot 10^{-7},\\
\mathrm{Br}(B^+ \to K^{*+}\tau^+\tau^-)_{\mathrm{LH}} &< 22.8 \cdot 10^{-7},\\
\mathrm{Br}(B^0 \to K^{*0}\tau^+\tau^-)_{\mathrm{LH}} &< 20.1 \cdot 10^{-7},\\
\mathrm{Br}(B_s \to \tau^+\tau^-)_{\mathrm{LH}} &< 1.5 \cdot 10^{-5}.
\end{aligned} \tag{293}$$

The q^2 regions are chosen as in Eq. (292). Enhancements beyond the above bounds are possible in the presence of right-handed currents [613]. Measurements of $b \to s, d\tau^+\tau^-$ modes are thus likely to play an important role in the search for lepton non-universality and indirectly may also provide useful information on lepton flavor violation (see, for instance, the discussion in Ref. [649]).

9.6.2. Experimental prospects for tauonic EW penguin decays

Contributing author: A. Ishikawa

Studies of the $B^+ \to K^+\tau^+\tau^-$ and $B_{d,s} \to \tau^+\tau^-$ decay modes are interesting because they allow searches for new physics which affects EW penguin B decays involving third-generation leptons. Since the final states contain multiple neutrinos, tagging of the other B meson is needed to search for these decays. Recently, Belle demonstrated that hadronic B_s tagging for rare decays is possible, despite the dominant mode of production proceeding through intermediate excited states, which degrades resolution. After tagging the other B meson, tau leptons can be reconstructed in single-prong decays. Even with the improved reconstruction techniques, observations of the SM branching ratios of $B^+ \to K^+\tau^+\tau^-$ and $B_{d,s} \to \tau^+\tau^-$ are unlikely. The expected upper limits on the branching ratios that Belle II should be able to place are of order 10^{-5} and 10^{-4} for B_d and B_s decays, respectively.

Searches for lepton flavor violating $B^+ \to K^+\tau^\pm\ell^\mp$ and $B_{s,d} \to \tau^\pm\ell^\mp$ ($\ell = e, \mu$) decays are relatively easy compared to the ditau modes, since the τ can be reconstructed in hadronic B tagged events. In the three-body $B^+ \to K^+\tau^\pm\ell^\mp$ decays, the τ four-momentum can be determined from the momentum of the B, K, and $\ell^\mp$, and in the two-body $B_{s,d} \to \tau^\pm\ell^\mp$ decays the ℓ is monochromatic. These clear signatures allow the setting of better upper limits of the order of 10^{-6} for these decays.

The Belle II sensitivities for the various observables which contain taus in the final state are summarized in Table 70.

9.7. Conclusions

The study of radiative and EW penguin B decays remains an important area of precision physics with its overarching goal to discover new physics indirectly by finding deviations between measurements and the corresponding SM predictions. This research direction has been established by a joint effort within the theory community and experimental results from BaBar, Belle, and LHCb.

Belle II will contribute to the flavor precision program in two ways. First, by improving the measurements of various FCNC key observables. The inclusive and exclusive $b \to s, d\,\gamma$ channels as well as the inclusive $b \to s\ell^+\ell^-$ transition (see Tables 61, 62, and 64 for the expected Belle II sensitivities) are well-known examples, but the studies performed in this chapter also show that Belle II can perform measurements that are competitive with those at LHCb for exclusive $b \to s\ell^+\ell^-$

Table 70. The Belle II sensitivities for the EW penguin B decays involving taus in the final states. We assume that 5 ab^{-1} of data will be taken on the $\Upsilon(5S)$ resonance. Some numbers at Belle are extrapolated to 0.71 ab^{-1} (0.12 ab^{-1}) for the $B_{u,d}$ (B_s) decay.

Observables	Belle 0.71 ab^{-1} (0.12 ab^{-1})	Belle II 5 ab^{-1}	Belle II 50 ab^{-1}
$\mathrm{Br}(B^+ \to K^+\tau^+\tau^-) \cdot 10^5$	< 32	< 6.5	< 2.0
$\mathrm{Br}(B^0 \to \tau^+\tau^-) \cdot 10^5$	< 140	< 30	< 9.6
$\mathrm{Br}(B_s^0 \to \tau^+\tau^-) \cdot 10^4$	< 70	< 8.1	—
$\mathrm{Br}(B^+ \to K^+\tau^\pm e^\mp) \cdot 10^6$	—	—	< 2.1
$\mathrm{Br}(B^+ \to K^+\tau^\pm \mu^\mp) \cdot 10^6$	—	—	< 3.3
$\mathrm{Br}(B^0 \to \tau^\pm e^\mp) \cdot 10^6$	—	—	< 1.6
$\mathrm{Br}(B^0 \to \tau^\pm \mu^\mp) \cdot 10^6$	—	—	< 1.3

channels, including obervables that test lepton flavor universality (see Tables 65, 66, and 67 for the Belle II prospects). As exemplified by Fig. 94 for the case of the $b \to s\ell^+\ell^-$ transitions, this complementarity and synergy can play a crucial role in indirectly discovering (or constraining) BSM physics.

Belle II will, furthermore, push the frontier in the field of radiative and EW penguin B decays by measuring modes at the level predicted by the SM that have so far not been observed by any other experiment. The prime examples for such *discovery channels* are $B_d \to \gamma\gamma$ and $B \to K^{(*)}\nu\bar{\nu}$ (see Tables 63 and 69 for the expected Belle II sensitivities). In other cases, such as $B_s \to \nu\bar{\nu}$ or B decays to final states containing $\tau^+\tau^-$, $\tau^\pm e^\mp$, or $\tau^\pm\mu^\mp$ pairs, Belle II will not be able to observe them at the SM level. However with 50 ab^{-1} of data the existing limits will be improved by orders of magnitude (see Table 70 for the future Belle II constraints), which will further constrain possible new physics couplings to neutrinos and taus as well as flavor violation in the lepton sector.

10. Time-dependent CP asymmetries of B mesons and determination of ϕ_1, ϕ_2

Editors: A. Gaz, L. Li Gioi, S. Mishima, J. Zupan
Additional section writers: F. Abudinén, F. Bishara, M. Gronau, Y. Grossman, S. Jaeger, M. Jung, S. Lacaprara, A. Martini, A. Mordà, D. Robinson, A. Tayduganov

10.1. Introduction

The measurements of the CKM unitarity triangle angles ϕ_1, ϕ_2, ϕ_3 amount, within the SM, to different ways of measuring the single CP-violating phase in the CKM matrix. In the presence of NP, additional phases might lead to an overall inconsistency of the constraints on the CKM unitarity triangle. This would be a clear indication of NP.

In this section we describe the methods for determining the angles

$$\phi_1 \equiv \arg[-V_{cb}^* V_{cd}/(V_{tb}^* V_{td})] \tag{294}$$

and

$$\phi_2 \equiv \arg[-V_{tb}^* V_{td}/V_{ub}^* V_{ud}]. \tag{295}$$

All of these methods are sensitive to the B–$\bar{B}$ mixing phase. In the SM this is induced at one-loop level and can be modified by many NP models. The angle ϕ_3 is determined from tree-level processes, and is less sensitive to NP.

Precision measurements of angles ϕ_1 and ϕ_2 are crucial inputs into the CKM unitarity triangle fits. For the time-dependent CP asymmetry parameter $S_{J/\psi K^0}$, the most precise measurement determining the ϕ_1 angle, Belle II is projected to reduce the present world average error of 0.022 [230] down to 0.0052 (see Table 97). For penguin-dominated modes, ϕK^0, $\eta' K^0$, ωK^0_S, $K^0_S\pi^0\gamma$, $K^0_S\pi^0$, that are particularly sensitive to NP from penguin contributions, Belle II is expected to improve the world average precision by a factor of two with 5 ab^{-1} (see Table 97). The experimental errors on the measurements that enter the determination of the angle ϕ_2 will have errors reduced by factors between 2 and 10 depending on the sources of systematic uncertainties (see Tables 91 and 92). Additionally, the novel measurement of the time-dependent CP asymmetry parameter $S_{\pi^0\pi^0}$ will help to reduce the ambiguities in the determination of ϕ_2 within the $B \to \pi\pi$ decays. Considering the decays $B \to \pi\pi$ and $B \to \rho\rho$ together, the total uncertainty on ϕ_2 is projected to be about 0.6° (the current world average error is about 4.2° [650]). An important requirement is that the theoretical uncertainties within the SM predictions, to be discussed below, are controlled sufficiently well.

The general strategies for extracting $\phi_{1,2}$ use time-dependent CP asymmetries due to the interference between B–$\bar{B}$ mixing and B decay amplitudes. Interference between the two neutral B meson evolution eigenstates $|B_\pm\rangle = p|B\rangle \pm q|\bar{B}\rangle$ generates the time-dependent CP asymmetry

$$a_{\rm CP}(t) \equiv \frac{\Gamma(\bar{\mathcal{D}};t) - \Gamma(\mathcal{D};t)}{\Gamma(\bar{\mathcal{D}};t) + \Gamma(\mathcal{D};t)} = \frac{S_f \sin(\Delta m\, t) + A_f \cos(\Delta m\, t)}{\cosh(\Delta\Gamma\, t/2) + A^f_{\Delta\Gamma} \sinh(\Delta\Gamma\, t/2)}, \tag{296}$$

where

$$S_f = \frac{2\,{\rm Im}[\lambda_f]}{1+|\lambda_f|^2}, \quad -A_f \equiv C_f = \frac{1-|\lambda_f|^2}{1+|\lambda_f|^2}, \quad A^{\Delta\Gamma}_f = -\frac{2\,{\rm Re}[\lambda_f]}{1+|\lambda_f|^2}. \tag{297}$$

Here, $\mathcal{D} : B(t) \to f$ and $\bar{\mathcal{D}} : \bar{B}(t) \to f$, with f a common CP eigenstate with eigenvalue $\eta_f = \pm 1$, and $\Delta m \equiv m_H - m_L > 0$ and $\Delta\Gamma \equiv \Gamma_L - \Gamma_H$ are respectively the mass and decay rate splittings of the heavy (H) and light (L) eigenstates. The initial, $t = 0$, states are flavor tagged, i.e. $B(0) = B$ and $\bar{B}(0) = \bar{B}$. In the B_d system the decay width splitting $\Delta\Gamma$ can be safely set to zero up to sub-percent precisions [230]. However, it is non-negligible in the B_s system, as discussed below.

The interference between mixing and decay is described by the parameter

$$\lambda_f \equiv (q/p)(\bar{\mathcal{A}}_f/\mathcal{A}_f), \tag{298}$$

where the decay amplitudes are $\mathcal{A}_f \equiv \langle f|H_{\rm ew}|B\rangle$ and $\bar{\mathcal{A}}_f \equiv \langle f|H_{\rm ew}|\bar{B}\rangle$ ($\mathcal{A}_f$ should not be confused with $A_f \equiv -C_f$). In the B–$\bar{B}$ system, CP violation in mixing ($|q/p| \neq 1$) is measured separately and is negligible [230]. We can thus safely assume that $q/p = e^{-i\phi_d}$, where the B–$\bar{B}$ mixing phase is strictly

$$\phi_d = \arg[V_{tb}V^*_{td}/(V^*_{tb}V_{td})] \approx 2\phi_1, \tag{299}$$

up to negligible corrections in the SM, but possibly large corrections if there are NP contributions.

In this section we present sensitivity studies based on Belle II simulation for the following four final states: $B^0 \to \phi K^0$, $\eta' K^0$, $K^0_S\pi^0\gamma$, and $\pi^0\pi^0$. The complete analysis, from the reconstruction

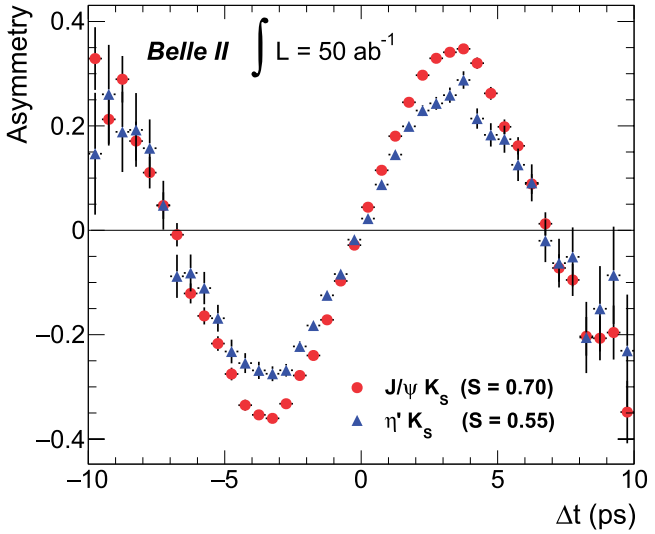

Fig. 98. Time-dependent CP asymmetries for the final states $J/\psi\, K^0_S$ (red dots) and $\eta' K^0_S$ (blue triangles), using $S_{J/\psi\, K^0_S} = 0.70$ and $S_{\eta' K^0_S} = 0.55$ as inputs to the Monte Carlo. With the full integrated luminosity of 50 ab^{-1} the two values would be unambiguously distinguishable, signifying the existence of new physics.

of intermediate resonances to the final maximum likelihood fit, is performed. In estimating the final sensitivity we take into account the expected improvements, most notably those affecting the reconstruction efficiencies.

Based on these studies and on the reconstruction efficiencies obtained by the BaBar and Belle experiments we also extrapolate the present sensitivities to Belle II for the channels $B^0 \to J/\psi\pi^0$, $B^0 \to \omega K^0_S$, and $B^0 \to K^0_S\pi^0$, which are related to the measurement of the angle ϕ_1, and for the channels $B^0 \to \pi^+\pi^-$, $B^+ \to \pi^+\pi^0$, $B^0 \to \rho^0\rho^0$, $B^0 \to \rho^+\rho^-$, and $B^+ \to \rho^+\rho^0$, which are related to the measurement of ϕ_2. We discuss in detail the systematic uncertainties that will affect the cleanest and highest statistics channel $B^0 \to J/\psi K^0$ for the measuerement of ϕ_1. Based on this discussion we also estimate the systematic uncertainties which will affect the channels $B \to \pi\pi$ and $B \to \rho\rho$ for the measurement of ϕ_2.

Figure 98 shows the time-dependent CP asymmetry distributions that can be measured at Belle II in the $B^0 \to J/\psi\, K^0_S$ and $\eta' K^0_S$ channels with an integrated luminosity of 50 ab^{-1}. As inputs to the simulations we set $S_{J/\psi\, K^0_S} = 0.70$ and $S_{\eta' K^0_S} = 0.55$, see Eq. (297). Such a difference between $S_{J/\psi\, K^0_S}$ and $S_{\eta' K^0_S}$ would be an unambiguous sign of new physics and would be easily detectable by the Belle II experiment.

10.2. Determination of ϕ_1

Contributing authors: M. Jung, L. Li Gioi, D. Robinson

10.2.1. Theory: $\sin 2\phi_1$ *from* $b \to c\bar{c}s$

The angle ϕ_1 is the most precisely measured CP-violating quantity to date. As such, it is one of the most important inputs in the global CKM fits and a cornerstone input to the tests of the SM.

The sensitivity to ϕ_1 comes from the CP asymmetry parameter S_f in Eq. (297), which measures the sum of the mixing phase $-\phi_d$ and the relative phase $\arg(\bar{\mathcal{A}}_f/\mathcal{A}_f)$—see Eq. (298). For $b \to c\bar{c}s$

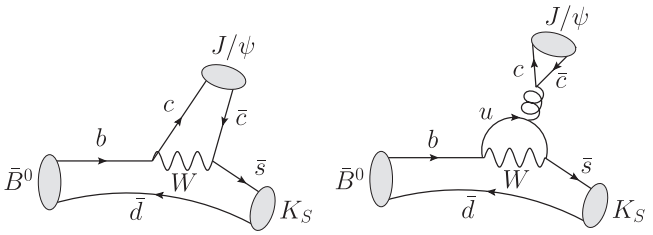

Fig. 99. Examples of diagrams for the T_f (left) and P_f (right) amplitudes in Eq. (300) for the $B \to J/\psi K^0_S$ decay. Only part of the contributions to T_f and P_f are shown.

transitions, CKM unitarity permits the decay amplitudes to be written as[28]

$$\mathcal{A}_f = \lambda_c^s T_f + \lambda_u^s P_f, \qquad \lambda_i^q \equiv V_{ib}^* V_{iq}. \tag{300}$$

While P_f and T_f correspond at leading order to penguin and tree $b \to c\bar{c}s$ contributions, respectively (see also Fig. 99), for the sub-percent precision measurements of S_f anticipated by Belle II subleading corrections become important, and such a diagrammatic interpretation of these contributions is no longer possible.

Since λ_u^s is doubly CKM-suppressed compared to λ_c^s, one has $\bar{\mathcal{A}}_f/\mathcal{A}_f \approx \eta_f \lambda_c^{s*}/\lambda_c^s$, and therefore

$$S_f \approx -\eta_f \sin(\phi_d) + \mathcal{O}\big(\lambda_u^s/\lambda_c^s\big), \tag{301}$$

while the direct CP asymmetry $A_f \approx 0$. The time-dependent CP asymmetry in $b \to c\bar{c}s$ decays thus allows a theoretically clean extraction of ϕ_1, up to doubly CKM-suppressed corrections. The control of the latter constitutes the main challenge with the available and future data precision.

Despite this challenge, as we will show below, the determination of the B mixing phase ϕ_1 via $b \to c\bar{c}s$ transitions remains an excellent way to search for NP that gives additional contributions to meson mixing. The SM uncertainties need to be brought under control at the present level of experimental precision, and even more so with the precision aimed at with Belle II.

$\sin\phi_1$ *from* $B \to J/\psi K^0_S$ The "golden mode" for measuring $\sin\phi_d$ is $B \to J/\psi K^0_S$ because of the expected small theoretical uncertainty and clean experimental signature.[29] Let us denote the corresponding $\mathcal{O}(\lambda_u^s/\lambda_c^s)$ terms in Eq. (301) by $\Delta S_{J/\psi K^0_S}$, so that

$$S_{J/\psi K^0_S} \equiv \sin\phi_d + \Delta S_{J/\psi K^0_S} \equiv \sin(\phi_d + \delta\phi_{J/\psi K^0_S}), \tag{302}$$

where $\delta\phi_{J/\psi K^0_S}$ is also $\mathcal{O}(\lambda_u^s/\lambda_c^s)$. The small parameters $\Delta S_{J/\psi K^0_S}$ or $\delta\phi_{J/\psi K^0_S}$ are often referred to as the "penguin pollution" in the extraction of ϕ_d from $S_{J/\psi K^0_S}$. The only potentially sizeable contribution to $\Delta S_{J/\psi K^0_S}$ is expected to arise from insertions of tree-level operators $\mathcal{O}^u_{1,2}$ in the SM effective Hamiltonian for non-leptonic $b \to s$ transitions, and then closing the up quark loop. This

[28] Reparameterization invariance permits the decay amplitude to always be expressed in terms of $\lambda^s_{u,c}$ and matrix elements, $A_{u,c}$, i.e. as $\mathcal{A}_f = \lambda_c^s A_u + \lambda_u^s A_c$, even in the presence of an additional NP contribution with an arbitrary weak phase [651–653]. However, in this case the interpretation of $A_{u,c}$ as matrix elements of SM currents does not hold anymore, and symmetry relations are potentially affected.

[29] Note that $f = J/\psi K^0_S$ is a CP eigenstate up to ϵ_K corrections that arise at the sub-percent level [654]. Note furthermore that $\eta_{J/\psi K^0_S} = -1$. The discussion here also applies trivially to the determination of $\sin\phi_d$ from $B \to J/\psi K^0_L$, except that $\eta_{J/\psi K^0_L} = 1$. This mode is harder to measure, however.

loop is expected to generate another suppression factor in addition to the CKM suppression, but the resulting net effect is hard to quantify.

A naive estimate of $\Delta S_{J/\psi K^0_S}$ from the CKM suppression alone yields $\delta\phi_{J/\psi K^0_S} \lesssim 2°$, comparable to the experimental uncertainty in the current world-average $S_{J/\psi K^0_S} = 0.682 \pm 0.021$ ($\phi_1 = (22.5 \pm 0.9)°$) [80,655,656]. Belle II is projected to improve the experimental precision to the sub-degree level with 50 ab^{-1} integrated luminosity, well inside the estimated theory uncertainty. In the remainder of this subsection we therefore discuss various strategies to either compute, bound, or control $\Delta S_{J/\psi K^0_S}$.

To this end, it is helpful to write a parameterization of $\Delta S_{J/\psi K^0_S}$ to leading order in CKM suppression. Using the definitions of Eqs. (297) and (300), together with the definitions $\bar{\lambda}^2 \equiv -\lambda_u^s \lambda_c^d / \lambda_c^s \lambda_u^d$ and $\phi_3 \equiv \arg(-\lambda_u^d / \lambda_c^d)$,

$$\Delta S_{J/\psi K^0_S} = 2\bar{\lambda}^2 \mathrm{Re} \frac{P_f}{T_f} \sin\phi_3 \cos\phi_d + \mathcal{O}(\bar{\lambda}^4), \tag{303}$$

in which we have used the fact that $\bar{\lambda}^2$ (≈ 0.05) [91,657] is real up to higher-order CKM corrections, so that $\mathrm{Im}(\lambda_u^s/\lambda_c^s) \approx \bar{\lambda}^2 \sin\phi_3$. All terms are well known experimentally, apart from the reduced matrix element ratio P_f/T_f.

Theoretical calculations or estimations of P_f/T_f provide one path to controlling $\Delta S_{J/\psi K^0_S}$. Formally, this term is not only CKM-suppressed, but is also expected to receive a loop suppression $\lesssim 5\%$ [658]. Attempts to calculate $\Delta S_{J/\psi K^0_S}$ via QCD factorization (QCDF) techniques [659], or by combining QCDF with perturbative QCD [660], yield estimates in the range $\Delta S_{J/\psi K^0_S} \sim 10^{-3}$. The $\mathcal{O}(1/m_{c,b})$ correction may, however, be large, specifically the leading corrections that scale as $\Lambda_{\mathrm{QCD}}/(\alpha_s m_c)$, which is of order unity for realistic charm quark masses [244]. Long-distance rescattering effects from intermediate charmless states may enhance P_f/T_f, although perhaps only moderately [661].

The ratio P_f/T_f may also be estimated via an OPE-type approach, by integrating out the u quark loop, on the basis that the typical momentum flow is large ($\sim m_{J/\psi}$) [662]. This approach produces a factorization formula for the penguin contributions, relying on the observation that soft and collinear divergences formally cancel or factorize up to $\Lambda_{\mathrm{QCD}}/m_{J/\psi}$ corrections. The remaining matrix elements are estimated in the large-N_c limit ($N_c = 3$ is the number of colors in QCD). This leads to the estimate $|\delta\phi_{J/\psi K^0_S}| < 0.68°$ [662].

Light-quark flavor symmetries, either flavor SU(3) or its subgroup U-spin, provide an alternate avenue to control P_f/T_f and thereby $\Delta S_{J/\psi K^0_S}$. The simplest manifestations of this approach use a single mode related to $B \to J/\psi K^0_S$ by such a flavor symmetry. In the U-spin limit, the $B \to J/\psi K^0_S$ amplitude in Eq. (300) is related to the $B_s \to J/\psi K^0_S$ amplitude, denoted $\mathcal{A}'$, via [663–665]

$$\mathcal{A}'_f = \lambda_c^d T_f + \lambda_u^d P_f. \tag{304}$$

Since $B_s \to J/\psi K^0_S$ constitutes a $b \to c\bar{c}d$ process, the $\lambda_u^d P_f$ term is no longer CKM-suppressed. Therefore, both $\Delta S'_{J/\psi K^0_S}$ and $C'_{J/\psi K^0_S}$ can be sizeable and hence be more easily determined. Using external knowledge of the B_s mixing phase, ϕ_s, permits the extraction of an estimate for $\mathrm{Re}(P_f/T_f)$ and thus $\Delta S_{J/\psi K^0_S}$. Similarly, $B \to J/\psi \pi^0$ can be used as a partner mode [666–668]. This mode has the advantage that it is more easily measurable than $B_s \to J/\psi K^0_S$ at Belle II, at which the B_s dataset will be limited. However, in this case a dynamical assumption regarding small annihilation contributions in P_f is necessary in addition to U-spin to obtain the analogue of Eq. (304). A drawback of using $b \to c\bar{c}d$ transitions in this procedure is that the rates of these modes are suppressed by a

Table 71. Theory expectations for $\Delta S_{J/\psi K^0_S}$ or $\delta\phi_{J/\psi K^0_S}$, related via $\Delta S_{J/\psi K^0_S} \approx \delta\phi_{J/\psi K^0_S} \cos\phi_1$. The highlighted values are not given in the corresponding reference, but have been calculated for convenience via Eq. (302).

Strategy	$\Delta S_{J/\psi K^0_S}$ [%]	$\delta\phi_{J/\psi K^0_S}$ [°]
QCDF/pQCD [659,660]	$\lesssim 0.1$	$\lesssim 0.1$
OPE [662]	$\lesssim 0.9$	$\lesssim 0.68$
Broken U-spin [666,668]	0 ± 2	0.0 ± 1.6
Broken U-spin [667]	$[-5, -0.5]$	$[-2.0, -0.4]$
SU(3) at $\mathcal{O}(\varepsilon)$ [669]	$\lesssim 1$	$\lesssim 0.8$
Broken SU(3) [665]	$-(1.4^{+0.9}_{-1.1})$	$-(1.10^{+0.70}_{-0.85})$

factor of $\lambda^2 \sim 1/20$. This problem is to be overcome with high-luminosity experiments like Belle II as discussed in Sect. 10.2.2.

The U-spin limit approach is limited by the size of U-spin-breaking corrections parameterized by the parameter $\varepsilon \sim m_s/\Lambda_{\rm QCD} \sim 0.2$. The flavor-breaking corrections cannot be controlled with a single partner mode, and hence such U-spin analyses require additional assumptions. More sophisticated flavor symmetry analyses therefore include fits from multiple decay modes, using a combination of CP asymmetries and CP-averaged rates [665,669]. Differences arise in the treatment of SU(3) breaking in these fits. One approach uses a model-independent expansion to first order in the breaking [669]; another considers only factorizable breaking as a starting point, while an additional non-factorizable part is assumed to be smaller [665]. Differing dynamical assumptions, e.g. about the smallness of annihilation contributions, are also necessary to obtain a well-constrained fit. Importantly, these methods are data-driven, such that their precision improves with additional data. In Table 71 we summarize the theory expectations from analyses performed over the last decade.

The importance of measuring CP-averaged rates is emphasized by the SU(3) relation [670]

$$(1+\bar{\lambda}^2)\sin\phi_d = S_{J/\psi K^0_S} - \bar{\lambda}^2 S_{J/\psi\pi^0} - 2(\Delta_K + \bar{\lambda}^2\Delta_\pi)\cos\phi_d \tan\phi_3, \tag{305}$$

in which penguin pollution effects are cancelled to $\mathcal{O}(\varepsilon)$ and leading corrections arise from isospin-breaking terms. Here, $\Delta_{K,\pi}$ are splittings of the charged and neutral CP-averaged rates,

$$\begin{aligned}\Delta_K &\equiv \frac{\bar{\Gamma}_{B_d\to J/\psi K^0} - \bar{\Gamma}_{B^+\to J/\psi K^+}}{\bar{\Gamma}_{B_d\to J/\psi K^0} + \bar{\Gamma}_{B^+\to J/\psi K^+}},\\ \Delta_\pi &\equiv \frac{2\bar{\Gamma}_{B_d\to J/\psi\pi^0} - \bar{\Gamma}_{B^+\to J/\psi\pi^+}}{2\bar{\Gamma}_{B_d\to J/\psi\pi^0} + \bar{\Gamma}_{B^+\to J/\psi\pi^+}}.\end{aligned} \tag{306}$$

Determining $\Delta_{\pi,K}$ at the desired precision requires the control of potentially enhanced isospin-breaking effects in the B^0/B^+ production ratio from independent measurements, which is possible using data from Belle and Belle II, but requires a dedicated analysis [671].

10.2.2. Experiment $\sin 2\phi_1$ *from* $b \to c\bar{c}s$ *decay modes*

$B^0 \to J/\psi K^0_S$ The $B^0 \to J/\psi K^0_S$ decay mode leads to an experimentally very clean signature. Moreover, it presents a relatively large branching fraction, so a large signal yield is expected. Even if the contribution of penguin diagrams with a different CKM phase is expected to be at less than the 1% level, this effect can become appreciable at the end of the Belle II data-taking and should be taken into account for the ϕ_1 determination.

Belle has updated the time-dependent CP asymmetry measurement using the whole data sample [80], obtaining:

$$S_{J/\psi K^0_S} = +0.670 \pm 0.029(\text{stat}) \pm 0.013(\text{syst}),$$
$$A_{J/\psi K^0_S} = -0.015 \pm 0.021(\text{stat}) \,^{+0.045}_{-0.023}(\text{syst}). \quad (307)$$

While $S_{J/\psi K^0_S}$ is still dominated by the statistical error, the measurement of $A_{J/\psi K^0_S}$ is already dominated by the systematic uncertainties. For the extrapolation of the statistical errors, we assume the same $B\bar{B}$ vertex separation capability as Belle. We then scale the statistical error according to the square root of the integrated luminosity. Systematic errors include uncertainties in the wrong tag fractions, a possible fit bias, uncertainties in the signal fractions, the background Δt distribution, τ_{B^0}, and Δm_d. All these depend on control samples or on Monte Carlo statistics and are expected to scale with the square root of the integrated luminosity, as the statistical errors. The two remaining systematic errors, tag-side interference and uncertainty due to the vertex reconstruction algorithm, do not scale with the integrated luminosity. A dedicated study is thus needed.

In the Belle measurement [80] the error due to the tag-side interference was evaluated by comparing the fit results with and without the tag-side interference term [672]. This term, however, is well defined in the case of the $B^0 \to D^{*-} l^+ \nu$ decay mode. The systematic error from tag-side interference can then be reduced in the measurement of the CP parameters of $B^0 \to J/\psi K^0_S$, taking into account the tag-side interference term in the default fitter and assigning as error the tag-side interference term uncertainty. Another way of avoiding the effect of the tag-side interference is to use only leptonic categories for the flavor tagging. However, this would reduce the tagging efficiency by about a factor of three, which results in an increase of statistical error.

The systematic uncertainty due to the vertex reconstruction had, at Belle, different causes: alignment of the vertex detector, the vertex algorithms, and the vertex resolution. All these components are expected to be reduced at Belle II. The uncertainty on the alignment of the vertex detector (see Sect. 5.3.3) has two components: one that depends on the size of the control samples that will be used to perform the alignment (and thus will scale as the statistical uncertainties), and an irreducible component. The new vertex algorithm for the tag side removes the systematic effect coming from the selection of the tracks used for the vertex fit, and improves, by almost a factor two, its resolution. The vertex resolution of the CP side will improve by a factor of two compared to Belle thanks to the new pixel vertex detector. We assume, for this study, a factor of two for the reduction of the systematic uncertainty due to the vertex reconstruction.

Table 72 shows the expected Belle II sensitivity to the $B^0 \to J/\psi K^0_S$ CP asymmetry parameters. The measurement is expected to be dominated by systematic errors. In the case of $A_{J/\psi K^0_S}$, the smallest total error is obtained when performing the analysis using only the leptonic categories for flavor tagging.

Expected sensitivity of the time-dependent asymmetries of $B^0 \to J/\psi \pi^0$ The $B^0 \to J/\psi \pi^0$ decay mode, proceeding through the $b \to c\bar{c}d$ transition, can be used to constrain the theoretical uncertainties in $B^0 \to J/\psi K^0_S$. Both BaBar [673] and Belle [674] have performed time-dependent analysis of $B^0 \to J/\psi \pi^0$, the latter obtaining

$$S_{J/\psi \pi^0} = -0.65 \pm 0.21(\text{stat}) \pm 0.05(\text{syst}),$$
$$A_{J/\psi \pi^0} = -0.08 \pm 0.16(\text{stat}) \pm 0.05(\text{syst}),$$

Table 72. Belle II expected sensitivity on the CP parameters of $B^0 \to J/\psi K^0_S$. The expected statistical, reducible systematic, and non-reducible systematic uncertainties are shown. An integrated luminosity of $50\,\text{ab}^{-1}$ is assumed. Three cases are considered: "No improvement," where Belle irreducible systematic uncertainties are assumed not to improve in Belle II; "Vertex improvement," where an improvement of 50% is assumed for the systematic uncertainty due to the vertex positions; "Leptonic categories," where the analysis is performed using only the leptonic categories for flavor tagging.

	No improvement	Vertex improvement	Leptonic categories
$S_{J/\psi K^0_S}$ $(50\,\text{ab}^{-1})$			
Statistical	0.0035	0.0035	0.0060
Systematic reducible	0.0012	0.0012	0.0012
Systematic irreducible	0.0082	0.0044	0.0040
$A_{J/\psi K^0_S}$ $(50\,\text{ab}^{-1})$			
Statistical	0.0025	0.0025	0.0043
Systematic reducible	0.0007	0.0007	0.0007
Systematic irreducible	$^{+0.043}_{-0.022}$	$^{+0.042}_{-0.011}$	0.011

Table 73. Belle II expected sensitivity to the $B^0 \to J/\psi\pi^0$ CP asymmetry parameters for an integrated luminosity of $50\,\text{ab}^{-1}$. See also Table 72.

	No improvement	Vertex improvement	Leptonic categories
$S_{J/\psi\pi^0}$ $(50\,\text{ab}^{-1})$			
Statistical	0.027	0.027	0.047
Systematic reducible	0.009	0.009	0.009
Systematic irreducible	0.050	0.025	0.025
$A_{J/\psi\pi^0}$ $(50\,\text{ab}^{-1})$			
Statistical	0.020	0.020	0.035
Systematic reducible	0.004	0.004	0.004
Systematic irreducible	0.045	0.042	0.017

largely dominated by statistical errors. A precise measurement will be possible using the high integrated luminosity collected by Belle II at the end of its data-taking. Table 73 shows the expected sensitivity to the time-dependent CP asymmetry parameters assuming an integrated luminosity of $50\,\text{ab}^{-1}$. The algorithm for calculating the expected statistical and systematic uncertainties is the same as in the previous section. A relative uncertainty of a few percent is expected. This will translate to an uncertainty of $\sim 0.1^\circ$ on ϕ_1 from $B^0 \to J/\psi K^0_S$ when using Eq. (305) to estimate the penguin pollution and ignoring for now the $\mathcal{O}(\epsilon^2)$ effects from SU(3) breaking.

Expected sensitivity from the combined analysis of $b \to c\bar{c}s$ decay modes We show next the projected sensitivity to ϕ_1 for the combination of the most relevant $b \to c\bar{c}s$ decay modes. Belle has published a combined analysis of decay modes with $\eta_f = -1$ CP eigenvalue ($B^0 \to J/\psi K^0_S$, $B^0 \to \psi(2S)K^0_S$, $B^0 \to \chi_{c1}K^0_S$) and with $\eta_f = +1$ CP eigenvalue ($B^0 \to J/\psi K^0_L$) [675]. The

Table 74. Belle II expected sensitivity for the CP asymmetry parameters in the combination of $b \to c\bar{c}s$ modes. An integrated luminosity of $50\,\text{ab}^{-1}$ is assumed.

	No improvement	Vertex improvement	Leptonic categories
$S_{c\bar{c}s}$ ($50\,\text{ab}^{-1}$)			
Statistical	0.0027	0.0027	0.0048
Systematic reducible	0.0026	0.0026	0.0026
Systematic irreducible	0.0070	0.0036	0.0035
$A_{c\bar{c}s}$ ($50\,\text{ab}^{-1}$)			
Statistical	0.0019	0.0019	0.0033
Systematic reducible	0.0014	0.0014	0.0014
Systematic irreducible	0.0106	0.0087	0.0035

averaged CP asymmetry parameters,

$$\begin{aligned} S_{c\bar{c}s} &= 0.667 \pm 0.023(\text{stat}) \pm 0.012(\text{syst}), \\ A_{c\bar{c}s} &= 0.006 \pm 0.016(\text{stat}) \pm 0.012(\text{syst}), \end{aligned} \tag{308}$$

are still dominated by the statistical errors.

The combination of CP-odd and CP-even final states returns a combined tag-side interference systematic that is smaller than the systematic in each individual mode. The tag-side interference term has the opposite sign for different CP eigenstates, which produces a partial cancellation in the combined result.

Table 74 shows the expected sensitivity for the CP asymmetry parameters in the combined $b \to c\bar{c}s$ analysis at Belle II. The $B^0 \to J/\psi K_{\text{S,L}}$ decay modes contribute the largest fraction of the yield. The addition of the remaining channels improves the statistical uncertainty by about 10%. While all the modes will be important for the measurements performed during the first years of data-taking, the opportunity of including them in the final analysis performed using the full expected luminosity should be considered only if the resulting systematic uncertainties will be better than those reported in Table 74. A precision better than 1% is expected when setting aside the theoretical issue of penguin pollution. The strategies to deal with the latter differ from mode to mode as discussed above, and may also be combined in a global analysis.

10.2.3. Other $b \to c\bar{c}X$ decay modes

The arguments above hold equally well for the other initial and final states, as long as the corresponding amplitude is dominated by the $b \to c\bar{c}X$ transition. The following three decay channels are the most relevant: (i) $B \to \psi(X)K^0_{\text{S}}$, i.e. replacing the J/ψ by other charmonia; (ii) $B \to J/\psi V$, i.e. replacing the pseudoscalar in the final state by a vector meson (or two pseudoscalars), specifically the decay $B_s \to J/\psi\phi$; (iii) $B \to D^{(*)}D^{(*)}$, i.e. two charmed mesons in the final state. These options are briefly discussed in the remainder of this section.

(i) Replacing the J/ψ by other charmonia makes little difference theoretically, but the experimentally convenient $\ell^+\ell^-$ final state becomes unavailable. The SU(3) symmetry analysis for controlling penguin pollution proceeds analogously to the $J/\psi K^0_{\text{S}}$ case. Of course, the relevant SU(3)-related modes need to be remeasured with each charmonium state. For the $\psi(2S)K^0_{\text{S}}$ final state, the penguin pollution has been estimated in Ref. [662].

(ii) The main change when replacing the K^0_S by a vector meson is that an angular analysis becomes necessary in order to disentangle the different polarization amplitudes which transform differently under CP. Doing so presently provides the best extraction of ϕ_s via $B_s \to J/\psi\,\phi$ [230]. Regarding ϕ_d, the fact that K^* is not a CP eigenstate complicates the extraction. However, the final state $K^* \to K^0_S\pi^0$ can be used. The penguin pollution in the $B \to J/\psi\,K^*(\to K^0_S\pi^0)$ mode has been estimated from a theoretical calculation to be of a similar size as in $B \to J/\psi\,K^0_S$ [662].

A flavor SU(3) symmetry analysis is again possible [665,676], but complicated by the fact that the three polarization amplitudes per channel require three independent sets of matrix elements, introducing a larger number of nuisance parameters into the analysis. Furthermore, the fact that the ϕ meson is an admixture of flavor SU(3) octet and singlet states has to be taken into account. When using $J/\psi\,\rho$ or $J/\psi\,K^*$ final states as control modes, only the octet amplitude can be restricted, while in order to control the singlet amplitude, data for $B_{d,s} \to J/\psi\,\omega$ and $B_d \to J/\psi\,\phi$ are necessary. So far, the corresponding singlet amplitudes, stemming, e.g., from exchange diagrams, have been neglected. This type of amplitude, however, has been shown in $B \to DD$ decays to be larger than naively expected [677,678]. While this does not allow one to infer anything regarding $B \to J/\psi\,V$ decays, it demonstrates that experimental data should be used to control these amplitudes instead of theoretical assumptions.

Apart from $B_d \to J/\psi K^0_S$ and $B_s \to J/\psi\phi$, the $B_s \to J/\psi f_0(980)$ decay has also been proposed as a means to extract ϕ_s [679], $f_0(980)$ being the largest resonance in $B_s \to J/\psi\pi^+\pi^-$. Since it is a scalar meson, this mode does not require an angular analysis. Of concern in this case is the unclear hadronic nature of the $f_0(980)$, and its mixing with the $\sigma(f_0(500))$ resonance. This renders a symmetry analysis of the type described above more complicated [680]. It therefore seems hard to achieve the control of sub-leading contributions to a comparable level as in $B_s \to J/\psi\phi$.

(iii) The $B \to D^{(*)}D^{(*)}$ modes exhibit essentially the same features as $B \to J/\psi\,K^0_S$, only they are not as straightforward to interpret. The corresponding "golden" channels are the tree-level $b \to c$ transitions into CP eigenstates, specifically $B_d \to D^+D^-$, sensitive to ϕ_1, and $B_s \to D_s^+D_s^-$, sensitive to ϕ_s [663]. This strategy has been model-independently extended to full SU(3), including symmetry-breaking corrections [677]. The strategy requires precision measurements of many branching fractions and CP asymmetries [677,678]. Explicit calculation of penguin pollution in these modes is very challenging, since even in the formal limit $m_{b,c} \to \infty$ these decays do not factorize [244]. Some analyses have nonetheless employed this approximation [678].

10.3. Determination of ϕ_1 in gluonic penguin modes

10.3.1. Theory: $\sin 2\phi_1$ *from* $b \to q\bar{q}s$, $q = u, d, s$

Contributing author S. Jäger

The penguin-dominated modes $b \to q\bar{q}s$ ($q = u, d, s$), see Fig. 100, are interesting for at least the following three reasons:

(1) They probe the B_d–$\bar{B}_d$ mixing phase through different short-distance vertices than the tree-dominated $b \to c\bar{c}s$ decays.
(2) They are loop dominated in the SM, and hence may be more sensitive to NP effects than the tree-dominated modes.
(3) They comprise a large number of different final states, which can help in disentangling nonperturbative long-distance physics from short-distance information such as ϕ_1 or BSM contributions to the weak Hamiltonian.

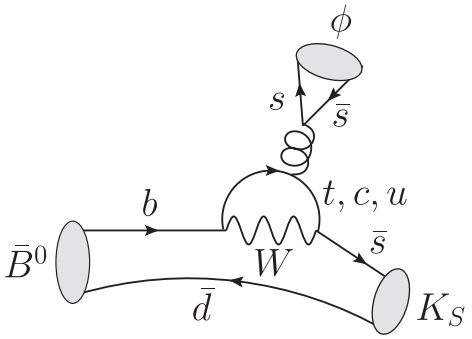

Fig. 100. The QCD penguin contributions to $B \to \phi K_S^0$ decay. The T_f amplitude receives a contribution from the c quark in the loop, while the t and u quarks contribute to both T_f and P_f in Eq. (309).

On general grounds, the charmless $b \to q\bar{q}s$ decay amplitude $\mathcal{A}_f \equiv \mathcal{A}(\bar{B} \to f)$ can be written as

$$\mathcal{A}_f = \lambda_c^s P_f + \lambda_u^s T_f + \mathcal{A}_f^{\rm NP}. \tag{309}$$

Note that compared to the $b \to sc\bar{c}$ decays in Eq. (300), here the "penguin amplitude" P_f is multiplied by a large CKM factor, λ_c^s, while the "tree amplitude", T_f, is CKM suppressed. $\mathcal{A}_f^{\rm NP}$ is a possible BSM contribution. The latter will, in general, have indefinite CP properties, i.e. $|\bar{\mathcal{A}}^{\rm NP}| \neq |\mathcal{A}^{\rm NP}|$. It is worth noting that the "tree amplitude" T_f as defined here contains effects not only from tree-level W exchange (operators Q_1 and Q_2, including their "up loop" contractions) but also part of the QCD and electroweak penguin operator contributions (top loops). These carry the combination of CKM matrix elements $\lambda_t^{(s)} = V_{ts}V_{tb}^* = -(1+\epsilon_{uc})\lambda_c^{(s)}$ (where we have defined $\epsilon_{uc} \equiv \lambda_u^{(s)}/\lambda_c^{(s)} = \mathcal{O}(\lambda^2)$), which differs slightly in weak phase from the penguin amplitude in Eq. (309).

In the SM and when ϵ is neglected, the $b \to q\bar{q}s$ modes are pure penguin with the same weak phase (indeed, CKM combination) as the tree-dominated $b \to c\bar{c}s$ decays. As a consequence, direct CP asymmetries vanish in this limit. If f is a CP eigenstate, the coefficient S_f in the time-dependent CP asymmetry then measures the same phase ϕ_1 as in the $b \to c\bar{c}s$ decays. Departures from this limit may come from the tree amplitude T_f (often called the "tree pollution"), as well as from possible NP effects. Introducing the tree-to-penguin ratio $r_f^T = T_f/P_f$ and the BSM-to-SM ratio $r_f^{\rm NP} \equiv \mathcal{A}_f^{\rm NP}/(\lambda_c^{(s)}P_f)$, one can make the following statements:

- Branching ratios are affected at $\mathcal{O}\big(|\epsilon_{uc}r_f^T|, |r_f^{\rm NP}|\big)$.
- Direct CP asymmetries in the SM are of $\mathcal{O}\big(|\epsilon_{uc}|{\rm Im}\, r_f^T\big)$. A possible BSM contribution to the direct CP asymmetry will likewise require both a weak and a strong phase difference relative to the SM penguin.
- The sine coefficients in time-dependent CP asymmetry differ from $\sin 2\phi_1$ by ΔS_f (see, e.g., Ref. [681]),

$$-\eta_f^{\rm CP} S_f = \sin 2\phi_1 + \Delta S_f, \tag{310}$$

where

$$\Delta S_f = 2\cos 2\phi_1 \sin\phi_3 |\epsilon_{uc}| {\rm Re}\, r_f^T + \Delta S_f^{\rm NP}. \tag{311}$$

Table 75. The predictions for ΔS_f in Eq. (310) for the charmless two-body final states listed in the first column, using different theoretical approaches, are listed in the second, third, and fourth columns, while the experimental values are given in the last column.

Mode	QCDF [681]	QCDF (scan) [681]	SU(3)	Data [230]
$\pi^0 K^0_S$	$0.07^{+0.05}_{-0.04}$	$[0.02, 0.15]$	$[-0.11, 0.12]$ [683]	$-0.11^{+0.17}_{-0.17}$
$\rho^0 K^0_S$	$-0.08^{+0.08}_{-0.12}$	$[-0.29, 0.02]$		$-0.14^{+0.18}_{-0.21}$
$\eta' K^0_S$	$0.01^{+0.01}_{-0.01}$	$[0.00, 0.03]$	$(0 \pm 0.36) \times 2\cos(\phi_1)\sin\gamma$ [684]	-0.05 ± 0.06
ηK^0_S	$0.10^{+0.11}_{-0.07}$	$[-1.67, 0.27]$		—
ϕK^0_S	$0.02^{+0.01}_{-0.01}$	$[0.01, 0.05]$	$(0 \pm 0.25) \times 2\cos(\phi_1)\sin\gamma$ [684]	$0.06^{+0.11}_{-0.13}$
ωK^0_S	$0.13^{+0.08}_{-0.08}$	$[0.01, 0.21]$		$0.03^{+0.21}_{-0.21}$

The first term on the right-hand side is due to the SM tree pollution, while $\Delta S_f^{\rm NP}$ denotes the potential NP contribution.

To measure ϕ_1 it is crucial to control the effects due to non-vanishing r_f^T. Since $\mathrm{Re}\, r_f^T \propto \cos\delta_f = 1 - \delta_f^2/2 + \cdots$, with $\delta_f = \arg r_f^T$ the strong phase difference, it is less sensitive to final-state rescattering effects. Small strong phases are predicted in the heavy quark expansion, see below. In addition, a given NP scenario will affect different modes in different ways.

Theoretical information on r_f^T comes from the use of flavor SU(3) relations and the heavy quark expansion. The methods based on SU(3) relate the $b \to q\bar{q}s$ transitions to the $b \to q\bar{q}d$ transitions, such as $B \to \pi\pi$, $B \to \pi\eta'$, and so on, i.e. the modes that are related by the U-spin subgroup of SU(3) to $B \to \pi K, K\eta'$, …In $b \to q\bar{q}d$ transitions the tree contributions are CKM enhanced compared to the penguins, making it possible to obtain experimental information on r_f^T.

The heavy quark expansion gives rise to QCDF of charmless hadronic $B \to M_1 M_2$ decay amplitudes [244,415,416] (see also Ref. [682]), allowing the calculation of the decay amplitudes directly in terms of weak decay form factors and meson light cone distribution amplitudes. Qualitatively, the QCDF formula implies the following:

- Naive factorization holds up to perturbative corrections and power corrections. In particular, there is a limit—the heavy quark limit—in which naive factorization holds.
- Imaginary parts of strong amplitudes (strong phases) are small, $\mathcal{O}(\alpha_s; \Lambda/m_B)$.
- Real parts of strong amplitudes, and thus also $\mathrm{Re}\, r_f^T$, are roughly approximated by their naive-factorization expressions. The exception are color-suppressed tree amplitudes, for which there are strong cancellations at the naive-factorization level.

ΔS_f phenomenology for $B_d \to \phi K^0_S, \eta' K^0_S$, etc. Many S_f measurements for charmless final states have been performed at the B factories. A selection of them is shown in Table 75. The last column lists the experimental values for $\Delta S_f = -\eta_f^{\rm CP} S_f - (\sin\phi_1)_{c\bar{c}s}$, combining errors in quadrature. Here, $(\sin\phi_1)_{c\bar{c}s}$ is the HFLAV average of $\sin\phi_1$ measurements using final states with charmonia [230], while S_f are the HFLAV averages for each individual penguin ($q\bar{q}s$) mode. These data can be compared to theory predictions.

A systematic treatment in QCD factorization has been given in Ref. [681] for each of the listed modes. The calculation constrains the QCD penguin amplitudes through the branching fraction

measurements (see Ref. [681] for details). The second and third columns of Table 75 show two different error estimates, one combining individual errors in quadrature, the other scanning over them. One observes that deviations are mostly predicted to be small, notably in the $\eta' K^0_S$ and ϕK^0_S final states. Typically they have a definite, mode-dependent, sign. The fourth column of Table 75, shows mode-specific predictions for ΔS_f obtained with the help of flavor SU(3) to fix or constrain tree-to-penguin ratios from data; see, e.g., Refs. [683–686]. To obtain further control of the predictions one could use global fits of SU(3) amplitudes, as in, e.g., Ref. [687], but it would be crucial to include SU(3)-breaking effects to control the systematic errors associated with them. A first step in this direction could be the NP tests using sum rules valid to higher orders in SU(3) breaking [688].

QCDF generally predicts definite or preferred signs of the ΔS_f shift, similarly to predictions from naive factorization. This implies a definite pattern of shifts to be compared with data. At present there is no significant tension between these predictions and data. The theoretical errors are generally much smaller than the experimental ones. The measurements of $b \to q\bar{q}s$ time-dependent CP asymmetries thus provide theoretically clean NP discovery modes for Belle II.

NP can give rise to peculiar patterns of shifts in certain scenarios. For instance, BSM scenarios with "right-handed currents" can enhance the weak Hamiltonian QCD and electroweak penguin operators with a right-handed strange quark field, Q'_i, well above their SM values. Their matrix elements are related to the "SM" operators with left-handed strange quark field, Q_i, through

$$\langle f|Q'_i|\bar{B}^0\rangle = \eta_P \langle f|Q_i|\bar{B}^0\rangle,$$

where f was assumed to have definite parity, and $\eta_P = \pm 1$. An example of such a scenario is low-scale supersymmetry with substantial mixing between right-handed squark flavors [689] (for grand-unified scenarios where this naturally arises see, e.g., Refs. [690,691]). This modifies the QCD penguin amplitudes and can produce parity-dependent shifts ΔS_f. (The parameter values in Ref. [689] are ruled out by the LHC SUSY searches and measurements of CP violation in B_s mixing. However, the correlation between B_s mixing and $\Delta F = 1$ decays is model dependent.)

ΔS versus ΔA in $B \to \pi^0 K^0_S$ For $\pi^0 K^0_S$ it is possible, with very limited theory input, to relate $S_{\pi^0 K^0_S}$ and $A_{\pi^0 K^0_S}$ from the four measured branching ratios in the $B \to \pi K$ system [692,693]. The reason why this is possible is that most of the required hadronic matrix elements can be obtained using isospin. The starting point is the isospin relation

$$\sqrt{2}\,\mathcal{A}(B^0 \to \pi^0 K^0) + \mathcal{A}(B^0 \to \pi^- K^+) = -\left[(\hat{T} + \hat{C})e^{i\phi_3} + \hat{P}_{\rm ew}\right] \equiv 3\mathcal{A}_{3/2}, \tag{312}$$

in which the QCD penguin amplitudes cancel out on the left-hand side. The subscript of $\mathcal{A}_{3/2}$ reminds us that the πK final state has isospin $I = 3/2$. A similar relation holds for the CP-conjugate amplitudes, with $\mathcal{A}_{3/2} \to \bar{\mathcal{A}}_{3/2}$ and $\phi_3 \to -\phi_3$. Here, $\hat{T}$, $\hat{C}$, and $\hat{P}_{\rm ew}$ are, respectively, the color-allowed tree, color-suppressed tree, and electroweak penguin contributions.

The important point is that $\mathcal{A}_{3/2}$ can be obtained with good accuracy. The SU(3) flavor symmetry relates $|\hat{T} + \hat{C}|$ to $\mathcal{B}(B \to \pi^+\pi^0)$, while $P_{\rm ew}/(\hat{T} + \hat{C})$ is given directly by the $C_{9,10}$ Wilson coefficients and CKM elements [694,695]. Measurements of $\mathcal{B}(B^0 \to \pi^0 K^0)$, $\mathcal{B}(B^0 \to \pi^+ K^-)$, and the corresponding CP asymmetries then suffice to determine $S_{\pi^0 K^0_S}$.

It is instructive to remove $A_{\pi^0 K^0_S}$ from the input data set and view the construction as a mostly data-driven prediction of the relation between $A_{\pi^0 K^0_S}$ and $S_{\pi^0 K^0_S}$ (left panel of Fig. 101). Differently shaped points along the bands are distinguished by different values of the strong phase of the tree-to-penguin ratio $r_c \equiv (\hat{T} + \hat{C})/\hat{P}$. There is a four-fold ambiguity in the construction, due to an ambiguity

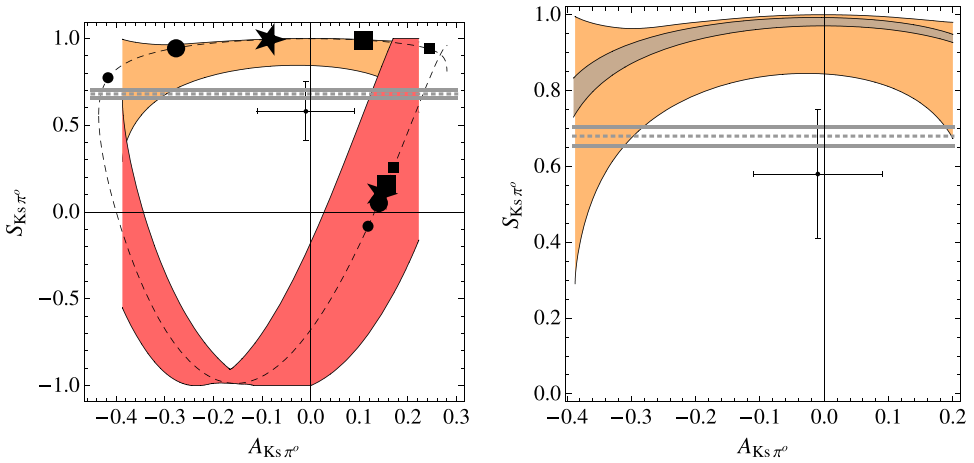

Fig. 101. Data-driven prediction for time-dependent CP violation in $B \to \pi^0 K^0_S$. Figures from Ref. [692]. Left panel: Existing constraints. Only the top (orange, horizontal) band is consistent with SU(3) and the heavy quark limit. Right panel: Belle II projection for about 10 ab^{-1} of integrated luminosity (thin brown band). For details, see text.

in determining the $I = 3/2$ amplitudes. The ambiguity is partly resolved by taking the strong phase of r_c to be small, leading to a single closed "loop" of solutions in Fig. 101. The smallness of the phase is implied by QCDF [696,697], or alternatively from SU(3) relations with CP violation in $B \to \pi^+\pi^-$, see Ref. [692] for a detailed discussion. Of the remaining two solutions, one is again wildly inconsistent with both QCDF predictions and with SU(3) relations with $B \to \pi\pi$ data. This leaves the top orange band in Fig. 101. The experimental data on $A_{K^0_S\pi^0}, S_{K^0_S\pi^0}$ (cross) and $\sin\phi_1$ from $b \to c\bar{c}s$ (gray horizontal band) at the time of Ref. [692] are also displayed.

The data-driven nature of the method implies that Belle II measurements can be used to sharpen predictions considerably. This is illustrated in the right panel of Fig. 101, where the 2008 situation is displayed in orange (broad band) and a projected uncertainty in brown (thin band), assuming unchanged central values of $B \to \pi K$ with 10 times larger datasets. The uncertainty (width of the brown band) is then determined by the SU(3) breaking, which were taken to be $\mathcal{O}(20\%)$ at the level of the amplitudes.

In summary, time-dependent CP violation in $b \to q\bar{q}s$ penguin-dominated transitions provides complementary ways to access ϕ_1 in the SM, and provides good sensitivity to BSM scenarios. The tree pollution in the S_f coefficients is theoretically understood and small in several of the charmless two-body final states. In the special case of the $B \to \pi K$ system, an isospin analysis in conjunction with the use of the heavy quark expansion provides a data-driven determination for $S_{\pi^0 K^0_S}$ at Belle II with percent-level accuracy.

10.3.2. Experiment: $\sin 2\phi_1$ *from* $b \to q\bar{q}s$, $q = u, d, s$

Contributing authors: A. Gaz, S. Lacaprara

In this section we present a complete sensitivity study for the time-dependent CP violation parameters in the penguin-dominated modes $B^0 \to \phi K^0$ and $\eta' K^0$, and an extrapolation of the sensitivity for $B^0 \to \omega K^0_S$.

For time-dependent CP violation analysis the current implementation of the Belle II simulation and reconstruction software gives a realistic estimate of the Δt resolution and the effective tagging efficiency. The reconstruction efficiencies, on the other hand, are most probably underestimated,

especially for neutral particles. As more realistic estimates we thus use the values for the reconstruction efficiencies that were achieved by BaBar and Belle in the previous analyses (we also quote the efficiencies obtained with the current simulation).

The analyses of $b \to q\bar{q}s$ decays have several common features. The dominant background is due to random combinations of particles produced in continuum events ($e^+e^- \to q\bar{q}, q = u, d, s, c$) and, to a much smaller extent, from B meson decays to charmed particles. To study it we simulated a large sample of $e^+e^- \to u\bar{u}, d\bar{d}, s\bar{s}, c\bar{c}$ events corresponding to 1–5 ab^{-1} of equivalent luminosity. The combinatorial background is without any peaking structure in the main analysis variables $M_{\rm bc}$ and ΔE. It can be easily modeled from data, selecting sidebands of the $M_{\rm bc}$ and/or ΔE distributions.

The other significant background components are due to charmless B decays with topologies similar to the decay under study. While much less frequent than the combinatorial background, they do require modeling of peaking structures in the main variables of the analysis, including $M_{\rm bc}$ and to a smaller extent ΔE. This is more sensitive to extra or missing particles. Background charmless B decays can also be CP violating and can potentially bias the main measurement. We study these effects using a 5.0 ab^{-1} equivalent-luminosity sample of simulated $B\bar{B}$ decays.

The CP-violating parameters S and A are extracted from an unbinned multidimensional maximum likelihood fit which includes the proper decay time difference Δt, and variables that discriminate against backgrounds: $M_{\rm bc}$, ΔE, the output of the continuum suppression multivariate discriminator, the invariant masses of resonances, helicity angles, etc. We assume that all these variables are uncorrelated.

For some of the modes there will be competition from the LHCb experiment. Their plan is to measure $S_{\phi K^0}$ with uncertainty of 0.06 for an integrated luminosity of 50 fb^{-1} and extensive upgrade in their hadronic trigger [698]. From this projection it is therefore reasonable to expect that LHCb will approach the sensitivity of BaBar and Belle at the end of Run2 in the year 2018. LHCb is expected to be less competitive in the $B^0 \to \eta' K^0$ and $\omega K^0_{\rm S}$ channels.

The systematic uncertainties for $B^0 \to \eta' K^0$, the channel with higher yield, have been extrapolated from Belle results using the same assumption used for $B^0 \to J/\psi K^0$. They become comparable to statistical uncertainties for an integrated luminosity of about 10 ab^{-1}. The other $b \to q\bar{q}s$ decay channels will be statistically limited up to 50 fb^{-1}.

The equivalent integrated luminosity used for these studies is 5 ab^{-1}. With this dataset, the measurements will still be dominated by statistical uncertainties. We verified that the statistical sensitivity of the analyses scales well with $1/\sqrt{\mathcal{L}}$.

$B_d \to \phi K^0$.

Contributing author: A. Gaz

BaBar and Belle extracted the $B_d \to \phi K^0$ CP asymmetry parameters from time-dependent analysis of the $K^+K^-K^0$ final state [699,700]. We perform a sensitivity study using a quasi-two-body approach, taking into account the decay channels $\phi(K^+K^-)K^0_{\rm S}(\pi^+\pi^-)$, $\phi(K^+K^-)K^0_{\rm S}(\pi^0\pi^0)$, $\phi(\pi^+\pi^-\pi^0)K^0_{\rm S}(\pi^+\pi^-)$, and $\phi(K^+K^-)K^0_{\rm L}$. The channel $\phi(\pi^+\pi^-\pi^0)K^0_{\rm S}(\pi^+\pi^-)$ has never been used before due to its very low significance with small integrated luminosity. For the $K^0_{\rm L}$ channel we extrapolate previous BaBar and Belle results and do not perform a simulation.

Analysis strategy In the $B^0 \to \phi(K^+K^-)K^0$ decay there is a non-negligible non-resonant s-wave contribution, even when restricting the K^+K^- invariant mass to a narrow range around the ϕ resonance. The s-wave has a CP phase that differs from the resonant contribution and, if ignored,

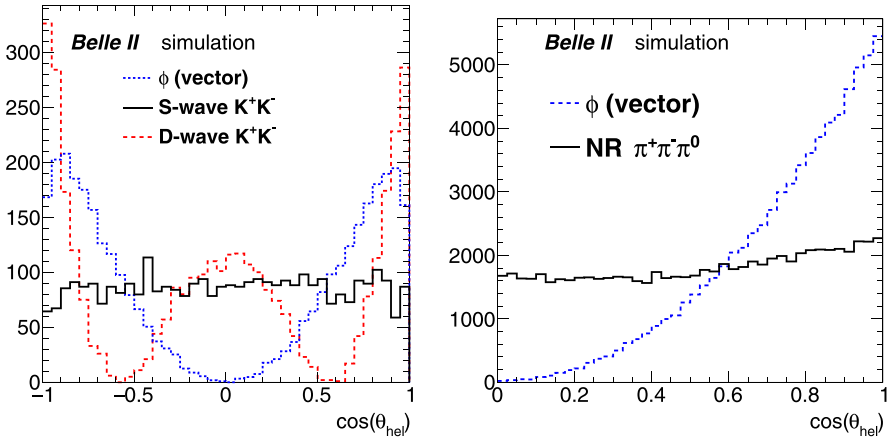

Fig. 102. Distributions of $\cos\theta_{\rm H}$ for the $\phi \to K^+K^-$ case (left plot) and for the $\phi \to \pi^+\pi^-\pi^0$ case (right). The plots include effects due to the detector acceptance, easily visible at the edges of the distributions.

would lead to a significant bias in the measurement. This component could also include a contribution from $f_0(980) \to K^+K-$ decays which, in a more refined version of the analysis, could be treated as an additional component.

The two components can be disentangled using a full Dalitz plot analysis. An alternative, much simpler, option is to include in the maximum likelihood fit the helicity angle, $\theta_{\rm H}$, of the ϕ candidate. For $\phi \to K^+K^-$, $\theta_{\rm H}$ is the angle between the K^+ and B flight directions in the ϕ rest frame, while for $\phi \to \pi^+\pi^-\pi^0$, $\theta_{\rm H}$ is the angle between the normal to the plane formed by the three pions and the B momentum in the ϕ rest frame. Figure 102 (left) shows the $\cos\theta_{\rm H}$ distributions for the scalar, vector, and tensor components for $\phi \to K^+K^-$, while Fig. 102 (right) shows the $\cos\theta_{\rm H}$ distributions for the scalar and vector components for $\phi \to \pi^+\pi^-\pi^0$. Toy Monte Carlo studies show that this approach gives unbiased results for the CP asymmetry parameters for both the vector and the scalar components, provided that each component has an adequate number of events, typically $\mathcal{O}(100)$.

Event selection Table 76 summarizes the main selection cuts applied for each of the investigated channels. Cuts are applied to the main discriminating variables $M_{\rm bc}$ and ΔE, and to the invariant masses of the intermediate resonances; all these are intentionally set quite loose so that backgrounds can be fitted and modeled from the sidebands. Furthermore, requirements on the flight length significance (flLenSig, the ratio between the measured flight length and its estimated uncertainty) of the $K^0_{\rm S}$ candidates, on the PID of the charged kaons, and on the probability that final state particles originate from a common vertex (PrbVtx) are set. The requirements on the distance of closest approach d_0, its z coordinate z_0, and on the number of PXD hits associated to the tracks that originate from the ϕ decay, reject poorly reconstructed events that are expected to have significantly worse Δt resolution.

The selection efficiencies and candidate multiplicities for signal events are reported at the bottom of Table 76. While the efficiency for the $\phi(K^+K^-)K^0_{\rm S}(\pi^+\pi^-)$ mode is comparable to what was achieved at BaBar and Belle, the modes with π^0 are performing significantly worse. We expect that the planned developments on the reconstruction software of the calorimeter and the selection of photon candidates will significantly improve the overall efficiency as we approach the start of data-taking.

Table 76. Main selection requirements for the channels used in the ϕK^0_S sensitivity study. The selection efficiency ε and candidate multiplicity for signal events are given at the bottom.

Variable	$\phi(K^+K^-)K^0_S(\pi^+\pi^-)$	$\phi(K^+K^-)K^0_S(\pi^0\pi^0)$	$\phi(\pi^+\pi^-\pi^0)K^0_S(\pi^+\pi^-)$
$M_{\rm bc}$ (GeV)	> 5.25	> 5.25	> 5.25
ΔE (GeV)	in $[-0.2, 0.2]$	in $[-0.1, 0.2]$	in $[-0.1, 0.2]$
$m(\pi^0)$ (GeV)	—	in $[0.10, 0.14]$	in $[0.10, 0.14]$
$E(\pi^0)$ (GeV)	—	—	> 0.35
$m(\phi)$ (GeV)	in $[1.00, 1.05]$	in $[1.00, 1.05]$	in $[0.97, 1.04]$
$m(K^0_S)$ (GeV)	in $[0.48, 0.52]$	in $[0.44, 0.51]$	in $[0.48, 0.52]$
flLenSig(K^0_S)	> 5	—	> 5
PIDk($K^\pm$)	> 0.2	> 0.2	—
PrbVtx(ϕ)	$> 10^{-4}$	$> 10^{-4}$	$> 10^{-4}$
PrbVtx(K^0_S)	$> 10^{-4}$	—	$> 10^{-4}$
PrbVtx(B)	$> 10^{-4}$	$> 10^{-4}$	$> 10^{-4}$
	For each track coming from the ϕ decay:		
d_0 (cm)	< 0.08	< 0.08	< 0.08
z_0	< 0.3	< 0.3	< 0.3
#PXDhits	≥ 1	≥ 1	≥ 1
ε	31.1%	14.2%	17.4%
Cand. multiplicity	1.0008	1.0701	1.0470

Table 77. Δt resolution obtained with the *iptube* constraint and, when applicable, the K^0_S flight direction constraint. The value reported is the weighted average of the σs of the three Gaussians.

Channel	Δt resolution (ps)
$\phi(K^+K^-)K^0_S(\pi^+\pi^-)$	0.75
$\phi(K^+K^-)K^0_S(\pi^0\pi^0)$	0.77
$\phi(\pi^+\pi^-\pi^0)K^0_S(\pi^+\pi^-)$	0.78

Δt resolution The resolution on the proper decay time difference Δt is one of the critical aspects of time-dependent CP violation analyses. The $\phi \to K^+K^-$ decay is particularly challenging, since the $\phi \to K^+K^-$ decay is just above the kinematical threshold. The $K^\pm$ momenta are soft in the ϕ rest frame, while the ϕ boost leads to quite unfavorable angles between the kaon momenta.

From a simple geometric vertex fit to the tracks originating from the signal B decay vertex we thus expect a resolution that is much worse than for the $J/\psi \to \mu^+\mu^-$ decays. Fitting with three Gaussians, the $\Delta t_{\rm gen} - \Delta t_{\rm meas}$ distribution without any external constraint gives $\Delta t = 2.08$ ps (1.18 ps) resolution for the $\phi \to K^+K^-$ ($\phi \to \pi^+\pi^-\pi^0$) decay.

External constraints greatly improve the Δt resolution. One can apply the *iptube* constraint (see Sect. 6.2.3) and, in the case of $K^0_S \to \pi^+\pi^-$, we can also add a constraint from the K^0_S flight direction. Figure 103 shows an example of a fit to the Δt resolution, while Table 77 summarizes the best achievable resolutions for the three $B^0 \to \phi K^0_S$ channels investigated.

Continuum background The discrimination between $B\bar{B}$ and continuum events relies on variables that are sensitive to the different event topologies (spherical for $B\bar{B}$, events, jet-like for continuum). We utilize a FastBDT [70] multivariate discriminator for efficient separation between signal $B \to \phi K^0_S$ and continuum events. The algorithm takes as input 30 variables that provide at least some

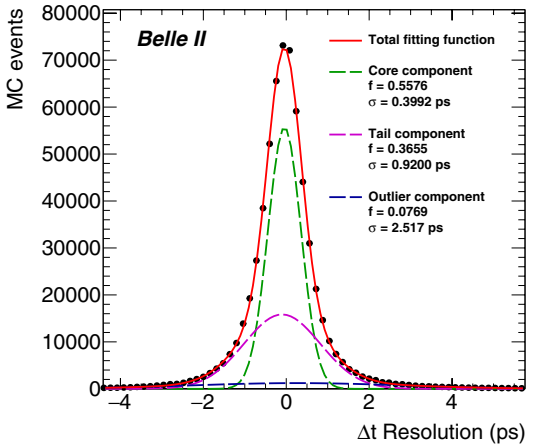

Fig. 103. Example of three-Gaussian fit on the Δt resolution. The (integral) fractions and the widths of the three Gaussian components are reported on the figure.

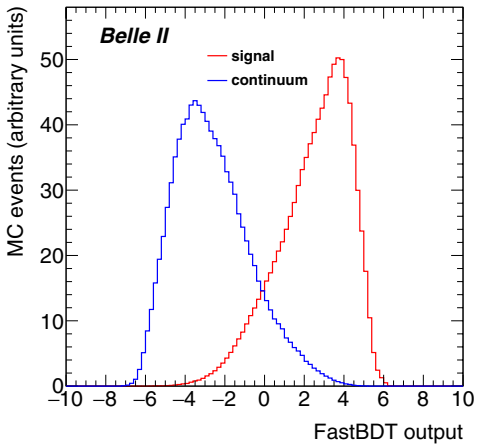

Fig. 104. Output of the FastBDT multivariate discriminator utilized for continuum suppression in the channel $\phi(K^+K^-)K^0_S(\pi^+\pi^-)$. The red (blue) histogram corresponds to the output of signal $B^0 \to \phi K^0_S$ (continuum) events.

discrimination power between the two categories. The most powerful among those are the cosine of the angle between the thrust axis of the B candidate and the thrust axis of the rest of the event, the ratio between the second and zeroth Fox–Wolfram moments, the cosine of the angle between the B candidate flight direction and the z axis, the Cleo cones, and the KSFW moments (see Sect. 6.4).

Figure 104 shows an example of the separation that is achievable with the FastBDT algorithm and the selected set of variables. Just to illustate the discrimination power of the method, by setting a cut on the output variable of the FastBDT discriminator that retains 95% of the signal events, we reject 82.7% of the continuum background in the $\phi(K^+K^-)K^0_S(\pi^+\pi^-)$ case, 85.5% in $\phi(K^+K^-)K^0_S(\pi^0\pi^0)$, and 75.9% in $\phi(\pi^+\pi^-\pi^0)K^0_S(\pi^+\pi^-)$.

In order to keep the selection efficiency as high as possible for signal events, we do not apply cuts on the output of the FastBDT discriminator, but rather use it as a variable in the maximum likelihood fit when extracting the S and A parameters.

Table 78. Number of generic $B\bar{B}$ events passing the selection (see Table 76) for the different channels. The equivalent luminosity of the generic MC sample used is 5 ab^{-1}. For comparison, the expected signal yield is also given.

Channel	B^+B^-	$B^0\bar{B}^0$	Expected signal
$\phi(K^+K^-)K^0_S(\pi^+\pi^-)$	43	97	2280
$\phi(K^+K^-)K^0_S(\pi^0\pi^0)$	39	58	765
$\phi(\pi^+\pi^-\pi^0)K^0_S(\pi^+\pi^-)$	627	1512	545

$B\bar{B}$ background A preliminary estimate of the yield of $B\bar{B}$ backgrounds is obtained by checking how many events of generic B^+B^- and $B^0\bar{B}^0$ Monte Carlo events pass the selection. For this estimate we use the full 5 ab^{-1} available at the time of writing.

Table 78 summarizes the number of generic $B\bar{B}$ background events passing the selection for different channels. The numbers are quite high for the $\phi(\pi^+\pi^-\pi^0)K^0_S(\pi^+\pi^-)$ channel, so further work is needed in order to optimize the selection and reject more background.

For the $\phi(K^+K^-)K^0_S(\pi^+\pi^-)$ channel, one of the modes that has highest probability of passing the selection is $B^0 \to \phi K^{*0}$, with $K^{*0} \to K^0_S\pi^0$ (with the π^0 not being reconstructed). For the real data analysis, further studies on this background mode will be needed in order to avoid biases on the S and A parameters.

Maximum likelihood fit In the multidimensional maximum likelihood fit, the time-independent variables are $M_{\rm bc}$, ΔE, the output of the FastBDT discriminator used for continuum suppression, $m(\phi)$, and $\cos\theta_{\rm H}$. The first three variables are very powerful in discriminating between signal and continuum background events, while the latter two mostly separate the signal from real ϕ candidates from the non-resonant K^+K^- (or $\pi^+\pi^-\pi^0$) events.

For each of the decay channels under study, we consider five components:

(1) Signal from real ϕ mesons.
(2) SXF: self cross-feed events originating from real signal events in which the reconstruction of the B signal candidate utilized one or more particles from the decay of the other B in the event.
(3) Non-resonant: events in which the selected ϕ candidate originates from non-resonant K^+K^- or $\pi^+\pi^-\pi^0$ events.
(4) Combinatorial: mostly arising from continuum background.
(5) $B\bar{B}$ background.

Estimate of sensitivity from pseudo-experiment studies To estimate the sensitivity of the analysis we performed an ensemble test with 1 ab^{-1} and 5 ab^{-1} equivalent Monte Carlo samples. For the signal, SXF, and non-resonant events, the full MC simulation is used and combinatorial and $B\bar{B}$ background events are generated by the parameters of each corresponding PDF determined by the fully simulated generic MC datasets. To study the sensitivity on the signal and background yields, we perform a scan varying the number of injected signal and background events, covering approximately one order of magnitude about the expected values. For each mode and each of the investigated signal/background hypotheses we perform 1000 pseudo-experiments.

We confirm that the fit returns unbiased results about the signal for both scalar and vector components as well as background yields. To perform the test under an extreme condition, we study the

Table 79. Sensitivity estimates for the $S_{\phi K^0}$ and $A_{\phi K^0}$ parameters for 1 ab^{-1} and 5 ab^{-1} integrated luminosity. The efficiency $\varepsilon_{\rm reco}$ used in this estimate has not been taken from the simulation, but is rather an estimate taking into account the expected improvements. Systematic uncertainties, negligible for these integrated luminosities, are not included.

Channel	$\varepsilon_{\rm reco}$	Yield	$\sigma(S_{\phi K^0})$	$\sigma(A_{\phi K^0})$
1 ab^{-1} luminosity:				
$\phi(K^+K^-)K^0_S(\pi^+\pi^-)$	35%	456	0.174	0.123
$\phi(K^+K^-)K^0_S(\pi^0\pi^0)$	25%	153	0.295	0.215
$\phi(\pi^+\pi^-\pi^0)K^0_S(\pi^+\pi^-)$	28%	109	0.338	0.252
K^0_S modes combination		400	0.135	0.098
$K^0_S + K^0_L$ modes combination			0.108	0.079
5 ab^{-1} luminosity:				
$\phi(K^+K^-)K^0_S(\pi^+\pi^-)$	35%	2280	0.078	0.055
$\phi(K^+K^-)K^0_S(\pi^0\pi^0)$	25%	765	0.132	0.096
$\phi(\pi^+\pi^-\pi^0)K^0_S(\pi^+\pi^-)$	28%	545	0.151	0.113
K^0_S modes combination		2000	0.060	0.044
$K^0_S + K^0_L$ modes combination			0.048	0.035

case with opposite values of S for the signal (+0.7) and for the non-resonant component (−0.7). We find these two components are correctly separated and the CP violation parameters obtained are consistent with inputs. We also see that the dependence of the uncertainty $\sigma(S)$ depends very mildly on the background yields, and that the dependence on the signal yield is, as expected, $1/\sqrt{N_{\rm sig}}$.

Table 79 summarizes the sensitivity estimates for the two integrated luminosity scenarios considered. We estimate the expected yield of ϕK^0_L based on previous BaBar and Belle analyses (but use the same Δt resolution we estimate in $\phi \to K^+K^-$ for Belle II).

$B_d \to \eta' K^0_S$.

Contributing authors: S. Lacaprara, A. Mordà

The $\eta' K^0$ decay channel shares many features with ϕK^0. The main differences are that the η' is a pseudoscalar particle, its decay channels are more complex, and that the branching fraction is about 10 times larger [701].

The BaBar and Belle collaborations performed CP violation analyses for this channel using $467 \cdot 10^6$ [702] and $772 \cdot 10^6$ $B\bar{B}$ pairs [703], respectively. The published results for $S_{\eta' K^0_S}$ are still dominated by statistical uncertainties: $S_{\eta' K^0_S} = +0.57 \pm 0.08 \pm 0.02$ (BaBar), $S_{\eta' K^0_S} = +0.68 \pm 0.07 \pm 0.03$ (Belle).

The η' decay chains considered for this analysis are:

(1) $\eta'(\to \eta(\to \gamma\gamma)\pi^+\pi^-) : \eta'(\eta_{\gamma\gamma}\pi^\pm)$
(2) $\eta'(\to \eta(\to \pi^+\pi^-\pi^0)\pi^+\pi^-)$: $\eta'(\eta_{3\pi}\pi^\pm)$
(3) $\eta'(\to \rho^0(\to \pi^+\pi^-)\gamma)$: $\eta'(\rho\gamma)$.

The K^0 can be a K^0_S, decaying into $K^0_S \to \pi^+\pi^-$ ($K^{(\pm)}_S$) or $\pi^0\pi^0$ ($K^{(00)}_S$), or a K^0_L. At the time of writing the sensitivity study for the channel $\rho^0\gamma$ is not yet ready, and the modes with K^0_L have not yet been studied. Among the four remaining channels we put more emphasis on the final states where the K^0_S decays into charged pions. In particular, the channel with η decaying into three π and K^0_S

Table 80. Selection requirements for the channels used in the $\eta'(\to \eta\pi^{\pm})K^0_S$ sensitivity study.

$\eta'(\eta_{\gamma\gamma}\pi^{\pm})K_S^{(\pm)}$	$\eta'(\eta_{\gamma\gamma}\pi^{\pm})K_S^{(00)}$	$\eta'(\eta_{3\pi}\pi^{\pm})K_S^{(\pm)}$	$\eta'(\eta_{3\pi}\pi^{\pm})K_S^{(00)}$
$M_{\rm bc} > 5.25\,\text{GeV}$			
$-0.2 < \Delta E < 0.2\,\text{GeV}$	$-0.15 < \Delta E < 0.2\,\text{GeV}$	$-0.15 < \Delta E < 0.15\,\text{GeV}$	$-0.15 < \Delta E < 0.25\,\text{GeV}$
$0.06 < E_\gamma < 6\,\text{GeV}$			
—		$0.1 < m_{\pi^0} < 0.15\,\text{GeV}$	
$0.52 < m_\eta < 0.57\,\text{GeV}$	$0.48 < m_\eta < 0.57\,\text{GeV}$	$0.52 < m_\eta < 0.57\,\text{GeV}$	$0.52 < m_\eta < 0.57\,\text{GeV}$
$0.93 < m_{\eta'} < 0.98\,\text{GeV}$	$0.93 < m_{\eta'} < 0.98\,\text{GeV}$	$0.93 < m_{\eta'} < 0.98\,\text{GeV}$	
$0.48 < m_{K^0_S} < 0.52\,\text{GeV}$	$0.42 < m_{K^0_S} < 0.52\,\text{GeV}$	$0.48 < m_{K^0_S} < 0.52\,\text{GeV}$	$0.40 < m_{K^0_S} < 0.52\,\text{GeV}$
For each track coming from the η' decay:			
$\Delta\log\mathcal{L}(\pi, K) > -10$			
$d_0 < 0.16\,\text{cm}$			
$z_0 < 0.2\,\text{cm}$			

into a pair of π^0 has not been used by Belle and BaBar due to the very low reconstruction efficiency on signal events and large background yields.

Signal reconstruction, backgrounds, and selection For each final state, signal candidates are found by reconstructing the whole decay chains. This is done by reconstructing all the intermediate particles, starting from the final state tracks and proceeding back up to the head of the decay (B^0 or $\bar{B}^0$).

The selection criteria listed in Table 80 are applied on each of the reconstructed particles in the decay chain. In particular, the requirements on the invariant masses of the intermediate particles efficiently reduce the number of candidates arising from random combinations of tracks and photons in the event (combinatoric backgrounds). The selection criteria are, in general, looser for channels with neutral particles decaying to a pair of photons.

Once the signal B^0 decay chain has been reconstructed, the rest of the event is fed to the flavor tagger algorithm (see Sect. 6.5) to determine the flavor of the B on the tag side.

Self cross-feed and multiple candidates Given the complex final states considered, often more than one candidate per event fulfills the selection requirements, especially for the modes with $\eta \to \pi^+\pi^-\pi^0$. For signal events, the average number of candidates per event is 1.1 and 2.7 for the $\eta'(\eta_{\gamma\gamma}\pi^{\pm})K_S^{(\pm)}$ and $\eta'(\eta_{3\pi}\pi^{\pm})K_S^{(\pm)}$ channels respectively. For channels with K^0_S decaying into a pair of π^0, preliminary studies show that the multiplicity is even higher: ∼5 and ∼30 for the final states with $\eta \to \gamma\gamma$ and $\eta \to \pi^+\pi^-\pi^0$ respectively.

Among the selected candidates there is usually the one reconstructed with the proper combination of tracks corresponding to the actual decay chain, together with others built with a wrong combination of the final state tracks. Those candidates will be referred in the following (according to the notation used in the previous section) as self cross-feed (SXF) candidates.

The increased fraction of SXF candidates compared to the previous analyses from Belle is mostly due to the higher level of background arising from the beam interactions in the higher-luminosity regime. Currently the tracking and photon reconstruction algorithms for Belle II are still under development and, once optimized, will likely end up in an increased true signal purity of the sample

Table 81. Selection efficiency ε and fraction of signal cross-feed candidates $\varepsilon_{\rm SXF}$ for the $\eta'(\eta_{\gamma\gamma}\pi^{\pm})K_S^{(\pm)}$ and $\eta'(\eta_{3\pi}\pi^{\pm})K_S^{(\pm)}$ channels when selecting only one (A), two (B), or all (C) the candidates in the event. The selected strategy is labeled with $\star$.

Channel	Strategy	ε [%]	$\varepsilon_{\rm SXF}$ [%]
$\eta'(\eta_{\gamma\gamma}\pi^{\pm})K_S^{(\pm)}$	C$\star$	23.0	3.8
$\eta'(\eta_{3\pi}\pi^{\pm})K_S^{(\pm)}$	A	6.7	2.6
	B$\star$	8.0	6.0
	C	9.5	28.6

of selected candidates; in the meanwhile, a novel strategy has been designed to deal with the larger fraction of SXF candidates.

In order to discriminate the true signal against the cross-feed-selected candidates, a multivariate BDT algorithm [239] has been trained using kinematic and geometrical variables. These include invariant masses of intermediate particles, vertex χ^2, impact parameters of the pion tracks, and the variables describing the photons reconstructed by the ECL. The BDT output variable, $BDT_{\rm SXF}$ henceforth, is used as an additional input to the final fit. Indeed, it provides good separation between the true and cross-feed-selected signal candidates, and it also improves the discrimination of background events (described in the next subsection) which behave like the cross-feed ones. The respective distributions are shown in Fig. 105 for the $\eta(3\pi)$ channel.

Selected candidates are ranked according to the value of the $BDT_{\rm SXF}$, and the following three strategies have been explored in order to deal with multiple candidates:

- Strategy A: For each event keep only the candidate with the highest $BDT_{\rm SXF}$ value.
- Strategy B: For each event keep only the two candidates with the highest $BDT_{\rm SXF}$ values.
- Strategy C: Keep all the candidates in each event.

The advantage of strategy A is that it leads to only one candidate per event. The cost is the reduced signal efficiency. The other two strategies give higher signal efficiencies, but also increase the number of cross-feed candidates. These can still be separated in the maximum likelihood fit that uses $BDT_{\rm SXF}$. Strategy B uses just two candidates, because in most cases the signal has the highest or second highest $BDT_{\rm SXF}$. Including the third candidate does not increase the signal efficiency significantly.

For the $\eta'(\eta_{\gamma\gamma}\pi^{\pm})K_S^{(\pm)}$ final state the candidate multiplicity is very close to 1 and the three strategies are almost equivalent. Strategy C was chosen in order to keep the signal efficiency as high as possible. For $\eta'(\eta_{3\pi}\pi^{\pm})K_S^{(\pm)}$, strategy B has been adopted instead since it allows for good signal efficiency while keeping the fraction of cross-feed events at a reasonable level; see Table 81. The goodness of such a choice has also been checked quantitatively by computing (through ensemble tests) the expected statistical uncertainty and the bias on the S_f parameters for each of the abovementioned scenarios: strategy B has been found to give the smallest statistical uncertainty while keeping a negligible bias.

Despite the improvement in the K_S^0 reconstruction, the computed signal efficiencies of the modes with $K_S^0 \to \pi^+\pi^-$ decays are comparable with those achieved by Belle and BaBar; this is likely due to the low reconstruction efficiency of the intermediate η and π^0 decaying into photons. Preliminary studies on modes with $K_S^0 \to \pi^0\pi^0$ decays show a significantly lower efficiency with respect to those estimated for the channels with K_S^0 decaying into charged pions. The reconstruction efficiencies

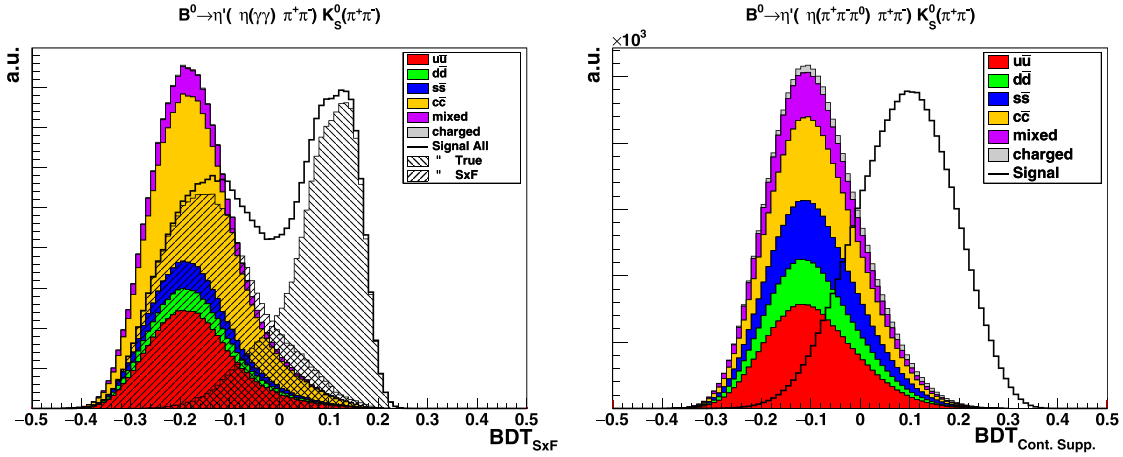

Fig. 105. Left: Distribution of the $BDT_{\rm SXF}$ variable for true signal events, self cross-feed candidates, and background events for the $\eta'(\eta_{\gamma\gamma}\pi^{\pm})K_S^{(\pm)}$ channel. Right: Output of the BDT multivariate discriminator used for continuum suppression in the channel $\eta'(\eta_{3\pi}\pi^{\pm})K_S^0(\pi^{\pm})$ ("signal" distribution accounts for both the true and the SXF signal candidates).

for modes with η and π^0 intermediate states are expected to improve with better reconstruction algorithms.

Background suppression Background candidates originate from two sources: random combinations of particles from continuum events, and from actual $B\bar{B}$ events (peaking).

Among the two sources of background, the former is relatively easy to model by looking at sidebands of $M_{\rm bc}$ and ΔE in the data, whose selection requirements are kept rather loose. At present the expected yields of this contribution are estimated from a large MC production (0.7 ab^{-1}). As for ϕK_S^0, the best discrimination between the continuum background and the signal is achieved by a multivariate algorithm sensitive to the event topology (spherical for $B\bar{B}$ events, jet-like for continuum). For this analysis we used a BDT algorithm, using the same set of variables presented for the ϕK^0. These variables are explained in detail in Sect. 6.4. The output distribution of the BDT algorithm is shown in Fig. 105 for the $\eta(\gamma\gamma)K_S^0(\pi^{\pm})$ channel.

This variable allows good separation between background and signal, e.g. it is possible to retain 95% of the signal and remove 50% of the background, or reject 97.5% of the background with a relative signal efficiency of 50%. Given the relative ease with which one can tell apart signal and continuum background events using $M_{\rm bc}$, ΔE, and the BDT, an even better strategy is to include the BDT as a discriminating variable in the multidimensional maximum likelihood fit.

The peaking background from $B\bar{B}$ events was estimated from Monte Carlo simulation by analysing a data sample corresponding to $\sim$0.7 ab^{-1}.

Table 82 summarizes the amount of continuum and peaking background for different channels, for an integrated luminosity of 1 ab^{-1}. In general, the peaking background is much smaller than the continuum, and the continuum mostly comes from $c\bar{c}$ events and $u\bar{u}$ for the $\eta \to 2\gamma$ channel.

Δt resolution The signal vertex precision ultimately determines the resolution on the proper time difference Δt. In the case of the decay $\eta' \to \eta(2\gamma)\pi^+\pi^-$ only the two charged pions can be used to build the B decay vertex, whereas for decay $\eta' \to \eta(3\pi)\pi^+\pi^-$, two additional charged pions are present and are used for vertex reconstruction. The decay topology is thus more favorable than the

Table 82. Expected yields of continuum and peaking ($B\bar{B}$) events passing the selection for the different channels. The equivalent luminosity of the generic MC sample used is 1 ab^{-1}. The continuum background yield is before any cut on the continuum suppression variable.

Channel	Continuum	$B^0\bar{B}^0$	B^+B^-
$\eta'(\eta_{\gamma\gamma}\pi^\pm)K_S^{(\pm)}$	16 413	1834	57
$\eta'(\eta_{3\pi}\pi^\pm)K_S^{(\pm)}$	4508	304	13

Table 83. The Δt resolution for true, SXF, and all selected candidates for $\eta'(\eta_{\gamma\gamma}\pi^\pm)K_S^{(\pm)}$ and $\eta'(\eta_{3\pi}\pi^\pm)K_S^{(\pm)}$ channels (obtained by fitting the B^0 signal vertex with the *iptube* constraint and the information on the K_S^0 flight direction).

Channel	True [ps]	SXF [ps]	All [ps]
$\eta'(\eta_{\gamma\gamma}\pi^\pm)K_S^{(\pm)}$	1.22	2.87	1.45
$\eta'(\eta_{3\pi}\pi^\pm)K_S^{(\pm)}$	1.17	2.36	1.50

$\phi \to K^+K^-$ case described before, but not as good as the golden $J/\psi \to \mu^+\mu^-$ one, given the invariant mass of the parent particle η'.

The resolution on Δt is estimated as for the ϕK^0 analysis, with a three-Gaussian fit to the Δt–$\Delta t_{\rm true}$ distribution, expressing the resolution as the weighted average of the σ of each component. As for the case of ϕK^0, the vertex resolution can be improved by using the *iptube* constraint (see Sect. 6.2.3), as well as using the K_S^0 flight direction, for the $K_S^0 \to \pi^+\pi^-$ decays. Without beam background, the resolution for the $\eta \to \gamma\gamma$ final state decreases from 1.89 ps without any constraints to 1.62 ps including the constraints of K_S^0, and to 0.91 ps by adding the *iptube* constraint. In this last case the resolutions of the three Gaussian components of the time resolution models are 0.49 ps, 1.14 ps, and 2.97 ps, each of them accounting respectively for 56.5%, 36.2%, and 7.3% of the full model. Similarly, the Δt resolution for the channel with $\eta \to \pi^+\pi^-\pi^0$ improves from 1.25 ps to 0.88 ps with *iptube* and K_S^0 flight direction information (in this case the resolutions of the three Gaussians are 0.45 ps, 1.07 ps, and 2.88 ps respectively, with weights 56.5%, 34.2%, and 9.3%). For both channels the larger improvement comes from the *iptube* constraint, while that due to the K_S^0 direction is marginal.

Beam background causes a degradation of the Δt resolution for signal events, plus tails due to the larger fraction of cross-feed candidates. The values of the Δt resolution for the true, cross-feed, and all candidates for channels $\eta(\gamma\gamma)K_S^0(\pi^\pm)$ and $\eta(\to \pi^+\pi^-\pi^0)K_S^0(\pi^\pm)$ are reported in Table 83.

Estimate of sensitivity from ensemble test studies To estimate the statistical uncertainties expected from this analysis, we performed a set of ensemble test studies. As input parameters we used $S_{\eta' K_S^0} = 0.7$ and $A_{\eta' K_S^0} = 0$. Using MC we performed a multivariate maximum likelihood fit and extracted the PDF for the various distributions. For the time-independent part we used $M_{\rm bc}$, ΔE, the cross-feed discriminating BDT variable, and the continuum suppression BDT variables, both described above. The generated ensemble MC datasets, including signal, self cross-feed, continuum background, and peaking background, correspond to integrated luminosities of 1 and 5 ab^{-1}. The signal, as well as the signal cross-feed, were obtained by extracting a random sub-sample from the

Table 84. The estimated resolutions (statistical uncertainties only) from ensemble test studies for CP-violating S_f and A_f parameters for integrated luminosities of 1 and 5 ab^{-1} for different channels.

	1 ab^{-1}			5 ab^{-1}		
Channel	Yield	$\sigma(S_f)$	$\sigma(A_f)$	Yield	$\sigma(S_f)$	$\sigma(A_f)$
$\eta'(\eta_{\gamma\gamma}\pi^{\pm})K_S^{(\pm)}$	969	0.13	0.08	4840	0.06	0.04
$\eta'(\eta_{\gamma\gamma}\pi^{\pm})K_S^{(00)}$	215	0.27	0.17	1070	0.12	0.09
$\eta'(\eta_{3\pi}\pi^{\pm})K_S^{(\pm)}$	283	0.25	0.16	1415	0.11	0.08
$\eta'(\rho\gamma)K_S^{(\pm)}$	2100	0.09	0.05	10 500	0.04	0.03
$\eta'(\rho\gamma)K_S^{(00)}$	320	0.22	0.14	1600	0.10	0.07
K_S^0 modes	3891	0.065	0.040	19 500	0.028	0.021
K_L^0 modes	1546	0.17	0.11	7730	0.08	0.05
$K_S^0 + K_L^0$ modes	5437	0.060	0.038	27 200	0.027	0.020

full signal MC dataset. Both the background samples were instead randomly generated from the PDF fitted from the full sample.

The expected statistical uncertainties for the extracted $S_{\eta' K_S^0}$ and $A_{\eta' K_S^0}$ are summarized in Table 84. A comparison with BaBar and Belle published results shows that these preliminary results are comparable for similar integrated luminosities.

No significant bias is observed for $S_{\eta' K_S^0}$, while a non-negligible bias arises in the estimation of $A_{\eta' K_S^0}$, which is likely due to a correlation between the BDT_{SXF} and continuum suppression BDT variables. Such an effect can be mitigated by further optimizing the sets of input variables of each of the two classifiers, in order to reduce the correlation; another solution consists in taking into account such a correlation by implementing it in the likelihood fit model.

Table 84 also shows the channel $\eta'(\eta_{\gamma\gamma}\pi^{\pm})K_S^{(00)}$. The efficiency found in this sensitivity study is a factor of two lower, suffering from the poor π^0 reconstruction currently available. Improvements are expected before data-taking, so we used instead an efficiency taken from a similar study performed at Belle. The sensitivity for the decay channel with $\eta'(\rho\gamma)K_S^{(00)}$ has been estimated using the expected yield, based on the Belle efficiency, and with the resolution found in the analysis for the $\eta'(\eta_{\gamma\gamma}\pi^{\pm})K_S^{(\pm)}$ channel. The K_L^0 modes have not yet been analyzed, so the values in Table 84 are obtained by extrapolation of the Belle measurement to the Belle II expected luminosity.

Systematic uncertainties A precise determination of the systematic uncertainties is not available at the time of writing, so we estimate them following the guidelines described in Sect. 10.2.1. The current measurement by Belle [703] reports contributions of several sources of systematic uncertainty. Some are irreducible, such as vertex reconstruction (± 0.014) and tag-side interference (± 0.001), and some are reducible, like Δt resolution, signal fraction, background Δt PDF, flavor tagging, fit bias (accounting, summed in quadrature, to ± 0.038). We can assume that the reducible systematics will scale with the luminosity, since they are evaluated via control samples and Monte Carlo simulated events. As in the $J/\psi K^0$ channel, the vertex-related systematics are expected to be reduced by a factor of two thanks to the new pixel vertex detector and improved tracking and alignment algorithms (see Sect. 10.2.2). As a conservative scenario we also consider the case when the vertex-related systematics do not change.

Table 85. Estimated systematic uncertainties on S_f for $B^0 \to \eta' K^0$ decay for two different luminosities and with two different hypotheses concerning the vertex-related uncertainties: conservative and optimistic (in parentheses).

Luminosity (ab^{-1})	Stat. (10^{-2})	Syst. (10^{-2})	Total (10^{-2})
5	2.7	2.1 (1.7)	3.4 (3.2)
50	0.85	1.8 (1.3)	2.0 (1.5)

Table 86. Extrapolated sensitivity for the ωK^0_S mode. The Δt resolution is taken from the $\eta' K^0_S$ study, while we assume a reconstruction efficiency of 21%.

$\omega(\pi^+\pi^-\pi^0)K^0_S(\pi^\pm)$			
Luminosity	Yield	$\sigma(S)$	$\sigma(A)$
$1\,ab^{-1}$	334	0.17	0.14
$5\,ab^{-1}$	1670	0.08	0.06
$50\,ab^{-1}$	16 700	0.024	0.020

The expected systematic uncertainties are summarized in Table 85 for two luminosities (5 and $50\,ab^{-1}$) and two scenarios: conservative, without scaling down the vertex-related systematic, and optimistic, including that rescaling.

The measurement of S with this channel will be affected by a systematic uncertainty similar to the statistical one at an integrated luminosity of $L = 10\ (20)\,ab^{-1}$ in the conservative (optimistic) scenario.

Extrapolation of the ωK^0_S sensitivity Given the similarity of the decay channels of $\eta' \to \eta\pi^+\pi^-$ and $\omega \to \pi^0\pi^+\pi^-$, we extrapolate the Belle II sensitivity to the time-dependent CP violation parameters on $B^0 \to \omega K^0_S$. We assume the Δt resolution to be the same for these two modes. We thus rescale the uncertainties on S_f and A_f from the $\eta(2\gamma)K^0_S(\pi^\pm)$ channel by the expected ωK^0_S yields. For these we use a reconstruction efficiency of 21%, which is derived from the efficiency quoted in the latest BaBar paper [702], rescaled by the ratio of Belle II and BaBar efficiencies for the $\eta' K^0$ channel. The results are collected in Table 86.

10.4. Determination of ϕ_2

10.4.1. Theory: ϕ_2 from $B \to \pi\pi$, $B \to \rho\rho$, and $B \to \rho\pi$

Contributing authors: Y. Grossman, M. Gronau

The theoretically most precise way of determining the phase ϕ_2 is based on applying isospin symmetry to $B \to \pi\pi, \rho\rho$ decays [704]. The decays $B^+ \to \pi^+\pi^0$, $B^0 \to \pi^+\pi^-$, $B^0 \to \pi^0\pi^0$, including their charge conjugates, and corresponding B decays involving longitudinally polarized ρ mesons, ρ_L, provide sufficient information to determine ϕ_2. A complete study of these processes resolves discrete ambiguities in ϕ_2. The discrete ambiguities are also resolved by a more complex study of $B \to \rho\pi$ that involves non-identical final state particles [705]. We describe the current status of the isospin method for determining ϕ_2 in $B \to \pi\pi$ and $B \to \rho_L\rho_L$, pointing out its sensitivity to specific measurements and the potential of improving the precision at Belle II. This discussion largely follows the very recent study in Ref. [706], where further details can be found.

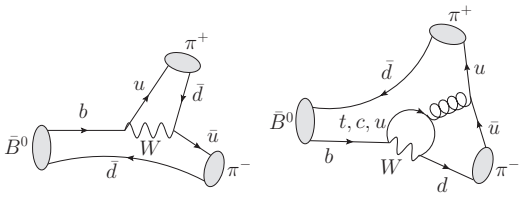

Fig. 106. Sample diagrams for the T (left) and P (right) amplitudes in Eq. (313) for the $\bar{B}^0 \to \pi^+\pi^-$ decay.

Determination of ϕ_2 from $B \to \pi\pi$ and $B \to \rho\rho$ Using the unitarity of the CKM matrix one can write in full generality for the decay amplitude (an equal formalism applies to $B \to \rho_L\rho_L$):

$$\mathcal{A}_{+-} \equiv \mathcal{A}(B^0 \to \pi^+\pi^-) = |T_{+-}|e^{i\phi_3} + |P_{+-}|e^{i\delta}, \tag{313}$$

where $|T|$ is the magnitude of the tree amplitude with weak phase ϕ_3, while P is the magnitude of the penguin amplitude with strong phase δ (see Fig. 106). The tree amplitude for $b \to u\bar{u}d$ transitions carries isospin 1/2 and 3/2, while the $b \to d$ penguin amplitude carries only isospin 1/2. The spinless two-pion state can only have isospin 0 and 2, so that the $B \to \pi\pi$ amplitudes, denoted by the pion charges, obey the relation

$$\mathcal{A}_{+-}/\sqrt{2} + \mathcal{A}_{00} = \mathcal{A}_{+0}. \tag{314}$$

The $\Delta I = 3/2$ amplitude $\mathcal{A}_{+0}$ has no penguin contribution and thus has the weak phase ϕ_3, while $\bar{\mathcal{A}}_{-0}$ has weak phase $-\phi_3$. Defining $\tilde{\mathcal{A}} \equiv e^{2i\phi_3}\bar{\mathcal{A}}$, we have

$$\tilde{\mathcal{A}}_{+-}/\sqrt{2} + \tilde{\mathcal{A}}_{00} = \tilde{\mathcal{A}}_{-0}, \tag{315}$$

where the two triangles in Eqs. (314) and (315) have a common base, $\mathcal{A}_{+0} = \tilde{\mathcal{A}}_{-0}$. The sides of these two triangles are determined by decay rates and direct asymmetries. This fixes two angles, $\theta_{+-} = \arg(\mathcal{A}_{+-}/\mathcal{A}_{+0})$ and $\theta_{00} \equiv \arg(\mathcal{A}_{00}/\mathcal{A}_{+0})$ for B decays, and $\tilde{\theta}_{+-} = \arg(\tilde{\mathcal{A}}_{+-}/\tilde{\mathcal{A}}_{-0})$ and $\tilde{\theta}_{00} \equiv \arg(\tilde{\mathcal{A}}_{00}/\tilde{\mathcal{A}}_{-0})$ for $\bar{B}$ decays. The two differences between these pairs of angles, $\Delta\theta_{+-} = \tilde{\theta}_{+-} - \theta_{+-}$, $\Delta\theta_{00} \equiv \tilde{\theta}_{00} - \theta_{00}$, then determine ϕ_2 via the relations

$$\begin{aligned} \sin(2\phi_2 + \Delta\theta_{+-}) &= \frac{S_{+-}}{\sqrt{1-(A_{+-})^2}}, \\ \sin(2\phi_2 + \Delta\theta_{00}) &= \frac{S_{00}}{\sqrt{1-(A_{00})^2}}. \end{aligned} \tag{316}$$

A discrete ambiguity in $\Delta\theta_{+-}$ and $\Delta\theta_{00}$ may remain due to the possibility of flipping either triangle about its base.

The above determination of ϕ_2 receives corrections from isospin breaking, either due to electroweak penguins or due to mass difference of up and down quarks and their electric charges. We discuss the induced errors below.

Determination of ϕ_2 from $B \to \rho\pi$ There is a major difference between ϕ_2 determination from $B \to \rho\pi$ and from $B \to \pi\pi$ and $B \to \rho\rho$. From the overlaps of the resonances in the Dalitz plot of the time-dependent decay $B \to \rho\pi \to \pi^+\pi^-\pi^0$ one can now determine both the magnitudes and relative phases of the decay amplitudes $\mathcal{A}_{ij} \equiv \mathcal{A}(B^0 \to \rho^i\pi^j)$, $i,j = +,-,0$, as well as their

CP conjugate counterparts. For instance, the time-dependent decay rate for the initial B^0 is given by [705,707,708]

$$\Gamma(B^0 \to \pi^+\pi^0\pi^0(t)) \propto (|\mathcal{A}_{+-0}|^2 + |\bar{\mathcal{A}}_{-+0}|^2) + (|\mathcal{A}_{+-0}|2 - |\bar{\mathcal{A}}_{-+0}|^2)\cos(\Delta mt) - 2\mathrm{Im}(e^{-2i\phi_1}\bar{\mathcal{A}}_{-+0}\mathcal{A}^*_{+-0})\sin(\Delta mt), \quad (317)$$

where we shortened $\mathcal{A}_{+-0} \equiv \mathcal{A}(B^0 \to \pi^+\pi^-\pi^0)$, $\bar{\mathcal{A}}_{+-0} \equiv A(\bar{B}^0 \to \pi^+\pi^-\pi^0)$. Each of these decay amplitudes to the three-body final state is a sum of the quasi-two-body decay amplitudes, $\mathcal{A}_{ij}$, that overlap in the corners of the Dalitz plot.

For $B \to \rho\pi$ decays it is convenient to split the amplitudes into the tree and penguin amplitudes according to the so-called "t-convention" (see, e.g., Ref. [708]),

$$e^{i\phi_1}\mathcal{A}_a = e^{-i\phi_2}\mathcal{T}_a + \mathcal{P}_a,$$
$$e^{-i\phi_1}\bar{\mathcal{A}}_a = e^{i\phi_2}\mathcal{T}_a + \mathcal{P}_a, \quad (318)$$

where $a = +-, -+, 00$. The relative phases between the two amplitudes on the left-hand side are directly measured from the coefficient of $\sin(\Delta mt)$ in Eq. (317). Note that $\mathcal{T}_{\pm,0}$ and $\mathcal{P}_{\pm,0}$ also contain the strong phases. There are thus 11 observables: 6 magnitudes and 5 relative phases between decay amplitudes. These are described by 12 unknown parameters: the weak phase ϕ_2, 6 magnitudes of tree and penguin amplitudes, and 5 relative strong phases between these amplitudes. A complex isospin relation [705,707]

$$\mathcal{P}_{-+} + \mathcal{P}_{+-} + 2\mathcal{P}_{00} = 0 \quad (319)$$

reduces the number of unknowns by two, leading to an over-constrained system. Unlike in $B \to \pi\pi$ and $B \to \rho\rho$, here the isospin was used only to relate the penguin amplitudes. Since these are smaller than the tree amplitudes, the error induced by isospin breaking is expected to be smaller as a result [709].

Current status of $B \to \pi\pi$ Current $B \to \pi\pi$ measurements are summarized in Table 2 of Ref. [706] and include the six variables $\mathcal{B}^{+0}_{\rm av}$, $\mathcal{B}^{+-}_{\rm av}$, $\mathcal{B}^{00}_{\rm av}$, A_{+-}, A_{00}, and S_{+-}, where the subscript "av" denotes an average for the process and its CP conjugate. Values of $\mathcal{B}^{00}_{\rm av}$ and A_{00} in the table are based on preliminary Belle measurements [710] averaged with those measured by BaBar [711]. Final Belle results for $\mathcal{B}^{00}_{\rm av}$ and A_{00} have recently been published in Ref. [712]. Solutions for ϕ_2 were obtained in Ref. [706] using a Monte Carlo program generating the above six observables assuming they obey Gaussian distributions and calculating corresponding values for χ^2. A minimum value $\chi^2_{\rm min} = 0.338$ occurs at four values of ϕ_2, $\phi_2 = 95°, 128.9°, 141.1°, 175°$. $\Delta\chi^2 \equiv \chi^2 - \chi^2_{\rm min} \leq 1$ is satisfied for ϕ_2 in the range $[87°, 104°], [120°, 150°], [166°, 183°]$, in agreement with ranges found by the CKMfitter Collaboration [657]. The error on ϕ_2 scales roughly as the error on *all* six variables, while reducing the error on any individual variable does not significantly affect the error on ϕ_2.

Future measurements of S_{00} at Belle II using external photon conversion [713] will distinguish solutions near $\phi_2 = 129°$ and 141°, yielding $S_{00} \approx -0.70$ for the $\chi^2_{\rm min}$ solution, from those near 95° and 175°, yielding $S_{00} \approx 0.67$.

Current status of $B \to \rho_{\rm L}\rho_{\rm L}$ In order to perform a similar analysis for $B \to \rho_{\rm L}\rho_{\rm L}$ one uses branching ratios multiplied by fractions $f_{\rm L}$ for decays leading to longitudinal ρ polarization. In

Table 87. Inputs to the determination of ϕ_2 from an isospin analysis of $B \to \rho\rho$. Branching fractions are multiplied by longitudinal ρ polarization fractions [88,230].

Quantity	Value ($\times 10^{-6}$)	Quantity	Value
$f_L\mathcal{B}_{av}(B^+ \to \rho^+\rho^0)$	21.18 ± 1.71^a	A_{+-}	0.00 ± 0.09
$f_L\mathcal{B}_{av}(B^0 \to \rho^+\rho^-)$	27.42 ± 1.95	A_{00}	0.20 ± 0.85
$f_L\mathcal{B}_{av}(B^0 \to \rho^0\rho^0)$	0.67 ± 0.12^b	S_{+-}	-0.14 ± 0.13
		S_{00}	0.3 ± 0.73

[a]Branching ratio corrected by factor $\tau(B^0)/\tau(B^+) = 0.929$ [88].
[b]Averaged values of branching ratio and longitudinal fraction also using Ref. [714].

addition to these three branching fractions and corresponding CP asymmetries, A_{+-}, A_{00}, S_{+-}, the BaBar collaboration has also measured S_{00} [715]. The seven averaged measured observables are listed in Table 87. The value of ϕ_2 corresponding to $\Delta\chi^2 \leq 1$ is now $(92.0^{+4.7}_{-5.0})^\circ$. Since the B and $\bar{B}$ isospin triangles are exactly flat for the solution of $\chi^2_{\rm min} = 0.202$, there exists merely a single second solution near $\phi_2 = 180^\circ$ which is ruled out by the measurement of ϕ_1, assuming the unitarity of the CKM matrix. The precision in ϕ_2 may be improved by reducing errors on $f_L\mathcal{B}_{av}(B^0 \to \rho^+\rho^-)$ and $f_L\mathcal{B}_{av}(B^+ \to \rho^+\rho^0)$, for which the Belle analysis [716] was based on only about 10% of its $\Upsilon(4S)$ sample, and in particular by improving the current rather crude measurement of S_{00}. A data sample of 10^{10} $B\bar{B}$ pairs can reduce all current errors by at least a factor of two, for which one finds $\Delta\chi^2 \leq 1$ for $\phi_2 = (92.0 \pm 2.5)^\circ$.

Current status of $B \to \rho\pi$ Both BaBar [717] and Belle [718] performed time-dependent Dalitz plot analyses of $B \to \rho\pi \to \pi^+\pi^-\pi^0$ decays. The results of these analyses are the 27 coefficients multiplying the bilinears of quasi-two-body $\rho\pi$ decay form factors. These coefficients are directly related to the magnitudes and relative phases of the quasi-two-body $B \to \rho\pi$ decay amplitudes. In addition to the isospin relation in Eq. (319), the experiments also include the information from $B^+ \to \rho^+\pi^0, \rho^0\pi^+$ decays using an isospin pentagon relation [719] between the decay amplitudes.

From this, Belle [718] obtained the constraint $68^\circ < \phi_2 < 95^\circ$ at 68.3% CL for the ϕ_2 solution, consistent with the SM. BaBar [717] did not attach a CL interval to the scan of ϕ_2 that they presented, since their study indicated that the scan itself was not yet statistically robust.

Electroweak penguin corrections Higher-order electroweak penguin (EWP) operators contribute to $B \to \pi\pi$ and $B \to \rho\rho$. Neglecting EWP operators multiplied by tiny Wilson coefficients (C_7, C_8), isospin symmetry relates dominant EWP operators to the $\Delta I = 3/2$ current–current operator in the effective Hamiltonian [720]. Hadronic matrix elements of the latter operator form the bases of the isospin triangles for $B \to \pi\pi$ and $B \to \rho_L\rho_L$. Consequently, the bases for B and $\bar{B}$ form a small calculable relative angle [695,721],

$$\arg(\tilde{\mathcal{A}}_{-0}\mathcal{A}^*_{+0}) = -3\left(\frac{C_9(m_b) + C_{10}(m_b)}{C_1(m_b) + C_2(m_b)}\right)\frac{|V_{tb}V_{td}|}{|V_{ub}V_{ud}|}\sin\phi_2 \tag{320}$$

$$= 3.42\,\alpha(m_W)\,\frac{\sin(\phi_1+\phi_2)\sin\phi_2}{\sin\phi_1}. \tag{321}$$

Using $\alpha(m_W) = 1/129$, $\phi_1 = 22.6^\circ$ [91], and $\phi_2 \approx 90^\circ$, obtained from $B \to \rho_L\rho_L$, one calculates a small negative shift in ϕ_2 due to EWP corrections, $\Delta\phi_2(\text{EWP}) = -\frac{1}{2}\arg(\tilde{\mathcal{A}}_{-0}\mathcal{A}^*_{+0}) = -1.8^\circ$. A shift of a similar size applies to ϕ_2 determined from $B \to \rho\pi$ [709].

Other isospin-breaking effects Not all isospin-breaking effects on ϕ_2 can be included at present. We can judge the expected size of the bias in ϕ_2 through the isospin-breaking effects that we can estimate. One example is π^0–η–η' mixing, which introduces isospin breaking in $B \to \pi\pi$ through an additional $I = 1$ amplitude, while isospin-conserving terms obey the triangle relation in Eq. (314) [709,722]. We follow the discussion in Ref. [709], updating bounds on B decays involving η and η'. Mixing of π^0, η, and η' adds a small isospin singlet component to the dominantly isotriplet neutral pion state, $|\pi^0\rangle = |\pi_3\rangle + \epsilon|\eta\rangle + \epsilon'|\eta'\rangle$, where $\epsilon = 0.017 \pm 0.003$, $\epsilon' = 0.004 \pm 0.001$ [723]. Applying flavor SU(3) to B decays into pairs of non-strange pseudoscalar mesons [724] (thereby keeping an uncertainty at the level of 30% in isospin-breaking terms), one reaches two conclusions:

(1) The isospin relation in Eq. (314) becomes $\mathcal{A}_{+-}/\sqrt{2} + \mathcal{A}_{00} = \mathcal{A}_{+0}(1 - \epsilon_0)$, where $\epsilon_0 = \sqrt{2/3}\,\epsilon + \sqrt{1/3}\,\epsilon' = 0.016 \pm 0.003$. This affects very slightly the current range in ϕ_2, becoming $(94.5^{+9.2}_{-8.5})^\circ$ instead of $(95^{+9}_{-8})^\circ$.
(2) The amplitude $\mathcal{A}_{+0}$ can be written in terms of the pure $\Delta I = 3/2$ amplitude $\mathcal{A}_{+3}$ carrying a weak phase ϕ_3, corrected by isospin-breaking terms involving $\mathcal{A}_{0\eta}$ and $\mathcal{A}_{0\eta'}$, $\mathcal{A}_{+0} = (1 + \epsilon_0)\mathcal{A}_{+3} + \sqrt{2}\,\epsilon\mathcal{A}_{0\eta} + \sqrt{2}\,\epsilon'\mathcal{A}_{0\eta'}$. This can be shown to imply an upper bound on the correction to ϕ_2 [709]: $|\Delta\phi_2| \leq \sqrt{2\tau(B^+)/\tau(B^0)}(\epsilon\sqrt{\mathcal{B}_{0\eta}/\mathcal{B}_{+0}} + \epsilon'\sqrt{\mathcal{B}_{0\eta'}/\mathcal{B}_{+0}})$. Using the above values of ϵ and ϵ', and updated branching ratios [88], we find $|\Delta\phi_2| < 1.2^\circ$.

The shift in ϕ_2 from this effect is expected to be much smaller for $B \to \rho\pi$. The reason is that, unlike for $B \to \pi\pi$ and $B \to \rho\rho$, here the isospin relations are used only to relate the penguin contributions. Thus the ϕ_2 determination from $B \to \rho\pi$ are not affected by the isospin breaking in tree amplitudes, but only in penguin amplitudes. Since penguin amplitudes are sub-leading to tree amplitudes, the isospin-breaking effects on ϕ_2 extraction are expected to be suppressed [709].

Another two effects that we can analyze are due to the finite ρ width and the ρ–ω mixing on ϕ_2 extraction from $B \to \rho_L\rho_L$. Amplitudes for $B \to \rho\rho$ depend on dipion invariant masses, $m_{12}^2 \equiv (p_{\pi_1} + p_{\pi_2})^2$, $m_{34}^2 \equiv (p_{\pi_3} + p_{\pi_4})^2$, for the two pion pairs forming ρ mesons. The isospin method assumes equal ρ masses, $m_{12} = m_{34}$, leading to the absence of an $I = 1$ final state for the two identical bosons. Choosing the two invariant masses to lie in a common mass range around the ρ peak, e.g. $400\,\mathrm{MeV}/c^2 < m_{12}, m_{34} < 1150\,\mathrm{MeV}/c^2$ [725], introduces an $I = 1$ amplitude for unequal masses [726]. The $I = 1$ amplitude, which is antisymmetric in $m_{12} \leftrightarrow m_{34}$, does not interfere in the decay rate with the symmetric $I = 0, 2$ amplitudes. Its contribution is expected to be of order $(\Gamma_\rho/m_\rho)^2$. Furthermore, isospin breaking leads to ρ^0–ω mixing of the order of a few percent. Its effect is to form a prominent peak at the ω mass followed by a sharp dip [709]. These effects have to be studied and resolved experimentally by a judicious choice of ranges for the two dipion masses.

There are isospin effects that have not been captured in the above estimates. For instance, the reduced matrix elements of operators in the effective Hamiltonian between initial B^0 and B^+ states and final states involving π^3, π^+ were assumed to obey exact SU(2) relations. Furthermore, the $\Delta I = 5/2$ corrections were assumed to vanish. Further information could be gained from QCDF/SCET calculations, if the relevant isospin breaking in light cone distribution amplitudes is available from the lattice [709].

Formally going beyond leading order So far we have discussed isospin breaking and ways to overcome and estimate it. Here we remark that in principle there are observables where the

theoretical error is only of second order in isospin breaking and thus below the permille level. It may be impossible to measure them to the required level of accuracy, and thus these ideas are challenging experimentally. Nevertheless, they may point to a way forward in tests for the presence of NP.

The main point is the following. The $B \to n\pi$ amplitudes have a sum rule that holds to $n-2$ level in isospin breaking. The proof of this statement is based on the following facts:

(1) There are $n+1$ different decay modes in $B \to n\pi$. In terms of isospin these $n+1$ amplitudes have ΔI equal to

$$\frac{1}{2},\ \frac{3}{2},\ \cdots,\ \frac{2n+1}{2}. \tag{322}$$

(2) To leading order the weak Hamiltonian has only $\Delta I = 1/2,\ 3/2$.
(3) Isospin-breaking effects are always $\Delta I = 1$.

Thus, in order to generate non-zero $(2n+1)/2$ amplitudes, $n-1$ spurion insertions are needed. That is, the isospin sum rules are completely broken at the $n-1$ level.

This is a known result in $B \to \pi\pi$ where the sum rule is broken at first order in isospin breaking. The non-trivial result is that with three pions we have a sum rule that is broken only at the second order in isospin breaking.

Having a sum rule that is broken only by second-order effects does not guarantee that we can get ϕ_2 to the same accuracy. It is thus quite non-trivial that one can indeed determine ϕ_2 from $B \to \pi\pi\pi$ even when including the first-order isospin breaking. The problem is that the method requires measuring the time-dependent CP asymmetry in $B \to \pi^0\pi^0\pi^0$ to an accuracy of less than 1%. Such a measurement is very unlikely to be done at Belle II.

10.4.2. Experiment: Sensitivity study of the branching fraction and CP violation parameters in $B^0 \to \pi^0\pi^0$ and the expected ϕ_2 sensitivity from $B \to \pi\pi$, $B \to \rho\rho$, and $B \to \rho\pi$

Contributing authors: F. Abudinén, L. Li Gioi

We estimate the Belle II sensitivity on the ϕ_2 angle with isospin analysis of the decay modes $B \to \pi\pi$ and $B \to \rho\rho$. The input parameters of the isospin analysis are the branching fractions $\mathcal{B}_{+-}$, $\mathcal{B}_{00}$, and $\mathcal{B}_{+0}$, as well as the CP violation parameters A_{+-}, S_{+-}, A_{00}, and S_{00}. In the case of $B \to \rho\rho$ the isospin analysis applies only for decays with longitudinally polarized ρ mesons, therefore the branching fractions are multiplied by the fraction f_{L} of decays leading to longitudinal ρ polarization.

We present sensitivity studies of the CP violation parameters and the branching fraction of $B^0 \to \pi^0\pi^0$. We estimate the sensitivity to $S_{\pi^0\pi^0}$, performing a feasibility study of the time-dependent CP analysis using converted photons and π^0 Dalitz decays. The sensitivity to $A_{\pi^0\pi^0}$ and $\mathcal{B}_{\pi^0\pi^0}$ is estimated from a time-integrated CP analysis considering only photons which are reconstructed as clusters in the calorimeter. For the other $B \to \pi\pi$ and for all the $B \to \rho\rho$ input parameters, we estimated the sensitivity through extrapolation of the Belle results.

$B^0 \to \pi^0\pi^0$ At present, there is not enough data to perform a time-dependent CP analysis of the decay mode $B \to \pi^0\pi^0$. Neutral pions decay at about $(98.823 \pm 0.034)\%$ [88] into two photons, and, without external photon conversion $\gamma \to e^+e^-$, they do not provide information to reconstruct the vertex of the B^0. Also, the fraction of useful Dalitz decays $\pi^0 \to e^+e^-\gamma$ is very small at $(1.174 \pm 0.035)\%$ [88]. Consequently, the isospin analysis of the $B \to \pi\pi$ decay mode has been

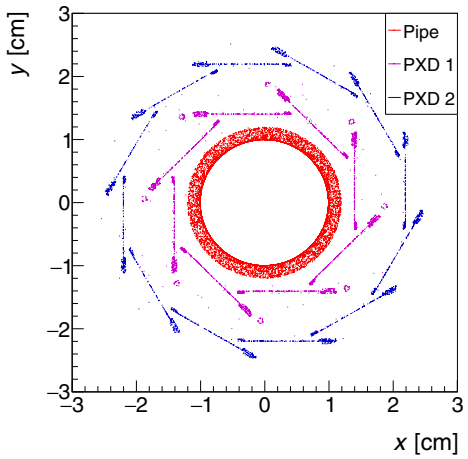

Fig. 107. Conversion vertices in the x–y plane inside the PXD. Conversions in the beam pipe and the first and second layers of the PXD are shown in red, magenta, and blue, respectively.

performed without $S_{\pi^0\pi^0}$, leading to an eightfold ambiguity in the solution of ϕ_2 in the range $[0, \pi]$. Only a measurement of $S_{\pi^0\pi^0}$ could reduce the number of possible solutions.

For this study, we generate and reconstruct signal MC events with $B_{\rm sig} \to \pi^0\pi^0$ and $B_{\rm tag} \to$ generic. Assuming that $\mathcal{B}_{\pi^0\pi^0} = 1.91 \cdot 10^{-6}$ [88], the total number of expected events in 50 ab^{-1} is about 103 000. For the CP analyses, the following three decay modes are considered as signal:

- $B^0_{\rm sig} \to \pi^0_{\gamma\gamma}(\to \gamma\gamma)\, \pi^0_{\gamma\gamma}(\to \gamma\gamma)$,
- $B^0_{\rm sig} \to \pi^0_{\rm dal}(\to e^+e^-\gamma)\, \pi^0_{\gamma\gamma}(\to \gamma\gamma)$,
- $B^0_{\rm sig} \to \pi^0_{\gamma_c\gamma}(\to \gamma_c(\to e^+e^-)\gamma)\, \pi^0_{\gamma\gamma}(\to \gamma\gamma)$.

We found out that only about 3% of the generated events contain at least one photon that undergoes conversion within the PXD volume. Of these, two-thirds of the conversions take place in the beam pipe, and the remaining convert in the PXD material. Figure 107 shows the MC vertices of converted photons inside the PXD in the x–y plane. Additionally, about 6% of the generated events contain at least one converted photon in the SVD volume outside of the PXD.

Signal reconstruction For each event, signal candidates are found by reconstructing the whole decay chain for the three signal decay modes considered. Photons and $\pi^0_{\gamma\gamma}$ are reconstructed in a similar way to Belle [712]. Photons correspond to neutral clusters in the ECL; the energy of the clusters is required to be greater than 50 MeV in the barrel region, 100 MeV in the front-end cap, and 150 MeV in the back-end cap of the ECL. The reconstruction of $\pi^0_{\gamma\gamma}$ is performed using pairs of photons with invariant masses in the range $105\,{\rm MeV}/c^2 < m_{\gamma\gamma} < 165\,{\rm MeV}/c^2$, corresponding to about $\pm 2.5\,\sigma$ around the nominal π^0 mass, where σ is the current mass resolution shown in Fig. 108 (left). To reduce the combinatorial background, $\pi^0_{\gamma\gamma}$ candidates with small helicity angles ($|\cos(\theta_{\rm H})| > 0.95$) are rejected. The helicity angle $\theta_{\rm H}$ is defined as the angle between the π^0 boost direction in the laboratory frame and the momentum of one of the γ daughters in the π^0 rest frame.

Electron–positron pairs are reconstructed using pairs of oppositely charged tracks, where both tracks have an electron PID $\mathcal{L}(e : \pi) > 0.8$ (see Eq. (5) in Sect. 5.5) and an impact parameter $d_0 < 5$ cm. For each electron–positron pair, we require that one or both tracks have at least one PXD

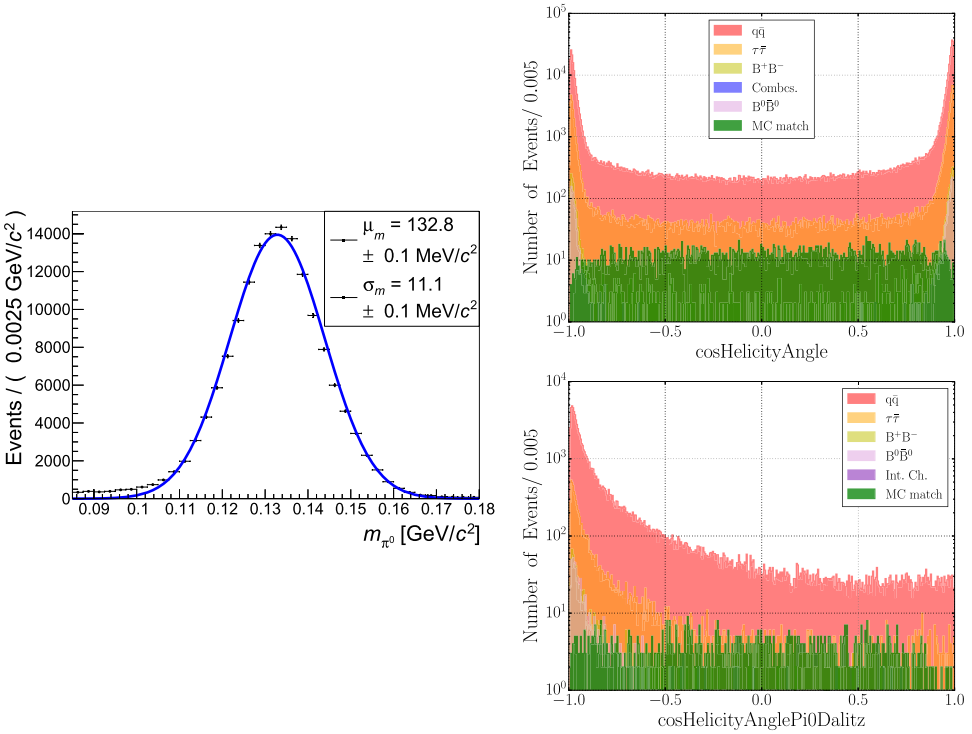

Fig. 108. Mass distribution of the reconstructed $\pi^0 \to \gamma\gamma$ (left). Distributions of $\cos\theta_{\rm H}$ for the $\pi^0_{\gamma\gamma} \to \gamma\gamma$ case (right top) as well as for the $\pi^0_{\rm dal} \to e^+e^-\gamma$ and $\pi^0_{\gamma_{\rm c}\gamma}(\to \gamma_{\rm c}(\to e^+e^-)\gamma)$ cases (right bottom).

hit. Events with electron–positron pairs without PXD hits, including also events with SVD hits, are not suitable for a time-dependent CP analysis since their time resolution is at least a factor of three worse than for the events used in this analysis.

Converted photons $\gamma_{\rm c}$ are reconstructed using e^+e^- pairs with invariant masses $m_{e^+e^-} < 0.3\,{\rm GeV}/c^2$. The non-zero mass $m_{e^+e^-}$ results from the fact that the momentum of the tracks is determined at the point of closest approach to the interaction point (IP) and not at the conversion vertex. The $\gamma_{\rm c}$ momentum is obtained by adding the momenta of the e^+ and the e^- tracks.

The reconstruction of neutral pions with one converted photon $\pi^0_{\gamma_{\rm c}\gamma}$ is performed using pairs consisting of a reconstructed converted photon $\gamma_{\rm c}$ and a photon corresponding to a neutral cluster. Dalitz pions $\pi^0_{\rm dal}$ are reconstructed using three particles for each candidate: an e^+e^- pair and a photon corresponding to a neutral cluster.

All three kinds of pions are reconstructed within the same mass range chosen for $\pi^0_{\gamma\gamma}$ ($105\,{\rm MeV}/c^2 < m_{\pi^0} < 165\,{\rm MeV}/c^2$). The reason is that the mass resolution for $\pi^0_{\gamma_{\rm c}\gamma}$ ($\sigma \sim 12\,{\rm MeV}$) and the mass resolution for $\pi^0_{\rm dal}$ ($\sigma \sim 10\,{\rm MeV}$) differ only by about $1\,{\rm MeV}/c^2$ from the mass resolution of $\pi^0_{\gamma\gamma}$ ($\sigma \sim 11\,{\rm MeV}$). For $\pi^0_{\gamma_{\rm c}\gamma}$ and $\pi^0_{\rm dal}$ candidates, the helicity angle $\theta_{\rm H}$ is defined as the angle between the π^0 boost direction in the laboratory frame and the momentum of the neutral ECL cluster γ in the π^0 rest frame. Candidates with helicity angles $|\cos(\theta_{\rm H})| > 0.95$ are rejected. Figure 108 (right) shows the $\cos(\theta_{\rm H})$ distributions for signal and background π^0 candidates. The asymmetry in the case of $\pi^0_{\gamma_{\rm c}\gamma}$ and $\pi^0_{\rm dal}$ occurs because tracks are less affected by low-momentum background in comparison with neutral clusters (the momentum threshold for tracks is higher than for neutral clusters).

At the end, $B^0_{\rm sig}$ candidates are reconstructed requiring that $M_{\rm bc} > 5.26\,{\rm GeV}/c^2$ and $-0.3\,{\rm GeV} < \Delta E < 0.2\,{\rm GeV}$ for the three signal decay modes considered. The same requirements for $M_{\rm bc}$ and ΔE were applied previously by Belle in the time-integrated analysis of $B^0 \to \pi^0\pi^0$ [712].

We found that almost half of the reconstructed $B^0_{\rm sig}$ candidates with a reconstructed Dalitz $\pi^0_{\rm dal}$ are in reality generated B^0s with a converted photon and vice versa. This occurs because the final state particles are in the same kinematic phase space and because the topology of the decay is very similar if at least one of the e^+e^- tracks is required to have a PXD hit.

We select only one $B^0_{\rm sig}$ candidate per event. If an event contains both a $B^0_{\rm sig}$ candidate with a reconstructed converted photon and a $B^0_{\rm sig}$ candidate with a reconstructed Dalitz $\pi^0_{\rm dal}$, we select the candidate with the reconstructed Dalitz $\pi^0_{\rm dal}$. After reconstruction and final selection, about 270 events with $B^0_{\rm sig}$ candidates reconstructed with Dalitz $\pi^0_{\rm dal}$ and about 50 events with $B^0_{\rm sig}$ candidates reconstructed with converted photons remain in a signal MC sample corresponding to $50\,{\rm ab}^{-1}$. The latter number of events is too small for a time-dependent CP violation analysis. Since reconstructed $B^0_{\rm sig}$ candidates with converted photons have a worse Δt resolution and a worse value of the figure of merit (see the definition in Eq. (325)), they cannot be added to the sample with reconstructed Dalitz $B^0_{\rm sig}$ candidates. Therefore, the sensitivity study for time-dependent CP violation is performed only for events with reconstructed Dalitz $B^0_{\rm sig}$ candidates. The $B^0_{\rm sig}$ candidates reconstructed from two $\pi^0_{\gamma\gamma}$ are used for the time-integrated CP violation study. There is no event overlap between events with $B^0_{\rm sig}$ candidates reconstructed from two $\pi^0_{\gamma\gamma}$ and events containing Dalitz decays or converted photons.

Δt resolution For the time-dependent CP analysis, we use only events reconstructed as Dalitz events $B^0_{\rm sig} \to \pi^0_{\rm dal}(\to e^+e^-\gamma)\,\pi^0_{\gamma\gamma}(\to \gamma\gamma)$. Using MC information, we find that about 54% of these events correspond to signal events with true Dalitz $\pi^0_{\rm dal}$ decays and about 46% correspond to events with a converted photon. The vertex of the $B^0_{\rm sig}$ is reconstructed using the two tracks (e^+e^-) together with the *iptube* constraint, an ellipsoid constraint whose transverse size corresponds to the beam size at the IP and is oriented along the boost direction (see Sect. 6.3.2).

The reconstruction of the $B^0_{\rm tag}$ vertex is performed as explained in Sect. 6.2. The time difference Δt is calculated from the difference Δl in the lab frame, which corresponds to the difference between the reconstructed decay vertices of $B^0_{\rm sig}$ and $B^0_{\rm tag}$ in the boost direction.

Figure 109 shows the $\Delta t^{\rm rec} - \Delta t^{\rm gen}$ residuals for fully reconstructed events. The Δt resolution $\sigma_{\Delta t}$ for events with a converted photon is about 0.3 ps larger than for true Dalitz events. Therefore, these two types of signal events have to be considered separately.

Separation between B^0_{sig} candidates with a true Dalitz π^0_{dal} decay and with a converted photon from one of the two π^0s In order to distinguish the two types of signal candidates used for the time-dependent CP analysis, i.e. between $B^0_{\rm sig}$ candidates with a true Dalitz $\pi^0_{\rm dal}$ decay and $B^0_{\rm sig}$ candidates with a converted photon from one of the two π^0s, a FastBDT [70] multivariate method was trained with four input variables that provide separation capacity. These input variables make use of the information related to the properties of the reconstructed e^+e^- pair, for which at least one of the tracks is required to have a PXD hit. The first two variables, $r_{\rm L}$ and $r_{\rm U}$, correspond to the possible two solutions for the e^+e^- vertex in the x–y plane (r–ϕ plane): $r_{\rm L}$ is the solution closest to the IP and $r_{\rm U}$ the farthest one. For the calculation, we consider the e^+e^- tracks as two circles with radii r_1 and r_2 and calculate the intersections between them. The line connecting the two intersection

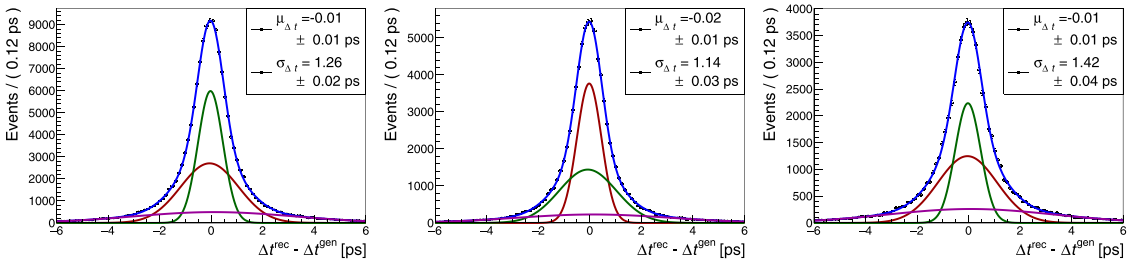

Fig. 109. Δt residual distributions for events with reconstructed Dalitz $\pi^0_{\rm dal}$: for all the events (left); only for true Dalitz events (middle); and only for events with a converted photon (right). All events are reconstructed as Dalitz events. The fits are performed with three Gaussian distributions. The shift $\mu_{\Delta t}$ and the resolutions $\sigma_{\Delta t}$ are the weighted averages of the mean values and the standard deviations of the three Gaussian functions.

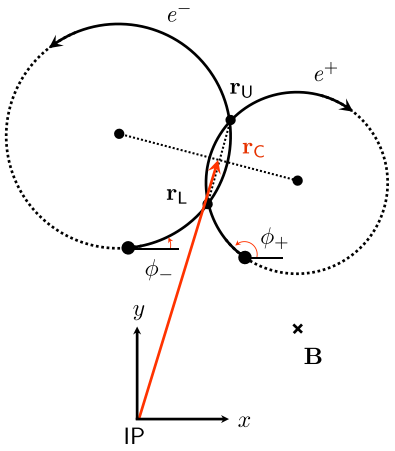

Fig. 110. Illustration of $\mathbf{r}_{\rm C}$, $\mathbf{r}_{\rm L}$, $\mathbf{r}_{\rm U}$, ϕ_{e^+}, and ϕ_{e^-} on the x–y plane (r–ϕ plane). The vector $\mathbf{B}$ corresponds to the magnetic field.

points crosses the line connecting the centers $\mathbf{c}_1$ and $\mathbf{c}_2$ of the two circles at the point

$$\mathbf{r}_{\rm C} = \mathbf{c}_1 + \frac{\mathbf{c}_2 - \mathbf{c}_1}{2}\left(1 + \frac{r_1^2 - r_2^2}{|\mathbf{c}_2 - \mathbf{c}_1|^2}\right). \tag{323}$$

One can then write

$$\mathbf{r}_{\rm U,L} = \mathbf{r}_{\rm C} \pm y \cdot \mathbf{n}, \tag{324}$$

where $\mathbf{n}$ is a unit vector perpendicular to the line connecting the centers of the two circles. If there are two intersections, y is a real number such that $y > 0$. If there is only one intersection, $y = 0$. In the case that there is no intersection, we set $\mathbf{r}_{\rm L,U} = \mathbf{r}_{\rm C}$. An illustration of the two-circle approach is shown in Fig. 110.

The fourth and the fifth variables correspond to the angular differences $\Delta\theta_{e^+e^-} = \theta_{e^+} - \theta_{e^-}$ and $\Delta\phi_{e^+e^-} = \phi_{e^+} - \phi_{e^-}$, where the angles θ and ϕ for each track are calculated at the respective point of closest approach to the IP; within the Belle II software, the tracks are represented by the helix parameters calculated at the point of closest approach to the IP.

Figure 111 shows the distributions of the four input variables and the output $y_{\rm DC}$ of the FastBDT classifier for $B^0_{\rm sig}$ candidates with true Dalitz $\pi^0_{\rm dal}$ decays and for $B^0_{\rm sig}$ candidates with converted

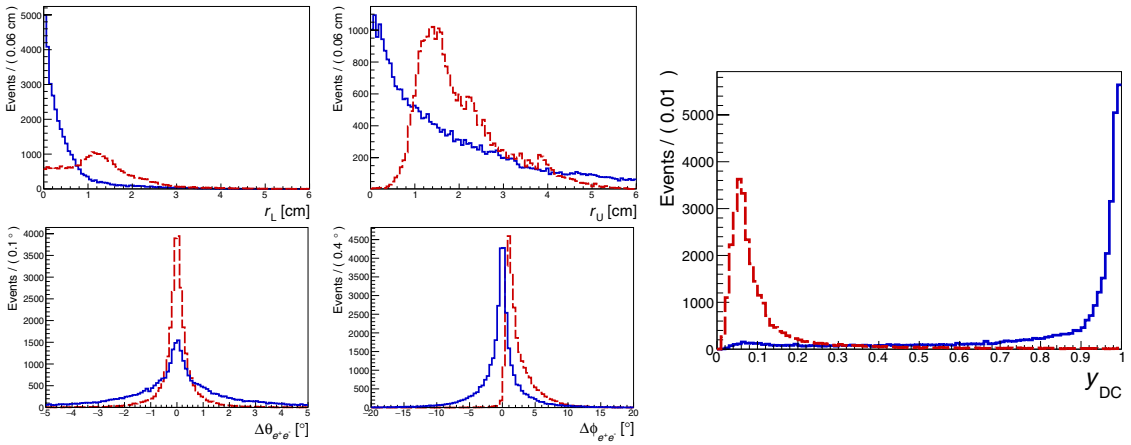

Fig. 111. The four input variables, r_L (left top), r_U (middle top), $\Delta\theta_{e^+e^-}$ (left bottom), and $\Delta\phi_{e^+e^-}$ (middle bottom), together with the output y_{DC} of the dalitz conversion classifier (right). B^0_{sig} candidates with true Dalitz π^0_{dal} decays and with converted photons are shown by the solid blue and the long dashed red curves, respectively.

photons. In particular, the input variable $\Delta\phi_{e^+e^-}$ has a large separation power. For events with Dalitz π^0_{dal} decays, the $\Delta\phi_{e^+e^-}$ distribution is symmetric around zero degrees. In this case, the B^0 decay vertex is only a few microns away from the IP in the r–ϕ plane and then the π^0_{dal} decay follows immediately; therefore, the angles at the point of closest approach correspond to a good approximation to the true opening angles at the decay vertex. In contrast, the distribution of $\Delta\phi_{e^+e^-}$ for converted photons is asymmetric. For these events, the vertex is far from the interaction point (at least 1 cm). Thus, the ϕ angles at the point of closest approach to the IP are biased with respect to the true values at the conversion vertex. Because the curvature of reconstructed electrons always has the same sign, which is opposite to the sign of the curvature of the reconstructed positrons, the angular difference $\Delta\phi_{e^+e^-}$ is always biased in the same direction.

Continuum suppression and flavor tagging Continuum events ($e^+e^- \to q\bar{q},\ q = u, d, s, c$) are the dominant source of background. The continuum background is studied using an available MC sample which corresponds to $2\,\text{ab}^{-1}$. We employ a FastBDT multivariate method to discriminate between $B^0 \to \pi^0\pi^0$ and continuum events. The method is trained with variables that have a separation power between spherical $B\bar{B}$ events and jet-like continuum events (see Sect. 6.4). From the available set of 30 continuum suppression variables, three variables were discarded because of their strong correlation with M_{bc} and ΔE: the magnitude of the B_{sig} thrust together with the first and the second Cleo cones. The output of the multivariate method is normalized to the range $[0, 1]$. We select events where the output of the multivariate method is larger than 0.976, maximizing the figure of merit

$$\text{FoM} = \frac{n_{sig}}{\sqrt{n_{sig} + n_{cont}}}, \tag{325}$$

where n_{sig} is the number of signal events and n_{cont} is the number of continuum events. The flavor of the remaining B^0_{tag} is determined using the flavor tagger algorithm explained in Sect. 6.5. The output flavor dilution $r \in [0, 1]$ peaks at 0 for continuum background and at 1 for signal events. In order to additionally remove some continuum background, events with $r < 0.1$ are rejected. In this way, only signal events which do not provide flavor separation power are discarded.

Table 88. Fraction of generated events in the acceptance $n^{\rm acc}_{\rm gen}/n_{\rm gen}$, reconstruction efficiency $n_{\rm rec}/n^{\rm acc}_{\rm gen}$, and efficiency after final selection $n^{\rm FS}_{\rm rec}/n^{\rm acc}_{\rm gen}$ (the efficiencies are normalized to the number of generated events in the acceptance $n^{\rm acc}_{\rm gen}$). Events with converted photons and Dalitz π^0s (first and second rows) were reconstructed as $B^0_{\rm sig} \to \pi^0_{\rm dal}\,\pi^0_{\gamma\gamma}$. The highlighted row corresponds to the whole set used for time-dependent CP analysis.

Decay Channel	$n^{\rm acc}_{\rm gen}/n_{\rm gen}$ [%]	$n_{\rm rec}/n^{\rm acc}_{\rm gen}$ [%]	$n^{\rm FS}_{\rm rec}/n^{\rm acc}_{\rm gen}$ [%]
$B^0 \to \pi^0_{\rm dal}\,\pi^0_{\gamma\gamma}$	2.0	52.0	7.2
$B^0 \to \pi^0_{\gamma{\rm c}\gamma}\,\pi^0_{\gamma\gamma}$	3.0	48.8	4.2
Dal. + Conv.	5.0	50.1	5.4
$B^0 \to \pi^0_{\gamma\gamma}\,\pi^0_{\gamma\gamma}$	76.2	86.0	19.2

$B\bar{B}$ background Sources of background from $B\bar{B}$ events are studied with a $4\,{\rm ab}^{-1}$ MC sample. The largest contribution comes from $B^+ \to \rho^+(\to \pi^+\pi^0)\pi^0$ decays, where the π^+ is lost. Events where the remaining π^0 pair decays into four photons which arrive at the ECL are the main $B\bar{B}$ background for $B^0 \to \pi^0_{\gamma\gamma}\pi^0_{\gamma\gamma}$ candidates. Those events which contain a converted photon or a Dalitz π^0 are the main background $B\bar{B}$ source for $B^0 \to \pi^0_{\rm dal}\pi^0_{\gamma\gamma}$ candidates. This background peaks at the same value of $M_{\rm bc}$, but is shifted in ΔE towards negative values due to the missing π^+.

Efficiencies Table 88 presents the absolute reconstruction efficiency and the efficiency after final selection including the requirements on flavor dilution and on continuum suppression for the different decay modes. We verified that the reconstruction efficiency is constant over the whole Δt fit range. The events with converted photons and Dalitz π^0s are reconstructed as $B^0_{\rm sig} \to \pi^0_{\rm dal}\,\pi^0_{\gamma\gamma}$.

Estimate of sensitivity from pseudo-experiments The expected statistical uncertainties are estimated by performing sets of pseudo-experiments based on simulated experiments. A time-integrated CP analysis is performed for events reconstructed as $B^0 \to \pi^0_{\gamma\gamma}(\to \gamma\gamma)\,\pi^0_{\gamma\gamma}(\to \gamma\gamma)$, and a time-dependent CP analysis for events reconstructed as $B^0_{\rm sig} \to \pi^0_{\rm dal}(\to e^+e^-\gamma)\,\pi^0_{\gamma\gamma}(\to \gamma\gamma)$. We extracted PDFs for the distributions of the different components and performed an unbinned extended multi-dimensional maximum likelihood fit using MC. For the time-dependent and the time-integrated analyses we used ΔE and $M_{\rm bc}$ as fit variables. For the time-dependent analysis, the classifier output $y_{\rm DC}$ was used in addition. The fit was performed assuming no correlation between the fit variables.

The generated toy MC for each pseudo-experiment set corresponds to an integrated luminosity of $50\,{\rm ab}^{-1}$ including signal, background from wrongly reconstructed signal events (WRS), $B\bar{B}$ background, and continuum background. The signal and the background from wrongly reconstructed signal events were obtained by extracting random sub-samples from the generated signal MC. Wrongly reconstructed signal events correspond to signal events where the $B^0_{\rm sig}$ candidate was reconstructed by a wrong combination of final state particles. Different input values of $A_{\pi^0\pi^0}$ and $S_{\pi^0\pi^0}$ were used to generate the signal MC: we considered the world averages $A_{\pi^0\pi^0} = 0.43$ (2016) [88], $A_{\pi^0\pi^0} = 0.34$ (2017) [650], the latest Belle measurement $A_{\pi^0\pi^0} = 0.14$ [712], and the predicted value $S_{\pi^0\pi^0} = 0.65$ [650]. The assumed branching fraction $\mathcal{B}_{\pi^0\pi^0} = 1.91 \cdot 10^{-6}$ [88] yields 15 068 signal events for the time-integrated analysis and 271 for the time-dependent analysis. The latter number of events is composed of 147 signal events with Dalitz decays and 124 signal events with conversions. These two types of signal events are considered as two independent signal components

Table 89. Purity and fraction of wrongly reconstructed signal events after the final selection.

Decay Channel	Purity [%]	$\frac{n_{\rm WRS}}{n_{\rm sig}+n_{\rm WRS}}$ [%]
Dal. + Conv.	17.6	1.1
$B^0 \to \pi^0_{\gamma\gamma}\,\pi^0_{\gamma\gamma}$	15.8	1.0

in the maximum likelihood fit which can be distinguished by the $y_{\rm DC}$ fit variable. The purity,

$$\text{Purity} = \frac{n_{\rm sig}}{n_{\rm sig} + n_{\rm WRS} + n_{B\bar{B}} + n_{\rm cont}}, \tag{326}$$

and the fractions of wrongly reconstructed signal events are presented in Table 89. The continuum and the $B\bar{B}$ background events were generated from PDFs which were modeled using MC samples corresponding to 2 and 4 ab^{-1}, respectively. For each combination of input values $A_{\pi^0\pi^0}$ and $S_{\pi^0\pi^0}$, we generated 527 pseudo-experiments performing time-dependent and time-integrated analyses. Projections of the fit results for one example pseudo-experiment are shown in Figs. 112 and 113 for the time-dependent and the time-integrated analysis, respectively.

We verify that the signal yields and the CP violation parameters are determined without bias and without over- or under-estimation of the error through examination of the fit pulls. Figure 114 shows the residuals distributions for the CP violation parameters extracted from the time-dependent analysis. Figure 115 shows the residuals distributions for $n_{\rm sig}$ and $A_{\pi^0\pi^0}$ extracted from the time-integrated analysis. These distributions are fitted with a single Gaussian function and the value of σ is taken as the statistical uncertainty of the measured parameters. For the statistical uncertainty of the branching fraction we use $\Delta\mathcal{B}_{\pi^0\pi^0}/\mathcal{B}_{\pi^0\pi^0} = \sigma_{n_{\rm sig}}/n_{\rm sig}$. Table 90 shows the estimated statistical uncertainties of $A_{\pi^0\pi^0}$, $S_{\pi^0\pi^0}$, and $\Delta\mathcal{B}_{\pi^0\pi^0}/\mathcal{B}_{\pi^0\pi^0}$ for different values of the input parameters $A_{\pi^0\pi^0}$ and $S_{\pi^0\pi^0}$ used for the generation of the signal MC.

Extrapolation of the $B^0 \to \pi\pi$ sensitivities The expected statistical uncertainties for $\mathcal{B}_{\pi^+\pi^-}$, $\mathcal{B}_{\pi^+\pi^0}$, $A_{\pi^+\pi^-}$, and $S_{\pi^+\pi^-}$ are estimated through extrapolation of Belle measurements at 0.8 ab^{-1} assuming a final integrated luminosity of 50 ab^{-1} at Belle II. For $\mathcal{B}_{\pi^0\pi^0}$, $A_{\pi^0\pi^0}$, and $S_{\pi^0\pi^0}$, the statistical uncertainties are taken from the sensitivity study that was performed using the current world averages for $A_{\pi^0\pi^0}$ and $S_{\pi^0\pi^0}$ as input values (first row of Table 90).

An estimation of possible systematic uncertainties is performed following the guidelines in Sect. 10.2.1. We assume that reducible systematics will scale with the luminosity since they are evaluated with control samples and MC events. We sum in quadrature the irreducible and the extrapolated reducible systematic uncertainties. For $\mathcal{B}_{\pi^+\pi^-}$ and $\mathcal{B}_{\pi^+\pi^0}$, the list of sources of systematic uncertainties in Table II of Ref. [727] is considered, and, for $\mathcal{B}_{\pi^0\pi^0}$ and $A_{\pi^0\pi^0}$, the lists in Ref. [712]. We assume all sources in these lists to be reducible apart from the number of B mesons (1.37% for $\mathcal{B}_{\pi^+\pi^-}$ and $\mathcal{B}_{\pi^+\pi^0}$ as well as 1.4% for $\mathcal{B}_{\pi^0\pi^0}$) and the contribution from the PHOTOS MC generator (0.8%). We add an additional reducible flavor tagging contribution of ± 0.0034 to $A_{\pi^0\pi^0}$, considering Table VI of Ref. [711]. For $A_{\pi^+\pi^-}$ and $S_{\pi^+\pi^-}$ the systematic sources in Table II of Ref. [728] are considered. Apart from the tag-side interference (± 3.18 for $A_{\pi^+\pi^-}$ and ± 0.17 for $S_{\pi^+\pi^-}$) and the Δt resolution (± 0.42 for $A_{\pi^+\pi^-}$ and ± 1.01 for $S_{\pi^+\pi^-}$), we assume all sources in this list to be reducible. The Δt resolution contribution is reduced by a factor of two considering the improvement

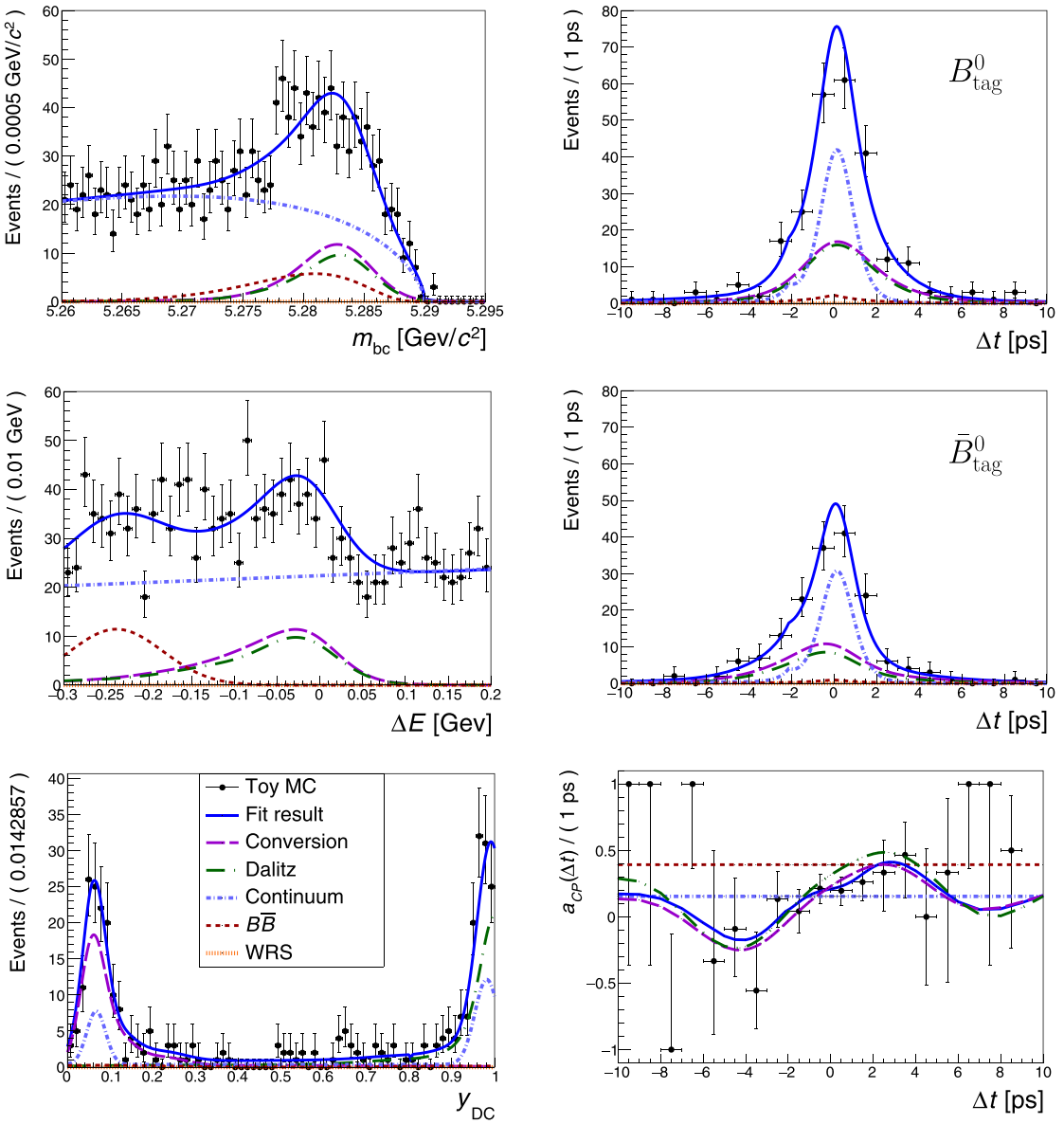

Fig. 112. Projections of the fit results for candidates reconstructed as $B^0 \to \pi^0 \left(\to e^+e^-\gamma\right)\pi^0 \left(\to \gamma\gamma\right)$. The projections for one example pseudo-experiment are shown onto M_{bc} (left top), ΔE (left middle), y_{DC} (left bottom) and Δt (right). The Δt projection is shown for B^0 mesons tagged as B^0 (right top) and as $\bar{B}^0$ (right middle) together with the CP asymmetry (right bottom). Points with error bars represent the toy MC sample. The full fit results are shown by the solid blue curves. Contributions from signal with Dalitz decays, signal with conversions, generic $B\bar{B}$, continuum background, and background from wrongly reconstructed signal events are shown by the long dashed-dotted green, long dashed violet, short dashed red, dash-dotted blue, and dotted orange curves, respectively. The input values used for this pseudo-experiment are $A_{\pi^0\pi^0} = 0.34$ and $S_{\pi^0\pi^0} = 0.65$.

due to the PXD and the new reconstruction algorithms (see Sect. 10.2.1). A summary of the Belle measurements and the extrapolated uncertainties is presented in Table 91.

The systematic uncertainty for $S_{\pi^0\pi^0}$ is assumed to be about 10% of the statistical uncertainty and in the order of magnitude of the systematic uncertainties of $A_{\pi^+\pi^-}$ and $S_{\pi^+\pi^-}$. This gives in total $\Delta S_{\pi^0\pi^0} = \pm 0.28 \pm 0.03$.

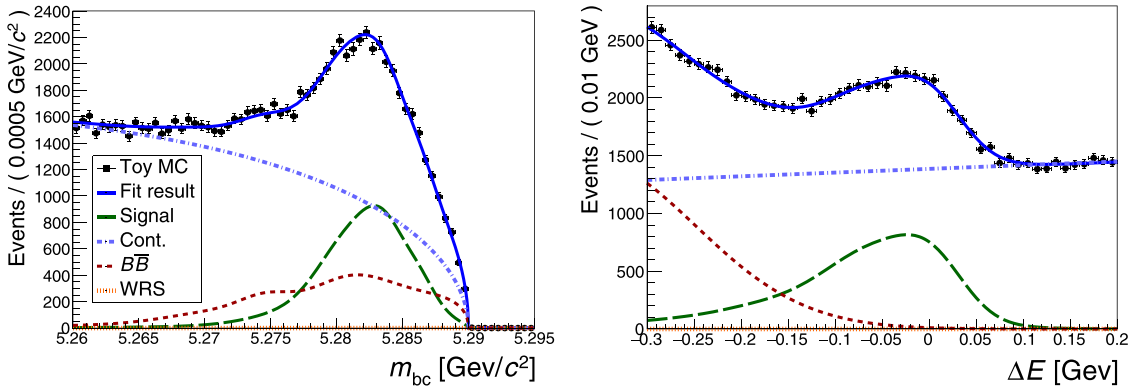

Fig. 113. Projections of the fit results for candidates reconstructed as $B^0 \to \pi^0(\to \gamma\gamma)\,\pi^0(\to \gamma\gamma)$. The projections for one example pseudo-experiment are shown onto $M_{\rm bc}$ (left) and ΔE (right). Points with error bars represent the toy sample. The full fit results are shown by the solid blue curves. Contributions from signal, generic $B\bar{B}$ events, continuum background, and background from wrongly reconstructed signal events are shown by the long dashed green, short dashed red, dash-dotted blue, and dotted orange curves, respectively. The input values used for this pseudo-experiment are $A_{\pi^0\pi^0} = 0.34$ and $S_{\pi^0\pi^0} = 0.65$.

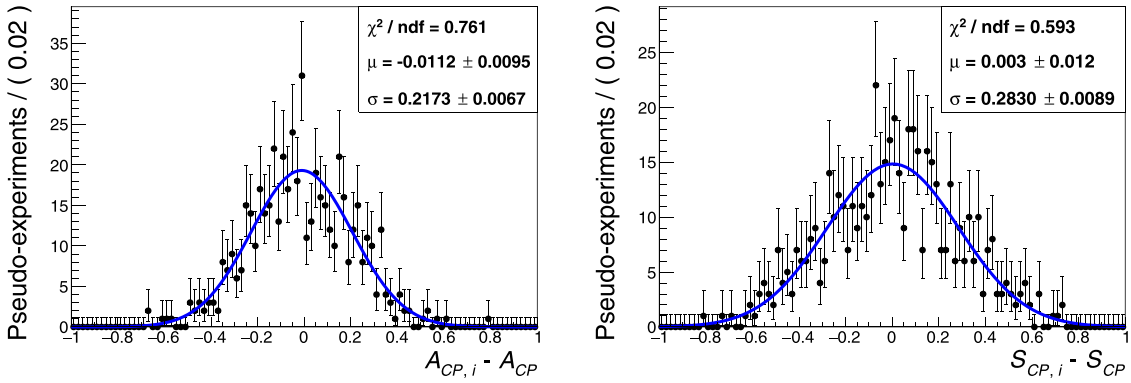

Fig. 114. Residuals distributions of $A_{\rm CP}$ (left) and $S_{\rm CP}$ (right) for the fit of $B^0 \to \pi^0\left(\to e^+e^-\gamma\right)\pi^0(\to \gamma\gamma)$. The input values used for these pseudo-experiments are $A_{\pi^0\pi^0} = 0.34$ and $S_{\pi^0\pi^0} = 0.65$.

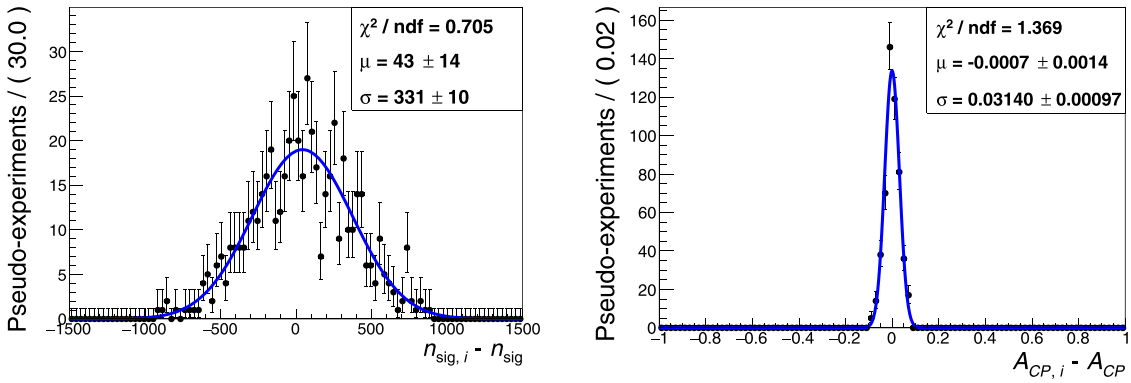

Fig. 115. Residuals distributions of the signal yield $n_{\rm sig}$ (left) and the parameter $A_{\rm CP}$ (right) for the fit of $B^0 \to \pi^0(\to \gamma\gamma)\,\pi^0(\to \gamma\gamma)$. The input values used for these pseudo-experiments are $A_{\pi^0\pi^0} = 0.34$ and $S_{\pi^0\pi^0} = 0.65$.

Table 90. Statistical uncertainties $\Delta A_{\pi^0\pi^0}$, $\Delta S_{\pi^0\pi^0}$, and $\Delta\mathcal{B}_{\pi^0\pi^0}/\mathcal{B}_{\pi^0\pi^0}$ for different input values of $A_{\pi^0\pi^0}$ and $S_{\pi^0\pi^0}$ used for the generation of signal MC.

Input values		Time-dependent		Time-integrated	
$A_{\pi^0\pi^0}$	$S_{\pi^0\pi^0}$	$\Delta A_{\pi^0\pi^0}$	$\Delta S_{\pi^0\pi^0}$	$\Delta A_{\pi^0\pi^0}$	$\Delta\mathcal{B}_{\pi^0\pi^0}/\mathcal{B}_{\pi^0\pi^0}$ [%]
0.34 [650]	0.65 [650]	0.22	0.28	0.03	2.2
0.43 [88]	0.79	0.23	0.29	0.03	2.2
0.14 [712]	0.83	0.21	0.26	0.03	2.4
0.14 [712]	0.40	0.20	0.29	0.03	2.3
0.14 [712]	−0.61	0.22	0.27	0.03	2.3
0.14 [712]	−0.94	0.22	0.28	0.03	2.4

Table 91. Branching fractions and CP asymmetry parameters entering in the isospin analysis of the $B \to \pi\pi$ system: Belle measurements at 0.8 ab^{-1} together with the expected Belle II sensitivity at 50 ab^{-1}.

	Value	0.8 ab^{-1}	50 ab^{-1}
$\mathcal{B}_{\pi^+\pi^-}$ [10^{-6}]	5.04	$\pm0.21 \pm 0.18$ [727]	$\pm0.03 \pm 0.08$
$\mathcal{B}_{\pi^0\pi^0}$ [10^{-6}]	1.31	$\pm0.19 \pm 0.19$ [712]	$\pm0.03 \pm 0.03$
$\mathcal{B}_{\pi^+\pi^0}$ [10^{-6}]	5.86	$\pm0.26 \pm 0.38$ [727]	$\pm0.03 \pm 0.09$
$A_{\pi^+\pi^-}$	0.33	$\pm0.06 \pm 0.03$ [728]	$\pm0.01 \pm 0.03$
$S_{\pi^+\pi^-}$	−0.64	$\pm0.08 \pm 0.03$ [728]	$\pm0.01 \pm 0.01$
$A_{\pi^0\pi^0}$	0.14	$\pm0.36 \pm 0.10$ [712]	$\pm0.03 \pm 0.01$

Extrapolation of the $B^0 \to \rho\rho$ sensitivities The expected statistical uncertainties for all the parameters entering in the isospin analysis of the $B \to \rho\rho$ decay mode are estimated through extrapolation of Belle and BaBar measurements assuming a final integrated luminosity of 50 ab^{-1} at Belle II. We consider BaBar measurements only for $A_{\rho^0\rho^0}$ and $S_{\rho^0\rho^0}$ since these measurements have not been performed by Belle.

An estimation of possible systematic uncertainties is performed in a similar way as in the previous section for the $B \to \pi\pi$ system: the irreducible and the extrapolated reducible systematic uncertainties are summed in quadrature. For $\mathcal{B}_{\rho^+\rho^-}$ and $f_{L,\rho^+\rho^-}$, the list of sources of systematic uncertainties in Table VIII of Ref. [725] is considered; for $\mathcal{B}_{\rho^0\rho^0}$ and $f_{L,\rho^0\rho^0}$, the list in Table VIII of Ref. [729]; and for $\mathcal{B}_{\rho^+\rho^0}$ and $f_{L,\rho^+\rho^0}$, the list of sources given in Ref. [716]. We assume all sources in these lists to be reducible apart from the number of B mesons (1.4%). For $A_{\rho^+\rho^-}$ and $S_{\rho^+\rho^-}$, the list in Table VIII of Ref. [725] is taken into account. Apart from the tag-side interference ($\pm1.02 \cdot 10^{-2}$ for $A_{\rho^+\rho^-}$ and $\pm0.08 \cdot 10^{-2}$ for $S_{\rho^+\rho^-}$), we assume all sources in this list to be reducible. Although the measurement of $A_{\rho^0\rho^0}$ and $S_{\rho^0\rho^0}$ was performed by BaBar, we consider for these parameters the sources of systematic uncertainties taken into account by Belle for the measurement of $A_{\rho^+\rho^-}$ and $S_{\rho^+\rho^-}$. A summary of the Belle and BaBar measurements together with the extrapolated uncertainties is presented in Table 92.

ϕ_2 expected sensitivity using isospin analysis We estimate the Belle II sensitivity to the ϕ_2 angle by performing the isospin analysis introduced in Sect. 10.4.1 for $B \to \pi\pi$ and $B \to \rho\rho$. We perform a scan of the confidence for ϕ_2 from a χ^2 distribution which is obtained by minimizing

Table 92. Branching fractions, fractions of longitudinally polarized events, and CP asymmetry parameters entering in the isospin analysis of the $B \to \rho\rho$ system: Belle measurements at 0.8 ab^{-1} and 0.08 ab^{-1}, BaBar measurements at 0.5 ab^{-1}, and expected Belle II sensitivity at 50 ab^{-1}.

	Value	0.8 ab^{-1}	50 ab^{-1}
$f_{L,\rho^+\rho^-}$	0.988	$\pm0.012 \pm 0.023$ [725]	$\pm0.002 \pm 0.003$
$f_{L,\rho^0\rho^0}$	0.21	$\pm0.20 \pm 0.15$ [729]	$\pm0.03 \pm 0.02$
$\mathcal{B}_{\rho^+\rho^-}$ [10^{-6}]	28.3	$\pm1.5 \pm 1.5$ [725]	$\pm0.19 \pm 0.4$
$\mathcal{B}_{\rho^0\rho^0}$ [10^{-6}]	1.02	$\pm0.30 \pm 0.15$ [729]	$\pm0.04 \pm 0.02$
$A_{\rho^+\rho^-}$	0.00	$\pm0.10 \pm 0.06$ [725]	$\pm0.01 \pm 0.01$
$S_{\rho^+\rho^-}$	−0.13	$\pm0.15 \pm 0.05$ [725]	$\pm0.02 \pm 0.01$
	Value	0.08 ab^{-1}	50 ab^{-1}
$f_{L,\rho^+\rho^0}$	0.95	$\pm0.11 \pm 0.02$ [716]	$\pm0.004 \pm 0.003$
$\mathcal{B}_{\rho^+\rho^0}$ [10^{-6}]	31.7	$\pm7.1 \pm 5.3$ [716]	$\pm0.3 \pm 0.5$
	Value	0.5 ab^{-1}	50 ab^{-1}
$A_{\rho^0\rho^0}$	−0.2	$\pm0.8 \pm 0.3$ [715]	$\pm0.08 \pm 0.01$
$S_{\rho^0\rho^0}$	0.3	$\pm0.7 \pm 0.2$ [715]	$\pm0.07 \pm 0.01$

$-2\log(\mathcal{L})$. The likelihood $\mathcal{L}$ has the form of a multivariate normal distribution,

$$\chi^2 = -2\log\left[\frac{\exp\left\{\frac{1}{2}\left(\mathbf{x}_{\text{data}} - \mathbf{x}_{\text{theo}}\right)^{\mathrm{T}} \Sigma^{-1} \left(\mathbf{x}_{\text{data}} - \mathbf{x}_{\text{theo}}\right)\right\}}{\sqrt{(2\pi)^n \det \Sigma}}\right], \tag{327}$$

where $\mathbf{x}_{\text{data}}$ and $\mathbf{x}_{\text{theo}}$ are vectors containing respectively the measured values and the theoretical predictions of the parameters $\mathcal{B}_{+-}, \mathcal{B}_{00}, \mathcal{B}_{+0}, A_{+-}, S_{+-}, A_{00}$, and S_{00}. For the theoretical predictions, we adopt the alternative amplitude parameterization proposed in Ref. [730]. The covariance matrix Σ contains the uncertainties in the diagonal and the correlations between the measured parameters in the non-diagonal part.

Figure 116 shows the results of the scan of the confidence for the ϕ_2 angle performing the isospin analysis of $B \to \pi\pi$. We use the Belle measurements and the projection for Belle II summarized in Table 91 without and with the $S_{\pi^0\pi^0}$ constraint. One can recognize the eight possible solutions and the improvement of rejection power at Belle II even without $S_{\pi^0\pi^0}$. The scan including the $S_{\pi^0\pi^0}$ constraint is performed for several $S_{\pi^0\pi^0}$ central values. Compatible $S_{\pi^0\pi^0}$ values are estimated by calculating the theoretical predictions. For these calculations we used the fit parameters obtained at the solutions of the scan performed without the $S_{\pi^0\pi^0}$ constraint. The compatible values of $S_{\pi^0\pi^0}$ were used as input values for the sets of pseudo-experiments in Sect. 10.4.2 (see Table 90). As can be seen in Fig. 116 (right), the solutions for each value of $S_{\pi^0\pi^0}$ that are compatible with the scan performed without the $S_{\pi^0\pi^0}$ constraint overlap with two of the eight possible solutions, thus reducing the ambiguities in the determination of the ϕ_2 angle by a factor of four.

Because of the experimental precision, it is possible that the value of $S_{\pi^0\pi^0}$ that will be measured at Belle II will not be compatible with any of the four predicted values obtained from the the scan without the $S_{\pi^0\pi^0}$ constraint. Figure 117 shows different possible scenarios: a value of $S_{\pi^0\pi^0}$ that is compatible with the solution around 88°, and two values that are not compatible with any of the eight solutions. In both situations there is a large range that can be excluded at $1\,\sigma$. In the case of the compatible value $S_{\pi^0\pi^0} = 0.83$, the width of the solution around 88° corresponding to a confidence of $1\,\sigma$ is about 4° and thus $\Delta\phi_2 \approx 2°$.

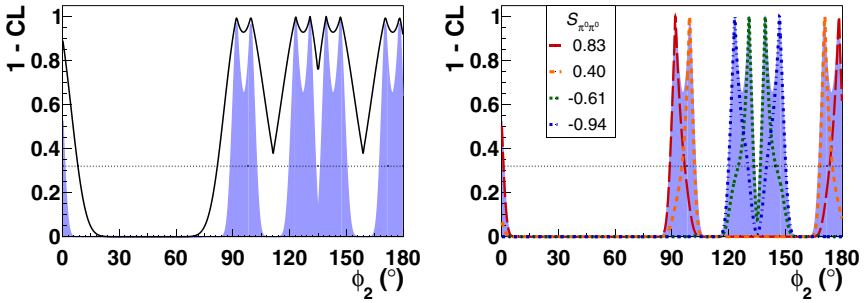

Fig. 116. Scan of the confidence for ϕ_2 performing isospin analysis of the $B \to \pi\pi$ system. (Left): The black solid line shows the result of the scan using data from Belle measurements (see Table 91). The blue shaded area in both plots shows the projection for Belle II. (Right): Results of the scan adding the $S_{\pi^0\pi^0}$ constraint. Each line shows the result for a different $S_{\pi^0\pi^0}$ value. The dotted horizontal lines correspond to $1\,\sigma$.

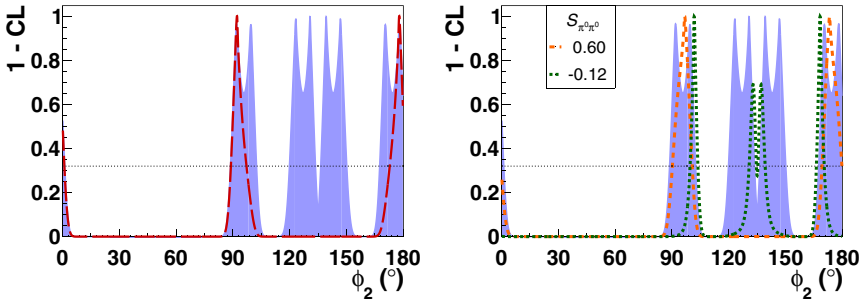

Fig. 117. Scan of the confidence for ϕ_2 performing isospin analysis of the $B \to \pi\pi$ system. The blue shaded area in both plots shows the projection of the Belle measurements (see Fig. 116) for Belle II. Results of the scan with additional $S_{\pi^0\pi^0}$ constraints are shown by dashed lines. Each line correspond to different input $S_{\pi^0\pi^0}$ values. The red long dashed line on the left figure shows the result for $S_{\pi^0\pi^0} = 0.83$. The dotted horizontal line correspond to $1\,\sigma$.

Figure 118 (left) shows the results of the scan of the confidence for the ϕ_2 angle performing the isospin analysis of $B \to \rho\rho$. The analysis was performed using the current Belle measurements without the $S_{\rho^0\rho^0}$ constraint. The results of the scan are consistent with the Belle results presented in Fig. 7 of Ref. [729]. Since the $B \to \rho\rho$ system exhibits a twofold ambiguity, we focus on the range which is consistent with the current measurements of the unitarity triangle. Figure 118 (left) also shows projections for Belle II without and with the $S_{\rho^0\rho^0}$ constraint. The measurements and the projections are summarized in Table 92. The estimated sensitivity for Belle II at the $1\,\sigma$ level without the $S_{\rho^0\rho^0}$ constraint is found to be about $\Delta\phi_2 \sim 1°$. For the case with the $S_{\rho^0\rho^0}$ constraint, an estimation was performed using the central value $S_{\rho^0\rho^0} = -0.14$. This value was chosen such that the solutions of the scan using this value are compatible with the solutions of the scan performed without the $S_{\rho^0\rho^0}$ constraint. The improvement with $S_{\rho^0\rho^0}$ at the $1\,\sigma$ level is about one third: $\Delta\phi_2 \sim 0.7°$.

Figure 118 (right) shows the results of the scan of the confidence for ϕ_2 combining the isospin analyses of $B \to \pi\pi$ and $B \to \rho\rho$. In order to have consistent central values of the input parameters for the study of the Belle II sensitivity, the value of $\mathcal{B}_{\pi^0\pi^0}$ was adjusted to be $1.27 \cdot 10^{-6}$. This adjustment, which is within $1\,\sigma$ of the measured value (see Table 91), ensures that the solutions of the isospin analyses of $B \to \pi\pi$ and $B \to \rho\rho$ correspond to the same true value of ϕ_2. The ϕ_2 scan using current Belle measurements was performed without S_{00} constraints. The projections for Belle II were performed for both cases, without and with S_{00} constraints. For the former case,

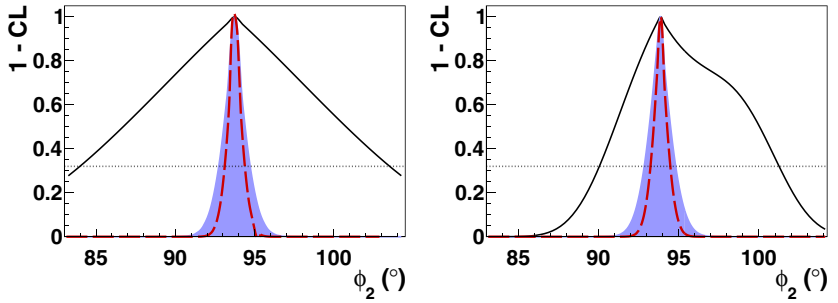

Fig. 118. Scans of the confidence for ϕ_2 performing an isospin analysis of the $B \to \rho\rho$ system (left) and combining the isospin analyses of the $B \to \pi\pi$ and the $B \to \rho\rho$ systems (right). The black solid lines show the results of the scans using data from measurements at the current precision (see Tables 92 and 91). The blue shaded areas show the projections for Belle II. The red long-dashed lines show the results of the scans adding the S_{00} constraints: $S_{\rho^0\rho^0} = -0.14$ and $S_{\pi^0\pi^0} = 0.75$. The dotted horizontal lines correspond to $1\,\sigma$.

the estimated sensitivity is found to be about $\Delta\phi_2 \sim 1°$. For the case with the S_{00} constraints, the analysis is performed with central values of $S_{\rho^0\rho^0}$ and $S_{\pi^0\pi^0}$ which are compatible in terms of ϕ_2 ($S_{\rho^0\rho^0} = -0.14$ and $S_{\pi^0\pi^0} = 0.75$). The improvement in the ϕ_2 precision at the $1\,\sigma$ level with the S_{00} constraints is about a factor of 2: from $\Delta\phi_2 \sim 1°$ to $\Delta\phi_2 \sim 0.6°$.

ϕ_2 from $B^0 \to \rho\pi$ The measurement of ϕ_2 from a Dalitz plot analysis of $B^0 \to \pi^+\pi^-\pi^0$ has been pioneered by Belle [718] and BaBar [717]. Both teams succeeded in extracting meaningful information about ϕ_2; however, BaBar performed some studies on the robustness of the extraction of ϕ_2 and discovered the existence of two *secondary solutions* on either side of the expected primary solution. These secondary solutions do not arise from ambiguities intrinsic in the method, but are rather artefacts that result from the limited statistics of the sample that was analyzed and are expected to vanish with significantly larger datasets.

This strongly motivates the repetition of the analysis at Belle II, with a data sample of at least a few ab^{-1}. The dominant background will arise from random combinations of particles arising from continuum events, and the model for the signal component will include the $\rho(770)$, $\rho(1450)$, and $\rho(1700)$ resonances.

For the reasons explained above, and due to the difficulty of realistically simulating the full Dalitz plot analysis using Monte Carlo, we do not provide any prediction of the sensitivity attainable by Belle II.

10.5. Time-dependent CP violation analysis of $B^0 \to K^0_S\pi^0(\gamma)$

10.5.1. Theory: Probing new physics with $B^0 \to K^0_S\pi^0\gamma$

Contributing authors: F. Bishara, A. Tayduganov

The radiative loop $b \to s\gamma$ processes have been extensively studied as a probe of NP beyond the SM. In the SM $b_L \to s_R\gamma_R$ is m_s/m_b suppressed compared to $b_R \to s_L\gamma_L$, if QCD interactions are switched off. In order to use this as a probe of NP it is important to estimate reliably the QCD corrections to these expectations. We review the current status below.

The short-distance contributions to $b \to s\gamma$ are given by

$$\mathcal{O}_7^{(\prime)} = \frac{e}{16\pi^2} m_b \bar{s}_{L(R)} \sigma^{\mu\nu} b_{R(L)} F_{\mu\nu} \tag{328}$$

in the effective weak Hamiltonian. The operator $\mathcal{O}_7$ describes the $b_R \to s_L\gamma_L$, while $\mathcal{O}'_7$ describes the $b_L \to s_R\gamma_R$ process. Due to chiral suppression, in the SM $C'_7/C_7 \approx m_s/m_b$. The $b \to s\gamma$ also receives long-distance contributions, most notably from the "charm loop" contributions from insertion of $\mathcal{O}^c_{1,2}$ operators.

We focus on the $B \to K^*\gamma$ decay. An analysis of $1/m_b$ expansion based on the soft collinear effective theory (SCET) in Refs. [506,731] shows that the right-handed helicity amplitude is suppressed. The largest contribution is expected to come from the $\mathcal{O}_2 = (\bar{s}_L\gamma_\mu c_L)(\bar{c}_L\gamma^\mu b_L)$ operator, giving a parametric estimate:

$$\frac{\mathcal{M}(\bar{B} \to \bar{K}^*\gamma_R)}{\mathcal{M}(\bar{B} \to \bar{K}^*\gamma_L)} \sim \frac{(C_2/3)}{C_7}\frac{\Lambda_{\rm QCD}}{m_b} \sim 10\%. \tag{329}$$

The numerical value was obtained using naive dimensional analysis for the relevant matrix element.

A light cone sum rule based assessment of the matrix element shows, however, that this is further suppressed [491,507] (for previous works see Refs. [490,511,732]). The matrix element $\mathcal{M}(\bar{B} \to \bar{K}^*\gamma_R)$ receives two types of contributions. The $m_b \to \infty$ contribution is perturbatively calculable and is $\mathcal{O}(m_s/m_b)$ suppressed compared to $\mathcal{M}(\bar{B} \to \bar{K}^*\gamma_L)$. The contributions to $\mathcal{M}(\bar{B} \to \bar{K}^*\gamma_L)$ from hard collinear gluon exchanges vanish, while the contributions from soft gluons are $1/m_b$ suppressed. This gives the estimate

$$\frac{\mathcal{M}(\bar{B} \to \bar{K}^*\gamma_R)}{\mathcal{M}(\bar{B} \to \bar{K}^*\gamma_L)} \sim \frac{(C_2/3)}{C_7}\frac{\Lambda^2_{\rm QCD}}{m_b^2} \sim \text{few}\%. \tag{330}$$

In conclusion, the charm loop effect could entail a theoretical uncertainty $\sim(2 \div 10)\%$ on the ratio of the right-handed polarization amplitude over the left-handed one, though most likely on the lower end of this range. The NP effects can be clearly established only if the deviation from the SM is sufficiently large.

One way to measure the photon polarization is to study the time-dependent CP asymmetry in the radiative decays of the neutral B mesons into the final hadronic self-conjugate state $f_{\rm CP}$ [502]. The asymmetry arises from the interference between the $B \to f_{\rm CP}\gamma$ and $B \to \bar{B} \to f_{\rm CP}\gamma$ amplitudes (and similarly for CP conjugated decays). Since the $B(\bar{B})$ meson decays predominantly into a photon with right- (left-)handed helicity, the dominant amplitudes are $B \to f_{\rm CP}\gamma_R$ and $B \to \bar{B} \to f_{\rm CP}\gamma_L$, which cannot interfere. In the SM the time-dependent asymmetry is thus generated by suppressed amplitudes, of order $\mathcal{O}(m_s/m_b)$ or $\mathcal{O}(\Lambda^2/m_b^2)$, as discussed above. NP can induce a much larger contribution to the "wrong" helicity amplitudes, inducing a larger time-dependent CP asymmetry.

For the radiative decay $B(t) \to f_{\rm CP}\gamma$, neglecting direct CP violation and the small width difference between two B mesons,[30] the CP asymmetry is given by [502]

$$\mathcal{A}_{\rm CP}(t) \equiv \frac{\Gamma(\bar{B}(t) \to f_{\rm CP}\gamma) - \Gamma(B(t) \to f_{\rm CP}\gamma)}{\Gamma(\bar{B}(t) \to f_{\rm CP}\gamma) + \Gamma(B(t) \to f_{\rm CP}\gamma)} \approx S_{f_{\rm CP}\gamma}\sin(\Delta m t), \tag{331}$$

with

$$S_{f_{\rm CP}\gamma} \equiv \eta_f \frac{2{\rm Im}[e^{-i2\phi_1}\,\mathcal{M}_L\mathcal{M}_R]}{|\mathcal{M}_L|^2 + |\mathcal{M}_R|^2} \simeq \eta_f \frac{2{\rm Im}[e^{-i2\phi_1}\,C_7C'^*_7]}{|C_7|^2 + |C'_7|^2}, \tag{332}$$

[30] Non-negligible width difference $\Delta\Gamma_s$ in B_s mesons leads to one more measurable quantity proportional to $\sinh(\Delta\Gamma t/2)$, also sensitive to the right-handed currents (see, e.g., Ref. [503]).

where $\mathcal{M}_{L(R)}$ are the amplitudes of $\bar{B} \to f_{\rm CP}\gamma_{L(R)}$, $\eta_f = \pm 1$ is the CP eigenvalue of $f_{\rm CP}$, and ϕ_1 the phase in B–$\overline{B}$ mixing. The measurement of $\mathcal{A}_{\rm CP}(t)$ allows us to determine the ratio of two amplitudes $\mathcal{M}_{L,R}$ together with the CP-violating phase ϕ_1, but not each of them separately.

The decay $B \to K^*(\to K^0_S\pi^0)\gamma$ has the largest branching fraction and hence has the largest potential for the time-dependent CP asymmetry search. The SM prediction for this asymmetry is [494]

$$S^{\rm SM}_{K^0_S\pi^0\gamma} \sim -2\frac{m_s}{m_b}\sin 2\phi_1 = -(2.3 \pm 1.6)\%, \tag{333}$$

which is to be compared with the current world average [230]

$$S^{\rm exp}_{K^0_S\pi^0\gamma} = -0.16 \pm 0.22. \tag{334}$$

Another method to search for the non-SM right-handed photon is to use $B \to K^*(\to K^+\pi^-)\gamma$ events with $\gamma \to e^+e^-$ conversions that occur in the detector [596]. If the photon helicity is mixed, the photon has an elliptical polarization (or linear polarization if the size of the left- and right-handed amplitudes are the same). Interference between the intermediate on-shell photon polarizations produces oscillations in the angular kinematic observable ψ (the relative twist between the e^+e^- conversion plane and the K–π decay plane) [516]. Measuring the amplitude and phase of these oscillations, or equivalently two quadrant-type asymmetries, would permit extraction of the absolute value and the relative weak phase of the polarization amplitudes ratio $\mathcal{M}_R/\mathcal{M}_L$.

This method requires high angular resolution in order to reconstruct the lepton kinematics after conversion. Moreover, a detector whose thickness is of the order of one radiation length or less is required to avoid multiple leptonic rescattering. All of the above makes this approach experimentally challenging.

10.5.2. Experiment: Sensitivity study of the time-dependent CP asymmetries in $B^0 \to K^0_S\pi^0\gamma$

Contributing author: A. Martini

In this section we use the Belle II simulation to estimate the sensitivity for measuring the time-dependent CP asymmetry on the $B^0 \to K^0_S\pi^0\gamma$ decay:

$$\wp(\Delta t) = \frac{\exp\left\{-\frac{\Delta t}{\tau_{B^0}}\right\}}{4\tau_{B^0}}(1 \pm S_{K^0_S\pi^0\gamma}\sin(\Delta m\Delta t) \pm A_{K^0_S\pi^0\gamma}\cos(\Delta m\Delta t)). \tag{335}$$

The experimental results from BaBar and Belle on the CP violation parameters are, respectively, $S_{K^0_S\pi^0\gamma} = -0.78\pm0.59\pm0.09, A_{K^0_S\pi^0\gamma} = 0.36\pm0.33\pm0.04$ [733] and $S_{K^0_S\pi^0\gamma} = -0.10\pm0.31\pm0.07$, $A_{K^0_S\pi^0\gamma} = -0.20 \pm 0.20 \pm 0.06$ [519], all of which are still dominated by statistical errors.

We focus in particular on the reconstruction of the signal-side B decay (B^0_{sig}) and on evaluating the Δt resolution using a constraint on the beam spot size. Refined event selection strategies and the impact of beam backgrounds are not considered in this study.

Signal reconstruction A Monte Carlo sample containing 10^4 $B^0_{sig} \to K^0_S\pi^0\gamma$ decays, with the decay of the other B meson in the event (B^0_{tag}) undergoing a generic decay, has been generated and reconstructed. No beam background has been added to the simulation. To avoid effects due to possible incorrect assignment in the reconstruction of the intermediate resonances, all reconstructed particles are matched to the generated ones by using Monte Carlo truth information.

Table 93. Selection criteria for photon candidates in $B \to K^0_S \pi^0 \gamma$ reconstruction.

Detector region	Forward	Barrel	Backward
Energy (MeV)	>103	>97	>72
$E9/E25$	>0.80	>0.78	>0.71
minC2Hdist (cm)	55	36	49

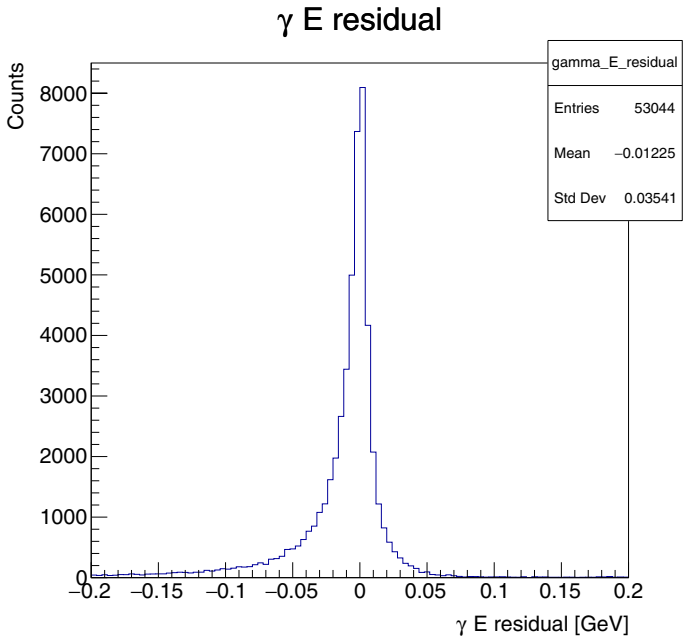

Fig. 119. Momentum residual distribution of all photons reconstructed in the events.

Photons are selected using four different variables, with the selection criteria listed in Table 93. The $E9/E25$ variable is the ratio of deposited energies in the 3×3 and the 5×5 calorimeter cell blocks, while "minC2Hdist" is the minimum distance between the photon's estimated position and the closest track. Figure 119 shows the residuals of the momentum distribution of all the photons in the event. The long negative tail is due to calorimeter leakages and to interactions of photons with material in front of the calorimeter.

Neutral pions are reconstructed through the decay $\pi^0 \to \gamma\gamma$, with the invariant mass of the photon pair in the range [110, 150] MeV. A kinematic mass fit, requiring a p-value $> 1‰$ (this is supposed to retain 99.9% of the true π^0 candidates) is then performed. The residuals distribution of the π^0 mass is shown in Fig. 120 (left plot). The residuals are slightly negatively biased and the σ value of the pull distribution (not shown here) is significantly larger than 1. This is due to a non-optimized selection of photons, which will be improved with the next versions of the reconstruction algorithms.

The reconstruction of K^0_S is one of the crucial points of this analysis, because this is practically the only source of information to determine the vertex position of $B^0_{\rm sig}$. For this reason K^0_Ss are reconstructed only through the decay into charged pions $K^0_S \to \pi^+\pi^-$. Kaon candidates are selected in the invariant mass range between 400 MeV and 600 MeV; a vertex fit with a p-value greater than

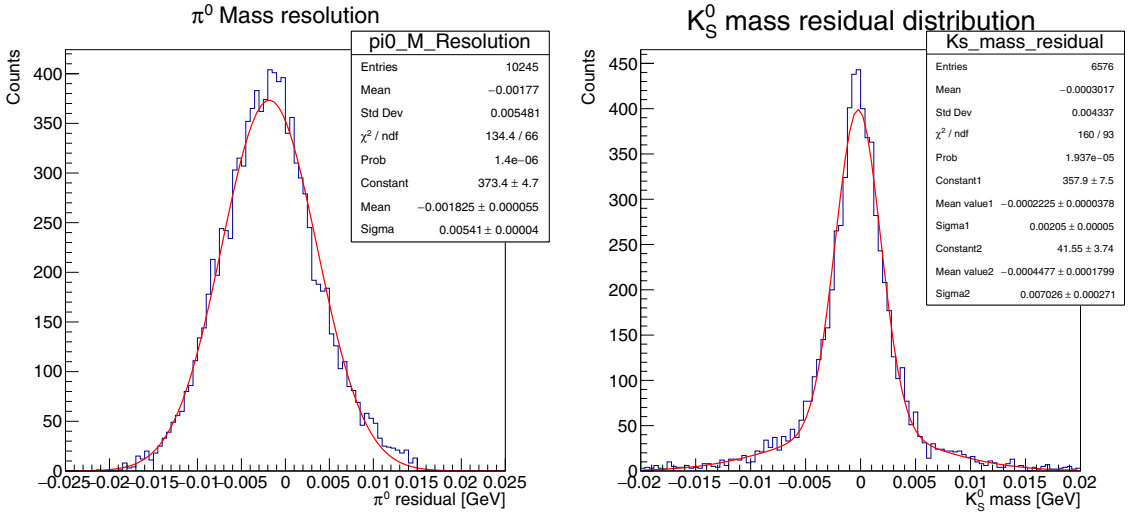

Fig. 120. Residuals of the reconstructed mass for the π^0 (left) and K^0_S (right) candidates.

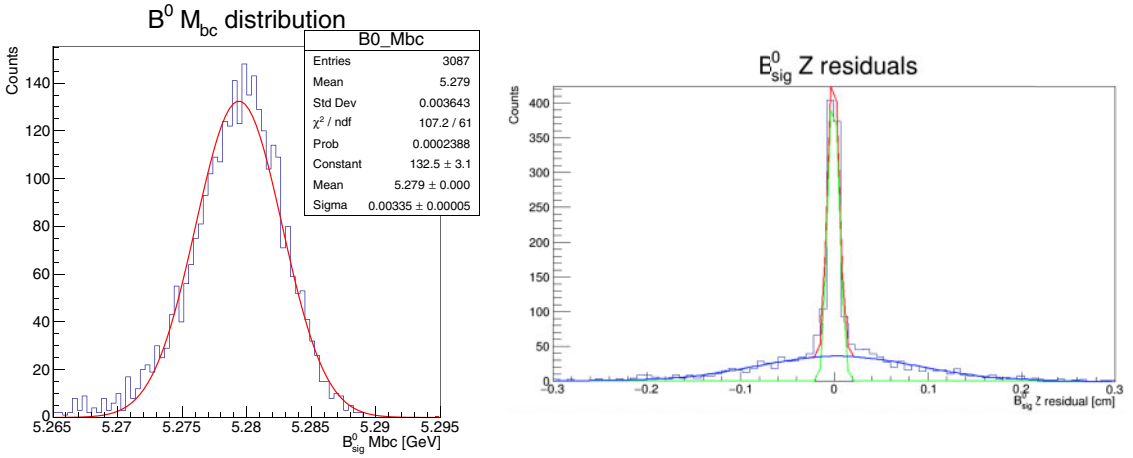

Fig. 121. Top: $M_{\rm bc}$ distribution of $B^0_{\rm sig}$, fitted with a single Gaussian giving $\sigma \sim 3.3$ MeV mass resolution. Bottom: Residual distribution of the $B^0_{\rm sig}$ vertex. The resolution provided by the core and the tail Gaussian are respectively $\sim$58 μm and $\sim$850 μm.

1‰ is subsequently performed. The residuals distribution of the K^0_S mass is shown in Fig. 120 (right).

The $B^0_{\rm sig}$ is reconstructed by requiring its mass to be between 5.0 GeV and 5.5 GeV and performing a vertex fit demanding a p-value >1‰. The K^0_S flight direction is extrapolated backwards and matched to the estimated region in which the e^+e^- collisions take place. Given the non-negligible flight length of the B^0 candidates, and to avoid any biases in the time-dependent analysis, the beam spot constraint is applied only in the plane perpendicular to the boost direction, hence the name *iptube* constraint. The ellipsoid in the transverse plane has semi-axes $\sigma_x \approx 6$ μm and $\sigma_y \approx 42$ nm.

The $M_{\rm bc}$ (beam-constrained mass) distribution and the $B^0_{\rm sig}$ vertex residual distribution are reported in Fig. 121 (upper plot).

The distribution of the $B^0_{\rm sig}$ vertex position along the boost axis (lower plot of Fig. 121) is fitted with a combination of two Gaussians with two very different widths. This is dominated by the resolution

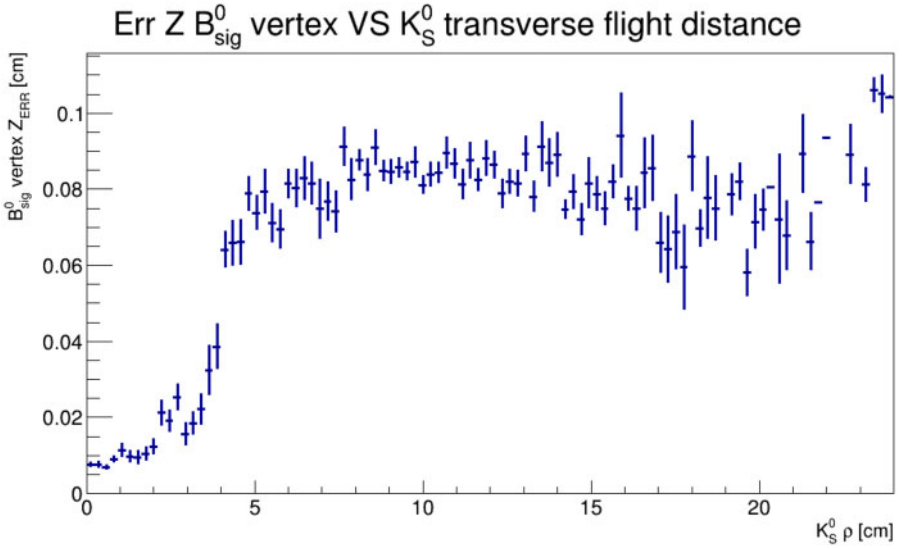

Fig. 122. Profile plot of the errors on the z coordinate of the $B^0_{\rm sig}$ vertex versus the $K^0_{\rm S}$ transverse flight distance (ρ). $K^0_{\rm S}$s decaying within the PXD volume have a significantly better resolution.

Table 94. Reconstruction efficiencies of particles involved in the decay of $B^0_{\rm sig}$ (with the current version of the Belle II software).

	$K^0_{\rm S}$	π^0	γ	B^0
$\varepsilon^{\rm reco}$	58.6%	53.7%	83.4%	26.2%

of the reconstruction of charged tracks. Kaons that decay outside the SVD (transverse flight distance $\rho > 3.8$ cm) are reconstructed from charged pions that are only seen by the CDC. Without SVD hit information, the precision on the $K^0_{\rm S}$ vertices becomes significantly worse. The profile plot in Fig. 122 shows the error on the $B^0_{\rm sig}$ vertex position with respect to the $K^0_{\rm S}$ transverse flight distance (radius ρ).

The step at around 3.8 cm is visible, while there is no transition at 16 cm, corresponding to the inner radius of the CDC. This is due to the fact that the tracking algorithms are still under development (we expect an improvement for $K^0_{\rm S}$s decaying within the SVD volume).

The other contribution to the uncertainty in Δt measurement comes from the $B^0_{\rm tag}$ vertex determination, which uses the standard algorithm that is common to the other time-dependent analyses. The resolution of the $B^0_{\rm tag}$ vertex position along the boost axis is $\sim$42 μm.

Efficiency studies The reconstruction efficiency was studied using a Monte Carlo sample in which $B^0_{\rm sig}$ is forced to decay to the $K^0_{\rm S}\pi^0\gamma$ final state, while $B^0_{\rm tag}$ decays to a $\nu\bar{\nu}$ pair. In this way any cross-feed between the two B meson decays is avoided.

The efficiencies obtained are summarized in Table 94.

Δt resolution The distance of the $B^0_{\rm sig}$ and $B^0_{\rm tag}$ decay vertices along the boost direction (Δz) is related (with very good approximation) to Δt via the formula $\Delta z = \beta\gamma c\Delta t$, with β and γ characterizing the Lorentz boost of the $\Upsilon(4S)$ in the laboratory system. The Δt resolution is measured from the residual distribution shown in Fig. 123. The distribution is fitted with the sum of two

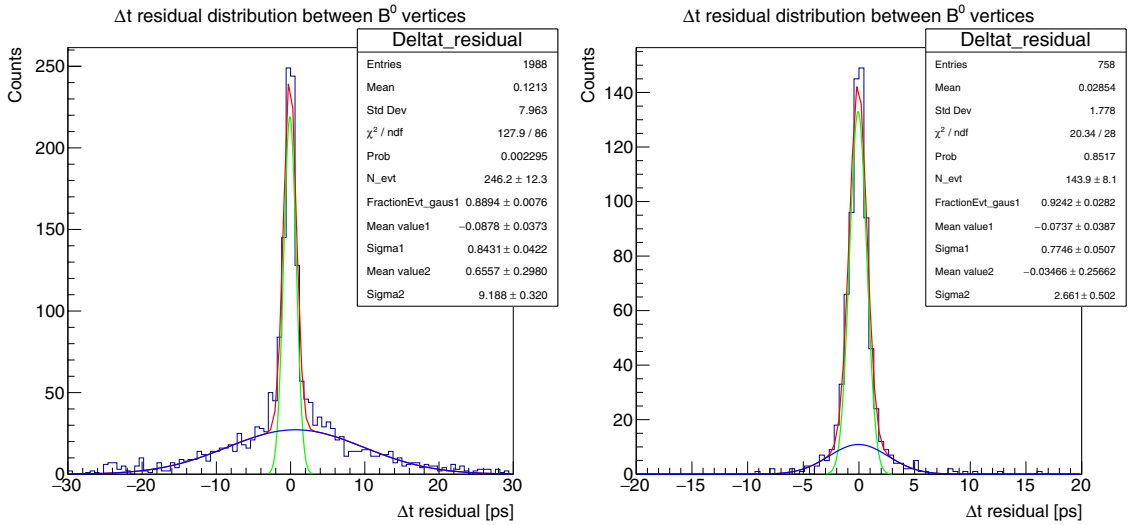

Fig. 123. Δt residual distribution for $B \to K^0_S \pi^0 \gamma$ without (left) and with (right) SVD hit requirements.

Table 95. Sensitivity estimation on the S and A parameters at different values of integrated luminosity.

Integrated Luminosity (ab^{-1})	Stat. (S)	Stat. (A)
2	0.15	0.10
10	0.07	0.05
50	0.031	0.021

Gaussians where the narrow Gaussian (core) has $\sigma \approx 0.84$ ps while the wide one (tail Gaussian) has $\sigma \approx 9.2$ ps. The wide component can be suppressed by imposing that both the pions coming from K^0_S have at least one SVD hit associated to their tracks. The Δt residual distribution relative to the new sample of K^0_S is shown in Fig. 123.

The results show a significant improvement, but by selecting only the sub-samples of K^0_S with better resolution we can use only ∼35% of the events. The resolution values are ∼0.77 ps (from the core Gaussian) and ∼2.66 ps (from the tail Gaussian). Requiring $M_{K\pi} < 1.8$ GeV (the region in which the SCET framework can provide reliable predictions), the statistic drops by a further factor of ∼6, but the residual distribution does not change significantly. Considering the resolution as the weighted average of the two σ values, we obtain an average of ∼0.94 ps.

Sensitivity studies An estimate of the sensitivity of Belle II on the CP violation parameters S and A is obtained using a study based on pseudo-experiments, in which the expected Δt resolution is used. The results, reported in Table 95, are very promising, especially considering that significant improvements are expected in the reconstruction software. On the other hand, the impact of physics and beam backgrounds still needs to be estimated.

Extrapolation of the $K^0_S \pi^0$ sensitivity We estimate the sensitivity to the $S_{K^0_S \pi^0}$ and $A_{K^0_S \pi^0}$ parameters of the $K^0_S \pi^0$ mode analogously to Sect. 10.3.2. The vertex reconstruction position resolution is taken from the study of $K^0_S \pi^0 \gamma$ presented above, and we assume a reconstruction efficiency of 30%, based on the performance of BaBar and Belle. The results are presented in Table 96.

Table 96. Extrapolated sensitivity for the $K^0_S\pi^0$ mode. The Δt resolution is taken from the $K^0_S\pi^0\gamma$ study and we assume for this mode a reconstruction efficiency of 30%.

Channel	Yield	$\sigma(S)$	$\sigma(A)$
$1\,\text{ab}^{-1}$			
$K^0_S(\pi^\pm)\pi^0$	1140	0.20	0.13
$5\,\text{ab}^{-1}$			
$K^0_S(\pi^\pm)\pi^0$	5699	0.09	0.06

Table 97. Expected uncertainties on the S and A parameters for the channels sensitive to $\sin 2\phi_1$ discussed in this chapter for an integrated luminosity of 5 and $50\,\text{ab}^{-1}$. The present (2017) world average [230] errors are also reported.

	WA (2017)		$5\,\text{ab}^{-1}$		$50\,\text{ab}^{-1}$	
Channel	$\sigma(S)$	$\sigma(A)$	$\sigma(S)$	$\sigma(A)$	$\sigma(S)$	$\sigma(A)$
$J/\psi K^0$	0.022	0.021	0.012	0.011	0.0052	0.0090
ϕK^0	0.12	0.14	0.048	0.035	0.020	0.011
$\eta' K^0$	0.06	0.04	0.032	0.020	0.015	0.008
ωK^0_S	0.21	0.14	0.08	0.06	0.024	0.020
$K^0_S\pi^0\gamma$	0.20	0.12	0.10	0.07	0.031	0.021
$K^0_S\pi^0$	0.17	0.10	0.09	0.06	0.028	0.018

10.6. Conclusions

We summarize in Table 97 the expected uncertainties to the S and A CP-violating parameters in the channels sensitive to $\sin 2\phi_1$ discussed in this chapter. For the $J/\psi K^0$ mode, we provide the estimate, dominated by systematic uncertainties, for the full $50\,\text{ab}^{-1}$ dataset. For the penguin-dominated modes the estimates are based on an integrated luminosity of $5\,\text{ab}^{-1}$, for which we can safely assume that all the channels will still be dominated by the statistical uncertainties and that the assumptions on which the current studies are based are valid. In the fifth and last columns of Table 97 we also report the present HFLAV world average (WA) errors on each of the observables. For most of the penguin-dominated modes Belle II is projected to reduce the WA errors by a factor of 2–3 already with $5\,\text{ab}^{-1}$.

We projected the uncertainty on the determination of ϕ_2 considering the isospin analyses of $B \to \pi\pi$ and $B \to \rho\rho$. The $B \to \rho\pi$ system, which is usually considered together with $B \to \pi\pi$ and $B \to \rho\rho$, was not taken into account due to the difficulty of realistically simulating the full Dalitz plot analysis of $B^0 \to \pi^+\pi^-\pi^0$ in MC. The expected uncertainties on ϕ_2 extracted via isospin analysis of $B \to \pi\pi$ and $B \to \rho\rho$ and via combined isospin analysis of these two decay systems are summarized in Table 98. The projections of the experimental errors and the central values of previous measurements that enter the isospin analysis of $B \to \pi\pi$ and $B \to \rho\rho$ are presented in Tables 91 and 92, respectively. Additionally, we performed a feasibility study for the novel time-dependent CP analysis of the decay $B \to \pi^0\pi^0$. The uncertainty on the measurement of the time-dependent asymmetry $S_{\pi^0\pi^0}$ is estimated to be $\Delta S_{\pi^0\pi^0} = \pm 0.28 \pm 0.03$. Consequently, the current eightfold ambiguity in the determination of ϕ_2 performing the isospin analysis of $B \to \pi\pi$ will be reduced by factor of four (see Fig. 116). It is also possible that the values of ϕ_2 extracted from the isospin analysis including $S_{\pi^0\pi^0}$ have a tension to the values expected within the SM (see Fig. 117). The

Table 98. Current world average error [650] and expected uncertainties on the determination of ϕ_2 performing isospin analyses of the decay systems $B \to \pi\pi$ and $B \to \rho\rho$ together with a combined isospin analysis of these two systems. For the current world average error, the decay system $B \to \rho\pi$ was also considered.

Channel	$\Delta\phi_2$ [°]
Current world average	$^{+4.4}_{-4.0}$
$B \to \pi\pi$	2.0
$B \to \rho\rho$	0.7
$B \to \pi\pi$ and $B \to \rho\rho$ combined	0.6

Table 99. Summary of the current and expected sensitivities on the CKM angles ϕ_1 and ϕ_2. As explained in the text, theoretical uncertainties based on data-driven techniques (e.g. those releted to EWP amplitudes in the determination of ϕ_2) can be given only with a large degree of uncertainty.

	Current	50 ab^{-1} projection
ϕ_1:		
Experimental	0.7°	0.2°
Theoretical: QCDF and pQCD	0.1°	0.1°
Theoretical: SU(3)	1.7°	0.8°
ϕ_2:		
Experimental	4.2°	0.6°
Theoretical	1.2°	$< 1.0°$

sensitivity study of $B \to \pi^0\pi^0$ and the projections of previous measurements were performed for a total Belle II integrated luminosity of 50 ab^{-1}. So far, we did not consider isospin-breaking effects on the projection of the sensitivity to ϕ_2. Possible ways to extract the size of the bias in ϕ_2 due to isospin-breaking effects were discussed in Sect. 10.4. At present, isospin-breaking effects can be only partially included. In principle there are observables where the theoretical error is only of second order in isospin breaking and thus below the permille level. However, it may be impossible to measure them to the required level of accuracy.

Finally, Table 99 summarizes the current and expected experimental and theoretical uncertainties on the CKM angles ϕ_1 and ϕ_2. We should stress once more that, as explained above, the theoretical uncertainties based on data-driven techniques cannot be precisely estimated at this stage.

11. Determination of the UT angle ϕ_3

Editors: M. Blanke, Y. Grossman, J. Libby
Additional section writers: J. Brod, G. Tetlalmatzi-Xolocotzi, I. Watson, J. Zupan

11.1. Introduction

This working group is dedicated to examining the Belle II potential to determine the unitarity triangle angle ϕ_3 (also denoted as γ), defined as

$$\phi_3 \equiv -\arg\left(V_{ub}^* V_{ud} / V_{cb}^* V_{cd}\right), \tag{336}$$

Table 100. Methods and D decay modes used in $B^- \to DK^-$ and $B^- \to D^*K^-$ measurements. Those in parentheses have not been published by Belle.

Type of D decay	Method	D final states studied
CP eigenstates	GLW	CP-even: K^+K^-, $\pi^+\pi^-$; CP-odd: $K^0_S\pi^0$, $K^0_S\eta$
CF and DCS	ADS	$K^\pm\pi^\mp$, $K^\pm\pi^\mp\pi^0$, $(K^\pm\pi^\mp\pi^+\pi^-)$
Self-conjugate	GGSZ	$K^0_S\pi^+\pi^-$, $(K^0_SK^+K^-)$, $(\pi^+\pi^-\pi^0)$, $(K^+K^-\pi^0)$, $(\pi^+\pi^-\pi^+\pi^-)$
SCS	GLS	$(K^0_SK^\pm\pi^\mp)$

in $B \to DK$, $B \to D\pi$, and related modes. In general, when we talk about $B \to DK$ we refer to a family of related decays like B^- decay into DK, D^*K, DK^*, and D^*K^*, as well as multi-body decays, as they are all sensitive to ϕ_3 as well. Only the hadronic part of the amplitude is different.

The key feature of $B \to DK$ decays is that they arise solely from the interference of tree-level diagrams of differing weak and strong phases. No B mixing or penguin amplitudes are involved. Here, D represents a general superposition of D^0 and $\overline{D}^0$. The tree-level nature of the amplitudes involved in $B \to DK$ allows the theoretically clean extraction of ϕ_3. Clearly, improved knowledge of the unitarity triangle angle ϕ_3 is very useful to further test the SM. The current precision on ϕ_3 is an order of magnitude worse than that on ϕ_1 [77] and it is the only measurement of the unitarity triangle that can be improved significantly by experimental advances alone.

We move to a very brief discussion of the main idea. Sensitivity to ϕ_3 can be obtained by studying CP-violating observables in $B \to DK^-$ decays. There are two tree amplitudes contributing to $B^- \to DK^-$ decays: $B^- \to D^0K^-$ and $B^- \to \overline{D}^0K^-$. The amplitude for the second decay is both CKM and color suppressed with respect to that for the first. The ratio of the suppressed to favored amplitudes is written as

$$\frac{A(B^- \to \overline{D}^0K^-)}{A(B^- \to D^0K^-)} = r_Be^{i(\delta_B-\phi_3)}, \tag{337}$$

where $r_B \approx 0.1$ is the ratio of magnitudes and δ_B is the strong phase difference. The fact that the hadronic parameters r_B and δ_B can be determined from data together with ϕ_3 makes these measurements essentially free of theoretical uncertainties.

Several different types of D decay are utilized to determine ϕ_3. Examples of D decays include CP eigenstates, proposed by Gronau, London, and Wyler [734,735], Cabibbo-favored (CF) and doubly Cabibbo-suppressed (DCS) decays, proposed by Atwood, Dunietz, and Soni [736,737], self-conjugate modes, proposed by Giri, Grossman, Soffer, and Zupan [738], and singly Cabibbo-suppressed (SCS) decays, proposed by Grossman, Ligeti, and Soffer [739]. The different methods are known by their proponents' initials, as shown in Table 100, along with the D final states that have so far been studied. Note that $K^0_S\phi$ has also been included in early GLW measurements but has been dropped from more recent analyses given that the same data forms part of the $K^0_SK^+K^-$ sample, which can be studied with the GGSZ method.

The remainder of this chapter is structured as follows. In Sects. 11.2 and 11.3 the theoretical limits on the accuracy of the measurements of ϕ_3 and the scope for new physics to appear in these measurements is discussed, respectively. Section 11.4 provides a snapshot of the latest Belle II sensitivity studies related to ϕ_3. In Sect. 11.5 we review the charm decay measurements that are

required to reach the ultimate precision. Section 11.6 compares the current and future sensitivity of LHCb to that of Belle II, before the outlook and conclusions are given in Sect. 11.7.

11.2. The ultimate precision

In the original formulations of the methods for extracting ϕ_3 from $B^- \to DK^-$ and $B_d \to DK^0_S$, the small effects due to D–$\bar{D}$ and K–$\bar{K}$ mixing, as well as due to CP violation in the D and K sectors, were neglected. Several studies of the impact of mixing and direct CP violation in charm decays have been made since then [740–749]. These studies show that ϕ_3 can be extracted without bias as long as appropriate modifications of the formalism are made and the measured values of the mixing and direct CP violation parameters are included as external inputs. Even if the effect of mixing is neglected, the size of the induced bias is less than 1° [748]. The inclusion of direct CP violation in D decays does require that at least one decay mode has no direct CP violation. This breaks the phase shift reparameterization symmetry which would otherwise prevent the model-independent determination of ϕ_3 [745]. It is expected that Cabibbo-allowed D decays have vanishingly small direct CP asymmetry, a fact that can be checked experimentally.

Measurements of ϕ_3 can also be made using the $B^- \to D\pi^-$ decay mode, which has sensitivity to ϕ_3 in the same manner as $B^- \to DK^-$. However, the size of the direct CP asymmetry is much smaller due to the ratio r_B of the suppressed to favored amplitudes being very small, approximately 0.005. The reduced sensitivity due to the smaller interference is compensated to some degree by the much larger branching fraction for $B^- \to D\pi^-$ compared to $B^- \to DK^-$ [77]. D mixing and direct CP violation must be accounted for carefully in $B^- \to D\pi^-$ measurements of ϕ_3 because the bias on the extracted value of ϕ_3 would be $\mathcal{O}(10°)$ otherwise [748].

For both the $B \to DK$ and the $B \to D\pi$ modes, the irreducible theoretical uncertainty is due to diagrams of higher order in the electroweak expansion. Second-order weak box diagrams have a dependence on the CKM parameters that differs from the tree diagrams. This can induce a shift, $\delta\phi_3$, in the extracted value of ϕ_3. An effective field theory calculation including a resummation of the large logarithms $\log(m_b/m_W)$ in the corrections to the Wilson coefficients gives $\delta\phi_3 \sim 2 \times 10^{-8}$ [750]. Long-distance contributions are at most a factor of a few larger than the calculated short-distance contribution. For $B \to DK$, the relative shift in ϕ_3 due to neglecting these weak box diagrams is $\lesssim 10^{-7}$ [750]. This is many orders of magnitude below the present experimental precision, as well as that anticipated at Belle II. The estimate of the analogous uncertainty for the extraction of ϕ_3 from $B \to D\pi$ decays suffers from a possible approximate cancellation in the leading term so that the relative shift can be up to $\delta\phi_3 < 10^{-4}$ [751]. More data can exclude the possibility of a large cancellation, so that the estimate of $\delta\phi_3$ can also be made more precise for the $B \to D\pi$ mode.

11.3. New physics in ϕ_3

The traditional way of testing for NP contributions to the angle ϕ_3 is to compare the value obtained from tree-level decays with the one obtained from penguin-dominated processes, and to look for deviations. This strategy relies on negligible NP contributions to SM tree-level processes.

Recent studies, however, have shown that, when state-of-the-art experimental measurements and theoretical determinations are taken into account, NP contributions of up to $\mathcal{O}(40\%)$ and $\mathcal{O}(20\%)$ to the tree-level Wilson coefficients C_1 and C_2 respectively are not excluded [752,753]. Allowing for general complex contributions $\Delta C_{1(2)}$ to the tree-level Wilson coefficients $C_{1(2)}$, and using that $|C_1(m_b)/C_2(m_b)| \approx 0.22$ and that $|\Delta C_1(m_b)/C_2(m_b)|$ and $|\Delta C_2(m_b)/C_2(m_b)|$ are small, Eq. (337)

should be modified according to

$$r_B e^{i(\delta_B-\phi_3)} \to r_B e^{i(\delta_B-\phi_3)} \cdot \left[1 + (r_{A'} - r_A)\frac{\Delta C_1}{C_2}\right], \tag{338}$$

with

$$r_{A(A')} = \frac{\langle \bar{D}^0 K^- | Q_1^{\bar{c}us}\left(Q_1^{\bar{u}cs}\right) | B^- \rangle}{\langle \bar{D}^0 K^- | Q_2^{\bar{c}us}\left(Q_2^{\bar{u}cs}\right) | B^- \rangle} \tag{339}$$

and

$$\begin{aligned} Q_1^{\bar{u}_1 u_2 d_1} &= (\bar{u}_1^\alpha b^\beta)_{V-A}(\bar{d}_1^\beta u_2^\alpha)_{V-A}, \\ Q_2^{\bar{u}_1 u_2 d_1} &= (\bar{u}_1^\alpha b^\alpha)_{V-A}(\bar{d}_1^\beta u_2^\beta)_{V-A}. \end{aligned} \tag{340}$$

Here, α, β are color indices and u_1, u_2 label the combinations of the up-type quarks u, c.

A fit to the semi-leptonic asymmetries $a_{\rm sl}^{d(s)}$, the B_s decay width difference $\Delta\Gamma_s$, the branching ratio for the process $B \to X_s\gamma$, and the total lifetime of B hadrons, as well as various observables associated with the hadronic decays $B \to \pi\pi$, $B \to \rho\rho$, $B \to \rho\pi$, $\bar{B}_d^0 \to D^{*+}\pi^-$, and $\bar{B}_d^0 \to D^{(*)0}h^0$ (with $h^0 = \pi^0, \eta, \omega$), such as indirect CP asymmetries and hadronic to semi-leptonic ratios, yields the allowed ranges for ΔC_1 and ΔC_2 quoted above (see Refs. [752] and [753] for details).

From Eq. (338) we can see that the shift in the CKM phase ϕ_3 is sensitive mainly to new complex weak phases in ΔC_1. The main impediment in evaluating the impact on ϕ_3 quantitatively is the unknown hadronic matrix elements in Eq. (338). Naive color counting gives $r_A \approx \mathcal{O}(1)$, $r_{A'} \approx \mathcal{O}(N_c = 3)$, while naive factorization yields

$$r_A \approx \frac{f_D F_0^{B\to K}(0)}{f_K F_0^{B\to D}} \approx 0.4. \tag{341}$$

There are large uncertainties in this determination, but it is unlikely that the two ratios r_A and $r_{A'}$ cancel accidentally. Using $r_A - r_{A'} \approx -0.6$ as a conservative (and rough) estimate, it follows that deviations in ϕ_3 of $\mathcal{O}(4°)$ are consistent with the current experimental constraints [753]. A more detailed statistical study leads to similar conclusions [754]. It also reveals how the shifts in ϕ_3 due to possible NP at tree level can be reduced if the theoretical and experimental status of different B-physics observables and hadronic parameters are improved, for instance the observable $\sin(2\beta)$, extracted from the transition $B \to J/\psi K_S^0$.

The possible deviations on ϕ_3 induced by NP at tree level are close to the current precision achieved in direct measurement. This result is a strong motivation for the 1° precision being pursued by Belle II, and for further study of the NP contributions and the associated theoretical uncertainties.

11.4. Belle II sensitivity study

In this section we summarize the status of the Belle II studies related to ϕ_3. Sections 11.4.1 to 11.4.3 report a preliminary study of the determination of ϕ_3 using the GGSZ analysis of $B^\pm \to [K_S^0\pi^+\pi^-]_D K^\pm$, which is the golden mode for Belle II. This study uses the Belle II simulation, though some aspects are not yet optimized. Section 11.4.4 then describes an extrapolation of the combination of the GGSZ measurements with the ADS and GLW measurements of $B \to D^{(*)}K$ based on Belle measurements to give an indication of the precision that can be reached by Belle II.

11.4.1. Model-independent Dalitz analysis overview

The $B^\pm \to DK^\pm$ mode using the GGSZ method was the most sensitive channel to ϕ_3 at Belle. Therefore, our initial efforts are concentrated on this decay. The sensitivity in this method arises when a D decays to a self-conjugate three-body final state that allows a comparison of the Dalitz plot for B^+ and B^- from which ϕ_3, r_B, and δ_B can be determined from a single decay [738,755]. This technique with $B^\pm \to [K^0_S\pi^+\pi^-]_D K^\pm$ has been seen to be the most sensitive single analysis at Belle because of the significant $D^0 \to K^0_S\pi^+\pi^-$ branching fraction of $(2.85 \pm 0.20)\%$ [77] and good K^0_S reconstruction efficiency. Therefore, we perform a sensitivity analysis in this mode to understand how the ϕ_3 measurement will evolve as a function of the amount of data collected at Belle II.

The decay rate for $B^\pm \to [K^0_S\pi^+\pi^-]_D K^\pm$ can be written as

$$\begin{aligned} d\Gamma_{B^-}(m^2_+, m^2_-) \propto\ & |A_+|^2 + r_B^2|A_-|^2 \\ & + 2r_B|A_+|\,|A_-|\,(\cos\delta_D\cos(\delta_B+\phi_3) - \sin\delta_D\sin(\delta_B+\phi_3))\,dp, \end{aligned} \tag{342}$$

where m^2_+ (m^2_-) is the invariant mass of the $K^0_S\pi^+$ ($K^0_S\pi^-$) from the D decay, $A_+ = A_D(m^2_+, m^2_-)$ and $A_- = A_D(m^2_-, m^2_+)$ are the D^0 and $\bar{D}^0$ decay amplitudes, δ_D is the phase difference between A_+ and A_-, δ_B is the phase difference between D^0 and $\bar{D}^0$ diagrams in the $B^- \to DK^-$ decay, and dp is an infinitesimal phase space element. Similarly, the B^+ decay is found by substituting $\phi_3 \leftrightarrow -\phi_3$ and $A_+ \leftrightarrow A_-$.

Thus, in order to measure ϕ_3 with these decays, we need to know the phase difference between $A_D(m^2_+, m^2_-)$ and $A_D(m^2_-, m^2_+)$ at each point in the Dalitz plot. This suggests that the strategy for the measurement is, first, to construct a model for $A_D(m^2_+, m^2_-)$. This can be done by reconstructing D mesons produced in the decay $D^{*\pm} \to D\pi^\pm$, which gives a known flavor state for the D. An amplitude model can be fitted to the flavor sample to determine $A_D(m^2_+, m^2_-)$. Then, one can use this model as input to fit a $B^\pm \to DK^\pm$ sample to the parameters r_B, δ_B, and ϕ_3. It has been found, though, that in order to eliminate bias due to the physical boundary $r_B = 0$, it is better to convert the physics parameters into Cartesian coordinates for the fit:

$$(x_\pm, y_\pm) = r_B(\cos(\delta_B \pm \phi_3), \sin(\delta_B \pm \phi_3)),$$

which can then be reinterpreted in terms of r_B, δ_B, and ϕ_3.

This method has been followed at previous experiments, for example in a Belle analysis for $B^\pm \to DK^\pm$ and $B^\pm \to D^*K^\pm$ [756]. The analysis found, however, that the amplitude model leads to a systematic uncertainty of 8.9° on ϕ_3. With the much larger data sample anticipated at Belle II, the statistical uncertainty on ϕ_3 will reduce below 1°. Therefore, a method which eliminates the model systematic uncertainty, replacing it with a model-independent uncertainty measured from data, has been proposed [738].

To remove the model dependency and obtain degree-level precision, a binned approach is used. The Dalitz plot is divided into $2N$ bins numbered $-N$ to N, excluding 0, where interchanging bin i with bin $-i$ corresponds to interchanging m^2_- with m^2_+. Further, we choose positive bins to lie in the region $m^2_- > m^2_+$. The binning used in the current analysis is shown in Fig. 124. The number of events expected in a given bin i can then be found by integrating the amplitude over the phase space $\mathcal{D}_i$ of the Dalitz bin. For the flavor Dalitz plot in $D^{*\pm} \to D\pi^\pm$ the number of events K_i is simply

$$K_i \propto \int_{\mathcal{D}_i} |A_+|^2 dp,$$

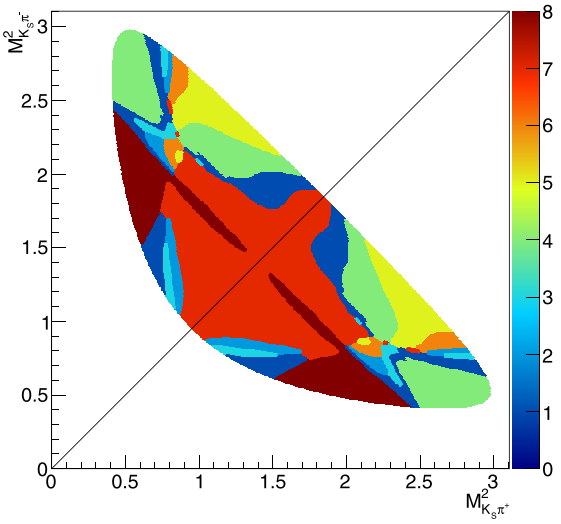

Fig. 124. Dalitz binning used for the $D \to K^0_S\pi^+\pi^-$ analyses.

where $\mathcal{D}_i$ indicates that the integration is over the ith bin. The values of K_i can be measured directly, then used as inputs to the $B^\pm \to DK^\pm$ analysis. The number of $B^+ \to DK^+$ events in each bin is given by

$$\begin{aligned} N_i^+ &\propto \int_{\mathcal{D}_i} |A_-|^2 + r_B^2|A_+|^2 + 2|A_+|\,|A_-|(x_+\cos\delta_D + y_+\sin\delta_D)dp, \\ &\propto K_{-i} + r_B^2 K_i + 2\sqrt{K_i K_{-i}}(x_+c_i - y_+s_i). \end{aligned}$$

Here, we introduced the amplitude-averaged phase variations over the Dalitz plot bins:

$$\begin{aligned} c_i = \quad c_{-i} &= \frac{\int_{\mathcal{D}_i} |A_+|\,|A_-|\cos\delta_D dp}{\sqrt{\int_{\mathcal{D}_i}|A_+|^2dp}\sqrt{\int_{\mathcal{D}_i}|A_-|^2dp}}, \\ s_i = -s_{-i} &= \frac{\int_{\mathcal{D}_i} |A_+|\,|A_-|\sin\delta_D dp}{\sqrt{\int_{\mathcal{D}_i}|A_+|^2dp}\sqrt{\int_{\mathcal{D}_i}|A_-|^2dp}}. \end{aligned}$$

A similar expression can be derived for the number of events N_i^- expected in $B^- \to DK^-$ with replacements as before. If we also explicitly split the positive and negative Dalitz bins, and introduce an overall normalization h_B, then the numbers of events expected in each of the Dalitz bins are given by

$$\begin{aligned} N_i^+ &\propto K_{-i} + r_B^2 K_i + 2\sqrt{K_i K_{-i}}(x_+c_i + y_+s_i), \\ N_i^- &\propto K_i + r_B^2 K_i + 2\sqrt{K_i K_{-i}}(x_-c_i - y_-s_i). \end{aligned} \tag{343}$$

This approach was used by Belle to measure ϕ_3 in $B^\pm \to DK^\pm$ [757] and $D \to K^0_S\pi^+\pi^-$, and by LHCb for $B^\pm \to DK^\pm$, $D \to K^0_S\pi^+\pi^-$, and $D \to K^0_S K^+K^-$ [758].

The phase difference parameters have been measured by CLEO-c from quantum-correlated $D\bar{D}$ decays of the $\psi(3770)$, which is discussed further in Sect. 11.5. The binning can be set to minimize the phase variation or to optimize sensitivity to ϕ_3 including information about the B decay yields by also taking into account the amplitude variation; the latter approach is adopted here. Setting the

binning based on these criteria requires a model in order to divide the Dalitz plot. However, a model dependency is not introduced by this procedure. Instead, if the model is incorrect, then the binning selected will simply not be optimal, since the direct measurement of the parameters is still valid and does not depend on the details of how the binning was derived.

11.4.2. Signal reconstruction at Belle II

The dataset used is the MC5 production dataset without beam background, and corresponds to an integrated luminosity of $2\,\text{ab}^{-1}$. For purely hadronic modes which do not use calorimeter-based observables, like the one studied here, the beam background is expected to have little effect. The selection is not as refined as that of the Belle analysis due to the lack of multivariate continuum suppression and tuning of the K^0_S reconstruction. However, the implementation of the whole analysis even with a non-optimal selection gives a conservative estimate of what can be achieved.

From the dataset, a sample for further study is selected based on a loose final state particle requirement, using the decay chains $D^{*\pm} \to \pi^\pm D$, $B^\pm \to D\pi^\pm$, and $B^\pm \to DK^\pm$, with $D \to K^0_S\pi^+\pi^-$ in all cases. The final state hadronic particles are selected with the Belle II framework's standard particle selection. The K^0_S is selected with a BDT trained on the K^0_S flight distance, mass, the minimum distance between the vertex and the electron beam direction, and vertex p-value, after an initial dipion selection satisfying $0.477 < M(\pi^+\pi^-) < 0.518\,\text{GeV}$. After selecting D candidates, a mass vertex fit using `RAVE` is performed to improve the resolution of the Dalitz plot variables.

In the $D^{*\pm} \to D\pi^\pm$ channel, it is additionally required that D candidates have $1.82 < M(D) < 1.9\,\text{GeV}$, $\Delta M = M(D\pi^\pm) - M(D) < 0.155\,\text{GeV}$, and $p_D > 1.8\,\text{GeV}$. The momentum selection is chosen so that the mean of the momentum spectrum of the $D^{*\pm}$ and B signal events are the same; this partially eliminates any systematic effects due to the differing acceptance of the two samples over the Dalitz plot. In the $B^\pm \to DK^\pm$ channel, the additional requirements are $\Delta E < 0.15\,\text{GeV}$, $M_{\text{bc}} > 5.25\,\text{GeV}$, and $1.85 < M(D) < 1.88\,\text{GeV}$.

Following the previous Belle analysis of the GGSZ mode, the $D^{*\pm}$ sample is fitted in $M(D)$ and $\Delta M = M(D\pi^\pm) - M(D)$ to extract the number of signal events in each Dalitz bin. There are two background types: combinatorial and a correctly reconstructed D candidate (true D) paired with a slow pion not originating from a D^*. The D mass distribution is modeled by a sum of a Gaussian and two bifurcated Gaussians in the D^* and true D background component, and a third-order Chebyshev polynomial for the combinatorial background. The ΔM component is modeled by a bifurcated Student's t-function in the $D^{*\pm}$ component, and an Argus background function for the true D and purely combinatorial components. These distributions are fixed by fitting to the full generic MC separated into the three components by matching the reconstructed $D^{*\pm}$ to the event generator information. Figure 125 shows the fits to the components.

The full generic MC is then divided into Dalitz bins and the number of events for each component is obtained by fitting the sum of the components. Figure 126 shows an example fit in one of the Dalitz bins.

The signal and background components in $B^\pm \to DK^\pm$ are separated by fitting in two dimensions of M_{bc} and ΔE. The signal $B^\pm \to DK^\pm$ component is modeled with three Gaussians in ΔE and a correlated Gaussian in M_{bc}, where the Gaussian mean of the M_{bc} is allowed to vary with ΔE. The peaking $B^\pm \to D\pi^\pm$ background component, where the π is mis-identified as a K, is modeled with the sum of two Gaussians in M_{bc} and a sum of two Gaussian distributions in ΔE, without correlation between the components. The generic $B\bar{B}$ component is modeled with a sum of a Gaussian and an exponential function in ΔE, and in M_{bc} a sum of an Argus background and a Gaussian for the fully

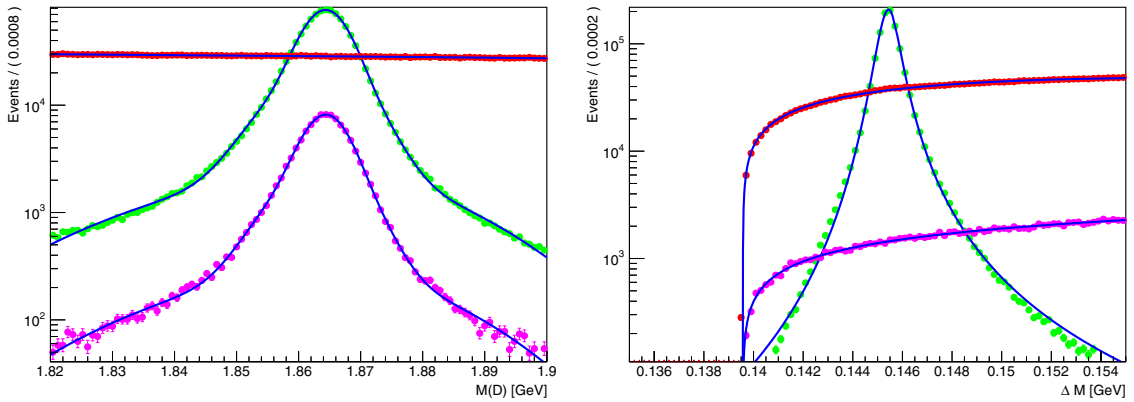

Fig. 125. Fits to the signal (green), fake slow pion background (blue), and combinatorial background (red) components of the D^* in $M(D)$ (top) and ΔM (bottom) distributions.

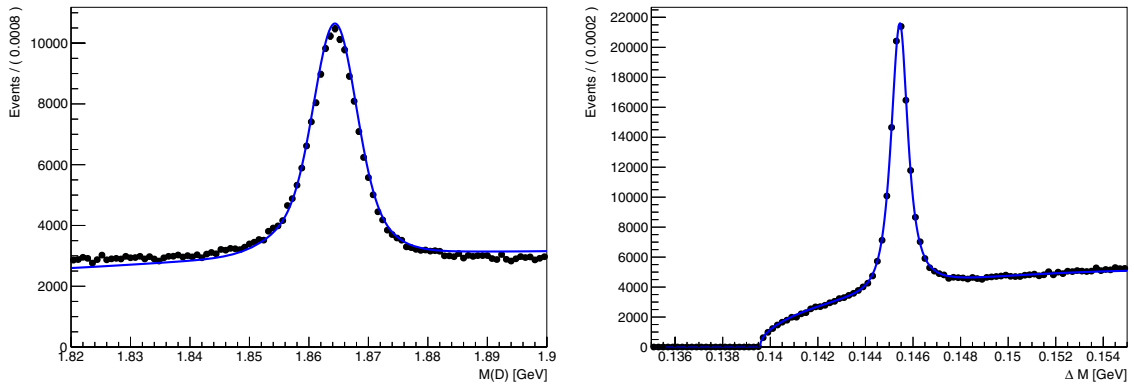

Fig. 126. Example fit to bin 4 of $D^{*\pm} \to D\pi^{\pm}$ in generic Belle II MC. (Left): The overall fit to the D mass. (Right): shows $\Delta M = M(D\pi^{\pm}) - M(D)$.

reconstructed component. The continuum background is modeled with a second-order Chebyshev in ΔE and an Argus function in $M_{\rm bc}$. The fits to these components are shown in Fig. 127. A subsequent fit to the whole of the MC with fixed shapes for the components is presented in Fig. 128. In a more realistic analysis the abundant $B \to D\pi$ sample that has limited sensitivity to ϕ_3 will act as a control sample on which to tune the probability density functions that will be used in the fit.

The whole MC sample is then divided into Dalitz bins, and the MC is fitted again to measure the (x, y) parameters. For the background components, the number of events of the component in each separate bin is allowed to vary freely. For the $B^{\pm} \to DK^{\pm}$ signal the overall number of events is allowed to vary, while the number of events in the individual bins is governed by Eq. (343).

11.4.3. Sensitivity to ϕ_3 with increased luminosity

To study the sensitivity to ϕ_3 versus luminosity, toy Monte Carlo studies were performed. The signal and background components were each individually binned into an $M_{\rm bc} \times \Delta E$ grid, and an uncorrelated Dalitz bin array. The grid and Dalitz bin were then sampled the expected number of times for a given luminosity to produce a distribution for each individual component at that luminosity. These distributions were added together, then the fitting procedure of the previous section was performed to obtain an (x, y) measurement. This procedure was repeated several hundred times per luminosity to build up an (x, y) distribution expected at that luminosity.

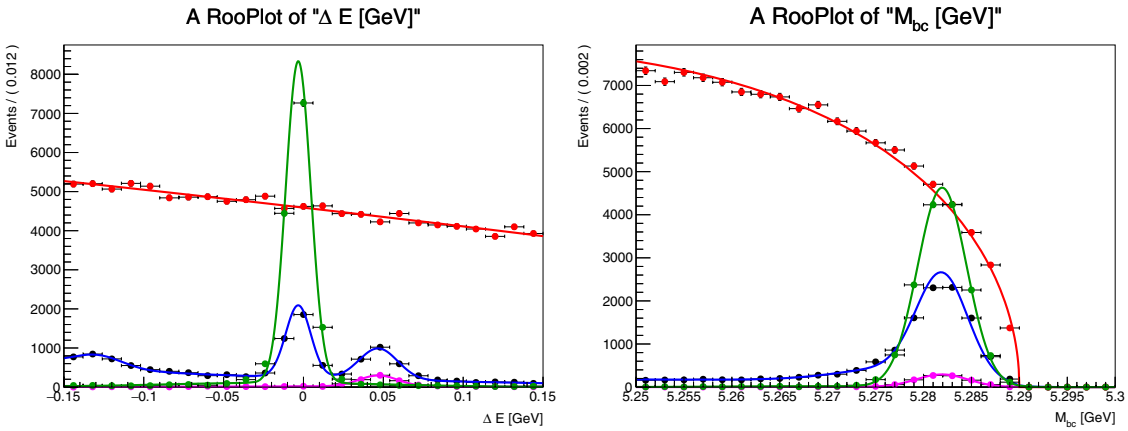

Fig. 127. Fits to the signal and background components of the Belle II Monte Carlo in $B^{\pm} \to [K^0_S\pi^+\pi^-]_D K^{\pm}$. The left panel shows ΔE and the right shows $M_{\rm bc}$. The red component is from events reconstructed from e^+e^- to u, d, s, or c quarks pairs, the green component from a dedicated MC sample of signal $B^{\pm} \to [K^0_S\pi^+\pi^-]_D K^{\pm}$ events, and the blue from arbitrary $B\bar{B}$ (not excluding signal) in the generic MC.

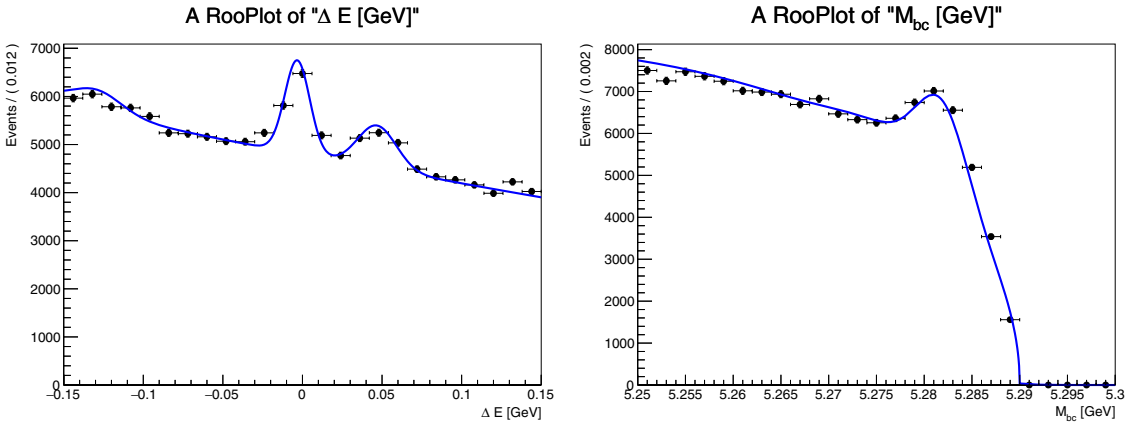

Fig. 128. Overall fit to the generic Monte Carlo in the $B^{\pm} \to [K^0_S\pi^+\pi^-]_D K^{\pm}$ mode. The fit is subsequently performed in Dalitz bins in order to measure the (x, y) physics parameters which can be used extract ϕ_3.

The standard deviations of these toy distributions are taken as the expected uncertainty for a given luminosity. From these widths, and taking the current world average [759] *[UTfit average]* of ϕ_3 parameters to fix the underlying true (x, y), the ϕ_3 resulting from these (x, y) uncertainties is derived. This is done by generating pairs of (x, y) for B^+ and B^- using the (x, y) derived from the UTFit parameters as the mean and the uncertainties from the toys as a width (assuming no correlation) and running this procedure several hundred times to generate a distribution for ϕ_3 whose width we take as the expected ϕ_3 uncertainty. Figure 129 shows how the expected uncertainty in ϕ_3 scales with luminosity based on these toy Monte Carlo studies. It shows that the expected uncertainty with an integrated 50 ab^{-1} is approximately 3°.

There are several possible future refinements of this study:

(1) Include additional channels such as $D^0 \to K^0_S K^+ K^-$ and $B^+ \to D^{*0} K^+$.
(2) Better signal-to-background separation by including a continuum suppression variable in the signal extraction fit.

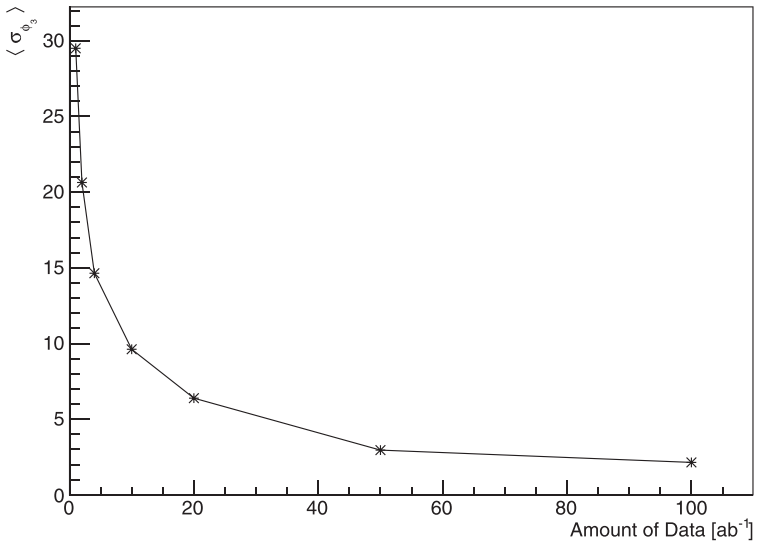

Fig. 129. The expected uncertainty (based on toy Monte Carlo studies) versus luminosity for ϕ_3.

(3) Derive the ϕ_3 estimators from a likelihood profile fit of the (x, y) that includes information about the correlation information for each of the several hundred toys.

However, this preliminary study clearly demonstrates the excellent capabilities of Belle II to determine ϕ_3 from this mode.

11.4.4. Extrapolation of the combination of measurements to Belle II luminosities

The value of ϕ_3 from a combination of Belle measurements alone is $(68\pm13)^\circ$ (see, e.g., Ref. [760]) and is dominated by the GGSZ measurement of $B^- \to D^{(*)}(K^0_S\pi^+\pi^-)K^-$ [756], which should be considered the golden mode for Belle II. However, there have also been measurements using the ADS and GLW techniques [761–763] that have non-negligible weight in the combination. This includes an ADS/GLW analysis of $B^+ \to D^*(D\{\gamma, \pi^0\})K^+$ [762], which has only been measured at the e^+e^- B factories. Therefore, the ϕ_3 programme at Belle II must at least include all these modes and possibly others (see Sect. 11.7) to realize its full potential.

To be quantitative we will just restrict ourselves to the measurements made so far and extrapolate this combination to Belle II luminosities. Therefore, the expectation is a sensitivity of 3.6° and 1.6° with datasets corresponding to $10\,\text{ab}^{-1}$ and $50\,\text{ab}^{-1}$, respectively. The most important systematic uncertainties are related to the inputs from charm physics, which will be discussed in Sect. 11.5, the signal extraction fits, and backgrounds from charmless B decay. The latter two sources can be controlled using the $B^+ \to D\pi^+$ sample and sidebands of the M_D distribution, respectively, so they should scale with the statistical uncertainty.

11.5. Auxiliary measurements

The precise determination of ϕ_3 using $B^- \to DK^-$ is reliant upon external inputs from the charm sector. The accurate determination of charm-mixing parameters [764] means that any bias from this source in the determination of ϕ_3 can be corrected for as discussed in Sect. 11.2. In addition, D meson branching fractions of both CF and DCS decays provide important inputs to ADS measurements [765,766].

However, the most important auxiliary measurements are related to D decay strong phases, which are an essential input to interpret the measurements related to ϕ_3. In principle these parameters could be extracted from the B data along with ϕ_3, δ_B, and r_B, but the sensitivity to ϕ_3 would be diluted. Therefore, measurements of the strong phases are taken from elsewhere.

The strong phase difference between the D^0 and $\overline{D}^0$ decays to $K^+\pi^-$ is required for two-body ADS measurement and is accurately determined using a combination of charm-mixing measurements [764]. For multibody ADS measurements, two parameters must be determined due to the variation of the strong phase difference over the allowed phase space: the coherence factor R and average strong phase difference δ_D. Recently there has been a new analysis to determine R and δ_D for $D \to K^-\pi^+\pi^0$ and $D \to K^-\pi^+\pi^+\pi^-$ [767], which uses quantum-correlated $D^0\overline{D}^0$ pairs produced at the $\psi(3770)$. (For a comprehensive review of quantum-correlated measurements relevant to ϕ_3 see Ref. [768].) At the $\psi(3770)$ the D decay of interest is tagged in events where the other D decays to a CP eigenstate, a state with a kaon of opposite or same-sign charge as the signal or $K^0_{S,L}\pi^+\pi^-$. The last of these tags is an addition since the first determination of R and δ_D reported by the CLEO-c Collaboration [769]. The updated results are used to perform the combinations reported elsewhere in these proceedings.

The model-independent GGSZ method requires two parameters related to the strong phase difference to be determined for each bin of the Dalitz plot. Such measurements have been reported by the CLEO Collaboration [770] using a data sample corresponding to an integrated luminosity of 818 pb^{-1}. These measurements have been used by both the Belle [757] and LHCb [758] collaborations to determine ϕ_3 from $B^- \to DK^-$ data. The systematic uncertainty on ϕ_3 related to the statistical precision of the CLEO measurements is currently $\sim 2^\circ$, which is not dominant, but it will become much more significant with the future running of LHCb and Belle II. Therefore, improvements in the measurements of the strong phase parameters are desirable. BESIII has accumulated an integrated luminosity of 2.92 fb^{-1} at the $\psi(3770)$, which is 3.5 times larger than that analyzed by CLEO. Preliminary results for the $D \to K^0_S\pi^+\pi^-$ parameters using the same binning as CLEO have been reported [771], which give a significant improvement in the statistical uncertainty on the measurements. BESIII can accumulate around 4 fb^{-1} of integrated luminosity per year of running at the $\psi(3770)$; therefore, a two-year run at the $\psi(3770)$ by BESIII would reduce the uncertainty on ϕ_3 from the determination of strong phases in the GGSZ method to a negligible level.

Quantum-correlated measurements are also opening up new pathways to determining ϕ_3. A measurement of the CP content of $D \to \pi^+\pi^-\pi^0$ and $D \to K^+K^-\pi^0$ [772] using the full CLEO-c $\psi(3770)$ dataset has shown that $D \to \pi^+\pi^-\pi^0$ is $(96.8 \pm 1.7 \pm 0.6)\%$ CP-even. Therefore, this mode can be used as an additional GLW measurement to augment $D \to h^+h^-$, given it has a significantly larger branching fraction [77]. Most recently, a preliminary study of using $D \to K^0_S\pi^+\pi^-\pi^0$ as a GLW and GGSZ mode has been reported [773]. This mode has a large branching fraction of 5.2% [77] and is largely CP-odd, with a CP-even fraction of only (0.246 ± 0.018), which has been measured using the full CLEO-c dataset. Therefore, this mode can be used in a GLW analysis. Furthermore, by binning the five-dimensional phase space, the values of c_i and s_i can be determined in the quantum correlated data, which then allows a GGSZ-type measurement. This has been done with nine bins using the CLEO-c data. A toy simulation study based on these quantum-correlated measurements indicates a statistical uncertainty of 3.5° may be possible with a Belle II sample of 50 ab^{-1}. There is no reliable amplitude model of this final state to guide the choice of binning to maximize ϕ_3 sensitivity as there is for $D \to K^0_S\pi^+\pi^-$; this means there is scope to improve the sensitivity of this mode to ϕ_3 if an amplitude model is developed.

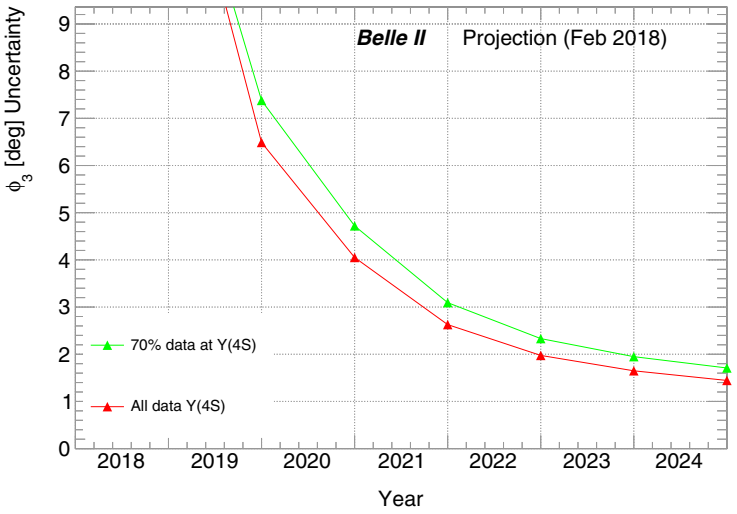

Fig. 130. The future prospect of Belle II sensitivity to ϕ_3.

11.6. Review of LHCb $B \to D^{(*)}K^{(*)}$ measurements

LHCb have recently updated their ϕ_3 average using the data collected at a center-of-mass energy of 7 TeV and 8 TeV. The combination of $B \to DK$ modes gives $\phi_3 = (72.2^{+6.8}_{-7.3})^\circ$ [774], the most precise determination from a single experiment. The balance of the contributions to the average at LHCb is somewhat different due to the lower relative selection efficiency for K^0_S in the forward hadronic environment. Here, GGSZ and ADS/GLW, including the four-body final states $K^-\pi^+\pi^-\pi^+$ and $\pi^+\pi^-\pi^+\pi^-$, are on an almost equal footing in terms of sensitivity to ϕ_3.

An extrapolation of these results under a variety of assumptions about the size of the available BESIII dataset has been performed [775]. These studies predict a precision of around 4° after Run 2 and a precision of around 1° after the phase-1 upgrade. Therefore, the precision possible with an upgraded LHCb and Belle II is very similar and is a true area of competition between the two experiments. The future prospect of Belle II sensitivity to ϕ_3 is plotted in Fig. 130.

11.7. Outlook and conclusions

We have reviewed the exquisite theoretical cleanliness of determining ϕ_3 in $B \to DK$ decays, hence allowing these measurements to be a standard candle against which other SM CKM measurements can be compared. Further, the current level of precision of the measurements of ϕ_3 is such that there can still be NP contributions at the level of 4°. Both of these observations provide the motivation to produce a degree-level precision measurement at Belle II.

The first study of the sensitivity of Belle II based on the full simulation has been made for the GGSZ analysis of $B^+ \to (K^0_S\pi^+\pi^-)_D K^+$ using a generic MC sample corresponding to an integrated luminosity of $2\,\text{ab}^{-1}$. Based on these studies a 3° precision is anticipated from a $50\,\text{ab}^{-1}$ dataset, in line with naive expectations. Further, there is still much scope to refine the analysis further. However, the anticipated precision based on the combination of all Belle results, including GLW and ADS as well, is not completely dominated by the GGSZ measurement alone, such that once the full combination is extrapolated the uncertainty is expected to be 1.6° with a $50\,\text{ab}^{-1}$ dataset. A caveat is that the extrapolation is predicated on there being sufficient BESIII data collected at the $\psi(3770)$, approximately $10\,\text{fb}^{-1}$, to determine the strong phase difference parameters required. If

such a sample does not exist there will be a few degrees' systematic uncertainty that will limit the impact of the GGSZ measurements on the combination.

However, further improvements are possible as several $B \to DK$ modes have not been exploited at Belle. In particular there are several modes with significant branching fractions that have neutral particles $K^0_{S,L}$, π^0, and η that are yet to be exploited:

- CP-even: $\pi^0\pi^0$, $K^0_L\pi^0$, $K^0_S\pi^0\pi^0$, $K^0_S\eta\pi^0$, $K^0_SK^0_SK^0_S$;
- CP-odd: $K^0_SK^0_SK^0_L$, $\eta\pi^0\pi^0$, $\eta'\pi^0\pi^0$, $K^0_SK^0_S\pi^0$, $K^0_SK^0_S\eta$; and
- Self-conjugate: $K^0_L\pi^+\pi^-$, $K^0_LK^+K^-$, $K^0_S\pi^+\pi^-\pi^0$, $\pi^+\pi^-\pi^0\pi^0$.

The improved particle identification, energy resolution in the electromagnetic calorimeter, and continuum suppression algorithms at Belle II will all benefit the selection of these modes. The fully charged four-body modes $D \to K^-\pi^+\pi^+\pi^-$, $D \to \pi^+\pi^-\pi^+\pi^-$, $D \to K^-K^-\pi^+\pi^+$ are also of interest, but LHCb will reconstruct significantly larger samples because of the absence of neutral particles in the final state. Another type of measurement that appears to have excellent potential is the double Dalitz analysis of $B^0 \to D(K^0_S\pi^+\pi^-)K^+\pi^-$ [776], which so far has received no attention at Belle or Belle II.

In summary, ϕ_3 is the single place where a purely experimental improvement can be made in determining the unitarity triangle at Belle II, that in turn will allow for comparison with NP-sensitive measurements. The sensitivity has been established using the golden mode $B^+ \to (K^0_S\pi^+\pi^-)_DK^+$ and extrapolating the Belle measurements. However, given the improvements in detector performance and the many modes that are yet to be explored, there is scope to go beyond this baseline sensitivity.

12. Charmless hadronic B decays and direct CP violation

Editors: M. Beneke, C-W. Chiang, P. Goldenzweig
Additional section writers: B. Pal, G. Bell, C. Bobeth, H-Y. Cheng, A. Datta, T. Feldmann, T. Huber, C-D. Lu, J. Virto

12.1. Introduction

Charmless hadronic final states in B decays have branching fractions of order 10^{-5} or less, since either the final state is reached by the $b \to u$ transition, which is suppressed by the small CKM matrix element $|V_{ub}|$, or the transition is loop-suppressed. Charmless decays are a good place to observe direct CP violation, since the smallness of the leading amplitude often implies that another amplitude with a different CKM factor is of similar size. If the two amplitudes also have a substantial (strong) phase difference, this leads to sizeable direct CP violation, which has indeed been observed. There are a large number of potentially interesting decay modes. There are 130 (quasi) two-body final states, where the two mesons are from the ground-state pseudoscalar or vector nonet alone. The number multiplies when more exotic mesons or three-body final states are considered. Belle II is expected to considerably extend the knowledge of such hadronic final states.

The theoretical description of hadronic B decays starts from the effective weak interaction Lagrangian for $\Delta B = 1$ transitions,

$$\mathcal{L}_{\rm eff} = -\frac{G_{\rm F}}{\sqrt{2}} \sum_{p=u,c} \lambda_p^{(D)} \sum_i C_i \, Q_i^p, \tag{344}$$

where Q_i^p denotes the so-called tree, QCD, and electroweak penguin, and dipole operators, and $\lambda_p^{(D)} \equiv V_{pb}V_{pD}^*$ $(p = u, c, D = d, s)$. Any B decay to a final state f can then be expressed in the form

$$A(\bar{B} \to f) = \lambda_u^{(D)} A_f^u + \lambda_c^{(D)} A_f^c, \tag{345}$$

where A_f^p are the matrix elements of the above Lagrangian. The Wilson coefficients C_i include the physics from the highest scales, including M_W, down to the scale m_b, and their calculation is under complete theoretical control. $\mathcal{L}_{\text{eff}}$ above assumes the SM, and the convention that $\lambda_t^{(D)}$ is eliminated by the unitarity relation $\lambda_u^{(D)} + \lambda_c^{(D)} + \lambda_t^{(D)} = 0$. The structure of the operators Q_i, the values of their Wilson coefficients, and the flavor structures can be modified in extensions of the SM. The decay amplitude $A(\bar{B} \to f) = \langle f|\mathcal{L}_{\text{eff}}|\bar{B}\rangle$ then requires the computation of the hadronic matrix elements $\langle f|Q_i|\bar{B}\rangle$ of the local operators Q_i. When f consists of two or more hadrons this is a difficult strong interaction problem, which cannot be solved with lattice QCD. Systematic expansions can be performed in the heavy quark mass, that is in Λ/m_b, where Λ is the strong interaction scale, or in light quark masses, that is in m_q/Λ $(q = u, d, s)$. The corresponding theoretical approaches are referred to as the "factorization" and "SU(3)" frameworks, respectively.

This chapter summarizes recent developments in the field of charmless hadronic B decays with possible relevance to Belle II physics, collected from contributions to the B2TIP workshop series (see Chapter 1 for details). It does not provide a comprehensive discussion of the field. A compact introduction to the theory of charmless decay and a summary of experimental results from BaBar and Belle can be found in the "Charmless B decays" chapter of Ref. [2]. The present chapter provides only a few projections for Belle II results and uncertainties, since the large number of potential final states and observables, many of them not measured before, do not allow a more detailed study.

The chapter is divided into two main parts. The larger first part deals with aspects of two-body or quasi-two-body final states, and starts with a discussion of global SU(3) analyses of charmless B decays. This is followed by several contributions related to the factorization framework, a section on πK final states and the corresponding ones with vector mesons, a brief discussion on CP violation in B_s decays, specifically $B_s \to K_S^0 K_S^0$, and concludes with a focus on polarization and angular distributions in vector–vector final states. The second part features two sections devoted to the theoretically less developed and experimentally less explored subject of three-body decays.

12.2. SU(3) analysis of two-body decays

Contributing author: Cheng-Wei Chiang

When the difference between the masses of the light quarks (up, down, and strange) is neglected, QCD exhibits an exact SU(3) flavor symmetry. For charmless B decays this implies that the hadronic decay amplitudes (with their CKM factors stripped off) of many different decays are related to a few reduced matrix elements multiplied by known Clebsch–Gordan coefficients. This approach to hadronic decays of heavy mesons was developed in the 1980s [777–780], originally for charmed meson decays, and has since been used extensively for hadronic B decays (see Ref. [781] and references therein). In practice, the SU(3) treatment amounts to an expansion in m_s/Λ. Since usually only the leading SU(3)-symmetric term is considered, the approximation amounts to ignoring the effect of the strange quark mass on the long-distance dynamics.

Valuable knowledge about strong dynamics in various decay topologies has been obtained via this approach. With sufficient data it enables us to extract the (reduced) decay matrix elements directly from data without reference to further theoretical assumptions. The results include the effects of the strong interaction to all orders, including long-distance rescattering. This provides a good guide to

the sizes and strong phases of certain amplitudes, such as the unexpectedly large color-suppressed tree amplitude discussed below. On the other hand, being primarily data-driven through fits, the SU(3) approach does not by itself provide an explanation of such findings and the result depends on the quality of the experimental data.

Once the hadronic SU(3) amplitudes are determined from sufficient data, one can use the obtained information to make predictions for as yet unmeasured observables. For example, the best-fit results from a fit to B^0 and B^+ decays have been used to predict B_s decays and obtained a fairly good agreement with those few observables that have been measured.

Within the limitations of its approximation, the quality of the SU(3) analysis depends on the quality of the data. Belle II is expected to collect a substantial amount of new information that should allow us to extend the SU(3) analysis to final states with two light vector mesons ("VV modes"), and to attain a precision that requires the inclusion of sub-leading amplitudes, as well as SU(3)-breaking effects on the dominant amplitudes.

In the following we briefly discuss the formalism and the main results from the analysis of present pseudoscalar–pseudoscalar (PP) and pseudoscalar–vector (PV) final state data. We then provide a short outlook on relevant issues for Belle II.

SU(3) amplitudes In practice, instead of the group-theoretical reduced matrix elements, one uses an equivalent set of transition amplitudes for heavy meson decays categorized according to the topology of their flavor flow. Among these flavor diagrams seven types have been identified to play an indispensable role in explaining the current data. Leaving out the CKM factors, they are:

- T, the color-favored tree diagram with an external W emission;
- C, the color-suppressed tree diagram with an internal W emission;
- E, the W-exchange diagram;
- P, the QCD penguin diagram;
- S, the flavor-singlet QCD penguin diagram;
- $P_{\rm EW}$, the electroweak (EW) penguin diagram;
- PA, the penguin annihilation diagram.

A graphical representation of these amplitudes is shown in Fig. 131.

The first three amplitudes, T, C, and E, are generated at tree level in the electroweak interaction. T is the dominant amplitude, whereas C is naively suppressed relative to T by a color factor of $N_c = 3$, and E by helicity conservation and hadronic form factors. The remaining four amplitudes are induced only at the one-loop level. Compared to the first five amplitudes, the EW penguin amplitude is one order higher in the weak interaction and thus even smaller in magnitude. However, due to non-perturbative strong interaction dynamics, the hierarchy of the amplitudes is not seen as clearly in the current data as suggested by the above arguments.

The physical η and η' mesons are mixtures of the SU(3) singlet and octet states or, alternatively, of $\eta_q = \frac{1}{\sqrt{2}}(u\bar{u} + d\bar{d})$ and $\eta_s = s\bar{s}$, according to Ref. [782]:

$$\begin{pmatrix} \eta \\ \eta' \end{pmatrix} = \begin{pmatrix} \cos\varphi & -\sin\varphi \\ \sin\varphi & \cos\varphi \end{pmatrix} \begin{pmatrix} \eta_q \\ \eta_s \end{pmatrix}, \tag{346}$$

where the mixing angle φ is determined by lattice calculations as $\varphi \approx 46^\circ$ [783]. For vector mesons, the ϕ meson is usually assumed to be a pure $s\bar{s}$ state. Since the mixing is as SU(3) breaking effect,

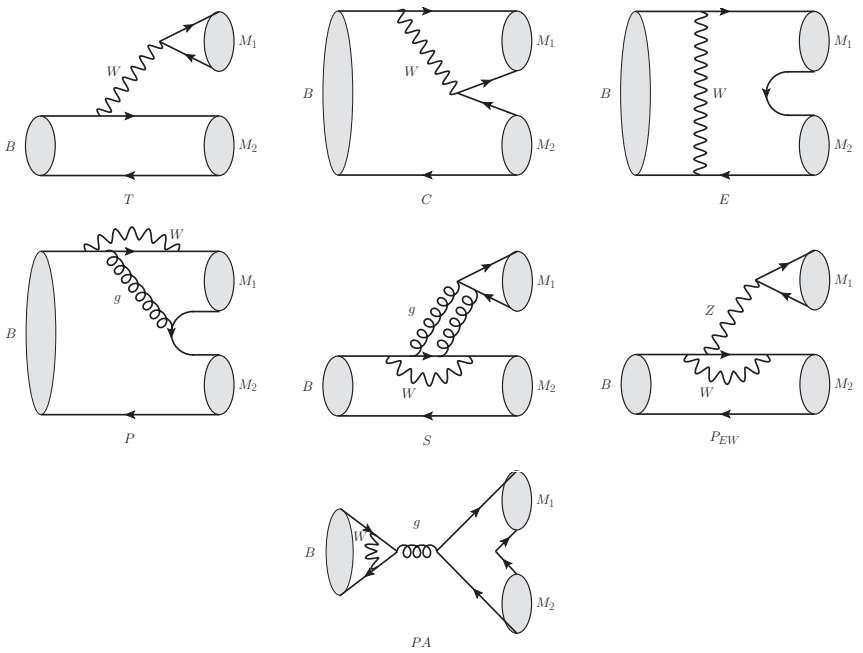

Fig. 131. Graphical representation of the most important SU(3) amplitudes of $B \to M_1 M_2$ decays in the flavor topology classification.

including the η, η', ω, and ϕ by assuming a universal mixing angle for all amplitudes is an assumption that goes beyond the systematic SU(3) treatment, which, however, greatly enhances the global fit, since it enlarges the set of final states at the expense of adding only one new topological amplitude, S. It is noted [781] that when the η–η' mixing angle φ is included as a free parameter in the fit, one obtains a value consistent with the lattice result quoted above.

Amplitude analyses using the current data show that SU(3) flavor symmetry is a satisfactory working assumption at the current level of experimental precision, meaning that the magnitude and strong phase of each flavor diagram can be taken to be the same for $\Delta S = 0$ and $|\Delta S| = 1$ transitions. In physical processes, the abovementioned flavor amplitudes always appear in certain combinations, multiplied by appropriate CKM factors. In the case of strangeness-conserving ($\Delta S = 0$) transitions, we have

$$\begin{aligned} t &= \lambda_u^{(d)} T - \left(\lambda_u^{(d)} + \lambda_c^{(d)}\right) P_{\rm EW}^{\rm C}, \\ c &= \lambda_u^{(d)} C - \left(\lambda_u^{(d)} + \lambda_c^{(d)}\right) P_{\rm EW}, \\ e &= \lambda_u^{(d)} E, \\ p &= -\left(\lambda_u^{(d)} + \lambda_c^{(d)}\right)\left(P - \frac{1}{3} P_{\rm EW}^{\rm C}\right), \\ s &= -\left(\lambda_u^{(d)} + \lambda_c^{(d)}\right)\left(S - \frac{1}{3} P_{\rm EW}\right), \\ pa &= -\left(\lambda_u^{(d)} + \lambda_c^{(d)}\right) PA. \end{aligned} \tag{347}$$

In the SU(3) limit, the corresponding amplitudes for strangeness-changing ($|\Delta S| = 1$) transitions are obtained by replacing d by s in the CKM factors. Even though the color-suppressed EW penguin diagram $P_{\rm EW}^{\rm C}$, which is both loop suppressed and sub-leading in weak interactions, is not strongly

required by the data (and was therefore not shown in Fig. 131), we include it in the above expressions for completeness. A full flavor amplitude decomposition of all PP and VP modes can be found, for example, in Ref. [781].

Whether a particular flavor amplitude is important phenomenologically is determined by the available data and their precision. Currently, the above seven flavor diagrams are sufficient to explain the observed data of PP decays. In the case of the PV modes, both the E and PA diagrams are not yet called for. Moreover, in this case one has to distinguish whether the spectator quark in the B meson ends up in the vector or pseudoscalar meson. Therefore, the number of flavor amplitudes required for PV modes is doubled, with the corresponding flavor amplitude denoted with a subscript V or P. These two sets of amplitudes are a priori different in both strength and strong phase, yet they can be related to each other under the assumption of (naive) factorization. The SU(3) approach can also be applied to VV final states, in which case one needs three parameters for each flavor diagram, one for every helicity amplitude. A global fit then requires polarization data for every decay mode in the fit, which is not yet available.

In the following, we highlight some results of recent global analyses. We adopt the convention of fixing T (in the case of PP decays) and $T_{\rm P}$ (in the case of PV decays) to be real and positive. All other strong phases, denoted by δ_X for amplitude X, are then defined relative to these amplitudes. The experimental observables include the CP-averaged branching fractions and CP asymmetries (direct and indirect). The former primarily determine the magnitude of each flavor amplitude, while the latter are more useful in fixing the associated strong phase.

PP decays In the case of PP final states, Ref. [781] shows that the magnitudes of the flavor amplitudes follow the hierarchy $|T| \gtrsim |C| > |P|, |E| > |S| > |P_{\rm EW}| \sim |PA|$. The importance of the E and PA annihilation amplitudes mainly comes from the data on $B^0 \to K^+K^-$, $\pi^+\pi^-$, and $\pi^0\pi^0$ decays. The E amplitude is seen to have a size about the same as the QCD penguin amplitude P and a phase of $\sim -130°$. On the other hand, the PA amplitude has a similar phase to E but is one order of magnitude smaller in size than P.

An unexpected outcome is the value of the color-suppressed tree amplitude. Not only does the C amplitude have a non-trivial phase of about $-70°$, its magnitude is about 70% of $|T|$. The combination of both is at odds with QCD factorization calculations [784,785]. Large $|C|$ is not attributed only to the branching fractions of a small set of observables such as of $B^0 \to \pi^0\pi^0$ and/or $K^0\pi^0$, as might naively be expected. Rather, a large complex C amplitude is a consequence of fitting to the observed direct CP asymmetries in $B \to K\pi$ decays. In particular, it is required to explain the so-called $K\pi$ CP puzzle, that is, the observation of the CP asymmetry difference $\Delta A_{K\pi} \equiv A_{\rm CP}^{K^+\pi^0} - A_{\rm CP}^{K^+\pi^-} = 0.122 \pm 0.022$ by SM hadronic physics. Moreover, it helps alleviate the rate deficit problem of the $B^0 \to \pi^0\pi^0$ decay.

The electroweak penguin amplitude $P_{\rm EW}$ is found to have a strong phase of about $-80°$, and a similar phase is also found in the $P_{\rm EW,V}$ amplitude for the PV decays. Such a large phase is not only unexpected in the factorization formalism, but difficult to understand from the basic structure of the weak effective Hamiltonian [720,721,786]. It is an open question whether better data from Belle II or a better theoretical understanding of SU(3)-breaking effects in the dominant amplitudes can resolve this apparent contradiction in the subdominant $P_{\rm EW}$ amplitude. Similarly, the status of the singlet amplitude S has not been clarified. In the SU(3) fit it plays an essential role, particularly in explaining the branching fractions of $\eta' K$ decays [687]. It is found to be $\sim$60% of the P amplitude and $\sim$4 times larger than the $P_{\rm EW}$ amplitude, and has a strong phase of about $-100°$. On the other

hand, the explanation in terms of the interference pattern of standard QCD penguin amplitudes P [787,788] suggests a less important role of S.

The SU(3) determination of flavor amplitudes from B_d and $B^\pm$ decays leads to predictions for B_s decays. The $\eta\eta'$ and $\eta'\eta'$ modes are expected to have the largest decay rates among the B_s decays.

PV decays This sector shows the hierarchy $|T_{\rm P,V}| > |C_{\rm P,V}| > |P_{\rm P,V}| \sim |P_{\rm EW,V}| > |P_{\rm EW,P}| \sim |S_{\rm P,V}|$. Current data do not significantly constrain the magnitudes and phases of the $E_{\rm P,V}$ amplitudes. A global fit without the singlet $S_{\rm P,V}$ amplitudes gives essentially the same values for most parameters except for $C_{\rm V}$ and $P_{\rm EW,V}$, but has a much worse quality, indicating a strong need for $S_{\rm P,V}$ to describe data in the SU(3) framework. Unlike in the PP sector, the singlet amplitudes are smaller than the electroweak penguin amplitudes $P_{\rm EW,P,V}$.

The $C_{\rm V}$ amplitude is about twice as large in magnitude as the $C_{\rm P}$ amplitude, giving the ratios $|C_{\rm V}/T_{\rm P}| \sim 0.6$ and $|C_{\rm P}/T_{\rm V}| \sim 0.35$. Although with large errors, $C_{\rm P}$ and $C_{\rm V}$ have strong phases around $-30°$ and $-90°$, respectively. It thus appears that $C_{\rm V}$ receives large corrections beyond factorization, as in the PP sector.

The QCD penguin amplitudes are about one order of magnitude smaller than the color-allowed tree amplitudes, with $|P_{\rm P}|$ slightly larger than $|P_{\rm V}|$. It is noted that $P_{\rm P}$ and $P_{\rm V}$ are almost opposite in phase, in agreement with the proposal made in Refs. [787,789] and the predictions from factorization. This property results in constructive and destructive interference effects in the ηK^* and $\eta' K^*$ modes, respectively. Besides, $P_{\rm P}$ has only a small strong phase of $\sim -20°$ relative to $T_{\rm P}$, so that $P_{\rm V}$ is almost opposite to both $T_{\rm P}$ and $T_{\rm V}$. This leads to a significant interference effect on modes involving $C_{\rm P,V}$ and $P_{\rm P,V}$. For example, among the B_s decays to PV final states, the $B_s \to \rho^+ K^-$ mode is predicted to have the largest branching fraction of order 15×10^{-6}.

A striking finding is that $|P_{\rm EW,V}|$ is comparable to $|P_{\rm V}|$. In contrast, in the PP sector $|P_{\rm EW}|$ is suppressed by one order of magnitude relative to $|P|$. This observation has some important implications for CP violation in the $K^*\pi$ modes and for the branching fractions of $B_s \to \phi\pi^0$ (and $\phi\rho^0$). In the absence of the color-suppressed amplitude, the $K^{*+}\pi^0$ and $K^{*+}\pi^-$ decays should have the same CP asymmetry. Just as in the $B \to K\pi$ decays, a sign flip in $A_{\rm CP}(K^{*+}\pi^0)$ will occur in the presence of a large complex $C_{\rm V}$. This is in contradiction to the experimental observation that CP asymmetries of $K^{*+}\pi^0$ and $K^{*+}\pi^-$ are of the same sign. This enigma can be resolved by noting that since $|\lambda_c^{(s)}| \gg |\lambda_u^{(s)}|$ and $|P_{\rm EW,V}| \sim |P_{\rm V}|$, $P_{\rm EW,V}$ contributes substantially and renders $A_{\rm CP}(K^{*+}\pi^0)$ the correct sign. In the $K\pi$ case, $P_{\rm EW}$ is suppressed relative to P, only affecting the magnitude of $A_{\rm CP}(K^+\pi^0)$ but not its sign.

The experimental status of the $K\pi$ and $K^*\pi$ systems is discussed in Sect. 12.4. For $B_s \to \phi\pi^0$ decays, there is currently no measurement. Theoretical predictions of its branching fraction within the SM are $(1.6^{+1.1}_{-0.3}) \times 10^{-7}$ in the framework of QCD factorization [790] and $(1.94 \pm 1.14) \times 10^{-6}$ in the framework of flavor symmetry [781]. Preliminary studies at Belle [791] (unpublished) show that one can expect a signal yield of 0.5–1.14 with the full 121 fb^{-1} of $\Upsilon(5S)$ data for this range of predicted branching fractions. In a theoretical analysis motivated by the $K\pi$ CP puzzle (Sect. 12.3.4), it has been shown [790] that in models with modified or additional Z bosons an increase of the branching fraction by an order of magnitude is possible without inconsistencies with other measurements. The $K\pi$ decays are dominated by isospin-conserving processes, but have a small contribution from isospin-violating penguin processes as well. In the isospin-violating process $B_s \to \phi\pi^0$ the penguin processes are expected to dominate, which means that potential NP contributions can have a much larger relative effect. If these contributions exist, an observation of the $B_s \to \phi\pi^0$ decay is possible. For $B_s \to \phi\rho^0$

decays, LHCb reports $4\,\sigma$ evidence with a branching fraction of $(2.7 \pm 0.7) \times 10^{-7}$ [792], which is lower than, but still consistent with, the SM prediction of $(4.4^{+2.2}_{-0.7}) \times 10^{-7}$. While $B_s \to \phi\rho^0$ tests some of the same physics models as $B_s \to \phi\pi^0$, there are cases, e.g. with parity-symmetric NP models, where only $B_s \to \phi\pi^0$ is sensitive.

Further discussion and outlook Beyond the hierarchy of amplitudes the SU(3) approach makes many specific predictions for observables that are not yet well measured. For example, better or new measurements of branching fractions such as $\mathrm{Br}(\pi^0 K^0)$, $\mathrm{Br}(\eta K^0)$, $\mathrm{Br}(\eta' K^0)$, as well as for the $\bar{K}^{*0}\pi^0$, $\rho^+ K^-$, $\bar{K}^{*0}\eta$, $\bar{K}^{*0}\eta'$, $\omega\bar{K}^0$, $\phi\bar{K}^0$, $\phi\pi^0$, and $\phi\eta'$ modes, the direct CP asymmetries $A_{\mathrm{CP}}^{\eta\pi^0}$, $A_{\mathrm{CP}}^{\eta\eta'}$, $A_{\mathrm{CP}}^{\eta' K^+}$, $A_{\mathrm{CP}}^{\eta K^0_S}$, and the time-dependent CP asymmetries $\mathcal{S}^{\pi^0 K^0_S}$, $\mathcal{S}^{\eta K^0_S}$, $\mathcal{S}^{\eta' K^0_S}$, $\mathcal{S}^{K^0 K^0}$, $\mathcal{S}^{\eta\pi^0}$, $\mathcal{S}^{\eta'\pi^0}$ at Belle II will be very useful in discriminating between different theoretical approaches. We refer to Ref. [781] for a detailed discussion of these and other specific examples.

With more and better data from Belle II, the flavor SU(3) symmetry approach will enable us to learn more about the role of each flavor amplitude in the PP and PV decays and inform us whether additional smaller amplitudes are called for. More insights can be obtained from applying the approach to the helicity amplitudes of VV final states. At the same time, more precise data will allow us to address the question of whether the SU(3) limit continues to be a satisfactory working assumption. A better understanding or parameterization of SU(3) breaking is necessary to distinguish reliably the smaller amplitudes from potential SU(3)-breaking effects in the dominant amplitudes. Also, it is known that decay constants and form factors, which appear in the factorization framework, exhibit sizeable SU(3) breaking. If there are significant corrections to perturbative factorization, as appears to be indicated for some amplitudes, this creates an ambiguity in the treatment of SU(3) breaking, which can only be resolved in terms of a complete parameterization of SU(3) breaking of the charmless decay amplitudes. The likely lack of predictivity due to the increase in independent amplitudes may be compensated by the amount of data anticipated from Belle II, or may motivate combinations of the SU(3) and factorization approaches [793]. Due to its data-driven nature, the SU(3) approach will profit like no other theoretical approach from the input of Belle II and hence contribute to the possible discovery of NP in charmless B meson decays.

12.3. Factorization approach to two-body decays

12.3.1. Introduction

Contributing author: M. Beneke

The notion of factorization in B physics originally referred to an approximation of the hadronic matrix elements $\langle f|Q_i|\bar{B}\rangle$ relevant to charmless two-body decays in terms of the product of a light meson decay constant and a B to light meson transition form factor [794]. In contrast, "factorization" or "QCD factorization" now refers to a systematic separation of scales in $\langle f|Q_f|\bar{B}\rangle$. Contrary to the (useful but ad hoc) approximation of "naive" factorization, QCD factorization implies an expansion of the matrix element in the small parameters $\alpha_s(\mu)$ and Λ/m_b, with $\mu = m_b$ or $\sqrt{m_b\Lambda}$, one of the perturbative scales. Since the α_s series can be calculated order by order (with increasing effort), but only the leading term in the $1/m_b$ expansion assumes a simple form, the generic accuracy of this approach is limited by power corrections of generic size $\Lambda/m_b \approx (10\text{–}20)\%$ at the amplitude level. The actual importance of power corrections depends, however, on the specific amplitude and observable.

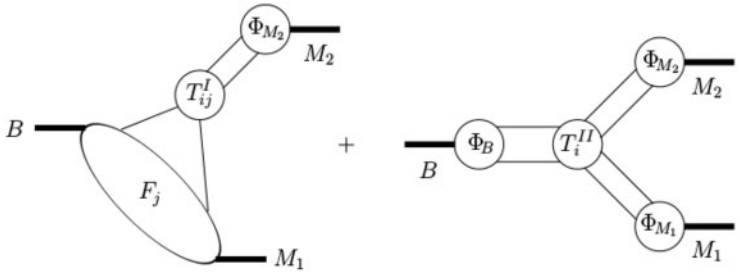

Fig. 132. Graphical representation of the factorization formula given in Eq. (348). Figure taken from Ref. [244].

The QCD factorization approach developed in Refs. [244,415,416] replaces the naive factorization ansatz by a factorization formula that includes radiative corrections and spectator-scattering effects. The basic formula for the hadronic matrix elements is

$$\begin{aligned}\langle M_1 M_2|Q_i|\bar{B}\rangle &= F^{BM_1}(0)\int_0^1 du\, T_i^{\rm I}(u)\Phi_{M_2}(u)\\ &\quad + \int_0^\infty d\omega \int_0^1 du \int_0^1 dv\, T_i^{\rm II}(\omega,u,v)\,\Phi_B(\omega)\Phi_{M_1}(v)\Phi_{M_2}(u)\\ &= F^{BM_1}\, T_i^{\rm I}\star\Phi_{M_2} + \Phi_B\star[H_i^{\rm II}\star J^{\rm II}]\star\Phi_{M_1}\star\Phi_{M_2}, \end{aligned} \tag{348}$$

where $F^{BM_1}(0)$ is a (non-perturbative) B to light meson transition form factor, Φ_{M_i} and Φ_B are light-cone distribution amplitudes, and $T_i^{\rm I,II}$ are perturbatively calculable hard-scattering kernels. M_1 is the meson that picks up the spectator quark from the B meson.[31] The equation is illustrated in Fig. 132. The third line uses a shorthand notation $\star$ for convolutions and indicates that the spectator-scattering effect in the second line is a convolution of physics at the hard scale m_b, encoded in $H_i^{\rm II}$, and the hard-collinear scale $\sqrt{m_b\Lambda}$, encoded in the jet function $J^{\rm II}$. Equation (348) shows that there is no long-distance interaction between the constituents of the meson M_2 and the (BM_1) system at leading order in $1/m_b$. This is the precise meaning of "factorization." Strong interaction scattering phases are generated at leading order in the heavy quark expansion only by perturbative loop diagrams contributing to the kernels $T_i^{\rm I}$ and $H_i^{\rm II}$. Thus, the strong phases and therefore direct CP asymmetries are generically of order $\delta\sim\mathcal{O}(\alpha_s(m_b),\Lambda/m_b)$.

Factorization as embodied by Eq. (348) is not expected to hold at sub-leading order in $1/m_b$. Some power corrections related to scalar currents are enhanced by factors such as $m_\pi^2/((m_u+m_d)\Lambda)$. Some corrections of this type, in particular those related to scalar penguin amplitudes, nevertheless appear to be calculable and turn out to be numerically important. On the other hand, attempts to compute sub-leading power corrections to hard spectator-scattering in perturbation theory usually result in infrared divergences, which signal the breakdown of factorization. These effects are usually estimated and included in the error budget. All weak annihilation contributions belong to this class of effects and often constitute the dominant source of theoretical error, in particular for the direct CP asymmetries. Factorization as above applies to pseudoscalar flavor-non-singlet final states and to the longitudinal polarization amplitudes for vector mesons. Final states with η and η' require additional considerations, but can be included [788]. The transverse helicity amplitudes for vector mesons are formally power-suppressed but can be sizeable, and do not factorize in a simple form [795,796].

[31] The definition of M_1 and M_2 in Eq. (348) and Fig. 132 are opposite to what is shown in Fig. 131.

The description of polarization is therefore more model dependent than branching fractions and CP asymmetries. QCD factorization results are available for a variety of complete sets of final states. References [696,796] contain the theoretical predictions for pseudoscalar and vector meson final states. A similar analysis has been performed for final states with a scalar meson [797], axial-vector mesons [798,799], and a tensor meson [800]. We refer to these papers for the present status of charmless B decay calculations in the factorization approach, and to Ref. [2] for an extended version of this very brief theoretical introduction.

Several variations of factorization have been considered in the literature. In this chapter we shall also refer to the "perturbative QCD" (PQCD) framework [801,802]. PQCD makes the stronger additional assumption that the B meson transition form factors $F^{B\to M_1}(0)$ are also dominated by short-distance physics and factorize into light-cone distribution amplitudes. Both terms in Eq. (348) can then be combined to

$$\langle M_1 M_2|Q_i|\bar{B}\rangle = \phi_B \star [T_i^{\rm PQCD} \star J^{\rm PQCD}] \star \phi_{M_1} \star \phi_{M_2}. \tag{349}$$

It should be mentioned that while the assumptions that lead to Eq. (348) are generally accepted and have been verified in the computation of radiative corrections, the additional assumption required for Eq. (349) has remained controversial, since it relies on regularizing the infrared sensitivity by intrinsic transverse momentum, and the power counting in $1/m_b$ has not been clarified. The original PQCD factorization formula Eq. (349) was revised due to infrared divergences in loop effects [803], which weakens its predictive power. Most phenomenological analyses predate this revision, with few exceptions [804].

Making first-principle calculations of charmless B decay amplitudes precise requires good knowledge of hadronic input parameters such as form factors and moments of distribution amplitudes, accurate perturbative computations, and some understanding of power corrections, either from theory or guided by data. While many issues involved are discussed in the references quoted above, the following summarizes recent theoretical progress on each of them. In order to facilitate comparison with the SU(3) terminology, we note that there is a one-to-one correspondence between the amplitudes notation α_i, β_i introduced in Ref. [696] and used below, and the topological flavor amplitudes, provided SU(3) breaking effects are neglected in the former. The correspondence is

$$T \leftrightarrow \alpha_1,\ C \leftrightarrow \alpha_2,\ E \leftrightarrow \beta_2,\ P \leftrightarrow \alpha_4 + \beta_3,\ S \leftrightarrow \alpha_3,\ P_{\rm EW} \leftrightarrow \alpha_{3,\rm EW},\ PA \leftrightarrow \beta_4,\ \text{etc.} \tag{350}$$

A complete list can be found in Ref. [805].

12.3.2. B meson light-cone distribution

Contributing author: T. Feldmann

The B meson light-cone distribution amplitudes (LCDAs) constitute essential hadronic input parameters not only in the QCD factorization formula Eq. (348) for exclusive charmless B decays, but also for the computation of spectator corrections to heavy-to-light form factors and rare radiative decays. They also enter correlation functions in certain variants of the QCD sum rule approach. The most important parameter is the inverse moment [415]

$$\frac{1}{\lambda_B} \equiv \int_0^\infty \frac{d\omega}{\omega}\, \Phi_B(\omega), \tag{351}$$

which enters the overall size of spectator-scattering effects in Eq. (348) through the quantity

$$r_{\rm sp} = \frac{9 f_\pi f_B^{\rm HQET}}{m_b F^{B\to\pi}(0)} \frac{1}{\lambda_B}, \tag{352}$$

where $f_B^{\rm HQET}$ denotes the B meson decay constant in heavy quark effective theory (HQET) and $F^{B\to\pi}(0)$ the $B \to \pi$ transition form factor at $q^2 = 0$. For example, the color-suppressed tree amplitude α_2 for $B \to \pi\pi$ decays has been calculated as [785]

$$\alpha_2(\pi\pi) = 0.220 - [0.179 + 0.077\, i]_{\rm NLO} + \left[\frac{r_{\rm sp}}{0.445}\right]\left\{[0.114]_{\rm LOsp} + [0.067]_{\rm tw3}\right\} + \cdots . \tag{353}$$

It is to be noted that spectator-scattering effects tend to partly cancel the NLO vertex corrections, which enhances the sensitivity on λ_B. The inverse moment λ_B also enters the factorization formula for the partial rate of the $B \to \gamma\ell\nu$ decay with large photon energy $E_\gamma \gg \Lambda$ [806–808]. Since, at leading power,

$$\frac{d\Gamma}{dE_\gamma} \propto \frac{1}{\lambda_B^2}, \tag{354}$$

this process can be used to determine λ_B experimentally, providing crucial input to the phenomenology of charmless decays.

The strongest experimental bound on λ_B (from Belle) using the up-to-date theoretical results from Refs. [223,246] are still rather weak [247]. Belle II is uniquely suited to improving the measurement of λ_B with $B \to \ell\nu\gamma$ decays (Sect. 8.4.1). In the following, we therefore summarize recent theoretical progress in the understanding of the leading-twist B meson LCDA.

The formal definition of the relevant LCDA[32] $\Phi_B(\omega)$ is given in terms of the Fourier transform of the hadronic matrix element of a light-cone operator in HQET [809],

$$m_B f_B^{(\rm HQET)}\, \phi_B^+(\omega) = \int \frac{d\tau}{2\pi}\, e^{i\omega\tau}\, \langle 0|\bar q(\tau n)\,[\tau n,\,0]\, \not{n}\gamma_5\, h_v^{(b)}(0)|\bar B(m_B v)\rangle, \tag{355}$$

where v^μ is the heavy quark velocity, n^μ a light-like ($n^2 = 0$) vector, and $[\tau n, 0]$ denotes a light-like Wilson line connecting the two field positions 0 and τn. The LCDA $\phi_B^+(\omega)$ can be interpreted as the probability amplitude for the distribution of the light antiquark's momentum k in a two-particle Fock state of the B meson, more precisely its light-cone projection $\omega \equiv n \cdot k$.

The LCDA ϕ_B^+ is a scale-dependent quantity. The scale dependence is controlled by an RG equation [810]. Recent progress is related to the identification of the eigenfunctions of the one-loop RG kernel [811]

$$f_{\omega'}(\omega) \equiv \sqrt{\frac{\omega}{\omega'}}\, J_1\left(2\sqrt{\frac{\omega}{\omega'}}\right) \tag{356}$$

with eigenvalues

$$\gamma_{\omega'} = -\left(\Gamma_{\rm cusp}\, \ln\frac{\mu}{\hat\omega'} + \gamma_+\right). \tag{357}$$

[32] Now denoted as $\phi_B^+(\omega)$. There is another Dirac structure, which defines a sub-leading twist LCDA, denoted as $\phi_B^-(\omega)$.

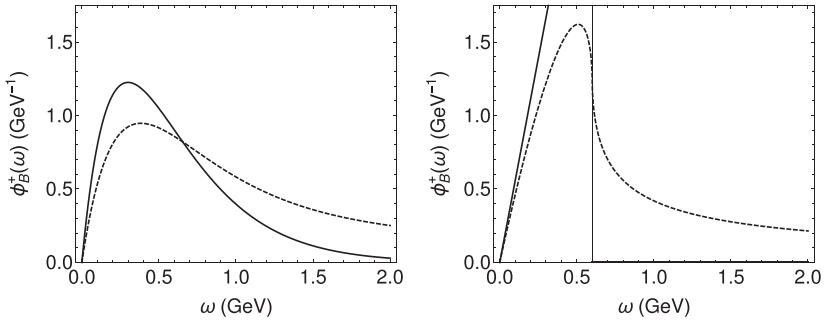

Fig. 133. Two models for $\phi_B^+(\omega)$ (solid lines): "Exponential" (left panel) and "Parton" (right panel), as defined in Eq. (359). The dashed lines illustrate the effect of RG evolution; see Ref. [811] for further details.

Here, $J_1(z)$ is a Bessel function. It has been noted that Eq. (357) can also be constructed from the symmetries of collinear conformal transformations [812]. The eigenfunctions are labelled by a continuous parameter ω', which can be viewed as a "dual momentum" (we also use the notation $\hat{\omega}' \equiv \omega' e^{-2\gamma_E}$ below). The spectrum in ω' defines the "dual" representation of the B meson LCDA in terms of a function $\rho_B^+(\omega')$, related to the original LCDA via

$$\phi_B^+(\omega) = \int_0^\infty \frac{d\omega'}{\omega'} f_{\omega'}(\omega)\, \rho_B^+(\omega') \quad \Leftrightarrow \quad \rho_B^+(\omega') = \int_0^\infty \frac{d\omega}{\omega} f_{\omega'}(\omega)\, \phi_B^+(\omega). \tag{358}$$

The key result is that the scale dependence of the dual function $\rho_B^+(\omega')$ is described by a simple multiplicative RG factor [811], which facilitates the construction and interpretation of models for the LCDA.

The effect of the RG evolution is illustrated in Fig. 133 for two models,

$$\text{"Exponential" [809]:} \quad \phi_B^+(\omega,\mu_0) = \frac{\omega\, e^{-\omega/\omega_0}}{\omega_0^2} \leftrightarrow \rho_B^+(\omega',\mu_0) = \frac{e^{-\omega_0/\omega'}}{\omega'},$$

$$\text{"Parton" [813]:} \quad \phi_B^+(\omega,\mu_0) = \frac{\omega\,\theta(2\bar{\Lambda}-\omega)}{2\bar{\Lambda}^2} \leftrightarrow \rho_B^+(\omega',\mu_0) = \frac{1}{\bar{\Lambda}} J_2\left(2\sqrt{\frac{2\bar{\Lambda}}{\omega'}}\right), \tag{359}$$

where ω_0 and $\bar{\Lambda} = M_B - m_b$ are the two parameters of the model, and the model form is supposed to hold at a particular reference scale μ_0. One then observes from the figure that the RG evolution towards higher scales generates a "radiative tail" at large values of ω.

In applications of QCD factorization the jet function in the factorization theorem takes the form of a polynomial in $\ln\omega$, or $\ln\omega'$ in dual space. One thus generically needs the logarithmic moments[33]

$$L_n(\mu) \equiv \int_0^\infty \frac{d\omega'}{\omega'} \ln^n\left(\frac{\hat{\omega}'}{\mu}\right) \rho_B^+(\omega',\mu) \tag{360}$$

for $n = 0, 1, 2, \ldots$ These obey the RG equation [811]

$$\frac{dL_n(\mu)}{d\ln\mu} = \Gamma_{\text{cusp}}(\alpha_s)\, L_{n+1}(\mu) - \gamma_+(\alpha_s) L_n(\mu) - n\, L_{n-1}(\mu), \tag{361}$$

[33] The relation to the convention used, for instance, in Ref. [814] reads

$$L_0 \equiv \frac{1}{\lambda_B(\mu)}, \qquad L_1 \equiv L_0\,\sigma_1(\mu), \qquad L_2 \equiv L_0\,\sigma_2(\mu).$$

which mixes neighboring moments. For phenomenological applications one may consider—either in dual space or in the original ω space—a truncated set $\{L_0, L_1, \ldots, L_N\}$ of logarithmic moments, or a particular *model* for $\rho_B^+(\omega')$ or $\phi_B^+(\omega)$, respectively.

An advantage of the dual representation is that large and small values of ω' are clearly separated because they do not mix under renormalization. This is useful, since large values of ω' can be described by perturbative dynamics which implements the QCD-improved parton model, subject to constraints from a local operator product expansion (OPE) in the context of HQET [814–816]. At fixed order in the strong coupling one finds the model-independent result [817]

$$\rho_B^+(\omega')_{\text{pert.}} = C_0 \, \frac{1}{\bar{\Lambda}} J_2\left(2\sqrt{\frac{2\bar{\Lambda}}{\omega'}}\right) + (C_0 - C_1)\, \frac{4}{\bar{\Lambda}} J_4\left(2\sqrt{\frac{2\bar{\Lambda}}{\omega'}}\right) + \cdots \tag{362}$$

for $\omega' \gg \bar{\Lambda}$ with matching coefficients

$$\begin{aligned} C_0 &= 1 + \frac{\alpha_s C_F}{4\pi}\left(-2L^2 + 2L - 2 - \frac{\pi^2}{12}\right) + \mathcal{O}(\alpha_s^2), \\ C_0 - C_1 &= \frac{\alpha_s C_F}{4\pi}\left(-\frac{13}{4}\right) + \mathcal{O}(\alpha_s^2), \end{aligned} \tag{363}$$

and $L = \ln \mu/\hat{\omega}'$. Equation (362) reduces to the free parton result in Eq. (359) for $\alpha_s \to 0$. Furthermore, the RG equations can be used to resum large logarithms $|L| \gg 1$. This implies that the function $\rho_B^+(\omega')$ falls off faster than $1/\omega'$ [817]. If one splits the logarithmic moments in Eq. (360) as $L_n = L_n^+ + L_n^-$ by separating the ω' integral at $\omega' = \mu$ into a large ω' part (+) and small ω' part (−), one concludes that

- L_n^+ are completely determined by the (RG-improved) OPE and contain the information on the HQET parameters $\bar{\Lambda}$, etc.;
- L_n^- depend on (non-local) IR dynamics and are *unrelated* to HQET parameters $\bar{\Lambda}$, etc.

Numerically, one typically finds that $L_n^- \gg L_n^+$, and thus the information from the LCDAs needed in phenomenological applications of the QCD factorization approach in *exclusive B* decays, is basically unrelated to the information on the HQET parameters entering the OPE analysis of *inclusive B* decays. While the non-local effects entering L_n^- are notoriously difficult to estimate with lattice QCD simulations, a dedicated analysis within the QCD sum rule approach, using the dual representation of the B meson LCDA, might improve the situation on the theoretical side. Information on the first few moments L_n^- can then be used in the future as a theory prior in a global analysis of exclusive radiative, semi-leptonic, and charmless B decays.

12.3.3. Weak annihilation

Contributing author: C. Bobeth

Weak annihilation (WA) corresponds to parts of the decay amplitude where the constituent quarks of the decaying B meson are annihilated by one of the local $|\Delta B| = 1$ four-quark operators in the weak effective Lagrangian in Eq. (344), and two quarks of the final state are created by the operator. The remaining quark pair in the final state is created via QCD interactions.

The flavor amplitudes E and PA in Fig. 131 represent the subset of annihilation topologies that are most relevant for the SU(3) approach. In factorization approaches to charmless two-body decays,

WA is of sub-leading order in $1/m_b$, but is a potentially important contribution in all of those cases where the leading-order amplitudes are small. This obviously applies to pure annihilation modes, but also to penguin-dominated transitions, especially when there is a vector meson in the final state.

Such $1/m_b$ corrections are not covered by the factorization formula in Eq. (348). Technically, this manifests itself in so-called "end-point divergences" in convolutions of the hard scattering kernels with light meson distribution amplitudes, if one attempts such a factorization. In Refs. [416,696] a parameterization of the annihilation amplitudes has been introduced that replaces the divergent expressions by hadronic parameters, ρ_A. There are WA amplitudes $b_{1,2}$ due to current–current operators ($Q_{1,2}$), $b^p_{3,4}$ due to QCD penguin operators ($Q_{3,4,5,6}$), and $b^p_{3,4,\mathrm{EW}}$ due to electroweak penguin operators ($Q_{7,8,9,10}$), which in QCD factorization are parameterized as

$$\begin{aligned} b_1 &\propto C_1 A_1^{\mathrm{i}}, \\ b_2 &\propto C_2 A_1^{\mathrm{i}}, \\ b_3^p &\propto C_3 A_1^{\mathrm{i}} + C_5 (A_3^{\mathrm{i}} + A_3^{\mathrm{f}}) + N_c C_6 A_3^{\mathrm{f}}, \\ b_4^p &\propto C_4 A_1^{\mathrm{i}} + C_6 A_2^{\mathrm{i}}, \\ b_{3,\mathrm{EW}}^p &\propto C_9 A_1^{\mathrm{i}} + C_7 (A_3^{\mathrm{i}} + A_3^{\mathrm{f}}) + N_c C_8 A_3^{\mathrm{f}}, \\ b_{4,\mathrm{EW}}^p &\propto C_{10} A_1^{\mathrm{i}} + C_8 A_2^{\mathrm{i}}. \end{aligned} \tag{364}$$

As already mentioned, $E \leftrightarrow b_2$ and $PA \leftrightarrow b_4^p$ in terms of flavor amplitudes, while b_3^p can always be absorbed into P. The b_i coefficients are identical to the β_i coefficients, which appear in Eq. (350), up to a proportionality factor defined in Ref. [696]. In the above equation C_i denote the Wilson coefficients of operators Q_i, and $p = u, c$. $A^{\mathrm{i}}_{1,2,3}$ and A^{f}_3 can be regarded as non-perturbative objects[34] with strong phases. They are further expressed in terms of quantities $\rho^{\mathrm{i,f}}_{A_{1,2,3}}$ [696], where the superscript indicates whether the gluon that creates the second quark–antiquark pair in the final state was radiated off the initial (i) or final (f) state (anti-)quarks. The sizes of the Wilson coefficients determine greatly the importance of the various WA amplitudes in CP-averaged observables.

The theoretical uncertainties due to WA are estimated by varying the complex-valued ρ_As within ranges given by naive dimensional arguments for each observable separately. This conservative procedure yields large uncertainties, especially in CP asymmetries and, of course, all pure annihilation modes, that allow for agreement with most of the data, in part because it allows the situation where different values of the ρ_As lead to agreement between predictions and measurements of different observables of one and the same decay mode.

Note that in the framework of light cone sum rules, WA contributions are free of endpoint divergences [818] due to different assumptions and approximations. This approach yields the same dependence on Wilson coefficients C_i as given in Eq. (364), and the non-perturbative $A^{\mathrm{i,f}}_{1,2,3}$ can be evaluated explicitly. We also mention that WA tree diagrams are calculated within the PQCD framework [802,819].

The explicit dependence of amplitudes on WA contributions $b_i^{(p)}$ for charmless $B \to$ PP, PV, VP Refs. [416,696] and $B \to$ VV [796,820] can be quite different, such that certain groups of decays and/or certain observables have an enhanced sensitivity to a particular $A^{\mathrm{i,f}}_{1,2,3}$. For example,

[34] A proper factorization theorem would establish a relation to matrix elements of well-defined operators. These matrix elements have to be either determined from data or calculated by non-perturbative means.

$b \to (s,d)q\bar{q}$ transitions dominated by QCD and QED penguin operators depend mainly on b_3^p, where $A_3^{\rm f}$ is enhanced by a color factor $N_c = 3$ such that $C_6 \approx 8C_5 \approx 3C_3$ in the SM at the renormalization scale $\mu \sim m_b$. Further, the pure annihilation decays $B_d \to K^+K^-$, $B_s \to \pi^+\pi^-$ depend on b_4^p and b_1, being sensitive to $A_{1,2}^{\rm i}$. It is therefore of utmost importance to improve and extend measurements for as many decay systems as possible to test these predictions and relations.

Belle II is the only experiment that can provide measurements of complete decay systems related by $u \leftrightarrow d$ quark exchange such as, for example, $B^+ \to K^+\pi^0, K^0\pi^+$ and $B^0 \to K^+\pi^-, K^0\pi^0$, due to its identification capabilities for charged *and* neutral particles. This enables Belle II to provide combinations of observables within such decay systems accounting for cancellations of common experimental systematic uncertainties. Prominent examples are ratios of branching fractions such as

$$R_n = \frac{1}{2}\frac{\mathrm{Br}(B^0 \to K^+\pi^-)}{\mathrm{Br}(B^0 \to K^0\pi^0)}, \tag{365}$$

or differences of CP asymmetries such as $\Delta A_{K\pi} = A_{\rm CP}^{K^+\pi^0} - A_{\rm CP}^{K^+\pi^-}$, etc., which are less sensitive to theory uncertainties.

Some phenomenological studies supplement the leading-power QCDF predictions with WA contributions and infer the latter from data. The two main strategies can be classified as

(1) *either* fit whole WA amplitudes $b_i^{(p)}$, see Ref. [821] for the $B \to K\pi$ system;[35]
(2) *or* use short-distance Wilson coefficients from a given model and fit only long-distance parts $A_{1,2,3}^{\rm i,f}$ [822–826].

The advantage of strategy (2) over (1) is that it consistently uses the Wilson coefficients of a given model, SM or extensions thereof, in both the leading $1/m_b$ and WA contributions.

The relative size of WA contributions to leading amplitudes has been determined from recent data of $b \to (s,d)q\bar{q}$ transitions for the decay systems $B \to K + (\pi, \eta^{(\prime)}, K)$, $B_s \to \pi\pi, K\pi, KK$; $B \to K + (\rho, \phi, \omega)$, $B \to K^* + (\pi, \eta^{(\prime)})$; $B \to K^* + (\rho, \phi, \omega, K^*)$, $B_s \to \phi\phi, K^*\phi, K^*K^*$ following strategy (2) [823], assuming one universal ρ_A per decay system. These systems depend primarily on the WA amplitude b_3^p being dominated by $A_3^{\rm f}$. The fits show that within the SM data do not require a huge b_3^p, but usually they are a sizeable fraction of the leading amplitude α_4^p. For example, at 68% probability the minimal required fraction varies among the $B \to$ PP systems in the range 0–60%, and is larger (40–80%) for $B \to$ PV systems as well as for $B \to$ VV systems (20–90%). This is related to the larger absolute size of the QCD penguin coefficient $\alpha_4^p = a_4^p \pm r_\chi^{M_2} a_6^p$ for PP compared to PV and VV final states (see the following subsection). Only in a few cases can the data be explained at 95% probability without WA. Within current large experimental uncertainties, the goodness-of-fit is always excellent except for the $B \to K\pi$ system, where tensions of around 2–3 σ are observed for observable combinations R_n and $\Delta A_{K\pi}$. The potential underlying mechanism (WA or sub-leading hard scattering contributions) of this so-called $K\pi$ CP puzzle can be further scrutinized by improved measurements of direct and mixing-induced CP asymmetries in $B^0 \to K^0\pi^0$ expected from Belle II.

Pure WA decays, such as the observed modes $B^0 \to K^+K^-$ and $B_s \to \pi^+\pi^-$, depend on $A_{1,2}^{\rm i}$, but not on the hadronic quantity λ_B and form factors. The fit of the preferred regions of a universal $\rho_A = \rho_A^{\rm i}$ from branching fractions of $B^0 \to K^+K^-$ and $B_s \to \pi^+\pi^-$ shows a strong incompatibility

[35] Reference [821] fits sub-leading contributions in general, of which one is WA.

[823,827], but experimental uncertainties are still large. In the case $A_1^{\rm i} \approx A_2^{\rm i}$ only one strong phase would be present, yielding tiny CP asymmetries. It is important to measure the latter and to search for other pure WA decays, such as $B^0 \to K^- K^{*+}$, $K^{*-} K^+$, $K^{*-} K^{*+}$ and related B_s decays.

In view of the large number of $\rho_{A_{1,2,3}}^{\rm i,f}$ but limited set of observables per decay, the assumption that the dependence on u, d, and s quarks is small in initial- and final-state interactions would allow one to combine different decay systems to fit for universal $\rho_A^{\rm i}$ and $\rho_A^{\rm f}$ parameters. However, due to the aforementioned incompatibility of purely WA decays $B^0 \to K^+ K^-$ and $B_s \to \pi^+ \pi^-$, different $\rho_A^{\rm i,f}$s are often assumed in $B_{u,d}$ and B_s decays. This has been done for $B_{u,d,s} \to \pi\pi, \pi K, KK$ in Ref. [822], $B_{u,d} \to$ PV in Ref. [824] and in combination with $B_s \to$ PV in Ref. [825], as well as $B_{u,d} \to$ VV in Ref. [826]. In these papers, λ_B and in part sub-leading hard scattering contributions have also been included as fit parameters.

For example, in $B \to$ PP the $\rho_A^{\rm i}$s are constrained from the pure annihilation decays $B_d \to K^+ K^-$ and $B_s \to \pi^+ \pi^-$, where current data allow for similar size $\rho_A^{\rm i}$s in $B_{u,d}$ and B_s decays, and the same has been tested for $\rho_A^{\rm f}$. In the global fit the aforementioned tension between $B^0 \to K^+ K^-$ and $B_s \to \pi^+ \pi^-$ is less significant, such that there are no indications of SU(3) flavor breaking within the current experimental accuracy. However, the data prefer $\rho_A^{\rm i} \neq \rho_A^{\rm f}$. These fits also prefer values of $\lambda_B \approx 200\,\text{MeV}$, similar to values inferred from data of tree-dominated decays $B \to \pi\pi$, $\pi\rho$, $\rho\rho$ [785]. Based on the stronger assumption of equal $\rho_A^{\rm i}$ in $B_{u,d}$ and B_s decays, and analogously for $\rho_A^{\rm f}$, predictions for not yet measured $B_s \to P^0 P^0$ ($P = \pi, K$) modes are given, which can be tested in the future.

In the case of $B \to$ PV, the currently large experimental uncertainties in B_s decays also allow for universal $\rho_A^{\rm i}$ and $\rho_A^{\rm f}$ in $B_{u,d}$ and B_s decays, and again prefer $\rho_A^{\rm i} \neq \rho_A^{\rm f}$. Improved measurements of $B_s \to$ PV are necessary to investigate whether there is sizeable SU(3) breaking, demanding a dedicated B_s physics run of Belle II.

Additional polarization dependence enters through $A_h^{\rm i,f}$ ($h = L, T$, with $T = \perp, \parallel$) in $B \to$ VV decays, which also allows for the assumption of polarization-dependent $\rho_{A,h}^{\rm i,f}$. The assumption of polarization-independent $\rho_{A,L}^{\rm i,f} = \rho_{A,T}^{\rm i,f}$ leads to similar observations as in $B \to$ PP, PV decays. On the other hand, it is found that the data of $B \to$ VV decays can be also described with polarization-dependent but universal $\rho_{A,h}^{\rm i} = \rho_{A,h}^{\rm f}$ for initial and final state radiation.

The preferred regions of $\rho_A^{\rm f}$ from $B \to$ PP, PV, VV decays are close to each other, which is not the case for the $\rho_A^{\rm i}$.

12.3.4. Direct CP asymmetries at NLO

Contributing authors: G. Bell, T. Huber

Direct CP asymmetries require the interference of two decay amplitudes with different CP ("weak") and rescattering ("strong") phases. As already observed, within QCD factorization strong phases are generated only through loop effects proportional to $\alpha_s(m_b)$ or power corrections proportional to Λ/m_b. One therefore generically expects that direct CP asymmetries are small, which is in qualitative agreement with experimental data. Larger strong phases and hence larger CP asymmetries may arise whenever the leading-order term is suppressed, e.g. by color factors or Wilson coefficients.

The dependence on the strong phases makes theoretical calculations of direct CP asymmetries more involved than those of branching ratios or mixing-induced CP asymmetries. A clear picture about the relative size and sign of direct CP asymmetries requires, in particular, controlling sub-leading terms in the double expansion in $\alpha_s(m_b)$ and Λ/m_b. Whereas the former can be systematically computed

using loop techniques, the latter cannot be calculated at present and their modeling introduces sizeable theoretical uncertainties.

The various contributions to the decay amplitudes are typically classified according to their topological structure into tree, QCD penguin, electroweak penguin, and annihilation topologies. In the notation of Ref. [696], the $\bar{B} \to \pi \bar{K}$ amplitudes, which play an important role in the following discussion, are parameterized as

$$\begin{aligned}
\mathcal{A}_{B^- \to \pi^- \bar{K}^0} &= \lambda_p \, A_{\pi \bar{K}} \big[\hat{\alpha}_4^p - \tfrac{1}{2}\alpha_{4,\mathrm{EW}}^p\big], \\
\sqrt{2}\,\mathcal{A}_{B^- \to \pi^0 K^-} &= \lambda_p \, A_{\pi \bar{K}} \big[\delta_{pu}\,\alpha_1 + \hat{\alpha}_4^p + \alpha_{4,\mathrm{EW}}^p\big] + \lambda_p \, A_{\bar{K}\pi} \big[\delta_{pu}\,\alpha_2 + \tfrac{3}{2}\alpha_{3,\mathrm{EW}}^p\big], \\
\mathcal{A}_{\bar{B}^0 \to \pi^+ K^-} &= \lambda_p \, A_{\pi \bar{K}} \big[\delta_{pu}\,\alpha_1 + \hat{\alpha}_4^p + \alpha_{4,\mathrm{EW}}^p\big], \\
\sqrt{2}\,\mathcal{A}_{\bar{B}^0 \to \pi^0 \bar{K}^0} &= \lambda_p \, A_{\pi \bar{K}} \big[-\hat{\alpha}_4^p + \tfrac{1}{2}\alpha_{4,\mathrm{EW}}^p\big] + \lambda_p \, A_{\bar{K}\pi} \big[\delta_{pu}\,\alpha_2 + \tfrac{3}{2}\alpha_{3,\mathrm{EW}}^p\big]
\end{aligned} \tag{366}$$

up to power-suppressed annihilation topologies, which are not shown for simplicity (the exact expressions can be found in Ref. [696]). The corresponding amplitudes with $\pi \to \rho$ or/and $K \to K^*$ take the same form with the appropriate meson substitution. Here, $\lambda_p = V_{pb} V_{ps}^*$ and the terms must be summed over $p = u, c$. The prefactors $A_{M_1 M_2} \propto f_{M_2} F^{BM_1}(M_2^2)$ reflect the factorized structure of the hadronic matrix elements in terms of a form factor and a decay constant.

The above $\Delta S = 1$ amplitudes are dominated by the charm penguin topology $\hat{\alpha}_4^c$. A non-zero direct CP asymmetry is then generated via its interference with the contribution $\propto \lambda_u$. If this is the color-allowed tree topology α_1—and if one neglects the other topologies for the moment—one obtains $\Delta A_{K\pi} = A_{\mathrm{CP}}^{K^+\pi^0} - A_{\mathrm{CP}}^{K^+\pi^-} = 0$. The observed value $\Delta A_{K\pi} = (12.2 \pm 2.2)\%$ constitutes the so-called $B \to \pi K$ CP puzzle, which has attracted a lot of attention in the past, since it could hint at a NP contribution to the electroweak penguin amplitude $\alpha_{3,\mathrm{EW}}^c$. This interpretation is, however, flawed by the fact that the remaining topologies cannot be neglected. It is equally possible to explain the $B \to \pi K$ CP puzzle by purely hadronic effects, if the color-suppressed tree amplitude α_2 and its phase are larger than naively expected.

In order to better understand the pattern of direct CP asymmetries, perturbative corrections to the QCD factorization framework have been worked out to NNLO, i.e. $\mathcal{O}(\alpha_s^2)$, accuracy.[36] According to the factorization formula in Eq. (348), this includes two sets of hard-scattering kernels—vertex corrections (T_i^{I}) and spectator-scattering contributions (T_i^{II})—for each topological amplitude.

Both types of $\mathcal{O}(\alpha_s^2)$ corrections have been worked out for the tree topologies [784,785,828–831]. Using the input parameters specified in Ref. [785], the color-allowed tree amplitude for the $\pi\pi$ final states becomes (see also Ref. [831,832])

$$\alpha_1(\pi\pi) = 1.000^{+0.029}_{-0.069} + (0.011^{+0.023}_{-0.050})i, \tag{367}$$

which is close to its leading-order value 1.009. As the amplitude is stable under radiative corrections, the theoretical uncertainties are small and the strong phase is negligible.

The situation is quite different for the color-suppressed tree amplitude. In order to understand why the respective uncertainties are much larger, it is instructive to disentangle the various perturbative contributions. Extending Eq. (353) to NNLO [785,831], the expression for $\alpha_2(\pi\pi)$ reads

$$\alpha_2(\pi\pi) = 0.220 - [0.179 + 0.077\,i]_{\mathrm{NLO}} - [0.031 + 0.050\,i]_{\mathrm{NNLO}}$$

[36] As direct CP asymmetries first arise at $\mathcal{O}(\alpha_s)$, the counting of the perturbative orders is shifted by one unit, and the α_s^2 correction represents an NLO effect in this case.

$$+\left[\frac{r_{\rm sp}}{0.445}\right]\left\{[0.114]_{\rm LOsp}+[0.049+0.051i]_{\rm NLOsp}+[0.067]_{\rm tw3}\right\}$$
$$=0.240^{+0.217}_{-0.125}+(-0.077^{+0.115}_{-0.078})i. \tag{368}$$

Here, the first term is the leading-order result, and the next two terms represent corrections to the vertex kernel $T_i^{\rm I}$. Note that the real part almost cancels in this sum, which makes this amplitude particularly sensitive to the spectator-scattering mechanism ($T_i^{\rm II}$). Unfortunately, the normalization of this contribution—encoded in $r_{\rm sp}$—is currently only poorly constrained, which is mainly related to the B meson light cone distribution amplitude ($r_{\rm sp}\propto 1/\lambda_B$, see Sect. 12.3.2). It is therefore possible to enhance the color-suppressed tree amplitude by tuning the hadronic parameters, but the relative strong phase between α_1 and α_2 is stable under this variation, and predicted to be small. Thus, the $B\to\pi K$ CP puzzle cannot be explained by perturbative corrections to α_2.

The NNLO calculation of the penguin topologies is incomplete to date. Whereas the spectator-scattering contributions are known [786], only the current–current [833] and magnetic dipole [834] operator insertions to the kernels $T_i^{\rm I}$ have been computed so far. The new $\mathcal{O}(\alpha_s^2)$ corrections are particularly important for the imaginary part of the QCD penguin amplitudes [833,835]. The partial NNLO result reads

$$a_4^u(\pi\bar K)/10^{-2}=(-2.46^{+0.49}_{-0.24})+(-1.94^{+0.32}_{-0.20})i,$$
$$a_4^c(\pi\bar K)/10^{-2}=(-3.34^{+0.43}_{-0.27})+(-1.05^{+0.45}_{-0.36})i. \tag{369}$$

The most recent numbers for the electroweak penguin amplitudes can be found in Ref. [786].

The full QCD penguin amplitude $\hat\alpha_4^p$ in Eq. (366) is a combination of three terms,

$$\hat\alpha_4^p=a_4^p\pm r_\chi^{M_2}a_6^p+\beta_3^p, \tag{370}$$

where a_4^p is the leading-power contribution from above, $r_\chi^{M_2}a_6^p$ is a power-suppressed scalar penguin amplitude (currently known to NLO [416]), and β_3^p is the penguin annihilation amplitude. The plus (minus) sign applies to decays where the meson M_1, which picks up the spectator quark, is a pseudoscalar (vector) meson; see Fig. 132. Equation (370) has two important implications. First, as the second term depends on the spins of the final-state mesons, QCD factorization predicts a specific hierarchy of the penguin amplitudes for final states with pseudoscalar and vector mesons. This pattern is clearly reflected in the experimental data [833]. Second, although the first term in Eq. (370) is the only leading-power contribution, all terms may numerically be of similar magnitude. The NNLO correction to a_4^p is therefore diluted in the full QCD penguin amplitude $\hat\alpha_4^p$.

These features are essential for understanding the theoretical predictions for direct CP asymmetries. As an example, Table 101 shows (partial) NNLO numbers for $\bar B\to\pi\bar K^{(*)}$ and $\bar B\to\rho\bar K$ decays [833].[37] First, one notes that the predicted CP asymmetries are generically larger for $\pi\bar K^*$ and $\rho\bar K$ final states, and have larger uncertainties than for $\pi\bar K$ final states. The reason is that the a_6^p term, which exceeds the formally leading term a_4^p and adds up constructively for $\pi\bar K$, is practically absent for $\pi\bar K^*$ and adds destructively for $\rho\bar K$. The charm penguin amplitude $\hat\alpha_4^c$ is therefore smaller and

[37] The table does not provide results for the $\rho\bar K^*$ final states, because (partial) NNLO accuracy is available only for the longitudinal polarization amplitude, while the transverse amplitudes are much more uncertain; see Sect. 12.6. Polarization effects in the $\rho\bar K^*$ final states are discussed in Sect. 12.6.3, and Table 103 quotes results for the direct CP asymmetries.

Table 101. Direct CP asymmetries A_{CP}, difference of direct CP asymmetry ΔA, and the isospin-breaking parameter I (all in percent) for the πK, πK^*, and ρK final states. The theoretical values are taken from Ref. [833]. The column NNLO+LD (long distance) includes an estimate of non-factorizable annihilation contributions. The theoretical errors are due to CKM and hadronic parameters, respectively. The errors on the experimental values of ΔA and I are computed from those of the individual observables appearing in Eq. (371) for πK (and analogous sum rules for πK^* and ρK), ignoring possible correlations. The fourth column contains the experimental world average (WA) values from Ref. [230]. The last column includes the precision on I determined by fitting Eq. (371), using the complete set of measurements from Belle for $I_{K\pi}$, and from BaBar for $I_{K^*\pi}$ and $I_{K\rho}$ (Sect. 12.4). The first and second errors in parentheses are obtained by repeating the fit with the errors on the branching fractions and A_{CP} scaled to the expected results with 5 and 50 ab^{-1} of Belle II data, respectively.

	NLO	NNLO	NNLO + LD	Exp (WA)	Exp (Belle II)
$A_{CP}^{\pi^-\bar{K}^0}$	$0.71^{+0.13+0.21}_{-0.14-0.19}$	$0.77^{+0.14+0.23}_{-0.15-0.22}$	$0.10^{+0.02+1.24}_{-0.02-0.27}$	-1.7 ± 1.6	
$A_{CP}^{\pi^0 K^-}$	$9.42^{+1.77+1.87}_{-1.76-1.88}$	$10.18^{+1.91+2.03}_{-1.90-2.62}$	$-1.17^{+0.22+20.00}_{-0.22-6.62}$	4.0 ± 2.1	
$A_{CP}^{\pi^+ K^-}$	$7.25^{+1.36+2.13}_{-1.36-2.58}$	$8.08^{+1.52+2.52}_{-1.51-2.65}$	$-3.23^{+0.61+19.17}_{-0.61-3.36}$	-8.2 ± 0.6	
$A_{CP}^{\pi^0 \bar{K}^0}$	$-4.27^{+0.83+1.48}_{-0.77-2.23}$	$-4.33^{+0.84+3.29}_{-0.78-2.32}$	$-1.41^{+0.27+5.54}_{-0.25-6.10}$	1 ± 10	-14 ± 13
$\Delta A_{K\pi}$	$2.17^{+0.40+1.39}_{-0.40-0.74}$	$2.10^{+0.39+1.40}_{-0.39-2.86}$	$2.07^{+0.39+2.76}_{-0.39-4.55}$	12.2 ± 2.2	
$I_{K\pi}$	$-1.15^{+0.21+0.55}_{-0.22-0.84}$	$-0.88^{+0.16+1.31}_{-0.17-0.91}$	$-0.48^{+0.09+1.09}_{-0.09-1.15}$	-14 ± 11	$-27 \pm 14(7)(3)$
$A_{CP}^{\pi^-\bar{K}^{*0}}$	$1.36^{+0.25+0.60}_{-0.26-0.47}$	$1.49^{+0.27+0.69}_{-0.29-0.56}$	$0.27^{+0.05+3.18}_{-0.05-0.67}$	-3.8 ± 4.2	
$A_{CP}^{\pi^0 K^{*-}}$	$13.85^{+2.40+5.84}_{-2.70-5.86}$	$18.16^{+3.11+7.79}_{-3.52-10.57}$	$-15.81^{+3.01+69.35}_{-2.83-15.39}$	-6 ± 24	-6 ± 24
$A_{CP}^{\pi^+ K^{*-}}$	$11.18^{+2.00+9.75}_{-2.15-10.62}$	$19.70^{+3.37+10.54}_{-3.80-11.42}$	$-23.07^{+4.35+86.20}_{-4.05-20.64}$	-23 ± 6	
$A_{CP}^{\pi^0 \bar{K}^{*0}}$	$-17.23^{+3.33+7.59}_{-3.00-12.57}$	$-15.11^{+2.93+12.34}_{-2.65-10.64}$	$2.16^{+0.39+17.53}_{-0.42-36.80}$	-15 ± 13	
$\Delta A_{CP}^{K^*\pi}$	$2.68^{+0.72+5.44}_{-0.67-4.30}$	$-1.54^{+0.45+4.60}_{-0.58-9.19}$	$7.26^{+1.21+12.78}_{-1.34-20.65}$	17 ± 25	
$I_{K^*\pi}$	$-7.18^{+1.38+3.38}_{-1.28-5.35}$	$-3.45^{+0.67+9.48}_{-0.59-4.95}$	$-1.02^{+0.19+4.32}_{-0.18-7.86}$	-5 ± 45	$69 \pm 32(15)(6)$
$A_{CP}^{\rho^-\bar{K}^0}$	$0.38^{+0.07+0.16}_{-0.07-0.27}$	$0.22^{+0.04+0.19}_{-0.04-0.17}$	$0.30^{+0.06+2.28}_{-0.06-2.39}$	-12 ± 17	
$A_{CP}^{\rho^0 K^-}$	$-19.31^{+3.42+13.95}_{-3.61-8.96}$	$-4.17^{+0.75+19.26}_{-0.80-19.52}$	$43.73^{+7.07+44.00}_{-7.62-137.77}$	37 ± 11	
$A_{CP}^{\rho^+ K^-}$	$-5.13^{+0.95+6.38}_{-0.97-4.02}$	$1.50^{+0.29+8.69}_{-0.27-10.36}$	$25.93^{+4.43+25.40}_{-4.90-75.63}$	20 ± 11	
$A_{CP}^{\rho^0 \bar{K}^0}$	$8.63^{+1.59+2.31}_{-1.65-1.69}$	$8.99^{+1.66+3.60}_{-1.71-7.44}$	$-0.42^{+0.08+19.49}_{-0.08-8.78}$	6 ± 20	5 ± 26
$\Delta A_{K\rho}$	$-14.17^{+2.80+7.98}_{-2.96-5.39}$	$-5.67^{+0.96+10.86}_{-1.01-9.79}$	$17.80^{+3.15+19.51}_{-3.01-62.44}$	17 ± 16	
$I_{K\rho}$	$-8.75^{+1.62+4.78}_{-1.66-6.48}$	$-10.84^{+1.98+11.67}_{-2.09-9.09}$	$-2.43^{+0.46+4.60}_{-0.42-19.43}$	-37 ± 37	$-44 \pm 49(25)(11)$

more uncertain, and the interference with the tree amplitudes is more important for $\pi\bar{K}^*$ and $\rho\bar{K}$. For the same reason, the NNLO corrections to a_4^p are more pronounced for the $\pi\bar{K}^*$ and $\rho\bar{K}$ direct CP asymmetries. If one adds the weak annihilation term β_3^p to the short-distance contribution, one is left with the column NNLO+LD (long distance). The weak annihilation has a large impact on the direct CP asymmetries, and the parameterization in Eq. (364) from Ref. [416] introduces sizeable theoretical errors.

The table also shows the direct CP asymmetry difference $\Delta A_{K\pi}$ and the corresponding quantity for the PV final states, in which the color-allowed tree amplitude cancels out to good approximation, and the value of the asymmetry sum rule parameter

$$I_{K\pi} = A_{CP}^{K^+\pi^-} + A_{CP}^{K^0\pi^+}\frac{\mathrm{Br}(K^0\pi^+)}{\mathrm{Br}(K^+\pi^-)}\frac{\tau_{B^0}}{\tau_{B^+}} - 2A_{CP}^{K^+\pi^0}\frac{\mathrm{Br}(K^+\pi^0)}{\mathrm{Br}(K^+\pi^-)}\frac{\tau_{B^0}}{\tau_{B^+}} - 2A_{CP}^{K^0\pi^0}\frac{\mathrm{Br}(K^0\pi^0)}{\mathrm{Br}(K^+\pi^-)}, \quad (371)$$

Table 102. Branching fractions (top) and A_{CP} (bottom) measurements for $B \to K\pi$ decays from Ref. [230].

Mode	BaBar	Belle	LHCb
$\mathcal{B}(10^{-6})$			
$K^+\pi^-$	$19.1 \pm 0.6 \pm 0.6$	$20.0 \pm 0.34 \pm 0.60$	
$K^+\pi^0$	$13.6 \pm 0.6 \pm 0.7$	$12.62 \pm 0.31 \pm 0.56$	
$K^0\pi^+$	$23.9 \pm 1.1 \pm 1.0$	$23.97 \pm 0.53 \pm 0.71$	
$K^0\pi^0$	$10.1 \pm 0.6 \pm 0.4$	$9.68 \pm 0.46 \pm 0.50$	
A_{CP}			
$K^+\pi^-$	$-0.107 \pm 0.016^{+0.006}_{-0.004}$	$-0.069 \pm 0.014 \pm 0.007$	$-0.080 \pm 0.007 \pm 0.003$
$K^+\pi^0$	$0.030 \pm 0.039 \pm 0.010$	$0.043 \pm 0.024 \pm 0.002$	
$K^0\pi^+$	$-0.029 \pm 0.039 \pm 0.010$	$-0.011 \pm 0.021 \pm 0.006$	$-0.022 \pm 0.025 \pm 0.010$
$K^0\pi^0$	$-0.13 \pm 0.13 \pm 0.03$	$0.14 \pm 0.13 \pm 0.06$	

where the color-suppressed tree amplitude cancels out. The parameter $I_{K\pi}$ is expected to be small on general grounds [836], but all $K\pi$ CP asymmetries must be measured to high precision.

The experimental uncertainty of the asymmetry sum rule is currently dominated by the $\pi^0\bar{K}^0$ direct CP asymmetry, which will be one of the key measurements at Belle II (see the following subsection). The related $\pi\bar{K}^*$, $\rho\bar{K}$, and $\rho\bar{K}^*$ channels provide additional insights on the pattern of direct CP asymmetries in penguin-dominated $\Delta S = 1$ transitions. As discussed above, all interference effects, and also the theoretical uncertainties, are expected to be enhanced in these channels, which are therefore of significant interest for both NP searches and theory testing.

The theoretical predictions shown in Table 101 can be further improved in the future. On the one hand, this requires completing the NNLO calculation of the leading-power penguin amplitude a_4^p. In view of its phenomenological relevance, one should also consider computing the scalar penguin amplitude a_6^p to the same precision. In addition, one should attempt to improve the modeling of the weak annihilation amplitudes, e.g. through a data-driven approach (see previous section).

While this short review has focused on the πK channels and their relatives, many more direct CP asymmetries can be measured in charmless two-body decays. In general, one expects that the same theoretical methods hold for the leading amplitudes in the heavy quark limit (in the case of $B \to VV$ decays, this applies then only to the longitudinal amplitude).

12.4. Experimental status of $B \to \pi K^{(*)}$ and $\rho K^{(*)}$ decays

Contributing author: P. Goldenzweig

The experimental status of the branching fraction and A_{CP} measurements of the $K\pi$ system are displayed in Table 102. Both Belle and BaBar report a complete set of measurements of the eight observables, while LHCb only reports the values for $A_{CP}^{K^+\pi^-}$ and $A_{CP}^{K^0\pi^+}$. The most demanding of these measurements is the all-neutral final state $K^0\pi^0$. It requires vertex reconstruction of the charged pions from the neutral kaon decays and depends crucially on a vertex detector with a large radial acceptance. Belle measures $A_{CP}^{K^0\pi^0} = +0.14 \pm 0.13 \pm 0.06$ with a data sample of approximately 600 fb^{-1} [837]. The main systematic uncertainty contributions are ordered from largest to smallest as follows: tag-side interference (± 0.054), vertex reconstruction (± 0.022), background fraction (± 0.022), and potential fit biases (± 0.020). These are expected to improve with the larger dataset, particularly since similar systematic uncertainties in the analyses of the other $K\pi$ modes, which all have more signal events, are all substantially smaller.

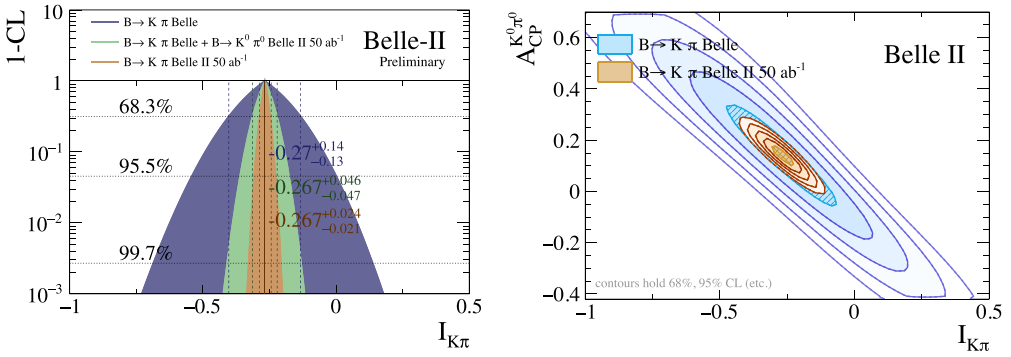

Fig. 134. (Left): Precision of $I_{K\pi}$ with current Belle results; $K^0\pi^0$ with 50 ab^{-1}; all channels with 50 ab^{-1}. (Right): Two-dimensional comparison of $I_{K\pi}$ vs. $A_{\rm CP}^{K^0\pi^0}$ with current Belle results and all channels with 50 ab^{-1}.

Belle has found the value of the isospin-breaking identity parameter, $I_{K\pi}$ as defined in Eq. (371), to be $-0.270\pm0.132\pm0.060$ [727]. To determine the effect on the precision of $I_{K\pi}$ with Belle II data, the errors on Belle's measurements of the branching fractions and $A_{\rm CP}$ are scaled to the expectations at 5 and 50 ab^{-1}, and fits are performed with the `GammaCombo` fit package [838] to extract $I_{K\pi}$. The only possible correlated errors for the $A_{\rm CP}$ measurements are detector bias errors, which are estimated with different methods for each channel; thus, the bias errors are assumed to be uncorrelated. Additionally, the systematic uncertainties are conservatively estimated and they are still smaller than the statistical errors. With the large Belle II dataset, the correlations will need to be taken into account. The precision with 5 ab^{-1} (50 ab^{-1}) is found to be 0.07 (0.03). These results are shown in the first horizontal block of Table 101, alongside the NLO, NNLO, and NNLO+LD predictions (described in detail in Sect. 12.3.4), all in %. To isolate the effect of the all-neutral mode, an additional fit is performed where only the $K^0\pi^0$ measurements are scaled to the expectation at 50 ab^{-1}. Clearly the precision is limited by $K^0\pi^0$, as displayed in Fig. 134 (left). The dependence on the precision of $I_{K\pi}$ is further demonstrated by the simplistic two-dimensional comparison of $I_{K\pi}$ vs. $A_{\rm CP}^{K^0\pi^0}$ shown in Fig. 134 (right).

The experimental results for the branching fractions and $A_{\rm CP}$ measurements for the $K^*\pi$, $K\rho$, and $K^*\rho$ systems are tabulated in Ref. [230]. To determine the effect on the precision of the isospin-breaking parameters $I_{K^*\pi}$, $I_{K\rho}$, and $I_{K^*\rho}$ with Belle II data, the errors on the branching fractions and $A_{\rm CP}$ measurements are scaled to the expectations at 5 and 50 ab^{-1}, and fits are performed to extract the corresponding I (analogous to the $K\pi$ system). The results of the fits to $I_{K^*\pi}$ and $I_{K\rho}$ are listed in the second and third blocks of Table 101, respectively, alongside the theoretical predictions. Here, the inputs to the fits are from BaBar's complete set of branching fraction and $A_{\rm CP}$ measurements, as Belle does not yet have results for all observables. The vector–vector decay $K^*\rho$ is discussed in detail in Sect. 12.6.3. Here, the comparison of NNLO results to experiment is presently not possible, as the longitudinal $A_{\rm CP}$ for K^{*0} ρ^+ has not been measured. Furthermore, the NNLO computation is not possible for transverse amplitudes, as they are power-suppressed and there is no complete QCD factorization theorem for them. The results for the fit to the $K^*\rho$ system (also using BaBar's complete set of branching fractions) are $I_{K^*\rho} = 0.4 \pm 26.4(12.4)(4.4)\%$, where the first and second errors in parentheses are obtained by repeating the fit with the errors on the branching fractions and $A_{\rm CP}$ scaled to the expected results with 5 and 50 ab^{-1} of Belle II data, respectively. Analogous to the $K\pi$ system, two-dimensional contours are plotted for the isospin-breaking parameters vs. the

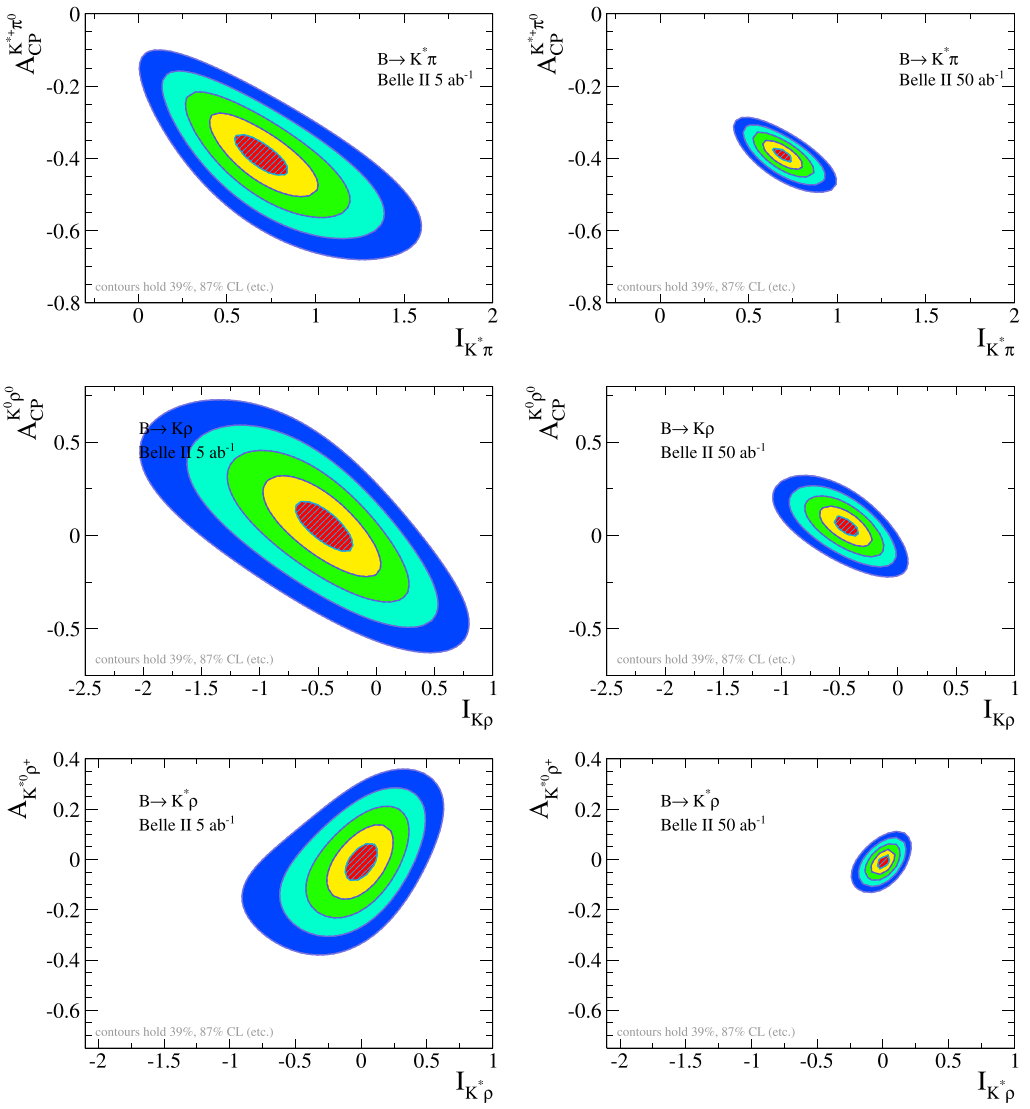

Fig. 135. Demonstration of the limitations on the measurments of the isospin sum rules due to the precision of $A_{\rm CP}^{K^{*+}\pi^0}$ for $I_{K^*\pi}$ (top), $A_{\rm CP}^{K^0\rho^0}$ for $I_{K\rho}$ (middle), and $A_{\rm CP}^{K^{*0}\rho^+}$ for $I_{K^*\rho}$ (bottom) for 5 ab^{-1} (top) and 50 ab^{-1} (bottom) of Belle II data. The results for I are listed in Table 101.

channel with the largest error in $A_{\rm CP}$ (Fig. 135): $K^{*+}\pi^0$, $K^0\rho^0$, and $K^{*0}\rho^+$ for the $K^*\pi$, $K\rho$, and $K^*\rho$ systems, respectively.

A summary of the world average results for $A_{\rm CP}$ and $\Delta A_{\rm CP}$ for all four systems is provided in Fig. 136 and Table 101. While the uncertainty has improved greatly in $K\pi$, it is still too large in the PV and VV systems to be conclusive and thus requires high-precision measurements from Belle II.

12.5. CP violation in B_s^0 decays and $B_s^0 \to K^0\bar{K}^0$

Contributing author: B. Pal

The observation of the decay $B_s^0 \to K^0\bar{K}^0$ (candidate K^0 mesons are reconstructed via the decay $K_{\rm S}^0 \to \pi^+\pi^-$) by the Belle Collaboration [839] is the first observation of a charmless two-body B_s^0 decay involving only neutral hadrons in the final state. In the SM, this decay proceeds mainly via a $b \to s$ penguin transition, and thus is sensitive to any NP that propagates in the internal loop.

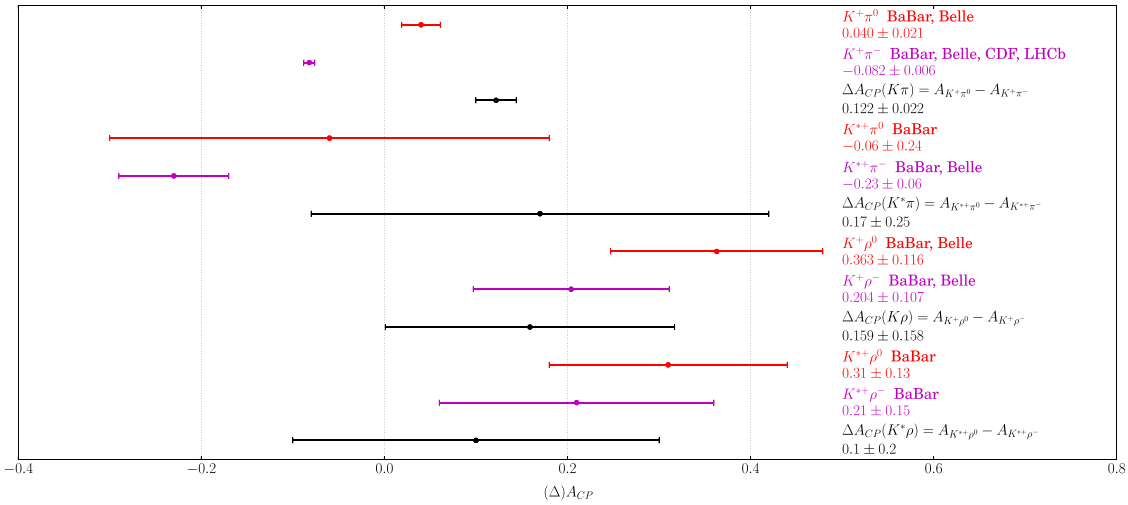

Fig. 136. World averages of $A_{\rm CP}$ and $\Delta A_{\rm CP}$ for the $K\pi$, $K^*\pi$, $K\rho$, and $K^*\rho$ systems.

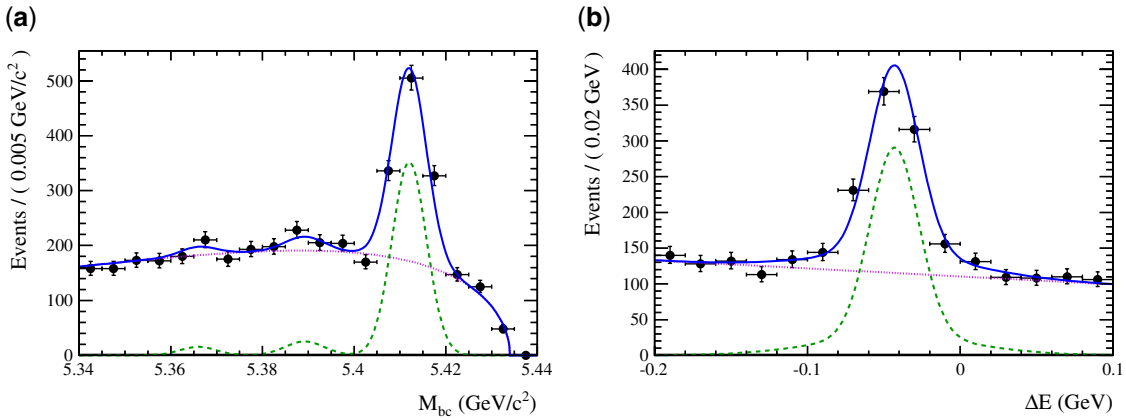

Fig. 137. Projections for $B_s \to K^0\overline{K}^0$ decay by a toy MC study for 5 ab^{-1} of Belle II $\Upsilon(5S)$ data, based on the Belle measurement [839]: (a) $M_{\rm bc}$ in $\Delta E \in (-0.11, 0.02)$ GeV; (b) ΔE in $M_{\rm bc} \in (5.405, 5.427)$ GeV/c^2. Both projections contain a cut on the continuum suppression network output variable of $C'_{\rm NN} > 0.5$. The points with error bars are data, the (green) dashed curves show the signal, (magenta) dotted curves show the continuum background, and (blue) solid curves show the total. The three peaks in $M_{\rm bc}$ arise from $\Upsilon(5S) \to B_s^0\bar{B}_s^0$, $B_s^{*0}\bar{B}_s^0 + B_s^0\bar{B}_s^{*0}$, and $B_s^{*0}\bar{B}_s^{*0}$ decays.

With the full Belle $\Upsilon(5S)$ dataset of 121.4 fb^{-1}, a total of $29.0\,^{+8.5}_{-7.6}$ signal candidates are observed with a significance of $5.1\,\sigma$. The measured branching fraction is $\mathcal{B}(B_s^0 \to K^0\bar{K}^0) = (19.6\,^{+5.8}_{-5.1} \pm 1.0 \pm 2.0) \times 10^{-6}$, where the first uncertainty is statistical, the second is systematic, and the third reflects the uncertainty due to the total number of $B_s^0\bar{B}_s^0$ pairs. This result is in good agreement with SM predictions [697,781,822,827,840–843]. This branching fraction implies that Belle II will reconstruct over 1000 of these decays with 5 ab^{-1} of $\Upsilon(5S)$ data (assuming similar reconstruction efficiency to Belle). The results of a toy MC study are shown in Fig. 137, where the signal region projections are identical to Ref. [839]. Such a sample would allow for a much higher-sensitivity search for NP in this $b \to s$ penguin-dominated decay. In particular, the SM prediction for CP violation in $B_s^0 \to K^0\bar{K}^0$ is very small, and thus any CP asymmetry observed could be an indication of NP. It has been argued in Refs. [844,845] that the direct CP asymmetry of the decay $B_s^0 \to K^0\bar{K}^0$ is a very promising observable to search for the effects of NP. It was shown that the direct CP

asymmetry, which is $\lesssim 1\%$ in the SM, can be an order of magnitude larger in the presence of SUSY, while the branching fraction remains unaffected.

Measuring CP violation in B_s^0 decays at e^+e^- B factories, however, cannot be performed using conventional time-dependent techniques, which require the two B_s^0 vertices to be reconstructed with an accuracy of $\sim 10\,\mu$m. The current Belle II detector design will not achieve $\sim 10\,\mu$m resolution. Additionally, determining the flavor of the initial state B_s^0 will be difficult, due to the rapid B_s^0 oscillations. However, it can be studied in a manner similar to CP violation studies in K^0 decays [846,847]. In the SM, the lifetime distribution of B_s^0 decays into a fixed CP eigenstate, $f_{\rm CP}$ (e.g. the $K_S^0 K_S^0$ final state is a CP-even eigenstate) is governed by a single exponential. CP violation would be established if a second exponential component were observed in the decay, i.e. the CP eigenstate would not be a mass eigenstate. The Belle II experiment will be able to perform this study and will clarify the presence of NP in the decay $B_s^0 \to K^0 \bar{K}^0$.

12.6. $B_{(s)} \to$ VV decays

Theoretically, $B_{(s)} \to$ VV decays are two-body final states. However, experimentally they are at least four-body decays, since the vector mesons decay via the strong interaction with a non-negligible width. Vector mesons can be produced in three polarization states, corresponding to the longitudinal and the two helicity ± 1 amplitudes. The fraction of a given polarization state is an interesting observable, as well as other observables constructed from the helicity amplitudes, in addition to the branching fractions. The phenomenology of $B \to$ VV decays offers rich opportunities for our understanding of the mechanism for hadronic weak decays and their CP asymmetry, and the search for physics beyond the SM. The following three subsections provide first an overview of the theoretical and experimental status of VV final states, then a discussion of triple-product observables, and finally of polarization in the system of the ρK^* final states.

12.6.1. Polarization

Contributing authors: M. Beneke, C.-D. Lu

In the SM, all charmless B decays occur through the V–A weak interaction. This implies that the outgoing light quark in the current containing the b quark is left-handed, while the anti-quark from the other current is right-handed. This makes one of the final-state vector mesons naturally longitudinally polarized, as in Fig. 138. The other must then also be longitudinal for pseudoscalar B meson decay. To form a negatively polarized vector meson, one has to flip the spin of the energetic anti-quark, which results in a negative helicity and $1/m_b$ suppression [795]. To obtain a vector meson in the positive helicity state, one has to flip the spin orientation of two energetic quarks, which is even further suppressed. Therefore, it is naively expected that the helicity amplitudes A_i in heavy meson decay satisfy the power-counting hierarchy [848]

$$A_0 : A_- : A_+ = 1 : \frac{\Lambda}{m_b} : \left(\frac{\Lambda}{m_b}\right)^2 , \tag{372}$$

where Λ denotes the strong interaction scale. In the naive factorization approach, longitudinal polarization dominates the branching fractions of $B \to$ VV decays [849]. In the QCD factorization (QCDF) approach this continues to hold formally in the leading-power approximation [850,851], but is violated numerically by several large power-suppressed effects [795,796].

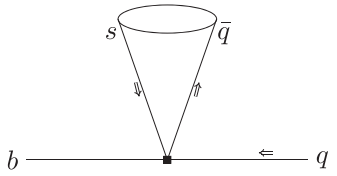

Fig. 138. Naive quark helicities in the charmless $B_{(s)} \to$ VV decays.

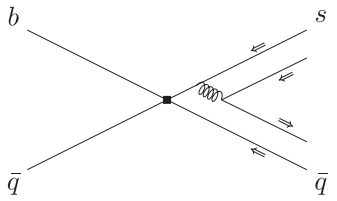

Fig. 139. Quark helicities in the penguin annihilation diagram of charmless $B \to$ VV decays.

The hierarchy in Eq. (372) is indeed verified in the experimental measurements of tree-dominated final states such as $B \to \rho^+\rho^-$, etc. In sharp contrast to the expectations, however, a large transverse polarization fraction (around 50%) was observed in $B \to K^*\phi$ decays by Belle [852] and BaBar [853]. Large transverse polarization of order 50% has subsequently also been observed for $B \to K^*\rho$, $B_s \to K^*\phi$, and $B_s \to \phi\phi$ decays. The fact that the scaling behavior shown in Eq. (372) is apparently violated—at least numerically—in penguin-dominated B decays has triggered considerable theoretical interest both in the QCD factorization approach [795,796,799,854–856] and in the perturbative QCD (PQCD) approach [841,857–860].

Several mechanisms have been proposed to explain the observation of large transverse polarization in penguin-dominated decays. The most convincing appears to be a large annihilation contribution from the scalar $(S-P)\times(S+P)$ penguin operator Q_6 in the weak effective Hamiltonian, originally introduced in Ref. [795] and further analyzed in the QCDF framework in Ref. [796]. This operator is already known to contribute significantly to final states with pseudoscalar mesons [802,819]. From Fig. 139, one can see that one quark spin needs to be flipped to obtain longitudinal or negative polarizations. As a result, although power-suppressed, the contribution from this diagram is of the same order for the longitudinal and negative helicity amplitude. Since the annihilation contribution to the longitudinal amplitude is already sizeable for longitudinally polarized vector mesons, whose factorizable penguin amplitude is suppressed, it is plausible that the polarization fractions satisfy

$$f_{\rm L} \approx f_\parallel \approx f_\perp. \tag{373}$$

The basic picture is confirmed in the perturbative QCD approach [841], that is, both QCDF and PQCD invoke penguin annihilation to explain the observed large transverse polarization fraction in the penguin-dominated $B \to$ VV decays $B \to K^*\phi, B \to K^*\rho$. Recent updates of the respective results of branching ratios, longitudinal and transverse polarization fractions, relative strong phases, and the CP asymmetry variables in $B \to$ VV decays can be found in Refs. [855,856,861]. Other explanations of the large transverse polarization include its attribution to the charm-penguin amplitude, final-state interactions [862,863], form factor tuning [864], and even NP [865,866], some of which have already been ruled out by experiment, since they cannot produce the relation $f_\parallel \approx f_\perp$ and the observed relative strong phases between different polarization states.

We note that, theoretically, the longitudinal amplitude for VV final states is similar to the single decay amplitude in PV and VP final states. However, the helicity ± 1 amplitudes are power-suppressed and theoretically not as well understood. As a consequence, the prediction of polarization-related observables in $B \to$ VV modes are not on the same footing as the calculations of branching fractions and even CP asymmetries for the PP, PV, and VP final states. When transverse polarization is sizeable as for penguin-dominated final states, even the calculation of branching fractions and CP asymmetries from first principles is on less solid ground. This should be kept in mind when comparing observations to theoretical predictions. As an aside, we mention that the hierarchy in Eq. (372) is not respected by electromagnetic effects, which generate a transverse electroweak penguin amplitude, which instead of Eq. (372) satisfies [854]

$$A_0 : A_- : A_+ = 1 : \frac{\alpha_{\rm em} m_b}{\Lambda} : \alpha_{\rm em}. \tag{374}$$

The measurement and theoretical interpretation of polarization in color-suppressed B decays is also not completely settled. The branching fraction $B^0 \to \rho^0\rho^0$ was measured by BaBar and Belle in 2008 as $(0.9 \pm 0.32 \pm 0.14) \times 10^{-6}$ [715] and $(0.4 \pm 0.4^{+0.2}_{-0.3}) \times 10^{-6}$ [867], respectively. With such a small decay rate of $B^0 \to \rho^0\rho^0$, by isospin symmetry the rate for the decay $B^0 \to \rho^+\rho^-$ ought to be twice that of $B^+ \to \rho^+\rho^0$. Experimentally, however, the first is only slightly larger than the second, indicating significant isospin violation. In 2012, Belle updated its $B^0 \to \rho^0\rho^0$ to $1.02 \pm 0.30 \pm 0.15$ [729], in better agreement with the isospin triangle expectation. However, the increase comes from the transverse polarization, which results in a very small longitudinal polarization fraction $f_{\rm L} = 0.21^{+0.18}_{-0.22} \pm 0.13$ [729] in the Belle measurement, which is in conflict with the BaBar measurement and in particular the LHCb result [714] $f_{\rm L} = 0.745^{+0.048}_{-0.058} \pm 0.034$, which dominates the world average. The theoretical interpretation also remains somewhat ambiguous. Leading-order PQCD calculations find the longitudinal polarization fraction for the $B^0 \to \rho^0\rho^0$ decay to be as small as 12% [861]. This results from a large cancellation of two hard-scattering emission diagrams and the annihilation diagram in the longitudinal polarization amplitude, while the chirally enhanced annihilation and hard-scattering emission diagrams provide a sizeable transverse amplitude. On the other hand, in the QCDF approach Ref. [796] finds $f_{\rm L} = (90^{+3+8}_{-4-63})\%$, which supports a larger value, although with a very large uncertainty, which arises from non-factorizable spectator-scattering contributions. The current situation leaves much room for better measurements of the branching fractions and the longitudinal polarization fractions of color-suppressed VV final states and their theoretical understanding. The existing $f_{\rm L}$ measurements in B decays are summarized in Fig. 140. Besides the currently measured channels, other modes such as $B^0 \to \rho^0\omega$, $B^0 \to \omega\omega$, $B^0 \to K^{*+}K^{*-}$, $B^- \to \phi\rho^-$, $B^0 \to \phi\rho^0$, and $B^0 \to \phi\omega$ will provide further insight into the QCD dynamics that governs the different helicity amplitudes.

The experimental effort to study the charmless $B_s \to$ VV decays has already started, for example with the measurements of branching ratios and polarization fractions of the decays $B_s \to \bar{K}^{*0}K^{*0}$, $B_s \to \phi\bar{K}^{*0}$, and $B_s \to \phi\phi$. However, most of the $B_s \to$ VV decays have not yet been measured, leaving much room for the Belle II experiment. Many of the branching ratios and direct CP observables need the input from Belle II, since it is more difficult for the LHCb experiment to measure absolute branching fractions. The results of the existing $f_{\rm L}$ measurements for B_s decays are also summarized in Fig. 140.

Theoretically, the prediction of $B_s \to$ VV decays follows similar patterns to $B \to$ VV, but there is a larger uncertainty for the non-perturbative input parameters, such as the form factors

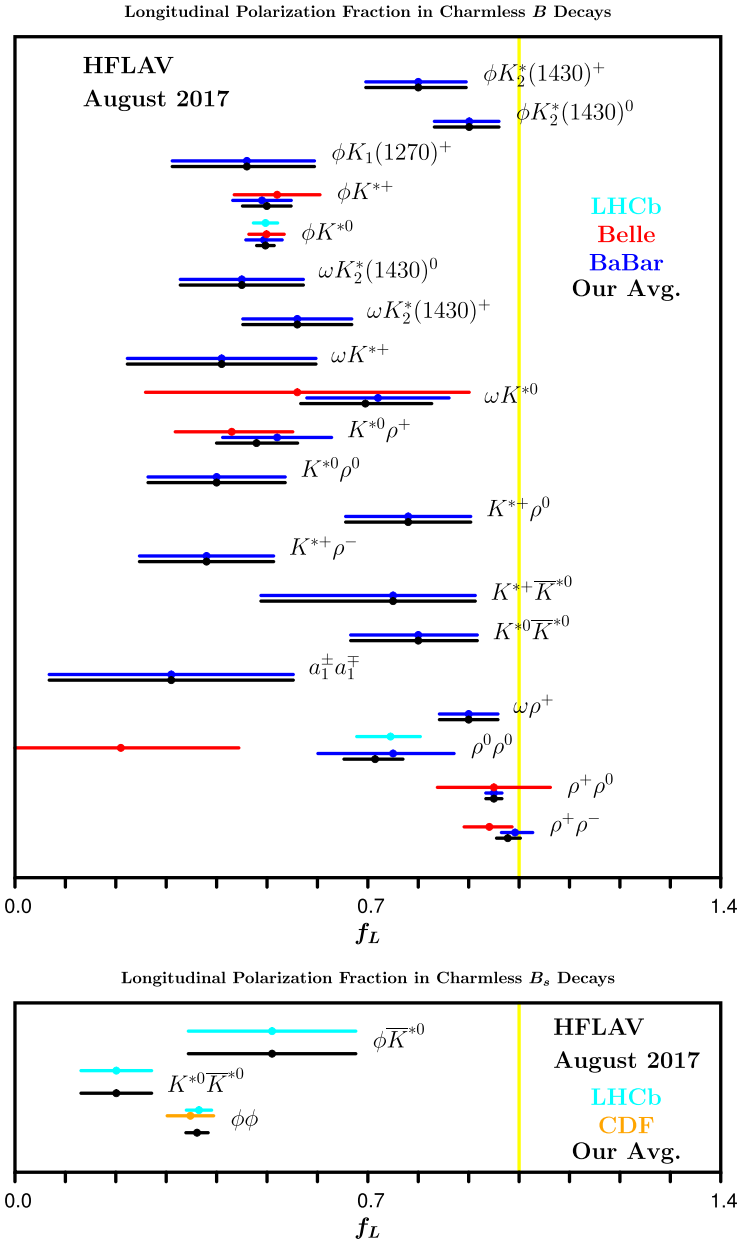

Fig. 140. Longitudinal polarization fraction in charmless B and B_s decays from Ref. [230].

and light cone wave functions/distribution amplitudes. Results for all $B_s \to$ VV modes can be found in Refs. [796,856] and Ref. [861] in the QCDF and PQCD approaches, respectively, and show agreements and disagreements depending on whether there is agreement on the underlying dynamical mechanism governing a particular decay. In general, the QCDF approach adopts a more conservative approach on theoretical uncertainties due to power-suppressed effects, including all helicity amplitudes. The abovementioned references also contain a comprehensive coverage of direct CP asymmetries and the parameters $f_\perp$, $\phi_\parallel = \arg(A_\parallel/A_0)$, and $\phi_\perp = \arg(A_\perp/A_0)$, which enter the complete angular analysis. These parameters (and the corresponding CP asymmetries) are in part related to the positive-helicity amplitude, which is expected to be strongly suppressed in the SM, but is otherwise poorly understood theoretically. Many of the existing polarization results refer only to f_L, while the perpendicular polarization fraction, $f_\perp$, the relative phases $\phi_\parallel$, $\phi_\perp$, and the

helicity-specific CP asymmetry parameters $A_{\rm CP}^0$ and $A_{\rm CP}^\perp$ have been measured only in five channels: $B^0(B^+) \to K^*(K^{*+})\phi$ and $B_s \to \bar{K}^{*0}\phi$, $B_s \to \bar{K}^{*0}K^{*0}$ and $B_s \to \phi\phi$. Complete angular analyses of penguin-dominated and color-suppressed VV final states are expected to provide further insight on the surprisingly complex dynamics of these decays, and are, at least in principle (see Ref. [868] for an example), sensitive to NP with right-handed currents.

12.6.2. Triple product asymmetries

Contributing author: A. Datta

In addition to the standard polarization observables, one can measure the so-called triple product asymmetries (TPAs) [869,870] in the angular distribution of $B \to V_1V_2$ decays. As with any CP-violating quantity, a non-vanishing TPA needs the interference of at least two amplitudes with a weak phase difference $\Delta\phi$. However, while direct CP asymmetries are proportional to $\sin\Delta\phi \sin\Delta\delta$ and therefore also require a strong phase difference $\Delta\delta$, TPAs go as $\sin\Delta\phi\cos\Delta\delta$. Hence, direct CP violation and TPAs complement each other. If the strong phases are small, then the TPA is maximal. Even in the absence of CP-violating effects, T-odd triple products (also called "fake" TPAs), which go as $\cos\Delta\phi\sin\Delta\delta$, can provide useful complementary information on NP [871].

Basic definitions The general amplitude for $B(p) \to V_1(k_1,\varepsilon)V_2(k_2,\eta)$ is

$$A_{\lambda_1,\lambda_2} = a\,\varepsilon^*_{\lambda_1}\cdot\eta^*_{\lambda_2} + \frac{b}{m_B^2}(p\cdot\varepsilon^*_{\lambda_1})(p\cdot\eta^*_{\lambda_2}) + i\frac{c}{m_B^2}\epsilon_{\mu\nu\rho\sigma}p^\mu q^\nu \varepsilon^{*\rho}_{\lambda_1}\eta^{*\sigma}_{\lambda_2}, \tag{375}$$

where $q \equiv k_1 - k_2$. The amplitude c has $L = 1$ and is parity-odd, while the amplitudes a and b are combinations of the $L = 0$ and $L = 2$ partial waves. We note that in the B meson rest frame the last term takes the form of a triple product $TP \equiv \vec{q}\cdot(\vec{\epsilon}^*\times\vec{\eta}^*)$. The TPAs are related to the interference of this amplitude with the other two, Im (ac^*) and Im (bc^*).

The polarization vectors can be transverse $(\epsilon_\pm, \eta_\pm)$ or longitudinal (ϵ_0, η_0). Helicity conservation allows $A_{+,+}, A_{-,-}, A_{0,0}$, which we will denote as A_+, A_-, A_0. The amplitudes in the transversity bases are related to a, b, and c above by

$$\begin{aligned} A_0 &= -ax - \frac{m_1m_2}{m_B^2}b(x^2-1) \approx -(2a+b)\frac{m_B^2}{4m_1m_2}, \\ A_\parallel &= \sqrt{2}a, \\ A_\perp &= 2\sqrt{2}\,\frac{m_1m_2}{m_B^2}c\sqrt{x^2-1} \approx \sqrt{2}c, \end{aligned} \tag{376}$$

where $x = k_1\cdot k_2/(m_1m_2) \approx m_B^2/(2m_1m_2)$ and the approximation holds for $m_B \gg m_1, m_2$. The relations between the transversity and helicity amplitudes are

$$A_+ = (A_\parallel + A_\perp)/\sqrt{2}, \qquad A_- = (A_\parallel - A_\perp)/\sqrt{2}. \tag{377}$$

The asymmetry

$$A_{\rm T} = \frac{\Gamma[TP>0] - \Gamma[TP<0]}{\Gamma[TP>0] + \Gamma[TP<0]}$$

is T-odd. In terms of the transversity amplitudes that appear in the $B \to V_1 V_2$ angular distribution, we can define

$$A_{\rm T}^{(1)} \equiv \frac{{\rm Im}(A_\perp A_0^*)}{A_0^2 + A_\parallel^2 + A_\perp^2}, \qquad A_{\rm T}^{(2)} \equiv \frac{{\rm Im}(A_\perp A_\parallel^*)}{A_0^2 + A_\parallel^2 + A_\perp^2}, \tag{378}$$

and

$$\bar{A}_{\rm T}^{(1)} \equiv -\frac{{\rm Im}(\bar{A}_\perp \bar{A}_0^*)}{\bar{A}_0^2 + \bar{A}_\parallel^2 + \bar{A}_\perp^2}, \qquad \bar{A}_{\rm T}^{(2)} \equiv -\frac{{\rm Im}(\bar{A}_\perp \bar{A}_\parallel^*)}{\bar{A}_0^2 + \bar{A}_\parallel^2 + \bar{A}_\perp^2} \tag{379}$$

for the CP-conjugate decay. While all these observables are T-odd, they do not by themselves violate time-reversal invariance. It is evident from the definition that they can be generated by a strong phase difference between the transversity amplitudes alone. Assuming CPT invariance, a CP-violating observable is obtained from comparing $A_{\rm T}$ and $\bar{A}_{\rm T}$. One therefore constructs

$$A_{\rm TP}^{\rm true,1,2} = \frac{1}{2}\left(A_{\rm T}^{(1,2)} + \bar{A}_{\rm T}^{(1,2)}\right) \propto \sin\Delta\phi \cos\Delta\delta, \tag{380}$$

$$A_{\rm TP}^{\rm fake,1,2} = \frac{1}{2}\left(A_{\rm T}^{(1,2)} - \bar{A}_{\rm T}^{(1,2)}\right) \propto \cos\Delta\phi \sin\Delta\delta. \tag{381}$$

The first quantity is the CP-violating TPA; the second, which is non-zero even for $\Delta\phi = 0$ if there is a strong phase difference, is referred to as "fake TPA."

As is the case with rate asymmetries and the full angular distribution, when the $V_1 V_2$ final state be reached by both B and $\bar{B}$ mesons, such as in $B_d \to K^* \bar{K}^*$ and $B_s \to J/\psi\phi, \phi\phi$, etc., mixing effects have to be included and the measurement of TPAs becomes a time-dependent problem.

When the final-state particles can be reached through a scalar background (resonant or non-resonant)—for example, $B \to V_1 V_2 \to f$ and $B \to V_1 S \to f$—one has to include the interference effects. In particular, when a neutral vector meson is detected via its decay $V \to PP'$ (P, P' are pseudoscalars), there is usually a background from the decay of a scalar resonance $S \to PP'$, or from the scalar non-resonant PP' production [679,872]. Then it is necessary to add another (scalar) helicity to the angular analysis of $B_s \to V_1(\to P_1 P_1') V_2(\to P_2 P_2')$ in presence of the scalar background [873]. The most general amplitude contains six helicities: $h =$ VV (3), VS, SV, and SS, each with a corresponding amplitude A_h. After squaring the amplitude the general angular analysis contains 21 terms. Allowing for time dependence due to B_s–$\bar{B}_s$ mixing, the angular distribution can be written as

$$\frac{d^4\Gamma(t)}{dt d\cos\theta_1 d\cos\theta_2 d\phi} = \frac{9}{8\pi} \sum_{i=1}^{21} K_i(t) X_i(\theta_1, \theta_2, \phi), \tag{382}$$

where θ_1, θ_2, and ϕ are the helicity angles in Fig. 141. We can express

$$K_i(t) = [a_i \cosh(\Delta\Gamma/2)t + b_i \sinh(\Delta\Gamma/2)t + c_i \cos\Delta m t + d_i \sin\Delta m t], \tag{383}$$

where the individual functions $a_i, b_i, c_i,$ and d_i for $i = 1, \ldots, 21$ are time independent. The expressions for these coefficients in terms of the helicity amplitudes and mixing phase can be found in Ref. [873].

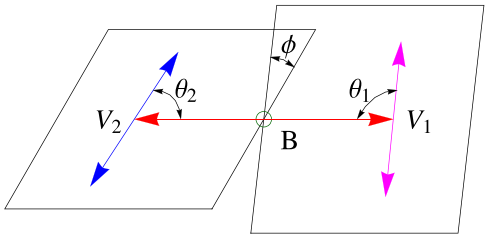

Fig. 141. Definition of the helicity angles in Eq. (382).

Various CP-violating quantities including TPAs are related to these coefficients as follows:

- Direct CP asymmetries are represented by c_i ($i = 1$–$4, 7, 13$–$16, 18, 20, 21$), a_i ($i = 8$–11).
- The indirect CP asymmetries are: d_i ($i = 1$–$4, 7, 13$–$16, 18, 20, 21$), b_i ($i = 8$–11).
- The triple products are: a_i ($i = 5, 6, 17, 19$), c_{12}.
- The mixing-induced triple products: b_i ($i = 5, 6, 17, 19$), d_{12}.

SM expectations and observations The TPAs $A_{\rm T}^{(1,2)}$ both involve the transverse polarization amplitudes $A_\perp, A_\parallel$. For the reasons discussed in the general overview on VV final states this makes it difficult to make reliable theoretical predictions from first principles. Nevertheless, a few general observations can be made, based on the amplitude hierarchy in Eq. (372) as well as the existing observations of longitudinal polarization fractions $f_{\rm L}$ and direct CP asymmetries.

- Due to the left-handedness of the the weak interaction, $A_+ \ll A_-$ is expected. Within uncertainties, there is no experimental evidence of a violation of this hierarchy, which implies $A_\parallel \approx A_\perp$, hence $A_{\rm T}^{(2)}$ is power-suppressed by Λ/m_B relative to $A_{\rm T}^{(1)}$. An observation of $A_{\rm T}^{(2)} \sim A_{\rm T}^{(1)}$ in any pure vector–vector decay mode would indicate a departure from pure left-handedness.
- The hierarchy in Eq. (372) also implies that $A_{\rm T}^{(1)}$ is itself a power-suppressed quantity. However, as discussed in the previous section, this hierarchy is numerically not respected by penguin-dominated decays and is possibly also violated in color-suppressed decay modes. Thus, final states with large transverse amplitude fractions are favorable for the measurement of TPAs and can then provide valuable complementary information on CP violation without requiring the generation of a sizeable strong phase difference.
- Strangeness-changing penguin-dominated decays are dominated by an amplitude with a single weak phase, hence one does not expect large "true" TPAs $A_{\rm TP}^{\rm true,1,2}$. They are therefore especially sensitive to NP [865,874]. In addition, the "fake" TPAs are of interest, since they provide information on the helicity structure of NP interactions, see above.

TPAs have already been measured in some B decay final states at BaBar, Belle, and at hadron machines by CDF and LHCb [875–878]. These measurements have in turn provided strong constraints on various NP models [871]. TPAs can also be probed in b baryon decays [879–881], as well as in semi-leptonic B decays [882–884]. In $B^0_{s,d}$ decays, where the final state can be reached by $B^0_{s,d}$ and $\bar{B}^0_{s,d}$ decays, the TPAs appear in the time-integrated untagged angular distribution [873,874].

Analyses including amplitudes for scalar backgrounds have been performed by Babar [853] and LHCb [885] in their studies of the decays $B_s \to J/\psi\phi$ [886] and $B_s \to \phi\phi$. In both cases the ϕ is detected through its decay to K^+K^-, and there is a resonant (f_0) or non-resonant scalar background.

The angular analyses were performed with four and five helicities, respectively. TPAs have been measured in $B_s \to \phi\phi$ [887] with results consistent with the SM expectation of no CP violation. In addition, LHCb has studied the decay $B_s \to K^{*0}(892)\bar{K}^{*0}(892)$ [888], and found that each of these vector mesons has a background coming from the scalar resonance $K_0^{*0}(1430)$. In this case, as one does not have identical particles in the final state (in contrast to $B_s \to \phi\phi$), all six helicities and the general angular distribution in Eq. (382) must be considered. Some of these asymmetries in the $K_i(t)$ appear in the untagged distribution and have been measured in Ref. [888]. They were found to be consistent with SM predictions with the present precision of the measurements. Recently, a flavor-tagged decay-time-dependent amplitude analysis of $B_s \to (K^+\pi^-)(K^+\pi^-)$ decays was presented in Ref. [889] where the $K\pi$ combinations come from intermediate K^* resonances with spin 0, 1, and 2. Many TPAs can be obtained from the interference of the various helicity amplitudes in this decay.

New physics, if present in B decays, is more likely to be observed in rare decays where it can compete with the SM contribution. For a number of years there has been a certain inconsistency among the measurements of the branching ratios and CP asymmetries of the four $B \to \pi K$ decays, as discussed earlier in this chapter. If the data is interpreted in terms of NP then it points to a new contribution to the electroweak penguin amplitude, which may come from models with a new neutral gauge boson (Z'). These models would also produce TPAs in vector–vector final states that proceed through the $b \to s\bar{q}q$ transitions where $q = u, d, s$. More precise measurements of TPAs in decays where TPAs have been measured as well as TPA measurements in new decays like $B \to \rho K^*$ (see also the following subsection) would be very interesting.

12.6.3. Electroweak penguins in $B \to \rho K^*$ decays

Contributing author: M. Beneke

The system of the four $B \to \rho K^*$ decays and their CP conjugates deserves special mention here, since it represents the VV cousin of the much discussed πK final states. There are two main reasons for the particular interest in the ρK^* final states: (i) The dominant QCD penguin amplitude is at least a factor of two smaller than for the πK system, while the tree and electroweak penguin amplitudes are of similar size; hence, all interference effects are enhanced for the ρK^* final states, possibly providing a clue to the "πK puzzles." (ii) The polarization degree of freedom can provide additional clues. Furthermore, there is an electromagnetic penguin effect in the transverse amplitudes, which modifies the electroweak penguin amplitude. In the SM, it appears only in the negative helicity amplitude [854]. It is therefore of great interest to measure the full angular distributions for all four ρK^* final states, which should be feasible at Belle II owing to its high statistics and good particle identification.

We briefly elaborate on these two facts and refer to Refs. [796,854] for further details. The amplitude decomposition of $B \to \rho K^*$ decays, similar to Eq. (366) for πK, reads

$$\begin{aligned} A_h(\rho^-\bar{K}^{*0}) &= P_h, \\ \sqrt{2}\,A_h(\rho^0 K^{*-}) &= [P_h + P_h^{\rm EW}] + \epsilon_{\rm KM} e^{-i\gamma}\,[T_h + C_h], \\ A_h(\rho^+ K^{*-}) &= P_h + \epsilon_{\rm KM} e^{-i\gamma}\,T_h, \\ -\sqrt{2}\,A_h(\rho^0\bar{K}^{*0}) &= [P_h - P_h^{\rm EW}] + \epsilon_{\rm KM} e^{-i\gamma}\,[-C_h]. \end{aligned} \tag{384}$$

Table 103. CP-averaged branching fractions and direct CP asymmetries of the ρK^* final states. Theoretical values correspond to an update of Ref. [796]. Experimental values are taken from the HFLAV compilation [230] (August 2017 web update) except for the $B^- \to \bar{K}^{*0}\rho^-$ branching fraction, which is the average of the BaBar and Belle measurements reported in Refs. [890,891].

Mode	BrAv/10^{-6}		A_{CP} / percent	
	Theory	*Experiment*	Theory	*Experiment*
$B^- \to \bar{K}^{*0}\rho^-$	$6.6^{+0.3+3.3+0.3}_{-0.3-1.4-0.7}$	9.2 ± 1.5	1^{+0+1+1}_{-0-1-2}	-1 ± 16
$B^- \to K^{*-}\rho^0$	$5.1^{+1.6+2.1+0.5}_{-1.4-1.0-0.8}$	4.6 ± 1.1	$18^{+5+9+31}_{-5-9-22}$	31 ± 13
$\bar{B}^0 \to K^{*-}\rho^+$	$6.1^{+1.8+2.9+0.5}_{-1.6-1.3-0.6}$	10.3 ± 2.6	$10^{+3+8+38}_{-2-7-27}$	21 ± 15
$\bar{B}^0 \to \bar{K}^{*0}\rho^0$	$2.4^{+0.2+1.1+0.2}_{-0.2-0.6-0.1}$	3.9 ± 0.8	$-16^{+4+16+10}_{-5-14-6}$	-6 ± 9

Here we have used the topological amplitude notation,[38] and neglected the color-suppressed electroweak penguin amplitude $\alpha^p_{4,\mathrm{EW}}$. The subscript $h = 0, \pm 1$ denotes the helicity amplitudes, and $\epsilon_{\mathrm{KM}} = |V_{ub}V^*_{us}|/|V_{cb}V^*_{cs}| \sim 0.025$ implies the CKM suppression of the tree amplitudes. The system is ideally suited to probe the electroweak penguin amplitudes, which enter in three different combinations $P_h + k \cdot P^{\mathrm{EW}}_h$, or, in factorization notation,

$$A_{\rho\bar{K}^*}\,\hat{\alpha}^{p,h}_4 + k \cdot A_{\bar{K}^*\rho}\,\frac{3}{2}\alpha^{p,h}_{3,\mathrm{EW}}, \qquad k = 1, 0, -1, \tag{385}$$

allowing various kinds of interferences. The smallness of P_h implies that $|P^{\mathrm{EW}}_h/P_h|$ is sizeable and the interference can be large. Similarly, one expects sizeable direct CP asymmetries in the final states with charged K^* mesons due to the enhanced interference with the color-allowed tree amplitude. A comparison of theoretical predictions and present experimental results for the CP-averaged branching fractions and direct CP asymmetries summed over all helicity states is shown in Table 103. The theoretical results represent an update of the QCD factorization results [796], where the QCD penguin amplitude P_h is determined from the ϕK^* angular distribution rather than from the theoretical calculation. The qualitative pattern of the branching fractions and especially the CP asymmetries is in good agreement with observations, given uncertainties, but a helicity-specific analysis would provide interesting further insights.

A full angular analysis is not presently available for any of the ρK^* final states. Table 104 summarizes the averages of the existing longitudinal polarization fraction measurements and the theoretical prediction [796]. The difficulties with calculating the transverse QCD penguin amplitudes reliably have been discussed in Sect. 12.6.1. One notes that the agreement is quite satisfactory for the final states with the neutral ρ meson, especially concerning the largely different f_{L}. The charged ρ final states, however, show a discrepancy, even with uncertainties, which appears surprising given their simpler amplitude structure in Eq. (384).

A full angular analysis of the ρK^* final states is especially interesting in view of the fact that there is a contribution from the electromagnetic dipole operator $Q_{7\gamma}$ to the transverse polarization amplitudes, which dramatically changes the power counting in the heavy quark limit. Comparing Eqs. (372) and (374) in Sect. 12.6.1, one notes that the negative helicity amplitude is enhanced by a factor $(m_B/\Lambda)^2$ compared to the counting in the absence of the electromagnetic dipole effect. This arises due to the transition $b \to s\gamma^\star$ to a photon with virtuality m^2_ρ, which then converts to a ρ

[38] For the relation to the factorization notation, see the end of Sect. 12.3.1.

Table 104. Longitudinal polarization fraction of the ρK^* final states. Theoretical values correspond to an update of Ref. [796]. Experimental values are taken from the HFLAV compilation [230] (August 2017 web update).

Mode	f_L / percent	
	Theory	Experiment
$B^- \to \bar{K}^{*0}\rho^-$	$67^{+0+14+0}_{-0-10-3}$	48 ± 8
$B^- \to K^{*-}\rho^0$	89^{+1+6+1}_{-2-5-3}	78 ± 12
$\bar{B}^0 \to K^{*-}\rho^+$	$70^{+3+13+1}_{-4-10-6}$	38 ± 13
$\bar{B}^0 \to \bar{K}^{*0}\rho^0$	$34^{+3+23+2}_{-3-14-0}$	40 ± 14

meson. This process modifies the electroweak penguin amplitude as

$$\alpha_{3,\mathrm{EW}}^{p,-} = \alpha_{3,\mathrm{EW}|\text{no } C_{7\gamma}}^{p,-} - \frac{2\alpha_{\mathrm{em}}}{3\pi} C_{7\gamma}^{\mathrm{eff}} \frac{m_B m_b}{m_\rho^2}, \tag{386}$$

where the double power enhancement is evident in the additional contribution. It changes the real part from $-0.010^{+0.002}_{-0.002}$ to the value $+0.015^{+0.004}_{-0.003}$. Due to the change in sign, the pattern of interference between the electroweak penguin and QCD penguin amplitude is now opposite for the longitudinal and negative-helicity amplitude.

Due to the left-handed nature of the weak interaction, $Q_{7\gamma}$ contributes through the above effect only to the negative-helicity amplitude. Since the term proportional to the Wilson coefficient of the electromagnetic dipole operator, $C_{7\gamma}^{\mathrm{eff}}$, is the largest contribution to the negative-helicity electroweak penguin amplitude, the interference patterns in Eq. (385) are sensitive to possible anomalous contributions to $C_{7\gamma}^{\mathrm{eff}}$, including its phase. An anomalous right-handed component would lead to a corresponding enhancement of the positive-helicity amplitude, which otherwise is strongly suppressed in the SM.

The numerical effect of the electromagnetic dipole contribution to the branching fractions, direct CP asymmetries, and longitudinal polarization fractions of the final states containing ρ^0 is shown in Table 105 by including and excluding the second term on the right-hand side of Eq. (386) in the theoretical prediction.[39] Already in the "excluded" results, the longitudinal polarization fractions of the ρK^* final states are predicted to differ such that $f_L(K^{*-}\rho^0) > f_L(\bar{K}^{*0}\rho^-) > f_L(\bar{K}^{*0}\rho^0)$. This follows from the large longitudinal electroweak penguin contribution. The transverse electromagnetic dipole effect amplifies the hierarchy among the three f_L predictions.

The present situation is inconclusive. Observables more sensitive to the electroweak penguin amplitudes can be defined by taking the helicity-specific CP-averaged decay rate ratios [854]

$$S_h \equiv \frac{2\bar{\Gamma}_h(\rho^0\bar{K}^{*0})}{\bar{\Gamma}_h(\rho^-\bar{K}^{*0})}, \qquad S_h' \equiv \frac{2\bar{\Gamma}_h(\rho^0 K^{*-})}{\bar{\Gamma}_h(\rho^- K^{*0})}, \tag{387}$$

and $S_h'' \equiv S_h/S_h'$. In particular, S_h'' differs by up to a factor of four depending on whether or not the electromagnetic dipole contribution is included [796]. It would be very interesting to detect this effect in the complete angular distribution, which is essentially equivalent to a measurement of

[39] These theoretical numbers are *not* updated relative to Ref. [796] and therefore differ from those in the previous tables. The difference is small except for the longitudinal polarization fraction of the $\bar{K}^{*0}\rho^0$ final state. The main purpose of this table is to show the difference of the two results.

Table 105. Predicted branching fraction, longitudinal polarization, and direct CP asymmetry of the two ρK^* final states sensitive to the electroweak penguin amplitude with the power-enhanced transverse contribution proportional to $C_{7\gamma}$ included or excluded. Experimental results for comparison (exp.).

	$B^- \to K^{*-}\rho^0$			$\bar{B}^0 \to \bar{K}^{*0}\rho^0$		
	Incl.	Excl.	Exp.	Incl.	Excl.	Exp.
BrAv/10^{-6}	4.5	5.4	4.6 ± 1.1	2.4	1.4	3.9 ± 0.8
f_L / %	84	70	78 ± 12	22	37	40 ± 14
A_{CP} / %	16	14	31 ± 13	-15	-24	-6 ± 9

photon polarization in the radiative decay $B \to K^*\gamma$. It should be emphasized that the CP average of helicity-specific decay rates is not the same as the CP average of polarization fractions f_h. When the standard variables are used, the relation involves CP asymmetries. The S-observables defined above are better suited to an investigation of helicity-specific effects. Experimentally they can be determined from the same data as the standard observables, thus avoiding unfolding complicated correlations in the errors of CP asymmetries, branching, and polarization fractions.

12.7. Three-body charmless B decays

In the final section of this chapter we focus on the relatively new and much less developed subject of three-body charmless B decays. Two subsections approach the topic from the general theoretical and the phenomenological points of view. Particular interest in the subject arises from the observation of large local CP asymmetries in Dalitz plot analyses by LHCb [892–894].

12.7.1. Theoretical framework

Contributing author: J. Virto

In complete analogy with two-body decays (see Sect. 12.1), three-body B decay amplitudes can be decomposed according to their CKM structure:

$$A(\bar{B} \to f) = \lambda_u^{(D)} A_f^u + \lambda_c^{(D)} A_f^c, \tag{388}$$

where now $f = M_a M_b M_c$ is a three-body charmless final state and A_f^p are given by the corresponding matrix elements of dimension-six operators in the weak effective Lagrangian in Eq. (344),

$$A_f^p = -\frac{G_F}{\sqrt{2}} \sum_{i=1,\ldots,6,8} C_i(\mu) \langle f | Q_i^p(\mu) | \bar{B} \rangle. \tag{389}$$

As in two-body decays, the theory challenge is to calculate the matrix elements $\langle M_a M_b M_c | Q_i(\mu) | \bar{B} \rangle$ from first principles in QCD, or else to establish rigorous relationships between various of these matrix elements that can be exploited phenomenologically. In this respect three-body decays are considerably more challenging than two-body decays (and correspondingly less well understood), but provide a number of theoretical and phenomenological advantages:

- The number of different three-body final states is about ten times larger than the number of two-body decays. In addition, each final state has a non-trivial kinematic multiplicity (a two-dimensional phase space) as opposed to two-body decays where the kinematics is fixed by the masses. This leads to a much richer phenomenology.

- "Quasi-two-body" decays $\bar{B} \to M_a M(\to M_b M_c)$, where M decays strongly, are only well defined in the context of the three-body decay, in the narrow-width approximation, and neglecting any "non-resonant" background (e.g. the overlap with other nearby or very wide resonances in the $M_b M_c$ channel). Therefore, full understanding of the three-body decay provides corrections to the quasi-two-body approximation. In addition, this allows for performing spectroscopy by looking for resonant structures in the kinematic distributions, and to measure their spin.
- Factorization properties of three-body decays depend continuously on two kinematic invariants, thus allowing for more detailed data-driven studies of factorization and power corrections in B decays.
- Strong phases in two-body decays are either perturbative [$\mathcal{O}(\alpha_s(m_b))$] or power-suppressed [$\mathcal{O}(\Lambda/m_b)$]. Therefore, the corresponding CP asymmetries are predicted to be suppressed correspondingly, and leading-power predictions are on a less solid footing, since $\alpha_s(m_b)/\pi \sim \Lambda/m_b$. On the contrary, strong phases in three-body decays arise non-perturbatively already at the leading power, through complex phases in matrix elements such as $F_\pi \sim \langle 0|j|\pi\pi\rangle$ and $F^{B\pi\pi} \sim \langle \pi\pi|j|\bar{B}\rangle$. These matrix elements and their phases can in principle be obtained from data from other, unrelated, decay modes. Localized direct CP asymmetries can therefore be large, potentially leading to improved extraction of CKM angles from direct CP violation.

The theory of three-body non-leptonic decays is still in an early stage of development. Here we provide a brief overview of the subject (see Ref. [895] for an extended version).

Kinematics We consider a decay

$$\bar{B}(p_B) \to M_a(p_1) M_b(p_2) M_c(p_3). \tag{390}$$

Fixing the masses of the initial and final hadrons, the kinematics is completely specified by two invariant masses of two pairs of final-state particles (e.g. s_{ab} and s_{ac}, with $s_{ab} \equiv 2(p_1 \cdot p_2)/m_B^2$, etc.). All physical kinematic configurations thus define a two-dimensional region in the s_{ab}–s_{ac} plane, which in the limit where all final particles are massless is a triangle defined by $s_{ab} > 0$, $s_{ac} > 0$, $s_{ab} + s_{ac} < 1$ (see Fig. 142). The amplitude of the process is a function of these two invariant masses $\mathcal{A}(s_{ab}, s_{ac})$, and the density plot of the differential decay rate

$$\frac{d^2\Gamma}{ds_{ab}\, ds_{ac}} = \frac{m_B}{32(2\pi)^3} |\mathcal{A}(s_{ab}, s_{ac})|^2 \tag{391}$$

in that region is called the Dalitz plot. Labeling particles by their momenta removes any ambiguity related to identical particles, but reduces the relative physical phase space (Dalitz plot) to one half, or one sixth (see Fig. 142).

The Dalitz plot contains different regions with "special" kinematics (Fig. 142). The central region corresponds to the case in which all three final particles fly apart at ∼120° angles with large energy ($E \sim m_B/3$). The corners correspond to the case in which one final-state particle is approximately at rest (i.e. soft), and the other two fly back-to-back with large energy ($E \sim m_B/2$). The central parts of the edges correspond to the case in which two particles move collinearly with large energy and the other particle recoils back. The significance of these special kinematic configurations is that different theoretical approaches may be applicable in these different regions, as will be discussed below.

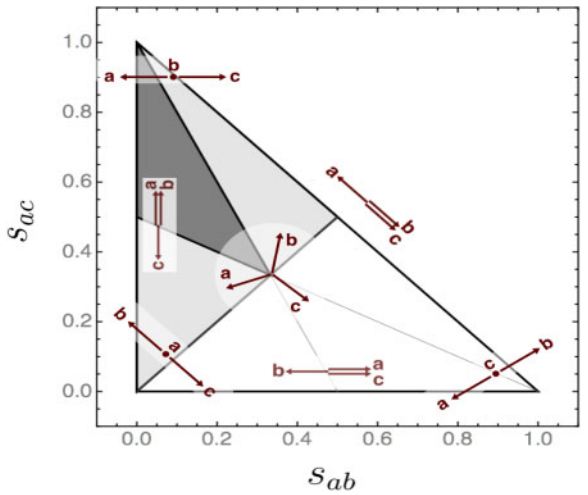

Fig. 142. Phase space of the three-body decay $B \to M_a M_b M_c$ in terms of the normalized invariants s_{ab}, s_{ac}. Special kinematic configurations are indicated. If $M_b = M_c$ or $M_a = M_b = M_c$ then $s_{ab} \to s_{ab}^{\rm low}$ and $s_{ac} \to s_{ab}^{\rm high}$, and the phase space is reduced to the light gray and dark gray regions respectively.

Partial wave expansions and isobars The Dalitz plot is typically dominated by resonant quasi-two-body contributions along the edges. Therefore, a first-order approximation is to regard the three-body decay as a coherent sum of quasi-two-body decays $\bar{B} \to R_{ij}^{(\ell)}(\to M_i M_j) M_k$, where $R_{ij}^{(\ell)}$ denotes a resonance in the (ij) channel with spin ℓ. This resonance contributes to the region $s_{ij} \sim (m_{R_{ij}} \pm \Gamma_{R_{ij}})^2/m_B^2$, where $m_{R_{ij}}, \Gamma_{R_{ij}}$ are the mass and width respectively, and the profile of this contribution in the other Dalitz plot variable s_{ik} is specified by the spin ℓ. In each channel it is thus convenient to expand the amplitude in partial waves. For example, one may trade the variable s_{ac} by the angle θ_c between the momenta $\vec{p}_3$ and $\vec{p}_B$ in the $(M_a M_b)$ rest frame, which in the massless limit is given by $(1 - s_{ab}) \cos\theta_c = s_{ab} + 2s_{ac} - 1$. The amplitude $\mathcal{A}(s_{ab}, s_{ac})$ can then be expanded in Legendre polynomials,

$$\mathcal{A}(s_{ab}, s_{ac}) = \sum_{\ell=0}^{\infty} (2\ell + 1) \mathcal{A}^{(\ell)}(s_{ab}) P_\ell(\cos\theta_c), \tag{392}$$

and spin ℓ resonances in the (ab) channel contribute only to the corresponding partial wave. Note, however, that truncating the wave expansion to any finite order makes the right-hand side of Eq. (392) algebraic in s_{ac}, while the left-hand side typically contains singularities in the physical region in the s_{ac} (and s_{bc}) channels [896]. Therefore, the series cannot converge. A popular solution to this issue is provided by the *isobar* model, where the amplitude is modeled by a finite set of partial waves simultaneously in all three channels:

$$\mathcal{A}(s_{ab}, s_{ac}) = \sum_{\ell=0}^{\ell_{\rm max}} (2\ell + 1)\, a_\ell^{ab}(s_{ab}) P_\ell(\cos\theta_c) + (abc \to bca) + (abc \to cab). \tag{393}$$

Typically, the isobaric amplitudes $a_\ell(s)$ are modeled by energy-dependent Breit–Wigner amplitudes. In addition, a "non-resonant" (smooth) component can be added to the amplitude, but the exact kinematic dependence of this component is rather arbitrary.

Final-state interactions and CPT constraint Final-state interactions are often invoked as a possible source of non-perturbative strong phases, leading to large localized CP asymmetries in

three-body decays. However, the isobar model does not include coupled channel effects (beyond resonance interference) or three-body rescattering. These effects may be modeled separately, or analyzed by means of dispersive methods (see, e.g., Refs. [118,896–898]).

Additional constraints may be obtained by combining CPT invariance and unitarity, which imply that [899]

$$\sum_f \left[\Gamma(B \to f) - \Gamma(\bar{B} \to \bar{f})\right] = 0, \tag{394}$$

where the sum runs over all states f with the same flavor quantum numbers. The individual exclusive rates need not be equal, as there might be direct CP violation in exclusive modes, but all CP asymmetries of exclusive decays to same-flavor final states must sum to zero. Due to the large phase space available in B meson decays, the multiplicity of such final states is very large, and so the constraint in Eq. (394) is by itself of little use. However, this constraint may be imposed on simple models with a few coupled channels, leading to some insight on the importance of final-state interactions and resonance interference, and a qualitative understanding of the patterns of CP asymmetries in different modes. For example, a two-channel model with coupled S-wave $(\pi^+\pi^-)$ and (K^+K^-) states satisfying the CPT constraint [900] shows good qualitative agreement for the observed CP asymmetries in $B^\pm \to K^\pm\pi^+\pi^-$ and $B^\pm \to K^\pm K^+K^-$ in the region $1\,\text{GeV}^2 \lesssim m^2_{\pi\pi,KK} \lesssim 2.2\,\text{GeV}^2$, where S-wave $\pi^+\pi^- \leftrightarrow K^+K^-$ scattering is expected to be important, and explains qualitatively why these asymmetries (properly weighted by the branching ratios) are equal and of opposite sign. The same pattern is observed in $B^\pm \to \pi^\pm\pi^+\pi^-$ and $B^\pm \to \pi^\pm K^+K^-$. More complicated models including resonant contributions from $\rho(770)$ and $f_0(980)$ have also been studied in this context [901].

Flavor symmetries and SU(3) relations The approximate SU(3) flavor symmetry of QCD has been used extensively to study two-body charmless decays (see Sect. 12.2), and it is equally useful in the case of three-body decays. By arranging all three-body final states and effective operators into SU(3) representations, the matrix elements $\langle M_aM_bM_c|Q_i(\mu)|\bar{B}\rangle$ can be expressed in terms of reduced matrix elements and Clebsch–Gordan coefficients. Some relationships can be established between observables where reduced matrix elements cancel exactly or approximately, or global fits to data can be performed to determine the reduced matrix elements and CKM parameters. In the remainder of this section we discuss the methods based on factorization.

Naive factorization For two-body charmless B decays, naive factorization is a prediction of QCD in the heavy quark limit and at the leading order in $\alpha_s(m_b)$ [415], and perturbative "non-factorizable" corrections can be computed consistently (see Sect. 12.3.1). While such a theory has not been fully developed in the three-body case, many phenomenological analyses have been performed *assuming* that "naive factorization plus $\mathcal{O}(\alpha_s)$ corrections" is a good approach to three-body decays, too. It is very likely that this is the case in the kinematic regions where one invariant mass is small and the other two are large (near the edges of the Dalitz plot). Indeed, these regions contain "quasi-two-body" configurations corresponding to two-body decays with one strong resonance in the final state (such as $B \to \rho\pi$), to which the QCD factorization formula applies [696].

Considering the kinematic region where $s_{bc} \ll 1$, and denoting the two-meson system with small invariant mass by $[M_bM_c]$, the naive factorization formula for the amplitude $A^p_{M_a[M_bM_c]}$ in Eq. (389)

is given by [902]

$$A^p_{M_a[M_bM_c]} = \sum_k \left[\alpha^p_k(M_a,[M_bM_c])A^k_{M_a,[M_bM_c]} + \alpha^p_k([M_bM_c],M_a)A^k_{[M_bM_c],M_a}\right], \tag{395}$$

where

$$A^k_{M_a,[M_bM_c]} = -\frac{G_F}{\sqrt{2}}\langle M_a|j^1_k|\bar{B}\rangle\langle[M_bM_c]|j^2_k|0\rangle, \tag{396}$$

$$A^k_{[M_bM_c],M_a} = -\frac{G_F}{\sqrt{2}}\langle[M_bM_c]|j^1_k|\bar{B}\rangle\langle M_a|j^2_k|0\rangle. \tag{397}$$

Here, $j^{1,2}_k$ are local bilinear color-singlet currents and a^p_k are the usual coefficients in QCD factorization [696]. Annihilation contributions as well as hard-scattering corrections are typically neglected. A simple way to make sense of NLO vertex corrections and penguin contractions in $a^p_k(M_a,[M_bM_c])$, which would involve a light cone distribution amplitude of the system $[M_bM_c]$, is to adopt a multi-resonance model [902]. This requires partial wave decomposition in the (M_bM_c) channel, which immediately involves all values of s_{ab}, including the kinematic regions where either M_b or M_c are soft (the corners of the Dalitz plot). The resonance model is also used for the matrix elements $\langle[M_bM_c]|j^1_k|\bar{B}\rangle$ and $\langle[M_bM_c]|j^2_k|0\rangle$.

An even more aggressive approach is to extend this factorization formula to the whole Dalitz plot [903,904]. This provides a more complete set of predictions but a loss of theoretical justification. These phenomenological analyses (see the following subsection) also include an estimate of non-resonant contributions, by calculating the $B\to M_bM_c$ form factors $\langle[M_bM_c]|j^1_k|\bar{B}\rangle$ within the heavy meson chiral perturbation theory at an unphysical kinematic point where the two mesons are soft, and then using an exponential one-parameter ansatz to extrapolate to the physical region. This parameter is assumed universal, is fitted to the "non-resonant" component of $B^-\to\pi^-\pi^+\pi^-$ provided by the B factories, and is used to predict non-resonant contributions in other modes. These (model-dependent) predictions are in reasonable agreement with data for $B^-\to K^-K^+K^-$ and $B^-\to K^-\pi^+\pi^-$ branching fractions [904], but the significance of this agreement is not always easy to interpret.

QCD factorization Different forms of factorization theorems may be conjectured depending on the scaling of the two kinematic invariants with m_b [905–907].

In the central region of the Dalitz plot, where all invariant masses are of order m_B ($s_{ab}\sim s_{ac}\sim 1/3$), the following factorization formula can be proposed [907]:

$$\langle M_aM_bM_c|Q_i|\bar{B}\rangle_{\text{center}} = F^{B\to M_a}\,T^{\rm I}_i\star\Phi_b\star\Phi_c + T^{\rm II}_i\star\Phi_B\star\Phi_a\star\Phi_b\star\Phi_c, \tag{398}$$

where the convolutions of hard-scattering kernels and distribution amplitudes are written schematically, as in Eq. (348). The hard kernels $T^{\rm I,II}_i$ can be computed perturbatively in QCD. To the lowest order (at order α_s) only $T^{\rm I}_i$ contributes, and arises from diagrams with an insertion of the operator Q_i and all possible insertions of a hard gluon which splits into a quark–antiquark pair with large invariant mass. The convolutions of the resulting perturbative kernels $T^{\rm I}_i$ with the pion light cone distributions can be computed without encountering end-point singularities, thus providing a check of the factorization formula. This check is non-trivial since the kernels $T^{\rm I}_i(u,v)$ already depend on the momentum fraction of the quarks at the leading order, making the convolutions non-trivial.

At certain edges of the Dalitz plot, where one invariant mass becomes small, the gluon propagator in some of the diagrams becomes soft, leading to a $1/s$ behavior in the amplitude. This behavior is related to non-perturbative dynamics that results, for example, in the formation of resonances. This is the case, e.g., for $B^\pm \to \pi^\pm\pi^-\pi^+$ in the region where $m_{\pi^+\pi^-} \sim m_\rho$. The decay thus looks very much like a two-body decay, and one expects a similar factorization formula [905,907]:

$$\langle M_a M_b M_c|Q_i|B\rangle_{s_{bc}\ll 1} = F^{B\to\pi^a}\, T_a^{\rm I} \star \Phi_{bc} + F^{B\to M^b M^c}\, T_{bc}^{\rm I} \star \Phi_a + T^{\rm II} \otimes \Phi_B \star \Phi_a \star \Phi_{bc}. \quad (399)$$

Here, Φ_{bc} denotes a two-meson distribution amplitude (2MLCDA), and $F^{B\to M_b M_c}$ denotes a $B \to M_b M_c$ form factor. Conceptually, this factorization formula is at the same level of theoretical rigor as the factorization formula for two-body decays to unstable particles (e.g. $B \to \rho\pi$), but requires more complicated hadronic input (discussed below). This is the cost of generalizing quasi-two-body decays beyond the narrow-width approximation.

The three-body amplitude in the central region is power- and $\mathcal{O}(\alpha_s)$-suppressed with respect to the amplitude at the edge [905,906]. The interpolation between one region and the other can be understood by noting that some parts of the central-region amplitude arise from factorization of 2MLCDAs or $B \to M_b M_c$ form factors at large s_{bc}, and one can check analytically the correspondence of such parts of the amplitudes [907]. Numerically, it is found that, in the case of $B^- \to \pi^-\pi^+\pi^-$, a good matching of the 2MLCDA part of the amplitude between the center and the edge happens only for $m_B \gtrsim 20\,\text{GeV}$, but not for physical values ($m_B \sim 5\,\text{GeV}$), suggesting that power corrections to Eq. (398) are too large in reality, and preclude a description of the central region in terms of single pion states.

We finish this section summarizing a few facts about two-pion distribution amplitudes and $B \to \pi\pi$ form factors that are relevant for three-body decays with two collinear pions.

Generalized distribution amplitudes An example of a 2πLCDA in Eq. (399) is given by the matrix element [907,908]

$$\Phi_{\pi\pi}(z,\zeta,k_{12}^2) = \int \frac{dx^-}{2\pi} e^{iz(k_{12}^+ x^-)} \langle \pi^+(k_1)\pi^0(k_2)|\bar{u}(x^- n_-)\, \not{n}_+ d(0)|0\rangle,$$

where $k_{12}^\mu = k_1^\mu + k_2^\mu \approx (k_{12}^+/2)n_+^\mu$, $\zeta = k_{12}^+/k_1^+$, and we have suppressed a Wilson line that makes the non-local quark current gauge invariant. At the leading order the kernel $T_a^{\rm I}$ in Eq. (399) does not depend on z, and only the normalization for $\Phi_{\pi\pi}$ is needed [905]:

$$\int dz\, \Phi_{\pi\pi}^q(z,\zeta,s) = (2\zeta - 1)F_\pi(s), \quad (400)$$

where $F_\pi(s)$ is the pion vector form factor. The absolute value of the pion form factor is well known experimentally in a wide range of energies (see Ref. [907, Fig. 5]). Higher moments of the 2πLCDA are needed at higher orders, but these are not well known.

$B \to \pi\pi$ form factors $B \to \pi\pi$ form factors are accessible from measurements of $B \to \pi\pi\ell\nu$ observables [909]. At low dipion masses and at large recoil of the dipion, these form factors can be studied by means of light cone sum rules. One may consider light cone sum rules with two-pion distribution amplitudes [910] or with B meson distribution amplitudes [911]. In the first case one arrives at a closed expression for the form factors in terms of moments of the 2πLCDAs:

$$F^{B\to\pi\pi}(k_{12}^2,\zeta) \sim \frac{1}{f_B}\int du f(u,k_{12}^2)\, \Phi_{\pi\pi}(u,\zeta,k_{12}^2). \quad (401)$$

The disadvantage of this method is that moments of 2π LCDAs are not well known.

In the second case, one obtains sum rules that depend on weighted convolutions of the form factors with the pion form factor $F_\pi(s)$ [911]:

$$\int ds\, g(s)\, F_\pi^\star(s)\, F^{B\to\pi\pi}(s,\zeta) \sim f_B \int d\omega\, h(\omega)\, \phi_B^+(\omega), \tag{402}$$

and depend on moments of the B meson LCDA ϕ_B^+ discussed in Sect. 12.3.2. These sum rules allow for testing of models for the $B \to \pi\pi$ form factors. In the limit where the pion form factor is dominated by an infinitely narrow ρ meson, the sum rules reduce analytically to the known sum rules for the $B \to \rho$ form factors [912].

A factorization formula for $B \to \pi\pi$ form factors at large dipion masses has also been proven at NLO recently [913]. This also proves part of the factorization formula in Eq. (398) at NLO.

12.7.2. Phenomenological analysis

Contributing author: H-Y. Cheng

Evidence of inclusive integrated direct CP asymmetries $A_{\rm CP}^{\rm incl}$ in charmless three-body decays of charged B mesons, $B^+ \to \pi^+\pi^+\pi^-$ ($4.2\,\sigma$), $B^+ \to K^+K^+K^-$ ($4.3\,\sigma$), and $B^+ \to K^+K^-\pi^+$ ($5.6\,\sigma$), has been found by LHCb [892–894]. LHCb has also observed very large asymmetries $A_{\rm CP}^{\rm low}$ of the order of 60%–70% in some small invariant-mass regions of phase space. For example, $A_{\rm CP}^{\rm low}(K^-\pi^+\pi^-) = 0.678 \pm 0.085$ for $m^2_{K^-\pi^+\ \rm high} < 15\,{\rm GeV}^2$ and $0.08 < m^2_{\pi^+\pi^-\ \rm low} < 0.66\,{\rm GeV}^2$.

As is evident from the previous subsection, three-body decays of heavy mesons are much more complicated than the two-body ones, in particular as they receive both resonant and non-resonant contributions. Contrary to three-body D decays where the non-resonant signal is usually rather small and less than 10% [914], non-resonant contributions play an essential role in penguin-dominated three-body B decays. For example, the non-resonant fraction of KKK modes is of order 70%–90%. It follows that non-resonant contributions to the penguin-dominated modes should also be dominated by the penguin mechanism. The relevance and importance of non-resonant effects are often not appreciated in the literature. Resonant effects are conventionally described within the isobar model in terms of the usual Breit–Wigner formalism. For charmless three-body decays of B mesons into three pseudoscalar mesons, there exist vector and scalar resonances.

CP violation in three-body decays is also more intricate than in the two-body case. While CP violation is just a number in the latter case, it is the distribution of the CP asymmetry in the Dalitz plot that is measured in three-body decays. Hence, the Dalitz plot analysis of $A_{\rm CP}$ distributions can reveal very rich information about CP violation. Besides the integrated CP asymmetry, the local asymmetry can be large and positive in some region and negative in another. A successful model must explain not only the inclusive asymmetry but also regional CP violation. Therefore, the measured CP asymmetry Dalitz distributions put stringent constraints on the models.

The following discussion is based on the model and results of Refs. [904,915], which examined CP violation in three-body decays and stressed the crucial role played by the non-resonant contributions. Indeed, if the non-resonant term is essential to account for the total rate, it should play a role for CP violation, too.

Decay rates Unlike hadronic two-body B decays, established frameworks such as QCDF [415] or PQCD [801,802] are not yet on the same footing for three-body decays (see the previous subsection and the original papers in Refs. [905–907] and Refs. [916,917]). Hence, Refs. [903,915] take the

factorization approximation in Eqs. (395)–(397) of the three-body decay amplitudes as a working hypothesis rather than starting from first principles.

Non-resonant contributions In general, the decay amplitude is the coherent sum of resonant contributions together with the non-resonant background

$$A = \sum_R A_R + A_{\rm NR}. \tag{403}$$

Consider the non-resonant contributions induced by the $b \to u$ transition to the tree-dominated $B^- \to K^+K^-\pi^-$ and $B^- \to \pi^+\pi^-\pi^-$ decays. The non-resonant amplitude induced by the $b \to u$ transition process reads

$$\begin{aligned} A^{\rm HMChPT}_{\rm transition} &\equiv \langle P_3(p_3)|(\bar{q}u)_{V-A}|0\rangle\, \langle P_1(p_1)P_2(p_2)|(\bar{u}b)_{V-A}|B\rangle_{\rm NR} \\ &= -\frac{f_{P_3}}{2}\big[2m_3^2 r + (m_B^2 - s_{12} - m_3^2)\omega_+ + (s_{23} - s_{13} - m_2^2 + m_1^2)\omega_-\big], \end{aligned} \tag{404}$$

where $(\bar{q}_1 q_2)_{V-A} = \bar{q}_1\gamma_\mu(1-\gamma_5)q_2$. The form factors $r, \omega_\pm$, and h can be evaluated in the framework of heavy meson chiral perturbation theory (HMChPT) [918]. However, as pointed out in Refs. [903, 915], the predicted non-resonant rates based on HMChPT are then too large for tree-dominated decays. The branching fractions of non-resonant $B^- \to \pi^+\pi^-\pi^-$ and $B^- \to K^+K^-\pi^-$ are found to be of order 75×10^{-6} and 33×10^{-6}, respectively, one order of magnitude larger than the corresponding measured total branching fractions of 15.2×10^{-6} and 5.0×10^{-6}. The issue has to do with the applicability of HMChPT. In order to apply this approach, the two final-state pseudoscalars in the $B \to P_1P_2$ transition matrix element have to be soft, which is not generally the case. Hence, an ansatz for the momentum dependence of non-resonant amplitudes in an exponential form,

$$A_{\rm transition} = A^{\rm HMChPT}_{\rm transition}\, e^{-\alpha_{\rm NR} p_B\cdot(p_1+p_2)} e^{i\phi_{12}}, \tag{405}$$

is assumed, so that the HMChPT results are recovered in the soft meson limit of $p_1, p_2 \to 0$.

For penguin-dominated decays $B \to KKK$ and $B \to K\pi\pi$, the non-resonant background induced by the $b \to u$ transition process is small compared to experiment due to the large CKM suppression $|V_{ub}V_{us}^*| \ll |V_{cb}V_{cs}^*| \approx |V_{tb}V_{ts}^*|$ associated with the $b \to u$ tree transition relative to the $b \to s$ penguin process. This implies that the two-body matrix element of scalar densities such as $\langle K\bar{K}|\bar{s}s|0\rangle$ induced from the penguin diagram should have a large non-resonant component. The measured kaon electromagnetic form factors can be used to extract $\langle K\bar{K}|\bar{q}\gamma_\mu q'|0\rangle^{\rm NR}$ and $\langle K\bar{K}|\bar{s}s|0\rangle^{\rm NR}$ first, then SU(3) flavor symmetry is applied to relate them to other two-body matrix elements [903]. The non-resonant component of the matrix element of scalar density is given by [903]

$$\langle K^+(p_2)K^-(p_3)|\bar{s}s|0\rangle_{\rm NR} = \frac{v}{3}(3F_{\rm NR} + 2F'_{\rm NR}) + \sigma_{\rm NR}\, e^{-\alpha s_{23}}, \tag{406}$$

with $v = m_{K^+}^2/(m_u + m_s) = (m_K^2 - m_\pi^2)/(m_s - m_d)$.

Resonant contributions In general, vector and scalar resonances contribute to the two-body matrix elements $\langle P_1P_2|V_\mu|0\rangle$ and $\langle P_1P_2|S|0\rangle$, respectively. The intermediate vector meson contributions to three-body decays are identified through the vector current, while the scalar resonances are mainly

Table 106. Branching fractions (in units of 10^{-6}) of resonant and non-resonant (NR) contributions to $B^- \to K^+K^-K^-, K^-\pi^+\pi^-$ [904].

$B^- \to K^+K^-K^-$			
Decay mode	BaBar [699]	Belle [919]	Theory
ϕK^-	$4.48 \pm 0.22^{+0.33}_{-0.24}$	$4.72 \pm 0.45 \pm 0.35^{+0.39}_{-0.22}$	$4.4^{+0.0+0.8+0.0}_{-0.0-0.7-0.0}$
$f_0(980)K^-$	$9.4 \pm 1.6 \pm 2.8$	< 2.9	$11.2^{+0.0+2.7+0.0}_{-0.0-2.1-0.0}$
$f_0(1500)K^-$	$0.74 \pm 0.18 \pm 0.52$		$0.63^{+0.0+0.11+0.0}_{-0.0-0.10-0.0}$
$f_0(1710)K^-$	$1.12 \pm 0.25 \pm 0.50$		$1.2^{+0+0.2+0}_{-0-0.2-0}$
$f_2'(1525)K^-$	$0.69 \pm 0.16 \pm 0.13$		
NR	$22.8 \pm 2.7 \pm 7.6$	$24.0 \pm 1.5 \pm 1.8^{+1.9}_{-5.7}$	$21.1^{+0.8+7.2+0.1}_{-1.1-5.7-0.1}$
Total	$33.4 \pm 0.5 \pm 0.9$	$30.6 \pm 1.2 \pm 2.3$	$28.8^{+0.5+7.9+0.1}_{-0.6-6.4-0.1}$
$B^- \to K^-\pi^+\pi^-$			
Decay mode	BaBar [919]	Belle [920]	Theory
$\bar{K}^{*0}\pi^-$	$7.2 \pm 0.4 \pm 0.7^{+0.3}_{-0.5}$	$6.45 \pm 0.43 \pm 0.48^{+0.25}_{-0.35}$	$8.4^{+0.0+2.1+0.0}_{-0.0-1.9-0.0}$
$\bar{K}_0^{*0}(1430)\pi^-$	$19.8 \pm 0.7 \pm 1.7^{+5.6}_{-0.9} \pm 3.2$	$32.0 \pm 1.0 \pm 2.4^{+1.1}_{-1.9}$	$11.5^{+0.0+3.3+0.0}_{-0.0-2.8-0.0}$
$\rho^0 K^-$	$3.56 \pm 0.45 \pm 0.43^{+0.38}_{-0.15}$	$3.89 \pm 0.47 \pm 0.29^{+0.32}_{-0.29}$	$2.9^{+0.0+0.7+0.0}_{-0.0-0.2-0.0}$
$f_0(980)K^-$	$10.3 \pm 0.5 \pm 1.3^{+1.5}_{-0.4}$	$8.78 \pm 0.82 \pm 0.65^{+0.55}_{-1.64}$	$6.7^{+0.0+1.6+0.0}_{-0.0-1.3-0.0}$
NR	$9.3 \pm 1.0 \pm 1.2^{+6.7}_{-0.4} \pm 1.2$	$16.9 \pm 1.3 \pm 1.3^{+1.1}_{-0.9}$	$15.7^{+0.0+8.1+0.0}_{-0.0-5.2-0.0}$
Total	$54.4 \pm 1.1 \pm 4.6$	$48.8 \pm 1.1 \pm 3.6$	$42.2^{+0.2+16.1+0.1}_{-0.1-10.7-0.1}$

associated with the scalar density. Both scalar and vector resonances can contribute to the three-body matrix element $\langle P_1P_2|J_\mu|B\rangle$. The intermediate resonances are described by a coherent sum of Breit–Wigner expressions:

$$\begin{aligned}\langle P_1P_2|\bar{q}_1\gamma_\mu q_2|0\rangle^R &= \sum_i \langle P_1P_2|V_i\rangle\langle V_i|\bar{q}_1\gamma_\mu q_2|0\rangle \times \frac{1}{s_{12} - m_{V_i}^2 + im_{V_i}\Gamma_{V_i}},\\ &+ \sum_i \langle P_1P_2|S_i\rangle\langle S_i|\bar{q}_1\gamma_\mu q_2|0\rangle \times \frac{-1}{s_{12} - m_{S_i}^2 + im_{S_i}\Gamma_{S_i}},\\ \langle P_1P_2|\bar{q}_1 q_2|0\rangle^R &= \sum_i \langle P_1P_2|S_i\rangle\langle S_i|\bar{q}_1 q_2|0\rangle \times \frac{-1}{s_{12} - m_{S_i}^2 + im_{S_i}\Gamma_{S_i}},\end{aligned} \tag{407}$$

where $V_i = \phi, \rho, \omega, \ldots$ and $S_i = f_0(980), f_0(1370), f_0(1500), \ldots$ for $P_1P_2 = \pi^+\pi^-$; $V_i = K^*(892), K^*(1410), K^*(1680), \ldots$ and $S_i = K_0^*(1430), \ldots$ for $P_1P_2 = K^\pm\pi^\mp$.

Branching fractions Table 106 summarizes the calculated branching fractions of resonant and non-resonant components in the penguin-dominated decays $B^- \to K^+K^-K^-$ and $K^-\pi^+\pi^-$. It is known that the predicted rates for penguin-dominated channels $K^-\phi$ in $B^- \to K^+K^-K^-$ decays, and $K^*\pi$, $K_0^*(1430)\pi$, and ρK in $B^- \to K^-\pi^+\pi^-$, within the factorization approach are substantially smaller than the data. To overcome this problem, the penguin annihilation induced power corrections calculated in Ref. [855] have been used. Regarding the quasi-two-body mode $B^- \to \bar{K}_0^{*0}(1430)\pi^-$, BaBar has measured the three-body decay $B^- \to K_S^0\pi^-\pi^0$ and obtained $\mathrm{Br}(B^- \to \bar{K}_0^{*0}(1430)\pi^- \to K^-\pi^+\pi^-) = (31.0 \pm 3.0 \pm 3.8^{+1.6}_{-1.6}) \times 10^{-6}$ [921], in good agreement with the Belle result $(32.0 \pm 1.0 \pm 2.4^{+1.1}_{-1.9}) \times 10^{-6}$ [920]. Hence, the rate predicted by naive

factorization is too small by a factor of three. This is still an unresolved puzzle in both the QCD factorization and PQCD approaches [922,923].

The non-resonant component of $B \to KKK$ is governed by the $K\bar{K}$ matrix element of scalar density $\langle K\bar{K}|\bar{s}s|0\rangle$. By the same token, the non-resonant contribution to the penguin-dominated $B \to K\pi\pi$ decays should also be dominated by the $K\pi$ matrix element $\langle K\pi|\bar{s}q|0\rangle$ of the scalar density. Applying the SU(3) symmetry relation, $\langle K^-(p_1)\pi^+(p_2)|\bar{s}d|0\rangle_{\rm NR} = \langle K^+(p_1)K^-(p_2)|\bar{s}s|0\rangle_{\rm NR}$, one finds too-large non-resonant and total branching fractions, namely ${\rm Br}(B^- \to K^-\pi^+\pi^-)_{\rm NR} \sim 29.7 \times 10^{-6}$ and ${\rm Br}(B^- \to K^-\pi^+\pi^-)_{\rm tot} \sim 68.5 \times 10^{-6}$. It also leads to negative asymmetries $A_{\rm CP}^{\rm incl}(B^- \to K^-\pi^+\pi^-) \sim -0.8\%$ and $A_{\rm CP}^{\rm resc}(B^- \to K^-\pi^+\pi^-) \sim -6.4\%$, opposite in sign compared with the data. To accommodate the rates, as argued in Ref. [915], some sort of power corrections such as final-state interactions are assumed to give a large strong phase δ to the non-resonant component of $\langle K^-\pi^+|\bar{s}d|0\rangle$, parameterized as

$$\langle K^-(p_1)\pi^+(p_2)|\bar{s}d|0\rangle_{\rm NR} = \frac{v}{3}(3F_{\rm NR} + 2F'_{\rm NR}) + \sigma_{\rm NR}e^{-\alpha s_{12}}e^{i\delta}. \tag{408}$$

It is then found that $\delta \approx \pm\pi$ accommodates both the non-resonant branching fractions and the CP asymmetry for $B^- \to K^-\pi^+\pi^-$. Yet, it should be stressed again that the predicted total rate of $B^- \to K^-\pi^+\pi^-$ is smaller than the measurements of both BaBar and Belle. This is ascribed to the fact that the calculated $K_0^*(1430)\pi^-$ rate in naive factorization is too small by a factor of three.

Direct CP violation In Refs. [904,915], there are three sources of strong phases: effective Wilson coefficients, propagators of resonances, and the matrix element of the scalar density $\langle M_1M_2|\bar{q}_1q_2|0\rangle$. There are two sources for the phase in the penguin matrix element of scalar densities: $\sigma_{\rm NR}$ and δ for $K\pi$ vacuum matrix elements, see Eq. (408).

The LHCb data indicate that decays involving a K^+K^- pair have a larger CP asymmetry ($A_{\rm CP}^{\rm incl}$ or $A_{\rm CP}^{\rm resc}$) than their partner channels. The asymmetries are positive for channels with a $\pi^+\pi^-$ pair and negative for those with a K^+K^- pair. In other words, when K^+K^- is replaced by $\pi^+\pi^-$, the CP asymmetry flips its sign. This can be understood in terms of U-spin symmetry, which leads to the relations [924,925]

$$R_1 \equiv \frac{A_{\rm CP}(B^- \to \pi^-\pi^+\pi^-)}{A_{\rm CP}(B^- \to K^-K^+K^-)} = -\frac{\Gamma(B^- \to K^-K^+K^-)}{\Gamma(B^- \to \pi^-\pi^+\pi^-)}, \tag{409}$$

$$R_2 \equiv \frac{A_{\rm CP}(B^- \to \pi^-K^+K^-)}{A_{\rm CP}(B^- \to K^-\pi^+\pi^-)} = -\frac{\Gamma(B^- \to K^-\pi^+\pi^-)}{\Gamma(B^- \to \pi^-K^+K^-)}. \tag{410}$$

The predicted signs of the ratios R_1 and R_2 are confirmed by experiment. However, because of the momentum dependence of three-body decay amplitudes, U-spin or flavor SU(3) symmetry do not lead to any testable relations between $A_{\rm CP}(\pi^-K^+K^-)$ and $A_{\rm CP}(\pi^-\pi^+\pi^-)$ and between $A_{\rm CP}(K^-\pi^+\pi^-)$ and $A_{\rm CP}(K^+K^-K^-)$. That is, symmetry arguments alone do not give hints at the relative sign of the CP asymmetries in the pair of $\Delta S = 0(1)$ decays.

Following the framework of Refs. [903,915] we present in Table 107 the calculated inclusive and regional CP asymmetries in the adopted model, including both resonant and non-resonant mechanisms and their interference. For the non-resonant contributions, direct CP violation arises solely from the interference of tree and penguin non-resonant amplitudes. For example, in the absence of resonances, the CP asymmetry in $B^- \to K^-\pi^+\pi^-$ stems mainly from the interference of the non-resonant tree amplitude $\langle\pi^+\pi^-|(\bar{u}b)_{V-A}|B^-\rangle_{\rm NR}\langle K^-|(\bar{s}u)_{V-A}|0\rangle$ with the non-resonant penguin amplitude $\langle\pi^-|\bar{d}b|B^-\rangle\langle K^-\pi^+|\bar{s}d|0\rangle_{\rm NR}$.

Table 107. Predicted inclusive and regional CP asymmetries (in %) for various charmless three-body B decays [904]. Two local regions of interest for regional CP asymmetries are the low-mass regions specified in Refs. [892,893] for A_{CP}^{low} and the rescattering region of $m_{\pi\pi}$ and $m_{K\bar{K}}$ between 1.0 and 1.5 GeV for A_{CP}^{resc}. Resonant (RES) and non-resonant (NR) contributions to direct CP asymmetries are considered.

	$\pi^-\pi^+\pi^-$	$K^+K^-\pi^-$	$K^-\pi^+\pi^-$	$K^+K^-K^-$
$(A_{CP}^{incl})_{NR}$	$25.0^{+4.4+2.1+0.0}_{-2.7-3.1-0.1}$	$-25.6^{+2.2+1.7+0.2}_{-3.0-1.1-0.1}$	$9.1^{+1.3+2.2+0.1}_{-1.8-2.0-0.1}$	$-7.8^{+1.4+1.3+0.1}_{-0.9-1.5-0.1}$
$(A_{CP}^{incl})_{RES}$	$5.3^{+0.0+1.6+0.0}_{-0.0-1.3-0.0}$	$-16.3^{+0.0+0.9+0.1}_{-0.0-0.8-0.1}$	$6.9^{+0.0+2.1+0.1}_{-0.0-1.8-0.1}$	$1.2^{+0.0+0.0+0.0}_{-0.0-0.0-0.0}$
$(A_{CP}^{incl})_{NR+RES}$	$8.3^{+0.5+1.6+0.0}_{-1.1-1.5-0.0}$	$-10.2^{+1.6+1.5+0.1}_{-2.5-1.4-0.1}$	$7.3^{+0.2+2.1+0.1}_{-0.2-2.0-0.1}$	$-6.0^{+1.8+0.8+0.1}_{-1.2-0.9-0.1}$
$(A_{CP}^{incl})_{expt}$	5.8 ± 2.4	-12.3 ± 2.2	2.5 ± 0.9	-3.6 ± 0.8
$(A_{CP}^{low})_{NR}$	$58.3^{+3.6+2.6+0.8}_{-3.7-4.0-0.8}$	$-25.0^{+2.8+2.7+0.3}_{-5.4-2.5-0.3}$	$48.9^{+\ 7.0+7.6+0.3}_{-10.5-8.2-0.3}$	$-13.0^{+2.0+2.8+0.2}_{-1.2-3.2-0.2}$
$(A_{CP}^{low})_{RES}$	$4.5^{+0.0+1.6+0.0}_{-0.0-1.2-0.0}$	$-4.9^{+0.0+0.5+0.0}_{-0.0-0.4-0.0}$	$57.1^{+0.0+\ 7.9+0.9}_{-0.0-16.6-0.9}$	$1.6^{+0.0+0.1+0.0}_{-0.0-0.1-0.0}$
$(A_{CP}^{low})_{NR+RES}$	$21.9^{+0.5+3.0+0.0}_{-0.4-3.3-0.1}$	$-17.5^{+0.6+1.7+0.1}_{-0.9-1.5-0.1}$	$49.4^{+0.7+\ 9.4+0.8}_{-1.0-14.2-0.8}$	$-16.8^{+3.5+2.8+0.2}_{-2.3-3.2-0.2}$
$(A_{CP}^{low})_{expt}$	58.4 ± 9.7	-64.8 ± 7.2	67.8 ± 8.5	-22.6 ± 2.2
$(A_{CP}^{resc})_{NR}$	$36.7^{+6.2+3.2+0.1}_{-3.7-4.6-0.2}$	$-27.7^{+3.1+3.0+0.4}_{-5.9-2.7-0.4}$	$31.8^{+4.6+4.6+0.3}_{-6.7-4.5-0.3}$	$-10.8^{+1.8+2.2+0.2}_{-1.2-2.5-0.2}$
$(A_{CP}^{resc})_{RES}$	$7.0^{+0.0+1.8+0.0}_{-0.0-1.5-0.0}$	$-5.6^{+0.0+0.5+0.0}_{-0.0-0.4-0.0}$	$1.1^{+0.0+0.6+0.0}_{-0.0-0.5-0.0}$	$0.96^{+0.00+0.02+0.01}_{-0.00-0.02-0.01}$
$(A_{CP}^{resc})_{NR+RES}$	$13.4^{+0.5+2.0+0.0}_{-1.1-2.1-0.0}$	$-20.4^{+1.2+2.0+0.2}_{-1.8-1.8-0.2}$	$4.1^{+0.2+0.9+0.0}_{-0.3-0.9-0.0}$	$-3.8^{+1.5+0.5+0.1}_{-1.0-0.5-0.1}$
$(A_{CP}^{resc})_{expt}$	17.2 ± 2.7	-32.8 ± 4.1	12.1 ± 2.2	-21.1 ± 1.4

It is clear from Table 107 that non-resonant CP violation is usually much larger than resonant CP violation and that the interference effect is generally quite significant. If non-resonant contributions are turned off in the $K^+K^-K^-$ mode, the predicted asymmetries will be wrong in sign when compared with experiment. The main contributions to $(A_{CP}^{incl})_{RES}$ arise from ϕK^-,$f_0(1500)K^-$,$f_0(1710)K^-$, all giving positive contributions. This is not a surprise because the mode $B^- \to K^+K^-K^-$ is dominated by the non-resonant background. Hence, the magnitude and the sign of its CP asymmetry should also be governed by the non-resonant term. The observed negative $A_{CP}^{incl}(K^+K^-K^-)$ is a strong indication of the importance of non-resonant effects.

From Table 107, it is also evident that, except for the $K^+K^-K^-$ mode, the resonant contributions to integrated inclusive CP asymmetries are of the same sign as and have similar magnitudes to A_{CP}^{incl}. On the other hand, the predicted $(A_{CP}^{low})_{RES}$ and $(A_{CP}^{resc})_{RES}$ by resonances alone for other modes are usually too small compared to the data, especially for the former.

The LHCb data indicate that the CP asymmetries are positive for channels with a $\pi^+\pi^-$ pair and negative for those with a K^+K^- pair, as discussed above. This observation appears to imply that final-state rescattering may play an important role for direct CP violation. Based on the constraint of CPT invariance on final-state interactions, the authors of Refs. [897,900] have studied CP violation in charmless three-body charged B decays. They assumed that only the two channels $\alpha = \pi^+\pi^-P^-$ and $\beta = K^+K^-P^-$ ($P = \pi, K$) in B^- decays are strongly coupled through strong interactions and treated the third meson P as a bachelor. Applying the CPT relation to describe the CP asymmetry distribution in $B^- \to K^+K^-P^-$ decays after fitting the model to the $B^- \to \pi^+\pi^-P^-$ channels, they found that final-state rescattering of $\pi^+\pi^- \leftrightarrow K^+K^-$ dominates the asymmetry in the mass region between 1 and 1.5 GeV. In Refs. [904,915], the partial rates and CP asymmetries were calculated in the model based on naive factorization as discussed above, without taking into account final-state interactions explicitly and without data fitting. While the calculated direct CP asymmetries for $K^+K^-K^-$ and $\pi^+\pi^-\pi^-$ modes are in good agreement with experiment in both magnitude and sign,

the predicted asymmetries in $B^- \to \pi^- K^+ K^-$ and $B^- \to K^- \pi^+ \pi^-$ are wrong in sign compared to experiment. In order to accommodate the non-resonant branching fraction and CP asymmetry observed in $B^- \to K^- \pi^+ \pi^-$, the matrix element $\langle K\pi|\bar{s}q|0\rangle$ is modified by extra strong phase δ of order $\pm\pi$ in addition to the phase characterized by the parameter $\sigma_{\rm NR}$, as mentioned above. The phase δ may arise from final-state interactions.

In the study of $B^- \to \pi^- \pi^+ \pi^-$, Refs. [903,915] encountered a conflict between theory and experiment for the CP asymmetry $A_{\rm CP}^{\rho^0\pi^-}$. Both BaBar [926] and LHCb [894] measurements of $B^- \to \pi^+\pi^-\pi^-$ indicate a positive CP asymmetry in the $m(\pi^+\pi^-)$ region peaked at m_ρ. On the other hand, all theories predict large and negative CP violation in $B^- \to \rho^0\pi^-$. Therefore, the issue with CP violation in $B^- \to \rho^0\pi^-$ needs to be resolved.

As mentioned at the beginning, the magnitude and sign of CP asymmetries in the Dalitz plot vary from region to region. The CP asymmetry Dalitz distributions in some (large) invariant mass regions have been studied in the factorization model [904], finding qualitative agreement with experiment for $K^+K^-K^-$ and $\pi^+\pi^-\pi^-$ modes and the correct sign for $K^-\pi^+\pi^-$. However, it appears that the phase δ needs to vanish in the large invariant mass region for $K^+K^-\pi^-$ in order to accommodate the observations. Thus it is possible that the phase δ must be allowed to be energy dependent. This issue needs to be investigated.

The large Belle II dataset will enable the study of additional three-body channels with neutral final state particles which may exhibit large local CP asymmetries, such as $B^0 \to K^+K^-K^0_S$, $B^0 \to K^+K^-\pi^0$, $B^0 \to K^+\pi^0\pi^0$, $B^+ \to K^0_S\pi^+\pi^0$, $B^+ \to K^0_S K^0_S K^+$, and $B^+ \to K^0_S K^0_S \pi^+$.

12.8. Conclusions

The large datasets collected by Belle, BaBar, and LHCb have enabled the study of many charmless hadronic $B_{(s)}$ decays, and have allowed for a detailed comparison with theoretical predictions and models. Some tantalizing questions have emerged and await the large dataset of Belle II to be further understood. The expected precision in $B \to K^0\pi^0$ with $50\,{\rm ab}^{-1}$ of data will be sufficient for NP studies and may resolve the $K\pi$ CP puzzle. The analogous isospin sum rules for the multi-body πK^* and $\rho K^{(*)}$ decays are also promising avenues to resolve this puzzle, but are statistically limited and must be measured with high precision to reveal whether an anomalous pattern of direct CP violation is emerging. The study of $B \to$ VV decays requires large statistics to perform full angular analyses, and thus there remains enormous potential. While the majority of analyses at Belle and BaBar were limited to only measuring the longitudinal polarization fraction, full angular analyses will be possible for many VV channels at Belle II. Of particular interest are ρK^* decays, where a polarization analysis will reveal if there is an enhanced contribution proportional to electromagnetic penguins. Belle II will also be uniquely suited to search for CP asymmetries in $B \to 3h$ decays with multiple neutral particles in the final state, which will serve to complement related searches at LHCb, where the observation of large local CP asymmetries in multiple channels has generated enormous interest from the theoretical and phenomenological communities. A sizeable B_s dataset will also be necessary to study rare decays such as the penguin dominated $B_s \to \phi\pi^0$, where an excess above the SM prediction would be a clear indication of NP, and, e.g., the recently observed $B^0_s \to K^0\bar{K}^0$ decay, where Belle II expects to reconstruct $\mathcal{O}(1000)$ events with $5\,{\rm ab}^{-1}$ which will enable a CP violation study and will serve to clarify the presence of NP in the decay. There are countless additional charmless hadronic $B_{(s)}$ decays which will be within the reach of Belle II. This will open up a new era of discovery and complementarity with other experiments.

13. Charm physics

Editors: G. Casarosa, A. L. Kagan, A. A. Petrov, A. J. Schwartz
Additional section writers: J. Bennett, R. Briere, G. De Pietro, S. Fajfer, M. Jung, L. Li, T. Nanut, U. Nierste, S. Schacht, S. Sharpe

13.1. Introduction

Studies of transitions involving the charm quark play an important role in both searches for NP and in understanding QCD. The large yields of charmed mesons and baryons that will be produced at Belle II make searches for NP in charm transitions a vibrant avenue for research. At the $\Upsilon(4S)$ resonance, the charm production cross section is approximately 2.7 nb: 1.6 nb from prompt $c\bar{c}$ production, and 1.1 nb from secondary $\Upsilon(4S) \to B \to D$ production. Thus the number of D (D_s) mesons produced is expected to be $> 10^9$ ($> 10^8$) per ab^{-1} of data. Decays of charmed mesons and baryons probe a variety of NP scenarios, e.g. couplings to intermediate charged Higgs states, and decays to light dark matter particles.

Searches for NP in charm decays fall into three categories: (i) searches for processes that are forbidden in the SM, (ii) studies of processes that are forbidden at tree level in the SM, and (iii) studies of processes that are allowed at tree level. The first category probes violations of principles upon which modern quantum field theories are based, such as locality, unitarity, gauge invariance, and Lorentz invariance. The second category includes processes that occur via higher-order electroweak diagrams, such as flavor-changing neutral currents (FCNC). However, the relatively small mass of the intermediate-state b quark and tiny values of the CKM matrix elements V_{cb}, V_{ub} make the short-distance SM amplitudes very small. Thus, these processes tend to be long-distance dominated, and SM predictions of most FCNC $|\Delta C| = 1$ and $|\Delta C| = 2$ processes have significant uncertainties. Finally, charm transitions allowed at tree level also test the SM. For example, measurements of leptonic and semi-leptonic decays can be directly compared to lattice QCD calculations, which have greatly improved in precision over the past few years. In addition, SM sum rules and symmetry relations among decay amplitudes based on SU(2) and SU(3) can be tested experimentally, e.g. by measuring branching fractions. Violations of such relations would indicate the presence of NP.

Experimentally, an e^+e^- collider experiment is ideal for studying charm decays, including those that are very rare or forbidden. Backgrounds are much lower than at a hadron machine, trigger efficiencies are much higher, and acceptances tend to be flat across Dalitz plots. There are usually numerous control samples available with which to study backgrounds and estimate systematic uncertainties. Because the recorded luminosity can be determined by measuring Bhabha scattering, absolute (in addition to relative) branching fractions can be measured. Because the initial state is known, unknown particles can be searched for via energy-momentum conservation: one calculates the difference between the four-momentum of the initial state and the sum of the four-momenta of all visible particles, squares that "missing four-momentum" to get a "missing mass," and looks for structure in the missing mass spectrum. Finally, photons, π^0s, and final state particles decaying to π^0s such as η, η', ρ^+, ω, and K^{*+} are much easier to reconstruct in an e^+e^- experiment than in a hadron collider experiment.

This chapter is organized as follows. We first review experimental techniques such as flavor tagging and partial reconstruction, and then we discuss some highlights from the Belle II charm physics program. The latter is not a complete discussion but rather focuses on several topics of high interest that the Belle II detector is well suited to address. These topics are divided into the following

categories: leptonic and semi-leptonic decays, rare and radiative decays, mixing and indirect CP violation, and direct CP violation. Within each category there is a theory discussion followed by a discussion of experimental sensitivity. A dedicated section on lattice QCD calculations is also included. Finally, we conclude with a listing of "golden modes," i.e. those decay modes that Belle II should measure well and also have especially good sensitivity to NP.

13.2. Experimental techniques

Authors: G. Casarosa, G. De Pietro

The Belle II detector will offer improved performance in the reconstruction of charm events with respect to the previous generation of B factories. Before presenting the physics reach of Belle II, we discuss charm flavor-tagging techniques, and expected improvements in decay vertex resolution and reconstruction efficiency.

13.2.1. Flavor-tagging methods

In order to measure CP violation it is crucial to determine the flavor of the D^0 or $\bar{D}^0$ at production. At B factories this was achieved by selecting the D^0 coming from the $D^{*+} \to D^0\pi^+$ with the charge of the pion determining the charm-quark flavor of the neutral meson. The D^0 mesons coming from B decays were excluded[40] in order to have a better measurement of the decay proper time, therefore only D^0 from D^{*+} in $c\bar{c}$ events were used. After a brief summary of the expected performance of the D^* method at Belle II, we present a new flavor-tagging method, the ROE method, that could potentially increase statistics and also provide useful control samples for our measurements. We will also comment on the possibility of exploiting D^0 mesons from a partial reconstruction of B decays for time-integrated measurements. In Table 108 we report a summary of efficiencies and mistagging rates for the methods presented.

D^* method This is the "golden" flavor-tagging method: it provides a clean sample of flavor-tagged D^0 and it has been used extensively at B factories. The primary purpose of the method is to identify the flavor of the D^0 meson at its production through the charge of the pion emitted with the D^0 in the D^{*+} decay. The low Q value of the $D^{*+} \to D^0\pi^+$ decay allows for a powerful criterion to be applied to the reconstructed difference of D^{*+} and D^0 masses, which eliminates a considerable fraction of the combinatorial background, as shown in Fig. 143. At Belle II we achieve a resolution on Δm of $\sim$180 keV/c^2 (estimated for D^*-tagged $D^0 \to K\pi$ candidates), a factor of two better than that achieved by Belle and BaBar; this will increase the background rejection power.

The typical reconstruction efficiency at BaBar was around $\epsilon_{D*} = 80\%$, with a mistagging rate of approximately $\omega_{D*} = 0.2\%$. Studies on simulated events show that Belle II will have a similar reconstruction efficiency.

ROE method We present a new flavor-tagging method with the goal of increasing the size of the sample of tagged D^0 candidates. This is achieved by adding D^0 mesons produced in $c\bar{c}$ events that are not coming from D^{*+} decays.

This new method consists in looking at the so-called rest of the event (ROE) with respect to the neutral D meson whose flavor we want to tag. The principle of the ROE method is shown in Fig. 144.

[40] To remove D^0 candidates from B decays, at Belle and BaBar D^0 mesons were usually required to have momentum in the CM frame greater than $\sim$2.5 GeV/c.

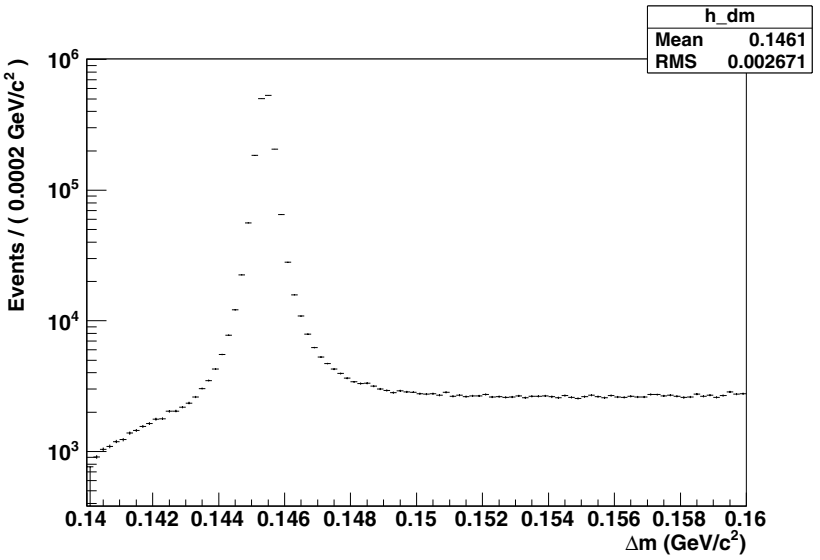

Fig. 143. $\Delta m = m(D^{*+}) - m(D^0)$ distribution for reconstructed D^*-tagged $D^0 \to K\pi$.

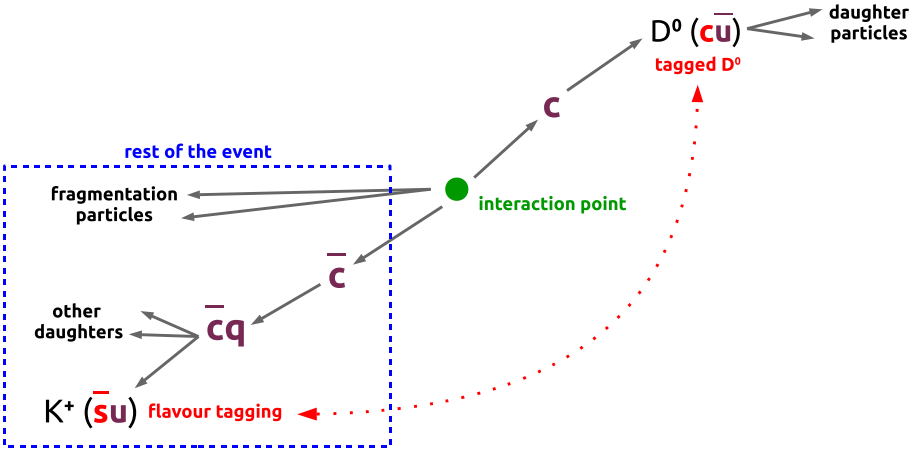

Fig. 144. The principle on which the ROE flavor-tagging method is based. Events with only one $K^\pm$ in the ROE are selected; the flavor of the neutral D meson is determined by the charge of the kaon.

Suppose a c quark hadronizes into a D^0 meson, and $\bar{c}$ hadronizes into an anti-charmed meson or an anti-charmed baryon. Since the Cabibbo-favored transition for an anti-charm quark is $\bar{c} \to \bar{s}$, we expect to find at least one hadron containing an $\bar{s}$ quark in the ROE, namely a K^+ ($u\bar{s}$) or a K^0 ($d\bar{s}$).

The flavor-tagging is performed by selecting events with only one $K^\pm$ in the ROE and using the charge of the kaon to determine the flavor of the other D^0 at the time of its production. A correctly identified $K^\pm$ produced by a Cabibbo-favored (CF) decay ($c \to su\bar{d}$) of a charmed hadron is labeled as "signal $K^\pm$."

Of course, not every event with a single $K^\pm$ in the ROE correctly determines the flavor of the neutral D. The main source of mistagging is kaons produced from s or $\bar{s}$ quarks in the primary fragmentation. If the $K^\pm$ in the ROE is generated from the hadronization of an s ($\bar{s}$) quark instead of a CF decay, the charge of the kaon is not correlated with the flavor of the neutral D meson; i.e. the $K^\pm$ in the ROE will randomly tag the flavor of the neutral D meson. This type of background is labeled as "$K^\pm$ from $c\bar{c}s\bar{s}$." There are two other minor sources of mistagging: a charged kaon in the

Table 108. Flavor-tagging summary. The number of D^0 mesons produced is relative to the number originating from D^* decays. The numbers regarding partial B reconstruction are estimated from a BaBar analysis [927], while the others are extracted from Belle II simulations using a cut on the D^0 center-of-mass momentum ($p^* > 2.5\,\mathrm{GeV}/c$). Criteria A, B, and C are described in the text.

Flavor-tagging	Produced D^0	Mistagging	Efficiency (%)	
method	N_{D^0}	ω (%)	ϵ	$Q = \epsilon\,(1-2\omega)^2$
D^*	1	0.2	80	79.7
ROE, criteria A	3	13.3	26.7	20.1
ROE, criteria B	3	9.8	16.8	13.7
ROE, criteria C	3	4.9	15.9	15.7
Partial B reconstruction	0.13	< 1	65	$\sim$62

ROE produced by a doubly Cabibbo-suppressed (DCS) decay ($c \to du\bar{s}$) labeled as "$K^\pm$ from DCS decay," and a charged kaon produced by a CF decay of a D^0 that has undergone mixing (labeled as "$K^\pm$ from mixing"). This last type of background is heavily suppressed, since the time-integrated probability for D^0–$\bar{D}^0$ oscillations is measured to be very small. Thus this background is neglected in the following.

Other sources of mistagging arise from the reconstruction of the charged kaons in the ROE. Applying a soft selection, we risk contaminating the list of $K^\pm$ candidates with tracks produced by other charged particles, mainly charged pions and protons (background from "fake $K^\pm$"). On the other hand, if the selection is too tight, we risk missing some $K^\pm$ candidates in the ROE and miscounting the number of $K^\pm$ (background from "missing $K^\pm$").

The crucial part of this new method consists of the selection of the $K^\pm$ candidates in the ROE, and this is performed using a multivariate classification. The chosen classifier method is the fast boosted decision tree, FBDT [70]. To reject poorly measured candidates, a preselection of the tracks based on PID and track fit probability is applied before the multivariate classification. The FBDT makes use of the following variables: track momentum in the lab frame, cosine of the track polar angle, track impact parameters, track fit probability, number of hits in PXD, SVD, CDC, and PID selectors for K, μ, e, p. A two-step selection based on the FBDT output variable is applied: first, a soft cut is applied to correctly count the number of charged kaons in the ROE, then a tighter cut is applied in order to remove the fake charged kaons from the list. The resulting tagging efficiency is $\epsilon = 26.7\%$ and the mistagging rate is $\omega = 13.3\%$. This is referred to as "criteria A" in Table 108. With this selection, 87.8% of the selected events have a single $K^\pm$ at the generator level (ρ_{1K}).

More than half of the mistagged events are due to $K^\pm$ from $c\bar{c}s\bar{s}$. A veto on the K^0_S (reconstructed in the $\pi^+\,\pi^-$ final state) in the ROE is applied after the FBDT selection in order to reduce the mistagging due to $c\bar{c}s\bar{s}$ events. Since the two charm quarks are produced back-to-back, a signal $K^\pm$ in the ROE tends to be produced in the opposite direction with respect to the neutral D meson. A cut on the relative angle (θ^*_{rel}) between the direction of the charged kaon and the direction of the neutral D meson in the center-of-mass frame further helps in reducing the mistagging rate. Applying these two post-FBDT selection criteria, the performance of the flavor-tagging method becomes $\epsilon = 16.8\%$, $\omega = 9.8\%$, and $\rho_{1K} = 90.9\%$. This is referred to as "criteria B" in Table 108.

Since this analysis has been made with the Belle II offline software (`BASF2`) version released at the time of writing, some tools that will be available with the final version of the software were

missing. In particular, the K_L^0 reconstruction was missing. Moreover, some improvements in the K_S^0 reconstruction and in the PID are expected. In order to evaluate how much the performance of this new flavor tagging could change with further versions of the software, we studied the limiting case in which all generated $K_S^0 \to \pi^+\pi^-$ and K_L^0 decays in the ROE are vetoed. With this special veto and with the same cut on $\theta^*_{\rm rel}$ as before, we obtain the following performance for the ROE flavor-tagging method: $\epsilon = 15.9\%$, $\omega = 4.9\%$, and $\rho_{1K} = 93.3\%$. This is referred to as "criteria C" in Table 108.

The final evaluation of the efficiency and mistagging rate can be performed directly with data events that are double tagged, i.e. tagged with *both* the D^{*+} and ROE methods. We estimate that Belle II can measure the mistagging rate of the ROE method with a statistical uncertainty of $\sim 1\%$ using an integrated luminosity of 13 fb^{-1}.

It should be noted that the number of D^0 mesons that are taggable using the ROE method, i.e. produced via $e^+e^- \to D^0\bar{D}X$, is similar to the number of mesons taggable using the D^* method, i.e. produced via $e^+e^- \to D^{*+}\bar{D}X$.

Partial reconstruction of B decays Most B mesons decay into a charmed hadron plus other particles. Charm measurements at B factories have not fully exploited this large sample of charmed hadrons. Here we briefly present a reconstruction technique used to measure the absolute branching fraction of the $D^0 \to K^-\pi^+$ channel [927].

The technique consists of partially reconstructing the semi-leptonic decay $B^0 \to D^{*+}\ell^-\nu$ with $D^{*+} \to D^0\pi^+$. Experimentally, only two tracks are required to be reconstructed: the charged lepton and the low-momentum (or "slow") pion of the D^{*+} decay. These two oppositely charged tracks are geometrically fitted to a common vertex. Two assumptions have to be made in order to reconstruct the decay tree:

- the momentum of the B^0 in the $\Upsilon(4S)$ reference frame is neglected since it is small compared to the momenta of the reconstructed tracks;
- the momentum vector of the D^{*+} is estimated by rescaling the momentum of the slow pion: the low Q-value of the D^{*+} decay allows the approximation that the pion is at rest in the D^{*+} rest frame.

With these assumptions, the missing mass squared (M_ν^2) of events can be calculated via

$$M_\nu^2 = (\sqrt{s}/2 - E_{D^{*+}} - E_\ell)^2 - (\vec{p}_{D^{*+}} + \vec{p}_\ell)^2, \tag{411}$$

where E and $\vec{p}$ are the energy and momentum of the subscript particle, and $\sqrt{s}$ is the center-of-mass energy. The M_ν^2 distribution peaks at zero for signal events and is fitted to obtain the signal yield.

We note that although the D^0 is not reconstructed, its presence is indicated by a small value of M_ν^2, and its flavor is identified by both the charge of the slow pion and the charge of the lepton. Although this reconstruction technique has a high efficiency of around 65% and a low mistagging rate, it suffers from the low branching fraction of the B^0 semi-leptonic decay. As listed in Table 108, considering $\ell = e, \mu$, only 13 D^0 are reconstructed for every 100 reconstructed with the D^{*+} technique. The application of this technique is therefore limited by the low D^0 yield. However, it can be used to improve the measurement of branching fractions and also to search for rare processes where the uniqueness of a $B\bar{B}$ event environment can be exploited. Further studies are needed to understand the effective power of this reconstruction technique at Belle II.

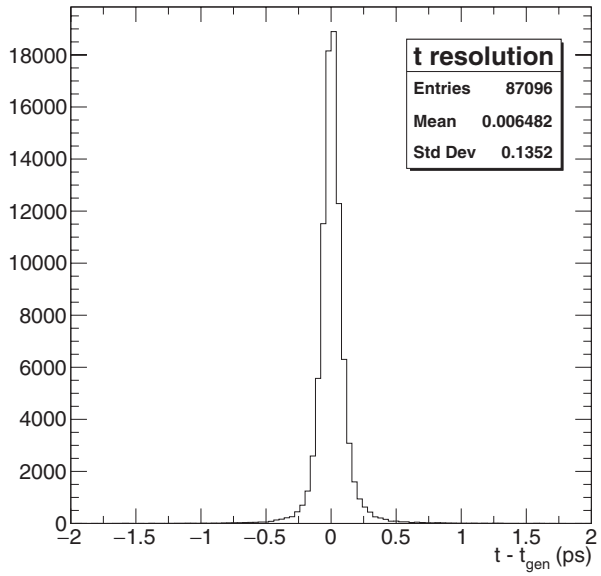

Fig. 145. D^0 proper time residuals for D^*-tagged $D^0 \to K^+K^-$ reconstructed decays.

Table 109. Typical mean and RMS of proper time resolutions. These values are obtained for candidates reconstructed in the D^*-tagged $D^0 \to K^+K^-$ channel.

Experiment	t resolution [fs]	
	Mean	RMS
Belle II	6.5	135
BaBar	−0.48	271

13.2.2. D proper time resolution

The Belle II vertex detector allows one to reconstruct the D^0 decay vertex with a precision of $\sim$40 μm, a significant improvement with respect to Belle and BaBar. This ability is due to the reduced distance between the first pixel layer and the interaction point. The resolution on the D^0 decay time is improved by a factor of two, and this should greatly improve the precision of time-dependent measurements of D^0–$\overline{D}^0$ mixing and searches for CP violation.

Figure 145 shows the residuals of the proper decay time $t = (\vec{p}\cdot\vec{d})/|\vec{p}|$, where $\vec{p}$ is the reconstructed momentum and $\vec{d}$ is the vector connecting the D^0 production and decay vertices. For comparison, Table 109 lists typical resolutions of proper decay time and errors on decay time for Belle II and BaBar. The average proper time error is a factor of three smaller at Belle II. The same improvement in resolution is also achieved for prompt D^0 production, i.e. D^0 mesons that do not originate from D^{*+} decays.

13.3. Leptonic and semi-leptonic decays

Leptonic and semi-leptonic decays of charm involve both well-understood weak interaction physics and non-perturbative strong interaction effects. Leptonic decays of charm mesons are used to extract the product of a decay constant and a CKM matrix element: $|V_{cd}|f_D$ or $|V_{cs}|f_{D_s}$. Semi-leptonic decays are used to extract the product of a form factor normalization at $q^2 = m^2_{\ell\nu} = 0$ and a CKM matrix element: $|V_{cd}|f^{\pi}_+(0)$ or $|V_{cs}|f^{K}_+(0)$. In each case, there is a factor parameterizing strong interaction

effects due to the fact that the quarks are bound in mesons. These factors can now be calculated with good precision via lattice QCD. One typically uses the experimental data in three ways:

- inputting CKM matrix elements to yield a measurement of decay constants or form factors, then comparing these to theoretical calculations tests lattice QCD;
- taking ratios of branching fractions such that CKM matrix elements cancel, which can provide a high-precision test of lattice QCD;
- inputting lattice QCD values for decay constants or form factors to yield a measurement of CKM matrix elements $|V_{cd}|$ and $|V_{cs}|$.

13.3.1. Theory

Author: S. Fajfer

Searching for NP at the LHC is the most efficient way to see the effects of NP at energies larger than 1 TeV. The alternative way to search for NP is via high-precision measurements at low energies. For example, measuring flavor-changing neutral-current processes is often considered to be a promising way to detect NP. However, indications of a difference between the measured branching fraction for $B \to D^{(*)}\tau\nu_\tau$ and the theoretical predictions (see, e.g., Ref. [291]) have stimulated discussions on the presence of NP in *charged current* processes. The $c \to s\ell\nu_\ell$ transition within charm mesons offers interesting tests of the SM as well as non-perturbative QCD dynamics.

Precise values of the decay constants for D and D_s mesons are now known from unquenched lattice QCD calculations that include the effects of dynamical up, down, strange, and charm quarks [928, 929]. The shapes of the semi-leptonic form factors $f_{+,0}(q^2)$ for the process $D \to K\ell\nu$ over the whole physical q^2 region were also recently calculated using lattice QCD [929,930]. In order to extract the $|V_{cs}|$ and $|V_{cd}|$ elements of the CKM matrix, the theoretical predictions performed within the SM can be compared to the experimental values of the total or differential branching fractions. Alternatively, constraints on the effects of NP can be derived by fixing the value of the CKM matrix element using another independent source.

The relevant NP states are usually assumed to be much heavier than the typical hadronic energy scale, in which case they can be integrated out together with the W boson. The result is that NP appears as non-standard higher-dimensional operators in the low-energy effective description of $c \to s\ell\nu_\ell$ transitions. In general, the effective Lagrangian can be written [931]:

$$\mathcal{L}_{\text{eff}} = -\frac{4G_{\text{F}}}{\sqrt{2}} V_{cs} \sum_{\ell=e,\mu,\tau} \sum_i c_i^{(\ell)} \mathcal{O}_i^{(\ell)} + \text{h.c.} \tag{412}$$

The usual four-fermion operator is $\mathcal{O}_{\text{SM}}^{(\ell)} = \left(\bar{s}\gamma_\mu P_L c\right)\left(\bar{\nu}_\ell \gamma^\mu P_L \ell\right)$ with the coefficient $c_{\text{SM}}^{(\ell)} = 1$. The non-SM effective operators that involve only the (pseudo)scalar quark and lepton densities and keep only the SM neutrinos are:

$$\mathcal{O}_{L(R)}^{(\ell)} = \left(\bar{s}P_{L(R)}c\right)\left(\bar{\nu}_\ell P_R \ell\right). \tag{413}$$

These operators might be induced by integrating out the new non-SM charged scalar boson at the tree level. Such a boson can arise in a two-Higgs doublet model (THDM), i.e. the extension of the SM with an additional scalar doublet [932]. In the approach of Ref. [931], the coefficients $c_{S,R(L)}^{(\ell)}$ are complex valued and depend on the flavor of the charged lepton. The additional dependence (besides the factor of m_ℓ) on the charged lepton's flavor is present in the THDM of the type-III [279] or in the

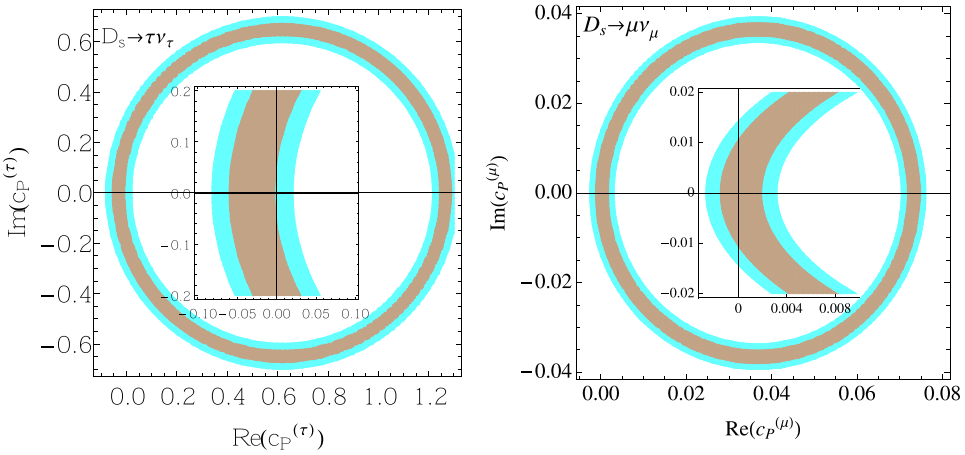

Fig. 146. Allowed regions of the effective coupling $c_{\rm P}^{(\tau)}$ (left panel) and $c_{\rm P}^{(\mu)}$ (right panel), extracted from the branching fraction of the decay mode $D_s \to \tau(\mu)\nu$, respectively. The 68% (95%) CL regions of the parameters are shown in darker (lighter) shades.

aligned THDM [280,933]. The tensor operator $\left(\bar{s}\sigma_{\mu\nu}P_R c\right)\left(\bar{\nu}_\ell \sigma^{\mu\nu}P_R \ell\right)$ could also appear together with the (pseudo)scalar operators, after integrating out a scalar leptoquark at the tree level. Such contributions are ignored due to the lack of reliable information on the tensor form factors. First, the constraints on the linear combination of the Wilson coefficients $c_{L(R)}^{(\ell)}$ from the measured branching fractions of the purely leptonic $D_s \to \ell\nu$ decay mode can be determined. The hadronic matrix element of the corresponding axial vector current is parameterized by the decay constant f_{D_s} via $\langle 0|\bar{s}\gamma_\mu\gamma_5|D_s(k)\rangle = f_{D_s}k_\mu$. Following the procedure described in Ref. [931], the branching fraction is then modified to

$$\mathcal{B}(D_s \to \ell\nu_\ell) = \tau_{Ds}\frac{m_{Ds}}{8\pi}f_{Ds}^2\left(1-\frac{m_\ell^2}{m_{Ds}^2}\right)^2 G_{\rm F}^2 \times (1+\delta_{em}^{(\ell)})|V_{cs}|^2 m_\ell^2\left|1 - c_{\rm P}^{(\ell)}\frac{m_{Ds}^2}{(m_c+m_s)m_\ell}\right|^2, \quad (414)$$

where the pseudoscalar combination of the couplings is $c_{\rm P}^{(\ell)} \equiv c_R^{(\ell)} - c_L^{(\ell)}$. In evaluating these constraints on $c_{\rm P}$, the authors of Ref. [931] used the most recent theoretical value of the decay constant $f_{D_s} = 249.0(0.3)(^{+1.1}_{-1.5})$ MeV, as calculated with sub-percent precision by the Fermilab Lattice and MILC collaborations [928]. The allowed regions for the real and imaginary parts of $c_{\rm P}$ are shown in Fig. 146.

The leptonic branching fractions for $D_s^+ \to \tau^+(\mu^+)\nu$ have been measured by the Belle Collaboration [934]. Belle also sets an upper limit $\mathcal{B}(D_s^- \to e^-\nu) < 1.0\times10^{-4}$ (95% CL) [934], which leads to the constraint $|c_{\rm P}^{(e)}| < 0.005$ [931]. This calculation uses the value $|V_{cs}| = 0.97317^{+0.00053}_{-0.00059}$ resulting from a global fit of the unitary CKM matrix as performed by the CKMFitter Collaboration [91].

One can consider the ratio of the branching fractions, i.e. $R_{\tau/\mu} = \mathcal{B}(D_s \to \tau\nu)/\mathcal{B}(D_s \to \mu\nu)$, in order to test the lepton flavor universality of the charged current. The pseudoscalar Wilson coefficient $c_{\rm P}^{(\ell)}$ also appears in the semi-leptonic decays of the pseudoscalar to vector mesons, which then offer a larger number of observables than the two-body leptonic decays due to the existence of the non-trivial angular distributions as described in Ref. [931]. Information about the helicity-suppressed contribution can be extracted experimentally by comparing the decays that involve electrons and muons in the final state. The helicity-suppressed contributions [931] are sub-dominant; this results in the small sensitivity of $D \to K^*\ell\nu_\ell$ and $D_s \to \phi\ell\nu_\ell$ to the coefficient $c_{\rm P}^{(\ell)}$ when compared to that of purely leptonic decays. Also, the knowledge of the form factors in these transitions is

currently less precise. Information about the decay mode $D \to K^* \ell \nu$ is obtained from $D \to K\pi\ell\nu$ decays, in which the dominant vector intermediate state interferes with the scalar $K\pi$ amplitude and also, to a smaller extent, with higher waves [935]. Extraction of the possible NP effects from the angular analysis thus requires careful disentangling of such resonant (and also other non-resonant) contributions. Lattice calculations would provide easier access to the form factors for $D_s \to \phi\ell\nu$, in which neither of the two mesons contain light valence quarks.

In order to analyze NP effects in $D \to K^*\ell\nu$, one needs to know the behavior of the form factors. Most of the experimental approaches to the form factors assume single pole dominance, in which the main contribution arises from the lowest pole outside the physically allowed region. An analysis of $D \to K\pi\ell\nu$ decays was performed by BaBar [936] and more recently by BESIII [937]. Both groups used the simple pole parameterization of form factors and extracted the ratios of form factors for the $D \to K^*$ transition at a single kinematic point. In Ref. [931], the ratio of the decay widths of the longitudinally and transversally polarized K^* fractions $R_{L/T}$ was considered as an observable that is sensitive to $c_{\rm P}^{(\ell)}$. However, the resulting constraint is much weaker than that shown in Fig. 146.

The scalar combination of Wilson coefficients $c_{\rm S}^{(\ell)} = c_R^{(\ell)} + c_L^{(\ell)}$ enters the amplitude for semi-leptonic $D \to K\ell\nu$ decays. In this case there are lattice evaluations of the form factors, performed by the HPQCD collaboration in Ref. [930], and there are measured values of the branching ratios [77]. These can then constrain the values of $c_{\rm S}^{(\ell)}$, $\ell = e, \mu$. Using lattice QCD results [930] and the measured decay rates [77], one can derive a constraint on the Wilson coefficient $c_{\rm S}^{(\mu)} \equiv c_R^{(\mu)} + c_L^{(\mu)}$, e.g. $|c_{\rm S}^{(e)}| < 0.2$ at 95% CL [931].

The most interesting observables in which to search for NP are the forward–backward asymmetry and the CP-violating transverse muon polarization in decays involving muons in the final state. Deviations from the SM in these observables have not been excluded. In Ref. [931] it was found that the differential forward–backward asymmetry for low q^2 can be about 10%. It was also found that the ratio $R_{\mu/e}(q^2) \equiv (d\Gamma^{(\mu)}/dq^2)/(d\Gamma^{(e)}/dq^2)$ can be used to test lepton flavor universality [931]. By allowing the first generation of leptons to interact as in the SM, and NP to affect the second generation, it was found that this ratio can deviate from the SM value by (10–20)%.

13.3.2. Experiment

Authors: J. Bennett, R. Briere, A. J. Schwartz

Leptonic decays $D^+ \to \ell^+\nu$ The low backgrounds of an e^+e^- experiment allow one to study purely leptonic $D_{(s)}^- \to \ell^-\bar{\nu}$ decays. Belle has measured the branching fractions for $D_s^- \to \mu^-\bar{\nu}$ and $D_s^- \to \tau^-\bar{\nu}$ [934], and inputting the value of f_{D_s} as calculated from lattice QCD [140] results in the world's most precise determination of $|V_{cs}|$. The $D_s^- \to \ell^-\bar{\nu}$ event sample for Belle II will be significantly larger than that for Belle, and this will allow for a more precise determination of $|V_{cs}|$. In addition, Belle II should measure $D^- \to \mu^-\bar{\nu}$ decays, and, from the branching fraction, determine $|V_{cd}|$ with an uncertainty of $< 2\%$.

The method used by Belle to reconstruct $D_s^- \to \mu^-\bar{\nu}$ decays is as follows [934]. First, a "tag-side" D^0, D^+, or Λ_c^+ is reconstructed, nominally recoiling against the signal D_s^-. The decay modes used for this are listed in Table 110. In addition, tag-side D^0 and D^+ mesons can be paired with a π^+, π^0, or γ candidate to make a tag-side $D^{*+} \to D^0\pi^+$, $D^{*+} \to D^+\pi^0$, $D^{*0} \to D^0\pi^0$, or $D^{*0} \to D^0\gamma$ candidate. The remaining pions, kaons, and protons in the event are then grouped together into what is referred to as the "fragmentation system" $X_{\rm frag}$. The particle combinations allowed for $X_{\rm frag}$ are also listed in Table 110. Because the signal decay is a D_s^-, $X_{\rm frag}$ must include a K^+ or $K_{\rm S}^0$ in order

Table 110. List of tag modes and $X_{\rm frag}$ used for analysis of $D_s^- \to \ell^- \nu$ decays at Belle [934].

Tag side:	D^0	D^+	Λ_c^+
	$K^-\pi^+$	$K^-\pi^+\pi^+$	$pK^-\pi^+$
	$K^-\pi^+\pi^0$	$K^-\pi^+\pi^+\pi^0$	$pK^-\pi^+\pi^0$
Final	$K^-\pi^+\pi^+\pi^-$	$K^0_S\pi^+$	pK^0_S
state:	$K^-\pi^+\pi^+\pi^-\pi^0$	$K^0_S\pi^+\pi^0$	$\Lambda\pi^+$
	$K^0_S\pi^+\pi^-$	$K^0_S\pi^+\pi^+\pi^-$	$\Lambda\pi^+\pi^0$
	$K^0_S\pi^+\pi^-\pi^0$	$K^+K^-\pi^+$	$\Lambda\pi^+\pi^+\pi^-$
	$K^0_S\pi^+$	K^0_S	
	$K^0_S\pi^+\pi^0$	$K^0_S\pi^0$	
	$K^0_S\pi^+\pi^+\pi^-$	$K^0_S\pi^+\pi^-$	same as for
$X_{\rm frag}$:	K^+	$K^0_S\pi^+\pi^-\pi^0$	D^+ tag
	$K^+\pi^0$	$K^+\pi^-$	$+\bar{p}$
	$K^+\pi^+\pi^-$	$K^+\pi^-\pi^0$	
	$K^+\pi^+\pi^-\pi^0$	$K^+\pi^-\pi^+\pi^-$	

Table 111. Belle's $D_s^- \to \mu^-\bar{\nu}$ [934] and inclusive D^0 [939] signal yields, and the yields expected for Belle II. The latter are obtained by either scaling the Belle results or from MC simulation studies.

Mode	Belle ($0.91, 0.92\,{\rm ab}^{-1}$)	Belle II ($50\,{\rm ab}^{-1}$)
$D_s^- \to \mu^-\bar{\nu}$	492 ± 26	27 000
$D^- \to \mu^-\bar{\nu}$	—	1250
Inclusive $D^0 \to$ anything	$(695 \pm 2) \times 10^3$	38×10^6

to conserve strangeness. If the tag side were a Λ_c^+, then $X_{\rm frag}$ must include a $\bar{p}$ in order to conserve baryon number. After $X_{\rm frag}$ is identified, a photon recoiling against $D_{\rm tag}$ and having $p > 120\,{\rm MeV}/c$ is required. This photon is considered to originate from $D_s^{*-} \to D_s^-\gamma$; the missing mass squared, $M^2_{\rm miss} = (P_{\rm CM} - P_{\rm tag} - P_{X_{\rm frag}} - P_\gamma)^2$, is required to be within a narrow window centered around $M^2_{D_s}$. The event is subsequently required to have a μ^- candidate, presumably originating from $D_s^- \to \mu^-\bar{\nu}$. The signal yield is obtained by fitting the distribution of "neutrino" missing mass $M^2_\nu = (P_{\rm CM} - P_{\rm tag} - P_{X_{\rm frag}} - P_\gamma - P_{\mu^-})^2$, which should peak at zero. The Belle signal yield, and the much larger yield expected for Belle II, are listed in Table 111.

The above method can also be used to search for $D^- \to \mu^-\bar{\nu}$ and $D^0 \to \nu\bar{\nu}$ decays [938]. In the latter case, the D^0 is required to originate from $D^{*+} \to D^0\pi^+$, and the daughter π^+ momentum is used when calculating the missing mass. Requiring that $M_{\rm miss}$ lie within a narrow window centered around M_{D^0} results in an inclusive sample of D^0 decays. The Belle yield for this sample, and the expected Belle II yield, are also listed in Table 111. The Belle II yield would allow for a seven times more sensitive search for $D^0 \to \nu\bar{\nu}$ (or any invisible final state) than that achieved by Belle.

Semi-leptonic decays $D \to h\ell^+\nu$ Both Belle and BaBar have measured semi-leptonic D decays. An early Belle analysis used $280\,{\rm fb}^{-1}$ of data to reconstruct 126 ± 12 (106 ± 12) $\pi e\nu$ ($\pi\mu\nu$) decays with an average purity of $S/(S+B) = 79\%$ [940]. A more efficient BaBar analysis used $380\,{\rm fb}^{-1}$ of data to reconstruct 5303 ± 121 $\pi e\nu$ decays, but with more background: $S/(S+B) = 53\%$ [941]. However, the systematic error on the branching fraction for the BaBar result was in fact less than

Table 112. List of tag modes and $X_{\rm frag}$ used for analysis of D^0 semi-leptonic decays at Belle II.

Tag side:	D^0	D^+
Final state:	$K^-\pi^+$	$K^-\pi^+\pi^+$
	$K^-\pi^+\pi^0$	$K^-\pi^+\pi^+\pi^0$
	$K^-\pi^+\pi^+\pi^-$	$K^0_S\pi^+$
	$K^-\pi^+\pi^+\pi^-\pi^0$	$K^0_S\pi^+\pi^0$
	$K^0_S\pi^+\pi^-$	$K^0_S\pi^+\pi^+\pi^-$
	$K^0_S\pi^+\pi^-\pi^0$	$K^+K^-\pi^+$
$X_{\rm frag}$:	π^+	none
	$\pi^+\pi^0$	π^0
	$\pi^+\pi^+\pi^-$	$\pi^+\pi^-$
		$\pi^+\pi^-\pi^0$

that of Belle. Scaling the BaBar result to the expected Belle II integrated luminosity, one predicts for Belle II a very large sample of 7.0×10^5 $\pi e\nu$ decays in 50 ab^{-1} of data.

As a feasibility study, semi-leptonic charm decays have been studied using the 1 ab^{-1} sample of $c\bar{c}$ MC. Events are reconstructed according to the reaction $e^+e^- \to c\bar{c} \to D^{0/+}_{\rm tag} D^{*-} X^{+/0}_{\rm frag}$, where $D^{*-} \to D^0_{\rm sig}\pi^-$ (charge conjugation is assumed throughout). Finally, the $D^0_{\rm sig}$ decays to the $hl\nu$ final state, where $h = K, \pi$ and $l = e, \mu$. The $D_{\rm tag}$ can be either a D^0 or D^+ reconstructed in several decay modes. The number and charge of fragmentation particles depends on the charge of the $D_{\rm tag}$. A preliminary list of tag and fragmentation modes to be implemented is given in Table 112.

The details of the missing neutrino are determined using the recoil reconstruction method, as described above for leptonic $D^+ \to \ell^+\nu$ decays. For semi-leptonic decays at Belle II, the reconstruction proceeds in two steps. First, the signal D^* is reconstructed using the recoil against the $D_{\rm tag}X_{\rm frag}$ system. Next, the search for semi-leptonic decays of the $D^0_{\rm sig}$ is conducted by reconstructing the mass recoiling against the $D_{\rm tag}X_{\rm frag}\pi_s^- hl$ system, where π_s is the slow pion from the D^* decay. The four-momentum of the missing neutrino is determined by the equation

$$P_{\rm miss} = P_{e^+} + P_{e^-} - P_{D_{\rm tag}} - P_{X_{\rm frag}} - P_h - P_l. \tag{415}$$

Then, the missing mass is constructed as $M_{\rm miss} = \sqrt{P^2_{\rm miss}}$, or, alternatively, the missing energy as $U_{\rm miss} = E_{\rm miss} - |\vec{p}_{\rm miss}|$. For correctly reconstructed events, both $M_{\rm miss}$ and $U_{\rm miss}$ peak at zero. Due to its superior resolution, $U_{\rm miss}$ is used in this analysis.

With relatively few selection criteria, it is possible to get a clean $U_{\rm miss}$ spectrum. In each event, the reconstructed charged tracks must originate at the interaction point ($|z_0| < 4$ cm, $|d_0| < 2$ cm) and survive a loose cut on the track fit quality. Hadrons must satisfy a standard requirement on the particle identification likelihood $\mathcal{L}$ ($\mathcal{L}(K) > 0.50$, $\mathcal{L}(\pi) > 0.50$), while leptons must satisfy only a loose requirement ($\mathcal{L}(\mu) > 0.10$, $\mathcal{L}(e) > 0.10$). Each K^0_S is reconstructed from $\pi^+\pi^-$ pairs, subjected to a vertex fit, and required to have an invariant mass within 20 MeV/c^2 of the nominal K^0_S mass [77].

Each $D_{\rm tag}$ candidate within a 30 MeV/c^2 mass window of the nominal D mass is subjected to a vertex fit. The mass recoiling against the $D_{\rm tag}$ candidate and fragmentation particles must fall within a 500 MeV/c^2 window of the nominal D^* mass. Finally, the difference in recoil masses for the $D_{\rm tag}X_{\rm frag}$ and $D_{\rm tag}X_{\rm frag}\pi_s$ system (equivalent to the difference in invariant mass of the D^* and D_0 candidates) must be less than 0.15 GeV/c^2.

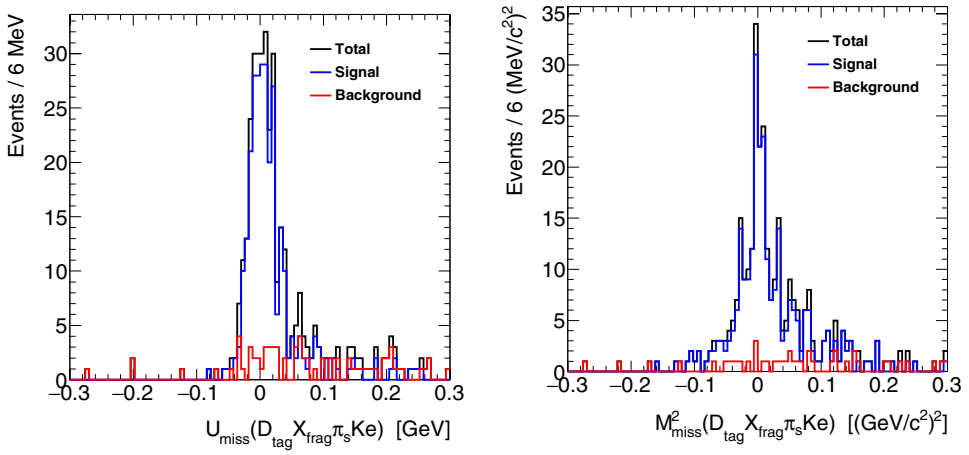

Fig. 147. $U_{\rm miss}$ (top) and missing mass squared (bottom) for semi-leptonic charm decays reconstructed using a 1 ab^{-1} sample of generic $c\bar{c}$ events using `basf2` release-00-07-00. Only a single tag mode, $D^0_{\rm tag} \to K^-\pi^+$, and a single fragmentation pion are reconstructed.

Additional selection criteria are still under investigation but will possibly include restrictions on the PID likelihood ratio for leptons, lepton momenta, the number of extra tracks in the event, and the unassociated ECL energy in the event. Imposing loose restrictions on these values, one obtains the $M_{\rm miss}$ and $U_{\rm miss}$ distributions shown in Fig. 147. The missing mass resolution is comparable to that of the most recent Belle analysis [942]. A similar analysis of Belle II MC light quark continuum samples yields no events, indicating that the continuum background for this analysis will be small.

Discussion As branching fraction measurements of leptonic and semi-leptonic decays do not require measuring decay times, they can be performed with high statistics at BESIII. Thus we compare the sensitivity of Belle II to that of BESIII.

All decays of interest involve unobservable neutrinos. With charm threshold data, one has simple initial states, either $e^+e^- \to \psi(3770) \to D^0\bar{D}^0, D^+D^-$ or $e^+e^- \to D_s^{*+}D_s^-$ + c.c. near 4170 MeV. The lack of additional fragmentation particles allows one to fully reconstruct ("tag") one $D_{(s)}$ decay to a hadronic final state, and then study the other decay. The neutrino may be inferred via energy-momentum conservation, leading to rather clean signal peaks. With continuum charm data at B factory energies, one produces more complex final states. Not only are there an unknown number of fragmentation particles, but the c and $\bar{c}$ quarks may appear in many different pairings of charm hadrons (e.g. $D^0D_s^-, \Lambda_c\bar{D}^0$). Belle overcomes this by fully reconstructing a tag-side D or Λ decay. To obtain enough efficiency, Belle sums over many different exclusive states. For both experiments there is sufficient phase space (and reduced helicity suppression) for the $\tau\nu$ mode to be important for the D_s but not the D decay.

For $D_s^+ \to \tau^+\nu, \mu^+\nu$ decays, we note that the error of 1.4% on the D_s lifetime contributes a significant 0.7% to the systematic error on f_{D_s}. As discussed above, Belle used 0.91 ab^{-1} to measure $f_{D_s} = (255.5 \pm 4.2 \pm 5.1)$ MeV [934]; this has higher precision than a similar measurement using 3 fb^{-1} by BESIII. While BESIII may take more data, they cannot match the factor of 50 increase in data that Belle II will have over Belle. The Belle result is systematics limited, with the largest contributions to the systematic uncertainty being due to normalization, efficiency, and particle identification. These uncertainties are determined by studying control samples, and thus the uncertainties should be reduced with increased luminosity.

For $D^+ \to \mu^+\nu$ decays, both CLEOc (0.82 fb^{-1}) [943] and BESIII (2.9 fb^{-1})[944] have measured $|V_{cd}|f_D$. For the latter, the statistical error on the leptonic branching fraction is 5%. While Belle has not yet published a measurement, Belle II is expected to reconstruct over 1200 of these decays, giving a statistical error of 2.8% and a resulting uncertainty on $|V_{cd}|f_D$ of half of this: 1.4%. This precision is similar to what BESIII would achieve with its planned final dataset of 15 fb^{-1}. For both experiments, the measurement should be statistics dominated.

For semi-leptonic $D \to (K/\pi)\ell\nu$ decays, those for the charged meson, D^+, provide identical information to the neutral meson, D^0, but are reconstructed less efficiently due to the presence of neutral hadrons K_S, π^0. This disadvantage is partially offset by the 2.5 times longer D^+ lifetime, i.e. the semi-leptonic branching fractions are 2.5 times larger. In addition, studying a mode such as $D^+ \to K^{*0}\ell^+\nu$, $K^{*0} \to K^-\pi^+$ avoids having to reconstruct a neutral hadron with a cost of reconstructing an additional track relative to $h^-\ell^+\nu$ modes. However, the production of D^{*+} mesons with the subsequent decay $D^{*+} \to D^0\pi^+$ will produce larger samples of D^0 mesons than D^+ at Belle II. The yield of $D^0 \to \pi^-e^+\nu$ decays estimated for Belle II, 7.0×10^5 in 50 ab^{-1} of data, can be compared to that for BESIII. The latter experiment reconstructed 6297 ± 87 events in 2.9 fb^{-1} of data [945], implying that the final BESIII data sample of 15 fb^{-1} would yield 33 000 $D^0 \to \pi^-e^+\nu$ decays. This is a large sample but an order of magnitude less than that of the full Belle II dataset.

13.4. Rare decays

13.4.1. Theory

Author: A. A. Petrov

In general, rare decays of D mesons are mediated by quark-level FCNC transitions $c \to u\ell^+\ell^-$ and $c \to u\gamma^*$ (followed by $\gamma^* \to \ell^+\ell^-$). Both these decays and D^0–$\overline{D}^0$ mixing proceed only at one loop in the SM, and these amplitudes are highly suppressed by the GIM mechanism.

Rare decays with charged leptons The simplest rare decay is purely leptonic: $D^0 \to \ell^+\ell^-$. This transition has a very small SM contribution, so it can serve as a clean probe of amplitudes due to NP. Other rare decays such as $D \to \rho\gamma$ receive significant SM contributions, which are often difficult to calculate [946–949]. There exist several experimental constraints on $D^0 \to \ell_1^+\ell_2^-$ branching fractions [230,950–952]:

$$\begin{aligned} \mathcal{B}(D^0 \to \mu^+\mu^-) &< 7.6 \times 10^{-9}, \\ \mathcal{B}(D^0 \to e^+e^-) &< 7.9 \times 10^{-8}, \\ \mathcal{B}(D^0 \to \mu^\pm e^\mp) &< 1.3 \times 10^{-8}. \end{aligned} \tag{416}$$

Theoretically, all NP contributions to $c \to u\ell^+\ell^-$ transitions (and also to D^0–$\overline{D}^0$ mixing) can be parameterized in terms of an effective Hamiltonian:

$$\mathcal{H}_{\rm NP}^{\rm rare} = \sum_{i=1}^{10} \frac{\widetilde{\rm C}_i(\mu)}{\Lambda^2}\,\widetilde{Q}_i, \tag{417}$$

where $\widetilde{C}_i$ are Wilson coefficients, $\widetilde{Q}_i$ are the effective operators, and Λ represents the energy scale of NP interactions that generate the $\widetilde{Q}_i$. There are only ten of these operators with canonical dimension six:

$$\begin{aligned}
\widetilde{Q}_1 &= (\bar{\ell}_L\gamma_\mu\ell_L)(\bar{u}_L\gamma^\mu c_L), & \widetilde{Q}_2 &= (\bar{\ell}_L\gamma_\mu\ell_L)(\bar{u}_R\gamma^\mu c_R),\\
\widetilde{Q}_3 &= (\bar{\ell}_L\ell_R)\ (\bar{u}_R c_L), & \widetilde{Q}_4 &= (\bar{\ell}_R\ell_L)(\bar{u}_R c_L),\\
\widetilde{Q}_5 &= (\bar{\ell}_R\sigma_{\mu\nu}\ell_L)(\bar{u}_R\sigma^{\mu\nu} c_L),
\end{aligned} \tag{418}$$

and five additional operators $\widetilde{Q}_6,\ldots,\widetilde{Q}_{10}$ obtained from those in Eq. (418) by interchanging $L \leftrightarrow R$, e.g. $\widetilde{Q}_6 = (\bar{\ell}_R\gamma_\mu\ell_R)(\bar{u}_R\gamma^\mu c_R)$, $\widetilde{Q}_7 = (\alpha/4)(\bar{\ell}_R\gamma_\mu\ell_R)(\bar{u}_L\gamma^\mu c_L)$, etc.

The Hamiltonian of Eq. (417) is quite general, and thus it also contains the SM contribution usually denoted by the operators $Q_9 = (\alpha/4)(\widetilde{Q}_1+\widetilde{Q}_7)$ and $Q_{10} = (\alpha/4)(\widetilde{Q}_7-\widetilde{Q}_1)$ (together with a substitution $\Lambda \to \sqrt{G_{\rm F}^{-1}}$). It is worth noting that matrix elements of several operators or their linear combinations vanish in the calculation of $\mathcal{B}(D^0\to\ell^+\ell^-)$: $\langle\ell^+\ell^-|\widetilde{Q}_5|D^0\rangle = \langle\ell^+\ell^-|\widetilde{Q}_{10}|D^0\rangle = 0$ (identically), $\langle\ell^+\ell^-|Q_9|D^0\rangle \equiv (\alpha/4)\langle\ell^+\ell^-|(\widetilde{Q}_1+\widetilde{Q}_7)|D^0\rangle = 0$ (vector current conservation), etc. The most general $D^0\to\ell^+\ell^-$ decay amplitude can be written

$$\mathcal{M}(D^0\to\ell^+\ell^-) = \bar{u}(p_-,s_-)\,[\,A+\gamma_5 B\,]\,v(p_+,s_+). \tag{419}$$

Any NP contribution described by the operators of Eq. (417) gives, for the amplitudes A and B,

$$|A| = \frac{f_D M_D^2}{4\Lambda^2 m_c}\big[\widetilde{C}_{3-8}+\widetilde{C}_{4-9}\big], \tag{420}$$

$$|B| = \frac{f_D}{4\Lambda^2}\left[2m_\ell\big(\widetilde{C}_{1-2}+\widetilde{C}_{6-7}\big)+\frac{M_D^2}{m_c}\big(\widetilde{C}_{4-3}+\widetilde{C}_{9-8}\big)\right], \tag{421}$$

with $\widetilde{C}_{i-k} \equiv \widetilde{C}_i - \widetilde{C}_k$. The amplitude of Eq. (419) results in the following branching fractions for the lepton flavor-diagonal and off-diagonal decays:

$$\mathcal{B}(D^0\to\ell^+\ell^-) = \frac{M_D}{8\pi\Gamma_{\rm D}}\sqrt{1-\frac{4m_\ell^2}{M_D^2}}\times\left[\left(1-\frac{4m_\ell^2}{M_D^2}\right)|A|^2+|B|^2\right], \tag{422}$$

$$\mathcal{B}(D^0\to\mu^+e^-) = \frac{M_D}{8\pi\Gamma_{\rm D}}\left(1-\frac{m_\mu^2}{M_D^2}\right)^2\times\big[|A|^2+|B|^2\big]. \tag{423}$$

In the latter expression, the electron mass is safely neglected. Any NP model that contributes to $D^0\to\ell^+\ell^-$ can be constrained by bounds on the Wilson coefficients appearing in Eqs. (420) and (421). We note that, because of helicity suppression, studies of $D^0\to e^+e^-$ (and consequently analyses of lepton universality using this channel) are experimentally challenging. Experimental limits on $\mathcal{B}(D^0\to\mu^+e^-)$ give constraints on lepton-flavor-violating interactions via Eq. (423). Similar limits can also be obtained from two-body charmed quarkonium decays [953].

In studying NP contributions to rare decays in charm, it can be advantageous to study *correlations* of various processes, for example D^0–$\overline{D}^0$ mixing and rare decays [954]. In general, one cannot predict the rare decay rate by knowing just the mixing rate, even if both x_D and $\mathcal{B}(D^0\to\ell^+\ell^-)$ are dominated by a single operator contribution. It is, however, possible to do so for a restricted subset of NP models [954]; these results are presented in Table 113.

Table 113. Predictions for the $D^0 \to \mu^+\mu^-$ branching fraction from correlations of rare decays and D^0–$\overline{D}^0$ mixing for $x_D \sim 1\%$ (from [954]). Notice that experimental constraints are beginning to probe the charm sector of R-parity-violating SUSY models.

Model	$\mathcal{B}(D^0 \to \mu^+\mu^-)$
Standard Model (LD)	$\sim$several $\times\ 10^{-13}$
$Q = +2/3$ singlet	4.3×10^{-11}
$Q = -1/3$ singlet	$1 \times 10^{-11}\ (m_S/500\,\text{GeV})^2$
Fourth family	$1 \times 10^{-11}\ (m_S/500\,\text{GeV})^2$
Z' model	$2.4 \times 10^{-12}/(M_{Z'}\ (\text{TeV}))^2$
Family symmetry	0.7×10^{-18} (Case A)
RPV-SUSY	$4.8 \times 10^{-9}\ (300\,\text{GeV}/m_{\tilde{d}_k})^2$
Experiment	$\leq 7.6 \times 10^{-9}$

Rare charm decays with missing energy High-luminosity e^+e^- flavor factories such as Belle II provide a perfect opportunity to search for rare processes that require high purity of the final states. In particular, searches for D decays to final states that contain neutrinos, such as $D \to \pi(\rho)\nu\overline{\nu}$, are possible at those machines due to the fact that pairs of D mesons are produced in a charge-correlated state. The SM predicts extremely small branching fractions for D decay processes with neutrinos in the final state, i.e. $\mathcal{B}(D^0 \to \nu\overline{\nu}) \approx 1 \times 10^{-30}$ and $\mathcal{B}(D^0 \to \nu\overline{\nu}\gamma) \approx 3 \times 10^{-14}$ [955]. Thus, any detection of decays of D states into channels with missing energy in the current round of experiments would indicate NP. It is important to note that these NP models could be substantially different from models described in previous sections: experimentally, it is impossible to say if the missing energy signature were generated by a neutrino or by some other weakly interacting particle.

Recently, a variety of models with light ($\sim$ MeV) dark matter (DM) particles have been proposed to explain the null results of experiments indirectly searching for dark matter (see, e.g., Refs. [956,957]). Such models predict couplings between quarks and DM particles that can be described using EFT methods [958]. These models can be tested at e^+e^- flavor factories by studying D (or B) mesons decaying into a pair of light DM particles or a pair of DM particles and a photon. The latter process eliminates helicity suppression of the final state [955]. It is conceivable that searches for light DM in heavy meson decays could even be more sensitive than direct detection and other experiments, as DM couplings to heavy quarks could be enhanced (e.g. the "Higgs portal" model of Ref. [956]).

Branching fractions for the heavy meson states decaying into $\chi_s\overline{\chi}_s$ and $\chi_s\overline{\chi}_s\gamma$, where χ_s is a DM particle of spin s, can be calculated in the EFT framework. Since production of scalar χ_0 states avoids helicity suppression, these are discussed here. For the cases $s = 1/2$ and $s = 1$, see Ref. [955].

A generic effective Hamiltonian for scalar DM interactions has the simple form

$$\mathcal{H}_{\text{eff}} = 2\sum_i \frac{C_i}{\Lambda^2} O_i, \tag{424}$$

where Λ is the energy scale associated with the particle(s) mediating interactions between the SM and DM fields, and C_i are the Wilson coefficients. The effective operators O_i are

$$\begin{aligned} O_1 &= m_c(\overline{u}_R c_L)(\chi_0^*\chi_0), \\ O_2 &= m_c(\overline{u}_L c_R)(\chi_0^*\chi_0), \\ O_3 &= (\overline{u}_L\gamma^\mu c_L)(\chi_0^* \overleftrightarrow{\partial}_\mu \chi_0), \end{aligned} \tag{425}$$

$$O_4 = (\bar{u}_R \gamma^\mu c_R)(\chi_0^* \overset{\leftrightarrow}{\partial}_\mu \chi_0),$$

where $\overset{\leftrightarrow}{\partial} = (\overset{\rightarrow}{\partial} - \overset{\leftarrow}{\partial})/2$ and the DM *anti-particle* $\overline{\chi}_0$ may or may not coincide with χ_0. The branching fraction for the two-body decay $D^0 \to \chi_0 \chi_0$ is

$$\mathcal{B}(D^0 \to \chi_0 \chi_0) = \frac{(C_1 - C_2)^2}{4\pi M_D \Gamma_{D^0}} \left[\frac{f_D M_D^2 m_c}{\Lambda^2 (m_c + m_q)} \right]^2 \times \sqrt{1 - 4x_\chi^2}, \tag{426}$$

where $x_\chi = m_\chi / M_{D^0}$ is a rescaled DM mass. This rate is not helicity-suppressed, so it could allow one to study DM properties at an e^+e^- flavor factory.

Using the formalism above, the photon energy distribution and the decay width of the radiative transition $D^0 \to \chi_0 \, \chi_0 \, \gamma$ can be calculated:

$$\frac{d\Gamma}{dE_\gamma}(D^0 \to \chi_0 \chi_0 \gamma) = \frac{f_D^2 \alpha C_3 C_4}{3\Lambda^4} \left(\frac{F_D}{4\pi} \right)^2 \times \frac{2 M_D^2 E_\gamma (M_D(1 - 4x_\chi^2) - 2E_\gamma)^{3/2}}{\sqrt{M_D - 2E_\gamma}} \tag{427}$$

$$\mathcal{B}(D^0 \to \chi_0 \chi_0 \gamma) = \frac{f_D^2 \alpha C_3 C_4 M_D^5}{6\Lambda^4 \Gamma_{D^0}} \left(\frac{F_D}{4\pi} \right)^2 \times \left(\frac{1}{6} \sqrt{1 - 4x_\chi^2} (1 - 16x_\chi^2 - 12x_\chi^4) - 12 x_\chi^4 \log \frac{2x_\chi}{1 + \sqrt{1 - 4x_\chi^2}} \right). \tag{428}$$

We observe that Eqs. (427) and (428) are independent of $C_{1,2}$; this is due to the fact that $D \to \gamma$ form factors of scalar and pseudoscalar currents vanish. In this manner, studies of $D^0 \to$ (missing energy) and $D^0 \to (\gamma +$ missing energy) processes probe complementary operators in the effective Hamiltonian of Eq. (424). Similar conclusions hold for decays of B mesons into final states with missing energy.

13.4.2. Experiment

Radiative modes $D \to V\gamma$

Author: T. Nanut

Radiative decays $D^0 \to V\gamma$ are a promising probe of NP, as theoretical studies [959,960] predict that NP contributions can enhance the time-integrated CP asymmetry

$$A_{\rm CP} \equiv \frac{\Gamma(D^0 \to f) - \Gamma(\bar{D}^0 \to \bar{f})}{\Gamma(D^0 \to f) + \Gamma(\bar{D}^0 \to \bar{f})} \tag{429}$$

up to an order of magnitude relative to the SM expectation, which is $\sim 10^{-3}$. As these decays are dominated by long-distance contributions, measurement of their branching fractions can test non-perturbative QCD calculations [961,962].

Belle has recently made the first measurements of $A_{\rm CP}$ in $D^0 \to V\gamma$ decays, where $V = \phi, \overline{K}^{*0}$, or ρ^0. The results are

$$A_{\rm CP}(D^0 \to \rho^0 \gamma) = +0.056 \pm 0.152 \pm 0.006,$$
$$A_{\rm CP}(D^0 \to \phi \gamma) = -0.094 \pm 0.066 \pm 0.001,$$
$$A_{\rm CP}(D^0 \to \overline{K}^{*0} \gamma) = -0.003 \pm 0.020 \pm 0.000,$$

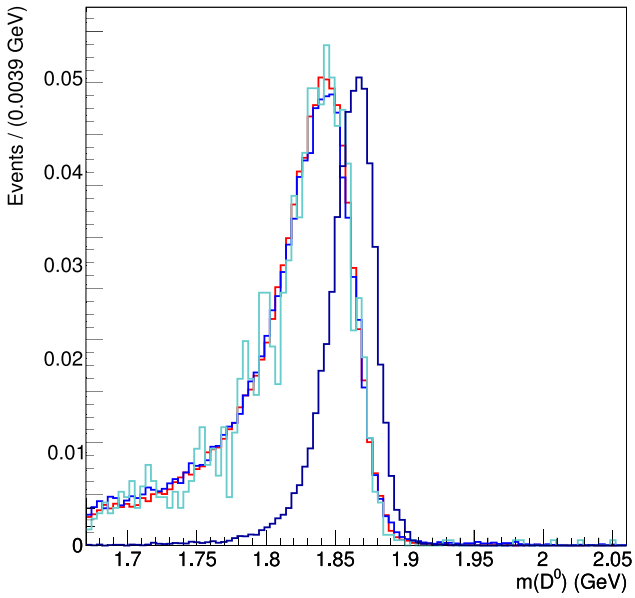

Fig. 148. Comparison of normalized distributions for $m(D^0)$ of signal (right-most distribution) and various π^0-type backgrounds, for $D^0 \to \overline{K}^{*0}\gamma$ decays at Belle.

where the first error is statistical and the second is systematic. These results are consistent with no CP violation. The dominant error is by far the statistical one, which implies that the precision will be significantly improved at Belle II, with its much larger dataset.

The extraction of signal and the corresponding statistical uncertainty depend heavily on backgrounds. The dominant background arises from $D^0 \to X\pi^0$ decays in which one of the photons from the subsequent $\pi^0 \to \gamma\gamma$ decay is undetected. For example, $D^0 \to \phi\pi^0$ is background to $D^0 \to \phi\gamma$; $D^0 \to K^-\rho^+$, $\rho^+ \to \pi^+\pi^0$ is background to $D^0 \to \overline{K}^{*0}\gamma$; and $D^0 \to \rho^+\pi^-$, $\rho^+ \to \pi^+\pi^0$ is background to $D^0 \to \rho^0\gamma$. As these backgrounds have the same charged final state particles and only one photon is missed in the reconstruction, the distribution of the reconstructed D^0 mass is shifted towards lower values but still overlaps with the signal peak, as shown in Fig. 148. Since there are many such decays of this type and their branching fractions can exceed that of the signal by several orders of magnitude, it is crucial to suppress this type of background as much as possible.

The separation power between signal and π^0 background, which is reflected in the statistical error, is governed by the D^0 mass resolution of signal and background (i.e. the extent of overlap of the peaks), and the signal-to-background ratio. We study these two aspects using MC simulation. As the three signal decays studied by Belle share the same kinematics and have similar backgrounds, we investigate the Belle II sensitivity to only one signal mode and one π^0-type background: $D^0 \to \phi\gamma$ signal and $D^0 \to \phi\pi^0$ background. We generate Belle II MC samples of both signal and background events and reconstruct $D^0 \to \phi\gamma$ candidates in both.

To reduce the substantial π^0 background for this type of analysis, Belle developed a dedicated π^0 veto. This veto employs a neural network utilizing two mass veto variables. Each variable is obtained by pairing the signal candidate photon with all other photons in the event whose energy exceeds a specific minimum value. The diphoton mass combination that lies closest to the mass of the π^0 is recorded and assigned to the signal candidate photon. To reject background with minimal signal loss, the energy of the second photon is required to be >75 MeV for the first veto variable and >30 MeV for the second. This minimum energy requirement is effective as there is a high multiplicity of soft

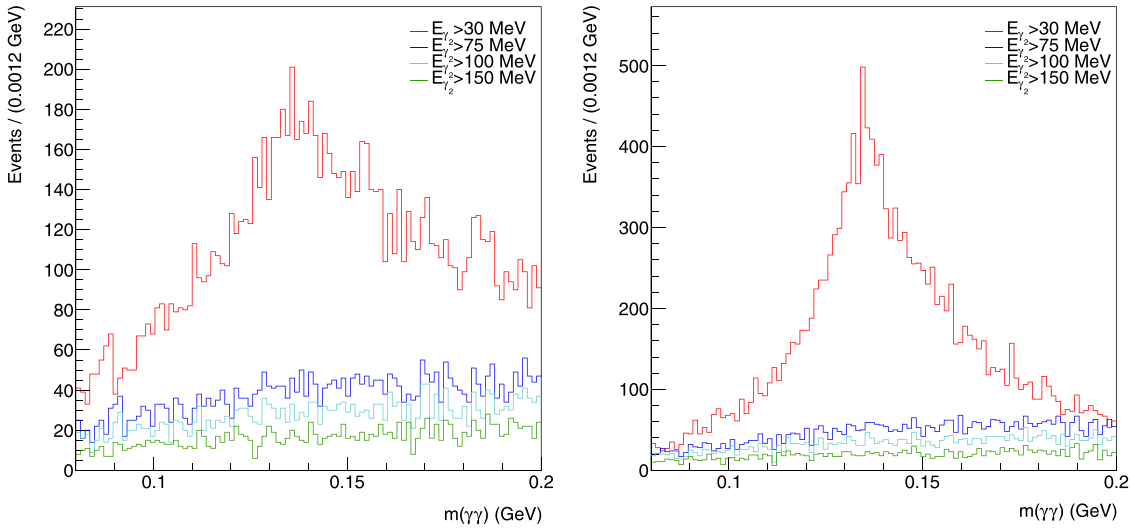

Fig. 149. Comparison between the diphoton invariant mass distributions with different requirements on the energy of the second photon for $D^0 \to \phi\gamma$ signal MC events, for Belle (left) and Belle II (right).

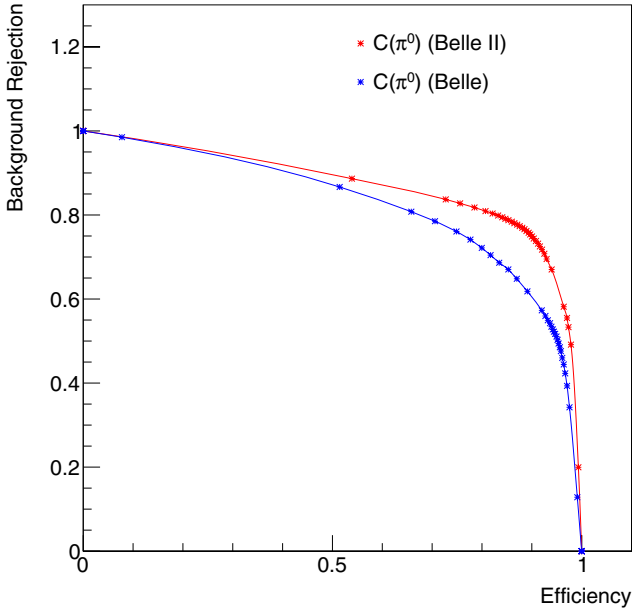

Fig. 150. Performance of the π^0 veto for Belle and Belle II: $D^0 \to \phi\pi^0$ background rejection as a function of $D^0 \to \phi\gamma$ signal efficiency.

photons, which increases the chance that a random combination of photons will have a diphoton mass close to that of the π^0. This is demonstrated in Fig. 149, which shows that, even for MC signal events in which there is *no* π^0 background, there is a peak in the diphoton mass distribution near $M(\pi^0)$ when the energy requirement on the second photon is low. This false peak can cause a signal inefficiency.

The performance of the π^0 veto in Belle II has been studied using MC simulation, and the results are shown in Fig. 150. This figure plots $D^0 \to \phi\pi^0$ background rejection as a function of $D^0 \to \phi\gamma$ signal efficiency for both Belle and Belle II. Comparing the two curves indicates that the performance

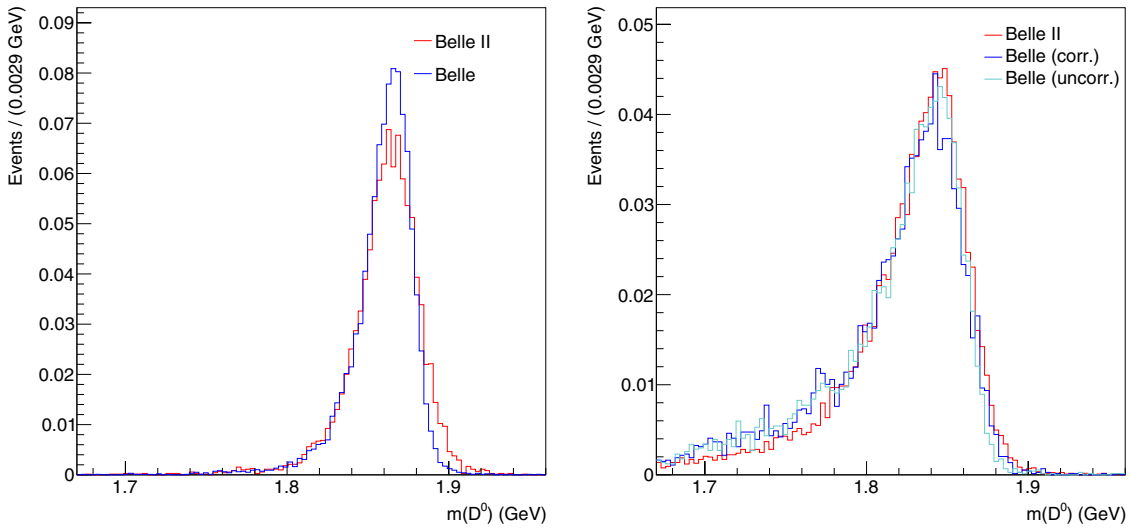

Fig. 151. Comparison of $m(D^0)$ distributions between Belle and Belle II for signal $D^0 \to \phi\gamma$ decays (left), and for background events reconstructed as $D^0 \to \phi\gamma$ (right), from MC simulation. For Belle, a corrected distribution is also shown; this distribution was calibrated to match that of the data.

is very similar; in fact the Belle II results indicate slightly higher background rejection for a given signal efficiency.

The variables that are used in the fit to measure the signal yield are the reconstructed D^0 mass and the cosine of the helicity angle, which is the angle between the D^0 and daughter particles of the vector meson in the rest frame of the vector meson. The comparison of D^0 mass distributions between Belle and Belle II MC samples for both signal and background is shown in Fig. 151. The fitted widths for the Belle and Belle II signal samples are 0.0122 ± 0.0001 GeV and 0.0164 ± 0.0002 GeV, respectively. For the background samples, the widths are 0.0162 ± 0.0004 GeV and 0.0194 ± 0.0003 GeV, respectively. The Belle II resolution is comparable to, but slightly worse than, that of Belle. The means of the Belle and Belle II mass distributions are very similar. The decrease in the resolution of Belle II is attributed to slightly worse energy resolution of the ECL. However, the ECL reconstruction software is still under development, and the Belle II resolution is expected to improve, eventually reaching the level of Belle. Figure 152 shows analogous plots for the second fit variable, $\cos\theta_{\rm H}$. The distributions for Belle and Belle II samples match well.

As the resolution of both fitted variables is very similar for Belle and Belle II, and the performance of the π^0 veto is similar, we conclude that the ratio of signal to background will be similar for the two experiments. Thus, we estimate the Belle II sensitivity for $A_{\rm CP}$ of $D^0 \to V\gamma$ decays by scaling (reducing) the Belle statistical uncertainty by the ratio of integrated luminosities. The resulting sensitivities for 5, 15, and 50 ab^{-1} of data are listed in Table 114. The table shows that the statistical error should be reduced to the level of 1%–2% for the full Belle II dataset. As these $A_{\rm CP}$ measurements are relative, i.e. $A_{\rm CP}(\phi\gamma)$ is measured relative to $A_{\rm CP}(D^0 \to K^+K^-)$ (which has a similar final state), most systematic uncertainties should cancel. Thus the overall systematic error for Belle II should be similar to that for Belle, and the statistical error will remain the dominant one. We conclude that the final results for Belle II will provide an order of magnitude greater sensitivity to NP than achieved by Belle.

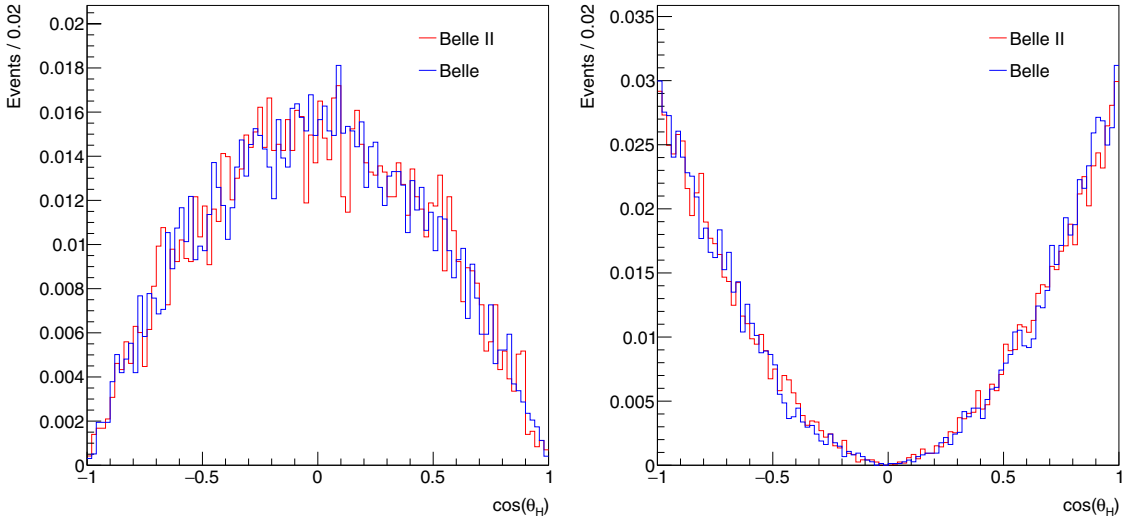

Fig. 152. Comparison of $\cos\theta_{\rm H}$ distributions between Belle and Belle II for signal $D^0 \to \phi\gamma$ decays (left), and for background events reconstructed as $D^0 \to \phi\gamma$ (right), from MC simulation.

Table 114. $A_{\rm CP}$ results of the Belle study and extrapolation of the statistical uncertainty to Belle II, for different values of integrated luminosity.

	Int. luminosity			
		$A_{\rm CP}(D^0 \to \rho^0\gamma)$		
Belle result	$1\,{\rm ab}^{-1}$	$+0.056$	±0.152	±0.006
	$5\,{\rm ab}^{-1}$		±0.07	
Belle II statistical error	$15\,{\rm ab}^{-1}$		±0.04	
	$50\,{\rm ab}^{-1}$		±0.02	
		$A_{\rm CP}(D^0 \to \phi\gamma)$		
Belle result	$1\,{\rm ab}^{-1}$	-0.094	±0.066	±0.001
	$5\,{\rm ab}^{-1}$		±0.03	
Belle II statistical error	$15\,{\rm ab}^{-1}$		±0.02	
	$50\,{\rm ab}^{-1}$		±0.01	
		$A_{\rm CP}(D^0 \to \overline{K}^{*0}\gamma)$		
Belle result	$1\,{\rm ab}^{-1}$	-0.003	±0.020	±0.000
	$5\,{\rm ab}^{-1}$		±0.01	
Belle II statistical error	$15\,{\rm ab}^{-1}$		±0.005	
	$50\,{\rm ab}^{-1}$		±0.003	

13.5. Charm mixing

13.5.1. CP violation theory

Author: A. L. Kagan

In the SM, CP violation in mixing enters at $O(|V_{cb}V_{ub}/V_{cs}V_{us}|) \sim 10^{-3}$. What is the resulting theoretical uncertainty on the indirect CP violation observables? How large is the current window for NP? What is an appropriate parameterization for indirect CP-violating effects, given the expected sensitivity in the LHCb/Belle II era? These points are addressed below, based on work to appear in Y. Grossman et al. (in preparation)—see also Refs. [963,964].

We begin with an introduction to the formalism for treating CP violation in mixing. The transition amplitudes for D^0–$\overline{D}^0$ mixing are written as

$$\langle D^0|H|\overline{D}^0\rangle \;=\; M_{12} - \frac{i}{2}\Gamma_{12}, \tag{430}$$

where M_{12} is the dispersive mixing amplitude. In the SM it is dominated by long-distance contributions of off-shell intermediate states. A significant short-distance effect would be due to NP. Γ_{12} is the absorptive mixing amplitude, and is due to long-distance contributions of on-shell intermediate states. The D meson mass eigenstates, obtained by diagonalizing the 2×2 Hamiltonian $H = M - i\Gamma/2$, are $|D_{1,2}\rangle = p|D^0\rangle \pm q|\overline{D}^0\rangle$. The differences between their eigenvalues are parameterized as $x \equiv (m_2 - m_1)/\,\Gamma$ and $y \equiv (\Gamma_2 - \Gamma_1)/2\Gamma$. The subscripts label the masses and widths of the two mass eigenstates; by convention the "2" state usually corresponds to the CP-even state in the absence of CP violation. The parameters x, y give rise to D^0–$\overline{D}^0$ mixing and can be measured.

We define the following three underlying theoretical parameters: x_{12}, y_{12}, ϕ_{12}. The first two are CP conserving:

$$x_{12} \;\equiv\; \frac{2|M_{12}|}{\Gamma} \qquad \text{and} \qquad y_{12} \;\equiv\; \frac{|\Gamma_{12}|}{\Gamma}, \tag{431}$$

while the last is a phase difference that gives rise to CP violation in mixing:

$$\phi_{12} \;\equiv\; \arg\left(\frac{M_{12}}{\Gamma_{12}}\right). \tag{432}$$

It can be shown that $x \approx x_{12}$ and $y \approx y_{12}$ up to small corrections quadratic in the amount of CP violation. CP violation in mixing occurs due to sub-leading $O(V_{cb}V_{ub})$ suppressed SM decay amplitudes (containing the CKM phase γ), and possible NP short-distance mixing amplitudes and decay amplitudes containing new weak phases.

There are in fact two types of CP violation due to mixing; both are referred to as "indirect" CP violation. The first is CP violation in the mixing ("CPVMIX"), which arises when $\phi_{12} \neq 0$, and is due to interference between the dispersive and absorptive mixing amplitudes. CPVMIX can be directly measured via the semi-leptonic CP asymmetry

$$A_{\rm SL} \;\equiv\; \frac{\Gamma(D^0 \to K^+\ell^-\nu) - \Gamma(\overline{D}^0 \to K^-\ell^+\nu)}{\Gamma(D^0 \to K^+\ell^-\nu) + \Gamma(\overline{D}^0 \to K^-\ell^+\nu)} \;=\; \frac{|q/p|^4 - 1}{|q/p|^4 + 1} \;=\; \frac{2x_{12}y_{12}}{x_{12}^2 + y_{12}^2}\sin\phi_{12}. \tag{433}$$

The second type of CP violation is due to interference between a direct decay amplitude and a "mixed" amplitude followed by decay ("CPVINT"), i.e. interference between $D^0 \to f$ and $D^0 \to \overline{D}^0 \to f$. For decays to a CP eigenstate final state, there are two CPVINT observables (introduced in Ref. [965]),

$$\lambda_f^M \;\equiv\; \frac{M_{12}}{|M_{12}|}\,\frac{A_f}{\overline{A}_f} \;=\; \eta_f^{\rm CP}\left|\frac{A_f}{\overline{A}_f}\right| e^{i\phi_f^M}, \quad \lambda_f^\Gamma \;\equiv\; \frac{\Gamma_{12}}{|\Gamma_{12}|}\,\frac{A_f}{\overline{A}_f} \;=\; \eta_f^{\rm CP}\left|\frac{A_f}{\overline{A}_f}\right| e^{i\phi_f^\Gamma}, \tag{434}$$

that parameterize the interference for a dispersive mixing amplitude and an absorptive mixing amplitude, respectively. Here, ϕ_f^M and ϕ_f^Γ are the corresponding weak phases, $A_f \;=\; \langle f|H|D^0\rangle$ and $\overline{A}_f = \langle f|H|\overline{D}^0\rangle$ are the decay amplitudes, and $\eta_f^{\rm CP} = +\,(-)$ for CP even (odd) final states. For

decays to a non-CP-eigenstate final state f, and its CP conjugate $\bar{f}$, there are two pairs of observables,

$$\lambda_f^M \equiv \frac{M_{12}}{|M_{12}|}\frac{A_f}{\overline{A}_f} = \left|\frac{A_f}{\overline{A}_f}\right| e^{i(\phi_f^M - \Delta_f)}, \quad \lambda_f^\Gamma \equiv \frac{\Gamma_{12}}{|\Gamma_{12}|}\frac{A_f}{\overline{A}_f} = \left|\frac{A_f}{\overline{A}_f}\right| e^{i(\phi_f^\Gamma - \Delta_f)}, \tag{435}$$

and $\lambda_{\bar{f}}^M$, $\lambda_{\bar{f}}^\Gamma$, obtained by substituting $f \to \bar{f}$ and $\Delta_f \to -\Delta_f$ in Eq. (435), where Δ_f is the strong phase difference between the decay amplitudes. Note that the absorptive and dispersive phases are related to the pure mixing phase ϕ_{12} as

$$\phi_{12} = \phi_f^M - \phi_f^\Gamma. \tag{436}$$

In general, the weak phases ϕ_f^M and ϕ_f^Γ are final state specific due to "non-universal" weak and strong phases entering SM CKM-suppressed contributions and possible NP contributions to the sub-leading decay amplitudes. However, in the case of the Cabibbo-favored / doubly Cabibbo-suppressed (CF/DCS) decays in the SM, these phases are universal. More generally, NP phases entering the CF/DCS amplitudes would need to be very exotic in origin, or tuned, to evade the ϵ_K constraint [966]. Thus it is a well-motivated assumption to take ϕ_f^M and ϕ_f^Γ to be final state independent, in general, for CF/DCS decays.

Non-vanishing ϕ_f^M and ϕ_f^Γ cause *time-dependent* CP asymmetries. For example, in SCS decays to the CP eigenstates $f = K^+K^-$ and $f = \pi^+\pi^-$, the effective lifetimes $\hat{\tau}$ (or inverse lifetimes $\hat{\Gamma} = 1/\hat{\tau}$) for D^0 and $\overline{D}{}^0$ decays will differ:

$$\Delta Y_f \equiv \frac{\hat{\Gamma}_{\overline{D}{}^0 \to f} - \hat{\Gamma}_{D^0 \to f}}{2\Gamma_D} = -x_{12} \sin\phi_f^M + a_f^d\, y_{12}. \tag{437}$$

The second term on the right-hand side is the direct CP-violating contribution, where the direct CP asymmetry is defined as

$$a_f^d = 1 - \left|\bar{A}_f / A_f\right|. \tag{438}$$

It can, in principle, be disentangled experimentally from the dispersive CPVINT contribution with the help of time-integrated CP violation measurements, in which a_f^d also enters without a mixing suppression [967],

$$A_{\rm CP} \equiv \frac{\Gamma(D^0 \to f) - \Gamma(\overline{D}{}^0 \to \bar{f})}{\Gamma(D^0 \to f) + \Gamma(\overline{D}{}^0 \to \bar{f})} = \frac{\langle t \rangle}{\tau_D} \cdot \Delta Y_f + a_f^d. \tag{439}$$

At Belle II, the factor $\langle t \rangle / \tau_D$ is very close to unity, whereas at LHCb this factor is close to two [968]. Examples of time-dependent CP asymmetries in decays to non-CP eigenstates include the SCS final states $f = K^*K$ or $f = \rho\pi$, and CF/DCS final states $f = K^\pm\pi^\mp$. These asymmetries generally depend on both ϕ_f^M and ϕ_f^Γ because of the additional strong phase Δ_f (Y. Grossman et al., in preparation).

Finally, we relate the dispersive and absorptive observables to the more familiar parameterization of indirect CP violation currently in use; see, e.g., Ref. [969]. The latter consists of the CPVMIX parameter $|q/p| - 1$, and the CPVINT observables

$$\lambda_f \equiv \frac{q}{p}\frac{\bar{A}_f}{A_f} = -\eta_f^{\rm CP} \left|\lambda_f\right| e^{i\,\phi_{\lambda_f}} \tag{440}$$

for CP eigenstate final states, and their generalization to pairs of observables λ_f, $\lambda_{\bar{f}}$ for non-CP-eigenstate final states, with arguments $\phi_{\lambda_f} \pm \Delta_f$. The relation between $|q/p| - 1$ and ϕ_f^M, ϕ_f^Γ follows from Eqs. (433) and (436), while ϕ_{λ_f} is given by (Y. Grossman et al., in preparation)

$$\tan 2\phi_{\lambda_f} = -\frac{x_{12}^2 \sin 2\phi_f^M + y_{12}^2 \sin 2\phi_f^\Gamma}{x_{12}^2 \cos 2\phi_f^M + y_{12}^2 \cos 2\phi_f^\Gamma}. \tag{441}$$

Indirect CP violation can be equivalently described in terms of the parameters ϕ_f^M, ϕ_f^Γ, x_{12}, y_{12} emphasized in this report, or the more familiar ones $|q/p|, \phi_{\lambda_f}, x, y$. The same number of independent parameters is employed in each case.

The superweak limit Until recently, fits to measurements of indirect CP violation have been sensitive to values of ϕ_{12} down to the 100 mrad level. This level of precision probes large short-distance NP effects. In particular, the effects of weak phases in the sub-leading decay amplitudes can be safely neglected in the indirect CP violation observables. In this limit, referred to as the superweak limit, a non-vanishing ϕ_{12} would be entirely due to short-distance NP in M_{12}. Thus, the dispersive and absorptive weak phases satisfy

$$\phi_f^M = \phi_{12}, \qquad \phi_f^\Gamma = 0, \tag{442}$$

and the ϕ_{λ_f} reduce to the familiar "universal" CPVINT phase ϕ entering current fits. Note that the phase ϕ_{12} would be the only source of indirect CP violation. Therefore, CPVMIX and CPVINT would be related as [970–972]

$$\tan 2\phi \approx -\frac{x_{12}^2}{x_{12}^2 + y_{12}^2} \sin 2\phi_{12}, \qquad \tan\phi \approx \left(1 - \left|\frac{q}{p}\right|\right) \frac{x}{y}, \tag{443}$$

where the first relation is the superweak limit of Eq. (441). However, in the superweak limit, the effects of weak phases in the SCS decay amplitudes are kept in the *direct* CP violation observables (where they are not suppressed by x_{12}, y_{12}). For example, Eq. (437) reduces to $\Delta Y_f = -x_{12} \sin\phi_{12}$, while the second term on the right-hand side of Eq. (439) is kept.

With only one phase ϕ_{12} controlling all indirect CP violation, the superweak fits to CP violation data are highly constrained. In particular, HFLAV [230] and the UTfit Collaboration [964] obtained the following $1\,\sigma$ and 95% CL fit results (in radians):

$$\begin{aligned} \text{HFLAV} &: \phi_{12} = 0.00 \pm 0.03, \quad [-0.09, +0.08], \\ \text{UTfit} &: \phi_{12} = 0.01 \pm 0.05, \quad [-0.10, +0.15]. \end{aligned} \tag{444}$$

The HFLAV fit uses all available charm mixing and CP violation data. The HFLAV superweak results for ϕ and $|q/p|$ are:

$$\phi = 0.00 \pm 0.01 \text{ [rad]}, \qquad |q/p| = 0.999 \pm 0.014. \tag{445}$$

Approximate universality With the continuing improvement in experimental sensitivity expected from Belle II and LHCb, achieving $O(10\,\text{mrad})$ precision for ϕ_{12} may be possible. Thus, we must consider possible deviations from the superweak limit due to the sub-leading decay amplitudes, and how best to parameterize such deviations. In particular, we need to estimate the size of the final state dependence in ϕ_f^M and ϕ_f^Γ. We accomplish this via a U-spin flavor symmetry decomposition

of the D^0–$\overline{D}^0$ mixing amplitudes. Crucially, this also yields order of magnitude estimates of indirect CP-violating effects in the SM (Y. Grossman et al., in preparation).

Employing CKM unitarity, the U-spin decomposition of the SM mixing amplitude Γ_{12} can be written as ($\lambda_i \equiv V_{ci}V_{ui}^*$)

$$\Gamma_{12} = \frac{(\lambda_s - \lambda_d)^2}{4}\,\Gamma_2 + \frac{(\lambda_s - \lambda_d)\lambda_b}{2}\,\Gamma_1 + \frac{\lambda_b^2}{4}\,\Gamma_0, \tag{446}$$

and similarly for M_{12}, with substitutions $\Gamma_i \to M_i$. The U-spin amplitudes $\Gamma_{2,1,0}$ and $M_{2,1,0}$ are the $\Delta U_3 = 0$ elements of $\Delta U = 2$, 1, 0 (5-plet, triplet, and singlet) multiplets, respectively. The $\Delta U = 2, 1, 0$ amplitudes enter at $O(\epsilon^2)$, $O(\epsilon)$, and $O(1)$, respectively, in $\mathrm{SU(3)_F}$ flavor symmetry breaking. The expansion parameter ϵ characterizes the size of the symmetry breaking. Although M_2, Γ_2 enter at $O(\epsilon^2)$, they dominate due to their large CKM factors, and yield the mass and lifetime differences, i.e. x_{12} and y_{12}. CP violation in the SM is due to M_1, Γ_1, and arises at $O(\epsilon)$ via the CKM phase $\gamma = \arg(\lambda_b)$ entering the SCS decays. The effects of M_0, Γ_0 are of $O(\lambda_b^2)$, and therefore negligible.

We define a pair of theoretical absorptive and dispersive CP violation phases, ϕ_2^Γ and ϕ_2^M, respectively, with respect to the $\Delta U = 2$ direction in the mixing amplitude complex plane, proportional to $(\lambda_s - \lambda_d)^2$, i.e. the direction of the Γ_2 and M_2 contributions, cf. Eq. (446):

$$\phi_2^\Gamma \equiv \arg\left(\frac{\Gamma_{12}}{\Gamma_{12}^{\Delta U=2}}\right) \approx \mathrm{Im}\left(\frac{2\lambda_b}{\lambda_s - \lambda_d}\frac{\Gamma_1}{\Gamma_2}\right) \sim \left|\frac{\lambda_b}{\theta_c}\right| \sin\gamma \times \frac{1}{\epsilon}, \tag{447}$$

and similarly for ϕ_2^M, with the substitution $\Gamma \to M$ everywhere in Eq. (447). The second relation in Eq. (447) is obtained from the ratio of Γ_1 to Γ_3 contributions in Eq. (446), while $\Gamma_1/\Gamma_3 = O(1/\epsilon)$ is used in the last relation. In addition, $\phi_{12} = \phi_2^M - \phi_2^\Gamma$. Taking the nominal value $\epsilon \sim 0.2$ for U-spin breaking in Eq. (447), we arrive at the rough SM estimates

$$\phi_{12} \sim \phi_2^\Gamma \sim \phi_2^M \sim 3 \times 10^{-3}. \tag{448}$$

Thus, values for these phases as large as $\sim$10 mrad are certainly plausible.

The phases ϕ_2^M and ϕ_2^Γ are the theoretical analogs of the final-state-dependent phases ϕ_f^M and ϕ_f^Γ, respectively. Another useful theoretical phase defined with respect to the $\Delta U = 2$ direction is the theoretical analog of the final-state-dependent phases ϕ_{λ_f}. It is given by

$$\phi_2 \equiv \arg\left(\frac{q}{p}\frac{1}{\Gamma_{12}^{\Delta U=2}}\right). \tag{449}$$

The estimate, $\phi_2 \sim 3 \times 10^{-3}$, follows from Eq. (448) and the substitutions $\phi_f^{\Gamma(M)} \to \phi_2^{\Gamma(M)}$, $\phi_{\lambda_f} \to \phi_2$ in Eq. (448).

Next, we assess the deviations of the final-state-dependent phases ϕ_f^M, ϕ_f^Γ, and ϕ_{λ_f}, cf. Eqs. (434), (435), and (440), from their theoretical counterparts, in order to arrive at the appropriate minimal parameterization of indirect CP-violating effects in the LHCb/Belle II era. The misalignments between these phases, for given final state f, satisfy

$$\delta\phi_f \equiv \phi_f^\Gamma - \phi_2^\Gamma = \phi_f^M - \phi_2^M = \phi_2 - \phi_{\lambda_f}. \tag{450}$$

We can characterize the magnitude of the misalignment in the SM as follows: (i) For CF/DCS decays it is precisely known and negligible, i.e. $\delta\phi_f = O(\lambda_b^2/\theta_c^2)$, implying that, to excellent

approximation, $\phi_f^{\Gamma(M)} = \phi_2^{\Gamma(M)}$, and $\phi_{\lambda_f} = \phi_2$. (ii) In SCS decays, $\delta\phi_f$ is related to direct CP violation as $\delta\phi_f = a_f^d \cot\delta$ (via the U-spin decomposition of the decay amplitudes [973]), where a strong phase $\delta = O(1)$ is expected due to large rescattering at the charm mass scale. Thus, for $f = \pi^+\pi^-, K^+K^-$, the experimental bounds $a_f^d \lesssim O(10^{-3})$ imply that $\delta\phi_f \lesssim O(10^{-3})$. (iii) In SCS decays, $\delta\phi_f = O(\lambda_b \sin\gamma/\theta_c) \times \cot\delta$, i.e. it is $O(1)$ in SU(3)$_F$ breaking. Thus, Eq. (447) yields $\delta\phi_f/\phi_2^\Gamma = O(\epsilon)$, implying an order-of-magnitude suppression of the misalignment.

We conclude that in the SM, the deviations of the final-state-dependent phases from the theoretical phases are entirely negligible for CF/DCS decays, whereas for SCS decays they yield ∼10% corrections. Thus, in the LHCb/Belle II era, with a potential sensitivity of 10 mrad, a single pair of dispersive and absorptive phases suffices to parameterize all indirect CP-violating effects, which we can identify with our theoretical phases ϕ_2^M and ϕ_5^Γ, respectively. We refer to this fortunate circumstance as *approximate universality*. Moreover, approximate universality generalizes beyond the SM under the following conservative assumptions about NP decay amplitudes containing new weak phases: (i) they can be neglected in CF/DCS decays [966]; (ii) in SCS decays their magnitudes are similar to, or smaller than, the SM QCD penguin amplitudes, as already hinted at by the experimental bounds on the direct CP asymmetries $a_{K^+K^-}^d$, $a_{\pi^+\pi^-}^d$. These assumptions can ultimately be tested by future direct CP-violating measurements.

Under approximate universality, the final-state-dependent CPVINT phases ϕ_f^M, ϕ_f^Γ are replaced with the final-state-independent phases ϕ_2^M, ϕ_2^Γ in the expressions for the time-dependent CP asymmetries. For example, $\Delta Y_f = -x_{12} \sin\phi_2^M + y_{12}\, a_f^d$, cf. Eq. (437). A global fit to the CP violation data with any two of the three phases ϕ^M, ϕ^Γ, ϕ_{12} is equivalent to the traditional two-parameter fit for the parameters $|q/p|$ and $\phi = \phi_2$. The relations

$$\left|\frac{q}{p}\right| - 1 \approx \frac{|x||y|}{x^2+y^2}\sin\phi_{12}, \qquad \tan 2(\phi_2 + \phi^\Gamma) \approx -\frac{x_{12}^2}{x_{12}^2+y_{12}^2}\sin 2\phi_{12}, \tag{451}$$

together with $\phi_{12} = \phi_2^M - \phi_2^\Gamma$, allow one to translate between $(\phi_2, |q/p|)$ and $(\phi_2^M, \phi_2^\Gamma)$—the second relation in Eq. (451) follows from Eq. (441) in the approximate universality limit. In this manner it is possible to separately determine the dispersive and absorptive CP violation phases. Large short-distance NP contributions, which would reside in the former, could therefore be isolated.

Theory summary We have described indirect CP-violating effects in terms of the (final-state-dependent) dispersive and absorptive CP-violating weak phases. This description allowed us to estimate the size of indirect CP violation in the SM, and to arrive at a minimal parameterization appropriate for the LHCb/Belle II era. Up until recently, the sensitivity of indirect CP violation measurements has been sufficient to probe for large short-distance NP contributions. Fits to the CP violation data carried out in the superweak limit have therefore been appropriate. In the superweak limit the only source of indirect CP violation is the mixing phase ϕ_{12}. The UTfit and HFLAV fits yield $\phi_{12} \lesssim 0.10$ [rad] at the 95% CL. A U-spin-based decomposition of the mixing amplitudes implies that ϕ_{12} could be as large as ∼10 mrad in the SM, cf. Eq. (448). Hence, we concluded that there is currently an $O(10)$ window for NP in indirect CP violation.

As the sensitivity of indirect CP violation measurements improves towards 10 mrad in the indirect CP violation phases, it becomes necessary to take into account the effects of weak phases in sub-leading decay amplitudes. We have argued that their contributions to the indirect CP violation observables can be accounted for in the SM, and under conservative assumptions for NP, with only

two theoretical dispersive and absorptive phases ϕ_2^M and ϕ_2^Γ (denoted as approximate universality), cf. Eq. (447). These phases could be as large as $\sim$10 mrad in the SM, while the final-state-dependent corrections are an order of magnitude smaller.

The parameterization in terms of ϕ_2^M and ϕ_2^Γ is equivalent to the traditional two-parameter fits to ϕ and $|q/p|$, where ϕ is identified with the theoretical phase ϕ_2 in Eq. (449), with direct CP asymmetries in the CF/DCS decays set to zero. The translation between them is given in Eq. (451). In the second relation, the left-hand side contains the combination $\phi_2 + \phi_2^\Gamma$. However, our U-spin-based estimates for these phases in the SM are not far from the $1\,\sigma$ error on ϕ in the superweak fit, cf. Eqs. (445) and (448). Going forward, this confirms that we must move beyond the superweak limit (in which $\phi_2^\Gamma = 0$), and fit for the independent parameters ϕ_2^M and ϕ_2^Γ. The two-parameter fit yields much larger errors on $\phi = \phi_2$ and $|q/p|$. For example, the current HFLAV errors increase by $O(10)$ compared to the superweak fit results. However, this should ultimately be overcome by the improved statistics at Belle II and LHCb.

13.5.2. Lattice calculations

Author: S. Sharpe

To search for new physics using charmed mesons, it is obviously crucial to accurately predict the SM contributions to the decay and mixing amplitudes. The issue addressed in this section is the extent to which lattice QCD (LQCD) can, over the next few years, provide such predictions.

LQCD provides a method for determining the strong interaction contributions to certain types of hadronic amplitudes, using numerical simulations of the partition function of QCD. All approximations that are made (finite lattice spacing, finite volume, etc.) can be systematically removed, so that results with fully controlled errors are possible. For those quantities that are presently accessible, LQCD results have now achieved percent-level precision or better. These quantities include the light hadron spectrum, decay constants (including those of the D and D_s), semi-leptonic form factors (including those for $D \to K$ and $D \to \pi$ decays), and mixing matrix elements (such as B_K and B_B). For a recent review of the status of such calculations see Ref. [140]. The results confirm that QCD indeed describes the strong interactions in the non-perturbative regime, and provides predictions that play a crucial role in the search for new physics by looking for inconsistencies in unitarity triangle analyses.

At present, however, results with high precision are only available for processes involving single hadrons and a single insertion of a weak operator. For charmed mesons, the only high-precision quantities are thus the abovementioned decay constants and semi-leptonic form factors, as well as the short-distance part of the D^0–$\overline{D^0}$ mixing amplitude. The decay amplitudes (e.g. those for $D \to \pi\pi$ and $D \to K\bar{K}$), as well as the long-distance part of the mixing amplitude, are more challenging quantities because they involve multiple-particle states. The progress towards LQCD calculations of these quantities will be discussed below.

Before doing so we give an update on results for the short-distance contributions to D^0–$\overline{D^0}$ mixing. We recall that, in the SM, these arise only from loops involving b quarks, and contribute only a small part of the mixing amplitude. The largest contribution involves intermediate light quarks and is long-distance dominated. This holds also for the CP-violating part of the mixing amplitude, which is, in any case, expected to be very small in the SM due to the CKM factors and lack of enhancement from the top-quark loop. In light of these considerations, D^0 mixing is an excellent place to look for contributions from new physics. Integrating out the heavy particles in generic beyond-the-SM (BSM) theories leads to Lorentz scalar $|\Delta C| = 2$ operators with all possible chiral structures, eight

in all. Their matrix elements can be parameterized in terms of five B parameters, generalizations of the single B parameter that is needed for the SM operator composed of left-handed currents. Explicit forms of these operators and the definitions of the corresponding B parameters are given, for example, in Ref. [193]. Analogous matrix elements are needed to parameterize the BSM contributions to kaon and B mixing.

Recently, the first fully controlled results for the D-mixing B parameters have become available [193]. These were obtained by the ETM collaboration using simulations with dynamical up, down, strange, and charm quarks (with up and down degenerate). The quarks were discretized with the twisted-mass action. The results have errors ranging from 3%–8%, larger than the state-of-the-art quantities mentioned above, but sufficiently small for most phenomenological purposes. The values of the five B parameters range from 0.65 up to 0.97.

There are also preliminary results from the Fermilab Lattice plus MILC collaborations [974]. These use staggered light quarks and the Fermilab heavy quark action for the charm quark, with up, down, and strange sea quarks. The results have larger errors than those of Ref. [193], but have similar central values [975]. Final results are expected soon.

We now return to the more challenging, and more interesting, case of the D decay amplitudes. To understand the challenges facing a lattice calculation of, say, the $D \to \pi\pi$ amplitude, it is useful to begin by discussing the simpler case of $K \to \pi\pi$ decays. For the latter decays, an LQCD calculation is now possible, and indeed first results have been obtained. For the $\Delta I = 3/2$ transition, these have fully controlled errors [178], while for the $\Delta I = 1/2$ case a complete result is available only at a single lattice spacing [179,976]. Nevertheless, the successful calculation of both real and imaginary (CP-violating) parts of the $\Delta I = 1/2$ amplitude is a *tour de force*, and substantially moves the boundaries of what is possible from LQCD.

There are three main technical challenges for $K \to \pi\pi$ calculations: (i) the fact that one necessarily works in a finite volume so the states are not asymptotic two-particle states; (ii) the need to calculate Wick contractions (such as the penguin-type contractions) that involve gluonic intermediate states in some channels; and (iii) the presence of an effective weak Hamiltonian with many operators, some of which can mix in lattice regularization with lower-dimension operators. The former challenge was solved some time ago [177]. It has taken many years, however, for methods, algorithms, and computational power to improve to the point that the numerical aspects of all three challenges can be overcome. Fully controlled results for all amplitudes, and in particular for the SM prediction for ϵ', are expected in the next few years.

To extend these results to the charm case one faces two additional challenges. The first is that to calculate a decay matrix element one must use final states with energy $E = M_D$, and these are highly excited compared to the strong interaction ground states. For example, in the $I = S = 0$ sector, with total momentum $\vec{P} = 0$, the lightest state consists of two pions at rest, with $E \approx 2M_\pi$ (up to small finite-volume corrections). In a correlation function, the contribution of this lightest state will dominate over that from states with $E = M_D$ by an exponential factor, $e^{(M_D - 2M_\pi)\tau}$ (where τ is Euclidean time). This is relevant because, in an LQCD calculation, the weak Hamiltonian is able to connect states having different energies. Thus if one simply considers a correlator in which one first creates a D meson, then inserts the weak Hamiltonian, and finally destroys two pions, the dominant contribution will be from the unphysical (and uninteresting) amplitude for $D \to (\pi\pi)\big|_{\text{rest}}$. In order to obtain the desired physical amplitude one must therefore project the final state onto one having $E = M_D$. This can be done in principle by using appropriate final state operators, tuned to avoid couplings to lighter states. While this will certainly be challenging, it is encouraging that over the

last five years there have been tremendous advances in the methodology for extracting excited state energies, using the methods described in Refs. [977,978]. These have allowed the first calculations of resonance properties in several channels (as reviewed, for example, in Ref. [979]). Thus we expect this challenge to be solvable using adaptations of existing methods.

The second, and more difficult, challenge is as follows. Even when one has fixed the quantum numbers of a final state, say to $I = S = 0$, the strong interactions necessarily mix together all kinematically allowed states having these quantum numbers. When $E = M_D$, this means that even if one creates a state with a two-pion operator, it will mix with states containing $K\overline{K}$, $\eta\eta$, 4π, 6π, etc. This is an inevitable feature of working in a finite volume, where the particles do not lie in asymptotic states and repeatedly scatter off one another. It means that even if one could calculate the matrix element between a D meson and one of these finite-volume states, this would not be related to the desired infinite-volume amplitudes. This is the generalization of the problem solved by Lellouch and Lüscher for a single two-particle channel. We stress that this is not an issue introduced by discretization of space-time, but instead by the computational necessity of working with a finite system.

There has been significant progress towards a solution to this theoretical problem in the last few years. The first step, taken in Ref. [189], was to solve the analogous problem for a particle that can decay to any number of two-particle channels (and assuming that the scattering is dominantly s-wave). Thus, if the D decayed only to $\pi\pi$, $K\bar{K}$, and $\eta\eta$, for example, then the problem is solved in principle.

The next major step was to determine the "quantization condition" for a finite-volume three-particle system, e.g. three pions in a box [980,981]. This relates the finite-volume energies to the two- and three-particle infinite-volume scattering amplitudes, and generalizes to three particles the two-particle formalism of Lüscher. The result is quite complicated, but has recently been checked by comparing the threshold expansion to results obtained using non-relativistic quantum mechanics and perturbation theory [982]. Other checks are underway. The derivation also makes various simplifying assumptions (e.g. not allowing any $2 \leftrightarrow 3$ transitions) and work is actively underway to relax these. We expect that a fully general three-particle quantization condition will be available within a year, and that the next step, a generalization of the Lellouch–Lüscher method to decays involving two and three particles, will follow shortly after.

Extension of the theoretical work to four or more particles will be the next challenge. No work has been done on this to date, and it is difficult to give a timescale for expected progress. We do note, however, that there is great interest in the development of these methods in the hadron spectroscopy community.

Finally, we comment briefly on the possibility of calculating long-distance contributions to D^0–$\overline{D^0}$ mixing using lattice methods. Here the challenge is that there are two insertions of the weak Hamiltonian, with many allowed states propagating between them. Significant progress has been made recently on the corresponding problem for kaons [983,984], but the D^0 system is much more challenging. The main problem is that there are many strong interaction channels having $E < m_D$, and these lead to exponentially enhanced contributions that must be subtracted and corrected for. Further theoretical work is needed to develop a practical method.

13.5.3. Experiment

The experimental status of D^0–$\bar{D}^0$ mixing and CP violation measurements is summarized in Table 115. The first evidence for mixing was obtained by Belle in $D^0 \to h^+h^-$ decays [985] and by BaBar in $D^0 \to K^+\pi^-$ decays [986]. The first observations of mixing with more than $5\,\sigma$

Table 115. The experimental status of D^0–$\overline{D}^0$ mixing and CP violation in different decays.

Decay type	Final state	LHCb	Belle	BaBar	CDF	CLEO	BESIII
DCS 2-body (WS)	$K^+\pi^-$	★	★	●	★	✓	
DCS 3-body (WS)	$K^+\pi^-\pi^0$		✓ A_{CP}	●		✓ A_{CP}	
CP eigenstate	K^+K^-, $\pi^+\pi^-$	● (a) A_{CP}	●	●	✓ A_{CP}	✓	
Self-conjugated 3-body decay	$K^0_S\pi^+\pi^-$ $K^0_S K^+K^-$	✓	✓ ✓ (b)	✓ A_{CP} ✓	✓		
Self-conjugated SCS 3-body decay	$\pi^+\pi^-\pi^0$ $K^+K^-\pi^0$	✓ A_{CP}	✓ A_{CP}	✓ mixing A_{CP} ✓ A_{CP}			
SCS 3-body	$K^0_S K^\pm\pi^\mp$	✓ $_\delta{}^{K^0_S K\pi}$				✓ $_\delta{}^{K^0_S K\pi}$	
Semi-leptonic decay	$K^+\ell^-\nu_\ell$		✓	✓		✓	
Multi-body ($n \geq 4$)	$\pi^+\pi^-\pi^+\pi^-$ $K^+\pi^-\pi^+\pi^-$ $K^+K^-\pi^+\pi^-$	✓ A_{CP} ★ ✓ (c) A_{CP}	✓ A_{CP}	✓ ✓ A_T		✓ A_{CP}	
$\psi(3770) \to D^0\overline{D}$ via correlations						✓ $_\delta{}^{K\pi}$	✓ y_{CP}

★: observation ($>5\,\sigma$); ●: evidence ($>3\,\sigma$); ✓: measurement.
(a) LHCb measured the indirect CP asymmetry in Phys. Rev. Lett. **112**, 041801 (2014).
(b) Belle measured y_{CP} in $D^0 \to K^0_S\phi$ in Phys. Rev. D **80**, 052006 (2009).
(c) LHCb searched for CP violation using T-odd correlations in J. High Energy Phys. **10**, 005 (2014).

significance were made by LHCb [987] and CDF [988]. To date, no evidence of CP violation in D^0 decays has been obtained by any experiment.

Wrong-sign decays $D^0 \to K^+\pi^-$
Author: A. Schwartz

Given the much larger samples of flavor-tagged DCS $D^0 \to K^+\pi^-$ decays Belle II will collect over those collected by Belle and BaBar, and also the improved decay time resolution, one expects that Belle II will have significantly greater sensitivity to mixing and CP violation in D^0 decays than the first generation of B factories. To study this, we have performed a "toy" MC study in which "wrong-sign" $D^0 \to K^+\pi^-$ and $\overline{D}{}^0 \to K^-\pi^+$ decays are generated, their decay times smeared by the expected decay time resolution of Belle II, and the resulting decay times fitted for mixing parameters x, y and CP-violating parameters $|q/p|$, ϕ. The fit results are compared with the generated (true) values and the residuals plotted. The RMS of these distributions are taken as the precision Belle II should achieve for these parameters. Below we provide details of this study and the results.

The yield of flavor-tagged $D^0 \to K^+\pi^-$ decays collected by Belle was 4024 ± 88 in 400 fb^{-1} of data and 11478 ± 177 in 976 fb^{-1} of data, corresponding to two independent analyses. Scaling the latter result, which has higher statistics, by luminosity gives the expected Belle II signal yields listed in Table 116 for 5 ab^{-1}, 20 ab^{-1}, and 50 ab^{-1} of data. Thus, for our MC study we generate samples of $D^{*+} \to D^0\pi^+$, $D^0 \to K^+\pi^-$ and $D^{*-} \to \overline{D}{}^0\pi^-$, $\overline{D}{}^0 \to K^-\pi^+$ decays corresponding to these integrated luminosities. It is expected that it will take Belle II approximately two years, five years, and ten years, respectively, to collect these samples.

Table 116. Flavor-tagged $D^{*+} \to D^0\pi^+$, $D^0 \to K^+\pi^-$ signal yields (including charge conjugates) obtained by Belle and expected for Belle II.

Luminosity (ab^{-1})	Belle	Belle II
0.400	4024	
0.976	11 478	
5.0		58 800
20		235 200
50		588 000

The $D^0 \to K^+\pi^-$ decay times are generated according to the following probability density functions (PDFs):

$$\frac{N(D^0 \to f)}{dt} \propto e^{-\overline{\Gamma}t}\left\{R_D + \left|\frac{q}{p}\right|\sqrt{R_D}(y'\cos\phi - x'\sin\phi)(\overline{\Gamma}t) + \left|\frac{q}{p}\right|^2\frac{(x'^2+y'^2)}{4}(\overline{\Gamma}t)^2\right\},$$
$$\frac{N(\overline{D}^0 \to \bar{f})}{dt} \propto e^{-\overline{\Gamma}t}\left\{\overline{R}_D + \left|\frac{p}{q}\right|\sqrt{\overline{R}_D}(y'\cos\phi + x'\sin\phi)(\overline{\Gamma}t) + \left|\frac{p}{q}\right|^2\frac{(x'^2+y'^2)}{4}(\overline{\Gamma}t)^2\right\}, \quad (452)$$

where $x' = x\cos\delta + y\sin\delta$, $y' = y\cos\delta - x\sin\delta$, and δ is the strong phase difference between the $D^0 \to K^-\pi^+$ and $\bar{D}^0 \to K^-\pi^+$ amplitudes. The parameter R_D is the squared ratio of the magnitudes of $D^0 \to K^+\pi^-$ to $D^0 \to K^-\pi^+$ amplitudes, and $\overline{R}_D$ is the squared ratio of the magnitudes of $\bar{D}^0 \to K^-\pi^+$ to $\bar{D}^0 \to K^+\pi^-$ amplitudes. We subsequently smear these decay times using a Gaussian resolution function with a mean of zero and a width set equal to the expected decay time resolution of Belle II: 135 fs. Finally, we fit these distributions with the PDFs of Eq. (452) convolved with the Gaussian resolution function. This convolution is done analytically, resulting in a PDF consisting of error functions [$\mathrm{erf}(x)$]:

$$\begin{aligned}\frac{N(D^0 \to f)}{dt} \propto\ & R_D\,\sigma\sqrt{\frac{\pi}{2}}\,e^{\sigma^2/(2\tau^2)}\,[1+\mathrm{erf}(x)]\,e^{-t/\tau} \\ & + \left|\frac{q}{p}\right|\sqrt{R_D}\,(y'\cos\phi - x'\sin\phi)\sigma^2 e^{-t^2/(2\sigma^2)} \\ & + \frac{\sigma}{\tau}\sqrt{\frac{\pi}{2}}\,e^{\sigma^2/(2\tau^2)}(t\tau-\sigma^2)\,[1+\mathrm{erf}(x)]\,e^{-t/\tau} \\ & + \left|\frac{q}{p}\right|^2\frac{(x'^2+y'^2)}{4}\left(\sigma^2 t - \frac{\sigma^4}{\tau}\right)e^{-t^2/(2\sigma^2)} \\ & + \frac{\sigma}{\tau^2}\sqrt{\frac{\pi}{2}}\,e^{\sigma^2/(2\tau^2)}(\tau t-\sigma^2)\left[\sigma^4 - 2\sigma^2\tau t + \tau^2(t^2+\sigma^2)\right][1+\mathrm{erf}(x)]\,e^{-t/\tau},\end{aligned}$$

where $\sigma = 135\,\mathrm{fs}$, $\tau = \tau_D = 410\,\mathrm{fs}$, and $x = t/(\sigma\sqrt{2}) - \sigma/(\tau\sqrt{2})$. The corresponding smeared PDF for $\overline{D}^0$ decays is the same as that above but with the substitutions $R_D \to \overline{R}_D$, $\phi \to -\phi$, and $|q/p| \to |p/q|$.

Two distinct generation + fitting procedures are performed: assuming CP conservation and allowing for CP violation. For the first procedure we set $R_D = \overline{R}_D$, $|q/p| = 1$, and $\phi = 0$. In this case the PDFs for D^0 and $\overline{D}^0$ decays are identical [see Eqs. (452)], and the fitted parameters are R_D, x'^2, and

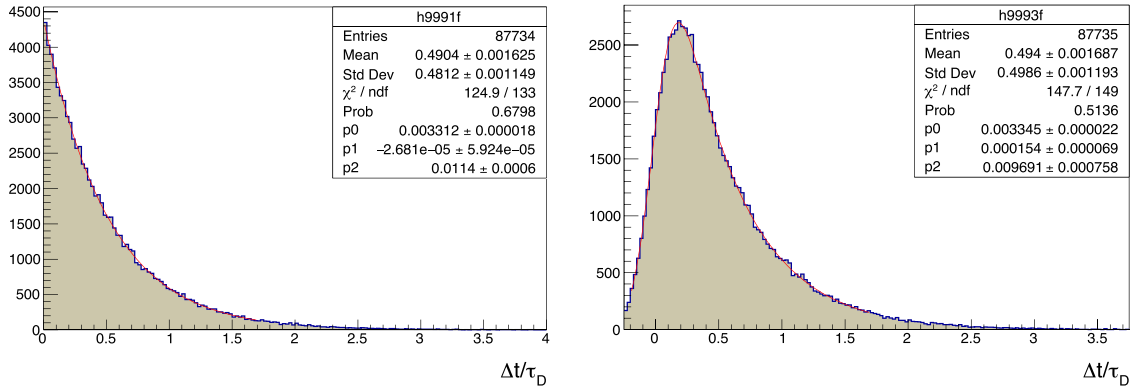

Fig. 153. Unsmeared (left) and smeared (right) decay time distributions for $D^{*+} \to D^0\pi^+$, $D^0 \to K^+\pi^-$ decays, and projections of the fit result, for 20 ab^{-1} of Belle II data. The fit shown is for no CP violation; the fitted parameters are $p_0 = R_D$, $p_1 = x'^2$, and $p_2 = y'$. The generated values are $R_D = 0.335\%$, $x'^2 = (0.01)^2$, and $y' = 0.01$.

Table 117. Uncertainties on mixing parameters x, y and CP-violating parameters $|q/p|$, ϕ resulting from fitting Belle II samples of flavor-tagged $D^0 \to K^+\pi^-$ and $\overline{D}{}^0 \to K^-\pi^+$ decays. The first two rows correspond to no CP violation; the last four rows correspond to allowing for CP violation.

Parameter	5 ab^{-1}	20 ab^{-1}	50 ab^{-1}
$\delta x'^2$ (10^{-5})	6.2	3.2	2.0
$\delta y'$ (%)	0.093	0.047	0.029
$\delta x'$ (%)	0.32	0.22	0.13
$\delta y'$ (%)	0.23	0.15	0.097
$\delta\lvert q/p\rvert$	0.174	0.073	0.043
$\delta\phi$ (°)	13.2	8.4	5.4

y'. For the second fit we float all six parameters: R_D, $\overline{R}_D$, x', y', $|q/p|$, and ϕ. Typical unsmeared and smeared decay time distributions are shown in Fig. 153, along with the fit result, for a typical fit assuming CP conservation. For this fit the generated values were $R_D = 0.335\%$, $x'^2 = (0.01)^2$, and $y' = 0.01$. For fits allowing for CP violation, the samples were generated with $|q/p| = 0.90$ and $\phi = \pi/4$.

The generation + fitting procedure is repeated for an ensemble of 1000 experiments, and the differences between the fit results and the true (generated) values are plotted in Fig. 154. The RMS of these distributions of residuals are taken as the uncertainties on these parameters and are listed in Table 117. We note that the residuals for x' and ϕ for the CP-allowed fits exhibit a bifurcated structure. This is due to non-linearities in the PDF, which cause the fitter to occasionally converge to a local (rather than global) minimum. This problem can be alleviated by fitting for a better-behaved set of parameters, for example $\alpha \equiv x' \sin\phi$, $\beta \equiv y' \cos\phi$, and $\gamma \equiv \tan\phi$. However, we do not study such transformations here.

We also plot the MINOS errors for these parameters as returned by the fits; see Fig. 155. The mean values of these errors should nominally match the RMS of the residuals distributions of Fig. 154. This is confirmed for the case of no CP violation, but for the CP-allowed case the situation is more complicated: the mean of the MINOS errors for $|q/p|$ matches the RMS of the residuals distribution, but the mean for x' is somewhat larger, and those for y' and ϕ are about twice as large.

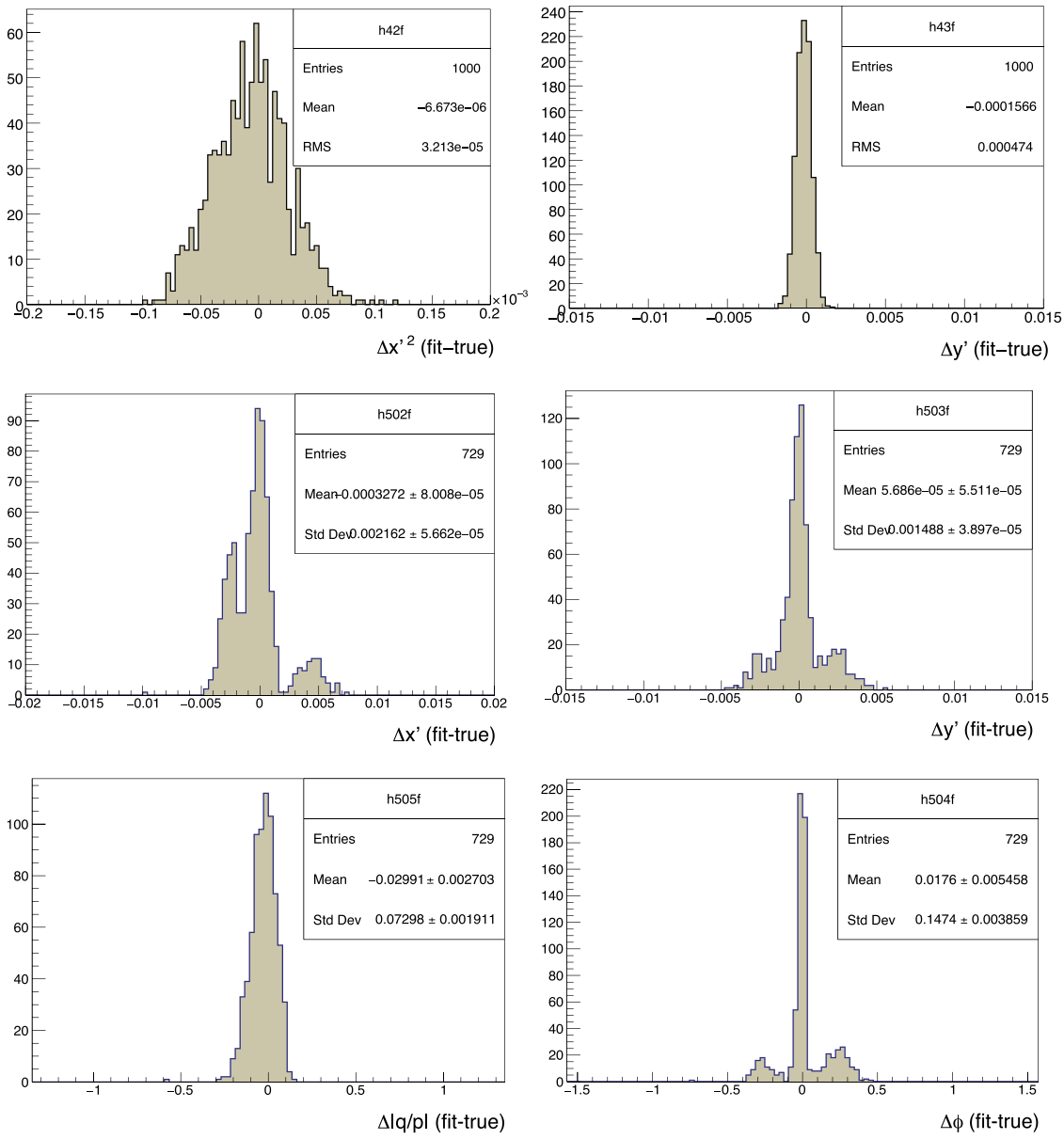

Fig. 154. Residual distributions obtained by simultaneously fitting the decay time distributions of $D^0 \to K^+\pi^-$ and $\overline{D}{}^0 \to K^-\pi^+$ decays for an ensemble of 1000 experiments (see text). Each experiment corresponds to $20\,\text{ab}^{-1}$ of data. The top row corresponds to no CP violation; the middle and bottom rows correspond to allowing for CP violation. The units for $\Delta\phi$ are radians.

This study does not yet include backgrounds, which are expected to be modest. A preliminary look at the effect of backgrounds indicates that the fitted errors on the mixing and CP violation parameters increase by ∼20%. We have also neglected systematic uncertainties, which are expected to be small (for the Belle analysis including CP violation, the systematic uncertainties increased the errors on the fitted parameters by 12% [989]).

Wrong-sign decays $D^0 \to K^+\pi^-\pi^0$

Authors: L. Li, A. Schwartz

The "wrong-sign" (WS) decay $D^0 \to K^+\pi^-\pi^0$ proceeds via the same weak amplitudes as the WS decay $D^0 \to K^+\pi^-$: directly via a doubly Cabibbo-suppressed decay, and indirectly via mixing

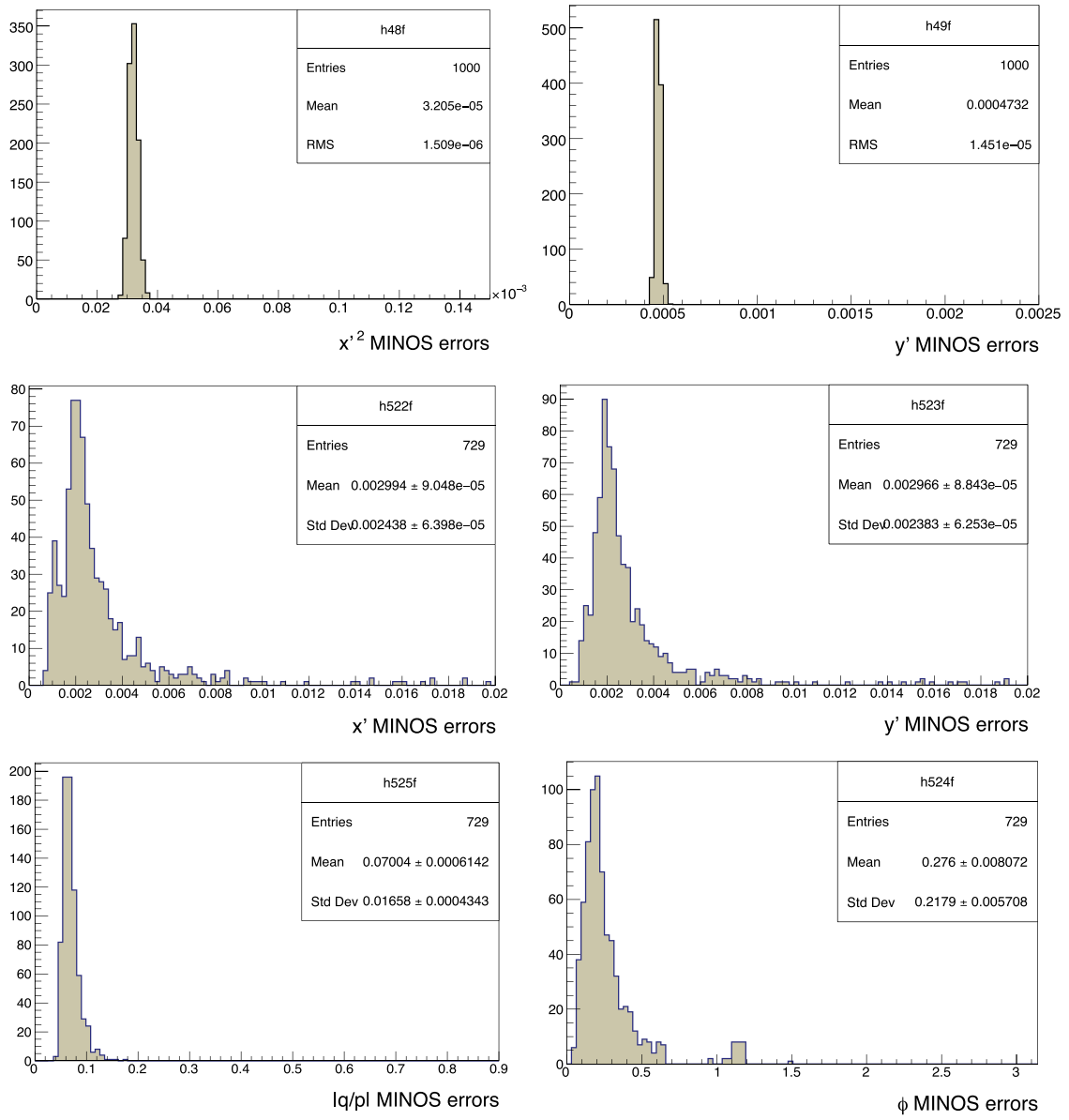

Fig. 155. MINOS errors obtained by simultaneously fitting the decay time distributions of $D^0 \to K^+\pi^-$ and $\overline{D}{}^0 \to K^-\pi^+$ decays for an ensemble of 1000 experiments (see text). Each experiment corresponds to 20 ab^{-1} of data. The top row corresponds to no CP violation; the middle and bottom rows correspond to allowing for CP violation. The units for ϕ are radians.

followed by a Cabbibo-favored decay. The latter amplitude provides sensitivity to mixing and indirect CP violation. However, fitting for mixing parameters requires understanding the decay amplitude, which typically contains numerous intermediate resonances. The different magnitudes and phases of the intermediate states necessitates performing a time-dependent Dalitz plot analysis to measure mixing.

Both Belle and BaBar have studied $D^0 \to K^+\pi^-\pi^0$ decays. Belle has measured the ratio of rates for WS decays to "right-sign" $D^0 \to K^-\pi^+\pi^0$ decays: $R_{\text{WS}} = (0.229 \pm 0.015)\%$ [990]. BaBar has performed a time-dependent fit to the $(m^2_{K^+\pi^-}, m^2_{\pi^-\pi^0})$ Dalitz plot to measure the effective mixing parameters $x'' = x \cdot \cos\delta_{K\pi\pi^0} + y \cdot \sin\delta_{K\pi\pi^0}$ and $y'' = y \cdot \cos\delta_{K\pi\pi^0} - x \cdot \sin\delta_{K\pi\pi^0}$, where $\delta_{K\pi\pi^0}$ is

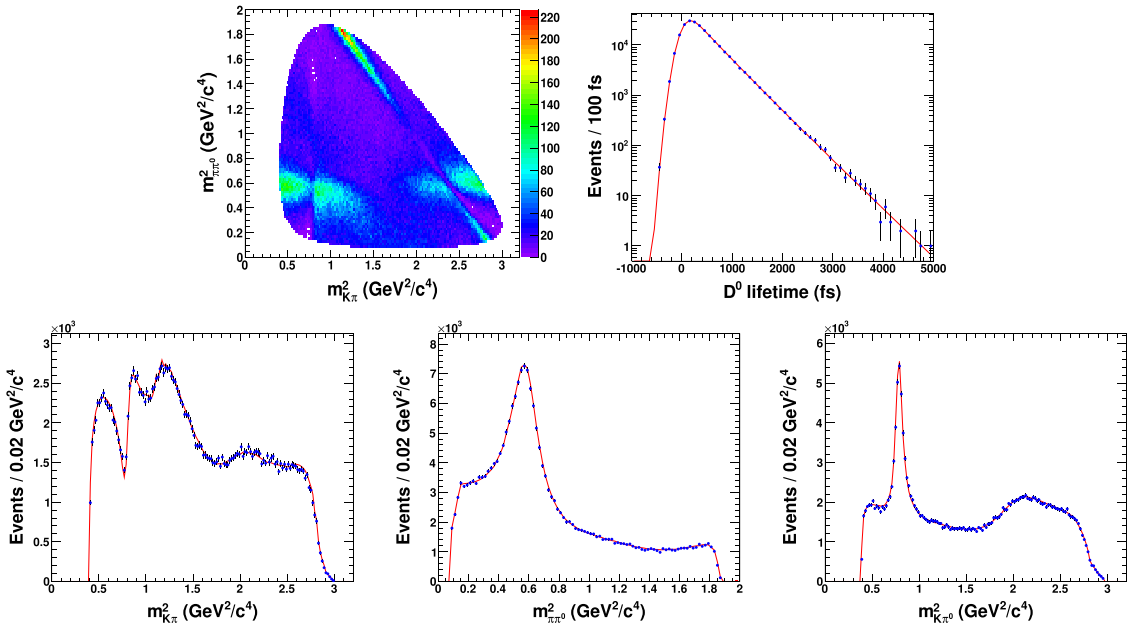

Fig. 156. Time-dependent fit to the Dalitz plot of WS $D^0 \to K^+\pi^-\pi^0$ decays. The decay times are smeared by the expected Belle II decay time resolution of 140 fs. The second row shows projections of the fitted Dalitz variables $m^2_{K^+\pi^-}$ (left), $m^2_{\pi^-\pi^0}$ (middle), and $m^2_{K^+\pi^0}$ (right).

the strong phase difference between the amplitudes for $D^0 \to K^+\rho^-$ and $\overline{D}{}^0 \to K^+\rho^-$. The results are $x'' = (2.61^{+0.57}_{-0.68} \pm 0.39)\%$ and $y'' = (-0.06^{+0.55}_{-0.64} \pm 0.34)\%$ [991].

Assuming Belle II has the same $D^0 \to K^+\pi^-\pi^0$ reconstruction efficiency as BaBar, we estimate the Belle II signal yield by scaling the BaBar yield by the ratio of luminosities. The result is 225 000 flavor-tagged signal decays in 50 ab^{-1} of data. We estimate the Belle II sensitivity to x'' and y'' by performing an MC simulation study, generating 10 independent data sets of 225 000 WS events each. We also generate corresponding samples of RS events, which are needed to determine the ratio of the magnitudes of the WS and RS decay amplitudes. To generate WS decays, we use a seven-resonance decay model as measured by BaBar [991], whereas to generate RS decays we use an 11-resonance decay model as measured by Belle [992].[41]

For both samples the decay times are smeared by an assumed resolution of $\sigma = 140$ fs. The mixing parameters used for the event generation are $x'' = 2.58\%$, $y'' = 0.39\%$, and $\delta_{K\pi\pi^0} = 10°$. After generation, we fit the samples for parameters x'' and y'' as well as for the magnitudes and phases of the intermediate states. A typical time-dependent fit to the Dalitz plot is shown in Fig. 156.

The resulting fit residuals for the 10 experiments are plotted in Fig. 157, and the RMS of these distributions is taken as the expected precision of Belle II for these parameters. This precision is:

$$\sigma_{x''} = 0.057\% \quad \text{(stat. error only, } 50\,\text{ab}^{-1}\text{)},$$
$$\sigma_{y''} = 0.049\% \quad \text{(stat. error only, } 50\,\text{ab}^{-1}\text{)}. \tag{453}$$

[41] For this decay there are 13 possible resonances. However, the $\rho(1450)$ and $\rho(1700)$ have masses whose peaks are outside the Dalitz plot boundary but whose widths are sufficiently wide that their tails extend into the region of interest. As their phases differ by close to 180°, it is difficult for the fitter to distinguish them, and therefore we keep only the $\rho(1700)$. We also remove the $K^*(1680)^0$, whose fitted fraction is negligibly small (<0.1%).

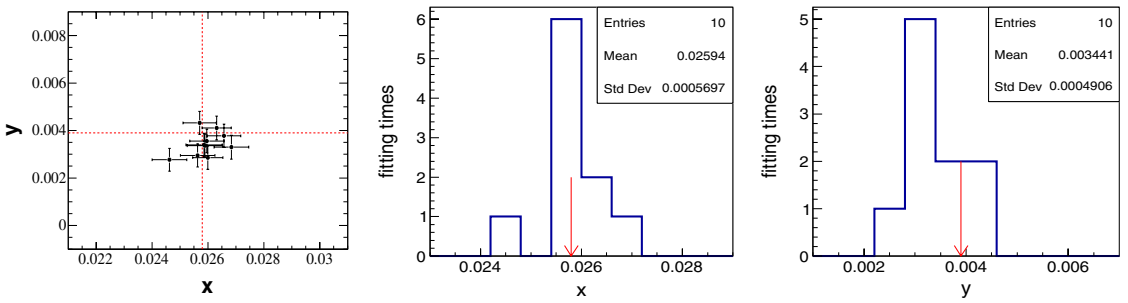

Fig. 157. Residuals resulting from fitting the time-dependent Dalitz plot of WS $D^0 \to K^+\pi^-\pi^0$ decays for 10 experiments corresponding to 50 ab^{-1} of data (see text). The red lines and arrows show the input (true) values of x'' and y''.

These uncertainties are an order of magnitude smaller than the errors obtained by BaBar. These errors do not include systematic uncertainties, which are expected to be small and are discussed below. In addition, these errors do not include the effect of backgrounds. From a study with Belle data, we find that the presence of backgrounds increases the fitted errors on x'' and y'' by approximately 40%. Applying this scaling to the values of Eq. (453) gives errors of $\sigma_{x''} = 0.080\%$ and $\sigma_{y''} = 0.070\%$. These estimates are probably conservative, as backgrounds should be smaller at Belle II than at Belle due to improved vertex resolution, improved mass resolution, and improved particle identification.

The systematic errors in this measurement can be classified as "reducible," i.e. those that decrease with increasing data sample size, and "irreducible," i.e. those that do not. The reducible systematic errors in the BaBar analysis [991] were dominated by uncertainty in the RS decay model (0.22 times the statistical uncertainty), uncertainty in the WS decay model (0.22 times the statistical uncertainty), and uncertainties due to the decay time resolution (0.10 times the statistical uncertainty). The irreducible systematic errors were dominated by the choice of fitted decay time range (0.3–0.5 times the statistical uncertainty). This last uncertainty should be notably smaller at Belle II, as the decay time resolution is only half that at BaBar.

In summary, Belle II can measure the mixing parameters x'' and y'' by fitting the time-dependent Dalitz plot of $D^0 \to K^+\pi^-\pi^0$ decays, and the resulting uncertainties should be almost an order of magnitude smaller than those obtained previously by BaBar. As the strong phase $\delta_{K\pi\pi^0}$ can be independently measured by BESIII using double-tagged events recorded at the $\psi(3770)$ resonance, this measurement can provide strong constraints on the underlying mixing parameters x and y.

Self-conjugate decays $D^0 \to K^0_S\pi^+\pi^-$

Authors: L. Li, A. Schwartz

The self-conjugate decays $D^0 \to K^0_S\pi^+\pi^-$ and $D^0 \to \pi^0\pi^+\pi^-$ proceed via the Cabibbo-favored (K^0_S daughter) and singly-Cabibbo-suppressed (π^0 daughter) interfering amplitudes shown in Fig. 158. This interference gives sensitivity to D^0–$\overline{D}^0$ mixing. By separately fitting samples of D^*-flavor-tagged D^0 and $\overline{D}^0$ decays, one can also measure indirect CP-violating parameters $|q/p|$ and ϕ.

Denoting the two interfering amplitudes as A_1 and A_2, the overall decay amplitudes squared have the form

$$|\mathcal{M}_f|^2 = \left\{|A_1|^2 e^{-y\Gamma t} + |A_2|^2 e^{y\Gamma t} + 2\Re[A_1 A_2^*]\cos(x\Gamma t) + 2\Im[A_1 A_2^*]\sin(x\Gamma t)\right\} e^{-\Gamma t},$$
$$|\bar{\mathcal{M}}_f|^2 = \left\{|\bar{A}_1|^2 e^{-y\Gamma t} + |\bar{A}_2|^2 e^{y\Gamma t} + 2\Re[\bar{A}_1 \bar{A}_2^*]\cos(x\Gamma t) + 2\Im[\bar{A}_1 \bar{A}_2^*]\sin(x\Gamma t)\right\} e^{-\Gamma t}.$$

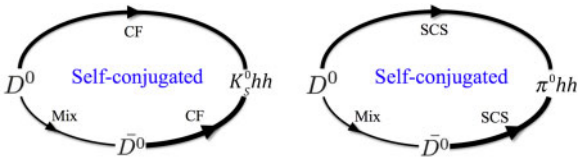

Fig. 158. Interfering amplitudes for $D^0 \to K^0_S\pi^+\pi^-$ (left) and $D^0 \to \pi^0\pi^+\pi^-$ (right).

Table 118. Measurements of mixing and CP violation in self-conjugate three-body decays. The errors listed are statistical, systematic, and systematic due to the decay amplitude model.

No CP violation	$D^0 \to K^0_S\pi^+\pi^-$ (Belle 921 fb^{-1})	$x = \left(+0.56 \pm 0.19\,^{+0.03\,+0.06}_{-0.09\,-0.09}\right)\%$ $y = \left(+0.30 \pm 0.15\,^{+0.04\,+0.03}_{-0.05\,-0.06}\right)\%$
	$D^0 \to K^0_S\pi^+\pi^-$, $K^0_S K^+K^-$ (BaBar 469 fb^{-1})	$x = (+0.16 \pm 0.23 \pm 0.12 \pm 0.08)\%$ $y = (+0.57 \pm 0.20 \pm 0.13 \pm 0.07)\%$
	$D^0 \to K^0_S\pi^+\pi^-$ (LHCb 1.0 fb^{-1})	$x = (-0.86 \pm 0.53 \pm 0.17)\%$ $y = (+0.03 \pm 0.46 \pm 0.13)\%$
	$D^0 \to \pi^0\pi^+\pi^-$ (BaBar 468 fb^{-1})	$x = (+1.5 \pm 1.2 \pm 0.6)\%$ $y = (+0.2 \pm 0.9 \pm 0.5)\%$
Indirect CP violation	$D^0 \to K^0_S\pi^+\pi^-$ (Belle 921 fb^{-1})	$x = \left(+0.56 \pm 0.19\,^{+0.04\,+0.06}_{-0.08\,-0.08}\right)\%$ $y = \left(+0.30 \pm 0.15\,^{+0.04\,+0.03}_{-0.05\,-0.07}\right)\%$ $\lvert q/p\rvert = 0.90\,^{+0.16\,+0.05\,+0.06}_{-0.15\,-0.04\,-0.05}$ $\arg(q/p) = \left(-6 \pm 11 \pm 3\,^{+3}_{-4}\right)^\circ$

These expressions show that self-conjugate decays provide sensitivity directly to x and y, i.e. without being "rotated" by a strong phase difference between D^0 and $\overline{D}{}^0$ decays. The current status of mixing and CP violation measurements in self-conjugate three-body decays is summarized in Table 118.

We estimate the sensitivity of Belle II to mixing parameters x, y, and CP-violating parameters $|q/p|$, ϕ from $D^0 \to K^0_S\pi^+\pi^-$ decays by scaling from a recent Belle measurement. The Belle analysis reconstructed 1.23×10^6 D^*-flavor-tagged decays in 0.921 ab^{-1} of data. Assuming Belle II has the same reconstruction efficiency, we estimate the Belle II signal yield by scaling by the ratio of luminosities. The result is 67×10^6 signal decays in 50 ab^{-1} of data. The Belle errors on x and y were $\sigma_x = 0.19\%$ and $\sigma_y = 0.15\%$. We divide these errors into three parts: statistical uncertainty, reducible systematic uncertainty, and irreducible systematic uncertainty. We scale the first two uncertainties by the ratio of luminosities between Belle and Belle II, and then add the result in quadrature to the irreducible systematic uncertainty. The resulting errors are listed in Table 119. These estimates are conservative, as they do not account for the improved decay-time resolution of Belle II over Belle.

With the high statistics of Belle II, the systematic uncertainty due to the D^0 decay model is expected to become the dominant uncertainty. This can be avoided by using strong phase differences measured experimentally, i.e. by BESIII using double-tagged events recorded on the $\psi(3770)$ resonance. Using this method, the authors of Ref. [993] estimated the resulting precision for x, y. The resulting statistical errors for a sample of 100×10^6 reconstructed $D^0 \to K^0_S\pi^+\pi^-$ decays are $\sigma_x = 0.017\%$ and $\sigma_y = 0.019\%$. The systematic errors are estimated by propagating the errors on the binned strong phases as measured by CLEOc [770]; the results are $\sigma_x(\text{syst}) = 0.076\%$ and $\sigma_y(\text{syst}) = 0.087\%$. These systematic errors, while larger than the statistical errors, constitute upper bounds, as more precise measurements of the binned strong phases are expected from BESIII.

Table 119. Expected precision for mixing parameters x, y and CP-violating parameters $|q/p|$, ϕ from $D^0 \to K^0_S\pi^+\pi^-$ decays.

Data	Stat.	Syst.		Total	Stat.	Syst.		Total
		Red.	Irred.			Red.	Irred.	
	σ_x (10^{-2})				σ_y (10^{-2})			
976 fb^{-1}	0.19	0.06	0.11	0.20	0.15	0.06	0.04	0.16
5 ab^{-1}	0.08	0.03	0.11	0.14	0.06	0.03	0.04	0.08
50 ab^{-1}	0.03	0.01	0.11	0.11	0.02	0.01	0.04	0.05
	$\lvert q/p\rvert$ (10^{-2})				ϕ (°)			
976 fb^{-1}	15.5	5.2–5.6	7.0–6.7	17.8	10.7	4.4–4.5	3.8–3.7	12.2
5 ab^{-1}	6.9	2.3–2.5	7.0–6.7	9.9–10.1	4.7	1.9–2.0	3.8–3.7	6.3–6.4
50 ab^{-1}	2.2	0.7–0.8	7.0–6.7	7.0–7.4	1.5	0.6	3.8–3.7	4.0–4.2

Table 120. Most precise measurements of A_{CP} in singly Cabibbo-suppressed $D \to PP'$ decays. For older measurements and world averages, see Ref. [230].

Mode	A_{CP} [%]	Ref.
$D^0 \to K^+K^-$	$0.04 \pm 0.12 \pm 0.10$	[1022]
$D^0 \to \pi^+\pi^-$	$0.07 \pm 0.14 \pm 0.11$	[1022]
$D^0 \to K^0_S K^0_S$	$-0.02 \pm 1.53 \pm 0.17$	[1023]
$D^0 \to \pi^0\pi^0$	$-0.03 \pm 0.64 \pm 0.10$	[1024]
$D^+ \to K^0_S K^+$	$0.03 \pm 0.17 \pm 0.14$	[1025]
$D^+_s \to K^0_S \pi^+$	$-0.36 \pm 0.09 \pm 0.07$	[1026]

Singly Cabibbo-suppressed decays $D^0 \to K^0_S K^\pm \pi^\mp$

Authors: L. Li, A. Schwartz

Whereas the CF and DCS amplitudes producing a $K^+\pi^-$ final state give rise to branching fractions that differ by a factor of ∼300, for singly Cabibbo-suppressed (SCS) final states there is approximate equality between the two branching fractions, i.e. $B(D^0 \to K^0_S K^-\pi^+) = (0.35 \pm 0.05)\%$ and $B(D^0 \to K^0_S K^+\pi^-) = (0.26 \pm 0.05)\%$. This similarity implies that the decay amplitudes have similar magnitudes, which in turn gives greater interference between the amplitudes and thus greater sensitivity to mixing and indirect CP violation.

Experimentally, SCS $D^0 \to K^0_S K^\pm \pi^\mp$ decays should have greater purity than DCS $D^0 \to K^+\pi^-$ decays due to the larger branching fraction. These SCS decays have been studied by both CLEO [994] and LHCb [995]. An MC study [996] indicates that the precision obtainable for y should be similar to that obtained for y' using $D^0 \to K^+\pi^-$ decays.

13.6. CP asymmetries of $D \to PP'$ decays

13.6.1. Theory

Authors: M. Jung, U. Nierste, S. Schacht

CP asymmetries in non-leptonic D decays have long been considered a quasi-null test of the SM, since they vanish for Cabibbo-allowed and doubly suppressed modes, and are very small for singly suppressed decays;[42] the latter is mainly due to the fact that they are strongly CKM-suppressed by

[42] We do not consider CP violation in the kaon system, which affects decays that produce K^0 or $\overline{K}^0$.

the factor $\mathrm{Im}[(V_{cb}^* V_{ub})/(V_{cs}^* V_{us})] \sim 10^{-3}$. However, recent experimental progress—see Table 120—changed this situation: several measurements achieved sensitivity down to the SM level, such that a potential significant measurement cannot easily be considered NP anymore, apart from exceptional channels like $D^+ \to \pi^+\pi^0$ [997,998]. The main challenge at this level is therefore the distinction between NP and the SM, taking into account finite contributions from the SM; this has been a main focus in recent theory analyses, see, e.g., Refs. [967,973,999–1021].

Determining the SM contributions precisely turns out to be extremely difficult. The reason is that there is so far no reliable method to determine the corresponding hadronic matrix elements (MEs), related to the fact that the charm quark is neither very heavy nor light compared to a typical QCD scale $\Lambda_{\mathrm{QCD}} \sim 300$–$500\,\mathrm{MeV}$. This is in contrast to the situation in B or K decays. So far there are also no lattice calculations available for the relevant three-body MEs; see, however, Ref. [189] for recent progress in that direction. Direct calculation can be avoided when employing symmetry methods, specifically the $\mathrm{SU}(3)_F$ and isospin flavor symmetries. Instead of calculating the MEs in question, symmetries *relate* them and thereby allow one to determine them from data. The main concern in such analyses becomes symmetry-breaking contributions. These can be systematically included but yield additional degrees of freedom, complicating the determination of the MEs, as will be discussed below. Nevertheless, they allow for the identification of NP contributions in the presence of a sizeable SM background, in the form of sum rules and patterns that hold in the SM but can be violated by NP. This type of analysis relies on experimental input not only of (many) CP asymmetries, but also of branching fractions, and the results improve with more precise inputs.

In order to discuss the future key impact of Belle II in this context, we provide an overview of two theoretical frameworks for $D \to PP'$ decays, which are both based on the approximate $\mathrm{SU}(3)_F$ symmetry of QCD. After that we give our predictions for key measurements at Belle II.

Theoretical framework The $\mathrm{SU}(3)_F$ symmetry approach can be implemented in two different ways, whose close connection has been realized from the start [777,1027,1028]. In the "plain group theory" approach (see recent Refs. [1001,1011,1016–1018]), one uses directly the Wigner–Eckart theorem in order to obtain a decomposition of the amplitudes in terms of reduced $\mathrm{SU}(3)_F$ matrix elements and Clebsch–Gordan coefficients [1029–1031]. In the "dynamical" approach (see recent Refs. [1002,1003,1019–1021]), one uses a decomposition of the decay amplitudes in terms of topological diagrams. These diagrams, which are defined by their flavor flow, are meant to include all-order QCD effects. In both approaches one can include $\mathrm{SU}(3)_F$-breaking effects in a systematic way. These come into play through the different masses of the light quarks. The mass terms can be written as

$$m_u \bar{u}u + m_d \bar{d}d + m_s \bar{s}s = \mathcal{H}_1 + \mathcal{H}_8^{I} + \mathcal{H}_8^{\Delta I=0}. \tag{454}$$

In the limit $m_u = m_d = m_s$, the $\mathrm{SU}(3)_F$ limit is restored; i.e. only the $\mathrm{SU}(3)_F$ singlet operator $\mathcal{H}_1$ survives, which does not break $\mathrm{SU}(3)_F$. The second operator, $\mathcal{H}_8^{I} \sim m_u - m_d$, breaks isospin and can be neglected to very good approximation, leaving $\mathcal{H}_8^{\Delta I=0} \sim m_s$ to determine the major part of $\mathrm{SU}(3)_F$-breaking. In order to apply the Wigner–Eckart theorem, initial and final states as well as the relevant Hamiltonian are classified according to their $\mathrm{SU}(3)_F$ representations. The initial states (D^0, D^+, D_s^+) transform as a $\bar{\mathbf{3}}$. The two-body final states of kaons and pions are symmetrized due to a Bose symmetry and transform as

$$(\mathbf{8} \otimes \mathbf{8})_S = \mathbf{1} \oplus \mathbf{8} \oplus \mathbf{27}. \tag{455}$$

The SM operators have the flavor structure $\bar{u}c\bar{q}q'$ with $q,q' = d,s$, and correspond to the SU(3)$_F$ representations

$$\mathbf{3} \otimes \bar{\mathbf{3}} \otimes \mathbf{3} = \mathbf{3}_1 \oplus \mathbf{3}_2 \oplus \bar{\mathbf{6}} \oplus \mathbf{15}. \tag{456}$$

Note that this decomposition is only sensitive to the flavor structure of a given effective operator and not to its Dirac structure. The first-order SU(3)$_F$-breaking representations can be obtained from the tensor products of the SU(3)$_F$ limit representations with the perturbation operator $\mathcal{H}_8^{\Delta I=0}$. The CKM-leading part of the amplitude of a decay d can then be written as [1017]

$$\mathcal{A}^{\mathrm{C}}(d) = \lambda_{\mathrm{C}}\left(\sum_{i,k} c_{d;ik} A_i^k + \sum_{i,j} c_{d;ij} B_i^j\right), \tag{457}$$

with C=SCS, CF, DCS, and $\lambda_{\mathrm{CF}} \equiv V_{cs}^* V_{ud}$, $\lambda_{\mathrm{DCS}} \equiv V_{cd}^* V_{us}$, and

$$\lambda_{\mathrm{SCS}} \equiv \frac{V_{cs}^* V_{us} - V_{cd}^* V_{ud}}{2}. \tag{458}$$

The A_i^k and B_i^j denote the reduced SU(3)$_F$-limit and -breaking matrix elements for the final state representation i and the operator representation k,j, respectively. The Clebsch–Gordan coefficients $c_{d,ik}$ can be found in Ref. [1017]. To give an example, the CKM-leading SU(3)$_F$-limit decay amplitude of the decay channel $D_s^+ \to K^+\pi^0$ can be written as [1017]

$$\mathcal{A}^{\mathrm{SCS}}(D_s^+ \to K^+\pi^0)/\lambda_{\mathrm{SCS}} = -\frac{1}{5}A_{27}^{15} + \frac{1}{5}A_8^{15} + \frac{1}{\sqrt{10}}A_8^{\bar{6}}. \tag{459}$$

Note that, due to linear dependences of the parameterization, the number of matrix elements can be reduced by redefinitions; see Ref. [1017] for details. The same holds for the parameterization in terms of topological diagrams [1019]. $\mathcal{A}_X(d)$ is the part of the amplitudes that is obtained when setting all A_i^k in Eq. (457) to zero. In order to measure the maximal SU(3)$_F$ breaking present in the system of all 17 $D \to P_8 P_8'$ decays, we define

$$\delta_X \equiv \frac{\max_{ij}|B_i^j|}{\max\left(|A_{27}^{15}|, |A_8^{\bar{6}}|, |A_8^{15}|\right)}, \tag{460}$$

$$\delta_X' \equiv \max_d \left|\frac{\mathcal{A}_X(d)}{\mathcal{A}(d)}\right|, \tag{461}$$

which are complementary measures regarding interference effects between different SU(3)$_F$-breaking MEs. By performing a global fit to the available data, one can test whether the fit worsens significantly for given values of the measures for maximal SU(3)$_F$ breaking, $\delta_X^{(\prime)}$, compared to the null hypothesis, which does not constrain the amount of SU(3)$_F$ breaking. The result is shown in Fig. 159. One finds that the data can be described by SU(3)$_F$ breaking of $\sim$30%, i.e. the perturbative expansion is consistent with the data. This of course does not exclude larger values for SU(3)$_F$ breaking.

In the language of topological diagrams, the CKM-leading amplitude of the example decay channel $D_s^+ \to K^+\pi^0$ [see Eq. (459)] has the decomposition

$$\frac{\mathcal{A}(D_s^+ \to K^+\pi^0)}{\lambda_{\mathrm{SCS}}} = -\frac{1}{\sqrt{2}}\left(A + A_1^{(1)} + A_2^{(1)}\right) - \frac{1}{\sqrt{2}}\left(C + C_3^{(1)}\right) - \frac{1}{\sqrt{2}}P_{\mathrm{break}}, \tag{462}$$

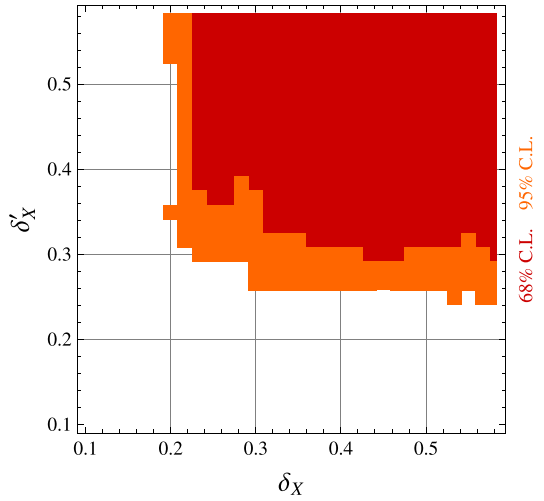

Fig. 159. Allowed regions for δ_X and δ'_X at 68% CL (red) and 95% CL (orange) with respect to the global minimum of a fit where the amount of $SU(3)_F$ breaking is unrestricted. Figure taken from Ref. [1017].

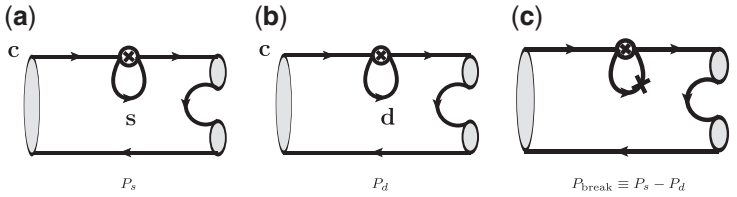

Fig. 160. The relevant penguin diagrams. Figures taken from Ref. [1019].

which includes $SU(3)_F$-breaking topologies denoted by the superscript $^{(1)}$ and also the $SU(3)_F$-breaking difference of penguin diagrams [973]

$$P_{\text{break}} \equiv P_s - P_d, \tag{463}$$

as shown in Fig. 160. The $SU(3)_F$-limit topological diagrams are shown in Fig. 161. As a Feynman rule for the perturbation $H_{\cancel{SU(3)_F}} = (m_s - m_d)\bar{s}s$, we write a cross on the corresponding quark line [1032]. Also, in the topological approach, one can define measures of $SU(3)_F$ breaking analogous to Eqs. (460) and (461); see Ref. [1019] for details.

The reduced matrix elements of the "plain group theory" approach and the topological diagrams of the "dynamical" approach can be mapped onto each other. For the explicit mapping including linear $SU(3)_F$ breaking, see Appendix B and Table XVII in Ref. [1019]. In both cases the dependence on the parameters has the same algebraic properties. The rank of the parameterization is identical, and so are the sum rules between the amplitudes [1011]. Consequently, as long as no dynamical input is assumed for the topological amplitudes, the two frameworks are equivalent to each other. Note, however, that assuming a certain amount of $SU(3)_F$ breaking in the form of ratios of $SU(3)_F$ matrix elements, and in the form of ratios of topological amplitudes, is in general not equivalent [1019]. This is a consequence of the fact that reduced matrix elements are a linear combination of several topological amplitudes, and vice versa.

For further dynamical input, one can utilize the $1/N_C$ expansion [1033,1034]. This is used in Refs. [1019,1020] for calculating tree and annihilation diagrams, and to estimate upper limits for exchange and color-suppressed diagrams.

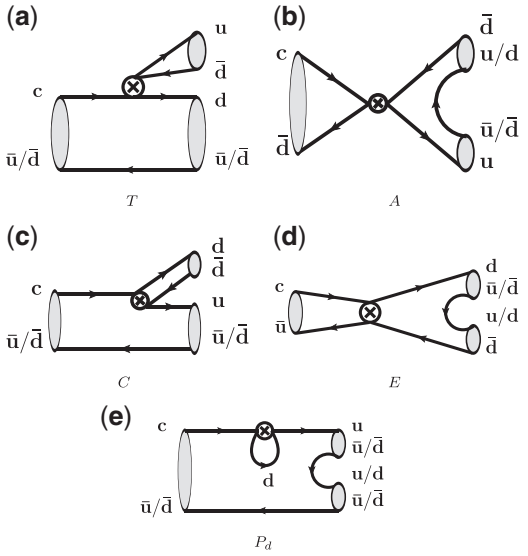

Fig. 161. SU(3)$_F$-limit topological amplitudes. Figures taken from Ref. [1019].

Table 121. Key measurements that Belle II can improve.

Observable	Current measurement	Phenomenological impact
$A_{CP}(D^0 \to \pi^0\pi^0)$	-0.0003 ± 0.0064 [230,1024,1036]	SM test with A_{CP} sum rule I
$A_{CP}(D_s^+ \to K^+\pi^0)$	$-0.266 \pm 0.238 \pm 0.009$ [1037]	SM test with A_{CP} sum rule II
$A_{CP}(D^+ \to \pi^+\pi^0)$	$0.023 \pm 0.012 \pm 0.002$ [1038]	SM null test
$A_{CP}(D^0 \to K_S^0 K_S^0)$	$-0.004 \pm 0.015^\dagger$ [1023,1036,1039]	Possible near-future observation channel of CP violation
$R(D_s^+)$	$0.02 \pm 0.35^*$	Distinguishing different theoretical treatments

†Our average, statistical, and systematic error added in quadrature.
*Our estimate from experimental data in Refs. [77,934,1035]; see text before Eq. (473).

Sum rules between amplitudes as given in Refs. [1011,1017] have the disadvantage that in most cases the corresponding relative strong phases are unknown. However, there are also sum rules between decay rates [1011] and between CP asymmetries [688,1020]. These are further discussed in the next section.

Predictions for key measurements at Belle II In this section we discuss several key measurements that Belle II can perform in the field of non-leptonic charm decays. The following discussion is summarized in Table 121.

The difficulty in predicting individual CP asymmetries is due to their dependence on independent combinations of hadronic matrix elements (sums of penguin diagrams), which are not constrained by a fit to branching fractions. The branching fractions contain only differences of these penguin diagrams, up to some heavily CKM-suppressed (i.e. negligible) corrections. Therefore, the corresponding predictions depend strongly on the assumptions regarding these penguin diagrams. The way out of this situation is to consider correlations of CP asymmetries that are determined by sum rules. These

sum rules depend only on topologies that can be extracted from a global fit to branching fractions, and thus they eliminate the dependence on the sum of penguins.

There are two exceptions to this general observation. First, in the isospin limit we have [997]

$$A_{CP}(D^+ \to \pi^+\pi^0) = 0, \tag{464}$$

up to corrections that are expected to be tiny: $\mathcal{O}(\%)$ relative to other CP asymmetries [998]. Second, generically one expects that $A_{CP}(D^0 \to K^0_S K^0_S)$ is enhanced [1010,1017,1021] with respect to other modes for the following reason: the CKM-leading part of the amplitude ($\propto \lambda_{SCS}$) vanishes in the SU(3)$_F$ limit, while the CKM-suppressed part ($\propto V^*_{cb}V_{ub}$) does not. Furthermore, $A_{CP}(D^0 \to K^0_S K^0_S)$ receives contributions from a large exchange diagram. Estimating penguin annihilation contributions through a perturbative calculation, the authors of Ref. [1021] found

$$\left|A_{CP}(D^0 \to K^0_S K^0_S)\right| \leq 1.1\% \quad (95\%\ \text{CL}), \tag{465}$$

i.e. this asymmetry could be as large as 1%. This is of similar size to recent measurements [1023, 1039], which makes this mode very promising for discovering CP violation in the up-quark sector. The observables $A_{CP}(D^+ \to \pi^+\pi^0)$ and $A_{CP}(D^0 \to K^0_S K^0_S)$ are especially well suited for Belle II because of the neutral particles in the final state.

Regarding correlations of CP asymmetries, in the SU(3)$_F$ limit we have

$$a^{dir}_{CP}(D^0 \to K^+K^-) = -a^{dir}_{CP}(D^0 \to \pi^+\pi^-), \tag{466}$$

$$a^{dir}_{CP}(D^+ \to K^0_S K^+) = -a^{dir}_{CP}(D^+_s \to K^0\pi^+). \tag{467}$$

Taking into account SU(3)$_F$-breaking corrections, these sum rules can be generalized to contain three direct CP asymmetries each:

I. Sum rule among $a^{dir}_{CP}(D^0 \to K^+K^-)$, $a^{dir}_{CP}(D^0 \to \pi^+\pi^-)$, and $a^{dir}_{CP}(D^0 \to \pi^0\pi^0)$;
II. Sum rule among $a^{dir}_{CP}(D^+ \to K^0_S K^+)$, $a^{dir}_{CP}(D^+_s \to K^0\pi^+)$, and $a^{dir}_{CP}(D^+_s \to K^+\pi^0)$.

In these sum rules, the coefficients contain only topological amplitudes that can be extracted from the branching fractions. Thus, the unknown penguin combination is eliminated. Details are given in Ref. [1020]. To fully benefit from the sum rules, one would perform a global fit to the $D \to PP'$ data. Note that the generalized sum rules do not include SU(3)$_F$-breaking corrections to the penguin contributions. Consequently, they have an inherent uncertainty of the order of the SU(3)$_F$ breaking, approximately 30% of the size of the CP asymmetry.

The correlation between $a^{dir}_{CP}(D^0 \to \pi^+\pi^-)$ and $a^{dir}_{CP}(D^0 \to \pi^0\pi^0)$ resulting from sum rule I is shown in Fig. 162. Also shown are contours corresponding to a future scenario in which uncertainties on the branching fractions are divided by a factor of $\sqrt{50}$. These latter contours illustrate that more precise measurements of branching fractions will significantly improve our knowledge of the uncalculable MEs, and this in turn improves our predictions for CP asymmetries. A similar correlation between direct CP asymmetries appearing in sum rule II can be plotted; however, to test this sum rule to an interesting level, a better measurement of $A_{CP}(D^+_s \to K^+\pi^0)$ is needed.

Better measurements of branching fractions can also test the theoretical description of the data. This is especially true for DCS modes. A good example is the asymmetry

$$R(D^+_s) = \frac{\mathcal{B}(D^+_s \to K^0_S K^+) - \mathcal{B}(D^+_s \to K^0_L K^+)}{\mathcal{B}(D^+_s \to K^0_S K^+) + \mathcal{B}(D^+_s \to K^0_L K^+)}. \tag{468}$$

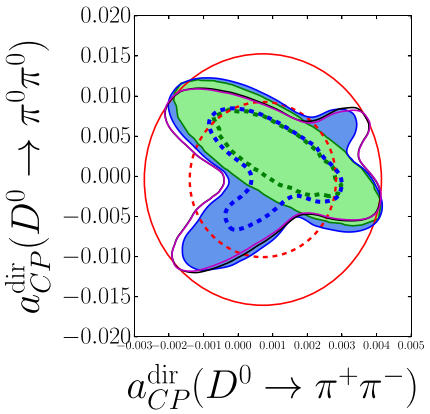

Fig. 162. Correlation between $a_{\rm CP}^{\rm dir}(D^0 \to \pi^0\pi^0)$ and $a_{\rm CP}^{\rm dir}(D^0 \to \pi^+\pi^-)$ from sum rule I. The solid (dashed) lines show allowed 95% (68%) CL regions. In red we show the current experimental data at the date of publication of Ref. [1020]. In blue we show the current fit result, including $1/N_c$ counting for the topological amplitudes. In green we show the same for a future data scenario where the errors of all branching ratios are improved by a factor $\sqrt{50}$. The solid black and magenta curve show current and future data scenarios, respectively, without including the $1/N_c$ counting. Note that the magenta and black curves lie partially on top of each other. Figure taken from Ref. [1020].

A fit with the topological amplitudes method results in [1019]

$$R(D_s^+) = 0.11^{+0.04}_{-0.14} \quad (1\,\sigma). \tag{469}$$

In the literature, several other predictions for this observable are available. In the SU(3)$_F$ limit, the authors of Ref. [1040] found

$$R(D_s^+)^{\text{SU(3)}_F\text{ limit}} = -0.0022 \pm 0.0087. \tag{470}$$

Partially including SU(3)$_F$-breaking effects, the authors of Ref. [1041] found

$$R(D_s^+)^{\text{partial }\cancel{\text{SU(3)}_F}} = -0.008 \pm 0.007. \tag{471}$$

This result is identical to a result found using QCD factorization [1042]. (QCD factorization involves an expansion in $2\Lambda_{\rm QCD}/m_c$, which, however, is close to one.) Note that the prediction of Eq. (469) has quite large uncertainties; these reflect the conservative treatment of SU(3)$_F$ breaking, which is allowed to be as large as 50% in the fit.

Belle has measured the combination [934]

$$\mathcal{B}(D_s^+ \to K_{\rm S}^0 K^+) + \mathcal{B}(D_s^+ \to K_{\rm L}^0 K^+) = 0.0295 \pm 0.0011 \pm 0.0009, \tag{472}$$

where the $K_{\rm S}^0$ or $K_{\rm L}^0$ is identified only by its missing mass. From Eq. (472) and the measurement $\mathcal{B}(D_s^+ \to K_{\rm S}^0 K^+) = (1.50 \pm 0.05)\%$ [77,1035], one obtains

$$R(D_s^+)^{\rm exp} = 0.02 \pm 0.35. \tag{473}$$

In the future, more precise data on $R(D_s^+)$ could allow one to quantify SU(3)$_F$ breaking in this mode.

Deviations from the SM for the observables in Table 121 can occur in several NP models. For example, the operator with flavor structure $\bar{u}c\bar{u}u$ studied in Ref. [1043] gives the additional SU(3)$_F$

representations [1017]

$$\mathcal{H}^{\mathrm{NP},\bar{u}c\bar{u}u} = -\frac{V_{cb}^* V_{ub}}{2}\left(\mathbf{15}_{3/2}^{\mathrm{NP}} + \frac{1}{\sqrt{2}}\mathbf{15}_{1/2}^{\mathrm{NP}} + \sqrt{\frac{3}{2}}\mathbf{3}_{1/2}^{\mathrm{NP}}\right). \tag{474}$$

The new quantity in Eq. (474) is the additional $\mathbf{15}_{3/2}^{\mathrm{NP}}$ representation, which comes with a weak phase relative to the $\mathbf{15}_{3/2}$ already present in the SM. This leads to the "smoking gun" signal for $\Delta I = 3/2$ NP models:

$$A_{\mathrm{CP}}(D^+ \to \pi^+\pi^0) \neq 0. \tag{475}$$

As another example, some models [1004] give rise to an operator with flavor structure $\bar{s}c\bar{u}s$ without a corresponding operator $\bar{d}c\bar{u}d$, breaking the discrete U-spin symmetry of $\mathcal{H}$. This results in the representations

$$\mathcal{H}^{\mathrm{NP},\bar{s}c\bar{u}s} = -\frac{V_{cb}^* V_{ub}}{2}\left(\sqrt{\frac{3}{2}}\mathbf{15}_{1/2}^{\mathrm{NP}} - \bar{\mathbf{6}}_{1/2}^{\mathrm{NP}} - \sqrt{\frac{3}{2}}\mathbf{3}_{1/2}^{\mathrm{NP}}\right). \tag{476}$$

A sign of this model would be violation of the CP asymmetry sum rules, for example a deviation from the SM prediction in Fig. (162). A proof of principle for distinguishing the above NP models from the SM has been given in Ref. [1017].

Conclusions We have highlighted key measurements of non-leptonic charm decays where Belle II is expected to have a large impact. The individual CP asymmetries $A_{\mathrm{CP}}(D^+ \to \pi^+\pi^0)$ and $A_{\mathrm{CP}}(D^0 \to K_S^0 K_S^0)$ can be used on their own as a test of the SM and as a discovery channel for CP violation in the up-quark sector, respectively. Due to the difficulty of estimating penguin diagrams, the best way to study further CP asymmetries is to look at their correlations. In order to test the CP asymmetry sum rules, further improvement of $A_{\mathrm{CP}}(D^0 \to \pi^0\pi^0)$ and the poorly measured $A_{\mathrm{CP}}(D_s^+ \to K^+\pi^0)$ is particularly important. Also, time-dependent measurements of CP asymmetries for D^0 decays would be helpful [1021,1044]. In addition, future measurements of the asymmetry $R(D_s^+)$ could distinguish different theoretical approaches to SM predictions for charm decays.

13.6.2. Experiment

Authors: G. Casarosa, A. J. Schwartz

The Belle II experiment is ideal for searching for time-integrated CP-violating effects in a variety of final states, and will reach precisions of the order of the 0.01% level. The LHCb experiment has provided extremely precise measurements of CP asymmetries in decays with charged particles in the final state. The excellent γ and π^0 reconstruction (and thus η, η', and ρ^+ reconstruction) will allow Belle II to search for CP violation in complementary final states that contain neutral particles. The high flavor-tagging efficiency with low dilution, the numerous control samples with which to study systematics, in addition to the excellent reconstruction of charged particles, will allow Belle II to compete with LHCb in measurements of time-integrated CP violation.

Extrapolations from Belle measurements A listing of D^0, D^+, and D_s^+ decay modes that Belle has studied is given in Table 122. The table lists the CP asymmetry $A_{\mathrm{CP}} = [\Gamma(D^0 \to f) - \Gamma(\bar{D}^0 \to \bar{f})]/[\Gamma(D^0 \to f) + \Gamma(\bar{D}^0 \to \bar{f})]$ measured by Belle, and the precision expected for Belle II. The latter is estimated by scaling the Belle statistical error (σ_{stat}) by the ratio of integrated luminosities,

Table 122. Time-integrated CP asymmetries measured by Belle, and the precision expected for Belle II in 50 ab^{-1} of data.

Mode	$\mathcal{L}$ (fb^{-1})	A_{CP} (%)	Belle II 50 ab^{-1}
$D^0 \to K^+K^-$	976	$-0.32 \pm 0.21 \pm 0.09$	± 0.03
$D^0 \to \pi^+\pi^-$	976	$+0.55 \pm 0.36 \pm 0.09$	± 0.05
$D^0 \to \pi^0\pi^0$	966	$-0.03 \pm 0.64 \pm 0.10$	± 0.09
$D^0 \to K^0_S\pi^0$	966	$-0.21 \pm 0.16 \pm 0.07$	± 0.02
$D^0 \to K^0_S K^0_S$	921	$-0.02 \pm 1.53 \pm 0.02 \pm 0.17$	± 0.23
$D^0 \to K^0_S\eta$	791	$+0.54 \pm 0.51 \pm 0.16$	± 0.07
$D^0 \to K^0_S\eta'$	791	$+0.98 \pm 0.67 \pm 0.14$	± 0.09
$D^0 \to \pi^+\pi^-\pi^0$	532	$+0.43 \pm 1.30$	± 0.13
$D^0 \to K^+\pi^-\pi^0$	281	-0.60 ± 5.30	± 0.40
$D^0 \to K^+\pi^-\pi^+\pi^-$	281	-1.80 ± 4.40	± 0.33
$D^+ \to \phi\pi^+$	955	$+0.51 \pm 0.28 \pm 0.05$	± 0.04
$D^+ \to \pi^+\pi^0$	921	$+2.31 \pm 1.24 \pm 0.23$	± 0.17
$D^+ \to \eta\pi^+$	791	$+1.74 \pm 1.13 \pm 0.19$	± 0.14
$D^+ \to \eta'\pi^+$	791	$-0.12 \pm 1.12 \pm 0.17$	± 0.14
$D^+ \to K^0_S\pi^+$	977	$-0.36 \pm 0.09 \pm 0.07$	± 0.02
$D^+ \to K^0_S K^+$	977	$-0.25 \pm 0.28 \pm 0.14$	± 0.04
$D^+_s \to K^0_S\pi^+$	673	$+5.45 \pm 2.50 \pm 0.33$	± 0.29
$D^+_s \to K^0_S K^+$	673	$+0.12 \pm 0.36 \pm 0.22$	± 0.05

and by dividing the systematic error into those that scale with luminosity, such as background shapes measured with control samples (σ_{syst}), and those that do not scale with luminosity, such as decay time resolution due to detector misalignment (σ_{irred}). The overall error estimate is calculated as

$$\sigma_{\text{Belle II}} = \sqrt{(\sigma^2_{\text{stat}} + \sigma^2_{\text{syst}}) \cdot (\mathcal{L}_{\text{Belle}}/50\,\text{ab}^{-1}) + \sigma^2_{\text{irred}}}.$$

For most of the decay modes listed, the expected uncertainty on A_{CP} is $\lesssim 0.10\%$.

It is important to note that the estimates in this table do not take into account expected improvements in reconstruction at Belle II with respect to Belle, and the additional flavor-tagging techniques that we have presented above. Also, the different background conditions are not included in the estimation.

Systematic uncertainties In this section we briefly discuss the main sources of systematic errors and we classify them as *reducible* or *irreducible* as they have been treated in Table 122.

Detection asymmetry: The determination of the flavor or charge of the D meson is achieved by looking at the charge of a final state pion or kaon. Any asymmetry in the detection and reconstruction between positive and negative tracks will induce a fake asymmetry in the final measurement. The detection asymmetry is measured in data using control samples, with different techniques employed by Belle [1045] and BaBar [1046], and a correction is applied to the number of D and $\bar{D}$ candidates, usually by weighting events. This correction depends on the direction and momentum of the track and can be as large as 3%. The associated systematic error depends on the precision to which the correction is determined, which in turn depends on the statistics of the control sample used. Hence it is a *reducible* systematic error.

Forward–backward asymmetry: The interference between the photon and the Z bosons in the e^+e^- interaction induces a forward–backward asymmetry (A_{FB}) in the direction of the c (and consequently $\bar{c}$) quark. A fake CP asymmetry is induced by a non-null A_{FB} coupled with the Belle II

detector acceptance. In order to decouple $A_{\rm FB}$ from $A_{\rm CP}$, the asymmetry measurement is performed in bins of the cosine of the polar angle in the center-of-mass of the charmed meson ($\cos\theta^*$). This angle is a good approximation for the direction of the charmed quark. The forward–backward asymmetry is an odd function of $\cos\theta^*$, while the CP asymmetry is of course independent; thus the value of $A_{\rm CP}$ can be extracted with a fit with a constant to the averages of the number-of-candidates asymmetry in symmetric bins of $\cos\theta^*$. This is also clearly a *reducible* systematic error since with more data the determination of $A_{\rm FB}$ will be more precise and less dependent on the binning in $\cos\theta^*$, and the impact on the determination of the CP asymmetry will be smaller.

K^0_S in the final state: Many interesting channels have a K^0_S in the final state. Particular attention must be paid in these cases because the final CP asymmetry will contain a contribution due to CP violation in the $K^0\overline{K}^0$ system. This contribution can be calculated; e.g., for the Belle $D^+ \to K^0_S K^+$ analysis [1047] it is $-(0.328 \pm 0.006)\%$.

Moreover, additional contributions to the measured asymmetry arise from:

- $K^0\overline{K}^0$ regeneration effect in the material;
- K^0_S–K^0_L interference.

These are conservatively considered *irreducible* systematics. However, for Belle II it may be possible to reduce these with further simulation studies, as the physics underlying them is well understood. (For Belle and BaBar analyses, it was not necessary to reduce these as the statistical error dominated.)

Other contributions: A few small systematic contributions related to the selection of events and the selection of the control sample used to correct for the detection asymmetry are also included. Other systematic contributions are related to the fitting of invariant mass distribution used to extract the number of D candidates, e.g. the estimation of the PDF of the background events from the sidebands, and extraction of the signal PDF resolution parameters. These contributions are usually all reducible, and they do not dominate the total error. With a much larger data sample their impact should be re-evaluated.

Expected improvements As described in Sect. 13.2, we expect that the reconstruction efficiency for charm will be higher at Belle II than it was at Belle or BaBar. The improved vertex resolution should result in improved rejection of random combinations of tracks. The improved tracking and the extended radius of the drift chamber should improve the K^0_S reconstruction efficiency, and also that of converted photons. The improved discrimination between $K^\pm$ and $\pi^\pm$ will reduce cross-feed backgrounds among topologically similar decay modes. Moreover, the measurements will benefit from the improved photon and π^0 reconstruction. However, the overall increase of backgrounds complicates simply extrapolating the overall reconstruction improvements of Belle II.

The high statistics that Belle II is expected to accumulate will allow estimation of the CP asymmetry in bins of proper time. This technique has already been used at LHCb and is expected be available at Belle II both for D^*-tagged D^0 decaying to at least two charged tracks (or one track and a K^0_S) and for prompt charmed mesons decaying to at least one charged track, or one K^0_S.

Beside the usual D^{*+}-tagged sample of D^0 mesons, an additional sample will be available, exploiting the ROE flavor-tagging method. The overlap of the two samples is estimated to be $<3\%$, and the overlapping events are assigned to only one of the two samples so that the samples are independent. We can conservatively estimate the reduction of the statistical error on $A_{\rm CP}$ assuming two independent $A_{\rm CP}$ measurements: one performed on the D^{*+}-tagged sample with a statistical error $\sigma^*_{A_{\rm CP}}$, and the other one performed on the ROE-tagged sample with a statistical error $\sigma^0_{A_{\rm CP}}$. We can then

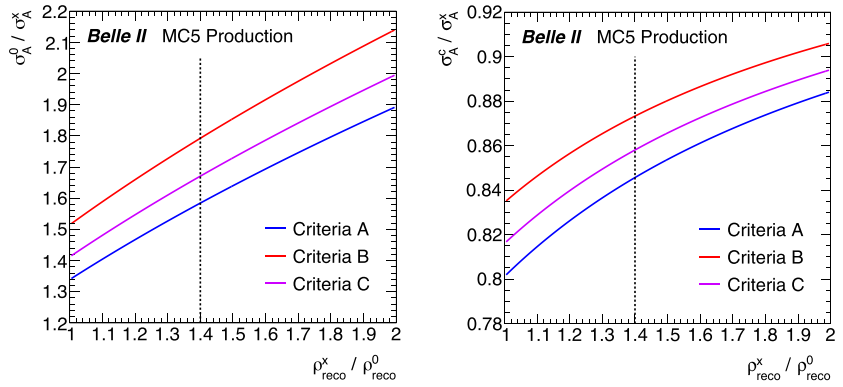

Fig. 163. Left: Trend of $\sigma^0_{A_{CP}}/\sigma^*_{A_{CP}}$ as a function of $\rho^*_{reco}/\rho^0_{reco}$. Right: Trend of $\sigma^c_{A_{CP}}/\sigma^*_{A_{CP}}$ as a function of $\rho^*_{reco}/\rho^0_{reco}$. In both cases the vertical dotted line is drawn at the value $\rho^*_{reco}/\rho^0_{reco} = 1.4$. Criteria A–C are described in Sect. 43 and Table 108.

evaluate the error of the combination of the two. The ratio of statistical errors of the two independent measurements is

$$\frac{\sigma^0_{A_{CP}}}{\sigma^*_{A_{CP}}} = \sqrt{\frac{1}{3}\cdot\frac{Q^*}{Q^0}\cdot\frac{\rho^*_{reco}}{\rho^0_{reco}}} \equiv \alpha, \tag{477}$$

where $Q = \epsilon_{tag}(1-2\omega)^2$ is the effective tagging efficiency, ρ_{reco} is the purity of the reconstructed sample, the symbol 0 ($*$) denotes the sample tagged with the ROE (D^{*+}) method, and the factor of three in the denominator accounts for the different number of generated prompt D^0 versus D^{*+}. Values of Q are listed in Table 108.

If $\sigma^c_{A_{CP}}$ is the statistical uncertainty associated to A_{CP} obtained combining the two independent measurements, we have

$$\frac{\sigma^c_{A_{CP}}}{\sigma^*_{A_{CP}}} = \frac{\alpha}{\sqrt{1+\alpha^2}}, \quad \text{with } \alpha \equiv \alpha(\rho^*_{reco}/\rho^0_{reco}).$$

The value of $\rho^*_{reco}/\rho^0_{reco}$ depends on the reconstruction performance of the detector, and also on the final state. We conservatively estimate the ratio $\rho^*_{reco}/\rho^0_{reco} = 1.4$ from a BaBar analysis [1048]. Plots of the two ratios $\sigma^0_{A_{CP}}/\sigma^*_{A_{CP}}$ and $\sigma^c_{A_{CP}}/\sigma^*_{A_{CP}}$ as functions of α are shown in Fig. 163, for different values of Q^0. The best scenario is obtained for criteria A, since the tagging efficiency ϵ^0_{tag} is significantly higher than for the other two cases (see Table 108). We estimate that the error on A_{CP} would be reduced by ∼15% if, in addition to using D^* decays for flavor tagging, one also used the ROE method for flavor tagging. Since $\sigma_{A_{CP}} \propto 1/\sqrt{\mathcal{L}}$, where $\mathcal{L}$ is the integrated luminosity, one can interpret this reduction of the statistical uncertainty as being equivalent to an effective increase in integrated luminosity of $(1/0.85)^2 - 1 = 38\%$.

A further improvement in the precision can be achieved with a simultaneous fit to the two separately tagged D^0 samples, instead of the *a posteriori* combination of two measurements. A quantitative estimation is not straightforward, but previous analyses [1048] have shown that a reduction of the statistical error of up to 5% is possible.

Estimate of δA_{CP} for $D^0 \to K^0_S K^0_S$ and $D^+ \to \pi^+\pi^0$ In this section we discuss two channels that have generated much theoretical interest:

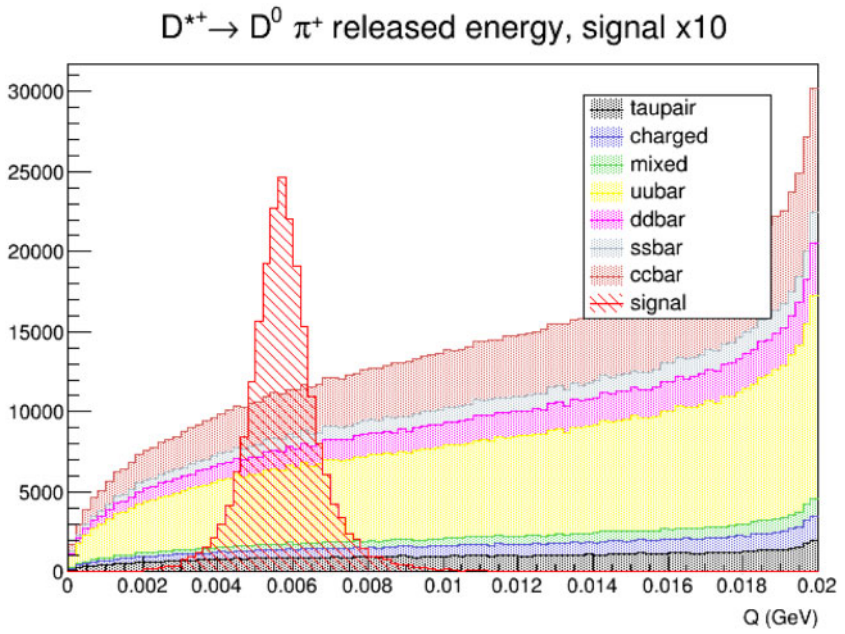

Fig. 164. Energy released, $Q \equiv M(D^+\pi^0) - M(D^+) - M_{\pi^0}$, for $D^{*+} \to D^+\pi^0$, $D^+ \to \pi^+\pi^0$ decays after a preliminary selection. The signal distribution (in red) is multiplied by 10. The overall background distribution consists of stacked contributions from different event types.

(1) $D^0 \to K^0_S K^0_S$: CP violation may be as large as 1% in the SM;
(2) $D^+ \to \pi^+\pi^0$: no CP violation is expected in the SM.

The first decay mode is a promising channel for obtaining first evidence of CP violation in the charm sector. The second decay mode is of particular interest in the search for NP contributions.

Both Belle [1023] and LHCb [1039] have measured A_{CP} for $D^0 \to K^0_S K^0_S$ decays using their full or current datasets (921 fb^{-1} and 3 fb^{-1} respectively). The statistical and systematic errors of the Belle measurement are significantly smaller than those of LHCb, and they will improve further at Belle II. The Belle result is $A_{CP}(D^0 \to K^0_S K^0_S) = (-0.02 \pm 1.53 \pm 0.17)\%$. The systematic uncertainty is very small because the measurement is normalized to the asymmetry in the $D^0 \to K^0_S\pi^0$ channel:

$$A_{CP}(D^0 \to K^0_S K^0_S) = A_{raw}(K^0_S K^0_S) - A_{raw}(K^0_S\pi^0) + A_{CP}(K^0_S\pi^0), \tag{478}$$

where $A_{raw}(f) = [N(D^0 \to f) - N(\bar{D}^0 \to f)]/[N(D^0 \to f) + N(\bar{D}^0 \to f)]$ is the raw asymmetry. Note that the asymmetry that arises from the difference in strong interactions in material of K^0 and $\bar{K}^0$ is null in this channel, as the final state is $K^0\bar{K}^0$. The systematic error is almost completely reducible, as it is dominated by the error on $A_{CP}(D^0 \to K^0_S\pi^0)$ (which will itself be improved at Belle II). Scaling the statistical error with luminosity and adding in quadrature the expected error on $A_{CP}(D^0 \to K^0_S\pi^0)$, we obtain an uncertainty for 50 ab^{-1} of data of 0.23%. This precision is notably smaller than the allowed window for CP violation in this decay, Eq. (465).

For $D^+ \to \pi^+\pi^0$ decays, to estimate the Belle II precision for A_{CP} we perform an MC simulation study. To reduce backgrounds, we require that the D^+ originate from $D^{*+} \to D^+\pi^0$ decays. We then apply a set of preliminary selection criteria in order to reduce the main sources of background. The resulting distribution of energy released, $Q \equiv M(D^+\pi^0) - M(D^+) - M_{\pi^0}$, where $M(D^+\pi^0)$ is the $\pi^+\pi^0\pi^0$ invariant mass and $M(D^+)$ is the $\pi^+\pi^0$ invariant mass, is plotted in Fig. 164. Both signal and background events plotted correspond to 50 ab^{-1} of data; the signal curve is scaled by

a factor of 10 for greater visibility. Mis-reconstructed signal candidates are included in the signal distribution. At this stage, a selection efficiency of approximately 30% and a background rejection of 96%–99% are achieved. This performance is good, but, as this study was done with an early version of the Belle II reconstruction code (release-00-06-00), we expect further improvements as the recontruction code is developed. As the signal-to-background ratio shown in Fig. 164 is similar to that achieved at Belle, we estimate the sensitivity of Belle II by simply scaling the Belle errors by the square root of the ratio of luminosities. The result is an uncertainty for 50 ab^{-1} of data of 0.17%.

13.7. The golden channels

In summary, the charm physics program of Belle II is quite broad, covering mixing, both indirect and direct CP violation, semi-leptonic decays, hadronic decays, rare and forbidden decays, etc. There is substantial discovery potential. We list some of the most promising channels and measurements for discovering NP in Table 123, and refer to this listing as the "golden channels."

14. Quarkonium(-like) physics

Editors: N. Brambilla, B. Fulsom, C. Hanhart, Y. Kiyo, R. Mizuk, R. Mussa, A. Polosa, S. Prelovsek, C. P. Shen

Additional section writers: S. Godfrey, F.-K. Guo, K. Moats, A. Nefediev, S. Olsen, P. Pakhlov, U. Tamponi, A. Vairo

14.1. Introduction

Authors: N. Brambilla, A. Vairo

This chapter is devoted to quarkonium(-like) states at Belle II. Quarkonium is a bound state of a heavy quark and a heavy antiquark, i.e. bound states of the type $c\bar{c}$, $b\bar{b}$, and $b\bar{c}$; $t\bar{t}$ cannot give rise to a quarkonium state because the t quark decays weakly before a proper bound state can be formed. We use "Quarkonium(-like)" as the title for the chapter since we also include the (potentially) exotic (non-$\bar{Q}Q$) X, Y, Z states that have been observed at Belle and at other accelerator-based experiments. Very likely they involve more degrees of freedom besides the heavy quark and the heavy antiquark. Quarkonium is a system of great physical interest in general, and of great interest for the Belle experiment in particular. Indeed, the most cited paper of the Belle collaboration [1049] concerns the first observation of an exotic quarkonium candidate (the famous $X(3872)$).

In this chapter we will report on the current status of our theory understanding of quarkonium and the present status of its experimental investigation within a discussion focused on the Belle II program.

The chapter is structured as follows. Section 14.2 discusses the physics of quarkonium, its impact, and relevance. Section 14.3 introduces the theoretical methods to study quarkonia within QCD, i.e. non-relativistic effective field theories and lattice. Then we present concrete theoretical descriptions of quarkonium processes and corresponding results and predictions. We separate the presentation of the theoretical concepts into Sect. 14.4, where quarkonia below the threshold for the decay into two open flavor mesons are discussed, and Sect. 14.5, where quarkonia and quarkonium-like states above this threshold are the subject. At this threshold many additional degrees of freedom become dynamical and should be considered in theory. Accordingly, the properties of quarkonium states appear to differ below and above this threshold, and all of the new exotic X, Y, Z states have been found at or above this strong decay threshold. In particular, Sect. 14.4 presents predictions for masses, decay widths, and transitions. We also discuss how to use high-order perturbative calculations inside

Table 123. The "golden channels" for charm physics.

Channel	Observable	Belle/BaBar measurement		Scaled	
		$\mathcal{L}$ [ab^{-1}]	Value	5 ab^{-1}	50 ab^{-1}
Leptonic decays					
$D_s^+ \to \ell^+\nu$	μ^+ events	0.913	492 ± 26	2.7k	27k
	τ^+ events		2217 ± 83	12.1k	121k
	f_{D_s}		2.5%	1.1%	0.34%
$D^+ \to \ell^+\nu$	μ^+ events	—	—	125	1250
	f_D	—	—	6.4%	2.0%
Rare and radiative decays					
$D^0 \to \rho^0\gamma$	A_{CP}	0.943	$+0.056 \pm 0.152 \pm 0.006$	± 0.07	± 0.02
$D^0 \to \phi\gamma$	A_{CP}		$-0.094 \pm 0.066 \pm 0.001$	± 0.03	± 0.01
$D^0 \to \overline{K}^{*0}\gamma$	A_{CP}		$-0.003 \pm 0.020 \pm 0.000$	± 0.01	± 0.003
Mixing and indirect (time-dependent) CP violation					
$D^0 \to K^+\pi^-$ (no CPV)	x'^2 (%)	0.976	0.009 ± 0.022	± 0.0075	± 0.0023
	y' (%)		0.46 ± 0.34	± 0.11	± 0.035
(CPV allowed)	$\lvert q/p\rvert$	World avg. [230]	$0.89^{+0.08}_{-0.07}$	± 0.20	± 0.05
	ϕ (°)	with LHCb	$-12.9^{+9.9}_{-8.7}$	$\pm 16°$	$\pm 5.7°$
$D^0 \to K^+\pi^-\pi^0$	x''	0.384	$2.61^{+0.57}_{-0.68} \pm 0.39$	—	± 0.080
	y''		$-0.06^{+0.55}_{-0.64} \pm 0.34$	—	± 0.070
$D^0 \to K^0_S\pi^+\pi^-$	x (%)	0.921	$0.56 \pm 0.19^{+0.04\ +0.06}_{-0.08\ -0.08}$	± 0.16	± 0.11
	y (%)		$0.30 \pm 0.15^{+0.04\ +0.03}_{-0.05\ -0.07}$	± 0.10	± 0.05
	$\lvert q/p\rvert$		$0.90^{+0.16\ +0.05\ +0.06}_{-0.15\ -0.04\ -0.05}$	± 0.12	± 0.07
	ϕ (°)		$-6 \pm 11 \pm 3^{+3}_{-4}$	± 8	± 4
Direct (time-integrated) CP violation in %					
$D^0 \to K^+K^-$	A_{CP}	0.976	$-0.32 \pm 0.21 \pm 0.09$	± 0.10	± 0.03
$D^0 \to \pi^+\pi^-$	A_{CP}	0.976	$+0.55 \pm 0.36 \pm 0.09$	± 0.16	± 0.05
$D^0 \to \pi^0\pi^0$	A_{CP}	0.966	$-0.03 \pm 0.64 \pm 0.10$	± 0.28	± 0.09
$D^0 \to K^0_S\pi^0$	A_{CP}	0.966	$-0.21 \pm 0.16 \pm 0.07$	± 0.08	± 0.02
$D^0 \to K^0_S K^0_S$	A_{CP}	0.921	$-0.02 \pm 1.53 \pm 0.17$	± 0.66	± 0.23
$D^0 \to K^0_S\eta$	A_{CP}	0.791	$+0.54 \pm 0.51 \pm 0.16$	± 0.21	± 0.07
$D^0 \to K^0_S\eta'$	A_{CP}	0.791	$+0.98 \pm 0.67 \pm 0.14$	± 0.27	± 0.09
$D^0 \to \pi^+\pi^-\pi^0$	A_{CP}	0.532	$+0.43 \pm 1.30$	± 0.42	± 0.13
$D^0 \to K^+\pi^-\pi^0$	A_{CP}	0.281	-0.60 ± 5.30	± 1.26	± 0.40
$D^0 \to K^+\pi^-\pi^+\pi^-$	A_{CP}	0.281	-1.80 ± 4.40	± 1.04	± 0.33
$D^+ \to \phi\pi^+$	A_{CP}	0.955	$+0.51 \pm 0.28 \pm 0.05$	± 0.12	± 0.04
$D^+ \to \pi^+\pi^0$	A_{CP}	0.921	$+2.31 \pm 1.24 \pm 0.23$	± 0.54	± 0.17
$D^+ \to \eta\pi^+$	A_{CP}	0.791	$+1.74 \pm 1.13 \pm 0.19$	± 0.46	± 0.14
$D^+ \to \eta'\pi^+$	A_{CP}	0.791	$-0.12 \pm 1.12 \pm 0.17$	± 0.45	± 0.14
$D^+ \to K^0_S\pi^+$	A_{CP}	0.977	$-0.36 \pm 0.09 \pm 0.07$	± 0.05	± 0.02
$D^+ \to K^0_S K^+$	A_{CP}	0.977	$-0.25 \pm 0.28 \pm 0.14$	± 0.14	± 0.04
$D_s^+ \to K^0_S\pi^+$	A_{CP}	0.673	$+5.45 \pm 2.50 \pm 0.33$	± 0.93	± 0.29
$D_s^+ \to K^0_S K^+$	A_{CP}	0.673	$+0.12 \pm 0.36 \pm 0.22$	± 0.15	± 0.05

non-relativistic effective field theories together with lattice or experimental data on quarkonium observables to obtain precise extractions of SM parameters like the heavy quark masses and the strong coupling constant α_s. Precise values for these parameters are relevant to the search for the BSM physics that is discussed later in this document: uncertainties in these quantities jeopardize the search for new physics. Section 14.5 explains the physics of quarkonium at or above the open flavor

threshold and compares several approaches to describing the X, Y, Z states and their predictions. The lattice- and QCD-based effective field theory descriptions of states at and above the threshold are currently being developed. We summarize the latest developments and progress that will likely take place in the near future, as well as their potential impact on prospects for Belle II.

Sections 14.6 and 14.7 present recent experimental results and the perspectives for Belle II for charmonium and bottomonium respectively, discussed in relation to the theoretical descriptions presented before.

Finally, Sect. 14.8 presents the early physics program of Belle II in relation to quarkonium, together with an analysis of competing experiments. Part of this section is dedicated to a quantitive analysis of the states that could be observed at Belle II and the relevant processes. Action items for experiment and theory are listed in Sect. 14.9, emphasizing the modes of greatest importance at Belle II. Conclusions are presented in Sect. 14.10.

14.2. Heavy quarkonium: physical picture

Authors: N. Brambilla, A. Vairo

The contemporary interest in heavy quarkoniua stems from the fact that, on one hand, a solid description of quarkonium has been developed from QCD, based on the recent advances in QCD non-relativistic effective field theories and lattice QCD [1050–1053], at least for what concerns states below and away from the open flavor strong decay threshold. On the other hand, a wealth of data on discoveries of new states, measurements of new processes, and increased statistics and precision have been accumulated thanks to the B factories [2], the tau–charm factories, and, at present, the experiments at LHC [1050,1051].

The theoretical interest in quarkonium states below the open flavor threshold stems from the hierarchy of the physical scales that characterize them. Heavy quarks have a mass m larger than the QCD scale $\Lambda_{\rm QCD}$, which is the scale at which non-perturbative effects become dominant (a few hundred MeV, say). This implies that processes happening at the scale of the heavy quark mass can be described by perturbative QCD while non-perturbative effects are suppressed by powers of $\Lambda_{\rm QCD}/m$. This is also true for heavy–light mesons. However, in the case of a bound state of two heavy quarks the situation becomes more interesting. Because the system is non-relativistic, quarkonium is characterized by the heavy quark bound state velocity, $v \ll 1$, ($v^2 \sim 0.3$ for $c\bar{c}$, $v^2 \sim 0.1$ for $b\bar{b}$ with $E = mv^2 \sim 500\,\text{GeV}$) and by a hierarchy of energy scales: the mass m (hard scale), the relative momentum $p \sim mv$ (soft scale), and the binding energy $E \sim mv^2$ (ultrasoft scale). For energy scales close to $\Lambda_{\rm QCD}$, perturbation theory breaks down and one has to rely on non-perturbative methods. Regardless, the non-relativistic hierarchy of scales,

$$m \gg p \sim 1/r \sim mv \gg E \sim mv^2, \tag{479}$$

where $r \sim 1/(mv)$ is the typical distance between the heavy quark and the heavy antiquark, also persists below the scale $\Lambda_{\rm QCD}$, since $m \gg \Lambda_{\rm QCD}$, $\alpha_s(m) \ll 1$, and phenomena occurring at the scale m can always be treated perturbatively. The coupling may also be small if $mv \gg \Lambda_{\rm QCD}$ and $mv^2 \gg \Lambda_{\rm QCD}$, in which case $\alpha_s(mv) \ll 1$ and $\alpha_s(mv^2) \ll 1$, respectively. This is likely to happen only for the lowest charmonium and bottomonium states, as for the excited states r becomes bigger and $r \ll 1/\Lambda_{\rm QCD}$ is no longer true. Direct information on the radius of the quarkonia systems is not available, and thus the attribution of some of the lowest bottomonia and charmonia states to the perturbative or the non-perturbative soft regime is at the moment still ambiguous.

Annihilation and production processes take place at the scale m, binding takes place at the scale mv, while very low-energy gluons and light quarks are sufficiently long-lived that a bound state

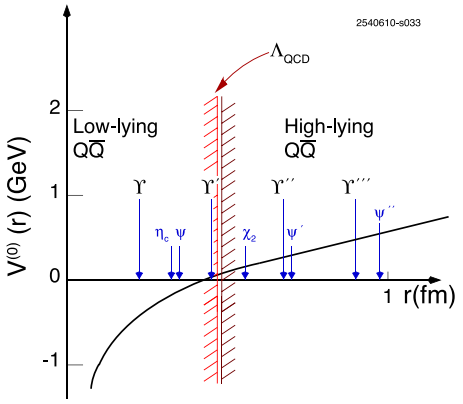

Fig. 165. The static $Q\bar{Q}$ potential plotted as a function of the $Q\bar{Q}$ distance r in comparison to typical quarkonia radii. The static potential has a Coulombic behavior (asymptotic freedom) for small r and a linearly rising behavior for large r (confinement). Low-lying quarkonia are quarkonia states with a typical radius smaller than the inverse of $\Lambda_{\rm QCD}$, the scale at which the non-perturbative effect becomes dominant. High-lying quarkonia are quarkonia states with typical radius bigger than $\Lambda_{\rm QCD}$.

has time to form and therefore are sensitive to the scale mv^2. Ultrasoft gluons are responsible for retardation (i.e. non-potential) effects analogous to the Lamb shift. The existence of several scales makes QCD calculations for quarkonium difficult. In perturbative calculations of loop diagrams the different scales get entangled, challenging our abilities to perform higher-order calculations. In lattice QCD, the existence of several scales for quarkonium sets requirements on the lattice spacing ($a < 1/m$) and the overall size of the lattice ($L > 1/(mv^2)$) that are challenging to be meet.

However, it is precisely this rich structure of separated energy scales that makes heavy quarkonium an ideal laboratory to test the interplay between perturbative and non-perturbative QCD within a controlled environment. Quarkonia with different radii have varying sensitivities to the Coulombic and confining interactions, as shown in Fig. 165. Additionally, the large mass of quarkonium also makes it a suitable system to probe some part of the parameter space of BSM models in decays.

The greatest excitement in the field came in the last decade from the discovery of a large number of states close to and above the open flavor strong decay threshold showing exotic properties: the X, Y, Z states (see Tables 125 and 126). Starting from the discovery of the $X(3872)$ in 2003 [1049], more than 20 candidates have been reported by various experiments with properties at odds with the expectations from quark models, which had until then been very successful. An interesting feature is that many of these exotic states have a comparatively small width. Most prominent among them are the charged states found in both the charmonium and bottomonium mass ranges. These states have to contain at least four quarks: they are explicitly exotic. Other states of explicit exotic nature, two pentaquark states in the charmonium mass region, have recently been discovered by the LHCb Collaboration [1054].

With these states we have for the first time the possibility of exploring the non-standard configurations that a non-Abelian theory like QCD can generate [1050] and have long been conjectured: hybrids, multiquark configurations, pentaquarks. Belle II will play a role of paramount importance for the characterization of these states, taking an important step towards a solution of what is among the most challenging problems in contemporary particle physics. The theory to describe such states from QCD lags behind, however. At present most of the studies are carried out at the level of models, which focus on a limited number of degrees of freedom assumed to be prominent. Initial applications of effective field theories based either on quark–gluon degrees of freedom or on hadronic degrees

of freedom, and of lattice QCD, to study these states have begun, and the field is likely to develop very rapidly.

14.3. Theory methods

Authors: N. Brambilla, A. Vairo

14.3.1. Introduction

The modern approach to heavy quarkonium is provided by lattice QCD and non-relativistic effective field theories (NR EFTs) [1053].

Lattice QCD is a reliable non-perturbative method for studying hadron properties based directly on QCD. It relies on numerical path integrations in finite and discretized Euclidean space-time.

On the other hand, taking advantage of the existence of a hierarchy of scales, one can substitute simpler but equivalent NR EFTs for QCD [1053]. A hierarchy of EFTs may be constructed by systematically integrating out modes associated with high-energy scales not relevant for a particular quarkonium system. Such integration is performed as part of a matching procedure that enforces the equivalence between QCD and the EFT at a given order of the expansion in the velocity v of the heavy quark in the bound state. The EFT realizes a factorization between the high-energy contributions carried by the matching coefficients and the low-energy contributions carried by the degrees of freedom left as dynamical in the EFT Lagrangian. The Poincaré symmetry remains intact at the level of the NR EFT in a non-linear realization that imposes exact relations among the EFT matching coefficients [1055].

14.3.2. Non-relativistic effective field theories

Physics at the scale m: NRQCD Quarkonium annihilation and production occur at the scale m. The suitable EFT is non-relativistic QCD (NRQCD) [1056,1057], which follows from QCD by integrating out the scale m. As a consequence, the effective Lagrangian is organized as an expansion in $1/m$ and $\alpha_s(m)$:

$$\mathcal{L}_{\rm NRQCD} = \sum_n \frac{c_n(\alpha_s(m),\mu)}{m^n} \times O_n(\mu, mv, mv^2, \ldots), \tag{480}$$

where O_n are the operators of NRQCD that are important at the low-energy scales mv and mv^2, μ is the NRQCD factorization scale, and c_n are the Wilson coefficients of the EFT that encode the contributions from the scale m and are non-analytic in m. Only the upper (lower) components of the Dirac fields matter for quarks (antiquarks) at energies lower than m. The low-energy operators O_n are constructed out of two or four heavy quark/antiquark fields plus gluons. Four-fermion operators have to be added. Matrix elements of O_n depend on the scales μ, mv, mv^2, and $\Lambda_{\rm QCD}$. Thus, operators are counted in powers of v. The imaginary part of the coefficients of the four-fermion operators contains the information on heavy quarkonium annihilation. The NRQCD heavy quarkonium Fock state is given by a series of terms, where the leading term is a $Q\overline{Q}$ in a color-singlet state, and the first correction, suppressed in v, comes from a $Q\overline{Q}$ in an octet state plus a gluon. Higher-order terms are sub-leading in increasing powers of v. NRQCD is suitable for spectroscopy studies on the lattice, and it is used especially to calculate properties of bottomonium since the large mass of the b quark would put stringent requirements on the lattice step. The latest lattice results on charmonium and bottomonium spectroscopy are reported in Sect. 14.4.3. Inclusive and exclusive quarkonium decays can be calculated in NRQCD [1053,1057] at higher order in the expansion in v and in α_s, the main

problem being the proliferation of low-energy non-perturbative matrix elements at higher order in the velocity expansion [1058,1059] that should still be calculated on the lattice. See Ref. [1060] for an example of such lattice calculations.

NRQCD is also the theory used to study quarkonium production—see Refs. [1050,1061]. One of the most interesting production processes for Belle is double quarkonium production, which turned out to also be a discovery tool for new states; see Sect. 14.6.4.

Physics at the scale mv, mv^2: pNRQCD To study the physics at the scales mv, mv^2 and bound state formation, it is convenient to also integrate out the scale of the momentum transfer, obtaining EFTs called potential NRQCD (pNRQCD) [1062,1063]. If the typical radius of the quarkonium state is smaller than the inverse of $\Lambda_{\rm QCD}$, the dynamical degrees of freedom are quark–antiquak pairs in either the color singlet or the color octet configuration as well as low-energy gluons (higher-energy gluons are integrated out). In this case the matching can be done in perturbation theory. The corresponding EFT is called "weakly coupled pNRQCD." Otherwise, the residual dynamical degree of freedom is only the color singlet and the matching is non-perturbative, i.e. the matching coefficients cannot be calculated via a perturbative expansion in α_s. However, the gauge-invariant gluon correlators (generalized Wilson loops) in terms of which the matching coefficients are written can be calculated using lattice QCD or in QCD vacuum models. This EFT is called "strongly coupled pNRQCD." In both cases the zeroth-order problem is a Schrödinger equation and the matching coefficients are the potentials which are directly obtained from QCD. We will present details of this and applications in the next section. In the case of strongly coupled pNRQCD, the singlet is the only degree of freedom (apart from ultrasoft pions). In this situation the non-relativistic EFT is similar to a quark potential model, though with a few important differences: the potentials are not modeled but obtained directly from QCD [1053,1064,1065], all the scales of the problem are considered systematically, and each observable is calculated within a well-defined power-counting scheme.

When we are close to or above the open flavor threshold, things become radically different. A description of quarkonium based on potentials (obtained from QCD using strongly coupled pNRQCD) emerges only below the strong decay threshold. At and above the the open heavy flavor threshold, new degrees of freedom become relevant containing explicitly light quarks and excited gluons, and many new states are expected. NRQCD is still a good EFT for states close to and just above the threshold, at least as long as their binding energies remain much smaller than the heavy quark mass. The heavy quarks move slowly in these states, and the static limit should remain a good starting point.

To construct a quark–gluon-based EFT description is difficult, because it entails identifying the dynamical degrees of freedom, symmetries, and an appropriate and small expansion parameter. Lattice *ab initio* calculations are also difficult because they require dealing with a plethora of excited states and also considering scattering states; however, we will present pioneering results in both directions.

In the next section we will deal with quarkonia below the threshold. For the case of charmonium, all such states have been observed. For bottomonium most S-wave and P-wave states have been observed with exception of the $\eta_b(3S)$ and most $3P$ states. Only one bottomonium $1D$-wave state below the $B\bar{B}$ threshold has been observed and no $2D$ states. Observation of $2D$ and other excited states is a challenging task from an experimental point of view; various search strategies are discussed in Sect. 14.7.

14.3.3. Lattice

N. Brambilla, S. Prelovsek

Lattice QCD obtains an expectation value of a desired quantity C via numerical path integration $\int \mathcal{D}G\mathcal{D}q_i\mathcal{D}\bar{q}_i e^{-S_{\rm QCD}} C$ formulated on a discretized and finite Euclidean space-time. The parameters of the lattice action $S_{\rm QCD}$ are the quark masses m_{q_i} and the strong coupling g_s. The quantity C that gives information on the quarkonium(-like) masses is the correlator $C(t) = \langle \Omega | \mathcal{O}(t) \mathcal{O}^\dagger(0) | \Omega \rangle$. Here, operators $\mathcal{O} \simeq \bar{Q}Q$ or $\bar{Q}q\bar{q}Q$ create/annihilate the system with quantum numbers of interest and $|\Omega\rangle$ is the vacuum. The correlator renders energies of QCD eigenstates and therefore hadron masses via Eq. (488) below. For a pedagogical introduction we refer to the excellent books of Refs. [1066] and [1067]. Some recent reviews on spectroscopy including quarkonium(-like) states are given in Refs. [1068–1070].

Two approaches concerning the heavy quark Q that enters the correlator C are employed: (i) Q can be a moving (i.e. non-static) quark, where particular care is needed in discretization due to the non-zero lattice spacing—the c quark is often treated with a proper relativistic formulation, while the heavier b is approached with $\mathcal{L}_{\rm NRQCD}$ or with improved discretizations of $\mathcal{L}_{\rm QCD}$. (ii) The heavy quark, particularly $Q = b$, can alternatively be treated as static in the zeroth order of strongly coupled pNRQCD (Sect. 14.4.2). The employed operator $\mathcal{O} = \bar{Q}(0)Q(r)$ or $\bar{Q}(0)q\bar{q}Q(r)$ keeps Q and $\bar{Q}$ at a fixed distance r and the correlator leads to the potential $V(r)$. Quarkonium masses are then extracted from the Schrödinger equation.

The matrix elements for electromagnetic and weak transitions are extracted from an analogous path integral with $C = \langle \Omega | \mathcal{O}_f(t_f)\, J^\mu(Q,t)\, \mathcal{O}_i(t_i) | \Omega \rangle$ which involves the transition matrix element $H_i \to H_f$ as detailed in Eq. (489).

The described procedure straightforwardly leads to hadron masses and transitions only for hadrons that are stable with respect to strong decay and are away from thresholds. This (approximately) applies for quarkonium below the $D\bar{D}$ and $B\bar{B}$ thresholds. The properties of the resonances $R \to H_1 H_2$ and states near the $m_{H_1} + m_{H_2}$ threshold have to be inferred from simulating the $H_1 H_2$ scattering on the lattice and extracting the scattering matrix. Pioneering work concerning quarkonium(-like) states has recently employed this strategy, and is discussed in Sect. 14.5.4.

14.4. Theory for heavy quarkonium states below the open flavor threshold

In this section we summarize the theory for states below the threshold and corresponding applications to spectra, transitions, and decays.

14.4.1. Weakly coupled pNRQCD

Authors: N. Brambilla, Y. Kiyo, A. Vairo

For systems with a small radius ($mv \gg \Lambda_{\rm QCD}$), the effective Lagrangian is organized as an expansion in $1/m$ and $\alpha_s(m)$, inherited from NRQCD, and an expansion in r (r being the quark–antiquark distance, $r \sim (mv)^{-1}$) [1062]:

$$\mathcal{L}_{\rm pNRQCD} = \int d^3 r \sum_n \sum_k \frac{c_n(\alpha_s(m),\mu)}{m^n} \times V_{n,k}(r,\mu',\mu)\, r^k \times O_k(\mu', mv^2, \ldots), \tag{481}$$

where O_k are the operators of pNRQCD that are dominant at the low-energy scale mv^2, μ' is the pNRQCD factorization scale, and $V_{n,k}$ are the Wilson coefficients of the EFT that encode the contributions from the scale r and are non-analytic in r: they are the potentials. The degrees of freedom that make up the operators O_k are $Q\overline{Q}$ states, color singlet S, color octet $O_a T^a$, and (ultrasoft)

gluons. The operators are defined in a multipole expansion. In the equations of motion of pNRQCD, we may identify $V_{n,0} = V_n$ with the $1/m^n$ potentials that enter the Schrödinger equation and $V_{n,k\neq 0}$ with the couplings of the ultrasoft degrees of freedom that provide non-potential corrections to the Schrödinger equation. Since the degrees of freedom that enter the Schrödinger description are, in this case, both $Q\overline{Q}$ color singlet and $Q\overline{Q}$ color octets, both singlet and octet potentials exist. The bulk of the interaction is contained in potential-like terms, but non-potential interactions, associated with the propagation of low-energy degrees of freedom, are, in general, present as well, and start to contribute at NLO in the multipole expansion. They are typically related to non-perturbative effects.

If the quarkonium system is small, the soft scale is perturbative and the potentials can be *entirely* calculated in perturbation theory. They are renormalizable, develop a scale dependence, and satisfy renormalization group equations that eventually allow resummation of potentially large logarithms.

The singlet potential V_S is a quantity of great relevance and it has been studied since the inception of QCD. When the soft scale is perturbative, it can be calculated in perturbation theory and it is given by the sum of the static singlet potential V_0 and $1/m$ and $1/m^2$ spin-dependent and velocity-dependent singlet potentials [1071,1072],

$$V_S = V_0(r) + V_{1/m}(r) + V_{1/m^2}(r) + \cdots \tag{482}$$

In particular, the static potential is $V_0(r) = -C_F\alpha_V(r)/r$, where $\alpha_V(r)$, which represents α_s in the V scheme and parameterizes the strength of the interquark force, is presently fully known at three loops [1073,1074]. The static potential develops a logarithmic divergence that is compensated in the static energy by the presence of low-energy gluons [1075].

The quark–antiquark static energy is given in perturbation theory by the sum of the static singlet potential and the ultrasoft correction (coming from the low-energy gluons), $E(r) = V_0(r) + \delta E_{us}$, and it is a function of the quark–antiquark distance r. It is known at next-to-next-to-next-to-leading (NNNLL) logarithmic accuracy [1076]. It is a physical quantity, to be identified with the QCD static energy, and its perturbative determination can be compared to the lattice determination.

In Fig. 166, such a comparison is shown [1074,1077,1078] in a short distance region, where the higher-order perturbative computation and the lattice determination agrees well—the agreement persists up to about 0.25 fm. The quark–antiquark distance r is given in terms of the lattice Sommer scale $r_0 \sim 0.5$ fm.

Spectroscopy and precise determination of SM parameters
Authors: N. Brambilla, Y. Kiyo, A. Vairo

Using the pNRQCD Lagrangian in Eq. (481), quarkonium energy levels have been calculated for general quantum number $n^{2s+1}L_j$ to NNLO [1079,1080] and NNNLO [1071,1072,1081]. To perform a phenomenological analysis it is necessary to cure the problem of the perturbative series (technically one should enforce the infrared renormalon cancellation [1082,1083] between the static potential $V_0(r)$ and heavy quark pole mass m_q). This can be conveniently done by using a variety of heavy quark short-distance masses. For the quarkonium spectroscopy such an analysis was performed in Refs. [1084] and [1085] at NNLO and NNNLO, respectively, using the $\overline{\rm MS}$ mass. The bottomonium spectrum below the $B\bar{B}$ threshold predicted at NNLO and NNNLO and the corresponding experimental values are summarized in Fig. 167. As input values, $\alpha_s^{(5)}(M_z) = 0.1184$, $m_b^{\overline{\rm MS}}(m_b^{\overline{\rm MS}}) = 4.20\,\text{GeV}$ are used, where $m_b^{\overline{\rm MS}}$ is adjusted to reproduce the experimentally measured mass $M_{\Upsilon(1S)} = 9.460\,\text{GeV}$.

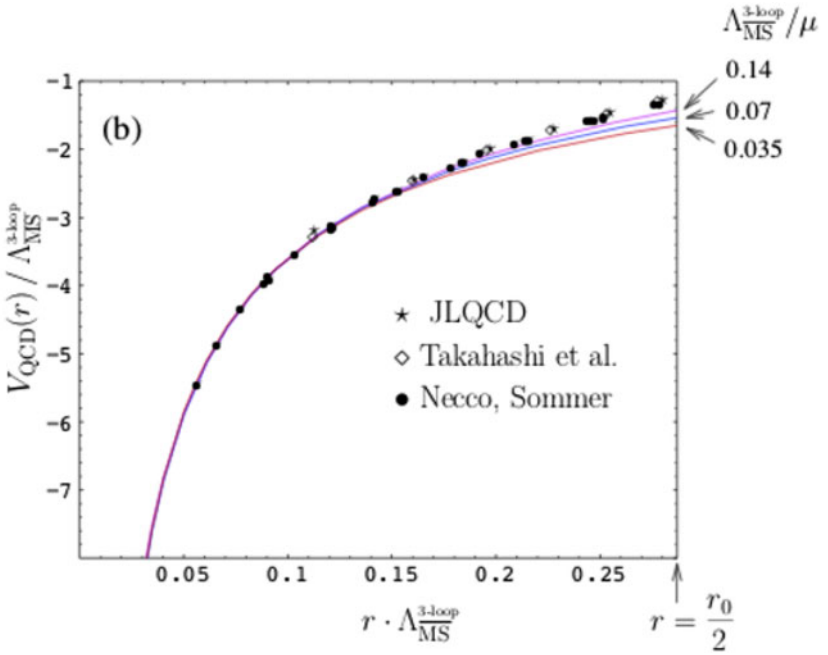

Fig. 166. Comparison in Ref. [1074] between the potential in the weak-coupling expansion in pNRQCD and lattice simulation of the static energy.

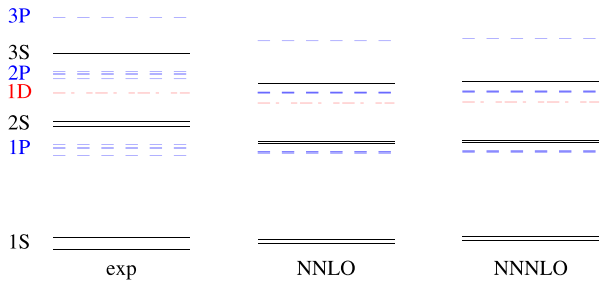

Fig. 167. Experimental and perturbative QCD results [1085] for bottomonium spectrum. The black, blue, and red lines correspond to S-wave ($\Upsilon(nS)$, $\eta_b(nS)$), P-wave ($\chi_b(nP)$, $h_b(nP)$), and D-wave ($\Upsilon(1D; J^{PC} = 2^{--})$). For $n = 3$ states, only the spin triplet states $\Upsilon(3S)$ (black line) and J-averaged $\chi_b(3P)$ (dashed blue line) are shown.

Although the overall structures are well explained by the fixed-order perturbative predictions, some of the level splittings are far from the experimental value. This is to be expected for excited states for which the typical radius is no longer smaller than the confinement scales, and for which non-perturbative effects become dominant at the level of the potential.

Dedicated studies of the ground state hyperfine splitting have been performed for bottomonium [1086,1087] with the result $M(\Upsilon(1S)) - M(\eta_b(1S) = 41 \pm 14\,\text{MeV}$, and for B_c with the result $M(B_c^*) - M(B_c) = 50 \pm 17(th)^{+15}_{-12}(\delta\alpha_s)\,\text{MeV}$ [1088], where *th* represents the uncertainty due to high-order perturbative corrections and non-perturbative effects, and $\delta\alpha_s$ the uncertainty in $\alpha_s(M_Z)$.

For most of the phenomenological analyses for bottomonia the charm quark mass effect is neglected, but there exist some theory predictions [1089–1092] for the $1S$ energy levels that include the effect of finite charm mass. Such an analysis becomes important for precision bottom quark mass extraction from experimentally measured $1S$ bottomonium masses. In Fig. 168 $1S$ bottomonium masses versus the $\overline{\text{MS}}$ bottom quark mass is shown. The extracted bottom quark masses are given

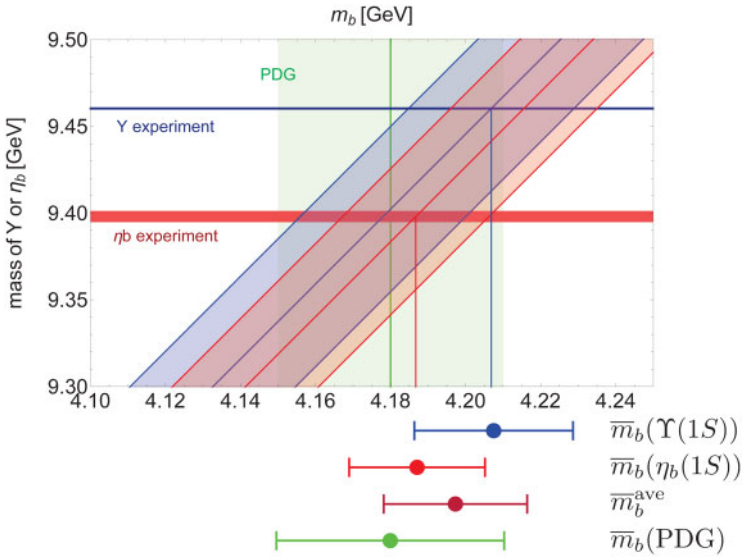

Fig. 168. $\Upsilon(1S)$, $\eta_b(1S)$ masses vs. bottom quark $\overline{\rm MS}$ mass taking into account finite charm quark mass [1091]. The blue and red regions indicate the theory ambiguity for $\Upsilon(1S)$ and $\eta_b(1S)$, respectively, for a given $m_b^{\overline{\rm MS}}$.

by $m_b^{\overline{\rm MS}}(m_b^{\overline{\rm MS}}) = 4.207$ and $4.187\,\text{GeV}$, which reproduce the experimental masses of $\Upsilon(1S)$ and $\eta_b(1S)$, respectively. Combining these values leads to one of the most precise bottom quark mass determinations from a perturbation approach,

$$\overline{m}_b^{\rm ave} = (4197 \pm 2(d_3) \pm 6(\alpha_s) \pm 18(\text{h.o.}) \pm 5(m_c))\ \text{MeV}, \tag{483}$$

where the errors correspond to uncertainties on a constant called d_3, in the potential, on α_s, higher-order terms (*h.o.*), and the input m_c value, respectively [1091]. This shows the importance of systematic computations in the effective field theory approach.

Although one can predict the charmonium masses with exactly the same formula used for bottomonium, replacing $(m_b, n_l = 4)$ by $(m_c, n_l = 3)$, most of the charmonium states have too large a radius and therefore a soft scale lying outside the perturbative regime. For instance, the minimal sensitivity scale for which the perturbative prediction is stable against the μ variation is given by $\mu \sim 2\,\text{GeV}$ $(\alpha_s \sim 0.3)$ for the low-lying states $\eta_c(1S), J/\Psi(1S)$, while for excited charmonium states $\mu \leq 0.8\,\text{GeV}$ $(\alpha_s \geq 0.6)$ and perturbative expansion in α_s fails to converge. As a result, except for the low-lying $\eta_c(1S)$ and $J/\psi(1S)$, the perturbative series for the energy levels does not converge well. For instance, the perturbative series with $m_c^{\overline{\rm MS}} = 1226, 1266\,\text{MeV}$ gives $M^{\rm pert}_{\eta_c(1S)} = (2452 + 242 + 162 + 103 + 24)\,\text{MeV}$, $M^{\rm pert}_{J/\psi(1S)} = (2532 + 263 + 170 + 109 + 23)\,\text{MeV}$, respectively, where the last terms represent the $\mathcal{O}(m_c\alpha_s^5)$ binding energy corrections. The values are obtained by evaluating the perturbative series in $\alpha_s(\mu) = 0.269, 0.288$ with $\mu = 2.45, 2.13\,\text{GeV}$ for $\eta_c(1S), J/\Psi(1S)$, respectively. On average the charm quark $\overline{\rm MS}$ mass is

$$\overline{m}_c^{\rm ave} = (1246 \pm 2(d_3) \pm 4(\alpha_s) \pm 23(\text{h.o.}))\ \text{MeV}. \tag{484}$$

By comparing the lattice calculation of the static energy and the static potential at NNNLL in perturbation theory it was possible to extract a precise determination of α_s: $\alpha_s(M_Z) = 0.116^{+0.0012}_{-0.0008}$ [1077,1078]. Precise lattice data at a smaller quark–antiquark distance will allow a more precise

extraction. Such extractions of the strong coupling constant from quarkonium are important because they are independent from other determinations and are done at high order in perturbation theory.

Decays and transitions

Authors: N. Brambilla, Y. Kiyo, A. Vairo

While the quarkonium energy levels are evaluated by computing expectation values of the non-relativistic Hamiltonian, the quarkonium decay widths depend on the square of the wave functions; for example, leptonic widths are determined by the wave function at the origin $|\psi(0)|^2$. Reliable predictions for the leptonic decays enable another useful check of the QCD dynamics. The leptonic decay width $\Upsilon(1S) \to \ell^+\ell^-$ for the bottomonium ground state is calculated to NNNLO QCD [1093] as

$$\begin{aligned}\Gamma(\Upsilon(1S) \to \ell^+\ell^-) &= \frac{32}{243}\alpha^2\alpha_s^3 m_b^{\rm PS}(1 + 0.37 + 0.95 - 0.04) \\ &= 1.08 \pm 0.05(\alpha_s)^{+0.01}_{-0.20}(\mu)\,\text{keV},\end{aligned} \tag{485}$$

to be compared with the measurement $\Gamma(\Upsilon(1S) \to e^+e^-) = 1.340\,\text{keV}$. In Eq. (485) the uncertainties are due to uncertainty of $\alpha_s(M_z)$ and the scale variation ($3\,\text{GeV} < \mu < 10\,\text{GeV}$). Here, the theory prediction was evaluated using a potential subtracted mass $m_b^{\rm PS} = 4.484\,\text{GeV}$, which corresponds to $m_b^{\overline{\rm MS}} = 4.163\,\text{GeV}$. This means that even at NNNLO the theory prediction lacks roughly a 30% contribution, which remains substantial even if the theoretical uncertainty is taken into account. There can be non-perturbative effects related to non-local gluon condensates [1053,1062] or local gluon condensate corrections [1094,1095], which are not well known and therefore not included or estimated in the above theory prediction. It would be important to develop estimates of such non-perturbative condensate corrections. The decays of charmonium are more challenging in perturbative QCD because of the bad convergence of the perturbation series.

The two-photon decay width $\eta_b(1S) \to \gamma\gamma$ and the leptonic decay width are proportional to the same wave function to NLO, due to the spin symmetry of heavy quarks. This suggests that the decay ratio $\Gamma(n^3S_1 \to e^+e^-)/\Gamma(n^1S_0) \to \gamma\gamma)$ [1096,1097] is more appropriate to obtain reliable results that are stable against the renormalization scale variation. Using $\Gamma(\Upsilon(1S) \to e^+e^-) = 1.340 \pm 0.018\,\text{keV}$ as an input, the spin ratio provides a prediction for the spin singlet decay width [1097]:

$$\Gamma(\eta_b(1S) \to \gamma\gamma) = (0.54 \pm 0.15)\,\text{keV}. \tag{486}$$

Among quarkonium transitions, electromagnetic transitions [1100] are theoretically clean and rather straightforward compared to the hadronic ones. The pNRQCD descriptions of magnetic dipole (M1) and electric dipole (E1) radiative transitions have been developed in Refs. [1098,1101], and the precision was raised to $k_\gamma^3/m^2 \times \mathcal{O}(\alpha_s^2, v^2)$ and $k_\gamma^3/m^2 \times \mathcal{O}(v^4)$ (k_γ emitted photon energy) for the allowed and hindered magnetic dipole transitions, respectively, in Ref. [1099]. In this latter work several improvements were obtained taking into account the higher-order corrections of the heavy quark static potential, $\mathcal{O}(\alpha_s^2)$ correction to the heavy quark anomalous magnetic moment, and the LL resummation of large logarithms for the NRQCD interactions. The results are summarized in Table 124. While there are no experimental data for $2^1S_0 \to 1^3S_1\gamma$, the radiative transition $2^3S_1 \to 1^1S_0\gamma$ is available and the theory prediction $\Gamma(\Upsilon(2S) \to \eta_b(1S)\gamma) = 6^{+26}_{-6}\,\text{eV}$ agrees within uncertainties with the experimental value $\Gamma_{\rm exp} = 12.5(4.8)\,\text{eV}$ [88].

Table 124. Widths for the magnetic dipole transitions in pNRQCD for bottomonium and charmonium in eV. Note that different values for the photon energy $k_\gamma = (M_i^2 - M_f^2)/(2M_i)$ are used for some theory predictions.

Decay	Ref. [1098]	Ref. [1099]
$\Upsilon(1S) \to \eta_b(1S)\gamma$	3.6(2.9)	15.18(51)
$h_b(1P) \to \chi_{b0}(1P)\gamma$	1.0(2)	0.962(35)
$h_b(1P) \to \chi_{b1}(1P)\gamma$	17(4)	$8.99(55) \times 10^{-3}$
$\chi_{b2}(1P) \to h_b(1P)\gamma$	90(20)	0.118(6)
$\Upsilon(2S) \to \eta_b(2S)\gamma$		0.668(60)
$\Upsilon(2S) \to \eta_b(1S)\gamma$		6^{+26}_{-06}
$\eta_b(2S) \to \Upsilon(1S)\gamma$		
$J/\psi(1S) \to \eta_c(1S)\gamma$	$1.5(1.0) \times 10^3$	$2.12(40) \times 10^3$

The radiative transition for J/ψ is also available and $\Gamma_{\rm exp}(J/\psi \to \eta_c(1S)\gamma) = (1.58 \pm 0.37)$ keV is consistent with the theory predictions.

Calculations of higher-order contribution in E1 transitions and related applications to the phenomenology are under way [1102].

The study of electromagnetic radiative transition in the EFT approach enables model-independent analyses of the decays, including photon energy line shapes [1103]. All this can provide additional insights into bound state dynamics, e.g. from the electromagnetic radius $\langle r^2 \rangle$ and expectation value $\langle p^2 \rangle$ of quarkonia based on first principles of QCD.

14.4.2. Strongly coupled pNRQCD

Authors: N. Brambilla, A. Vairo

For systems with a radius $r^{-1} \sim mv \sim \Lambda_{\rm QCD}$ the soft scale is non-perturbative. Only color singlet quark–antiquark operators can appear in the EFT at the soft scale. The matching to NRQCD is organized as an expansion in $1/m$, but no expansion in α_s can be made at the soft scale. Consequently the matching coefficients of pNRQCD (the potentials) are non-perturbative objects defined through QCD averages of gauge-invariant non-local operators called generalized Wilson loops.

Potentials, energy levels, inclusive decays

Authors: N. Brambilla, Y. Kiyo, A. Vairo

When $mv \sim \Lambda_{\rm QCD}$ the color singlet quark–antiquark pair S is the only dynamical degree of freedom and the pNRQCD Lagrangian is written as [1053,1064,1065]:

$$\mathcal{L}_{\rm pNRQCD} = S^\dagger \left(i\partial_0 - \frac{\mathbf{p}^2}{2m} - V_S(r) \right) S. \tag{487}$$

The singlet potential $V_S(r)$ can be expanded in powers of the inverse of the quark mass; static, $1/m$, and $1/m^2$ terms were calculated long ago [1064,1065]. The form of these potentials is summarized in Ref. [1053]. They involve NRQCD matching coefficients (containing the contribution from the hard scale) and low-energy non-perturbative parts given in terms of static Wilson loops and field strength insertions in the static Wilson loop (containing the contribution from the soft scale). In this regime of pNRQCD, we recover the quark potential singlet model. However, here the potentials are calculated from QCD by non-perturbative matching. These generalized Wilson loops have been calculated on the lattice (for the most precise recent determination, see Refs. [1104,1105]) and in QCD vacuum models [1106–1108].

Then, away from and below the open flavor thresholds, all the heavy quarkonium masses can be obtained by solving the Schrödinger equation with such potentials [1106,1109].

An example for the application of this method is the mass of the h_b. The lattice data show a vanishing long-range component of the spin–spin potential. Thus, the potential appears to be entirely dominated by its short-range, delta-like, part, suggesting that the $^1P_1$ state should be close to the center of gravity of the ^3P_J system. Indeed, this is consistent with measurements [1110,1111].

If we explicitly consider light quarks, each quarkonium state may develop a width due to decay through pion emission. Pions in this situation act as ultrasoft degrees of freedom. The heavy–light states develop a mass gap of order $\Lambda_{\rm QCD}$ with respect to quarkonium [1112]. The imaginary parts of the potentials give the quarkonium inclusive decay widths [1112]. In particular, the NRQCD low-energy matrix elements can be rewritten in pNRQCD in terms of quarkonium wave functions and a few universal purely gluonic correlators, reducing in this way the number of unknowns. However, lattice calculations of these gluonic correlators have not yet been performed.

14.4.3. Lattice QCD

Author: S. Prelovsek

Quarkonia $\bar{Q}Q$ below the open flavor threshold are discussed in this section—those that are (almost) stable in the approximation when heavy quark annihilation is omitted. This simplifying approximation of omitting the Wick contraction related to $\bar{Q}Q$ annihilation is undertaken in all the lattice studies presented below. We also present results on higher-lying charmonia that are treated as stable, i.e. their strong decay to a pair of charmed hadrons is ignored. Resonances that are considered as unstable and near-threshold states are discussed in Sect. 14.5.4.

The mass of a stable hadron $m_n = E_n(P=0)$ is obtained from the energy E_n of the lattice QCD eigenstate $|n\rangle$ at zero momentum. The eigenenergies E_n are extracted from the time dependence of the correlation functions

$$C_{ij}(t) = \langle \Omega | \mathcal{O}_i(t) \mathcal{O}_j^\dagger(0) | \Omega \rangle = \sum_n Z_i^n Z_j^{n*} e^{-E_n t}, \tag{488}$$

where $Z_i^n \equiv \langle \Omega | \mathcal{O}_i | n \rangle$ and $|\Omega\rangle$ denotes the vacuum. The $\mathcal{O}_i$ are the interpolating fields that create/annihilate the physical system with given quantum numbers J^{PC}, and only operators of type $\mathcal{O} \simeq \bar{Q}Q$ ($Q = c, b$) are used throughout this section. In fact, the continuum rotation group is reduced on the lattice to a discrete one, and operators correspond to irreducible representations of the discrete group. Several J^P contribute to a given irreducible representation and careful studies are needed to identify the quantum numbers of the eigenstates.

Spectra below the open flavor threshold The masses of charmonia $m_n = E_n(P=0)$ obtained from the correlation functions in Eq. 488 are extrapolated to continuum, infinite volume, and physical quark masses. The simulations involve light dynamical quarks and non-static heavy quarks with variety of heavy quark discretizations. Recent precision spectra [1114–1118] are in impressive agreement with the experimental masses, and there are no major open issues. The main remaining uncertainty is due to the omission of $c\bar{c}$ annihilation.

The spectrum of bottomonia below $B\bar{B}$ contains many more states. The recent lattice spectrum in Fig. 169 [1113] is based on non-static b quarks within NRQCD and presents valuable guidance for states that have not been found in experiment yet.

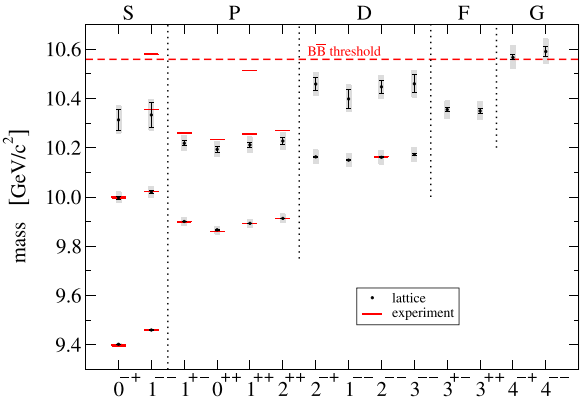

Fig. 169. Lattice spectra of bottomonia below the $B\bar{B}$ threshold from Ref. [1113]. The J^{PC} and L of the $\bar{b}b$ multiplet are shown.

The other approach considers the strongly coupled potential NRQCD introduced in Sect. 14.4.2, which determines $\bar{Q}Q$ potentials $V(r)$ at orders $1/m^0$, $1/m$, and $1/m^2$ in the heavy quark expansion [1064,1065]. The most precise lattice determination of those potentials has been done in the quenched approximation [1104,1105,1109], where the spin-independent $1/m^2$ corrections are still missing. The spectra of charmonia and bottomonia based on these potentials are shown in [1109, Figs. 2 and 3]. The analogous dynamical results suffer from large errors at present, but work is underway.

Charmonia within a single-hadron approach The most extensive spectra of the excited charmonia have been calculated within the so-called single-hadron approach by the Hadron Spectrum Collaboration. Several complete quark–antiquark multiplets nL were found in a recent simulation with $m_\pi \simeq 240\,\mathrm{MeV}$ [195] (green boxes in Fig. 170). Comparison with earlier spectra at $m_\pi \simeq 400\,\mathrm{MeV}$ [1119] and those at $m_\pi \simeq 240\,\mathrm{MeV}$ shows only mild light quark mass dependence [195, Fig. 6].[43] Multiplets of hybrid states were also found (shown in red and blue) and some of them carry exotic J^{PC}. Spectra of excited D and D_s mesons were also presented in Ref. [195]. The single-hadron treatment ignores strong decays of resonances and threshold effects. It provides valuable reference spectra, but cannot lead to reliable conclusions on the existence of near-threshold exotic states, for example.

Radiative transitions and leptonic widths Certain transitions were investigated between quarkonia that lie below the strong decay threshold. The transition $\langle H_f|J^\mu(Q)|H_i\rangle$ is typically determined from correlators of the type

$$\langle\Omega|\mathcal{O}_f(t_f)\,J^\mu(Q,t)\,\mathcal{O}_i(t_i)|\Omega\rangle \propto \sum_{H_i,H_f} \langle\Omega|\mathcal{O}_f|H_f\rangle e^{-E_{H_f}(t_f-t)}\langle H_f|J^\mu(Q,t)|H_i\rangle e^{-E_{H_i}(t-t_i)}\langle H_i|\mathcal{O}_i|\Omega\rangle, \quad (489)$$

where $\mathcal{O}_i$ ($\mathcal{O}_f$) are interpolators that create a tower of initial (final) hadrons with certain quantum numbers. The leptonic decay constants of vector mesons $V \to l^+l^-$ are obtained by extracting $\langle 0|J^\mu|V\rangle$ from correlators.

[43] For excited charmonia close to S-wave open charm thresholds, a non-analytic pion mass dependence is expected which could be sizeable [1120].

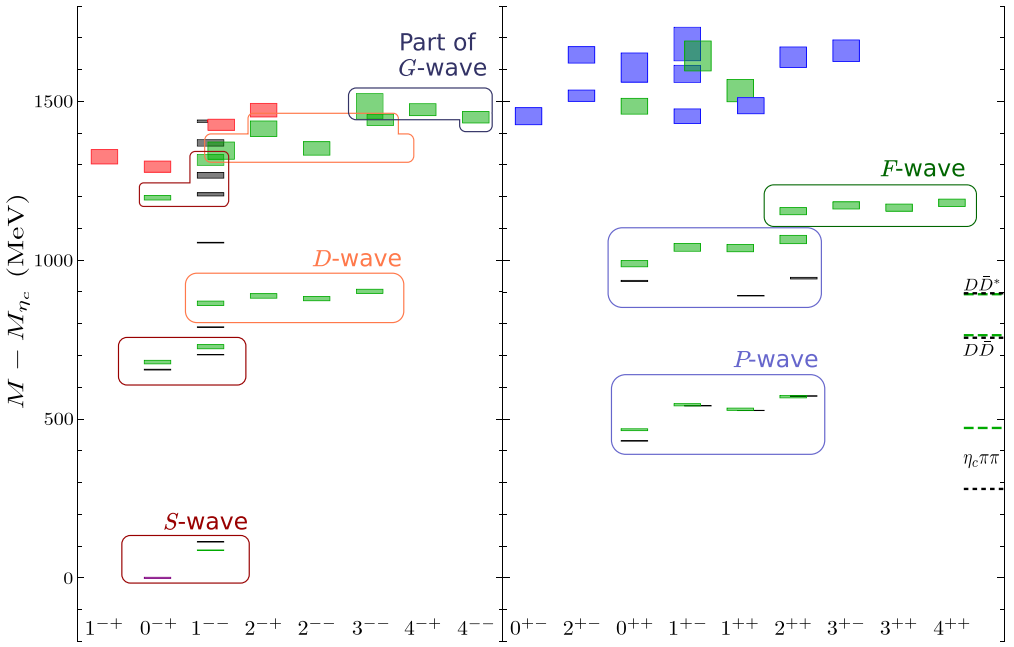

Fig. 170. Lattice spectra of excited charmonia within the single-hadron approximation at $m_\pi \simeq 240\,\mathrm{MeV}$ [195]. Lattice results are shown in green (conventional $c\bar{c}$ multiplets nL), red, and blue (hybrid candidates from lightest and first-excited supermultiplets, respectively). Experimental masses are shown by black lines. The multiplets are identified based on overlaps $\langle\Omega|\mathcal{O}_i|n\rangle$ [Eq. (488)].

An extensive study by the HPQCD collaboration with full error budget led to $\Gamma^{\mathrm{lat}}[\Upsilon(2S) \to \eta_b(1S)\gamma] = 1.72(55)\cdot 10^{-2}\,\mathrm{keV}$ using lattice NRQCD [1121]. This hindered M1 transition would have zero rate in the extreme non-relativistic limit due to the orthogonality of the radial wavefunctions. So its matrix element is sensitive to a multitude of effects such as relativistic corrections to the leading-order current and to the wave functions, particularly those which affect the hyperfine splitting. Such delicate effects also need to be considered when fitting the photon spectra from the experimental data.

The leptonic widths for $\Upsilon(1S, 2S, 3S)$ and the matrix elements for radiative transitions $\Upsilon(1S, 2S, 3S) \to \gamma\eta_b(1S)$, $\Upsilon(2S) \to \gamma\eta_b(2S)$, $\eta_b(2S, 3S) \to \gamma\Upsilon(1S)$ were determined with lattice NRQCD in Ref. [1122]. The subsequent higher-order corrections $O(v^6)$ [1123] led to better agreement with the observed widths $\Upsilon(2S, 3S) \to \gamma\eta_b(1S)$. It would be interesting to compare the rates of $\Upsilon(2S) \to \gamma\eta_b(1S)$ and $\eta_b(2S) \to \gamma\Upsilon(1S)$, since the difference of the rates arises solely from the spin-dependent interactions.

The quenched study of radiative transitions between charmonia [1124] considered ground states as well as excited states, states of high spin, and hybrids. The excited charmonia above the open charm threshold were treated in the simplified single-hadron approach discussed above. The dynamical simulation that also considered the extrapolation to the continuum limit rendered $\Gamma(J/\psi \to \eta_c\gamma) = 2.64(11)(3)\,\mathrm{keV}$, within $2\,\sigma$ of the experimental value, and predicted $\Gamma(\eta_c(2S) \to J/\psi\gamma) = (15.7 \pm 5.7)\,\mathrm{keV}$ and $\Gamma(h_c \to \eta_c\gamma) = 0.72(5)(2)\,\mathrm{MeV}$ [1125,1126]. The transitions between ground state charmonia were also determined in Ref. [1127], and favorable comparison with experiment is provided in [1127, Table IV]. A comparison of quenched and dynamical calculations can provide important information for the role of light quarks in heavy quarkonium systems [1120], which may lead to new insights into the XYZ structures to be discussed below.

Hadronic transitions between quarkonia (via π, η, $\pi\pi$, etc.) have not been considered in lattice QCD to our knowledge. The transitions via a single pion could potentially be addressed by studying

the matrix element $\langle H_2|u\gamma^m u\gamma_5 d|H_1\rangle$. The general hadronic transitions and related non-leptonic decays are challenging for lattice QCD study. The framework and prospects to study non-leptonic decays on the lattice are discussed in the theory overview of this report.

14.4.4. Summary

In summary, the theory for quarkonium states below threshold has been constructed and highly developed. Thanks to this, quarkonium can be described in QCD and becomes an important system to probe strong interactions. Lattice calculation of masses and electroweak matrix elements is generally straightforward for such states. On the EFT side, the soft scale is perturbative for systems characterized by a small radius (lowest states). Non-perturbative corrections appear in the form of local and non-local condensates; in this case, high-order resummed perturbation theory and lattice can be compared to experiment, and quarkonium becomes a tool for precision determinations. For systems characterized by a larger radius (higher states) the soft scale is non-perturbative, but quarkonium properties can still be calculated either with the EFT potentials or directly from the lattice, and quarkonium becomes a tool for the investigation of confinement. The alliance of EFTs and lattice will be important for further progress.

14.5. Theory and theory predictions for quarkonia at and above the open flavor threshold

14.5.1. Introduction

Authors: N. Brambilla, A. Vairo

When we consider the region close to or above the lowest open flavor threshold (see Tables 125 and 126), things change substantially compared to the physics of the previous section. First, let us consider the simplified case without light quarks, in which case the degrees of freedom are heavy quarkonium, heavy hybrids (i.e. bound states of heavy quark, heavy antiquark, and gluonic excitations), and glueballs. In the static limit, at and above the $\Lambda_{\rm QCD}$ threshold, a tower of hybrid static energies (i.e. of gluonic excitations) should be considered on top of the $Q\overline{Q}$ static singlet energy. The spectrum has been thoroughly studied on the lattice [1128]. At short quark–antiquark distance, the spectrum of the hybrid static energies is described in the leading multipole expansion of pNRQCD by the octet potential plus a non-perturbative mass scale, which is called *gluelump mass* [1062,1129]. At large distances the static energies resemble a string pattern. Some of these states may develop a width if decays to lower states with glueball emission (such as hybrid $\to$ glueball + quarkonium) are allowed.

Then, once light fermions have been incorporated into the spectrum to describe the realistic situation, new gauge-invariant states appear beside the heavy quarkonia, hybrids, and glueballs. In fact, close to the threshold there is no longer a mass gap between the heavy quarkonium and the creation of a $\overline{Q}q$–$Q\overline{q}$ pair. Thus, for a study of near-threshold heavy quarkonia, these degrees of freedom must be included in the spectrum and in the effective field theory Lagrangian. States made of $Q\bar{Q}$ and light quarks and antiquarks include those built on pairs of heavy–light mesons ($D\bar{D}$, $B\bar{B}$, …) and pairs of heavy–light baryons, like hadronic molecular states; states composed of the usual quarkonium states (built on the static potential) and light hadrons (hadro-quarkonium); tetraquark states; and likely many others. Moreover, how these different kinds of states "talk to each other" becomes an important issue. This explains why, from the QCD point of view, so many states of a new nature may appear in this region of the spectrum. However, a systematic QCD description of these states has not yet been developed and it is not yet possible to derive from QCD what the dominant degrees of freedom and their interactions are.

Table 125. Quarkonium-like states at the lowest open flavor thresholds.

State	M [MeV]	Γ [MeV]	J^{PC}	Process (mode)	Experiment ($\#\sigma$)	Year	Status
$X(3872)$	3871.69 ± 0.17	< 1.2	1^{++}	$B \to K(\pi^+\pi^- J/\psi)$	Belle [1049,1137] (>10), BaBar [1138] (8.6)	2003	Ok
				$p\bar{p} \to (\pi^+\pi^- J/\psi) \ldots$	CDF [1139–1141] (11.6), D0 [1142] (5.2)	2003	Ok
				$pp \to (\pi^+\pi^- J/\psi) \ldots$	LHCb [1143–1145] (np), CMS [1146] (np)	2012	Ok
				$Y(4260) \to \gamma\,(\pi^+\pi^- J/\psi)$	BESIII [1147] (6.3)	2013	NC!
				$B \to K(\omega J/\psi)$	Belle [1148] (4.3), BaBar [1149] (4.0)	2005	NC!
				$B \to K(\gamma\, J/\psi)$	Belle [1148,1150] (5.5), BaBar [1151,1152] (3.6), LHCb [1153] (> 10)	2005	Ok
				$B \to K(\gamma\, \psi(2S))$	BaBar [1152] (3.5), Belle [1150] (0.2), LHCb [1153] (4.4)	2008	NC!
				$B \to K(D^0 \bar{D}^{*0})$	Belle [1154,1155] (6.4), BaBar [1156] (4.9)	2006	NC!
$Z_c(3900)^+$	3891.2 ± 3.3	40 ± 8	1^{+-}	$Y(4260) \to \pi^-(\pi^+ J/\psi)$	BESIII [1157] (>8), Belle [1158] (5.2), CLEO data [1159] (>5)	2013	Ok
				$Y(4260, 4360) \to \pi^0(\pi^0 J/\psi)$	CLEO data [1159] (3.5), BESIII [1160] (10.4)	2013	Ok
				$Y(4260, 4390) \to \pi^-(\pi^+ h_c)$	BESIII [1161] (2.1)	2013	NC!
				$Y(4260) \to \pi^-(D\bar{D}^*)^+$	BESIII [1162,1163] (18)	2013	Ok
				$Y(4260) \to \pi^0(D\bar{D}^*)^0$	BESIII [1164] (>10)	2015	Ok
$Z_c(4020)^+$	4022.9 ± 2.8	7.9 ± 3.7	$?^{?-}$	$Y(4260, 4390) \to \pi^-(\pi^+ h_c)$	BESIII [1161] (8.9)	2013	NC!
				$Y(4260, 4390) \to \pi^0(\pi^0 h_c)$	BESIII [1165] (>5)	2014	NC!
				$Y(4360) \to \pi^-(\pi^+ \psi(2S))$	Belle [1166] (3.5), BESIII [1167] (9.2)	2014	NC!
				$Y(4260) \to \pi^-(D^*\bar{D}^*)^+$	BESIII [1168] (10)	2013	NC!
				$Y(4260) \to \pi^0(D^*\bar{D}^*)^0$	BESIII [1169] (5.9)	2015	NC!
$Z_b(10610)^+$	10607.2 ± 2.0	18.4 ± 2.4	1^{+-}	$\Upsilon(10860) \to \pi^-(\pi^+\Upsilon(1S, 2S, 3S))$	Belle [1170–1172] (>10)	2011	Ok
				$\Upsilon(10860) \to \pi^0(\pi^0\Upsilon(2S, 3S))$	Belle [1173] (6.5)	2013	NC!
				$\Upsilon(10860) \to \pi^-(\pi^+ h_b(1P, 2P))$	Belle [1170,1171] (16)	2011	Ok
				$\Upsilon(10860) \to \pi^-(B\bar{B}^*)^+$	Belle [1174,1175] (9.3)	2012	NC!
$Z_b(10650)^+$	10652.2 ± 1.5	11.5 ± 2.2	1^{+-}	$\Upsilon(10860) \to \pi^-(\pi^+\Upsilon(1S, 2S, 3S))$	Belle [1170–1172] (>10)	2011	Ok
				$\Upsilon(10860) \to \pi^-(\pi^+ h_b(1P, 2P))$	Belle [1170,1171] (16)	2011	Ok
				$\Upsilon(11020) \to \pi^-(\pi^+ h_b(1P))$	Belle [1176] (3.3)	2015	NC!
				$\Upsilon(10860) \to \pi^-(B^*\bar{B}^*)^+$	Belle [1174,1175] (8.1)	2012	NC!

The states are typically searched as poles in the hadron–hadron scattering matrix. First steps towards the extraction of this scattering matrix from lattice have been done for $D^{(*)}\bar{D}^{(*)}$, possibly coupled with a scattering of charmonium and a light meson.

On a parallel front, models are developed in order to obtain more detailed information on these systems. Exceptional cases, e.g. those for which the state is extremely close to a threshold (like the $X(3872)$), allow for a kind of "universal" effective field theory treatment [1130–1132] largely inspired by EFT treatments for the nucleon–nucleon interaction [1133]. The models, as detailed in the next sections, are based on a special choice of degrees of freedom assumed to be dominant. The resulting models are not equivalent because different dynamics are attributed to different configurations. Due to the absence of further theoretical input from QCD, many tetraquark studies at the moment rely just on phenomenological forms for the tetraquark interaction. This will change in the near future following the first pioneering lattice calculations of tetraquark static energies [1134,1135] and further explorations of the special hierarchy of dynamical scales on top of the non-relativistic and perturbative expansions discussed so far [211,1136].

In the next sections we will summarize the observed exotic states, and introduce various approaches and their predictions. After that we will turn to the lattice QCD and QCD-based effective field theory results existing at the moment.

14.5.2. Observed states

Authors: C. Hanhart, R. Mizuk

All hadrons containing $c\bar{c}$ or $b\bar{b}$ quarks with masses above the $D\bar{D}$ or $B\bar{B}$ thresholds are presented in Tables 125 and 126. The names of the recently observed states are not well established yet. We partly use the convention of the PDG [77]; however, vector and isovector states are denoted Y and Z, respectively. The tables give mass and width values, J^{PC} quantum numbers, a list of the processes in which the state is seen, corresponding references and significances (or "np" for "not provided"), discovery year, and the status for each production and decay channel (here, "NC!" stands for "need confirmation"). For isovector states the C parity is given for the neutral member of the isotriplet.

Table 125 shows the states that have masses very near the lowest open flavor thresholds, e.g. the $X(3872)$ near $D^0\bar{D}^{*0}$, and the $Z_b(10610)$ and $Z_b(10650)$ near $B\bar{B}^*$ and $B^*\bar{B}^*$, respectively. The threshold proximity is often interpreted as a signature for a hadronic molecule; however, also within the tetraquark scenario the appearance of very near threshold states could be natural—for a detailed discussion of these issues see the *Molecules* and *Tetraquarks* subsections of Sect. 14.5.3. All states have properties that make them distinct from quarkonia. The $X(3872)$ decays into $\rho J/\psi$ and $\omega J/\psi$ with comparable probabilities, which corresponds to strong violation of isospin symmetry and is unexpected for quarkonium. The Z_b states are isovectors, thus in addition to a $b\bar{b}$ pair they should contain light quarks. Another interesting property of Z_b is that they decay with comparable probabilities into spin-triplet and spin-singlet bottomonia [$\Upsilon(nS)$ $(n = 1, 2, 3)$ and $h_b(mP)$ $(m = 1, 2)$]. This would correspond to a strong violation of heavy quark spin symmetry (HQSS) for pure quarkonium, but can be explained naturally within both the tetraquark picture [1237] and the molecular scenario [1238]. The isovector states in the charmonium sector, the $Z_c(3900)$ and $Z_c(4020)$, seem to be close relatives of the Z_b states. Their masses as reported in the current literature are located somewhat above the $D\bar{D}^*$ and $D^*\bar{D}^*$ thresholds, which is disastrous for the molecular interpretation. However, those mass determinations take into account neither the interference between the Z_c signals and the non-resonant background, which could shift the peak position by as much as $\Gamma/2$, nor the proper analytic structure of the amplitudes.

Recently, BESIII studied the process $e^+e^- \to \pi^+\pi^-\psi(2S)$ and reported observation of an intermediate charged state [1167]. Previously, Belle had found evidence for this state [1166]. The state is only $2.8\,\sigma$ away from the $Z_c(4020)$[44] and likely corresponds to a new decay channel of that state.

As we move even higher above the lowest open flavor thresholds (see Table 126), the interpretation of the states becomes even more difficult. The number of states in the charmonium region is especially large. All states, except $\psi_2(3823)$ and $X(3860)$, possess properties unexpected for $c\bar{c}$ levels. Most of the states have hadronic transitions to lower charmonia with anomalously high rates. Not only do the recently observed XYZ states have this property, but it is shared by the $\psi(4040)$, $\psi(4160)$, and $\psi(4415)$, known since the 1970s. Indeed, Belle observed the above ψ states in the energy dependence of the $e^+e^- \to J/\psi\,\eta$ cross section using the initial state radiation (ISR) process [1194], and BESIII confirmed this measurement at several energies [1207]. BESIII has also found that the

[44] This number is possibly even smaller, since the errors in masses do not include systematic uncertainties due to neglecting interferences.

Table 126. Quarkonium(-like) states above the open flavor thresholds.

State	M [MeV]	Γ [MeV]	J^{PC}	Process (mode)	Experiment ($\#\sigma$)	Year	Status
$\psi(3770)$	3773.13 ± 0.35	27.2 ± 1.0	1^{--}	$e^+e^- \to (D\bar{D})$	PDG [77]	1977	Ok
				$B \to K(D\bar{D})$	Belle [1177,1178] (5.5), BaBar [1156] (6.4)	2003	Ok
				$e^+e^- \to (\pi^+\pi^- J/\psi)$	BES [1179] (3), CLEO [1180] (11.6)	2003	Ok
				$e^+e^- \to (\pi^0\pi^0 J/\psi)$	CLEO [1180] (3.4)	2005	NC!
				$e^+e^- \to (\eta J/\psi)$	CLEO [1180] (3.5)	2005	NC!
				$e^+e^- \to (\phi\,\eta)$	CLEO [1181] (5)	2005	NC!
				$e^+e^- \to (\gamma\,\chi_{c0,1})$	PDG [77]	2005	Ok
$\psi_2(3823)$ or $X(3823)$	3822.2 ± 1.2	< 16	2^{--}	$B \to K(\gamma\,\chi_{c1})$	Belle [1182] (3.8)	2013	NC!
				$e^+e^- \to \pi^+\pi^-(\gamma\,\chi_{c1})$	BESIII [1183] (6.2)	2015	NC!
$X(3860)$	3862^{+48}_{-35}	201^{+177}_{-106}	$0/2^{++}$	$e^+e^- \to J/\psi\,(D\bar{D})$	Belle [1184] (6.5)	2017	NC!
$X(3915)$ or $Y(3940)$	3918.4 ± 1.9	20 ± 5	$0/2^{?+}$	$B \to K(\omega J/\psi)$	Belle [1185] (8), BaBar [1149,1186] (19)	2004	Ok
				$e^+e^- \to e^+e^-(\omega J/\psi)$	Belle [1187] (7.7), BaBar [1188] (7.6)	2009	Ok
$\chi_{c2}(2P)$	3927.2 ± 2.6	24 ± 6	2^{++}	$e^+e^- \to e^+e^-(D\bar{D})$	Belle [1189] (5.3), BaBar [1190] (5.8)	2005	Ok
$X(3940)$	3942^{+9}_{-8}	37^{+27}_{-17}	$?^{?+}$	$e^+e^- \to J/\psi\,(D\bar{D}^*)$	Belle [1191,1192] (6)	2005	NC!
$\psi(4040)$	4039 ± 1	80 ± 10	1^{--}	$e^+e^- \to$ (hadrons)	PDG [77]	1978	Ok
				$e^+e^- \to (\eta J/\psi)$	BESIII [1193] (>10), Belle [1194] (6.0)	2012	NC!
$Z(4050)^+$	4051^{+24}_{-43}	82^{+51}_{-55}	$?^{?+}$	$\bar{B}^0 \to K^-(\pi^+\chi_{c1})$	Belle [1195] (5.0), BaBar [1196] (1.1)	2008	NC!
$X(4140)$ or $Y(4140)$	$4146.5^{+6.4}_{-5.3}$	83^{+30}_{-25}	1^{++}	$B^+ \to K^+(\phi J/\psi)$	CDF [1197,1198] (5.0), Belle [1199] (1.9), LHCb [1200] (1.4), CMS [1201] (>5), D0 [1202] (3.1), BaBar [1203] (1.6), LHCb [1204,1205] (8.4)	2009	Ok
				$p\bar{p} \to (\phi J/\psi)\ldots$	D0 [1206] (4.7)	2015	NC!
$\psi(4160)$	4153 ± 3	103 ± 8	1^{--}	$e^+e^- \to$ (hadrons)	PDG [77]	1978	Ok
				$e^+e^- \to (\eta J/\psi)$	Belle [1194] (6.5), BESIII [1207] (>5)	2013	NC!
$X(4160)$	4156^{+29}_{-25}	139^{+113}_{-65}	$?^{?+}$	$e^+e^- \to J/\psi\,(D^*\bar{D}^*)$	Belle [1192] (5.5)	2007	NC!
$Z(4200)^+$	4196^{+35}_{-32}	370^{+99}_{-149}	1^{+-}	$\bar{B}^0 \to K^-(\pi^+ J/\psi)$	Belle [1208] (6.2)	2014	NC!
$Z(4250)^+$	4248^{+185}_{-45}	177^{+321}_{-72}	$?^{?+}$	$\bar{B}^0 \to K^-(\pi^+\chi_{c1})$	Belle [1195] (5.0), BaBar [1196] (2.0)	2008	NC!
$Y(4260)$	4221.1 ± 2.5	47.7 ± 4.0	1^{--}	$e^+e^- \to (\pi^+\pi^- J/\psi)$	BaBar [1209,1210] (8), CLEO [1211,1212] (11), Belle [1158,1213] (15), BESIII [1157,1214] (np)	2005	Ok
				$e^+e^- \to (\pi^0\pi^0 J/\psi)$	CLEO [1211] (5.1), BESIII [1160] (np)	2006	Ok
				$e^+e^- \to (K^+K^- J/\psi)$	CLEO [1211] (3.7)	2006	NC!
				$e^+e^- \to (f_0(980)J/\psi)$	BaBar [1210] (np), Belle [1158] (np)	2012	Ok
				$e^+e^- \to (\pi^+\pi^- h_c)$	BESIII [1161,1215] (10)	2013	NC!
				$e^+e^- \to (\pi^0\pi^0 h_c)$	BESIII [1165] (np)	2014	NC!
				$e^+e^- \to (\omega\chi_{c0})$	BESIII [1216] (>9)	2014	NC!
				$e^+e^- \to (\gamma\,X(3872))$	BESIII [1147] (6.3)	2013	NC!
				$e^+e^- \to (\pi^- Z_c(3900)^+)$	BESIII [1157,1163] (>8), Belle [1158] (5.2)	2013	Ok
				$e^+e^- \to (\pi^0 Z_c(3900)^0)$	BESIII [1160,1164] (10.4)	2015	Ok
				$e^+e^- \to (\pi^{\mp,0} Z_c(4020)^{\pm,0})$	BESIII [1161,1168] [1165,1169] (>10)	2013	Ok

(continued)

Table 126. (continued)

State	M [MeV]	Γ [MeV]	J^{PC}	Process (mode)	Experiment ($\#\sigma$)	Year	Status
$X(4274)$ *or* $Y(4274)$	$4273.3^{+19.1}_{-9.0}$	$56.2^{+13.8}_{-15.6}$	1^{++}	$B^+ \to K^+(\phi J/\psi)$	CDF [1198] (3.1), LHCb [1200] (1.0), CMS [1201] (>3), D0 [1202] (np), LHCb [1204,1205] (6.0)	2011	NC!
$X(4350)$	$4350.6^{+4.6}_{-5.1}$	13^{+18}_{-10}	$0/2^{?+}$	$e^+e^- \to e^+e^-(\phi J/\psi)$	Belle [1217] (3.2)	2009	NC!
$Y(4360)$	4341.2 ± 5.4	101.9 ± 9.3	1^{--}	$e^+e^- \to (\pi^+\pi^-\psi(2S))$	Belle [1166,1218] (8), BaBar [1219] (np)	2007	Ok
				$e^+e^- \to (\pi^+\pi^- J/\psi)$	BESIII [1214] (7.6)	2016	NC!
				$e^+e^- \to (\pi^+\pi^-\psi_2(3823))$	BESIII [1183] (np)	2015	NC!
				$e^+e^- \to (\pi^0 Z_c(3900)^0)$	BESIII [1160] (np)	2015	NC!
				$e^+e^- \to (\pi^- Z_c(4020)^+)$	Belle [1166] (3.5), BESIII [1167] (9.2)	2014	NC!
$Y(4390)$	4391.6 ± 6.4	139.5 ± 16.1	1^{--}	$e^+e^- \to (\pi^+\pi^- h_c)$	BESIII [1215] (10)	2016	NC!
				$e^+e^- \to (\pi^{\mp,0} Z_c(4020)^{\pm,0})$	BESIII [1161,1165] (np)	2013	NC!
$\psi(4415)$	4421 ± 4	62 ± 20	1^{--}	$e^+e^- \to$ (hadrons)	PDG [77]	1976	Ok
				$e^+e^- \to (\eta J/\psi)$	Belle [1194] (np), BESIII [1207] (>5)	2013	NC!
				$e^+e^- \to (\omega\chi_{c2})$	BESIII [1220] (10.4)	2015	NC!
				$e^+e^- \to (D\bar{D}_2^*(2460))$	Belle [1221] (10)	2007	NC!
$Z(4430)^+$	4478^{+15}_{-18}	181 ± 31	1^{+-}	$\bar{B}^0 \to K^-(\pi^+\psi(2S))$	Belle [1222–1224] (6.4), BaBar [1225] (2.4), LHCb [1226,1227] (13.9)	2007	Ok
				$\bar{B}^0 \to K^-(\pi^+ J/\psi)$	Belle [1208] (4.0)	2014	NC!
$X(4500)$	4506^{+16}_{-19}	92^{+30}_{-29}	0^{++}	$B^+ \to K^+(\phi J/\psi)$	LHCb [1204,1205] (6.1)	2016	NC!
$Y(4660)$	4643 ± 9	72 ± 11	1^{--}	$e^+e^- \to (\pi^+\pi^-\psi(2S))$	Belle [1166,1218] (5.8), BaBar [1219] (5)	2007	Ok
				$e^+e^- \to (\Lambda_c^+\bar{\Lambda}_c^-)$	Belle [1228] (8.2)	2007	NC!
$X(4700)$	4704^{+17}_{-26}	120^{+52}_{-45}	0^{++}	$B^+ \to K^+(\phi J/\psi)$	LHCb [1204,1205] (5.6)	2016	NC!
$\Upsilon(4S)$	10579.4 ± 1.2	20.5 ± 2.5	1^{--}	$e^+e^- \to$ (hadrons)	PDG [77]	1985	Ok
				$e^+e^- \to (\pi^+\pi^-\Upsilon(1S,2S))$	BaBar [1229,1230] (>10), Belle [1231,1232] (11.2)	2006	Ok
				$e^+e^- \to (\eta\Upsilon(1S))$	BaBar [1230] (>11)	2008	Ok
				$e^+e^- \to (\eta h_b(1P))$	Belle [1110] (11)	2015	Ok
$\Upsilon(10860)$	10891 ± 4	54 ± 7	1^{--}	$e^+e^- \to$ (hadrons)	PDG [77]	1985	Ok
				$e^+e^- \to (\pi^+\pi^-\Upsilon(1S,2S,3S))$	Belle [1171,1233] [1172] (>10)	2007	Ok
				$e^+e^- \to (\pi^0\pi^0\Upsilon(1S,2S,3S))$	Belle [1173] (np)	2013	Ok
				$e^+e^- \to (f_0(980)\Upsilon(1S))$	Belle [1171–1173] (>8)	2011	Ok
				$e^+e^- \to (f_2(1275)\Upsilon(1S))$	Belle [1171–1173] (np)	2011	NC!
				$e^+e^- \to (\eta\Upsilon(1S,2S))$	Belle (10)	2012	NC!
				$e^+e^- \to (K^+K^-\Upsilon(1S))$	Belle [1233] (4.9)	2007	NC!
				$e^+e^- \to (\omega\chi_{b1,2}(1P))$	Belle [1234] (12)	2014	Ok
				$e^+e^- \to ((\pi^+\pi^-\pi^0)_{\text{non-}\omega}\chi_{b1,2}(1P))$	Belle [1234] (4.9)	2014	NC!
				$e^+e^- \to (\pi^+\pi^-\Upsilon_J(1D))$	Belle (9)	2012	NC!
				$e^+e^- \to (\eta\Upsilon_J(1D))$	Belle (np)	2014	NC!
				$e^+e^- \to (\pi Z_b(10610,10650))$	Belle [1171,1173] (>10)	2011	Ok
				$e^+e^- \to (B_s^*\bar{B}_s^*)$	Belle [1235] (np)	2016	NC!
$\Upsilon(11020)$	$10987.5^{+11.0}_{-3.4}$	61^{+9}_{-28}	1^{--}	$e^+e^- \to$ (hadrons)	PDG [77]	1985	Ok
				$e^+e^- \to (\pi^+\pi^-\Upsilon(1S,2S,3S))$	Belle [1236] (np)	2015	NC!
				$e^+e^- \to (\pi^\mp Z_b(10610,10650)^\pm)$	Belle [1176] (5.3)	2015	NC!

$e^+e^- \to \chi_{c2}\,\omega$ cross section peaks near $\psi(4415)$ [1220]. The only charmonium-like states for which hadronic transitions are not known yet are $X(3940)$ and $X(4160)$. However, their masses are quite far from the expectations derived from conventional quark models, thus they also have unexpected properties.

The rate of the $\psi(3770)$ decay to $J/\psi\pi^+\pi^-$ is not anomalously high. However, the decay to $J/\psi\eta$ is not strongly suppressed, which corresponds to violation of HQSS. The rates of the decays into charged and neutral $D\bar{D}$ pairs are substantially different, thus violating isospin conservation. These properties point to a multiquark admixture in the $\psi(3770)$ [1239].

Recently, Belle observed a new state, $X(3860)$, produced via $e^+e^- \to J/\psi(D\bar{D})$ [1184]. The mass and width of the state are $M = (3862^{+48}_{-35})\,\mathrm{MeV}/c^2$ and $(\Gamma = 201^{+177}_{-106})\,\mathrm{MeV}$, respectively. The spin parity hypothesis 0^{++} is favored over the 2^{++} at the $2.5\,\sigma$ level. The properties of $X(3860)$ agree well with expectations for the charmonium level $\chi_{c0}(2P)$.

Even before the observation of $X(3860)$, the authors of the phenomenological paper of Ref. [1240] interpreted the near-threshold enhancement in the $\gamma\gamma \to D\bar{D}$ cross section as a signal of the $\chi_{c0}(2P)$. The mass and width estimated in Ref. [1240] are consistent with the measurement by Belle.

It is puzzling that a 0^{++} state is already known in this mass region: the $X(3915)$, with $M = (3918.4 \pm 1.9)\,\mathrm{MeV}/c^2$ and $\Gamma = (20 \pm 5)\,\mathrm{MeV}$. Properties of $X(3915)$ do not fit expectations for the $\chi_{c0}(2P)$ [1240,1241]. The fact that this state is $190\,\mathrm{MeV}/c^2$ above the S wave $D\bar{D}$ threshold but is only 20 MeV wide is especially unusual.

Alternatively, the authors of Ref. [1242] proposed that the spin parity of the $X(3915)$ is in fact 2^{++}. Indeed, the 2^{++} assignment was found to be disfavored relative to the 0^{++} assignment by analysis of one-dimensional angular distributions in the $\gamma\gamma \to X(3915) \to J/\psi\,\omega$ process under the assumption that the 2^{++} state is produced only with helicities ± 2 [1188], as expected for pure charmonium. It has been pointed out [1242] that if $X(3915)$ has a non-$c\bar{c}$ admixture then the suppression of helicity 0 could be lifted, and with this contribution allowed, the 2^{++} hypothesis is no longer excluded. In this case the $X(3915)$ could correspond to a new decay channel of the $\chi_{c2}(2P)$ state [1242]. The large helicity 0 component would call for a prominent exotic component in the $\chi_{c2}(2P)$ state; Ref. [1243] discusses to what extent this pattern is consistent with a molecular nature of this state. Further experimental studies, to be performed both in B decays and in two-photon production, are needed to clarify the puzzle of the states near $3.9\,\mathrm{GeV}/c^2$.

Recently BESIII observed that the signal of the vector state $Y(4260)$ is in fact a sum of signals of two structures, an enhancement that may be traced to $Y(4360)$ and a state with mass near 4.22 GeV [1214]. Note that the original data already peaked at this energy; however, since the distribution is highly asymmetric, this feature was diminished in the experimental analysis using a symmetric Breit–Wigner distribution—note that the molecular picture for the $Y(4260)$ naturally leads to an asymmetric line shape as discussed in Sect. 14.5.3. This lower mass state is still called $Y(4260)$ by BESIII, though now its parameters have changed considerably (see Table 126). The new state decays to both spin-triplet and spin-singlet charmonia, which corresponds to a violation of HQSS and is unexpected for quarkonium. In addition, there are now a lot more vector states than expected $c\bar{c}$ levels in the considered mass region, and there might be even more than shown in the table. For example, here we list the decay $Y(4660) \to \Lambda_c\bar{\Lambda}_c$ following Refs. [1244,1245], although the distribution peaks at 4630 MeV and might in fact point to an additional state. The high-mass ψ states decay predominantly into $D^{(*(*))}\bar{D}^{(*)}$ channels, while no open flavor decays were found for the vector Y states, which is also puzzling for the charmonium assignment.

In the bottomonium sector there are only three states in the region above the open flavor thresholds, $\Upsilon(10580)$, $\Upsilon(10860)$, and $\Upsilon(11020)$ (see Table 126). For brevity, we will refer to them as $\Upsilon(4S)$, $\Upsilon(5S)$, and $\Upsilon(6S)$ according to the potential model assignment. However, they all show properties unexpected for pure $b\bar{b}$ pairs. The mass splitting between the $\Upsilon(4S)$ and $\Upsilon(5S)$ is larger by $(73 \pm 11)\,\mathrm{MeV}/c^2$ than that between the $\Upsilon(3S)$ and $\Upsilon(4S)$, while for a pure $b\bar{b}$ system it is

expected to be smaller by about 40 MeV/c^2 [1246]. The rates of $\Upsilon(5S) \to \Upsilon(nS)\pi^+\pi^-$ and $\Upsilon(6S) \to \Upsilon(nS)\pi^+\pi^-$ transitions are two orders of magnitude higher than expected for a pure bottomonium [1233,1236]. The η transitions, that in a pure bottomonium involve the spin flip of heavy quark and are suppressed by three orders of magnitude relative to $\pi^+\pi^-$ transitions, are not strongly suppressed in the case of $\Upsilon(5S)$ and are even enhanced for the $\Upsilon(4S)$ [1230]. In addition, the open-bottom two-body decays of the $\Upsilon(5S)$ show a sizeable breaking of HQSS (see, e.g., Refs. [1247,1248]), which is expected to be a very good approximation for bottomonia.

Thus, practically all known hadrons containing $c\bar{c}$ or $b\bar{b}$ quarks with masses above corresponding open flavor thresholds have properties unexpected for a pure $Q\bar{Q}$ state; their structure is possibly more complicated. Theoretical interpretations of these states are discussed in the next subsections.

In 2015, the LHCb Collaboration reported the observation of two pentaquark-like structures in the $\Lambda_b \to P_c K^-(P_c \to J/\psi p)$ channel [1054], with opposite parities. Similar models to the one discussed above have been proposed to explain these new resonances, e.g. the (compact) pentaquark [1249], or the meson–baryon molecule [1250,1251]. Reference [1252] also considers the possibility of the narrower peak being due to a kinematical singularity. Belle II can search for these (and similar) states in $c\bar{c}\,p$, both inclusively and in association with an antiproton.

14.5.3. Models

Author: C. Hanhart

As described below in more detail, most of the models for exotic states can be classified according to their clustering of the quarks and the relevant degrees of freedom:

- If the heavy quark–antiquark pair forms a compact quarkonium-like core surrounded by light quarks and antiquarks, the state is called *hadroquarkonium*.
- If the light and the heavy quark as well as the light and the heavy antiquark combine to form compact diquark and antidiquark substructures (diquarkonium), respectively, one speaks of *tetraquarks* (note, this applies to the most prominent tetraquark model, but there are also tetraquark models that do not assume any diquark clustering).
- If the quarks and antiquarks combine to form a pair of heavy hadrons, the object is called a *hadronic molecule*. When located close to the threshold of the molecular constituents the molecules can become quite extended—a feature that is crucial for a well-defined hadronic molecule and is claimed to lead to observable consequences.

In addition to those possibilities, there are exotics expected with gluons as active degrees of freedom:

- *Glueballs*: These are bound systems of gluons and do not carry any valence quarks. A lattice calculation based on quenched QCD, in which case glueballs do not mix with ordinary mesons, revealed glueball masses up to almost 5 GeV, with the lightest vector state having a mass of almost 4 GeV [1253].
- *Hybrid states*: Here, both the gluons and the quarks act as active degrees of freedom and contribute to the quantum numbers [1254].

Many of the exotic states are located near thresholds. This led various authors to claim that they are simply kinematical effects that find their origin in the non-analyticity of any S-wave meson loop when crossing a threshold [1255–1262]. However, as stressed in Ref. [1263], if this were correct,

those resonances should not show up as pronounced signals in the elastic channel (the channel close to whose threshold the actual state is located).[45] Based on this reasoning basically none of the near-threshold states found can be purely of kinematic origin; in other words, for all pronounced signals in elastic channels there must be a pole of the S-matrix nearby—they all classify as states.

In reality, all the physical wave functions might contain some fraction of all of the mentioned configurations and at least the neutral ones, even an admixture of regular quarkonium. Until now only a few studies have investigated the interplay of quark model poles and exotics in the quarkonium mass range; see, e.g., Refs. [1265–1270] for the quarkonium effect on hadronic molecules.

At present the main focus of research in the field is to identify the most prominent component in the wave function of some given state. This enterprise calls for refined theories that allow one to relate observables to the underlying sub-structures in a controlled way, as well as experiments of sufficient quality and quantity to be decisive.

Tetraquarks

Author: A. D. Polosa

The constituent quark model has been by far the most successful tool for the classification and interpretation of hadrons. Despite its obvious limitations, the systematic search of SU(3) multiplets provides the most reliable guideline in hadron spectroscopy. Exotic states with non-minimal quark content were forecast by Gell-Mann in the very first paper on the quark model [1271]. The proposal of diquarks as effective degrees of freedom inside baryons appeared in the late 1960s; it is based on the observation that a qq pair in the antisymmetric color configuration binds according to the tree-level calculation (one gluon exchange). Some phenomena, like the $x \to 1$ of the ratio of proton and neutron PDFs, or the ratio of fragmentation functions into Σ and Λ, can be qualitatively understood assuming the existence of these colored objects. Also, some evidence of a scalar diquark was found in lattice QCD [1272].

Diquarks can be the constituent bricks of a new, rich multiquark spectroscopy. In 2003, Jaffe and Wilczek [1273] proposed a diquark–diquark–antiquark explanation for the positive-strangeness Θ^+ baryon (whose existence was later contested by a higher statistics analysis). Soon after, Maiani et al. [1274,1275] interpreted the light scalar sector in terms of diquark–antidiquark states.

For the Hamiltonian of the multiquark system we take [1276]

$$H = \sum_i m_i + 2\sum_{i<j} \kappa_{ij} \mathbf{S}_i \cdot \mathbf{S}_j T_i^a T_j^a, \tag{490}$$

T being the SU(3) generators and $\mathbf{S}_i$ the spins of the constituent quarks. The spin–spin interaction is local (proportional to $\delta(\mathbf{r})$). The spin-one diquarks are heavier and less likely to be produced. The parity of S-wave tetraquarks is positive.

Taking heavy quarks into account one can produce spin-one diquarks as well. Hence, the S-wave states carry 0^{++}, 1^{++}, 1^{+-}, and 2^{++} quantum numbers [1277]. For each of them, the full SU(3) nonet is expected in principle. The natural assignment for the $X(3872)$ is the 1^{++} member of the multiplet. This allows one to fix the unknown diquark mass and get predictions for the masses of the other states. In the first version of the model, the chromomagnetic couplings κ were estimated from

[45] Reference [1264] questions the reasoning of Ref. [1263]. However, it should be stressed that in that work the mechanism to produce structures in the elastic and in the inelastic channels is very different and appears to be somewhat implausible.

the splittings in the ordinary meson and baryon spectra; however, this picture does not fit with the observed $Z_c'(4020)$ state.

On the other hand, if one thinks of the diquarks as point-like particles separated in space [1237], the only non-zero contribution is due to the κ_{cq} coupling inside the diquark itself; the Hamiltonian is diagonal in the diquark masses, and the resulting spectrum is compatible with the experiment.

An effective description of the tetraquark [1278] can be given in terms of a double-well potential segregating the two diquarks—a system with two length scales, namely the size of the diquark and that of the whole hadron. The tunneling amplitude of a heavy quark through the barrier separating the diquarks is exponentially suppressed with respect to the switching amplitude of the two light quarks to produce a pair of open charm/beauty mesons.

One can observe that if the ratio of the two tetraquark length scales is chosen appropriately (and for very reasonable values of it), the two neutral and charged $X_{u,d}, X^{\pm}$ states are expected to be all quasi-degenerate. They will preferably decay into open charm mesons and, with smaller rates, into charmonia, as observed. The charged components, however, are forced to decay only into the suppressed charmonia modes, because of the heavier $D^{\pm}D^{*0}$ thresholds.

The quasi-degenerate X_u and X_d particles will get mixed. One can show that there are mixing angle regions allowing us to explain, at the same time, the observed isospin-breaking pattern of the decays into $\psi\,\omega$ and $\psi\,\rho$, and to keep the $\psi\,\rho^{\pm}$ modes well below the neutral one in B decays [1278].

We notice that this approach can satisfactorily answer long-standing questions challenging the diquark–antidiquark model of exotic resonances. The tetraquark description of X and Z resonances is shown to be compatible with present limits on the non-observation of charged partners $X^{\pm}$ of the $X(3872)$ and the absence of a hyperfine splitting between the two different neutral states. The $Z_c(3900)$ can be described as the partner of the $X(3872)$ with reversed charge conjugation [1237]. In the same picture, Z_c and Z_b particles are expected to form complete isospin triplets plus singlets. It also explains why the decay rate into final states including quarkonia are suppressed with respect to those having open charm/beauty states.

The generalization to $J = 1$ and $L = 1$ excitations reproduces the spectrum of vector states; the extra contribution to the Hamiltonian is

$$\Delta H_{L=1,J=1} = B_c \frac{\mathbf{L}^2}{2} - 2a\mathbf{L}\cdot\mathbf{S}. \tag{491}$$

For a complete treatment of this problem see Ref. [1279], where tensor interactions are included.

The hadronic decay matrix elements depend on the details of the dynamics (see, for example, Ref. [1280]), and the most reliable predictions on the ratios of branching fractions are due to the fulfillment of heavy quark spin symmetry [1237,1281]. Predictions on radiative decays can also be achieved.

Other properties of diquark–antidiquark mesons were forecast in the late 1970s in the context of the so-called baryonium in dual theories [1282–1284]. The isospin violation was predicted to happen in heavy baryonia because of the smallness of $\alpha_s(m_Q)$, with $Q = c, b$: this quenches the light quark annihilations and leads the eigenstates to align with the flavor basis. Charmed baryonia have more recently been considered in Ref. [1244].

LHCb recently observed a rich structure in the $B^+ \to XK^+(X \to J/\psi\phi)$ channel, and confirmed the $X(4140)$ seen at Tevatron and CMS, albeit with a much broader width. Were these states to be confirmed, they would naturally constitute candidates for a $[cs][\bar{c}\bar{s}]$ tetraquark multiplet [1285].

In the bottomonium sector, tetraquark interpretations of the axial states were also proposed by Ali et al. [1281,1286].

The main drawback of the tetraquark model is the experimental absence of many of the predicted states, most notably of the charged partners of the $X(3872)$ and of its bottomonium analog; see the discussion above and Ref. [1278]. Moreover, in the original models the presence of several close meson–meson thresholds is ignored for it was supposed they had naturally to occur right below the mass of the observed states (since diquarks are less bound than a color singlet).

On the other hand, the tetraquark model predicted the presence of charged states as the $Z^+(4430)$ and the $Z^{\pm}_{c,b}$ resonances. With present data, all of them are *above* the respective meson–meson threshold with the corresponding quantum numbers. Since diquarks are slightly less bound than color singlets this explains why compact tetraquarks should be observed close to, but above, the corresponding meson–meson thresholds.

A tentative solution to the problem of charged states was also proposed in Ref. [1287], following some ideas presented in Refs. [1130,1288,1289]. In this picture the observed states are neither pure tetraquarks nor meson molecules, but rather the result of a hybridization between the first ones and the two-meson states. According to the Feshbach formalism, the scattering length for an unbound pair of particles (open channel) is dramatically enhanced whenever a discrete level of the same quantum numbers (closed channel) happens to be close and *above* the onset of the continuous spectrum. This hybridization is in contrast to the formation of a bound state, in which case the discrete level must be below the threshold.

In this model, the two-meson spectrum corresponds to the open channel, while the closed one is provided by the compact tetraquark previously described. The hybridization between the two consists in an inelastic scattering that temporarily rearranges the internal structure of the four-quark system.

The phenomenon described here induces a resonant enhancement in the production of tetraquarks and would be compatible (as any compact tetraquark model) with their production in high-energy and high-p_T proton–(anti)proton collisions, as opposed to what is expected for real loosely bound molecules, as discussed in the literature [1290,1291].[46]

The enhancement in the scattering length together with the fact that the energy of the pair must be smaller than some $E_{\rm max}$ also instruct us on the total width of the state. This is now expected to be $\Gamma \sim \sqrt{\delta}$, where δ is computed with respect to the *closest* threshold from below, as already explained.[47] This prediction correctly fits many of the observed X and Z states [1287].

The analysis does not straightforwardly generalize to excited orbital and radial states, and to better understand the absence of the isospin partners of the $X(3872)$ we need to turn to the more complete description introduced in Ref. [1278] and sketched at the beginning of this section, inspired in part by the Feshbach resonance idea.

The picture in Ref. [1278] strongly suggests some experimental tests to be done: (i) Improve on the bounds on $X^{\pm}$ in $J/\psi\rho^{\pm}$ decays by at least one order of magnitude. (ii) Improve on the precision on the mass measurement of the neutral component of the $X(3872)$ in various decay channels. (iii) Determine wether the $Z_c(3900)$ is produced or not in B decays and in prompt pp collisions—search all the X, Z states both in B decays and in prompt hadron collisions, and measure their production cross sections.

[46] Note that Refs. [1292–1295] come to a different conclusion about the production of shallow bound states.

[47] The fact that $\sqrt{\delta}$ is referred to the smallest detuning rather than to the larger available ones—those related to other decay modes—shows that this is not just a simple phase space effect.

Hybrid states

Author: A. V. Nefediev

Hybrid hadrons (or simply hybrids) are states where not only quarks and antiquarks but also gluons contribute to the quantum numbers and other properties of the system. Indeed, due to the non-Abelian nature of the interaction mediated by gluons, the latter can play the role of extra constituents of hadrons or even form a new type of compound: glueballs made entirely of two, three, or more gluons. In particular, in the language of the potential quark models, conventional mesons are described as radial and orbital excitations of the quark–antiquark pair connected by a confining potential or, in more sophisticated models, by a string-like object usually referred to as the flux-tube or the QCD string. Hybrid excitations correspond to the vibrational modes of this object formed by gluons. In the simplest realization, the hybrid meson is a quark–antiquark pair accompanied by a single excitation quantum of the glue. There exists a vast literature on theoretical approaches to hybrids. The corresponding predictions can be found, for example, in Refs. [1296,1297] (bag model), Ref. [1254] (flux-tube model), Refs. [1298–1300] (Coulomb-gauge QCD approach), Ref. [1136] (NRQCD approach), Ref. [1301] (potential quark model), Refs. [1302–1304] (constituent gluon model), and Refs. [1305–1313] (QCD string approach). Predictions of different models for the hybrids may differ slightly from each other. For example, in the flux-tube model [1314] the hybrid excitations are visualized as phonon-type objects, while in the constituent gluon model [1302–1304] the latter carry color and spin. This can lead to different predictions for the quantum numbers and other properties of the hybrids. Nevertheless, there is a consensus about the most general and most important features of hybrids, and these are discussed below.

One of the straightforward consequences of the presence of an extra degree of freedom in the system is a richer set of quantum numbers available for the hybrids. For example, while the quantum numbers 0^{+-}, 1^{-+}, and so on are not accessible in the standard J^{PC} scheme for the conventional quark–antiquark mesons, such options are allowed for hybrids. Thus, the experimental observation of a state containing a heavy quark–antiquark pair which at the same time has exotic quantum numbers would provide a strong candidate for a hybrid meson.

Another consequence of the excited glue in hybrids is a higher mass of the latter compared to the conventional mesons. Indeed, whatever model for the hybrid is used, its ground state is expected to have a mass of roughly $2m_Q + 1$ GeV, where m_Q is the mass of the heavy quark and the extra 1 GeV comes from the gluons. Therefore, in the spectrum of charmonium and bottomonium, it is natural to expect the lightest hybrid to have a mass slightly above 4 GeV and around 11 GeV, respectively. Indeed, the eight lowest $c\bar{c}g$ hybrids predicted in the flux-tube model [1254] reside around 4.1–4.2 GeV, with the 1^{--} and 1^{-+} states being among those. Other models give similar predictions. To mention just a few, in a potential model, with the $c\bar{c}$ pair considered as a color octet source, the tensor hybrid is predicted at 4.12 GeV [1301]; calculations within the QCD string model give for the mass of the exotic 1^{-+} charmonium hybrid 4.2 ± 0.2 GeV [1315] or 4.3–4.4 GeV [1312,1313]. The sibling states with a magnetic gluon and with the quantum numbers 0^{-+}, 1^{--}, and 2^{-+} are found in Refs. [1312,1313] to lie within the range 4.3–4.5 GeV; the non-relativistic effective field theory approach of Ref. [1136] predicts multiple hybrid states with different quantum numbers, including a total spin J as large as 3 or 4, in the range 4.0–4.7 GeV—this approach is discussed in some detail in Sect. 14.5.5. It should be noticed that the existence of the sibling hybrid states with different quantum numbers lying close to each other is yet another natural consequence of the extra degree of freedom introduced in the system. In the flux-tube model, the spin splittings between such hybrids are due to the long-range Thomas precession and they were found to be small [1316]. In the QCD string

model, these splittings are much larger, and they mostly come from the perturbative short-ranged forces [1312,1313]. In the EFT of Ref. [1136] they stem from different gluonic excitation operators which appear in the multipole expansion in perturbative NRQCD.

The situation with hybrids in the spectrum of bottomonium looks similar. Indeed, the most recent calculations place the lowest bottomonium hybrids around 11 GeV, in agreement with the simple estimate made above; see Refs. [1136,1313,1317] for more details.

An independent source of information about the masses and splittings of the hybrid mesons is provided by the results of the lattice calculations which are collected in the *Hybrids* subsection in Sect. 14.5.4.

To summarize, both theory and numerical simulations indicate that hybrids with different quantum numbers, including those with exotic ones, may exist in the mass region 4–5 GeV and around 11 GeV in the spectrum of charmonium and bottomonium, respectively.

However, it remains difficult to identify hybrid states in the experimental spectra. Therefore, it is important to establish selection rules which would allow one to disentangle the conventional mesons from the hybrids.

For the leptonic decays, a straightforward selection rule of this kind follows from the fact that the quark–antiquark pair in the conventional vector meson can easily annihilate into lepton pairs, but a similar decay is forbidden for hybrids which contain the $Q\bar{Q}$ pair in the color octet.

Open-flavor decays also provide a set of selection rules and criteria for hybrids. In particular, it was found long ago that, due to the symmetry of the wave function, a selection rule exists which forbids the decay of the vector hybrid with a magnetic gluon into a pair of S-wave open-flavor heavy–light mesons in the final state [1303,1304,1318–1320]. On the contrary, hybrids with electric gluons couple quite strongly to such S-wave pairs and, as a result, they are very broad and not observable experimentally. At the same time, for the allowed decays, for example into one S-wave and one P-wave open-flavor meson, the relative strength of such decays encoded in the corresponding coupling constants depends strongly on the pair creation mechanism for the light-quark pair $(\bar{q}q)$: it is created with the quantum numbers of the vacuum for conventional mesons, however it is coupled to the gluon for the hybrid, and as such it carries the quantum number of the vector. Thus, the recoupling coefficients for the decays into the $(\bar{Q}q)(\bar{q}Q)$ final state differ substantially for the $\bar{Q}Q$ mesons and for the $Q\bar{Q}g$ hybrids—see examples in Refs. [1312,1321].

It should be noted that, in the strict heavy-quark limit, the quadruplet of the P-wave heavy–light mesons turns to a pair of doubly degenerate states P_j corresponding to a particular total momentum of the light quark, $j = 1/2$ or $j = 3/2$. Since the $P_{1/2}$ and the $P_{3/2}$ mesons decay via pion emission to the lower-lying S-wave heavy–light mesons in the S-wave and in the D-wave, respectively, then the $P_{1/2}$ mesons appear to be much broader than the $P_{3/2}$ ones. This makes it hardly feasible to experimentally identify either of the two $P_{1/2}$ quadruplet members in the final state.

In the meantime, production of a heavy–light meson from the $P_{3/2}$ doublet accompanied by an S-wave meson is only possible if the produced light-quark pair has the total angular momentum equal to 1. This condition is not fulfilled for the vector bottomonium where $j_{q\bar{q}} = 0$ and, therefore, the amplitude for its decay into such a final state vanishes in the heavy-quark limit [1322,1323]. Meanwhile, as mentioned above, open-flavor decays of $Q\bar{Q}g$ hybrids proceed through gluon conversion into a light quark–antiquark pair which carries the quantum numbers of the vector, $j_{q\bar{q}} = 1$. This implies that there is no suppression for the amplitude of the vector hybrid decay into a pair of one S-wave and one $P_{3/2}$ open-bottom meson. Therefore, in the strict heavy-quark limit, the decays to

the open-flavor final states containing the members of the positive-parity quadruplet of heavy–light mesons could be used as test modes for the hybrid [1313].[48]

Beyond the strict heavy-quark limit, corrections of two types have to be taken into account. On the one hand, there exist corrections which are controlled by the parameter $\Lambda_{\rm QCD}/m_Q$. Such corrections are sizeable in the charm sector, so that the heavy-quark symmetry can provide only qualitative predictions for charmonia. In the meantime, since $m_b \gg \Lambda_{\rm QCD}$, the heavy-quark symmetry constraints are typically very well met in bottomonium systems. On the other hand, for a finite m_Q, the physical P-level heavy–light mesons come as certain mixtures of the $P_{1/2}$ and $P_{3/2}$ states governed by the mixing angle θ. Then, the probability of the decay of the genuine quarkonium $\bar{Q}Q$ (of the $Q\bar{Q}g$ hybrid) into the final state containing one S-level and one narrow P-level open-flavor meson is proportional to $\sin^2\theta$ ($\cos^2\theta$). Recent estimates of the mixing angle θ in the charmed and bottomed systems demonstrate that, at least in the b sector, the given selection rule may allow one to distinguish the hybrid from the conventional meson [1313].

Also, the final-state momentum distributions in the open-flavor decay channels can provide additional valuable information about the nature of the decaying state [1299,1324]. The method is reminiscent of the Franck–Condon factorization principle in molecular physics which is based on the so-called "velocity superselection rule." The rule states that the heavy quark does not change its velocity upon emitting or interacting with the light degrees of freedom, such as light quarks, gluons, pions, and so on, with a momentum of the order of the typical QCD scale $\Lambda_{\rm QCD}$. This entails that the momentum distribution of the heavy mesons in the open-flavor decays should be proportional to the momentum distribution of the heavy quarks inside the parent hadrons, thus giving a window on their internal structure. As mentioned above, excited glue brings a large contribution to the energy of the hybrid, so that the low-lying hybrids have the quark–antiquark pair in the ground state. Meanwhile, for a conventional meson, one needs to excite the radial motion of the quark–antiquark pair to arrive at the state with the same mass and the same J^{PC} quantum numbers. For example, in the framework of potential quark models, the vectors $\Upsilon(10860)$ and $\Upsilon(11020)$ lying in the mass range around 11 GeV correspond to the fourth and the fifth radial excitations of the $b\bar{b}$ pair, respectively, conventionally denoted as $\Upsilon(5S)$ and $\Upsilon(6S)$. Their wave functions possess four and five nodes, respectively, which is to be confronted with the nodeless wave function of the $b\bar{b}g$ hybrid. Since, for a given total energy, the relative momentum of the mesons in the final state is fixed by the energy conservation law, then different two- and three-body open-flavor final states probe different parts of the wave function of the decaying state—see Refs. [1299,1324] for further details. Therefore, studying the two- and three-body open-bottom final states, it should be possible to make a conclusion concerning the source of the B meson pair: a smooth distribution would identify the source as the hybrid while a distribution with residual (after smearing due to the quark recoil in B mesons) structures would indicate a conventional (highly radially excited) quarkonium as the corresponding source.

For hidden-charm decays of the charmonium hybrids two different types of transitions can be identified: with and without conventional charmonium production in the final state. In the former case, the decay proceeds through the $c\bar{c}$ pair conversion from color octet to color singlet via emission of a single gluon and with a consequent annihilation of the gluons into light hadrons [1325],

$$\psi_g(c\bar{c}g) \to (c\bar{c})(gg) \to \psi(c\bar{c}) + \text{light hadrons}, \tag{492}$$

[48] If the state is close to the threshold of the S-wave and P-wave heavy mesons, the strong coupling would also imply a sizeable hadronic molecule component, as discussed below.

where ψ_g is a hybrid while ψ is a conventional charmonium. Such decays populate final states with hidden charm which may provide a clear experimental signal if the charmonium $\psi(c\bar{c})$ is the J/ψ or a higher charmonium which decays into J/ψ through a cascade. On the contrary, in the latter case, the $c\bar{c}$ pair in the hybrid annihilates into gluons which then convert into light hadrons,

$$\psi_g(c\bar{c}g) \to (ng) \to \text{light hadrons}, \quad n \geqslant 2, \tag{493}$$

so that such decays enhance no-charm final states [1326]. See also Ref. [1327] for further details of the experimental signatures and search strategies for the charmonium hybrids in B meson decays.

Additional information on hybrids can be obtained from the production reactions where hybrids are created in line with the conventional mesons. For B factories, the most relevant production reaction of this kind is a decay of the B meson of the form $B \to \psi_g + X$, where X stands for the rest of the products of the decay. It should be noticed that, although both types of hybrids with a heavy quark–antiquark pair and with one heavy and one light quark can be produced in such B meson decays, only hybrids containing a $c\bar{c}$ pair are eigenstates of the C-parity operator and as such they can possess exotic quantum numbers to be regarded as a smoking-gun-like signature of an exotic state. Then the underlying weak transition is governed by the CKM-favored decay $b \to c\bar{c}s$. Since the $c\bar{c}$ pair in such a transition should not be in the color singlet, it is produced through the color octet intermediate state; the corresponding theoretical estimates can be found, for example, in Refs. [1327,1328]. In particular, in Ref. [1328] the branching fraction for the decay $B \to \psi_g(0^{+-}) + X$ is estimated at the level of 10^{-3}, while it is argued in Ref. [1327] that $\mathcal{B}[B \to \psi_g + X]$ can be as large as $\sim$1% for any quantum numbers of the hybrid, including the exotic ones 1^{-+}. Therefore, hybrids are produced in B meson decays with a probability comparable to that for the conventional charmonia.

The experimental status of hybrids is obscure because up to now not a single hybrid has been identified beyond doubt. One of the most prominent candidates for a hybrid state is $Y(4260)$ (see Table 126) which demonstrates some features expected for a charmonium hybrid. In particular, it has a mass close to the phenomenological and lattice predictions discussed above and, more importantly, it has a decay pattern (small electronic width and not seen open-charm decays of a particular type) that is not typical for conventional mesons but that is specific for hybrids. Thus, this state could be a hybrid charmonium with a spin-1 [1136,1329] or spin-0 $c\bar{c}$ core [1312,1319]. However, further studies of the open-charm decays of this state [1330] question its hybrid nature; alternative scenarios for the $Y(4260)$ are discussed below. In addition, if the resonant spectrum of transition $e^+e^- \to h_c(1P)\,\pi\pi$ around 4.22 GeV [1215] is found to be dominated by the $Y(4260)$ that also decays into $J/\psi\pi\pi$, the data might call for a mixture of two structures, since the appearance of both transitions would otherwise violate heavy quark spin symmetry.

To summarize, hybrids in the spectrum of charmonia and bottomonia are expected to possess a few specific features which are expected to allow one to disentangle them from conventional quarkonia. Among these are:

- exotic quantum numbers not accessible for the quark–antiquark system;
- coexistence in the same mass region with sibling states with different quantum numbers;
- abnormally small leptonic width;
- peculiar decay pattern into open-flavor meson pairs;
- smooth momentum distribution in the two- and three-body open-flavor decays.

Hadroquarkonia

Author: C. Hanhart

Triggered by the observation that a large number of exotic candidates decay into a quarkonium accompanied by one or more pions, these candidates were proposed in Refs. [1331,1332] to consist of a core provided by a heavy quarkonium surrounded by an excited state of light quark matter. In this picture the mentioned decays are understood as setting free the quarkonium core in the process of de-exciting the light quark cloud into one or more pions.

It is expected that the dominant decay modes of hadroquarkonia are given by light quarks in combination with the core quarkonium. In particular, since in heavy quark systems the spins of the heavy quarks and the total angular momentum of the light quarks are conserved individually, any given state should decay either into a spin 1 or a spin 0 quarkonium, but not into both. However, this spin symmetry selection rule can be evaded by mixing [1333]. Following this idea, $Y(4260)$ (potentially seen not only in the final state $J/\psi\pi\pi$ but also in $h_c\pi\pi$) and $Y(4360)$ (seen in $\psi'\pi\pi$) could be mixtures of two hadrocharmonia with spin triplet and spin singlet heavy quarkonium cores. The same kind of mixing could also operate for hybrids.

The mixing scenario of Ref. [1333] opens an interesting opportunity: using the proposed scenario for $Y(4260)$ and $Y(4360)$ as input one, can use spin symmetry to predict in total four spin partners of the mentioned states; most special among them is a pseudoscalar state, which is significantly lighter than $Y(4260)$ [1334]. Although this state appears at a similar mass to the second radial excitation predicted within typical quark models, it could still be identified via its prominent decay into $\eta_c^{(\prime)}\pi\pi$, while a decay into $D^*\bar{D}$ should not occur. Testing these predictions provides crucial tests for the hadroquarkonium model.

Since in leading order the light quark cloud does not feel the flavor of the quarkonium core, the masses of the bottomonium partners of hadrocharmonia can be found simply by adding the mass difference of the assumed core state and its bottomonium partner to the hadrocharmonium mass. Although this picture can get distorted to some extent via the interactions with neighboring states, it should be clear that a lot can be learned from a comparison of the bottomonium spectrum and the charmonium spectrum.

Hadronic molecules

Authors: F.-K. Guo, C. Hanhart

In contrast to the compact tetraquarks discussed above that are formed from coloured (anti-)diquarks, hadronic molecules are understood as bound states of two color neutral hadrons. This results in a different analytic structure of the corresponding amplitudes that leads to observable consequences, if the corresponding states are located close to the relevant threshold. For a recent review, see Ref. [1335]. To get a quantum mechanical understanding of this statement one may think of the wave function of a physical state being made of two components: a two-hadron copmonent and a compact component. In the modern literature the former is often called the molecular component. In 1963 Weinberg showed that the probability of finding the molecular component inside the physical wave function, $(1-\lambda^2)$, is related to the physical coupling of the state to the continuum channel via [1336]

$$\frac{g_{\rm eff}^2}{4\pi} = 4M_{\rm thr}^2(1-\lambda^2)\sqrt{\frac{2\epsilon}{\mu}} \leq 4M_{\rm thr}^2\sqrt{\frac{2\epsilon}{\mu}}, \tag{494}$$

where $M_{\rm thr} = m_1 + m_2$ denotes the threshold mass, and $m_{1,2}$ and μ denote the masses of the individual constituents and their reduced mass, respectively. The binding energy, ϵ, is defined with respect to the continuum threshold via

$$M = m_1 + m_2 - \epsilon, \tag{495}$$

where M denotes the mass of the state considered. Equation (494) is correct up to corrections of the order of γR, where $\gamma = \sqrt{2\mu\epsilon}$ denotes the binding momentum and R the range of forces. Since $g^2_{\rm eff}$ is nothing but the residue at the pole for the state considered, via Eq. (494) the amount of molecular component in a wave function becomes an observable, e.g. the scattering length scales as [1336]

$$a = -\left(\frac{1-\lambda^2}{1-\lambda^2/2}\right)\frac{1}{\gamma}. \tag{496}$$

For binding momenta γ much smaller than any intrinsic scale of the system considered and $\lambda^2 \to 0$, all physics gets controlled by the single scale γ. In particular the scattering length gets unnaturally large. This gives rise to various universal phenomena as detailed in Ref. [1337], as well as allowing for the construction of effective field theories based on hadronic degrees of freedom [1130–1132] largely inspired by EFT treatments for the nucleon–nucleon interaction [1133].

The derivation of Eq. (494) involves the normalization of a bound state wave function and it therefore holds rigorously only for stable bound states. However, it was shown that it can be generalized to states coupling to remote inelastic channels [96]. In addition, in order to keep the corrections small, the considered bound systems should be shallow. Generalizations of the Weinberg approach to coupled channels as well as resonances can be found in Refs. [1338–1341]. In any case, as soon as one also adopts the physical picture for somewhat more deeply bound systems, namely that the coupling of a state gets large when it has a sizeable molecular component, quite significant observable consequences emerge, like highly asymmetric line shapes, as was shown, e.g., in Refs. [1342,1343] on the example of the $Y(4260)$ as a $D_1\bar{D}$ molecular structure (for a recent discussion, which also contains the most recent BESIII data of relevance for the $Y(4260)$, we refer to Ref. [1344]).

While detailed predictions for new states within a molecular picture are difficult, since they require detailed dynamical modeling analogous to that necessary to describe few-nucleon systems, some general statements are still possible. For instance, molecules should form (predominantly) in S-waves since the centrifugal barrier is always repulsive. Therefore the quantum numbers of the constituents already define the molecules they can (most easily) form. In addition, only narrow states can form hadronic molecules, since a shallow bound state that contains a broad building block would be very short-lived or might not even have the time to be formed before the constituent decays [1345,1346].

In addition, it appears natural to expect that the one-pion exchange plays an important role in the formation of the bound states [1347], which after all is also understood as a crucial ingredient of the nuclear force. In this context it is important to acknowledge that the strength of the one-pion exchange changes by a factor $-1/3$ when switching from an isoscalar to an isovector channel. Thus, if the pion exchange provides a crucial contribution to the binding of the isoscalar $X(3872)$, one might be tempted to claim that there should be no charged molecules. However, there is an additional change in sign, when switching to systems of opposite C parity. As a result of this one should expect that, if there is an isoscalar molecule of a given C parity, the isovector partner, if it exists, should have opposite C parity [1334]. This is in contrast to the tetraquark picture where for each J^{PC} there should always be both an isoscalar and an isovector state, but in line with experiment at least for

the states near the $D\bar{D}^*$ threshold, since the $X(3872)$ has positive C parity while the $Z_c(3900)^+$ has negative C parity. Following this logic one might also expect an isoscalar partner of the $Z_c(4020)^+$ near the $D^*\bar{D}^*$ threshold with $J^{PC} = 1^{++}$, which, however, does not exist since an S-wave $D^*\bar{D}^*$ state with spin 1 has negative C parity [1348].

In heavy quark systems spin symmetry can provide an important diagnostic for the study of the structure of hadrons [1334]. Detailed studies for the implications of the heavy quark spin symmetry on both states in the charmonium and bottomonium sector can be found in Refs. [1238,1349–1353]. While the pattern does not get destroyed by the inclusion of the one-pion exchange, spin symmetry violations driven by the mass difference in the open flavor mesons might distort the pattern severely [1354,1355]. This becomes apparent, e.g., when looking at the spin 2 partner of the $X(3872)$. This state was predicted to be a shallow bound state of $D^*\bar{D}^*$ with the same binding energy as $X(3872)$ [1348,1353] and a narrow width [1356]. However, a crucial part of the one-pion exchange is its tensor force that induces sizeable transitions from S to D waves. In the case of the spin 2 partner of the $X(3872)$ these transitions allow for a decay of the state to $\bar{D}D$ in D wave, which might result not only in a significant mass shift but also in a sizeable width for this state [1354]. A recent study of the line shapes of $Z_b(10610)$ and $Z_b(10650)$ revealed that a proper renormalization of the full one-pion exchange contribution is possible only if a naively order-p^2 counter term that induces S–D transitions is promoted to leading order. The effect of this is that a significant fraction of the tensor force contribution gets canceled [1357]. What impact this counter term can have in the charmonium systems remains to be seen. Predictions based solely on interactions of a heavy meson pair could also be distorted due to the interplay with the preexisting charmonium states [1270]; for a more general discussion of this scenario we refer to Refs. [1265,1266]. In this context detailed knowledge of the bottonomium spectrum would be extremely valuable since the mentioned violations of spin symmetry should be suppressed significantly in those heavier systems. Moreover, the location of the open flavor thresholds relative to the quarkonia is expected to be different in the bottom sector compared to the charm sector.

Even without any detailed calculation it should be clear that, particularly by comparing charmonium and bottomonium sectors, a great deal of physics may be revealed, e.g. molecular states are located at a binding energy where the kinetic energy matches the potential energy. Accordingly, the binding momentum, $\gamma = \sqrt{2\mu\epsilon}$, is an important characteristic of a two-hadron bound state. In heavy–light two-hadron molecular states the reduced mass is close to the mass of the light hadron and as such the binding energies of, e.g., the $KD^{(*)}$ and the $K\bar{B}^{(*)}$ system should be similar. Therefore, if indeed $D_{s0}^*(2317)$ and $D_{s1}(2460)$ are bound states of KD and KD^*, respectively, as claimed in Refs. [1358–1362], which can naturally explain the otherwise puzzling fact that $M_{D_{s1}(2460)} - M_{D_{s0}^*(2317)} \simeq M_{D^*} - M_D$, the actual masses of the corresponding bottom states should reveal important information on the flavor dependence of the binding potential. In Ref. [1363], the radiative decays of these scalar and axial vector states are identified as the most promising discovery modes of these predicted bottom states (isospin-violating decay modes are estimated in Ref. [1363] within the molecular picture and in Refs. [1364,1365] using heavy meson chiral perturbation theory). In the scenario that the $D_{s0}^*(2317)$ and $D_{s1}(2460)$ are hadronic molecules, some quantitative predictions have been confronted with both lattice QCD and experimental data. Using the parameters fixed in Ref. [1366], which leads to an $\sim$70% DK component in the $D_{s0}^*(2317)$, the finite-volume energy levels in the scalar isoscalar $D\pi, D\eta$ and $D_s\bar{K}$ coupled channel system [1367] were found to be in remarkable agreement with the lattice results of the Hadron Spectrum Collaboration [174]. The same parameters also result in a good description [1368] of the precise measurements of the $D^+\pi^-$ and $\bar{D}^0K^-$ angular moments

in the $B^- \to D^+\pi^-\pi^-$ [336] and $B_s^0 \to \bar{D}^0 K^-\pi^+$ [1369] processes. These agreements may be regarded as strong support of the hadronic molecular scenario. Nevertheless, these comparisons are only in the scalar sector, since the quality of the data in the 1^+ sector [327] is not good enough. The much better data expected from Belle II will be crucial to allow for more firm statements.

In contrast to the heavy–light systems, the flavor dependence of the kinetic energy of heavy–heavy systems is much stronger, since here the reduced mass is of the order of the heavy meson mass. Thus, for heavy–heavy two-hadron molecular systems one should expect significant differences in the bottomonium and charmonium spectra, as exemplified by the large binding energy difference between the $X(3872)$ and X_b in Ref. [1353].

Before closing this subsection we would like to give a few examples of molecular candidates in the heavy hadron spectrum. One of the prime candidates for a molecular state is $X(3872)$. Its mass lies extremely close to the $D^0\bar{D}^{*0}$ threshold and therefore a natural explanation for this state might be a 1^{++} $D\bar{D}^*$ molecule [1370]. As a consequence of the separation to the D^+D^{*-} channel of only 8 MeV, strong isospin breaking is predicted in this scenario [1370,1371]. The comparable rates in the $\omega J/\psi$ and $\rho^0 J/\psi$ channels appear to be consistent with an interpretation of $X(3872)$ as an isoscalar $D\bar{D}^*$ molecule when the different widths of ρ and ω as well as the mass difference between the $D\bar{D}^*$ thresholds are taken into account [1372]. Also, in Ref. [1373] it becomes apparent that only an isoscalar structure is consistent with the decay properties of $X(3872)$. The copious production of $X(3872)$ at very high p_T in pp and $p\bar{p}$ collisions was claimed to be in conflict with a pure molecular assignment [1289,1290]; however, the role of rescattering could be crucial in enhancing the production cross sections [1292–1294]. Recently the production of shallow molecules was revisited from a different angle in Ref. [1295], again showing that the observed production rates are not in conflict with expectations. However, it is fair to say that this issue has still not been resolved in the literature. The comparison with light nuclei production at high p_T proposed in Ref. [1291] might shed further light on the molecular assignment. However, there is a crucial difference between a light nucleus and the $X(3872)$, namely that the former does not allow for a $q\bar{q}$ component, which can prevent a decisive conclusion from being drawn from this comparison [1335].

Other quarkonium-like states very close to open flavor thresholds include the charged $Z_b^{\pm}(10610, 10650)$ and $Z_c(3900, 4020)^{\pm}$. For these, a molecular interpretation was also proposed shortly after their discovery: $B\bar{B}^*$ and $B^*\bar{B}^*$ for the Z_b states [1238], and $D\bar{D}^*$, $D^*\bar{D}^*$ for the Z_c states [1353,1374]. The measured spin and parity of $J^P = 1^+$ for $Z_b(10610)$ and $Z_b(10650)$ [1172] and for $Z_c(3900)$ [1162,1163] correspond to heavy–light mesons in the S wave, in line with the molecular interpretation. The experimental fact that, e.g., the Z_b states decay predominantly into the open flavor channels despite being located in mass very close to their thresholds is claimed to be a "smoking gun" of a molecular structure [114,1238,1375]. A recent combined analysis of the $B^{(*)}\bar{B}^*$ and $h_b(mP)\pi$ channels using amplitudes consistent with unitarity and analyticity indicates that $Z_b(10610)$ and $Z_b(10650)$ may in fact be virtual molecular states with poles within 2 MeV of the corresponding thresholds [114]. A similar conclusion for the $Z_c(3900)$ was made in Ref. [1376], where an above-threshold resonance solution was also found in addition to the virtual state one. To fully pin down the pole locations of the Z_b and Z_c states, additional data of better statistics appear to be necessary. Those studies are really important: if the masses of all the charged states mentioned in this paragraph were indeed located above the corresponding thresholds, it would challenge the molecular interpretation (and might support the tetraquark interpretation—see the discussion in the tetraquark subsection above) for molecular structures that naturally appear either below threshold or are broad [1377] since the coupling of the given state to the channel that forms is large—see

Eq. (494). To further establish if indeed the Z_b states are of molecular nature or consist predominantly of more compact components like tetraquarks, in Ref. [1375] several decay ratios are given based on the molecular picture. In Ref. [1378], similar relations are derived for the Z_c states within both the molecular and the tetraquark picture. Indeed, given the heavy flavor symmetry of QCD, a detailed comparison of the charmonium and the bottomonium spectra should provide deep insights into the way nature forms hadrons.

The above examples concern candidates for hadronic molecules formed by two ground state heavy mesons. Molecules formed of other heavy hadrons are possible as well. The most discussed example is the $Y(4260)$, which was conjectured to be predominantly a $D_1(2420)\bar{D}$ molecule [1374]. If this were the case, the $D_1\bar{D}$ decay should play a significant role in the $Y(4260)$ physics, but data are still inconclusive on that [1162,1342]. The resulting binding energy of 70 MeV pushes this state out of the validity range of the Weinberg theorem [1336], and makes the $Y(4260)$ predictions more model dependent. However, this assignment not only provides a natural mechanism for the production of a $D\bar{D}^*$ molecule, $Z_c(3900)^+$, but also allows subsequently for the prediction of copious production of $X(3872)$, also assumed to be a $D\bar{D}^*$ molecular state, in $Y(4260)$ radiative decays [1379]. This prediction was confirmed shortly afterwards at BESIII [1147]. The same radiative transitions naturally occur if the $Y(4260)$ is identified as the orbital excitation of the $X(3872)$ tetraquark [1237]. The $Y(4360)$ with a large $D_1\bar{D}^*$ component could be the spin partner of the $Y(4260)$ [1380–1382], but a detailed microscopic calculation to make this connection solid is still lacking. The new value of the $Y(4260)$ mass of about 4.22 GeV (see Table 126) agrees better than the old one with the expectations for the molecule [1342,1343]. In addition, the mass difference between $Y(4260)$ and $Y(4360)$ is now closer to that between D and D^* mesons, as expected in the molecular picture.

The $\Upsilon(6S)$ is situated near the $B_1(5721)\bar{B}$ threshold, where $B_1(5721)$ is a narrow P-wave excitation with the spin parity of the light degrees of freedom $j^P = 3/2^+$, and can be the bottomonium analog of the $Y(4260)$. A contribution of the $B_1(5721)\bar{B}$ pairs to the $\Upsilon(6S)$ decays[49] has a very clear experimental signature: the $Z_b(10610)\pi$ final state should be produced, while the $Z_b(10650)\pi$ should not [1383], in full analogy to $Y(4260)$. This prediction is distinct from the observations at $\Upsilon(5S)$, where both Z_b states are produced in roughly equal proportions. Present data provide only a very loose constraint on the relative yields of $Z_b(10610)$ and $Z_b(10650)$, and do not exclude the single $Z_b(10610)$ hypothesis at a high confidence level [1176]. The observation of a possible analog of $Y(4260)$ and $\Upsilon(6S)$ also makes one suggest that the radiative decay of $\Upsilon(6S)$ to the X_b, the to-be-found bottomonium partner of $X(3872)$, should be sizeable and could well be an ideal discovery channel (e.g. via $\Upsilon(6S) \to \gamma X_b \to \gamma[\Upsilon(1S)\omega]$).

Effect of continuum channels on quarkonia

Authors: C. Hanhart, R. Mizuk

For hadronic molecules to be formed it is necessary that the scattering potential of two heavy mesons is sufficiently strong that its resummation leads to a pole in the scattering matrix. For this mechanism to be convincing one expects that the two-meson continuum also influences at least some properties of states that are believed to have a pronounced $Q\bar{Q}$ component. In the literature, the continuum contribution is sometimes called coupled-channel effects or molecular admixture.

[49] The coupling of a pair of $3/2^+$ and $1/2^-$ bottom mesons to an S-wave $b\bar{b}$ system, however, requires sizeable HQSS breaking to be present [1322,1323].

Table 127. The decomposition of P-wave $B^{(*)}\bar{B}^{(*)}$ pairs with $J^{PC} = 1^{--}$ into $b\bar{b}$ spin eigenstates [1396].

State	Decomposition into $b\bar{b}$ spin eigenstates
$B\bar{B}$	$\frac{1}{2\sqrt{3}}\,\psi_{10} + \frac{1}{2}\,\psi_{11} + \frac{\sqrt{5}}{2\sqrt{3}}\,\psi_{12} + \frac{1}{2}\,\psi_{01}$
$B\bar{B}^*$	$\frac{1}{\sqrt{3}}\,\psi_{10} + \frac{1}{2}\,\psi_{11} - \frac{\sqrt{5}}{2\sqrt{3}}\,\psi_{12}$
$(B^*\bar{B}^*)_{S=0}$	$-\frac{1}{6}\,\psi_{10} - \frac{1}{2\sqrt{3}}\,\psi_{11} - \frac{\sqrt{5}}{6}\,\psi_{12} + \frac{\sqrt{3}}{2}\,\psi_{01}$
$(B^*\bar{B}^*)_{S=2}$	$\frac{\sqrt{5}}{3}\,\psi_{10} - \frac{\sqrt{5}}{2\sqrt{3}}\,\psi_{11} + \frac{1}{6}\,\psi_{12}$

For most heavy quarkonium transitions, we notice that $M_{Q\bar{Q}} - 2M_{Q\bar{q}} \ll M_{Q\bar{q}}$, where $M_{Q\bar{Q}}$ and $M_{Q\bar{q}}$ are the masses of the heavy quarkonium and an open flavor heavy meson, respectively. As a result, the intermediate heavy mesons are non-relativistic with a small velocity

$$v \sim \sqrt{|M_{Q\bar{Q}} - 2m_{Q\bar{q}}|/m_{Q\bar{q}}} \ll 1, \tag{497}$$

and the coupled-channel effects in the transitions can be investigated using a non-relativistic effective field theory. A systematic analysis reveals that certain transitions acquire a $1/v$ enhancement compared to the transition captured by the quark model. This is especially the case if the quark model transition is suppressed either by a violation of flavor selection rules, as in $\psi' \to J/\psi\pi$ and $\psi' \to J/\psi\eta$ [1384], or by small wave function overlaps as in hindered M1 transitions between two P-wave $Q\bar{Q}$ states [1385,1386] (for a detailed discussion on the power counting and additional examples, see Ref. [1387]). On the other hand, based on the same power counting rules, it was argued that the transitions $\Upsilon(4S) \to h_b\pi^0/\eta$ have only a small pollution from the bottom meson loops. They are dominated by a short-distance contribution proportional to the light quark mass difference [1388] and could be used for the extraction of the light quark mass ratio. Furthermore, the prediction, made before the discovery of the $h_b(1P)$, on the branching fraction of the order of 10^{-3} for the decay $\Upsilon(4S) \to h_b\eta$ was verified by the Belle measurement, $(2.18 \pm 0.11 \pm 0.18) \times 10^{-3}$ [1110]. In addition, in Ref. [1120] it is pointed out that coupled-channel effects can even introduce sizeable and non-analytic pion mass dependence in heavy quarkonium systems which couple to open flavor heavy meson pairs in an S-wave.

A possible explanation for the unusual features of $\Upsilon(4S)$, $\Upsilon(5S)$, and $\Upsilon(6S)$ listed in Sect. 14.5.2 is the presence of heavy mesons in their wave functions. In this picture the $\Upsilon(4S)$, $\Upsilon(5S)$, and $\Upsilon(6S)$ states are mixtures of $b\bar{b}$ and $B_{(s)}^{((*)*)}\bar{B}_{(s)}^{((*)*)}$ pairs (where $B_{(s)}^{**}$ denotes the P-wave excitations of B or B_s mesons). It was realized at the time of observation of the $\Upsilon(4S)$, $\Upsilon(5S)$, and $\Upsilon(6S)$ in the 1980s [1389,1390] that the too large splitting between the $\Upsilon(4S)$ and $\Upsilon(5S)$ states is due to the contribution of hadron loops [1391], which is another language in which discuss the molecular admixture. Enhanced transitions into hidden flavor final states are due to rescattering of the on-shell heavy mesons [1392,1393]. Finally, the molecular admixture is also responsible for the violation of HQSS. Indeed, an admixture of a specific $B\bar{B}$, $B\bar{B}^*$, or $B^*\bar{B}^*$ meson pair is not an eigenstate of the $b\bar{b}$ total spin. Table 127 presents the decomposition of the P-wave $B^{(*)}\bar{B}^{(*)}$ pairs with $J^{PC} = 1^{--}$ into the $b\bar{b}$ spin eigenstates ψ_{ij}, where i is the total spin of the $b\bar{b}$ pair and j is the total angular momentum contributed by all other degrees of freedom, including both the spin of light quarks and the orbital angular momentum $L = 1$ [1394,1395]. Various ψ_{ij} components give rise to transitions that are forbidden by HQSS for pure $b\bar{b}$ states. Experimental signatures for ψ_{ij} components are presented in Table 128.

Table 128. Experimental signatures for the $b\bar{b}$ spin eigenstates ψ_{ij} [1396].

Spin eigenstate	Expected decays
ψ_{10}	$\Upsilon(nS)\,\pi^+\pi^-$, $\Upsilon(nS)\,K^+K^-$ in S wave
ψ_{11}	$\Upsilon(nS)\,\eta$, $\Upsilon(nS)\,\eta'$
ψ_{11}, ψ_{12}	$\Upsilon(nS)\,\pi^+\pi^-$, $\Upsilon(nS)\,K^+K^-$ in D wave
ψ_{01}	$\eta_b(nS)\,\omega$, $\eta_b(nS)\,\phi$, $h_b(nP)\,\eta$, $h_b(nP)\,\eta'$

One can expect that the closer the physical state to the threshold, the larger the admixture of the corresponding meson pairs. Therefore, $B\bar{B}$ should be the dominant admixture in the $\Upsilon(4S)$ wave function, while in case of the $\Upsilon(5S)$ the dominant HQSS-violating contribution could be the $B_s^*\bar{B}_s^*$ component [1395]. This picture gives a successful description of the observed decay pattern, while Tables 127 and 128 give guidance for further experimental searches.

The above analysis considers only the ground state S wave bottom mesons. Contributions of excited bottom mesons were recently discussed for the $\Upsilon(nS)$ states in a quark model [1397]. The $\Upsilon(6S)$ situated near the $B_1(5721)\bar{B}$ threshold may even qualify as a hadronic molecule, as discussed above in the hadronic molecular subsection.

The $\Upsilon(5S)$ and $\Upsilon(6S)$ states are not good candidates for compact tetraquarks, since their signals are seen in the total hadronic cross section, and thus the open flavor channels are likely to give a dominant contribution to the $\Upsilon(5S)$ and $\Upsilon(6S)$ peaks. The $\Upsilon(5S)$ is also not a good candidate for hadrobottomonia, since it decays into various final states with bottomonia, instead of a single one.

In this sense it is of paramount importance that we get better information on the hadron spectrum in the bottomonium sector above the $\bar{B}B$ threshold. Various possible strategies that could be followed at Belle II for discoveries for quantum numbers different from 1^{--} are listed in Sect. 14.7.2. Clearly, the same decay chains are also well suited to discovering new exotic candidates.

We are convinced that the spectrum of bottomonium(-like) states above the $\bar{B}B$ threshold will provide crucial information on the inner workings of QCD, and that Belle II can and will be a key player in this field in the years to come.

14.5.4. Lattice QCD

Author: S. Prelovsek

In the energy region near or above threshold, the masses of bound states and resonances have to be inferred from the infinite-volume scattering matrix $S(E)$ of the one-channel (elastic) or multiple-channel (inelastic) scattering of two hadrons. This has been done for QCD in practice only recently, and the approaches currently used or proposed are briefly summarized below. The poles of the resulting $S(E)$ provide the masses of resonances and bound states.

The most rigorous and the most widely used way to extract $S(E)$ is Lüscher's method. He has shown that the energy of eigenstate E in finite volume gives the scattering matrix $S(E)$ at that energy in infinite volume [196]. This leads to $S_l(E) = e^{2i\delta_l(E)}$ for partial wave l only for specific values of E, since the spectrum in a finite volume is discrete. The energies of lattice eigenstates are extracted from the correlation matrix, Eq. (488), where interpolators preferably span the most important Fock components. For quarkonium(-like) states one takes, for example, $\mathcal{O} \approx \bar{Q}\Gamma Q$, two-meson interpolators $\mathcal{O} = (\bar{Q}\Gamma_1 q)(\bar{q}\Gamma_2 Q)$, $(\bar{Q}\Gamma_1 Q)(\bar{q}\Gamma_2 q)$, and $\mathcal{O} = [\bar{Q}\Gamma_1\bar{q}][Q\Gamma_2 q]$ with $Q = c, b$ and $q = u, d, s$. The energy eigenstates $|n\rangle$ are predominantly "one-meson" states (e.g. χ_{c0}) or

predominantly "two-meson" states (e.g. $D\bar{D}$)—in interacting theory they are mixtures of those. The Lüscher approach has been thoroughly verified on the conventional resonances like ρ. The generalization of this approach to multi-channel scattering is discussed, e.g., in Refs. [185,1398]. The scattering of the particles with integer/half-integer spin in generic moving frames is considered, e.g., in Refs. [187,1399].

A modification of the Lüscher approach has been proposed, based on the use of unitary chiral perturbation theory in a finite volume [1400–1403]. Within this approach, the free parameters are directly fitted to the energy levels measured on the lattice. Using the same values of parameters, the infinite-volume formalism allows one to calculate the scattering amplitudes and determine the resonance pole positions in the complex plane.

Another possibility to extract $S(E)$ is the HALQCD approach [207], which starts by determining the two-hadron Bethe–Salpeter wave function and two-hadron potential $V(r)$ from the lattice. The phase shift $\delta(E)$ and $S(E)$ are then obtained using the Schrödinger equation for the given $V(r)$. This approach has not been verified on conventional resonances yet. There are ongoing discussions as to whether this approach is as rigorous as Lüscher's approach.

The Born–Oppenheimer approach may be applied for systems with heavy quarks Q, where static heavy quark sources are surrounded by light degrees of freedom. The static energy is calculated as a function of the distance r between a static pair $Q(0)Q(r)$ or $Q(0)\bar{Q}(r)$ in the presence of the light degrees of freedom. In Sects. 46 and 14.5.4 we refer to this static energy as the potential $V(r)$ as commonly used in the literature; there is a subtle difference[50] between the static energy and the potential mentioned shortly after Eq. (482). Related potentials were mentioned in the previous sections. The potential is then used in the Schrödinger equation to determine the properties of the system.

Recently, a novel method was suggested that allows direct extraction of the real and imaginary parts of the optical potential from lattice data [1404]. The method relies on the analytic continuation into the complex plane and is applicable even if the intermediate states contain more than two particles.

All the presented simulations of heavy quarkonia omit Wick contractions with $\bar{Q}Q$ annihilation, while all other Wick contractions are taken into account.

Vector and scalar resonances Until recently, all quarkonia above the $D\bar{D}$ ($B\bar{B}$) threshold were treated by ignoring the strong decay to a pair of charmed (beauty) mesons. The pioneering investigation of mixing between $c\bar{c}$ and $D\bar{D}$ was presented in Ref. [1405]. The first simulation that determined m_R and Γ_R for such resonances using Lüscher's approach considered vector and scalar charmonia [197]. The Breit–Wigner-type fit of the $D\bar{D}$ scattering matrix $S(E)$ in P wave leads to a resonance mass and width of $\psi(3770)$ that agree with experiment within sizeable errors (see Fig. 171).[51] The $\psi(2S)$ appears as a bound state pole below the threshold.

In the scalar channel, only the ground state $\chi_{c0}(1P)$ is understood and there was no commonly accepted candidate for its first excitation $\chi_{c0}(2P)$ until recently. Some identifed $X(3915)$ with this state, but this was seriously questioned in Refs. [1240–1242], as discussed in Sect. 14.5.2. The alternative candidate $X^*(3860)$ was observed by Belle in 2017 [1184] as a rather broad resonance in

[50] hey differ in perturbative QCD at three loops for ultrasoft corrections. In the non-perturbative regime such corrections are not there.

[51] Actually, the $\psi \to D\bar{D}$ coupling (g) is compared to the experiment, rather than the width $\Gamma = g^2 p^3/(6\pi m_R^2)$.

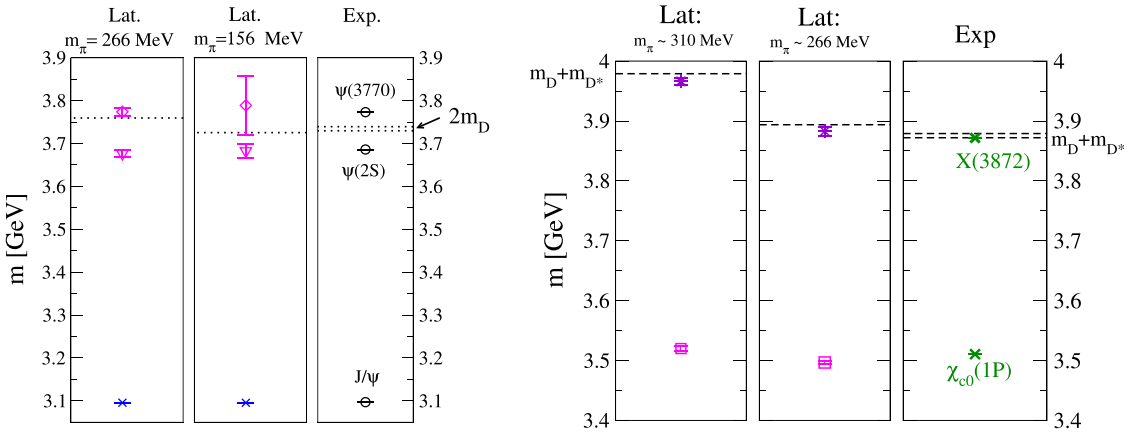

Fig. 171. Left: The spectrum of the vector charmonia from Ref. [197]: the diamond denotes the resonance mass of $\psi(3770)$, while the triangle denotes the pole mass of the bound state $\psi(2S)$; both are obtained from the $D\bar{D}$ scattering matrix. Right: The location of $X(3872)$ with $I = 0$ which emerges as a shallow bound state in $D\bar{D}^*$ scattering at $m_\pi \approx 266$ MeV [198] and $m_\pi \approx 310$ MeV (C. DeTar and S.-H. Lee, private communication, 2014, an update of Ref. [199]).

the $D\bar{D}$ invariant mass. The scattering matrix for $D\bar{D}$ in S wave was extracted from lattice [197] and provides an indication of a rather narrow resonance slightly below 4 GeV with a width of $\Gamma[\chi'_{c0} \to D\bar{D}] < 100$ MeV, which is compatible with the experimental $X^*(3860)$ at a 2.7σ level [1184]. Further experimental and lattice QCD efforts are required to map out the $D\bar{D}$ and $J/\psi\omega$ scattering in more detail.

Charmonium-like $X(3872)$ and $X(4140)$ $X(3872)$ lies experimentally on the $D^0\bar{D}^{0*}$ threshold and its existence on the lattice cannot be established without taking into account the effect of this threshold. This was first done by simulating $D\bar{D}^*$ scattering in Ref. [198] using $D\bar{D}^*$ and $c\bar{c}$ operators. The $D\bar{D}^*$ scattering matrix in the $I(J^{PC}) = 0(1^{++})$ channel was determined using Lüscher's approach. The pole was found just below the threshold (Fig. 171) and it was associated with a bound state $X(3872)$. The more recent simulation using the HISQ action confirms the existence of such a pole (C. DeTar and S.-H. Lee, private communication, 2014; [199]). The finite-volume corrections for such shallow bound states fall as exponentials of pL, where p is the binding momentum [1406]. For a discussion of the quark mass dependence of the $X(3872)$ we refer to Refs. [1407,1408].

The lattice study in Ref. [1409] investigated the overlaps of the different operators needed to make the $X(3872)$ with $I = 0$ visible on the lattice. The energy eigenstate related to $X(3872)$ appears in the simulation only if $D\bar{D}^*$ as well as $c\bar{c}$ interpolating fields are employed. The $X(3872)$ does not appear in the absence of $c\bar{c}$ interpolators, even if (localized) interpolators $[\bar{c}\bar{q}]_{3_c}[cq]_{\bar{3}_c}$ or $[\bar{c}\bar{q}]_{6_c}[cq]_{\bar{6}_c}$ are in the interpolator basis. Although the overlaps are scheme and scale dependent, and no theoretically strict conclusion can be driven from them, this might nevertheless suggest that the $c\bar{c}$ Fock component is most likely more essential for creating the $X(3872)$ than the diquark–antidiquark one.

A charged $X(3872)$ with $J^{PC} = 1^{++}$ was not found in Ref. [1409], although the diquark–antidiquark interpolators were incorporated. A reliable search for the neutral $I = 1$ state would need to incorporate isospin-breaking effects [1410], but that has not been performed on the lattice yet.

The experimental candidate $X(4140)$ with hidden strangeness and $J^{PC} = 1^{++}$ was recently confirmed by the high-statistics LHCb study [1204,1205]. The lattice search for it was performed

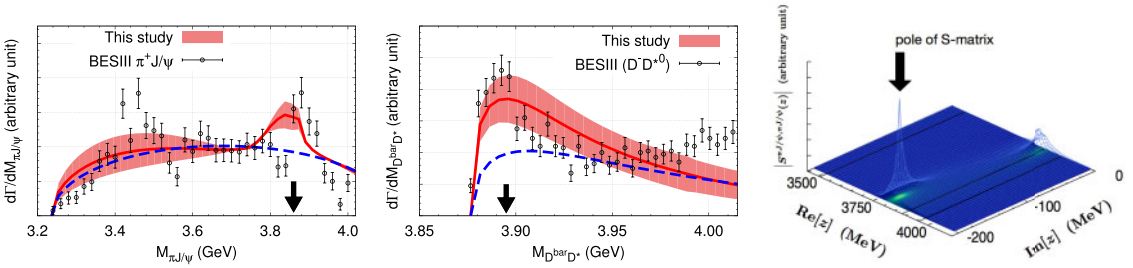

Fig. 172. Simulation of $Z_c^+(3900)$ based on the HALQCD method [208]. Left and center: The red lines present the lattice QCD results for $Y(4260) \to J/\psi\pi\pi$ and $Y(4260) \to D\bar{D}^*\pi$ differential rates, while the blue lines present the results if $J/\psi\pi$-$D\bar{D}^*$ coupling is turned off by setting $V_{J/\psi\pi,D\bar{D}^*} = 0$. Right: Poles of the scattering matrix in the complex energy plane.

with $J/\psi\phi$, $D_s\bar{D}_s^*$, and $[\bar{c}\bar{s}][cs]$ interpolators [1409]. If $X(4140)$ was an elastic resonance in $J/\psi\phi$ or $D_s\bar{D}_s^*$ where both channels are decoupled, one would expect an additional lattice eigenstate near m_X. Such an eigenstate was not found, so $X(4140)$ as a dominantly elastic resonance (on the unphysical sheet) is not supported. This may point to a coupled channel origin of this structure, which may still allow for the presence of a state as a pole in the infinite-volume coupled channel S matrix. The S-wave and P-wave $J/\psi\,\phi$ scattering matrices from the simulations of Ref. [1411], which omit $\bar{s}s$ annihilation, also do not support the elastic resonance $X(4140)$.

Charged $Z_{c,b}^+$ and $B\bar{B}$ potentials The lattice search for the manifestly exotic states Z_c^+ with flavor content $\bar{c}c\bar{d}u$ and $I^G(J^{PC}) = 1^+(1^{+-})$ is challenging since the experimental candidates lie above several thresholds and can decay to several final states via strong interaction. A reliable treatment requires the simulation of coupled channels and the extraction of the coupled channel scattering matrix.

The only simulation that determined the coupled channel $S(E)$ for such systems applied the HALQCD approach [208]. The potential $V_{\pi J/\psi,\pi J/\psi}(r)$ related to the Nambu–Bethe–Salpeter equation is determined between the J/ψ and π as a function of their separation, r. The other diagonal and off-diagonal potentials $V_{\alpha,\beta}(r)$ for three channels $\alpha, \beta = J/\psi\pi^+$, $D\bar{D}^*$, $\eta_c\rho$ were also determined [208] according to the formalism of Ref. [1412]. The off-diagonal potential between channels $\pi J/\psi$ and $D\bar{D}^*$ is larger than other ones, which seems to indicate a sizeable coupled channel effect near the $D\bar{D}^*$ threshold. The potentials render a 3×3 scattering matrix for three coupled two-meson channels [208]. This is then used to determine the three-body decay $Y(4260) \to J/\psi\pi\pi$ and $Y(4260) \to D\bar{D}^*\pi$ in a semi-phenomenological way. The differential rate indeed shows a peak around Z_c mass (the red line in Fig. 172). If the potential between $J/\psi\pi$ and $D\bar{D}^*$ is turned off, the peak disappears (blue dashed line). This indicates that the coupling of $J/\psi\pi$ and $D\bar{D}^*$ channels seems to be crucial for the existence of Z_c. This also needs to be verified by the Lüscher method. Notice that a virtual state pole deep in the complex plane was found in Ref. [208]. This is consistent with the fact that the obtained peaks in Fig. 172 are not as narrow as the observed ones. However, a phenomenological fit to the BESIII data for the $Z_c(3900)$ reveals a pole, as either a virtual state or a resonance, much closer to the threshold [1376].

The S-wave and P-wave scattering matrices near the $D\bar{D}^*$ threshold were determined using only $D\bar{D}^*$ interpolating fields in Ref. [1413], which may not be reliable since the ground state of the system is $J/\psi\pi$. The authors concluded that no evidence for $Z_c(3900)^+$ was found.

A simplified search for Z_c^+ states extracted the energies of eigenstates [199,1414] without determining $S(E)$. The simulation of the coupled channels (with a large number of meson–meson and diquark–antidiquark interpolators) renders eigenenergies close to the energies of the non-interacting two-meson states, e.g. $J/\psi\pi^+$, $D\bar{D}^*$. A scenario with elastic resonance poles[52] on the unphysical sheet predicts an additional eigenstate, but such an eigenstate was not found in the actual simulations [199,1414].[53] This could indicate that the effect of coupled channels is significant for experimental Z_c, in line with the HALQCD result [208]. Notice that the analytic study of coupled channels [1415], which renders the experimental differential rates [1376] and at the same time quantitatively agrees with the lattice energy levels [1414], allows for scenarios where Z_c can be a virtual state with a pole below the $D\bar{D}^*$ threshold.[54]

The lattice search for a pair of Z_b^+ from Belle [1170] is challenging as each of them can decay to at least five two-meson final states. The additional difficulty is that the discrete two-meson energies[55] are much denser than for the Z_c channel. The only exploratory study considered $B(0)\bar{B}^{(*)}(r)$ potentials within the Born–Oppenheimer approach [210]. The challenge is that the $\Upsilon(nS)\pi$ represents the ground state of the $\bar{Q}(0)Q(r)\bar{d}u$ system, which leads roughly to the energy $V_{Q\bar{Q}}(r) + m_\pi$. The $B(0)\bar{B}^*(r)$ potential had to be extracted from the first excited eigenstate, and the Schrödinger equation for this potential rendered a possible indication of a $\bar{b}b\bar{d}u$ bound state with a binding energy of (58 ± 71) MeV and $I(J^P) = 1(1^+)$ [210]. The effects of the heavy quark spin have been considered analytically and it was found that a bound state with binding energy 59^{+30}_{-38} MeV persists after their inclusion [1134]. Exploratory studies of related $B\bar{B}$ potentials for the $I = 0$ channel [1416,1417] followed the discovery of $Q\bar{Q}$ string breaking [1418]. Most of the interesting spectroscopic aspects related to $\bar{b}b$ and $B\bar{B}$ mixing are still unexplored on the lattice.

$\bar{q}\bar{q}QQ$ states, $BB^{(*)}$ and $DD^{(*)}$ potentials The $\bar{q}\bar{q}QQ$ system was considered with static quarks Q within the Born–Oppenheimer approximation [1417,1419–1421], and also with non-static Q [1135,1422–1424]. On the lattice, this open heavy-flavor channel is simpler than the closed heavy-flavor one since the ground state is $BB^{(*)}$ and leads to the potential/interaction of the $BB^{(*)}$ (for $Q = b$). Most lattice studies explored whether a bound state could exist in the $\bar{q}\bar{q}QQ$ system. Among all the investigated channels (including $q = u, d, s$, $Q = b, c$, $J = 0, 1, 2$), the channel $\bar{u}\bar{d}bb$ with $I(J^P) = 0(1^+)$ gives an indication for a bound state below BB^* in several studies [1419,1420,1424]. This is manifested as an eigenstate about 200 MeV below the BB^* threshold [1424], and the same study also favors $\bar{u}\bar{s}bb$ with $J^P = 1^+$ as a bound state. The $DD^{(*)}$ and $\bar{K}D$ ($cs\bar{u}\bar{d}$) systems are typically not found to form bound states on the lattice [1422,1423]. However, certain phenomenological studies favor DD^* bound by only few MeV [1425,1426], which prompts further lattice investigation to achieve such a precision. A search for DD^* bound states in double-charm production at Belle II is an exciting possibility, where the search strategies have been investigated in Refs. [1425,1426].

The possible existence of resonances in such systems remains yet to be explored.

[52] The resonance scenario [1415] does not predict an additional eigenstate since the phase shift does not pass through $\pi/2$ at resonance there.

[53] An extra eigenstate (in addition to the expected two-meson states) has been found for all resonances and all bound states that have been established on the lattice up to now.

[54] Or it can be a resonance above the threshold, but the phase shift does not pass through $\pi/2$ at resonance in this case [1415].

[55] The non-interacting energies $E \approx 2\sqrt{m_B^2 + n(2\pi/L)^2}$ for $B\bar{B}$ are denser than for $D\bar{D}$.

Hadro-quarkonium: $Q\bar{Q}$ and light hadrons The hadro-quarkonium picture [1332] consists of a color-singlet $Q\bar{Q}$ pair to which a color-singlet light hadron H is bound by residual QCD forces—see Sect. 14.5.3. This scenario was tested in the Born–Oppenheimer approach by determining the modification of the potential between a static quark–antiquark pair induced by the presence of a light hadron [1427]. The modification $\Delta V_H(r) = V_H(r) - V_0(r)$ was found to be negative, $\Delta V_H(r) < 0$, for all investigated hadrons: $H = \pi, K, \rho, K^*, N, \Sigma, \Lambda, \Delta, \Sigma^*, \Omega, \Xi, \Xi^*$. The main effect was as a reduction of the linear slope of the potential. At a distance of 0.5 fm the potential was lowered by only about 2–3 MeV for all these hadrons. The Schrödinger equation for these potentials yields quarkonia that are more tightly bound by 1–7 MeV in the presence of the light hadrons.

Hybrids and other exotics Hybrid states $\bar{Q}gQ$ have been discussed generally in the *Hybrid states* subsection of Sect. 14.5.3 and in Sect. 14.5.5. They have been addressed on the lattice, for example, in Refs. [209,1119,1428–1434]. The $\bar{Q}gQ$ are unstable resonances above the $(\bar{Q}q)(\bar{q}Q)$ threshold in dynamical QCD, while practically all previous lattice simulations neglected their strong decays. This challenge is the main reason why there has been little progress on this front recently. Quenched QCD is somewhat simpler in this respect as the threshold for the decay $\bar{Q}gQ \to (\bar{Q}Q) +$ glueball lies higher. Most studies consider $J^{PC} = 1^{-+}$, which are much easier to disentangle from the conventional mesons.

The recent results for the masses of $\bar{c}gc$ hybrids with relativistic quarks [195] are shown in red and blue in Fig. 170 above. The 1^{-+} state is obtained at 4.31(2) GeV [195], which is close to the other determinations, for example 4.4 GeV in Ref. [1429] and 4.405 ± 0.038 GeV in Ref. [1430]. The 1^{--} candidate resides at 4.41(2) GeV [195], close to 4.379 ± 0.149 GeV from [1431] (the authors claim that they have found a radially excited vector hybrid; however, such an interpretation was criticized in Ref. [1432]).

The lightest bottomonium hybrid was found to be 1^{-+} at 10.9 GeV in a quenched simulation with relativistic b quarks [1428]. The other approach is within the Born–Oppenheimer approximation, where hybrid static energies for excited static $Q(0)\bar{Q}(r)$ were calculated first. This was done long ago [209], but only in quenched approximation so far. The lightest hybrid $\bar{b}gb$ was also found at about 10.9 GeV, and the masses for the lowest few hybrids show reasonable agreement with the results based on quenched NRQCD [209].

An experimental search for hybrids, particularly those with exotic quantum numbers 0^{+-} and 1^{-+}, is of high importance.

$Q\bar{Q}$ potentials for other exotic states The $\bar{Q}(0)Q(r)$ potentials related to hybrids, mentioned in the previous section, represent just one of the possible types of interest. The potentials related to light adjoint mesons in static octet-color sources $(Q\bar{Q})$ were calculated in the quenched approximation [1435]. An analytic study proposed to calculate many interesting Born–Oppenheimer potentials related to $\bar{Q}(0)Q(r)$, accompanied with glue and/or light quarks with various angular momenta and flavor quantum numbers [211]. Most of these have not been calculated on the lattice yet, but recent dynamical simulations discussed above [210,1427] investigate along these lines.

Pentaquarks The NPLQCD collaboration finds an interesting indication for an $\eta_c N$ bound state approximately 20 MeV below the $\eta_c N$ threshold (N denotes a nucleon) [1436]. This is the only pentaquark candidate containing $c\bar{c}$ from lattice studies up to now. As the simulation was done at an SU(3) flavor symmetric point ($m_\pi \approx 800$ MeV), it is not clear yet whether this bound state persists

to physical m_π. A Belle II search for such a bound-state pentaquark and its siblings is of prime interest. An $\eta_c p$ (p = proton) resonance or a bound state could be searched for in inclusive decays $Y(nS) \to \eta_c p X$ by considering the invariant mass $M(\eta_c p)$. Here, η_c is reconstructed through its deacy to $K^*K\pi$, $2(\pi^+\pi^-)$, …, and X is anything or something with a reconstructed antiproton. An $\eta_c p$ structure would be found for $M(K^*K\pi\ p) < m_{\eta_c} + m_p$. Another production mechanism could be through Λ_b decays if $E_{cm} > 2m_{\Lambda_b}$ were reached at Belle II.

The simulation of two pentaquarks P_c discovered by LHCb [1054] will be more difficult as they are located 0.4 GeV above the $J/\psi p$ threshold and they have several open decay channels. Such lattice results are not available yet. Some light on such systems might be inferred from Ref. [1427], where the $\bar{Q}Q$ potential $V(r)$ in the presence of baryons is considered within the hadroquarkonium picture.

Lattice outlook Lattice QCD spectra of charmonia and bottomonia below the open flavor threshold are precise, under control, and in reasonable agreement with experiment. The decay constants and radiative transitions between some of these states have been determined, and the remaining ones are tractable. $\bar{Q}Q$ annihilation is omitted in all simulations presented here, and this presents the main remaining uncertainty for quarkonia below the open flavor threshold. This annihilation would invoke decays to light hadrons and presents a considerable challenge.

Information on the states above or slightly below threshold have to be inferred from the scattering matrix extracted on the lattice. The hadronic resonances that can strongly decay only to one two-hadron final state can be treated rigorously by simulating the scattering in this channel. The same applies for stable hadrons that are situated slightly below one threshold. Reasonable results can also be obtained for the hadrons where a coupling to one channel is dominant, while coupling to others may be neglected. Such an approximation is not reliable for exotic candidates that could involve important coupled channel effects. The radiative and weak transitions $\langle H_1|J^\mu|H_2\rangle$, where the initial or final hadron decays strongly via one channel, could be studied along the lines of a recent pioneering simulation [204] in the light sector.

The states that can decay into two or three different two-hadron final states are challenging, but manageable in principle. The scattering matrix for few-coupled channels has recently been extracted via a Lüscher-type method for other systems [174,206,1437].[56] Some analogous results relevant to quarkonium(-like) spectroscopy at Belle II can be expected by the time it starts operating.

Many interesting aspects related to systems containing $\bar{b}b$ or bb will be obtained by further investigations based on Born–Oppenheimer potentials. Other interesting future directions for lattice studies of quarkonium-like states were recently put forward in Refs. [1438,1439].

14.5.5. Exotics from QCD with EFTs

Authors: N. Brambilla, A. Vairo

In Ref. [1136] an effective field theory description of hybrid states was constructed on the basis of pNRQCD. Lattice calculation of the two lowest static hybrid energy curves (Σ_u and Π_u) is provided in the quenched approximation [209] (see the *Hybrids and other exotics* subsection of Sect. 14.5.4). The main uncertainty comes from the poor lattice knowledge of a non-perturbative parameter entering

[56] Special attention is neecssary to get rid of possible model dependence in the parameterizations of the coupled channel T matrix. Sometimes, even the number of poles in the relevant energy region could be different [174,1367].

Table 129. J^{PC} multiplets with $l \leq 2$ for the Σ_u^- and Π_u gluonic states. We follow the naming notation H_i used in Refs. [209,211], which orders the multiplets from lower to higher mass. The last column shows the gluonic static energies that appear in the Schrödinger equation of the respective multiplet.

	l	$J^{PC}\{s=0, s=1\}$	$E_n^{(0)}$
H_1	1	$\{1^{--}, (0,1,2)^{-+}\}$	Σ_u^-, Π_u
H_2	1	$\{1^{++}, (0,1,2)^{+-}\}$	Π_u
H_3	0	$\{0^{++}, 1^{+-}\}$	Σ_u^-
H_4	2	$\{2^{++}, (1,2,3)^{+-}\}$	Σ_u^-, Π_u
H_5	2	$\{2^{--}, (1,2,3)^{-+}\}$	Π_u

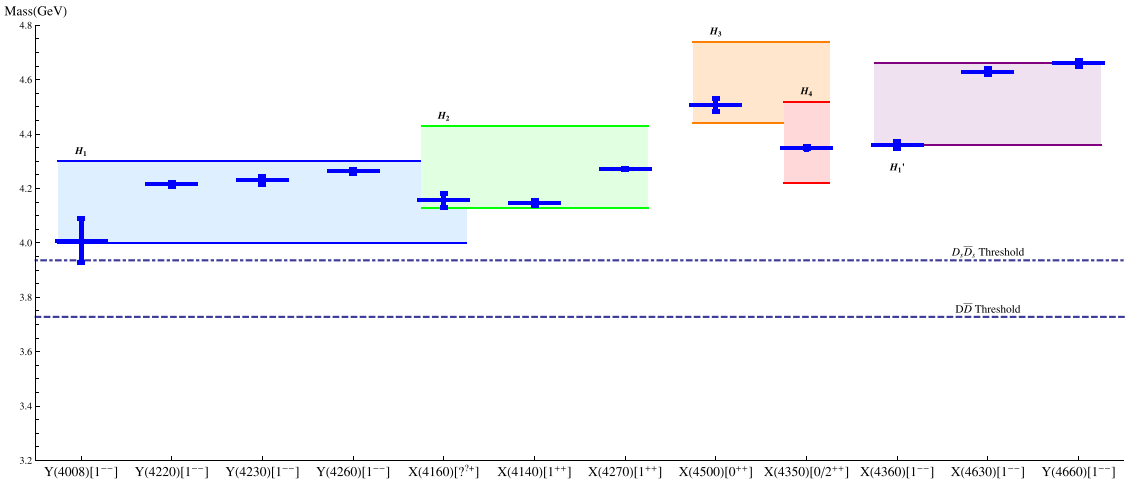

Fig. 173. Comparison of the experimental candidate masses for the charmonium sector with the results of Ref. [1136] for the hybrid masses. The experimental states are plotted in solid blue lines with error bars corresponding to the average of the lower and upper mass uncertainties. The results for the H_1, H_2, H_3, H_4, and H_1' multiplets have been plotted in error bands corresponding to the gluelump mass uncertainty of ± 0.15 GeV.

the calculation called gluelump mass. Up to now the EFT does not include spin but manages to obtain coupled Schrödinger equations at leading order that cause an effect on the energy level called Λ doubling already known from molecular physics. The multiplets obtained are given in Table 129 and compared to the neutral heavy quark mesons above the open flavor threshold in Fig. 173 and with a recent direct lattice calculation of the hybrid masses multiplets [195] in Fig. 174. It is interesting to compare these results to those obtained in other approaches.

The Born–Oppenheimer approximation for hybrids [211] produces spin-symmetry multiplets with the same J^{PC} constituents as the H_i multiplets in Table 129. However, in all the existing Born–Oppenheimer papers the mixing terms have been neglected and therefore the masses of opposite parity states are degenerate, in contrast with the EFT approach in which the degeneracy between opposite parity states is broken (Λ doubling).

In the constituent gluon picture hybrids are assumed to be composed of a gluonic excitation bound to a heavy quark–antiquark pair—see the *Hybrid states* subsection of Sect. 14.5.3. The gluons are assumed to appear in J^{PC} representations, unlike the case of pNRQCD or Born–Oppenheimer descriptions, in which the gluonic states appear in Λ_η^σ representations. The quantum numbers of the resulting hybrid are obtained by adding those of the gluon and those of the heavy quark–antiquark pair using the standard rules for addition of angular momenta. In this way one gets the same J^{PC}

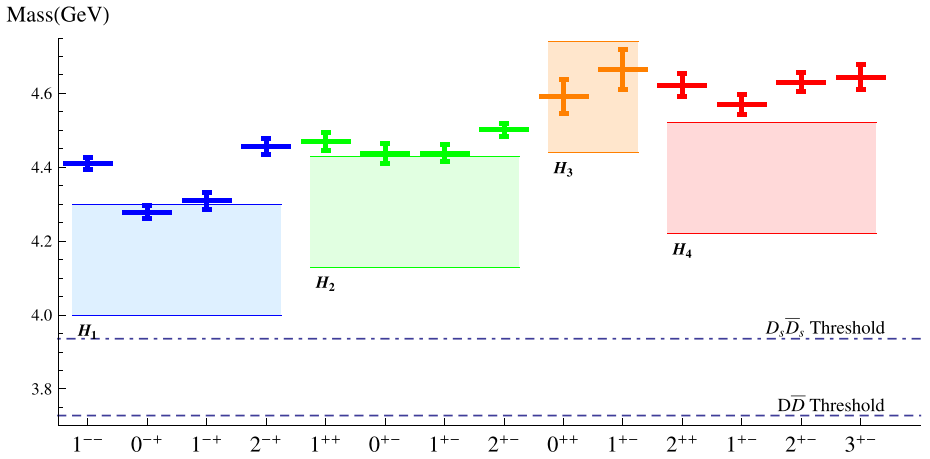

Fig. 174. Comparison of the results from direct lattice computations of the masses for charmonium hybrids [195] with the results of Ref. [1136] for the hybrid masses. The direct lattice mass predictions are plotted in solid lines with error bars corresponding to the mass uncertainties. The results for the H_1, H_2, H_3, and H_4 multiplets have been plotted in error bands corresponding to the gluelump mass uncertainty of ± 0.15 GeV.

quantum numbers but arranged in larger multiplets. If in the constituent gluon picture we add the gluon quantum numbers 1^{+-} to an S-wave heavy quark–antiquark pair in a spin singlet $\{0^{-+}\}$ or spin triplet $\{1^{--}\}$ state, then we get exactly the quantum numbers of H_1. Similarly, for P-wave quarkonia with quantum numbers $\{1^{+-}, (0, 1, 2)^{++}\}$ (corresponding to different spin states) we get $H_2 \cup H_3 \cup H_4$. H_5 would then be included in the combination with the next quarkonium quantum numbers. Since for pNRQCD in the limit $r \to 0$ we recover spherical symmetry, we can see the constituent gluon picture as the short-distance limit of the pNRQCD. Furthermore, one can interpret the finer multiplet structure of pNRQCD with respect to the constituent gluon picture as the effect of the finite distance r between the heavy quark pair.

The flux-tube model [1314] arises from the idea that for QCD in the strong coupling regime one can think of the gluonic degrees of freedom as having condensed into a collective string-like flux-tube. In this picture the spectrum of gluonic static energies can be interpreted as the vibrational excitation levels of the string. The lowest excitations of such a string will correspond to non-relativistic, small, transverse displacement oscillations, and as such should be well described by the Hamiltonian of a continuous string. The eigenstates of such a Hamiltonian are characterized by the phonon occupation number and their polarizations, while the spectrum eigenenergies correspond to the different phonon occupation numbers. The hybrid quantum numbers are constructed by specifying the gluonic states via phonon operators. The value of Λ corresponds to the number of phonons with clockwise polarization minus the number of phonons with anticlockwise polarization. From here one can construct the J^{PC} quantum numbers of the hybrid states in an analogous way to the Born–Oppenheimer picture. The first excited energy level is a one-phonon state, which necessarily corresponds to a $\Lambda = 1$ state, unlike in the pNRQCD case, where the first excited energy level can be $\Lambda = 0, 1$. Thus, the pattern of the spin symmetry multiplets emerging from the flux-tube model in the case of the first excited static energy is the one in Table 129, except for the non-existence of H_3.

In order to interpret the data it is necessary to include spin and enlarge the description to decay and transitions [1440]. Work in this direction is currently in progress. Moreover, by adding light quarks with isospin number into the picture [211,1136,1317] it will eventually be possible to

describe tetraquarks and molecular states directly from QCD, combining EFTs and lattice QCD. For a discussion of EFTs for molecular states based on hadronic degrees of freedom we refer to Sect. 14.5.3.

In Ref. [1441] the van der Waals forces between two $\Upsilon(1S)$ or two η_b states were studied to investigate the possibility of the formation of a bound state of two quarkonia. Van der Waals QCD forces may also play a role in the binding of the charmonium pentaquark.

14.5.6. Summary

In summary, the energy region at and above the strong decay threshold is very interesting for future investigation, holding the promise of unveiling new interactions and new binding mechanisms of the strong interactions. At the moment a plethora of new X, Y, Z states have been observed, in part paired with enormous theoretical activity with a number of phenomenological models. A theory description inside EFTs and lattice theory is currently being developed and new results will soon be available to match the experimental development.

14.6. Belle II prospects for charmonium(-like) states

Presently more than 20 charmonium-like states are known (see Tables 125 and 126). Their properties do not agree with the expectations for pure $c\bar{c}$ levels, which indicates that their structure is exotic. Theoretical approaches to the description of these states were presented in the previous section. For each state, several variants of interpretation exist (tetraquark, hybrid, hadroquarkonium, molecule, …), and thus the structures of the state remains unestablished. Existing experimental data are not precise enough or are not sufficiently full to discriminate the various interpretations. Thus, further experimental input is crucial for understanding the quarkonium-like states. This section describes future studies on charmonium and charmonium-like states that can be performed at Belle II. The states are grouped according to the processes in which they are produced: B decays, initial state radiation, two-photon processes, and double charmonium production. All the considered states are situated above the $D\bar{D}$ threshold.

14.6.1. B decays

Authors: R. Mizuk, S. L. Olsen

Charmonium(-like) states are produced in B meson decays in association with a kaon: $B \to K X_{c\bar{c}}$. Such processes are CKM favored and therefore have relatively large branching fractions, typically 10^{-4}–10^{-3}. Decays of B mesons produced at the $\Upsilon(4S)$ have very useful properties for studies of charmonium(-like) states:

- Both the B and the kaon are spinless, therefore the state $X_{c\bar{c}}$ is produced polarized (with $J_Z = 0$ relative to the kaon path). This helps to discriminate various spin and parity hypotheses for the $X_{c\bar{c}}$.
- Using hadronically tagged events (i.e. with a fully reconstructed second B) one can measure absolute branching fractions of the charmonium(-like) states, as discussed below.

In B decays, Belle observed two narrow charmonium levels: the $\eta_c(2S)$ reconstructed in its $K^0_S K^{\pm}\pi^{\mp}$ channel [1442], and the $\psi_2(1D)$ reconstructed via its radiative transition $\psi_2(1D) \to \gamma\, \chi_{c1}$ [1182]. The $\eta_c(2S)$ is a radial excitation of the spin singlet S-wave state, and its mass is below the $D\bar{D}$ threshold. By now all charmonium levels below the $D\bar{D}$ threshold are known. The $\psi_2(1D)$

is a spin triplet member of the $1D$ multiplet with $J^{PC} = 2^{--}$. It is above the $D\bar{D}$ threshold but, due to unnatural spin parity, cannot decay to this channel. Since the $\psi_2(1D)$ is below the $D\bar{D}^*$ threshold, it is very narrow [1443,1444]. Only one more narrow charmonium level remains unobserved: the $\eta_{c2}(1D)$, a spin singlet $1D$ state with $J^{PC} = 2^{-+}$. It is expected to reside between the $D\bar{D}$ and $D\bar{D}^*$ thresholds and, similarly to $\psi_2(1D)$, cannot decay to $D\bar{D}$ due to unnatural spin parity [1443,1444]. A promising search channel might be $B \to K\,(h_c\gamma)$ [1443]. The lattice QCD predictions for the mass of this state are presented in Fig. 169 and Sect. 46.

B decays have also been a rich source of charmonium-like mesons. Of the 24 known states, 10 have been observed in B decays (see Tables 125 and 126). In addition to the well-known $X(3872)$ observed in the $\pi^+\pi^- J/\psi$ channel, these include the $X(3915)$ seen in $\omega J/\psi$; $Z(4050)^+$ and $Z(4250)$ in $\pi^+\chi_{c1}$; $Z(4200)^+$ in $\pi^+ J/\psi$; $Z(4430)^+$ in $\pi^+\psi(2S)$ and in $\pi^+ J/\psi$; $X(4140)$, $X(4274)$, $X(4500)$, and $X(4700)$ in $\phi J/\psi$. With the possible exception of the $X(3872)$, the experimental information on all other states is very incomplete: the $Z(4050)^+$, $Z(4200)^+$, $Z(4250)^+$, and high-mass X states were seen in one experiment only and therefore need confirmation; the spin parities of the $X(3915)$, $Z(4050)$, and $Z(4250)$ are still not determined; for most states only one decay channel is known. Belle II can considerably improve this situation.

Belle and LHCb performed full amplitude analyses of the $B^0 \to K^\pm\pi^\mp J/\psi$, $B^0 \to K^\pm\pi^\mp\psi(2S)$, and $B^0 \to K\phi J/\psi$ decays, which permitted J^P quantum number determinations of the corresponding intermediate charmonium-like states. It is very important to apply full amplitude analyses to $B \to K\,\omega J/\psi$ and $B \to K\,\pi\,\chi_{c1}$ decays to determine the spin parities of the $X(3915)$, $Z(4050)$, and $Z(4250)$.

While the $X(3872)$ has been seen to decay into $D^0\bar{D}^{*0}$ final states, open flavor decays of the other states have yet to be seen. These can be investigated by comprehensive studies of the three-body decay processes $B \to K(D\bar{D})$, $B \to K(D\bar{D}^*)$, and $B \to K(D^*\bar{D}^*)$, for $D^{(*)}\bar{D}^{(*)}$ final states with both zero and non-zero total charge. The addition of one more pion will provide access to the final states with the P-wave D mesons: $K(D\bar{D}^{**})$ and $K(D^*\bar{D}^{**})$. Since the states are broad, full amplitude analyses will be necessary in all cases. It will also be of considerable interest to study decays that include D_s mesons.

Systematic investigations of charmonium plus light hadron final states, $B \to K\,(c\bar{c} + h)$, will be useful both for uncovering new decay channels of known charmonium-like mesons and for new charmonium-like meson searches. In this case, one should consider all narrow charmonium states (η_c, $\eta_c(2S)$, J/ψ, $\psi(2S)$, h_c, χ_{cJ}, and $\psi_2(1D)$) and light hadron systems such as π^0, $\pi^\pm$, $\pi^+\pi^-$, η, ω, and ϕ. Recently, Belle performed a systematic search for B decays into final states with an η_c meson—$B^\pm \to K^\pm\pi^0\eta_c$, $B^\pm \to K^\pm\pi^+\pi^-\eta_c$, $B^\pm \to K^\pm\eta\,\eta_c$, and $B^\pm \to K^\pm\omega\,\eta_c$ [1445]—but no signals were seen for any of these channels with the available data sample. Belle also studied the decays $B \to K\,\eta J/\psi$ [1446], $B \to K\pi\,\chi_{c2}$, and $B \to K\pi\pi\,\chi_{c1,2}$ [1447]; there is possibly a hint of the $Y(4140)$ in $\pi^+\pi^-\chi_{c1}$ [1448]. There is interest in searching for radiative transitions of new states, in which case a charmonium should be combined with a photon. Belle studied the $B \to K\,\gamma\,\chi_{c1,2}$ decays and this resulted in the first evidence for $\psi_2(1D)$ [1182]. Investigations of these channels with a charmonium replaced by $X(3872)$ might also be interesting; recently Belle observed the first decay of this kind, $B \to K\pi X(3872)$ [1449].

Apart from $X(3872)$, which likely has a dominant $D^0\bar{D}^{*0}$ molecule-like component, the interpretations of the other states produced in B decays remain unclear. An interesting possibility for the $X(3915)$ is that it is not a new state, but a new decay channel of the established $\chi_{c2}(2P)$ meson [1242] (see Sect. 14.5.2). To test this hypothesis one should determine the $X(3915)$ spin

parity using an amplitude analysis of $B \to K\,\omega J/\psi$ decays, and search for an intermediate $\chi_{c2}(2P)$ in the $B \to KD\bar{D}$ decays. Additional experimental information on the charmonium-like states, such as their spin parities, open flavor, and new hidden flavor decay channels, will facilitate their interpretation and help to discriminate between various models. More precise measurements of masses and widths of charmonium(-like) states are also important.

Determinations of absolute branching fractions of the XYZ states (and, thus, partial decay widths) are essential. This can be done at Belle II by identifying their inclusive production in $B \to KX$ decays via the missing mass recoiling against the kaon. For this, one needs to know the initial momentum vector of the B meson with good precision, which can be determined in $B\bar{B}$ events where the accompanying $\bar{B}$ meson is fully reconstructed (i.e. using techniques similar to those described in Ref. [1450]).

For many of the above-described measurements, Belle II will have competition from the LHCb experiment. However, for absolute branching fraction measurements and for studies of final states that include neutral particles, Belle II will have considerably lower background.

14.6.2. Initial state radiation

Author: C. P. Shen

The idea of utilizing initial state radiation (ISR) from a high-mass state to explore electron–positron processes at all energies below that state was outlined in Ref. [1451]. The possibility of exploiting such processes in high-luminosity ϕ and B factories was discussed in Refs. [1452–1454] and motivates the hadronic cross section measurement. States with $J^{PC} = 1^{--}$ can be studied with ISR technology using the huge Belle II data sample.

The ISR cross section for a hadronic final state f is related to the corresponding e^+e^- cross section $\sigma_f(s)$ by

$$\frac{\sigma_f(s,x)}{dx} = W(s,x)\sigma_f(s(1-x)),$$

where $x = \frac{2E_\gamma}{\sqrt{s}}$; E_γ is the energy of the ISR photon in the nominal e^+e^- center-of-mass frame; $\sqrt{s} = E_{\rm cm}$ is the nominal e^+e^- center-of-mass energy; and $\sqrt{s(1-x)}$ is the effective center-of-mass energy at which the final state f is produced. The function $W(s,x)$ is calculated with an accuracy better than 1% and describes the probability density function for ISR photon emission [1052].

Although dramatic progress has been made on the study of the XYZ states and the conventional charmonium states, there are still many questions to be studied in more detail. For example: Are the $X(3872)$ and $\psi_2(1D)$ in $e^+e^- \to \gamma\pi^+\pi^- J/\psi$ coming from resonance decays or continuum production? Are there other similar X states in similar processes such as $\chi_{c2}(2P), X(3915), X(4140)$, and $X(4350)$? Is there a Z_{cs} state decaying into $K^\pm J/\psi$ or $D_s^- D^{*0} + c.c.$, $D_s^{*-} D^0 + c.c.$? Can the Z_c states decay into light hadrons?

More data are necessary for ISR studies. Belle II will accumulate 10 ab^{-1} (50 ab^{-1}) data at around $\Upsilon(4S)$ by 2020 (2024). Compared to the current BESIII experiment, with ISR events the whole hadron spectrum is visible so that the line shape of the resonance and fine structures can be investigated. The disadvantage is that the effective luminosity and detection efficiency are relatively low. Figure 175 shows the effective luminosity from 3 to 5 GeV in the Belle II data samples. We can see that for 10 ab^{-1} Belle II data, we have about 400–500 pb^{-1} of data for every 10 MeV in the range 4–5 GeV. Of course, ISR analyses have a lower efficiency than in direct e^+e^- collisions because of the extra

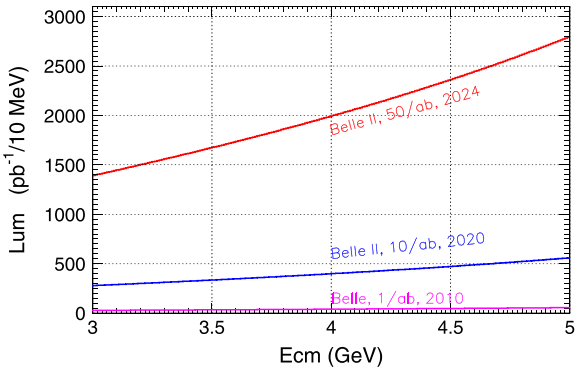

Fig. 175. Effective luminosity at low energy in the Belle and Belle II $\Upsilon(4S)$ data samples.

ISR photons and the boost given to events along the beam direction. Even taking these effects into account, the full Belle II data sample, which corresponds to about 2000–2300 pb^{-1} data for every 10 MeV from 4–5 GeV, will result in similar statistics as BESIII for modes like $e^+e^- \to \pi^+\pi^- J/\psi$. Belle II has the advantage that data at different energies are expected to be accumulated at the same time, making the analysis much simpler than at BESIII at 60 data points. In addition, Belle II gets access to events above 4.6 GeV, which is currently the maximum energy of BEPCII. Very interesting in this context would be the search for the predicted pseudoscalar spin partner of $Y(4660)$ that should have a mass of 4616 MeV [1349] and could be produced in radiative decays of $Y(4660)$. This state should exist, if indeed $Y(4660)$ has a prominent $f_0(980)\psi(2S)$ component as claimed in Ref. [1455].

With a data sample larger than 10 ab^{-1} at Belle II, ISR processes $e^+e^- \to \pi^+\pi^- J/\psi$, $\pi^+\pi^-\psi(2S), K^+K^- J/\psi, K^+K^-\psi(2S), \gamma X(3872), \pi^+\pi^-\psi_2(1D), \pi^+\pi^- h_c, \pi^+\pi^- h_c(2P), \omega\chi_{cJ}$, $\phi\chi_{cJ}, \eta J/\psi, \eta' J/\psi, \eta\psi(2S), \eta h_c, (D^*\bar{D}^*)^\pm\pi^\mp$, and so on can be studied. Some golden modes are:

$e^+e^- \to \pi^+\pi^- J/\psi$: The $Y(4260)$ state was observed and confirmed by BaBar [1209], CLEO [1212], and Belle experiments [1456]. Besides the $Y(4260)$, Belle also observed a broad excess near 4 GeV, called $Y(4008)$ [1213]. With the full BaBar data sample of 454 fb^{-1}, the $Y(4008)$ structure was not confirmed [1210]. The difference between the BaBar and Belle interpretation around 4.01 GeV is large. Recently, BESIII reported a precise measurement of the $e^+e^- \to \pi^+\pi^- J/\psi$ cross section from 3.77 to 4.60 GeV using data samples with an integrated luminosity of 9 fb^{-1} [1214]. While the nature of the events at around 4 GeV is still ambiguous, the dominant resonant structure, the so-called $Y(4260)$, was found to have a mass of $(4222.0 \pm 3.1 \pm 1.4)$ MeV/c^2 and a width of $(44.1 \pm 4.3 \pm 2.0)$ MeV. In addition, a new resonance with a mass of around 4.32 GeV/c^2 is needed to describe the high-precision data. With a 10 ab^{-1} (50 ab^{-1}) data sample at Belle II, the expected statistical error on the $e^+e^- \to \pi^+\pi^- J/\psi$ cross section will be 7.5% (3.0%) at 4.23 GeV/c^2. The questions on the existence of the $Y(4008)$ and whether there are more structures around 4.26 GeV/c^2 will be answered—note that such a light exotic vector state seems incompatible with a molecular interpretation while, e.g., the tetraquark picture calls for light vectors—see the discussions in Sect. 14.5.3. Belle also observed a charged charmonium-like state $Z_c(3900)$ in the $M_{\max}(\pi^\pm J/\psi)$ distributions [1158]. Its properties will be measured with much improved precision.

$e^+e^- \to \pi^+\pi^-\psi(2S)$: The $Y(4360)$ was discovered by BaBar [1457], while Belle observed two resonant structures at 4.36 and 4.66 GeV/c^2, denoted the $Y(4360)$ and $Y(4660)$ [1218]. BaBar confirmed the existence of the $Y(4660)$ state later [1219]. Subsequently, the $Y(4360)$

and $Y(4660)$ parameters were measured with improved precision with the full 980 fb^{-1} data sample of Belle [1166]. Belle also noticed a few events in the vicinity of the $Y(4260)$ mass, but the signal significance of the $Y(4260)$ was only $2.4\,\sigma$. Evidence for a charged charmonium-like structure at 4.05 GeV/c^2, denoted the $Z_c(4050)$, was observed in the $\pi^{\pm}\psi(2S)$ intermediate state in $Y(4360)$ decays, which might be the excited state of the $Z_c(3900)$. With a 10 ab^{-1} (50 ab^{-1}) data sample at Belle II, the expected statistical error on the $e^+e^- \to \pi^+\pi^-\psi(2S)$ cross section will be 12% (5.0%) at 4.36 GeV/c^2. The questions on the presence of the $Y(4260)$ in this channel and the existence of $Z_c(4050)$ will be answered.

$e^+e^- \to K^+K^-J/\psi$: In the updated analysis, a strange partner of the $Z_c(3900)^{\pm}$, called the Z_{cs}, was searched for in the $K^{\pm}J/\psi$ system [1458]. There are clear K^+K^-J/ψ signal events and the cross sections are measured from threshold to 6.0 GeV. Rich structures with large statistical errors are observed; different fits were tried with poor fit quality. No obvious structures were observed in the $K^{\pm}J/\psi$ system. With a 10 ab^{-1} (50 ab^{-1}) data sample at Belle II, the expected statistical error on the $e^+e^- \to K^+K^-J/\psi$ cross section is 15% (6.5%) at 4.53 GeV/c^2. Possible resonance structures to K^+K^-J/ψ and Z_{cs} to $K^{\pm}J/\psi$ can be searched for.

$e^+e^- \to \pi^+\pi^-h_c$: BESIII measured $e^+e^- \to \pi^+\pi^-h_c$ cross sections at 13 energies of 3.90–4.42 GeV [1161]. There is clear evidence for an exotic charmonium-like structure with a greater than $8.9\,\sigma$ statistical significance in the $\pi^{\pm}h_c$ system at 4.02 GeV/c^2, referred to as $Z_c(4020)$, and there are also some events at around 3.9 GeV/c^2, which could be $Z_c(3900)$. Adding $Z_c(3900)$ with fixed mass and width to the fit results in a statistical significance of $2.1\,\sigma$. BESIII also studied $e^+e^- \to (D^*\bar{D}^*)^{\pm}\pi^{\mp}$ at a center-of-mass energy of 4.26 GeV using an 827 pb^{-1} data sample. A structure near the $(D^*\bar{D}^*)^{\pm}$ threshold, denoted the $Z_c(4025)^{\pm}$, was observed [1168]. Very recently, the cross sections of $e^+e^- \to \pi^+\pi^-h_c$ at center-of-mass energies from 3.896 to 4.600 GeV were measured. Two structures are observed around 4.22 and 4.39 GeV/c^2, called $Y(4220)$ and $Y(4390)$, respectively [1215]. With a 10 ab^{-1} (50 ab^{-1}) data sample at Belle II, the expected statistical error on the $e^+e^- \to \pi^+\pi^-h_c$ cross section is 15% (6.5%) at 4.23 GeV/c^2. The $Y(4220)$, $Y(4390)$, and $Z_c(4020)/Z_c(4025)$ are expected to be confirmed or denied.

$e^+e^- \to \omega\chi_{c0}$: Based on data samples collected at nine center-of-mass energies from 4.21 to 4.42 GeV, BESIII searched for the production of $e^+e^- \to \omega\chi_{c0}$ [1216]. Assuming the $\omega\chi_{c0}$ events come from a single resonance, the fitted mass and width of the resonance are $(4230\pm8\pm6)$ MeV/c^2 and $(38\pm12\pm2)$ MeV, respectively. The position of this resonance is consistent with the $Y(4220)$ state observed in the cross section of $e^+e^- \to \pi^+\pi^-h_c$ [1459]. It also indicates that the $Y(4260)$ signals observed in $e^+e^- \to \pi^+\pi^-J/\psi$ may have fine structures, and the lower-mass structure at about 4230 MeV/c^2 has a sizeable coupling to the $\omega\chi_{c0}$ channel. With a 10 ab^{-1} (50 ab^{-1}) data sample at Belle II, the expected statistical error on the $e^+e^- \to \omega\chi_{c0}$ cross section is 35% (15%) at 4.23 GeV/c^2. The question on the existence of the $Y(4220)$ will be further investigated.

Table 130 shows the estimated statistical errors on the cross section measurements at some typical center-of-mass points for some golden ISR reactions with the total luminosity of 10 ab^{-1} (50 ab^{-1}) at Belle II and the *XYZ* states involved.

The PHOKHARA event generator is used at Belle II to simulate the ISR process at NLO accuracy. This includes virtual and soft photon corrections to one-photon emission events and the emission of two real hard photons. At the moment, version 9.1 has been transferred into the Belle II environment [1460], where only a few modes, such as $e^+e^- \to \pi^+\pi^-$, $\pi^+\pi^-\pi^0$, $p\bar{p}$, and $n\bar{n}$, are available.

Table 130. Estimated statistical errors on the cross section measurements at some typical center-of-mass points for some golden ISR reactions with the total luminosity of $10\,\text{ab}^{-1}$ ($50\,\text{ab}^{-1}$) at Belle II. Here the largest values of the cross sections from the latest measurements [1166,1214–1216,1458] are taken and the signal efficiency at Belle II is assumed to be around 22% of that at BESIII according to the measurements of $e^+e^- \to \pi^+\pi^- J/\psi$ at BESIII and Belle [1158,1214].

Golden channels	E_{cm} (GeV)	Statistical error (%)	Related XYZ states
$\pi^+\pi^- J/\psi$	4.23	7.5 (3.0)	$Y(4008)$, $Y(4260)$, $Z_c(3900)$
$\pi^+\pi^-\psi(2S)$	4.36	12 (5.0)	$Y(4260)$, $Y(4360)$, $Y(4660)$, $Z_c(4050)$
$K^+K^- J/\psi$	4.53	15 (6.5)	Z_{cs}
$\pi^+\pi^- h_c$	4.23	15 (6.5)	$Y(4220)$, $Y(4390)$, $Z_c(4020)$, $Z_c(4025)$
$\omega\chi_{c0}$	4.23	35 (15)	$Y(4220)$

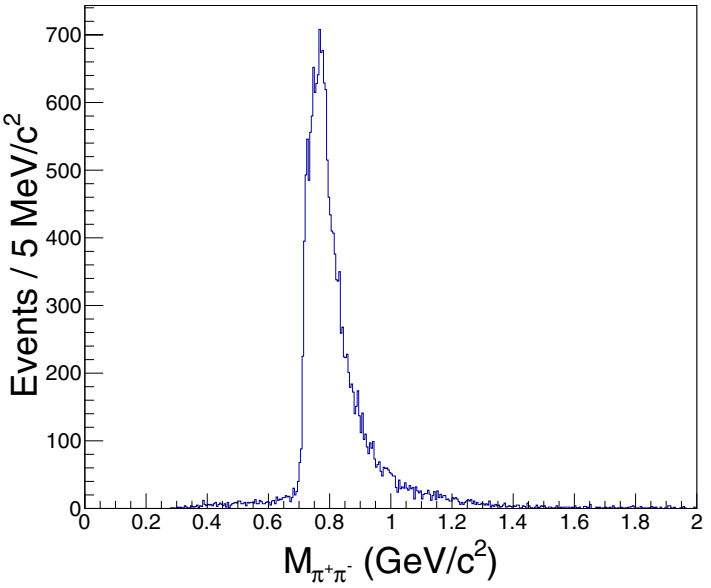

Fig. 176. The $\pi^+\pi^-$ invariant mass distribution from the $e^+e^- \to \pi^+\pi^-$ MC sample simulated with the PHOKHARA generator in the Belle II environment.

More modes with a charmonium final state have also been added by Belle II. Figure 176 shows the simulated $\pi^+\pi^-$ invariant mass distribution from the $e^+e^- \to \pi^+\pi^-$ MC sample simulated with the PHOKHARA generator in the Belle II environment.

14.6.3. Two-photon collisions

Author: C. P. Shen

At e^+e^- colliders, two-photon interactions are studied via the process $e^+e^- \to e^+e^-\gamma^*\gamma^* \to e^+e^-R$. Almost all of the beam energy is kept by the scattered electron and positron and usually those are not detected (non-tagged events). If the scattering angle is sufficiently large, they can be detected in the forward region (tagged events). This process gives access to the resonances with $J^{PC} = 0^{++}, 0^{-+}, 2^{++}, 2^{-+}, \ldots$

The total production cross section of $e^+e^- \to e^+e^-R$ is given by

$$\sigma(e^+e^- \to e^+e^-R) = \int \sigma(\gamma\gamma \to R)\frac{d\mathcal{L}_{\gamma\gamma}}{dW_{\gamma\gamma}}dW_{\gamma\gamma} = (2J+1)\cdot\mathcal{K}\cdot\Gamma_{\gamma\gamma},$$

where $\frac{d\mathcal{L}_{\gamma\gamma}(W_{\gamma\gamma})}{dW_{\gamma\gamma}}$ is the transverse two-photon luminosity function [1461], $W_{\gamma\gamma}$ is the effective center-of-mass energy of the two-photon system, and the factor $\mathcal{K}$ could be obtained from Monte Carlo integration:

$$\mathcal{K} = \int 8\pi^2\frac{d\mathcal{L}_{\gamma\gamma}(W_{\gamma\gamma})}{dW_{\gamma\gamma}}\delta(W_{\gamma\gamma}^2 - m_R^2)\frac{1}{m_R}dW_{\gamma\gamma} = 4\pi^2\frac{1}{m_R^2}\frac{d\mathcal{L}_{\gamma\gamma}(W_{\gamma\gamma})}{dW_{\gamma\gamma}}.$$

Here, $\int \delta(W_{\gamma\gamma}^2 - m_R^2)dW_{\gamma\gamma} = \frac{1}{2m_R}$ is used.

Experimental studies for two-photon physics at Belle II have merits since all the data at any energy point can be used to investigate the lower invariant mass region. Physics at higher invariant mass regions, $W_{\gamma\gamma} > 5\,\text{GeV}$, is not suitable because the luminosity function for two-photon collisions steeply decreases with increasing $W_{\gamma\gamma}$ and the backgrounds from single-photon annihilation processes are considerable. With the total integrated luminosity larger than $10\,\text{ab}^{-1}$ at Belle II, the two-photon processes listed below are our priorities.

A state at 3930 MeV was discovered by Belle in $\gamma\gamma \to D\bar{D}$ [1189], and later confirmed by BaBar [1190]. The experimental results on the mass, angular distributions, and $\Gamma(X(3930) \to \gamma\gamma)\mathcal{B}(X(3930) \to D\bar{D})$ are all consistent with the expectation for the $\chi_{c2}(2P)$. So far, this is the only unambiguously identified radially excited P-wave charmonium state found in experiment. The $X(3915)$ was discovered by Belle in $\gamma\gamma \to \omega J/\psi$ [1187]. Later, a spin parity analysis was performed for $X(3915) \to \omega J/\psi$ by BaBar [1188], and the results suggest that the quantum numbers of this state are $J^P = 0^+$. It was therefore identified as the $\chi_{c0}(2P)$. However, assigning the $X(3915)$ as the $\chi_{c0}(2P)$ state faces many problems, as discussed in Sect. 14.5.2. At Belle II, with higher statistics, the $\gamma\gamma \to D\bar{D}$ process needs to be analyzed carefully to give more precise parameters for the $\chi_{c2}(2P)$. The angular distribution for the broad bump below the narrow peak of the $\chi_{c2}(2P)$ should be determined to obtain the J^P value and checked to see if it could be assigned as the $\chi_{c0}(2P)$. For $\gamma\gamma \to D\bar{D}$, we expect obvious contributions from $\gamma\gamma \to D\bar{D}^* \to D\bar{D}\pi$ and $\gamma\gamma \to D\bar{D}(n)\gamma$. All of these processes are cross contaminated. Their cross sections can be measured, however, by applying iterative methods. The lattice QCD masses of $\chi_{c0,c2}(2P)$ within an approach that neglects their strong decays are given in Fig. 170. The results of an exploratory lattice simulation which takes into account their $D\bar{D}$ strong decays was discussed in the *Scalar resonances* subsection of Sect. 14.5.4.

Another important two-photon process is $\gamma\gamma \to \phi J/\psi$. With the full amplitude analysis of $B^+ \to K^+\phi J/\psi$ performed by LHCb, four $\phi J/\psi$ structures, $X(4140)$, $X(4274)$, $X(4500)$, and $X(4700)$, were observed [1204]. The structures in the $\phi J/\psi$ mass spectrum seem very rich. The $M(\phi J/\psi)$ distribution at Belle II needs to be revisited to confirm or deny the existence of the $X(4350)$ and search for more exotic states. Note here that because of the Landau–Yang theorem [1462], the $X(4140)$ and $X(4274)$ with $J^{PC} = 1^{++}$ cannot be produced in two-photon process $\gamma\gamma \to \phi J/\psi$.

With the somewhat smaller boost at Belle II, the efficiency in two-photon processes may be a little higher compared to that at Belle. With higher luminosity and detection efficiency, we expect interesting results from $\gamma\gamma \to \phi J/\psi$.

14.6.4. Double charmonium production

Author: P. Pakhlov

The discovery of a number of double charmonium production processes in e^+e^- annihilation at B factories was initiated by the observation of $e^+e^- \to J/\psi X$, where X is η_c, χ_{c0}, or $\eta_c(2S)$, at Belle [1463]. This production mechanism provides a powerful tool for an understanding of the interplay between perturbative QCD (pQCD) (and its expansions beyond the leading order) and non-perturbative effects, in particular with application of the light cone approximation and the NRQCD factorization approaches. The first calculations using NRQCD within the leading-order pQCD for the $e^+e^- \to J/\psi\,\eta_c$ cross section gave a value an order of magnitude smaller than the measured cross section [1464]. The importance of relativistic corrections was realized in Refs. [1465,1466]; the authors, using the light cone approximation to take into account the relative momentum of heavy quarks in the charmonium states, managed to calculate the cross section, which is close to the experimental value. Some authors have been able to reproduce the experimental result using NLO corrections [1467,1468]. The present variety of different alternative approaches that explain the experimental result points to the need to check the suggested models with new data.

For the moment, the production of J/ψ and $\psi(2S)$ with spin-0 charmonia is established with a very high significance [1469,1470]. The processes $e^+e^- \to J/\psi\, X$ are identified from peaks in the mass spectrum of the system recoiling against the reconstructed J/ψ in inclusive $e^+e^- \to J/\psi\, X$ events. Belle also reported strong evidence for the process $e^+e^- \to J/\psi\,\chi_{c1}$ [1471]. Furthermore, the latter process was reconstructed from both sides: with a fully reconstructed J/ψ and χ_{c1} signal seen in the recoil spectrum and vice versa, with a J/ψ peak seen recoiling against the reconstructed χ_{c1}. A hint of the process $e^+e^- \to J/\psi\,\chi_{c2}$ was also seen. At Belle II it is likely that the full list of possible charmonium pairs can be measured with good accuracy, which can be used to verify the charmonium production models. Another important mission for Belle II is to perform angular analyses (e.g. to measure the J/ψ production and J/ψ helicity angle distributions for $e^+e^- \to J/\psi X$) that gives access to the ratio of different orbital angular momentum contributions in the two-body process, which also allows checking of the consistency of the models with the experimental data. Finally, Belle II, with unprecedentedly high statistics and data taken at different energies from the $\Upsilon(1S)$ to $\Upsilon(6S)$ resonances, is capable of measuring the $\sqrt{s}$ dependence of the double charmonium cross sections.

This process can also serve as an efficient tool to study charmonium decays, in particular to measure their absolute branching fractions. The double charmonium production mechanisms provide efficient and clean tagging for charmonia states, produced recoiling against the J/ψ. At Belle the statistics of tagged η_c and $\eta_c(2S)$ from the process $e^+e^- \to J/\psi X$ was about 1000 and 700 events, respectively [1471]. With a 50 times higher dataset Belle II can measure the absolute branching fractions for $\eta_c, \eta_c(2S) \to K^0_S K\pi$ with a $\sim$1% accuracy.

On the other hand, the double charmonium production mechanism offers a unique opportunity to search for and study new C-even charmonium states, produced in association with the effectively reconstructed C-odd charmonia such as J/ψ or $\psi(2S)$. New states can be exclusively revealed as peaks in the recoil mass spectrum against the J/ψ or $\psi(2S)$, using two-body kinematics. Moreover, the decay channels of those new charmonia states can also be studied. Known examples from Belle [1191,1192] are $X(3940) \to D\bar{D}^*$ and $X(4160) \to D^*\bar{D}^*$, which are tagged by the $\bar{D}^*$ peak in the spectrum recoiling against reconstructed $J/\psi D$ or $J/\psi D^*$ combinations, respectively. These two states are the only charmonium-like states for which hidden flavor decay channels are not known. As

mostly spin-zero ordinary charmonia are produced in the process $e^+e^- \to J/\psi\, X$ and production of the radial excitations is not suppressed, the $X(3940)$ and $X(4160)$ could be naturally interpreted as the $\eta_c(3S)$ and $\eta_c(4S)$ states. As these assignments are not well accommodated by the potential models [1050,1051], it is important to perform a full amplitude analysis at Belle II to measure spin parities and finally identify these states. New states can appear at Belle II with much higher statistics in the processes which have been already studied at Belle (such as $e^+e^- \to J/\psi\, D\bar{D}$, $J/\psi\, D\bar{D}^*$, $J/\psi\, D^*\bar{D}^*$ [1184,1192]), or with new final states, which were not accessible at Belle because of low reconstruction efficiencies. They include charmonia other than J/ψ: $e^+e^- \to \eta_c X$, $e^+e^- \to h_c X$, $e^+e^- \to \chi_{cJ} X$, $e^+e^- \to \eta_c(2S)X$, $e^+e^- \to \psi(2S)X$, or other final states for new charmonium states (e.g. charmonium+light hadrons, or $D_s^{(*)}\bar{D}_s^{(*)}$, charmed baryon final states, or $D^{(*)}\bar{D}^{(*)}\pi$).

Interesting but experimentally challenging topics related to the $e^+e^- \to c\bar{c}c\bar{c}$ process are searches for doubly charmed molecules $DD^{(*)}$ and doubly charmed baryons. The former are discussed in Sect. 58; they can be formed in double $2(c\bar{c})$ production because the phase space in this process is limited. The DD^* molecular state can be searched for in the DD^*, $DD\pi$, or $DD\gamma$ channels. Experimental difficulties arise due to low efficiency of the full reconstruction of the final states and due to the large expected combinatorial background from single $(c\bar{c})$ production. Production of doubly charmed baryons in e^+e^- annihilation is discussed in Refs. [1472,1473]. It is predicted that the $c\bar{c}c\bar{c}$ events hadronize predominantly into doubly charmed baryons. However, their reconstruction is also difficult because of small expected branching fractions into the final states convenient for reconstruction, and high background. Thus far, the obtained upper limit for the cross section of the production of weakly decaying doubly charmed baryons, the Ξ_{cc}, by Belle [1474] is at least an order of magnitude higher than the theoretical expectation.

14.6.5. Summary

The only missing very narrow charmonium level, the spin-singlet $\eta_{c2}(1D)$ with $J^{PC} = 2^{-+}$, can be searched for at Belle II in B decays.

Experimental information about the charmonium-like states above the $D\bar{D}$ threshold is very incomplete. With the significant increase of statistics compared to Belle, the Belle II experiment can measure more precisely the line shapes of the states, determine their spin parities, search for new decay channels (in particular for the open flavor channels, which are not known for most of the states but are very important for their interpretation), and search for new states expected in various approaches. More precise and detailed experimental information about the states should facilitate their interpretation, and help to discriminate between various models.

14.7. Belle II prospects for bottomonium(-like) states

14.7.1. Bottomonia below the $B\bar{B}$ threshold

Authors: B. Fulsom, R. Mussa, U. Tamponi

At Belle II there are generally three ways to access bottomonia below the $B\bar{B}$ threshold: via decays of higher-mass states (e.g. $\Upsilon(4S, 5S, 6S)$), production of 1^{--} states via initial state radiation, or by direct production via operation at a lower center-of-mass energy. From the previous generation of B factories we learned that the spin-flipping transitions via charged bottomonium-like states are key to reaching the spin singlet sector of the spectrum (para-bottomonia). These studies can be performed at Belle II using the high statistics data samples that will be integrated at $\Upsilon(4S)$ and $\Upsilon(5S)$ peak energies. High-precision studies of the rare hindered transitions, which will allow measurement of

the small but sizeable relativistic effects in bottomonium, will in turn require one dedicated period of data-taking on the peak of the $\Upsilon(3S)$ resonance.

The lattice QCD results for masses and radiative transitions of bottomonia were given in Sect. 46. In particular, the almost complete spectrum of states below the $\bar{B}B$ threshold from lattice NRQCD is presented in Fig. 169. The calculated masses are generally in good agreement with masses of already observed states. Hadronic transitions are challenging for rigorous lattice treatment and have not been considered yet. Potential model predictions are collected in Table 132.

Below the $\Upsilon(4S)$ threshold there are several predicted bottomonium states that have yet to be positively identified: separation of the $\chi_b(3P)$ triplet, the $\Upsilon(2D_3)$ triplet, $\eta_b(3S)$, $\Upsilon(1D_{1,3})$, $\eta_b(1D)$, and the F-wave states. Evidence for $\eta_b(2S)$ is below the $5\,\sigma$ threshold [1111]. Of the known states there are several important parameters that either need to be measured or have conflicting experimental results in need of resolution. Examples include the masses and widths of the η_b states, χ_{b0} widths, and the mass splitting of the $\Upsilon(1D)$ states.

Experimentally, a few facts should be taken into account to understand the Belle II potential. Radiative and hadronic transitions can be identified either inclusively, by studying the η, ω, γ, or $\pi^+\pi^-$ recoil spectrum in hadronic events, or exclusively, when the final state of a decay chain can be fully reconstructed. In bottomonium, this restricts us to the $\Upsilon(nS) \to e^+e^-, \mu^+\mu^-$ modes, since the hadronic annihilations are known to result in many multi-body final states with small branching fraction. While the former technique grants a high-efficiency reconstruction almost insensitive to the quantum numbers of the final state, its power is limited by a small signal-versus-background ratio, due to the large combinatorial background arising by the final state annihilation or the underlying *continuum* process $e^+e^- \to q\bar{q}$. This latter process is dominant in the datasets collected above the $\Upsilon(4S)$ energy: Monte Carlo simulation of the $\Upsilon(6S) \to \eta h_b(1P)$ process show that more than 90% of the combinatorial background in the signal region is due to the continuum, even after applying a topological selection to suppress it based on the Fox–Wolfram moments. A strong commitment by the experimental community to finding better tools to further suppress the continuum contribution is therefore desirable and needed to improve the physics results on hadronic transitions of any run at $\Upsilon(4S)$, $\Upsilon(5S)$, and $\Upsilon(6S)$ energies.

Inclusive radiative transitions, on the other hand, are even more problematic. Even though the combinatorial background is in some cases smaller and the reconstruction efficiency much higher than any hadronic transition, the activity in the calorimeter arising from the beam background, which scales approximately with the instantaneous luminosity, limits the photon energy resolution and adds a large background. This makes it quite difficult to detect any transitions emitting a photon with energy in the center of mass frame lower than 50 MeV. While the improved Belle II tracking grants better resolution and much better tracking efficiency in the low transverse momentum region compared to Belle, no striking improvement in the photon detection performance is expected.

η_b measurements The combined BaBar [1475,1476] and CLEO [1477] results from $\Upsilon(mS) \to \gamma\eta_b(1S)$ decays give $m_{\eta_b(1S)} = (9391.1 \pm 2.9)$ MeV, while the combined Belle [1111,1478] measurements via $h_b(nP) \to \gamma\eta_b(1S)$ find $m_{\eta_b(1S)} = (9403.4 \pm 1.9)$ MeV. These measurements disagree at the $\sim 3.5\,\sigma$ level. Combining the two existing measurements of the $\eta_b(1S)$ width [1111,1478] still has an appreciable uncertainty, $\Gamma_{\eta_b(1S)} = 10.8^{+3.5}_{-3.0}$ MeV. As for $\eta_b(1S)$, Belle [1111] measured $m_{\eta_b(2S)} = 9999.0 \pm 3.5^{+2.8}_{-1.9}$ MeV in the decay $h_b(2P) \to \gamma\eta_b(2S)$, after disconfirming [1479] an independent analysis of the CLEO dataset which found $m_{\eta_b(2S)} = (9974.6 \pm 2.3 \pm 2.1)$ MeV [1480].

Ultimately, the best way to produce η_b states at Belle II could be via $\Upsilon(4S)$ decays. With 50 ab^{-1} of $\Upsilon(4S)$ data and $\mathcal{B}(\Upsilon(4S) \to \eta h_b(1P)) = (1.83 \pm 0.16 \pm 0.17) \times 10^{-3}$, $\sim$ 4M $\eta_b(1S)$ can be produced and reconstructed (accounting for efficiency and η branching ratios). An extended run of $\sim$2 ab^{-1} at $\Upsilon(5S)$ energy offers access to $h_b(1P, 2P)$, potentially resulting in 0.25M of both $\eta_b(1S, 2S)$ after efficiency and reconstruction. Given $\mathcal{B}(\Upsilon(3S) \to \gamma\eta_b(1S)) = (5.1 \pm 0.7) \times 10^{-4}$ [77], one expects roughly 0.6M $\eta_b(1S)$ events if 300 fb^{-1} is collected at the $\Upsilon(3S)$. The best limit for the suppressed $M1$ transition, $\mathcal{B}(\Upsilon(3S) \to \gamma\eta_b(2S)) < 6.2 \times 10^{-4}$ [1481], implies less than 0.5M $\eta_b(2S)$ events from a similar dataset. This last analysis would require a detailed understanding of nearby peaking contributions from χ_b, $\Upsilon(1D)$, and initial state radiation photon lines, and extraction of a signal above a large inclusive photon background. The $\pi\pi$ transitions from the $\Upsilon(5S)$ and the η transition from the $\Upsilon(4S)$ will allow the study of the $\eta_b \to \gamma\gamma$ transition with very little background in exclusive mode ($\pi\pi + 5\gamma$ or 5γ from the $\Upsilon(4S)$, and $\pi\pi + 3\gamma$ from the $\Upsilon(5S)$). Very precise prediction is available in NRQCD [1096,1482] for the two-photon decays of both $\eta_b(1S)$ and $\eta_b(2S)$, as discussed in the theory section.

Another potential unexplored pathway well suited to the initial running conditions could be via $\Upsilon(3S) \to \gamma\chi_{b0}(2P) \to \gamma\eta\eta_b(1S)$. The $\chi_b(2P) \to \eta\eta_b(1S)$ decay could have a branching fraction as large as 10^{-3} [1483]. When combined with $\mathcal{B}(\Upsilon(3S) \to \gamma\chi_{b0}(2P)) = (5.9 \pm 0.6)\%$ [77] and an estimated efficiency of 5%, one might expect $\sim$12 events per fb^{-1}, or a few thousand events with a 300 fb^{-1} $\Upsilon(3S)$ sample.

$\Upsilon(m^3D_J)$ measurements Although much progress has been made on understanding the $\Upsilon(1^3D_J)$ triplet by CLEO, BaBar, and Belle, isolation and identification of the individual $\Upsilon(1^3D_J)$ states remains elusive.

Belle observed $\Upsilon(5S) \to \eta\Upsilon(1D)$ decays with a branching fraction of $(2.8 \pm 0.7 \pm 0.4) \times 10^{-3}$, corresponding to a cross section $\sigma(e^+e^- \to \eta\Upsilon(1D)) \approx 400$ fb, in inclusive η transitions. Further preliminary studies investigated $\Upsilon(1D)$ decays to exclusive $\gamma\chi_b(1P) \to \gamma\Upsilon(1S)$ final states. The current level of statistics was insufficient to resolve the various J components.

From $\Upsilon(3S)$, two decay pathways have been employed: the four-photon radiative decay cascade [1484,1485], and radiative decays to $\Upsilon(1^3D_J)$ followed by a dipion decay to $\Upsilon(1S)$ [1486]. With an integrated luminosity of 250 fb^{-1}, thousands of 1^3D_J will be produced in radiative transitions for each J value, which should be sufficient to identify each of the 1^3D_J states and measure their masses precisely enough to test theoretical predictions for their splittings. The D-wave states may also be accessed via dipion transitions from $\Upsilon(5S)$ [1478]. In addition, the spin singlet state $\eta_b(1D)$ can only be reached via E1 radiative transitions from $h_b(2P)$, which can be reached only from $\Upsilon(5, 6S)$.

Based on the BaBar results [1486], a factor of 7–9 increase in statistics is needed to resolve and observe previous hints of $J = 1, 3$ $\Upsilon(1D) \to \pi^+\pi^-\Upsilon(1S)$ peaks, given a similar reconstruction efficiency (and if they are indeed significant). For the exclusive four-photon cascade, approximately 4, 15, and 2 events are expected per fb^{-1} for the $J = 1$, 2, and 3 states, respectively (assuming an efficiency of $\sim$15%). Good photon energy resolution is critical for disentangling overlapping photon energies in this decay mode.

Another possibility could be to search for the $\Upsilon(1D_1)$ state via the inclusive $\Upsilon(3S)$ photon spectrum ($\Upsilon(1D_1) \to \gamma\chi_{b0}(1P)$ produces a photon of $E^*_{CM} \sim 288$ MeV). This is the highest of the six $\Upsilon(1^3D_J) \to \gamma\chi_{bJ}(1P)$ photon transition energies, and may possibly be identified as a lone peak apart from a Gaussian encompassing several other photon transition lines. The energy resolution and higher statistics of running directly at $\Upsilon(3S)$ are necessary for such an analysis.

In addition to the $\Upsilon(1^3D_J)$ strategies noted above, there could also be the chance to produce the $J = 1$ states directly via a beam energy scan [1487]. $\Gamma_{e^+e^-}$ widths of the $\Upsilon(D)$ states are predicted to be very small (<2 eV) [1488,1489], but a dedicated scan with the high instantaneous luminosity of Belle II could cover this in a relatively short time. The production cross section is proportional to the BR to e^+e^-, which is roughly three orders of magnitude smaller than that for the S-wave states. The small number of signal events will also make it challenging to see the n^3D_1 states above backgrounds. With these caveats we estimate the number of n^3D_1 produced by multiplying the raito of $nD/2S$ BRs to e^+e^- times the 2^3S_1 cross section. This gives ∼13 pb for the 1^3D_1, which results in $\sim 1.3 \times 10^6$ 1^3D_1 for 100 fb^{-1} of integrated luminosity yielding ∼100 events in $1^3D_1 \to \mu^+\mu^-$ but many more in radiative decay chains via intermediate $1P$ states.

Similarly, we estimate $\sigma(e^+e^- \to 2^3D_1) \sim 18$ pb, yielding $\sim 2 \times 10^6$ 2^3D_1 for 100e fb^{-1} of integrated luminosity. It should thus be possible to observe the 2^3D_1 state, which is predicted to have mass around 10.45 GeV/c^2, above the $\Upsilon(3S)$. No known way to access these states with hadronic transitions is known, even if the observation of $\Upsilon(5S) \to \eta\Upsilon(1D)$ hints at a possible production of $\Upsilon(2D)$ via η transitions from $\Upsilon(6S)$. Preliminary MC simulations show that the cross section $\sigma[e^+e^- \to \eta\Upsilon(2D)]$ at the $\Upsilon(6S)$ energy must exceed 3.5 pb (0.5 pb) in order to observe this process with an integrated luminosity of 50 fb^{-1} (250 fb^{-1}) collected at the $\Upsilon(6S)$ energy, using the inclusive η meson recoil technique. These results can be largely improved by better rejection of the continuum background.

h_b measurements The h_b has been discovered in the process $\Upsilon(5S, 6S) \to \pi^+\pi^- h_b(1P, 2P)$ (via intermediate $Z_b^{\pm}$) [1111], and $\Upsilon(4S) \to \eta h_b(1P)$. The controversial evidence of $h_b(1P)$ in decays of $\Upsilon(3S) \to \pi^0 h_b(1P)$ [1490] deserves further studies. No evidence for $\Upsilon(3S) \to \pi^+\pi^- h_b(1P)$ has been found [1491].

η and dipion transitions from $\Upsilon(4S)$ and $\Upsilon(5S)$ to $h_b(nP)$ are the best production source for these states at Belle II, with branching fractions of $\sim 2 \times 10^{-3}$, in agreement with the prediction in Ref. [1388], and $(4\text{–}6) \times 10^{-3}$, respectively. Considering efficiency, this equates to approximately 11M $h_b(1P)$ events in the full Belle II $\Upsilon(4S)$ dataset. An additional 0.8M (1.4M) $n = 1$ (2) could be reconstructed from 2 ab^{-1} of $\Upsilon(5S)$ data.

For direct running at $\Upsilon(3S)$, the BaBar measurement of the $\Upsilon(3S) \to \pi^0 h_b(1P))$ efficiency of ∼15% implies about 250 events per fb^{-1}, though the background level for the π^0 transition is very high. A factor of ∼3 increase in statistics would be necessary to convert their evidence into an observation. Besides providing an alternative measurement of the masses of $h_b(1P)$ and $\eta_b(1S)$, this process is the only isospin-violating transition between narrow bottomonia, in striking contrast with the non-observation of the transition $\Upsilon(3S) \to \eta\Upsilon(1S)$. This process may also provide comparative information on the $\eta_b(1S)$ from a separate production method.

The dipion transition sets a branching fraction limit for $\Upsilon(3S) \to \pi^+\pi^- h_b(1P)$ of less than 1.2×10^{-4}, challenging most theoretical models, the lowest of which was of the order of $\mathcal{O}(10^{-4})$ [1492–1494].

$\chi_b(3P)$ bottomonia ATLAS, D0, and LHCb have observed radiative $\chi_b(3P)$ decays to $\Upsilon(1S, 2S, 3S)$. At Belle II, this could potentially be accessed by $\Upsilon(4S) \to \gamma\chi_b(3P)$ decays, though the rate is expected to be low. It is expected that several ab^{-1} of integrated luminosity will be accumulated at the $\Upsilon(4S)$. Assuming 10 ab^{-1} of integrated luminosity, roughly 10^{10} $\Upsilon(4S)$ will be produced, so that sufficient numbers of events will be produced in the decay chains proceeding via

the 3^3P_2 and 3^3P_1 that these states should be observed in radiative decays of the $\Upsilon(4S)$. We do not expect that the 3^3P_0 will be observed in this manner due to its larger width and consequently smaller branching ratios for radiative transitions. Another interesting possibility for studying the $3P$ states via radiative transitions from the $\Upsilon(4S)$ utilizes hadronic transitions from the $\Upsilon(3S)$ and $\Upsilon(2S)$ or $\Upsilon(1S)$ in the decay chain. In the full Belle II dataset, this would yield some tens of events for the 3^3P_2 and 3^3P_1 intermediate states, but only $\mathcal{O}(1)$ event for the 3^3P_0. This might be sufficient to resolve these states.

Lattice QCD guidance on where ^3P states are located is not available yet (see Fig. 169). This is an even more challenging task as it would need to also take into account the effect of the $\bar{B}B^{(*)}$ threshold.

The search for F-wave bottomonia The lattice QCD predictions for these states are given in Fig. 169. These states are likely best accessed via radiative decays of $\Upsilon(2^3D_J)$ (also yet to be discovered). Reaching $\Upsilon(2^3D_J)$ could potentially be accomplished by two-photon transitions from $\Upsilon(4S)$, a dipion transition from $\Upsilon(6S)$, or direct production from initial state radiation or operation at the appropriate energy. The F-wave states decay dominantly to $\gamma\Upsilon(1^3D_J)$, which also typically decay radiatively to $\chi_b(1P)$ states, or via rare dipion transitions to $\Upsilon(1S)$. Overall, this is a difficult experimental challenge. The production rate of these states is expected to be very low (indeed, the first step of reaching $\Upsilon(2^3D_J)$ has still not been realized). Assuming a beam energy scan to discover and directly produce $\Upsilon(2^3D_1)$, the most promising search method could be via the inclusive photon spectrum for a ~90 MeV photon corresponding to $\Upsilon(2D_1) \to \gamma\chi_{b2}(1F)$. This low-energy photon search would face high backgrounds and overlapping transition lines from other bottomonium and initial state radiation processes.

Hadronic transitions and decays CLEO and Belle have searched for or identified dozens of exclusive final states for χ_b and Υ [1495–1497] decays (generally at the level of $<\mathcal{O}(10^{-4})$. Two examples of interesting measurements with this approach are $\Upsilon \to \gamma\eta_b(nS) \to \gamma +$ hadrons [1479, 1480], or using the ratio of $\Upsilon(2S) \to \gamma\chi_b(1P) \to \gamma +$ hadrons to $\Upsilon(3S) \to \gamma\chi_b(1P) \to \gamma +$ hadrons to access $\Upsilon(3S) \to \gamma\chi_b(1P)$ [1495].

There are several allowed dipion transitions among bottomonium states that could be studied in detail, for example $\Upsilon(3S) \to \pi^+\pi^-\Upsilon(1S, 2S)$ and $\chi_b(2P) \to \pi^+\pi^-\chi_b(1P)$, and their neutral pion counterparts. While the dipion transitions between Υ states and their atypical $m_{\pi\pi}$ structure have been studied extensively [1498], the transitions between χ_b states have yet to be fully exploited and understood [1491,1499].

If the $\pi\pi$ invariant mass distributions for the dipion transitions were measured precisely, additional interesting physics aspects can be extracted. For instance, the $\pi\pi$ S-wave scattering length $a_0 - a_2$ can be measured precisely with an uncertainty of ~0.5% using the cusp effect at the $\pi^+\pi^-$ threshold with about 4M events for $\Upsilon(3S) \to \Upsilon(2S)\pi^0\pi^0$ [1500]. A fine measurement of the dipion mass spectrum at around 1 GeV in the transition $\Upsilon(4S) \to \Upsilon(1S)\pi^+\pi^-$ is necessary to see clearly the non-trivial behavior caused by the $f_0(980)$ [1501,1502], which is invisible in the present analysis [1232].

Radiative decays The lattice results on the radiative decays $\Upsilon(1S, 2S, 3S) \to \eta_b(1S, 2S)\gamma$ and $\eta_b(2S, 3S) \to \Upsilon(1S)\gamma$ were summarized in Sect. 46. The transition $\Upsilon(2S, 3S) \to \eta_b(1S)\gamma$, for example, would be absent in the strict non-relativistic limit and its rate crucially depends on a

multitude of interesting relativistic effects. Results on other, yet unobserved, transitions discussed below can be expected in the years to come.

Radiative decays between Υ and χ_b have been extensively studied by several experiments in the past, most recently by BaBar [1503,1504]. Two outstanding questions regarding these transitions are the observation of $\chi_{b0}(2P) \to \gamma\Upsilon(1S)$, and the understanding of $\Upsilon(3S) \to \gamma\chi_{bJ}(1P)$ decays. The former has a single claim [1505], while the recent high-statistics BaBar measurement could only reach a significance of $2.2\,\sigma$, putting this observation within reach with approximately five times the $\Upsilon(3S)$ dataset. These hindered E1 transitions are both experimentally difficult to measure due to overlapping photon transition energies, and theoretically difficult to calculate due to the effects of higher-order corrections. While they have been measured by both CLEO [1481,1506] and BaBar [1503], there remains some disagreement over the suppressed $\Upsilon(3S) \to \gamma\chi_{b1}(1P)$ transition.

The hindered M1 transitions $\chi_{bJ}(nP) \to \gamma h_b(mP)$ and $h_b(nP) \to \gamma\chi_{bJ}(mP)$ with $n > m$ are even more difficult to measure. However, any observation of such transitions would be a clear hint at non-trivial coupled channel effects due to light quarks [1386], and thus deserve to be searched for. The most promising processes are $h_b(2P) \to \gamma\chi_{bJ}(1P)$ and $\chi_{bJ}(2P) \to \gamma h_b(1P)$ [1386]. The former can be studied as part of the exclusive decay chain $\Upsilon(5S) \to \pi^+\pi^- h_b(2P) \to \pi^+\pi^-\gamma\chi_{bJ}(1P) \to \pi^+\pi^-\gamma\gamma\Upsilon(1S)$, with $\Upsilon(1S)$ reconstructed in dimuon or dielectron decay. We expect roughly $\mathcal{O}(10)$ reconstructed events per ab^{-1} at the $\Upsilon(5S)$ energy, with a small or negligible background coming from radiative QED processes or other transitions among bottomonia. The latter transition can be studied using a large dataset collected at the $\Upsilon(3S)$ energy. In this case the analysis should be done inclusively, studying single and multi-photon recoil mass spectra in hadronic events, in search of either the $\Upsilon(3S) \to \gamma\chi_{bJ}(2P) \to \gamma\gamma h_b(1P)$ or the $\Upsilon(3S) \to \gamma\chi_{bJ}(2P) \to \gamma\gamma h_b(1P) \to \gamma\gamma\gamma\eta_b(1S)$ cascade decays.

Another class of radiative transitions which should become statistically within reach at Belle II are the $b\bar{b} \to \gamma c\bar{c}$ transitions. This process is predicted in NRQCD [1507] and is expected to be enhanced by the interference of QCD and QED amplitudes. Weak evidence of these transitions was observed at Belle, but the final comparison with theory predictions will be feasible only at Belle II.

14.7.2. Dedicated runs above the $B\bar{B}$ threshold at Belle II

Author: R. Mizuk

Above the $B\bar{B}$ threshold there are five hadrons containing the $b\bar{b}$ quarks. Their properties are inconsistent with their structure being a pure $b\bar{b}$ pair. Unlike in the charmonium sector, there are clear winners in the interpretation of the bottomonium-like states. The vector states $\Upsilon(10580)$, $\Upsilon(10860)$, and $\Upsilon(11020)$ [or $\Upsilon(4S)$, $\Upsilon(5S)$, and $\Upsilon(6S)$] are likely mixtures of the $b\bar{b}$ pair and the molecular component of $B\bar{B}$ or $B_s\bar{B}_s$ mesons in ground or excited states. The isospin-one states $Z_b(10610)$ and $Z_b(10650)$ likely have purely molecular structures of $B\bar{B}^*$ and $B^*\bar{B}^*$, respectively.

Anomalous properties of $\Upsilon(4S)$ and $\Upsilon(5S)$ were established somewhat occasionally using on-resonance data samples that were collected to study B and B_s mesons. Subsequently Belle performed a high-statistics energy scan with a total luminosity of 27 fb^{-1} that played a crucial role in interpreting the $\Upsilon(5S)$ and $\Upsilon(6S)$. Further studies at Belle II should proceed along the same lines: in addition to increased data samples at the $\Upsilon(4S)$ and $\Upsilon(5S)$, it is useful to perform an energy scan with improved statistics, and to collect data at the $\Upsilon(6S)$ and at higher-mass states if they are found in the scan.

Energy scan Coupled channel analysis of exclusive cross sections: The total $b\bar{b}$ cross section above the $B\bar{B}$ threshold has several features: the $\Upsilon(4S)$, $\Upsilon(5S)$, and $\Upsilon(6S)$ peaks, and dips near

Table 131. Thresholds of narrow S- and P-wave mesons and baryons.

Particles	Threshold (GeV/c^2)
$B^{(*)}\bar{B}^{**}$	11.00–11.07
$B_s^{(*)}\bar{B}_s^{**}$	11.13–11.26
$\Lambda_b\,\bar{\Lambda}_b$	11.24
$B^{**}\bar{B}^{**}$	11.44–11.49
$B_s^{**}\bar{B}_s^{**}$	11.48–11.68
$\Lambda_b\,\bar{\Lambda}_b^{**}$	11.53–11.54
$\Sigma_b^{(*)}\,\bar{\Sigma}_b^{(*)}$	11.62–11.67
$\Lambda_b^{**}\,\bar{\Lambda}_b^{**}$	11.82–11.84

the $B\bar{B}^*$, $B^*\bar{B}^*$,and $B_s^*\bar{B}_s{}^*$ thresholds [1236,1508]. The exclusive cross sections for open flavor final states, such as $B^{(*)}\bar{B}^{(*)}$, $B^{(*)}\bar{B}^{(*)}\pi$, or $B_s^{(*)}\bar{B}_s^{(*)}$, that almost saturate the total $b\bar{b}$ cross section in this energy region are expected to have many more features. The unitarized quark model [1509] predicts several maxima and zeros in each exclusive cross section, which are shifted in different final states, producing a relatively featureless sum. The oscillatory behavior of exclusive cross sections is related to the nodes of the $\Upsilon(5S)$ and $\Upsilon(6S)$ wave functions. Exclusive cross sections contain complete information about the corresponding energy region. Combined coupled channel analysis of all exclusive cross sections will allow the determination of the pole positions of the Υ states, their electronic widths, and couplings to various channels. Thus, the ability of the currently favored interpretation to describe the data will be put to the test, and all relevant parameters will be determined.

Recently Belle measured the $B_s^{(*)}\bar{B}_s^{(*)}$ cross sections from corresponding thresholds up to 11.02 GeV [1235]. Results for $B\bar{B}$, $B\bar{B}^*$, $B^*\bar{B}^*$, and $B^{(*)}\bar{B}^{(*)}\pi$ are still expected. These measurements will provide the first attempt at a coupled channel analysis.

Search for new vector states: The final states with bottomonia, such as $\Upsilon(nS)\pi^+\pi^-$, $\Upsilon(nS)\eta$, or $h_b(nP)\pi^+\pi^-$, contribute only a few percent to the total $b\bar{b}$ cross section. They can be used in the coupled channel analysis and play an important role in searching for new states. A "smoking gun" of compact tetraquarks and hadrobottomonia are suppressed decays to the open flavor channels. Thus, hidden flavor cross sections provide a unique way to search for such states. Even for molecular states, for which open flavor channels dominate, the channels with bottomonia could have higher sensitivity because they usually have higher reconstruction efficiency and no non-resonant continuum contribution.

Recently Belle measured the $\Upsilon(nS)\pi^+\pi^-$ $(n = 1,2,3)$ and $h_b(mP)\pi^+\pi^-$ $(m = 1,2)$ cross sections [1176,1236]. They exhibit clear $\Upsilon(5S)$ and $\Upsilon(6S)$ peaks. With the available statistics no new significant structures are found.

Promising energy regions: The states with molecular admixture are naturally located near the corresponding threshold. The positions of the thresholds in the region above 11.0 GeV where no high-statistics data are available are listed in Table 131. We consider only pairs of narrow S- and P-wave mesons and baryons.

The present energy limit of the SuperKEKB accelerator of 11.24 GeV will allow investigation of the $B^{(*)}\bar{B}^{**}$ and $B_s^{(*)}\bar{B}_s^{**}$ threshold regions. The increase of maximal energy by at least 100 MeV will allow exploration of the $\Lambda_b\,\bar{\Lambda}_b$ threshold and the search for baryon–antibaryon molecular states. The presence of potentially interesting dynamics in a heavy baryon–antibaryon channel is strongly suggested by the data [1228] in the charmonium sector near the $\Lambda_c\bar{\Lambda}_c$ threshold. The region of promising

Table 132. Missing bottomonium levels below the $B\bar{B}$ threshold, their quantum numbers, potential model predictions for masses [1246], light hadrons emitted in the transitions from vector bottomonium-like states to the considered bottomonia, and the thresholds of these transitions [1396].

Name	L	S	J^{PC}	Mass (MeV/c^2)	Emitted hadrons [Threshold (GeV/c^2)]
$\eta_b(3S)$	0	0	0^{-+}	10336	ω [11.12], ϕ [11.36]
$h_b(3P)$	1	0	1^{+-}	10541	$\pi^+\pi^-$ [10.82], η [11.09], η' [11.50]
$\eta_{b2}(1D)$	2	0	2^{-+}	10148	ω [10.93], ϕ [11.17]
$\eta_{b2}(2D)$	2	0	2^{-+}	10450	ω [11.23], ϕ [11.47]
$\Upsilon_J(2D)$	2	1	$(1,2,3)^{--}$	10441–10455	$\pi^+\pi^-$ [10.73], η [11.00], η' [11.41]
$h_{b3}(1F)$	3	0	3^{+-}	10355	$\pi^+\pi^-$ [10.63], η [10.90], η' [11.31]
$\chi_{bJ}(1F)$	3	1	$(2,3,4)^{++}$	10350–10358	ω [11.14], ϕ [11.38]
$\eta_{b4}(1G)$	4	0	4^{-+}	10530	ω [11.31], ϕ [11.55]
$\Upsilon_J(1G)$	4	1	$(3,4,5)^{--}$	10529–10532	$\pi^+\pi^-$ [10.81], η [11.08], η' [11.49]

thresholds extends up to 12 GeV. The energy region 11.5–11.6 GeV is of special importance to search for partners of $Z_b(10610)$ and $Z_b(10650)$, as discussed in the next section.

In the high-statistics energy scan Belle collected about 1 fb^{-1} per point, and the statistical uncertainty in measured cross sections was quite high [1176,1235,1236]. Thus at Belle II it is useful to collect about 10 fb^{-1} per scan point. Since the expected energy smearing at Belle II is similar to that at Belle (close to 5 MeV), no narrow peak will be missed if the step of the scan is 10 MeV.

On resonance data at $\Upsilon(6S)$ and at higher-mass states Once a new state is found it is of interest to collect about 500 fb^{-1} at its peak. Searches for new transitions from vector states, searches for missing bottomonia and for molecular states in such transitions, and searches for excited B and B_s mesons are among the topics to be addressed with these data.

Mechanism of hadronic transitions and structure of vector bottomonium-like states: In Sect. 14.5.3 it is shown that the rates of hadronic transitions are sensitive to the structure of the parent state. Final states that have already been seen at $\Upsilon(4S)$ or $\Upsilon(5S)$ include $\Upsilon(nS)\pi^+\pi^-$, $\Upsilon(nS)\eta$, $\Upsilon(1S)K^+K^-$, $h_b(nP)\pi^+\pi^-$, $h_b(1P)\eta$, $\chi_{bJ}(1P)\omega$, $\Upsilon_J(1D)\pi^+\pi^-$, $\Upsilon_J(1D)\eta$, and $Z_b\pi$ (see the full list in Ref. [1396]). Further final states to be investigated are given in Table 128. These studies will benefit greatly from increased $\Upsilon(4S)$ and $\Upsilon(5S)$ data samples at Belle II. The final states that have already been investigated at the $\Upsilon(6S)$ energy are limited to the most prominent channels $\Upsilon(nS)\pi^+\pi^-$ and $h_b(nP)\pi^+\pi^-$ because only a small amount of scan data with an effective luminosity of 3 fb^{-1} is available. It is of interest to compare the transitions from $\Upsilon(6S)$ and $\Upsilon(5S)$ since the two states are relatively close in energy and the differences should be due to their different structures. The comparison requires an increase of statistics at the $\Upsilon(6S)$ peak, which is a good topic for initial data-taking at Belle II (see Sect. 14.8).

Search for missing conventional bottomonia below the $B\bar{B}$ threshold: The 121 fb^{-1} data sample at the $\Upsilon(5S)$ was highly instrumental in finding missing bottomonium levels, e.g. the first observation of $h_b(1P)$ and $h_b(2P)$, the first evidence for $\eta_b(2S)$, the first precise measurement of the $\eta_b(1S)$ mass, and the first measurement of its width [1111,1510]. Possible production channels for still missing bottomonium levels and their thresholds are shown in Table 132. Many thresholds are above the

Table 133. Expected molecular states with the structure $B\bar{B}$, $B\bar{B}^*$, and $B^*\bar{B}^*$ [1396].

$I^G(J^P)$	Name	Content	Co-produced particles [Threshold (GeV/c^2)]	Decay channels
$1^+(1^+)$	Z_b	$B\bar{B}^*$	π [10.75]	$\Upsilon(nS)\pi$, $h_b(nP)\pi$, $\eta_b(nS)\rho$
$1^+(1^+)$	Z_b'	$B^*\bar{B}^*$	π [10.79]	$\Upsilon(nS)\pi$, $h_b(nP)\pi$, $\eta_b(nS)\rho$
$1^-(0^+)$	W_{b0}	$B\bar{B}$	ρ [11.34], γ [10.56]	$\Upsilon(nS)\rho$, $\eta_b(nS)\pi$
$1^-(0^+)$	W_{b0}'	$B^*\bar{B}^*$	ρ [11.43], γ [10.65]	$\Upsilon(nS)\rho$, $\eta_b(nS)\pi$
$1^-(1^+)$	W_{b1}	$B\bar{B}^*$	ρ [11.38], γ [10.61]	$\Upsilon(nS)\rho$
$1^-(2^+)$	W_{b2}	$B^*\bar{B}^*$	ρ [11.43], γ [10.65]	$\Upsilon(nS)\rho$
$0^-(1^+)$	X_{b1}	$B\bar{B}^*$	η [11.15]	$\Upsilon(nS)\eta$, $\eta_b(nS)\omega$
$0^-(1^+)$	X_{b1}'	$B^*\bar{B}^*$	η [11.20]	$\Upsilon(nS)\eta$, $\eta_b(nS)\omega$
$0^+(0^+)$	X_{b0}	$B\bar{B}$	ω [11.34], γ [10.56]	$\Upsilon(nS)\omega$, $\chi_{bJ}(nP)\pi^+\pi^-$, $\eta_b(nS)\eta$
$0^+(0^+)$	X_{b0}'	$B^*\bar{B}^*$	ω [11.43], γ [10.65]	$\Upsilon(nS)\omega$, $\chi_{bJ}(nP)\pi^+\pi^-$, $\eta_b(nS)\eta$
$0^+(1^+)$	X_b	$B\bar{B}^*$	ω [11.39], γ [10.61]	$\Upsilon(nS)\omega$, $\chi_{bJ}(nP)\pi^+\pi^-$
$0^+(2^+)$	X_{b2}	$B^*\bar{B}^*$	ω [11.43], γ [10.65]	$\Upsilon(nS)\omega$, $\chi_{bJ}(nP)\pi^+\pi^-$

$\Upsilon(6S)$, which motivates investigation of the higher-mass region and increase of the SuperKEKB e^+e^- collision energy. Various kinematic effects in the production of excited states are discussed in Ref. [1396].

The transitions listed in Table 132 can be reconstructed inclusively using the missing mass of the emitted light hadrons. In case of the spin-triplet states there is also a possibility of exclusive reconstruction. The dominant transitions between the bottomonia below the $B\bar{B}$ threshold are radiative E1 transitions. Thus the chain $\Upsilon_J(1G) \to \gamma\chi_{bJ}(1F) \to \gamma\gamma\Upsilon_J(1D) \to \gamma\gamma\gamma\chi_{bJ}(1P) \to \gamma\gamma\gamma\gamma\Upsilon(1S)$ corresponds to dominant transitions and can be used for exclusive reconstruction, with $\Upsilon(1S) \to e^-e^-$ or $\mu^+\mu^-$. More details on the bottomonium decays can be found, e.g., in Ref. [1246].

Search for molecular states near the $B_{(s)}^{(*)}\bar{B}_{(s)}^{(*)}$ thresholds: The $Z_b(10610)$ and $Z_b(10650)$ states situated near the $B\bar{B}^*$ and $B^*\bar{B}^*$ thresholds, respectively, were observed in pionic transitions from the $\Upsilon(5S)$ and $\Upsilon(6S)$: $\Upsilon(nS) \to Z_b\pi$ (see Table 125). It is expected [1351] that there are other molecular states near the $B\bar{B}$, $B\bar{B}^*$, and $B^*\bar{B}^*$ thresholds (see Table 133), however there are difficulties with producing them at the $\Upsilon(5S)$ or $\Upsilon(6S)$. Indeed, all other than $Z_b^{(\prime)}$ isovector states have negative G-parity, therefore they cannot be produced with the emission of a single pion, but require the emission of a ρ meson. Production of isosinglet states requires the emission of η or ω mesons. All these processes have higher thresholds that are in the range 11.15–11.43 GeV (see Table 133). To search for them a new vector state has to be found above this range, and thus the SuperKEKB energy would need to be increased up to 11.5–11.6 GeV. Most of the states can also be reached via radiative transitions that have much lower thresholds; however, the corresponding rates carry the suppression factor of $\alpha_{\rm QED}$.

The state X_b near the $B\bar{B}^*$ threshold (see Table 133) would be a bottom partner of the $X(3872)$. However, the properties of the X_b are expected to differ vastly from the $X(3872)$: it should be dominantly an isoscalar state and the decays into $\Upsilon(nS)\pi\pi$, breaking isospin symmetry, should be strongly suppressed [1353]. Therefore, it should be searched for in final states such as $\Upsilon(nS)\pi\pi\pi$, $\chi_{bJ}\pi\pi$, and $\Upsilon(nS)\gamma$ [1294,1353]. A search for the $\Upsilon(1S)\omega$ final state using the Belle dataset at $\sqrt{s} = 10.867\,\text{GeV}/c^2$ was negative [1234].

One can also search for the Z_{bs} states with the structure of $B_s^*\bar{B}$, $B_s\bar{B}^*$, and $B_s^*\bar{B}^*$ [1396]. They can be produced in association with a kaon: $e^-e^- \to Z_{bs}K$, at energies above 11.20 GeV. These

resonances would decay into the states of bottomonium plus a kaon, and also to heavy meson pairs with one B meson being either B_s or B_s^*.

Spectroscopy of B and B_s mesons: Taking data at high energies potentially gives access to excited B and B_s mesons. The missing B_s mesons with $J^P = 0^+$ and 1^+ are expected not far below the BK and B^*K thresholds, respectively. The effect of thresholds was taken into account in the lattice study [1511], where the bound-state poles in the scattering matrices of BK and B^*K were found below thresholds. The predicted masses are $m_{B_{s0}} = 5.711(13)(19)$ GeV and $m_{B_{s1}} = 5.750(17)(19)$ GeV for the $J^P = 0^+$ and 1^+ states, respectively. Therefore they should be narrow, similar to the D_{sJ} case. They could be produced near the $B_s^{(*)}\bar{B}_s^{**}$ thresholds [1512] that are within the current reach of SuperKEKB.

D_s and B_s excited states The scalar B_{s0} and axial B_{s1} states have not been found experimentally yet and Belle II has the potential to search for them. They are expected not far below the BK and B^*K thresholds. The analogous study of $D_{s0}(2317)$ rendered it 37(17) MeV below DK, while $D_{s1}(2460)$ was found 44(10) MeV below DK [1513,1514], both in agreement with experiment.

14.7.3. Conclusion

Dedicated data-taking is needed to establish the current interpretation of known bottomonium-like states, check its predictions, and search for new states. An energy scan from the $B\bar{B}$ threshold up to the highest possible energy with $\sim$10 fb^{-1} per point and $\sim$10 MeV steps is of high interest. Measured exclusive open and hidden flavor cross sections will be used in coupled channel analyses to establish the nature of the vector states and in the searches for new states. At each new vector state it is useful to collect $\sim$500 fb^{-1} to perform a detailed study of corresponding transitions, and to search for missing conventional bottomonia, excited $B_{(s)}$ mesons, and molecular states—partners of $X(3872)$, $Z_b(10610)$, and $Z_b(10650)$.

It is of high interest to increase the maximal energy of the SuperKEKB collider, which is currently 11.24 GeV. An increase to about 11.35 GeV would allow it to cover the $\Lambda_b\bar{\Lambda}_b$ threshold region. A further increase to 11.5–11.6 GeV is of particular importance for searches for molecular states—partners of $X(3872)$ and Z_b. Studies of the whole resonance region require an increase up to 12 GeV. More detailed discussion of this subject can be found in Refs. [1247,1396].

14.8. Early physics program at Belle II

Author: B. Fulsom

The Belle II experiment is scheduled to begin its first "physics" run in early 2019. As a prelude to this, there were two commissioning periods known as "Phase 1" (early 2016) and "Phase 2" (early 2018) where a varied collection of smaller detectors were deployed to measure background rates and operating conditions. During Phase 1, beams were circulated, but the solenoid was inactive, no collisions took place, and the Belle II detector was not yet installed. For Phase 2 all the detector subsystems except for the vertex detector were fully deployed to study colliding beam events. A total of 0.5 fb^{-1} of collision data was collected for commissioning. The first physics run ("Phase 3") in early 2019 will involve the entire Belle II detector, with the machine expected to operate with an instantaneous luminosity of at least 1×10^{35} cm^{-2} s^{-1}. In addition to data collected at the nominal $\Upsilon(4S)$ energy for commissioning purposes, data collected at different center-of-mass energies during Phase 3 represent an important opportunity for the Belle II experiment to have an early scientific

Table 134. Existing Υ-related datasets.

Experiment	Scans	$\Upsilon(6S)$	$\Upsilon(5S)$		$\Upsilon(4S)$		$\Upsilon(3S)$		$\Upsilon(2S)$		$\Upsilon(1S)$	
	off res.	fb^{-1}	fb^{-1}	10^6	fb^{-1}	10^6	fb^{-1}	10^6	fb^{-1}	10^6	fb^{-1}	10^6
CLEO	17.1	—	0.1	0.4	16	17.1	1.2	5	1.2	10	1.2	21
BaBar	54		R_b scan		433	471	30	122	14	99	—	
Belle	100	∼5.5	36	121	711	772	3	12	25	158	6	102

impact. These opportunities largely lie in the realm of quarkonium and "new states" physics, as described previously in this chapter.

14.8.1. Potential operating points

Table 134 summarizes recent data collected at the Υ resonances. Since existing $\Upsilon(4S)$ and $\Upsilon(5S)$ datasets cannot be matched during the early periods, this leaves the possibility for quick acquisition of uniquely large samples at $\Upsilon(1S)$, $\Upsilon(2S)$, $\Upsilon(3S)$, $\Upsilon(6S)$, off-resonance, and $E_{\rm CM}$ scan points if sufficiently justified. One of the primary drivers of the physics will be the amount of integrated luminosity available during these early periods.

Based on the expected operating conditions and physics prospects, collecting data above the $\Upsilon(4S)$ offers the best physics opportunities during the early stages of the experiment. The $\Upsilon(6S)$ energy region (∼11020 MeV) is particularly interesting, both because only $<5.6\,\text{fb}^{-1}$ of data have been collected there previously, and also because of the discoveries of multiquark Z_b states in its midst [1176]. At ∼11 GeV, $20\,\text{fb}^{-1}$ could be used to understand $\Upsilon(6S) \to \pi^{\pm} Z_b^{\mp}$ decays, e.g. the relative production of $m_{Z_b} = 10610\,\text{MeV}/c^2$ versus $10650\,\text{MeV}/c^2$ in decays to $h_b(1P, 2P)$ and $\Upsilon(1S, 2S, 3S)$. It may also be possible to search for Z_b partners [1238] in the decays $\Upsilon(6S) \to \gamma W_b$ and $\Upsilon(6S) \to \pi^+\pi^- W_b$, and in analogy to $\Upsilon(5S)$ decays, study bottomonium transitions with sufficient phase space for $h_b(3P)$, $\Upsilon(2D)$, and F-wave discovery, as discussed in the previous section. Other Belle results for decays to $\pi\pi\Upsilon$ may point to cross section enhancements indicative of these intermediate states for energies in the range 10.7–10.8 GeV, where only $\sim 2\,\text{fb}^{-1}$ of data have been collected [1236].

Energies below $\Upsilon(4S)$ are useful for both the study of bottomonium states and their transitions, and BSM physics in searches for the dark sector and light Higgs. Datasets in the $>200\,\text{fb}^{-1}$ range during Phase 3 offer a chance to reach this type of physics from the $\Upsilon(3S)$. Another strategy could be an $E_{\rm cm}$ scan of the expected $\Upsilon(1^3D_1)$ and $\Upsilon(2^3D_1)$ mass regions (10160 MeV and 10450 MeV, respectively) to discover these states directly in e^+e^- collisions.

14.8.2. Operating conditions

The majority of Phase 2 focused on accelerator commissioning, ultimately reaching an instantaneous luminosity of $\sim 0.5 \times 10^{34}\,\text{cm}^{-2}\,\text{s}^{-1}$. A total of $500\,\text{pb}^{-1}$ of data was collected. It was found that the beam energy spread was near the expected value of ∼5 MeV, and this is promising for physics studies in Phase 3. The first full physics run of Belle II is expected to be with nominal operating conditions. During Phase 3, data will be collected at $\Upsilon(4S)$, with options for exploring other energy values once a suitable $B\overline{B}$ sample has been collected for validation, commissioning, and other early physics studies.

14.9. Action items

Experiment

- It is important to perform an energy scan from the $B\bar{B}$ threshold up to the highest possible energy with about 10 fb^{-1} per point, and to measure the energy dependence of exclusive open flavor ($B\bar{B}$, $B\bar{B}^*$, $B^*\bar{B}^*$, $B^{(*)}\bar{B}^{(*)}\pi$, $B_s\bar{B}_s$, etc.) and hidden flavor ($\Upsilon(nS)\pi^+\pi^-$, $h_b(nP)\pi^+\pi^-$, $\Upsilon(nS)\eta$, etc.) cross sections. This information is crucial for understanding vector bottomonium-like states.
- Collect data at $\Upsilon(6S)$ and at any new peak observed in the energy scan. These data will allow investigation of the decay mechanism of bottomonium-like states, search for missing conventional bottomonia, predicted bottomonium-like states, and missing P-wave excitations of B_s mesons.
- The maximal energy of SuperKEKB is expected to be 11.24 GeV. The region above this energy is previously unexplored and it is of paramount importance to increase the energy. There is a $\Lambda_b\bar{\Lambda}_b$ threshold at 11.24 GeV with potentially interesting baryon–antibaryon dynamics, and more promising thresholds all the way up to 12 GeV. Transitions from new vector states possibly provide a unique way to produce partners of the $X(3872)$, $Z_b(10610)$, and $Z_b(10650)$. Most of the relevant transitions are kinematically allowed if the mass of the vector state is above 11.5 GeV.
- The spin and parity of the quarkonium-like state are very important to discriminate various interpretations. For many states this information is missing. One should perform full amplitude analyses of the corresponding production processes to measure J^P.
- All quarkonium-like states are above the open flavor thresholds, and the decay patterns into open flavor channels and corresponding line shapes are crucial for understanding of them. One should systematically search for open flavor decays of all quarkonium-like states.

Theory

- Phenomenological approaches:
  - Within all approaches to QCD exotics predictions should be provided for states with quantum numbers not yet observed. This could be done, e.g., by employing the heavy quark spin symmetry. At Belle those could be searched for in the decay chains of heavy vector states.
  - For all predicted states, quantitative statements about partial decay widths, or at least branching ratios, should be provided, not only allowing one to identify potential discovery modes but also as a stringent test of the assumed dynamics.
  - Predictions for the bottom sector are also necessary, again for various quantum numbers.
  - The mixing of exotic states with regular quarkonia needs to be investigated.
- Lattice QCD:
  - Calculate scattering matrices for $D_{(s)}^{(*)}\bar{D}_{(s)}^{(*)}$ and for charmonium + light-hadron with non-static heavy quarks, first in the one-channel approximation and then taking as many coupled channels as possible. Determine the position of poles in the scattering matrix and try to connect poles with the experimentally observed states.
  - Approach bottomonium states close to the $B^{(*)}\bar{B}^{(*)}$ threshold with non-static b quarks and make an effort to take into account the effect of this threshold.
  - Determine as yet undetermined Born–Oppenheimer potentials for static heavy quarks using lattice QCD, for example those related to Z_b.

- Calculate as yet undetermined radiative transitions between quarkonia below threshold. Try also to take a step towards a rigorous treatment of this problem for states above the open-charm threshold.
- Consider effects of $\bar{Q}Q$ annihilation in lattice simulations.
- Consider effects of isospin breaking in lattice QCD for channels where it might be important, for example $X(3872)$.

14.10. Conclusions

Since the turn of the century a large number of states that cannot be explained by the so far very successful quark model have been discovered experimentally. These discoveries led to a renaissance of hadron spectroscopy with respect to both experimental and theoretical activities. On the theory side there are important developments in three branches: effective field theories, both based on quark–gluon dynamics nested in QCD and based on hadron–hadron dynamics, model building, and lattice QCD studies.

There are firm theoretical predictions for the spectrum of quarkonia below the open flavor threshold by means of lattice QCD and NRQCD, for example. All such charmonia have already been discovered experimentally and they agree with calculated masses well. The bottomonium spectrum below $\bar{B}B$ contains many more states and some of the predicted ones have not yet been discovered. The predicted spectra of highly excited charmonia should serve as a valuable guideline for experimental searches, although most of these lattice simulations ignore strong decays of these states. Meanwhile, first lattice attempts have been made to treat quarkonia above open flavor thresholds as strongly decaying resonances.

Most of the discovered exotic hadrons lie near some threshold and they are strongly decaying states. Suggested structures for the new states are hybrids ($\bar{Q}Q$ supplemented with an active gluon degree of freedom), tetraquarks (bound systems of heavy diquarks and antidiquarks), hadroquarkonia (compact $\bar{Q}Q$ cores surrounded by a light quark cloud), and hadronic molecules (bound states of color-neutral hadrons in analogy to nuclei). As of today there is no consensus yet achieved within the community as to which of those structures is the most relevant—it is not even excluded that there are groups of different nature, or that contributions of all kinds are significant for various states simultaneously. Currently most effort goes into generating more predictions within the different pictures individually, but mixing scenarios need to be on the agenda in the not too distant future both amongst exotic structures and between exotics and $\bar{Q}Q$ states.

This chapter has demonstrated that different assumed structures for each exotic state lead to different predictions for decay branching ratios. Moreover, the location of spin partner states that necessarily exist as a consequence of heavy quark spin symmetry is known to be sensitive to the intrinsic dynamics of the states. Therefore there is a lot of work waiting for Belle II, not only to complete our experimental knowledge of new states in the charm sector but especially to map out exotics in the bottom sector where so far only two exotic states have been identified unambiguously.

The experimental studies at Belle II should proceed along the same lines as at Belle: search for missing quarkonia and for expected partners of exotic states, search for new decay channels of known states, and detailed measurement of all accessible properties, including spin parities, absolute branching fractions, line shapes, and so on. All this should be possible given the expected significant increase in luminosity at Belle II. With only modest additional effort and time dedicated to operating at energies other than the $\Upsilon(4S)$ resonance, it is possible to make important scientific gains in this area. More detailed experimental information will help to resolve many puzzles currently present

in the field of heavy quarkonia. The high precision of recent, and especially future, data require analysis employing sound theoretical tools. This appears to be realized most efficiently within close collaborations of experimenters and theoreticians.

15. Tau and low-multiplicity physics

Editors: T. Ferber, K. Hayasaka, E. Passemar, J. Hisano
Additional section writers: H. Aihara, I. Bigi, V. Braun, G. Colangelo, H. Czyz, S. Eidelman, D. Epifanov, M. Hoferichter, M. Jamin, T. Konno, E. Kou, K. Maltman, B. Moussallam, D. Nomura, N. Offen, A. Pich, M. Procura, P. Roig, M. Roney, J. Sasaki, N. Shimizu, Y. Shimizu, B. Shwartz, P. Stoffer, F. Tenchini, T. Teubner, S. Uehara, Z. Was

15.1. Introduction

The enormous number of e^+e^- collisions that are expected from the Belle II experiment provides a unique environment for electroweak and QED studies: about 45 billion of both $\tau\tau$ and $\mu\mu$ pairs are expected in the full dataset. The Belle II experiment will therefore offer fantastic possibilities to study τ physics and low-multiplicity final states with high precision.

The τ lepton is an extremely convenient probe to search for BSM NP because of the well-understood mechanisms that govern its production and decay in electroweak interactions. With its large mass, it is the only lepton that can decay into hadrons, thus providing a clean laboratory to study QCD effects in the 1 GeV energy region.

The Belle II experiment will be well suited to studying τ physics; in fact, since the decays of τ leptons involve neutrinos in the final state, their study is very difficult at hadron colliders such as LHC.

Two experiments at e^+e^- colliders capable of producing tau leptons, BESIII at IHEP, Beijing, and KEDR at BINP, Novosibirsk, are statistically limited with respect to Belle II and therefore have a τ physics program basically limited to measuring its mass. Note that there are a few proposals for tau–charm factories for the future. τ decays offer a whole range of possible studies, from understanding strong interactions to precise tests of electroweak interactions and potential discoveries of NP with lepton flavor violation and lepton universality violation.

Non-τ physics such as ISR, two-photon physics, and dark sector searches will profit from both the significantly larger statistics compared to Belle or BaBar and from triggers specifically designed to collect data for these analyses.

15.2. Charged lepton flavor violation in τ decays

Contributing authors: K. Hayasaka, H. Hisano, T. Konno, E. Passemar, Y. Shimizu, F. Tenchini

In the SM, the presence of only left-handed neutrinos implies that lepton flavor is conserved and that neutrinos are massless. From experimental observations of neutrino oscillations, we now know that lepton flavor is violated in the neutrino sector. However, this alone does not necessarily mean that charged lepton flavor is violated and that charged LFV processes will be observed in near-future experiments. Even if we extend the SM to include neutrino masses generated by the Higgs mechanism, these processes are suppressed by the fourth power of the neutrino masses such that their branching ratios are too small to be observed [1515,1516] (e.g. $<10^{-54}$ for $\mu \to e\gamma$ and $<10^{-53}$ for $\tau \to \mu\gamma$, with the latest averages of the measured neutrino mass and mixing).

Lepton flavor symmetries are not exact in nature, rather they are only accidental. Many BSMs at the TeV scale predict charged LFV interactions at a level reachable in near-future experiments, such as

supersymmetric standard models [1517–1521], little Higgs models [1522], low-scale seesaw models [1523], leptoquark models [1524], Z' models [1525], and extended Higgs models [1526–1530].

Let us consider charged LFV transitions in tau lepton decays. Stringent bounds already exist for μ–e transitions, for example the latest result of the MEG experiment is $\mathrm{Br}(\mu^+ \to e^+\gamma) < 4.2 \times 10^{-13}$ (90% CL) [1531], and gives strong constraints on BSMs. On the other hand, the bounds on τ–μ or τ–e transitions are much weaker. Some NP scenarios, such as the SUSY seesaw model [1517], may have enhanced LFV couplings for tau leptons. Moreover, the CMS hint of Higgs LFV coupling suggested a τ–μ coupling at the 1% level [1532], which triggered many new theoretical activities. While it seems that the anomaly was not confirmed by more recent measurements at CMS and ATLAS [1533,1534], models that could explain such an anomaly have been presented. They typically show very interesting correlations between $H \to \mu\tau$ and LFV tau lepton decays. Constraining LFV from tau decays therefore offers a very interesting complementarity with energy frontier collider constraints.

Studying LFV processes in tau decays offers several advantages compared to muon decays. Since the tau lepton is much heavier than the muon, many more types of LFV processes can be studied: $\tau \to \mu/e+\gamma$ and $\tau \to \mu/e+l^+l^-$ ($l = \mu/e$), the counterparts of $\mu \to e\gamma$ and $\mu \to 3e$, respectively. In addition, the tau lepton has semi-leptonic LFV channels whose final states have one or two mesons (even more) of isospin zero or one. These final states allow us to test the LFV couplings between quarks and leptons. If charged LFV is discovered, we can identify fundamental LFV interactions by matching the pattern of the branching ratios to the predictions in BSMs. Furthermore, tau leptons can have more exotic LFV decay processes, such as $\tau^+ \to \mu^-e^+e^+$ (all lepton flavor symmetries are not conserved) and $\tau \to \Lambda\pi^-$ (baryon number is not conserved).

We choose $\tau \to 3\mu$ and $\tau \to \mu\gamma$ as the golden modes for studying charged LFV. Firstly, the $\tau \to 3\mu$ channel, with its purely leptonic final state, is expected to be free of background. This allows us to scale the experimental uncertainties linearly with the luminosity. Thus, we naturally expect at least a 50 times increase in discovery potential at SuperKEKB. We will briefly discuss the Belle II prospects as well as a comparison with the LHCb experiment at the end of the following section.

The $\tau \to \mu\gamma$ decay has the largest LFV branching ratio in models where the LFV processes are induced by one-loop diagrams including heavy particles, such as in supersymmetric models. For example, if $\tau \to 3\mu$ is induced by photon-penguin diagrams, the ratio of $\mathrm{Br}(\tau \to 3\mu)$ and $\mathrm{Br}(\tau \to \mu\gamma)$ is 2.2×10^{-2}. However, a search for $\tau \to \mu\gamma$ may suffer from background due to $\tau \to \mu\nu\bar{\nu}$ with radiated photons, or radiative dimuon events, such that the scaling of the sensitivity is non-trivial. At Belle II, the higher beam background will make the search more difficult, but at the same time its high luminosity will allow us to impose more stringent experimental criteria compared to Belle. In the following section we show the results of a Belle II sensitivity study.

We should also note the complementarity of semi-leptonic LFV transitions in τ or B decays, such as $\tau \to \mu h$ (h being hadrons), $B \to K^{(*)}\tau\mu$, and $\tau \to 3\mu$ channels. If the LFV processes are induced by a tree-level exchange of Higgs bosons or Z' bosons, the branching ratio of $\tau \to 3\mu$ may provide information for the normalization for the LFV couplings, and the ratios between the branching ratios of $\tau \to 3\mu$ and the semi-leptonic LFV processes allow us to discriminate between models. If $\tau \to 3\mu$ is not discovered, while the semi-leptonic LFV processes are, that would give us an indication that LFV couplings are generated from more exotic models such as those that contain leptoquarks.

15.2.1. Theory

Authors: J. Hisano, E. Passemar, Y. Shimizu

The low-energy effective operators for an LFV τ–μ transition are the following (those for an LFV τ–e transition are derived by exchanging μ and e) [124]:

$$\mathcal{L}_{\rm eff} = \mathcal{L}_{\rm eff}^{(D)} + \mathcal{L}_{\rm eff}^{(4l)} + \mathcal{L}_{\rm eff}^{(lq)} + \mathcal{L}_{\rm eff}^{(G)} + \cdots,$$

where

$$\begin{aligned}
\mathcal{L}_{\rm eff}^{(D)} &= -\frac{m_\tau}{\Lambda^2}\left[\left(C_{DL}\bar{\mu}\sigma^{\rho\sigma}P_L\tau + C_{DR}\bar{\mu}\sigma^{\rho\sigma}P_R\tau\right)F_{\rho\sigma} + h.c.\right],\\
\mathcal{L}_{\rm eff}^{(4l)} &= -\frac{1}{\Lambda^2}\left[C_{SLL}(\bar{\mu}P_L\tau)(\bar{\mu}P_L\mu) + C_{SRR}(\bar{\mu}P_R\tau)(\bar{\mu}P_R\mu) + C_{VLL}(\bar{\mu}\gamma^\mu P_L\tau)(\bar{\mu}\gamma_\mu P_L\mu)\right.\\
&\quad + C_{VRR}(\bar{\mu}\gamma^\mu P_R\tau)(\bar{\mu}\gamma_\mu P_R\mu) + C_{VRL}(\bar{\mu}\gamma^\mu P_R\tau)(\bar{\mu}\gamma_\mu P_L\mu)\\
&\quad \left. + C_{VLR}(\bar{\mu}\gamma^\mu P_L\tau)(\bar{\mu}\gamma_\mu P_R\mu) + h.c.\right],\\
\mathcal{L}_{\rm eff}^{(lq)} &= -\frac{1}{\Lambda^2}\sum_{q=u,d,s}\left[\left(C_{VL}^q\bar{\mu}\gamma^\rho P_L\tau + C_{VR}^q\bar{\mu}\gamma^\rho P_R\tau\right)\bar{q}\gamma_\rho q\right.\\
&\quad + \left(C_{AL}^q\bar{\mu}\gamma^\rho P_L\tau + C_{AR}^q\bar{\mu}\gamma^\rho P_R\tau\right)\bar{q}\gamma_\rho\gamma_5 q\\
&\quad + G_F m_\tau m_q\left(C_{SL}^q\bar{\mu}P_R\tau + C_{SR}^q\bar{\mu}P_L\tau\right)\bar{q}q\\
&\quad + G_F m_\tau m_q\left(C_{PL}^q\bar{\mu}P_R\tau + C_{PR}^q\bar{\mu}P_L\tau\right)\bar{q}\gamma_5 q\\
&\quad \left. + G_F m_\tau m_q\left(C_{TL}^q\bar{\mu}\sigma^{\rho\sigma}P_R\tau + C_{TR}^q\bar{\mu}\sigma^{\rho\sigma}P_L\tau\right)\bar{q}\sigma_{\rho\sigma}q + h.c.\right],\\
\mathcal{L}_{\rm eff}^{(G)} &= \frac{G_F m_\tau}{\Lambda^2}\frac{9\alpha_s}{8\pi}\left[\left(C_{GL}\bar{\mu}P_R\tau + C_{GR}\bar{\mu}P_L\tau\right)G^a_{\rho\sigma}G^{a\rho\sigma}\right.\\
&\quad \left. + \left(C_{\tilde{G}L}\bar{\mu}P_R\tau + C_{\tilde{G}R}\bar{\mu}P_L\tau\right)G^a_{\rho\sigma}\tilde{G}^{a\rho\sigma} + h.c.\right].
\end{aligned} \tag{498}$$

Here, $F_{\rho\sigma}$ and $G_{\rho\sigma}$ are field strength tensors for photons and gluons, respectively. For simplicity we show pure leptonic four-Fermi operators for $\tau \to 3\mu$ in $\mathcal{L}_{\rm eff}^{(4l)}$, though the inclusion of those for $\tau^- \to \mu^- e^+ e^-$ is straightforward.

The Wilson coefficients in Eq. (498) depend on the choice of UV model. The LFV dipole operators in $\mathcal{L}_{\rm eff}^{(D)}$ are induced by loop diagrams in the renormalizable models. In the SUSY SMs, slepton mass terms are sources of lepton flavor violation, and the integration of a SUSY particle generates the LFV dipole operators via the loop diagrams. The LFV dipole operators induce $\tau \to \mu/e\gamma$ and other LFV processes via the penguin diagrams. The Higgs or Z' boson can generate LFV four-Fermi operators in $\mathcal{L}_{\rm eff}^{(4l)}$ and $\mathcal{L}_{\rm eff}^{(lq)}$ if they have LFV interactions. In Eq. (498) heavy quarks (top, bottom, and charm quarks) are integrated out. The gluonic operators in $\mathcal{L}_{\rm eff}^{(G)}$ come from loop diagrams of those heavy quarks or unknown colored particles if they have LFV scalar or pseudoscalar couplings.

Table 135 shows the relations between LFV tau decay modes and effective operators. (The branching ratios for the LFV tau lepton decay modes are summarized as functions of the Wilson coefficients in Ref. [124].) When the LFV dipole operators are non-vanishing, the pure leptonic and semi-leptonic LFV tau lepton decay modes are predicted to proceed via penguin diagrams, in addition to $\tau \to \mu\gamma$. Their branching ratios are suppressed by α compared with $\mathrm{Br}(\tau \to \mu\gamma)$, such as $\mathrm{Br}(\tau^- \to \mu^-\mu^+\mu^-)/\mathrm{Br}(\tau^- \to \mu^-\gamma) \approx 2.2 \times 10^{-2}$, as mentioned above.

The specific decay modes of semi-leptonic LFV tau decays depend on the Wilson coefficients of the gluon and quark LFV operators. If the coefficients of the four-Fermi operators correspond

Table 135. Relations between LFV tau decay modes and effective operators. Here, I stands for the isospin of the final states. Table adapted from Ref. [124].

	$\tau \to \mu\gamma$	$\tau \to 3\mu$	$\tau \to \mu\pi^+\pi^-$	$\tau \to \mu K\bar{K}$	$\tau \to \mu\pi$	$\tau \to \mu\eta^{(\prime)}$
$C_{DL,R}$	$\surd$	$\surd$	$\surd$	$\surd$	—	—
$C_{SLL,RR}$	—	$\surd$	—	—	—	—
$C_{VLL,RR}$	—	$\surd$	—	—	—	—
$C_{VLR,RL}$	—	$\surd$	—	—	—	—
$C^q_{VL,R}$	—	—	$\surd\ (I=1)$	$\surd\ (I=0,1)$	—	—
$C^q_{SL,R}$	—	—	$\surd\ (I=0)$	$\surd\ (I=0,1)$	—	—
$C_{GL,R}$	—	—	$\surd$	$\surd$	—	—
$C^q_{AL,R}$	—	—	—	—	$\surd\ (I=1)$	$\surd\ (I=0)$
$C^q_{PL,R}$	—	—	—	—	$\surd\ (I=1)$	$\surd\ (I=0)$
$C_{\tilde{G}L,R}$	—	—	—	—	—	$\surd$

to vector or scalar couplings, the final states will include at least two mesons. If the coefficients correspond to a pseudoscalar or axial vector coupling, the final states may include only one meson. The final states of semi-leptonic LFV tau lepton decays will have isospin zero or one, depending on the Wilson coefficients. On the other hand, purely leptonic tau lepton decays, such as $\tau \to 3\mu$, are induced by any type of purely leptonic four-Fermi operators. Thus, from the branching ratios of the LFV tau lepton decay, we can identify the Wilson coefficients and the UV physics. If the golden mode $\tau \to 3\mu$ is discovered, it will provide the normalization for the LFV couplings, and we can discriminate models by comparing it with the branching ratios of other decay types.

We will discuss some predictions for the LFV tau lepton decay modes, assuming the SUSY extensions of the SM as benchmark models. In the SUSY SMs, the SUSY-breaking mass terms for the left-handed and/or right-handed sleptons may be lepton flavor violating such that the LFV dipole operators induce $\tau \to \mu/e\gamma$ and other LFV processes via penguin diagrams. In Fig. 177 we show the branching ratio for $\tau \to \mu\gamma$ by introducing the left-handed (right-handed) stau and smuon mixing mass term with black (red) dots. The branching ratio for the golden mode $\tau \to 3\mu$ is 2.2×10^{-2} times smaller than that for $\tau \to \mu\gamma$. Here, the bino, wino, and Higgsino masses are 250 GeV, 500 GeV, and 1 TeV, respectively, while $\tan\beta$ is 30. In the case of left-handed (right-handed) slepton mixing, the smuon and stau masses are taken from 500 GeV to 2 TeV, while the right-handed (left-handed) slepton masses are 5 TeV. We exclude the points where the sleptons are lighter than the second lightest neutralino or the light chargino, since the LHC results give constraints on these points. The left-handed sleptons interact as $SU(2)_L$, and the branching ratio is larger when the left-handed sleptons have non-zero mixing mass terms. It is found that the SUSY SMs could even exceed the current experimental bounds on the branching ratios.

In Fig. 178 we show the branching ratios of $\tau \to \mu\gamma$ and $\tau \to e\gamma$ in the SUSY seesaw model. Here, the CMSSM boundary conditions for the SUSY-breaking parameters are assumed, that is, $0.5 < m_0$, $m_{1/2} < 10$ TeV, $|A_0| < 3$, $\mu > 0$, while $\tan\beta = 30$. The mixing mass terms for left-handed sleptons are generated by renormalization group effects. The SUSY seesaw model is reconstructed from the observed oscillation parameters by assuming a specific set of Yukawa couplings that suppress $\mu \to e\gamma$. The procedure is detailed in Ref. [1535]. For the blue (red) points the normal (inverted) hierarchy is assumed for the neutrino mass ordering. The branching ratios in Fig. 178 are smaller than in Fig. 177. This is mainly from the observed Higgs mass, since it requires the SUSY particle masses

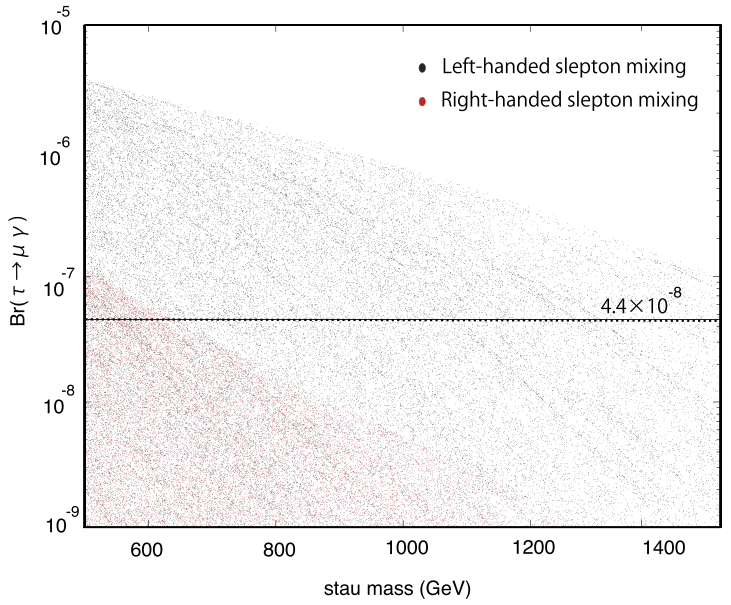

Fig. 177. Branching ratio of $\tau \to \mu\gamma$ in the SUSY SMs with left-handed (black) and right-handed (red) smuon–stau-mixing mass terms. The dashed line indicates the current experimental bound. See text for details on the input parameters.

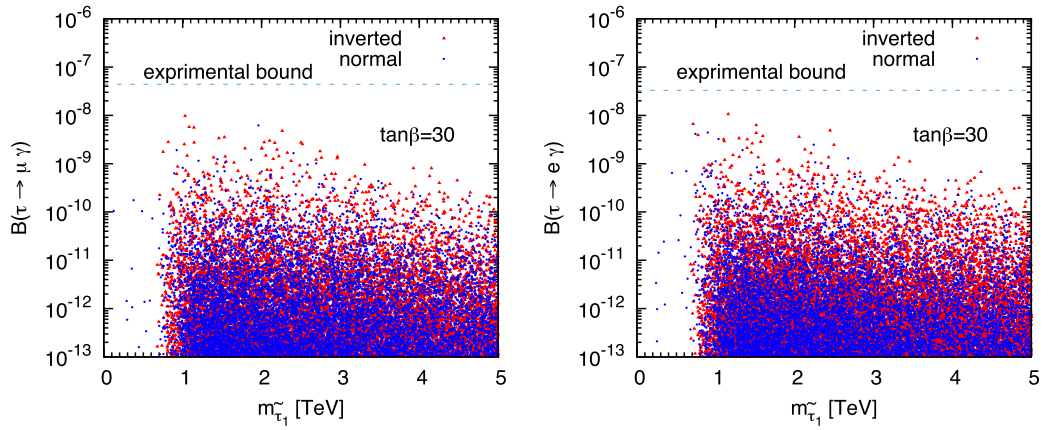

Fig. 178. Branching ratios of $\tau \to \mu\gamma$ and $\tau \to e\gamma$ in the SUSY seesaw model under the assumption of specific textures of Yukawa couplings which suppress $\mu \to e\gamma$. For the blue (red) points a normal (inverted) hierarchy is assumed for the neutrino mass ordering. CMSSM boundary conditions for SUSY-breaking parameters are assumed. See text for details on the input parameters.

to be heavier. These results demonstrate that the target of the Belle II experiment with $\tau \to \mu\gamma$ is a more generic flavor structure rather than a CMSSM-like structure.

15.2.2. Experiment

Authors: K. Hayasaka, T. Konno, F. Tenchini

In this subsection we describe the experimental techniques used to search for LFV signals based on Belle analyses. Belle performed searches for 46 LFV τ decay modes using nearly the entire data sample of approximately 1000 fb^{-1}. No evidence for LFV decays was observed in any of the modes studied, where 90% CL upper limits on the branching fractions at the $O(10^{-8})$ level were set. At

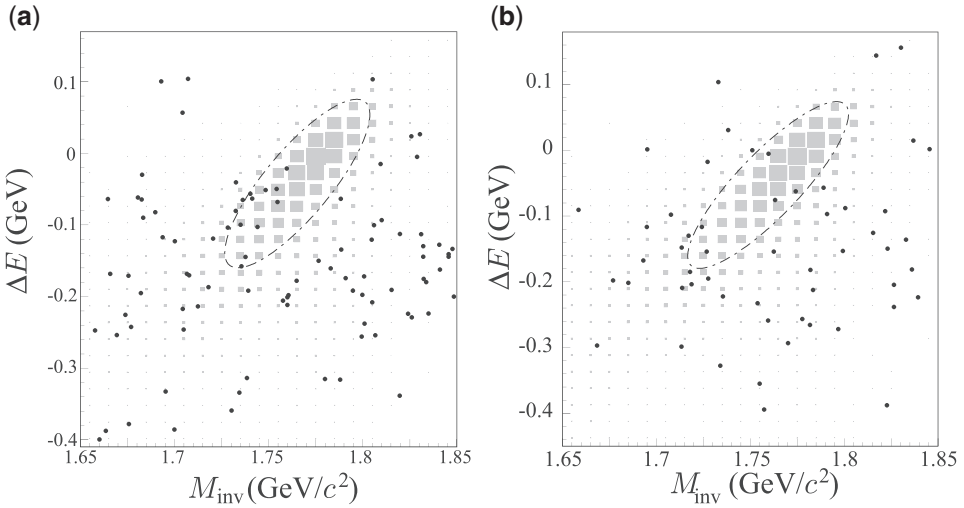

Fig. 179. $M_{\ell\gamma}$–ΔE distributions from the Belle search for (a) $\tau \to \mu\gamma$ and (b) $\tau \to e\gamma$ [1536]. The black dots and shaded boxes show the data and signal MC, respectively, and the ellipse is the $2\,\sigma$ signal region.

Belle II a sensitivity at the $O(10^{-9})$–$O(10^{-10})$ level is expected, allowing one to explore a wider region of parameter space in various NP scenarios.

$\tau \to \mu\gamma$ In LFV analyses, in order to evaluate the signal yield two independent variables are typically used: the reconstructed mass of the signal, and the difference between the sum of energies of the signal τ daughters and the beam energy (ΔE) in the CM frame. In the $\tau \to \mu\gamma$ case, these variables are defined as

$$M_{\mu\gamma} = \sqrt{E_{\mu\gamma}^2 - P_{\mu\gamma}^2}, \tag{499}$$

$$\Delta E = E_{\mu\gamma}^{\rm CM} - E_{\rm beam}^{\rm CM}, \tag{500}$$

where $E_{\mu\gamma}$ and $P_{\mu\gamma}$ are the sum of the energies and the magnitude of the vector sum of the momenta for the μ and the γ, respectively. The superscript CM indicates that the variable is defined in the CM frame; e.g. $E_{\rm beam}^{\rm CM}$ is the beam energy in the CM frame. For signal, $M_{\mu\gamma}$ and ΔE should peak at $M_{\mu\gamma} \sim m_\tau$ and $\Delta E \sim 0$ GeV, while for the background, $M_{\mu\gamma}$ and ΔE will smoothly vary without a peaking structure.

Taking into account the resolution of the detector and the correlation between $M_{\mu\gamma}$ and ΔE, we use an elliptical signal region. To avoid biases, we typically perform blind analyses, where the data in the signal region are blinded when determining the selection criteria and the systematic uncertainties.

The observed $M_{\ell\gamma}$–ΔE distributions at Belle (based on a sample of 4.9×10^8 $\tau^+\tau^-$ pairs [1536]) are shown in Fig. 179 for $\tau \to \mu\gamma$ and $\tau \to e\gamma$. The signal yield is evaluated from an extended unbinned maximum likelihood fit to the $M_{\ell\gamma}$–ΔE distributions. The main background (BG) is from $\tau \to \ell\nu_\ell\nu_\tau$ with radiated photons, radiative dimuon (for $\mu\gamma$), and Bhabha (for $e\gamma$) events. The event selection criteria used to reduce background are discussed further in the context of the Belle II sensitivity study later in this section. The upper limit obtained from this analysis yields Br($\tau \to \mu\gamma$ ($e\gamma$)) $= 4.5 \times 10^{-8}$ (1.2×10^{-7}) at 90% CL.

Beam background studies: At Belle II, the beam background to the τ LFV searches is potentially a more serious concern than at Belle, as the ultimate goal is to achieve background-free signal windows. However, beam background is likely to produce only low-energy photons, which would be removed

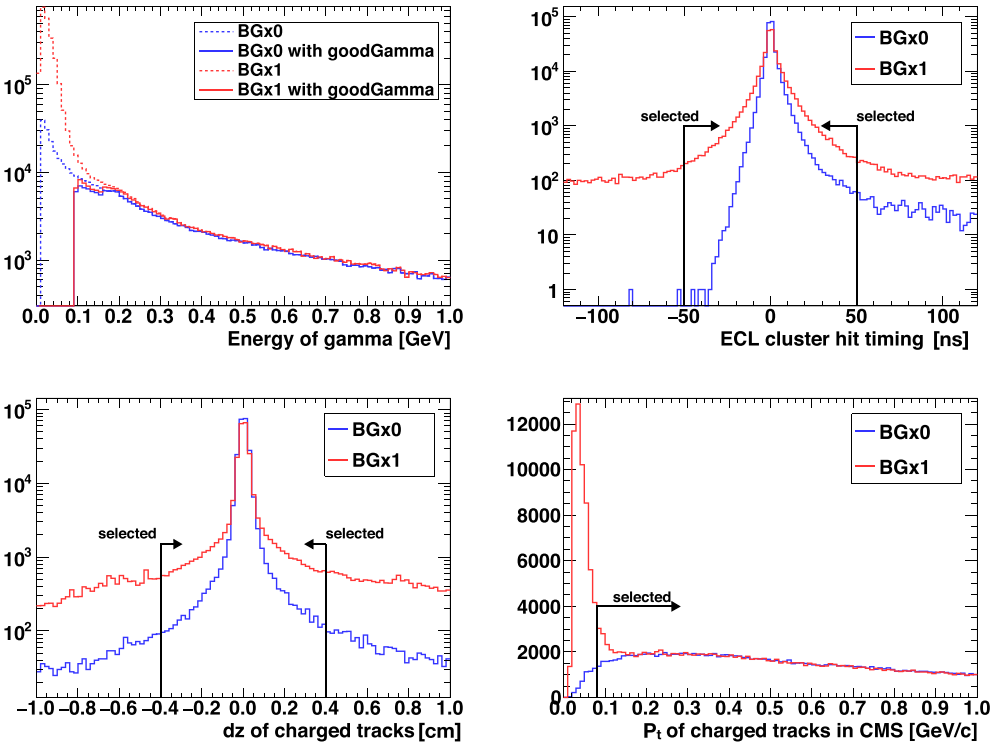

Fig. 180. Distribution of γ energy (top left), ECL cluster timing (top right), track distance from the interaction point along the beam, dz (defined in Sect. 5) (bottom left), and P_t of charged particle tracks (bottom right). The bold lines show the distributions after the Belle II quality cut, which rejects low-energy photons. The black arrows show the selection criteria adopted for background rejection.

by typical selection criteria. A preliminary Belle II $\tau \to \mu\gamma$ study with beam background was performed using MC samples, in order to determine the feasibility of τ LFV analyses in this more contaminated environment.

We first studied generic SM-decaying $\tau^+\tau^-$ pairs generated with nominal beam background (denoted BGx1) and without background (denoted BGx0) in order to study the background's impact on the distributions of various physics observables and develop background reduction techniques. As a result, we introduced the following basic selection criteria:

- For photon clusters:
  - $E_\gamma > 0.100$ GeV (forward endcap), 0.090 GeV (barrel), 0.160 GeV (backwards endcap);
  - $|\Delta t_{\text{cluster}}| < 50$ ns.
- For charged particles:
  - track fit p-value > 0.01;
  - track distance from interaction point (along the beam axis) $|dz| < 0.5$ cm;
  - $P_t > 0.08$ GeV.

The distributions of each of the above variables, except for the p-value, are shown in Fig. 180.

We examined the τ LFV decay mode $\tau \to \mu\gamma$ by loosely following the corresponding Belle analysis and reconstructing τ MC signal samples generated both with and without beam background. In addition to the signal side, a single charged particle in the accompanying (tag) side of the τ pair was also required for successful candidate selection.

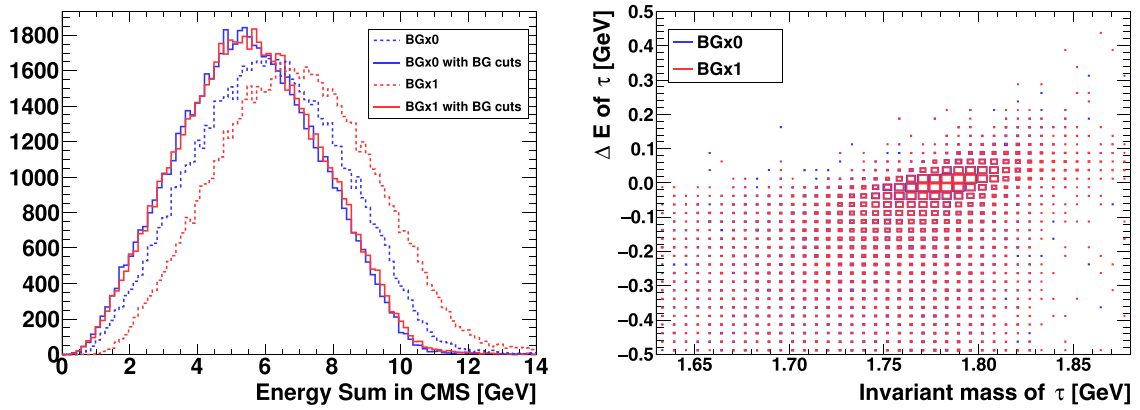

Fig. 181. (Left) Energy sum distribution in the CMS frame; dashed lines show histograms without any selection, while bold lines show histograms with all selection criteria applied. (Right) Correlation between invariant mass and energy difference, ΔE, of the signal τ after $\tau \to \mu\gamma$ preselection.

The final-state particle selection criterion was verified to largely mitigate the effect of beam background, as demonstrated by the distribution of the reconstructed τ energy in the center-of-mass frame (Fig. 181 (left)). The phase space in the invariant mass and the beam energy difference of the signal τ can also be seen in Fig. 181 (right), where 29.6% of BGx1 events and 35.1% of BGx0 events passed this selection; we can therefore estimate a 16% decrease in signal due to background.

Sensitivity studies: We perform a sensitivity study for a $\tau \to \mu\gamma$ analysis in Belle II, in order to validate the stated sensitivity projections, demonstrate measurement feasibility with the new beam conditions, and investigate new observables that could potentially improve the separation power for future analyses.

The expected ΔE resolution in Belle II is expected to be superior to Belle when neutral particles are part of the reconstructed decay. This is due to improvements in photon position measurement, and hence four-vector derivation. Overall, this means that better background separation is in principle achievable in order to achieve a background-free signal region.

The analysis approach mimics the previous Belle analysis in Ref. [1537], with several additional criteria to further reduce the background. We reconstruct the signal in the mode $\tau \to \mu\gamma$, while the tag side is reconstructed from one non-μ charged track which is assumed to originate from a SM tau decay. The study is performed on 3×10^6 signal MC events and $10^8 \div 10^9$ events for each process acting as a background to the analysis: $\tau \to \mu\nu\bar{\nu}$, $\tau \to e\nu\bar{\nu}$, $\tau \to \pi\nu$, $e^+e^- \to \mu^+\mu^-(\gamma)$, $e^+e^- \to e^+e^-(\gamma)$, $e^+e^- \to q\bar{q}$ (for each $q = u, d, s, c$), $e^+e^- \to B^+B^-$, and $e^+e^- \to B^0\bar{B}^0$. The channels are subsequently rescaled to a luminosity of 1 ab^{-1}, equivalent to the full Belle dataset, for ease of comparison. The selection criteria applied are similar to the Belle analysis, with some changes due to differences in the Belle II detector. The criteria described in the preceding section on beam background studies are applied as a preselection. In addition, several new criteria are implemented. We discuss the most significant ones below and show their impact against the dominant background processes, due to $e^+e^- \to \mu^+\mu^-(\gamma)$, $\tau \to \pi\nu$, or $\tau \to \mu\nu\bar{\nu}$ with random photons, as well as hadronic continuum where relevant. $e^+e^- \to \Upsilon(4S)$ is omitted from most plots to avoid clutter, as it is easily suppressed through basic event shape requirements.

Energy, momentum, timing: We expect tag side tracks from μ-pair backgrounds to peak at $p^{\text{tag}}_{\text{CM}} \sim 5.5\,\text{GeV}/c$ due to momentum conservation; we thus require $p^{\text{tag}}_{\text{CM}} < 2.5\,\text{GeV}/c$. As a significant

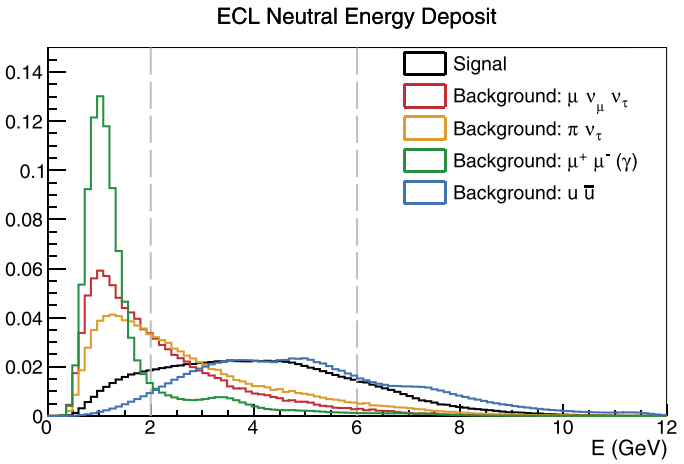

Fig. 182. Total energy deposit in the ECL by neutral particles. The dashed gray lines indicate the selection criteria.

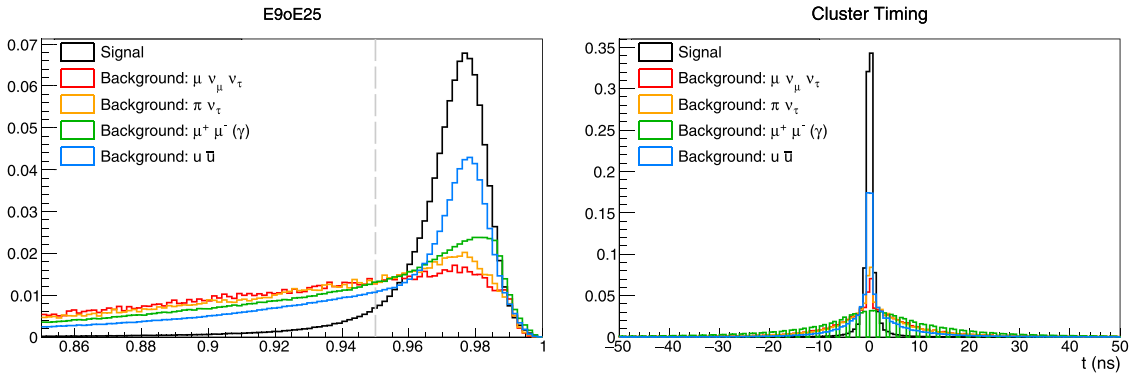

Fig. 183. Left: E9oE25 cluster ratio distributions. The dashed gray line indicates the selection criterion. Right: Cluster timing distributions.

portion of the background process is reconstructed from random combinations of charged tracks with low-energy photons, we require the total energy collected in the ECL from neutral clusters to be $2 < E_{\mathrm{ECL}} < 6\,\mathrm{GeV}$. This is shown in Figure 182.

We expect the ECL energy cluster ratio E9oE25 to be consistent with that of an EM shower (see Sect. 5.6.1) and peak close to 1. We require E9oE25 > 0.95—see Fig. 183 (left). In order to select time-coincident $\tau \to \mu\gamma$ decays, we require the value of cluster timing to be within ± 1 ns—see Fig. 183 (right).

Event thrust: We define the thrust scalar T for a collection of N particles as the value

$$T = \frac{\sum_{i=1}^{N} |\mathbf{T} \cdot \mathbf{p_i}|}{\sum_{i=1}^{N} |\mathbf{p_i}|}, \tag{501}$$

where the thrust axis $\mathbf{T}$ is the unit vector along which the total projection of the particle momenta is maximized. We calculate the thrust scalars for both the signal side and the rest of the event, i.e. the collection of particles (including the tag) belonging to the event but not used to build the signal side. The thrust distribution for the signal is shown in Fig. 184 (left).

Signal $\mu\gamma$ pairs have similar momenta with a small opening angle between them; therefore, the signal-side thrust shows a clear peak around 0.942. For most background events, the signal

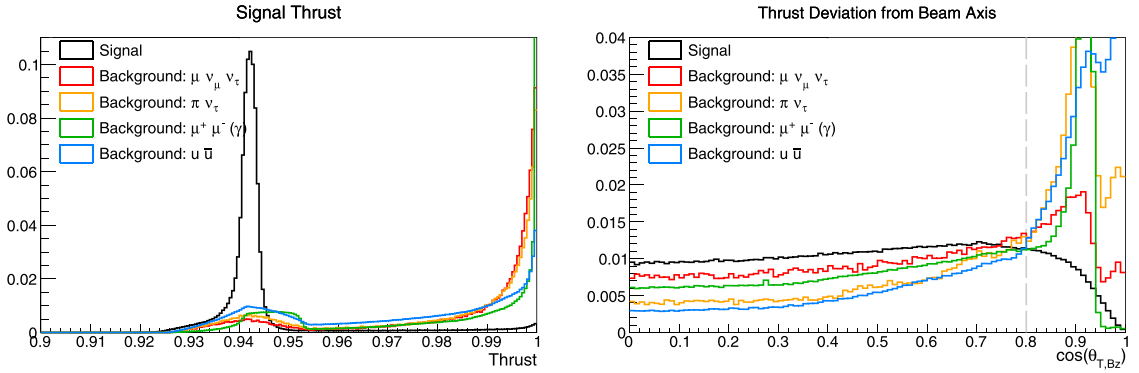

Fig. 184. (Left) Signal-side thrust scalar distributions. (Right) Angle between the signal thrust axis and the beam axis. The dashed gray line indicates the selection criterion.

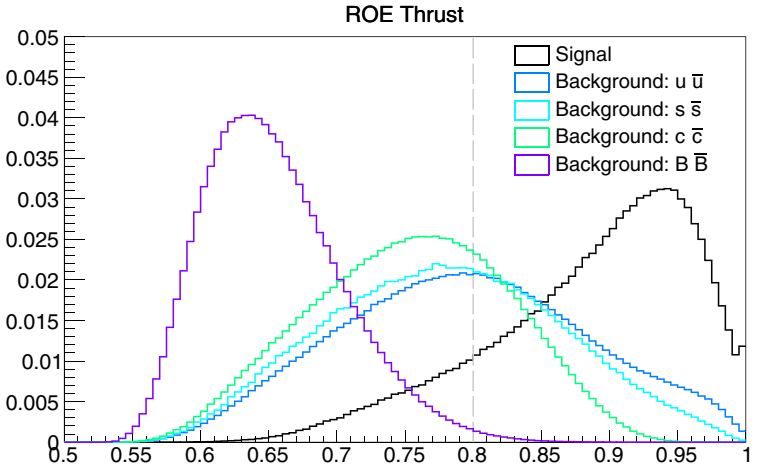

Fig. 185. Rest-of-event thrust scalar distributions. The dashed gray line indicates the selection criterion.

side is instead reconstructed from a high-energy track paired with a low-energy photon from bremsstrahlung, beam background, or other processes. As the track momentum alone dominates the thrust calculation, the distribution produces a peak at 1. We therefore require the signal thrust to be in the range 0.936 to 0.944. A similar criterion is also used in the Belle analysis, but in Belle II the improved photon momentum measurements allow for a tighter requirement. An additional criterion can be required on the angle between the signal thrust and the beam axis: $\cos\theta_{T,Bz} < 0.8$, as shown in Fig. 184 (right).

Due to the large number of tracks and photons produced in hadronic processes, mis-reconstructed $e^+e^- \to q\bar{q}$ and $e^+e^- \to B\bar{B}$ events have on average a lower rest-of-event thrust than leptonic channels. We can thus also select on the magnitude of the rest-of-event thrust vector to exclude $B\bar{B}$ events and strongly suppress $q\bar{q}$continuum. This is shown in Fig. 185.

Event shape: Further suppression can be achieved by selecting on higher-level event shape variables. The first such are CLEO cones [74], which are defined by binning the space around the signal thrust axis in nine 10° polar angle regions and then measuring the forward and backwards momentum flow through those regions in the laboratory frame. Distributions for the first and second CLEO cone are shown in Fig. 186, together with sample selections used for this study. The full set of selection criteria is given in Table 136. Event shape Fox–Wolfram moments can also provide

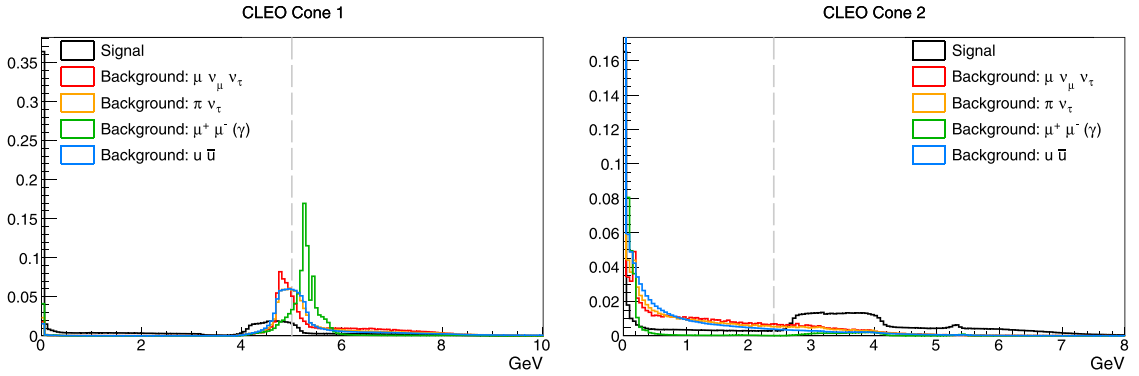

Fig. 186. Momentum flow distributions for the first (left) and second (right) CLEO cones. The dashed gray lines indicate the selection criteria.

Table 136. Sample selection criteria for CLEO cones.

CLEO		
cone	Lower	Upper
cc1	—	5
cc2	2.4	—
cc3	—	—
cc4	—	1.7
cc5	—	0.9
cc6	—	0.7
cc7	—	0.5
cc8	—	–
cc9	—	0.4

Table 137. Sample selection criteria for super and reduced Fox–Wolfram moments.

Fox–Wolfram		
moment	Lower	Upper
Hso(0,0)	0.05	1
Hso(0,1)	−0.05	0.3
Hso(0,2)	—	0.48
Hso(0,3)	−0.1	0.25
Hso(2,0)	−0.1	1
Roo(1)	−0.018	0.08
Roo(3)	−0.01	0.007
R_2	0.4	—

strong separation power. Sample criteria are shown in Table 137. These are especially effective in rejecting surviving continuum background events.

Table 138 lists the remaining events in the extended signal region ($-0.4 < \Delta E < 0.2\,\text{GeV}$, $1.65 < M_{\text{inv}} < 1.85\,\text{GeV}/c^2$) after the event selection. As can be seen, the expected background rate is vastly reduced. This selection has a 7.23% signal efficiency; the remaining signal distribution is fitted with asymmetric Gaussians yielding $\langle \Delta E \rangle \approx 47\,\text{MeV}$, $\langle M_{\text{inv}} \rangle \approx 1.79\,\text{GeV}/c^2$, which is consistent with our expectation of $\langle \Delta E \rangle \sim 0$ and $\langle M_{\text{inv}} \rangle \sim m_\tau$.

Table 138. Events remaining in the extended signal region after selection.

Channel	Events in sample (scaled to 1 ab^{-1})	Events after selection
$\tau \to \mu\nu\overline{\nu}$	1.60×10^8	163
$\tau \to \pi\nu$	3.34×10^8	40
$\tau \to e\nu\overline{\nu}$	1.64×10^8	0
$e^+e^- \to \mu^+\mu^-(\gamma)$	1.148×10^9	15
$e^+e^- \to e^+e^-(\gamma)$	3×10^{11}	0
$e^+e^- \to B^+B^-$	5.50×10^8	0
$e^+e^- \to B^0\overline{B}^0$	5.50×10^8	0
$e^+e^- \to q\overline{q}$	3.69×10^9	$9(u\overline{u})$+$3(d\overline{d})$+$3(c\overline{c})$

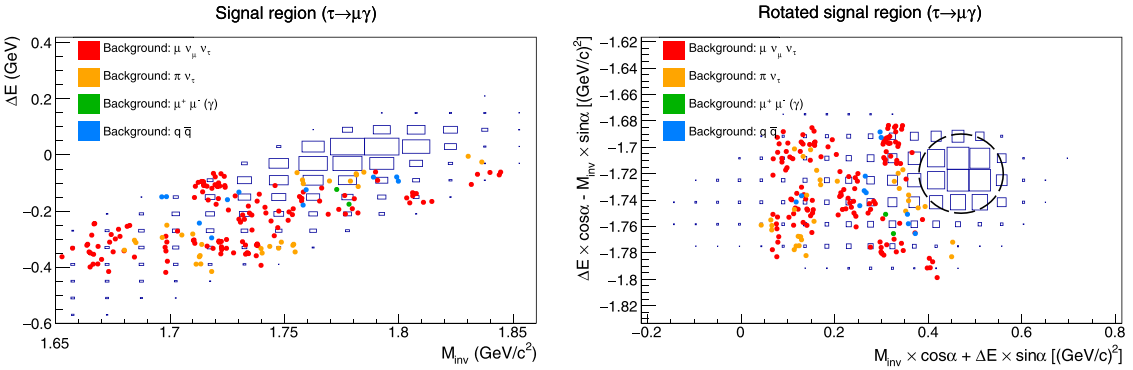

Fig. 187. $M_{\rm inv}$–ΔE extended signal region (top), and the same region rotated by $\alpha = 72°$ (bottom). Shaded boxes indicate the event distribution for $\tau \to \mu\gamma$; dots are unscaled background events colored according to the legend. The dotted ellipse represents the final, background-free, selection.

To determine an upper limit on the sensitivity to the branching fraction, we perform a 72° phase space rotation and select a smaller signal region centered on the means of the Gaussian fits. This is shown in Fig. 187. Selecting this sub-region reduces the signal efficiency to 4.59%; however, no MC background events are present. Assuming that the background distribution follows Poisson statistics, the sensitivity can be estimated without the need of likelihood fits, which is acceptable for a basic sensitivity study. Based on the observation of 0 events, we can set an upper limit of $n_{\rm events} < 2.3$ at 90% CL and convert it into an upper limit for the branching ratio under the hypothesis of no signal, for 1 ab^{-1} luminosity and a $e^+e^- \to \tau\tau$ production cross section of 0.919 nb:

$$B(\tau \to \mu\gamma) < \frac{n_{\rm events}}{\epsilon_{\rm signal} \times n_\tau} = \frac{2.3}{4.59 \times 10^{-2} \times 2 \times 9.19 \times 10^8} = 2.7 \times 10^{-8}\ (90\%\ \mathrm{CL}).$$

This compares favorably to the Belle result of $B(\tau \to \mu\gamma) < 4.5 \times 10^{-8}$ using 535 fb^{-1}. Although this is only a preliminary study, if a background-free selection were to be successfully achieved and maintained over the full Belle II dataset this would have a great impact, as the limit scales as $1/n_\tau$ in the zero-background hypothesis. This would lead to a factor of ∼100 improvement compared to the limit obtained by Belle.

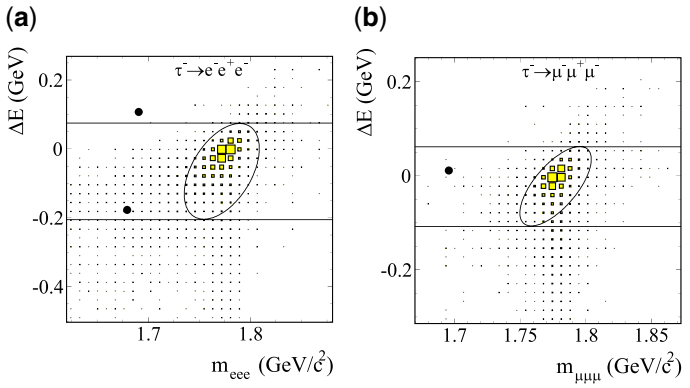

Fig. 188. $M_{\ell\ell\ell}$–ΔE distributions for the Belle analyses of the (a) $\tau^- \to e^-e^+e^-$ and (b) $\tau^- \to \mu^-\mu^+\mu^-$ modes [1537]. The black dots and shaded boxes show the data and signal MC, respectively. The ellipse is the signal region. The region formed by the two parallel lines, excluding the signal ellipse region, is the sideband region used to evaluate the expected number of background events in the signal region.

Table 139. Summary of the efficiency, the expected number of BG events, and the upper limit on the branching fraction at 90% CL for $\tau^- \to \ell^-\ell'^+\ell''^-$ at Belle.

Mode	Efficiency (%)	$N_{\rm BG}^{\rm exp}$	Upper limit (10^{-8})
$e^-e^+e^-$	6.0	0.21 ± 0.15	2.7
$e^-\mu^+\mu^-$	6.1	0.10 ± 0.04	2.7
$e^-e^+\mu^-$	9.3	0.04 ± 0.04	1.8
$\mu^-e^+\mu^-$	10.1	0.02 ± 0.02	1.7
$e^-\mu^+e^-$	11.5	0.01 ± 0.01	1.5
$\mu^-\mu^+\mu^-$	7.6	0.13 ± 0.06	2.1

Other modes Here we review some of the other τ LFV measurements performed at Belle, including the golden $\tau \to 3\mu$ mode. All of these channels are largely background free and therefore a sensitivity improvement of about two orders of magnitude can be expected with Belle II due to the increase in luminosity.

$\tau \to \ell\ell'\ell''$*:* For the decays $\tau \to \ell\ell'\ell''$, $M_{\ell\ell\ell}$ and ΔE are similarly used to identify signal events. Figures 188(a) and (b) show the three-lepton invariant mass versus ΔE ($M_{\ell\ell\ell}$–ΔE) distributions, respectively, for the $\tau^- \to e^-e^+e^-$ and $\tau^- \to \mu^-\mu^+\mu^-$ candidates after selection at Belle with nearly the entire data sample (7.2×10^8 $\tau^+\tau^-$ pairs) [1537]. No events in the signal region have been found in any of the six modes. The 90% CL upper limits on the branching fractions in units of 10^{-8} are given in Table 139.

LHC experiments have also studied $\tau \to 3\mu$; the current upper limit obtained by LHCb is 4.6×10^{-8} using a $1.0\,\text{fb}^{-1}$ data sample at 7 TeV and a $2.0\,\text{fb}^{-1}$ data sample at 8 TeV. LHCb has a plan to accumulate a $50\,\text{fb}^{-1}$ data sample at 14 TeV by 2029, and to improve the tau trigger efficiency through various upgrades. Since the LHCb analysis has a large background contribution, the sensitivity is expected to primarily run proportionally to the inverse of the square root of the data increase. Therefore, the expected upper limit of the branching fraction for $\tau \to 3\mu$ will be approximately $4.6 \times 10^{-8}/\sqrt{50/3 \times 2 \times 2} = 5.6 \times 10^{-9}$. So while the LHC experiments will be

Table 140. Summary of the efficiency, the expected number of BG events, and the upper limit on the branching fraction for $\tau \to \ell P^0$ at Belle, where (comb.) means the combined result from sub-decay modes.

Mode	Efficiency (%)	$N_{\rm BG}^{\rm exp}$	Upper limit (10^{-8})
$\mu\eta(\to \gamma\gamma)$	8.2	0.63 ± 0.37	3.6
$e\eta(\to \gamma\gamma)$	7.0	0.66 ± 0.38	8.2
$\mu\eta(\to \pi\pi\pi^0)$	6.9	0.23 ± 0.23	8.6
$e\eta(\to \pi\pi\pi^0)$	6.3	0.69 ± 0.40	8.1
$\mu\eta$(comb.)			2.3
$e\eta$(comb.)			4.4
$\mu\eta'(\to \pi\pi\eta)$	8.1	$0.00^{+0.16}_{-0.00}$	10.0
$e\eta'(\to \pi\pi\eta)$	7.3	0.63 ± 0.45	9.4
$\mu\eta'(\to \gamma\rho^0)$	6.2	0.59 ± 0.41	6.6
$e\eta'(\to \gamma\rho^0)$	7.5	0.29 ± 0.29	6.8
$\mu\eta'$(comb.)			3.8
$e\eta'$(comb.)			3.6
$\mu\pi^0$	4.2	0.64 ± 0.32	2.7
$e\pi^0$	4.7	0.89 ± 0.40	2.2

good competitors, Belle II is expected to have higher sensitivity owing to the background-free environment. The expected Belle II upper limit is $2.1 \times 10^{-8}/(50/0.8) = 3.3 \times 10^{-10}$ with the 50 ab^{-1} data sample.

$\tau \to \ell P^0$ ($P^0 = \pi^0, \eta, \eta'$)*:* The results for τ decays into a lepton and a neutral pseudoscalar (π^0, η, η') at Belle [1538] are summarized in Table 140. A single event is found in $\tau \to e\eta(\to \gamma\gamma)$, consistent with the expected background, while no events are observed in other modes. The obtained 90% CL upper limits on the branching fraction are in the range (2.2–4.4) $\times 10^{-8}$.

Summary of LFV projections We provide a naive set of 50 ab^{-1}projections for 90% CL upper limits based on zero-background scenarios in Fig. 189. In this case, all limits follow linearly with the increase in integrated luminosity, with a reasonable assumption that the Belle II analyses will have the same efficiency as Belle. As shown earlier in this section, it may be feasible to reach zero background in many channels, particularly those with all charged particle final states. A simulation study of a challenging case was presented, that of $\tau \to \mu\gamma$, which we found could conceivably be isolated from background with optimized analysis techniques. It would be realistic to assume that some modes with neutrals may eventually contain some irreducible background, in which case the improvement on the limits will be approximately one order of magnitude, rather than two in the zero-background case presented in the figure.

15.3. CP violation in τ decays

Contributing authors: I. Bigi, K. Hayasaka, E. Kou, B. Moussallam, E. Passemar

In the three-generation SM, the violation of CP is explained by the Kobayashi–Maskawa mechanism. It predicts the CP violation in the quark sector as well as an absence of CP violation in the lepton sector. Therefore, the study of CP violation in semi-hadronic τ decays offers a unique search of physics beyond the SM, namely a new source of CP violation beyond the Kobayashi–Maskawa

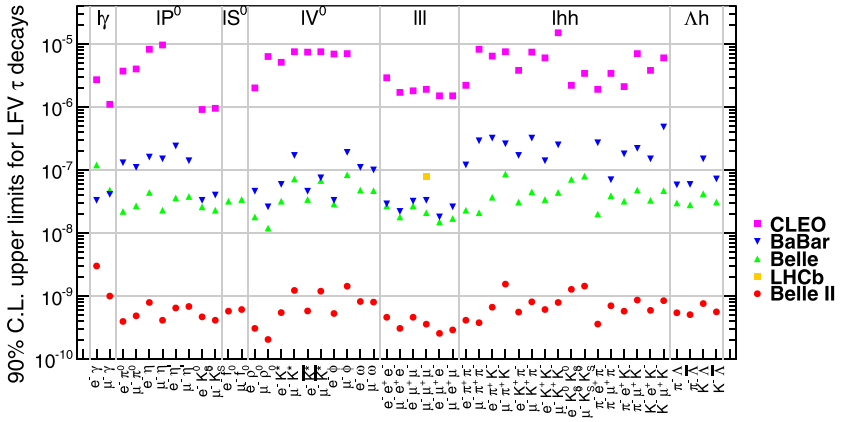

Fig. 189. Current 90% CL upper limits for the branching fraction of τ LFV decays obtained in the CLEO, BaBar, and Belle experiments. The purple boxes, blue inverted triangles, green triangles, and yellow boxes show CLEO, BaBar, Belle, and LHCb results, respectively, while the red circles express the Belle II future prospects, where they are extrapolated from Belle results assuming the integrated luminosity of 50 ab^{-1}.

mechanism. If τ CP violation is observed, it implies that there exists a new CP-violating coupling in the τ–ν_τ and/or d–u or s–u current in addition to the one induced in the SM by the K^0–$\overline{K}^0$ mixing.

The first CP asymmetry measurement in τ decays was performed using the decay rate difference between $\tau^+ \to \pi^+ K^0_S \bar{\nu}_\tau$ and $\tau^- \to \pi^- K^0_S \nu_\tau$:

$$\mathcal{A}_\tau = \frac{\Gamma(\tau^+ \to \pi^+ K^0_S \bar{\nu}_\tau) - \Gamma(\tau^- \to \pi^- K^0_S \nu_\tau)}{\Gamma(\tau^+ \to \pi^+ K^0_S \bar{\nu}_\tau) + \Gamma(\tau^- \to \pi^- K^0_S \nu_\tau)}. \tag{502}$$

This CP asymmetry is non-zero in SM due to the K^0–$\overline{K}^0$ mixing. Assuming CPT invariance, we can write the CP asymmetry in terms of the kaon mixing parameter ϵ. With a first-order approximation, and neglecting the effect from ϵ'/ϵ, the SM prediction yields [1539–1541]

$$\mathcal{A}^{\text{SM}}_\tau \approx 2\text{Re}(\epsilon) \approx (0.36 \pm 0.01)\%, \tag{503}$$

where we assume that the experimental results are obtained by time integration between a time much smaller than the K^0_S lifetime and much longer than the K^0_L lifetime (see Ref. [1541] for a discussion on the effects of time dependence). Note that we are discussing the simplest case with two hadrons in the final state, but we would obtain the same result adding more pions. Thus, more generally [1539],

$$\begin{aligned} &A_{\text{CP}}(\tau^- \to \nu K^0 X'_{S=0}) \\ &= A_{\text{CP}}(\tau^- \to \nu K^0_S X'_{S=0}) + A_{\text{CP}}(\tau^- \to \nu K^0_L X'_{S=0}) + A_{\text{CP}}(\tau^- \to \nu [K^0_S/K^0_L] X'_{S=0}) \\ &= 2\,\text{Re}\,\epsilon_K + 2\,\text{Re}\,\epsilon_K - 4\,\text{Re}\,\epsilon_K = 0, \end{aligned} \tag{504}$$

where $X' = \pi, \pi\pi, \pi\pi\pi, \ldots$ with corresponding charge, and $[K^0_S/K^0_L]$ represents the K^0_S–K^0_L interference term. The SM prediction in Eq. (503) must be compared to the result obtained by the BaBar collaboration [1542]:

$$\mathcal{A}_\tau = (-0.36 \pm 0.23 \pm 0.11)\%, \tag{505}$$

which is $2.8\,\sigma$ away from the SM expectation in Eq. (503). A similar level of CP violation, due to kaon mixing, should be observed in D meson decay,

$$\mathcal{A}_D = \frac{\Gamma(D^+ \to \pi^+ K^0_S) - \Gamma(D^- \to \pi^- K^0_S)}{\Gamma(D^+ \to \pi^+ K^0_S) + \Gamma(D^- \to \pi^- K^0_S)}.$$

These asymmetries are related to the τ CP asymmetry as $A_\tau = -A_D$ [1541]. The experimental average of D meson CP asymmetry is found to be $A_D = (-0.41 \pm 0.09)\%$, much more precise than $\mathcal{A}_\tau$. Thus, an improved measurement of $\mathcal{A}_\tau$ is certainly the first priority at Belle II.

This intriguing result motivates us to further investigate CP violation measurements in hadronic τ decays. The CP asymmetry $\mathcal{A}_\tau$ discussed above is an angular integrated observable (parity even) and is sensitive to a particular type of NP coupling. For example, in Ref. [1543] it was pointed out that a tensor coupling induced by an NP model may interfere with the SM vector coupling and produce such CP violation. However, in a recent study [1544] it has been shown that this tensor coupling cannot explain such a large effect. Moreover, they also showed that such a large asymmetry is incompatible with constraints coming from the neutron EDM and D^0–$\overline{D}^0$ mixing. An interesting NP search in the $D^+ \to K^0_S \pi^+$ process is proposed in Ref. [1545]. The prospect of the relevant measurement at Belle II is discussed in detail in Chapter 13. If this discrepancy persists at Belle II, it would point towards the existence of light BSM physics evading these constraints. On the other hand, in order to probe scalar or pseudoscalar couplings, which can be induced by charged Higgs bosons, a parity-odd angular observable is needed. In the following subsections we discuss some details of CP violation measurement using the angular observables.

We note an interesting CPT test that Belle II may be able to perform:

$$A_{\rm CP}(\tau^- \to \nu K^- X'_{S=0}) + A_{\rm CP}(\tau^- \to \nu K^0 X'_{S=0}) = 0, \tag{506}$$

where $X' = \pi, \pi\pi, \pi\pi\pi$, etc., with corresponding charges. This relation can be derived from the CPT invariance relation

$$\Gamma(\tau^- \to \nu X^-_{S=0}) = \Gamma(\tau^+ \to \bar{\nu} X^+_{S=0}), \quad \Gamma(\tau^- \to \nu X^-_{S=-1}) = \Gamma(\tau^+ \to \bar{\nu} X^+_{S=+1}). \tag{507}$$

15.3.1. CP violation in angular observables

The general angular formalism of hadronic τ decays contain 16 structure functions [1546]. Not all of them are measurable, as the final state neutrino direction is lost. Nevertheless, it has been shown in Ref. [1546] that 13 out of 16 are measurable if information is known about the azimuthal and polar angles of the hadronic system in the laboratory frame (ϕ, β)[57] in addition to the two angles (θ and ψ) which characterize the relative orientation of the laboratory, hadron, and tau rest frames, (find the details below) are known. We do not use the angle θ in the following discussion since it is useful only when the τ polarization is known [1548], which is not the case for Belle II. Various CP violation measurements have been proposed for the $\tau \to 2\pi\nu$ [1549], $\tau \to K\pi\nu$ [1547], $\tau \to 3\pi\nu$ [1550], $\tau \to K\pi\pi\nu, KK\pi\nu$ [1551–1553] decay channels.

Let us start with the two-hadron final state, $\tau \to P_1 P_2 \nu$ ($P_1 P_2 = \pi\pi, \pi\eta, \pi K, \eta K$). In Ref. [1547] it was shown that the CP-violating angular observable can be composed even without knowing the τ direction, as follows. Let us work in the $P_1 P_2$ momentum rest frame. In this frame, we first define the

[57] In Ref. [1546], the azimuthal angle is defined as α instead of ϕ. Note also that Ref. [1547] assumes that the laboratory frame coincides with the e^+e^- CM frame, which is not the case at Belle II.

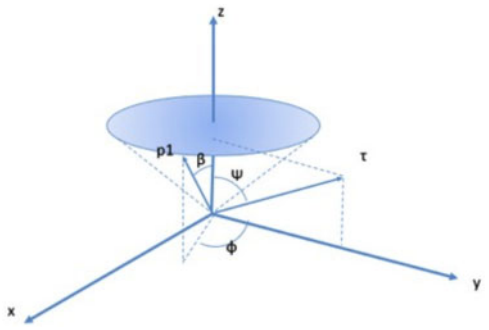

Fig. 190. Kinematics of $\tau \to K\pi\nu$.

laboratory direction as $+z$ and then the direction of P_1 by the polar angle β and the azimuthal angle ϕ (see Fig. 190). The direction of the τ cannot be measured due to the missing neutrino; however, the polar angle ψ can be computed with the following formula [1547]:

$$\cos\psi = \frac{x(m_\tau^2 + Q^2) - 2Q^2}{(m_\tau^2 - Q^2)\sqrt{x^2 - 4Q^2/s}}, \tag{508}$$

where $x = \frac{2E_{P_1}}{\sqrt{Q^2}}$ and E_{P_1} is the energy of the hadron P_1 in the laboratory frame. Q is the invariant mass of P_1, P_2. We fix the relative azimuthal angle such that τ is on the y–z plane to remove an unnecessary angle. As a result, we can write the angle between P_1 and τ in the hadronic rest frame as

$$\cos\alpha = \cos\beta\cos\psi + \sin\beta\sin\psi\cos\phi. \tag{509}$$

We are left with one angle, ϕ, undetermined,[58] though this does not cause any problem since the azimuthal angle does not carry additional information. We can therefore integrate it out, which cancels the second term in Eq. (509) (i.e. integration along the cone in Fig. 190). As we will see in the next subsection, using the term $\cos\beta\cos\psi$ we can construct one CP-violating observable for the two-hadron final state case that can be measured at Belle II.

Before closing this introduction, we briefly discuss three-hadron final states. While the CP violation search in $\tau \to P_1P_2\nu$ is sensitive to a new (pseudo)scalar contribution in the intermediate state, the CP violation search in $\tau \to P_1P_2P_3\nu$ is sensitive to a new pseudoscalar contribution (see, e.g., Refs. [1551–1553]) since $P_1P_2P_3$ proceeds mainly through axial vector resonances. For the three-hadron final states, we define the following angles for τ^-: β, which is an angle between the direction of the momentum for the $P_1P_2P_3$ system in the laboratory frame and the perpendicular direction of the plane which includes the momenta of P_1, P_2, and P_3 in the $P_1P_2P_3$ rest frame; and γ, which is the angle between the P_1 direction in the $P_1P_2P_3$ rest frame and the plane made from the two directions constructing β. Note that for τ^+, the charge conjugate must be considered (see [1552, Fig. 1]). Using these angles, it is found that three CP asymmetries, two T-even and one T-odd, can be constructed [1552]. Note that the T-even observable requires a strong phase to measure CP violation, while the T-odd one does not. Extracting the hadronic form factors in the three-hadron final states is

[58] The ϕ angle could be determined with the twofold ambiguity of using the other τ produced together from e^+e^- annihilation.

more difficult than in the two-hadron case, so we do not go into the details here. Nevertheless, we emphasize that three-hadron final states can offer an excellent null test: if non-zero CP violation is observed, it can be immediately interpreted as a signal of new physics.

15.3.2. CP violation measurement in $\tau \to P_1P_2\nu$ and determination of the hadronic form factors

As mentioned in the previous section, CP violation in two-hadron final states occurs due to the interference between vector and (pseudo)scalar currents that are accompanied by a strong phase. This amplitude is theoretically very well described by the form factors, which can be extracted from the same measurement. In this section we give a short account of the properties of these amplitudes and of the potential progress which could be achieved at Belle II.

Decays into two light pseudoscalar mesons $\tau^- \to P_1^- P_2^0 \nu_\tau$ with $P_i = \pi, K, \eta$ represent approximately 27% of the hadronic tau decays. Up to electromagnetic corrections, the decay amplitudes have the Fermi form

$$\mathcal{T} = -\frac{G_F}{\sqrt{2}} V_{uq}\, \bar{u}_\tau \gamma^\mu (1-\gamma^5) u_\nu \langle P_1^-(q_1) P_2^0(q_2)|\, \bar{\psi}_q \gamma_\mu \psi_u |0\rangle, \tag{510}$$

where q is the d or s quark and V_{uq} the corresponding CKM matrix element. The four-momenta q_1, q_2 are those of P_1 and P_2 in the laboratory frame.[59]

The hadronic matrix element involves the vector current only due to parity conservation in QCD, and can be expressed in terms of two form factors,

$$\langle P_1(q_1)P_2(q_2)|j_\mu^{qu}|0\rangle = C^{12}\big\{(q_1+q_2)_\mu f_-^{12}(Q^2) + (q_1-q_2)_\mu f_+^{12}(Q^2)\big\}, \tag{511}$$

where $Q^2 = (q_1+q_2)^2$ and the overall normalization factor C^{12} reads:

$$C^{\pi^-\pi^0} = \sqrt{2},\ C^{\pi^-\bar{K}^0} = -1,\ C^{\pi^-\eta} = \sqrt{2},\ C^{K^-\pi^0} = 1/\sqrt{2},\ C^{K^-\eta} = \sqrt{3/2},\ C^{K^-\bar{K}^0} = -1.$$

It is convenient to introduce the scalar form factor $f_0^{12}(s)$ as the following combination:

$$f_0^{12}(Q^2) = f_+^{12}(Q^2) + \frac{Q^2}{\Delta_{12}} f_-^{12}(Q^2), \quad \Delta_{12} = M_1^2 - M_2^2, \tag{512}$$

such that at $Q^2 = 0, f_0^{12}(0) = f_+^{12}(0)$. Expressing the two kinematical factors in Eq. (511) in the center-of-mass frame of the meson pair, one easily sees that $f_+^{12}(s)$ is associated with a pair in a $J = 1$ angular momentum state and is thus the vector form factor, while the scalar form factor f_0^{12} is associated with a pair in a $J = 0$ state.

The differential τ^- decay width reads

$$\begin{aligned}\frac{d\Gamma^{\tau^-}}{d\cos\alpha dW} = \frac{(C^{12}G_F V_{uq})^2}{128\pi^3}\left(\frac{m_\tau^2}{Q^2}-1\right)^2 \frac{q_{\rm cm}}{m_\tau} \\ \times \left\{|f_0^{12}(Q^2)|^2\Delta_{12}^2 + 4|f_+^{12}(Q^2)|^2 q_{\rm cm}^2 Q^2\left[\frac{Q^2}{m_\tau^2} + \left(1-\frac{Q^2}{m_\tau^2}\right)\cos^2\alpha\right]\right. \\ \left. - 4{\rm Re}\big[f_0^{12}(Q^2) f_+^{12}(Q^2)^*\big]\Delta_{12}\, q_{\rm cm}\sqrt{Q^2}\cos\alpha\right\},\end{aligned} \tag{513}$$

[59] Note that the formulae given in Ref. [1547] assume that the laboratory frame coincides with the e^+e^- CM frame, which is not the case at Belle II.

where $W = \sqrt{Q^2}$ and $q_{\rm cm}$ is the momentum in the hadronic center of mass system, $q_{\rm cm}^2 = ((Q^2)^2 - 2Q^2(M_1^2 + M_2^2) + \Delta_{12}^2)/4Q^2$. The decay widths integrated over $\cos\alpha$ are usually dominated by the vector form factor so that little is known at present on the scalar form factors from an experimental point of view. If one could measure the dependence on $\cos\alpha$, we would obtain more precise values of the two form factors and, furthermore, their relative phase, which is of particular interest in relation to the CP violation as shown below.

As pointed out in Ref. [1554], the interference of the vector and scalar form factors may be obtained using the forward–backward asymmetry:

$$\begin{aligned} A_{\rm FB}^{\tau^-}(Q^2) &= \frac{\int_0^1 \left[d\Gamma^{\tau^-}(\cos\alpha) - d\Gamma^{\tau^-}(-\cos\alpha)\right] d\cos\alpha}{\int_0^1 \left[d\Gamma^{\tau^-}(\cos\alpha) + d\Gamma^{\tau^-}(-\cos\alpha)\right] d\cos\alpha} \\ &= \frac{-2{\rm Re}\left[f_0^{12}(Q^2) f_+^{12}(Q^2)^*\right] \Delta_{12}\, q_{\rm cm}\sqrt{Q^2}}{|f_0^{12}(Q^2)|^2 \Delta_{12}^2 + 4|f_+^{12}(Q^2)|^2 q_{\rm cm}^2 Q^2 \left[\frac{Q^2}{m_\tau^2} + (1 - \frac{Q^2}{m_\tau^2})\frac{1}{3}\right]}, \end{aligned} \tag{514}$$

where ϕ in $\cos\alpha$ can be integrated—see Eq. (509)—so that, in practice, $\cos\alpha = \cos\beta\cos\psi$. Note that $A_{\rm FB}^{\tau^-}$ is related to the average weighted by $\cos\alpha$, $\langle\cos\alpha\rangle_{\tau^-}$,

$$\begin{aligned} \langle\cos\alpha\rangle_{\tau^-} &\equiv \frac{\int_{-1}^1 \cos\alpha\, d\Gamma^{\tau^-}(\cos\alpha)\, d\cos\alpha}{\int_{-1}^1 d\Gamma^{\tau^-}(\cos\alpha)\, d\cos\alpha} \\ &= \frac{2}{3} A_{\rm FB}^{\tau^-}(Q^2). \end{aligned} \tag{515}$$

In the presence of a charged Higgs boson exchange, the QCD scalar form factor is modified in the following way:

$$f_0^{12}(Q^2) \to f_0^{12}(Q^2)\left(1 + \eta_s \frac{Q^2}{m_H^2}\right). \tag{516}$$

As we expect $\left|\eta_s \frac{Q^2}{m_H^2}\right| \ll 1$, the phase difference between the vector and the scalar form factor can still be obtained by $A_{\rm FB}$ within a good approximation.

A new physics contribution as in Eq. (516) can induce CP violation, which can be measured with the CP-violating observable discussed in the introduction. It can be given (see, e.g.. Refs. [1555,1556]) as

$$\begin{aligned} A_{\rm CP}(Q^2) &= A_{\rm FB}^{\tau^-}(Q^2) - A_{\rm FB}^{\tau^+}(Q^2) \\ &= \frac{3}{2}\left(\langle\cos\alpha\rangle_{\tau^-} - \langle\cos\alpha\rangle_{\tau^+}\right). \end{aligned} \tag{517}$$

The decay rate for τ^+ can be obtained by $\eta_s \to \eta_s^*$ in Eq. (513). Thus, we find

$$A_{\rm CP}(Q^2) = \frac{4{\rm Im}\left[f_0^{12}(Q^2) f_+^{12}(Q^2)^*\right] {\rm Im}\left[\eta_s \frac{Q^2}{m_H^2}\right] \Delta_{12}\, q_{\rm cm}\sqrt{Q^2}}{|f_0^{12}(Q^2)|^2 \Delta_{12}^2 + 4|f_+^{12}(Q^2)|^2 q_{\rm cm}^2 Q^2 \left[\frac{Q^2}{m_\tau^2} + (1 - \frac{Q^2}{m_\tau^2})\frac{1}{3}\right]}, \tag{518}$$

where we have neglected the subdominant charged Higgs contribution in the denominator. We can see that, having the hadronic form factor information, we can determine the CP-violating parameter $\eta_s \frac{Q^2}{m_H^2}$ from this formula. Thus, obtaining the vector and scalar form factors is important.

It should be noted that $A_{CP}(Q^2)$ is a T-even observable so that the weak phase can be observed only when there is a strong phase. Fortunately, the strong phase in the $\tau \to P_1P_2\nu$ process is expected to be relatively large and it can be well defined theoretically. Recently, a model-independent parameterization of the form factors for this decay based on dispersion relations has been introduced (see, e.g., Ref. [1557]). This takes into account final state interactions, as has been done in the case of kaon decays [1558]. We will review this method below.

Vector form factors In the following we recall some properties of the form factors in QCD. Of particular importance is the property of analyticity, which follows from confinement. The $\pi\pi$ vector form factor, in particular, is of great interest in connection with a precise evaluation of the hadronic contributions to the $g-2$ of the muon. Analyticity-based descriptions provide improved extrapolations of the experimental data below the $\pi\pi$ threshold region. Both the vector and scalar form factors can be defined as analytic functions of the energy variable with a right-hand cut along the real axis, and they have the property of real analyticity, i.e. $f^{12}(z^*) = f^{12*}(z)$ (see, e.g., Ref. [1559] for a review, and also Sect. 7.4). This implies that one can express the form factors as a phase dispersive representation,

$$f^{12}(Q^2) = P_N(Q^2)\Omega^{12}(Q^2), \tag{519}$$

with

$$\Omega^{12}(Q^2) = \exp\left[\frac{Q^2}{\pi}\int_{s_0}^{\infty} ds' \frac{\phi^{12}(s')}{s'(s'-Q^2)}\right], \tag{520}$$

where $\phi^{12}(s')$ is the phase of the form factor and P_N is a polynomial. In QCD, we expect the form factors to vanish at infinity (see Ref. [1560] for a review),

$$f^{12}(Q^2) \sim \alpha_s(Q^2)/Q^2, \tag{521}$$

which constrains the degree N of the polynomial and the value of the phase at infinity to satisfy

$$N = \frac{\phi^{12}(\infty)}{\pi} - 1. \tag{522}$$

The phase representation is effective for the $\pi\pi$ or πK form factors, as Watson's theorem relates the phase of the form factor to the scattering phase shift of $\pi\pi$ or πK in a finite energy range where the scattering is elastic. As an illustration of this, a description of $f_+^{\pi\pi}$ of the following form was proposed [1561]:

$$f_+^{\pi\pi}(Q^2) = \Omega_1(Q^2)\,\Omega_{\rm in}(Q^2), \tag{523}$$

where Ω_1 is the Omnès function associated with the $I = J = 1\ \pi\pi$ phase shift δ_1^1 (recent parameterizations of δ_1^1, constrained by the Roy equations, can be found in Refs. [116,117]). The second term, $\Omega_{\rm in}$, takes into account the effect of the effective onset of inelasticity close to the $\omega\pi$ threshold via a simple polynomial of a conformally mapped variable (see Ref. [1561]). Similar types of parameterization can be used for the πK vector form factor; see, e.g., Ref. [1562], where such analytic

representations are used for combining $\tau \to K\pi\nu$ and K_{l3} data in order to derive and improve the determination of $V_{us}f_+^{K\pi}(0)$.

The $\tau \to \pi\eta\nu$ mode belongs to a category of so-called "second class current" processes, which are suppressed by isospin-breaking effects. The values of the form factors at $Q^2 = 0$ are proportional to the isospin-breaking quark mass ratio,

$$f_+^{\eta\pi}(0) = f_0^{\eta\pi}(0) = \frac{\sqrt{3}(m_d - m_u)}{4(m_s - (m_d + m_u)/2)}(1 + O(m_q)), \tag{524}$$

where the NLO chiral corrections can be found in Ref. [1563]. In the region of the $\rho(770)$ resonance, the discontinuity of the $\eta\pi$ vector form factor is dominated by the $\eta\pi \to \pi\pi$ amplitude, which is well constrained by a number of recent experiments on $\eta \to 3\pi$ decays. This information was used in Ref. [1564] to provide a quantitative estimate of the form factor (see Ref. [1565] for an update and a list of references).

Scalar form factors The Omnès phase representation is particularly useful for the scalar form factors because meson–meson interactions with $J = 0$ may contain broad resonances (like the "κ") or no resonances at all. This is the case for the $\pi^-\pi^0$ scalar form factor.

$\pi^-\pi^0$: $\pi^-\pi^0$ scattering in the S-wave corresponds to $I = 2$ isospin. Ignoring inelasticity effects in this channel we can identify the phase of the form factor with the scattering phase δ_0^2 and use the following Omnès representation for the form factor:

$$f_0^{\pi\pi}(Q^2) = \exp\left[\frac{Q^2}{\pi}\int_{4m_\pi^2}^{\infty} ds' \frac{\delta_0^2(s')}{s'(s' - Q^2)}\right]. \tag{525}$$

Parameterizations for the phase shift δ_0^2 can be found in Refs. [116,117]. Note that $f_0^{\pi\pi}$ is not particularly suppressed, but its influence on the decay width is, due to the multiplicative $M_{\pi^+}^2 - M_{\pi^0}^2$ factor. Equation (525) should provide a better estimate for $f_0^{\pi\pi}$ than that used in Ref. [1566] in their search for CP violation in the $\tau \to \pi\pi\nu$ channel. The parameter $f_0^{\pi\pi}$ induces a forward–backward asymmetry, which is visible in a small energy range close to the threshold, see Ref. [1565].

$K^-\pi^0$, $\bar{K}^0\pi^-$: The phase of the $K\pi$ scalar form factors corresponds to $K\pi$ scattering with $I = 1/2$ in the elastic region. Experimental measurements of the scattering phase shift (e.g. Ref. [1567] and references therein) have been performed. The phase representation encodes the influence of the broad $K_0^*(800)$ resonance and that of the more conventional $K_0^*(1430)$. Furthermore, the $K\pi$ scalar form factor obeys the Dashen–Weinstein chiral constraint [1568],

$$f_0^{K\pi}(m_K^2 - m_\pi^2) = \frac{F_K}{F_\pi} + O\left(\frac{m_\pi^2}{\Lambda^2}\right), \tag{526}$$

where the leading $O(m_\pi^2)$ corrective term was computed in Ref. [1569]. Results for $f_0^{K\pi}$ at $s = 0$ are available from lattice QCD (see Ref. [140]). Both constraints can be encoded in the dispersive representation. Inelastic scattering for $J = 0$ $K\pi$ was shown to remain small below the $K\eta'$ threshold and can be approximated by a two-channel T-matrix in a range suitable for τ decay. This was used in Ref. [1570] to derive the $K\pi$ scalar form factor from an Omnès matrix. This model should be valid over most of the τ decay range. At present, some evidence for $f_0^{K\pi}$ was observed at Belle [1571] below 800 MeV. Keeping track of the $\cos\beta\cos\psi$ dependence, substantial improvements can be achieved at Belle II.

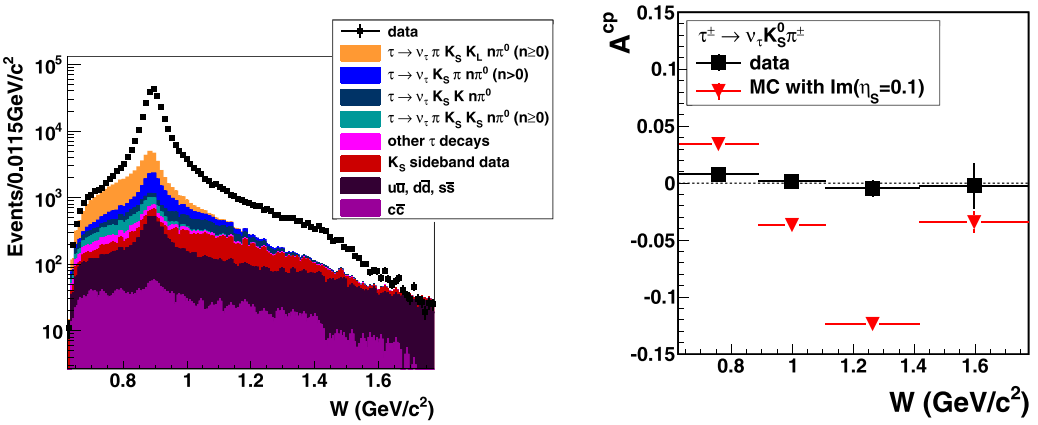

Fig. 191. Left: Invariant mass spectrum of the $K^0_S\pi^\pm$ system in $\tau \to K^0_S\pi^\pm\nu_\tau$ candidates [1574]. Right: Measured CP-violating asymmetry $A^{\rm CP}$ as a function of the $K^0_S\pi^\pm$ invariant mass W after subtraction of background (black squares) [1574]. The inverted red triangles show the expected asymmetry when $\mathrm{Im}(\eta_S) = 0.1$ (to obtain this prediction, a linear combination of Breit–Wigner shapes of the vector resonances $K^*(890)$ and $K^*(1410)$ and the scalar resonances $K^*_0(800)$ and $K^*_0(1430)$ are used [1574]). At Belle II, this CP asymmetry is expected to be improved by a factor of nearly $\sqrt{70} = 8.4$.

$\pi^-\eta$: The S-wave $\pi\eta$ scattering phase shift has not been measured but a qualitative picture emerges for its behavior around 1 GeV from Flatté-type parameterizations of a number of production processes (e.g. Ref. [1572]), while the behavior at low energy is constrained by chiral symmetry [1573]. Some progress in determining the phase shift from lattice simulations has also been achieved recently [1437]. The influence of the scalar form factor on the $\tau \to \pi\eta\nu$ branching fraction is usually estimated to be of comparable size to that of the vector form factor, or even larger, (see, e.g., Ref. [1565] and references therein). Measuring this mode with a number of energy bins would shed new light on the properties of the $\eta\pi$ interaction, as well as the quark content properties of the $a_0(980)$ scalar resonance (via the size of its coupling to the $\bar{u}d$ operator).

15.3.3. CP violation measurements with angular observables

Belle searched for CP violation, $A^{\rm CP}$, in angular observables of the mode $\tau^\pm \to K^0_S\pi^\pm\nu_\tau$ using a 699 fb^{-1} data sample [1574]. The $K^0_S\pi^\pm$ invariant mass distribution of the 3.2×10^5 $\tau^\pm \to K^0_S\pi^\pm\nu_\tau$ signal candidates is shown in Fig. 191 (left). We see clearly additional resonance structures on top of the $K^*(890)$. It is most important to first understand these resonance structures.

The measured CP asymmetry $A^{\rm CP}$ is shown in Fig. 191 (right) as a function of $K^0_S\pi^\pm$ invariant mass after correcting the known detector effects. At Belle, almost all contributions to the systematic uncertainty come from the detector bias on $A^{\rm CP}$ (see Table II in Ref. [1574]), which was evaluated using a control sample in which one tau decays into three charged pions and a neutrino, and the pions are not daughters of a K^0_S. Since this source of systematic uncertainty depends on the statistics of the control sample, it is expected that the systematic uncertainty of the Belle II analysis will follow the integrated luminosity of the data sample. Thus, with a 50 ab^{-1} data sample, we can expect around $\sqrt{70}$ times improvement for both the statistical and systematic uncertainties, i.e. $|A^{\rm CP}| < (0.4 - 2.6) \times 10^{-4}$ at 90% confidence level depending on $M_{K\pi}$ under the assumption that the central value of $|A^{\rm CP}|$ is zero. It should be emphasized that at such a high precision, the extraction of the CP parameter η_s has to be done in conjunction with the form factor determination.

Finally, we comment on the prospect of CP violation measurement with an angular analysis of the three-hadron final state. The most promising channel is $\tau \to K\pi\pi\nu$. The CP violation search can be performed by using the three observables $A_{(i)}^{\rm CP}$ $(i = 1, 2, 3)$; see Ref. [1552] for details). Note that this analysis was not done at Belle. To maximize the sensitivity of $A_{(i)}^{\rm CP}$ $(i = 1, 2, 3)$, the $M_{K\pi\pi}$, $M_{K\pi}$, and $M_{\pi\pi}$ distributions should all be measured. Similarly to the analysis of $\tau \to K_{\rm S}^0\pi\nu$, the $\tau \to \pi\pi\pi\nu$ channel can be used as a controlled sample to evaluate the detector bias by assuming that the CP violation in $\tau \to \pi\pi\pi\nu$ is much smaller than that in $\tau \to K\pi\pi\nu$. In this analysis, $\tau \to \pi\pi\pi\nu$ is also a major background since it has an almost 30 times larger branching fraction than $\tau \to K\pi\pi\nu$ and, due to the incompleteness of the particle identification, $\tau \to \pi\pi\pi\nu$ may enter into the $\tau \to K\pi\pi\nu$ sample. Since at Belle II the probability of misidentifying a π as a K will be reduced to around a half of that at Belle, we can expect a higher-purity $\tau \to K\pi\pi\nu$ sample.

15.4. Other τ measurements

15.4.1. Leptonic τ decays: Michel parameter determination

Authors: H. Aihara, D. Epifanov, J. Sasaki, N. Shimizu

In the SM, τ decays proceed via the charged weak interaction, which is described by the exchange of a $W^{\pm}$ with a pure vector coupling to only left-handed fermions. Decays of τ leptons, such as $\tau^- \to \ell^-\bar{\nu}_\ell\nu_\tau$, $\tau^- \to \ell^-\bar{\nu}_\ell\nu_\tau\gamma$, and $\tau^- \to \ell^-\ell'^+\ell'^-\bar{\nu}_\ell\nu_\tau$ $(\ell, \ell' = e, \mu)$, are of special interest as electroweak couplings in these decays can be probed without disturbance from the strong interaction. This makes them an ideal system to study the Lorentz structure of the charged weak current. Assuming left-handed neutrinos, the most general, Lorentz-invariant, derivative-free, and lepton-number-conserving four-lepton point interaction Lagrangian can be written as [1575]:

$$\mathcal{L} = \frac{4G_{\rm F}}{\sqrt{2}} \sum_{\substack{N=S,V,T \\ i,j=L,R}} g_{ij}^N \left[\bar{\Psi}_i(l)\Gamma^N\Psi_n(\nu_l)\right]\left[\bar{\Psi}_m(\nu_\tau)\Gamma_N\Psi_j(\tau)\right]; \tag{527}$$

$$\Gamma^S = 1, \quad \Gamma^V = \gamma^\mu, \quad \Gamma^T = \frac{i}{2\sqrt{2}}(\gamma^\mu\gamma^\nu - \gamma^\nu\gamma^\mu).$$

The Γ_N matrices (the γ^ν are Dirac matrices) define the properties of the two currents under a Lorentz transformation with $N = S, V, T$ for scalar, vector, and tensor interactions, respectively. The indices i and j label the right- or left-handedness (R, L) of the charged leptons. Ten non-trivial terms are characterized by ten complex coupling constants g_{ij}^N; those with g_{RR}^T and g_{LL}^T are identically zero. In the SM, the only non-zero coupling constant is $g_{LL}^V = 1$; this property is also known as the $(V - A) \otimes (V - A)$ Lorentz structure of the matrix element. As the couplings can be complex, with arbitrary overall phase, there are 19 independent parameters. The total strength is determined by the Fermi constant $G_{\rm F}$, which constrains the coupling constants to be $|g_{ij}^S| \leq 2$, $|g_{ij}^V| \leq 1$, and $|g_{ij}^T| \leq 1/\sqrt{3}$.

In leptonic τ decay, $\tau^- \to \ell^-\bar{\nu}_\ell\nu_\tau$, where neutrinos are not detected and the spin of the outgoing charged lepton is not determined, only four Michel parameters, ρ, η, ξ, and δ, are experimentally accessible. They are bilinear combinations of the g_{ij}^N coupling constants [1576] and appear in the predicted energy spectrum of the charged lepton. In the τ rest frame, neglecting radiative corrections, this spectrum is given by [914]:

$$\frac{d\Gamma(\tau^\mp)}{dx\, d\Omega_\ell} = \frac{4G_{\rm F}^2 m_\tau E_{\rm max}^4}{(2\pi)^4}\sqrt{x^2 - x_0^2}\left(x(1-x) + \frac{2}{9}\rho(4x^2 - 3x - x_0^2) + \eta x_0(1-x)\right.$$

$$\mp \frac{1}{3} P_\tau \cos\theta_\ell \xi \sqrt{x^2 - x_0^2} \left[1 - x + \frac{2}{3}\delta\left(4x - 4 + \sqrt{1 - x_0^2}\right) \right] \Bigg),$$

$$x = E_\ell / E_{\max}, \quad E_{\max} = m_\tau \left(1 + m_\ell^2/m_\tau^2\right)/2, \quad x_0 = m_\ell / E_{\max},$$

where P_τ is the τ polarization, Ω_ℓ is the solid angle of the outgoing lepton, and θ_ℓ is the angle between the τ spin and the lepton momentum. In the SM, the $(V-A)$ charged weak current is characterized by $\rho = 3/4$, $\eta = 0$, $\xi = 1$, and $\delta = 3/4$. In the radiative leptonic decay, $\tau^- \to \ell^- \bar{\nu}_\ell \nu_\tau \gamma$, three additional parameters, $\bar{\eta}$, η'', and $\xi\kappa$, can be extracted [1577]. The Michel formalism for the five-lepton τ decay, $\tau^- \to \ell^- \ell'^+ \ell'^- \bar{\nu}_\ell \nu_\tau$, can be found in Ref. [1578].

Measurement of the ξ, δ, and $\xi\kappa$ parameters requires knowledge of the τ spin direction. In experiments at e^+e^- colliders with unpolarized $e^\pm$ beams, the average polarization of a single τ is zero. However, spin–spin correlations between the τ^+ and τ^- produced in the reaction $e^+e^- \to \tau^+\tau^-$ can be exploited [1579]. The main idea of the method is to consider events where both taus decay to the selected final states. One tau decays to the signal mode while the opposite tau, which decays via $\tau^+ \to \pi^+\pi^0\bar{\nu}_\tau$, serves as a spin analyzer. We choose the $\tau^+ \to \pi^+\pi^0\bar{\nu}_\tau$ (it is characterized by the ξ_ρ parameter; in the SM $\xi_\rho = 1$) decay mode because it has the largest branching fraction as well as properly studied dynamics. To write the total differential cross section we follow the approach developed in Refs. [1580,1581]. The differential cross section is used to construct the PDF, and the Michel parameters are extracted in the unbinned maximum likelihood fit of the selected events.

Further, we describe the construction of the PDF for ordinary leptonic decay. The total differential cross section for the $\tau^- \to \ell^- \bar{\nu}_\ell \nu_\tau$, $\tau^+ \to \pi^+\pi^0\bar{\nu}_\tau$) (or, briefly, $(\ell^-;\, \rho^+)$) events in the full nine-dimensional phase space, $\frac{d\sigma}{d\vec{z}}(\vec{\Theta})$ ($\vec{\Theta} = \{1, \rho, \eta, \xi_\rho\xi, \xi_\rho\xi\delta\}$, $\vec{\Theta}_{\rm SM} = \{1, 3/4, 0, 1, 3/4\}$), is used to construct the PDF for the measurement vector $\vec{z} = \{p_\ell, \cos\theta_\ell, \phi_\ell, p_\rho, \cos\theta_\rho, \phi_\rho, m_{\pi\pi}, \cos\tilde{\theta}_\pi, \tilde{\phi}_\pi\}$. The main background processes, $(\ell^-;\, \pi^+\pi^0\pi^0)$, $(\pi^-;\, \rho^+)$, and $(\rho^-;\, \rho^+)$, with the fractions $\lambda_{3\pi}$, λ_π, and λ_ρ, respectively, are included in the PDF analytically. The remaining background with the fraction $\lambda_{\rm other}$ is described by the $\mathcal{P}_{\rm bg}^{\rm MC}(\vec{z})$ PDF, which is evaluated from the large Monte Carlo sample. The total PDF for the $(\ell^-;\, \rho^+)$ events is written as:

$$\mathcal{P}(\vec{z}) = \frac{\varepsilon(\vec{z})}{\bar{\varepsilon}} \Bigg((1 - \lambda_{3\pi} - \lambda_\pi - \lambda_\rho - \lambda_{\rm other}) \frac{S(\vec{z} \mid \vec{\Theta})}{\int \frac{\varepsilon(\vec{z})}{\bar{\varepsilon}} S(\vec{z} \mid \vec{\Theta}) d\vec{z}}$$
$$+ \lambda_{3\pi} \frac{B_{3\pi}(\vec{z} \mid \vec{\Theta})}{\int \frac{\varepsilon(\vec{z})}{\bar{\varepsilon}} B_{3\pi}(\vec{z} \mid \vec{\Theta}) d\vec{z}} + \lambda_\pi \frac{B_\pi(\vec{z})}{\int \frac{\varepsilon(\vec{z})}{\bar{\varepsilon}} B_\pi(\vec{z}) d\vec{z}} + \lambda_\rho \frac{B_\rho(\vec{z})}{\int \frac{\varepsilon(\vec{z})}{\bar{\varepsilon}} B_\rho(\vec{z}) d\vec{z}} + \lambda_{\rm other} \mathcal{P}_{\rm bg}^{\rm MC}(\vec{z}) \Bigg),$$

where $S(\vec{z} \mid \vec{\Theta})$, $B_{3\pi}(\vec{z} \mid \vec{\Theta})$, $B_\pi(\vec{z})$, and $B_\rho(\vec{z})$ are the cross sections for the $(\ell^-;\, \rho^+)$, $(\ell^-;\, \pi^+\pi^0\pi^0)$, $(\pi^-;\, \rho^+)$, and $(\rho^-;\, \rho^+)$ events, respectively; $\varepsilon(\vec{z})$ is the detection efficiency for signal events in the full phase space; and $\bar{\varepsilon} = \int \varepsilon(\vec{z}) S(\vec{z} \mid \vec{\Theta}_{\rm SM}) d\vec{z} / \int S(\vec{z} \mid \vec{\Theta}_{\rm SM}) d\vec{z}$ is an average signal detection efficiency. There are several corrections that must be incorporated into the procedure to take into account the real experimental situation. Physics corrections include electroweak higher-order corrections to the $e^+e^- \to \tau^+\tau^-$ cross section [1582,1583]. Apparatus corrections include the effect of the finite detection efficiency and resolution, the effect of the external bremsstrahlung for $(e^-;\, \rho^+)$ events, and the $e^\pm$ beam energy spread.

A study of the Michel parameters ρ, η, $\xi_\rho\xi$, and $\xi_\rho\xi\delta$ in leptonic τ decays using a 485 fb^{-1} data sample collected at Belle showed that their statistical uncertainties are already of the order of 10^{-3}; see Table 141 [1584]. Although systematic uncertainties coming from the physical and apparatus corrections as well as from the normalization are below 1%, there are still relatively large

Table 141. Statistical uncertainties of the Michel parameters ρ, η, $\xi_\rho\xi$, $\xi_\rho\xi\delta$, $\bar{\eta}$, and $\xi_\rho\xi\kappa$ in ordinary and radiative leptonic τ decays [1585] at Belle (with a 485 fb^{-1} (703 fb^{-1}) data sample for ordinary (radiative) leptonic decays).

$(\Delta\rho)_{\rm stat}$, 10^{-4}	$(\Delta\eta)_{\rm stat}$, 10^{-4}	$(\Delta\xi_\rho\xi)_{\rm stat}$, 10^{-4}	$(\Delta\xi_\rho\xi\delta)_{\rm stat}$, 10^{-4}	$(\Delta\bar{\eta})_{\rm stat}$	$(\Delta\xi_\rho\xi\kappa)_{\rm stat}$
13	62	39	25	1.5	0.4

systematic uncertainties from the experimental corrections to the detection efficiency. Currently, the largest contribution, $(1 \div 3)\%$, comes from the trigger efficiency correction. The expected statistical uncertainties of the Michel parameters at Belle II (with the total planned luminosity integral of 50 ab^{-1}) are already of the order of 10^{-4}. At Belle II the systematic uncertainties will be the dominant ones. To improve them, a high- and uniform-efficiency two-track trigger is needed.

15.4.2. Searches for second-class currents in τ decays

Authors: P. Roig, S. Eidelman

Theory Hadronic currents can be classified according to their spin, parity, and G-parity quantum numbers (J^{PG}) as [1586] first-class currents, with the quantum numbers $J^{PG} = 0^{++}$ (σ), 0^{--} (π), 1^{+-} (a_1), 1^{-+} (ρ), and second-class currents (SCC), which have $J^{PG} = 0^{+-}$ (a_0), 0^{-+} (η), 1^{++} (b_1), 1^{--} (ω), and are yet to be discovered. The mesons in brackets share J^{PG} with the preceding current, yielding easily the simplest meson systems for a given class current.

G-parity combines charge and isospin symmetries. The latter is broken both by $m_u \neq m_d$ and $q_u \neq q_d$. Since these violations are small, G-parity is a good approximate symmetry of the strong interactions. Thus, within the SM and for definite J^P, hadron systems with G-parity corresponding to the weak left-handed (light-)quark current are allowed and easily produced. Those with the "wrong" G-parity are suppressed and have SCC quantum numbers.

Within the SM, a small violation of G-parity is induced by isospin breaking, giving rise to *induced* SCCs. In addition to this suppressed effect one may have *genuine* weak SCCs from unknown new physics, which may show up either in rates above the expectations coming from isospin violation or distinguished from the calculable SM background.

In principle, SCCs could also be discovered in nuclear processes or in $\Sigma^\pm$ semi-leptonic decays [1586]. However, both face the challenge of separating possible violations of CVC from SCC effects [1587,1588].

The discovery of either of the decays $\tau^- \to b_1^- \nu_\tau$ or $\tau^- \to a_0^- \nu_\tau$ would be an unambiguous signature of SCCs [1589]. Since b_1 decays dominantly to $\omega\pi$ and this final state can also be produced via ordinary first-class current at a rate of $\sim$2%, angular analyses of the pions is needed to disentangle both types of currents. The resulting upper limits on SCCs are Br $\sim 1.4 \cdot 10^{-4}$ [1590], while Ref. [1591] roughly estimates Br $\sim 2.5 \cdot 10^{-5}$ based on spin-one meson dominance.

SCCs can also be searched for through $\tau^- \to \pi^-\eta\nu_\tau$ decays (not necessarily proceeding through a_0 exchange). In the SM, their suppressed amplitude can be understood in terms of the π^0–η mixing parameter $\epsilon_{\pi\eta}$ given by the value of Eq. (524), neglecting sub-leading m_q corrections. Since $\epsilon_{\pi\eta} \sim 10^{-2}$, Br$(\tau^- \to \pi^-\eta\nu_\tau) \sim 10^{-5}$ is expected in the SM [1592].

Both form factors will contribute sizeably to the $\tau^- \to \pi^-\eta\nu_\tau$ decays ($m_\eta^2 >> m_\pi^2$). While their low-energy behavior is determined by chiral perturbation theory [1563], resonance dynamics is needed to describe them appropriately throughout the available phase space. Recently, the vector

form factor contribution was estimated using $\eta \to 3\pi$ decay data as Br $\sim 0.36 \cdot 10^{-5}$ [1564]. This was done using a dispersive approach [1565]. According to Ref. [1593], the $\pi^-\eta$ vector form factor can be related to the very precisely measured 2π vector form factor [1594], which results in a negligible error in the corresponding prediction, Br $= (0.26 \pm 0.02) \cdot 10^{-5}$ [1593], in agreement with $[0.1, 0.4] \cdot 10^{-5}$ [1565].

The scalar form factor contribution is more involved theoretically. A phase-dispersive representation of this form factor is supplemented with a sum rule constraint for the inelastic region and a realistic model for the phase shift [1565]. The corresponding estimate for this contribution is $[0.1, 0.6] \cdot 10^{-5}$, versus $\sim 1.0 \cdot 10^{-5}$ [1564]. A coupled channel dispersive analysis of the $\pi\eta$–$K\bar{K}$–$\pi\eta'$ channels within U(3) chiral perturbation theory with resonances [1595] determines $(1.41 \pm 0.09) \cdot 10^{-5}$ [1593]. Recent COMPASS data on the partial waves of the $\pi\eta^{(\prime)}$ system [1596] will help to check this uncertainty.

Br$(\tau^- \to \pi^-\eta'\nu_\tau) \in [0.2, 1.4] \cdot 10^{-6}$ [1597], Br $\in [10^{-7}, 10^{-6}]$ [1593] suggest scalar form factor dominance with an associated order-of-magnitude error in Br. Although BaBar fixed the impressive upper bound Br $< 4.0 \cdot 10^{-6}$ on these decays, the inaccuracy of the theory predictions does not allow the conclusion if the first measurement of SCCs corresponds to $\tau^- \to \pi^-\eta'\nu_\tau$ decays.

With Br$(\tau^- \to \pi^-\eta\nu_\tau) \sim 1 \cdot 10^{-5}$, SCCs were not measured by BaBar or Belle because of the difficulty in controlling the associated backgrounds [2]. BaBar was able to set the upper limit Br $< 9.9 \cdot 10^{-5}$ [1598], while Belle determined the bound Br $< 7.3 \cdot 10^{-5}$ [1599]. Scaling the previous upper limits on both Br$(\tau^- \to \pi^-\eta^{(\prime)}\nu_\tau)$ according to Belle II statistics should warrant the discovery of SCCs at Belle II. New physics can manifest through abnormally large branching fractions in either of them, but only $\tau^- \to \pi^-\eta\nu_\tau$ is predicted with enough accuracy to allow setting competitive restrictions [1600] on a possible charged Higgs exchange if the Br is known with at least 20% accuracy [1565].

Experimental status The most frequently discussed SCC decay mode is $\tau^- \to \eta\pi^-\nu_\tau$, for which theory predicts the branching ratio to be in the range 10^{-5}–10^{-6}. The smallness of the branching ratio makes its search very sensitive to various background processes, such as that from $\tau^- \to \eta\pi^-\pi^0\nu_\tau$, which has a branching fraction $\sim 10^{-3}$, so that a missing π^0 mimics completely the decay looked for and thus produces background that is very difficult to suppress. To understand such backgrounds better, Belle performed a high-statistics study of various exclusive decays that include an η meson [1601].

In the BaBar search that used the $\eta \to \pi^+\pi^-\pi^0$ decay mode the abovementioned background dominates; however, other processes ($q\bar{q}+c\bar{c}$, $\eta K^0\pi^-\nu_\tau$, $\eta K^-\nu_\tau$) also give significant contributions, which in total are even larger than the first one. As a result, BaBar, with its much larger data sample than CLEO, set an upper limit of $<9.9 \times 10^{-5}$ [1598], only slightly improving on the upper limit of $<1.4 \times 10^{-4}$ from CLEO [1602], which used both $\eta \to \pi^+\pi^-\pi^0$ and $\eta \to \gamma\gamma$ decay modes. The latter decay mode looks more promising for future searches, although serious backgrounds are still expected from $\tau^- \to \eta\pi^-\pi^0\nu_\tau$ and $\tau^- \to \pi^-\pi^0\nu_\tau$.

For the process $\tau^- \to \eta'\pi^-\nu_\tau$, theory predicts the branching ratio at the level of 10^{-6} [1563]. The background situation is better than for the previous decay and BaBar set an upper limit of $<7.2 \times 10^{-6}$ [1603], improving by an order of magnitude that of $<7.4 \times 10^{-5}$ from CLEO [1604].

The decay $\tau^- \to \omega\pi^-\nu_\tau$ is expected to proceed through the hadronic vector current mediated by the ρ, ρ', ρ'', and higher excitations. If, however, second-class currents violating G-parity contribute to this decay, it can also proceed through a hadronic axial vector current mediated, e.g., by the $b_1(1235)$ resonance. The difference in spin parity assignments for each of these states is reflected in

Table 142. Summary of τ lepton mass measurements.

Group	$\sqrt{s}$, GeV	N_{ev}	m_τ, MeV
DELCO, 1978	3.1–7.4	692	1783^{+3}_{-4}
ARGUS, 1992	9.4–10.6	11k	$1776.3 \pm 2.4 \pm 1.4$
BES, 1996	3.54–3.57	65	$1776.96^{+0.18+0.25}_{-0.21-0.17}$
CLEO, 1997	10.6	98.5k	$1778.2 \pm 0.8 \pm 1.2$
OPAL, 2000	∼90	13.3k	$1775.1 \pm 1.6 \pm 1.0$
KEDR, 2007	3.54–3.78	81	$1776.81^{+0.25}_{-0.23} \pm 0.15$
Belle, 2007	10.6	∼400k	$1776.61 \pm 0.13 \pm 0.35$
BaBar, 2009	10.6	∼682k	$1776.68 \pm 0.12 \pm 0.41$
BESIII, 2015	3.54–3.60	1171	$1776.91 \pm 0.12^{+0.10}_{-0.13}$
PDG, 2016	—	—	1776.86 ± 0.12

different polarizations of the ω spin and hence in different expected angular distributions of $cos\chi$. The angle χ is defined as the angle between the normal to the ω decay plane and the direction of the fourth pion measured in the ω rest frame, and l is the orbital angular momentum of the $\omega\pi$ system. The expected forms of the $cos\chi$ distribution are listed in Ref. [1605].

15.4.3. Measurement of the τ lepton mass

Author: S. Eidelman

Mass is one of the most fundamental parameters of any particle and thus should be measured as accurately as possible. For the τ lepton this is particularly important since its width is proportional to the mass to the fifth power, so that any tests of the Standard Model, e.g. of leptonic universality, crucially depend on the mass value and its accuracy [1606].

Two methods of τ lepton mass measurement exist. In the threshold method, one studies the energy dependence of the $\tau^+\tau^-$ production cross section in the energy range close to threshold: $\sqrt{s} - 2m_\tau \leq 200$ MeV. One can reach very high accuracy even with a limited data sample—the current most precise result on the τ lepton mass from BESIII was obtained with only about 1000 events [1607]. Measurements of the τ lepton mass at higher accuracy with this method are limited by statistics, and the systematic uncertainties are due to the energy scale calibration and knowledge of the beam energy spread.

The B factories, on the contrary, can collect much larger data samples and have systematic uncertainties that differ from the threshold method. They are based on the so-called pseudo-mass determination in which mass is estimated from the edge of the spectrum of invariant mass based on four-momenta of the detected hadrons—products of τ decay [1608]. This method allows for a separate determination of the mass for positive and negative τ leptons to be performed, thus providing a test of CPT invariance first realized by the OPAL Collaboration [1609]. Table 142 summarises the current status of τ lepton mass measurements.

In the Belle measurement the three most important sources of systematic uncertainty were the beam energy and tracking system calibration (0.26 MeV), the parameterization of the spectrum edge (0.18 MeV), and the limited MC statistics (0.14 MeV) [1610]. One expects that the two latter values will be greatly improved upon: the ad hoc parameterization of the spectrum edge will be replaced with a theoretical spectrum directly following from the high-statistics measurement of the τ decay

into the corresponding final state (usually $\tau^- \to \pi^-\pi^+\pi^-\nu_\tau$), which will also be used for the MC generators. The tracking system calibration should benefit from the larger dataset of Belle II, whereas beam energy determination will improve following the progress achieved in the B meson mass and $\Upsilon(4S)$ width measurements [88]. Very optimistically, one can hope to reach a level of (0.15–0.20) MeV for the total uncertainty on the mass, making new τ lepton mass measurements an attractive independent test of threshold measurements and the SM in general.

15.4.4. Electric dipole moment of the τ

Authors: K. Hayasaka, E. Kou

The current limit for the τ electric dipole moment (EDM) (d_τ) is several orders of magnitude less restrictive than that for the electron, muon, or neutron. The difficulty of the τ EDM measurement comes from its short lifetime. Therefore, the τ EDM cannot be measured in an electrostatic field. At an e^+e^- collider, however, the τ EDM can be measured by using the correlation of decay product momenta in the process $e^+e^- \to \tau^+\tau^-$.

The matrix element for the process $e^+e^- \to \tau^+\tau^-$ is given by the sum of the SM term, $\mathcal{M}^2_{\rm SM}$, the EDM term, $|d_\tau|^2\mathcal{M}^2_{d^2}$, and the interference between them:

$$\mathcal{M}^2 = \mathcal{M}^2_{\rm SM} + {\rm Re}(d_\tau)\mathcal{M}^2_{\rm Re} + {\rm Im}(d_\tau)\mathcal{M}^2_{\rm Im} + |d_\tau|^2\mathcal{M}^2_{d^2}, \tag{528}$$

where ${\rm Re}(d_\tau)$ (${\rm Im}(d_\tau)$) is the real (imaginary) part of the EDM. These interference terms $\mathcal{M}^2_{\rm Re/Im}$ contain the following combinations of spin–momentum correlations:

$$\begin{aligned} \mathcal{M}^2_{\rm Re} &\propto (\boldsymbol{S}_+ \times \boldsymbol{S}_-)\cdot\hat{\boldsymbol{k}}, \quad (\boldsymbol{S}_+ \times \boldsymbol{S}_-)\cdot\hat{\boldsymbol{p}}, \\ \mathcal{M}^2_{\rm Im} &\propto (\boldsymbol{S}_+ - \boldsymbol{S}_-)\cdot\hat{\boldsymbol{k}}, \quad (\boldsymbol{S}_+ - \boldsymbol{S}_-)\cdot\hat{\boldsymbol{p}}, \end{aligned} \tag{529}$$

where $\boldsymbol{S}_\pm$ is a $\tau^\pm$ spin vector, and $\hat{\boldsymbol{k}}$ and $\hat{\boldsymbol{p}}$ are the unit vectors of the τ^- and e^- momenta in the CM system, respectively. These terms are CP odd since they change sign under a CP transformation.

One could evaluate the value of the matrix elements if the values of $\boldsymbol{S}_\pm$ and $\hat{\boldsymbol{k}}$ could be measured on an event-by-event basis from the τ decay products. Although one cannot know them completely due to missing neutrinos from τ decays, one can obtain the most probable values of $\boldsymbol{S}_\pm$ and $\hat{\boldsymbol{k}}$ by calculating approximate averages from measurements of the momenta of τ decay products. In the Beller analysis, the method of optimal observables [1611] is employed. In this method, the observables $\mathcal{O}_{\rm Re}$ and $\mathcal{O}_{\rm Im}$,

$$\mathcal{O}_{\rm Re} = \frac{\mathcal{M}^2_{\rm Re}}{\mathcal{M}^2_{\rm SM}}, \quad \mathcal{O}_{\rm Im} = \frac{\mathcal{M}^2_{\rm Im}}{\mathcal{M}^2_{\rm SM}}, \tag{530}$$

are evaluated using the most probable values of $\boldsymbol{S}_\pm$ and $\hat{\boldsymbol{k}}$. The means of $\mathcal{O}_{\rm Re}$, $\mathcal{O}_{\rm Im}$ are proportional to the EDM value and have maximal sensitivity. In order to obtain the maximal sensitivity, we measure as many modes as possible. For example, in the Belle analysis with a 29.5 fb^{-1} data sample [1612], the following eight modes are used: $\tau^+\tau^- \to (e\nu_e\nu_\tau)(\mu\nu_\mu\nu_\tau)$, $(e\nu_e\nu_\tau)(\pi\nu_\tau)$, $(\mu\nu_\mu\nu_\tau)(\pi\nu_\tau)$, $(e\nu_e\nu_\tau)(\rho\nu_\tau)$, $(\mu\nu_\mu\nu_\tau)(\rho\nu_\tau)$, $(\pi\nu_\tau)(\pi\nu_\tau)$, $(\pi\nu_\tau)(\rho\nu_\tau)$, and $(\rho\nu_\tau)(\rho\nu_\tau)$.

The current mean values for ${\rm Re}(d_\tau)$ and ${\rm Im}(d_\tau)$ have been obtained by taking the weighted mean of the eight modes to be

$${\rm Re}(d_\tau) = (1.15 \pm 1.70) \times 10^{-17}\, e{\rm cm}, \tag{531}$$

$$\mathrm{Im}(d_\tau) = (-0.83 \pm 0.86) \times 10^{-17}\, e\mathrm{cm}. \tag{532}$$

The 95% CL intervals are

$$-2.2 \times 10^{-17} < \mathrm{Re}(d_\tau) < 4.5 \times 10^{-17}\, e\mathrm{cm}, \tag{533}$$

$$-2.5 \times 10^{-17} < \mathrm{Im}(d_\tau) < 0.8 \times 10^{-17}\, e\mathrm{cm}. \tag{534}$$

These limits are ten times more restrictive than previous experiments.

Now let us discuss the prospects for EDM and $g-2$ searches in τ decays at Belle II. In the τ EDM analysis, the statistical errors for $\mathrm{Re}(d_\tau)$ and $\mathrm{Im}(d_\tau)$ are expected to be proportional to the inverse of the square root of the integrated luminosity, while the systematic error strongly depends on the understanding of MC and data samples since the dependence of the optimal observable for d_τ is evaluated with MC samples. In particular, the understanding of low-momentum tracking is a large and important systematic uncertainty. Trigger, track-finding, and PID efficiency systematics are, while slightly smaller, strongly correlated, demanding a nuanced approach to their evaluation. Their uncertainties are mostly data driven, and will continue to improve with more data. Therefore, we expect approximately a 40 times gain from the current result, i.e. $|\mathrm{Re}, \mathrm{Im}(d_\tau)| < 10^{-18}$–$10^{-19}$.

The tau $g-2$ can be evaluated in a way similar to that of the tau EDM, by giving $\frac{1}{2}\bar{\psi}\sigma^{\mu\nu}\psi\frac{ea_\tau}{2m_\tau}F_{\mu\nu}$ as a $g-2$ interaction term instead of $-\frac{1}{2}\bar{\psi}\sigma^{\mu\nu}\psi\frac{e\tilde{a}_\tau}{2m_\tau}\tilde{F}_{\mu\nu}$ in the case of tau EDM into the Lagrangian. However, it is expected that the sensitivity to tau $g-2$ will be worse than that of the tau EDM.

15.4.5. Inclusive τ decays: V_{us} and α_s

Authors: M. Jamin, K. Maltman, E. Passemar, A. Pich

Hadronic τ decays constitute a very interesting tool for studying QCD and performing precise extractions of some of the fundamental SM parameters. The most famous example is the determination of $\alpha_s(m_\tau)$, the strong coupling constant at the tau mass, and the test of the running of α_s from the tau mass m_τ to the Z mass M_Z. Another example is the determination of the CKM matrix element V_{us} and the test of the unitarity of the first row of the CKM matrix. This was rendered possible by the measurement of not only the branching fractions of $\tau \to$ hadrons, see Fig. 192, but also the experimental differential distributions with respect to the invariant squared mass of the hadronic system, which generate information on the so-called spectral functions. The inclusive isovector, vector (V), and axial vector (A) spectral functions, and, with lower statistics, the inclusive flavor *us* V+A spectral function sum, have been measured by ALEPH [1613–1616] and OPAL [1617,1618], but not yet at the *B* factories. The ALEPH isovector distribution results are shown in Fig. 192. These results have triggered intense theoretical activities.

The central observables for inclusive hadronic τ decays are the so-called R_τ ratio and its differential version, dR_τ/ds, with s the invariant mass squared of the hadronic system. R_τ is defined by

$$R_\tau = \frac{\Gamma(\tau^- \to \nu_\tau\ \mathrm{hadrons}^-\,(\gamma))}{\Gamma(\tau^- \to \nu_\tau e^- \bar{\nu}_e\,(\gamma))}. \tag{535}$$

The central theoretical object is the appropriate two-point correlation function of the color-singlet vector $V^\mu_{ij} \equiv \bar{\psi}_j\gamma^\mu\psi_i$ or axial vector $A^\mu_{ij} \equiv \bar{\psi}_j\gamma^\mu\gamma_5\psi_i$ quark currents with $i,j = u,d,s$:

$$\Pi^{\mu\nu}_{ij}(q) = i\int d^4x\, e^{iqx}\langle 0|T(\mathcal{J}^\mu_{ij}(x)\mathcal{J}^\nu_{ij}(0)^\dagger)|0\rangle, \tag{536}$$

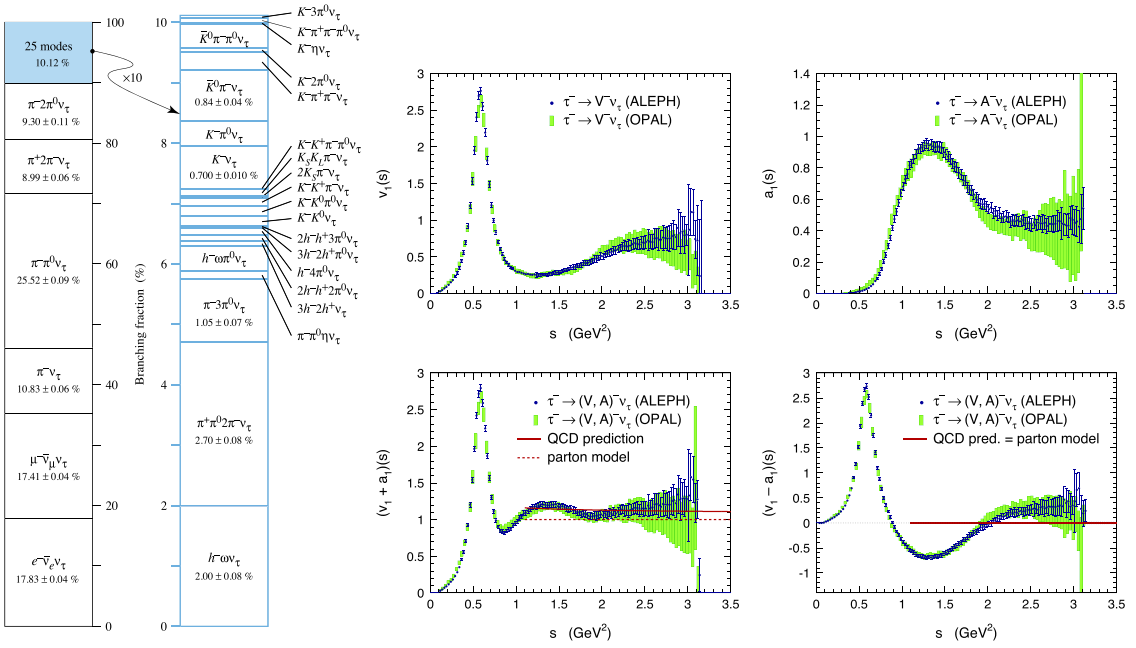

Fig. 192. Left: Measured tau branching fractions from the PDG [914]. Right: Spectral functions measured by ALEPH (blue data points) [1613] and OPAL (green rectangular blocks) [1617] in the vector (upper left) and axial (upper right) non-strange channels. The lower plots show the sum (left) and difference (right) of the vector and axial spectral functions, together with the perturbative QCD predictions (continuous red lines). Figures taken from Ref. [1614]. A recent update for the ALEPH collaboration has been given in Ref. [1615].

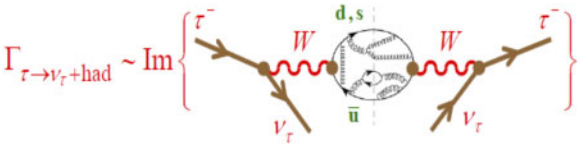

Fig. 193. Optical theorem. Figure taken from Ref. [1619].

with the current $\mathcal{J} = V, A$. The correlator has the Lorentz decomposition

$$\Pi^{\mu\nu}_{ij,\mathcal{J}}(q) = (-g^{\mu\nu}q^2 + q^\mu q^\nu)\Pi^{(1)}_{ij,\mathcal{J}} + q^\mu q^\nu \Pi^{(0)}_{ij,\mathcal{J}}, \tag{537}$$

with $\Pi^{(0)}_{ij,\mathcal{J}}$ the longitudinal component and $\Pi^{(1)}_{ij,\mathcal{J}}$ the transverse component in the hadronic rest frame. Using the optical theorem, the width for the decay to hadrons mediated by the flavor ij V or A current can be related to the imaginary part of the corresponding correlator, as shown schematically in Fig. 193.

Explicitly, in the SM one has [1579]

$$R_\tau = 12\pi S_{\text{EW}} \int_0^{m_\tau^2} \frac{ds}{m_\tau^2}\left(1 - \frac{s}{m_\tau^2}\right)^2 \left[\left(1 + 2\frac{s}{m_\tau^2}\right)\text{Im}\,\Pi^{(1)}(s) + \text{Im}\,\Pi^{(0)}(s)\right], \tag{538}$$

where $S_{\text{EW}} = 1.0201 \pm 0.0003$ [1620] is the short-distance electroweak correction. The appropriate combination of correlators entering this equation is

$$\Pi^{(J)}(s) = |V_{ud}|^2 \left(\Pi^{(J)}_{ud,V}(s) + \Pi^{(J)}_{ud,A}(s)\right) + |V_{us}|^2 \left(\Pi^{(J)}_{us,V}(s) + \Pi^{(J)}_{us,A}(s)\right). \tag{539}$$

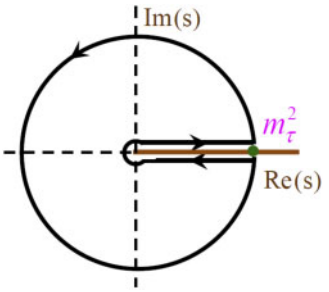

Fig. 194. Integration contour in the complex s plane, used to obtain Eq. (541). Figure taken from Ref. [1619].

We can separate the inclusive contributions associated with specific quark currents as follows:

$$R_\tau = R_{\tau,V} + R_{\tau,A} + R_{\tau,S}, \tag{540}$$

where $R_{\tau,V}$ and $R_{\tau,A}$ correspond to the first two terms in Eq. (539), while $R_{\tau,S}$ contains the remaining Cabibbo-suppressed contributions. Non-strange vector and axial vector hadronic τ decays can be distinguished experimentally, for the dominant n-pion decay modes, by counting the number of pions, with vector decays ($R_{\tau,V}$) producing an even number and axial vector decays ($R_{\tau,A}$) an odd number. Strange decays ($R_{\tau,S}$) are identified by the presence of an odd number of kaons in the final state. In principle we need to calculate the correlator in Eq. (538) from $s = 0$ to m_τ^2. Unfortunately this is an energy region where QCD is non-perturbative, displaying clear resonances, as can been seen in Fig. 192, and a calculation is at present not possible. Nevertheless, the integral itself can be calculated systematically by exploiting the analytic properties of the correlators $\Pi^{(0+1)}(s)$ and $s\Pi^{(0)}(s)$, which are analytic functions of s except along the positive real s axis, where their imaginary parts have discontinuities. Using the closed contour in Fig. 194, R_τ can then be expressed as a contour integral in the complex s plane running counterclockwise around the circle $|s| = m_\tau^2$ [1621–1623]:

$$R_\tau = 6\pi i S_{\rm EW} \oint_{|s|=m_\tau^2} \frac{ds}{m_\tau^2}\left(1-\frac{s}{m_\tau^2}\right)^2\left[\left(1+2\frac{s}{m_\tau^2}\right)\Pi^{(0+1)}(s) - 2\frac{s}{m_\tau^2}\Pi^{(0)}(s)\right]. \tag{541}$$

The advantage of writing R_τ using Eq. (541) rather than Eq. (538) is that we are at sufficiently high energy on the circle ($|s| = m_\tau^2$) that we can use operator product expansion (OPE) to calculate the correlator on the contour. OPE relates the QCD quark–gluon dynamics to the inclusive hadron distributions actually observed in hadronic tau decays. This is only justified for integrated quantities such as Eq. (541) (global quark–hadron duality). Local violations of quark–hadron duality can be expected from the integration region near the real axis, where the OPE is not valid. They are fortunately reduced by the presence of the kinematic factor $\left(1-\frac{s}{m_\tau^2}\right)^2$ which provides a double zero at $s = m_\tau^2$, suppressing the contribution from the region near the branch cut. Whether this suppression is sufficient to make duality-violating contributions negligible is the subject of intense theoretical debate; see, for instance, Ref. [1624].

The short-distance OPE can be used to organize the perturbative and non-perturbative contributions to the correlators into a systematic expansion in powers of $1/s$ [1625],

$$\Pi^{(J)}(s) = \sum_{D=2n}\sum_{\dim\mathcal{O}=D}\frac{C^{(J)}(s,\mu)\langle\mathcal{O}(\mu)\rangle}{(-s)^{D/2}}, \tag{542}$$

where the inner sum is over local gauge-invariant scalar operators of dimension $D = 0, 2, 4, \ldots$ The parameter μ is an arbitrary factorization scale, which separates long-distance non-perturbative

effects, which are absorbed into the vacuum matrix elements $\langle \mathcal{O}(\mu) \rangle$, from short-distance effects, which are included in the Wilson coefficients $C^{(J)}(s, \mu)$. Inserting $\Pi^{(J)}(s)$ from Eq. (542) into the contour integral representation of R_τ in Eq. (541), we obtain:

$$R_{\tau,V/A} = \frac{N_c}{2} |V_{ud}|^2 S_{\rm EW} \left(1 + \delta_P + \sum_{D=2,4,\ldots} \delta^{(D)}_{ud,V/A} \right),$$
$$R_{\tau,S} = N_c |V_{us}|^2 S_{\rm EW} \left(1 + \delta_P + \sum_{D=2,4,\ldots} \delta^{(D)}_{us} \right), \tag{543}$$

where $\delta^{(D)} = (\delta^{(D)}_V + \delta^{(D)}_A)/2$ is the average of the vector and axial vector corrections, and $N_C = 3$ is the number of colors. We have several contributions:

- $\delta_P \equiv \delta^{(D=0)}$: this term is the purely perturbative QCD correction, neglecting quark masses, which is the same for all the components of R_τ. This contribution is numerically dominant. It has been calculated up to $\mathcal{O}(\alpha_s^4)$ [1626]. The main uncertainties for this part come from the treatment of higher-order corrections, through the use of different renormalization group improvement prescriptions in the integration [1627–1630]. Its evaluation is subject to intense theoretical discussions [1624].
- $\delta^{(2)}$: this term represents the perturbative mass corrections. It is negligible for the non-strange part, where the leading contributions are proportional to $m^2_{u,d}$, but not for $R_{\tau,S}$, which has leading $D = 2$ contributions proportional to m^2_s [1631].
- $\delta^{(D\geq 4)}$: these are the non-perturbative contributions which involve $D = 4$ terms proportional to the gluon and quark condensates, and yet-higher-dimension condensate terms. We do not know in general how to calculate the non-perturbative condensates, but can attempt to fit them to data using s_0-dependent weighted integrals (moments) of the measured invariant mass distribution, involving alternate (typically polynomial) weights, $w(s/s_0)$. These moments, denoted $R^w_{\tau,V/A}(s_0)$ and $R^w_{\tau,S}(s_0)$, are the w-reweighted analogs of the kinematically weighted integrals $R_{\tau,V/A}(s_0)$ and $R_{\tau,S}(s_0)$ which correspond to a generalization of R_τ in Eq. (538). $R_\tau(s_0)$ is obtained by restricting the integral in Eq. (538) to $0 < s < s_0$ for any $s_0 \leq m^2_\tau$ and reweighting the kinematic prefactors. $R_\tau(s_0)$ has a contour integral representation analogous to that of R_τ, obtained by replacing in Eq. (541) the contour $|s| = m^2_\tau$ with $|s| = s_0$ and substituting m^2_τ by s_0 in the kinematic prefactors.

α_s determination By comparing the theoretical prediction of $R_{\tau,V+A}$, Eq. (543), in the non-strange sector to the measured τ branching fractions, as well as its moments $R^w_{\tau,V+A}(s_0)$, one can determine α_s [1632,1633]. The determination of α_s from these finite-energy sum rule (FESR) analyses of inclusive non-strange hadronic τ decay data [1623] has the lowest scale amongst the various current precision determinations and hence provides the strongest test of the running predicted by QCD. In addition, as a result of the decrease in relative error generated by running to higher scales, the τ decay result provides the second most precise determination at the Z scale.[60] The general situation for the determination of α_s remains somewhat unsettled, with determinations from shape observables, for example, lying significantly lower than those from τ decay and the lattice. Improvements of the

[60] For an overview of the various α_s determinations, see the PDG QCD review section at http://pdg.lbl.gov/2016/reviews/rpp2016-rev-qcd.pdf.

current situation are required to take advantage of the precision determinations of Higgs branching fractions anticipated at a future ILC in searching for BSM physics [1634].

Because of the relatively low τ mass scale, non-perturbative effects are not totally negligible in the τ-based α_s analysis. Moreover, even if one considers the inclusive non-strange experimental distribution, which sums vector (V) and axial vector (A) channel contributions and reduces the oscillatory behavior of the spectral distribution, one would like to estimate the uncertainty induced by duality violations in the upper part of the decay distribution. This necessitates some modeling of duality-violating (DV) contributions [1633,1635], even for the so-called pinched weights used in the FESR analyses, which suppress the relative role of such DV contributions. The ability to test and constrain this modeling, and hence to obtain sensible estimates of systematic errors associated with the presence of residual DV contributions, is currently limited by the size of the errors in the ALEPH differential distributions [1615] in the region above $s \sim 2\,\mathrm{GeV}^2$. In the V channel, it would be very useful to take advantage of the >1000 increase in statistics of the B factories relative to ALEPH and OPAL to reduce the errors on the differential distributions for the 4π exclusive modes, which dominate the V spectral function in this region. Improvements of the $\tau \to 4\pi\nu_\tau$ results are also motivated by the discrepancy remaining between expectations based on the ALEPH $\tau \to 4\pi\nu_\tau$ distributions and recent SND and BaBar $e^+e^- \to \pi^+\pi^-\pi^0\pi^0$ cross section results [1636,1637]. In the longer term, improved B factory determinations of the fully inclusive ud V and A spectral distributions are also highly desirable for improving the determination of α_s.

V_{us} determination Comparing the strange $|\Delta S| = 1$ and non-strange $|\Delta S| = 0$ tau decay widths gives the possibility to determine the CKM matrix element V_{us}. A determination of V_{us} using hadronic τ decay data is of interest both for providing an additional independent determination in the scenario where BSM contributions are negligible and in the context of the recently observed discrepancy between experimental results and SM expectations for the B decay ratios $R(D)$ and $R(D^*)$, which suggest the possibility of BSM contributions coupled more strongly to the third generation [1638].

If quark masses are neglected, or in the SU(3) limit, the experimental ratio of the strange to non-strange decay widths provides a direct measurement of $|V_{us}/V_{ud}|^2$. Away from this limit, one needs to take into account the small SU(3)-breaking contributions induced by the strange quark mass.

The original idea for extracting $|V_{us}|$ using hadronic τ decay data [1639,1640] involved the construction of the flavor-breaking (FB) combination δR_τ, defined by

$$\delta R_\tau \equiv \frac{R_{\tau,V+A}}{|V_{ud}|^2} - \frac{R_{\tau,S}}{|V_{us}|^2}, \tag{544}$$

where $R_{\tau,V+A}$ and $R_{\tau,S}$ are given in Eq. (540). In the SU(3) limit, $\delta R_\tau = 0$. The idea was to solve Eq. (544) for $|V_{us}|$, using the contour integral representation of the left-hand side, and, on the right-hand side, external input for $|V_{ud}|$ [1641] and experimental input for $R_{\tau,V+A}$ and $R_{\tau,S}$ [1639,1640, 1642–1652]. The result is

$$|V_{us}| = \left(\frac{R_{\tau,S}}{\frac{R_{\tau,V+A}}{|V_{ud}|^2} - \delta R_{\tau,th}} \right)^{1/2}. \tag{545}$$

This expression represents the conventional implementation of the flavor-breaking, inclusive finite-energy sum rule (FESR) approach to determining $|V_{us}|$ from inclusive hadronic τ decay data [1639, 1640].

The FESR approach can be formulated more generally using an arbitrary polynomial weight, w, and the analogs, $R^w_{\tau,V+A}(s_0)$ and $R^w_{\tau,S}(s_0)$, of $R_{\tau,V+A}$ and $R_{\tau,S}$ obtained by reweighting using the weight w rather than the SM kinematic weight, $w_\tau \equiv w(s/m_\tau^2)$, and integrating up to any kinematically allowed value, $s = s_0 \leq m_\tau^2$, rather than all the way to $s = m_\tau^2$. Generalized versions, $\delta R^w_\tau(s_0)$, of δR_τ, can then be constructed and more general w- and s_0-dependent analogs of Eq. (545) obtained.

The conventional implementation of this general FB, inclusive FESR approach, represented by Eq. (545) [1639,1640], employs, in this language, $s_0 = m_\tau^2$ and unreweighted versions of the experimental spectral integrals (corresponding to the choice $w = w_\tau$). With these choices, the spectral integrals entering the FESR are fixed by the inclusive non-strange and strange hadronic branching fractions. The cost of this experimental simplification is the presence, in the corresponding w_τ-weighted OPE integral, of in-general-unsuppressed dimension $D = 6$ and 8 OPE contributions whose values are not known from external sources. Past analyses dealt with this problem by using the crude vacuum saturation approximation (VSA) for the $D = 6$ contribution and neglecting $D = 8$ contributions on the grounds that the $D = 6$ VSA estimate was small. The result of these analyses with new inputs on branching ratios from B factories is a value of V_{us} more than $3\,\sigma$ below that implied by three-family unitarity[61] and the super-allowed nuclear β decay result for V_{ud} [1641]. This is mainly due to the fact that the branching ratios measured by BaBar and Belle are smaller than previous world averages, which translates into smaller results for $R_{\tau,S}$ and $|V_{us}|$. Replacing the three largest branching ratio results, $\mathrm{Br}\left(\tau^- \to \nu_\tau \mathrm{K}^-\right)$, $\mathrm{Br}\left(\tau^- \to \nu_\tau \bar{\mathrm{K}}^0 \pi^-\right)$, and $\mathrm{Br}\left(\tau^- \to \nu_\tau \mathrm{K}^- \pi^0\right)$ by information from leptonic kaon decays ($K^- \to \mu^- \bar{\nu}_\mu$) and the combination of the measured spectra in $\tau^- \to \nu_\tau (K\pi)^-$ decays with $K_{\ell 3}$ ($K \to \pi \ell \bar{\nu}_\ell$) data one gets a result for $|V_{us}|$ in better agreement with CKM unitarity; see Ref. [1653].

The V_{us} value, however, can also be obtained from FESRs with $s_0 < m_\tau^2$ and weights, w, other than w_τ. Varying s_0 and w, one finds a highly significant unphysical s_0 and w dependence [1654–1657]. These are eliminated when not just V_{us} but also the higher-dimension $D = 6$ and 8 OPE contributions are fitted to the data [1657]. Lattice data can also be used to obtain complementary information on the relevant OPE contributions [1657]. On the experimental side, with spectral integrals required over a range of s_0, inclusive branching fraction input no longer suffices; the full differential distributions are needed.

At present, the total V_{us} error is strongly dominated by the uncertainties in the weighted flavor *us* spectral integrals. Contributions to these errors from the exclusive $K\pi$ and $K\pi\pi$ modes studied by BaBar and Belle are at present dominated by uncertainties on the exclusive branching fractions which multiply the unit-normalized experimental distributions. Significantly reduced V_{us} errors should thus be possible through improvements of the low-multiplicity strange mode branching fractions. Thus, experimental efforts at Belle II are particularly important.

An additional inclusive hadronic τ decay method for determining V_{us} was also recently proposed in Refs. [976,1656]. A weighted dispersion relation is employed which (1) allows lattice input rather than the OPE to be used on the theory side, and (2) involves only the flavour *us* inclusive differential distribution on the experimental side. The weights used can be tuned to enhance relative contributions from the lower-multiplicity region of the *us* distribution without unduly inflating the associated lattice errors. The latest results in Ref. [976] show errors on V_{us} significantly reduced compared to those obtained from the FB FESR approach, and the V_{us} value is higher. This suggests the method has

[61] See, e.g., the HFLAV-Tau Spring 2017 report at http://www.slac.stanford.edu/xorg/hfag/tau/spring-2017.

the potential to become competitive with $K_{\ell 3}$ and $\Gamma[K_{\mu 2}]/\Gamma[\pi_{\mu 2}]$ determinations in future, making improvements of lower-multiplicity exclusive *us* experimental data highly desirable.

To summarize, the following experimental results would be useful for improving the FB FESR and new lattice-based *us* determinations of V_{us}:

- Improved $K^-\pi^0$ and $\bar{K}^0\pi^-$ branching fractions.
- Fully unfolded exclusive mode unit-normalized $K^-\pi^0$ and $\bar{K}^0\pi^-$ differential distributions, similar to Belle $\bar{K}^0\pi^-$ results, ideally including covariances, though improved overall normalization is most immediately useful.
- Improved $K\pi\pi$ branching fractions, if possible including the smaller $K^-\pi^0\pi^0$ mode.
- A fully unfolded unit-normalized $\bar{K}^0\pi^-\pi^0$ distribution, analogous to that for $K^-\pi^+\pi^-$ reported by BaBar [1658], ideally including covariances, but, again, with improved overall normalization of most immediate utility.
- If possible, a first *B* factory version of the unit-normalized $K^-\pi^0\pi^0$ distribution.

15.5. MC event generators for τ physics

Authors: Z. Was, D. Epifanov

15.5.1. KKMC *for τ lepton pair production*

Here we review status of the τ lepton production Monte Carlo generator KKMC. The main purpose of the program is the simulation of $f\bar{f} \to f'\bar{f}'$ processes at high energies. To achieve per-mille-level precision a substantial effort was required. In this section we concentrate on those effects which are necessary for high precision to be achieved at a center-of-mass energy of about 10 GeV. In such an energy regime many effects related to high-energy electroweak interactions can be neglected. On the other hand, effects due to masses of outgoing fermions, as well as electromagnetic vacuum polarization, have to be considered. The precise modeling of subsequent τ decays as well as radiative corrections in decays are important for precision measurements. Lessons learned from fits to BaBar and Belle data are discussed below.

The Monte Carlo program KKMC for $e^+e^- \to f'\bar{f}'n\gamma$ was developed and tested for center-of-mass energies above those necessary for Belle II (see Refs. [23,24,1659], and its recent upgrade for LHC applications in Ref. [1660]). It features a second-order matrix element for initial- and final-state QED effects, one-loop electroweak corrections including line shape corrections, and longitudinal and transverse spin effects of incoming electrons and outgoing fermions (τ leptons). Beamsstrahlung effects can be included in the simulation as well. A precision of 0.1% was achieved. For Belle II, applications of the effects mentioned above are limited, while specific effects for *B* factories discussed in Ref. [37] were not included and added in an ad hoc fashion later by BaBar. The achieved precision of 2–3 per-mille was considered to be sufficient, though more theoretical work is required to greatly improve on this limit.

One of the important features of KKMC is the possibility to generate τ lepton decays with all spin effects treated in the production process. The TAUOLA package [1661–1664] can then be used for the simulation of τ lepton decays, and PHOTOS [1665–1667] for simulation of QED radiative corrections in decays. Additional lepton pairs in the final state can also be generated with the help of the PHOTOS algorithm, described below, while the effect of both initial- and final-state pair emission can be simulated with the help of KORALW Monte Carlo [1668].

15.5.2. New currents in the TAUOLA *package*

In this subsection we will concentrate on physics extensions to and novel applications of the TAUOLA package. We will stress the importance of three aspects of the work: (i) construction and implementation of hadronic currents for τ decay currents obtained from models (evaluated from QCD), (ii) presentation of experimental data in a form suitable for fitting, and (iii) preparation of algorithms and determination of distributions useful for fits.

We have prepared two new sets of currents, the first based mainly on theoretical considerations, the second on an effort from the BaBar collaboration. References [1669,1670] showed how the resonance chiral Lagrangian approach was used for calculations of hadronic currents. This will be adapted for TAUOLA. Reference [1669] stressed that details such as additional resonances, more specifically the $f_2(1270)$, $f_0(1370)$, and $a_1(1640)$ observed by CLEO [1671], cannot be introduced if fits to one-dimensional invariant mass spectra of two- and three-pion systems are used. In Ref. [1671] two-dimensional mass scattergrams were used as input for a parameterization of TAUOLA currents (CLEO parameterization[62] [1664]). This should be considered as a minimum for comparisons with the present-day data. In fact, CLEO used a more detailed representation of the data in Ref. [1672]. It may be of interest to repeat such a data analysis, with the help of observables presented in Ref. [1546], adapted to the case of relativistic tau pair production in Belle II.

The physics of τ lepton decays requires sophisticated strategies for the confrontation of phenomenological models with experimental data, owing to the high precision of experimental data. Changing the parameterization for one channel may affect the background modeling of another. This demands simultaneous analysis of many decay channels. One has to keep in mind that the models used to obtain distributions in the fits may require refinement or even substantial rebuilding as a consequence of comparison with data. The topic was covered in detail in Ref. [1673].

One may wish to calculate alternative weights for each generated event (separately for the decay of τ^+ and/or τ^-): the ratios of the matrix element squared obtained with new currents, and the ones used in generation. A vector of weights can then be obtained and used in fits. Such a solution can be easily installed. For practical reasons, the use of semi-analytical distributions is much easier. It enables much faster calculation of errors for fit parameters including correlations, but experimental distributions must be available unfolded. This was important for fits of 3π currents obtained in Ref. [1674]. Modifications of the currents were necessary to obtain the results in Ref. [1675]. It is not clear whether such fitting, without additional help of observables as in Ref. [1546], can be used for the $KK\pi\nu_\tau$ and $K\pi\pi\nu_\tau$ τ decay channels, even if two-dimensional scattergrams are available. If experimental data are available as one- or at most two-dimensional histograms, then the associated currents still rely on models. With the present-day experimental precision, even use of the resonance chiral Lagrangian should not be expected to have sufficient predictive power to describe multidimensional distributions from the constraints of fits to one- or two-dimensional histograms [1676,1677]. This limitation is clearly visible in results for 4π currents [1678].

Currents have been developed for TAUOLA based on Refs. [1594,1675,1678,1679] for, respectively, two-, three-, four-, and five-pion final states. This is now available in FORTRAN and C++, with the option that users can introduce their own C++ currents. Note also that the parameterization for

[62] Note that for this parameterization, differences between hadronic currents of $\tau \to \pi^+\pi^-\pi^-\nu$ and $\tau \to \pi^-\pi^0\pi^0\nu$ were ignored and isospin symmetry was imposed ($\rho\pi$ dominance). A version of the current without this constraint is nonetheless distributed with TAUOLA (all versions), but as a non-active option.

TAUOLA, equivalent to the one used by the BaBar Collaboration for the default simulations, is given in Ref. [1677].

15.5.3. Status of the implementation of tau decays in TAUOLA

Tau decays into the final states with leptons that are currently implemented in TAUOLA include ordinary leptonic decay, $\tau^- \to \ell^- \bar{\nu}_\ell \nu_\tau$ ($\ell = e, \mu$), and radiative leptonic decay, $\tau^- \to \ell^- \bar{\nu}_\ell \nu_\tau \gamma$. These decays are simulated together and they are separated according to the gamma energy threshold (its value is set in TAUOLA). Also, the complete $\mathcal{O}(\alpha)$ QED corrections are implemented for the $\tau^- \to \ell^- \bar{\nu}_\ell \nu_\tau$ decay (LO matrix element, virtual and soft photon corrections) [1662], while the $\tau^- \to \ell^- \bar{\nu}_\ell \nu_\tau \gamma$ decay is generated according to the LO matrix element only. Hence, the accuracy of the simulation of the $\tau^- \to \ell^- \bar{\nu}_\ell \nu_\tau$ decay, estimated to be about 10^{-3}, is determined by the uncertainty of the theoretical formalism, i.e. contributions from various higher-order electroweak corrections, like Ref. [1680]. Recently, the NLO correction has been calculated for the $\tau^- \to \ell^- \bar{\nu}_\ell \nu_\tau \gamma$ decay; the corresponding corrections to the branching ratios were found to be about 3% for $\tau^- \to \mu^- \bar{\nu}_\ell \nu_\tau \gamma$ and about 10% for the $\tau^- \to e^- \bar{\nu}_\ell \nu_\tau \gamma$ mode [1681]. These corrections have not yet been implemented in TAUOLA, hence the accuracy of the simulation of the radiative leptonic decays is only $(3 \div 10)\%$. It should be mentioned that neither doubly radiative leptonic decay, $\tau^- \to \ell^- \bar{\nu}_\ell \nu_\tau \gamma \gamma$ (which is important for precision studies of radiative leptonic decay), nor five-body leptonic decays, $\tau^- \to \ell^- \ell'^+ \ell'^- \bar{\nu}_\ell \nu_\tau$, are implemented in the standard TAUOLA package. For all decay channels, configurations like $\tau^- \to l^- \gamma \gamma$ with additional photons and/or $\tau^- \to l^- l'^+ l'^-$ with an additional lepton pair can be introduced into a TAUOLA sample with the help of PHOTOS, mentioned below. Nevertheless, the code within the TAUOLA package for the simulation of the five-body leptonic tau decays, according to Ref. [1578], has been developed at Belle and can be easily embedded in the official version of TAUOLA [1682].

The multi-pion hadronic tau decays ($\tau \to (2\pi, 3\pi, 4\pi, 5\pi)\nu$) have been studied with high statistics in several experiments; for some of these modes optimal parameterizations of the hadronic currents (spectral functions) were obtained. The most precise description of the hadronic current in the $\tau^- \to \pi^- \pi^0 \nu_\tau$ decay was achieved at Belle from the fit of the experimental $\pi^- \pi^0$ invariant mass distribution [1594]. The parameterization of the hadronic current in the $\tau^- \to \pi^- \pi^0 \pi^0 \nu_\tau$ decay was established by CLEO in their unbinned analysis of the $e^+ e^- \to (\tau^- \to \pi^- \pi^0 \pi^0 \nu_\tau, \tau^+ \to \ell^+ \nu_\ell \bar{\nu}_\tau)$ process in the full phase space [1671]. Up to now, this is the most sophisticated and precise study of the dynamics of hadronic tau decay, and such analyses allow one to avoid the disadvantages of the studies of one- or two-dimensional distributions for tau decays into three or more pions mentioned above. It was found that the CLEO $\pi^- \pi^0 \pi^0$ hadronic current also fits the $\tau^- \to \pi^- \pi^+ \pi^- \nu_\tau$ decay well. For $\tau^- \to (\pi^- \pi^+ \pi^- \pi^0, \pi^- \pi^0 \pi^0 \pi^0) \nu_\tau$ decays the hadronic currents are written based on the experimentally measured cross sections of the reactions $e^+ e^- \to \pi^+ \pi^- \pi^0 \pi^0, \pi^+ \pi^- \pi^+ \pi^-$ [1678] and the conserved vector current (CVC) theorem. Basically, such an approach allows one to describe the dynamics of the four-pion production with small uncertainty determined by the degree of the CVC theorem violation (of the order of 1%). The hadronic currents in the $\tau^- \to (\pi^- \pi^+ \pi^- \pi^+ \pi^-, \pi^- \pi^+ \pi^- \pi^0 \pi^0) \nu_\tau$ decays are described by the model from Ref. [1679]. To choose the appropriate model, a high-statistics study of these decays in multidimensional phase space should be performed at Belle II.

15.5.4. PHOTOS *Monte Carlo for bremsstrahlung and its systematic uncertainties*

While PHOTOS is described in detail elsewhere [34], two aspects of recent development should be noted. First, the emission of additional lepton pairs was introduced, which contributes through

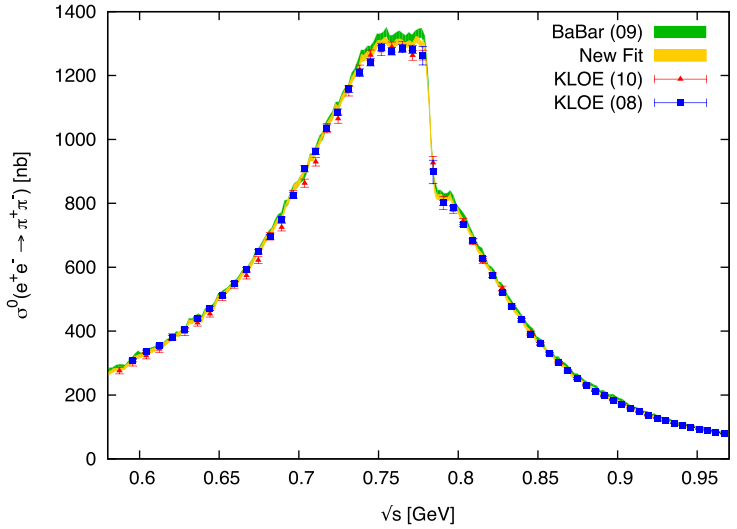

Fig. 195. The light (yellow) band shows the fit with all data in the 2π channel. The radiative return data from BaBar [1694] are shown by the darker (green) band, whereas the KLOE [1696–1698] data are displayed by the markers as indicated in the plot. (Reproduced from Ref. [1701].)

final-state bremsstrahlung. Second, the package is now fully written in C++ [34]. Recent work on numerical tests and new applications, especially in the domain of the LHC, have been performed with precision better than 10^{-3} [1683–1685]. Note that the PHOTOS algorithm features matrix element phase space separation. This is the case for the multi-photon mode of operation as well. That is why the decay channel dependent electromagnetic form factors can be implemented into matrix elements used for the decays of smaller multiplicity; see, e.g., Ref. [1686].

15.6. $e^+e^- \to \pi^+\pi^-$ cross section for $(g-2)_\mu$

Authors: H. Czyz, T. Ferber, D. Nomura, M. Roney, B. Shwartz, T. Teubner

The discrepancy between measurement and the SM calculations for the anomalous magnetic moment of the muon $(g-2)_\mu$ is close to $4\,\sigma$. With the upcoming experiments at Fermilab [1687] and J-PARC [1688] we can expect a factor of four improvement on the accuracy in each of them over the existing result [1689], reducing the experimental uncertainty to about 1.6×10^{-10}. The current theoretical uncertainty of 4.9×10^{-10} (see Refs. [1690–1693] for recent reviews) is dominated by experimental input for the calculation of the leading-order hadronic contribution. Of these experimental inputs, the largest contribution, and also the largest uncertainty, comes from the two-charged-pion channel in the mass region around the ω–ρ interference. Therefore, without significant improvements in the measurement of the $e^+e^- \to \pi^+\pi^-$ cross section, there is no hope of improving the error coming from the SM calculations. The situation here is inconclusive: the three recent most accurate experimental measurements of the cross section of the reaction $e^+e^- \to \pi^+\pi^-$ by BaBar [1694], BESIII [1695], and KLOE [1696–1698] show some tension (see Fig. 195). The spread between KLOE and BaBar, not accounted within their quoted uncertainties, is bridged by the BESIII results. The CMD-2 [1699] and SND [1700] results are not helping in sorting out this issue.

All experimental groups made a significant effort to control systematic errors, yet the difference is not understood at all and new experiments are needed. Moreover, in order to reduce the error on $(g-2)_\mu$ significantly, the goal for the final accuracy including both statistical and systematic uncertainties is to be 0.5% or lower.

15.6.1. Experiment

A measurement of $e^+e^- \to \pi^+\pi^-(\gamma)$ from threshold to approximately 3 GeV can be made with Belle II using the initial state radiation method [1451–1454]. The methodology published by BaBar [1694] can be used to estimate the precision reach of the Belle II dataset. The reduced center-of-mass energy ($\sqrt{s'}$) spectrum of $e^+e^- \to X\gamma_{\rm ISR}$ events gives the cross section for the process $e^+e^- \to X$ via

$$\frac{dN_{X\gamma_{\rm ISR}}}{d\sqrt{s'}} = \frac{dL^{\rm eff}_{\rm ISR}}{d\sqrt{s'}}\epsilon_{X\gamma_{\rm ISR}}(\sqrt{s'})\sigma^0_X(\sqrt{s'}), \tag{546}$$

where $\epsilon_{X\gamma_{\rm ISR}}$ is the detection efficiency estimated initially with MC simulation and subsequently corrected with control sample studies using data, $\sigma^0_X(\sqrt{s'})$ is the "bare" cross section that excludes vacuum polarization, and $\frac{dL^{\rm eff}_{\rm ISR}}{d\sqrt{s'}}$ is the effective initial state radiation luminosity. This ISR luminosity is obtained using $e^+e^- \to \mu\mu(\gamma)\gamma_{\rm ISR}$ events and Eq. 546, where the measured $\frac{dN_{\mu\mu\gamma_{\rm ISR}}}{d\sqrt{s'}}$ distribution, the bare cross section $\sigma^0_{\mu\mu(\gamma)}(\sqrt{s'})$ calculated using QED, and $\epsilon_{\mu\mu(\gamma)\gamma_{\rm ISR}}$ are used as input. With $\frac{dL^{\rm eff}_{\rm ISR}}{d\sqrt{s'}}$ in hand from these $e^+e^- \to \mu^+\mu^-(\gamma)\gamma_{\rm ISR}$ events, the measurement of $\sigma^0(e^+e^- \to \pi^+\pi^-(\gamma))$ is obtained using Eq. 546, the measured $\frac{dN_{\pi\pi\gamma_{\rm ISR}}}{d\sqrt{s'}}$ distribution, and $\epsilon_{\pi\pi(\gamma)\gamma_{\rm ISR}}$.

In essence, this is a precision measurement of the ratio $\sigma(e^+e^- \to \pi^+\pi^-(\gamma))/\sigma(e^+e^- \to \mu^+\mu^-(\gamma))$ as a function of the $\pi^+\pi^-$ and $\mu^+\mu^-$ invariant masses. The advantage is that it removes large components of the systematic effects related to the detection of the initial state radiation and most higher-order theoretical uncertainties. Such cancellations are required as every systematic uncertainty must be kept at a few-per-mille level.

The published BaBar measurement [1694] was performed using a sample of 232 fb^{-1}, which is approximately half of the entire BaBar dataset. That analysis selected $e^+e^- \to \pi^+\pi^-(\gamma)\gamma_{\rm ISR}$ and $e^+e^- \to \mu^+\mu^-(\gamma)\gamma_{\rm ISR}$ events, where the muon and pion samples were separated using μ/π charged particle identification. Backgrounds were suppressed using the χ^2 of kinematic fits to the $e^+e^- \to X\gamma_{\rm ISR}$ signal process that can allow for unmeasured photons radiated at small angles to the initial state electron and/or positron.

In Ref. [1694] the systematic error on the $\pi^+\pi^-$ cross section in the region of the ρ (0.6 GeV $< m_{\pi\pi} <$ 0.9 GeV), where most of the signal lies, is $\pm$0.5%, but is significantly larger below and above this region around the ρ resonance. The systematic error is dominated by π ID ($\pm$0.24%) and ISR luminosity from μ pairs ($\pm$0.34%). The ISR luminosity error itself, 0.34%, is dominated by the 0.29% systematic uncertainties on the μ ID, with smaller contributions from trigger, tracking, and acceptance uncertainties. The statistical error of the raw spectrum is 1.35% at the ρ mass, which includes the statistical error of the measured efficiency corrections (4.7×10^{-3} at the ρ). Although larger outside the ρ region, the systematic uncertainties did not exceed statistical errors over the full spectrum.

The lowest-order contribution of the $\pi\pi(\gamma)$ state to the muon magnetic anomaly is given by

$$a_\mu^{\pi\pi(\gamma),{\rm LO}} = \frac{1}{4\pi^3}\int_{4m_\pi^2} ds' K(s')\sigma^0_{\pi\pi(\gamma)}(s'), \tag{547}$$

where $K(s')$ is a known kernel [1702]. With 232 fb^{-1} of data, the BaBar integrated measurement from threshold to 1.8 GeV was $a_\mu = (514.1 \pm 2.2 \pm 3.1) \times 10^{-10}$, representing a statistical error of 0.4% and systematic error of 0.6%. Note that the systematic errors, though smaller in each mass

bin, are correlated across mass bins, and therefore in the evaluation of the error on a_μ the systematic error dominates.

Nonetheless, significant improvements can be expected with 1 ab^{-1} of Belle II data. Assuming similar selection approaches and that Belle II has a trigger for the $e^+e^- \to \pi^+\pi^-(\gamma)\gamma_{\rm ISR}$ and $e^+e^- \to \mu^+\mu^-(\gamma)\gamma_{\rm ISR}$ events that is at least as efficient as the BaBar trigger was, then one can expect a statistical error of 0.1%, or three times smaller than the error on a_μ expected from the next-generation experiments at FERMILAB and J-PARC. Consequently, the focus will be on reducing the systematic errors. As BaBar included all the statistical components of the systematic errors in the statistical error, there is no trivial projection of the potential systematic error reach for Belle II. Experience has shown, however, that with a significantly larger data sample potential opportunities to identify and reduce the systematic errors in dedicated studies could arise.

The BaBar analysis employed the `AfkQED` MC generator (based on Ref. [1703]) to compare the μ pair cross sections to NLO QED and provide MC efficiencies for both $\pi^+\pi^-$ and $\mu^+\mu^-$ channels. The more accurate `PHOKHARA` generator (see Sect. 15.6.2) was used to study the effects of additional ISR photons. With the anticipated improvements to `PHOKHARA` we anticipate not having to rely on `AfkQED` for Belle II.

As with the BaBar analysis, the efficiencies should be obtained from data-driven corrections to the MC. The PID efficiencies can be determined using the $x^+x^-\gamma_{\rm ISR}$ sample itself, where one of the final-state charged x particles ($x = \mu, \pi, K$) is tagged with stringent PID criteria, and the second ("opposite") track identification is probed (the "tag-and-probe" method). Such a sample was used in Ref. [1694] and set the level of the systematic errors associated with π ID and μ ID, the dominant components of the systematic errors. One can augment that tag-and-probe sample with high-statistics, pure samples of pions and kaons in low-multiplicity events from a high-purity sample of τ^- decays to three charged particles using the fact that $\tau^- \to K^+\pi^-\pi^-$ is forbidden. In that sample a clean sample of charged pions is obtained by making stringent requirements to select a $\pi^-\pi^-$ pair which forces the third charged particle to be π^+. The pure sample of kaons is obtained by making stringent requirements selecting a $K^+\pi^-$ pair in these τ decays, thereby forcing the third charged particle to be a K^-. In addition, a Belle II analysis can augment the tag-and-probe sample of muons using a dedicated sample of muons from $e^+e^- \to e^+e^-\mu^+\mu^-$ two-photon events where muons are selected in low total transverse momentum events with an electron tag and an oppositely charged, strictly identified, muon.

An important cross check on the sensitivity to higher-order radiative effects was provided by comparing the muon absolute cross section dependence on the reduced center-of-mass energy. This check was limited by the 1.1% error on the BaBar luminosity available at the time. It will be valuable for Belle II to have a few-per-mille-level uncertainty on the absolute luminosity, as this comparison can provide a means to reduce other systematic uncertainties in the analysis.

It is planned to have a purely neutral trigger based on a single, high-energy photon at Belle II. In order to keep the rate of this trigger sufficiently low, a three-dimensional veto for Bhabha events based on tracks and calorimeter clusters will be used. Preliminary studies using the Belle II trigger simulation of a 2 GeV photon trigger show a 100% efficiency for all $e^+e^- \to \pi^+\pi^-(\gamma_{\rm ISR})$ with the ISR photon in the barrel calorimeter. Additional triggers based on charged tracks only will allow a precision study of the trigger efficiencies using fully orthogonal triggers.

As mentioned, in the region of the ρ the largest systematic errors in the BaBar analysis arose from PID. If those errors were to be removed, the systematic error would drop by 1/3. A Belle II analysis that has a negligible PID error with 1 ab^{-1} of data would therefore have a total error on a_μ

of 2×10^{-10}, or 0.4%, which is approaching the 0.3% error on a_μ expected from the next-generation experiments at FERMILAB and J-PARC. One way to remove the PID uncertainties [1704] is to avoid using PID to separate the $e^+e^- \to \pi^+\pi^-(\gamma)$ and $e^+e^- \to \mu^+\mu^-(\gamma)$ event samples by exploiting the fact that they have different angular distributions in the center-of-mass system of the charge pair because of the different spins of the muon and pion: $e^+e^- \to \mu^+\mu^-(\gamma)$ events have a $1 + \cos^2\theta^*$ distribution and $e^+e^- \to \pi^+\pi^-(\gamma)$ events have a $\sin^2\theta^*$ distribution. Such an analysis conducted with a large Belle II dataset with a focus on further reducing the other classes of systematic errors reported by BaBar [1694] has a reasonable chance of reducing the total hadron vacuum polarization error to below the experimental error on a_μ expected from the FERMILAB and J-PARC experiments.

15.6.2. Monte Carlo generator

The measurement of the $e^+e^- \to \pi^+\pi^-$ cross section requires very precise Monte Carlo event generators. The Monte Carlo generator PHOKHARA, the most accurate generator to date, has an accuracy of the ISR radiator function of 0.5% [1705]. This should be improved. The PHOKHARA group is planning to include NNLO corrections to ISR emissions in the leading logarithmic approximation. This should, according to estimates, allow for a reduction of the error originating from this source to the level of (0.1–0.2)%. Including the complete NNLO radiative corrections to ISR emissions is more demanding.

Another issue to be addressed is to add the missing NLO corrections in the calculation of the cross section for $e^+e^- \to \pi^+\pi^-\gamma$. The complete NLO corrections were already added for the process $e^+e^- \to \mu^+\mu^-\gamma$ [1706], where it was found that the corrections, which were not included in PHOKHARA before, are small for all event selections used at experiments which used the radiative return method. For $e^+e^- \to \pi^+\pi^-\gamma$, if scalar QED is used for modeling of the photon–pion interactions, one expects that the results will be similar. However, when including the pion form factor effects, it is difficult to predict the results and the answer will be known only after simulating the process with the complete corrections and with realistic event selection cuts used at experiments.

15.7. Two-photon physics

15.7.1. π^0 and $\eta(')$ transition form factors

Authors: V. Braun, N. Offen, S. Uehara

Theory The $\gamma^*\gamma \to \pi, \eta, \eta'$ transition form factors (FFs) are widely recognized as golden modes that allow one to access meson wave functions at small transverse separations, usually referred to as distribution amplitudes (DAs). The standard theory framework is based on collinear factorization [1707–1709] complemented by estimates of soft end point contributions using a simplified version of the light cone sum rules [1710,1711] as first suggested in Ref. [1712]. Such calculations have reached a high degree of maturity [1713–1717].

An alternative approach to the calculation of transition form factors makes use of transverse-momentum-dependent (TMD) meson wave functions (TMD- or k_T-factorization [1718]). This is a viable technique that has been advanced recently to NLO (see, e.g., Ref. [1719,1720]) for the electromagnetic pion form factor and $\gamma^*\gamma \to \pi^0$, and which can be applied to the $\gamma^*\gamma \to \eta, \eta'$ transitions as well. Because of a more complicated non-perturbative input, interpretation of these results is not straightforward.

The recent measurements of the $\gamma^*\gamma \to \pi^0$ FF at space-like momentum transfers in the interval 4–40 GeV^2 by the BaBar and Belle collaborations [1721,1722] caused much excitement and stimulated

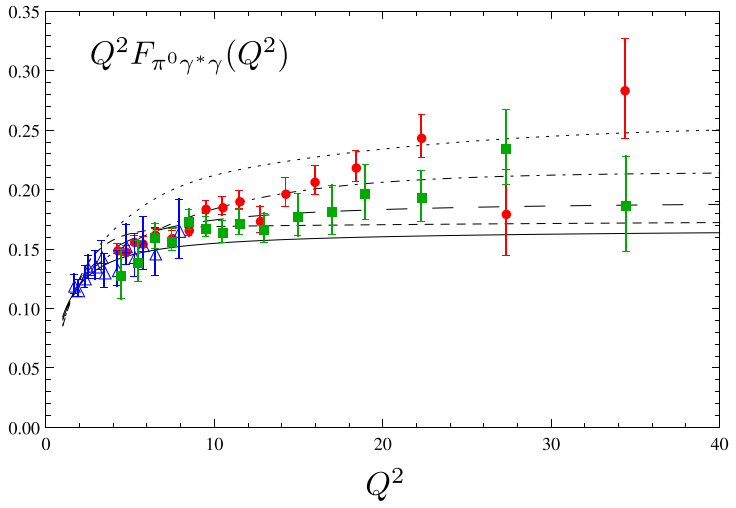

Fig. 196. The pion transition form factor for the "asymptotic" (solid line), "BMS" [1715] (short dashes), "holographic" (long dashes), "model II" of Ref. [1713] (dash-dotted), and "flat" (dots) pion DA. The experimental data are from BaBar [1721] (circles), Belle [1722] (squares), and CLEO [1723] (open triangles).

a flurry of theoretical activity. A strong scaling violation in the $Q^2 = 10$–$20\,\mathrm{GeV}^2$ range observed by BaBar [1721], see Fig. 196, necessitates a very large soft correction to the FF and a significant enhancement of the pion DA close to the end points. This would have profound implications for the studies of B decays to final states involving energetic pions using QCD factorization and/or LCSRs. The Belle data [1722] indicated a much softer scaling violation that is more consistent with common wisdom, although a certain enhancement of the end point behavior of the pion DA as compared to models based on truncated Gegenbauer expansion is favored in this case as well [1714]. A clarification of this discrepancy is extremely important.

The question at stake is whether hard exclusive hadronic reactions are under theoretical control, which is highly relevant for all future high-intensity, medium-energy experiments. Due to better pion identification and much higher statistics, the Belle II experiment will be able to measure the $\gamma^*\gamma \to \pi^0$ form factor with unprecedented precision in the whole Q^2 range. This effort will be complemented on the theory side by high-precision lattice calculations of the second moment of the pion DA [1724–1726] and the NNLO calculation of the leading-twist contribution [1727,1728].

The theory of $\gamma^*\gamma \to \eta, \eta'$ decays is similar to $\gamma^*\gamma \to \pi^0$ apart from a few technical elements. The most important question is whether the usual approach to η, η' based on the concept of state mixing (see, e.g., Ref. [782] and references therein) is adequate for the description of hard processes. Another issue is that η mesons, different to the π, can contain a significant admixture of the two-gluon state at low scales, and alias a comparably large two-gluon DA. Several different reactions were considered in an effort to extract or at least constrain these contributions. Non-leptonic exclusive isosinglet decays [1729] and central exclusive production [1730] act as prominent probes for the gluonic Fock state since the gluon production diagram enters already at LO. Exclusive semi-leptonic decays of heavy mesons were calculated in the framework of LCSRs [1731,1732] and k_T-factorization [1733]. These decays are simpler but the interesting gluon contribution enters only at NLO. Numerically it was shown that the gluonic contributions to η production are negligible, while they can reach a few percent in the η' channel. Up to now, experimental data are not conclusive in all these decays, with

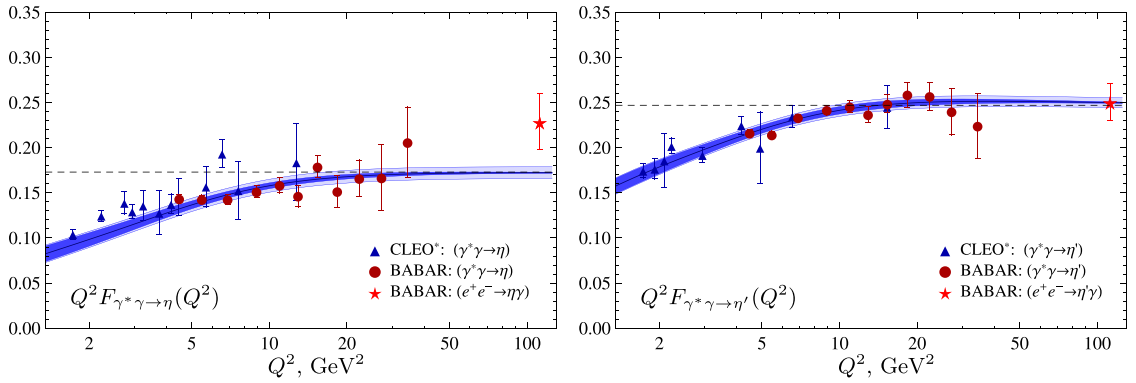

Fig. 197. Transition form factors $\gamma^*\gamma \to \eta$ (left panels) and $\gamma^*\gamma \to \eta'$ (right panels) [1723,1736] compared to the LCSR calculation [1716]. Asymptotic values at large photon virtualities are shown by the horizontal dashed lines. The dark blue shaded areas correspond to the uncertainty of the calculation due to the choice of various parameters. The light blue areas are obtained by adding the uncertainties in the mixing angles. The time-like data point [1737] at $|Q^2| = 112\,\text{GeV}^2$ is shown by red stars for comparison.

a vanishing gluonic DA being possible at a low scale. On the other hand, a large gluon contribution was advocated in Ref. [1734] from the analysis of $B_d \to J/\Psi\eta'$ transitions (see also Ref. [1735]).

The space-like FFs $\gamma^*\gamma \to \eta$ and $\gamma^*\gamma \to \eta'$ in the interval 4–40 GeV^2 were measured by BaBar [1736]. In addition, in Ref. [1737] the processes $e^+e^- \to \gamma^* \to (\eta, \eta')\gamma$ were studied at a center-of-mass energy of $\sqrt{s} = 10.58\,\text{GeV}$. The measurements can be interpreted in terms of the $\gamma^*\gamma \to \eta, \eta'$ FFs at remarkably high time-like photon virtuality $Q^2 = -112\,\text{GeV}^2$. Note that the time-like FFs are complex numbers, whereas only the absolute value is measured.

Next-to-leading-order QCD calculations for the FFs at Euclidean virtualities [1716] are, in general, in good agreement with data [1736], see Fig. 197, although the present statistical accuracy of the measurements is insufficient to distinguish between different models of the DAs and, in particular, determine the two-gluon DA. The most important effect of the NLO improvement is due to the finite renormalization of the flavor-singlet axial current which results in a 20% reduction of the asymptotic value of the $\gamma^*\gamma \to \eta'$ form factor at large photon virtualities. It is interesting that the experimental result for $\gamma^*\gamma \to \eta'$ at $Q^2 = -112\,\text{GeV}^2$ [1737] is very close to the contribution of the asymptotic η' meson DA, whereas the asymptotic contribution to $\gamma^*\gamma \to \eta$ is almost 50% below the data. This result urgently needs verification. If correct, it points to a much larger soft contribution aliasing a much broader DA of the η meson as compared to η', which would be in conflict with the state mixing approximation.

The Belle II experiment will be able to decrease the errors significantly. In addition, some of the parameters, most importantly the decay constants $f_\eta, f_{\eta'}$, will be calculated with high precision on the lattice. In this way, comparison of the QCD calculations with experimental results will allow one to study the structure of η, η' mesons at short interquark separations, encoded in the DAs, on a quantitative level. This, in turn, will benefit theory studies of B decays in final states involving η and η' mesons. The transition FF studies at time-like momentum transfers will eventually be complemented by studies of very rare exclusive decays of electroweak gauge bosons, e.g. $Z \to \eta\gamma$, in the high-luminosity run at the LHC or, later, at a future lepton collider [1738,1739].

Last, but not least, in recent years there has been increasing interest in hard exclusive production of tensor mesons such as $f_2(1270)$, $K_2^*(1430)$, etc. by virtual photons or in heavy meson decays. One motivation is that having three different polarizations of tensor mesons in weak B meson decays can

shed light on the helicity structure of the underlying electroweak interactions. A different symmetry of the wave function, and hence a different hierarchy of the leading contributions for the tensor mesons as compared to the vector mesons, can lead to the situation that the color-allowed amplitude is suppressed and becomes comparable to the color-suppressed one. This feature can give an additional handle on penguin contributions. These studies are, comparatively, at their infancy, but the first results [1740] on the $\gamma\gamma^* \to f_2(1270)$ transition FFs are quite encouraging and agree well with the theory predictions [1741]. Also, in this case Belle II has the potential to provide high-quality data.

To summarize, studies of electromagnetic transition form factors at Belle II will result in stringent tests of the QCD factorization formalism for hard exclusive reactions, provide one with quantitative information on the soft end point contributions, and in the long run enable novel searches for new physics.

Experiment The π^0 transition form factor in $\gamma^*\gamma \to \pi^0$ has been measured in Belle [1722], where one of beam particles scatters into the acceptance of the detector, by which the momentum transfer Q^2 of the virtual photon can be calculated, called a "single-tag measurement." Therefore, this event has an electron (or a positron) and two photons. Usually, such events in Belle are strongly suppressed by the trigger to veto Bhabha events. Due to this Bhabha veto, a complicated selection condition for the polar angle combinations of the electron and the two-photon system were imposed to reduce the uncertainty of the trigger inefficiency. As a result, it has turned out that the trigger efficiency is at the 10% level. The dominant sources for the systematic uncertainties are the extraction of the π^0 yield with the fit and the uncertainty of the trigger efficiency, and the total systematic uncertainty for the combined cross section is between 8% and 14% (and between 4% and 7% for the form factor), depending on the Q^2 region. Figure 198 (black dots with error bar) shows the Q^2 dependence of the form factor, $Q^2|F(Q^2)|$. It is found that the form factor approaches asymptotically 0.209 ± 0.016 GeV [1722], which is slightly higher but consistent with the pQCD prediction of $\sim$0.185 GeV [1742]. On the other hand, BaBar's measurement [1721] shows rapid growth with Q^2 in the higher Q^2 region. Belle II results will draw great attention whether they reproduce these results or not.

In Belle II, since the trigger system will be designed taking into account this analysis, the previous restrictions on statistical power by the trigger, and the systematic uncertainty on the trigger efficiency, will be improved upon. The statistical uncertainty is expected to reduce by a factor of 8 (from 759 fb^{-1} to 50 ab^{-1}) times 2.5 (expected improvement to the trigger efficiency), while the total systematic uncertainty should be at least two times smaller than at Belle (mostly due to improvements on the trigger efficiency uncertainty). As a result, a factor of three to five times more precise measurement is possible for the high Q^2 above 20 GeV^2, as shown in Fig. 198.

15.7.2. Inputs for determining the hadronic contribution to light-by-light scattering in $(g-2)_\mu$

Authors: G. Colangelo, M. Hoferichter, M. Procura, P. Stoffer, S. Uehara

Theory $\gamma\gamma$ physics allows one to constrain important input quantities needed for a data-driven analysis of the hadronic light-by-light (HLbL) contribution to the anomalous magnetic moment of the muon $(g-2)_\mu$, a relation that can be studied in a systematic way within dispersion theory [1743–1747], where the HLbL amplitude is reconstructed in terms of its analytic properties. Expanding in terms of the mass of intermediate states, the dominant contribution at low energies originates from pseudoscalar poles, π^0, η, η', followed by cuts generated by two-meson states, $\pi\pi$, $K\bar{K}$, and higher contributions, e.g. from multi-pion intermediate states, are further suppressed. This expansion

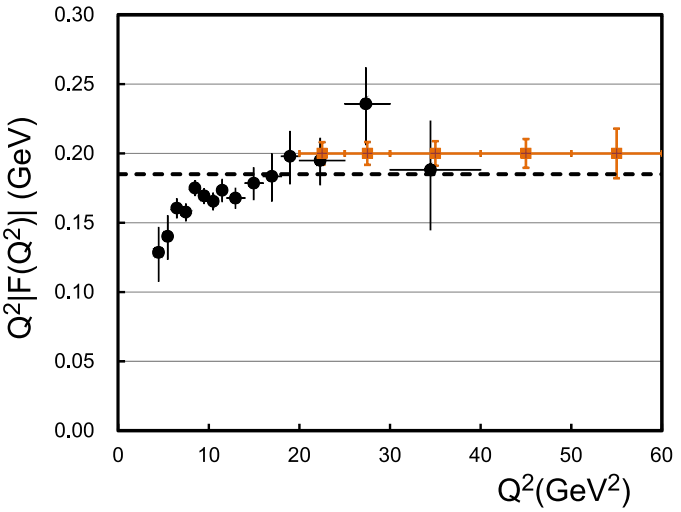

Fig. 198. Distribution of $Q^2|F(Q^2)|$. Black dots show the Belle result and the error bars for the red boxes show the Belle II expectation. The error bars are obtained from the quadratic sum of the statistical and systematic uncertainties. For the latter, the integrated luminosity is assumed to be 50 ab^{-1}. The central values for the red boxes are arbitrary. The dashed line is the asymptotic value of the TFF.

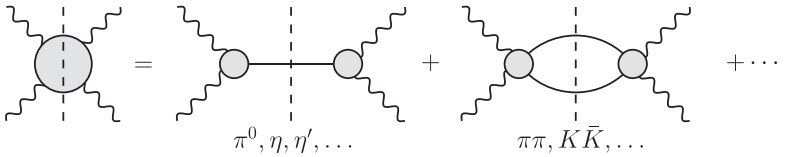

Fig. 199. Singularities of the HLbL amplitude. Solid lines denote meson intermediate states, wiggly lines the (virtual) photons, the gray blobs hadronic amplitudes, and the dashed lines indicate intermediate states taken on-shell.

scheme, illustrated in Fig. 199, ensures that all building blocks correspond to on-shell particles and are thus observable quantities, in the case of the pseudoscalar poles doubly virtual transition form factors, for the two-meson cuts doubly virtual helicity partial waves, and in principle similarly for higher intermediate states. Due to the suppression from phase space and energy thresholds the contributions from heavier states become more and more suppressed in a dispersive reconstruction of the amplitude, which together with the convolution with photon and muon propagators in the $(g-2)_\mu$ integral makes the low-energy region dominant. In practice, an explicit description in terms of individual channels is feasible for center-of-mass energies $\lesssim 1.5\,\text{GeV}$, and information on the virtuality dependence is most critical in the same region. However, information on larger virtualities can still be useful to assess the asymptotic behavior, with the pion transition form factor one prime example.

While the $(g-2)_\mu$ integral requires only space-like virtualities, measurements for time-like photons can provide additional invaluable information; see Ref. [1744] for a comprehensive list of processes that can help constrain one- and two-pion intermediate states, and Fig. 200 for the corresponding space-like and time-like processes in e^+e^- scattering. In fact, the singularity structure of the amplitudes is often dominated by (time-like) kinematics where the virtualities coincide with the mass of a vector meson, which can then be used to constrain the space-like amplitude. For instance, the pion vector form factor in the space-like region is predicted very accurately from the combination of time-like data and dispersion relations. Even though a direct measurement of the

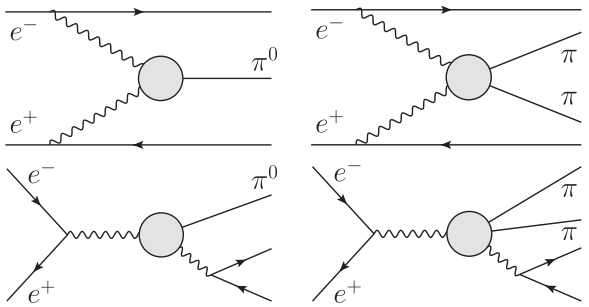

Fig. 200. $e^+e^- \to e^+e^-\pi^0$ and $e^+e^- \to e^+e^-\pi\pi$ in space-like (top) and time-like (bottom) kinematics.

full virtuality dependence is often unrealistic, strategies along those lines can help constrain the full amplitudes from experimentally accessible quantities. For π^0 intermediate states this includes $\gamma\pi \to \pi\pi$ [1748,1749], $\omega, \phi \to \pi^0\gamma^*$ [129], $\omega, \phi \to 3\pi$ [130], $e^+e^- \to 3\pi$ [1750], and similarly for η and η' in relation to $\eta, \eta' \to \pi\pi\gamma$ as well as crossed reactions [106,107,1751,1752]. A complete analysis along these lines has been carried out for the π^0 pole [1753,1754], indicating the impact of the various input quantities. In fact, a major component of the uncertainty estimate traces back to the asymptotic behavior of the singly virtual pion transition form factor, which could be clarified at Belle II. In the same way, data for the on-shell process $\gamma\gamma \to \pi\pi$ (and $\gamma\gamma \to K\bar{K}$) have become sufficiently precise to allow for a detailed understanding of the level of partial waves [1755–1757], while a partial wave analysis in the whole space of relevant virtualities is clearly beyond reach. However, less comprehensive virtual data already provide valuable constraints on the doubly virtual amplitude [1758,1759], as do several of the aforementioned processes by constraining the left-hand cut.

Finally, one way to estimate the impact of contributions beyond one- and two-meson intermediate states relies on the assumption that the dominant such terms are generated by resonances in the multi-meson systems [1760]. Information on their transition form factors crucial for this strategy can be partially reconstructed from light-by-light sum rules [1761,1762], but estimates along these lines could be improved with more information on the electromagnetic form factors of axial vector, scalar, and tensor resonances between 1 and 2 GeV.

Experiment Collisions of two space-like photons are measured through double-tagged two-photon processes at e^+e^- colliders. The reactions such as $\gamma^*\gamma^* \to \pi^0, \eta, \pi\pi$, etc. have a recoiling electron and positron, and a hadronic system in the final state. We "tag" both the electron and positron to measure the Q^2 of the two virtual photons, where $Q^2 \equiv -q^2$ is the negative of the four-momentum squared of the virtual photon. In general, we need to measure the final-state particles exclusively, including the hadronic system, as the double-tag production has a small cross section, and background rejection requires clear identification of the final state. No experimental measurement of double-tag production of a hadronic system below $W < 5\,\text{GeV}$ has been reported to date, where W is the center-of-mass energy of the two-photon collision system and is the same as the invariant mass of the hadronic system.

The double-tag process, like Bhabha scattering, is detected via the presence of a high-energy electron–positron pair. We typically apply a Bhabha veto to reduce the trigger rate in the low-level trigger, which should not reject the signals. It should be possible to keep good efficiency for this purpose by examining the angular correlation of the electron and positron and measuring activity

originating from the hadronic system. In the case that the hadronic system decays with a high final state multiplicity, the trigger and measurement is substantially easier.

The Q^2 range covered by the Belle II detector (with ECL) is typically above $Q^2 > 2\,\mathrm{GeV}^2$ for both electron- and positron-tag sides. The sensitivity to the high end of the Q^2 distribution will be limited by signal cross sections that steeply decrease with Q^2. As the accelerator energy and detector acceptance are asymmetric in the two beam directions, the dependence of the efficiency in Q^2 differs between the two tags. This feature can provide a method for a consistency check of efficiency evaluations, by swapping the Q^2 of the electron and positron sides (Q^2_- and Q^2_+, respectively) based on C symmetry of the differential cross section, $d^3\sigma/dWdQ^2_-dQ^2_+$. Pseudoscalar meson pair production below $W < 2\,\mathrm{GeV}$, dominated by tensor or scalar meson resonance formation processes, have been measured with zero-tag and single-tag two-photon events [2,1740].

The coupling of two time-like photons to a hadron (or a hadronic system) can be measured through an e^+e^- annihilation process to hadron(s) accompanied by a virtual photon, which converts to an electron or muon pair. In the case of the electron pair, the final state particle combination is just the same as that of the double-tag process. However, measurement methods of photon q^2 (Q^2) are different from the double-tag process case, and we have to distinguish them with the invariant mass of the electron pair.

We note that a hadronic system consisting of $\pi^+\pi^-$, K^+K^-, etc. can have a C-odd component that has converted from a single virtual photon, in addition to the targeted two-photon diagram. In some cases, the C-odd component can be larger than the C-even component and interfere with the latter, making it difficult to interpret the experimental results. Pure C eigenstate such as $\pi^0\pi^0$ and $K^0_S K^0_S$ should have an advantage on this point.

15.8. Conclusions

The high-luminosity data at Belle II will provide us with a unique opportunity to investigate the physics program of the tau lepton and low-multiplicity processes. The wealth of data will enable a great advance in this field in the coming years.

lepton flavor violating processes, such as $\tau \to \mu(e)\gamma$, $\tau \to \mu(e)h$ (h = hadrons), and $\tau \to \mu\mu\mu$ (or processes with μ replaced by e), are known to be very sensitive to new physics. In particular, we choose $\tau \to \mu\gamma$ and $\tau \to \mu\mu\mu$ as the Belle II golden channels and have discussed these processes in detail from both theoretical and experimental perspectives. $\tau \to \mu\gamma$ is known to be sensitive to SUSY GUT models. In this report we have discussed the status of this class of models after taking into account the recent results from the LHC (ATLAS and CMS). From these direct particle searches a large parameter space of such models has been excluded in recent years. Not having some obvious new physics benchmark models at hand, we also discussed LFV from an effective field theory point of view. On the experimental side, we have presented a beam background impact study based on Belle II simulation. We showed that the sensitivity to LFV processes will naturally improve as the integrated luminosity increases. At the same time, the high luminosity will allow us to impose further experimental criteria, which should help to reduce some systematic uncertainties.

CP violation in τ decays is another golden measurement chosen in this chapter. The observed hint of a deviation from the SM expectation in the $\tau^\pm \to \pi^\pm K_S \nu_\tau$ channel is extremely intriguing. If it is confirmed, this will be the first observation of CP violation in the leptonic sector, thus leading to a discovery of new physics. We also reviewed some CP violation measurements involving angular observables with hadronic two-body and three-body final states. In the two-hadron final states,

CP violation can occur from the interference between the vector and the scalar currents, when, for example, a scalar particle, such as a new Higgs particle, interacts with a coupling that is CP violating. The hadronic part of these processes is described by form factors. The form factor parameterization, which takes into account important final state interactions, has been discussed in detail. In particular, it was pointed out that the forward–backward asymmetry is one of the most interesting observables whose measurement will be largely improved in the era of Belle II.

In contrast to the other leptons, the tau lepton can decay into various leptonic and hadronic final states, which allow us to perform precise measurements of its properties. The Michel parameters have the advantage of allowing us to investigate the $V-A$ interaction of the SM for leptons without hadronic uncertainties. The study of the second-class currents provides a stringent test of the G-parity conservation in the SM. The Belle II measurement of the tau mass, which is a fundamental parameter of the SM, will offer an important test with respect to the threshold methods that are currently used, e.g., by BESIII and KEDR.

The $g-2$ and EDM of the tau lepton can also be measured: by knowing the initial e^+e^- energy, we can construct so-called optimal observables. The hadronic tau lepton decays can also be used to determine the CKM matrix element $|V_{us}|$, which constitutes an important input for the global CKM matrix parameter fits. Moreover, study of the hadronic tau decays is crucial to determining the strong coupling constant α_s, input for various new physics searches at collider experiments, including the Higgs mass. For this purpose, spectral function measurements of the inclusive tau decays are needed. These studies at the B factories have been very limited and the theory community is strongly hoping for new data from Belle II.

All the investigations using tau leptons require a specific Monte Carlo generator: `KKMC` for the production and `TAUOLA` for the decays. A mini-review of the status of `KKMC` and `TAUOLA` is presented.

The Belle II experiment will also contribute to the clarification of one of the most significant deviations from the SM (at a $4\,\sigma$ level) observed in the measurement of the muon anomalous magnetic moment, $(g-2)_\mu$. As the experimental measurement of $(g-2)_\mu$ at Fermilab and J-PARC will soon be improved, eventually by a factor of four, it is an urgent matter to improve the theoretical uncertainty, which is currently dominated by the uncertainty on the hadronic contributions. This can be achieved by measuring the cross section of $e^+e^- \to \pi^+\pi^-$ with the ISR technique. Belle was not able to perform such a measurement due to the lack of specific triggers. We reviewed the $e^+e^- \to \pi^+\pi^-$ cross section measurements following the BaBar analysis, and a first sensitivity estimate at Belle II was provided. The so-called two-photon processes, $e^+e^- \to \gamma\gamma e^+e^-$, provide information on the two-photon coupling to π, η, and η'. There are two types of experimental signals: single-tag, where either e^+ or e^- is detected, and double-tag, where both e^+ and e^- are detected. Both signals will be studied at Belle II. The former will provide information on the space-like pion form factor, which is a fundamental input for many of the theoretical computations of the B meson decays. The latter can be related and will improve the determination of the so-called light-by-light contribution to the theoretical prediction of the anomalous magnetic moment of the muon ($(g-2)_\mu$), which constitutes the most important theoretical uncertainty after the hadronic contribution mentioned above.

As presented in this section, the investigations of tau and low-multiplicity processes are unique to Belle II. Belle II will therefore play a major role in searching for new physics signals, either directly via LFV processes or CP-violating processes, or indirectly by providing crucial information for testing the SM such as for $(g-2)_\mu$, $|V_{us}|$ extractions, or α_s determination.

16. Dark sectors and light Higgs

Editors: T. Ferber, K. Hayasaka, E. Passemar, J. Hisano
Additional section writers: M. Dolan, S. Godfrey, C. Hearty, G. Inguglia, F. Kahlhoefer, H. Logan, J. Pradler, K. Schmidt-Hoberg

16.1. Theory

*Authors: M. Dolan, F. Kahlhoefer, J. Pradler, K. Schmidt-Hoberg**

Motivation and context In recent decades, an extensive experimental search program has been devoted to dark matter (DM) particles with mass and interaction strength comparable to the electroweak scale, the so-called weakly interacting massive particle (WIMP) paradigm. In recent years, however, the possibility that both DM and the particles mediating its interactions to the SM have a mass at or below the GeV scale has gained much traction; see, e.g., Ref. [1763] and references therein.

The interest in light DM and/or light mediators is not new [1764–1767]. Most notable is the frenzy of activity that set in once it was realized that the harder-than-expected cosmic ray positron fluxes [1768–1770] may be tied to DM and light mediators that leptonically couple to the SM; see Refs. [1771–1774], among many following works.

Another recent interest in light mediators, possibly (much) lighter than the DM particle, concerns DM self-interactions [1775–1778]. The ensuing heat transfer from outer to inner parts of DM halos may potentially explain the discrepancies between N-body simulations of collisionless cold DM and observations on small scales; see Ref. [1779] and references therein.

When the DM mass is at or below the GeV scale, cosmology provides another motivation for a richer dark sector, since achieving the correct relic abundance requires a light spin-1 vector (V) or spin-0 scalar particle S facilitating the annihilation of DM via $\chi\chi \to V^*, S^* \to$ SM or $\chi\chi \to VV$ or SS. In the latter case, V or S is required to be lighter than DM and offers the possibility of secluding it from the SM [956,1780]. At the same time, the mediator coupling to the SM cannot be made too weak, since it will eventually interfere with primordial nucleosynthesis [1781] (although the precise coupling values and lifetimes are model dependent).

Independently of all such motivations, NP below the GeV scale is a perfectly viable option *per se*, and therefore needs to be explored with all the experimental and observational tools available. The direct detection of sub-GeV DM particles is hampered by small energy depositions and finite detector thresholds, although it is still possible to set limits [1782,1783].

The efforts to detect dark matter in the sub-GeV mass bracket, as well as the particle mediating the interactions with SM states, have therefore been actively pursued at fixed-target experiments and with high-intensity, low-energy colliders. Searches at previous experiments such as Babar [1784,1785] have been the subject of theoretical interest and recasting [1786,1787], while neutrino experiments such as MiniBoone [1788] and the proposed DUNE facility [1789] also have sensitivity in this parameter space. Limits have also been derived using existing results from beam-dump experiments [1787,1790] and there are also proposals for multiple future experiments oriented towards low-mass dark sectors [1791,1792].

Light dark sectors There are only a small number of ways to couple a new light SM gauge singlet to the SM in a renormalizable way [1793]. A new vector or pseudovector particle V^μ can couple to

a SM current $J^{\mu}_{\rm SM}$ via the *vector portal*,

$$\mathcal{L} \supset \epsilon V_{\mu} J^{\mu}_{\rm SM}. \tag{548}$$

The most frequently studied example is when $J^{\mu}_{\rm SM}$ is the electromagnetic current and the coupling $\epsilon = \kappa e/\cos\theta_{\rm W}$ arises from kinetic mixing of the hypercharge (Y) and the vector field strengths, $(\kappa/2)V_{\mu\nu}F_Y^{\mu\nu}$ [1794], with κ the kinetic mixing parameter. In this case, V is then often called a "dark photon."

A new scalar particle S can couple to the SM Higgs field H via the *Higgs portal*,

$$\mathcal{L} \supset \lambda S^2 (H^{\dagger} H). \tag{549}$$

If this scalar acquires a vacuum expectation value, it will mix with the SM Higgs, leading to couplings to SM fermions of the form $\sin\theta\, y_q\, \bar{q} q\, S$ with θ the Higgs–singlet mixing angle and y_q the Yukawa coupling of q.

Finally,[63] for a pseudoscalar P, couplings to SM fermions can arise from the dimension-five *axion portal* [1795],

$$\mathcal{L} \supset \frac{\partial_{\mu} P}{f_A} \bar{f} \gamma^{\mu} \gamma^5 f. \tag{550}$$

This term is obtained, for example, from the spontaneous breaking of a global symmetry, where f_A is the scale at which the symmetry is broken. If the scale f_A is sufficiently large, the pseudoscalar naturally obtains a small mass and small couplings. While this operator is higher dimensional, there are very simple UV completions which give rise to such a term. For instance, such a term naturally arises in extended Higgs sectors such as in the two Higgs doublet model (2HDM), encountered in the context of supersymmetry. In particular, if an additional singlet is present, as e.g. in the NMSSM, there is a limit in which the singlet-like pseudoscalar is naturally at the GeV scale, precisely the region which will be probed by Belle II.

In addition to fermionic couplings, the axion portal generically induces couplings of the pseudoscalar to SM gauge bosons:

$$\mathcal{L} \supset -\sum_i \frac{\alpha_i}{8\pi} \frac{C_i}{f_A} F^b_{(i)\,\mu\nu} \tilde{F}^{b\,\mu\nu}_{(i)}\, P, \tag{551}$$

where $i = \{Y, 2, 3\}$ labels the different gauge groups of the SM, $F^{\mu\nu}_{(i)}$ denotes the corresponding field strength tensor, and we have furthermore defined the dual field strength tensors $\tilde{F}^{\mu\nu}_{(i)} = \frac{1}{2}\epsilon^{\mu\nu\rho\sigma} F_{(i)\,\rho\sigma}$. Similar interactions are expected to arise from string compactifications [1796], with $f_A \sim M_{\rm string}$ and coefficients C_i that are typically of order unity. Of particular interest is the pseudoscalar–photon coupling

$$\mathcal{L} \supset -\frac{g_{\gamma\gamma}}{4} F_{\mu\nu} \tilde{F}^{\mu\nu}\, P, \tag{552}$$

[63] For completeness, we also mention the *neutrino portal*, $N(LH)$, where N is a sterile neutrino. There is indeed ample chance that this portal is realized in nature, since N can be a (heavy) right-handed neutrino that is being invoked for generating an SM neutrino mass term. Nevertheless, we will not discuss this portal further in the present context.

where we have introduced the effective coupling

$$g_{\gamma\gamma} \equiv \frac{\alpha_i}{2\pi} \frac{C_Y \cos^2\theta_W + C_2 \sin^2\theta_W}{f_A}. \tag{553}$$

Light pseudoscalars with couplings to SM gauge bosons can play an interesting role in cosmology [1797] and can potentially explain the anomalous muon magnetic dipole moment $(g-2)_\mu$ via Barr–Zee diagrams and light-by-light scattering [1798]. Relevant constraints come from collider experiments [1799–1801], fixed-target experiments [1802], and searches for rare decays [1803]. The expected Belle II sensitivity is discussed in Sect. 16.2.2.

Each of the new particles introduced above can be a viable DM candidate [636], provided it is sufficiently light and its couplings to the SM are so small that it is stable on cosmological scales (or, in the case of the Higgs portal, if the Z_2 symmetry remains unbroken). Alternatively, the particles can be unstable and act as the *mediator* between the SM and another (stable) particle in the dark sector (which is itself an SM singlet and may be either a boson or a fermion). The role of the mediator may then be to keep the DM particle in thermal equilibrium with the SM in the early Universe and provide the annihilation processes that are necessary to reproduce the observed DM relic abundance via thermal freeze-out. Depending on the details of the model, the mediator can couple to both quarks and leptons, only to quarks (leptophobic), or only to leptons (leptophilic). In principle, it can also couple with different strength to down-type quarks and to up-type quarks. The scalar and the pseudoscalar mediator are furthermore expected to couple to fermions proportional to their mass.

The crucial point is that, in contrast to DM candidates from portal interactions, mediators from portal interactions may have sizeable couplings to the SM, which can potentially be probed in particle physics experiments. In the following section we discuss the general ways such a mediator can be produced in e^+e^- colliders and what experimental signatures would result from its various decay modes.

Production and decay modes There are three fundamentally different ways to produce light mediators ($M = S, P, V$) at B factories [616,1767,1804–1806]:

(1) direct (i.e. non-resonant) production from the annihilation of an electron–positron pair: $e^+e^- \to M + X$
(2) resonant production from a tree-level decay, for example $e^+e^- \to \Upsilon(nS) \to M + X$
(3) resonant production from a loop-level rare decay, for example $e^+e^- \to B + X \to K + M + X$.

Once produced, the mediator can have three different types of decays:

(1) invisible decays
(2) leptonic decays
(3) hadronic decays.

If the DM mass is less than half of the mediator mass, the first decay mode is expected to be the dominant one and the production of the mediator will lead to missing momentum in the detector. If invisible decays are kinematically forbidden, there will typically be both leptonic and hadronic decays (unless of course the mediator is either leptophilic or leptophobic). For scalar and pseudoscalar

mediators the leptonic decay modes will be dominated by the heaviest lepton that is kinematically accessible, while vector mediators decay equally into all available leptonic channels. Calculating the hadronic branching fractions for mediators in the GeV range is a difficult problem due to the onset of non-perturbative effects [1807,1808], so we will limit ourselves to the discussion of general signatures.

The first production mechanism relies on the coupling of the mediator to electrons, so it is most relevant for vector mediators. Depending on the decay modes of the mediator, it may be difficult to reliably trigger on this production. If the mediator decays invisibly, it is essential that additional visible particles are produced in association with the mediator. The most promising channel then is to search for the production of a single photon in association with missing energy [1786]. Provided the photon energy is sufficiently large, backgrounds can be efficiently suppressed and a high trigger acceptance can be achieved. For leptonic decays, the events are easier to identify. A possible way to enhance the trigger acceptance, although at the cost of a smaller cross section, would be to insist that the γ converts: $e^+e^- \to \gamma^* + M \to e^+e^- + M$ [1786]. For a (pseudo)scalar coupling to leptons proportional to their mass it may even be advantageous to consider $e^+e^- \to \gamma^* \to \tau^+\tau^-$ followed by final state radiation of the mediator from a tau lepton [1809].

A very efficient way to trigger on the second production mechanism is to focus on the case that the mediator is produced in the decay of an $\Upsilon(1S)$, which in turn is produced from the decay of $\Upsilon(2S)$ or $\Upsilon(3S)$: $e^+e^- \to \Upsilon(2S,3S) \to \Upsilon(1S) + \pi\pi \to M + X + \pi\pi$. For example, for a spin-0 mediator or a spin-1 mediator with axial couplings one can study the radiative decay $\Upsilon(1S) \to M + \gamma$ (for a spin-1 mediator with purely vectorial couplings this process is forbidden by C conservation [1767]). We note that although Belle II will take most of the data at higher center-of-mass energy (corresponding to the mass of $\Upsilon(4S)$ and $\Upsilon(5S)$), a sizeable number of $\Upsilon(2S)$ and $\Upsilon(3S)$ may still be produced if some of the center-of-mass energy is taken away by a photon from initial state radiation. In principle the mediator could also be produced directly in the radiative decay of a heavier resonance, e.g. $\Upsilon(3S)$, in which case the signature would resemble the mono-photon signal discussed above [1784].

If a new mediator is produced in radiative decays of an $\Upsilon(1S)$ resonance, this will lead to a bump in the photon energy, which can be readily identified experimentally. If in addition the mediator decays leptonically, one also obtains a peak in the invariant mass of the dilepton pair, leading to very efficient suppression of backgrounds [1810]. Even if the mediator decays into $\tau^+\tau^-$ [1811], gluons [1812], or hadrons [1813] it may be possible to search for features in the invariant mass of the decay products, providing the most promising search strategy for these channels.

The third production mode relies on loop-induced flavor-changing processes (involving, e.g., penguin diagrams with internal W-bosons and top quarks) [616]. The rate for these processes may depend on the details of the model in the UV as well as on uncertain hadronic form factors [1795,1808,1814,1815]. Nevertheless, the resulting experimental signatures are clear. For example, for an invisibly decaying mediator the process $B \to K + M$ will lead to $B \to K +$ invisible, which is experimentally very similar to the rare decay $B \to K\nu\bar{\nu}$ [1808,1816]. A measurement of this rare SM process can therefore be translated into a bound on the couplings of the new mediator, although the kaon momentum distribution may differ from the SM prediction, thus motivating a rather inclusive search. For a visibly decaying mediator the process $B \to K\mu^+\mu^-$ is of particular importance, as it often leads to the strongest limit on the SM coupling in the case of a scalar or pseudoscalar mediator [1795,1814]. Rare B decays may also have a unique sensitivity to photonic

decays of the mediator, which can be relevant for (pseudo)scalar mediators with a mass comparable to the muon threshold: $B \to K + M \to K + \gamma\gamma$ [1808].

Finally, we consider a somewhat more complicated setup and assume that decays of the mediator into DM are kinematically forbidden and couplings to SM particles are so small that the mediator decay length becomes sizeable. Such a scenario is in fact quite likely given the strong current bounds on the SM–mediator couplings (see, e.g., Ref. [1808]). The resulting signature would then be a leptonic or hadronic decay of the mediator from a displaced vertex. The most promising production mode in this case would be direct production of the mediator in association with a photon, so that there is no activity at all at the collision point and the displaced vertex can be readily identified. Searching for displaced vertices in the rare decay $B \to K\mu^+\mu^-$ may also place strong constraints on such models [1817].

Alternatively, it may be possible to produce such a mediator off-shell, such that decays into a pair of DM particles are allowed [1786]. This process can, for example, be searched for in radiative Υ decays, taking into account that the photon energy is now continuous rather than having a bump: $\Upsilon(1S) \to \gamma + M^* \to \gamma +$ invisible. For a vector mediator one can instead study the case that the $\Upsilon(1S)$ decays fully invisibly, such that the event is only visible due to the pions from the decay of the heavier Υ resonance: $\Upsilon(3S) \to \Upsilon(1S) + \pi\pi \to \pi\pi +$ invisible [1818]. These searches for non-resonant invisible decays may also allow the constraint of mediators with a mass above the center-of-mass energy of the collider, provided the DM mass is small enough [1819,1820]. For CP-even scalar mediators, an analogous search can be performed in the decays of scalar bottomium χ_b [1821]. These searches can be used to constrain the interactions of DM via heavy mediators in a model-independent effective operator approach.

To conclude this discussion, we note that it is also conceivable that there is more than one new mediator. For example, the mass for a vector mediator V could arise from a dark Higgs boson $H' = (h'+v')/\sqrt{v'}$ giving interactions such as $(m_V^2/v')h'V_\mu^2$ and $(m_V/v')^2 h'^2 V_\mu^2$, while H' couples to the SM via the Higgs portal. In such a scenario the dark Higgs may be produced via dark Higgsstrahlung from the vector mediator [1806], which can lead to striking signatures such as $e^+e^- \to 3\ell^+3\ell^-$ [1822, 1823].

Specific examples Let us discuss a few specific example cases to elucidate the projected sensitivity of Belle II. These examples are far from comprehensive, but they cover most of the search channels discussed above.

The first example is the search for invisibly decaying dark photons A into light DM χ, where A couples to the SM via the kinetic mixing parameter ϵ. The projected sensitivity and expected backgrounds are discussed in detail in Sect. 16.2.1. Existing limits and projections of future experiments searching for invisibly decaying dark photons are shown in Fig. 201. In the case of a discovery the energy distribution of the single photon may even allow a dark sector "spectroscopy" [1826] to be performed.

The second example, taken from Ref. [1809], considers a new scalar mediator coupling exclusively to leptons with coupling strength $g_\ell = \xi_\ell^S m_\ell/v$, with ξ_ℓ^S a mixing parameter. The presence of a light DM particle is not assumed, so the mediator decays dominantly into the heaviest lepton that is kinematically accessible. The left panel of Fig. 202 shows model-independent bounds, which only consider tree-level processes. In this case the leading constraints from Belle II result from processes where the scalar mediator is radiated from a tau lepton in the final state (orange dashed). If the mass

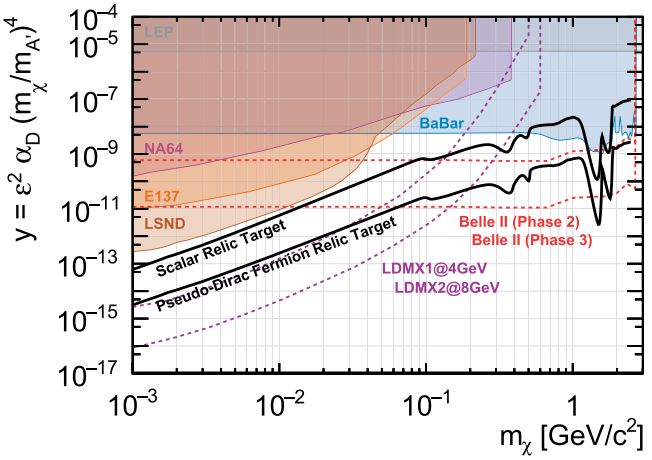

Fig. 201. Combined projections (LDMX, Belle II) and constraints, encapsulating direct production LDM constraints in the context of a kinetically mixed dark photon coupled to an LDM state that scatters elastically (or nearly elastically) at beam dump, missing energy, and missing momentum experiments (dark photon mass $m_{A'} = 3m_\chi$ and coupling of the dark photon to dark matter $g_\chi = 0.5$ where applicable) [1824,1825]. The Belle II projection for Phase 3 is extrapolated from the limit for Phase 2 (see Sect. 16.2.1). Note that the relic density lines assume a standard cosmological history and that there is only a single component of dark matter, which only interacts via dark photon exchange.

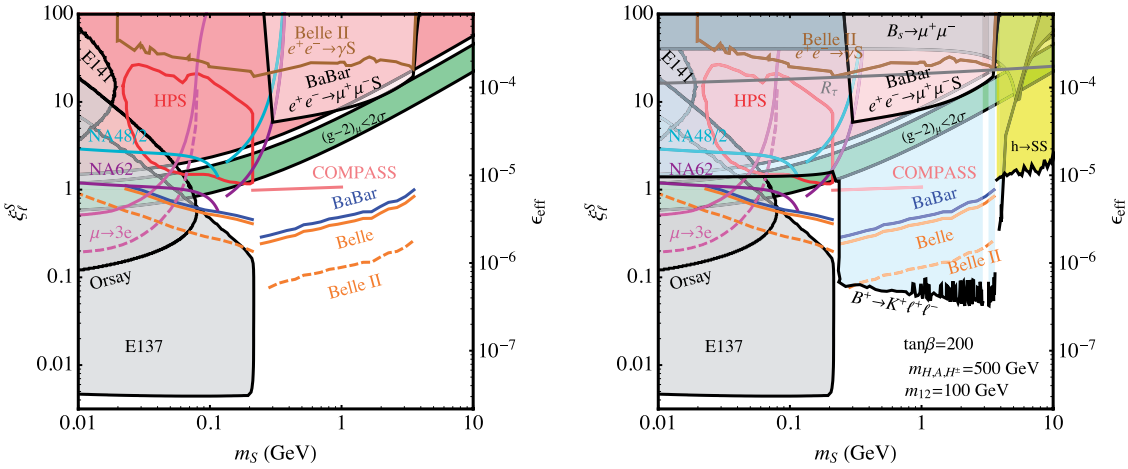

Fig. 202. Model-independent constraints on the effective coupling to leptons (left panel) and specific constraints for the leptonic two-Higgs doublet model (L2HDM+φ) UV completion (right panel) as a function of the scalar mass, reproduced from Ref. [1809].

of the scalar is below the muon threshold, its decay length can become comparable to the size of the detector, leading to constraints that become weaker for smaller mediator masses.

The right panel of Fig. 202 considers a specific UV completion in terms of a leptonic two-Higgs doublet model. In this case it is possible to calculate the rate for loop-induced rare decays, such as $B \to K\mu^+\mu^-$ or $B_s \to \mu^+\mu^-$. The corresponding searches from LHCb are found to give very strong constraints, which may further be improved by Belle II by searching for displaced vertices in B meson decays. We note that the leptonic two-Higgs doublet model also predicts additional tree-level processes, such as $h \to SS$, that can be constrained by low-energy experiments. We refer to Ref. [1809] for details.

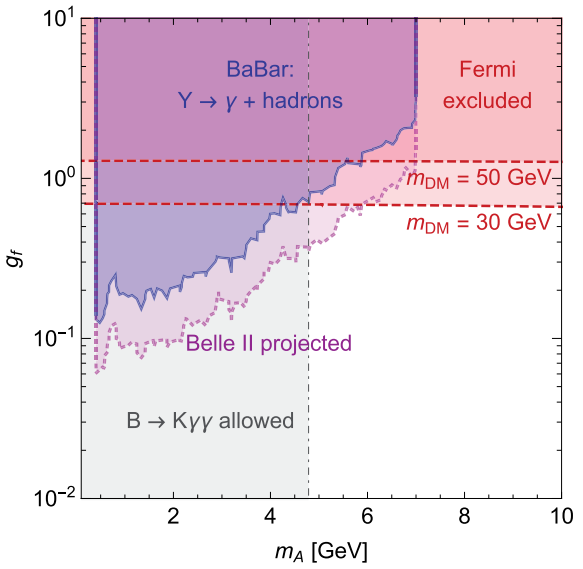

Fig. 203. Constraints on a leptophobic pseudoscalar from radiative Υ decays compared to bounds from Fermi-LAT. See Ref. [1808] for details.

For the third example, we consider a pseudoscalar coupling exclusively to quarks with coupling strength $g_q = g_f m_q/v$. Again, the pseudoscalar is assumed to decay visibly, so it can be observed in radiative Υ decays, e.g. $\Upsilon(2S) \to \gamma +$ hadrons. In Fig. 203 we show in blue the bound on this process from BaBar [1812], calculating the $\Upsilon(2S)$ branching ratio following Ref. [1808]. For the Belle II projection (purple dotted), we assume that the sensitivity scales proportional to the square root of the number of $\Upsilon(2S)$ and $\Upsilon(3S)$ produced, which we take to be a factor of 16 larger than in BaBar. The gray shaded region indicates the pseudoscalar masses for which the process $B \to K + P$ is kinematically allowed and additional (model-dependent) constraints may be obtained from rare decays such as $B \to K\gamma\gamma$.

It is intriguing to assume that such a light pseudoscalar mediator is responsible for setting the DM relic abundance via the processes $\chi\chi \to PP$ and $\chi\chi \to q\bar{q}$. Indeed, direct detection experiments are almost completely insensitive to DM particles interacting with quarks via pseudoscalar exchange, making it very difficult to experimentally test this scenario [1827]. For concreteness we consider Dirac fermion DM and fix the coupling of the DM particle to the pseudoscalar mediator (for given masses and coupling to quarks) by the requirement to reproduce the observed relic abundance. For a fixed DM mass, we can then show bounds on the process $\chi\chi \to b\bar{b}$ from Fermi-LAT observations of dwarf spheroidal galaxies [1828] in the same parameter plane (red dashed). We find Belle II to be competitive with these constraints, in particular for $m_{\rm DM} > 50\,{\rm GeV}$.

As a final example, taken from Ref. [1820], we consider the case that the mediator is so heavy that it cannot be produced on-shell in B factories, but the DM particle is kinematically accessible. In this case, the presence of a vector mediator can induce invisible $\Upsilon(1S)$ decays, while for a spin-0 mediator (or a spin-1 mediator with axial couplings) the Υ can decay into a photon and missing energy. Experimental bounds on these decays can then be translated to the suppression scale of the effective operator parameterizing the interactions of DM with quarks. The estimated bounds that can be set by Belle II (which have been obtained by scaling those in Ref. [1820] by a factor of four), shown in Fig. 204 for spin-0 mediators, depend on whether the DM particle is a scalar or a fermion

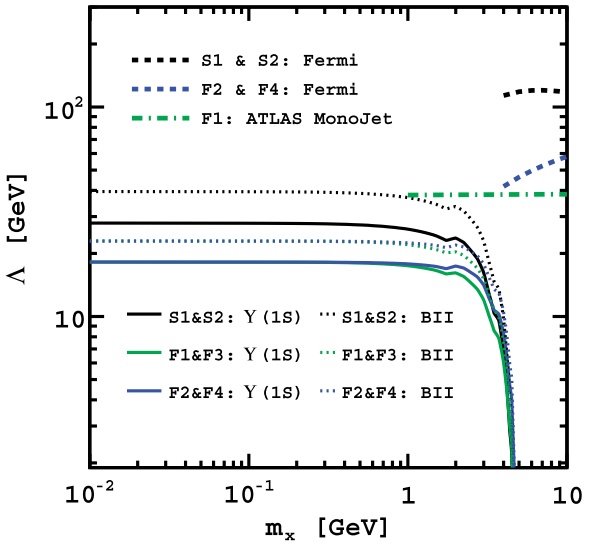

Fig. 204. Constraints on effective DM–quark interactions from radiative $\Upsilon(1S)$ decays followed by an invisible decay of the off-shell mediator as a function of the DM mass, reproduced from Ref. [1820]. BII stands for the expected sensitivity of Belle II.

as well as on the CP properties of the mediator. Again, these constraints can be compared to bounds from Fermi-LAT and LHC monojet searches.

16.2. Experiment: Scattering processes

Authors: T. Ferber, S. Godfrey, C. Hearty, G. Inguglia, H. Logan*

16.2.1. Search for dark photons decaying into light dark matter ("single-photon search")

A significant number of experiments have recently published results for A' searches where the A' decays visibly into charged lepton pairs. Several other dedicated experiments will proceed over the next several years. A recent search by BaBar for the radiative production of the A' in the e^+e^- and $\mu^+\mu^-$ final states used 514 fb^{-1} of data [1829]. The SM rates for $e^+e^- \to \gamma e^+e^-$ and $e^+e^- \to \gamma\mu^+\mu^-$ are large, and the search for the A' consists of a search for a narrow peak in the dilepton invariant mass spectrum on top of a large background. The cross section for this process is proportional to $\varepsilon^2\alpha^2/E^2_{\rm CM}$ [1805]. The decay branching fractions of the A' are the same as a virtual SM photon of mass $M_{A'}$.

If the A' is not the lightest dark sector particle, it will dominantly decay into light dark matter via $A' \to \chi\bar{\chi}$. Since the interaction probability of dark matter with the detector is negligible, the experimental signature of such a decay will be a monoenergetic ISR photon $\gamma_{\rm ISR}$ with energy $E_\gamma = (E^2_{\rm CM} - M^2_{A'})/(2E_{\rm CM})$. This search requires an L1 trigger that is sensitive to single photons, which was not available at Belle and was only partially available at BaBar. BaBar recorded 53 fb^{-1} of data with a single-photon trigger, primarily at the $\Upsilon(2S)$ and $\Upsilon(3S)$ resonances. The effective threshold was 1.8 GeV in the center-of-mass frame, resulting in limits on ε for dark photon masses up to 8 GeV/c^2 [1825]. The analysis had significant backgrounds at low masses (high photon energy) from $e^+e^- \to \gamma\gamma$ in which a photon was not detected in the calorimeter due to gaps between crystals, and which was also missed by the muon system. A subset of this data was used to produce a preliminary result with limits on invisible decays of a light Higgs produced in radiative decays of the $\Upsilon(3S)$ [1784].

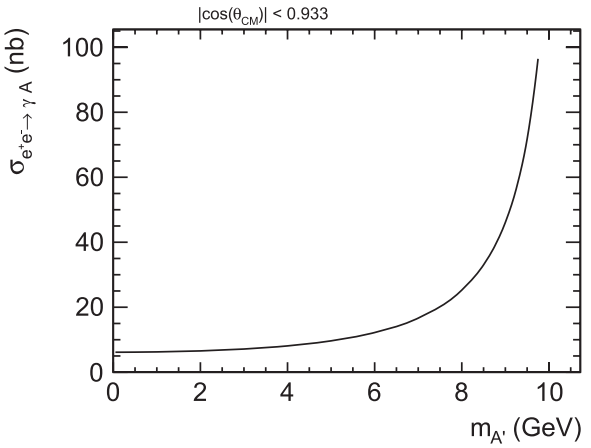

Fig. 205. Cross section for $e^+e^- \to \gamma A'$ as a function of dark photon mass $m_{A'}$ calculated using `MadGraph`.

Monte Carlo simulation Signal MC events ($e^+e^- \to \gamma A'$, $A' \to \chi\bar{\chi}$) are generated using `MadGraph` [1830] and a model based on Ref. [1831] that includes a dark photon A' and fermionic dark matter χ. Each signal sample is generated using a fixed dark photon mass $m_{A'} = [0.1, 0.5, 1.0, 2.0, 3.0, 4.0, 5.0, 6.0, 7.0, 8.0, 8.5, 8.75, 9.0, 9.25, 9.5, 9.75]$ GeV and contains 50 000 events for each mass hypothesis. Events are generated for a maximal photon pseudorapidity of $\eta^*_\gamma < 1.681$, which corresponds to $|\cos(\theta^*_\gamma)| = 0.933$. The beam energy is set to $E^* = 10.58$ GeV. We assume a dark matter mass $m_\chi = 1\,\mathrm{MeV}/c^2$, and we set the coupling to $g_\chi = g_e$. The decay width of the dark photon is set to the tree-level width which increases slowly with $m_{A'}$ and is of $\mathcal{O}(\mathrm{MeV}/c^2)$. We assume that all decays of the A' are into $\chi\bar{\chi}$ and set the kinetic mixing parameter to $\varepsilon = 1$. The resulting cross section, including vacuum polarization corrections (up to about 10%), is shown in Fig. 205.

The background in this analysis is dominated by high-cross-section QED processes $e^+e^- \to e^+e^-\gamma(\gamma)$ and $e^+e^- \to \gamma\gamma(\gamma)$ that produce one or more photons in the final states. If the charged tracks or additional photons are not detected or are out of detector acceptance, they can fake a single-photon event. $e^+e^- \to \gamma\gamma(\gamma)$ events are simulated using `BABAYAGA.NLO` (see Sect. 4.3) without any cut on the photon polar angles, and a minimum photon energy of 0.01 GeV, which results in an effective cross section of $\sigma_{\gamma\gamma} = 25.2$ nb. The phase space for radiative Bhabha events is split into three different regions: where both electrons are above $\theta^* > 1°$ (A), where one electron is below $\theta^* < 1°$ (B), and where both electrons are below $\theta^* < 1°$ (C). Case C has a negligible cross section after event selection (see Sect. 16.2.1), and is not included in the full simulation.

Case A is simulated using `BHWIDE` [1832] with a cut on the minimal electron energy of $E_e > 0.1$ GeV. `BHWIDE` generates multi-photon initial state radiation, final state radiation, and the interference of initial and final state radiation based on Yennie–Frautschi–Suura (YFS) exponentiation and exact NLO matrix elements. The main advantage over `BABAYAGA.NLO` for this particular configuration is a much higher generator speed. Some potential shortcomings of `BHWIDE`, like non-optimal vacuum polarization corrections and missing beam energy spread in the `basf2` implementation, are negligible for this analysis. The effective cross section for the `BHWIDE` sample is 30 950 nb which is, by far, the largest contribution before further preselection (see below).

The contribution for case B is simulated using three different modes of `TEEGG` [1833]: $\mathcal{O}(\alpha^3)$ (single hard photon emission), $\mathcal{O}(\alpha^4)$ with soft corrections, and $\mathcal{O}(\alpha^4)$ with hard corrections (double hard photon emission). The dominant diagram for these configurations is the t channel amplitude

and the processes are characterized by very small momentum transfers Q^2, where Z exchange is negligible and ignored here. The $\mathcal{O}(\alpha^3)$ calculation is exact and the $\mathcal{O}(\alpha^4)$ corrections are included in the equivalent photon approximation. Additional cuts are applied for the `TEEG` sample: we require at least one photon with $\theta^* > 10^\circ$ and an energy of $E^* > 1.4$ GeV, and no other photons above 0.1 GeV. The effective cross sections are 16.90 nb, 12.80 nb, and 4.90 nb. All background samples are preselected before the events are passed to the detector simulations. We require no charged particle with $p_T > 0.15$ GeV/c in $17^\circ < \theta^{\rm lab} < 150^\circ$, and one photon with $E^{\rm lab} > 1.4$ GeV/c and $17^\circ < \theta^{\rm lab} < 140^\circ$. We use a 0.1 fb^{-1} equivalent sample of all background processes with a reduced energy cut $E^{\rm lab} > 0.7$ GeV/c and a 5.0 fb^{-1} equivalent sample for `BABAYAGA.NLO` and `TEEGG`. The `BHWIDE` background has a very similar shape to the `TEEGG` samples and is scaled approximately according to the cross section.

The detector simulation and reconstruction use the Phase 2 BEAST 2 geometry as of release–00–07–01. All luminosity-dependent beam backgrounds are scaled to 0.025 of the nominal background and all other backgrounds are scaled to 0.10 of the nominal background. Two-photon background is not included. For technical reasons the backgrounds in the PXD and SVD octant are ignored.

Trigger efficiency The trigger efficiency has been evaluated using the `L1emulator` tool, which simulates the L1 trigger response using reconstructed quantities. These studies will need to be repeated using the full trigger simulation when it becomes available. We assume that the high-level trigger efficiency is high.

There are two single-photon triggers for physics use (i.e. not prescaled). Both look for an energy deposit in an ECL trigger tower, excluding the ring of towers closest to the beam line in each endcap. These innermost towers have very high rates of background from Bhabha showers in the VXD and CDC outside of the detector acceptance and depositing energy in the ECL with no accompanying charged track. The angular coverage of the triggers is $18.5^\circ < \theta < 139.2^\circ$. Prescaled versions will cover the full angular range of the ECL, $12^\circ < \theta < 157^\circ$.

The first trigger requires an energy deposition $E^* > 2$ GeV, where E^* is the center-of-mass (COM) energy. The event must not satisfy the Bhabha or $e^+e^- \to \gamma\gamma$ vetoes. An event is labeled as a Bhabha event if the highest-momentum track has $p^* > 3$ GeV/c, the second highest has $p^* > 1$ GeV/c, they are separated by at least 143° in the COM frame, and at least one of the two is associated with an ECL cluster with $E^* > 3$ GeV. An event is labeled a $\gamma\gamma$ event if the two most energetic ECL clusters have $E^* > 2$ GeV and are separated by at least 150° in the COM frame, and the event contains no tracks with $p_T > 300$ MeV/c in the laboratory frame. Note that this is not just a single-photon trigger. No requirement is placed on the number of charged tracks or additional clusters in the event, so that the trigger will be efficient for ISR production of $\pi^+\pi^-$ and similar final states. The effective cross section is estimated to be 4 nb, dominated by radiative Bhabha events.

The second trigger has a lower threshold, $E^* > 1$ GeV, and requires that the second cluster in the event be less than 0.2 GeV. There are no other vetoes applied. The cross section is estimated to be 2.5 nb, largely due to radiative Bhabha events in which there really is only a single photon in the acceptance of the detector.

The efficiency for signal MC, as a function of A' mass after combining the two triggers, is shown in Fig. 206. The loss of efficiency is primarily due to detector acceptance. The trigger efficiency for high-energy photons within the angular region $18.5^\circ < \theta < 139.2^\circ$ is 95% (not shown in Fig. 206).

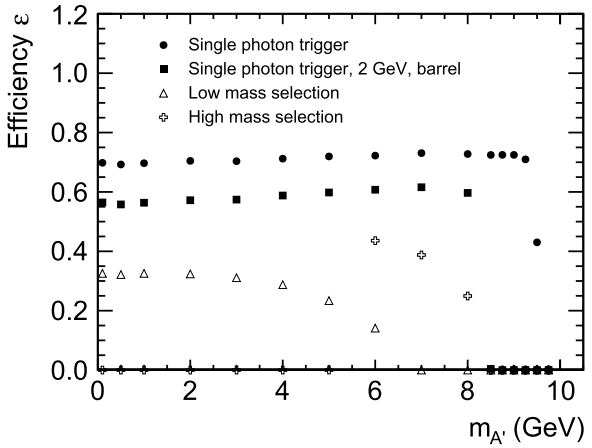

Fig. 206. Trigger efficiency for signal MC as a function of A' mass (filled circles). The filled squares show the efficiency if the acceptance is reduced to the ECL barrel, $E^* > 2\,\text{GeV}$, a selection more relevant for the subsequent event selection. The open symbols show the overall analysis efficiency for the low mass and high mass selections discussed in Sect. 16.2.1.

Event selection The basic event selection requires a calorimeter (ECL) cluster with COM energy $E^* > 1.8\,\text{GeV}$, no other ECL clusters with $E^* > 0.1\,\text{GeV}$, and no tracks with $p_T > 0.2\,\text{GeV}/c$ in the COM frame. The cuts on the second cluster and track momentum have not been optimized, but the results shown here are not sensitive to the specific values. These criteria have high efficiency for signal; the remaining criteria are designed to suppress physics backgrounds.

Backgrounds fall into two general categories. Irreducible backgrounds are those in which the final state includes one photon and no other particles in the acceptance of the detector, which for this purpose we consider to be the full coverage of the ECL, $12^\circ < \theta < 157^\circ$. In practice, efficient photon reconstruction is only available in the acceptance of the CDC, $17^\circ < \theta < 150^\circ$.

Simulation predicts approximately two million events of this type in $20\,\text{fb}^{-1}$ with $E^* > 1.8\,\text{GeV}$ and $22^\circ < \theta < 139^\circ$, 85% due to radiative Bhabhas, and the remainder due to radiative photon events $e^+e^- \to \gamma\gamma(\gamma)$ with at least three photons in the final state. Radiative muon pairs and other QED processes have small cross sections compared to these two sources. The kinematics of requiring all other particles to be outside of the detector acceptance produces a strong correlation between the maximum COM energy of the photon and θ (Fig. 207).

The dominant backgrounds at higher energies are those in which there is a second photon within the detector fiducial volume that is not detected. The event may also contain a third (or more) photon outside of the acceptance. Photon detection inefficiency in the ECL is due to the following, in order of importance:

(1) gap between the ECL barrel and the backwards endcap;
(2) gap between the ECL barrel and the forward endcap;
(3) 200 μm gaps between endcap crystals that are projective to the interaction point, plus 16 larger gaps for mechanical structure;
(4) a 1–1.5 mm gap for mechanical structure in the barrel at $\theta = 90^\circ$;
(5) photons not converting in the crystal, which occurs with a probability of 3×10^{-6}.

Note that the gaps between crystals in the barrel do not project to the beam spot in either polar or azimuthal angle.

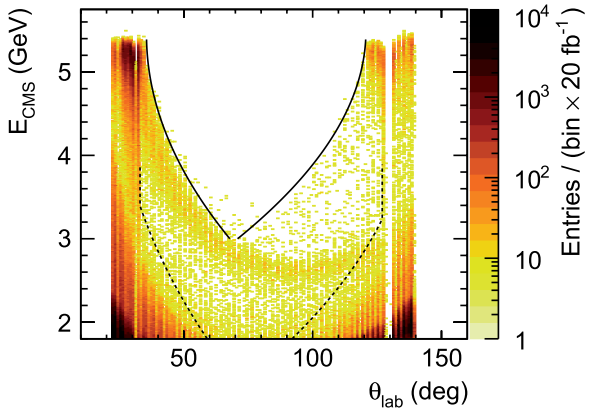

Fig. 207. COM energy E^* versus θ for background events satisfying all selection criteria other than the final cut on θ. The large population of events at low energies and wide angles is due to irreducible background processes. The beam energy events near θ of 30° and 130° are due to $e^+e^- \to \gamma\gamma$ where a photon goes undetected in a gap between the ECL barrel and an endcap. The band at intermediate energies (e.g. 2.6 GeV) at $\theta = 90°$ arises from three-photon final states in which a near-beam-energy photon is undetected in the backward barrel–endcap gap and a second (radiative) photon is near $\theta^* = 0$. The solid lines mark the fiducial region for $m_{A'} \leq 6\,\mathrm{GeV}/c^2$; the dashed lines are for higher masses.

The KLM can also be used to detect photons. Studies with signal MC indicate that most KLM clusters in such events are within 25° (3D, COM) of the signal photon. To suppress backgrounds due to ECL photon inefficiency we require that there be no KLM clusters outside of this 25° cone. At the background levels expected for Phase 2 running, 3.6% of signal MC fail this selection.

The KLM also has regions of inefficiency, primarily at the transitions from the barrel to the endcaps, at the location of the solenoid cryogenics chimney (located near the barrel / backwards endcap transition), between octants in the barrel KLM, and between sectors of the endcap KLM. The chimney and the backward transition overlap with the backwards gap in the ECL, and produce the majority of the non-irreducible backgrounds.

The kinematic distribution of background events passing the basic selection criteria plus the additional KLM requirement is shown in Fig. 207. The numbers of background events used to extract the final sensitivity are summarized in Table 143. Note that we have not yet used azimuthal information. Since KLM inefficiency is concentrated at specific values of ϕ, including this information—for example, as part of a neural net or BDT—will improve the final analysis.

The final step of the selection is an energy-dependent cut on θ, which rejects the vast majority of events in Fig. 207. Due to the limited background MC statistics in some regions of this two-dimensional histogram, a fully automatic process was not used to select the cuts, but rather a combination of optimization and manual intervention. For dark photon masses $m_{A'} \leq 6\,\mathrm{GeV}/c^2$ (roughly $E^* > 3$ GeV), the θ selection produces a low background region, marked with the solid lines in Fig. 207. This region is selected to reject the band in Fig. 207 corresponding to a three-photon final state, where one photon is lost in the backwards ECL gap, and another is at $\theta^* = 0$. Simulation predicts 300 events per $20\,\mathrm{fb}^{-1}$ with $E^* > 3\,\mathrm{GeV}$ between the solid lines, all due to $e^+e^- \to \gamma\gamma\gamma(\gamma)$.

At higher masses $6 < m_{A'} \leq 8\,\mathrm{GeV}/c^2$ (lower photon energy), a much wider θ region is used. It is chosen to almost completely reject the irreducible background, and to avoid the ECL endcaps, which have significantly lower efficiency. Simulation predicts 25 000 background events within this θ region with $1.8 < E^* < 3.9\,\mathrm{GeV}$, almost all due to $e^+e^- \to \gamma\gamma\gamma(\gamma)$.

Table 143. Expected numbers of background events after final selection, scaled to an integrated luminosity of 20 fb^{-1} (see text for details).

Dark photon mass m_A [GeV/c^2]	Low mass selection	High mass selection
0.5	4.3	15335
1	4.3	16012
2	4.3	14399
3	38.3	7931
4	42.6	5693
5	46.8	4659
6	51.1	3587
7	—	4251
8	—	1869

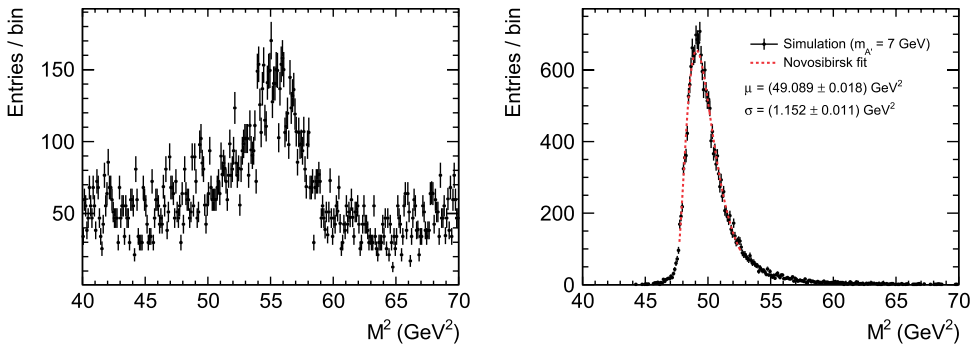

Fig. 208. (a) Recoil mass distribution squared for background events satisfying the selection criteria for the high A' mass region. (b) Distribution for a 7 GeV/c^2 A', fitted with a Novosibirsk function [1834].

Figure 208 shows the resulting background recoil mass distribution for the higher A' mass region, along with an example of a signal distribution.

Signal extraction The final analysis will fit the measured recoil mass squared distribution with a Novosibirsk function [1834] of appropriate width to measure the A' signal and an as yet unspecified function for the background. The kinematic features present in the background distribution will make this quite challenging in the high mass region, and a simpler process—not suitable for the final analysis, since it uses MC truth information—has been used for this study. The procedure uses the photon energy distribution, rather than the equivalent recoil mass. The expected upper limit has been obtained for different A' masses with $m_{A'} \leq 8$ GeV/c^2.

For each mass, the reconstructed photon COM energy has been fitted with a Novosibirsk function. The signal region is taken to be the photon energy range $[\mu_E - 3\sigma_E, \mu_E + 1.5\sigma_E]$, where μ_E and σ_E are the Novosibirsk fit parameters for that mass. This range contains between 83% and 88% of the signal.

For each mass, we obtain the expected 90% CL upper limit on the observed number of signal events μ_S from the expected number of background events μ_B. μ_B is the number of events in the signal region predicted by the generated background MC samples, scaled to 20 fb^{-1}. We assume that N, the number of events observed, is the integer closest to μ_B. μ_S is selected such that the Poisson probability of observing $\leq N$ events when expecting $\mu_B + \mu_S$ events is 0.1.

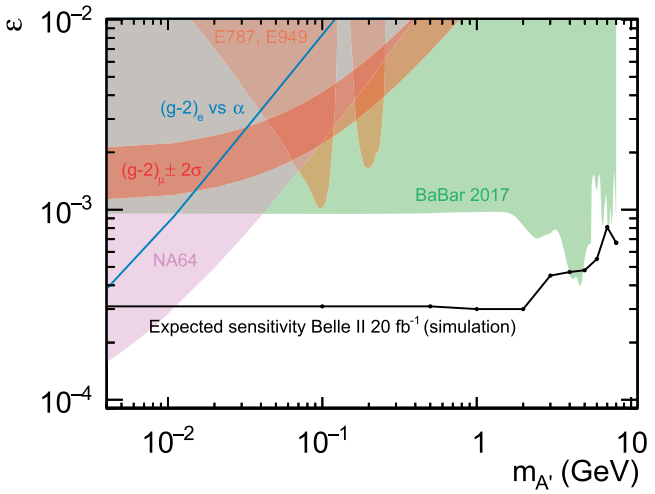

Fig. 209. Projected upper limits on ε for the process $e^+e^- \to \gamma A'$, $A' \to$ invisible, for a 20 fb^{-1} Belle II dataset (solid black curve).

The upper limit on the cross section for $e^+e^- \to \gamma A', A' \to$ invisible is $\sigma = \mu_S/\epsilon_S\mathcal{L}$, where ϵ_S is the signal efficiency (Fig. 206) and $\mathcal{L} = 20\,\text{fb}^{-1}$ is the integrated luminosity. The equivalent limit on ε is the square root of this cross section divided by the cross section calculated for $\varepsilon = 1$ (Fig. 205). Projected upper limits on ε are summarized as a function of A' mass in Fig. 209. The results are projected to be significantly better than BaBar due to the better hermeticity of the calorimeter and the efficiency of the KLM.

Systematic uncertainties We expect that the systematic uncertainties will be dominated by uncertainties in the predicted number and kinematic properties of background events. At low A' masses, we need to quantify the residual beam energy photon backgrounds from $e^+e^- \to \gamma\gamma$. This will require photon control samples, such as kinematically fitted radiative muon pairs, or $e^+e^- \to \gamma\gamma$ events in which one photon is reconstructed at full energy and the other has low energy, corresponding to a late conversion in the ECL crystal. The backgrounds for high A' masses are dominated by events with one photon in the backwards barrel/endcap gap and a second near $\theta^* = 0$. The kinematically fitted muon pair sample will be used to map the photon efficiency across this gap.

16.2.2. Search for axion-like particles

Axions were originally motivated by the strong CP problem and have a fixed relation between coupling strength and mass. While the axion and its parameters are related to QCD, the coupling and mass of axion-like particles (ALPs) are taken to be independent and can appear in a variety of extensions to the SM. ALPs are pseudoscalars ($J^P = 0^-$) with couplings to the different gauge bosons. The simplest search for an ALP at Belle II is via its coupling to $\gamma\gamma$ (Fig. 210) [1835]. Depending on the ALP mass m_a and the coupling constant $g_{a\gamma\gamma}$, the ALP is long lived, producing a single-photon final state, or decays in the detector to $\gamma\gamma$, producing a three-photon final state. A wide range of ALP coupling to photons and ALP masses has been ruled out by previous experiments, but two regions in the $g_{a\gamma\gamma}$–m_a plane are of particular interest for a Belle II analysis. The first region are light ALPs with $m_a \approx 1\,\text{MeV}$, $g_{a\gamma\gamma} \approx (10^{-5}\text{–}10^{-6})\,\text{GeV}^{-1}$, which is out of reach for beam-dump experiments and only disfavored by model-dependent limits from cosmology. The second region is heavier ALPs with $0.1\,\text{GeV} \lesssim m_a \lesssim 10\,\text{GeV}$. Hypercharge couplings are excluded for

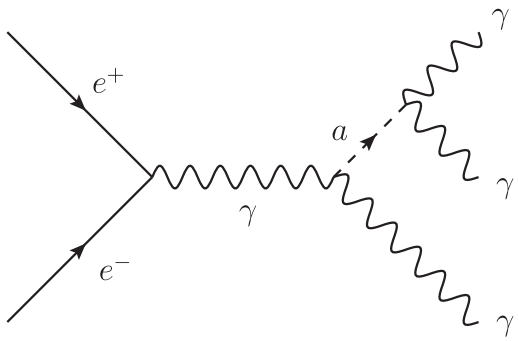

Fig. 210. Production of an axion-like particle in association with a photon.

$g_{aBB} \approx (10^{-2}\text{–}10^{-3})\,\text{GeV}^{-1}$ by reanalyzed LEP data, where the weaker limit is for coupling to photons only.

The three-photon search will provide access to parameter space that is not addressed by any current measurements. At higher masses, $m_a \gtrsim 200\,\text{MeV}/c^2$, the three photons are well separated. At lower masses, the ALP is sufficiently boosted that the two decay photons overlap in the calorimeter or, at the lowest masses, form a cluster that is reconstructed with only a single local maximum. The calorimeter group is developing software to reconstruct merged π^0 mesons that can be adapted for this analysis. However, the low-mass region will also be a challenge for the trigger system, particularly at level 1, where the signal is indistinguishable from $e^+e^- \to \gamma\gamma$. The problem is not that these signals are difficult to trigger on, but rather that the plan is to prescale the $\gamma\gamma$ final state to reduce the throughput to the high-level trigger, and to reduce the rate of events stored to disk. The preferred solution would be to delay the decision to reject $\gamma\gamma$ events to the HLT and apply no prescale at level 1 for the $\gamma\gamma$ trigger. The Belle II sensitivity for visible and invisible ALPs has been studied in detail in REf. [1836].

It has been suggested [1803] to search for the ALP in the flavor-changing neutral current decay $B^+ \to K^{(*)+}a$, which is governed by the coupling g_{aWW} of the ALP to W^+W^-. The decay $a \to \gamma\gamma$ produces a final state similar to $K^+\pi^0$. Both BaBar and Belle have measured this branching fraction with uncertainties of a few $\times 10^{-7}$ [727,1837]. Similar uncertainties in an ALP search would provide significant constraints on ALP coupling to heavy charged bosons. Extrapolating to the full Belle II dataset requires work, as the existing analyses are systematics dominated.

The $a \to$ invisible case produces a monoenergetic $K^{(*)+}$ in the B^+ rest frame. Such searches use the fully reconstructed B sample, and would be similar to the BaBar search for $B^+ \to K^{(*)+}J/\psi$, $J/\psi \to$ invisible [624]. This search was statistically limited, and could exploit the much larger dataset that will be available to Belle II.

16.2.3. Search for dark photons decaying into charged leptons and charged hadrons

If there are no kinematically accessible dark sector final states available, dark photons produced via the ISR reaction $e^+e^- \to \gamma_{\text{ISR}}A'$ will decay to SM particles, with branching fractions equal to a virtual photon of that mass. Particularly useful final states include $\mu^+\mu^-$, e^+e^-, and h^+h^-, where h is a charged pion or kaon. BaBar has searched for prompt decays to e^+e^- and $\mu^+\mu^-$ [1829], setting upper limits on the kinematic mixing parameter of 5×10^{-4}–10^{-3}, depending on mass. A search is ongoing at Belle for prompt decays to leptonic and hadronic final states, and for displaced decays to lepton pairs. With the large amount of data expected to be collected by the Belle II detector (about

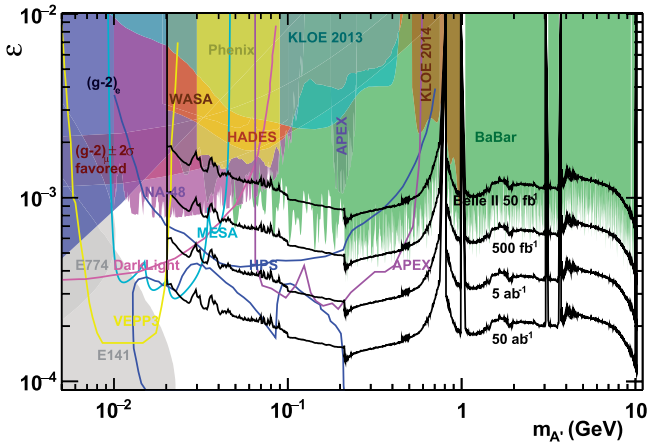

Fig. 211. Existing exclusion regions (90% CL) on the dark photon mixing parameter ε and mass $M_{A'}$ (solid regions) for $A' \to \ell\ell$, with projected limits for Belle II and other future experiments (lines). (Figure reproduced from Ref. [1838].)

two orders of magnitude larger than that available at BaBar), one can expect to observe an excess of events due to dark photon decays to charged leptons or charged hadrons with a mixing parameter of the order of a few $\times 10^{-4}$. This search requires the implementation of efficient L1 two-track triggers and it will also profit from photon triggers due to the presence of a single high-energetic ISR photon. In order to maintain a high L1 trigger efficiency for $A' \to e^+e^-$, the unavoidable prescale factor for radiative Bhabha events is ideally implemented as function of track charge and polar angle.

One can extrapolate the existing BaBar limits of dark photon decays into charged particles to Belle II. The larger drift chamber radius of Belle II will yield an improved invariant mass resolution (∼a factor of 2) and better trigger efficiency for both muons (∼a factor of 1.1) and electrons (∼a factor of 2) is expected. The projected upper limits for different values of integrated luminosity are shown in Fig. 211.

16.2.4. Search for dark photons decaying into light dark matter in $e^+e^- \to A'\ell^+\ell^-$

Dark photons can also be searched for in the reaction $e^+e^- \to A'\mu^+\mu^-$, with subsequent decays of the dark photon (also called a Z' in this context) into a variety of final states [1839,1840], including invisible ones. BaBar has performed this search for dark photon decays to muonic final states [1841], and the same analysis is in preparation at the Belle experiment. For the invisible case, a kinematic fit of the muons can be used to select events in which the missing energy is pointing into the barrel calorimeter, which has the best hermiticity. The trigger for this final state is the muon pair, which may be sensitive to higher A' masses than the single-photon trigger. A sensitivity to the mixing parameter at the level of 10^{-4}–10^{-3} can be expected in this channel.

16.3. Experiment: Quarkonium decay

16.3.1. Searches for BSM physics in invisible $\Upsilon(1S)$ decays

In the SM, invisible decays of $\Upsilon(1S)$ involving neutrinos in the final state are produced by $b\bar{b}$ annihilation with $\mathrm{Br}[\Upsilon(1S) \to \nu\bar{\nu}] \approx 10^{-5}$. Low-mass dark matter (i.e. with a mass smaller than the mass of the b quark), if it exists, should enhance this Br [1819,1842]. The ARGUS, CLEO, Belle, and BABAR experiments have studied this channel with limited data providing upper limits to $\mathrm{Br}[\Upsilon(1S) \to \text{invisible}] < 3.0 \times 10^{-4}$ at the 90% CL [1843–1846]. Low-mass dark matter can

also be probed in radiative $\Upsilon(1S)$ decays such as $\Upsilon(1S) \to \gamma +$ invisible. The next-to-minimal supersymmetric extension of the SM (NMSSM) allows for the existence of low-mass (GeV/c^2-scale) dark matter and of a low-mass CP-odd Higgs boson (A^0), therefore if $M_{\Upsilon(1S)} > M_{A^0}$ and $M_{A^0} > 2M_\chi$ one would be able to observe the Wilczek production of A^0 ($\Upsilon(1S) \to \gamma A^0$) followed by the decay into dark matter $A^0 \to \chi\bar{\chi}$ [1819,1842,1847,1848].

The main limitations for the study of transitions involving invisible decays of the $\Upsilon(1S)$ is that one has to find a tagging method that can be used to unambiguously infer the presence of the $\Upsilon(1S)$ even though its decay products are not seen in the detector. Generally one uses transitions such as $\Upsilon(2,3S) \to \pi^+\pi^-\Upsilon(1S)$ (with $\mathrm{Br}[\Upsilon(3S) \to \pi^+\pi^-\Upsilon(1S)] \approx 4.5\%$ and $\mathrm{Br}[\Upsilon(2S) \to \pi^+\pi^-\Upsilon(1S)] \approx 18.1\%$) followed by $\Upsilon(1S) \to$ invisible; in this case one has to trigger and reconstruct final states in which only two low-momentum pions are seen in the detector, trying to avoid collecting too many background events and at the same time maintaining a high trigger efficiency.

During Belle operations a special dedicated trigger was implemented to allow the search of $\Upsilon(1S) \to$ invisible from dipion transition of the $\Upsilon(3S)$ in e^+e^- collisions at the $\Upsilon(3S)$ peak, but no special triggers were implemented for the $\Upsilon(2S)$ data-taking. Based on the Belle experiment experience and on simulation studies performed with the Level 1 trigger emulator package (`L1TriggerEmulator`) of the Belle II analysis software (`basf2`), it is found that the special trigger conditions such as a *single-track trigger* with $p_t > 200\,\mathrm{MeV}/c$ (long track trigger) and opening angle between the tracks in the r–ϕ plane larger than 30° would allow a trigger efficiency comparable to that of Belle (i.e. 85–90%) in the process $\Upsilon(3S) \to \pi^+\pi^-\Upsilon(1S)$ and an efficiency of 30% for $\Upsilon(2S) \to \pi^+\pi^-\Upsilon(1S)$, $\Upsilon(1S) \to$ invisible. Simulation studies have shown that trigger efficiencies for $\Upsilon(2S) \to \pi^+\pi^-\Upsilon(1S)$ can still be improved if a second dedicated trigger is implemented for this case (for example realizing the p_t threshold of the single-track trigger).

If s ($= 10.0233, 10.3552\,\mathrm{GeV}/c^2$) is the center-of-mass energy of the collision, $M_{\pi^+\pi^-}$ the invariant mass of the two-pion system, and $E^{\mathrm{CMS}}_{\pi^+\pi^-}$ the energy of the two-pion system in the center-of-mass reference frame, one defines a recoil mass for the two-pion system as $M^2_{\mathrm{r}} = s + M^2_{\pi^+\pi^-} - 2\sqrt{s}E^{\mathrm{CMS}}_{\pi^+\pi^-}$. A signal of the decay $\Upsilon(1S) \to$ invisible is an excess of events in the M_{r} distribution at a mass equivalent to that of the $\Upsilon(1S)$ ($9.460\,\mathrm{GeV}/c^2$). Another possibility to produce and tag $\Upsilon(1S)$ consists in the search for the production of higher-spin resonances (such as $\Upsilon(2S)$ and $\Upsilon(3S)$) in ISR processes followed by their dipion transition to $\Upsilon(1S)$. While the electron and the positron approach before a head-on collision, either one or the other can radiate a photon, reducing the energy of the collision. As shown in Refs. [1849–1852], given the e^+e^- collision rate, it is possible to precisely calculate the ISR cross section $\sigma_f(s)$ for the production of any final state f. The cross section for untagged ISR production (ISR photon not reconstructed) of $\Upsilon(3S)$ ($\Upsilon(2S)$) is 29 pb (17 pb). This technique, which was already widely used by the Belle Collaboration, provides an additional source of $\Upsilon(nS)$ resonances. The search for $\Upsilon \to$ invisible is characterized by the presence of different backgrounds in the M_{r} distribution that will limit the final sensitivity: combinatorial and peaking backgrounds. The combinatorial background consists mostly of two-photon processes $e^+e^- \to e^+e^-X$ where the initial e^+e^- proceed along the beam pipe, escaping detection, and $X \to \pi^+\pi^-, \pi^+\pi^-\pi^0, \mu^+\mu^-$; this background can be easily parameterized by a first-order polynomial function. The peaking background is due to two-body decays of the $\Upsilon(1S)$ with both the decay products traveling outside the detector acceptance. Since the Br for $\Upsilon(1S)$ decays to lepton pairs are all of the order of 2.5%, this leads to a relatively large peaking background that needs to be carefully evaluated and that will constitute the main limitation to the measurement. An additional background source would be the

Table 144. Expected yields for various $\Upsilon(1S)$ tagging techniques, where $L_{\rm int}$ is the integrated luminosity considered for the extrapolation of the yields, ϵ is the expected total efficiency, $N(\Upsilon(1S))$ is the number of $\Upsilon(1S)$ produced in the process, and $N_{\Upsilon(1S)\to\nu\bar{\nu}}$ and $N_{\rm NP}$ are the expected number of observed $\Upsilon(1S) \to$ invisible events assuming SM (1×10^{-5}) and NP (3×10^{-4}) rates, respectively.

Process	$L_{\rm int}$ (ab^{-1})	ϵ	$N(\Upsilon(1S))$	$N_{\Upsilon(1S)\to\nu\bar{\nu}}$	$N_{\rm NP}$
$\Upsilon(2S) \to \pi^+\pi^-\Upsilon(1S)$	0.2, $\Upsilon(2S)$	0.1–0.2	2.3×10^8	232–464	6960–13920
$\Upsilon(3S) \to \pi^+\pi^-\Upsilon(1S)$	0.2, $\Upsilon(3S)$	0.1–0.2	3.2×10^7	32–64	945–1890
$\Upsilon(4S) \to \pi^+\pi^-\Upsilon(1S)$	50.0, $\Upsilon(4S)$	0.1–0.2	5.5×10^6	5.5–11	165–310
$\Upsilon(5S) \to \pi^+\pi^-\Upsilon(1S)$	5.0, $\Upsilon(5S)$	0.1–0.2	7.6×10^6	7.6–15.2	228–456
$\gamma\Upsilon(2S) \to (\gamma)\pi^+\pi^-\Upsilon(1S)$	50.0, $\Upsilon(4S)$	0.1–0.2	1.5×10^8	150–300	4500–9000
$\gamma\Upsilon(3S) \to (\gamma)\pi^+\pi^-\Upsilon(1S)$	50.0, $\Upsilon(4S)$	0.1–0.2	6.5×10^7	65–130	1950–3900

reaction $e^+e^- \to \pi^+\pi^-\nu\bar{\nu}$; however, due to the low cross section of the order of 10^{-6} pb, it would produce about 5 events out of 50 ab^{-1} of data collected at the $\Upsilon(4S)$ peak and can therefore be neglected in this study.

In order to extract the expected sensitivities we consider a scenario in which data are collected at different energies and different luminosities, as shown in Table 144. Taking into account the expected contribution from the peaking background, one can expect a sensitivity at the 90% CL (statistical only) of 1.3×10^{-5} to Br[$\Upsilon(1S) \to$ invisible] combining the various channels; this value is comparable to the SM prediction Br[$\Upsilon(1S) \to \nu\bar{\nu}$] $\approx 1.0 \times 10^{-5}$. For the search of the process $\Upsilon(1S) \to \gamma +$ invisible, it can be anticipated that taking into account the large data samples to be used and the expected total reconstruction efficiencies as outlined above, the Belle II experiment has the possibility of discovering an excess of events at the 90% confidence level either if Br[$\Upsilon(1S) \to \gamma A^0$] $\times$ Br[$A^0 \to$ invisible] $> 5 \times 10^{-7}$, or Br[$\Upsilon(1S) \to \gamma\chi\bar{\chi}$] $> 5 \times 10^{-6}$ for $0 < m_\chi < 4.5\,{\rm GeV}/c^2$.

16.3.2. Probe of new light CP-even Higgs bosons from bottomonium χ_{b0} decay

The decay of scalar bottomonium $\chi_{b0} \to \tau^+\tau^-$ can be sensitive to s channel exchange of CP-even neutral Higgs bosons via the process $\Upsilon(3S) \to \gamma\chi_{b0}(2P) \to \gamma\tau^+\tau^-$ [1821]. Although the event rate for SM Higgs exchange is a few orders of magnitude too small to be observed, this process can put significant constraints on the parameters of the type-II two-Higgs-doublet model [932] when the discovered 125 GeV Higgs boson is the heavier of the two CP-even scalars. In this model the scalar couplings to b quarks and τ leptons can be simultaneously enhanced for large values of the parameter $\tan\beta$, which is defined as the ratio of the vacuum expectation values of the two Higgs doublets. The model contains two CP-even neutral scalars, which we call H_{125} and $H_{\rm new}$. We identify H_{125} with the discovered Higgs boson at 125 GeV. In this model the SM expression for the partial width given by

$$\Gamma^H(\chi_0 \to \ell^+\ell^-) = \frac{M_{\chi_0}}{8\pi}\left[1 - \frac{4m_\ell^2}{M_{\chi_0}^2}\right]^{3/2}\left(\frac{m_q m_\ell}{v^2 M_H^2}\right)^2 f_{\chi_0}^2 \tag{554}$$

is modified by the presence of the second Higgs resonance,

$$\left(\frac{m_b m_\tau}{v^2 M_H^2}\right)^2 \to \left[\frac{m_b m_\tau}{v^2}\left(\frac{\kappa_b^{125}\kappa_\tau^{125}}{M_H^2} + \frac{\kappa_b^{\rm new}\kappa_\tau^{\rm new}}{M_{\rm new}^2 - M_{\chi b0}^2}\right)\right]^2, \tag{555}$$

where in the above equations $v^2 = 1/\sqrt{2}G_F$ is the SM Higgs vacuum expectation value, M_H is the Higgs mass, we have neglected $M_{\chi_0}^2$ relative to M_H^2 in the propagator, and f_{χ_0} is the χ_{b0} decay constant. $M_{\rm new}$ is the mass of the second scalar $H_{\rm new}$, and the κ factors represent the couplings of the two scalars to b quarks or τ leptons normalized to the corresponding coupling of the SM Higgs boson [1853]. We have kept the $p^2 = M_{\chi_{b0}}^2$ dependence in the second term in Eq. (555) corresponding to $H_{\rm new}$ exchange because we will be interested in low $M_{\rm new}$. There is also a contribution to the $\chi_0 \to \ell^+\ell^-$ decay through a two-photon intermediate state which we estimate to be $\mathrm{Br}^{2\gamma}(\chi_{b0}(2P) \to \tau^+\tau^-) \approx 6 \times 10^{-9}$ [1854].

To estimate the Br for $\chi_{b0} \to \tau^+\tau^-$ via SM Higgs exchange we estimate the $\chi_{b0}(2P)$ total width using the measured Br for $\chi_{b0} \to \gamma\Upsilon(1S)$ and the predicted partial with for this transition to obtain

$$\mathrm{Br}^{H}(\chi_{b0}(2P) \to \tau^+\tau^-) = (1.9 \pm 0.5) \times 10^{-12}. \tag{556}$$

In the 2HDM we set the couplings of the 125 GeV Higgs boson equal to their SM values (i.e. working in the *alignment limit* [1855]) and the branching ratios in Eq. (556) are modified by the multiplicative factor

$$\left[1 + \frac{M_H^2}{M_{\rm new}^2 - M_{\chi_{b0}}^2} \tan^2\beta\right]^2. \tag{557}$$

The number of signal events grows with increasing $\tan\beta$ and decreasing $M_{\rm new}$. For a large enough enhancement, the $H_{\rm new}$-exchange contribution will dominate over the SM two-photon intermediate state process.

There is also a continuum signal from $\Upsilon \to \gamma H_{\rm new}^* \to \gamma\tau^+\tau^-$, in which the photon is not monoenergetic. On the $\Upsilon(3S)$ the total continuum signal rate is only about 0.5% of the resonant rates through the $\chi_{b0}(2P)$ and $\chi_{b0}(1P)$ and is spread over a large photon energy range, so we neglect it in our results.

The resonant signal is a single photon, monoenergetic in the parent Υ rest frame, with the remainder of the collision energy taken up by the $\tau^+\tau^-$ pair. This must be discriminated from the reducible background $\Upsilon \to \gamma\chi_{b0}$ with χ_{b0} decaying to anything other than $\tau^+\tau^-$, as well as from the irreducible continuum background $e^+e^- \to \gamma\tau^+\tau^-$. We assume that the $\tau^+\tau^-$ identification purity will be good enough that the reducible backgrounds can be ignored. To estimate the sensitivity to the irreducible background we take as background the total number of $e^+e^- \to \gamma\tau^+\tau^-$ events with a photon energy within a window of width $2\delta E_\gamma$ around the characteristic photon energy.

In Fig. 212 we show the resulting $5\,\sigma$ discovery reach and 95% CL exclusion reach from 250 fb^{-1} of data on the $\Upsilon(3S)$. We plot the sensitivity reach as a function of $M_{\rm new}$ and $\tan\beta$, assuming that the couplings of the 125 GeV Higgs boson take their SM values. We also show, using dotted lines, the parameter region allowed by direct searches, as computed using `HiggsBounds` 4.2.0 [1856]. $H_{\rm new}$ masses below about 10 GeV are generally excluded by searches for $\Upsilon \to \gamma H_{\rm new}$ [1847,1857], which have not been included in `HiggsBounds`. We note that the 95% CL exclusion line for the $\Upsilon(3S)$-initiated process corresponds to 130 signal events on top of about 4300 background events, so that more sophisticated kinematic cuts could improve signal to background substantially, and even more so for the $5\,\sigma$ discovery curves.

On the $\Upsilon(3S)$, the sensitivity comes almost entirely from decays to $\chi_{b0}(2P)$; the signal rate from $\chi_{b0}(1P)$ is more than 100 times smaller but with comparable background. This process has the potential to probe a large region of the type-II 2HDM parameter space with $H_{\rm new}$ masses below

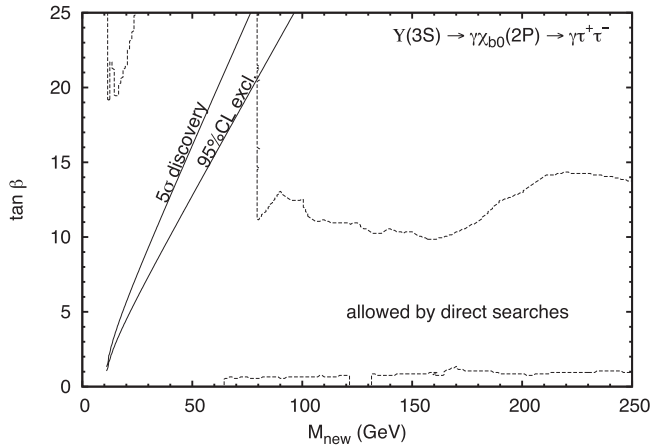

Fig. 212. $5\,\sigma$ discovery and 95% CL exclusion reach in the type-II 2HDM from 250 fb^{-1} of data on the $\Upsilon(3S)$. The sensitivity is to the regions to the left of the solid curves. We have set the couplings of the 125 GeV Higgs boson equal to their SM values. The dashed lines indicate the parameter regions still allowed by direct searches for $H_{\rm new}$, computed using `HiggsBounds` 4.2.0 [1856].

80 GeV and moderate to large $\tan\beta$ that is currently unconstrained by existing searches. On the $\Upsilon(2S)$ the sensitivity is not as good due to a combination of lower signal rate and a larger photon linewidth, resulting in more background.

16.3.3. Search for a CP-odd Higgs boson in radiative $\Upsilon(3S)$ decays

Radiative decays of vector bottomonium states can be used in the search for a low-mass CP-odd Higgs boson, A^0. Such a possibility has already been discussed in the case of invisible decays of A^0 to low-mass dark matter, but if dark matter is such that $2M_\chi > M_{A^0}$ then decays of a CP-odd Higgs boson to dark matter would be kinematically forbidden and A^0 would decay to SM final states; in particular, one would expect, for example, $A^0 \to h^+h^-, l^+l^-$ ($h = \pi, K$ and $l = e, \mu, \tau$). One reaction to be studied in this sense is, then, $e^+e^- \to \Upsilon(3S)$ followed by $\Upsilon(3S) \to A^0\gamma$ with $A^0 \to l^+l^-$ or $A^0 \to h^+h^-$. This reaction is characterized by the presence of one photon and two oppositely charged leptons/hadrons (same flavor) in the final state, and a peak in the photon energy spectrum is expected in correspondence with a peak in the lepton/hadron invariant mass distribution for a signal A^0 production and decays. Searches for A^0 decays to final states including l^+l^- ($l = \mu, \tau$) or hadrons have been performed by the BaBar experiment [1812,1858,1859]. No excess of events has been observed, and 90% CL upper limits have been set as follows:

- $\mathrm{Br}[\Upsilon(3S) \to \gamma A^0] \times \mathrm{Br}[A^0 \to \mu^+\mu^-] < 5.5 \times 10^{-6}$ for $0.2 < M_{A^0} < 9.3\,\mathrm{GeV}/c^2$ [1858];
- $\mathrm{Br}[\Upsilon(3S) \to \gamma A^0] \times \mathrm{Br}[A^0 \to \tau^+\tau^-] < 1.6 \times 10^{-4}$ for $4.3 < M_{A^0} < 9.5$ and $9.6 < M_{A^0} < 10.1\,\mathrm{GeV}/c^2$ [1859];
- $\mathrm{Br}[\Upsilon(3S) \to \gamma A^0] \times \mathrm{Br}[A^0 \to h^+h^-] < 8 \times 10^{-5}$ for $0.3 < M_{A^0} < 7\,\mathrm{GeV}/c^2$ [1812].

These results have been obtained by analyzing a sample of 122×10^6 $\Upsilon(3S)$ resonances equivalent to an integrated luminosity of 28 fb^{-1}. At Belle II, with improved detector performance and an integrated luminosity larger by a factor of 7–10, one can also expect large improvements in the search for CP-odd Higgs boson production and decays.

16.3.4. Prospects for lepton universality tests in $\Upsilon(1S)$ decays

Leptonic decays of $\Upsilon(1S)$ can be used to test lepton universality [1860,1861]. While the measured values for $\mathrm{Br}[\Upsilon(1S) \to l^+l^-]$ ($l = e, \mu, \tau$) are consistent with each other within statistical precision [77],

$$\mathrm{Br}[\Upsilon(1S) \to e^+e^-] = 2.38 \pm 0.11, \tag{558}$$

$$\mathrm{Br}[\Upsilon(1S) \to \mu^+\mu^-] = 2.48 \pm 0.05, \tag{559}$$

$$\mathrm{Br}[\Upsilon(1S) \to \tau^+\tau^-] = 2.60 \pm 0.10, \tag{560}$$

the central values might be hiding a tendency to increase as function of m_l; this might be a hint of lepton flavor non-universality. The values reported in Eqs. (558)–(560) are based on the average of results that are over a decade old, and the most recent results used in those averages are the following:

$$\mathrm{Br}[\Upsilon(1S) \to e^+e^-] = 2.29 \pm 0.08_{\mathrm{stat.}} \pm 0.11_{\mathrm{sys.}}, \tag{561}$$

$$\mathrm{Br}[\Upsilon(1S) \to \mu^+\mu^-] = 2.49 \pm 0.02_{\mathrm{stat.}} \pm 0.07_{\mathrm{sys.}}, \tag{562}$$

$$\mathrm{Br}[\Upsilon(1S) \to \tau^+\tau^-] = 2.53 \pm 0.13_{\mathrm{stat.}} \pm 0.05_{\mathrm{sys.}}. \tag{563}$$

Equations 561–563 show the values of Br as obtained in the most recent measurements [1862–1864] together with their statistics and systematic errors. It is important to notice that the values shown in Eqs. (561)–(563) are based on a very limited data sample of the order of few fb^{-1}, and consequently the statistical precision will be greatly improved with the data sample size expected at the Belle II experiment. The main systematic effects are due to the determination of the number of $\Upsilon(2S)$ resonances produced in the reaction $e^+e^- \to \Upsilon(2S) \to \pi^+\pi^-\Upsilon(1S)$ with $\Upsilon(1S) \to e^+e^-$ [1862], to the efficiency determination (dominated by uncertainties in the detector simulation) at the level of 1.8% and scale factor between on-resonance and off-resonance data in the determination of $\Upsilon(1S) \to \mu^+\mu^-$ with data collected at different center-of-mass energies [1863], and to τ, μ selection criteria at the level of 3% and $\Upsilon \to \tau^+\tau^-$ at the level of 2% in the search for $\Upsilon(1S) \to \tau^+\tau^-$ with data collected at different center-of-mass energies [1864]. Lepton universality implies that $\mathrm{Br}[\Upsilon(1S) \to e^+e^-] = \mathrm{Br}[\Upsilon(1S) \to \mu^+\mu^-] = \mathrm{Br}[\Upsilon(1S) \to \tau^+\tau^-]$ up to small corrections due to different available phase space, and consequently

$$R_{ll'} = \frac{\mathrm{Br}[\Upsilon(1S) \to l^+l^-]}{\mathrm{Br}[\Upsilon(1S) \to l'^+l'^-]} = 1, \tag{564}$$

where $l, l' = e, \mu, \tau$, and with the largest correction expected to appear in the $\tau\mu$ ratio with $R_{\tau\mu} = 0.992$. The observed $R_{ll'}$ values are all consistent with unity within 1–2 σ, so it is interesting to see how this will evolve as more precise measurements of $\mathrm{Br}[\Upsilon(1S) \to l^+l^-]$ become available. While detailed studies of these decay channels are not available, the Belle II experiment is expected to achieve a better control of systematic effects allowing an improved determination of $\mathrm{Br}[\Upsilon(1S) \to l^+l^-]$ and of the $R_{ll'}$ ($l, l' = e, \mu, \tau$) ratios.

16.4. Conclusions

Belle II offers exciting opportunities to explore dark sector physics both in scattering processes and in decays of Υ mesons in the MeV to GeV range. Unique triggers will already be available during the early running of Belle II that will allow the collection of events with a single photon in the final state. The better hermiticity of the Belle II detector compared to BaBarmakes these searches competitive

with even smaller datasets. With the final dataset the sensitivity of existing limits can be improved by almost an order of magnitude since these searches are generally not limited by systematics.

17. Physics beyond the Standard Model

Editors: F. Bernlochner, R. Itoh, J. Kamenik, V. Lubicz, U. Nierste, Y. Sato, L. Silvestrini
Additional section authors: A. Buras, M. Blanke, T. Deppisch, F. De Fazio, J. Jones, L. Hofer, W-S. Hou, N. Kosnik, J. Schwichtenberg, C. Smith, D. Straub

17.1. Introduction

This chapter describes new physics models with interesting imprints on flavor-changing transitions, specifically those testable at Belle II.

Flavor physics probes virtual effects of heavy particles with masses far above the reach of the high-p_T experiments ATLAS and CMS. In the SM all flavor-changing transitions originate from the Yukawa sector and are governed by very small numbers. Particularly sensitive to new physics are FCNC processes, which involve fermions of different generations but the same electric charge. Belle II can probe quark FCNC transitions of the type $b \to s$, $b \to d$, $c \to u$, and $s \to d$. Important observables for measuring these processes are the meson–antimeson mixing amplitudes, which are called $|\Delta F| = 2$ processes as the flavor quantum number $F = B, S, C$ changes by two units. Equally interesting are FCNC decays that belong to the class of $|\Delta F| = 1$ transitions. In the SM, FCNC amplitudes are tiny as they are governed by small CKM elements and are forbidden at tree level, proceeding instead through an electroweak loop diagram. In addition, the CKM-favored contribution to $s \to d$ and $c \to u$ transitions are GIM suppressed, with suppression factors of $(m_c^2 - m_u^2)/M_W^2$ and $(m_s^2 - m_d^2)/M_W^2$. The GIM suppression is most spectacular in FCNC decays of charged leptons (such as $\tau \to \mu\gamma$), which are suppressed by a factor of $\Delta m_\nu^2/M_W^2$ where Δm_ν^2 is a difference of squared neutrino masses. Furthermore, SM flavor-changing transitions involve only left-handed fermion fields. This feature leads to a chirality suppression of leptonic and radiative decays. For example, the chirality flips in the decay rates of $B \to \mu^+\mu^-$ and $B \to X_s\gamma$ come with factors of m_μ^2/m_b^2 and m_b^2/M_W^2, respectively.

Models of physics beyond the Standard Model need not involve any of the abovementioned suppression factors. For example, some of the models discussed in this chapter permit FCNC transitions at tree level. An important category in the classification of BSM theories is the property of *minimal flavor violation* (MFV) [621,1865]. In MFV theories the only sources of flavor violation are the Yukawa matrices of the SM and they enter the amplitudes in such a way that flavor-changing transitions involve the same CKM elements as the corresponding SM contribution. MFV theories may still have CP phases in addition to the Kobayashi–Maskawa phase. Usually the MFV property is an arbitrary add-on to a given model of new physics, for example the minimal supersymmetric standard model (MSSM) can be studied with or without MFV conditions.

New physics will modify measurements of effective Wilson coefficients (see Chapter 7) away from their SM expectation values. New operators can also be induced, meaning that Wilson coefficients that are negligible in the SM acquire non-zero values. In general, observables of different types may depend on the same Wilson operators, so that new physics will appear in different measurements in a correlated way. This is crucial for fully elucidating the nature of new physics. In this chapter we also discuss correlations with other experiments and observables outside the scope of Belle II, wherever appropriate. However, it is important to note that there are sectors of BSM flavor physics which are probed exclusively at Belle II.

Table 145. A snapshot of the discovery potential of the selected NP model for Belle II observables: charmless hadronic B decays including time-dependent CP asymmetry. The number of stars illustrates how well each model can accommodate a potential deviation from the SM in a given observable. The more stars the models have, the more they allow NP contributions. ×: the model does not permit significant NP contributions for those observables. □: there is no specific study available. The stars are given mainly based on the text in the given sections. "Experimental sensitivity" describes the competitiveness of Belle II—★★★: superior to LHCb; ★★: competitive with LHCb; ★: Belle II can contribute to the measurement, albeit with less sensitivity than LHCb.

Observables	Experimental sensitivity	Multi-Higgs models (Sect. 17.2)	Generic SUSY	MFV (Sect. 17.3)	Z' models (Sect. 17.6.1)	Gauged flavor (Sect. 17.6.2)	3-3-1 (Sect. 17.6.3)	Left–right (Sect. 17.6.4)	Leptoquarks (Sect. 17.6.5)	Compositeness (Sect. 17.7)	Dark sector (Sect. 16.1)
$b \to s$ gluonic penguins:											
$S_{CP}(B^0_d \to \eta^{(\prime)} K^0_S)$	★★★	★	★	★	★	★	★	★★	×	□	×
$S_{CP}(B^0_d \to K^0_S K^0_S K^0_S)$	★★	×	★	★	★	★	★	★★	×	□	×
$S_{CP}(B^0_d \to K^0_S \pi^0)$	★★★	×	★	★	★★	★	★★	★★	×	□	×
$b \to d$ gluonic penguins:											
$S_{CP}(B^0_d \to K^0_S K^0_S)$	★	×	★	★	★	★	★	★★	×	□	×
$b \to s$ EW penguins:											
$\Delta A_{CP}(B \to K^{(*)}\pi)$	★★★	×	★	×	★★★	★	★★★	□	×	□	×
$\mathcal{B}(B_s \to \phi\,\pi^0)$	★★	×	★	×	★★★	★	★★★	□	×	□	×
$\mathcal{B}(B_s \to \phi\,\rho^0)$	★	×	★	×	★★★	★	★★★	□	×	□	×
$b \to d$ EW penguins:											
$S_{CP}(B \to \pi\pi)$	★★★	×	×	×	★★★	★	★★★	□	□	□	×
$S_{CP}(B \to \rho\pi)$	★★	×	×	×	★★★	★	★★★	□	□	□	×
$S_{CP}(B \to \rho\rho)$	★★★	×	×	×	★★★	★	★★★	□	□	□	×

Tables 145–149 provide a summary of the experimental signatures accessible by Belle II that are sensitive to probe the new physics models described in this chapter.

17.2. Two Higgs doublet models

Authors: Wei-Shu Hou, Ryosuke Itoh

In this section we discuss the two Higgs doublet models (2HDM), in which the SM is extended by an additional Higgs boson doublet. Given the discovery of the 125 GeV boson h^0, it is mandatory to find out which Higgs sector is realized in nature. We consider only two 2HDMs: Model II, or 2HDM-II, which coincides with the tree-level Higgs sector of the MSSM, and the general 2HDM (G2HDM, also called 2HDM-III), i.e. without discrete Z_2 symmetry.

The charged Higgs boson (H^+) coupling to quarks in 2HDM-II is

$$\mathcal{L}_Y = \bar{u}_i \big[\cot\beta\, \lambda^u_i V_{ij} L + \tan\beta\, V_{ij} \lambda^d_j R \big] d_j\, H^+ + \text{h.c.}, \tag{565}$$

Table 146. A snapshot of the discovery potential of the selected NP model for Belle II observables: semi-leptonic and leptonic B decays. See the caption of Table 145 for an explanation of the symbols.

Observables	Experimental sensitivity	Multi-Higgs models (Sect. 17.2)	Generic SUSY	MFV (Sect. 17.3)	Z' models (Sect. 17.6.1)	Gauged flavor (Sect. 17.6.2)	3-3-1 (Sect. 17.6.3)	Left–right (Sect. 17.6.4)	Leptoquarks (Sect. 18.3.1)	Compositeness (Sect. 17.7)	Dark sector (Sect. 16.1)
Inclusive semi-leptonic B decays:											
$A_{\rm CP}(B^0_d \to X\ell\bar{\nu})$	★★★	★	★★★	★	★★★	×	★★★	★	×	□	★
$A_{\rm CP}(B^0_s \to X\ell\bar{\nu})$	★★★	★	★★★	★	★★★	×	★★★	★	×	□	×
$B \to D^{(*)}\tau\bar{\nu}$:											
Branching ratio	★★	★★	×	×	×	×	×	★	★★★	★	★
q^2	★★	★★★	×	×	×	×	×	★★	★★★	★	★
τ properties	★★★	★★★	×	×	×	×	×	★★	★★★	★	★
$B \to \pi\tau\bar{\nu}$:											
Branching ratio	★★	★★	×	×	×	×	×	★	★★★	□	★
q^2	★★	★★★	×	×	×	×	×	★★	★★★	□	★
τ properties	★★★	★★★	×	×	×	×	×	★★	★★★	□	★
Leptonic B decays:											
$\mathcal{B}(B^+ \to \tau^+\nu)$	★★★	★★★	×	★	×	×	×	★	★★	□	★★
$\mathcal{B}(B^+ \to \mu^+\nu)$	★★★	★★	×	★	×	×	×	★	★★★	×	★★★
$\mathcal{B}(B^0_{d,s} \to \tau\tau)$	★★★	★★	★★	★	★	×	★	×	★★★	□	×
$\mathcal{B}(B^0_{d,s} \to \tau^\pm\ell^\mp)$	□	★	★	×	★	×	★	×	★★★	□	×

where V is the CKM matrix, $\tan\beta$ is the ratio of the VEVs of the two doublets, and $\lambda_i \equiv \sqrt{2}m_i/v$ are the diagonalized Yukawa couplings related to the quark mass m_i and the Higgs vacuum expectation value $v = 246\,\text{GeV}$. In 2HDM-II the charged leptons couple analogously to d-type quarks.

Due to a power suppression of the leading SM contribution to the effective $bs\gamma$ coupling, it was found [1866] in the late 1980s that logarithmic corrections from the H^+ loop can have a significant impact. In addition, due to the dipole or $\sigma_{\mu\nu}m_bR$ form of the $bs\gamma$ coupling, one could have a $\cot\beta$ factor from the coupling to top at one side of the loop compensating a $\tan\beta$ factor at the other side needed for the m_b factor. There is thus a $\tan\beta$-independent H^+ effect that turns out to be constructive with the SM contribution, which makes $B \to X_s\gamma$ a powerful tool to constrain m_{H^+}. Of course, QCD corrections and other sophisticated effects have to be taken into account, which have seen dramatic progress over the past two decades, as discussed briefly in Sect. 9.2.1. The recent Belle update [425] of $B \to X_s\gamma$ is slightly lower than the SM expectation in central value, giving rise to the stringent bound $m_{H^+} > 570\,\text{GeV}$ [1867].

Table 147. A snapshot of the discovery potential of the selected NP model for Belle II observables: electroweak penguin and radiative B decays, including lepton flavor-violating channels. See the caption of Table 145 for an expkanation of the symbols.

Observables	Experimental sensitivity	Multi-Higgs models (Sect. 17.2)	Generic SUSY	MFV (Sect. 17.3)	Z' models (Sect. 17.6.1)	Gauged flavor (Sect. 17.6.2)	3-3-1 (Sect. 17.6.3)	Left–right (Sect. 17.6.4)	Leptoquarks (Sect. 18.3.1)	Compositeness (Sect. 17.7)	Dark sector (Sect. 16.1)
Semi-leptonic $b \to s$ penguin decays:											
$B \to K^{(*)}\ell\ell$ angular	★★	×	×	★★	★★	×	★★	×	★★★	★★	×
$R(K^*)$, $R(K)$	★★	×	×	×	★★	×	★★	×	★★★	★★	×
$\mathcal{B}(B \to X_s\ell\ell)$	★★★	×	×	★★★	★★	×	★★	×	★★★	★★	×
$R(X_s)$	★★★	×	×	×	★★	×	★★	×	★★★	★★	×
$\mathcal{B}(B \to K^{(*)}\tau\tau)$	★★★	★★★	×	★	★	×	★	×	★★★	★	×
$\mathcal{B}(B \to X_s\tau\tau)$	□	★★★	×	★	★	×	★	×	★★★	★	×
$\mathcal{B}(B \to K^{(*)}\nu\nu)$	★★★	×	×	★	★	×	★	×	★★★	★	×
$\mathcal{B}(B \to X_s\nu\nu)$	□	×	×	★	★	×	★	×	★★★	★	×
Semi-leptonic $b \to d$ penguin decays:											
$B \to \pi\ell\ell$ angular	★★	×	×	★★	★★	×	★★	×	★★★	★	×
$R(\rho)$, $R(\pi)$	★★	×	×	×	★★	×	★★	×	★★★	★	×
$\mathcal{B}(B \to X_d\ell\ell)$	★★★	×	×	★★★	★★	×	★★	×	★★★	★	×
$R(X_d)$	★★★	×	×	×	★★	×	★★	×	★★★	★	×
$\mathcal{B}(B \to \pi\tau\tau)$	□	★★★	×	★	★	×	★	★	★★★	★	×
$\mathcal{B}(B \to \pi\nu\nu)$	★★★	×	×	★	★	×	★	×	★★★	★	×
Semi-leptonic LFV B decays:											
$\mathcal{B}(B \to Xe^{\pm}\mu^{\mp})$	★★★	★	★	×	★	×	★	×	★★★	□	×
$\mathcal{B}(B \to K^{(*)}\tau\ell)$	★	★	★	×	★	×	★	×	★★★	□	×
$\mathcal{B}(B \to \pi\tau\ell)$	★	★	★	×	★	×	★	×	★★★	□	×
Radiative penguins:											
$\mathcal{B}(B \to X_s\,\gamma)$	★★★	★★★	★★★	★★★	★	★★	★	★	★	★★★	×
$A_{CP}(B \to X_{s+d}\,\gamma)$	★★★	★★★	★★★	×	★	★	★	★★	★	★	×
$S_{CP}(B^0_d \to K^0_S\pi^0\,\gamma)$	★★★	★★★	★★★	★★★	★	★	★	★★	★	★★★	×
$S_{CP}(B^0_d \to \rho\,\gamma)$	★★★	★★★	★★★	★★★	★	★	★	★★	★	□	×
$B^0_s \to \eta^{(\prime)}\gamma$ lifetime	★★★	★★★	★★★	★★★	★	★	★	★★	★	□	×

A second powerful constraint on H^+ comes from a tree-level effect in $B^+ \to \tau^+\nu_\tau$, as discussed in Sect. 8.3.1. It is rather interesting that [238] $\mathcal{B}^{\text{2HDM-II}}/\mathcal{B}^{\text{SM}}[B^+ \to \tau^+\nu_\tau] = r_H$, where

$$r_H = \left(1 - \tan^2 m^2_{B^+}/m^2_{H^+}\right) \tag{566}$$

Table 148. A snapshot of the discovery potential of the selected NP model for Belle II observables: τ decays. See the caption of Table 145 for an explanation of the symbols.

Observables	Experimental sensitivity	Multi-Higgs models (Sect. 17.2)	Generic SUSY	MFV (Sect. 17.3)	Z' models (Sect. 17.6.1)	Gauged flavor (Sect. 17.6.2)	3-3-1 (Sect. 17.6.3)	Left–right (Sect. 17.6.4)	Leptoquarks (Sect. 18.3.1)	Compositeness (Sect. 17.7)	Dark sector (Sect. 16.1)
τ tree decays:											
$\mathcal{B}(\tau \to K\nu)/\mathcal{B}(\tau \to \pi\nu)$	★★★	★★	×	×	×	×	×	★	★★★	□	★★
$\mathcal{B}(\tau \to K^*\nu)/\mathcal{B}(\tau \to \rho\nu)$	★★★	×	×	×	×	×	×	★	★★★	□	★★
$\tau \to \mu$ decays:											
$\tau \to \mu\gamma$	★★★	★	★★★	★	★	★	★	×	★	★★★	□
$\tau \to \mu\pi^0$	★★★	★	★★	×	★★★	×	★★★	×	★★★	□	□
$\tau \to \mu K^0_S$	★★★	★	★	×	★	×	★	×	★★★	□	□
$\tau \to \mu\rho^0$	★★★	×	★★	×	★★★	×	★★★	×	★★★	□	□
$\tau \to \mu K^{0*}$	★★★	×	★	×	★	×	★	×	★★★	□	□
$\tau^- \to \mu^-\ell^-\ell^+$	★★	★★	★	×	★★★	★★★	★★★	×	★	★★★	□
$\tau^- \to \mu^-\mu^-e^+$	★★	★	×	×	★	★★★	★	×	×	★★★	□
$\tau \to e$ decays:											
$\tau \to e\gamma$	★★★	★	★★★	★	★	★	★	×	★	★★★	□
$\tau \to e\pi^0$	★★★	★	★★	×	★★★	×	★★★	×	★★★	□	□
$\tau \to eK^0_S$	★★★	★	★	×	★	×	★	×	★★★	□	□
$\tau \to e\rho^0$	★★★	×	★★	×	★★★	×	★★★	×	★★★	□	□
$\tau \to eK^{0*}$	★★★	×	★	×	★	×	★	×	★★★	□	□
$\tau^- \to e^-\ell^-\ell^+$	★★	★★	★	×	★★★	★★★	★★★	×	★	★★★	□
$\tau^- \to e^-e^-\mu^+$	★★	★	×	×	★	★★★	★	×	×	★★★	□
τ CP violation:											
τ EDM	★★★	□	□	×	□	□	□	□	□	□	□
$A_{CP}(\tau \to K^0_S\pi\nu)$	★★★	★	★	×	×	×	×	★	★★★	□	□

involves only physical parameters, with no dependence on hadronic quantities. Measurements of $B \to \tau\nu$ came much later than $B \to X_s\gamma$ and provided another strong constraint on m_{H^+} and $\tan\beta$, as already discussed in Sect. 8.3, which has been a main driver for the Belle II upgrade, especially in earlier years.

In 2012, however, BaBar announced their measurements of $R_D \equiv B(B \to D\tau\nu)/B(B \to D\ell\nu)$ and the analogously defined R_{D^*}, and claimed to rule out 2HDM-II, albeit with a low statistical significance. The main feature of these data are branching ratios which are *higher* than the SM prediction, while the 2HDM-II predicts *lower* branching ratios, unless the 2HDM contribution is so large that it overcompensates the SM piece. While several measurements by Belle are closer

Table 149. A snapshot of the discovery potential of the selected NP model for Belle II observables: D decays and dark sector. See the caption of Table 145 for an explanation of the symbols.

Observables	Experimental sensitivity	Multi-Higgs models (Sect. 17.2)	Generic SUSY	MFV (Sect. 17.3)	Z' models (Sect. 17.6.1)	Gauged flavor (Sect. 17.6.2)	3-3-1 (Sect. 17.6.3)	Left–right (Sect. 17.6.4)	Leptoquarks (Sect. 18.3.1)	Compositeness (Sect. 17.7)	Dark sector (Sect. 16.1)
Charm tree decays:											
$\mathcal{B}(D^+ \to \ell\nu)/\mathcal{B}(D_s^+ \to \ell\nu)$	★★★	★	×	×	×	×	×	×	★★★	□	★
$\mathcal{B}(D_s^+ \to \tau\nu)$	★★★	★★	×	★	×	×	×	×	★★★	□	★
$\mathcal{B}(D^+ \to \tau\nu)/\mathcal{B}(D_s^+ \to \tau\nu)$	★★★	★★	×	×	×	×	×	×	★★★	□	★
$A_{CP}(D^+ \to \pi^+\pi^0)$	★★★	★	★	×	★★	×	★★	★★	×	□	×
$A_{CP}(D^0 \to \pi^0\pi^0)$	★★★	×	★	×	★	×	★	★	×	□	×
Charm FCNC decays:											
$D^0 \to \gamma\gamma$	★★★	★	★	×	★	×	★	×	★	□	×
$D^0 \to \mu^+\mu^-$	★★★	★	★	×	★	×	★	×	★★	□	×
$D^0 \to e^+e^-$	★★★	★	★	×	★	×	★	×	★★	□	×
$D^0 \to$ invisible	★★★	★	★	×	★	×	★	×	★★	□	×
Dark sector (boson A', fermion χ):											
$e^+e^- \to A' \to$ invisible	★★★	×	×	□	×	×	×	×	×	×	★★★
$e^+e^- \to A' \to \ell\ell$	★★★	★	×	□	★	×	★	×	×	×	★★★
$e^+e^- \to A'\gamma$	★★★	★	×	□	★	×	★	×	×	×	★★★
$B \to$ invisible	★★★	×	×	□	★	×	★	×	★★★	×	★★★
$B \to KA'$	★★★	×	×	□	×	×	×	×	×	×	★★★
$B \to \pi A'$	★★★	×	×	□	×	×	×	×	×	×	★★★
$B^+ \to \mu^+\chi$	★★★	×	×	□	×	×	×	×	×	×	★★★
$B^+ \to \mu^+\nu A'$	★★★	×	×	□	×	×	×	×	×	×	★★★
$\Upsilon(3S) \to \gamma A'$	★★★	×	×	□	×	×	×	×	×	×	★★★

to the SM than the BaBar result, the 2015 result of LHCb for R_{D^*} complied with the BaBar data, which elevated the interest from the broader community. This was for R_{D^*} using $\tau \to \mu\nu\nu$. In 2017, however, LHCb announced a second measurement of R_{D^*}, now via a three-prong decay of the τ, and the result is more consistent with the SM (and Belle). But the $R_{D^{(*)}}$ anomaly is far from gone and is a main target for Belle II, as discussed in Sect. 8.4.1. Combining various inputs, the effect of a scalar boson is not the most favored explanation. Given the volatility of the experimental situation, it only makes experimental clarification more imperative.

One impact of the $R_{D^{(*)}}$ anomaly is the gain in interest in G2HDM, i.e. 2HDM without a discrete Z_2 symmetry. As pointed out [1868] by Glashow and Weinberg in 1977, having two Yukawa matrices contributing to the mass matrix of each type of charged fermion would result in flavor-changing Higgs

couplings. They proposed the natural flavor conservation (or NFC) condition, that there can be only one Yukawa matrix per mass matrix, and hence these matrices can be simultaneously diagonalized. This is usually implemented by a Z_2 symmetry in 2HDM, such as u- and d-type quarks receive mass each from its own Higgs doublet, resulting in Eq. (565), where there is no additional free parameter other than $\tan\beta$. With the advent of the $R_{D^{(*)}}$ anomaly, models without NFC were proposed [254–256,279], utilizing the extra Yukawa couplings coming from the second Higgs doublet. Without any discrete Z_2 symmetry to implement NFC, this is in fact the "general" 2HDM, and was earlier called [1869] Model III, to distinguish it from the two types (if one discounts the freedom on the lepton side) of 2HDM with Z_2.

In G2HDM, which possesses flavor-changing neutral Higgs (FCNH) couplings, the full Yukawa couplings are [1870], in matrix notation,

$$\mathcal{L}_Y = -\sum_{f=u,d} \bar{\mathbf{f}}\left[\left(\frac{\mathbf{M}^f}{v}h^0 - \frac{\boldsymbol{\rho}^f}{\sqrt{2}}H^0\right)\sin(\beta-\alpha) + \left(\frac{\boldsymbol{\rho}^f}{\sqrt{2}}h^0 + \frac{\mathbf{M}^f}{v}H^0\right)\cos(\beta-\alpha) - i\,\mathrm{sgn}\,(Q_f)\frac{\boldsymbol{\rho}^f}{\sqrt{2}}A^0\right]\mathbf{f} - \left[\bar{\mathbf{u}}\left(\boldsymbol{\rho}^{u\dagger}\mathbf{V}L - \mathbf{V}\boldsymbol{\rho}^d R\right)\mathbf{d}\,H^+ + \text{h.c.}\right], \tag{567}$$

where $\mathbf{M}^f$ is the diagonal mass matrix for $f = u$- or d-type quarks, whereas $\boldsymbol{\rho}^f$ is likewise the Yukawa matrix for the doublet that is not responsible for mass generation. Keeping the convention of the 2HDM-II, $\cos(\beta-\alpha)$ is the h^0–H^0 mixing angle. But since $\tan\beta$ is unphysical when there is no Z_2 to distinguish the two doublets, a better notation is to call it $\cos\gamma$. Note that, in the $\cos(\beta-\alpha) \equiv \cos\gamma \to 0$ limit, h^0 couplings become diagonal and would be equal to that of the SM Higgs boson, while H^0 and A^0 can have exotic new Yukawa couplings. From the fact that we see no deviations so far [1871] in h^0 properties from SM Higgs, we seem to be either close to this "alignment" limit or close to the limit of a diagonal ρ^f. For a realization of the second possibility, see the Cheng–Sher ansatz [1872].

Comparing Eq. (567) with Eq. (565), the $\boldsymbol{\rho}^f$ couplings modulate the CKM matrix of the charged Higgs couplings, which various authors have utilized [254–256,279] to account for the $R_{D^{(*)}}$ anomaly, and the role of Belle II is to clarify the experimental situation. It is certainly more complicated than the $\cot\beta$, $\tan\beta$, and SM Yukawa factors of Eq. (565). It also means that the aforementioned bound [1867] on m_{H^+} for 2HDM-II no longer holds. G2HDM brings new flavor (exotic Yukawa couplings) parameters into the game, which should be welcome news for Belle II in terms of potential measurables. So, just what are the $\boldsymbol{\rho}^u$ and $\boldsymbol{\rho}^d$ (and likewise $\boldsymbol{\rho}^\ell$) matrices? Since one has two Higgs doublets, one combination of the two Yukawa matrices gives the mass matrix, $\mathbf{M}^f$, which is diagonalized in the usual way. An orthogonal combination of the two Yukawa matrices gives rise to $\boldsymbol{\rho}^f$.

The possibility of new Yukawa couplings ρ^f_{ij} should interest Belle II practitioners directly. Besides the $R_{D^{(*)}}$ anomaly, we mention two other examples. The ratio of $B^+ \to \tau^+\nu_\tau$ and $B^+ \to \mu^+\nu_\mu$, or $R_{\rm pl}$, is fixed kinematically for both SM and 2HDM-II. In G2HDM, ρ^ℓ_{ij} is non-trivial and modulated by both λ_μ and λ_τ, so both τ or μ channels can pick up NP effects. This makes the precision measurement of $B^+ \to \mu^+\nu_\mu$ of interest on its own, where the recent hint [242] from the untagged analysis of the full Belle dataset is encouraging. Second, we have already mentioned the link between $\tau \to \mu\gamma$ and $h^0 \to \tau\mu$, but the link is in fact more subtle. Naively, the link is through a one-loop diagram involving $\rho_{\tau\mu}$. However, even if this parameter is small, a two-loop mechanism [1527,1873] connects with ρ_{tt}! Thus, there are two sources which can generate $\tau \to \mu\gamma$, and can be probed at Belle II.

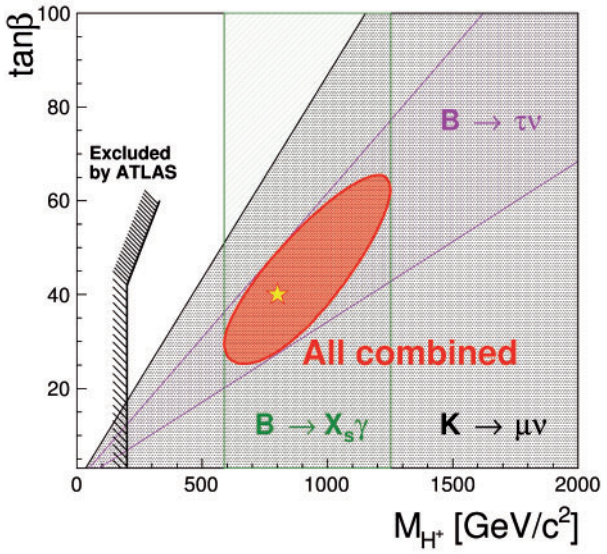

Fig. 213. tan β vs. the charged-Higgs mass M_{H^+} for a discovery scenario with M_H=800 GeV and tan $\beta = 40$ in type II 2HDM. Note that current data on $B \to D^{(*)}\tau\nu$ are incompatible with this model and are not included in this figure.

In 2HDM-II, the alignment phenomenon of $\cos(\beta-\alpha) \to 0$ arises automatically in the decoupling limit of very heavy non-standard Higgs bosons [1855]. In scenarios with lighter H^+, A^0, H^0 bosons the alignment limit can only be realized via fine-tuning. This is because α depends on details of the Higgs potential, and there is no reason for β and α to differ by $\pm\pi/2$.

To this end, a discovery scenario is studied for the charged Higgs with a mass of 800 GeV/c^2 at tan $\beta = 40$. Figure 213 shows the result for 50 ab^{-1} in a projection fit given by the NP-Japan group. The figure shows a region with a 1 σ signal confidence level constraint. The constraint is obtained with a global fit to the predicted branching fractions of $B \to \tau\nu$, $B \to X_s\gamma$, and $K \to \mu\nu$ in a 50 ab^{-1} projected data sample assuming the 2HDM of type II. The central values of the predictions are obtained using `SuperIso` [1874] with the given parameter values in the type-II 2HDM model. The errors on branching fraction measurements of $B \to \tau\nu$ and $B \to X_s\gamma$ are as described in the previous chapters. As for the $K \to \mu\nu$, the uncertainty on the lattice calculation is assumed to improve by a factor of three from the present, while the experimental error is assumed to be unchanged from the value quoted in HFLAV 2016 [230]. In the plot, the upper limit obtained by the ATLAS experiment in 2016 [1875] is overlaid.

17.3. Minimal flavor violation

Author: Christopher Smith

Phenomenologically, FCNC observables can be described as driven by effective operators. For example, $B \to X_{d,s}\nu\bar{\nu}$ and $B_{s,d} \to \mu^+\mu^-$ attract contributions from

$$\mathcal{H}_{\text{eff}} = \left[\frac{C_{\text{SM}}^{IJ}}{M_W^2} + \frac{C_{\text{NP}}^{IJ}}{\Lambda^2}\right](\bar{Q}^I\gamma_\mu Q^J)H^\dagger D_\mu H, \tag{568}$$

with $I, J = 1, 2, 3$, Q the left quark doublet, H the Higgs doublet, D^μ the SM covariant derivative, and the NP scale Λ presumably higher than M_W. What makes FCNC so interesting is that the SM Wilson coefficients C_{SM}^{IJ}, corresponding to the Z penguin [1876], are severely suppressed by small

CKM matrix elements. Since this is up to now in line with experimental results, the NP contributions tuned by $\mathcal{C}_{\rm NP}^{IJ}$ have to be at least as suppressed if Λ is to be only slightly above the electroweak scale, as required to prevent a strong hierarchy problem.

In practice there is no way to tell whether these suppressions are natural or not. Indeed, the naive definition of naturality—that Lagrangian parameters should be $\mathcal{O}(1)$—makes no sense in the flavor sector, where the known Yukawa couplings $\mathbf{Y}_{u,d,e}$ are already highly non-natural. So, the best strategy to define a meaningful naturality principle for the NP flavor couplings is to compare them with the Yukawa couplings. There would be no flavor puzzle if the hierarchies of the NP flavor couplings required to pass the experimental constraints are similar to those observed for the quark and lepton masses and mixing parameters.

Introducing minimal flavor violation To proceed, this similarity statement must be made precise. We ground it on a symmetry principle and deem natural those NP flavor couplings that respect minimal flavor violation [621]. This hypothesis can be defined in two steps [1877]: the first specifies how the flavor couplings are to be constructed, and the second requires the free parameters to be natural [1878,1879].

Construction principle The first condition for MFV is expressed straightforwardly in the spurion language: all the flavor couplings are required to be invariant under the flavor symmetry $G_{\rm F} = {\rm U}(3)^5$ exhibited by the flavor-independent SM gauge interactions [1865,1880], but only the spurions required to account for the fermion masses and mixings are allowed. By this we mean that $G_{\rm F}$ can be formally restored at the level of the whole SM if the Yukawa couplings $\mathbf{Y}_{u,d,e}$ are given definite $G_{\rm F}$ transformation rules, i.e. are promoted to spurions.[64] This purely formal manipulation provides us with a very useful tool. As soon as the SM Lagrangian becomes invariant under $G_{\rm F}$, the SM amplitude for any possible process must also be expressible as manifestly $G_{\rm F}$ invariant. Crucially, this invariance may require inserting Yukawa spurions in a very specific way in the amplitude. Its flavor structure can thus be established quite precisely without embarking on any computation.

In the presence of NP, allowing for only $\mathbf{Y}_{u,d,e}$ is clearly the minimal spurion content, since anything less would be insufficient to reproduce the well-known fermionic flavor structures. Typically, this does not forbid NP from introducing new flavor couplings, but forces them to be expressed as polynomials in the allowed spurions, that is, as functions of the Yukawa couplings $\mathbf{Y}_{u,d,e}$.

To illustrate this, let us take the effective operator in Eq. (568). Both Wilson coefficients $\mathcal{C}_{\rm SM}^{IJ}$ and $\mathcal{C}_{\rm NP}^{IJ}$ are 3×3 matrices of complex numbers in flavor space. They explicitly break $G_{\rm F}$ whenever $\mathcal{C}_{\rm SM}, \mathcal{C}_{\rm NP} \neq \mathbf{1}$, in which case their entries depend on the basis chosen for the quark fields. To formally restore the $G_{\rm F}$ invariance, $\mathcal{C}_{\rm SM}$ and $\mathcal{C}_{\rm NP}$ must transform contragradiantly to the fields. This can be achieved thanks to the presence of the spurions. There are infinitely many combinations of spurions transforming like $\mathcal{C}_{\rm SM,NP}$, so in full generality they are written as expansions,

$$\mathcal{C}_i = z_1^i \mathbf{1} + z_2^i \mathbf{Y}_u^\dagger \mathbf{Y}_u + z_3^i \mathbf{Y}_d^\dagger \mathbf{Y}_d + z_4^i \{\mathbf{Y}_d^\dagger \mathbf{Y}_d, \mathbf{Y}_u^\dagger \mathbf{Y}_u\} + \cdots , \tag{569}$$

for some a priori complex coefficients z_j^i.

Once this expansion is written down, the spurions have to be frozen back to their physical values in some basis. For example, we can now set $v\mathbf{Y}_u \sim \mathbf{m}_u V_{\rm CKM}$, $v\mathbf{Y}_d \sim \mathbf{m}_d$ with $\mathbf{m}_{u,d}$ the diagonal

[64] To force a Lagrangian parameter to transform under some symmetry, it is implicitly promoted to a non-propagating scalar field called a spurion, whose VEV matches the parameter's physical value.

quark mass matrices, and v the Higgs VEV. But, without any constraint on the z_i, any coupling can be expressed in this way [1881]. The infinite series of powers of $\mathbf{Y}_u^\dagger \mathbf{Y}_u$ and $\mathbf{Y}_d^\dagger \mathbf{Y}_d$ form a complete basis for the space of complex 3×3 matrices. So, the flavor couplings $\mathcal{C}_i$ can take on any value; they could even have all their entries of $\mathcal{O}(1)$.

Naturality principle The spurion expansions are not entirely void of physical content. The numerical value of a flavor coupling like $\mathcal{C}^{IJ}_{\text{SM,NP}}$ depends on the basis chosen for the quark fields, and this renders any assertion on the size of the NP flavor couplings ambiguous. On the other hand, by construction, the coefficients occurring in the spurion expansions are basis independent. In particular, the experimental information drawn from flavor observables can be unambiguously translated into values or bounds for the coefficients [1877]. Three situations can arise:

MFV flavor structure: The second condition for MFV is for all coefficients to be natural, $z_i \sim \mathcal{O}(1)$. In that case, all the flavor couplings inherit the peculiar numerical hierarchies of the spurions. For example, the leading non-diagonal effects for $\mathcal{C}_i$ arise from

$$\mathcal{C}_i^{I\neq J} \approx z_2^i \, (\mathbf{Y}_u^\dagger \mathbf{Y}_u)^{IJ} \approx z_2^i \, (m_t^2/v^2) \, V_{3I}^* V_{3J} \tag{570}$$

in the down-quark mass basis. This perfectly reproduces the CKM coefficients occurring for the SM Z penguin, with $z_2^{\text{SM}} \sim \alpha/4\pi$. If these suppressions of $\mathcal{C}_{\text{NP}}^{I\neq J}$ are necessary and sufficient for all FCNC processes, MFV solves the flavor puzzles.

Fine-tuned flavor structure: If some coefficients are still required to be very small, $z_i \ll 1$, the suppression brought in by MFV is not sufficient and one needs either an NP scale Λ much higher than TeV, or a complementary/alternative fine-tuning mechanism for that specific flavor coupling. At present, this is partly the case for flavor-blind CP-violating effects, both at the NP and SM levels (where it is known as the strong CP problem).

Generic flavor structure: Some coefficients are required to be very large, $z_i \gg 1$, for instance if some FCNC processes are found to significantly deviate from their SM values. This would signal NP, of course, but also the presence of a new flavor structure within its dynamics. Indeed, though the terms of the expansions in Eq. (570) form a complete basis, they barely do so; they nearly live in a lower-dimensional subspace. Therefore, a flavor structure not sufficiently aligned with $\mathbf{Y}_{u,d,e}$ generates huge coefficients when projected onto the expansions in Eq. (570).

MFV thus offers an unambiguous test of naturality. It permits precise characterization of the flavor puzzles and identification of non-standard flavor structures.

Why should we trust MFV? In view of the severe restrictions MFV imposes on the NP flavor structures, it would seem appropriate to ground it on some full-fledged dynamical mechanism. The problem is that this may be far too ambitious. Its origin may lie in the physics responsible for the observed patterns of quark and lepton masses and mixings, in which case MFV may be explained only once a comprehensive solution to all the flavor issues is found. A second point is that it is actually not necessary to explain the origin of MFV or the internal structures of the spurions dynamically to interpret the MFV hypothesis in very meaningful and universal ways. Let us discuss three such phenomenological interpretations.

Utilitarian interpretation: MFV is at the very least a convenient tool. First, it offers an improved parameterization. Instead of working with the ambiguous values of the couplings in some basis, one deals with the value of the coefficients of the expansions. There are as many free parameters in both descriptions [1881]. Second, the numerical size of the expansion coefficients is the only meaningful measure of the naturality of the NP couplings. It would not be consistent to say that an NP flavor coupling is unnatural if it is no more fine-tuned than those of the SM. So, MFV could be viewed as an *improved dimensional analysis* tool, designed to tackle the highly hierarchical flavor sector.

Pragmatic interpretation: Let us assume that some NP exists whose dynamics is blind to the flavor of the fields. Its flavor sector is thus trivial and the only G_F-breaking term in the whole SM plus NP Lagrangian are the usual Yukawa couplings only.

In practice, such a flavor-blind NP setting is not tenable because the SM is not flavor blind. The non-trivial SM flavor mixings will spill onto the NP flavor sector through radiative corrections and/or RG evolution [1881–1883]. At least at the loop level, the flavor-blind NP dynamics combined with the SM flavor mixings will generate new contributions to the FCNC. This is where MFV enters since all the flavor transitions remain tuned by the Yukawa couplings. MFV is not a hypothesis in this case; it is strictly valid. So, MFV emerges as *the least acceptable flavor violation* for the NP sector.

Redundancy interpretation: MFV can be understood as a statement about the mechanism at the origin of the flavor structures. To illustrate this, imagine a low-energy theory with two elementary flavor couplings $\mathbf{Y}$ and $\mathbf{A}$, which can be thought of as the Yukawa and NP couplings. At the very high scale, some flavor dynamics is active and introduces a single explicit breaking of G_F, which we call $\mathbf{X}$. The two low-energy flavor couplings are induced by this elementary flavor breaking, so it is possible to express them as

$$\begin{cases} \mathbf{Y} = x_1^Y \mathbf{1} + x_2^Y \mathbf{X} + x_3^Y \mathbf{X}^2, \\ \mathbf{A} = x_1^A \mathbf{1} + x_2^A \mathbf{X} + x_3^A \mathbf{X}^2. \end{cases} \tag{571}$$

If the flavor dynamics was known, these coefficients could be computed explicitly. Lacking this, we simply assume they are natural. Also, for these expansions to make sense, powers of $\mathbf{X}$ must not grow unchecked. A sufficient condition is $\langle \mathbf{X} \rangle \lesssim 1$, since then all $\mathbf{X}^{n>2}$ can be eliminated in terms of $\mathbf{1}$, $\mathbf{X}$, and $\mathbf{X}^2$ without upsetting $x_i \sim \mathcal{O}(1)$. Under this condition, from Eq. (571), we can get rid of the unknown high-energy spurion $\mathbf{X}$ and derive the low-energy MFV expansions

$$\begin{cases} \mathbf{A} = y_1 \mathbf{1} + y_2 \mathbf{Y} + y_3 \mathbf{Y}^2, \\ \mathbf{Y} = a_1 \mathbf{1} + a_2 \mathbf{A} + a_3 \mathbf{A}^2, \end{cases} \tag{572}$$

for some y_i, a_i coefficients. Naturality is preserved since $y_i, a_i \sim \mathcal{O}(1)$ when $x_i \sim \mathcal{O}(1)$. So, in this interpretation, neither the Yukawa $\mathbf{Y}$ nor the NP coupling $\mathbf{A}$ are fundamental, and the MFV expansions are understood as the only low-energy observable consequences of their *intrinsic redundancy*.

Some MFV frameworks and expectations MFV strongly constrain the NP flavor structures, but not the rest of the dynamics. Typically, MFV is very effective at relating different observables since their scaling essentially derives from that of the CKM coefficients, but not so much at predicting their overall size, which depends essentially on the masses of the NP particles. Let us give a few examples.

Table 150. Effective NP scales derived under various hypotheses for the Wilson coefficient $\mathcal{C}_{\rm NP}^{IJ}$, assuming its contribution at most totally saturates the experimental measurements. The last two columns correspond to MFV, with the CKM matrix elements $|V_{tI}^* V_{tJ}| \approx 4 \cdot 10^{-2}, 8 \cdot 10^{-3}, 3 \cdot 10^{-4}$ for $(I,J) = (b,s),(b,d),(s,d)$, respectively. The last column further assumes a loop-level NP contribution, in which case $\mathcal{C}_{\rm NP}$ essentially scales like $\mathcal{C}_{\rm SM}$ and Λ ends up close to the electroweak scale.

$\mathcal{C}_{\rm NP}^{IJ}$	$\mathcal{O}(1)$	$\mathcal{O}(g^2/4\pi)$	$\mathcal{O}(\lvert V_{tI}^* V_{tJ}\rvert)$	$\mathcal{O}(\lvert V_{tI}^* V_{tJ}\rvert \times g^2/4\pi)$
$B_s \to \mu^+\mu^-$	$\Lambda \gtrsim 12\,\text{TeV}$	$\Lambda \gtrsim 2.2\,\text{TeV}$	$\Lambda \gtrsim 2.5\,\text{TeV}$	$\Lambda \gtrsim 0.45\,\text{TeV}$
$B_d \to \mu^+\mu^-$	$\Lambda \gtrsim 17\,\text{TeV}$	$\Lambda \gtrsim 3\,\text{TeV}$	$\Lambda \gtrsim 1.5\,\text{TeV}$	$\Lambda \gtrsim 0.27\,\text{TeV}$
$K^+ \to \pi^+\nu\bar{\nu}$	$\Lambda \gtrsim 100\,\text{TeV}$	$\Lambda \gtrsim 18\,\text{TeV}$	$\Lambda \gtrsim 1.8\,\text{TeV}$	$\Lambda \gtrsim 0.33\,\text{TeV}$

Table 151. As Table 150, but for the meson mixing operator $\mathcal{Q}_{WW}^{IJ} \equiv (\bar{Q}^I \gamma_\mu Q^J)(\bar{Q}^I \gamma^\mu Q^J)$, induced in the SM by the W box diagram.

$(\mathcal{C}_{WW}^{IJ})_{\rm NP}$	$\mathcal{O}(1)$	$\mathcal{O}((g^2/4\pi)^2)$	$\mathcal{O}(\lvert V_{tI}^* V_{tJ}\rvert^2)$	$\mathcal{O}(\lvert V_{tI}^* V_{tJ}\rvert^2 \times (g^2/4\pi)^2)$
B_s–$\bar{B}_s^0$	$\Lambda \gtrsim 130\,\text{TeV}$	$\Lambda \gtrsim 4\,\text{TeV}$	$\Lambda \gtrsim 5\,\text{TeV}$	$\Lambda \gtrsim 0.17\,\text{TeV}$
B_d^0–$\bar{B}_d^0$	$\Lambda \gtrsim 650\,\text{TeV}$	$\Lambda \gtrsim 21\,\text{TeV}$	$\Lambda \gtrsim 5\,\text{TeV}$	$\Lambda \gtrsim 0.16\,\text{TeV}$
K^0–$\bar{K}^0$	$\Lambda \gtrsim 24\,000\,\text{TeV}$	$\Lambda \gtrsim 800\,\text{TeV}$	$\Lambda \gtrsim 8\,\text{TeV}$	$\Lambda \gtrsim 0.25\,\text{TeV}$

Model-independent MFV: Let us take again the operator in Eq. (568). The cleanest constraints on $\mathcal{C}_{\rm NP}^{IJ}$ come from leptonic and semi-leptonic processes because the hadronic matrix elements are well controlled theoretically. The golden modes are the $B_{d,s} \to \mu^+\mu^-$ decays, along with $K^+ \to \pi^+\nu\bar{\nu}$ (in principle, the $B_{d,s} \to (K,\pi,\ldots)\nu\bar{\nu}$ or $B_{d,s} \to (K,\pi,\ldots)\ell^+\ell^-$ processes could also be used). Assuming the NP contribution is at most saturating the experimental measurements, we find the values quoted in Table 150. For generic Wilson coefficients, the strongest constraints on Λ come from the kaon sector. Indeed, the experimental results are in good agreement with the SM, so they roughly scale like the corresponding SM contributions. The kaon sector is the most suppressed by the CKM scaling, hence it is the one leaving the least room for NP. On the other hand, once MFV scalings are enforced, $\mathcal{C}_{\rm NP}^{sd}$ is so suppressed that Λ is allowed to be much lower, and B physics takes the lead. Note, though, that this also means in practice that the NP scale should be very low to induce experimentally visible deviations, especially if the NP dynamics prevents tree-level FCNC.

Looking at Table 150, it is clear though that these B and K decay modes probe similar scales when MFV is active. In that case, and with the prospect of further experimental results on $K^+ \to \pi^+\nu\bar{\nu}$ in the near future, these B decay modes are not the best place to look for new physics. Let us thus consider other observables, and take the operator $\mathcal{Q}_{WW}^{IJ} \equiv (\bar{Q}^I \gamma_\mu Q^J)(\bar{Q}^I \gamma^\mu Q^J)$, relevant for meson–antimeson mixing, and $\mathcal{Q}_\gamma^{IJ} \equiv \bar{D}^I \sigma_{\mu\nu} Q^J F^{\mu\nu} H^C$, for $d^I \to d^J \gamma$ transitions, with Q the quark doublet, D the down-type quark singlet, and $F^{\mu\nu}$ the QED field strength. The corresponding scales are given in Tables 151 and 152. From the MFV point of view, meson mixing does not look very promising to go well beyond the scales probed with K^0–$\bar{K}^0$ (and this gets even worse in the presence of non-standard operators like $(\bar{D}^I Q^J)(\bar{Q}^I D^J)$ to which K^0–$\bar{K}^0$ is particularly sensitive). On the other hand, $b \to s\gamma$ and to a lesser extent $b \to d\gamma$ have the unique ability to probe the magnetic operator, to which K physics is essentially blind in the MFV case [1884]. The only caveat worth keeping in mind is the assumption that $\bar{D}^I \sigma_{\mu\nu} Q^J F^{\mu\nu} H^C$ is not accompanied by $\bar{D}^I \sigma_{\mu\nu} T^a Q^J G_a^{\mu\nu} H^C$, because the latter is already tightly bounded by ε'_K.

Table 152. As Table 150, but for the magnetic operator $\mathcal{Q}_\gamma^{IJ} \equiv \bar{D}^I \sigma_{\mu\nu} Q^J F^{\mu\nu} H^C$. In this case the SM contribution is not neglected, and we use the bounds set in Refs. [427,431,1884].

$(\mathcal{C}_\gamma^{I\neq J})_{\rm NP}$	$\mathcal{O}(1)$	$\mathcal{O}(m_{b,s}/v)$	$\mathcal{O}(\lvert V_{tI}^* V_{tJ}\rvert \times m_{b,s}/v)$	$\mathcal{O}(\lvert V_{tI}^* V_{tJ}\rvert \times g^2/4\pi \times m_{b,s}/v)$
$b \to s\gamma$	$\Lambda \gtrsim 220$ TeV	$\Lambda \gtrsim 34$ TeV	$\Lambda \gtrsim 7$ TeV	$\Lambda \gtrsim 1.2$ TeV
$b \to d\gamma$	$\Lambda \gtrsim 56$ TeV	$\Lambda \gtrsim 9$ TeV	$\Lambda \gtrsim 0.8$ TeV	$\Lambda \gtrsim 0.14$ TeV
$s \to d\gamma$	$\Lambda \gtrsim 220$ TeV	$\Lambda \gtrsim 5$ TeV	$\Lambda \gtrsim 0.1$ TeV	$\Lambda \gtrsim 0.02$ TeV

Supersymmetric MFV: Current constraints from direct searches at the LHC push the mass of supersymmetric particles quite far from the EW scale, so much so that if MFV is enforced, the prospect of observing any deviation in B physics looks dire (see Tables 150, 151, and 152).

There is, however, a caveat. While MFV only affects flavor couplings, this can influence the expected dynamics once in a supersymmetric setting. There are two interesting consequences. First, the squark masses derive nearly entirely from purely supersymmetric flavor couplings (the soft-breaking terms). So MFV restricts the squark mass spectrum, by requiring for example that the left squark mass matrix expresses itself as $\mathbf{M}_{LL}^2 = m_1^{LL}\mathbf{1} + m_2^{LL}\mathbf{Y}_u^\dagger\mathbf{Y}_u + \cdots$ [1885]. One of its predictions is that while in most cases the squarks should be quasi-degenerate, MFV nevertheless permits decoupling the stop. A so-called natural SUSY-like spectrum arises when $m_2^{LL} \approx -m_1^{LL}/\mathrm{tr}(\mathbf{Y}_u^\dagger\mathbf{Y}_u)$, which respects MFV naturality thanks to the large top quark Yukawa coupling [1886]. Thus, the stop could be much lighter than the other squarks, and could play a significant role in FCNC [1887–1889].

Second, the direct searches for supersymmetric particles usually assume that the so-called R parity is enforced. A typical signature then involves significant missing energy, that carried away by the stable lightest sparticle. But once MFV is present, this is not compulsory to satisfy proton decay bounds [1890–1893]. A perfectly viable supersymmetric setting with MFV then emerges, where baryon number violation would be significant when involving the stop. Current bounds on squark and gaugino masses would be evaded [1894]. With in addition a rather light stop from natural-SUSY-like soft-breaking terms, significant supersymmetric effects in FCNC could still occur.

Lepton-flavor violation under MFV: To deal with lepton flavor violation, let us assume that a seesaw mechanism is present. Two new spurions are then relevant at low energy [1895]: the tiny neutrino mass, $v^2\mathbf{Y}_\nu^T(\mathbf{M}_R^{-1})\mathbf{Y}_\nu = U^*\mathbf{m}_\nu U^\dagger$, where $\mathbf{m}_\nu$ is the diagonal left-handed neutrino mass matrix, $\mathbf{M}_R$ is the heavy ν_R Majorana mass matrix, $\mathbf{Y}_\nu$ is the neutrino Yukawa coupling, U the PMNS neutrino mixing matrix, and, more interestingly, an unsuppressed spurion $\mathbf{Y}_\nu^\dagger\mathbf{Y}_\nu$ (which cannot be fully reconstructed out of the available data on $\mathbf{m}_\nu$ and U [1896]).

Let us now consider the $P \to P'\nu^I\bar{\nu}^J$ and $P \to P'\ell^I\bar{\ell}^J$ decay modes with $I \neq J$. When enforcing MFV, operators involving right-handed fermions are heavily suppressed by light fermion masses. The least suppressed operators able to induce these transitions are then of the form $\bar{Q}^I(\mathbf{Y}_u^\dagger\mathbf{Y}_u)^{IJ}Q^J \otimes \bar{L}^K(\mathbf{Y}_\nu^\dagger\mathbf{Y}_\nu)^{KL}L^L$, with L the left-lepton doublet from which $\mathcal{B}(P \to P'\nu^I\bar{\nu}^J) \sim \mathcal{B}(P \to P'\ell^I\bar{\ell}^J)$.

Because the quark and lepton flavor sectors are completely disconnected under MFV (the flavor group factorizes), the hadronic current shows the same suppression as before. With an NP scale only slightly above the EW scale, the $\mathbf{Y}_u^\dagger\mathbf{Y}_u$ insertion alone naturally brings the NP contributions at most at around the SM ones. Then there remain the leptonic currents. Since $\mathbf{m}_\nu \sim \mathbf{Y}_\nu^T(\mathbf{M}_R^{-1})\mathbf{Y}_\nu$, it would appear that taking $\mathbf{M}_R$ sufficiently large would ensure $\mathbf{Y}_\nu \sim \mathcal{O}(1)$, leading to $P \to P'\nu^I\bar{\nu}^J \sim P \to P'\nu^I\bar{\nu}^I$. However, such large $\mathbf{Y}_\nu$ are forbidden by $\ell^I \to \ell^J\gamma$, tuned by the same spurion

insertion $E\mathbf{Y}_e(\mathbf{Y}_\nu^\dagger\mathbf{Y}_\nu)\sigma^{\mu\nu}LH^\dagger F_{\mu\nu}$. Conservatively, we can at most get $(\mathbf{Y}_\nu^\dagger\mathbf{Y}_\nu)^{I\neq J} \sim 1\%$, so that for $I \neq J$, $L = \nu, \ell$, $\mathcal{B}^{\rm MFV}(K \to \pi L^I \bar{L}^J) \lesssim 10^{-15}$ and $\mathcal{B}^{\rm MFV}(B \to (\pi, K) L^I \bar{L}^J) \lesssim 10^{-10}$, well beyond experimental reach. These modes are thus very powerful checks for the presence of new flavor structures, and would in particular react strongly to any NP spurion directly connecting the lepton and quark sectors.

17.4. Models with lepton flavor violation

Author: Nejc Košnik

Lepton flavor is exactly conserved in the SM due to the pattern of the lepton flavor group breaking due to Yukawa couplings, $\mathrm{U}(3)_L \otimes \mathrm{U}(3)_{e_R} \to \mathrm{U}(1)_e \otimes \mathrm{U}(1)_\mu \otimes \mathrm{U}(1)_\tau$, which keeps individual leptonic flavors conserved. To account for the observed neutrino mass differences one can simply introduce a singlet right-handed neutrino(s) with appropriate Yukawa term that breaks leptonic flavor down to lepton number $\mathrm{U}(1)_{e+\mu+\tau}$. LFV processes with charged leptons at low energies[65] are then induced by flavor mixing of virtual neutrinos, where only an extremely small GIM-violating effect of order m_ν^2/m_W^2 survives, making such a framework effectively lepton flavor conserving [1897]. Less theoretically ad hoc frameworks that induce neutrino masses possibly enhance charged LFV (CLFV) processes up to experimentally observable levels. The $\mathrm{U}(1)_e \otimes \mathrm{U}(1)_\mu \otimes \mathrm{U}(1)_\tau$ symmetry is accidental in the SM and is in general expected to be broken in NP models, which makes searches for CLFV processes a very interesting null test of the SM. From the above reasoning it is also evident that NP models can in general be expected to violate lepton flavor. Recent hints of lepton flavor non-universality in $B \to K\ell\ell$ decays and intriguing deviations from the SM predictions in $B \to K^{(*)}\mu\mu$ spectra, if true, generally imply accompanying LFV processes [623]. In this section we first introduce the effective Lagrangian for LFV, testable at Belle II, and provide a brief summary of the level of LFV in representative NP models.

Effective Lagrangian for LFV at Belle II Narrowing our focus, for the time being, to baryon and lepton number-conserving processes involving two (or four) charged leptons, we can set up a model-independent parameterization of heavy NP in terms of the effective Lagrangian of mass dimension six at the electroweak scale [619,620,1898]. There are in total 19 LFV-mediating operators that contain either two or four leptonic fields. This effective theory (SM-EFT) is a sensible starting point in studies of low-energy phenomenology of any NP model with degrees of freedom heavier than the weak scale. More suited to the processes to be studied at Belle II is the effective Lagrangian at scale m_B that is matched to the SM-EFT through renormalization group (RG) running due to the full SM group above the electroweak scale [1898] and due to strong and electromagnetic RG effects below the electroweak scale [396,1899].

The m_B-scale Lagrangian of dimension six can be systematically broken down to

$$\mathcal{L}_{\rm eff} = \mathcal{L}_{\rm eff}^{(D)} + \mathcal{L}_{\rm eff}^{(4\ell)} + \mathcal{L}_{\rm eff}^{(\ell q)} + \mathcal{L}_{\rm eff}^{(G)}, \tag{573}$$

where the definition of the above operators is given in Sect. 14.2.1. Here, $\mathcal{L}_{\rm eff}^{4\ell}$ is the Lagrangian containing four leptons and is mainly responsible for the purely leptonic LFV decays $\tau^- \to \ell'^-\ell'^\mp\ell''^\pm$, that are among the golden channels of Belle II. The semi-leptonic part of the LFV Lagrangian $\mathcal{L}_{\rm eff}^{\ell q}$

[65] Since the outgoing neutrino flavors are not accessible experimentally we need at least two charged leptons in the asymptotic states to tag LFV.

composed of $(\bar{q}q)(\bar{\ell}\ell)$ fields mediates LFV meson (M) decays, $M \to \ell\ell'$, $M \to M'\ell\ell'$, baryon (N) decays $N \to N'\ell\ell'$, and semi-leptonic τ decays, $\tau \to M\ell$ and $\tau \to PP\ell$. A very useful compilation of constraints on operators present in $\mathcal{L}_{\rm eff}^{\ell q}$ was presented in Ref. [1900]. The dipole Lagrangian

$$\mathcal{L}_{\rm eff}^{(D)} = -\frac{m_\tau}{\Lambda^2}\left[C_{DL}\bar{\mu}\sigma^{\mu\nu}P_L\tau + C_{DR}\bar{\mu}\sigma^{\mu\nu}P_R\tau\right]F_{\mu\nu} \tag{574}$$

triggers the radiative LFV decays that are accessible at Belle II, e.g. $\tau \to \mu\gamma, e\gamma$. Phenomenology of leptonic and semi-leptonic meson decays as induced by operators contained within $\mathcal{L}_{\rm eff}^{(\ell q)}$ has been studied in Ref. [1901], whereas the operator basis of $\mathcal{L}_{\rm eff}^{(4\ell)}$ adapted to the $\mu \to 3e$ decay can be found in Eq. (112) of Ref. [1902]. References [124,1903,1904] studied model-independent and model-discriminating aspects of $\tau \to \ell\ell\ell'$ decay. For the role of effective gluonic operators $\mathcal{L}_{\rm eff}^{(G)}$ in $\tau \to \mu\eta^{(\prime)}$ see Refs. [124,1905]. Finally, Belle II prospects for charged LFV in τ decays have been discussed in Sect. 14.2.

Model case studies for LFV LFV processes involving four-fermion vertices $(\bar{q}q)(\bar{\ell}\ell)$, $(\bar{\ell}\ell)(\bar{\ell}\ell)$ can be mediated by tree-level amplitudes with renormalizable couplings in models with neutral mediators such as additional Higgs or Z' gauge bosons. In the two Higgs doublet model (2HDM) with generic Yukawa couplings (also known as Type III 2HDM) leptonic decays of mesons $P \to \ell\ell'$ and purely leptonic decays $\mu \to eee$, $\tau \to \ell\ell\ell'$ are induced by tree-level exchanges of neutral scalars. For moderately large $\tan\beta$ the $\mathcal{B}(\tau \to \mu\gamma)/\mathcal{B}(\tau \to \mu\mu\mu)$ and $\mathcal{B}(\tau \to e\gamma)/\mathcal{B}(\tau \to e\mu\mu)$ could be between 0.1 and $\sim$1, and, taking into account better Belle II sensitivity to decays with three final-state leptons, makes the searches for $\tau \to 3\ell$ more promising [279]. For a study of LFV in the μ–τ sector of the MSSM, see Ref. [1906].

Non-diagonal Z couplings to leptons can be a signature of vector-like leptons where the most promising modes to search for at Belle II involve τ: $B_{(s)} \to \tau\mu, \tau e$, and $\tau \to \mu\phi$ can be of the order 10^{-10} and 10^{-8}, respectively [1907]. In models with additional U(1)$'$ gauge symmetries LFV couplings of a lepton pair to Z or Z' boson are induced at tree level [1908]. In the Z' models LFV is induced due to off-diagonal gauge couplings of Z or Z' to leptons. It was demonstrated that LFV B meson decays are correlated to another golden channel, $B \to K^{(*)}\nu\bar{\nu}$ [1909]. Models with very light Z' contribute dynamically at distances comparable to m_B^{-1} and their effects are not caught by the effective Lagrangian in Eq. (573). A light Z', with a mass above 2 MeV in order to avoid bounds on the number of relativistic degrees of freedom in the early universe, was considered as an explanation of the anomalous muon magnetic moment. However, in such cases $\tau \to \mu Z'$ with Z' subsequently decaying to neutrinos gives too strong a constraint if $m_{Z'} < m_\tau$. For heavier masses, $m_{Z'} > m_\tau$, the scenario can explain $(g-2)_\mu$ provided that Z' couples predominantly to right-handed fermions [1910].

Another mechanism for generating LFV processes is to introduce scalar or vector leptoquarks (LQs) close to the weak scale which are color triplet states and can be singlets, doublets, or triplets under SU(2)$_L$ in order to be able to induce tree-level LFV in $\mathcal{L}_{\rm eff}^{(\ell q)}$, while contributions to $\mathcal{L}_{\rm eff}^{(4\ell)}$ and $\mathcal{L}_{\rm eff}^{(D)}$ are loop induced [1911]. In the leptoquark scenarios it is usually assumed that a single LQ multiplet with well-defined SM quantum numbers is present at a time. Their typical UV embedding are the grand unified theories; however, composite scenarios with LQs can also be constructed [1911]. Tree-level LQ exchanges contribute to $\mathcal{L}_{\rm eff}^{(\ell q)}$ and can thus be most efficiently probed in LFV decays of hadrons or in $\tau \to \ell M$, where M denotes a meson [1912]. The decay $B \to K\mu\tau$ is an important test of the leptoquark scenarios designed to address the lepton flavor universality puzzle R_K and

related anomalies in $B \to K^{(*)}\mu\mu$ spectra [295]. Upper bounds on the golden channel $\tau \to \mu\gamma$ constrain the scalar leptoquark contribution in explaining $R_{D^{(*)}}$ [273] as well as prohibit the attempts at explaining the $h \to \tau\mu$ puzzle [1913]. At one-loop level, LQs contribute to the Belle II golden channel $\tau \to 3\ell$ [1524,1911].

Seesaw models of types I, II, and III could be distinguished by the imprint of heavy fermionic/scalar mediators on the dimension-six operator basis that leads to CLFV processes. These dimension-six effective operators, which are responsible for CLFV processes, are suppressed with M^{-2}, where M is the high scale linked to small neutrino masses [1914,1915]. For the vector quarkonia decays with LFV, Ref. [1901] demonstrated that in the inverse seesaw neutrino mass realization and in the sterile neutrino framework the quarkonia decays $\phi \to \ell\ell'$, $\psi \to \ell\ell'$, $\Upsilon \to \ell\ell'$ can be slightly enhanced, albeit no branching fraction can climb above the 10^{-12} level. In type I+III seesaw the semi-leptonic decays $\tau \to Pe$ and leptonic $\tau \to 3\ell$ present constraints that are slightly weaker compared to the constraints from the μ–e sector [1916]. In supersymmetry versions of seesaw mechanisms the $\tau \to \mu\gamma$ can be close to the current upper bound [1917]; however, LFV meson decay $B \to K\mu\tau$ is suppressed below 10^{-10} [1518]. In versions of the minimal flavor violation framework in the lepton sector it is well established that with the current value of the neutrino mixing angle, $\sin\theta_{13}$, the $\tau \to \mu\gamma$ decay is beyond the reach of Belle II [1895]. The gauged lepton flavor in the framework of the Pati–Salam model requires at least three to four orders of magnitude improvement in $\tau \to \mu\gamma$ and $\tau \to 3\mu$ experimental upper bounds in order to potentially test this model [1918].

In Randall–Sundrum models the golden channel $\tau \to \mu\gamma$ is reachable at Belle II. Another golden channel, $\tau \to 3\mu$, is currently constrained to lie below $\lesssim 10^{-8}$ [1919], and is thus a sensible probe of such models at Belle II.

Lepton number violation In the effective theory approach to the SM extensions the lowest-dimension operator is the dimension-five Weinberg operator [637] that violates leptonic number by two units ($\Delta L = 2$) and leads to the Majorana mass term for neutrinos. For heavy Majorana neutrinos, in addition to the LFV phenomena described above, Belle II could probe $\Delta L = 2$ processes that are resonantly enhanced [1920]. The authors point out the semi-leptonic $\Delta L = 2$ processes $\tau^- \to \ell^+ M^- M'^-$ and $B^- \to \ell^-\ell'^- M'^+$ involving two charged leptons and two charged mesons, which are suitable targets of study in Belle II. Better limits on the branching fraction of $\tau^- \to \ell^+ M^- M'^-$ would lead to stricter constraints on the mixing combination $|V_{\ell 4} V_{\tau 4}|$ in the mass range 0.1–1 GeV for the heavy Majorana neutrino. $B \to \ell^-\ell'^- M^+$ decays with e and μ in the final states are uniquely sensitive to mixing angles $|V_{e4}|$, $|V_{\mu 4}|$ in the mass range 2–5 GeV.

17.5. Minimal supersymmetric model with $\mathrm{U}(2)^5$ *symmetry*

Author: Joel Jones

Supersymmetric models with generic flavor structure (sfermion soft SUSY-breaking masses and trilinear couplings) suffer from severe flavor and CP violation constraints. These require that the sfermion states lie in the PeV range or above [1921], exacerbating the EW little hierarchy problem. The strongest constraints come from the measurement of ϵ_K, whose smallness in the SM is due to an approximate U(2) flavor symmetry respected by the quarks of the first two generations and which results in the efficient GIM suppression of all FCNCs among the light quarks. Similarly, LFV $\mu \to e$ transitions, whose null searches put severe constraints on the slepton sector of SUSY models, are absent in the U(2) symmetric limit, when the flavor group contains $\mathrm{U}(1)_\mu \times \mathrm{U}(1)_e$. This motivates

the consideration of NP models respecting approximate U(2) flavor symmetries acting on the light SM fermion generations.

In fact, with the improvement of theoretical input, a tension within CP-violating observables was first pointed out in Refs. [1922,1923]. This consisted of an incompatibility in the determination of ϵ_K, $S_{\psi K^0_S}$, and $\Delta M_d/\Delta M_s$, namely, with two of these observables one can predict the third, and this prediction would be in tension with the current experimental measurements [1924]. A recent analysis [1925] with updated theoretical data confirms that the problem is still present, at a level above $2\,\sigma$.

A $\mathrm{U}(2)^3$ flavor symmetry was proposed in Ref. [1926] as a way of solving the tension. This came naturally when considering the virtues of both MFV [621,1865] and U(2) flavor symmetry models [1927,1928]. The main idea consists of imposing a $\mathrm{U}(2)_Q \otimes \mathrm{U}(2)_u \otimes \mathrm{U}(2)_d$ symmetry acting on quarks, such that the first two generations transform as doublets, while the third generation remains a singlet. In order to reproduce the observed quark masses and mixings, one would need to introduce spurion fields transforming appropriately under the symmetries

$$\Delta Y_u \sim (2,\,2,\,1), \qquad \Delta Y_d \sim (2,\,1,\,2), \qquad V_q \sim (2,\,1,\,1). \tag{575}$$

With these spurions, the Yukawa matrices would acquire a structure following a definite pattern:

$$Y_f \sim \left(\begin{array}{c|c} \Delta Y_f & V_q \\ \hline 0 & y_f \end{array}\right), \tag{576}$$

where y_f should be of $\mathcal{O}(1)$.[66] Here, everything above the horizontal line has two rows, and everything to the left of the vertical lines has two columns. The parameters within the spurions are then fixed by requiring them to reproduce the quark masses and mixings. In the following we use $|V_{us}|$, $|V_{cb}|$, $|V_{ub}|$, and ϕ_3 to build the CKM matrix, and vary them in the following ranges [77,85,143,230,353,1929]:

$$|V_{us}| \in (0.2245,\,0.2261), \tag{577}$$

$$|V_{cb}| \in (3.97,\,4.30) \times 10^{-2}, \tag{578}$$

$$|V_{ub}| \in (3.56, 4.65) \times 10^{-3}, \tag{579}$$

$$\phi_3 \in (63.8^\circ,\,78.0^\circ). \tag{580}$$

As in MFV, the squark soft masses and trilinears are assumed to acquire a flavor structure based on the same spurions as in the Yukawas. One finds:

$$m^2_{\tilde{Q}} = \begin{pmatrix} I + \Delta_{LL} & x^*_Q V^*_q \\ x_Q V^T_q & m^2_{\text{light}}/m^2_{\text{heavy}} \end{pmatrix} m^2_{\text{heavy}}, \tag{581}$$

$$m^2_{\tilde{U}} = \begin{pmatrix} I + \Delta^u_{RR} & x^*_U \Delta Y^T_u V^*_q \\ x_U \Delta Y^*_u V^T_q & m^2_{\text{light}}/m^2_{\text{heavy}} \end{pmatrix} m^2_{\text{heavy}}, \tag{582}$$

$$m^2_{\tilde{D}} = \begin{pmatrix} I + \Delta^d_{RR} & x^*_D \Delta Y^T_d V^*_q \\ x_D \Delta Y^*_d V^T_q & m^2_{\text{light}}/m^2_{\text{heavy}} \end{pmatrix} m^2_{\text{heavy}}, \tag{583}$$

[66] For small values of $\tan\beta$, the suppression in y_b would be justified by the addition of an extra $\mathrm{U}(1)_b$ flavor symmetry.

where $\Delta_{LL} \sim V_q^* V^T + \Delta Y_u^* \Delta Y_u^T + \Delta Y_d^* \Delta Y_d^T$, $\Delta_{RR}^u \sim \Delta Y_u^T \Delta Y_u^*$, and $\Delta_{RR}^d \sim \Delta Y_d^T \Delta Y_d^*$. The trilinears follow the exact same structure as the Yukawas, proportional to $a_0\, m_{\text{heavy}}$, with different $\mathcal{O}(1)$ parameters.

The analyses carried out in Refs. [1926,1930–1933] considered the first two generations of squarks to be completely decoupled from the theory, as in effective supersymmetry [1934,1935]. In addition, no left–right mixing was considered, and only loops with gluinos were taken into account. In this limit, the SUSY contributions would modify ϵ_K, $S_{\psi K_S^0}$, and $\Delta M_d/\Delta M_s$ such that

$$\epsilon_K = \epsilon_K^{\text{SM(tt)}} \times \left(1 + x^2 F_0\right) + \epsilon_K^{\text{SM(tc+cc)}}, \tag{584}$$

$$S_{\psi K_S^0} = \sin\left(2\phi_1 + \arg\left(1 + x F_0 e^{-2i\gamma}\right)\right), \tag{585}$$

$$\frac{\Delta M_d}{\Delta M_s} = \left(\frac{\Delta M_d}{\Delta M_s}\right)^{\text{SM}}, \tag{586}$$

where x is a combination of $\mathcal{O}(1)$ constants, expected to be smaller than 10, F_0 is a loop function depending on $m_{\tilde{g}}^2$ and $m_{\tilde{Q}_3}^2$, and γ is an effective NP phase.

The results of Refs. [1926,1931,1933] confirmed that the new contributions could modify ϵ_K and $S_{\psi K_S^0}$ in the correct direction, such that the tension would be removed. In addition, a new contribution to $S_{\psi\phi}$ would be induced:

$$S_{\psi\phi} = \sin\left(2|\beta_s| - \arg\left(1 + x F_0 e^{-2i\gamma}\right)\right), \tag{587}$$

where one can see the same NP phase γ appearing. This means that the NP contributions to $S_{\psi K_S^0}$ and $S_{\psi\phi}$ would be correlated. In fact, this was used later in Ref. [1933] to demonstrate a more complete correlation between the latter two observables and the value of $|V_{ub}|$. Nevertheless, it was found in Refs. [1936,1937] that once the heavy squarks are included, non-negligible corrections appear. These corrections are related to the existence of a super-GIM mechanism, to contributions coming from the off-diagonal elements in the 1–2 block, and to left–right mixing.

In addition, with the increasing bounds on the gluino mass it is necessary to consider loops with lighter charginos or neutralinos [1937]. Even though the latter interact through smaller couplings, the bounds on their masses are not so stringent, so it is possible for them to give non-vanishing effects. The neutralino contribution should follow the same flavor structure as for the gluinos. In contrast, charginos and charged Higgs give an MFV-like contribution. All of these effects are expected to be small, but non-negligible.

In order to take all of these points into consideration, the framework has been implemented into `SPheno` 3.3.8 [1938,1939]. The appropriate Wilson coefficients have been generated using `SARAH-FlavorKit` 4.10.0 [1940–1942], and are used to generate our observables of interest. For the quark sector, these coefficients are processed with `flavio` 0.19.0 [618].

Using this implementation, a scan of the SUSY parameter space is performed in the parameter regions

$$\begin{aligned} m_{\text{heavy}} &\in (10, 30)\ \text{TeV}, & |a_0| &\in (0, m_{\text{heavy}}), \\ M_3 &\in (1.8, 3)\ \text{TeV}, & \mu &\in (0.1, 1)\ \text{TeV}, \\ M_{1,2} &\in (0.1, 1)\ \text{TeV}, & \tan\beta &\in (2, 10), \\ M_A &\in (1, 5)\ \text{TeV}, \end{aligned}$$

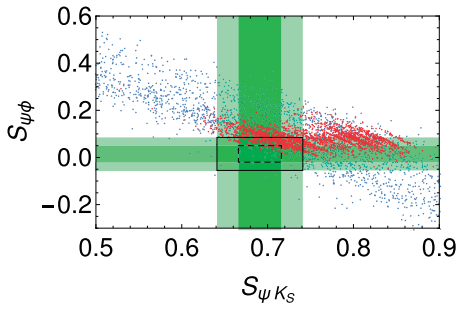

Fig. 214. Correlation between $S_{\psi K_S^0}$ and $S_{\psi\phi}$ in U(2)^3. Red points satisfy LHC mass constraints, and shaded green regions show bounds of experimental measurements at 1 and $2\,\sigma$. The dashed (solid) rectangles show the region where both bounds are satisfied at $1\,\sigma$ $(2\,\sigma)$ using current world average values [88,230].

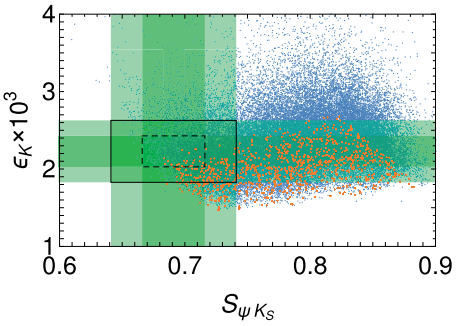

Fig. 215. Correlation between $S_{\psi K_S^0}$ and ϵ_K in U(2)^3. All points satisfy LHC mass constraints, and shaded green regions show bounds at 1 and $2\,\sigma$. The dashed (solid) rectangles show the region where both bounds are satisfied at $1\,\sigma$ $(2\,\sigma)$ using current world average values [88]. Orange points show the prediction without SUSY.

while m^2_{light} is set to appropriate values such that tachyons are absent, and so that the latest bounds on gluino, stop, and sbottom masses are satisfied. One also needs to check that the LSP is neutral.

We first demonstrate the correlation between $S_{\psi K_S^0}$ and $S_{\psi\phi}$. In Fig. 214, we show how both of these are modified in this framework. Points in red (blue) do (do not) satisfy the LHC constraints above. In addition, in regions shaded in green $S_{\psi K_S^0}$ and $S_{\psi\phi}$ are satisfied up to $2\,\sigma$. From the figure we can see that a smaller $S_{\psi K_S^0}$ will imply larger values of $S_{\psi\phi}$. Moreover, the current LHC bounds are not in conflict with the region where both observables satisfy their bounds. However, we also see that it is very difficult to have $S_{\psi K_S^0}$ on its lower end and simultaneously pass the bounds on $S_{\psi\phi}$.

It is interesting to note that many red points have very large values of $S_{\psi K_S^0}$. As we shall see, most of these cases are due to the value of V_{ub}, and not to SUSY effects. In fact, the current bounds on squark and gluino masses have a strong impact on the SUSY contributions to ϵ_K and $S_{\psi K_S^0}$. The bounds force F_0 to be small, which then requires x to be large in order to give a large enough effect in $S_{\psi K_S^0}$. However, since x appears quadratically in ϵ_K, this can cause the latter to overshoot. This can be seen in Fig. 215. Comparing the SM-only points (orange) and those with SUSY contributions (blue) helps us understand how U(2)^3 can reduce the tension. Although this is still possible, it is also common to have too large a contribution to ϵ_K. It is interesting that, as with $S_{\psi\phi}$, it is not favorable to have a small $S_{\psi K_S^0}$.

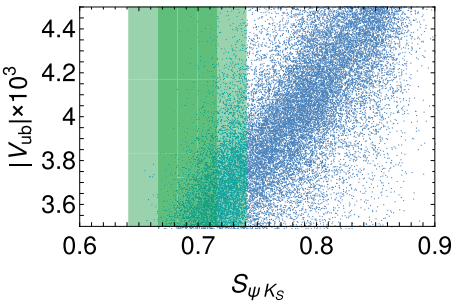

Fig. 216. Correlation between $S_{\psi K_S^0}$ and $|V_{ub}|$ in $U(2)^3$. All points satisfy LHC mass constraints, and have ϵ_K satisfying its bounds at $2\,\sigma$. Shaded green regions show bounds at 1 and $2\,\sigma$ using current world average values [88,143,353].

One attains further insight on the situation by selecting those points where the ϵ_K bounds are satisfied. One can then plot $|V_{ub}|$ as a function of $S_{\psi K_S^0}$, as is done in Fig. 216. The plots show that values of $|V_{ub}|$ close to its exclusive determination are favored. This is consistent to what we mentioned before. If we take $|V_{ub}|$ close to its inclusive value, we find that the SUSY contribution to $S_{\psi K_S^0}$ must be much larger. This, however, is correlated with the contribution to ϵ_K through the parameter x, which causes the former to exceed its bounds.

Thus, for this framework to solve the flavor tension would imply a future measurement of $S_{\psi K_S^0}$ to favor its current upper range, and a future measurement of $|V_{ub}|$ to approach its exclusive value. For $\Delta F = 1$ decays, one does not find strong distinctions with respect to MFV. However, CP asymmetries in $\Delta F = 1$ decays have been studied in detail in Ref. [1930]. For the lepton sector, there exist two possible approaches. The first one is to expand the $U(2)^3$ symmetry into $U(2)^5$ in the lepton sector by analogy, and generate LFV processes directly [1931]. The second approach, which is the one we discuss in detail below, is to modify the symmetry in order to generate neutrino masses and mixing, and then consider how that affects LFV.

In this second approach, there exist two realizations so far. The first one [1943] starts with a $U(3)^5$ symmetry, which is broken into $U(2)^5$ for the Yukawa couplings and $O(3)$ for the Majorana masses (denoted $U(3)^5_{\text{broken}}$). In this case, the neutrino masses are almost degenerate, such that one would expect an observation of neutrinoless double beta decay very soon. However, for the SUSY masses, one finds it more difficult to obtain a split spectrum, requiring a slight tuning in order to do so.

Another possibility [1944] is to start with $U(2)^5$, but then shift the $U(2)^2$ symmetry in the lepton sector towards the last two generations (denoted $U(2)^5_{\text{shifted}}$). This is achieved by the addition of two new U(1) symmetries for the lepton sector, with their own spurions. Here, one favors a normal ordering for the neutrino masses, with no possibility of observing neutrinoless double beta decay. An important feature of this case is that one would expect the selectron to be the lightest slepton, instead of the stau.

The main SUSY signature of both realizations is LFV decays. As one can see in Fig. 217, both scenarios have comparable $\mu \to e\gamma$ rates, and can be severely constrained by the MEG II upgrade. However, if MEG does observe a signal, there is a small chance to differentiate $U(3)^5_{\text{broken}}$ from $U(2)^5_{\text{shifted}}$ by observing $\tau \to \mu\gamma$ decay. Needless to say, if one observes the latter and does not see $\mu \to e\gamma$ in MEG II, then both frameworks would be simultaneously excluded. The predicted $\tau \to e\gamma$ branching ratio in both realizations is unfortunately too small to be observed in the near future.

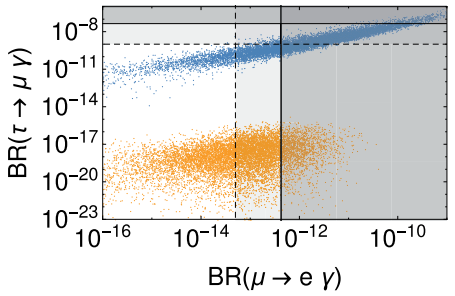

Fig. 217. Correlation between $\mu \to e\gamma$ and $\tau \to \mu\gamma$ in leptonic extension to $U(2)^3$. Blue points correspond to the $U(3)^5_{\text{broken}}$ scenario, while yellow points correspond to $U(2)^5_{\text{shifted}}$. Solid lines indicate current constraints [1531,1945], dashed lines indicate future prospects [1946].

17.6. Models with extended gauge sector

17.6.1. Z' models and modified Z couplings

Author: Lars Hofer

The simplest extension of the SM gauge sector is obtained by adding an extra $U(1)'$ symmetry. This modification augments the particle content by an additional gauge boson, Z', coupling to those fermions that carry a non-vanishing $U(1)'$ charge. After $U(1)'$ and EW symmetry breaking, the corresponding part of the Langrangian takes the most general form

$$\begin{aligned}\mathcal{L}_{Z'} = \Gamma^L_{uu'}\bar{u}\gamma^\mu P_L u' Z'_\mu + \Gamma^R_{uu'}\bar{u}\gamma^\mu P_R u' Z'_\mu + \Gamma^L_{dd'}\bar{d}\gamma^\mu P_L d' Z'_\mu + \Gamma^R_{dd'}\bar{d}\gamma^\mu P_R d' Z'_\mu + \\ \Gamma^L_{\ell\ell'}\bar{\ell}\gamma^\mu P_L \ell' Z'_\mu + \Gamma^R_{\ell\ell'}\bar{\ell}\gamma^\mu P_R \ell' Z'_\mu + \Gamma^L_{\nu_\ell\nu_{\ell'}}\bar{\nu}_\ell\gamma^\mu P_L \nu_{\ell'} Z'_\mu + \text{h.c.},\end{aligned} \tag{588}$$

where $u = (u, c, t)$, $d = (d, s, b)$, $\ell = (e, \mu, \tau)$, and $\nu_\ell = (\nu_e, \nu_\mu, \nu_\tau)$ denote the SM fermion fields in the mass eigenbasis. If the scale associated with the Z' is assumed to be well above that of the electroweak interactions, its couplings to left-handed fermions have to preserve $SU(2)_L$ invariance, implying the model-independent relations

$$\Gamma^L_{uu'} = V_{ud}\Gamma^L_{dd'}V^\dagger_{u'd'}, \qquad \Gamma^L_{\ell\ell'} = \Gamma^L_{\nu_\ell\nu_{\ell'}}, \tag{589}$$

with V denoting the CKM matrix.

Any further constraints on the couplings $\Gamma^{L,R}_{ij}$ depend on the $U(1)'$ charges assigned to the SM fermions and on a potential embedding of the $U(1)'$ model in a more fundamental theory (see, e.g., the models described in the following sections). Of interest for quark flavor physics are Z' scenarios featuring flavor off-diagonal quark couplings $\Gamma^{L,R}_{bs}$, $\Gamma^{L,R}_{bd}$, or $\Gamma^{L,R}_{uc}$. Such couplings can be obtained at tree level with a family non-universal assignment of $U(1)'$ charges, see, e.g., Refs. [1947,1948], requiring an extension of the Higgs sector in order to comply with the experimentally observed fermion masses and mixings. Alternatively, flavor off-diagonal couplings can be generated as effective couplings in an underlying more fundamental theory. A typical mechanism to generate these effective couplings involves heavy vector-like quarks that are charged under the $U(1)'$ symmetry and that mix with the SM fermions [599,648,1949,1950].

In the lepton sector the most popular class of Z' models is based on gauging the $L_\tau - L_\mu$ lepton number [599,648,1947,1949,1951]. Such models are anomaly free [1952–1954] and phenomenologically appealing as they lead to a PMNS matrix that provides a good tree-level approximation for the measured pattern of neutrino mixing angles [1955–1957]. The vanishing coupling of the Z' to electrons further allows an explanation of the present tensions in the LHCb measurement [391] of

the LFUV observable $R_K = \mathrm{Br}(B \to K\mu^+\mu^-)/\mathrm{Br}(B \to Ke^+e^-)$ and helps to avoid LEP bounds on the Z' mass $M_{Z'}$.

Tree-level exchange of the Z' boson contributes to various $\Delta F = 1$ and $\Delta F = 2$ FCNC processes. The contributions to the respective Wilson coefficients are quadratic in the reduced Z' couplings,

$$\widetilde{\Gamma}_{ij}^{L,R} \equiv \Gamma_{ij}^{L,R}/M_{Z'}, \tag{590}$$

and the absence of a loop suppression compared to the SM contribution boosts the sensitivity of FCNC observables to high Z' masses beyond the reach of direct searches. In the following we discuss in a model-independent way, based on the general Lagrangian in Eq. (588), the Z' phenomenology in B physics.

$B_{d,s}$–$\bar{B}_{d,s}$ mixing The observables in B_q–$\bar{B}_q$ mixing ($q = d, s$) probe the reduced Z' couplings $\widetilde{\Gamma}_{bq}^{L}$ and $\widetilde{\Gamma}_{bq}^{R}$. They constrain all $B_{d,s}$ decay modes discussed in the following, as a non-vanishing Z' contribution to any of them necessarily also implies a contribution to B_q–$\bar{B}_q$ mixing. In the absence of an additional CP phase, i.e. for $\arg(\Gamma_{bq}^{L,R}) = \arg(V_{tq}^* V_{tb})$, the Z' contribution leads to an enhancement of ΔM_{B_q} for purely left-handed, purely right-handed, or axial $Z'bs$ couplings, while it leads to a decrease for a vectorial $Z'bs$ coupling [1909,1958].

(Semi-)leptonic B decays (Semi-)leptonic B decays are the natural place to search for Z' bosons in quark flavor physics due to their partial protection from polluting QCD effects. They probe the four products of couplings $\widetilde{\Gamma}_{bq}^{L,R}\,\widetilde{\Gamma}_{\ell\ell}^{L,R}$, generating the four Wilson coefficients $C_{9,10}^{(\prime)}$. Since only three out of the four products $\widetilde{\Gamma}_{bq}^{L,R}\,\widetilde{\Gamma}_{\ell\ell}^{L,R}$ are independent, the relation

$$C_9 \cdot C_{10}' \;=\; C_9' \cdot C_{10} \tag{591}$$

is valid in models with a single Z' boson, with the ratio $C_9'/C_9 = C_{10}'/C_{10}$ being free from the leptonic couplings and fixed from B_q–$\bar{B}_q$ mixing [1959].

Global fits to current $b \to s\ell^+\ell^-$ data including (among other modes) $B_s \to \mu^+\mu^-$, $B \to K^{(*)}\ell^+\ell^-$, $B_s \to \phi\mu^+\mu^-$ show some significant tensions pointing towards NP in these coefficients, in particular a negative contribution to the coefficient C_9 [497,524,612,647,1960]. A Z' boson with a left-handed coupling to quarks and a vectorial coupling to leptons precisely generates this coefficient, whereas a Z' boson with purely left-handed couplings to both quarks and leptons generates the pattern $C_9 = -C_{10}$. A solution of the present tensions in exclusive semi-leptonic $B_{(s)}$ decays via the latter scenario implies a reduced branching ratio for the purely leptonic mode $B_s \to \mu^+\mu^-$, consistent with current LHC data. An unambiguous discrimination between a Z' model and non-perturbative QCD contributions as origin of the observed tensions requires an increased resolution in the invariant dilepton mass in the above-mentioned exclusive semi-leptonic channels, as well as the exploitation of neutrino modes like $B \to K^{(*)}\nu\bar{\nu}$ and additional more exotic modes like the baryonic $\Lambda_b \to \Lambda\mu^+\mu^-$ [162,1961,1962] or inclusive $B \to X_s\ell^+\ell^-$.

If the Z' mediates $b \to s$ transitions, it can be expected that it also generates $b \to d$ transitions. In an MFV scenario, for instance, the corresponding couplings would be related as $|\Gamma_{bd}^{L,R}/\Gamma_{bs}^{L,R}| = |V_{td}/V_{ts}|$. Therefore, the corresponding $b \to d\ell\ell$ modes $B_d \to \ell\ell$, $B \to \pi\ell\ell$, and $B \to \rho\ell\ell$ also need to be studied in detail. Belle II should be able to provide complementary input on $b \to d$ transitions through radiative decay measurements.

LFUV and LFV $B_{d,s}$ decays Z' models based on the gauged $L_\tau - L_\mu$ lepton number introduce lepton flavor universality violation (LFUV), a possibility also suggested by the current LHCb data [391] on the ratio $R_K = \mathrm{Br}(B \to K\mu^+\mu^-)/\mathrm{Br}(B \to Ke^+e^-)$. The hypothesis of LFUV can be tested by measuring a certain $b \to q\ell^+\ell^-$ decay for different lepton families $\ell = e, \mu, \tau$ and considering the ratio of the respective branching ratios, a theoretically clean observable due to the cancellation of hadronic uncertainties. For decays into vector mesons more elaborate observables can also be constructed from the full angular distribution [600].

It has been proposed to search for LFV B decay modes as well [623]. In $L_\tau - L_\mu$ models, for example, the symmetry breaking, which is needed for a realistic neutrino phenomenology, can induce such decays. Combined bounds from B_s–$\bar{B}_s$ mixing, $\tau \to 3\mu$, and $\tau \to \mu\nu\bar{\nu}$ constrain branching ratios of $b \to s\tau^\pm\mu^\mp$ modes to $\mathcal{O}(10^{-8})$–$\mathcal{O}(10^{-6})$, depending on the amount of fine-tuning allowed in the B_s–$\bar{B}_s$ mixing [1909,1963]. For $b \to s\mu^\pm e^\mp$, sizeable branching ratios (up to $\mathcal{O}(10^{-7})$ if a certain fine-tuning in B_s–$\bar{B}_s$ is permitted) are only possible in a region disfavored by current $b \to s\mu^+\mu^-$ data.

Hadronic $B_{(s)}$ decays To fully scrutinize the Z' model it is not sufficient to examine (semi-)leptonic B decays; purely hadronic decays $B_{(s)} \to M_1 M_2$ of the $B_{(s)}$ meson into two light mesons M_1, M_1, mediated by quark-level transitions $b \to q\bar{q}'q'$ ($q = d, s$, $q' = u, d, s, c$), should also be explored. Governed by the products of couplings $\widetilde{\Gamma}^{L,R}_{bq}\,\widetilde{\Gamma}^{L,R}_{q'q'}$, these decays are in general independent of the (semi-)leptonic ones and open a portal to probe the Z' boson even in leptophobic models.

While the plethora of hadronic channels allows for over-constraining measurements, the fact that these modes are typically dominated by QCD penguin topologies hampers the sensitivity to high-scale NP. An exception occurs for isospin-violating Z' models, i.e. for scenarios in which the Z' couples in a different way to u and d quarks, leading to observable effects that cannot be mimicked by the isospin-conserving QCD penguins. As a consequence of the $\mathrm{SU}(2)_L$ relation in Eq. (589), isospin violation is CKM suppressed in the left-handed Z' couplings $\Gamma^L_{uu} \approx \Gamma^L_{dd}$, but can be introduced via the right-handed couplings $\Gamma^R_{uu} \neq \Gamma^R_{dd}$.

The two B_s decay modes $B_s \to \phi\rho^0$ and $B_s \to \phi\pi^0$ are purely $\Delta I = 1$ decays and thus golden modes to search for an isospin-violating Z' boson [790]. The absence of a QCD penguin amplitude renders their branching ratios particularly small within the SM, $\mathrm{Br}(B_s \to \phi\rho^0) = 4.4^{+2.7}_{-0.7} \times 10^{-7}$ and $\mathrm{Br}(B_s \to \phi\pi^0) = 1.6^{+1.1}_{-0.3} \times 10^{-7}$.

The decay $B \to K\pi$ is also sensitive to isospin-violating Z' models. Its transition amplitude decomposes into a $\Delta I = 0$ part (dominated by QCD penguins) and a $\Delta I = 1$ part (free from QCD penguins). By combining the four different modes $B^- \to \bar{K}^0\pi^-$, $B^- \to K^-\pi^0$, $\bar{B}^0 \to K^-\pi^+$, and $\bar{B}^0 \to \bar{K}^0\pi^0$ it is possible to construct observables that project out the $\Delta I = 1$ component. In the last decade some discrepancies in such observables have led to speculations about a "$B \to K\pi$ puzzle" [1964–1967], but in the meantime measurements have fluctuated towards the SM predictions, reducing the "$B \to K\pi$ puzzle" to a $\gtrsim 2\,\sigma$ tension [1968] in the difference of direct CP asymmetries $\Delta A_{\mathrm{CP}} = A_{\mathrm{CP}}(B^- \to K^-\pi^0) - A_{\mathrm{CP}}(\bar{B}^0 \to K^-\pi^+)$.

Modified Z couplings A scenario where high-scale NP generates effective FCNC couplings for the SM Z boson is phenomenologically similar to a Z' model and can thus be probed by the same processes. Differences compared to the Z' case arise from the fact that the Z boson mass as well as its flavor-diagonal lepton couplings are known precisely from the LEP measurements. This significantly lowers the potential for observable departures from SM predictions in B decays, in particular in the

$b \to s$ transition, where the observed $b \to s\ell^+\ell^-$ anomalies cannot be accommodated. In $b \to d$ transitions measurable imprints are still possible [1958,1959].

17.6.2. Gauged flavor models

Author: Jernej F. Kamenik

The idea of assuming horizontal (flavor) symmetries to be true (gauged) symmetries of nature has a long history (see Ref. [1969] for a review). Unfortunately, contrary to the (global) symmetry arguments underlying MFV, such an assumption is itself not enough to suppress flavor violation below the experimental bounds when the flavor symmetry is broken at low scales. Namely, in this case the associated flavor gauge bosons can mediate dangerous FCNCs and their masses generally must be well above the TeV scale. In the minimal flavor-breaking scenarios, where the masses of the gauge bosons are proportional to the SM Yukawa couplings (as the only sources of flavor breaking), they generate tree-level four-fermion operators proportional to inverse powers of the SM Yukawa couplings, enhancing FCNC among the first generations, and resulting in severe constraints from FCNC and CP violation observables in the kaon sector.

A way out, exploited in Ref. [1970], is for the fields breaking the flavor symmetry to be instead proportional to the inverse of the SM Yukawa couplings. Then, the effective operators generated by integrating out the flavor gauge bosons will be roughly proportional to positive powers of the Yukawa couplings, suppressing flavor-violating effects for the light generations, much like in MFV models. The spectrum of the extra flavor states will thus present an inverted hierarchy, with states associated to the third generation much lighter than those associated to the first two.

Another particularity of gauged flavor symmetry models is that in general extra flavorful fermions have to be added to cancel flavor gauge anomalies. Such fermions are also welcome as they can make the dynamical SM Yukawa terms arise from a renormalizable Lagrangian. In the quark sector, the smallest set of fermions cancelling all anomalies in the $\mathrm{SU}(3)^3$ case was found in Ref. [1970] and leads automatically to the inverted hierarchy structure mentioned above (see also Ref. [1971] for examples of $\mathrm{SU}(2)^3$ gauged models). The SM fermion masses arise via a seesaw-like mechanism, after integrating out the extra fermions.

The strongest constraints on this kind of model do not necessarily come from flavor-violating observables but also from electroweak precision tests (EWPT) and direct searches for new particles, opening the possibility of direct discoveries of flavor dynamics at the LHC [1970]. The lightest new states are the top partners in the quark sector and a few flavor gauge bosons that behave as flavor non-universal (but diagonal) Z' (see also Sect. 17.6.1). Depending on the flavor gauge group a few flavor gauge bosons could lie in the TeV range. Most of the spectrum, however, is much heavier than a TeV and can only be probed through precision flavor observables.

An extensive analysis of $\Delta F = 2$ observables and of $B \to X_s\gamma$ in the minimal gauged quark $\mathrm{SU}(3)^3$ flavor model was studied in detail in Ref. [1972]. The model allows in principle for significant deviations from the SM predictions for ϵ_K, $\Delta m_{B_{d,s}}$, mixing-induced CP asymmetries $S_{\psi K^0_S}$ and $S_{\psi\phi}$, and $B \to X_s\gamma$ decay. Some predicted correlations among Belle II-relevant observables are shown in Fig. 218.

The gauging of the lepton flavor group was considered in Ref. [1973]. In contrast to the quark case, the unknown nature of neutrino masses allows for several possibilities for constructing a consistent model. In particular, the maximal lepton flavor symmetry group is $\mathrm{U}(3)^3$ for the case of purely Dirac neutrinos, and $\mathrm{U}(3)^2 \times O(3)$ for the Majorana case. In this latter case, which results in a type-I inverse seesaw scenario, $\mu \to eee$ is at present generically the most sensitive flavor non-conserving

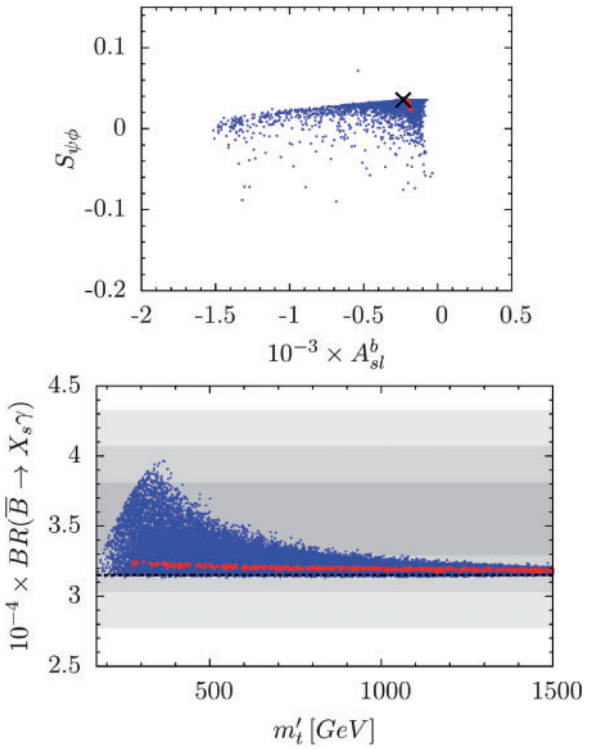

Fig. 218. Correlation plot of $S_{\psi\phi}$ and the b semi-leptonic CP asymmetry A_{sl}^{b} on the left and Br($\bar{B} \to X_s\gamma$) and the mass of the lightest new fermionic resonance (m_t') on the right in the minimal gauged SU(3)^3 flavor model (taken from Ref. [1972]). Gray regions refer to the present experimental error ranges. The big cross mark refers to the SM values reported in Ref. [1972]. The points for which the current experimental tension between $\Delta m_{B_{d,s}}$, $S_{\psi K_S^0}$, and ϵ_K is resolved are shown in red, all others in blue.

channel. However, the model also predicts potentially observable effects in LFV tau decays (see Fig. 219).

17.6.3. The 3-3-1 model

Authors: Andrzej Buras and Fulvia De Fazio

The name 3-3-1 generically indicates a set of models based on the gauge group $SU(3)_C \times SU(3)_L \times U(1)_X$ [1974,1975]; this group is at first spontaneously broken to the SM group $SU(3)_C \times SU(2)_L \times U(1)_Y$ and then to $SU(3)_C \times U(1)_Q$. The enlargement of the gauge group with respect to SM has two interesting consequences. The first one is that the number of generations must necessarily be equal to the number of colors, if one requires anomaly cancellation as well as asymptotic freedom of QCD; this might be viewed as an explanation for the existence of three generations. Moreover, quark generations should have different transformation properties under the action of $SU(3)_L$. In particular, two quark generations should transform as triplets, one as an antitriplet. Identifying the latter with the third generation, this difference could be at the origin of the large top quark mass. This choice imposes that the leptons should transform as antitriplets. However, one could also choose to exchange the role of triplets and antitriplets, provided that the number of triplets equals that of antitriplets, in order to fulfill the anomaly cancellation requirement. As a consequence, different variants of the model are obtained corresponding to the way one fixes the fermion representations.

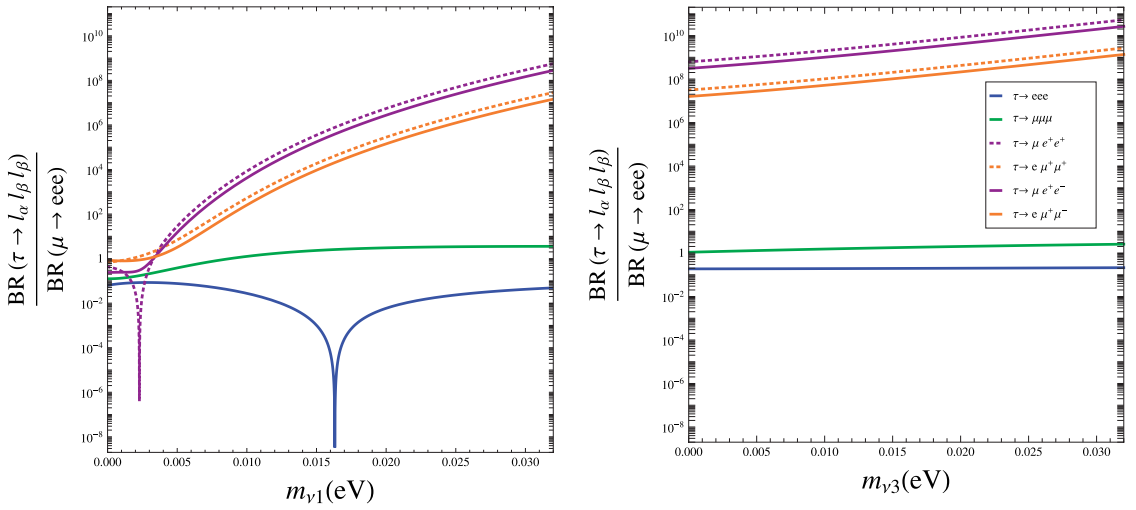

Fig. 219. Predictions of the gauged-flavor type-I seesaw scenario in a CP-even case (taken from Ref. [1973], to which the reader is referred for details): branching ratios for the different lepton rare decays over that for $\mu \to eee$ as functions of the lightest neutrino mass, for neutrino normal ordering (m_{ν_1}, left) and inverted ordering (m_{ν_3}, right).

The following relation holds among some of the generators of the group:

$$Q = T_3 + \beta T_8 + X, \tag{592}$$

where Q indicates the electric charge, T_3 and T_8 are the two diagonal generators of $\mathrm{SU}(3)_L$, and X is the generator of $\mathrm{U}(1)_X$. β is a parameter that, together with the choice for the fermion representations, defines a specific version of the model.

Several new particles are predicted to exist in 3-3-1 models. Known SM fermions fill the two upper components of the (anti)triplets; the third one is in general a new heavy fermion with electric charges depending on β. (An exception is the model having $\beta = \sqrt{3}$, called the minimal 3-3-1 model, where only new heavy quarks are present but no new leptons.) The Higgs system is also enlarged.

Five new gauge bosons exist due to the extension of the SM gauge group $\mathrm{SU}(2)_L$ to $\mathrm{SU}(3)_L$. A new neutral boson (Z') is always present, together with the other four that might be charged depending on the selected variant of the model. An important difference with respect to the SM is the existence of tree-level FCNC mediated by Z'. These arise only in the quark sector, due to the universality of the coupling of the Z' to leptons that guarantees that no FCNC show up in this case. Moreover, the new FCNC are purely left-handed since universality is also realized in the Z' couplings to right-handed quarks. Such tree-level transitions turn out to be no larger than the corresponding loop-induced SM contribution, due to the smallness of the relevant couplings. This is a very appealing feature of this model, since Z' could be responsible for the anomalies recently emerged in the flavor sector.

As in the SM, quark mass eigenstates are obtained upon rotation of flavor eigenstates through two unitary matrices V_L (for down-type quarks) and U_L (for up-type quarks). In analogy with the SM case, the relation

$$V_{\mathrm{CKM}} = U_L^\dagger V_L \tag{593}$$

holds. However, while in the SM the two rotation matrices never appear individually and $V_{\rm CKM}$ enters only in charged current interactions, this is not the case in 3-3-1 models and both U_L and V_L enter in tree-level FCNCs mediated by Z' in the up-quark and down-quark sector, respectively. Due to the relation in Eq. (593), one can choose to write U_L in terms of V_L and $V_{\rm CKM}$.

A suitable parameterization for V_L is

$$V_L = \begin{pmatrix} \tilde{c}_{12}\tilde{c}_{13} & \tilde{s}_{12}\tilde{c}_{23}e^{i\delta_3} - \tilde{c}_{12}\tilde{s}_{13}\tilde{s}_{23}e^{i(\delta_1-\delta_2)} & \tilde{c}_{12}\tilde{c}_{23}\tilde{s}_{13}e^{i\delta_1} + \tilde{s}_{12}\tilde{s}_{23}e^{i(\delta_2+\delta_3)} \\ -\tilde{c}_{13}\tilde{s}_{12}e^{-i\delta_3} & \tilde{c}_{12}\tilde{c}_{23} + \tilde{s}_{12}\tilde{s}_{13}\tilde{s}_{23}e^{i(\delta_1-\delta_2-\delta_3)} & -\tilde{s}_{12}\tilde{s}_{13}\tilde{c}_{23}e^{i(\delta_1-\delta_3)} - \tilde{c}_{12}\tilde{s}_{23}e^{i\delta_2} \\ -\tilde{s}_{13}e^{-i\delta_1} & -\tilde{c}_{13}\tilde{s}_{23}e^{-i\delta_2} & \tilde{c}_{13}\tilde{c}_{23} \end{pmatrix}. \tag{594}$$

The interaction Lagrangian describing Z' couplings to down quarks in 3-3-1 models can be written as follows:

$$i\mathcal{L}_L(Z') = i\left[\Delta_L^{sd}(Z')(\bar{s}\gamma^\mu P_L d) + \Delta_L^{bd}(Z')(\bar{b}\gamma^\mu P_L d) + \Delta_L^{bs}(Z')(\bar{b}\gamma^\mu P_L s)\right]Z'_\mu, \tag{595}$$

with the first upper index denoting the outgoing quark and the second incoming one. As a consequence,

$$\Delta_L^{ji}(Z') = (\Delta_L^{ij}(Z'))^*. \tag{596}$$

With this parameterization, the Z' couplings to quarks for the three meson systems K, B_d, and B_s,

$$\Delta_L^{sd}(Z'), \qquad \Delta_L^{bd}(Z'), \qquad \Delta_L^{bs}(Z'), \tag{597}$$

being proportional to $v_{32}^* v_{31}$, $v_{33}^* v_{31}$, and $v_{33}^* v_{32}$, respectively, depend on only four new parameters (explicit formulae can be found in Ref. [1976]):

$$\tilde{s}_{13}, \quad \tilde{s}_{23}, \quad \delta_1, \quad \delta_2. \tag{598}$$

Here, $\tilde{s}_{13}$ and $\tilde{s}_{23}$ are positive definite and δ_i vary in the range $[0, 2\pi]$. Therefore, for fixed $M_{Z'}$ and β, the Z' contributions to all processes discussed in the following depend only on these parameters and on their size, implying very strong correlations between NP contributions to various observables. Indeed, as seen in Eq. (594), the B_d system involves only the parameters $\tilde{s}_{13}$ and δ_1 while the B_s system depends on $\tilde{s}_{23}$ and δ_2. Furthermore, stringent correlations between observables in the $B_{d,s}$ sectors and in the kaon sector are found since kaon physics depends on $\tilde{s}_{13}, \tilde{s}_{23}$, and $\delta_2 - \delta_1$. Additional non-negligible contributions come from tree-level Z exchanges generated by the the Z–Z' mixing that depends on an additional parameter $\tan\bar{\beta}$ [1977]. The fact that in 3-3-1 models deviations from SM predictions are mainly related to Z' exchanges implies that NP effects in these models are likely to come from scales beyond the reach of the LHC. On the other hand they can be suitably investigated at Belle II, where the effects of a virtual Z' can be detected even if its mass is too high to be detected at the LHC.

Extensive recent flavor analyses in these models can be found in Refs. [1976–1980]. References to earlier analysis of flavor physics in 3-3-1 models can be found there and in Refs. [1981,1982]. In particular, in Ref. [1977] considered 24 different models corresponding to four values of β, three values of $\tan\bar{\beta}$, and two fermion representations. With the help of electroweak precision data it was possible to reduce the number of these models to seven.

The most recent updated analyses in Refs. [1979,1980] concentrated on the ratio ε'/ε and its correlation with ε_K and B physics observables such as $\Delta M_{s,d}$, $B_s \to \mu^+\mu^-$, and the Wilson coefficient C_9. They were motivated by the anomalies in ε'/ε [178–180,1983], tension between ε_K and $\Delta M_{s,d}$ within the SM [1925] implied by the recent lattice data [151], and, in the case of C_9, by the LHCb anomalies in $B \to K^*(K)\mu^+\mu^-$ summarized in Refs. [524,612]. We briefly recall the main results of these two papers, putting the emphasis on the last analysis in Ref. [1980] which could take into account new lattice QCD results from the Fermilab Lattice and MILC Collaborations [151] on $B^0_{s,d}$–$\bar{B}^0_{s,d}$ hadronic matrix elements.

The new analyses in Refs. [1979,1980] showed that the requirement of an enhancement of ε'/ε has a significant impact on other flavor observables. Moreover, in Ref. [1980] it was also shown that the results are rather sensitive to the value of $|V_{cb}|$, as illustrated by choosing two values: $|V_{cb}| = 0.040$ and $|V_{cb}| = 0.042$. There is also some sensitivity to V_{ub}, which is less precisely known than V_{cb}. In this context an improved determination of V_{cb} and V_{ub} at Belle II will allow higher precision for predictions made in 3-3-1 models and the ability to choose between the various scenarios for these two CKM elements discussed below.

The main findings of Refs. [1979,1980] for $M_{Z'} = 3$ TeV are as follows:

- Among seven 3-3-1 models selected in Ref. [1977] on the basis of the electroweak precision study, only three (M8, M9, M16) can provide, for both choices of $|V_{cb}|$, a significant shift of ε'/ε, even though not larger than 6×10^{-4}.
- The tensions between $\Delta M_{s,d}$ and ε_K pointed out in Ref. [1925] can be removed in these models (M8, M9, M16) for both values of $|V_{cb}|$.
- Two of them (M8 and M9) can simultaneously suppress $B_s \to \mu^+\mu^-$ by at most 10% and 20% for $|V_{cb}| = 0.042$ and $|V_{cb}| = 0.040$, respectively. This can still bring the theory within $1\,\sigma$ range of the combined result from CMS and LHCb, and for $|V_{cb}| = 0.040$ one can even reach the present central experimental value of this rate. On the other hand, the maximal deviations from SM in the Wilson coefficient C_9 are $C_9^{\rm NP} = -0.1$ and $C_9^{\rm NP} = -0.2$ for these two $|V_{cb}|$ values, respectively. Due to this moderate shift, these models do not really help in the case of $B_d \to K^*\mu^+\mu^-$ anomalies that require deviations as high as $C_9^{\rm NP} = -1.0$ [524,612].
- In M16 the situation is reversed. It is possible to reduce the rate for $B_s \to \mu^+\mu^-$ for $M_{Z'} = 3$ TeV for the two $|V_{cb}|$ values by at most 3% and 10%, respectively, but with the corresponding values $C_9^{\rm NP} = -0.3$ and -0.5 the anomaly in $B_d \to K^*\mu^+\mu^-$ can be significantly reduced.
- The maximal shifts in ε'/ε decrease quickly with increasing $M_{Z'}$ in the case of $|V_{cb}| = 0.042$ but are practically unchanged for $M_{Z'} = 10$ TeV when $|V_{cb}| = 0.040$ is used.
- On the other hand, for larger values of $M_{Z'}$ the effects in $B_s \to \mu^+\mu^-$ and $B_d \to K^*\mu^+\mu^-$ are much smaller. NP effects in rare K decays and $B \to K(K^*)\nu\bar{\nu}$ remain small in all 3-3-1 models, even for $M_{Z'}$ of a few TeV. This could be challenged by NA62, KOTO, and Belle II experiments in this decade.

We show these correlations for $M_{Z'} = 3$ TeV and $|V_{cb}| = 0.040$ in Fig. 220, plotting the shift $\Delta\left(\varepsilon'/\varepsilon\right)$ versus $\bar{B}(B_s \to \mu^+\mu^-)$ (left plots) or versus the NP contribution $\mathrm{Re}[C_9^{\rm NP}]$ (right plots). Since recent data would favor a suppression of the former as well as a large negative shift in the latter, on the basis of this figure we conclude that the first requirement would select M8 (upper plots) while the second would favor M16 (lower ones). Therefore, a substantial improvement in the experimental measurements of the angular observables in $B \to K^*\mu^+\mu^-$, expected from Belle II, could select

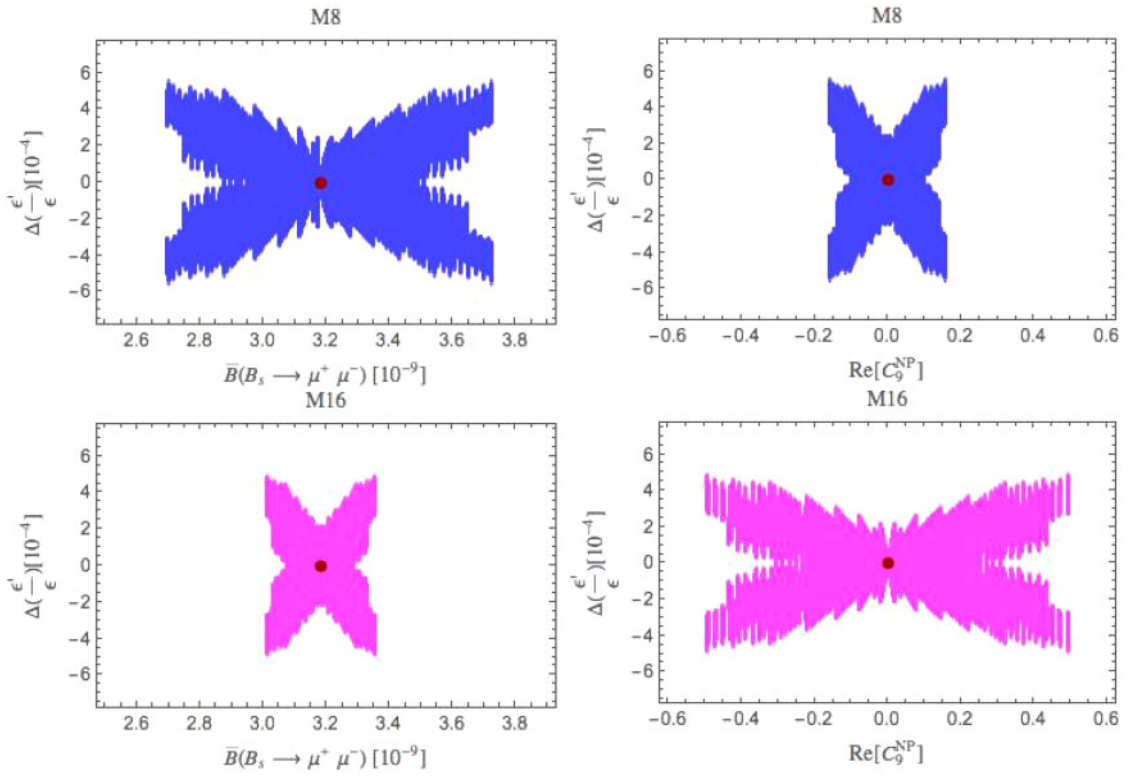

Fig. 220. Correlations of $\Delta(\varepsilon'/\varepsilon)$ with $B_s \to \mu^+\mu^-$ (left panels) and with C_9^{NP} (right panels) for M8 and M16. Red dots represent central SM values. $M_{Z'} = 3$ TeV and $|V_{cb}| = 0.040$.

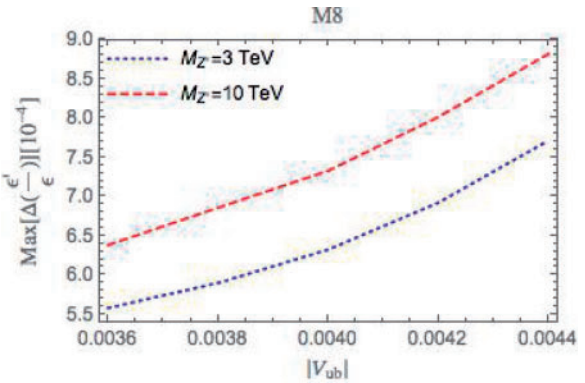

Fig. 221. Maximal values of $\Delta(\varepsilon'/\varepsilon)$ for $|V_{cb}| = 0.040$ as a function of $|V_{ub}|$ for $M_{Z'} = 3$ TeV and $M_{Z'} = 10$ TeV.

which one among the 3-3-1 models has a chance to survive. This in turn means that the size of the deviations in $B_s \to \mu^+\mu^-$ and in ε'/ε can be assessed and contrasted with data.

All these statements are valid for $|V_{ub}| = 0.0036$ as favored by the exclusive decays. For larger values of $|V_{ub}|$ the maximal shifts in ε'/ε are larger. We illustrate this in Fig. 221, where we show these shifts as functions of $|V_{ub}|$ for $|V_{cb}| = 0.040$ and two values of $M_{Z'}$.

The main message from Refs. [1979,1980] is that NP contributions in 3-3-1 models can simultaneously solve $\Delta F = 2$ tensions, enhance ε'/ε, and suppress either the rate for $B_s \to \mu^+\mu^-$ or the C_9 Wilson coefficient without any significant NP effects on $K^+ \to \pi^+\nu\bar{\nu}$ and $K_{\mathrm{L}} \to \pi^0\nu\bar{\nu}$ and $b \to s\nu\bar{\nu}$ transitions. While sizeable NP effects in $\Delta F = 2$ observables and ε'/ε can persist for $M_{Z'}$

outside the reach of the LHC, such effects in $B_s \to \mu^+\mu^-$ will only be detectable provided Z' is discovered soon.

Let us finally mention that even though we have stressed that deviations from SM predictions in 3-3-1 models are mainly expected due to the existence of FCNC mediated by Z', it is possible that the other new gauge bosons also present in these models can lead to interesting NP effects. Indeed, the gauge bosons denoted by $V^{\pm Q_V}$ and $Y^{\pm Q_Y}$ have electric charge depending on β and lepton number $L = \mp 2$, but carry no lepton generation number, so that the lepton generation number can be violated due to such new gauge boson mediation. Recent studies of the lepton sector in this scenario can be found in Refs. [1984,1985].

17.6.4. Left–right symmetry models

Author: Monika Blanke

In left–right symmetric models [1986–1989] the SM gauge group is extended by an additional $SU(2)_R$ factor under which the right-handed quarks and leptons transform as doublets. Parity can hence be restored at high scales, and the model contains right-handed neutrinos, thereby giving rise to non-vanishing neutrino masses.

Despite extensive searches, the W' and Z' gauge bosons associated with $SU(2)_R$ have not yet been observed and the current direct limits from the LHC reach up to about 2.5 TeV [1990–1992]. A significant improvement is expected from the growing 13 TeV dataset. Indirect constraints on the right-handed scale arise from electroweak precision constraints [1993] and from flavor-violating decays [1994–1997].

In analogy to the SM, the W' gauge boson mediates right-handed charged currents. The coupling strength of right-handed quarks is given by the unitary mixing matrix V_R. Unlike for the CKM matrix, all six complex phases of this matrix are physical.

The presence of right-handed flavor-changing charged current interactions can be tested in semi-leptonic decays [1998–2001]. Processes which are used to determine the elements of the CKM matrix from tree-level processes are sensitive to right-handed contributions. The crucial ingredient to identify right-handed contributions is their non-universal effect: different decays sensitive to the same CKM element are affected by right-handed charged currents in a different manner, manifesting in discrepancies between the various determinations of CKM elements. The current tensions between inclusive and exclusive determinations of $|V_{ub}|$ and $|V_{cb}|$ cannot, however, be explained by the presence of right-handed currents, as the pattern of effects is inconsistent with the theoretical prediction [2002]. In addition, the size of effect necessary to remove the tension in $|V_{ub}|$ determinations is in tension with the constraints from meson mixing observables and only achievable with large fine-tuning [1997]. With improved theoretical description of semi-leptonic decays and their precise measurement at Belle II, it will be possible to put much tighter constraints on the presence of right-handed charged currents, or to unravel their presence. Measurements must directly examine propagator chirality through decay helicities.

In addition to the enhanced gauge symmetry, left–right symmetric models are often equipped with a discrete symmetry, usually parity, charge conjugation symmetry, or CP, thus making the restoration of the corresponding symmetry at high scales manifest [2003–2007]. These scenarios imply specific structures for the right-handed mixing matrix, with a hierarchy close to the CKM one. These models have in common that a large amount of fine-tuning is required to satisfy the constraints from neutral kaon mixing [1996,2008–2012].

In the absence of a discrete symmetry the structure of the V_R matrix is not restricted theoretically and has to be determined from data. The most stringent constraints are obtained from meson mixing observables, allowing only for very specific structures of V_R. If in addition small fine-tuning is required, then all off-diagonal elements of V_R are found to be close to zero [1997,2013]. The most stringent constraints again stem from neutral kaon mixing, but $B_{d,s}$ mixing observables also play a prominent role. A further decrease of uncertainties will therefore be crucial for constraining the structure of V_R [2014].

An important contribution to meson mixing observables in left–right models is generated by tree-level flavor-changing heavy Higgs exchanges [1994–1997]. These heavy Higgs particles are generally present as a remnant of the $\mathrm{SU}(2)_R$ symmetry breaking. In minimal left–right models their contributions to $\Delta F = 2$ observables require their masses to be pushed well above 10 TeV. Simultaneously keeping the W' and Z' gauge bosons at the few TeV scale then forces the Higgs potential to be close to the non-perturbative regime. While it can be rigorously proven that it is not possible to avoid tree-level flavor-changing Higgs couplings in left–right models [2015], the model can be augmented by discrete symmetries that suppress these couplings to a safe level even for heavy Higgs bosons around the TeV scale [2016].

Another interesting probe of left–right symmetric models is given by $b \to s\gamma$ and $b \to d\gamma$ transitions [1997,2017–2020]. While in a significant portion of the parameter space of these models the effects are rather modest, it is possible to generate a sizeable contribution to the chirality-flipped magnetic penguin operator O_7'. Its presence could most easily be detected in observables sensitive to the photon polarization [504,505].

Last but not least, left–right symmetric models can also generate visible effects in lepton flavor-violating τ decays [2021,2022]. In models with Higgs triplet representations, which are theoretically appealing due to the natural realization of TeV-scale right-handed Majorana neutrinos, the doubly charged Higgs bosons mediate the decays $\tau \to \ell_i \ell_j \ell_k$ with branching ratios in the reach of Belle II.

17.6.5. E6-inspired models

Authors: Thomas Deppisch, Jakob Schwichtenberg

E_6 unification The exceptional rank 6 group E_6 is one of the most popular unification groups [2023–2026], due, for example, to the automatic absence of anomalies and the fact that all SM fermions of one generation live in the fundamental representation. Moreover, E_6 is in a unique position among the suitable groups, because it is not a member of an infinite family and the only exceptional group with complex representations. (In contrast, SU(5) is part of the infinite $\mathrm{SU}(N)$ family, and SO(10) of the infinite $\mathrm{SO}(N)$ family.) In addition, E_6 models are a rich source of inspiration for phenomenological studies [2027–2030].

Vector-like quarks A generic prediction of E_6 models is the existence of a vector-like quark, D, in each generation, which lives in the $(3, 1, -\frac{1}{3})$ representation of $G_{\mathrm{SM}} = \mathrm{SU}(3)_C \times \mathrm{SU}(2)_L \times \mathrm{U}(1)_Y$. In contrast to chiral quarks in a sequential fourth generation, which are ruled out by precision electroweak measurements [2031] and the Higgs discovery [2032], such vector-like quarks are still a viable extension of the SM.

Mass terms for vector-like quarks are G_{SM} invariant and therefore one usually expects that they are "superheavy" [2033]. Formulated differently, one expects that only fermions which cannot get a G_{SM}-invariant mass term are light. This is known as the "survival hypothesis" [2034,2035], which

is an explanation for the lightness of the chiral SM fermions. However, the term "superheavy" is not very precise. The exotic quarks acquire their mass through the Higgs mechanism and therefore their mass depends on the breaking chain. For example, in the breaking chain

$$\begin{aligned} \mathrm{E}_6 &\to \mathrm{SO}(10) \\ &\to \mathrm{SU}(4)_C \times \mathrm{SU}(2)_L \times \mathrm{U}(1)_R \\ &\to \mathrm{SU}(3)_C \times \mathrm{SU}(2)_L \times \mathrm{U}(1)_R \times \mathrm{U}(1)_X \\ &\to \mathrm{SU}(3)_C \times \mathrm{SU}(2)_L \times \mathrm{U}(1)_Y \end{aligned} \tag{599}$$

the vector-like quarks can be the lightest exotic fermions and acquire their mass through the vacuum expectation value which breaks the $\mathrm{SU}(4)_C \times \mathrm{SU}(2)_L \times \mathrm{U}(1)_R$ intermediate symmetry. The masses of the vector-like quarks are therefore proportional to the scale at which this symmetry breaks. Symmetry-breaking scales in GUTs can be calculated by solving the renormalization group equations for the gauge couplings. For the breaking chain in Eq. (599) this was recently done in Ref. [2036], with the result:[67] $M_{3221} = 10^3$–$10^{10.5}$ GeV, $M_{421} = 10^{10.5}$ GeV, $M_{\mathrm{SO}10} = 10^{14.7}$ GeV. The E_6 scale cannot be computed since the gauge couplings are already unified at the SO(10) scale and therefore there is no boundary condition left. Although $M_{\mathrm{SO}10} = 10^{14.7}$ GeV corresponds to a proton lifetime well below the present bound from Super-Kamiokande of $\tau_p(p \to e^+\pi^0) > 10^{34}$ yr [77], this does not necessarily exclude this scenario, because it is well known that threshold corrections can alter these results dramatically [2038].

To estimate the masses of the vector-like quarks, we observe that in E_6 models the Yukawa couplings of the SM fermions and the exotic fermions have a common origin. The general Yukawa sector above the E_6 scale reads [2039]

$$\mathcal{L}_{\mathrm{Y}} = \Psi^T i\sigma_2 \Psi (Y_{27}\varphi + Y_{351'}\phi + Y_{351}\xi) + \mathrm{h.c.}, \tag{600}$$

where Ψ denotes the fermionic 27, Y_i thw Yukawa couplings, and φ, ϕ, and ξ the scalar representations 27, 351′, 351, respectively. Therefore the Yukawa couplings of the lightest generation of the vector-like quarks could be as small as the Yukawa couplings of the first SM generation. Together with M_{421} from above this means that the masses for the lightest vector-like quarks could be in the region 10–100 TeV, which will be probed in the near future through precision measurements of flavor observables [2040].

The pattern of flavor violation in models with vector-like quarks was recently discussed extensively in Ref. [1950]. Among the main findings is, for example, that tree-level Z contributions can increase ϵ'/ϵ sufficiently to remove the current tension between the SM prediction [178–181] and the latest data [2041]. The patterns of flavor violation through vector-like E_6 quarks are summarized in Tables 5, 6, and 10 in Ref. [1950]. Significant effects are possible in $B \to K^* \nu\nu$ processes and could therefore be observed by Belle II.

Leptoquarks in E_6-inspired SUSY models In supersymmetric E_6 models [2026,2042,2043] the situation is quite different. Because of $\mathcal{R}$ parity conservation the vector-like quarks are not allowed to

[67] The authors of Ref. [2036] "find a sharp disagreement" with the result of an earlier study [2037] and "this difference brings [this breaking chain] back among the potentially realistic ones," because M_{3221} can be sufficiently high to yield realistic light neutrino masses.

mix with the SM down-type quarks, but there can be interesting flavor signatures from other sectors. The flavor physics in an E_6-inspired SUSY model was recently discussed in Ref. [2044]. Of special phenomenological interest in this model are the leptoquark couplings in the superpotential,

$$\mathcal{W}_{\text{leptoquark}} = \lambda_3 \, (L \cdot Q) \, D^c + \lambda_4 \, u^c e^c D. \tag{601}$$

With these fields in the multi-TeV range, the dominant contributions to flavor physics come from neutral current operators induced by the scalar leptoquarks. The effective Hamiltonian with dimension six operators then becomes

$$\begin{aligned}\mathcal{H}_{\text{eff}} = & \frac{1}{2}\lambda_3^{ijm}(m_D^2)^{-1}_{mn}\lambda_4^{kln}\,\mathcal{O}_b + \frac{1}{2}\lambda_3^{ijm}(m_D^2)^{-1}_{mn}\lambda_3^{*,kln}\,\mathcal{O}_c \\ & + \frac{1}{2}\lambda_3^{ijm}(m_D^2)^{-1}_{mn}\lambda_3^{*,kln}\,\mathcal{O}_e + \frac{1}{2}\lambda_4^{ijm}(m_D^2)^{-1}_{mn}\lambda_4^{*,kln}\,\mathcal{O}_f,\end{aligned} \tag{602}$$

with

$$\mathcal{O}_b = (\bar{u}_l P_L u_j)(\bar{e}_k P_L e_i) - \tfrac{1}{4}(\bar{u}_l \, \sigma^{\mu\nu} P_L u_j)(\bar{e}_k \, \sigma_{\mu\nu} P_L e_i), \tag{603}$$

$$\mathcal{O}_c = (\bar{\nu}_l \gamma^\mu P_L \nu_i)(\bar{d}_k \gamma_\mu P_L d_j), \tag{604}$$

$$\mathcal{O}_e = (\bar{e}_l \gamma^\mu P_L e_i)(\bar{u}_k \gamma_\mu P_L u_j), \tag{605}$$

$$\mathcal{O}_f = (\bar{e}_l \gamma^\mu P_R e_i)(\bar{u}_k \gamma_\mu P_R u_j). \tag{606}$$

Here, i, j, k, l, m, n are flavor indices and $(m_D^2)^{-1}$ is the inverse of the squared leptoquark mass matrix.

It is an interesting fact that these E_6 leptoquarks couple down-type quarks to neutrinos and up-type quarks to charged leptons. Further, these operators are lepton flavor non-universal. Therefore they open new (semi-)leptonic decay channels not present in the SM. Summing over all neutrino final states can also enhance decay rates in comparison to SM processes. Hence, improved measurements of the following rare decays may be sensitive to this kind of new physics:

- Leptonic decays of the D^0 meson are highly suppressed in the SM. The operators $\mathcal{O}_b$, $\mathcal{O}_e$, and $\mathcal{O}_f$ can significantly enhance these processes, also inducing LFV decays.
- Operator $\mathcal{O}_c$ contributes to the decay modes $B \to X_s \nu\overline{\nu}$ and $K \to \pi \nu\overline{\nu}$. In these cases, future measurements can reach the sensitivity of the SM predictions. This may allow either finding or excluding E_6 leptoquarks for a large region of the parameter space. Figure 222 shows the allowed regions using current data [77]. The mean values x and y are defined by

$$\frac{\lambda_3^{\ell 21}\lambda_3^{*,3\ell' 1}}{2m_D^2} \equiv \frac{x + \mathrm{i}y}{2m_D^2}, \qquad \ell, \ell' = 1, 2, 3, \tag{607}$$

  and m_D is the mass of the lightest leptoquark.

Apart from the neutral current operators, there are also charged current operators which have to compete with the contributions from three families of Higgs doublets and also with W boson exchange. Searches for SUSY Higgs couplings, e.g. in $b \to s\gamma$, also put relevant constraints on this model.

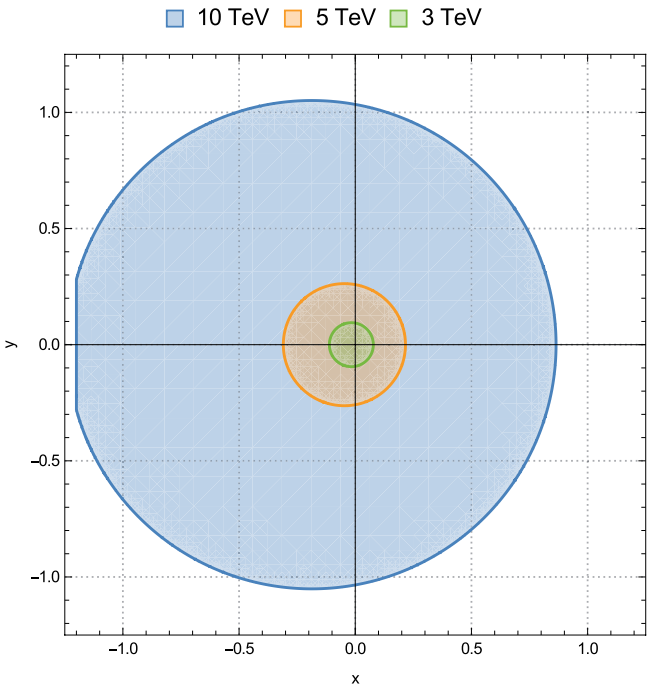

Fig. 222. Constraints from current data of $B \to X_s \nu\bar{\nu}$ on E_6 leptoquarks. The allowed regions for the parameters x and y that parameterize the couplings are shown for several values of the leptoquark mass m_D.

17.7. Models of compositeness

Author: David Straub

Introduction Partially composite SM quarks or leptons are predicted by several NP models. In composite Higgs models that are motivated by solving the SM's Higgs naturalness problem, they are a consequence of the linear coupling of the elementary fermion fields to composite operators that are required to generate fermion masses while avoiding the flavor problems of extended technicolor theories [2045]. In extra-dimensional models, e.g. of Randall–Sundrum type, partial compositeness in the four-dimensional dual picture arises from bulk fermions coupled to a bulk or brane Higgs [2046–2049]. If quarks were partially composite, the hierarchies in their masses and mixing angles could be a consequence of different degrees of compositeness (sticking to the four-dimensional language for definiteness), the first generation corresponding to the "mostly elementary" and the third generation to the "significantly composite" quarks.

Most effects in flavor physics in these models arise from the presence of heavy spin-1 states (composite resonances or KK modes) with the quantum numbers of the SM gauge bosons, and are thus closely related to Z' models (see, e.g., Refs. [2050–2053]). While the collider phenomenology is often distinct from renormalizable models with extended gauge sectors since the resonances tend to be broad, these differences are less relevant for flavor physics. The characteristic flavor effects arise from the flavor structure of the composite–elementary mixings.

Since some of the spin-1 resonances can mix with the elementary electroweak gauge bosons, flavor-changing Z couplings can also be generated. This leads to an interplay between flavor and electroweak precision tests. While the strong constraints on modifications of the electroweak T parameter suggest the presence of a global custodial symmetry $SU(2)_L \times SU(2)_R$ in the strong sector, the constraints on modifications of the $Z \to b\bar{b}$ partial width from LEP require a "custodial

protection" of the $Z\bar{b}b$ couplings within this class of models, which can be achieved by an appropriate choice of the representation of the composite fermions under this global symmetry [2054]. This in turn leads to forbidden or suppressed flavor-changing Z couplings for one chirality of down-type quarks (see, e.g., Refs. [2055,2056]).

Flavor structure An interesting possibility for the flavor structure is *flavor anarchy*, implying that the couplings in the strongly coupled composite sector are structureless (i.e. do not exhibit pronounced hierarchies), while the CKM and quark mass hierarchies arise purely from the composite–elementary mixings. Writing the rotation between the composite–elementary basis and the mass basis as

$$\begin{pmatrix} \psi^{\text{light}} \\ \Psi^{\text{heavy}} \end{pmatrix} = \begin{pmatrix} \cos\phi & -\sin\phi \\ \sin\phi & \cos\phi \end{pmatrix} \begin{pmatrix} \psi^{\text{ele}} \\ \Psi^{\text{comp}} \end{pmatrix}, \tag{608}$$

where ψ^{light} is an SM fermion, Ψ^{heavy} a new heavy fermion, and only the field Ψ^{comp} couples to the Higgs field; $s_\psi \equiv \sin\phi$ is the degree of compositeness of ψ^{light}. In the case of flavor anarchy, one finds the approximate relations

$$m_{u^i} \sim v\, g_\rho s_{q_L^i} s_{u_R^i} \tag{609}$$

for the up-type quark masses, where g_ρ is a generic strong-sector coupling, and analogously for the down-type quark masses, while the off-diagonal elements of the CKM matrix are roughly given by

$$V_{ij} \sim s_{q_L^i}/s_{q_L^j}, \qquad i > j. \tag{610}$$

This dependence leads to an automatic parametric suppression of FCNCs. For instance, the K^0–$\bar{K}^0$ mixing operator $(\bar{s}_L\gamma_\mu d_L)^2$ is proportional to $s^2_{q_L^2} s^2_{q_L^1} \sim s^4_{q_L^3} V^2_{td} V^2_{ts}$, which is the same CKM-like suppression as in the SM. However, the model is not minimally flavor violating (MFV) as FCNC operators with right-handed quarks are also generated. Using the naive parametric counting, this leads to a constraint on the NP scale of around 15 TeV from indirect CP violation in K^0–$\bar{K}^0$ mixing [2051,2052,2057].

To ameliorate this problem, it has been suggested that the composite sector is exactly invariant under a large flavor symmetry which is only broken minimally (i.e. by the amount required to reproduce CKM mixing) by the composite–elementary mixings.[68] A maximal symmetry based on U(3) rotations in three-generation space can be invoked to obtain MFV models [2067,2068], but these tend to struggle with strong constraints from electroweak precision tests or quark compositeness searches as they tie the compositeness of light quarks to the top quark. An alternative is to restrict the flavor symmetry to the first two generations, i.e. use U(2) rotations, which avoids these problems but still leads to CKM-like flavor violation [1931,2053].

Signals in flavor physics The most likely observables to be affected by models with partial quark compositeness strongly depend on the flavor structure and the implementation of custodial protection. We will discuss the most relevant cases in turn.

[68] For alternative mechanisms, see, e.g., Refs.[2058–2066].

Anarchic flavor structure: The most sensitive observables are expected to be ϵ_K, hadronic electric dipole moments (EDMs), ϵ'/ϵ, and the mass differences and CP violation in B_d and B_s mixing. While the mass differences have already been measured to a very good precision, their constraining power is currently limited by the limited knowledge of CKM elements from tree-level processes, e.g. V_{cb} and V_{ub} from semi-leptonic decays. Improved measurements of these decays by Belle II will thus play an important role in scrutinizing these models.

MFV with left-handed compositeness: In these models the flavor symmetry is maximal and only broken by the composite–elementary mixings of *right-handed* quarks. In this case, no FCNCs arise at tree level. Constraints from loop-level processes are expected to be weak given the strong bounds from electroweak precision tests. However, there can be sizeable contributions to hadronic EDMs.

MFV with right-handed compositeness: In this case the flavor symmetry is only broken by the composite–elementary mixings of *left-handed* quarks. Again, there can be sizeable contributions to hadronic EDMs, but also FCNCs are generated at tree level. The most sensitive observables are expected to be ϵ_K as well as B_d and B_s mixing.

U(2) *models:* In these models, both $\Delta F = 1$ and $\Delta F = 2$ processes with kaons or B mesons are sensitive to tree-level new physics effects. Up to sub-leading effects in the (flavor-symmetry-breaking) spurion expansion, effects arise in operators with the same chirality as those present in the SM, which potentially allows us to distinguish these models from the anarchic ones. In the $\Delta F = 1$ sector, signals at Belle II could arise in $b \to s\ell\ell$ and $b \to s\nu\bar{\nu}$ transitions (see, e.g., Refs. [613,2056]).

17.8. Conclusions

Belle II has a unique potential to reveal physics beyond the Standard Model. In this chapter we have described 10 BSM model classes and elucidated their imprints on the observables to be studied at Belle II. Tables 145–149 list 80 interesting observables which can be measured by Belle II and summarizes the sensitivity of these observables to effects from the various BSM model classes. The plethora of measurements (giving complementary information) will eventually help to pin down many features of the next theory superseding the SM. We may hope that Belle II will guide the high-p_T experiments to the discovery of new particles.

18. Global analyses

Editors: F. Bernlochner, R. Itoh, J. Kamenik, V. Lubicz, U. Nierste, Y. Sato, L. Silvestrini
Additional section writers: W. Altmannshofer, F. Beaujean, M. Bona, M. Ciuchini, J. A. Evans, S. Jahn, F. Mahmoudi, A. Paul, J. Rosiek D. Shih, D. Straub P. Urquijo, D. Van Dyk, R. Watanabe

18.1. Introduction

To interpret results of Belle II measurements requires global analyses when those observables are related theoretically to the other observables which have or have not yet been measured. In particular, when a signal of new physics is discovered, a consistency check has to be done thoroughly, including numbers of observables. Obviously, this is not an easy task since each observable has very complicated theoretical expressions and inputs, as we have seen throughout this book. Thus, developing tools is of primary importance in performing global analyses. In this final chapter we present some results of the global analyses and also the tools developed for this purpose.

A very successful example of global analysis in our field is the CKM unitary matrix fit, which contains four free parameters and must explain all observed flavor-changing phenomena, both CP conserving and violating, in the SM. Two tools have been developed independently, the `CKMfitter` and `UTfit` packages. In Sect. 18.2 we demonstrate the NP sensitivity of the Belle II experiment using these tools. Taking into account the future achievable precisions for various observables obtained in the previous chapters, we assess the reach of the precision in the case of SM and the discovery potential of new physics at Belle II through CKM unitarity triangle analysis.

In the SM, flavor phenomena are described by using the effective Hamiltonian (see Chapter 7). The Wilson coefficients in this Hamiltonian include information on the weak interaction (e.g. the dependence of the W boson and top quark masses) as well as QCD radiative corrections. An NP effect can appear as deviations between the experimentally determined values of the Wilson coefficients and their SM expectations. Thus, the Wilson coefficient fit is the most useful method for global analyses. In Sect. 18.3 we extend the effective Hamiltonian in a generic manner (with a model-independent method), yet limiting the extension by focusing on the two kinds of flavor-changing processes where hints of NP have been seen recently. We discuss what kind of deviations from SM appear in those Wilson coefficients and its expected sensitivity at the Belle II experiment.

There are more and more global analys-s tools available for flavor physics, and in the B2TiP framework we have organized dedicated workshops to discuss and compare them, inviting their developers. The tools we have discussed are those that fit the Wilson coefficients or the NP parameters (`Flavio`, `HEPfit`, `EOS`), those that compute the flavor physics observables, including contributions from the supersymmetric models (`SuperIso`, `SUSY_Flavor`, `FormFlavor`), and one that is a statistical tool (`pypmc`). In Sect. 18.4 we describe the characteristics of these tools.

18.2. CKM unitarity triangle global fits

In the SM, the weak charged current mixes different quark generations. The strength of such transitions are encoded in the unitary CKM matrix. In the case of three generations of quarks, the physical content of this matrix reduces to four real parameters, among which there is one phase, the only source of CP violation in the quark sector (see Sect. 7). These four real parameters are defined independently of the phase convention as

$$\lambda^2 = \frac{|V_{us}|^2}{|V_{ud}|^2 + |V_{us}|^2}, \quad A^2\lambda^4 = \frac{|V_{cb}|^2}{|V_{ud}|^2 + |V_{us}|^2}, \quad \bar{\rho} + i\bar{\eta} = -\frac{V_{ud}V_{ub}^*}{V_{cd}V_{cb}^*}. \tag{611}$$

At Belle II the attention on the combined analysis of the CKM unitarity triangle constraints will shift from pure metrology of the SM to investigation of deviations in flavor physics and manifestations of NP.

In order to perform global analyses of the CKM unitarity triangle two tools have been developed, `CKMfitter` and `UTfit`, which use different statistical methods. In this section, using these two packages, we present case studies to demonstrate the potential of discovering NP through the CKM unitarity triangle analysis at the Belle II experiment.

18.2.1. `CKMfitter`

Author: Phillip Urquijo

Here we discuss the future prospects of unitarity triangle global analyses using the `CKMfitter` package, which uses a frequentist approach based on the Rfit model to describe systematic uncertainties (see Ref. [91] for details). The key inputs used in the SM global fit are presented in Table 153.

Table 153. The `CKMFitter` input parameter values for the current situation (as of 2016) and for each scenario, year 2025 for the world average scenario [scenario (1)], and year 2025 for the SM-like scenario [scenario (2)]. The values in brackets are where Belle II and LHCb upgrade projections are combined.

Input	Current 2016	Scenario (1) Belle II (+LHCb) 2025	Scenario (2) Belle II (+LHCb) 2025
$\|V_{ub}\|$ (semi-leptonic) $[10^{-3}]$	$4.01 \pm 0.08 \pm 0.22$	± 0.10	3.71 ± 0.09
$\|V_{cb}\|$ (semi-leptonic) $[10^{-3}]$	$41.00 \pm 0.33 \pm 0.74$	± 0.57	41.80 ± 0.60
$\mathcal{B}(B \to \tau\nu)$	1.08 ± 0.21	± 0.04	0.817 ± 0.03
$\sin 2\phi_1$	0.691 ± 0.017	± 0.008	0.710 ± 0.008
ϕ_3 [°]	$73.2^{+6.3}_{-7.0}$	± 1.5 (± 1.0)	67 ± 1.5 (± 1.0)
ϕ_2 [°]	$87.6^{+3.5}_{-3.3}$	± 1.0	90.4 ± 1.0
Δm_d	0.510 ± 0.003	—	—
Δm_s	17.757 ± 0.021	—	—
$\mathcal{B}(B_s \to \mu\mu)$	$2.8^{+0.7}_{-0.6}$	(± 0.5)	$3.31^{+0.7}_{-0.6}$ (± 0.5)
f_{B_s}	$0.224 \pm 0.001 \pm 0.002$	0.001	—
B_{B_s}	$1.320 \pm 0.016 \pm 0.030$	0.010	—
f_{B_s}/f_{B_d}	$1.205 \pm 0.003 \pm 0.006$	0.005	—
B_{B_s}/B_{B_d}	$1.023 \pm 0.013 \pm 0.014$	0.005	—
$\|V_{cd}\|(\nu N)$	0.230 ± 0.011	—	—
$\|V_{cs}\|(W \to c\bar{s})$	$0.94^{+0.32}_{-0.26} \pm 0.13$	—	—
f_{D_s}/f_{D_d}	$1.175^{+0.001}_{-0.004}$	—	—
$\mathcal{B}(D \to \mu\nu)$	0.374 ± 0.017	± 0.010	—
ϵ_K	2.228 ± 0.011	—	—
$\|V_{us}\|f_+^{K\to\pi}(0)$	0.2163 ± 0.0005	—	0.22449 ± 0.0005
$\mathcal{B}(K \to e\nu)$	1.581 ± 0.008	—	1.5689 ± 0.008
$\mathcal{B}(K \to \mu\nu)$	0.6355 ± 0.0011	—	0.6357 ± 0.0011
$\mathcal{B}(\tau \to K\nu)$	0.6955 ± 0.0096	—	0.7170 ± 0.0096
$\|V_{ud}\|$	0.97425 ± 0.00022	—	—

Low-energy strong interactions constitute a central issue in flavor physics, which explains the need for accurate inputs for hadronic quantities such as decay constants, form factors, and bag parameters. `CKMfitter` mostly relies on lattice QCD simulations, with a specific averaging procedure to combine the results from different collaborations. A similar approach is followed in order to combine the inclusive and exclusive determinations of $|V_{ub}|$ and $|V_{cb}|$, which are not in excellent agreement. The current constraints on the unitarity triangle parameters are depicted in the $\bar{\rho}$–$\bar{\eta}$ plane in Fig. 223.

We consider two key scenarios in the Belle II era, defined as follows.

(1) World average scenario: the central values of the CKM matrix parameters stay at the world average ($c2016$) central values while for the uncertainties we consider Belle II + LHCb + LQCD future projections using the world average values as of 2017. For reference we show the precision of Belle II-only scenarios (rather than Belle II + LHCb).
(2) SM-like scenario: the central values are chosen such that they satisfy the SM (i.e. closed unitarity triangle) while the uncertainties are projected to the future Belle II + LHCb + LQCD data. For reference we show the precision of the Belle II-only cases as well.

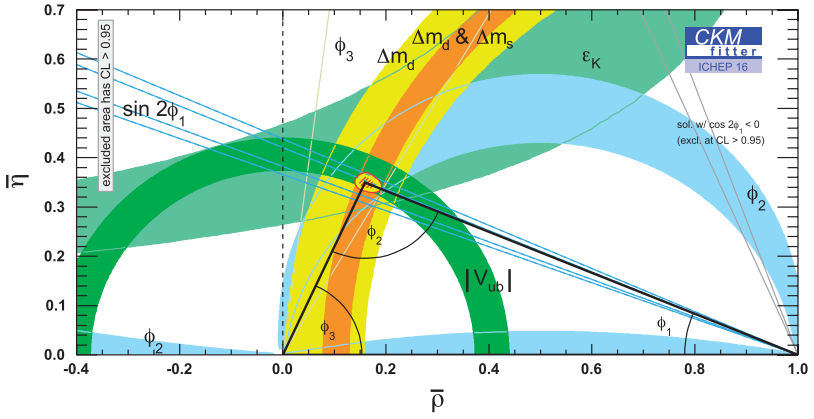

Fig. 223. Current unitarity triangle fit as determined with `CKMFitter`.

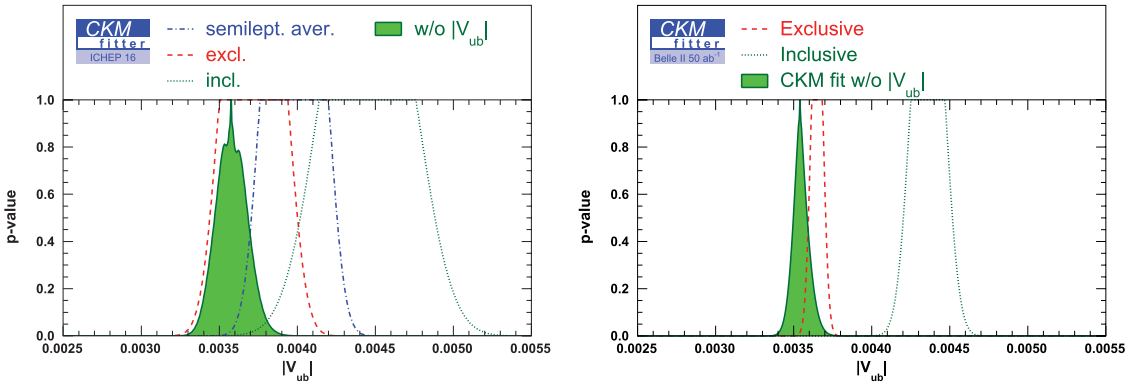

Fig. 224. $|V_{ub}|$ today (left) and extrapolated to the 50 ab^{-1} scenario (right).

The inputs to the fits are shown in Table 153. While the projections include input from Belle II and LHCb, it is expected that Belle II will provide the most precise measurements of many key observables used in the determination of these parameters. The exceptions are ϕ_3, which will be of similar precision at LHCb, and B_s and B mixing, which will be measured with greater precision at LHCb.

One of the most important inputs from Belle II will be the measurement of $|V_{ub}|$ from exclusive and inclusive semi-leptonic B decays. Figure 224 shows the current and projected precision of exclusive and inclusive world averages, their combination performed by `CKMFitter`, and the expected value based on CKM unitarity. An interesting test in the Belle II era will be the comparison between Br($B \to \tau\nu$) and $\sin 2\phi_1$. We depict the projected precision for these inputs compared to the constraints from the global fit in Fig. 225.

The fit results for scenarios (1) and (2) are shown in Fig. 226, and summarized in Table 154. For scenario (1) we show the associated p-values for the fits. For scenario (2) we show the numerical precision of the CKM unitarity triangle parameters.

The current and projected (Belle II combined with LHCb) fits for the world average scenario with various data subsets are shown in Fig. 227. The plots show constraints from loop, tree, CP-conserving, and CP-violating scenarios respectively.

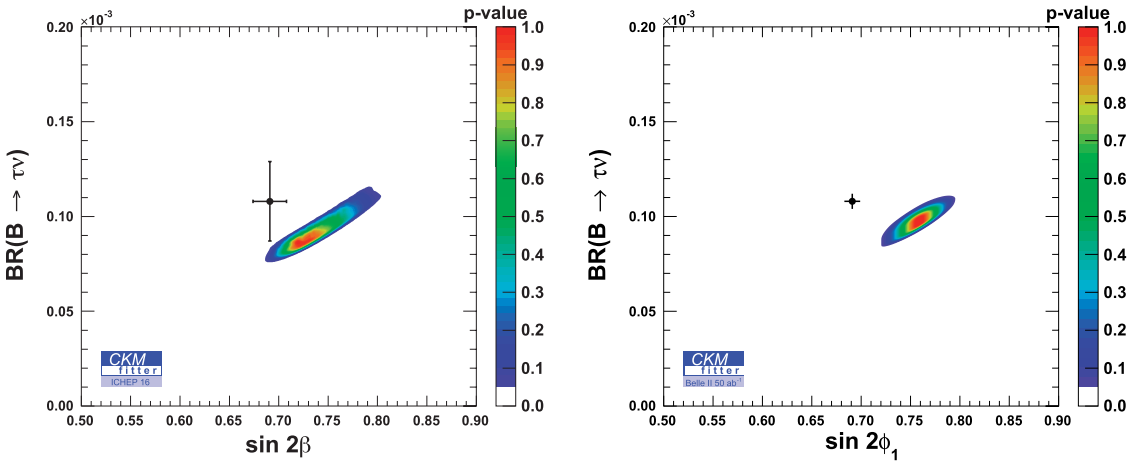

Fig. 225. $\sin 2\phi_1$ versus $\mathrm{Br}(B \to \tau\nu)$ derived from the global fit (contour) and direct measurements (data points) for current world average values (left) and Belle II projections (right).

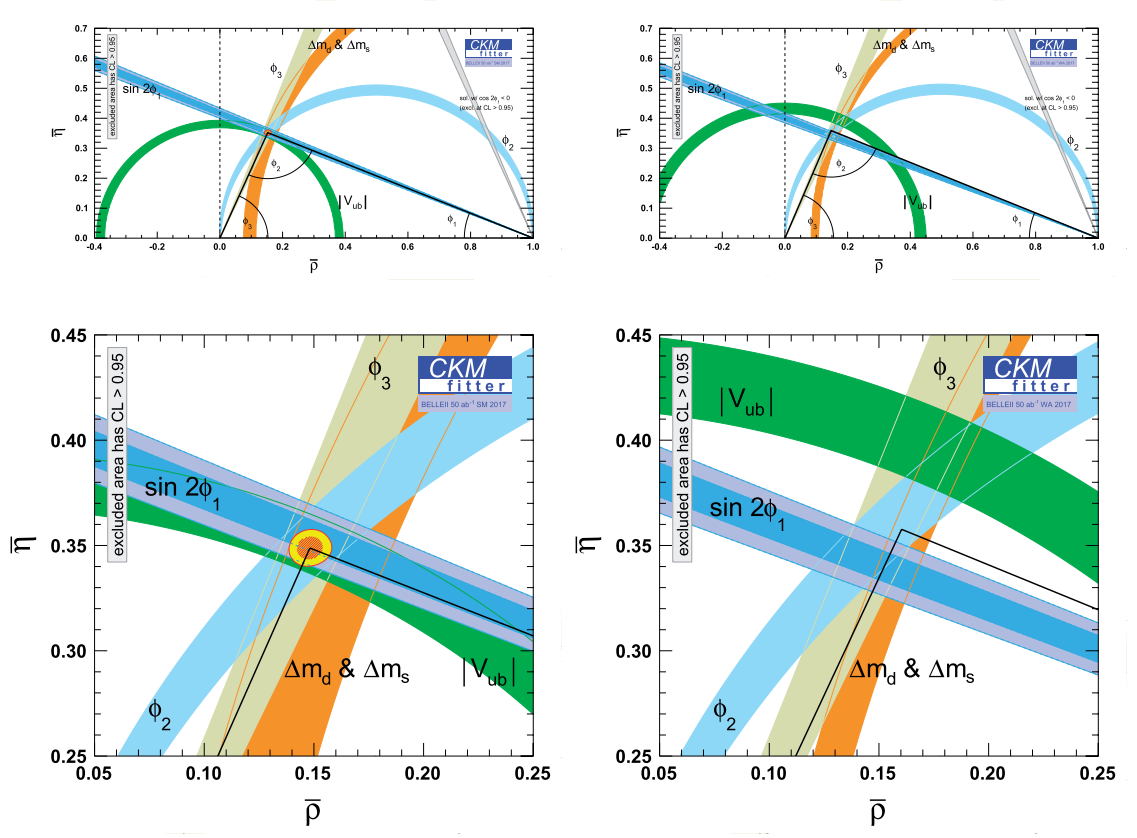

Fig. 226. Current unitarity triangle fit extrapolated to the 50 ab^{-1} scenario for an SM-like scenario (left) and world average values (right).

The `CKMFitter` group has performed analyses of new physics in mixing, in particular $\Delta B = 2$ operators, assuming that tree decays are not affected by NP effects. Within this framework, NP contributions to the $B_{d,s}$ mixing amplitudes can be parameterized as

$$M_{12}^{d,s} = (M_{12}^{d,s})_{\mathrm{SM}} \times \left(1 + h_{d,s} e^{2i\sigma_{d,s}}\right). \tag{612}$$

The results of fits with current constraints and with the full Belle II dataset are shown in Fig. 228.

Table 154. `CKMFitter` results for the Wolfenstein parameters with current world averages, and with the SM-like scenario with Belle II precision and with Belle II combined with LHCb by the year 2025.

Input	Current world average	SM value Belle II	SM value Belle II + LHCb
A	$0.8227^{+0.0066}_{-0.0136}$	$^{+0.0025}_{-0.0027}$	$^{+0.0024}_{-0.0028}$
λ	$0.22543^{+0.00042}_{-0.00031}$	$^{+0.00036}_{-0.00030}$	$^{+0.00035}_{-0.00030}$
$\bar{\rho}$	$0.1504^{+0.0121}_{-0.0062}$	$^{+0.0054}_{-0.0044}$	$^{+0.0042}_{-0.0040}$
$\bar{\eta}$	$0.3540^{+0.00069}_{-0.0076}$	$^{+0.0037}_{-0.00040}$	$^{+0.0036}_{-0.00037}$

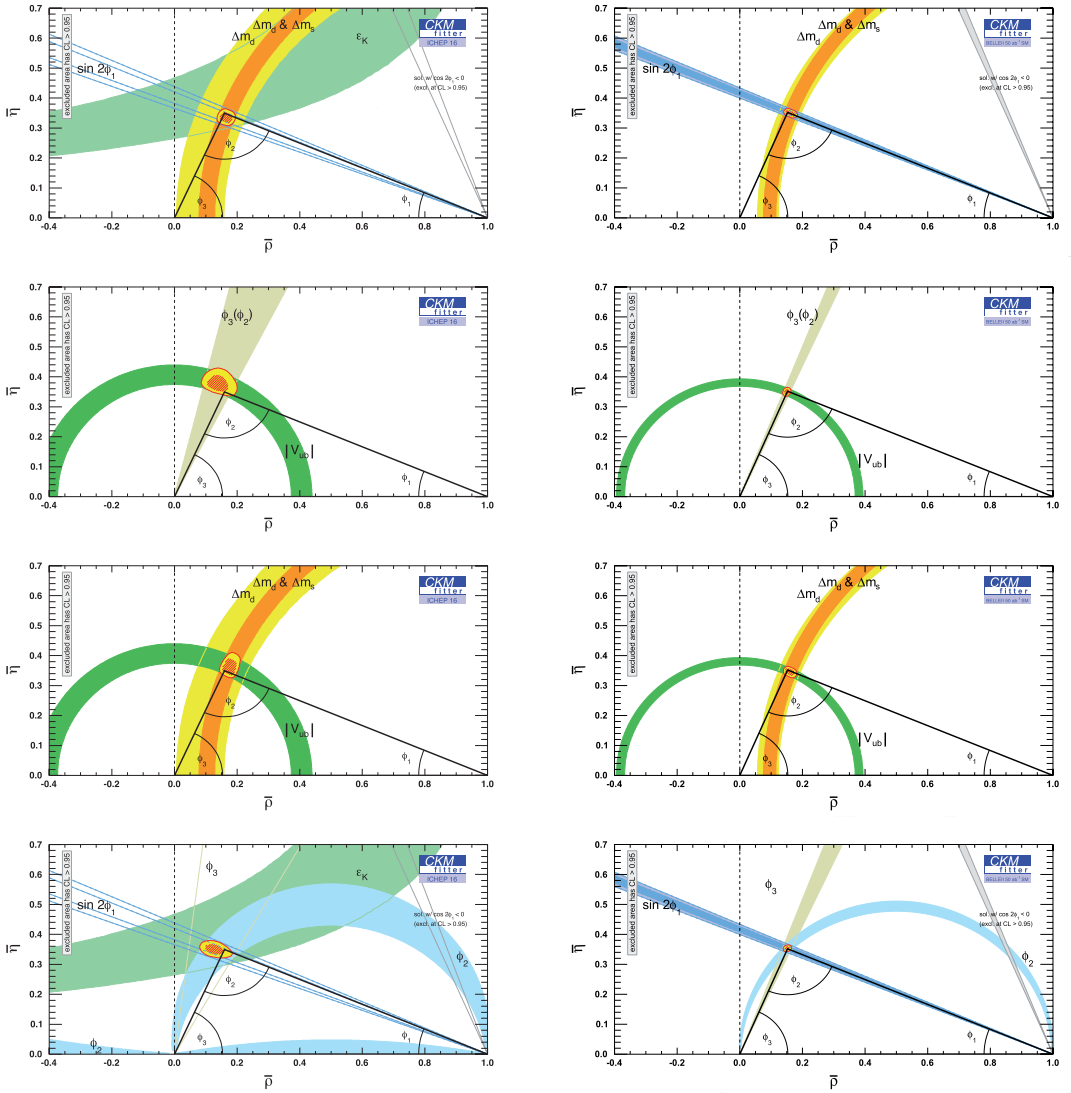

Fig. 227. Current unitarity triangle fit (left) and extrapolated to the 50 ab^{-1} scenario for the SM-like scenario (right). Four sets of fits are shown using loop, tree, CP-conserving and CP-violating data subsets, respectively.

For an NP contribution to the mixing of a meson with $q_i\bar{q}_j$ flavor quantum numbers due to the operator

$$\frac{C_{ij}^2}{\Lambda^2}\left(\bar{q}_{i,L}\gamma^\mu q_{j,L}\right)^2, \tag{613}$$

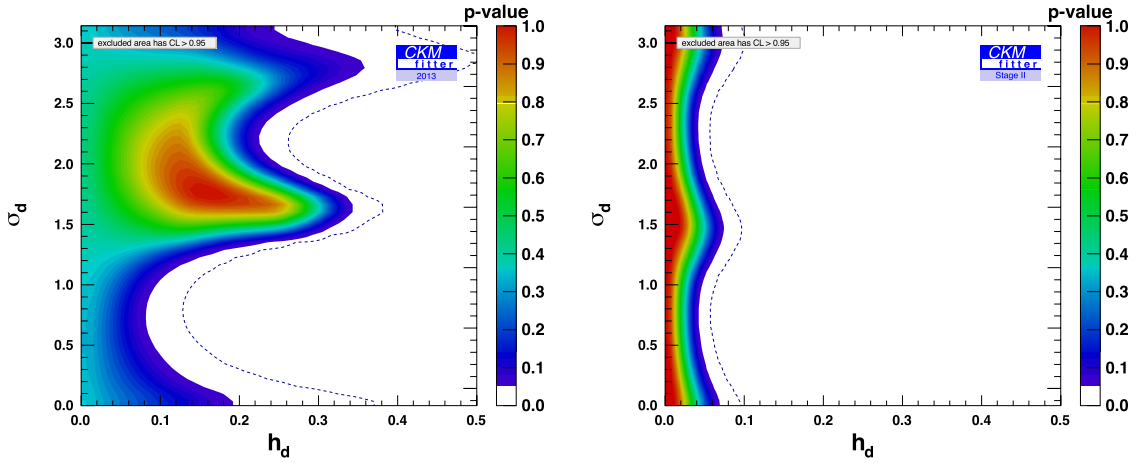

Fig. 228. Results of the fit to NP in mixing, for current constraints (left) and year 2025 constraints (right).

one finds that

$$h \simeq 1.5 \frac{|C_{ij}|^2}{|\lambda_{ij}^t|^2} \frac{(4\pi)^2}{G_F \Lambda^2} \simeq \frac{|C_{ij}|^2}{|\lambda_{ij}^t|^2} \left(\frac{4.5\,\text{TeV}}{\Lambda} \right), \quad \sigma = \arg(C_{ij} \lambda_{ij}^{t*}), \tag{614}$$

where $\lambda_{ij}^t = V_{ti}^* V_{tj}$ and V is the CKM matrix. The scales of the operators probed in B_d mixing by the end of Belle II data-taking will be 17 TeV and 1.4 TeV for CKM-like couplings in tree- and one-loop-level NP interactions respectively. For scenarios with no hierarchy, i.e. $|C_{ij}| = 1$, the corresponding scale of operators probed will be 2×10^3 TeV and 2×10^2 TeV in tree- and one-loop-level NP interactions respectively.

18.2.2. `UTfit`

Authors: Marcella Bona, Marco Ciuchini

Here we discuss the impact of Belle II on the unitarity triangle analysis within and beyond the SM in the Bayesian approach of the UTfit Collaboration [759,2069–2072]. We consider the two scenarios from Table 1.3. In particular, we present results using experimental uncertainties corresponding to 5 and 50 ab^{-1} for $|V_{cb}|$, $|V_{ub}|$, $\sin 2\phi_1$, ϕ_3, and ϕ_2, while central values are tuned to the SM. For other input parameters, in the 50 ab^{-1} scenario we use the uncertainties reported in Table 155, based on extrapolation of Ref. [2073, Appendix B.2].

The projected uncertainties of the SM fit for the CKM parameters, UT angles, and $\text{Br}(B \to \tau\nu)$ (not used in the fit) are reported in Table 156 and Fig. 229.

Generalizing the analysis beyond the SM following the notation introduced in Ref. [2071]:

$$C_{B_d} e^{2i\phi_{B_d}} = \frac{\langle B_d^0 | H_{\text{eff}}^{\text{full}} | \bar{B}_d^0 \rangle}{\langle B_d^0 | H_{\text{eff}}^{\text{SM}} | \bar{B}_d^0 \rangle}, \tag{615}$$

where $H_{\text{eff}}^{\text{SM}}$ includes only the SM box diagrams, while $H_{\text{eff}}^{\text{full}}$ also includes the NP contribution to the B_d–$^0B_d^0$ mixing, we obtain the uncertainties presented in Table 157 and Fig. 230 for the CKM parameters and the parameters representing NP contributions to B_d–$\bar{B}_d$ mixing.

Table 155. Uncertainties on external input parameters in the 5 and 50 ab^{-1} scenarios used in the UTFit study. In the 5 ab^{-1} study it is assumed that there is no improvement with respect to the present uncertainties.

Parameter	Error (5 ab^{-1})	Error (50 ab^{-1})
$\alpha_s(M_Z)$	±0.0012	±0.0004
m_t (GeV)	±0.73	±0.6
$\lvert V_{us}\rvert$	±0.0011	±0.0002
B_K	±0.029	±0.002
f_{B_s} (GeV)	±0.05	±0.001
f_{B_s}/f_{B_d}	±0.013	±0.006
B_{B_s}/B_{B_d}	±0.036	±0.007
B_{B_s}	±0.053	±0.007

Table 156. Extrapolated uncertainties of the fit in the 5 and 50 ab^{-1} scenarios. For comparison, we also report the uncertainties of the current fit.

Parameter	Error		
	Current	5 ab^{-1}	50 ab^{-1}
λ	±0.0007	±0.0007	±0.0002
A	±0.012	±0.008	±0.005
$\bar{\rho}$	±0.013	±0.007	±0.004
$\bar{\eta}$	±0.011	±0.006	±0.004
R_b	±0.013	±0.007	±0.005
R_t	±0.022	±0.006	±0.004
ϕ_2 (°)	±2.0	±0.9	±0.6
ϕ_1 (°)	±0.8	±0.4	±0.3
ϕ_3 (°)	±1.9	±1.0	±0.6
β_s (°)	±0.034	±0.02	±0.01
$J_{\rm CP}$	±0.093	±0.06	±0.04
Br($B \to \tau\nu$)	±0.06	±0.05	±0.02

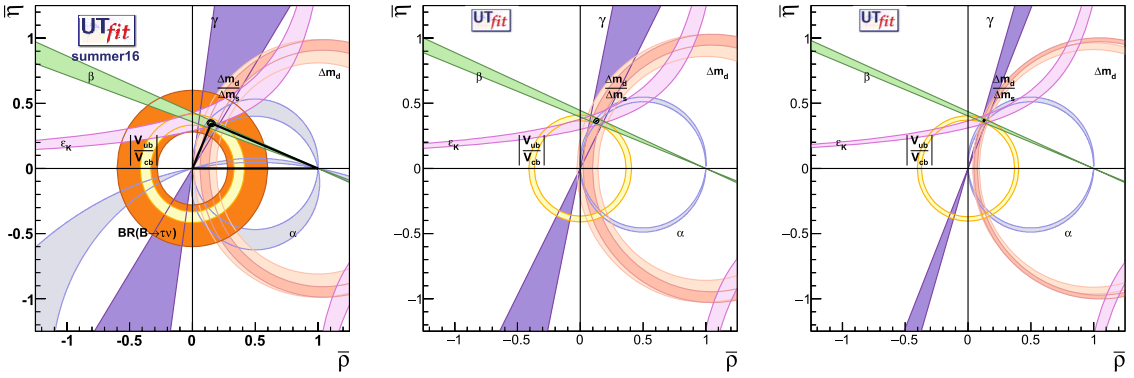

Fig. 229. SM unitarity triangle fit today (left) and extrapolated to the 5 ab^{-1} (center) and 50 ab^{-1} (right) cases.

18.3. Model-independent analyses of new physics

One can parameterize all possible types of new physics in terms of Wilson coefficients of the weak effective Hamiltonian. In hadronic decays this approach involves too many coefficients to be feasible in practice. However, in some cases only a restricted set of Wilson coefficients contributes and such model-independent fits are possible. These cases are discussed in this section.

Table 157. Extrapolated uncertainties on $\bar{\rho}$, $\bar{\eta}$, and the NP parameters C_{B_d} and ϕ_{B_d} in the 5 and 50 ab^{-1} scenarios. For comparison, we also report the uncertainties of the current fit.

Parameter	Error		
	Current	5 ab^{-1}	50 ab^{-1}
$\bar{\rho}$	±0.027	±0.008	±0.006
$\bar{\eta}$	±0.025	±0.009	±0.007
C_{B_d}	±0.11	±0.09	±0.03
ϕ_{B_d} (°)	±1.7	±0.8	±0.6

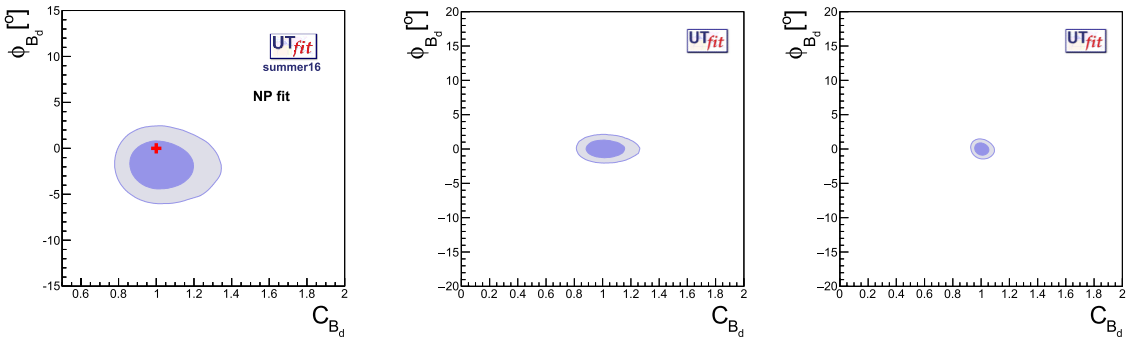

Fig. 230. Constraints on the NP parameters C_{B_d} and ϕ_{B_d} today (left) and extrapolated to the 5 ab^{-1} (center) and 50 ab^{-1} (right) scenarios.

18.3.1. Tree-level decays

Author: Ryoutaro Watanabe

(Semi-)leptonic B meson decays are derived from the quark-level process $b \to q\ell\nu$ for $q = u$ and c. Belle II has sufficient sensitivity to precisely measure a variety of observables for $\bar{B} \to D^{(*)}\ell\bar{\nu}$, $\bar{B} \to \pi\ell\bar{\nu}$, and $\bar{B} \to \ell\bar{\nu}$ (for $\ell = \tau, \mu, e$). The observed $4\,\sigma$ discrepancy from the SM in $R_{D^{(*)}} \equiv \mathcal{B}(\bar{B} \to D^{(*)}\tau\bar{\nu})/\mathcal{B}(\bar{B} \to D^{(*)}\ell\bar{\nu})$ (for $\ell = \mu$ or e) must be characterized in terms of new physics scenarios.

In the presence of all possible NP contributions in the process $b \to q\tau\nu$, the effective Lagrangian can be described by

$$-\mathcal{L}_{\text{eff}} = 2\sqrt{2}G_F V_{qb}\left[(\delta_{\nu_\tau,\nu_\ell} + C_{V_1}^{(q,\nu_\ell)})\mathcal{O}_{V_1}^{(q,\nu_\ell)} + \sum_{X=V_2,S_1,S_2,T} C_X^{(q,\nu_\ell)}\mathcal{O}_X^{(q,\nu_\ell)}\right] \tag{616}$$

for $q = u$ and c, where the four-Fermi operators $\mathcal{O}_X$ are written as

$$\mathcal{O}_{V_1}^{(q,\nu_\ell)} = (\bar{q}\gamma^\mu P_L b)(\bar{\tau}\gamma_\mu P_L \nu_\ell), \tag{617}$$

$$\mathcal{O}_{V_2}^{(q,\nu_\ell)} = (\bar{q}\gamma^\mu P_R b)(\bar{\tau}\gamma_\mu P_L \nu_\ell), \tag{618}$$

$$\mathcal{O}_{S_1}^{(q,\nu_\ell)} = (\bar{q}P_R b)(\bar{\tau}P_L \nu_\ell), \tag{619}$$

$$\mathcal{O}_{S_2}^{(q,\nu_\ell)} = (\bar{q}P_L b)(\bar{\tau}P_L \nu_\ell), \tag{620}$$

$$\mathcal{O}_T^{(q,\nu_\ell)} = (\bar{q}\sigma^{\mu\nu}P_L b)(\bar{\tau}\sigma_{\mu\nu}P_L \nu_\ell), \tag{621}$$

and C_X denotes the Wilson coefficient of $\mathcal{O}_X$ normalized by $2\sqrt{2}G_F V_{qb}$. The SM contribution is presented as $\delta_{\nu_\tau,\nu_\ell}$ in Eq. (616). The superscript (q, ν_ℓ) specifies the flavors of the quark q and the

neutrino ν_ℓ in $b \to q\tau\nu_\ell$; $\mathcal{O}_X^{(c,\nu_\ell)}$ contributes to $\bar{B} \to D^{(*)}\tau\bar{\nu}$, whereas $\mathcal{O}_X^{(u,\nu_\ell)}$ to $\bar{B} \to \pi\tau\bar{\nu}$ and $\bar{B} \to \tau\bar{\nu}$. Note that it is not necessary that the neutrino flavor is the same as ν_τ for new physics since it is not identified by the experiment. Equation (616) is the most general form without considering the right-handed neutrinos.

In addition to each V_1, V_2, S_1, S_2, and T scenario, the specific scenarios $C_{\mathrm{LQ}_{1,2}} \equiv C_{S_2} = \pm 4C_T$ are also considered here. These specific combinations of the Wilson coefficients are realized in some leptoquark (LQ) models;[69] see, e.g., the E^6-inspired model in Sect. 17.6.5.

In the following subsection we report on measurable observables that can probe new physics in the processes and their potentials expected at Belle II.

Ratio to the light-leptonic modes As for the semi-tauonic B decays, it is useful to define the ratios

$$R_{D^{(*)}} = \frac{\mathcal{B}(\bar{B} \to D^{(*)}\tau\bar{\nu})}{\mathcal{B}(\bar{B} \to D^{(*)}\ell\bar{\nu})}, \quad R_\pi = \frac{\mathcal{B}(\bar{B} \to \pi\tau\bar{\nu})}{\mathcal{B}(\bar{B} \to \pi\ell\bar{\nu})}, \tag{622}$$

where $\ell = \mu$ or e, since the uncertainty in $|V_{qb}|$, which is dominant in the SM, is cancelled out. These ratios also cancel out many experimental uncertainties. The current experimental analyses result in $R_D^{\mathrm{ex}} = 0.397 \pm 0.040 \pm 0.028$ [230], $R_{D^*}^{\mathrm{ex}} = 0.316 \pm 0.016 \pm 0.010$ [230], and $R_\pi^{\mathrm{ex}} = 1.05 \pm 0.51$ [297]. On the other hand, the SM predicts $R_D^{\mathrm{sm}} = 0.305 \pm 0.012$, $R_{D^*}^{\mathrm{sm}} = 0.252 \pm 0.004$, and $R_\pi^{\mathrm{sm}} = 0.641 \pm 0.016$. Large deviations are seen in $R_{D^{(*)}}^{\mathrm{ex/sm}}$. Since it is expected that these observables will be measured with high accuracy at Belle II, they will ultimately become very powerful NP tests.

The dominant sources of theoretical uncertainty in the purely tauonic decay, $\bar{B} \to \tau\bar{\nu}$, are f_B and $|V_{ub}|$. Then we potentially have two observables to reduce such uncertainties:

$$R_{\mathrm{ps}} = \frac{\tau_{B^0}}{\tau_{B^-}} \frac{\mathcal{B}(B^- \to \tau^-\bar{\nu}_\tau)}{\mathcal{B}(\bar{B}^0 \to \pi^+\ell^-\bar{\nu}_\ell)}, \quad R_{\mathrm{pl}} = \frac{\mathcal{B}(B^- \to \tau^-\bar{\nu}_\tau)}{\mathcal{B}(B^- \to \mu^-\bar{\nu}_\mu)}. \tag{623}$$

The former has ∼10% uncertainty [243], e.g. $R_{\mathrm{ps}}^{\mathrm{sm}} = 0.574 \pm 0.046$ from f_B and a form factor in $\bar{B} \to \pi\ell\bar{\nu}$, whereas the latter has a very accurate SM prediction, e.g. $R_{\mathrm{pl}}^{\mathrm{sm}} = 222.36$. The experimental status is obtained as $R_{\mathrm{ps}}^{\mathrm{ex}} = 0.73 \pm 0.14$, while $R_{\mathrm{pl}}^{\mathrm{ex}}$ has not been measured yet. These observables will also be good tools for testing new physics scenarios in $b \to q\tau\nu$ at Belle II.

In the presence of one NP operator of $\mathcal{O}_X^{(c,\nu_\ell)}$, R_D and R_{D^*} are correlated via the shared Wilson coefficient $C_X^{(c,\nu_\ell)}$. In Fig. 231 we show possible regions of R_D and R_{D^*}. Each shaded region can be obtained by each NP operator (as indicated in the figure) with some value of $C_X^{(c,\nu_\ell)}$. We also show regions for the two LQ scenarios with dot-dashed boundaries. We can see that R_D is sensitive to the scalars, whereas R_{D^*} ose sensitive to the tensor as it is reflecting spin properties of the charmed mesons. Thus, precisely measuring these two ratios may provide us a hint of the type of an existing NP operator if (one of) the measured values deviate from the SM predictions.

A similar conclusion can be seen for the correlation between R_π and R_{ps} in the presence of $\mathcal{O}_X^{(u,\nu_\ell)}$. For the tensor scenario, R_{ps} is fixed as the SM value since the tensor current does not contribute to $\bar{B} \to \tau\bar{\nu}$.

[69] To be precise, the relations are given as $C_{S_2} \approx \pm 7.8 C_T$ at the B meson scale while $C_{S_2} = \pm 4C_T$ is obtained at the scale where the LQ model is defined (∼O(TeV)).

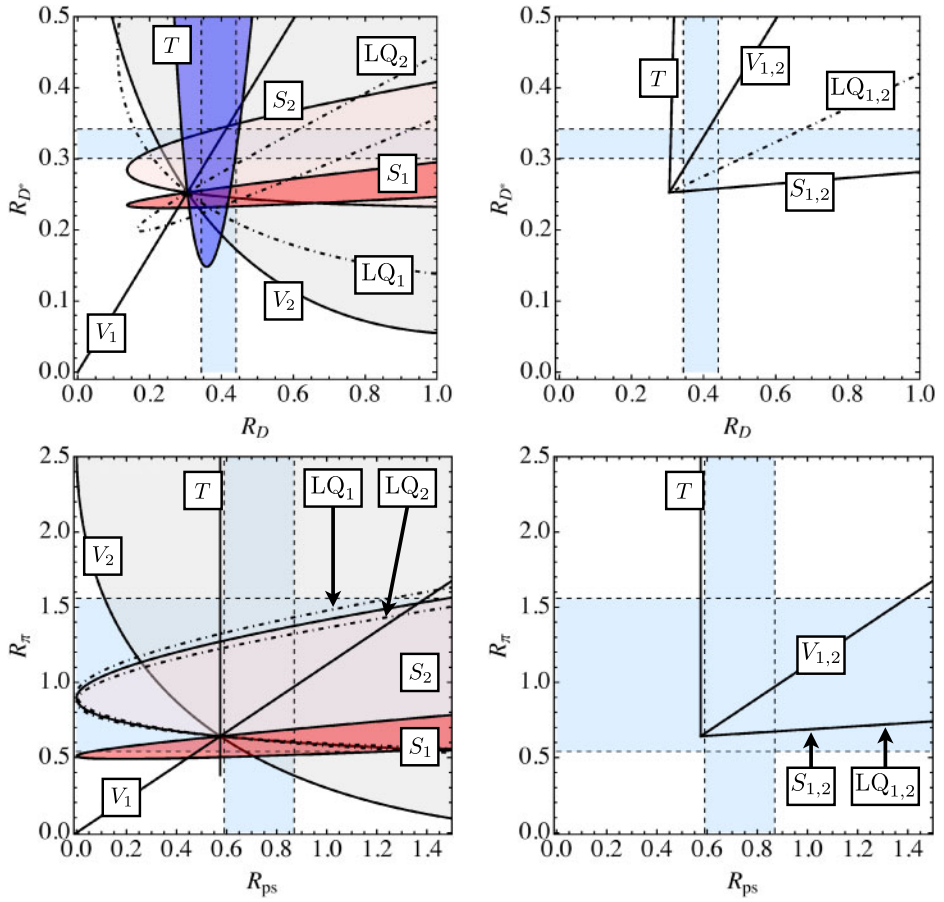

Fig. 231. (Upper) Possible covered regions of R_D and R_{D^*} in the presence of one new physics operator of $\mathcal{O}_X^{(c,\nu_\tau)}$ and $\mathcal{O}_X^{(c,\nu_{\mu,e})}$ in the left and right panels, respectively. The boundaries for the LQ scenarios are also shown with dot-dashed lines. The light blue horizontal and vertical bands are the experimental values with 1 σ ranges. (Lower) Similar results for $R_{\rm ps}$ and R_π.

Next, we discuss the maximum reach of limits on NP contributions $C_X^{(q,\nu_\tau)}$ at Belle II. The reach can be evaluated by assuming *reference central values of experimental data to be the same as the SM values* and taking theoretical and expected uncertainties into account. For the evaluations, we have taken the NP contributions to be real and omitted regions which do not include the SM points ($C_X^{(q,\nu_\tau)} = 0$).

In Table 158 we show the expected limits from $R_{D^{(*)}}$ obtained at the early and final stages of Belle II (5 ab^{-1}, 50 ab^{-1}). We can make sure that the scalar scenarios are sensitive to R_D while the tensor scenario is sensitive to R_{D^*}, as mentioned above. At the early stage we see that the $V_{1,2}$ scenario with more than 3% of the SM contribution, $|C_{V_{1,2}}| \gtrsim 0.03$, can be tested. Similarly, the NP scenarios with $|C_{S_{1,2},\,\mathrm{LQ}_{1,2}}| \gtrsim 0.07$–$0.08$ and $|C_T| \gtrsim 0.01$ can be examined. The limits will be further improved at the final stage. The expected ranges, however, are reduced only by half at most as the theoretical uncertainties in $R_{D^{(*)}}$ become dominant. Thus, further precise evaluations of the form factors are necessary to exploit the maximum potential of Belle II for new physics in $R_{D^{(*)}}$.

In Table 159 we show the expected limits from R_π and $R_{\rm ps}$ obtained at Belle II with 5 ab^{-1} and 50 ab^{-1}. At the early stage of Belle II, R_π provides loose constraints on the NP contributions, while the exclusion limits from $R_{\rm ps}$ can be $|C_{V_{1,2}}| \gtrsim 0.14$ for the $V_{1,2}$ scenarios and $|C_{S_{1,2}}| \gtrsim 0.04$ for

Table 158. 95% CL expected limits of the NP contributions C_X obtained by measuring $R_{D^{(*)}}$ at Belle II ($5\,\text{ab}^{-1}$, $50\,\text{ab}^{-1}$). The reference values of experimental data are given in the main text. The NP contribution C_X is assumed to be real, and the ranges which include the SM point ($C_X = 0$) are shown.

	R_D		R_{D^*}	
NP scenario	Belle II ($5\,\text{ab}^{-1}$)	Belle II ($50\,\text{ab}^{-1}$)	Belle II ($5\,\text{ab}^{-1}$)	Belle II ($50\,\text{ab}^{-1}$)
C_{V_1}	$[-0.08, 0.09]$	$[-0.05, 0.06]$	$[-0.04, 0.04]$	$[-0.02, 0.02]$
C_{V_2}	$[-0.08, 0.09]$	$[-0.05, 0.06]$	$[-0.04, 0.04]$	$[-0.02, 0.02]$
C_{S_1}	$[-0.12, 0.12]$	$[-0.07, 0.08]$	$[-0.82, 0.52]$	$[-0.26, 0.26]$
C_{S_2}	$[-0.12, 0.12]$	$[-0.07, 0.08]$	$[-0.52, 0.82]$	$[-0.26, 0.26]$
C_T	$[-0.21, 0.17]$	$[-0.12, 0.11]$	$[-0.01, 0.02]$	$[-0.007, 0.007]$
C_{LQ_1}	$[-0.11, 0.11]$	$[-0.06, 0.07]$	$[-0.10, 0.10]$	$[-0.04, 0.04]$
C_{LQ_2}	$[-0.13, 0.13]$	$[-0.08, 0.08]$	$[-0.18, 0.14]$	$[-0.07, 0.06]$

Table 159. 95% CL expected limits of the NP contributions C_X obtained by measuring R_π and R_{ps} at Belle II ($5\,\text{ab}^{-1}$, $50\,\text{ab}^{-1}$). The reference values of experimental data are given in the main text. The NP contribution C_X is assumed to be real and the ranges which include the SM point ($C_X = 0$) are shown.

	R_π		R_{ps}	
NP scenario	Belle II ($5\,\text{ab}^{-1}$)	Belle II ($50\,\text{ab}^{-1}$)	Belle II ($5\,\text{ab}^{-1}$)	Belle II ($50\,\text{ab}^{-1}$)
C_{V_1}	$[-0.45, 0.30]$	$[-0.12, 0.11]$	$[-0.13, 0.14]$	$[-0.08, 0.10]$
C_{V_2}	$[-0.45, 0.30]$	$[-0.12, 0.11]$	$[-0.14, 0.13]$	$[-0.10, 0.08]$
C_{S_1}	$[-1.26, 0.42]$	$[-0.32, 0.17]$	$[-0.03, 0.04]$	$[-0.02, 0.03]$
C_{S_2}	$[-1.26, 0.42]$	$[-0.32, 0.17]$	$[-0.04, 0.03]$	$[-0.03, 0.02]$
C_T	$[-1.30, 0.26]$	$[-0.13, 0.10]$	—	—
C_{LQ_1}	$[-1.34, 0.40]$	$[-0.23, 0.16]$	$[-0.04, 0.03]$	$[-0.03, 0.02]$
C_{LQ_2}	$[-1.18, 0.45]$	$[-0.93, 0.19]$	$[-0.04, 0.03]$	$[-0.03, 0.02]$

the $S_{1,2}$ scenarios. On the other hand, the T scenario is constrained only from R_π since the tensor operator does not contribute to R_{ps}. Thus, the $\text{LQ}_{1,2}$ scenarios, the combination of S_2 and T, have the same contribution as S_2 for R_{ps}. At the stage of Belle II with $50\,\text{ab}^{-1}$, $|C_{V_{1,2}}| \gtrsim 0.1$ can be obtained from both R_π and R_{ps}. As for the $S_{1,2}$ and $\text{LQ}_{1,2}$ scenarios, the limit is slightly improved as $|C_{S_{1,2}}| \gtrsim 0.03$ for R_{ps}. Finally, the T scenario with $|C_T| \gtrsim 0.1$ can be tested by measuring R_π.

The ratio of purely leptonic decays, R_{pl}, also provides exclusion limits of C_X. It is compared with R_{ps}, and it turns out that the sensitivity of R_{pl} is a factor of two weaker than that of R_{ps} [243]. Nevertheless, R_{pl} is a good observable in the sense that it has a very accurate theoretical prediction and could be used as a consistency check.

To conclude, measuring the ratios R_D, R_{D^*}, R_π, R_{ps}, and R_{pl} at Belle II can probe new physics with contributions up to $O(1\%–10\%)$ of the SM values.

Distributions Besides integrated quantities such as the ratios shown above, several distributions and asymmetries are measurable in semi-tauonic decays. As for $\bar{B} \to D^{(*)}\tau\bar{\nu}$, a variety of such observables has been proposed to test NP scenarios in the literature [225,254–257,264,265,276,284,296,883,884,2074–2080]. Among them, the distribution of $q^2 = (p_B - p_{D^{(*)}})^2$ has already been analyzed [251,270] and thus is expected to be measured at a relatively early stage of Belle II, compared

Table 160. Maximum p values for the NP scenarios obtained from the fit to the BaBar q^2 distribution.

Model	$\bar{B} \to D\tau\bar{\nu}$	$\bar{B} \to D^*\tau\bar{\nu}$	$\bar{B} \to (D+D^*)\tau\bar{\nu}$
SM	54%	65%	67%
V_1	54%	65%	67%
V_2	54%	65%	67%
S_2	0.02%	37%	0.1%
T	58%	0.1%	1.0%
LQ_1	13%	58%	25%
LQ_2	21%	72%	42%

with the other observables. Below we illustrate potential of the q^2 distribution in $\bar{B} \to D^{(*)}\tau\bar{\nu}$ at Belle II for discriminating the NP scenarios.

In Ref. [270], BaBar measured background-subtracted and efficiency-corrected q^2 distributions for signal events of $\bar{B} \to D^{(*)}\tau\bar{\nu}$. Comparing with those for the NP scenarios, we obtain the p values shown in Table 160. One finds that the S_2 and T scenarios are disfavored by the observed q^2 data while the others (including the SM) have larger (but not significant) p values. This is totally different from what is obtained from the integrated quantities $R_{D^{(*)}}$. However, we should note that the given q^2 data from BaBar does not include systematic errors, and the normalizations of the data are left as a free parameter of the fit. Therefore, the results in the table are not conclusive, although we can see that the q^2 distributions are useful for testing the NP scenarios.

The above analysis will be improved as data is accumulated at Belle II. A discriminative potential for q^2 distributions has been discussed using the following quantities [296]:

$$R_{D^{(*)}}(q^2) \equiv \frac{d\mathcal{B}(\bar{B} \to D^{(*)}\tau\bar{\nu})/dq^2}{d\mathcal{B}(\bar{B} \to D^{(*)}\ell\bar{\nu})/dq^2} N_{D^{(*)}}(q^2), \tag{624}$$

where the normalization $N_{D^{(*)}}(q^2)$ (to avoid rapid suppression of the phase spaces at $q^2 = m_\tau^2$) is defined in Ref. [296]. Here, we consider whether we can distinguish the NP scenarios by measuring $R_{D^{(*)}}(q^2)$ in the case that the present status of the anomalies on the integrated quantities, $R_{D^{(*)}}$, remains in future. In order to see this, we simulate "experimental data" for $R_{D^{(*)}}(q^2)$ assuming *one of the NP scenarios that can explain the present values of* $R_{D^{(*)}}$ and compare them with other NP scenarios. The q^2 distributions are binned as given in the BaBar hadronic tag analysis. Statistical uncertainties in each bin of $R_{D^{(*)}}(q_i^2)$ are approximately described by

$$\delta^{\rm stat} R_{D^{(*)}}(q_i^2) \sim \frac{1}{\sqrt{N_{B\bar{B}}\epsilon_i^\tau}} \frac{\sqrt{\mathcal{B}_i^\tau}}{\mathcal{B}_i^\ell} N_{D^{(*)}}(q_i^2), \tag{625}$$

where $N_{B\bar{B}} = \mathcal{L} \times \sigma(e^+e^- \to B\bar{B})$ is the number of produced $B\bar{B}$ pairs for an integrated luminosity, $\mathcal{B}_i^{\tau(\ell)}$ are the partial branching ratios of $\bar{B} \to D^{(*)}\tau\bar{\nu}$ ($\bar{B} \to D^{(*)}\ell\bar{\nu}$) for the ith bin, and ϵ_i^τ denotes the efficiency for the signal process $\bar{B} \to D^{(*)}\tau\bar{\nu}$. In the following test, the total experimental uncertainty (including the systematic one) is assumed as $\delta^{\rm exp} R_{D^{(*)}}(q_i^2) = 2\delta^{\rm stat} R_{D^{(*)}}(q_i^2)$, and then the efficiency is taken universally as $\epsilon_i^\tau = 10^{-4}$. Theoretical uncertainties are correlated between the q^2 bins and then taken as appropriate.

Given the above setup, we evaluate the required luminosities so that we can discriminate simulated data and the NP scenarios by measuring $R_{D^{(*)}}(q^2)$ at 99.9% CL. The results are shown in Table 161. As a comparison, we also show (in parentheses) results obtained by measuring $R_{D^{(*)}}$. One can see

Table 161. Luminosity required to discriminate various simulated "data" and tested model at 99.9% CL using $R_{D^{(*)}}(q^2)$ (or $R_{D^{(*)}}$ in parentheses). (—) indicates that it is impossible to discriminate between data and model.

$\mathcal{L}$ [fb^{-1}]		Model						
		SM	V_1	V_2	S_2	T	LQ_1	LQ_2
Data	V_1	1170 (270)		10^6 (—)	500 (—)	900 (—)	4140 (—)	2860 (1390)
	V_2	1140 (270)	10^6 (—)		510 (—)	910 (—)	4210 (—)	3370 (1960)
	S_2	560 (290)	560 (13750)	540 (36450)		380 (—)	1310 (35720)	730 (4720)
	T	600 (270)	680 (—)	700 (—)	320 (—)		620 (—)	550 (1980)
	LQ_1	1010 (270)	4820 (—)	4650 (—)	1510 (—)	800 (—)		5920 (1940)
	LQ_2	1020 (250)	3420 (1320)	3990 (1820)	1040 (20560)	650 (4110)	5930 (1860)	

that some cases of "data"–model, such as "S_2"–T or "S_2"–$V_{1,2}$, require only $\sim 500\,\mathrm{fb}^{-1}$ and thus can already be tested by $R_{D^{(*)}}(q^2)$ using the present data, while this is not the case for $R_{D^{(*)}}$. One also finds that we need 1–6 ab^{-1} to test the LQ scenarios, which will be achieved at an early stage of Belle II, as already pointed out. Interestingly, the discriminative potential of $R_{D^{(*)}}(q^2)$ is different from and complementary to that of $R_{D^{(*)}}$, as is shown in the table.

Connection to collider physics Here, we illustrate how the $R_{D^{(*)}}$ anomalies can be examined by the high-energy experiment at the 14 TeV LHC. A comprehensive study of such a test should be done for every specific model and is beyond the scope of this report. Instead, we show an LHC study for a scalar leptoquark model, which leads contributions with the form of C_{LQ_2}, as an example. The minimum requirement to accommodate the $R_{D^{(*)}}$ anomalies for this model is given in the Lagrangian as

$$\mathcal{L}_{S_1} = \left(g_{1L}^{33}\bar{Q}_L^{c,3}(i\sigma_2)L_L^3 + g_{1R}^{23}\bar{u}^{c,2}\ell_R^3\right)S_1, \tag{626}$$

where S_1 is an SU(2)$_L$ singlet scalar leptoquark, $Q^{c,3} = (t^c\ b^c)^T$, $L^3 = (\nu_\tau\ \tau)^T$, $u^{c,2} = c^c$, and $\ell^3 = \tau$. The contribution of C_{LQ_2} is presented by

$$2\sqrt{2}G_{\mathrm{F}}V_{cb}\,C_{\mathrm{LQ}_2} = -\frac{g_{1L}^{33}\,g_{1R}^{23*}}{M_{S_1}^2}, \tag{627}$$

and then the central values of the present anomalies can be explained with $C_{\mathrm{LQ}_2} \approx 0.26$. In this setup, one can see that the scalar LQ boson decays only into $S_1 \to c\tau$, $b\nu$, and $t\tau$. Since leptoquark bosons are dominantly pair-produced due to QCD interaction at the LHC, there are six possible final

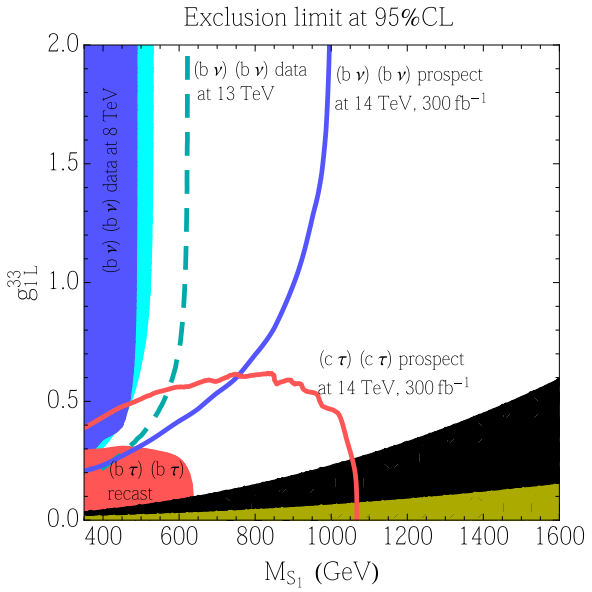

Fig. 232. Current excluded regions obtained from 8–13 TeV data and exclusion limits expected at $\mathcal{L} = 300\,\text{fb}^{-1}$ of the 14 TeV LHC in the (g^{33}_{1L}, M_{S_1}) plane at 95% CL. The black region indicates the area for $\Gamma_{S_1}/M_{S_1} > 0.2$ in which a narrow-width approximation becomes invalid. The dark yellow region is theoretically unacceptable due to $g^{23}_{1R} > 4\pi$.

states. All of them are worth analyzing at ATLAS and CMS to probe evidence of the $R_{D^{(*)}}$ anomalies measured at Belle, BaBar, and LHCb.

Reference [2081] studied two final states, $(b\nu)(\bar{b}\bar{\nu})$ and $(c\tau)(\bar{c}\bar{\tau})$, in great detail by doing numerical simulations, adopting optimized cut analyses. To see a connection between LHC direct searches and the $R_{D^{(*)}}$ anomalies, it is assumed that g^{33}_{1L} and g^{23}_{1R} are related, keeping $C_{\text{LQ}_2} = 0.26$.

As a result, the 95% CL current and expected excluded regions in the (g^{33}_{1L}, M_{S_1}) plane are shown in Fig. 232. The shaded regions in blue, cyan, and red are excluded at 95% CL by the current 8 TeV data of $(b\nu)(\bar{b}\bar{\nu})$ and $(c\tau)(\bar{c}\bar{\tau})$, respectively.[70] The blue and red curves show the 95% CL exclusion limits from $(b\nu)(\bar{b}\bar{\nu})$ and $(c\tau)(\bar{c}\bar{\tau})$ obtained at $\mathcal{L} = 300\,\text{fb}^{-1}$ of the 14 TeV LHC. Note that for the $(c\tau)(\bar{c}\bar{\tau})$ analysis, the realistic values of tagging/mistagging efficiencies of the c-jet are taken into account [2086]. Through the condition $C_{\text{LQ}_2} = 0.26$ required by the $R_{D^{(*)}}$ anomalies, both the searches of $(b\nu)(\bar{b}\bar{\nu})$ and $(c\tau)(\bar{c}\bar{\tau})$ can constrain the model parameters (g^{33}_{1L}, g^{23}_{1R}, and M_{S_1}), and then one can see from the figure that we can probe the S_1 leptoquark up to at least $M_{S_1} = 0.8$ TeV at 14 TeV LHC.

Similar correlations between the collider study and the flavor anomalies should be functional in other specific models. This will enable us to improve searching for new physics that explains the $R_{D^{(*)}}$ anomalies and that may exist in R_π and R_{ps}.

[70] For the blue and cyan regions, both the translated bound from the $(b\tilde{\chi}^0_1)(\bar{b}\tilde{\chi}^0_1)$ searches [2082,2083] and the direct bound from the $(b\nu)(\bar{b}\bar{\nu})$ searches [2083,2084] are taken into account. For the red region, the CMS search for $(b\tau)(\bar{b}\bar{\tau})$ [2085] is recast as a bound for $(c\tau)(\bar{c}\bar{\tau})$ by evaluating misidentification of the c-jet as the b-jet.

18.3.2. Loop-level decays

Author: Wolfgang Altmannshofer

Theoretical framework We extend the discussion of the effective Hamiltonian in Sect. 9.1.1 to the most generic NP scenario including the violation of lepton universality and/or lepton flavor. The effective Hamiltonian that enables model-independent studies of the leptonic decays $B^0 \to \ell^+\ell^-$ and $B_s \to \ell^+\ell^-$ as well as semi-leptonic transitions of the type $b \to d\ell\ell$, $b \to s\ell\ell$, $b \to d\nu\nu$, and $b \to s\nu\nu$ can be written as

$$\mathcal{H}_{\rm eff} = \mathcal{H}_{\rm eff}^{\rm SM} - \frac{4G_{\rm F}}{\sqrt{2}} V_{tq}^* V_{tb} \sum_i C_i^{\rm NP} \mathcal{O}_i, \tag{628}$$

where $\mathcal{H}_{\rm eff}^{\rm SM}$ is the effective Hamiltonian of the SM, $C_i^{\rm NP}$ are the Wilson coefficients encoding the effect of new physics, and $\mathcal{O}_i$ are dimension-six operators built from light SM particles.[71] Following the notation of Ref. [2087], the most relevant operators are dipole operators,

$$(\mathcal{O}_7^{(\prime)})_q = \frac{e}{16\pi^2} m_b (\bar{q}\sigma^{\mu\nu} P_{R(L)} b) F_{\mu\nu}, \tag{629}$$

$$(\mathcal{O}_8^{(\prime)})_q = \frac{g_s}{16\pi^2} m_b (\bar{q}\sigma^{\mu\nu} T^a P_{R(L)} b) G^a_{\mu\nu}, \tag{630}$$

as well as various semi-leptonic four-fermion contact interactions,

$$(\mathcal{O}_9^{(\prime)})_q^\ell = \frac{e^2}{16\pi^2} (\bar{q}\gamma_\mu P_{L(R)} b)(\bar{\ell}\gamma^\mu \ell), \tag{631}$$

$$(\mathcal{O}_{10}^{(\prime)})_q^\ell = \frac{e^2}{16\pi^2} (\bar{q}\gamma_\mu P_{L(R)} b)(\bar{\ell}\gamma^\mu \gamma_5 \ell), \tag{632}$$

$$(\mathcal{O}_\nu^{(\prime)})_q^\ell = \frac{e^2}{8\pi^2} (\bar{q}\gamma_\mu P_{L(R)} b)(\bar{\nu}_\ell \gamma^\mu P_L \nu_\ell), \tag{633}$$

$$(\mathcal{O}_S^{(\prime)})_q^\ell = \frac{e^2}{16\pi^2} (\bar{q} P_{R(L)} b)(\bar{\ell}\ell), \tag{634}$$

$$(\mathcal{O}_P^{(\prime)})_q^\ell = \frac{e^2}{16\pi^2} (\bar{q} P_{R(L)} b)(\bar{\ell}\gamma_5 \ell), \tag{635}$$

$$(\mathcal{O}_T^{(\prime)})_q^\ell = \frac{e^2}{16\pi^2} (\bar{q}\sigma_{\mu\nu} P_{L(R)} b)(\bar{\ell}\sigma^{\mu\nu} P_{L(R)} \ell), \tag{636}$$

where $\ell = e, \mu, \tau$. We explicitly allow for lepton universality violation. In the presence of lepton flavor violation, the semi-leptonic contact interactions can also contain leptons of different flavor, e.g.

$$(\mathcal{O}_9^{(\prime)})_q^{\ell\ell'} = \frac{e^2}{16\pi^2} (\bar{q}\gamma_\mu P_{L(R)} b)(\bar{\ell}\gamma^\mu \ell'), \tag{637}$$

and analogously for the other four-fermion interactions.

[71] Note that it is far from established whether the SM particles are the only dynamical degrees of freedom below the electroweak scale. If new light particles interact sufficiently weakly with the SM, they can evade direct detection. Examples are axions, light Higgs particles, light dark matter, sterile neutrinos, and dark photons. If such new degrees of freedom are lighter than B mesons, novel exotic decay modes of B mesons can open up that are not described by the effective Hamiltonian formalism but require the explicit addition of light new particles to the SM [616]. Exotic signatures include the decays of B mesons into invisible particles or resonances in the dilepton invariant mass spectra [1795].

Using the experimental result on leptonic and semi-leptonic B decays, allowed ranges for the new physics Wilson coefficients can be determined in a model-independent fashion [493,497,498,524, 592,612,647,1960,2088–2101]. Reparameterizing the effective Hamiltonian as

$$\mathcal{H}_{\rm eff} = \mathcal{H}_{\rm eff}^{\rm SM} - \sum_i \frac{1}{\Lambda_i^2}\mathcal{O}_i \tag{638}$$

allows us to translate information on the NP Wilson coefficients $C_i^{\rm NP}$ defined in Eq. (628) into constraints on the new physics scales Λ_i that suppress the dimension-six operators $\mathcal{O}_i$.[72]

In many classes of new physics, relations exist between the Wilson coefficients of the above operators. For example, in MFV models [621,1865] and in models with a minimally broken $\mathrm{U}(2)^3$ flavor symmetry [1931], the dominant Wilson coefficients are universal for down and strange quarks, $(C_i)_d = (C_i)_s$. In models that do not contain any sources of lepton flavor universality violation beyond the SM Yukawa couplings, one has, for instance, $(C_i^{(\prime)})_q^e = (C_i^{(\prime)})_q^\mu = (C_i^{(\prime)})_q^\tau$ for $i = 9, 10, \nu$, while the scalar, pseudoscalar, and tensor operators scale with the mass of the involved leptons, $(C_i^{(\prime)})_q^e/m_e = (C_i^{(\prime)})_q^\mu/m_\mu = (C_i^{(\prime)})_q^\tau/m_\tau$ for $i = S, P, T$. If new physics is heavy compared to the electroweak scale and it can be described by the SM effective field theory (SMEFT) with a linearly realized Higgs boson [620], one finds relations among the scalar and pseudoscalar operators $(C_S)_q^\ell = -(C_P)_q^\ell$, $(C_S')_q^\ell = (C_P')_q^\ell$, and vanishing tensor operators $(C_T^{(\prime)})_q^\ell = 0$ [622].[73] Moreover, due to $\mathrm{SU}(2)_L$ invariance, the operators involving neutrinos and left-handed charged leptons are related. At the level of $\mathrm{SU}(2)_L$-invariant dimension-six operators one has $(C_\nu^{(\prime)})_q = ((C_9^{(\prime)})_q - (C_{10}^{(\prime)})_q)/2$.

Leptonic decays The leptonic decays $B^0 \to \ell^+\ell^-$ and $B_s \to \ell^+\ell^-$, with $\ell = e, \mu, \tau$, are very well known to be highly sensitive probes of new physics.

The existing measurements from LHCb, CMS, and ATLAS of the branching ratios of the muonic decays $B^0 \to \mu^+\mu^-$ and $B_s \to \mu^+\mu^-$ can be interpreted in a model-independent way as constraints on the Wilson coefficients of the operators $(\mathcal{O}_{10,S,P}^{(\prime)})_s^\mu$ [2094]. Under the assumption that one operator dominates, the corresponding constraints on the NP scale Λ are at the level of $\Lambda \gtrsim 30\,\mathrm{TeV}$ for $(\mathcal{O}_{10}^{(\prime)})_s^\mu$ and $\Lambda \gtrsim 100\,\mathrm{TeV}$ for the scalar and pseudoscalar operators $(\mathcal{O}_S^{(\prime)})_s^\mu$, $(\mathcal{O}_P^{(\prime)})_s^\mu$. The constraints on the operators involving the down quark instead of the strange quark are slightly stronger. These bounds demonstrate the exquisite sensitivity of these rare B meson decays to new physics.

Combining the $B_s \to \mu^+\mu^-$ results with measurements of the decay rate and angular distribution of the semi-leptonic decay $B \to K\mu^+\mu^-$ allows the lifting of flat directions in NP parameter space that can appear when more than one operator is considered simultaneously [2104].

In the absence of BSM sources of lepton flavor universality violation, the branching ratios of the leptonic decays scale with the lepton masses squared. Given the current and foreseeable experimental sensitivities, dimuon decays are therefore the most sensitive probes of new physics in such scenarios. Searches for the dielectron and ditau decays $B \to e^+e^-$ and $B \to \tau^+\tau^-$ are sensitive probes of new sources of lepton flavor universality violation and well motivated [537].

Exclusive semi-leptonic decays Exclusive semi-leptonic decays like $B \to K^{(*)}\ell^+\ell^-$ and $B_s \to \phi\ell^+\ell^-$ give access to a plethora of observables. Beyond the corresponding decay rates, these decays

[72] See Ref. [2102] for a complementary discussion in the context of "simplified models."

[73] These relations can be violated in the presence of non-standard dynamics triggering electroweak symmetry breaking [2103].

offer, for example, angular distributions, CP asymmetries, and lepton flavor universality tests that can all be used to probe the SM and its extensions.

The differential decay distribution of the $B \to K\ell^+\ell^-$ decays as function of the angle θ_ℓ, defined as the angle between the direction of the ℓ^+ and the direction of the B in the dilepton rest frame, reads [590]

$$\frac{d\Gamma}{dz} \propto \frac{3}{4}(1-F_H)(1-z^2) + \frac{1}{2}F_H + A_{\rm FB}z, \tag{639}$$

with $z = \cos\theta_\ell$. The forward–backward asymmetry $A_{\rm FB}$ and the flat term F_H are functions of the dilepton invariant mass q^2. They are powerful probes of the scalar and tensor interactions $(\mathcal{O}^{(\prime)}_{S,P,T})^\ell_s$. Combined with the measurement of the branching ratio of $B_s \to \mu^+\mu^-$, existing data allows us to constrain the corresponding complex-valued Wilson coefficients involving muons in one fit [2099].

The differential decay distribution of the $B \to K^*\ell^+\ell^-$ decays is more complex and involves three angles (see, e.g., Ref. [588]),

$$\frac{d^3\Gamma}{d\cos\theta_\ell d\cos\theta_K d\phi} = \frac{9}{32\pi}\sum_i I_i f_i(\theta_\ell, \theta_K, \phi), \tag{640}$$

with angular coefficients I_i that depend on the dilepton invariant mass q^2. Analogous distributions describe the decays $B_s \to \phi\ell^+\ell^-$ and $B^0 \to \rho\ell^+\ell^-$. Many useful observables can be constructed out of the angular coefficients both at low q^2 and at high q^2, e.g. the CP-averaged angular coefficients S_i [588], CP asymmetries A_i [2105], and the P'_i observables [593]. Many of these observables are sensitive probes of new physics in the dipole operators $(\mathcal{O}^{(\prime)}_7)_q$ and the four-fermion contact interactions $(\mathcal{O}^{(\prime)}_{9,10})^\ell_q$.

The $B \to K^*e^+e^-$ decay also provides theoretically clean observables in the very low q^2 region $4m_e^2 < q^2 < 1\,{\rm GeV}^2$ [490,507] that allow for interesting tests of new physics in the dipole operators $(\mathcal{O}^{(\prime)}_7)_s$.

Among the various CP-violating observables there are the direct CP asymmetries in $B \to K^{(*)}\ell^+\ell^-$ decays as well as CP asymmetries of the angular coefficients in $B \to K^*\ell^+\ell^-$. Particularly interesting are the three T-odd angular observables A_7, A_8, and A_9, as they are not suppressed by small strong phases and therefore could be of $O(1)$ in the presence of CP-violating new physics [2105]. These CP-violating observables nearly vanish in the SM with very small uncertainties even in the presence of non-factorizable long-distance effects. Observation of non-zero CP asymmetries in $b \to s\ell^+\ell^-$ decays would be a clear signature of new physics. In the absence of a non-zero signal, precise measurements of the CP asymmetries $A_{7,8,9}$ can provide important bounds on BSM sources of CP violation in the form of imaginary parts of the $(C^{(\prime)}_9)^\ell_q$ and $(C^{(\prime)}_{10})^\ell_q$ Wilson coefficients, which are still only weakly constrained at the moment. Interesting CP observables can also be extracted from time-integrated and time-dependent analyses of decays into CP eigenstates like $B^0 \to K^*(\to K^0_S\pi^0)\ell^+\ell^-$ [2106].

Already existing measurements of decay rates and angular observables in the exclusive semi-leptonic decays based on the $b \to s\mu\mu$ transition show an intriguing pattern of deviations from

SM predictions that consistently point to non-standard effects in a single operator, $(\mathcal{O}_9)^{\mu}_{s}$ [497,647]. Assuming that hadronic effects are estimated in a sufficiently conservative way, the latest global fits [498,524,612,2100] find a preference for an NP contribution $(C_9)^{\mu}_{s} \approx -1$ at the level of $\sim 4\,\sigma$. Translated into an NP scale in the effective Hamiltonian of Eq. (638), this corresponds to $\Lambda \approx 35$ TeV, a scale that is not far above the direct reach of future high-energy colliders. However, unexpectedly large long-distance effects cannot be excluded as an explanation for the apparent discrepancies at this time [491,2107].

Very interesting in this context are lepton flavor universality tests where hadronic effects cancel to a very high precision and the SM predictions are robust, with accuracies at the 1% level or better [597]. Lepton flavor universality tests include ratios of branching ratios involving muons and electrons in the final state [598,2108]:

$$R_{K^{(*)}} = \frac{\mathrm{Br}(B \to K^{(*)}\mu\mu)}{\mathrm{Br}(B \to K^{(*)}ee)}, \quad R_{\phi} = \frac{\mathrm{Br}(B_s \to \phi\mu\mu)}{\mathrm{Br}(B_s \to \phi ee)}. \tag{641}$$

Interestingly enough, LHCb has measured $R_K = 0.745^{+0.090}_{-0.074} \pm 0.036$ [391] for $1\,\mathrm{GeV}^2 < q^2 < 6\,\mathrm{GeV}^2$, which differs from the SM prediction $R_K^{\mathrm{SM}} \approx 1$ by approximately $2.5\,\sigma$. This result is in striking agreement with NP explanations of the anomalies in the $b \to s\mu\mu$ transitions discussed above, assuming that the new physics affects the dimuon decays but not the dielectron decays, i.e. $(C_9)^{\mu}_{s} \approx -1$ and $(C_9)^{e}_{s} \approx 0$. Various explicit NP models have been constructed that realize such a scenario (see, e.g., Refs. [287,292,599,623,648,2109]). Future measurements of the LFU ratios showing significant deviations from 1 would establish clean and robust evidence for new physics.

Other tests of LFU are given by ratios or differences of angular observables in decays to final states with dielectrons vs. dimuons [491,524,599,600]. Examples are the difference of the forward–backward asymmetries A_{FB} or the angular observables S_5 [599]:

$$D_{A_{\mathrm{FB}}} = A_{\mathrm{FB}}(B \to K^*\mu\mu) - A_{\mathrm{FB}}(B \to K^*ee, \tag{642}$$

$$D_{S_5} = S_5(B \to K^*\mu\mu) - S_5(B \to K^*ee). \tag{643}$$

Measurements of these LFU differences provide additional means to probe lepton flavor non-universal new physics in rare B decays. For $(C_9)^{\mu}_{s} \approx -1$ and $(C_9)^{e}_{s} \approx 0$, non-standard effects at the level of $O(10\%)$ are generically predicted in these observables. The LFU differences might also serve as discriminants between NP models if precision measurements are feasible [599].

Furthermore, measurements of double ratios of branching ratios like R_{K^*}/R_K and R_{ϕ}/R_K provide a clean probe of flavor non-universal physics coupling to right-handed quarks [598,2110].

New physics models that contain new sources of LFU violation typically also lead to distinct non-standard effects in decays involving taus in the final state, like $B \to K^{(*)}\tau\tau$. If the new physics couples dominantly to the third generation of quarks and leptons, the tauonic decays could be enhanced by an order of magnitude or more compared to the SM predictions [287,623]. Another class of NP models that feature LFU violation are based on gauging $L_\mu - L_\tau$, the difference of muon number and tau number [648]. Such setups predict modifications in decays with muon and taus in the final state that are comparable in size but opposite in sign.

Some NP scenarios that contain new sources of LFU violation also lead to lepton flavor violating decays of B mesons like $B \to K^{(*)}\mu e$, $B \to K^{(*)}\tau e$, and $B \to K^{(*)}\tau\mu$ [287,623]. The rates for such decays could be just below current limits from BaBar [2111,2112], which are at the level of

10^{-7} in the case of μe and at the level of a few $\times 10^{-5}$ in the case of final states containing taus. $B \to K^{(*)}\tau\mu$ branching ratios at the level of a few $\times 10^{-7}$ are predicted in models with extended Higgs sectors that propose a new source of first- and second-generation fermion masses [2113]. Interesting complementarity exists between LFV B decays, flavor-violating charged lepton decays like $\ell \to \ell'\gamma$, $\ell \to 3\ell'$, and $\mu \to e$ conversion in nuclei. Any observation of an LFV process would constitute indisputable evidence for new physics.

Inclusive semi-leptonic decays The inclusive decays $B \to X_s\ell^+\ell^-$ are expected to be theoretically cleaner compared to the exclusive decays that are limited by the knowledge of hadronic form factors and non-factorizable long-distance effects. SM predictions for decay rates and angular observables at low q^2 have reached an accuracy of 5%–10% both for the muon and electron modes [567]. Due to the theoretically clean nature of the inclusive decays, Belle II measurements have the unique opportunity to establish lepton universal new physics in $b \to s\ell\ell$ transitions.

The double differential decay width of the $B \to X_s\ell^+\ell^-$ decay provides three independent observables, H_T, H_L, and H_A [554],

$$\frac{d^2\Gamma}{dq^2dz} = \frac{3}{8}\big[(1+z^2)H_T(q^2) + 2zH_A(q^2) + 2(1-z^2)H_L(q^2)\big], \tag{644}$$

where $z = \cos\theta$, with θ the angle between the ℓ^+ and the B meson momenta in the dilepton rest frame. The observable H_A is equivalent to the forward–backward asymmetry, and the differential decay rate is given by $H_T + H_L$. Precise measurements of these observables allows clean determinations of the Wilson coefficients $(C_7^{(\prime)})_s$, $(C_9^{(\prime)})_s^\ell$, and $(C_{10}^{(\prime)})_s^\ell$, and therefore crucial cross checks of the discrepancies in the recent LHCb data on the related exclusive modes. Global fits of the LHCb data (if interpreted as a sign of new physics) predict a ∼25% suppression of the $B \to X_s\mu^+\mu^-$ decay rate compared to the SM prediction, both at low and high dimuon invariant mass.

Similar to the case of the exclusive decays, LFU tests in $B \to X_s\ell^+\ell^-$ offer very clean probes of new physics. If the value of $R_K \approx 0.75$ measured by LHCb is due to new physics, LVU violating effects of similar size can generically be expected in the inclusive decays. Measurements of the ratio of $B \to X_s\mu^+\mu^-$ and $B \to X_se^+e^-$ branching ratios, R_{X_s} [524,598], as well as measurements of ratios or differences of the lepton flavor specific angular coefficients H_i [599] will help to distinguish the chirality structure of the underlying NP interactions.

Also interesting is the tauonic $B \to X_s\tau^+\tau^-$ decay that could be enhanced by orders of magnitude by new physics, and the lepton flavor violating decay modes $B \to X_s\mu e$, $B \to X_s\tau e$, and $B \to X_s\tau\mu$. The LFV modes are absent in the SM and any observation of them would be an unambiguous sign of new physics.

Decays with neutrinos in the final state New physics in decays with neutrinos in the final state is described by the operators $(\mathcal{O}_\nu^{(\prime)})_q^\ell$. Because the final state neutrinos cannot be detected in the experiment, there are only three observables that are accessible in the $B \to K^{(*)}\nu\bar{\nu}$ decays as functions of the dineutrino invariant mass (or equivalently as functions of the missing energy). These are the two branching ratios $\mathrm{Br}(B \to K\nu\bar{\nu})$ and $\mathrm{Br}(B \to K^*\nu\bar{\nu})$ as well as F_L, the K^* longitudinal polarization fraction in the $B \to K^*\nu\bar{\nu}$ decay [614].

Assuming lepton flavor universality, NP effects in all observables in $b \to s\nu\bar{\nu}$ transitions depend on two combinations of the complex Wilson coefficients C_ν and C'_ν [614,2114]:

$$\epsilon^2 = \frac{|C_\nu|^2 + |C'_\nu|^2}{|C_\nu^{\rm SM}|^2}, \quad \eta = -\frac{{\rm Re}(C'_\nu C_\nu^*)}{|C_\nu|^2 + |C'_\nu|^2}. \tag{645}$$

Measurements of $B \to K^{(*)}\nu\bar{\nu}$ observables can be interpreted as constraints in the ϵ–η plane. Significant deviation from the SM point $(\epsilon, \eta) = (1, 0)$ signals the presence of new physics; a non-zero value of η signals the presence of right-handed currents. Equivalently, one can look at the correlation of NP effects in ${\rm Br}(B \to K^*\nu\bar{\nu})$ and ${\rm Br}(B \to K\nu\bar{\nu})$ to identify the presence of right-handed currents [613]. Current bounds on the $B \to K^{(*)}\nu\bar{\nu}$ branching ratios [624,625] give the limit $0.5 \lesssim \epsilon \lesssim 3$, while η is currently largely unconstrained. This corresponds to the bounds on the NP scale in Ref. (638) at the order of $\Lambda \sim 10\,{\rm TeV}$.

The ${\rm SU}(2)_L$ gauge symmetry relates neutrinos to left-handed charged leptons and therefore NP effects in $b \to s\nu\nu$ and $b \to s\ell\ell$ and transitions can be related as long as the new physics respects ${\rm SU}(2)_L$ symmetry. Assuming lepton flavor universality, any NP effect in $B \to K^{(*)}\nu\bar{\nu}$ decays necessarily implies NP effects of the same order in $B \to K^{(*)}\mu^+\mu^-$. On the other hand, new physics in $B \to K^{(*)}\mu^+\mu^-$ does *not* necessarily imply new physics in $B \to K^{(*)}\nu\bar{\nu}$, if the new physics is specific to right-handed leptons. The decays involving neutrinos and charged leptons therefore give complementary information.

The complementarity between $b \to s\nu\nu$ and $b \to s\ell\ell$ transitions is even more pronounced if we consider the possibility of LFU violation [613]. For example, NP models based on the gauged L_μ–L_τ symmetry predict effects in $b \to s\mu^+\mu^-$ and $b \to s\tau^+\tau^-$ transitions, while $B \to K^{(*)}\nu\bar{\nu}$ decays remain approximately SM-like, as the individual effects in $B \to K^{(*)}\nu_\mu\bar{\nu}_\mu$ and $B \to K^{(*)}\nu_\tau\bar{\nu}_\tau$ cancel in the sum over neutrino flavors [648]. Other NP scenarios that are described by operators involving left-handed taus are best probed by the $B \to K^{(*)}\nu\bar{\nu}$ decays that are sensitive to the modified $B \to K^{(*)}\nu_\tau\bar{\nu}_\tau$ rates. New physics operators involving right-handed taus, on the other hand, can only be probed by searching for the $b \to s\tau^+\tau^-$ transitions.

The simultaneous study of the decays $B \to K^{(*)}\nu\bar{\nu}$, $B \to K^{(*)}\ell^+\ell^-$, $B \to X_s\ell^+\ell^-$, and $B \to \ell^+\ell^-$ will teach us a lot about possible new dynamics at scales in the reach of the LHC and beyond. Future Belle II results on the $B \to K^{(*)}\nu\bar{\nu}$ decays will give valuable complementary information and will be key to disentangling the ${\rm SU}(2)_L$ structure of new physics in rare decays.

Future sensitivities with Belle II and LHCb.
Author: F. U. Bernlochner

In this section, prospects for new physics searches in $b \to s$ transitions are studied under the SM hypothesis as well as in several NP scenarios in a global fit setting. Special attention is given to present anomalies; the `flavio` [618] framework further described in Sect. 18.4.2 is used for the fits. The future uncertainties for LHCb and all figures and tables have been taken from Ref. [2115].

Most measurements included will be dominated by the statistical uncertainty for the studied luminosity milestones, with only a few exceptions sucg as, e.g., the differential branching fractions $d\mathcal{B}/dq^2$ of $B \to K^{(*)}\mu\mu$, where the dominant systematic uncertainties arise from the branching ratio of the respective normalization channels, the form factor models, and data–simulation differences. Correlations between the systematic uncertainties are assumed to be negligible. The development of theoretical uncertainties is much harder to predict, and an overall improvement of all form factor uncertainties by a factor of two is assumed by the end of the Belle II data-taking. For the remaining

Table 162. New physics scenarios for LHCb, Belle II exclusive, and Belle II inclusive Wilson coefficient scans. Contributions to the Wilson coefficients arising from new physics are given for each scan. The values are from Ref. [2115].

	$(C_9^{\mathrm{NP}\mu\mu}, C_{10}^{\mathrm{NP}\mu\mu})$	$(C_9'^{\mu\mu}, C_{10}'^{\mu\mu})$	$(C_9^{\mathrm{NP}\mu\mu}, C_9^{\mathrm{NP}ee})$	$(\mathrm{Re}(C_7'^{\mathrm{NP}}), \mathrm{Im}(C_7'^{\mathrm{NP}}))$	$(\mathrm{Re}(C_7^{\mathrm{NP}}), \mathrm{Im}(C_7^{\mathrm{NP}}))$
LHCb	$(-1.0, 0.0)$	$(-0.2, -0.2)$	$(-1.0, 0.0)$	$(0.00, 0.04)$	$(-0.075, 0.000)$
Belle II exclusive	$(-1.4, 0.4)$	$(0.4, 0.2)$	$(-1.4, -0.7)$	$(0.08, 0.00)$	$(-0.050, 0.050)$
Belle II inclusive	$(-0.8, 0.6)$	$(0.8, 0.2)$	$(-0.8, 0.4)$	$(0.02, -0.06)$	$(-0.050, -0.075)$

uncertainties, in particular systematic uncertainties due to non-factorizable hadronic contributions, it is assumed that they will stay the same as at present.

In what follows, three milestones are considered. Milestones I and II correspond to integrated luminosities of $5\,\mathrm{ab}^{-1}$ and $50\,\mathrm{ab}^{-1}$ or $8\,\mathrm{fb}^{-1}$ and $22\,\mathrm{fb}^{-1}$ for Belle II and LHCb, respectively. In addition, milestone III assumes a luminosity of $50\,\mathrm{fb}^{-1}$ for LHCb.

In the following considerations, the effective Wilson coefficient C_7^{eff} (see, e.g., Ref. [2087]) is used instead of C_7 as this effective coefficient is independent of the regularization scheme, where we define

$$C_7^{\mathrm{eff}} = C_7^{\mathrm{eff\,SM}} + C_7^{\mathrm{NP}}, \tag{646}$$

$$C_7'^{\mathrm{eff}} = C_7'^{\mathrm{eff\,SM}} + C_7'^{\mathrm{NP}}. \tag{647}$$

The impact of future measurements is studied by performing scans of the NP contribution to the Wilson coefficients at a scale of $\mu = 4.8\,\mathrm{GeV}$, under the SM hypothesis and several different NP scenarios, listed in Table 162. The measurements are separated depending on whether they are inclusive or exclusive. This allows for a proper comparison given that their respective uncertainties have different origins. Various NP scenarios are chosen for each class of measurement and each scan parameter on the basis of existing global fits [493,2100,2116]. Scans to C_S and C_P (see, e.g., Ref. [2087]) are omitted as these are dominated by contributions from purely leptonic $B \to \ell^+\ell^-$ decays.

The scans of the electromagnetic dipole coefficients $C_7^{(\prime)}$ derive their sensitivity from measurements of the branching fractions of $B_s \to \phi\gamma$, $B^+ \to K^{*+}\gamma$, $B^0 \to K^{*0}\gamma$, $B \to X_s\gamma$, on $\mathcal{A}^{\Delta\Gamma}(B_s \to \phi\gamma)$ and $S_{K^*\gamma}$, as well as from $A_T^{(2)}$ and A_T^{Im} extracted from $B^0 \to K^{*0}\mathrm{e}^+\mathrm{e}^-$ decays at very low q^2. In addition, the angular observables $A_{7,8,9}$ in $B^0 \to K^{*0}\mu^+\mu^-$ constrain the imaginary part of $C_7^{(\prime)}$.

The measurements entering the scans of the semi-leptonic coefficients $C_{9,10}^{(\prime)}$ comprise the inclusive $\mathcal{B}(B \to X_s\mu^+\mu^-)$ at low and high q^2; the low q^2 range is split equally for extrapolations. The forward–backward asymmetry $A_{\mathrm{FB}}(B \to X_s\ell^+\ell^-)$ has been measured at low and high q^2, and extrapolations to future sensitivities are available in several low and high q^2 ranges. The differential branching fractions $d\mathcal{B}/dq^2$ of $B^+ \to K^+\mu^+\mu^-$, $B^0 \to K^{*0}\mu^+\mu^-$, and $B_s \to \phi\mu^+\mu^-$ decays in both low and high q^2 regions are included in the scans, as well as the angular observables $S_{3,4,5}$, F_{L}, A_{FB} in several bins of q^2 from LHCb. The angular observables available for Belle (II) are $P'_{4,5}(B^0 \to K^{*0}\mu^+\mu^-)$ in similar ranges. Scans of $C_{10}^{(\prime)}$ further include the branching fraction of the decay $B_s \to \mu^+\mu^-$.

In the scan of $C_9^{\mathrm{NP}\mu\mu}$ vs. $C_9^{\mathrm{NP}ee}$, the observables $P'_{4,5}$ extracted from $B^0 \to K^{*0}\mathrm{e}^+\mathrm{e}^-$ decays are included in addition to the muonic final state as Belle II will have good sensitivity to determine these. Information on electrons is further obtained from the ratios of the branching fraction between muon and electron final states for $R(X_s)$, $R(K)$, $R(K^*)$, and $R(\phi)$. The results of the Belle collaboration on $R(K)$ and $R(K^*)$ in the region $0.0 < q^2 < 22.0\,\mathrm{GeV}^2$ were not considered as input in this scan as the charmonium region is included [602]. The inclusive measurement of $R(X_s)$ will become accessible at Belle II.

The results of scans of the unprimed and primed semi-leptonic and electromagnetic dipole Wilson coefficients of the five scenarios summarized in Table 162 are shown in Figs. 233 and 234, respectively. Belle II and LHCb will be able to probe new physics in semi-leptonic decays with unprecedented precision. If NP is present in $C_9^{\mathrm{NP}\mu\mu}$ and the current anomalies in $\mathrm{b} \to \mathrm{s}\ell^+\ell^-$ persist at a comparable strength, both experiments will be able to rule out the SM with great significance.

18.4. Global analysis tools

18.4.1. `SuperIso`

Author: Farvah Mahmoudi

`SuperIso`[74] [1874,2117,2118] is public code written in C, dedicated to the calculation of flavor physics observables and the muon anomalous magnetic moment. In addition to the full calculations in the SM and generic implementation based on additional NP contributions to the Wilson coefficients, `SuperIso` is able to perform the calculations in specific NP models such as general 2HDM, general MSSM, and NMSSM. An extension towards automatic calculations in a given NP model is ongoing. The code incorporates the state of the art publicly available calculations, with particular attention paid to avoiding approximations and using the most accurate calculations available.

A broad set of flavor physics observables sensitive to NP contributions is implemented in `SuperIso`. This includes rare decays such as branching ratios of $B_{d,s} \to \ell^+\ell^-$ (with $\ell = e, \mu, \tau$), branching ratios of $B \to X_{d,s}\gamma$, isospin asymmetry of $B \to K^*\gamma$, inclusive and exclusive semi-leptonic $b \to s$ transitions, namely branching ratios and angular observables of $B_s \to X_s\ell^+\ell^-$, $B \to K^{(*)}\ell^+\ell^-$, $B_s \to \phi\ell^+\ell^-$, in addition to leptonic and semi-leptonic decays such as the branching ratio of $B_u \to \tau\nu_\tau$, branching ratios of $B \to D^{(*)}\tau\nu_\tau$, the branching ratio of $K \to \mu\nu_\mu$ and of $D \to \mu\nu_\mu$, and the branching ratios of $D_s \to \tau\nu_\tau$ and $D_s \to \mu\nu_\mu$, as well as meson mixings. The code is modular, and other observables can be added easily.

The calculation of the Wilson coefficients is done in two steps. First, they are calculated at the matching scale, $\mathcal{O}(M_W)$. They are subsequently evolved using the renormalization group equations (RGEs) to a lower scale, $\mathcal{O}(m_b)$, relevant for the B physics observables. The Wilson coefficients are calculated at the μ_W scale at NNLO in the SM and 2HDM, and NLO in the MSSM (including some partial NNLO calculations). The RGEs are implemented at NNLO.

Particular care has been taken to avoid having hard-coded values in the code so that the input parameters can be safely chosen by the users.

`SuperIso` can use a SUSY Les Houches Accord (SLHA) file [2119,2120] as input, which can be generated automatically by the program via a call to a spectrum generator or provided by the user. The direct calls are available for 2HDM (types I, II, III, and IV), different supersymmetric scenarios, such as the constrained MSSM (CMSSM), the non-universal Higgs mass model (NUHM), the

[74] The `SuperIso` package can be downloaded from http://superiso.in2p3.fr.

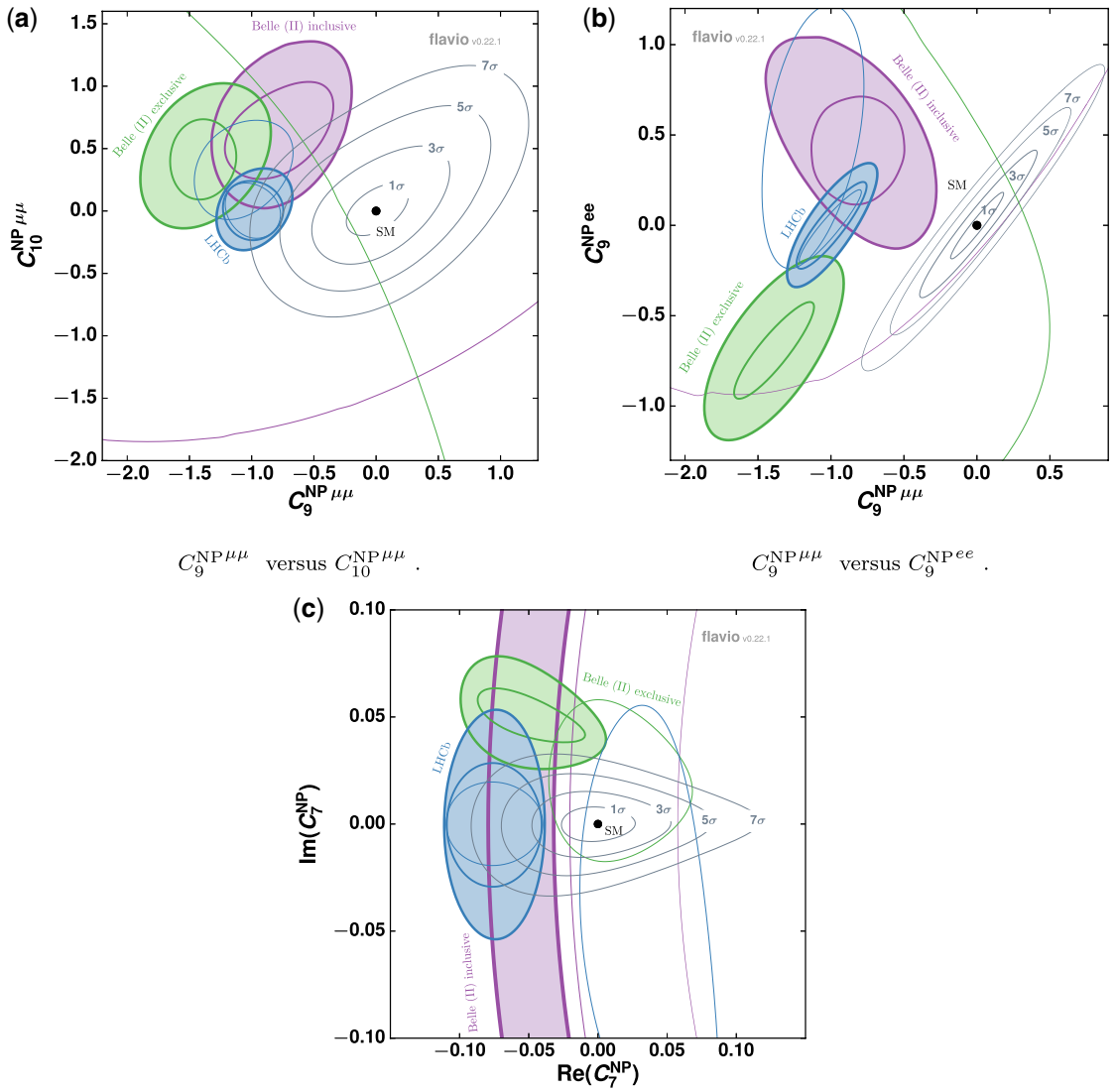

$C_9^{\mathrm{NP}\,\mu\mu}$ versus $C_{10}^{\mathrm{NP}\,\mu\mu}$. $C_9^{\mathrm{NP}\,\mu\mu}$ versus $C_9^{\mathrm{NP}\,ee}$.

$\mathcal{R}e\,(C_7^{\mathrm{NP}})$ versus $\mathcal{I}m\,(C_7^{\mathrm{NP}})$.

Fig. 233. In the two-dimensional scans of pairs of Wilson coefficients, the current average (not filled) as well as the extrapolations to future sensitivities (filled) of LHCb at milestones I, II, and III (exclusive) and Belle II at milestones I and II (inclusive and exclusive) are given and are progressively overlaid. The central values of the extrapolations have been evaluated in the NP scenarios listed in Table 162. The future projections at milestones I, II, and III are given by the filled contours. The contours correspond to $1\,\sigma$ uncertainty bands. The SM point (black dot) with the $1\,\sigma$, $3\,\sigma$, $5\,\sigma$, and $7\,\sigma$ exclusion contours with a combined sensitivity of Belle II's $50\,\mathrm{ab}^{-1}$ and LHCb's $50\,\mathrm{fb}^{-1}$ datasets is indicated in light gray. The primed operators show no tensions with respect to the SM; hence, no SM exclusions are provided. The figures are taken from Ref. [2115].

anomaly mediated supersymmetry breaking scenario (AMSB), the hypercharge anomaly mediated supersymmetry breaking scenario (HCAMSB), the mixed modulus anomaly mediated supersymmetry breaking scenario (MMAMSB), the gauge mediated supersymmetry breaking scenario (GMSB), and the phenomenological MSSM (pMSSM), and for the NMSSM scenarios, namely CNMSSM, NGMSB, and NNUHM.

Several example `main` programs are given in the package providing the values of the observables in different models. `SuperIso` respects the Flavor Les Houches Accord (FLHA) [2121],

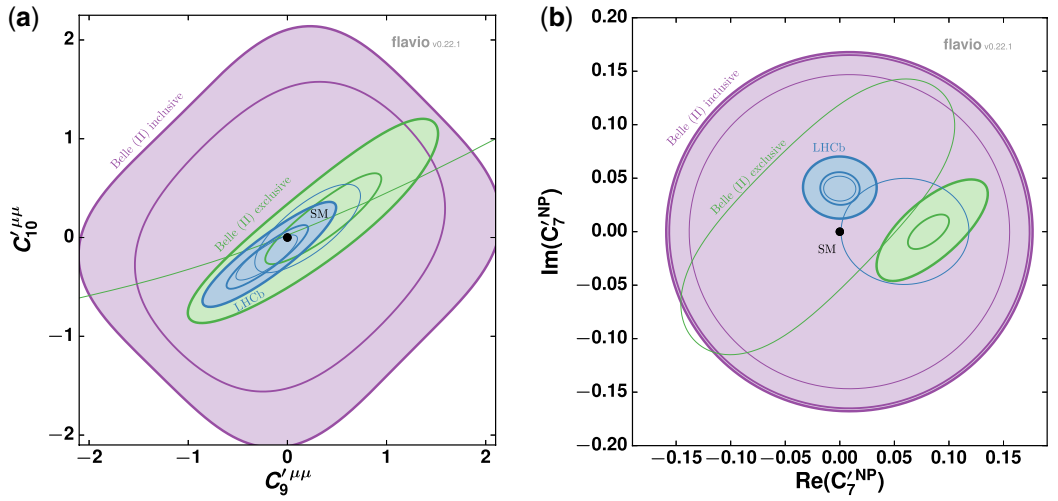

$C_9^{\prime\mu\mu}$ versus $C_{10}^{\prime\mu\mu}$. $\mathcal{R}e\,(C_7^{\prime\mathrm{NP}})$ versus $\mathcal{I}m\,(C_7^{\prime\mathrm{NP}})$.

Fig. 234. See the caption of Fig. 233. The figures are taken from Ref. [2115].

which is a standard format for flavor-related quantities. An output FLHA file can be subsequently generated.

In brief, the code first scans the SLHA file and transfers the parameters needed into a structure which is used by most of the internal routines. Alternatively, the structure can be filled directly in the `main` file. The observables which do not depend on the Wilson coefficients can then be computed directly. For the other observables, it is first necessary to use routines to compute the Wilson coefficients at the μ_W scale, then to use RGE routines to get Wilson coefficients at the μ_b scales. Alternatively, the Wilson coefficients can be directly given in the `main` program or through an FLHA interface. All the observables can then be computed with the appropriate routines.

For $B \to K^*\ell^+\ell^-$ and $B_s \to \phi\ell^+\ell^-$ decays, both the full and soft form factor approaches are implemented, and several parameterizations for the non-factorizable power corrections are provided. In addition, the lepton flavor is generic, allowing for the computation of lepton flavor ratios such as $R_K^{(*)}$.

The correlation matrices between the observables dependent on the Wilson coefficient are also available. The theoretical correlations and errors have been computed in the SM by varying all the parameters in a Monte Carlo program, also taking into account the form factor correlations. The theoretical correlation matrices have been added to the latest experimental correlations matrices.

An automatic and parallel calculation of the errors and correlations is possible by combining the elementary uncertainties. A function computing χ^2 is also available. The choice of observables included in the χ^2 can be easily achieved by commenting/uncommenting the observables in the `main` file. Recent examples of model-independent fits and studies using `SuperIso` can be found in Refs. [2122–2124]. In addition, `SuperIso` is interfaced in the `FlavBit` module of `GAMBIT` [2125, 2126], which provides a thorough set of tools for performing fits.

The calculation duration for one point depends on the number of selected observables; a standard calculation with χ^2 and about 100 observables takes less than one second on a laptop.

An extension of `SuperIso` including the dark matter relic density calculation as well as direct and indirect detection experiments, `SuperIso Relic`, is also publicly available [2127,2128].

18.4.2. `Flavio`

Author: David Straub

`Flavio`[75] is an open-source Python package to compute flavor physics observables in the SM and beyond. Rather than implementing specific new physics models, NP contributions to all processes can be supplied as contributions to Wilson coefficients of local dimension-six operators, while an interface to other software (e.g. BSM Wilson coefficient calculators `SARAH`/`FlavorKit` [1941] or `FormFlavor` [2129]) is realized through the Wilson coefficient exchange format (WCxf) [2130]. In this way, `flavio` can serve as an interface between model building and precision flavor measurements.

The package not only includes numerical values and uncertainties of all relevant input parameters that allow prediction of flavor observables including theoretical uncertainties, but also a library of experimental measurements of these observables that allows the construction of likelihood functions. Statistical inference of SM parameters or Wilson coefficients using these likelihoods is implemented in both Bayesian and frequentist frameworks. In the Bayesian case, interfaces to the Markov chain Monte Carlo libraries `pypmc`[76] and `emcee` [2131] are implemented. In the frequentist case, `flavio` implements its own one- and two-dimensional likelihood profilers. Performing the same analysis with Bayesian or frequentist statistics within the same framework allows for powerful cross-checks of the dependence of the fit results on the statistical approach.

Being written in Python and thus not requiring compilation, a main feature of the code is that it can be run interactively and can be easily modified at run time, including parameter values but also parameterizations of quantities such as hadronic form factors. At the same time, parallelization of computationally intensive routines makes it suitable for large-scale numerical analyses.

At present, `flavio` includes the following observables:

- mass differences in B^0 and B_s mixing and mixing-induced CP asymmetries in $B^0 \to J/\psi K^0_S$ and $B_s \to J/\psi\phi$
- CP violation parameter ϵ_K in K^0 mixing
- binned and differential branching ratios, angular observables, and angular CP asymmetries in rare $B_q \to M\ell^+\ell^-$ decays, where $M = K, K^*, \phi$
- binned and differential branching ratios and angular observables in $\Lambda_b \to \Lambda\ell^+\ell^-$ decays
- binned branching ratio and forward–backward asymmetry in $B_q \to X_s\ell^+\ell^-$ decays
- rare radiative decays $B \to X_s\gamma$, $B \to K^*\gamma$, $B_s \to \phi\gamma$
- rare leptonic B decays $B_q \to \ell^+\ell^-$
- rare B decays $B \to M\nu\bar{\nu}$ with $M = \pi, \rho, K, K^*$
- rare kaon decays $K^+ \to \pi^+\nu\bar{\nu}$ and $K^0_L \to \pi^0\nu\bar{\nu}$
- charged-current kaon and pion decays $K \to \pi\ell\nu$, $K \to \ell\nu$, $\pi \to e\nu$
- binned and differential branching ratios and angular observables in charged-current semi-leptonic B decays $B \to M\ell\nu$ with $M = \pi, \rho, \omega, D, D^*$
- charged-current inclusive B decay $B \to X_c\ell\nu$
- charged-current leptonic B decays $B \to \ell\nu$ and $B_c \to \ell\nu$
- charged-current D decays $D \to \ell\nu$ and $D_s \to \ell\nu$.

[75] The installation instructions and online manual can be found on the `flavio` website, https://flav-io.github.io. The public source code repository can be found at https://github.com/flav-io/flavio, where code contributions can also be submitted.

[76] https://pypi.org/project/pypmc/.

In all processes with leptons in the final state, NP contributions to the channels with different lepton flavor can be specified separately, allowing the analysis of models with violation of lepton flavor universality. In many cases, charged lepton flavor violating final states, forbidden in the SM, are also implemented.

`Flavio` has already been used in numerous publications.[77] Examples include fits of Wilson coefficients in radiative B decays [493], model-independent analysis of new physics in $b \to s\ell\ell$ transitions [611,2132], and an analysis of new physics in $b \to c\ell\nu$ transitions [262].

18.4.3. `HEPfit`

Author: Ayan Paul

`HEPfit`[78] is a computational tool for the combination of indirect and direct constraints on high-energy physics models. The code is built in a modular structure so that one can select observables and models of interest. It can be used to build customized models and customized observables. It has a statistical framework based on Markov chain Monte Carlo (MCMC) driven Bayesian analysis; however, any statistical framework can be used as an alternative. `HEPfit` allows for the use of parametric and experimental correlations and can read likelihood distributions directly from `ROOT` histograms.

The goal of `HEPfit` is to implement electroweak, Higgs, and flavor physics observables to the highest degree of precision with minimum theoretical assumptions built in. This has been done in the SM and in several models beyond SM, such as MSSM, THDM, L–R symmetric models, and several EFTs. Since the statistical treatment in `HEPfit` is based on MCMC, optimized computational time is of utmost importance. `HEPfit` is massively parallelized to run over a large number of CPUs using `openMPI`.

Here we focus on how `HEPfit` can be used for a B factory both by experimentalists for making predictions for observables and by theorists to fit model parameters to data. The list of observables implemented in `HEPfit` includes leptonic and semi-leptonic decays of the B mesons, flavor violation in the lepton sector, and oscillations and CP violation in the B and K meson systems. Some of these have been implemented in models beyond the SM. We list all of these observables below.

`HEPfit` has a dedicated flavor program in which several $\Delta B = 2$, $\Delta B = 1$ [2107,2133,2134], and $\Delta S = 2$ observables have been implemented to state-of-the-art precision in the SM and models beyond the SM. `HEPfit` also includes observables with lepton flavor violation. In Table 163 we list the processes and corresponding models that have either been fully implemented (✓) or are currently under development (○). H_{eff} refers to the implementation of a model with generalized Wilson coefficients at a given scale. Since `HEPfit` is continuously under development, the list of available observables keeps increasing and a more complete list is available in the online resource.

While the primary goal of HEPfit is to provide a fast multi-purpose MCMC-based fitting framework with a host of models implemented, the code offers a few other options in case the user wants to implement their own statistical framework or use the code to generate a large set of values for the observables given certain ranges for the parameter set.

[77] See https://flav-io.github.io/papers.html for a full list.

[78] Detailed documentation of the code, along with instructions on how to install and run it, can be found on the `HEPfit` website, http://hepfit.roma1.infn.it. The MCMC core is implemented in `BAT` [2135].

Table 163. The processes that have been implemented (✓) or are under development (○) in `HEPfit` for flavor physics.

Processes	SM	THDM	MSSM	$H_{\rm eff}$
$\Delta B = 2$	✓	✓	○	○
$\Delta S = 2$	✓		○	○
$B \to \tau\nu$	✓	✓	○	○
$B \to D^{(*)}\tau\nu$	○	✓		○
$B_{s/d} \to \mu\mu$	✓	○	○	○
Rare K decays	○			○
$B \to X_s\gamma$	✓	✓	○	○
$B \to V\gamma$	✓			○
$B \to P/V\ell^+\ell^-$	✓			○
$B \to X_s\ell^+\ell^-$	○			○
$B \to PP/PV$	○			○
$\ell_i \to \ell_j\gamma$			✓	
$\ell_i \to 3\ell_j$			✓	
$(g-2)_\mu$			✓	

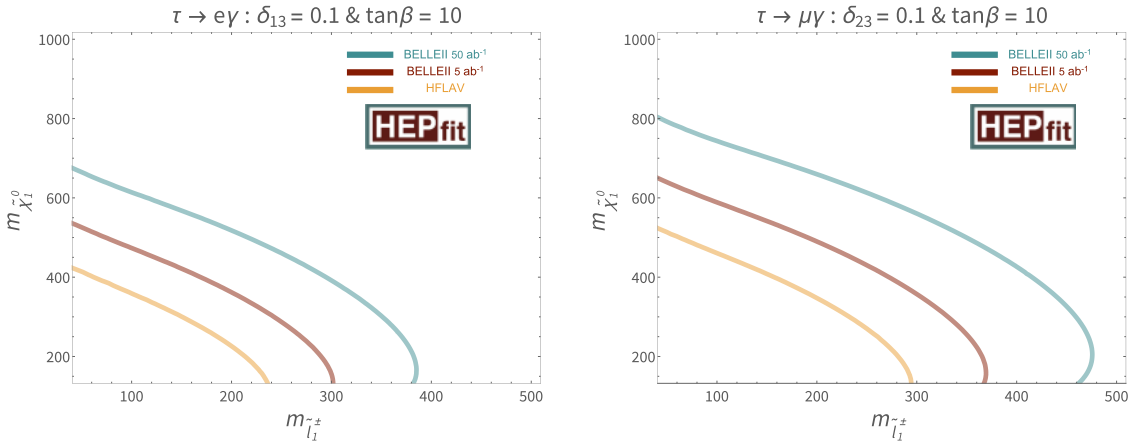

Fig. 235. Constraints on neutralino mass ($m_{\tilde{\chi}_1^0}$) vs. slepton mass ($m_{\tilde{l}_1^\pm}$) from $\tau \to e\gamma$ and $\tau \to \mu\gamma$ measurements at Belle II. The orange, red, and green lines display the bounds at 90% CL from current HFLAV averages, 5 ab^{-1}, and 50 ab^{-1} data, respectively.

While HEPfit provides a set of models and observables of relevance, it also allows the user to build their own standalone model or one that inherits from an existing model. The user can also define their own observables, with or without defining a new model.

Some example plots for lepton flavor violating tau decays produced using `HEPfit` are shown in Figs. 235 and 236.

18.4.4. `SUSY_Flavor`

Author: Janusz Rosiek

`SUSY_FLAVOR` [2136–2138][79] is a library of numerical routines designed to calculate over 30 low-energy observables related to flavor and CP violation within the most general R parity conserving MSSM.

[79] http://www.fuw.edu.pl/susy_flavor.

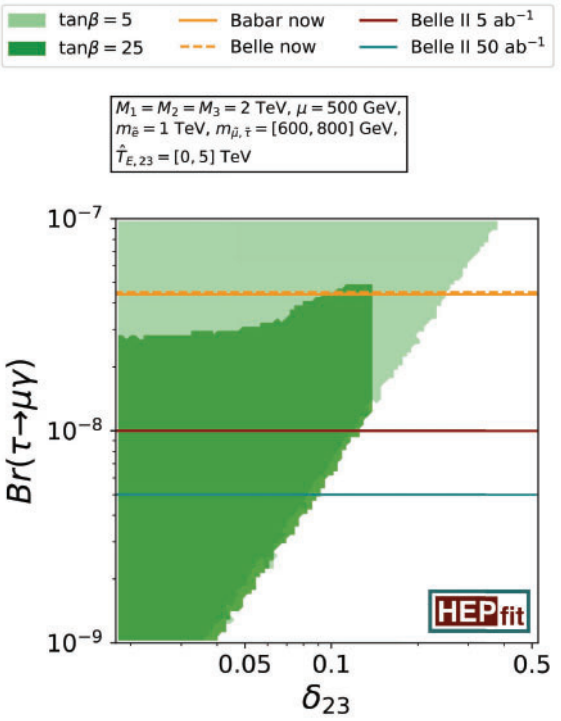

Fig. 236. Possible values for the branching ratio of the process $\tau \to \mu\gamma$ for the given MSSM inputs (see box), depending on δ_{23}. The light green region features $\tan\beta = 5$, and for the dark green contour we set $\tan\beta = 25$. The current 90% CL upper limits by BaBar and Belle are given by the orange lines; the expected future limits by Belle II with 5 and 50 ab^{-1} of data are marked by the red and green lines, respectively.

Due to its ability to calculate numerous observables simultaneously, the code is well equipped to carry out multi-process analyses. It can combine the input from high-p_T experiments, like FCNC decay constraints from the top or Higgs sectors, with the range of measurements Belle II has particular sensitivty to ($b \to s, d$ or $c, s \to u$ transitions). This allows testing of the SM and connecting direct and indirect constraints.

The main features of `SUSY_FLAVOR` are:

- Routines which calculate the observables summarized in Table 164.
- The code implements the full general structure of the MSSM, assuming only R-parity conservation. The implementation has no limitations on the size of complex phases or flavor-violating entries of the soft term matrices. In addition, it takes into account the non-vanishing non-holomorphic trilinear soft terms (cf. Ref. [2146,2147]):

$$L_{nh} = A'_l H_u^\dagger LE + A'_d H_u^\dagger QD + A'_u H_d^\dagger QU.$$

- The program is able to perform resummation of the chirally enhanced corrections arising in the regime of large $\tan\beta$ and/or large trilinear SUSY breaking. The resummation is implemented to all orders of perturbation theory, including the case of the non-minimal flavor structure of soft breaking terms [2148].
- The output is written to SLHA2-like structured files, with custom-defined blocks summarizing the results for $\Delta F = 0, 1, 2$ transitions.

Table 164. Observables calculated by SUSY_FLAVOR v2.5 and references with details of calculations (if published).

Observable	Reference
$\Delta F = 0$:	
$\frac{1}{2}(g-2)_\ell$, $\ell = \mu, \tau$	
EDM_ℓ, $\ell = e, \mu, \tau$	[2139]
$\mathrm{EDM}_{\mathrm{neutron}}$	[2139]
$\Delta F = 1$:	
$\mathrm{Br}(\mu \to e\gamma)$, $\mathrm{Br}(\tau \to e\gamma)$, $\mathrm{Br}(\tau \to \mu\gamma)$	
$\mathrm{Br}(K_\mathrm{L} \to \pi^0\nu\nu)$, $\mathrm{Br}(K^+ \to \pi^+\nu\nu)$	[2140]
$\mathrm{Br}(B_d \to \ell\ell')$, $\ell, \ell' = e, \mu, \tau$	[2141]
$\mathrm{Br}(B_s \to \ell\ell')$, $\ell, \ell' = e, \mu, \tau$	[2141]
$\mathrm{Br}(B^+ \to \tau^+\nu)$	
$\mathrm{Br}(B \to D\tau\nu)/\mathrm{Br}(B \to Dl\nu)$	
$\mathrm{Br}(B \to D^\star\tau\nu)/\mathrm{Br}(B \to D^\star l\nu)$	
$\mathrm{Br}(B \to X_s\gamma)$	[2142]
$\mathrm{Br}(t \to ch, uh)$	[2143]
$\Delta F = 2$:	
$\lvert\epsilon_K\rvert$, ΔM_K	[2144,2145]
ΔM_D	
ΔM_{B_d}, ΔM_{B_s}	[2144,2145]

18.4.5. EOS

Authors: Danny Van Dyk

The open-source EOS[80] [2149] software package fulfills multiple use cases. First, it provides estimates for flavor physics observables within the SM and in model-independent frameworks of effective field theories (EFTs). Second, EOS can be used to infer parameters from flavor observables within a Bayesian statistics framework. Finally, EOS is capable of producing MC pseudo-events for signal PDFs with a given theory uncertainty. While the complete set of observables that EOS features is too extensive to be listed here, in Table 165 we list the set of processes and a subset of the references to the corresponding theoretical predictions used in the package.

EOS features numerical implementations of QCD sum rules, which can be used to determine decay constants and form factors that arise in the computation of the above observables. Several parameterizations, and their default parameter values, of $B \to$ P(seudoscalar) and $B \to$ V(ector) form factors are implemented and selectable within EOS.

The remainder of this section gives an introduction to EOS and discusses three of its use cases.

For the first use case we consider the leptonic forward–backward asymmetry A_FB in the decay $B \to K^*\mu^+\mu^-$. Its prediction is provided by two different theory approaches, both implemented in EOS, which work in two different parts of the dilepton phase space. For small values of the dilepton mass squared, $q^2 \ll m_b^2$, or equivalently large recoil energy $E_{K^*} = \mathcal{O}(m_b)$ of the K^* in the B rest frame, the framework of QCD-improved factorization is applicable [483,484]. Conversely, for $q^2 \approx m_b^2$, or equivalently low hadronic recoil of the K^*, an operator product expansion exists [642,2154].

[80] https://github.com/eos/eos/.

Table 165. Processes featured in EOS and references to theoretical predictions.

Process	Reference
Semi-leptonic b decays:	
$B \to \ell\nu$, with $\ell = e, \mu, \tau$	[2150]
$B_s \to K^*\ell\nu$, with $\ell = e, \mu$	[2150]
$B \to \{\pi, D^{(*)}\}\,\ell\nu$, with $\ell = e, \mu, \tau$	[2150,2151]
$B \to \pi\pi\ell\nu$, with $\ell = e, \mu$	[909]
Rare b decays:	
$B_{(s)} \to \ell^+\ell^-$, with $\ell = e, \mu, \tau$	[2152]
$B \to X_s\gamma$	[2153]
$B \to K^*\gamma$	[484]
$B \to X_s\ell^+\ell^-$, with $\ell = e, \mu$	[565]
$B \to K^{(*)}\ell^+\ell^-$, with $\ell = e, \mu, \tau$	[484,2154,2155]
$\Lambda_b \to \Lambda\ell^+\ell^-$, with $\ell = e, \mu$	[2156]

Predictions can be obtained with either

- the central value and naive Gaussian uncertainty propagation, or
- a rigorous calculation of uncertainties, producing MC samples of either a prior- or posterior-predictive distribution for the observables of interest.

Here we use $A_{\rm FB}$ in the decay $B \to K^*\mu^+\mu^-$ as an example, which is binned in $s \equiv q^2$, the dilepton mass squared. The respective EOS method requires specification of the kinematic variables, for example $1\,\text{GeV}^2 \leq q^2 \leq 4\,\text{GeV}^2$. The prediction and uncertainty is then provided through one of the two methods listed above.

In order to facilitate the task of parameter inference, EOS provides a program to construct a (log-)posterior distribution from univariate uniform, Gaussian, and (asymmetric) log gamma distributions. The (log-)likelihood can be constructed from either univariate uniform or Gaussian distributions, or from a database of built-in multivariate constraints. The latter applies to both experimental measurements and theoretical constraints. The client program draws and stores random variates from the (log-)posterior using a Markov chain based Metropolis–Hastings algorithm or a mixture density based on a population Monte Carlo algorithm. The application of the population Monte Carlo algorithm allows for the calculation of the Bayesian *evidence* for the fit, which in turn can be used for model comparisons.

EOS has support to draw pseudo-events from kinematic distributions. Sampling is carried out using the same Metropolis–Hastings implementation as above. Again we will consider the production of pseudo-events for two decay processes, $B \to K^*\mu^+\mu^-$ and $B \to K^*e^+e^-$, for $1\,\text{GeV}^2 \leq q^2 \leq 6\,\text{GeV}^2$. Both are accessed using predefined signal PDFs for $B \to K^*\ell\ell$ at large recoil. Lepton flavor can be specified for each process. Wilson coefficients $\mathcal{C}_i^\ell$ for the $b \to s\ell^+\ell^-$ transitions can be configured as free parameters, which default to the SM values. Lepton flavor non-universality in these transitions can be introduced by setting $\mathcal{C}_9^{\ell=\mu}$ to non-SM values.

In summary, EOS is a multi-purpose software framework with a library of numerical implementations for radiative and semi-leptonic b hadron decays. It features methods for uncertainty propagation, parameter inference, and PDF sampling.

18.4.6. pypmc

Authors: Frederik Beaujean, Stephan Jahn

In global fits of rare B decays, one is interested in determining the most probable values of Wilson coefficients, as they are sensitive to new physics at short distances. A departure from the values predicted by the SM would provide clues as to the nature of NP. The overarching question in these global fits is whether the SM or some alternative NP model is favored by the data. In the Bayesian approach to global fits, one seeks the marginal distributions of the Wilson coefficients to determine their probable ranges, and the Bayes factor, or ratio of evidences, between models. Typically only a handful of Wilson coefficients are studied in one fit, but in order to fully account for theory uncertainties it is necessary to include a number of nuisance parameters relating to, for example, quark masses, the CKM matrix, form factors, or non-perturbative corrections. Both the marginal posterior and the evidence have to be computed numerically, which requires integration of the posterior over some (marginal) or all (evidence) parameters in the respective model.

Evaluating the posterior can take up to seconds if many observables need to be predicted, so an algorithm is preferred that produces samples from the posterior and estimates the evidence while exploiting a cluster of CPUs. Implementing a toolbox of such algorithms was the motivation to create `pypmc`,[81] an open-source Python package.

Among others, `pypmc` implements the Metropolis–Hastings algorithm with an adaptive multivariate Gaussian function producing a random walk Markov chain in parameter space. This algorithm is stable and efficient for unimodal problems with dozens of parameters but is known to fail if there are multiple modes or strong correlations among parameters.

Adaptive importance sampling Given the posterior P, the basic idea of importance sampling (IS) is to approximate the evidence as

$$\int dx\, P(x) = \int dx\, q(x) \frac{P(x)}{q(x)} \approx \frac{1}{N} \sum_{i=1}^{N} \frac{P(x_i)}{q(x_i)} \tag{648}$$

using a proposal function q. IS also produces independent weighted samples from P as a by-product, whereas the Metropolis–Hastings algorithm only yields correlated samples from P but not the evidence. Another advantage of IS is that it is trivially parallel, allowing one to spread the costly evaluation of P across a cluster of compute nodes. But for IS to be efficient, we need $q \approx P$. A generic and flexible proposal is a mixture density

$$q(x) = \sum_j \alpha_j q_j(x) \text{ with } \sum_j \alpha_j = 1, \tag{649}$$

where q_j is either a Gaussian or Student's t distribution. The key challenge is to infer the parameters of q_j and the weights α_j such that $q \approx P$. The core of `pypmc` revolves around updating a mixture based on samples using population Monte Carlo or variational Bayes [2135]. Typically one would start to analyze P with several Markov chains. These samples can be used to form an initial guess of the proposal, q_0, even if the chains do not mix or show strong autocorrelation. Then one can create additional samples through importance sampling with q_0 and update to q_1. In all cases of practical interest, only a handful of updates are needed to optimize q. Samples from all q_t can be combined

[81] https://github.com/fredRos/pypmc.

for the final inference step. This approach was used in Ref. [2099] to perform a global analysis to infer tensor and scalar Wilson coefficients by using a predecessor to the Python interface to `EOS`, described elsewhere in this report. In total, the analysis had up to 60 parameters. Beyond that, the efficiency of IS degrades too much due to the curse of dimensionality.

18.4.7. `FormFlavor`

Authors: Jared A. Evans, David Shih

`FormFlavor`[82] is a powerful, modular, Mathematica-based tool for the evaluation of low-energy flavor and CP observables in BSM models of physics. `FormFlavor` can be viewed as three distinct, model-independent, modular components: `CalcAmps`, `FFWilson`, and `FFObservables`. A final component, the `FFModel`, contains elements pertinent to the particular BSM model being studied.

The `CalcAmps` package, built upon the machinery of `FeynArts` and `FormCalc` facilitates the automatic generation of one-loop Feynman diagrams. These loops are then converted into analytic expressions of the NP contribution to the Wilson coefficients. The automated nature of `CalcAmps` greatly increases the reliability of the amplitudes, as an analog computation of the individual diagrams followed by a transcription into code would be prone to error and need to be repeated for each and every model. `CalcAmps` only needs to be run once per model, as the output files are stored for later access. These output files contain analytic expressions for Wilson coefficients that can be manipulated with the `FormFlavor` machinery.

`FFWilson` allows one to compile the analytic output from `CalcAmps`. The compiled code can then be used to numerically evaluate the Wilson coefficients at particular parameter points. Within `FFWilson` there are two separate compiling modes provided to allow for either a faster or more reliable determination of the Wilson coefficients. The compiling step should be performed once per `FormFlavor` session, while determining the numerical value of Wilson coefficients at a parameter point is performed once for each parameter point.

`FFObservables` takes as input numerical Wilson coefficients and converts these into flavor observables. Within `FFObservables` there are additional routines that can be used to assess whether the parameter point is constrained by particular flavor observables. Adding new observables to the code is straightforward, and explicit instructions are provided in the manual [2129]. Translating the numerical Wilson coefficients to flavor observables via `FFObservables` is performed once for each parameter point. Importantly, `FFObservables` is its own standalone program; flavor observables can be evaluated just by passing numerical Wilson coefficients, without using a specific model or any of the infrastructure within `CalcAmps` and `FFWilson`.

The `FFModel` directories contain model-specific elements that allow the model-independent routines of `CalcAmps` and `FFWilson` to interface with the syntax of the `FeynArts`/`FormCalc` model, and the parameter input format. One `FFModel`, the fully general MSSM, is included in `FormFlavor`, and reads SLHA2 files or a Mathematica-specific input format.

[82] The most up-to-date version of the `FormFlavor` code and manual can be downloaded from https://formflavor.hepforge.org. The manual contains explicit instructions on how to get started with the code, add new observables, and utilize the more advanced machinery within the package. Additionally, the base package contains the Mathematica notebook `FormFlavor.nb` with a tutorial covering the basic usage of the code.

18.5. Conclusions

The Belle II experiment has large varieties of observables sensitive to new physics. An NP effect may manifest itself in a single observable or in several observables simultaneously. Either way, we need a consistent picture including NP effects to interpret obtained experimental results, which requires a global analysis. Therefore, global analyses and associated tools will become more and more important in the future.

One successful example of global analysis is the CKM matrix elements fitted using the `CKMfitter` or `UTfit` packages. Although the CKM matrix elements are not predictable from the SM, measuring them independently from numbers of observables may exhibit an inconsistency. We demonstrated how the future precision measurements by the Belle II experiment will improve the CKM matrix fit for testing the SM and, furthermore, have the potential of discovering new physics.

The flavor-changing observables are described by the Wilson coefficients of the weak interaction in the SM. This description can be extended by including NP operators with new Wilson coefficients. Global analyses are essential since the NP effects would appear in many Wilson coefficients simultaneously with some patterns. Using the recent hints of NP in the $b \to c\tau\nu_\tau$ and $b \to s\ell\ell$ decays, we discussed how these effects appear in the Wilson coefficient fits and the future prospects at the Belle II experiments.

The ultimate goal for global analysis tool development is to make the computation fully automatic, but at the same time flexible enough to allow different theoretical and experimental inputs. In order to achieve higher reliability, independent groups developing tools with the same functions is ideal. We have introduced a few global analysis tools and their characteristics. We hope those tools will be further developed in the future and will make it possible for more users to perform NP searches with Belle II data.

19. Summary

The Belle II detector will provide a major step forward in precision heavy flavor physics, quarkonium and exotic states, searches for dark sectors, and many other areas. The sensitivity to a large number of key observables can be improved by about an order of magnitude compared to the current measurements, and up to two orders in very clean search measurements. This increase in statistical precision arises not only due to the increased luminosity, but also from improved detector efficiency and precision for many channels. Many of the most interesting observables tend to have very small theoretical uncertainties that will therefore not limit the physics reach.

This book has presented many new ideas for measurements, both to elucidate the nature of current anomalies seen in flavor, and to search for new phenomena in a plethora of observables that will become accessible with the Belle II dataset.

The simulation used for the studies in this book was state of the art at the time, though we are learning a lot more about the experiment during the commissioning period. The detector is in operation, and working spectacularly well.

Acknowledgements

This work was supported by the following funding sources: Australian Research Council and research grant nos. DP180102629, DP170102389, DP170102204, DP150103061, FT130100303, FT130100018; Austrian Academy of Sciences, Austrian Science Fund no. P 31361-N36, and New Frontiers Program; Natural Sciences and Engineering Research Council of Canada and Compute Canada; Chinese Academy of Sciences and research grant nos. QYZDB-SSW-SYS013 and QYZDJ-SSW-SLH011, and National Natural Science

Foundation of China and research grant nos. CRC 110 "Symmetries," PHY-1414345, PHY-1520966, PHY-1714253, PHY-1720252, 11521505, 11575017, 11675166, 11621131001 "The Emergence of Structure in QCD," 11761141009, 11475187, 11621131001, 11705209, and 11747601; the Ministry of Education, Youth and Sports of the Czech Republic under contract no. LTT17020, and Charles University grants SVV 260448 and GAUK 404316; European Research Council, 7th Framework PIEF-GA-2013-622527, Horizon 2020 Marie Sklodowska-Curie grant agreement no. 700525 "NIOBE," Horizon 2020 Marie Sklodowska-Curie RISE project JENNIFER grant agreement no. 644294, Horizon 2020 ERC-Advanced Grant no. 267104, and NewAve no. 638528 (European grants); L'Institut national de physique nucléaire et de physique des particules (IN2P3) du CNRS (France); BMBF, DFG, HGF, MPG, and AvH Foundation (Germany); Department of Atomic Energy and Department of Science and Technology (India); Israel Science Foundation grant no. 2476/17 and United States–Israel Binational Science Foundation grant no. 2016113; Istituto Nazionale di Fisica Nucleare and the research grants BELLE2 and Iniziativa Specifica QFT-HEP; Japan Society for the Promotion of Science, Grants-in-Aid for Scientific Research nos 16H03968, 16H03993, 16K05323, 17H01133, 17H05405, 18H03710, 18K03621, 16H06492, 26400255, and 26220706, and the Ministry of Education, Culture, Sports, Science, and Technology (MEXT) of Japan; National Research Foundation (NRF) of Korea Grant nos. 2015H1A2A1033649, 2016R1D1A1B01010135, 2016K1A3A7A09005603, 2016R1D1A1B02012900, 2018R1A2B3003643, 2018R1A6A1A06024970, and 2018R1D1A1B07047294, Radiation Science Research Institute, Foreign Large-size Research Facility Application Supporting project, the Global Science Experimental Data Hub Center of the Korea Institute of Science and Technology Information, and KREONET/GLORIAD; Frontiers of Science Program contracts FOINS-296, CB-221329, CB-236394, CB-254409, CB-180023 and the Thematic Networks program (Mexico); Foundation for Fundamental Research of Matter no. 156, "Higgs as Probe and Portal" and National Organization for Scientific Research (Netherlands); National Science Center, Poland and research grant nos. 2015/19/B/ST2/02848, 2017/25/B/ST2/00191, 2017/27/B/ST2/01391, and UMO-2015/18/M/ST2/00518, HARMONIA; Russian Ministry of Education and Science Funding no. 14.W03.31.0026; Slovenian Research Agency (research grant no. J1-8137 and research core funding nos. P1-0135, P1-0035); Agencia Estatal de Investigacion, Spain grant nos. FPA2014-55613-P and FPA2017-84445-P; CERN; Swiss National Science Foundation and research grant no. P300P2_167751; Ministry of Science and Technology and research grant no. MOST104-2628-M-002-014-MY4 and the Ministry of Education (Taiwan); Thailand Center of Excellence in Physics; TUBITAK ULAKBIM (Turkey); STFC no. ST/P000290/1 (United Kingdom); Ministry of Education and Science of Ukraine; the US National Science Foundation and research grant nos. PHY-1614545, PHY-1714253, PHY-1414345, PHY-1720252, and PHY-1520966, and the US Department of Energy and research grant nos. DE-SC0010118, DE-SC0012704, DE-SC0009973, DE-SC0012391, DE-SC0010504, DE-AC06-76RLO1830, DE-AC02-05CH11231, DE-AC05-06OR23177, DE-FG02-00ER41132, DE-SC0007983, DE-SC0011637, DE-SC0011726, and DE-SC0011784; International Centre of Physics (under the auspices of UNESCO), IOP, Hanoi, Viet Nam, and the National Foundation for Science and Technology Development (NAFOSTED) of Vietnam under contract no. 103.01-2017.76.

We thank the members of the advisory committee for useful input at the early stages of the document. We thank the KEK theory group and the EU-Rise Japan and Europe Network for Neutrino and Intensity Frontier Experimental Research for offering constant support for the many theorists involved.

Funding

Open Access funding: SCOAP[3].

References

[1] D. Boutigny et al., The BABAR physics book: Physics at an asymmetric *B* factory, in *Workshop on Physics at an Asymmetric B Factory (BaBar Collaboration Meeting) Pasadena, California, September 22–24, 1997* (1998).
[2] A. J. Bevan et al., Eur. Phys. J. C **74**, 3026 (2014) [arXiv:1406.6311 [hep-ex]] [Search INSPIRE].
[3] J. Charles et al., Phys. Rev. D **89**, 033016 (2014) [arXiv:1309.2293 [hep-ph]] [Search INSPIRE].
[4] Y. Ohnishi et al., Prog. Theor. Exp. Phys. **2013**, 03A011 (2013).
[5] M. Bona et al., arXiv:0709.0451 [hep-ex] [Search INSPIRE].
[6] T. Abe, et al., arXiv:1011.0352 [physics.ins-det] [Search INSPIRE].
[7] J. Kemmer et al., Nucl. Instrum. Meth. A **253**, 378 (1987).
[8] P. Fischer et al., Nucl. Instrum. Meth. A **582**, 843 (2007).

[9] M. Akatsu et al., Nucl. Instrum. Meth. A **440**, 124 (2000) [arXiv:physics/9904009] [Search INSPIRE].
[10] M. Staric et al., Nucl. Instrum. Meth. A **595**, 252 (2008).
[11] M. Akatsu et al., Nucl. Instrum. Meth. A **528**, 763 (2004).
[12] L. L. Ruckman and G. S. Varner, Nucl. Instrum. Meth. A **602**, 438 (2009) [arXiv:0805.2225 [physics.ins-det]] [Search INSPIRE].
[13] H. Kichimi et al., JINST **5**, P03011 (2010) [arXiv:1001.1194 [physics.ins-det]] [Search INSPIRE].
[14] T. Iijima et al., Nucl. Instrum. Meth. A **548**, 383 (2005) [arXiv:physics/0504220] [Search INSPIRE].
[15] P. Krizan et al., Nucl. Instrum. Meth. A **565**, 457 (2006) [arXiv:physics/0603022] [Search INSPIRE].
[16] S. Nishida et al., Nucl. Instrum. Meth. A **595**, 150 (2008).
[17] S. Nishida et al., Nucl. Instrum. Meth. A **766**, 28 (2014).
[18] S. Longo and J. M. Roney, JINST **11**, P08017 (2016) [arXiv:1608.07556 [physics.ins-det]] [Search INSPIRE].
[19] A. Kuzmin [Belle ECL Collaboration], Nucl. Instrum. Meth. A **623**, 252 (2010).
[20] V. Balagura et al., Nucl. Instrum. Meth. A **564**, 590 (2006) [arXiv:physics/0504194] [Search INSPIRE].
[21] D. J. Lange, Nucl. Instrum. Meth. A **462**, 152 (2001).
[22] T. Sjöstrand et al., Comput. Phys. Commun. **191**, 159 (2015) [arXiv:1410.3012 [hep-ph]] [Search INSPIRE].
[23] S. Jadach et al., Comput. Phys. Commun. **130**, 260 (2000) [arXiv:hep-ph/9912214] [Search INSPIRE].
[24] S. Jadach et al., Phys. Rev. D **63**, 113009 (2001) [arXiv:hep-ph/0006359] [Search INSPIRE].
[25] N. Davidson et al., Comput. Phys. Commun. **183**, 821 (2012) [arXiv:1002.0543 [hep-ph]] [Search INSPIRE].
[26] G. Balossini et al., Phys. Lett. B **663**, 209 (2008) [arXiv:0801.3360 [hep-ph]] [Search INSPIRE].
[27] G. Balossini et al., Nucl. Phys. B **758**, 227 (2006) [arXiv:hep-ph/0607181] [Search INSPIRE].
[28] C. M. Carloni Calame et al., Nucl. Phys. Proc. Suppl. **131**, 48 (2004) [arXiv:hep-ph/0312014] [Search INSPIRE].
[29] C. M. Carloni Calame, Phys. Lett. B **520**, 16 (2001) [arXiv:hep-ph/0103117] [Search INSPIRE].
[30] C. M. Carloni Calame et al., Nucl. Phys. B **584**, 459 (2000) [arXiv:hep-ph/0003268] [Search INSPIRE].
[31] F. A. Berends et al., Nucl. Phys. B **253**, 441 (1985).
[32] F. A. Berends et al., Comput. Phys. Commun. **40**, 285 (1986).
[33] F. A. Berends et al., Nucl. Phys. B **253**, 421 (1985).
[34] N. Davidson et al., Comput. Phys. Commun. **199**, 86 (2016) [arXiv:1011.0937 [hep-ph]] [Search INSPIRE].
[35] D. Bardin, Comput. Phys. Commun. **133**, 229 (2001) [arXiv:hep-ph/9908433] [Search INSPIRE].
[36] A. B. Arbuzov et al., Comput. Phys. Commun. **174**, 728 (2006) [arXiv:hep-ph/0507146] [Search INSPIRE].
[37] S. Banerjee et al., Phys. Rev. D **77**, 054012 (2008) [arXiv:0706.3235 [hep-ph]] [Search INSPIRE].
[38] Strategic accelerator design (SAD) (available at http://acc-physics.kek.jp/SAD, date last accessed May 6, 2016).
[39] S. Agostinelli et al., Nucl. Instrum. Meth. A **506**, 250 (2003).
[40] J. Allison et al., IEEE Trans. Nucl. Sci. **53**, 270 (2006).
[41] R. Brun et al., ROOT, an object oriented data analysis framework, in *Proc. 2000 CERN School of Computing, Marathon, Greece* (2000).
[42] A. Dotti, Proc. Int. Conf. Calorimetry for the High Energy Frontier (CHEF 2013), p. 247 (2013).
[43] Geant4, *Physics Reference Manual Ver. 10.1* (2014) (available at: http://geant4-userdoc.web.cern.ch/geant4-userdoc/UsersGuides/PhysicsReferenceManual/html/index.html, date last accessed: November 4, 2019).
[44] D. H. Wright, Proc. Int. Conf. Calorimetry for the High Energy Frontier (CHEF 2013), p. 254 (2013).
[45] B. Andersson et al., Nucl. Phys. B **281**, 289 (1987).
[46] V. V. Uzhinsky, Proc. Int. Conf. Calorimetry for the High Energy Frontier (CHEF 2013), p. 260 (2013).
[47] V. Ivanchenko et al., Recent improvements in Geant4 electromagnetic physics models and interfaces, in *Progress in Nuclear Science and Technology*, vol. 2, (2011), p. 898.

[48] Geant4, *User's Guide for Application Developers Ver. 10.2* (2015) (available at: http://geant4-userdoc.web.cern.ch/geant4-userdoc/UsersGuides/ForApplicationDeveloper/html/index.html, date last accessed: November 4, 2019).
[49] Y. Arimoto et al., Proc. 5th Int. Particle Accelerator Conf. (IPAC 2014), p. WEPRI086 (2014).
[50] Cobham Technical Services, *Opera-3D User Guide Ver. 15R3* (Vector Fields Ltd, Oxford, 2012).
[51] R. Fruhwirth et al., Nucl. Instrum. Meth. A **732**, 95 (2013).
[52] T. Lueck et al., EPJ Web Conf. **150**, 00007 (2017).
[53] P. V. C. Hough, U.S. Patent 3069654 (1962).
[54] R. Fruhwirth and A. Strandlie, Comput. Phys. Commun. **120**, 197 (1999).
[55] R. Fruhwirth, Nucl. Instrum. Meth. A **262**, 444 (1987).
[56] C. Hoppner et al., Nucl. Instrum. Meth. A **620**, 518 (2010) [arXiv:0911.1008 [hep-ex]] [Search INSPIRE].
[57] J. Rauch and T. Schlueter, J. Phys. Conf. Ser. **608**, 012042 (2015) [arXiv:1410.3698 [physics.ins-det]] [Search INSPIRE].
[58] H. Ishino et al., Belle internal note BN715 (2005).
[59] W. Waltenberger et al., IEEE Trans. Nucl. Sci. **58**, 434 (2011).
[60] V. Blobel and C. Kleinwort, arXiv:hep-ex/0208021 [Search INSPIRE].
[61] V. Blobel, Nucl. Instrum. Meth. A **566**, 5 (2006).
[62] C. Kleinwort, Nucl. Instrum. Meth. A **673**, 107 (2012).
[63] J. Rauch et al. (2014), arXiv:1410.3698 [physics.ins-det] [Search INSPIRE].
[64] M. Staric, Nucl. Instrum. Meth. A **639**, 252 (2011).
[65] K. Nakamura et al., J. Phys. G **37**, 075021 (2010).
[66] M. Staric, Nucl. Instrum. Meth. A **766**, 237 (2014).
[67] P. Baillon, Nucl. Instrum. Meth. A **238**, 341 (1985).
[68] R. Forty, Nucl. Instrum. Meth. A **433**, 257 (1999).
[69] R. Fruhwirth, Nucl. Instrum. Meth. **262**, 444 (1987).
[70] T. Keck, arXiv:1609.06119 [cs.LG] [Search INSPIRE].
[71] W. D. Hulsbergen, Nucl. Instrum. Meth. A **552**, 566 (2005) [arXiv:physics/0503191] [Search INSPIRE].
[72] W. Waltenberger, CERN-CMS-NOTE-2008-033 (2008).
[73] D. Weyland, MSc thesis, Karlsruher Institut für Technologie (2017).
[74] D. M. Asner et al., Phys. Rev. D **53**, 1039 (1996) [arXiv:hep-ex/9508004] [Search INSPIRE].
[75] G. C. Fox and S. Wolfram, Phys. Rev. Lett. **41**, 1581 (1978).
[76] F. Abudinén, PhD thesis, Ludwig-Maximilians-Universität (2018).
[77] K. A. Olive et al., Chin. Phys. C **38**, 090001 (2014).
[78] S. Nissen, *Implementation of a Fast Artificial Neural Network Library (FANN)*, Technical report, Department of Computer Science University of Copenhagen (DIKU) (2003).
[79] S. Pohl, PhD thesis, Ludwig-Maximilians-Universität (2017).
[80] I. Adachi et al., Phys. Rev. Lett. **108**, 171802 (2012) [arXiv:1201.4643 [hep-ex]] [Search INSPIRE].
[81] H. Kakuno et al., Nucl. Instrum. Meth. A **533**, 516 (2004) [arXiv:hep-ex/0403022] [Search INSPIRE].
[82] T. Keck et al., arXiv:1807.08680 [hep-ex] [Search INSPIRE].
[83] M. Feindt et al., Nucl. Instrum. Meth. A **654**, 432 (201).
[84] A. Sibidanov et al., Phys. Rev. D **88**, 032005 (2013) [arXiv:1306.2781 [hep-ex]] [Search INSPIRE].
[85] R. Glattauer et al., Phys. Rev. D **93**, 032006 (2016) [arXiv:1510.03657 [hep-ex]] [Search INSPIRE].
[86] M. Kobayashi and T. Maskawa, Prog. Theor. Phys. **49**, 652 (1973).
[87] L.-L. Chau and W.-Y. Keung, Phys. Rev. Lett. **53**, 1802 (1984).
[88] C. Patrignani et al., Chin. Phys. C **40**, 100001 (2016).
[89] L. Wolfenstein, Phys. Rev. Lett. **51**, 1945 (1983).
[90] A. J. Buras et al., Phys. Rev. D **50**, 3433 (1994) [arXiv:hep-ph/9403384] [Search INSPIRE].
[91] J. Charles et al., Eur. Phys. J. C **41**, 1 (2005) [arXiv:hep-ph/0406184] [Search INSPIRE].
[92] I. I. Bigi (2015), arXiv:1509.03899 [hep-ph] [Search INSPIRE].
[93] D. Boito et al., Phys. Rev. D **96**, 113003 (2017) [arXiv:1709.09739 [hep-ph]] [Search INSPIRE].
[94] M. E. Peskin and D. V. Schroeder, *An Introduction to Quantum Field Theory* (Addison-Wesley, Reading, MA, 1995).
[95] M. Doring et al., Nucl. Phys. A **829**, 170 (2009) [arXiv:0903.4337 [nucl-th]] [Search INSPIRE].

[96] V. Baru et al., Phys. Lett. B **586**, 53 (2004) [arXiv:hep-ph/0308129] [Search INSPIRE].
[97] C. Hanhart et al., Phys. Rev. D **75**, 074015 (2007) [arXiv:hep-ph/0701214] [Search INSPIRE].
[98] C Hanhart et al., Phys. Rev. D **76**, 034007 (2007) [arXiv:0704.0605 [hep-ph]] [Search INSPIRE].
[99] A. Svarc et al., Phys. Rev. C **89**, 045205 (2014) [arXiv:1401.1947 [nucl-th]] [Search INSPIRE].
[100] S. M. Flatte, Phys. Lett. B **63**, 224 (1976).
[101] S. Gardner and U.-G. Meißner, Phys. Rev. D **65**, 094004 (2002) [arXiv:hep-ph/0112281] [Search INSPIRE].
[102] D. Babusci et al., Phys. Lett. B **718**, 910 (2013) [arXiv:1209.4611 [hep-ex]] [Search INSPIRE].
[103] K. M. Watson, Phys. Rev. **95**, 228 (1954).
[104] F. Klingl et al., Z. Phys. A **356**, 193 (1996) [arXiv:hep-ph/9607431] [Search INSPIRE].
[105] C. Hanhart, Phys. Lett. B **715**, 170 (2012) [arXiv:1203.6839 [hep-ph]] [Search INSPIRE].
[106] F. Stollenwerk et al., Phys. Lett. B **707**, 184 (2012), [arXiv:1108.2419 [nucl-th]] [Search INSPIRE].
[107] B. Kubis and J. Plenter, Eur. Phys. J. C **75**, 283 (2015) [arXiv:1504.02588 [hep-ph]] [Search INSPIRE].
[108] J.-J. Wu et al., Phys. Rev. Lett. **108**, 081803 (2012) [arXiv:1108.3772 [hep-ph]] [Search INSPIRE].
[109] A. P. Szczepaniak, Phys. Lett. B **747**, 410 (2015) [arXiv:1501.01691 [hep-ph]] [Search INSPIRE].
[110] Q. Wang et al., Phys. Lett. B **725**, 106 (2013) [arXiv:1305.1997 [hep-ph]] [Search INSPIRE].
[111] J. T. Daub et al., J. High Energy Phys. **01**, 179 (2013) [arXiv:1212.4408 [hep-ph]] [Search INSPIRE].
[112] M. Battaglieri et al., Acta Phys. Polon. B **46**, 257 (2015) [arXiv:1412.6393 [hep-ph]] [Search INSPIRE].
[113] C. Hanhart et al., Phys. Rev. Lett. **115**, 202001 (2015) [arXiv:1507.00382 [hep-ph]] [Search INSPIRE].
[114] F. K. Guo et al., Phys. Rev. D **93**, 074031 (2016) [arXiv:1602.00940 [hep-ph]] [Search INSPIRE].
[115] G. Barton, *Introduction to Dispersion Techniques in Field Theory* (W.A. Benjamin, New York, 1965).
[116] B. Ananthanarayan et al., Phys. Rept. **353**, 207 (2001) [arXiv:hep-ph/0005297] [Search INSPIRE].
[117] R. Garcia-Martin et al., Phys. Rev. D **83**, 074004 (2011) [arXiv:1102.2183 [hep-ph]] [Search INSPIRE].
[118] J. T. Daub et al., J. High Energy Phys. **02**, 009 (2016) [arXiv:1508.06841 [hep-ph]] [Search INSPIRE].
[119] R. Aaij et al., Phys. Rev. D **90**, 012003 (2014) [arXiv:1404.5673 [hep-ex]] [Search INSPIRE].
[120] R. Aaij et al., Phys. Rev. D **89**, 092006 (2014) [arXiv:1402.6248 [hep-ex]] [Search INSPIRE].
[121] J. F. Donoghue et al., Nucl. Phys. B **343**, 341 (1990).
[122] S. Eidelman and L. Lukaszuk, Phys. Lett. B **582**, 27 (2004) [arXiv:hep-ph/0311366] [Search INSPIRE].
[123] A. Celis et al., Phys. Rev. D **89**, 013008 (2014) [arXiv:1309.3564 [hep-ph]] [Search INSPIRE].
[124] A. Celis et al., Phys. Rev. D **89**, 095014 (2014) [arXiv:1403.5781 [hep-ph]] [Search INSPIRE].
[125] N. N. Khuri and S. B. Treiman, Phys. Rev. **119**, 1115 (1960).
[126] J. Kambor et al., Nucl. Phys. B **465**, 215 (1996) [arXiv:hep-ph/9509374] [Search INSPIRE].
[127] A. V. Anisovich and H. Leutwyler, Phys. Lett. B **375**, 335 (1996) [arXiv:hep-ph/9601237] [Search INSPIRE].
[128] S. P. Schneider et al., J. High Energy Phys. **02**, 028 (2011) [arXiv:1010.3946 [hep-ph]] [Search INSPIRE].
[129] S. P. Schneider et al., Phys. Rev. D **86**, 054013 (2012) [arXiv:1206.3098 [hep-ph]] [Search INSPIRE].
[130] F. Niecknig et al., Eur. Phys. J. C **72**, 2014 (2012) [arXiv:1203.2501 [hep-ph]] [Search INSPIRE].
[131] F. Niecknig and B. Kubis, J. High Energy Phys. **10**, 142 (2015) [arXiv:1509.03188 [hep-ph]] [Search INSPIRE].
[132] I. V. Danilkin et al., Phys. Rev. D **91**, 094029 (2015) [arXiv:1409.7708 [hep-ph]] [Search INSPIRE].
[133] A. S. Kronfeld, Ann. Rev. Nucl. Part. Sci. **62**, 265 (2012) [arXiv:1203.1204 [hep-lat]] [Search INSPIRE].
[134] Sz. Borsanyi et al., Science **347**, 1452 (2015) [arXiv:1406.4088 [hep-lat]] [Search INSPIRE].
[135] R. Horsley et al., J. Phys. G **43**, 10LT02 (2016) [arXiv:1508.06401 [hep-lat]] [Search INSPIRE].
[136] B. A. Thacker and G. P. Lepage, Phys. Rev. D **43**, 196 (1991).
[137] A. X. El-Khadra et al., Phys. Rev. D **55**, 3933 (1997) [arXiv:hep-lat/9604004] [Search INSPIRE].
[138] J. Heitger and R. Sommer, J. High Energy Phys. **02**, 022 (2004) [arXiv:hep-lat/0310035] [Search INSPIRE].

[139] B. Blossier et al., J. High Energy Phys. **04**, 049 (2010) [arXiv:0909.3187 [hep-lat]] [Search INSPIRE].
[140] S. Aoki et al., Eur. Phys. J. C **77**, 112 (2017) [arXiv:1607.00299 [hep-lat]] [Search INSPIRE].
[141] J. M. Flynn et al., Phys. Rev. D **91**, 074510 (2015) [arXiv:1501.05373 [hep-lat]] [Search INSPIRE].
[142] E. Dalgic et al., Phys. Rev. D **73**, 074502 (2006); **75**, 119906 (2007) [erratum] [arXiv:hep-lat/0601021] [Search INSPIRE].
[143] J. A. Bailey et al., Phys. Rev. D **92**, 014024 (2015) [arXiv:1503.07839 [hep-lat]] [Search INSPIRE].
[144] J. A. Bailey et al., Phys. Rev. D **89**, 114504 (2014) [arXiv:1403.0635 [hep-lat]] [Search INSPIRE].
[145] J. A. Bailey et al., Phys. Rev. D **92**, 034506 (2015) [arXiv:1503.07237 [hep-lat]] [Search INSPIRE].
[146] H. Na et al., Phys. Rev. D **92**, 054510 (2015); **93**, 119906 (2016) [erratum] [arXiv:1505.03925 [hep-lat]] [Search INSPIRE].
[147] J. Harrison et al., Phys. Rev. D **97**, 054502 (2018) [arXiv:1711.11013 [hep-lat]] [Search INSPIRE].
[148] E. Gamiz et al., Phys. Rev. D **80**, 014503 (2009) [arXiv:0902.1815 [hep-lat]] [Search INSPIRE].
[149] N. Carrasco et al., J. High Energy Phys. **03**, 016 (2014) [arXiv:1308.1851 [hep-lat]] [Search INSPIRE].
[150] Y. Aoki et al., Phys. Rev. D **91**, 114505 (2015) [arXiv:1406.6192 [hep-lat]] [Search INSPIRE].
[151] A. Bazavov et al., arXiv:1602.03560 [hep-lat] [Search INSPIRE].
[152] A. Patella, PoS **LATTICE2016**, 020 (2017) [arXiv:1702.03857 [hep-lat]] [Search INSPIRE].
[153] N. Carrasco et al., Phys. Rev. D **91**, 074506 (2015) [arXiv:1502.00257 [hep-lat]] [Search INSPIRE].
[154] V. Lubicz et al., PoS **LATTICE2016**, 290 (2016) [arXiv:1610.09668 [hep-lat]] [Search INSPIRE].
[155] C. M. Bouchard et al., Phys. Rev. D **90**, 054506 (2014) [arXiv:1406.2279 [hep-lat]] [Search INSPIRE].
[156] F. Bahr et al., PoS **LATTICE2016**, 295 (2016) [arXiv:1701.03299 [hep-lat]] [Search INSPIRE].
[157] C. Bouchard et al., Phys. Rev. D **88**, 054509 (2013); **88**, 079901 (2013) [erratum] [arXiv:1306.2384 [hep-lat]] [Search INSPIRE].
[158] J. A. Bailey et al., Phys. Rev. D **93**, 025026 (2016) [arXiv:1509.06235 [hep-lat]] [Search INSPIRE].
[159] J. A. Bailey et al., Phys. Rev. Lett. **115**, 152002 (2015) [arXiv:1507.01618 [hep-ph]] [Search INSPIRE].
[160] W. Detmold et al., Phys. Rev. D **88**, 014512 (2013) [arXiv:1306.0446 [hep-lat]] [Search INSPIRE].
[161] W. Detmold et al., Phys. Rev. D **92**, 034503 (2015) [arXiv:1503.01421 [hep-lat]] [Search INSPIRE].
[162] W. Detmold and S. Meinel, Phys. Rev. D **93**, 074501 (2016) [arXiv:1602.01399 [hep-lat]] [Search INSPIRE].
[163] M. Crisafulli et al., Nucl. Phys. B **457**, 594 (1995) [arXiv:hep-ph/9506210] [Search INSPIRE].
[164] V. Gimenez et al., Phys. Lett. B **393**, 124 (1997) [arXiv:hep-lat/9607018] [Search INSPIRE].
[165] V. Gimenez et al., Nucl. Phys. B **486**, 227 (1997) [arXiv:hep-lat/9607055] [Search INSPIRE].
[166] A. Ali Khan et al., Phys. Rev. D **62**, 054505 (2000) [arXiv:hep-lat/9912034] [Search INSPIRE].
[167] A. S. Kronfeld and J. N. Simone, Phys. Lett. B **490**, 228 (2000); **495**, 441 (2000) [erratum] [arXiv:hep-ph/0006345] [Search INSPIRE].
[168] S. Aoki et al., Phys. Rev. D **69**, 094512 (2004) [arXiv:hep-lat/0305024] [Search INSPIRE].
[169] P. Gambino et al., Phys. Rev. D **96**, 014511 (2017) [arXiv:1704.06105 [hep-lat]] [Search INSPIRE].
[170] S. Hashimoto, arXiv:1703.01881 [hep-lat] [Search INSPIRE].
[171] M. T. Hansen et al., arXiv:1704.08993 [hep-lat] [Search INSPIRE].
[172] L. Maiani and M. Testa, Phys. Lett. B **245**, 585 (1990).
[173] D. J. Wilson et al., Phys. Rev. D **91**, 054008 (2015) [arXiv:1411.2004 [hep-ph]] [Search INSPIRE].
[174] G. Moir et al., J. High Energy Phys. **10**, 011 (2016) [arXiv:1607.07093 [hep-lat]] [Search INSPIRE].
[175] M. Luscher, Commun. Math. Phys. **105**, 153 (1986).
[176] M. Luscher, Nucl. Phys. B **354**, 531 (1991).
[177] L. Lellouch and M. Luscher, Commun. Math. Phys. **219**, 31 (2001) [arXiv:hep-lat/0003023] [Search INSPIRE].
[178] T. Blum et al., Phys. Rev. D **91**, 074502 (2015) [arXiv:1502.00263 [hep-lat]] [Search INSPIRE].
[179] Z. Bai et al., Phys. Rev. Lett. **115**, 212001 (2015) [arXiv:1505.07863 [hep-lat]] [Search INSPIRE].
[180] A. J. Buras et al., J. High Energy Phys. **11**, 202 (2015) [arXiv:1507.06345 [hep-ph]] [Search INSPIRE].
[181] T. Kitahara et al., J. High Energy Phys. **12**, 078 (2016) [arXiv:1607.06727 [hep-ph]] [Search INSPIRE].

[182] K. Rummukainen and S. A. Gottlieb, Nucl. Phys. B **450**, 397 (1995) [arXiv:hep-lat/9503028] [Search INSPIRE].
[183] C. H. Kim et al., Nucl. Phys. B **727**, 218 (2005) [arXiv:hep-lat/0507006] [Search INSPIRE].
[184] N. H. Christ et al., Phys. Rev. D **72**, 114506 (2005) [arXiv:hep-lat/0507009] [Search INSPIRE].
[185] M. Lage et al., Phys. Lett. B **681**, 439 (2009) [arXiv:0905.0069 [hep-lat]] [Search INSPIRE].
[186] S. He et al., J. High Energy Phys. **07**, 011 (2005) [arXiv:hep-lat/0504019] [Search INSPIRE].
[187] R. A. Briceno, Phys. Rev. D **89**, 074507 (2014) [arXiv:1401.3312 [hep-lat]] [Search INSPIRE].
[188] K. Polejaeva and A. Rusetsky, Eur. Phys. J. A **48**, 67 (2012) [arXiv:1203.1241 [hep-lat]] [Search INSPIRE].
[189] M. T. Hansen and S. R. Sharpe, Phys. Rev. D **86**, 016007 (2012) [arXiv:1204.0826 [hep-lat]] [Search INSPIRE].
[190] R. A. Briceno and Z. Davoudi, Phys. Rev. D **88**, 094507 (2013) [arXiv:1204.1110 [hep-lat]] [Search INSPIRE].
[191] R. A. Briceño, M. T. Hansen, and S. R. Sharpe, Phys. Rev. D **95**, 074510 (2017) [arXiv:1701.07465 [hep-lat]] [Search INSPIRE].
[192] N. Carrasco et al., Phys. Rev. D **90**, 014502 (2014) [arXiv:1403.7302 [hep-lat]] [Search INSPIRE].
[193] N. Carrasco et al., Phys. Rev. D **92**, 034516 (2015) [arXiv:1505.06639 [hep-lat]] [Search INSPIRE].
[194] N. H. Christ et al., Phys. Rev. D **93**, 114517 (2016) [arXiv:1605.04442 [hep-lat]] [Search INSPIRE].
[195] G. K. C. Cheung et al., J. High Energy Phys. **12**, 089 (2016) [arXiv:1610.01073 [hep-lat]] [Search INSPIRE].
[196] M. Lüscher, Nucl. Phys. B **364**, 237 (1991).
[197] C. B. Lang et al., J. High Energy Phys. **09**, 089 (2015) [arXiv:1503.05363 [hep-lat]] [Search INSPIRE].
[198] S. Prelovsek and L. Leskovec, Phys. Rev. Lett. **111**, 192001 (2013) [arXiv:1307.5172 [hep-lat]] [Search INSPIRE].
[199] S.-H. Lee et al., arXiv:1411.1389 [hep-lat] [Search INSPIRE].
[200] V. M. Abazov et al., Phys. Rev. Lett. **117**, 022003 (2016) [arXiv:1602.07588 [hep-ex]] [Search INSPIRE].
[201] C. B. Lang et al., Phys. Rev. D **94**, 074509 (2016) [arXiv:1607.03185 [hep-lat]] [Search INSPIRE].
[202] R. Aaij et al., Phys. Rev. Lett. **117**, 152003 (2016); **118**, 109904 (2017) [addendum] [arXiv:1608.00435 [hep-ex]] [Search INSPIRE].
[203] R. A. Briceño et al., Phys. Rev. D **91**, 034501 (2015) [arXiv:1406.5965 [hep-lat]] [Search INSPIRE].
[204] R. A. Briceño et al., Phys. Rev. Lett. **115**, 242001 (2015) [arXiv:1507.06622 [hep-ph]] [Search INSPIRE].
[205] L. Leskovec et al., PoS **LATTICE2016**, 159 (2016) [arXiv:1611.00282 [hep-lat]] [Search INSPIRE].
[206] J. J. Dudek et al., Phys. Rev. Lett. **113**, 182001 (2014) [arXiv:1406.4158 [hep-ph]] [Search INSPIRE].
[207] N. Ishii et al., Phys. Lett. B **712**, 437 (2012) [arXiv:1203.3642 [hep-lat]] [Search INSPIRE].
[208] Y. Ikeda et al., arXiv:1602.03465 [hep-lat] [Search INSPIRE].
[209] K. J. Juge et al., Phys. Rev. Lett. **82**, 4400 (1999) [arXiv:hep-ph/9902336] [Search INSPIRE].
[210] A. Peters et al., J. Phys. Conf. Ser. **742**, 012006 (2016) [arXiv:1602.07621 [hep-lat]] [Search INSPIRE].
[211] E. Braaten et al., Phys. Rev. D **90**, 014044 (2014) [arXiv:1402.0438 [hep-ph]] [Search INSPIRE].
[212] A. Bussone et al., Phys. Rev. D **93**, 114505 (2016) [arXiv:1603.04306 [hep-lat]] [Search INSPIRE].
[213] C. McNeile et al., Phys. Rev. D **85**, 031503 (2012) [arXiv:1110.4510 [hep-lat]] [Search INSPIRE].
[214] H. Na et al., Phys. Rev. D **86**, 034506 (2012) [arXiv:1202.4914 [hep-lat]] [Search INSPIRE].
[215] A. Bazavov et al., Phys. Rev. D **85**, 114506 (2012) [arXiv:1112.3051 [hep-lat]] [Search INSPIRE].
[216] N. H. Christ et al., Phys. Rev. D **91**, 054502 (2015) [arXiv:1404.4670 [hep-lat]] [Search INSPIRE].
[217] R. J. Dowdall et al., Phys. Rev. Lett. **110**, 222003 (2013) [arXiv:1302.2644 [hep-lat]] [Search INSPIRE].
[218] C. Bourrely et al., Phys. Rev. D **79**, 013008 (2009); **82**, 099902 (2010) [erratum] [arXiv:0807.2722 [hep-ph]] [Search INSPIRE].
[219] C. Bobeth et al., Phys. Rev. Lett. **112**, 101801 (2014) [arXiv:1311.0903 [hep-ph]] [Search INSPIRE].
[220] G. Burdman et al., Phys. Rev. D **51**, 111 (1995) [arXiv:hep-ph/9405425] [Search INSPIRE].
[221] B. A. Dobrescu and A. S. Kronfeld, Phys. Rev. Lett. **100**, 241802 (2008) [arXiv:0803.0512 [hep-ph]] [Search INSPIRE].

[222] V. Cirigliano and I. Rosell, J. High Energy Phys. **10**, 005 (2007) [arXiv:0707.4464 [hep-ph]] [Search INSPIRE].
[223] M. Beneke and J. Rohrwild, Eur. Phys. J. C **71**, 1818 (2011) [arXiv:1110.3228 [hep-ph]] [Search INSPIRE].
[224] J. G. Körner and G. A. Schuler, Z. Phys. C **46**, 93 (1990).
[225] Y. Sakaki et al., Phys. Rev. D **88**, 094012 (2013) [arXiv:1309.0301 [hep-ph]] [Search INSPIRE].
[226] A. S. Kronfeld, PoS **LATTICE2008**, 282 (2008) [arXiv:0812.2030 [hep-lat]] [Search INSPIRE].
[227] Z. Ligeti et al., J. High Energy Phys. **01**, 083 (2017) [arXiv:1610.02045 [hep-ph]] [Search INSPIRE].
[228] D. Atwood and W. J. Marciano, Phys. Rev. D **41**, 1736 (1990).
[229] S. de Boer et al., Phys. Rev. Lett. **120**, 261804 (2018) [arXiv:1803.05881 [hep-ph]] [Search INSPIRE].
[230] Y. Amhis et al., Eur. Phys. J. C **77**, 895 (2017) [arXiv:1612.07233 [hep-ex]] [Search INSPIRE].
[231] A. Bazavov et al., arXiv:1712.09262 [hep-lat] [Search INSPIRE].
[232] K. Ikado et al., Phys. Rev. Lett. **97**, 251802 (2006) [arXiv:hep-ex/0604018] [Search INSPIRE].
[233] K. Hara et al., Phys. Rev. D **82**, 071101 (2010) [arXiv:1006.4201 [hep-ex]] [Search INSPIRE].
[234] I. Adachi et al., Phys. Rev. Lett. **110**, 131801 (2013) [arXiv:1208.4678 [hep-ex]] [Search INSPIRE].
[235] B. Aubert et al., Phys. Rev. D **81**, 051101 (2010) [arXiv:0912.2453 [hep-ex]] [Search INSPIRE].
[236] J. P. Lees et al., Phys. Rev. D **88**, 031102 (2013) [arXiv:1207.0698 [hep-ex]] [Search INSPIRE].
[237] N. Satoyama et al., Phys. Lett. B **647**, 67 (2007) [arXiv:hep-ex/0611045] [Search INSPIRE].
[238] B. Aubert et al., Phys. Rev. D **79**, 091101 (2009) [arXiv:0903.1220 [hep-ex]] [Search INSPIRE].
[239] A. Höcker et al., PoS **ACAT**, 040 (2007) [arXiv:physics/0703039] [Search INSPIRE].
[240] B. Kronenbitter et al., Phys. Rev. D **92**, 051102 (2015) [arXiv:1503.05613 [hep-ex]] [Search INSPIRE].
[241] Y. Yook et al., Phys. Rev. D **91**, 052016 (2015) [arXiv:1406.6356 [hep-ex]] [Search INSPIRE].
[242] A. Sibidanov et al., arXiv:1712.04123 [hep-ex] [Search INSPIRE].
[243] M. Tanaka and R. Watanabe, Prog. Theor. Exp. Phys. **2017**, 013B05 (2017) [arXiv:1608.05207 [hep-ph]] [Search INSPIRE].
[244] M. Beneke et al., Nucl. Phys. B **591**, 313 (2000) [arXiv:hep-ph/0006124] [Search INSPIRE].
[245] T. Feldmann, arXiv:1408.0300 [hep-ph] [Search INSPIRE].
[246] V. M. Braun and A. Khodjamirian, Phys. Lett. B **718**, 1014 (2013) [arXiv:1210.4453 [hep-ph]] [Search INSPIRE].
[247] A. Heller et al., Phys. Rev. D **91**, 112009 (2015) [arXiv:1504.05831 [hep-ex]] [Search INSPIRE].
[248] M. Gelb et al., Phys. Rev. D **98**, 112016 (2018) [arXiv:1810.12976 [hep-ex]] [Search INSPIRE].
[249] A. Matyja et al., Phys. Rev. Lett. **99**, 191807 (2007) [arXiv:0706.4429 [hep-ex]] [Search INSPIRE].
[250] J. P. Lees et al., Phys. Rev. Lett. **109**, 101802 (2012) [arXiv:1205.5442 [hep-ex]] [Search INSPIRE].
[251] M. Huschle et al., Phys. Rev. D **92**, 072014 (2015) [arXiv:1507.03233 [hep-ex]] [Search INSPIRE].
[252] R. Aaij et al., Phys. Rev. Lett. **115**, 111803 (2015); **115**, 159901 (2015) [addendum] [arXiv:1506.08614 [hep-ex]] [Search INSPIRE].
[253] A. Vaquero Avilés-Casco et al., EPJ Web Conf. **175**, 13003 (2018) [arXiv:1710.09817 [hep-lat]] [Search INSPIRE].
[254] U. Nierste et al., Phys. Rev. D **78**, 015006 (2008) [arXiv:0801.4938 [hep-ph]] [Search INSPIRE].
[255] M. Tanaka and R. Watanabe, Phys. Rev. D **82**, 034027 (2010) [arXiv:1005.4306 [hep-ph]] [Search INSPIRE].
[256] S. Fajfer et al., Phys. Rev. D **85**, 094025 (2012) [arXiv:1203.2654 [hep-ph]] [Search INSPIRE].
[257] J. A. Bailey et al., Phys. Rev. Lett. **109**, 071802 (2012) [arXiv:1206.4992 [hep-ph]] [Search INSPIRE].
[258] D. Bigi and P. Gambino, Phys. Rev. D **94**, 094008 (2016) [arXiv:1606.08030 [hep-ph]] [Search INSPIRE].
[259] F. U. Bernlochner et al., Phys. Rev. D **95**, 115008 (2017); **97**, 059902 (2018) [erratum] [arXiv:1703.05330 [hep-ph]] [Search INSPIRE].
[260] D. Bigi et al., J. High Energy Phys. **11**, 061 (2017) [arXiv:1707.09509 [hep-ph]] [Search INSPIRE].
[261] S. Jaiswal et al., J. High Energy Phys. **12**, 060 (2017) [arXiv:1707.09977 [hep-ph]] [Search INSPIRE].
[262] M. Jung and D. M. Straub, arXiv:1801.01112 [hep-ph] [Search INSPIRE].
[263] R. Alonso et al., Phys. Rev. D **95**, 093006 (2017) [arXiv:1702.02773 [hep-ph]] [Search INSPIRE].

[264] M. Tanaka and R. Watanabe, Phys. Rev. D **87**, 034028 (2013) [arXiv:1212.1878 [hep-ph]] [Search INSPIRE].
[265] A. K. Alok et al., arXiv:1606.03164 [hep-ph] [Search INSPIRE].
[266] A. Bozek et al., Phys. Rev. D **82**, 072005 (2010) [arXiv:1005.2302 [hep-ex]] [Search INSPIRE].
[267] Y. Sato et al., Phys. Rev. D **94**, 072007 (2016) [arXiv:1607.07923 [hep-ex]] [Search INSPIRE].
[268] S. Hirose et al., Phys. Rev. Lett. **118**, 211801 (2017) [arXiv:1612.00529 [hep-ex]] [Search INSPIRE].
[269] A. Abdesselam et al., arXiv:1904.08794 [hep-ex] [Search INSPIRE].
[270] J. P. Lees et al., Phys. Rev. D **88**, 072012 (2013) [arXiv:1303.0571 [hep-ex]] [Search INSPIRE].
[271] R. Aaij et al., Phys. Rev. Lett. **120**, 171802 (2018) [arXiv:1708.08856 [hep-ex]] [Search INSPIRE].
[272] S. Hirose et al., Phys. Rev. D **97**, 012004 (2018) [arXiv:1709.00129 [hep-ex]] [Search INSPIRE].
[273] I. Doršner et al., J. High Energy Phys. **11**, 084 (2013) [arXiv:1306.6493 [hep-ph]] [Search INSPIRE].
[274] P. Krawczyk and S. Pokorski, Phys. Rev. Lett. **60**, 182 (1988).
[275] W-S. Hou, Phys. Rev. D **48**, 2342 (1993).
[276] M. Tanaka, Z. Phys. C **67**, 321 (1995) [arXiv:hep-ph/9411405] [Search INSPIRE].
[277] T. Miki et al., Proc. 3rd Workshop on Higher luminosity B factories, Shonan Village, Japan, p. 116 (2002) [arXiv:hep-ph/0210051] [Search INSPIRE].
[278] A. G. Akeroyd and S. Recksiegel, J. Phys. G **29**, 2311 (2003) [arXiv:hep-ph/0306037] [Search INSPIRE].
[279] A. Crivellin et al., Phys. Rev. D **87**, 094031 (2013) [arXiv:1303.5877 [hep-ph]] [Search INSPIRE].
[280] M. Jung et al., J. High Energy Phys. **11**, 003 (2010) [arXiv:1006.0470 [hep-ph]] [Search INSPIRE].
[281] X.-D. Cheng et al., Eur. Phys. J. C **74**, 3081 (2014) [arXiv:1401.6657 [hep-ph]] [Search INSPIRE].
[282] T. Enomoto and R. Watanabe, J. High Energy Phys. **05**, 002 (2016) [arXiv:1511.05066 [hep-ph]] [Search INSPIRE].
[283] A. Crivellin et al., Phys. Rev. D **86**, 054014 (2012) [arXiv:1206.2634 [hep-ph]] [Search INSPIRE].
[284] A. Celis et al., J. High Energy Phys. **01**, 054 (2013) [arXiv:1210.8443 [hep-ph]] [Search INSPIRE].
[285] A. Crivellin et al., Phys. Rev. Lett. **116**, 081801 (2015) [arXiv:1507.07567 [hep-ph]] [Search INSPIRE].
[286] B. Bhattacharya et al., Phys. Lett. B **742**, 370 (2015) [arXiv:1412.7164 [hep-ph]] [Search INSPIRE].
[287] A. Greljo et al., J. High Energy Phys. **07**, 142 (2015) [arXiv:1506.01705 [hep-ph]] [Search INSPIRE].
[288] L. Calibbi et al., Phys. Rev. Lett. **115**, 181801 (2015) [arXiv:1506.02661 [hep-ph]] [Search INSPIRE].
[289] S. M. Boucenna et al., Phys. Lett. B **760**, 214 (2016) [arXiv:1604.03088 [hep-ph]] [Search INSPIRE].
[290] B. Bhattacharya et al., J. High Energy Phys. **01**, 015 (2017) [arXiv:1609.09078 [hep-ph]] [Search INSPIRE].
[291] S. Fajfer et al., Phys. Rev. Lett. **109**, 161801 (2012) [arXiv:1206.1872 [hep-ph]] [Search INSPIRE].
[292] R. Alonso et al., J. High Energy Phys. **10**, 184 (2015) [arXiv:1505.05164 [hep-ph]] [Search INSPIRE].
[293] M. Freytsis et al., Phys. Rev. D **92**, 054018 (2015) [arXiv:1506.08896 [hep-ph]] [Search INSPIRE].
[294] M. Bauer and M. Neubert, Phys. Rev. Lett. **116**, 141802 (2015) [arXiv:1511.01900 [hep-ph]] [Search INSPIRE].
[295] S. Fajfer and N. Košnik, Phys. Lett. B **755**, 270 (2016) [arXiv:1511.06024 [hep-ph]] [Search INSPIRE].
[296] Y. Sakaki et al., Phys. Rev. D **91**, 114028 (2015) [arXiv:1412.3761 [hep-ph]] [Search INSPIRE].
[297] P. Hamer et al., Phys. Rev. D **93**, 032007 (2016) [arXiv:1509.06521 [hep-ex]] [Search INSPIRE].
[298] P. del Amo Sanchez et al., Phys. Rev. D **83**, 032007 (2011) [arXiv:1005.3288 [hep-ex]] [Search INSPIRE].
[299] H. Ha et al., Phys. Rev. D **83**, 071101 (2011) [arXiv:1012.0090 [hep-ex]] [Search INSPIRE].
[300] J. P. Lees et al., Phys. Rev. D **86**, 092004 (2012) [arXiv:1208.1253 [hep-ex]] [Search INSPIRE].
[301] Y. Grossman et al., Nucl. Phys. B **465**, 369 (1996); **480**, 753 (1996) [erratum] [arXiv:hep-ph/9510378] [Search INSPIRE].
[302] Y. Grossman et al., Phys. Rev. D **55**, 2768 (1997) [arXiv:hep-ph/9607473] [Search INSPIRE].
[303] F. U. Bernlochner et al., Phys. Rev. D **85**, 094033 (2012) [arXiv:1202.1834 [hep-ph]] [Search INSPIRE].
[304] T. Mannel, A. V. Rusov, and F. Shahriaran, Nucl. Phys. B **921**, 211 (2017) [arXiv:1702.01089 [hep-ph]] [Search INSPIRE].

[305] S. Bhattacharya, S. Nandi, and S. Kumar Patra, Eur. Phys. J. C **79**, 268 (2019) [arXiv:1805.08222 [hep-ph]] [Search INSPIRE].
[306] F. U. Bernlochner and Z. Ligeti, Phys. Rev. D **95**, 014022 (2016) [arXiv:1606.09300 [hep-ph]] [Search INSPIRE].
[307] A. F. Falk et al., Phys. Lett. B **326**, 145 (1994) [arXiv:hep-ph/9401226] [Search INSPIRE].
[308] S. Balk et al., Z. Phys. C **64**, 37 (1994) [arXiv:hep-ph/9312220] [Search INSPIRE].
[309] L. Koyrakh, Phys. Rev. D **49**, 3379 (1994) [arXiv:hep-ph/9311215] [Search INSPIRE].
[310] Z. Ligeti and F. J. Tackmann, Phys. Rev. D **90**, 034021 (2014) [arXiv:1406.7013 [hep-ph]] [Search INSPIRE].
[311] A. V. Manohar and M. B. Wise, Phys. Rev. D **49**, 1310 (1994) [arXiv:hep-ph/9308246] [Search INSPIRE].
[312] T. Mannel and F. J. Tackmann, Phys. Rev. D **71**, 034017 (2005) [arXiv:hep-ph/0408273] [Search INSPIRE].
[313] F. J. Tackmann, Phys. Rev. D **72**, 034036 (2005) [arXiv:hep-ph/0503095] [Search INSPIRE].
[314] Z. Ligeti et al., Phys. Rev. D **78**, 114014 (2008) [arXiv:0807.1926 [hep-ph]] [Search INSPIRE].
[315] C. Bauer et al., Phys. Rev. D **70**, 094017 (2004) [arXiv:hep-ph/0408002] [Search INSPIRE].
[316] F. U. Bernlochner et al., PoS **ICHEP2012**, 370 (2013) [arXiv:1303.0958 [hep-ph]] [Search INSPIRE].
[317] I. Caprini et al., Nucl. Phys. B **530**, 153 (1998) [arXiv:hep-ph/9712417] [Search INSPIRE].
[318] B. Aubert et al., Phys. Rev. D **77**, 032002 (2008) [arXiv:0705.4008 [hep-ex]] [Search INSPIRE].
[319] B. Aubert et al., Phys. Rev. D **79**, 012002 (2009) [arXiv:0809.0828 [hep-ex]] [Search INSPIRE].
[320] A. Abdesselam et al., (2018) [arXiv:1809.03290 [hep-ex]] [Search INSPIRE].
[321] B. Aubert et al., Phys. Rev. Lett. **104**, 011802 (2010) [arXiv:0904.4063 [hep-ex]] [Search INSPIRE].
[322] C. G. Boyd et al., Phys. Rev. Lett. **74**, 4603 (1995) [arXiv:hep-ph/9412324] [Search INSPIRE].
[323] D. Bigi et al., Phys. Lett. B **769**, 441 (2017) [arXiv:1703.06124 [hep-ph]] [Search INSPIRE].
[324] A. Abdesselam et al., (2017) arXiv:1702.01521 [hep-ex] [Search INSPIRE].
[325] W. Dungel et al., Phys. Rev. D **82**, 112007 (2010) [arXiv:1010.5620 [hep-ex]] [Search INSPIRE].
[326] B. Aubert et al., Phys. Rev. D **79**, 112004 (2009) [arXiv:0901.1291 [hep-ex]] [Search INSPIRE].
[327] K. Abe et al., Phys. Rev. D **69**, 112002 (2004) [arXiv:hep-ex/0307021] [Search INSPIRE].
[328] V. M. Abazov et al., Phys. Rev. Lett. **95**, 171803 (2005) [arXiv:hep-ex/0507046] [Search INSPIRE].
[329] J. Abdallah et al., Eur. Phys. J. C **45**, 35 (2006) [arXiv:hep-ex/0510024] [Search INSPIRE].
[330] B. Aubert et al., Phys. Rev. Lett. **101**, 261802 (2008) [arXiv:0808.0528 [hep-ex]] [Search INSPIRE].
[331] D. Liventsev et al., Phys. Rev. D **77**, 091503 (2008) [arXiv:0711.3252 [hep-ex]] [Search INSPIRE].
[332] P. del Amo Sanchez et al., Phys. Rev. D **82**, 111101 (2010) [arXiv:1009.2076 [hep-ex]] [Search INSPIRE].
[333] R. Aaij et al., J. High Energy Phys. **1309**, 145 (2013) [arXiv:1307.4556 [hep-ex]] [Search INSPIRE].
[334] R. Aaij et al., Phys. Rev. D **91**, 092002 (2015); **93**, 119901 (2016) [erratum] [arXiv:1503.02995 [hep-ex]] [Search INSPIRE].
[335] R. Aaij et al., Phys. Rev. D **92**, 032002 (2015) [arXiv:1505.01710 [hep-ex]] [Search INSPIRE].
[336] R. Aaij et al., Phys. Rev. D **94**, 072001 (2016) [arXiv:1608.01289 [hep-ex]] [Search INSPIRE].
[337] A. Le Yaouanc et al., Phys. Lett. B **387**, 582 (1996) [arXiv:hep-ph/9607300] [Search INSPIRE].
[338] N. Uraltsev, Phys. Lett. B **501**, 86 (2001) [arXiv:hep-ph/0011124] [Search INSPIRE].
[339] V. Morenas et al., Phys. Lett. B **386**, 315 (1996) [arXiv:hep-ph/9605206] [Search INSPIRE].
[340] V. Morenas et al., Phys. Rev. D **56**, 5668 (1997) [arXiv:hep-ph/9706265] [Search INSPIRE].
[341] D. Ebert et al., Phys. Lett. B **434**, 365 (1998) [arXiv:hep-ph/9805423] [Search INSPIRE].
[342] D. Ebert et al., Phys. Rev. D **61**, 014016 (2000) [arXiv:hep-ph/9906415] [Search INSPIRE].
[343] A. K. Leibovich et al., Phys. Rev. Lett. **78**, 3995 (1997) [arXiv:hep-ph/9703213] [Search INSPIRE].
[344] I. I. Bigi et al., Eur. Phys. J. C **52**, 975 (2007) [arXiv:0708.1621 [hep-ph]] [Search INSPIRE].
[345] J. Segovia et al., Phys. Rev. D **84**, 094029 (2011) [arXiv:1107.4248 [hep-ph]] [Search INSPIRE].
[346] R. Klein et al., Phys. Rev. D **91**, 094034 (2015) [arXiv:1503.00569 [hep-ph]] [Search INSPIRE].
[347] B. Aubert et al., Phys. Rev. Lett. **100**, 151802 (2008) [arXiv:0712.3503 [hep-ex]] [Search INSPIRE].
[348] T. Lueck, PoS **EPS-HEP2015**, 562 (2015).
[349] M. Atoui, Proc. 48th Rencontres de Moriond on QCD and High Energy Interactions, La Thuile, Italy p. 143 (2013) [arXiv:1305.0462 [hep-lat]] [Search INSPIRE].
[350] M. Atoui et al., Eur. Phys. J. C **75**, 376 (2015) [arXiv:1312.2914 [hep-lat]] [Search INSPIRE].
[351] B. Blossier, arXiv:1411.3563 [hep-ph] [Search INSPIRE].

[352] P. Gambino and C. Schwanda, Phys. Rev. D **89**, 014022 (2014) [arXiv:1307.4551 [hep-ph]] [Search INSPIRE].
[353] A. Alberti et al., Phys. Rev. Lett. **114**, 061802 (2015) [arXiv:1411.6560 [hep-ph]] [Search INSPIRE].
[354] P. Gambino et al., Phys. Lett. B **763**, 60 (2016) [arXiv:1606.06174 [hep-ph]] [Search INSPIRE].
[355] T. Mannel et al., J. High Energy Phys. **11**, 109 (2010) [arXiv:1009.4622 [hep-ph]] [Search INSPIRE].
[356] J. Heinonen and T. Mannel, Nucl. Phys. B **889**, 46 (2014) [arXiv:1407.4384 [hep-ph]] [Search INSPIRE].
[357] J. P. Lees et al., Phys. Rev. D **85**, 011101 (2012) [arXiv:1110.5600 [hep-ex]] [Search INSPIRE].
[358] C. Oswald et al., Phys. Rev. D **87**, 072008 (2013) [arXiv:1212.6400 [hep-ex]] [Search INSPIRE].
[359] M. Gronau and J. L. Rosner, Phys. Rev. D **83**, 034025 (2011) [arXiv:1012.5098 [hep-ph]] [Search INSPIRE].
[360] I. I. Bigi et al., J. High Energy Phys. **1109**, 012 (2011) [arXiv:1105.4574 [hep-ph]] [Search INSPIRE].
[361] V. M. Abazov et al., Phys. Rev. Lett. **102**, 051801 (2009) [arXiv:0712.3789 [hep-ex]] [Search INSPIRE].
[362] R. Aaij et al., Phys. Lett. B **698**, 14 (2011) [arXiv:1102.0348 [hep-ex]] [Search INSPIRE].
[363] C. Oswald et al., Phys. Rev. D **92**, 072013 (2015) [arXiv:1504.02004 [hep-ex]] [Search INSPIRE].
[364] M. Neubert, Phys. Rev. D **49**, 4623 (1994) [arXiv:hep-ph/9312311] [Search INSPIRE].
[365] I. I. Y. Bigi et al., Int. J. Mod. Phys. A **9**, 2467 (1994) [arXiv:hep-ph/9312359] [Search INSPIRE].
[366] C. W. Bauer et al., Phys. Rev. D **68**, 094001 (2003) [arXiv:hep-ph/0102089] [Search INSPIRE].
[367] K. S. M. Lee and I. W. Stewart, Nucl. Phys. B **721**, 325–406 (2005), [arXiv:hep-ph/0409045] [Search INSPIRE].
[368] P. Gambino et al., J. High Energy Phys. **0710**, 058 (2007) [arXiv:0707.2493 [hep-ph]] [Search INSPIRE].
[369] B. O. Lange et al., Phys. Rev. D **72**, 073006 (2005) [arXiv:hep-ph/0504071] [Search INSPIRE].
[370] S. W. Bosch et al., Nucl. Phys. B **699**, 335 (2004) [arXiv:hep-ph/0402094] [Search INSPIRE].
[371] S. W. Bosch et al., J. High Energy Phys. **11**, 073 (2004) [arXiv:hep-ph/0409115] [Search INSPIRE].
[372] P. Gambino, K. J. Healey, and C. Mondino, Phys. Rev. D **94**, 014031 (2016) [arXiv:1604.07598 [hep-ph]] [Search INSPIRE].
[373] J. R. Andersen and E. Gardi, J. High Energy Phys. **0601**, 097 (2006) [arXiv:hep-ph/0509360] [Search INSPIRE].
[374] U. Aglietti and G. Ricciardi, Phys. Rev. D **70**, 114008 (2004) [arXiv:hep-ph/0407225] [Search INSPIRE].
[375] U. Aglietti et al., Nucl. Phys. B **768**, 85 (2007) [arXiv:hep-ph/0608047] [Search INSPIRE].
[376] U. Aglietti et al., Eur. Phys. J. C **59**, 831 (2009) [arXiv:0711.0860 [hep-ph]] [Search INSPIRE].
[377] P. Urquijo et al., Phys. Rev. Lett. **104**, 021801 (2010) [arXiv:0907.0379 [hep-ex]] [Search INSPIRE].
[378] J. P. Lees et al., Phys. Rev. D **86**, 032004 (2012) [arXiv:1112.0702 [hep-ex]] [Search INSPIRE].
[379] A. Bornheim et al., Phys. Rev. Lett. **88**, 231803 (2002) [arXiv:hep-ex/0202019] [Search INSPIRE].
[380] A. Limosani et al., Phys. Lett. B **621**, 28 (2005) [arXiv:hep-ex/0504046] [Search INSPIRE].
[381] J. P. Lees et al., Phys. Rev. D **95**, 072001 (2017) [arXiv:1611.05624 [hep-ex]] [Search INSPIRE].
[382] C. W. Bauer et al., Phys. Rev. D **64**, 113004 (2001) [arXiv:hep-ph/0107074] [Search INSPIRE].
[383] I. Bigi et al., J. High Energy Phys. **1004**, 073 (2010) [arXiv:0911.3322 [hep-ph]] [Search INSPIRE].
[384] P. Gambino and J. F. Kamenik, Nucl. Phys. B **840**, 424 (2010) [arXiv:1004.0114 [hep-ph]] [Search INSPIRE].
[385] Z. Ligeti et al., Phys. Rev. D **82**, 033003 (2010) [arXiv:1003.1351 [hep-ph]] [Search INSPIRE].
[386] N. Brambilla et al., Phys. Rev. D **97**, 034503 (2018) [arXiv:1712.04983 [hep-ph]] [Search INSPIRE].
[387] A. Bazavov et al., arXiv:1802.04248 [hep-lat] [Search INSPIRE].
[388] R. Aaij et al., J. High Energy Phys. **08**, 131 (2013) [arXiv:1304.6325 [hep-ex]] [Search INSPIRE].
[389] R. Aaij et al., J. High Energy Phys. **02**, 104 (2016) [arXiv:1512.04442 [hep-ex]] [Search INSPIRE].
[390] S. Wehle et al., Phys. Rev. Lett. **118**, 111801 (2017) [arXiv:1612.05014 [hep-ex]] [Search INSPIRE].
[391] R. Aaij et al., Phys. Rev. Lett. **113**, 151601 (2014) [arXiv:1406.6482 [hep-ex]] [Search INSPIRE].
[392] R. Aaij et al., arXiv:1705.05802 [hep-ex] [Search INSPIRE].
[393] V. Khachatryan et al., Phys. Lett. B **753**, 424 (2016) [arXiv:1507.08126 [hep-ex]] [Search INSPIRE].
[394] G. Aad et al., Angular analysis of $B_d^0 \to K^* \mu^+ \mu^-$ decays in pp collisions at $\sqrt{s} = 8$ TeV with the ATLAS detector, Technical Report ATLAS-CONF-2017-023, CERN, Geneva (2017).
[395] A. M Sirunyan et al., arXiv:1710.02846 [hep-ex] [Search INSPIRE].

[396] G. Buchalla et al., Rev. Mod. Phys. **68**, 1125 (1996) [arXiv:hep-ph/9512380] [Search INSPIRE].
[397] K. G. Chetyrkin et al., Phys. Lett. B **400**, 206 (1997); **425**, 414 (1998) [erratum] [arXiv:hep-ph/9612313] [Search INSPIRE].
[398] M. Czakon et al., J. High Energy Phys. **03**, 008 (2007) [arXiv:hep-ph/0612329] [Search INSPIRE].
[399] C. Bobeth et al., Nucl. Phys. B **574**, 291 (2000) [arXiv:hep-ph/9910220] [Search INSPIRE].
[400] P. Gambino et al., Nucl. Phys. B **673**, 238 (2003) [arXiv:hep-ph/0306079] [Search INSPIRE].
[401] M. Gorbahn and U. Haisch, Nucl. Phys. B **713**, 291 (2005) [arXiv:hep-ph/0411071] [Search INSPIRE].
[402] M. Misiak and J. Urban, Phys. Lett. B **451**, 161 (1999) [arXiv:hep-ph/9901278] [Search INSPIRE].
[403] G. Buchalla and A. J. Buras, Nucl. Phys. B **548**, 309 (1999) [arXiv:hep-ph/9901288] [Search INSPIRE].
[404] T. Hermann et al., J. High Energy Phys. **12**, 097 (2013) [arXiv:1311.1347 [hep-ph]] [Search INSPIRE].
[405] J. Brod et al., Phys. Rev. D **83**, 034030 (2011) [arXiv:1009.0947 [hep-ph]] [Search INSPIRE].
[406] C. Bobeth et al., Phys. Rev. D **89**, 034023 (2014) [arXiv:1311.1348 [hep-ph]] [Search INSPIRE].
[407] B. Blok et al., Phys. Rev. D **49**, 3356 (1994); **50**, 3572 (1994) [erratum] [arXiv:hep-ph/9307247] [Search INSPIRE].
[408] M. Neubert, Phys. Rev. D **49**, 3392 (1994) [arXiv:hep-ph/9311325] [Search INSPIRE].
[409] S. J. Lee et al., Phys. Rev. D **75**, 114005 (2007) [arXiv:hep-ph/0609224] [Search INSPIRE].
[410] M. Benzke et al., J. High Energy Phys. **08**, 099 (2010) [arXiv:1003.5012 [hep-ph]] [Search INSPIRE].
[411] S. Aoki et al., Eur. Phys. J. C **74**, 2890 (2014) [arXiv:1310.8555 [hep-lat]] [Search INSPIRE].
[412] C. Bouchard et al., Phys. Rev. Lett. **111**, 162002 (2013); **112**, 149902 (2014) [erratum] [arXiv:1306.0434 [hep-ph]] [Search INSPIRE].
[413] R. R. Horgan et al., Phys. Rev. D **89**, 094501 (2014) [arXiv:1310.3722 [hep-lat]] [Search INSPIRE].
[414] J. Flynn et al., arXiv:1511.06622 [hep-lat] [Search INSPIRE].
[415] M. Beneke et al., Phys. Rev. Lett. **83**, 1914 (1999) [arXiv:hep-ph/9905312] [Search INSPIRE].
[416] M. Beneke et al., Nucl. Phys. B **606**, 245 (2001) [arXiv:hep-ph/0104110] [Search INSPIRE].
[417] A. Khodjamirian and R. Rückl, Adv. Ser. Direct. High Energy Phys. **15**, 345 (1998) [arXiv:hep-ph/9801443] [Search INSPIRE].
[418] P. Ball and R. Zwicky, Phys. Rev. D **71**, 014029 (2005) [arXiv:hep-ph/0412079] [Search INSPIRE].
[419] A. Bharucha et al., arXiv:1503.05534 [hep-ph] [Search INSPIRE].
[420] B. Aubert et al., Phys. Rev. D **77**, 051103 (2008) [arXiv:0711.4889 [hep-ex]] [Search INSPIRE].
[421] P. del Amo Sanchez et al., Phys. Rev. D **82**, 051101 (2010) [arXiv:1005.4087 [hep-ex]] [Search INSPIRE].
[422] J. P. Lees et al., Phys. Rev. D **86**, 052012 (2012) [arXiv:1207.2520 [hep-ex]] [Search INSPIRE].
[423] J. P. Lees et al., Phys. Rev. Lett. **109**, 191801 (2012) [arXiv:1207.2690 [hep-ex]] [Search INSPIRE].
[424] T. Saito et al., Phys. Rev. D **91**, 052004 (2015) [arXiv:1411.7198 [hep-ex]] [Search INSPIRE].
[425] A. Abdesselam et al., arXiv:1608.02344 [hep-ex] [Search INSPIRE].
[426] M. Czakon et al., J. High Energy Phys. **04**, 168 (2015) [arXiv:1503.01791 [hep-ph]] [Search INSPIRE].
[427] M. Misiak et al., Phys. Rev. Lett. **114**, 221801 (2015) [arXiv:1503.01789 [hep-ph]] [Search INSPIRE].
[428] O. Buchmüller and H. Flächer, Phys. Rev. D **73**, 073008 (2006) [arXiv:hep-ph/0507253] [Search INSPIRE].
[429] G. Paz, arXiv:1011.4953 [hep-ph] [Search INSPIRE].
[430] F. U. Bernlochner et al., arXiv:1101.3310 [hep-ph] [Search INSPIRE].
[431] A. Crivellin and L. Mercolli, Phys. Rev. D **84**, 114005 (2011) [arXiv:1106.5499 [hep-ph]] [Search INSPIRE].
[432] H. M. Asatrian and C. Greub, Phys. Rev. D **88**, 074014 (2013) [arXiv:1305.6464 [hep-ph]] [Search INSPIRE].
[433] P. Gambino and M. Misiak, Nucl. Phys. B **611**, 338 (2001) [arXiv:hep-ph/0104034] [Search INSPIRE].
[434] G. Buchalla et al., Nucl. Phys. B **511**, 594 (1998) [arXiv:hep-ph/9705253] [Search INSPIRE].
[435] M. Kaminski et al., Phys. Rev. D **86**, 094004 (2012) [arXiv:1209.0965 [hep-ph]] [Search INSPIRE].
[436] T. Huber et al., J. High Energy Phys. **01**, 115 (2015) [arXiv:1411.7677 [hep-ph]] [Search INSPIRE].

[437] I. R. Blokland et al., Phys. Rev. D **72**, 033014 (2005) [arXiv:hep-ph/0506055] [Search INSPIRE].
[438] K. Melnikov and A. Mitov, Phys. Lett. B **620**, 69 (2005) [arXiv:hep-ph/0505097] [Search INSPIRE].
[439] H. M. Asatrian et al., Phys. Lett. B **647**, 173 (2007) [arXiv:hep-ph/0611123] [Search INSPIRE].
[440] T. Ewerth, Phys. Lett. B **669**, 167 (2008) [arXiv:0805.3911 [hep-ph]] [Search INSPIRE].
[441] H. M. Asatrian et al., Phys. Rev. D **82**, 074006 (2010) [arXiv:1005.5587 [hep-ph]] [Search INSPIRE].
[442] Z. Ligeti et al., Phys. Rev. D **60**, 034019 (1999) [arXiv:hep-ph/9903305] [Search INSPIRE].
[443] A. Ferroglia and U. Haisch, Phys. Rev. D **82**, 094012 (2010) [arXiv:1009.2144 [hep-ph]] [Search INSPIRE].
[444] M. Misiak and M. Poradzinski, Phys. Rev. D **83**, 014024 (2011) [arXiv:1009.5685 [hep-ph]] [Search INSPIRE].
[445] S. J. Brodsky et al., Phys. Rev. D **28**, 228 (1983).
[446] K. Bieri et al., Phys. Rev. D **67**, 114019 (2003) [arXiv:hep-ph/0302051] [Search INSPIRE].
[447] R. Boughezal et al., J. High Energy Phys. **09**, 072 (2007) [arXiv:0707.3090 [hep-ph]] [Search INSPIRE].
[448] M. Misiak and M. Steinhauser, Nucl. Phys. B **764**, 62 (2007) [arXiv:hep-ph/0609241] [Search INSPIRE].
[449] M. Misiak and M. Steinhauser, Nucl. Phys. B **840**, 271 (2010) [arXiv:1005.1173 [hep-ph]] [Search INSPIRE].
[450] M. Misiak, A. Rehman, and M. Steinhauser, Phys. Lett. B **770**, 431 (2017) [arXiv:1702.07674 [hep-ph]] [Search INSPIRE].
[451] J. Charles et al., Phys. Rev. D **91**, 073007 (2015) [arXiv:1501.05013 [hep-ph]] [Search INSPIRE].
[452] T. Ewerth et al., Nucl. Phys. B **830**, 278 (2010) [arXiv:0911.2175 [hep-ph]] [Search INSPIRE].
[453] A. Alberti et al., J. High Energy Phys. **01**, 147 (2014) [arXiv:1311.7381 [hep-ph]] [Search INSPIRE].
[454] I. I. Y. Bigi et al., Phys. Lett. B **293**, 430 (1992); **297**, 477 (1992) [erratum] [arXiv:hep-ph/9207214] [Search INSPIRE].
[455] A. F. Falk et al., Phys. Rev. D **49**, 3367 (1994) [arXiv:hep-ph/9308288] [Search INSPIRE].
[456] C. W. Bauer, Phys. Rev. D **57**, 5611 (1998); **60**, 099907 (1999) [erratum] [arXiv:hep-ph/9710513] [Search INSPIRE].
[457] T. Becher and M. Neubert, Phys. Lett. B **637**, 251 (2006) [arXiv:hep-ph/0603140] [Search INSPIRE].
[458] M. Beneke et al., J. High Energy Phys. **06**, 071 (2005) [arXiv:hep-ph/0411395] [Search INSPIRE].
[459] G. Paz, J. High Energy Phys. **06**, 083 (2009) [arXiv:0903.3377 [hep-ph]] [Search INSPIRE].
[460] B. O. Lange et al., J. High Energy Phys. **0510**, 084 (2005) [arXiv:hep-ph/0508178] [Search INSPIRE].
[461] B. O. Lange, J. High Energy Phys. **01**, 104 (2006) [arXiv:hep-ph/0511098] [Search INSPIRE].
[462] A. Ali and C. Greub, Phys. Lett. B **361**, 146 (1995) [arXiv:hep-ph/9506374] [Search INSPIRE].
[463] A. Kapustin et al., Phys. Lett. B **357**, 653 (1995) [arXiv:hep-ph/9507248] [Search INSPIRE].
[464] J. F. Donoghue and A. A. Petrov, Phys. Rev. D **53**, 3664 (1996) [arXiv:hep-ph/9510227] [Search INSPIRE].
[465] M. B. Voloshin, Phys. Lett. B **397**, 275 (1997) [arXiv:hep-ph/9612483] [Search INSPIRE].
[466] Z. Ligeti et al., Phys. Lett. B **402**, 178 (1997) [arXiv:hep-ph/9702322] [Search INSPIRE].
[467] A. K. Grant et al., Phys. Rev. D **56**, 3151 (1997) [arXiv:hep-ph/9702380] [Search INSPIRE].
[468] M. Benzke et al., Phys. Rev. Lett. **106**, 141801 (2011) [arXiv:1012.3167 [hep-ph]] [Search INSPIRE].
[469] J. M. Soares, Nucl. Phys. B **367**, 575 (1991).
[470] A. Ali et al., Phys. Lett. B **429**, 87 (1998) [arXiv:hep-ph/9803314] [Search INSPIRE].
[471] A. L. Kagan and M. Neubert, Phys. Rev. D **58**, 094012 (1998) [arXiv:hep-ph/9803368] [Search INSPIRE].
[472] T. Hurth et al., Nucl. Phys. B **704**, 56 (2005) [arXiv:hep-ph/0312260] [Search INSPIRE].
[473] M. Misiak, Acta Phys. Polon. B **40**, 2987 (2009) [arXiv:0911.1651 [hep-ph]] [Search INSPIRE].
[474] J. P. Lees et al., Phys. Rev. D **86**, 112008 (2012) [arXiv:1207.5772 [hep-ex]] [Search INSPIRE].
[475] A. Limosani et al., Phys. Rev. Lett. **103**, 241801 (2009) [arXiv:0907.1384 [hep-ex]] [Search INSPIRE].
[476] S. Chen et al., Phys. Rev. Lett. **87**, 251807 (2001) [arXiv:hep-ex/0108032] [Search INSPIRE].
[477] B. Aubert et al., Phys. Rev. D **72**, 052004 (2005) [arXiv:hep-ex/0508004] [Search INSPIRE].
[478] S. Watanuki et al., arXiv:1807.04236 [hep-ex] [Search INSPIRE].
[479] B. Aubert et al., Phys. Rev. Lett. **95**, 042001 (2005) [arXiv:hep-ex/0504001] [Search INSPIRE].

[480] L. Pesantez et al., Phys. Rev. Lett. **114**, 151601 (2015) [arXiv:1501.01702 [hep-ex]] [Search INSPIRE].
[481] J. P. Lees et al., Phys. Rev. D **90**, 092001 (2014) [arXiv:1406.0534 [hep-ex]] [Search INSPIRE].
[482] S. W. Bosch and G. Buchalla, Nucl. Phys. B **621**, 459 (2002) [arXiv:hep-ph/0106081] [Search INSPIRE].
[483] M. Beneke et al., Nucl. Phys. B **612**, 25 (2001) [arXiv:hep-ph/0106067] [Search INSPIRE].
[484] M. Beneke et al., Eur. Phys. J. C **41**, 173 (2005) [arXiv:hep-ph/0412400] [Search INSPIRE].
[485] M. Dimou et al., Phys. Rev. D **87**, 074008 (2013) [arXiv:1212.2242 [hep-ph]] [Search INSPIRE].
[486] A. Ali and V. M. Braun, Phys. Lett. B **359**, 223 (1995) [arXiv:hep-ph/9506248] [Search INSPIRE].
[487] A. Khodjamirian et al., Phys. Lett. B **358**, 129 (1995) [arXiv:hep-ph/9506242] [Search INSPIRE].
[488] J. Lyon and R. Zwicky, Phys. Rev. D **88**, 094004 (2013) [arXiv:1305.4797 [hep-ph]] [Search INSPIRE].
[489] R. Aaij et al., Phys. Rev. Lett. **112**, 161801 (2014) [arXiv:1402.6852 [hep-ex]] [Search INSPIRE].
[490] D. Becirevic et al., J. High Energy Phys. **08**, 090 (2012) [arXiv:1206.1502 [hep-ph]] [Search INSPIRE].
[491] S. Jäger and J. Martin Camalich, Phys. Rev. D **93**, 014028 (2016) [arXiv:1412.3183 [hep-ph]] [Search INSPIRE].
[492] M. Borsato, PhD thesis, Santiago de Compostela U. (2015).
[493] A. Paul and D. M. Straub, J. High Energy Phys. **04**, 027 (2017) [arXiv:1608.02556 [hep-ph]] [Search INSPIRE].
[494] P. Ball, G. W. Jones, and R. Zwicky, Phys. Rev. D **75**, 054004 (2007) [arXiv:hep-ph/0612081] [Search INSPIRE].
[495] R. Aaij et al., Phys. Rev. D **85**, 112013 (2012) [arXiv:1202.6267 [hep-ex]] [Search INSPIRE].
[496] R. Aaij et al., Nucl. Phys. B **867**, 1 (2013) [arXiv:1209.0313 [hep-ex]] [Search INSPIRE].
[497] S. Descotes-Genon et al., Phys. Rev. D **88**, 074002 (2013) [arXiv:1307.5683 [hep-ph]] [Search INSPIRE].
[498] W. Altmannshofer et al., Proc. 50th Rencontres de Moriond Electroweak interactions and unified theories, p. 333 (2015)
[499] R. Aaij et al., J. High Energy Phys. **09**, 179 (2015) [arXiv:1506.08777 [hep-ex]] [Search INSPIRE].
[500] A. Ali and A. Y. Parkhomenko, Eur. Phys. J. C **23**, 89 (2002) [arXiv:hep-ph/0105302] [Search INSPIRE].
[501] A. L. Kagan and M. Neubert, Phys. Lett. B **539**, 227 (2002) [arXiv:hep-ph/0110078] [Search INSPIRE].
[502] D. Atwood et al., Phys. Rev. Lett. **79**, 185 (1997) [arXiv:hep-ph/9704272] [Search INSPIRE].
[503] F. Muheim et al., Phys. Lett. B **664**, 174 (2008) [arXiv:0802.0876 [hep-ph]] [Search INSPIRE].
[504] E. Kou et al., J. High Energy Phys. **12**, 102 (2013) [arXiv:1305.3173 [hep-ph]] [Search INSPIRE].
[505] N. Haba et al., J. High Energy Phys. **03**, 160 (2015) [arXiv:1501.00668 [hep-ph]] [Search INSPIRE].
[506] B. Grinstein et al., Phys. Rev. D **71**, 011504 (2005) [arXiv:hep-ph/0412019] [Search INSPIRE].
[507] S. Jäger and J. M. Camalich, J. High Energy Phys. **05**, 043 (2013) [arXiv:1212.2263 [hep-ph]] [Search INSPIRE].
[508] P. Ball and R. Zwicky, J. High Energy Phys. **04**, 046 (2006) [arXiv:hep-ph/0603232] [Search INSPIRE].
[509] A. Khodjamirian et al., J. High Energy Phys. **09**, 089 (2010) [arXiv:1006.4945 [hep-ph]] [Search INSPIRE].
[510] J. Gratrex and R. Zwicky, arXiv:1804.09006 [hep-ph] [Search INSPIRE].
[511] P. Ball and R. Zwicky, Phys. Lett. B **642**, 478 (2006) [arXiv:hep-ph/0609037] [Search INSPIRE].
[512] M. Gronau et al., Phys. Rev. Lett. **88**, 051802 (2002) [arXiv:hep-ph/0107254] [Search INSPIRE].
[513] M. Gronau and D. Pirjol, Phys. Rev. D **66**, 054008 (2002) [arXiv:hep-ph/0205065] [Search INSPIRE].
[514] E. Kou et al., Phys. Rev. D **83**, 094007 (2011) [arXiv:1011.6593 [hep-ph]] [Search INSPIRE].
[515] R. Aaij et al., J. High Energy Phys. **04**, 064 (2015) [arXiv:1501.03038 [hep-ex]] [Search INSPIRE].
[516] F. Bishara and D. J. Robinson, J. High Energy Phys. **09**, 013 (2015) [arXiv:1505.00376 [hep-ph]] [Search INSPIRE].
[517] D. Atwood et al., Phys. Rev. D **71**, 076003 (2005) [arXiv:hep-ph/0410036] [Search INSPIRE].
[518] R. Ammar et al., Phys. Rev. Lett. **71**, 674 (1993).
[519] Y. Ushiroda et al., Belle, Phys. Rev. D **74**, 111104 (2006) [arXiv:hep-ex/0608017] [Search INSPIRE].

[520] H. Nakano et al., Belle, Phys. Rev. D **97**, 092003 (2018) [arXiv:1803.07774 [hep-ex]] [Search INSPIRE].
[521] J. Li et al., Belle, Phys. Rev. Lett. **101**, 251601 (2008) [arXiv:0806.1980 [hep-ex]] [Search INSPIRE].
[522] H. Sahoo et al., Phys. Rev. D **84**, 071101 (2011) [arXiv:1104.5590 [hep-ex]] [Search INSPIRE].
[523] T. Horiguchi et al., Phys. Rev. Lett. **119**, 191802 (2017) [arXiv:1707.00394 [hep-ex]] [Search INSPIRE].
[524] W. Altmannshofer and D. M. Straub, Eur. Phys. J. C **75**, 382 (2015) [arXiv:1411.3161 [hep-ph]] [Search INSPIRE].
[525] K. Abe et al., Phys. Rev. Lett. **96**, 221601 (2006) [arXiv:hep-ex/0506079] [Search INSPIRE].
[526] Y. Ushiroda et al., Phys. Rev. Lett. **100**, 021602 (2008) [arXiv:0709.2769 [hep-ex]] [Search INSPIRE].
[527] N. Taniguchi et al., Phys. Rev. Lett. **101**, 111801 (2008); **101**, 129904 (2008) [erratum] [arXiv:0804.4770 [hep-ex]] [Search INSPIRE].
[528] B. Aubert et al., Phys. Rev. D **78**, 112001 (2008) [arXiv:0808.1379 [hep-ex]] [Search INSPIRE].
[529] D. Dutta et al., Phys. Rev. D **91**, 011101 (2015) [arXiv:1411.7771 [hep-ex]] [Search INSPIRE].
[530] A. Drutskoy et al., Phys. Rev. Lett. **98**, 052001 (2007) [arXiv:hep-ex/0608015] [Search INSPIRE].
[531] P. del Amo Sanchez et al., Phys. Rev. D **83**, 032006 (2011) [arXiv:1010.2229 [hep-ex]] [Search INSPIRE].
[532] S. Villa et al., Phys. Rev. D **73**, 051107 (2006) [arXiv:hep-ex/0507036] [Search INSPIRE].
[533] S. W. Bosch and G. Buchalla, J. High Energy Phys. **08**, 054 (2002) [arXiv:hep-ph/0208202] [Search INSPIRE].
[534] K. De Bruyn et al., Phys. Rev. D **86**, 014027 (2012) [arXiv:1204.1735 [hep-ph]] [Search INSPIRE].
[535] S. W. Bosch, PhD thesis, Munich, Max Planck Inst. (2002) [arXiv:hep-ph/0208203] [Search INSPIRE].
[536] J. L. Hewett et al. (eds.), arXiv:hep-ph/0503261 [Search INSPIRE].
[537] C. Bobeth and U. Haisch, Acta Phys. Polon. B **44**, 127 (2013) [arXiv:1109.1826 [hep-ph]] [Search INSPIRE].
[538] T. M. Aliev and G. Turan, Phys. Rev. D **48**, 1176 (1993).
[539] T. M. Aliev et al., Nucl. Phys. B **515**, 321 (1998) [arXiv:hep-ph/9708382] [Search INSPIRE].
[540] S. Bertolini and J. Matias, Phys. Rev. D **57**, 4197 (1998) [arXiv:hep-ph/9709330] [Search INSPIRE].
[541] I. I. Bigi et al., GESJ Phys. **2006N1**, 57 (2006) [arXiv:hep-ph/0603160] [Search INSPIRE].
[542] A. Gemintern et al., Phys. Rev. D **70**, 035008 (2004) [arXiv:hep-ph/0404152] [Search INSPIRE].
[543] H. M. Asatrian et al., Phys. Rev. D **85**, 014020 (2012) [arXiv:1110.1251 [hep-ph]] [Search INSPIRE].
[544] H. M Asatrian and C. Greub, Phys. Rev. D **89**, 094028 (2014) [arXiv:1403.4502 [hep-ph]] [Search INSPIRE].
[545] H. Simma and D. Wyler, Nucl. Phys. B **344**, 283 (1990).
[546] L. Reina et al., Phys. Lett. B **396**, 231 (1997) [arXiv:hep-ph/9612387] [Search INSPIRE].
[547] L. Reina et al., Phys. Rev. D **56**, 5805 (1997) [arXiv:hep-ph/9706253] [Search INSPIRE].
[548] J. Cao et al., Phys. Rev. D **64**, 014012 (2001) [arXiv:hep-ph/0103154] [Search INSPIRE].
[549] H. M. Asatrian et al., Phys. Rev. D **93**, 014037 (2016) [arXiv:1511.00153 [hep-ph]] [Search INSPIRE].
[550] H. M. Asatrian et al., Phys. Rev. D **95**, 053006 (2017) [arXiv:1611.08449 [hep-ph]] [Search INSPIRE].
[551] C-H. V. Chang et al., Phys. Lett. B **415**, 395 (1997) [arXiv:hep-ph/9705345] [Search INSPIRE].
[552] I. Adachi et al., Phys. Lett. B **662**, 323 (2008) [arXiv:hep-ex/0608037] [Search INSPIRE].
[553] R. Aaij et al., J. High Energy Phys. **1307**, 084 (2013) [arXiv:1305.2168 [hep-ex]] [Search INSPIRE].
[554] K. S. M. Lee et al., Phys. Rev. D **75**, 034016 (2007) [arXiv:hep-ph/0612156] [Search INSPIRE].
[555] A. Ali et al., Phys. Lett. B **273**, 505 (1991).
[556] H. H. Asatryan et al., Phys. Rev. D **65**, 074004 (2002) [arXiv:hep-ph/0109140] [Search INSPIRE].
[557] H. H. Asatrian et al., Phys. Lett. B **507**, 162 (2001) [arXiv:hep-ph/0103087] [Search INSPIRE].
[558] H. H. Asatryan et al., Phys. Rev. D **66**, 034009 (2002) [arXiv:hep-ph/0204341] [Search INSPIRE].
[559] A. Ghinculov et al., Nucl. Phys. B **648**, 254 (2003) [arXiv:hep-ph/0208088] [Search INSPIRE].
[560] H. M. Asatrian et al., Phys. Rev. D **66**, 094013 (2002) [arXiv:hep-ph/0209006] [Search INSPIRE].
[561] H. M. Asatrian et al., Mod. Phys. Lett. A **19**, 603 (2004) [arXiv:hep-ph/0311187] [Search INSPIRE].
[562] A. Ghinculov et al., Nucl. Phys. B **685**, 351 (2004) [arXiv:hep-ph/0312128] [Search INSPIRE].
[563] C. Greub et al., J. High Energy Phys. **12**, 040 (2008) [arXiv:0810.4077 [hep-ph]] [Search INSPIRE].

[564] C. Bobeth et al., J. High Energy Phys. **04**, 071 (2004) [arXiv:hep-ph/0312090] [Search INSPIRE].
[565] T. Huber et al., Nucl. Phys. B **740**, 105 (2006) [arXiv:hep-ph/0512066] [Search INSPIRE].
[566] T. Huber et al., Nucl. Phys. B **802**, 40 (2008) [arXiv:0712.3009 [hep-ph]] [Search INSPIRE].
[567] T. Huber et al., J. High Energy Phys. **06**, 176 (2015) [arXiv:1503.04849 [hep-ph]] [Search INSPIRE].
[568] A. Ali et al., Phys. Rev. D **55**, 4105 (1997) [arXiv:hep-ph/9609449] [Search INSPIRE].
[569] J.-W. Chen et al., Phys. Lett. B **410**, 285 (1997) [arXiv:hep-ph/9705219] [Search INSPIRE].
[570] G. Buchalla and G. Isidori, Nucl. Phys. B **525**, 333 (1998) [arXiv:hep-ph/9801456] [Search INSPIRE].
[571] C. W. Bauer and C. N. Burrell, Phys. Rev. D **62**, 114028 (2000) [arXiv:hep-ph/9911404] [Search INSPIRE].
[572] Z. Ligeti and F. J. Tackmann, Phys. Lett. B **653**, 404 (2007) [arXiv:0707.1694 [hep-ph]] [Search INSPIRE].
[573] M. Benzke et al., J. High Energy Phys. **10**, 031 (2017) [arXiv:1705.10366 [hep-ph]] [Search INSPIRE].
[574] B. Aubert et al., Phys. Rev. Lett. **93**, 081802 (2004) [arXiv:hep-ex/0404006] [Search INSPIRE].
[575] J. P. Lees et al., arXiv:1312.5364 [hep-ex] [Search INSPIRE].
[576] J. Kaneko et al., Phys. Rev. Lett. **90**, 021801 (2003) [arXiv:hep-ex/0208029] [Search INSPIRE].
[577] M. Iwasaki et al., Phys. Rev. D **72**, 092005 (2005) [arXiv:hep-ex/0503044] [Search INSPIRE].
[578] Y. Sato et al., Phys. Rev. D **93**, 032008 (2016); **93**, 059901 (2016) [addendum] [arXiv:1402.7134 [hep-ex]] [Search INSPIRE].
[579] K. S. M. Lee and I. W. Stewart, Phys. Rev. D **74**, 014005 (2006) [arXiv:hep-ph/0511334] [Search INSPIRE].
[580] K. S. M. Lee et al., Phys. Rev. D **74**, 011501 (2006) [arXiv:hep-ph/0512191] [Search INSPIRE].
[581] K. S. M. Lee and F. J. Tackmann, Phys. Rev. D **79**, 114021 (2009) [arXiv:0812.0001 [hep-ph]] [Search INSPIRE].
[582] G. Bell et al., Nucl. Phys. B **843**, 143 (2011) [arXiv:1007.3758 [hep-ph]] [Search INSPIRE].
[583] F. Krüger and L. M. Sehgal, Phys. Lett. B **380**, 199 (1996) [arXiv:hep-ph/9603237] [Search INSPIRE].
[584] H. M. Asatrian et al., Phys. Rev. D **69**, 074007 (2004) [arXiv:hep-ph/0312063] [Search INSPIRE].
[585] D. Seidel, Phys. Rev. D **70**, 094038 (2004) [arXiv:hep-ph/0403185] [Search INSPIRE].
[586] G. Buchalla et al., Phys. Rev. D **63**, 014015 (2000) [arXiv:hep-ph/0006136] [Search INSPIRE].
[587] F. Krüger et al., Phys. Rev. D **61**, 114028 (2000); **63**, 019901 (2001) [erratum] [arXiv:hep-ph/9907386] [Search INSPIRE].
[588] W. Altmannshofer et al., J. High Energy Phys. **01**, 019 (2009) [arXiv:0811.1214 [hep-ph]] [Search INSPIRE].
[589] J. Gratrex et al., Phys. Rev. D **93**, 054008 (2016) [arXiv:1506.03970 [hep-ph]] [Search INSPIRE].
[590] C. Bobeth et al., J. High Energy Phys. **12**, 040 (2007) [arXiv:0709.4174 [hep-ph]] [Search INSPIRE].
[591] J. Matias et al., J. High Energy Phys. **04**, 104 (2012) [arXiv:1202.4266 [hep-ph]] [Search INSPIRE].
[592] S. Descotes-Genon et al., J. High Energy Phys. **01**, 048 (2013) [arXiv:1207.2753 [hep-ph]] [Search INSPIRE].
[593] S. Descotes-Genon et al., J. High Energy Phys. **05**, 137 (2013) [arXiv:1303.5794 [hep-ph]] [Search INSPIRE].
[594] F. Kruger and J. Matias, Phys. Rev. D **71**, 094009 (2005) [arXiv:hep-ph/0502060] [Search INSPIRE].
[595] D. Becirevic and E. Schneider, Nucl. Phys. B **854**, 321 (2012) [arXiv:1106.3283 [hep-ph]] [Search INSPIRE].
[596] Y. Grossman and D. Pirjol, J. High Energy Phys. **06**, 029 (2000) [arXiv:hep-ph/0005069] [Search INSPIRE].
[597] M. Bordone et al., Eur. Phys. J. C **76**, 440 (2016) [arXiv:1605.07633 [hep-ph]] [Search INSPIRE].
[598] G. Hiller and M. Schmaltz, J. High Energy Phys. **02**, 055 (2015) [arXiv:1411.4773 [hep-ph]] [Search INSPIRE].
[599] W. Altmannshofer and I. Yavin, Phys. Rev. D **92**, 075022 (2015) [arXiv:1508.07009 [hep-ph]] [Search INSPIRE].
[600] B. Capdevila et al., J. High Energy Phys. **10**, 075 (2016) [arXiv:1605.03156 [hep-ph]] [Search INSPIRE].
[601] J. P. Lees et al., Phys. Rev. D **86**, 032012 (2012) [arXiv:1204.3933 [hep-ex]] [Search INSPIRE].
[602] J.-T. Wei et al., Phys. Rev. Lett. **103**, 171801 (2009) [arXiv:0904.0770 [hep-ex]] [Search INSPIRE].

[603] K. Abe et al., Phys. Rev. Lett. **88**, 021801 (2002) [arXiv:hep-ex/0109026] [Search INSPIRE].
[604] A. Ishikawa et al., Phys. Rev. Lett. **91**, 261601 (2003) [arXiv:hep-ex/0308044] [Search INSPIRE].
[605] A. Ishikawa et al., Phys. Rev. Lett. **96**, 251801 (2006) [arXiv:hep-ex/0603018] [Search INSPIRE].
[606] T. Aaltonen et al., Phys. Rev. Lett. **108**, 081807 (2012) [arXiv:1108.0695 [hep-ex]] [Search INSPIRE].
[607] J. P. Lees et al., Phys. Rev. D **93**, 052015 (2016) [arXiv:1508.07960 [hep-ex]] [Search INSPIRE].
[608] R. Aaij et al., J. High Energy Phys. **11**, 047 (2016) [arXiv:1606.04731 [hep-ex]] [Search INSPIRE].
[609] V. Khachatryan et al., Measurement of the P_1 and P_5' angular parameters of the decay $B^0 \to K^{*0}\mu^+\mu^-$ in proton–proton collisions at $\sqrt{s} = 8$ TeV, Technical Report CMS-PAS-BPH-15-008, CERN, Geneva (2017).
[610] R. Aaij et al., Phys. Rev. Lett. **111**, 191801 (2013) [arXiv:1308.1707 [hep-ex]] [Search INSPIRE].
[611] W. Altmannshofer et al., Eur. Phys. J. C **77**, 377 (2017) [arXiv:1703.09189 [hep-ph]] [Search INSPIRE].
[612] S. Descotes-Genon et al., J. High Energy Phys. **06**, 092 (2016) [arXiv:1510.04239 [hep-ph]] [Search INSPIRE].
[613] A. J. Buras et al., J. High Energy Phys. **02**, 184 (2015) [arXiv:1409.4557 [hep-ph]] [Search INSPIRE].
[614] W. Altmannshofer et al., J. High Energy Phys. **04**, 022 (2009) [arXiv:0902.0160 [hep-ph]] [Search INSPIRE].
[615] J. F. Kamenik and C. Smith, Phys. Lett. B **680**, 471 (2009) [arXiv:0908.1174 [hep-ph]] [Search INSPIRE].
[616] J. F. Kamenik and C. Smith, J. High Energy Phys. **03**, 090 (2012) [arXiv:1111.6402 [hep-ph]] [Search INSPIRE].
[617] R. R. Horgan et al., PoS **LATTICE2014**, 372 (2015) [arXiv:1501.00367 [hep-lat]] [Search INSPIRE].
[618] David Straub (2019), Flavio V0.20. doi.org/10.5281/zenodo.375591.
[619] W. Buchmuller and D. Wyler, Nucl. Phys. B **268**, 621 (1986).
[620] B. Grzadkowski et al., J. High Energy Phys. **10**, 085 (2010) [arXiv:1008.4884 [hep-ph]] [Search INSPIRE].
[621] G. D'Ambrosio et al., Nucl. Phys. B **645**, 155 (2002) [arXiv:hep-ph/0207036] [Search INSPIRE].
[622] R. Alonso et al., Phys. Rev. Lett. **113**, 241802 (2014) [arXiv:1407.7044 [hep-ph]] [Search INSPIRE].
[623] S. L. Glashow et al., Phys. Rev. Lett. **114**, 091801 (2015) [arXiv:1411.0565 [hep-ph]] [Search INSPIRE].
[624] J. P. Lees et al., Phys. Rev. D **87**, 112005 (2013) [arXiv:1303.7465 [hep-ex]] [Search INSPIRE].
[625] O. Lutz et al., Phys. Rev. D **87**, 111103 (2013) [arXiv:1303.3719 [hep-ex]] [Search INSPIRE].
[626] P. del Amo Sanchez et al., Phys. Rev. D **82**, 112002 (2010) [arXiv:1009.1529 [hep-ex]] [Search INSPIRE].
[627] J. Grygier et al., Phys. Rev. D **96**, 091101 (2017) [arXiv:1702.03224 [hep-ex]] [Search INSPIRE].
[628] J. P. Lees et al., Phys. Rev. D **86**, 051105 (2012) [arXiv:1206.2543 [hep-ex]] [Search INSPIRE].
[629] C. L. Hsu et al., Phys. Rev. D **86**, 032002 (2012) [arXiv:1206.5948 [hep-ex]] [Search INSPIRE].
[630] B. Bhattacharya, C. M. Grant, and A. A. Petrov arXiv:1809.04606 [hep-ph] [Search INSPIRE].
[631] M. Feindt et al., Nucl. Instrum. Meth. A **654**, 432 (2011) [arXiv:1102.3876 [hep-ex]] [Search INSPIRE].
[632] R. D. Peccei and H. R. Quinn, Phys. Rev. Lett. **38**, 1440 (1977).
[633] R. D. Peccei and H. R. Quinn, Phys. Rev. D **16**, 1791 (1977).
[634] S. Weinberg, Phys. Rev. Lett. **40**, 223 (1978).
[635] F. Wilczek, Phys. Rev. Lett. **40**, 279 (1978).
[636] J. Jaeckel and A. Ringwald, Ann. Rev. Nucl. Part. Sci. **60**, 405 (2010) [arXiv:1002.0329 [hep-ph]] [Search INSPIRE].
[637] S. Weinberg, Phys. Rev. Lett. **43**, 1566 (1979).
[638] J. F. Kamenik and C. Smith, Phys. Rev. D **85**, 093017 (2012) [arXiv:1201.4814 [hep-ph]] [Search INSPIRE].
[639] K. De Bruyn, Search for the rare decays $B^0_{(s)} \to \tau^+\tau^-$, Technical Report LHCb-CONF-2016-011. CERN-LHCb-CONF-2016-011, CERN, Geneva (2016).
[640] J. P. Lees et al., Phys. Rev. Lett. **118**, 031802 (2017) [arXiv:1605.09637 [hep-ex]] [Search INSPIRE].
[641] A. Morda, On the possibility of measuring br($b_s \to \tau\tau$) at LHCb, LHCb-TALK-2014-313, (2014).

[642] M. Beylich et al., Eur. Phys. J. C **71**, 1635 (2011) [arXiv:1101.5118 [hep-ph]] [Search INSPIRE].
[643] J. Lyon and R. Zwicky, arXiv:1406.0566 [hep-ph] [Search INSPIRE].
[644] R. Aaij et al., Phys. Rev. Lett. **111**, 112003 (2013) [arXiv:1307.7595 [hep-ex]] [Search INSPIRE].
[645] D. Du et al., Phys. Rev. D **93**, 034005 (2016) [arXiv:1510.02349 [hep-ph]] [Search INSPIRE].
[646] U. Haisch, arXiv:1206.1230 [hep-ph] [Search INSPIRE].
[647] W. Altmannshofer and D. M. Straub, Eur. Phys. J. C **73**, 2646 (2013) [arXiv:1308.1501 [hep-ph]] [Search INSPIRE].
[648] W. Altmannshofer et al., Phys. Rev. D **89**, 095033 (2014) [arXiv:1403.1269 [hep-ph]] [Search INSPIRE].
[649] J. F. Kamenik et al., Eur. Phys. J. C **77**, 701 (2017) [arXiv:1705.11106 [hep-ph]] [Search INSPIRE].
[650] J. Charles et al., arXiv:1705.02981 [hep-ph] [Search INSPIRE].
[651] D. London et al., Phys. Rev. D **60**, 074020 (1999) [arXiv:hep-ph/9905404] [Search INSPIRE].
[652] F. J. Botella and J. P. Silva, Phys. Rev. D **71**, 094008 (2005) [arXiv:hep-ph/0503136] [Search INSPIRE].
[653] T. Feldmann et al., J. High Energy Phys. **08**, 066 (2008) [arXiv:0803.3729 [hep-ph]] [Search INSPIRE].
[654] Y. Grossman, A. L. Kagan, and Z. Ligeti, Phys. Lett. B **538**, 327 (2002) [arXiv:hep-ph/0204212] [Search INSPIRE].
[655] B. Aubert et al., Phys. Rev. D **79**, 072009 (2009) [arXiv:0902.1708 [hep-ex]] [Search INSPIRE].
[656] R. Aaij et al., Phys. Rev. Lett. **115**, 031601 (2015) [arXiv:1503.07089 [hep-ex]] [Search INSPIRE].
[657] A. Höcker et al., Eur. Phys. J. C **21**, 225 (2001) [arXiv:hep-ph/0104062] [Search INSPIRE].
[658] M. Gronau, Phys. Rev. Lett. **63**, 1451 (1989).
[659] H. Boos, T. Mannel, and J. Reuter, Phys. Rev. D **70**, 036006 (2004) [arXiv:hep-ph/0403085] [Search INSPIRE].
[660] H.-N. Li and S. Mishima, J. High Energy Phys. **03**, 009 (2007) [arXiv:hep-ph/0610120] [Search INSPIRE].
[661] M. Gronau and J. L. Rosner, Phys. Lett. B **672**, 349 (2009) [arXiv:0812.4796 [hep-ph]] [Search INSPIRE].
[662] P. Frings et al., Phys. Rev. Lett. **115**, 061802 (2015) [arXiv:1503.00859 [hep-ph]] [Search INSPIRE].
[663] R. Fleischer, Eur. Phys. J. C **10**, 299 (1999) [arXiv:hep-ph/9903455] [Search INSPIRE].
[664] R. Fleischer, Nucl. Instrum. Meth. A **446**, 1 (2000) [arXiv:hep-ph/9908340] [Search INSPIRE].
[665] K. De Bruyn and R. Fleischer, J. High Energy Phys. **1503**, 145 (2015) [arXiv:1412.6834 [hep-ph]] [Search INSPIRE].
[666] M. Ciuchini et al., Phys. Rev. Lett. **95**, 221804 (2005) [arXiv:hep-ph/0507290] [Search INSPIRE].
[667] S. Faller et al., Phys. Rev. D **79**, 014030 (2009) [arXiv:0809.0842 [hep-ph]] [Search INSPIRE].
[668] M. Ciuchini et al., arXiv:1102.0392 [hep-ph] [Search INSPIRE].
[669] M. Jung, Phys. Rev. D **86**, 053008 (2012) [arXiv:1206.2050 [hep-ph]] [Search INSPIRE].
[670] Z. Ligeti and D. J. Robinson, Phys. Rev. Lett. **115**, 251801 (2015) [arXiv:1507.06671 [hep-ph]] [Search INSPIRE].
[671] M. Jung, Phys. Lett. B **753**, 187 (2016) [arXiv:1510.03423 [hep-ph]] [Search INSPIRE].
[672] O. Long et al., Phys. Rev. D **68**, 034010 (2003) [arXiv:hep-ex/0303030] [Search INSPIRE].
[673] B. Aubert et al., Phys. Rev. Lett. **101**, 021801 (2008) [arXiv:0804.0896 [hep-ex]] [Search INSPIRE].
[674] S. E. Lee et al., Phys. Rev. D **77**, 071101 (2008) [arXiv:0708.0304 [hep-ex]] [Search INSPIRE].
[675] I. Adachi et al., Phys. Rev. Lett. **108**, 171802 (2012).
[676] S. Faller et al., Phys. Rev. D **79**, 014005 (2009) [arXiv:0810.4248 [hep-ph]] [Search INSPIRE].
[677] M. Jung and S. Schacht, Phys. Rev. D **91**, 034027 (2015) [arXiv:1410.8396 [hep-ph]] [Search INSPIRE].
[678] L. Bel et al., J. High Energy Phys. **07**, 108 (2015) [arXiv:1505.01361 [hep-ph]] [Search INSPIRE].
[679] S. Stone and L. Zhang, Phys. Rev. D **79**, 074024 (2009) [arXiv:0812.2832 [hep-ph]] [Search INSPIRE].
[680] R. Fleischer et al., Eur. Phys. J. C **71**, 1832 (2011) [arXiv:1109.1112 [hep-ph]] [Search INSPIRE].
[681] M. Beneke, Phys. Lett. B **620**, 143 (2005) [arXiv:hep-ph/0505075] [Search INSPIRE].
[682] M. Beneke et al., Eur. Phys. J. C **61**, 439 (2009) [arXiv:0902.4446 [hep-ph]] [Search INSPIRE].
[683] M. Gronau et al., Phys. Lett. B **579**, 331 (2004) [arXiv:hep-ph/0310020] [Search INSPIRE].
[684] Y. Grossman et al., Phys. Rev. D **68**, 015004 (2003) [arXiv:hep-ph/0303171] [Search INSPIRE].
[685] M. Gronau et al., Phys. Lett. B **596**, 107 (2004) [arXiv:hep-ph/0403287] [Search INSPIRE].

[686] M. Gronau and J. L. Rosner, Phys. Rev. D **71**, 074019 (2005) [arXiv:hep-ph/0503131] [Search INSPIRE].
[687] C-W. Chiang et al., Phys. Rev. D **70**, 034020 (2004) [arXiv:hep-ph/0404073] [Search INSPIRE].
[688] Y. Grossman et al., J. High Energy Phys. **01**, 066 (2014) [arXiv:1308.4143 [hep-ph]] [Search INSPIRE].
[689] S. Khalil and E. Kou, Phys. Rev. Lett. **91**, 241602 (2003) [arXiv:hep-ph/0303214] [Search INSPIRE].
[690] D. Chang et al., Phys. Rev. D **67**, 075013 (2003) [arXiv:hep-ph/0205111] [Search INSPIRE].
[691] J. Girrbach et al., J. High Energy Phys. **06**, 044 (2011); **07**, 001 (2011) [erratum] [arXiv:1101.6047 [hep-ph]] [Search INSPIRE].
[692] R. Fleischer et al., Phys. Rev. D **78**, 111501 (2008) [arXiv:0806.2900 [hep-ph]] [Search INSPIRE].
[693] M. Gronau and J. L. Rosner, Phys. Lett. B **666**, 467 (2008) [arXiv:0807.3080 [hep-ph]] [Search INSPIRE].
[694] M. Neubert and J. L. Rosner, Phys. Rev. Lett. **81**, 5076 (1998) [arXiv:hep-ph/9809311] [Search INSPIRE].
[695] A. J. Buras and R. Fleischer, Eur. Phys. J. C **11**, 93 (1999) [arXiv:hep-ph/9810260] [Search INSPIRE].
[696] M. Beneke and M. Neubert, Nucl. Phys. B **675**, 333 (2003) [arXiv:hep-ph/0308039] [Search INSPIRE].
[697] A. R. Williamson and J. Zupan, Phys. Rev. D **74**, 014003 (2006); **74**, 03901 (2006) [erratum] [arXiv:hep-ph/0601214] [Search INSPIRE].
[698] R. Aaij et al., Eur. Phys. J. C **73**, 2373 (2013) [arXiv:1208.3355 [hep-ex]] [Search INSPIRE].
[699] J. P. Lees et al., Phys. Rev. D **85**, 112010 (2012) [arXiv:1201.5897 [hep-ex]] [Search INSPIRE].
[700] Y. Nakahama et al., Phys. Rev. D **82**, 073011 (2010) [arXiv:1007.3848 [hep-ex]] [Search INSPIRE].
[701] T. E. Browder et al., Phys. Rev. Lett. **81**, 1786 (1998) [arXiv:hep-ex/9804018] [Search INSPIRE].
[702] B. Aubert et al., Phys. Rev. D **79**, 052003 (2009) [arXiv:0809.1174 [hep-ex]] [Search INSPIRE].
[703] L. Santelj et al., J. High Energy Phys. **10**, 165 (2014) [arXiv:1408.5991 [hep-ex]] [Search INSPIRE].
[704] M. Gronau and D. London, Phys. Rev. Lett. **65**, 3381 (1990).
[705] A. E. Snyder and H. R. Quinn, Phys. Rev. D **48**, 2139 (1993).
[706] M. Gronau and J. L. Rosner, arXiv:1608.06224 [hep-ph] [Search INSPIRE].
[707] H. R. Quinn and J. P. Silva, Phys. Rev. D **62**, 054002 (2000) [arXiv:hep-ph/0001290] [Search INSPIRE].
[708] M. Gronau and J. Zupan, Phys. Rev. D **70**, 074031 (2004) [arXiv:hep-ph/0407002] [Search INSPIRE].
[709] M. Gronau and J. Zupan, Phys. Rev. D **71**, 074017 (2005) [arXiv:hep-ph/0502139] [Search INSPIRE].
[710] P. Vanhoefer, PoS **EPS-HEP2015**, 558 (2015) [arXiv:1509.06548 [hep-ex]] [Search INSPIRE].
[711] J. P. Lees et al., Phys. Rev. D **87**, 052009 (2013) [arXiv:1206.3525 [hep-ex]] [Search INSPIRE].
[712] T. Julius et al., Phys. Rev. D **96**, 032007 (2017) [arXiv:1705.02083 [hep-ex]] [Search INSPIRE].
[713] H. Ishino et al., arXiv:hep-ex/0703039 [Search INSPIRE].
[714] R. Aaij et al., Phys. Lett. B **747**, 468 (2015) [arXiv:1503.07770 [hep-ex]] [Search INSPIRE].
[715] B. Aubert et al., Phys. Rev. D **78**, 071104 (2008) [arXiv:0807.4977 [hep-ex]] [Search INSPIRE].
[716] J. Zhang et al., Phys. Rev. Lett. **91**, 221801 (2003) [arXiv:hep-ex/0306007] [Search INSPIRE].
[717] J. P. Lees et al., Phys. Rev. D **88**, 012003 (2013) [arXiv:1304.3503 [hep-ex]] [Search INSPIRE].
[718] A. Kusaka et al., Phys. Rev. Lett. **98**, 221602 (2007) [arXiv:hep-ex/0701015] [Search INSPIRE].
[719] H. J. Lipkin et al., Phys. Rev. D **44**, 1454 (1991).
[720] M. Neubert and J. L. Rosner, Phys. Lett. B **441**, 403 (1998) [arXiv:hep-ph/9808493] [Search INSPIRE].
[721] M. Gronau et al., Phys. Rev. D **60**, 034021 (1999); **69**, 119901 (2004) [erratum] [arXiv:hep-ph/9810482] [Search INSPIRE].
[722] S. Gardner, Phys. Rev. D **59**, 077502 (1999) [arXiv:hep-ph/9806423] [Search INSPIRE].
[723] P. Kroll, Int. J. Mod. Phys. A **20**, 331 (2005) [arXiv:hep-ph/0409141] [Search INSPIRE].
[724] M. Gronau et al., Phys. Rev. D **50**, 4529 (1994) [arXiv:hep-ph/9404283] [Search INSPIRE].
[725] P. Vanhoefer et al., Phys. Rev. D **93**, 032010 (2016); **94**, 099903 (2016) [addendum] [arXiv:1510.01245 [hep-ex]] [Search INSPIRE].
[726] A. F. Falk et al., Phys. Rev. D **69**, 011502 (2004) [arXiv:hep-ph/0310242] [Search INSPIRE].
[727] Y. T. Duh et al., Phys. Rev. D **87**, 031103 (2013) [arXiv:1210.1348 [hep-ex]] [Search INSPIRE].

[728] I. Adachi et al., Phys. Rev. D **88**, 092003 (2013) [arXiv:1302.0551 [hep-ex]] [Search INSPIRE].
[729] I. Adachi et al., arXiv:1212.4015 [hep-ex] [Search INSPIRE].
[730] M. Pivk et al., Eur. Phys. J. C **39**, 397 (2005) [arXiv:hep-ph/0406263] [Search INSPIRE].
[731] B. Grinstein and D. Pirjol, Phys. Rev. D **73**, 014013 (2006) [arXiv:hep-ph/0510104] [Search INSPIRE].
[732] A. Khodjamirian et al., Phys. Lett. B **402**, 167 (1997) [arXiv:hep-ph/9702318] [Search INSPIRE].
[733] B. Aubert et al., Phys. Rev. D **78**, 071102 (2008) [arXiv:0807.3103 [hep-ex]] [Search INSPIRE].
[734] M. Gronau and D. London, Phys. Lett. B **253**, 483 (1991).
[735] M. Gronau and D. Wyler, Phys. Lett. B **265**, 172 (1991).
[736] D. Atwood et al., Phys. Rev. Lett. **78**, 3257 (1997) [arXiv:hep-ph/9612433] [Search INSPIRE].
[737] D. Atwood et al., Phys. Rev. D **63**, 036005 (2001) [arXiv:hep-ph/0008090] [Search INSPIRE].
[738] A. Giri et al., Phys. Rev. D **68**, 054018 (2003) [arXiv:hep-ph/0303187] [Search INSPIRE].
[739] Y. Grossman et al., Phys. Rev. D **67**, 071301 (2003) [arXiv:hep-ph/0210433] [Search INSPIRE].
[740] J. P. Silva and A. Soffer, Phys. Rev. D **61**, 112001 (2000) [arXiv:hep-ph/9912242] [Search INSPIRE].
[741] Y. Grossman et al., Phys. Rev. D **72**, 031501 (2005) [arXiv:hep-ph/0505270] [Search INSPIRE].
[742] M. Gronau et al., Phys. Lett. B **649**, 61 (2007) [arXiv:hep-ph/0702011] [Search INSPIRE].
[743] A. Bondar et al., Phys. Rev. D **82**, 034033 (2010) [arXiv:1004.2350 [hep-ph]] [Search INSPIRE].
[744] W. Wang, Phys. Rev. Lett. **110**, 061802 (2013) [arXiv:1211.4539 [hep-ph]] [Search INSPIRE].
[745] M. Martone and J. Zupan, Phys. Rev. D **87**, 034005 (2013) [arXiv:1212.0165 [hep-ph]] [Search INSPIRE].
[746] B. Bhattacharya et al., Phys. Rev. D **87**, 074002 (2013) [arXiv:1301.5631 [hep-ph]] [Search INSPIRE].
[747] A. Bondar et al., Eur. Phys. J. C **73**, 2476 (2013) [arXiv:1303.6305 [hep-ph]] [Search INSPIRE].
[748] M. Rama, Phys. Rev. D **89**, 014021 (2014) [arXiv:1307.4384 [hep-ex]] [Search INSPIRE].
[749] Y. Grossman and M. Savastio, J. High Energy Phys. **03**, 008 (2014) [arXiv:1311.3575 [hep-ph]] [Search INSPIRE].
[750] J. Brod and J. Zupan, J. High Energy Phys. **01**, 051 (2014) [arXiv:1308.5663 [hep-ph]] [Search INSPIRE].
[751] J. Brod, Phys. Lett. B **743**, 56 (2015) [arXiv:1412.3173 [hep-ph]] [Search INSPIRE].
[752] C. Bobeth et al., J. High Energy Phys. **06**, 040 (2014) [arXiv:1404.2531 [hep-ph]] [Search INSPIRE].
[753] J. Brod et al., Phys. Rev. D **92**, 033002 (2015) [arXiv:1412.1446 [hep-ph]] [Search INSPIRE].
[754] T. Jubb et al., Nucl. Phys. B **915**, 431 (2017) [arXiv:1603.07770 [hep-ph]] [Search INSPIRE].
[755] A. Bondar, Proc. BINP Special Analysis Meeting on Dalitz Analysis, unpublished (2002).
[756] A. Poluektov et al., Phys. Rev. D **81**, 112002 (2010) [arXiv:1003.3360 [hep-ex]] [Search INSPIRE].
[757] H. Aihara et al., Phys. Rev. D **85**, 112014 (2012) [arXiv:1204.6561 [hep-ex]] [Search INSPIRE].
[758] R. Aaij et al., J. High Energy Phys. **10**, 097 (2014) [arXiv:1408.2748 [hep-ex]] [Search INSPIRE].
[759] M. Bona et al., J. High Energy Phys. **10**, 081 (2006) [arXiv:hep-ph/0606167] [Search INSPIRE].
[760] J. Libby, arXiv:1412.4269 [hep-ex] [Search INSPIRE].
[761] Y. Horii et al., Phys. Rev. Lett. **106**, 231803 (2011) [arXiv:1103.5951 [hep-ex]] [Search INSPIRE].
[762] K. Trabelsi, arXiv:1301.2033 [hep-ex] [Search INSPIRE].
[763] M. Nayak et al., Phys. Rev. D **88**, 091104 (2013) [arXiv:1310.1741 [hep-ex]] [Search INSPIRE].
[764] M. Gersabeck, arXiv:1411.4595 [hep-ex] [Search INSPIRE].
[765] G. Bonvicini et al. [CLEO Collaboration], Phys. Rev. D **89**, 072002 (2014); **91**, 019903 (2015) [erratum] [arXiv:1312.6775 [hep-ex]] [Search INSPIRE].
[766] E. White et al., Phys. Rev. D **88**, 051101 (2013) [arXiv:1307.5935 [hep-ex]] [Search INSPIRE].
[767] J. Libby et al., Phys. Lett. B **731**, 197 (2014) [arXiv:1401.1904 [hep-ex]] [Search INSPIRE].
[768] R. A. Briere, arXiv:1411.7327 [hep-ex] [Search INSPIRE].
[769] N. Lowrey et al. [CLEO Collaboration], Phys. Rev. D **80**, 031105 (2009) [arXiv:0903.4853 [hep-ex]] [Search INSPIRE].
[770] J. Libby et al., Phys. Rev. D **82**, 112006 (2010) [arXiv:1010.2817 [hep-ex]] [Search INSPIRE].
[771] D. Ambrose, Measurement of the relative strong-phase difference between D^0 and $\overline{D}^0 \to K^0_S\pi^+\pi^-$, Presented on behalf of the BESIII Collaboration at the APS April Meeting, 5–8 April, 2014, Savannah, Georgia (2014).
[772] M. Nayak et al., Phys. Lett. B **740**, 1 (2015) [arXiv:1410.3964 [hep-ex]] [Search INSPIRE].
[773] Resmi P. K. et al., PoS **CKM2016**, 112 (2017) [arXiv:1703.10317 [hep-ex]] [Search INSPIRE].

[774] R. Aaij et al., J. High Energy Phys. **12**, 087 (2016) [arXiv:1611.03076 [hep-ex]] [Search INSPIRE].
[775] S. Malde, Synergy of BESIII and LHCb physics programmes, Technical Report LHCb-PUB-2016-025. CERN-LHCb-PUB-2016-025, CERN, Geneva (2016).
[776] T. Gershon and A. Poluektov, Phys. Rev. D **81**, 014025 (2010) [arXiv:0910.5437 [hep-ph]] [Search INSPIRE].
[777] D. Zeppenfeld, Z. Phys. C **8**, 77 (1981).
[778] L. L. Chau and H. Y. Cheng, Phys. Rev. Lett. **56**, 1655 (1986).
[779] M. J. Savage and M. B. Wise, Phys. Rev. D **39**, 3346 (1989); **40**, 3127 (1989) [erratum].
[780] L.-L. Chau et al., Phys. Rev. D **43**, 2176 (1991); **58**, 019902 (1998) [erratum] (1991).
[781] H.-Y. Cheng, C.-W. Chiang, and A.-L. Kuo, Phys. Rev. D **91**, 014011 (2015) [arXiv:1409.5026 [hep-ph]] [Search INSPIRE].
[782] T. Feldmann et al., Phys. Rev. D **58**, 114006 (1998) [arXiv:hep-ph/9802409] [Search INSPIRE].
[783] C. Michael et al., Phys. Rev. Lett. **111**, 181602 (2013) [arXiv:1310.1207 [hep-lat]] [Search INSPIRE].
[784] M. Beneke and S. Jager, Nucl. Phys. B **751**, 160 (2006) [arXiv:hep-ph/0512351] [Search INSPIRE].
[785] M. Beneke et al., Nucl. Phys. B **832**, 109 (2010) [arXiv:0911.3655 [hep-ph]] [Search INSPIRE].
[786] M. Beneke and S. Jager, Nucl. Phys. B **768**, 51 (2007) [arXiv:hep-ph/0610322] [Search INSPIRE].
[787] H. J. Lipkin, Phys. Lett. B **433**, 117 (1998).
[788] M. Beneke and M. Neubert, Nucl. Phys. B **651**, 225 (2003) [arXiv:hep-ph/0210085] [Search INSPIRE].
[789] H. J. Lipkin, Phys. Lett. B **254**, 247 (1991).
[790] L. Hofer et al., J. High Energy Phys. **02**, 080 (2011) [arXiv:1011.6319 [hep-ph]] [Search INSPIRE].
[791] F. Fichter, MSc thesis, Karlsruher Institut für Technologie (2016).
[792] R. Aaij et al., arXiv:1610.05187 [hep-ex] [Search INSPIRE].
[793] S-H. Zhou et al., arXiv:1608.02819 [hep-ph] [Search INSPIRE].
[794] M. Bauer et al., Z. Phys. C **34**, 103 (1987).
[795] A. L. Kagan, Phys. Lett. B **601**, 151 (2004) [arXiv:hep-ph/0405134] [Search INSPIRE].
[796] M. Beneke et al., Nucl. Phys. B **774**, 64 (2007) [arXiv:hep-ph/0612290] [Search INSPIRE].
[797] H.-Y. Cheng et al., Phys. Rev. D **77**, 014034 (2008) [arXiv:0705.3079 [hep-ph]] [Search INSPIRE].
[798] H.-Y. Cheng and K.-C. Yang, Phys. Rev. D **76**, 114020 (2007) [arXiv:0709.0137 [hep-ph]] [Search INSPIRE].
[799] H.-Y. Cheng and K.-C. Yang, Phys. Rev. D **78**, 094001 (2008); **79**, 039903 (2009) [erratum] [arXiv:0805.0329 [hep-ph]] [Search INSPIRE].
[800] H.-Y. Cheng and K.-C. Yang, Phys. Rev. D **83**, 034001 (2011) [arXiv:1010.3309 [hep-ph]] [Search INSPIRE].
[801] Y. Y. Keum et al., Phys. Rev. D **63**, 054008 (2001) [arXiv:hep-ph/0004173] [Search INSPIRE].
[802] C.-D. Lu et al., Phys. Rev. D **63**, 074009 (2001) [arXiv:hep-ph/0004213] [Search INSPIRE].
[803] H.-Nan Li and S. Mishima, Phys. Rev. D **83**, 034023 (2011) [arXiv:0901.1272 [hep-ph]] [Search INSPIRE].
[804] H.-N. Li and S. Mishima, Phys. Rev. D **90**, 074018 (2014) [arXiv:1407.7647 [hep-ph]] [Search INSPIRE].
[805] H.-Y. Cheng and S. Oh, J. High Energy Phys. **09**, 024 (2011) [arXiv:1104.4144 [hep-ph]] [Search INSPIRE].
[806] S. Descotes-Genon and C. T. Sachrajda, Nucl. Phys. B **650**, 356 (2003) [arXiv:hep-ph/0209216] [Search INSPIRE].
[807] E. Lunghi et al., Nucl. Phys. B **649**, 349 (2003) [arXiv:hep-ph/0210091] [Search INSPIRE].
[808] S. W. Bosch et al., Phys. Rev. D **67**, 094014 (2003) [arXiv:hep-ph/0301123] [Search INSPIRE].
[809] A. G. Grozin and M. Neubert, Phys. Rev. D **55**, 272 (1997) [arXiv:hep-ph/9607366] [Search INSPIRE].
[810] B. O. Lange and M. Neubert, Phys. Rev. Lett. **91**, 102001 (2003) [arXiv:hep-ph/0303082] [Search INSPIRE].
[811] G. Bell et al., J. High Energy Phys. **11**, 191 (2013) [arXiv:1308.6114 [hep-ph]] [Search INSPIRE].
[812] V. M. Braun and A. N. Manashov, Phys. Lett. B **731**, 316 (2014) [arXiv:1402.5822 [hep-ph]] [Search INSPIRE].
[813] H. Kawamura et al., Phys. Lett. B **523**, 111 (2001); **536**, 344 (2002) [erratum] [arXiv:hep-ph/0109181] [Search INSPIRE].

[814] V. M. Braun et al., Phys. Rev. D **69**, 034014 (2004) [arXiv:hep-ph/0309330] [Search INSPIRE].
[815] S. J. Lee and M. Neubert, Phys. Rev. D **72**, 094028 (2005) [arXiv:hep-ph/0509350] [Search INSPIRE].
[816] H. Kawamura and K. Tanaka, Phys. Lett. B **673**, 201 (2009) [arXiv:0810.5628 [hep-ph]] [Search INSPIRE].
[817] T. Feldmann et al., Phys. Rev. D **89**, 114001 (2014) [arXiv:1404.1343 [hep-ph]] [Search INSPIRE].
[818] A. Khodjamirian et al., Phys. Rev. D **72**, 094012 (2005) [arXiv:hep-ph/0509049] [Search INSPIRE].
[819] Y.-Y. Keum et al., Phys. Lett. B **504**, 6 (2001) [arXiv:hep-ph/0004004] [Search INSPIRE].
[820] M. Bartsch et al., arXiv:0810.0249 [hep-ph] [Search INSPIRE].
[821] M. Ciuchini et al., Phys. Lett. B **674**, 197 (2009) [arXiv:0811.0341 [hep-ph]] [Search INSPIRE].
[822] Q. Chang et al., Phys. Lett. B **740**, 56 (2015) [arXiv:1409.2995 [hep-ph]] [Search INSPIRE].
[823] C. Bobeth et al., Eur. Phys. J. C **75**, 340 (2015) [arXiv:1409.3252 [hep-ph]] [Search INSPIRE].
[824] J. Sun et al., Phys. Lett. B **743**, 444 (2015) [arXiv:1412.2334 [hep-ph]] [Search INSPIRE].
[825] Q. Chang et al., Phys. Rev. D **91**, 074026 (2015) [arXiv:1504.04907 [hep-ph]] [Search INSPIRE].
[826] Q. Chang et al., J. Phys. G **43**, 105004 (2016).
[827] K. Wang and G. Zhu, Phys. Rev. D **88**, 014043 (2013) [arXiv:1304.7438 [hep-ph]] [Search INSPIRE].
[828] N. Kivel, J. High Energy Phys. **05**, 019 (2007) [arXiv:hep-ph/0608291] [Search INSPIRE].
[829] V. Pilipp, Nucl. Phys. B **794**, 154 (2008) [arXiv:0709.3214 [hep-ph]] [Search INSPIRE].
[830] G. Bell, Nucl. Phys. B **795**, 1 (2008) [arXiv:0705.3127 [hep-ph]] [Search INSPIRE].
[831] G. Bell, Nucl. Phys. B **822**, 172 (2009) [arXiv:0902.1915 [hep-ph]] [Search INSPIRE].
[832] G. Bell and V. Pilipp, Phys. Rev. D **80**, 054024 (2009) [arXiv:0907.1016 [hep-ph]] [Search INSPIRE].
[833] G. Bell et al., Phys. Lett. B **750**, 348 (2015) [arXiv:1507.03700 [hep-ph]] [Search INSPIRE].
[834] C. S. Kim and Y. W. Yoon, J. High Energy Phys. **11**, 003 (2011) [arXiv:1107.1601 [hep-ph]] [Search INSPIRE].
[835] G. Bell and T. Huber, J. High Energy Phys. **12**, 129 (2014) [arXiv:1410.2804 [hep-ph]] [Search INSPIRE].
[836] M. Gronau, Phys. Lett. B **627**, 82 (2005) [arXiv:hep-ph/0508047] [Search INSPIRE].
[837] M. Fujikawa et al., Phys. Rev. D **81**, 011101 (2010) [arXiv:0809.4366 [hep-ex]] [Search INSPIRE].
[838] M. Kenzie, GammaCombo (available at: https://gammacombo.github.io, date last accessed: November 5, 2019).
[839] B. Pal et al., Phys. Rev. Lett. **116**, 161801 (2016) [arXiv:1512.02145 [hep-ex]] [Search INSPIRE].
[840] C-H. Chen, Phys. Lett. B **520**, 33 (2001) [arXiv:hep-ph/0107189] [Search INSPIRE].
[841] A. Ali et al., Phys. Rev. D **76**, 074018 (2007) [arXiv:hep-ph/0703162] [Search INSPIRE].
[842] C.-K. Chua, Phys. Rev. D **78**, 076002 (2008) [arXiv:0712.4187 [hep-ph]] [Search INSPIRE].
[843] J.-J. Wang et al., Phys. Rev. D **89**, 074046 (2014) [arXiv:1402.6912 [hep-ph]] [Search INSPIRE].
[844] S. Baek et al., J. High Energy Phys. **12**, 019 (2006) [arXiv:hep-ph/0610109] [Search INSPIRE].
[845] A. Hayakawa et al., Prog. Theor. Exp. Phys. **2014**, 023B04 (2014) [arXiv:1311.5974 [hep-ph]] [Search INSPIRE].
[846] I. Dunietz, Phys. Rev. D **52**, 3048 (1995) [arXiv:hep-ph/9501287] [Search INSPIRE].
[847] Y. Grossman, Phys. Lett. B **380**, 99 (1996) [arXiv:hep-ph/9603244] [Search INSPIRE].
[848] J. G. Korner and G. R. Goldstein, Phys. Lett. **89B**, 105 (1979).
[849] A. Ali et al., Phys. Rev. D **58**, 094009 (1998) [arXiv:hep-ph/9804363] [Search INSPIRE].
[850] H.-Y. Cheng and K.-C. Yang, Phys. Lett. B **511**, 40 (2001) [arXiv:hep-ph/0104090] [Search INSPIRE].
[851] X.-Q. Li et al., Phys. Rev. D **68**, 114015 (2003); **71**, 019902 (2005) [erratum] [arXiv:hep-ph/0309136] [Search INSPIRE].
[852] K. F. Chen et al., Phys. Rev. Lett. **91**, 201801 (2003) [arXiv:hep-ex/0307014] [Search INSPIRE].
[853] Bernard Aubert et al., Phys. Rev. D **78**, 092008 (2008) [arXiv:0808.3586 [hep-ex]] [Search INSPIRE].
[854] M. Beneke et al., Phys. Rev. Lett. **96**, 141801 (2006) [arXiv:hep-ph/0512258] [Search INSPIRE].
[855] H.-Y. Cheng and C.-K. Chua, Phys. Rev. D **80**, 114008 (2009) [arXiv:0909.5229 [hep-ph]] [Search INSPIRE].
[856] H.-Y. Cheng and C.-K. Chua, Phys. Rev. D **80**, 114026 (2009) [arXiv:0910.5237 [hep-ph]] [Search INSPIRE].
[857] J. Zhu et al., Phys. Rev. D **72**, 054015 (2005) [arXiv:hep-ph/0504187] [Search INSPIRE].
[858] J. Zhu et al., J. Phys. G **32**, 101 (2006) [arXiv:hep-ph/0506316] [Search INSPIRE].

[859] Y. Li and C.-D. Lu, Phys. Rev. D **73**, 014024 (2006) [arXiv:hep-ph/0508032] [Search INSPIRE].
[860] H.-W. Huang et al., Phys. Rev. D **73**, 014011 (2006) [arXiv:hep-ph/0508080] [Search INSPIRE].
[861] Z.-T. Zou et al., Phys. Rev. D **91**, 054033 (2015) [arXiv:1501.00784 [hep-ph]] [Search INSPIRE].
[862] P. Colangelo et al., Phys. Lett. B **597**, 291 (2004) [arXiv:hep-ph/0406162] [Search INSPIRE].
[863] H.-Y. Cheng et al., Phys. Rev. D **71**, 014030 (2005) [arXiv:hep-ph/0409317] [Search INSPIRE].
[864] H.-N. Li, Phys. Lett. B **622**, 63 (2005), [arXiv:hep-ph/0411305] [Search INSPIRE].
[865] S. Baek et al., Phys. Rev. D **72**, 094008 (2005) [arXiv:hep-ph/0508149] [Search INSPIRE].
[866] Q. Chang et al., J. High Energy Phys. **06**, 038 (2007) [arXiv:hep-ph/0610280] [Search INSPIRE].
[867] C. C. Chiang et al., Phys. Rev. D **78**, 111102 (2008) [arXiv:0808.2576 [hep-ex]] [Search INSPIRE].
[868] M. Beneke et al., Eur. Phys. J. C **61**, 429 (2009) [arXiv:0901.4841 [hep-ph]] [Search INSPIRE].
[869] G. Valencia, Phys. Rev. D **39**, 3339 (1989).
[870] A. Datta and D. London, Int. J. Mod. Phys. A **19**, 2505 (2004) [arXiv:hep-ph/0303159] [Search INSPIRE].
[871] A. Datta et al., Phys. Lett. B **701**, 357 (2011) [arXiv:1103.2442 [hep-ph]] [Search INSPIRE].
[872] Y. Xie et al., J. High Energy Phys. **09**, 074 (2009) [arXiv:0908.3627 [hep-ph]] [Search INSPIRE].
[873] B. Bhattacharya et al., Phys. Rev. D **88**, 016007 (2013) [arXiv:1306.1911 [hep-ph]] [Search INSPIRE].
[874] A. Datta et al., Phys. Rev. D **86**, 076011 (2012) [arXiv:1207.4495 [hep-ph]] [Search INSPIRE].
[875] B. Aubert et al., Phys. Rev. D **76**, 031102 (2007) [arXiv:0704.0522 [hep-ex]] [Search INSPIRE].
[876] R. Itoh et al., Phys. Rev. Lett. **95**, 091601 (2005) [arXiv:hep-ex/0504030] [Search INSPIRE].
[877] T. Aaltonen et al., Phys. Rev. Lett. **107**, 261802 (2011) [arXiv:1107.4999 [hep-ex]] [Search INSPIRE].
[878] R. Aaij et al., Phys. Lett. B **713**, 369 (2012) [arXiv:1204.2813 [hep-ex]] [Search INSPIRE].
[879] W. Bensalem et al., Phys. Lett. B **538**, 309 (2002) [arXiv:hep-ph/0205009] [Search INSPIRE].
[880] W. Bensalem et al., Phys. Rev. D **66**, 094004 (2002) [arXiv:hep-ph/0208054] [Search INSPIRE].
[881] M. Gronau and J. L. Rosner, Phys. Lett. B **749**, 104 (2015) [arXiv:1506.01346 [hep-ph]] [Search INSPIRE].
[882] Ashutosh K. Alok et al., J. High Energy Phys. **11**, 122 (2011) [arXiv:1103.5344 [hep-ph]] [Search INSPIRE].
[883] M. Duraisamy and A. Datta, J. High Energy Phys. **09**, 059 (2013) [arXiv:1302.7031 [hep-ph]] [Search INSPIRE].
[884] M. Duraisamy et al., Phys. Rev. D **90**, 074013 (2014) [arXiv:1405.3719 [hep-ph]] [Search INSPIRE].
[885] R. Aaij et al., Phys. Rev. Lett. **110**, 241802 (2013) [arXiv:1303.7125 [hep-ex]] [Search INSPIRE].
[886] R. Aaij et al., Phys. Rev. Lett. **108**, 101803 (2012) [arXiv:1112.3183 [hep-ex]] [Search INSPIRE].
[887] R. Aaij et al., Phys. Rev. D **90**, 052011 (2014) [arXiv:1407.2222 [hep-ex]] [Search INSPIRE].
[888] R. Aaij et al., J. High Energy Phys. **07**, 166 (2015) [arXiv:1503.05362 [hep-ex]] [Search INSPIRE].
[889] R. Aaij et al., arXiv:1712.08683 [hep-ex] [Search INSPIRE].
[890] J. Zhang et al., arXiv:hep-ex/0505039 [Search INSPIRE].
[891] B. Aubert et al., Phys. Rev. Lett. **97**, 201801 (2006) [arXiv:hep-ex/0607057] [Search INSPIRE].
[892] R. Aaij et al., Phys. Rev. Lett. **111**, 101801 (2013) [arXiv:1306.1246 [hep-ex]] [Search INSPIRE].
[893] R. Aaij et al., Phys. Rev. Lett. **112**, 011801 (2014) [arXiv:1310.4740 [hep-ex]] [Search INSPIRE].
[894] R. Aaij et al., Phys. Rev. D **90**, 112004 (2014) [arXiv:1408.5373 [hep-ex]] [Search INSPIRE].
[895] J. Virto, PoS **FPCP2016**, 007 (2017) [arXiv:1609.07430 [hep-ph]] [Search INSPIRE].
[896] P. Guo et al., Eur. Phys. J. A **51**, 135 (2015) [arXiv:1409.8652 [hep-ph]] [Search INSPIRE].
[897] I. Bediaga and P. C. Magalhaes, [arXiv:1512.09284 [hep-ph]] [Search INSPIRE].
[898] J. H. Alvarenga Nogueira et al., Few Body Syst. **58**, 98 (2017) [arXiv:1609.01568 [hep-ph]] [Search INSPIRE].
[899] L. Wolfenstein, Phys. Rev. D **43**, 151 (1991).
[900] I. Bediaga et al., Phys. Rev. D **89**, 094013 (2014) [arXiv:1307.8164 [hep-ph]] [Search INSPIRE].
[901] J. H. Alvarenga Nogueira et al., Phys. Rev. D **92**, 054010 (2015) [arXiv:1506.08332 [hep-ph]] [Search INSPIRE].
[902] J. P. Dedonder et al., Acta Phys. Polon. B **42**, 2013 (2011) [arXiv:1011.0960 [hep-ph]] [Search INSPIRE].
[903] H.-Y. Cheng et al., Phys. Rev. D **76**, 094006 (2007) [arXiv:0704.1049 [hep-ph]] [Search INSPIRE].
[904] H.-Y. Cheng et al., Phys. Rev. D **94**, 094015 (2016) [arXiv:1607.08313 [hep-ph]] [Search INSPIRE].

[905] M. Beneke, Quasi-two-body and three-body decays in the heavy quark expansion, Proc. Three-Body Charmless B Decays Workshop, Paris, France (2006).
[906] I. Stewart, SCET methods for quasi-two-body and three-body decays, Proc. Three-Body Charmless B Decays Workshop, Paris, France (2006).
[907] S. Krankl et al., Nucl. Phys. B **899**, 247 (2015) [arXiv:1505.04111 [hep-ph]] [Search INSPIRE].
[908] M. V. Polyakov, Nucl. Phys. B **555**, 231 (1999) [arXiv:hep-ph/9809483] [Search INSPIRE].
[909] S. Faller et al., Phys. Rev. D **89**, 014015 (2014) [arXiv:1310.6660 [hep-ph]] [Search INSPIRE].
[910] C. Hambrock and A. Khodjamirian, Nucl. Phys. B **905**, 373 (2016) [arXiv:1511.02509 [hep-ph]] [Search INSPIRE].
[911] S. Cheng et al., J. High Energy Phys. **05**, 157 (2017) [arXiv:1701.01633 [hep-ph]] [Search INSPIRE].
[912] A. Khodjamirian et al., Phys. Rev. D **75**, 054013 (2007) [arXiv:hep-ph/0611193] [Search INSPIRE].
[913] P. Böer et al., J. High Energy Phys. **02**, 133 (2017) [arXiv:1608.07127 [hep-ph]] [Search INSPIRE].
[914] C. Patrignani et al., Chin. Phys. C **40**, 100001 (2016).
[915] H.-Y. Cheng and C.-K. Chua, Phys. Rev. D **88**, 114014 (2013) [arXiv:1308.5139 [hep-ph]] [Search INSPIRE].
[916] C.-H. Chen and H.-N. Li, Phys. Lett. B **561**, 258 (2003) [arXiv:hep-ph/0209043] [Search INSPIRE].
[917] W.-F. Wang et al., Phys. Rev. D **89**, 074031 (2014) [arXiv:1402.5280 [hep-ph]] [Search INSPIRE].
[918] C. L. Y. Lee et al., Phys. Rev. D **46**, 5040 (1992).
[919] A. Garmash et al., Phys. Rev. D **71**, 092003 (2005) [arXiv:hep-ex/0412066] [Search INSPIRE].
[920] A. Garmash et al., Phys. Rev. Lett. **96**, 251803 (2006) [arXiv:hep-ex/0512066] [Search INSPIRE].
[921] J. P. Lees et al., Phys. Rev. D **96**, 072001 (2017) [arXiv:1501.00705 [hep-ex]] [Search INSPIRE].
[922] H.-Y. Cheng et al., Phys. Rev. D **87**, 114001 (2013) [arXiv:1303.4403 [hep-ph]] [Search INSPIRE].
[923] H.-Y. Cheng et al., Phys. Rev. D **73**, 014017 (2006) [arXiv:hep-ph/0508104] [Search INSPIRE].
[924] B. Bhattacharya et al., Phys. Lett. B **726**, 337 (2013) [arXiv:1306.2625 [hep-ph]] [Search INSPIRE].
[925] D. Xu et al., Int. J. Mod. Phys. A **29**, 1450011 (2014) [arXiv:1307.7186 [heb-ph]] [Search INSPIRE].
[926] B. Aubert et al., Phys. Rev. D **79**, 072006 (2009) [arXiv:0902.2051 [hep-ex]] [Search INSPIRE].
[927] B. Aubert, Phys. Rev. Lett. **100**, 051802 (2008).
[928] A. Bazavov et al., Phys. Rev. D **90**, 074509 (2014) [arXiv:1407.3772 [hep-lat]] [Search INSPIRE].
[929] A. Vladikas, PoS **FPCP2015**, 016 (2015) [arXiv:1509.01155 [hep-lat]] [Search INSPIRE].
[930] J. Koponen et al., arXiv:1305.1462 [hep-lat] [Search INSPIRE].
[931] S. Fajfer et al., Phys. Rev. D **91**, 094009 (2015) [arXiv:1502.07488 [hep-ph]] [Search INSPIRE].
[932] G. C. Branco et al., Phys. Rept. **516**, 1 (2012) [arXiv:1106.0034 [hep-ph]] [Search INSPIRE].
[933] A. Pich and P. Tuzon, Phys. Rev. D **80**, 091702 (2009) [arXiv:0908.1554 [hep-ph]] [Search INSPIRE].
[934] A. Zupanc et al., J. High Energy Phys. **09**, 139 (2013) [arXiv:1307.6240 [hep-ex]] [Search INSPIRE].
[935] J. M. Link et al., Phys. Lett. B **535**, 43 (2002) [arXiv:hep-ex/0203031] [Search INSPIRE].
[936] P. del Amo Sanchez et al., Phys. Rev. D **83**, 072001 (2011) [arXiv:1012.1810 [hep-ex]] [Search INSPIRE].
[937] M. Ablikim et al., Phys. Rev. D **94**, 032001 (2016) [arXiv:1512.08627 [hep-ex]] [Search INSPIRE].
[938] A. Zupanc, presentation at Belle II Theory Interface Platform Meeting, KEK, Oct 2014 (2014).
[939] Y. T. Lai et al., Phys. Rev. D **95**, 011102 (2017) [arXiv:1611.09455 [hep-ex]] [Search INSPIRE].
[940] L. Widhalm et al., Phys. Rev. Lett. **97**, 061804 (2006) [arXiv:hep-ex/0604049] [Search INSPIRE].
[941] B. Aubert et al., Phys. Rev. Lett. **87**, 091801 (2001).
[942] L. et al Widhalm, Phys. Rev. Lett. **97**, 061804 (2006) [arXiv:hep-ex/0604049] [Search INSPIRE].
[943] B. I. Eisenstein et al., Phys. Rev. D **78**, 052003 (2008) [arXiv:0806.2112 [hep-ex]] [Search INSPIRE].
[944] M. Ablikim et al., Phys. Rev. D **89**, 051104 (2014) [arXiv:1312.0374 [hep-ex]] [Search INSPIRE].
[945] M. Ablikim et al., Phys. Rev. D **92**, 072012 (2015) [arXiv:1508.07560 [hep-ex]] [Search INSPIRE].
[946] S. de Boer and G. Hiller, Phys. Rev. D **93**, 074001 (2016) [arXiv:1510.00311 [hep-ph]] [Search INSPIRE].
[947] S. Fajfer et al., Phys. Rev. D **76**, 074010 (2007) [arXiv:0706.1133 [hep-ph]] [Search INSPIRE].
[948] S. Fajfer and N. Košnik, Eur. Phys. J. C **75**, 567 (2015) [arXiv:1510.00965 [hep-ph]] [Search INSPIRE].
[949] A. Paul et al., Phys. Rev. D **83**, 114006 (2011) [arXiv:1101.6053 [hep-ph]] [Search INSPIRE].
[950] R. Aaij et al., LHCb, Phys. Lett. B **725**, 15–24 (2013), [arXiv:1305.5059 []] [Search INSPIRE].
[951] R. Aaij et al., Phys. Lett. B **754**, 167 (2016) [arXiv:1512.00322 [hep-ex]] [Search INSPIRE].
[952] M. Petric et al., Phys. Rev. D **81**, 091102 (2010) [arXiv:1003.2345 [hep-ex]] [Search INSPIRE].

[953] D. E. Hazard and A. A. Petrov, Phys. Rev. D **94**, 074023 (2016) [arXiv:1607.00815 [hep-ph]] [Search INSPIRE].
[954] E. Golowich et al., Phys. Rev. D **79**, 114030 (2009) [arXiv:0903.2830 [hep-ph]] [Search INSPIRE].
[955] A. Badin and A. A Petrov, Phys. Rev. D **82**, 034005 (2010) [arXiv:1005.1277 [hep-ph]] [Search INSPIRE].
[956] M. Pospelov et al., Phys. Lett. B **662**, 53 (2008) [arXiv:0711.4866 [hep-ph]] [Search INSPIRE].
[957] J. L. Feng and J. Kumar, Phys. Rev. Lett. **101**, 231301 (2008) [arXiv:0803.4196 [hep-ph]] [Search INSPIRE].
[958] A. A. Petrov and A. E. Blechman, *Effective Field Theories* (World Scientific, Singapore, 2016).
[959] G. Isidori and J. F. Kamenik, Phys. Rev. Lett. **109**, 171801 (2012) [arXiv:1205.3164 [hep-ph]] [Search INSPIRE].
[960] J. Lyon and R. Zwicky, arXiv:1210.6546 [hep-ph] [Search INSPIRE].
[961] G. Burdman et al., Phys. Rev. D **52**, 6383 (1995) [arXiv:hep-ph/9502329] [Search INSPIRE].
[962] S. Fajfer, arXiv:1509.01997 [hep-ph] [Search INSPIRE].
[963] A. Kagan, Talk at 7th Int. Workshop on Charm Physics (Charm 2015), Detroit, MI, May 18–22 2015 (available at: https://indico.fnal.gov/event/8909/session/17/contribution/69/material/slides/0.pdf, date last accessed: November 5, 2019).
[964] L. Silvestrini, Talk at Implications of LHCb Measurements and Future Prospects, CERN, Nov 3–5, 2015 (available at: https://indico.cern.ch/event/395704/contributions/1834102/attachments/1180736/1709272/silvestriniLHCb.pdf, date last accessed: November 5, 2019).
[965] G. C. Branco et al., Int. Ser. Monogr. Phys. **103**, 1 (1999).
[966] S. Bergmann and Y. Nir, J. High Energy Phys. **09**, 031 (1999) [arXiv:hep-ph/9909391] [Search INSPIRE].
[967] Y. Grossman et al., Phys. Rev. D **75**, 036008 (2007) [arXiv:hep-ph/0609178] [Search INSPIRE].
[968] R. Aaij et al., LHCb, Phys. Rev. Lett. **108**, 111602 (2012), [arXiv:1112.0938 []] [Search INSPIRE].
[969] Yosef Nir, Conf. Proc. C **9207131**, 81 (1992).
[970] M. Ciuchini et al., Phys. Lett. B **655**, 162 (2007) [arXiv:hep-ph/0703204] [Search INSPIRE].
[971] Y. Grossman et al., Phys. Rev. Lett. **103**, 071602 (2009) [arXiv:0904.0305 [hep-ph]] [Search INSPIRE].
[972] A. L. Kagan and M. D. Sokoloff, Phys. Rev. D **80**, 076008 (2009) [arXiv:0907.3917 [hep-ph]] [Search INSPIRE].
[973] J. Brod et al., J. High Energy Phys. **10**, 161 (2012) [arXiv:1203.6659 [hep-ph]] [Search INSPIRE].
[974] J. Simone, PoS **LATTICE2015**, 332 (2016).
[975] C. C. Chang, arXiv:1509.07088 [hep-lat] [Search INSPIRE].
[976] P. A. Boyle et al., Phys. Rev. Lett. **110**, 152001 (2013) [arXiv:1212.1474 [hep-lat]] [Search INSPIRE].
[977] M. Peardon et al., Phys. Rev. D **80**, 054506 (2009) [arXiv:0905.2160 [hep-lat]] [Search INSPIRE].
[978] C. Morningstar et al., Phys. Rev. D **83**, 114505 (2011) [arXiv:1104.3870 [hep-lat]] [Search INSPIRE].
[979] J. J. Dudek, AIP Conf. Proc. **1735**, 020014 (2016).
[980] M. T. Hansen and S. R. Sharpe, Phys. Rev. D **90**, 116003 (2014) [arXiv:1408.5933 [hep-lat]] [Search INSPIRE].
[981] M. T. Hansen and S. R. Sharpe, Phys. Rev. D **92**, 114509 (2015) [arXiv:1504.04248 [hep-lat]] [Search INSPIRE].
[982] M. T. Hansen and S. R. Sharpe, Phys. Rev. D **93**, 096006 (2016) [arXiv:1602.00324 [hep-lat]] [Search INSPIRE].
[983] Z. Bai et al., Phys. Rev. Lett. **113**, 112003 (2014) [arXiv:1406.0916 [hep-lat]] [Search INSPIRE].
[984] N. H. Christ et al., Phys. Rev. D **91**, 114510 (2015) [arXiv:1504.01170 [hep-lat]] [Search INSPIRE].
[985] M. Staric et al., Phys. Rev. Lett. **98**, 211803 (2007) [arXiv:hep-ex/0703036] [Search INSPIRE].
[986] B. Aubert et al., Phys. Rev. Lett. **98**, 211802 (2007) [arXiv:hep-ex/0703020] [Search INSPIRE].
[987] R Aaij et al., Phys. Rev. Lett. **110**, 101802 (2013) [arXiv:1211.1230 [hep-ex]] [Search INSPIRE].
[988] T. Aaltonen et al., Phys. Rev. Lett. **111**, 231802 (2013) [arXiv:1309.4078 [hep-ex]] [Search INSPIRE].
[989] L. M. Zhang et al., Phys. Rev. Lett. **96**, 151801 (2006) [arXiv:hep-ex/0601029] [Search INSPIRE].
[990] X. C. Tian et al., Phys. Rev. Lett. **95**, 231801 (2005) [arXiv:hep-ex/0507071] [Search INSPIRE].
[991] B. Aubert et al., Phys. Rev. Lett. **103**, 211801 (2009) [arXiv:0807.4544 [hep-ex]] [Search INSPIRE].

[992] W. B. Yan, L. K. Li, and Z. P. Zhang, Belle Note 1381 (2016).
[993] C. Thomas and G. Wilkinson, J. High Energy Phys. **10**, 185 (2012) [arXiv:1209.0172 [hep-ex]] [Search INSPIRE].
[994] J. Insler et al., [CLEO Collaboration], Phys. Rev. D **85**, 092016 (2012) [arXiv:1203.3804 [hep-ex]] [Search INSPIRE].
[995] R. Aaij et al., Phys. Rev. D **93**, 052018 (2016) [arXiv:1509.06628 [hep-ex]] [Search INSPIRE].
[996] S. Malde and G. Wilkinson, Phys. Lett. B **701**, 353 (2011) [arXiv:1104.2731 [hep-ph]] [Search INSPIRE].
[997] F. Buccella et al., Phys. Lett. B **302**, 319 (1993) [arXiv:hep-ph/9212253] [Search INSPIRE].
[998] Y. Grossman et al., Phys. Rev. D **85**, 114036 (2012) [arXiv:1204.3557 [hep-ph]] [Search INSPIRE].
[999] G. Isidori et al., Phys. Lett. B **711**, 46 (2012) [arXiv:1111.4987 [hep-ph]] [Search INSPIRE].
[1000] J. Brod et al., Phys. Rev. D **86**, 014023 (2012) [arXiv:1111.5000 [hep-ph]] [Search INSPIRE].
[1001] D. Pirtskhalava and P. Uttayarat, Phys. Lett. B **712**, 81 (2012) [arXiv:1112.5451 [hep-ph]] [Search INSPIRE].
[1002] H.-Y. Cheng and C.-W. Chiang, Phys. Rev. D **85**, 034036 (2012); **85**, 079903 (2012) [erratum] [arXiv:1201.0785 [hep-ph]] [Search INSPIRE].
[1003] B. Bhattacharya et al., Phys. Rev. D **85**, 054014 (2012) [arXiv:1201.2351 [hep-ph]] [Search INSPIRE].
[1004] W. Altmannshofer et al., J. High Energy Phys. **04**, 049 (2012) [arXiv:1202.2866 [hep-ph]] [Search INSPIRE].
[1005] T. Feldmann et al., J. High Energy Phys. **06**, 007 (2012) [arXiv:1202.3795 [hep-ph]] [Search INSPIRE].
[1006] H.-N. Li et al., Phys. Rev. D **86**, 036012 (2012) [arXiv:1203.3120 [hep-ph]] [Search INSPIRE].
[1007] E. Franco et al., J. High Energy Phys. **05**, 140 (2012) [arXiv:1203.3131 [hep-ph]] [Search INSPIRE].
[1008] B. Bhattacharya et al., arXiv:1207.6390 [hep-ph] [Search INSPIRE].
[1009] B. Bhattacharya et al., arXiv:1207.0761 [hep-ph] [Search INSPIRE].
[1010] D. Atwood and A. Soni, Prog. Theor. Exp. Phys. **2013**, 093B05 (2013) [arXiv:1211.1026 [hep-ph]] [Search INSPIRE].
[1011] Y. Grossman and D. J. Robinson, J. High Energy Phys. **04**, 067 (2013) [arXiv:1211.3361 [hep-ph]] [Search INSPIRE].
[1012] G. Hiller et al., Phys. Rev. D **85**, 116008 (2012) [arXiv:1204.1046 [hep-ph]] [Search INSPIRE].
[1013] F. Buccella et al., Phys. Rev. D **88**, 074011 (2013) [arXiv:1305.7343 [hep-ph]] [Search INSPIRE].
[1014] M. Gronau, Phys. Lett. B **730**, 221 (2014); **735**, 282 (2014) [addendum] [arXiv:1311.1434 [hep-ph]] [Search INSPIRE].
[1015] A. Lenz, arXiv:1311.6447 [hep-ph] [Search INSPIRE].
[1016] M. Gronau, Phys. Rev. D **91**, 076007 (2015) [arXiv:1501.03272 [hep-ph]] [Search INSPIRE].
[1017] G. Hiller et al., Phys. Rev. D **87**, 014024 (2013) [arXiv:1211.3734 [hep-ph]] [Search INSPIRE].
[1018] G. Hiller et al., PoS **EPS-HEP2013**, 371 (2013) [arXiv:1311.3883 [hep-ph]] [Search INSPIRE].
[1019] S. Müller et al., Phys. Rev. D **92**, 014004 (2015) [arXiv:1503.06759 [hep-ph]] [Search INSPIRE].
[1020] S. Müller et al., Phys. Rev. Lett. **115**, 251802 (2015) [arXiv:1506.04121 [hep-ph]] [Search INSPIRE].
[1021] U. Nierste and S. Schacht, Phys. Rev. D **92**, 054036 (2015) [arXiv:1508.00074 [hep-ph]] [Search INSPIRE].
[1022] R. Aaij et al., Phys. Lett. B **767**, 177 (2017) [arXiv:1610.09476 [hep-ex]] [Search INSPIRE].
[1023] N. Dash et al., arXiv:1705.05966 [hep-ex] [Search INSPIRE].
[1024] N. K. Nisar et al., Phys. Rev. Lett. **112**, 211601 (2014) [arXiv:1404.1266 [hep-ex]] [Search INSPIRE].
[1025] R. Aaij et al., J. High Energy Phys. **10**, 25 (2014) [arXiv:1406.2624 [hep-ex]] [Search INSPIRE].
[1026] B. R. Ko et al., Phys. Rev. Lett. **109**, 021601 (2012); **109**, 119903 (2012) erratum] [arXiv:1203.6409 [hep-ex]] [Search INSPIRE].
[1027] L.-L. C. Wang, Flavor mixing and charm decay, in *Cnference on Theoretical Particle Physics, v.2*, p. 1218 (Science Press, Beijing, 1980).
[1028] L.-L. Chau, Phys. Rept. **95**, 1 (1983).
[1029] J. J. de Swart, Rev. Mod. Phys. **35**, 916 (1963); **37**, 326 (1965) [erratum].
[1030] T. A. Kaeding, Atom. Data Nucl. Data Tabl. **61**, 233 (1995) [arXiv:nucl-th/9502037] [Search INSPIRE].

[1031] T. A. Kaeding and H. T. Williams, Comput. Phys. Commun. **98**, 398 (1996) [arXiv:nucl-th/9511025] [Search INSPIRE].
[1032] M. Gronau et al., Phys. Rev. D **52**, 6356 (1995) [arXiv:hep-ph/9504326] [Search INSPIRE].
[1033] A. J. Buras et al., Nucl. Phys. B **268**, 16 (1986).
[1034] A. J. Buras and L. Silvestrini, Nucl. Phys. B **569**, 3 (2000) [arXiv:hep-ph/9812392] [Search INSPIRE].
[1035] P. U. E. Onyisi et al., Phys. Rev. D **88**, 032009 (2013) [arXiv:1306.5363 [hep-ex]] [Search INSPIRE].
[1036] G. Bonvicini et al., Phys. Rev. D **63**, 071101 (2001) [arXiv:hep-ex/0012054] [Search INSPIRE].
[1037] H. Mendez et al., Phys. Rev. D **81**, 052013 (2010) [arXiv:0906.3198 [hep-ex]] [Search INSPIRE].
[1038] V. Babu et al., Phys. Rev. D **97**, 011101 (2018) [arXiv:1712.00619 [hep-ex]] [Search INSPIRE].
[1039] R. Aaij et al., J. High Energy Phys. **10**, 055 (2015) [arXiv:1508.06087 [hep-ex]] [Search INSPIRE].
[1040] B. Bhattacharya and J. L. Rosner, Phys. Rev. D **81**, 014026 (2010) [arXiv:0911.2812 [hep-ph]] [Search INSPIRE].
[1041] H.-Y. Cheng and C.-W. Chiang, Phys. Rev. D **81**, 074021 (2010) [arXiv:1001.0987 [hep-ph]] [Search INSPIRE].
[1042] D.-N. Gao, Phys. Rev. D **91**, 014019 (2015) [arXiv:1411.0768 [hep-ph]] [Search INSPIRE].
[1043] Y. Hochberg and Y. Nir, Phys. Rev. Lett. **108**, 261601 (2012) [arXiv:1112.5268 [hep-ph]] [Search INSPIRE].
[1044] A. J. Bevan et al., Phys. Rev. D **84**, 114009 (2011); **87**, 039905 (2013) [erratum] [arXiv:1106.5075 [hep-ph]] [Search INSPIRE].
[1045] M. Staric et al., Phys. Lett. B **670**, 190 (2008) [arXiv:0807.0148 [hep-ex]] [Search INSPIRE].
[1046] P. del Amo Sanchez et al., Phys. Rev. D **83**, 071103 (2011) [arXiv:1011.5477 [hep-ex]] [Search INSPIRE].
[1047] B. R. Ko et al., J. High Energy Phys. **02**, 098 (2013) [arXiv:1212.6112 [hep-ex]] [Search INSPIRE].
[1048] J. P. Lees et al., Phys. Rev. D **87**(1), 012004 (2013) [arXiv:1209.3896 [hep-ex]] [Search INSPIRE].
[1049] S. K. Choi et al., Phys. Rev. Lett. **91**, 262001 (2003) [arXiv:hep-ex/0309032] [Search INSPIRE].
[1050] N. Brambilla et al., Eur. Phys. J. C **74**, 2981 (2014) [arXiv:1404.3723 [hep-ph]] [Search INSPIRE].
[1051] N. Brambilla et al., Eur. Phys. J. C **71**, 1534 (2011) [arXiv:1010.5827 [hep-ph]] [Search INSPIRE].
[1052] N. Brambilla et al., arXiv:hep-ph/0412158 [Search INSPIRE].
[1053] N. Brambilla et al., Rev. Mod. Phys. **77**, 1423 (2005) [arXiv:hep-ph/0410047] [Search INSPIRE].
[1054] R. Aaij et al., Phys. Rev. Lett. **115**, 072001 (2015) [arXiv:1507.03414 [hep-ex]] [Search INSPIRE].
[1055] N. Brambilla et al., Phys. Lett. B **576**, 314 (2003) [arXiv:hep-ph/0306107] [Search INSPIRE].
[1056] W. E. Caswell and G. P. Lepage, Phys. Lett. B **167**, 437 (1986).
[1057] G. T. Bodwin et al., Phys. Rev. D **51**, 1125 (1995); **55**, 5853 (1997) [erratum] [arXiv:hep-ph/9407339] [Search INSPIRE].
[1058] N. Brambilla et al., Phys. Rev. D **79**, 074002 (2009); **83**, 079904 (2011) [erratum] [arXiv:0810.2259 [hep-ph]] [Search INSPIRE].
[1059] N. Brambilla et al., J. High Energy Phys. **08**, 039 (2006); **04**, 058 (2011) [erratum] [arXiv:hep-ph/0604190] [Search INSPIRE].
[1060] G. T. Bodwin et al., Phys. Rev. D **65**, 054504 (2002) [arXiv:hep-lat/0107011] [Search INSPIRE].
[1061] G. T. Bodwin, arXiv:1208.5506 [hep-ph] [Search INSPIRE].
[1062] N. Brambilla et al., Nucl. Phys. B **566**, 275 (2000) [arXiv:hep-ph/9907240] [Search INSPIRE].
[1063] A. Pineda and J. Soto, Nucl. Phys. Proc. Suppl. **64**, 428 (1998) [arXiv:hep-ph/9707481] [Search INSPIRE].
[1064] N. Brambilla et al., Phys. Rev. D **63**, 014023 (2001) [arXiv:hep-ph/0002250] [Search INSPIRE].
[1065] A. Pineda and A. Vairo, Phys. Rev. D **63**, 054007 (2001); **64**, 039902 (2001) [erratum] [arXiv:hep-ph/0009145] [Search INSPIRE].
[1066] C. Gattringer and C. B. Lang, Lect. Notes Phys. **788**, 1 (2010).
[1067] T. DeGrand and C. E. Detar, *Lattice Methods for Quantum Chromodynamics*, (World Scientific, Hackensack, NJ, 2006).
[1068] C. Liu, arXiv:1612.00103 [hep-lat] [Search INSPIRE].
[1069] S. M. Ryan, EPJ Web Conf. **130**, 01002 (2016).
[1070] S. Prelovsek, arXiv:1508.07322 [hep-lat] [Search INSPIRE].
[1071] N. Brambilla et al., Phys. Lett. B **470**, 215 (1999) [arXiv:hep-ph/9910238] [Search INSPIRE].
[1072] B. A. Kniehl et al., Nucl. Phys. B **635**, 357 (2002) [arXiv:hep-ph/0203166] [Search INSPIRE].
[1073] A. V. Smirnov et al., Phys. Rev. Lett. **104**, 112002 (2010) [arXiv:0911.4742 []] [Search INSPIRE].

[1074] C. Anzai et al., Phys. Rev. Lett. **104**, 112003 (2010) [arXiv:0911.4335 [hep-ph]] [Search INSPIRE].
[1075] N. Brambilla et al., Phys. Rev. D **60**, 091502 (1999) [arXiv:hep-ph/9903355] [Search INSPIRE].
[1076] N. Brambilla et al., Phys. Rev. Lett. **105**, 212001 (2010); **108**, 269903 (2012) [erratum] [arXiv:1006.2066 [hep-ph]] [Search INSPIRE].
[1077] A. Bazavov et al., Phys. Rev. D **86**, 114031 (2012) [arXiv:1205.6155 [hep-ph]] [Search INSPIRE].
[1078] A. Bazavov et al., Phys. Rev. D **90**, 074038 (2014) [arXiv:1407.8437 [hep-ph]] [Search INSPIRE].
[1079] A. Pineda and F. J. Yndurain, Phys. Rev. D **58**, 094022 (1998) [arXiv:hep-ph/9711287] [Search INSPIRE].
[1080] S. Titard and F. J. Yndurain, Phys. Rev. D **49**, 6007 (1994) [arXiv:hep-ph/9310236] [Search INSPIRE].
[1081] Y. Kiyo and Y. Sumino, Nucl. Phys. B **889**, 156 (2014) [arXiv:1408.5590 [hep-ph]] [Search INSPIRE].
[1082] A. H. Hoang et al., Phys. Rev. D **59**, 114014 (1999) [arXiv:hep-ph/9804227] [Search INSPIRE].
[1083] M. Beneke, Phys. Lett. B **434**, 115 (1998) [arXiv:hep-ph/9804241] [Search INSPIRE].
[1084] N. Brambilla et al., Phys. Lett. B **513**, 381 (2001) [arXiv:hep-ph/0101305] [Search INSPIRE].
[1085] Y. Kiyo and Y. Sumino, Phys. Lett. B **730**, 76 (2014) [arXiv:1309.6571 [hep-ph]] [Search INSPIRE].
[1086] B. A. Kniehl et al., Phys. Rev. Lett. **92**, 242001 (2004); **104**, 199901 (2010) [erratum] [arXiv:hep-ph/0312086] [Search INSPIRE].
[1087] S. Recksiegel and Y. Sumino, Phys. Lett. B **578**, 369 (2004) [arXiv:hep-ph/0305178] [Search INSPIRE].
[1088] A. A. Penin et al., Phys. Lett. B **593**, 124 (2004); **677**, 343 (2009) [erratum] [arXiv:hep-ph/0403080] [Search INSPIRE].
[1089] A. H. Hoang, arXiv:hep-ph/0008102 [Search INSPIRE].
[1090] N. Brambilla et al., Phys. Rev. D **65**, 034001 (2002) [arXiv:hep-ph/0108084] [Search INSPIRE].
[1091] Y. Kiyo et al., Phys. Lett. B **752**, 122 (2016) [arXiv:1510.07072 [hep-ph]] [Search INSPIRE].
[1092] C. Ayala et al., J. High Energy Phys. **09**, 045 (2014) [arXiv:1407.2128 [hep-ph]] [Search INSPIRE].
[1093] M. Beneke et al., Phys. Rev. Lett. **112**, 151801 (2014) [arXiv:1401.3005 [hep-ph]] [Search INSPIRE].
[1094] M. B. Voloshin, Sov. J. Nucl. Phys. **36**, 143 (1982).
[1095] A. Pineda, Nucl. Phys. B **494**, 213 (1997) [arXiv:hep-ph/9611388] [Search INSPIRE].
[1096] A. A. Penin et al., Nucl. Phys. B **699**, 183 (2004); **829**, 398 (2010) [erratum] [arXiv:hep-ph/0406175] [Search INSPIRE].
[1097] Y. Kiyo et al., Nucl. Phys. B **841**, 231 (2010) [arXiv:1006.2685 [hep-ph]] [Search INSPIRE].
[1098] N. Brambilla et al., Phys. Rev. D **73**, 054005 (2006) [arXiv:hep-ph/0512369] [Search INSPIRE].
[1099] A. Pineda and J. Segovia, Phys. Rev. D **87**, 074024 (2013) [arXiv:1302.3528 [hep-ph]] [Search INSPIRE].
[1100] E. Eichten et al., Rev. Mod. Phys. **80**, 1161 (2008) [arXiv:hep-ph/0701208] [Search INSPIRE].
[1101] N. Brambilla et al., Phys. Rev. D **85**, 094005 (2012) [arXiv:1203.3020 [hep-ph]] [Search INSPIRE].
[1102] S. Steinbeißer and J. Segovia, arXiv:1701.02513 [hep-ph] [Search INSPIRE].
[1103] N. Brambilla et al., AIP Conf.Proc. **1343**, 418 (2011) [arXiv:1012.0773 [hep-ph]] [Search INSPIRE].
[1104] Y. Koma et al., Phys. Rev. Lett. **97**, 122003 (2006) [arXiv:hep-lat/0607009] [Search INSPIRE].
[1105] Y. Koma et al., PoS **LAT2007**, 111 (2007) [arXiv:0711.2322 [hep-lat]] [Search INSPIRE].
[1106] N. Brambilla et al., Phys. Rev. D **90**, 114032 (2014) [arXiv:1407.7761 [hep-ph]] [Search INSPIRE].
[1107] N. Brambilla and A. Vairo, Phys. Rev. D **55**, 3974 (1997) [arXiv:hep-ph/9606344] [Search INSPIRE].
[1108] M. Baker et al., Phys. Rev. D **54**, 2829 (1996); **56**, 2475 (1997) [erratum] [arXiv:hep-ph/9602419] [Search INSPIRE].
[1109] Y. Koma and M. Koma, PoS **LATTICE2012**, 140 (2012) [arXiv:1211.6795 [hep-lat]] [Search INSPIRE].
[1110] U. Tamponi et al., Phys. Rev. Lett. **115**, 142001 (2015) [arXiv:1506.08914 [hep-ex]] [Search INSPIRE].
[1111] R. Mizuk et al., Phys. Rev. Lett. **109**, 232002 (2012) [arXiv:1205.6351 [hep-ex]] [Search INSPIRE].
[1112] N. Brambilla et al., Phys. Rev. D **67**, 034018 (2003) [arXiv:hep-ph/0208019] [Search INSPIRE].
[1113] M. Wurtz et al., Phys. Rev. D **92**, 054504 (2015) [arXiv:1505.04410 [hep-lat]] [Search INSPIRE].
[1114] Y.-B. Yang et al., arXiv:1410.3343 [hep-lat] [Search INSPIRE].
[1115] B. A. Galloway et al., PoS **LATTICE2014**, 092 (2014) [arXiv:1411.1318 [hep-lat]] [Search INSPIRE].

[1116] P. Perez-Rubio et al., Phys. Rev. D **92**, 034504 (2015) [arXiv:1503.08440 [hep-lat]] [Search INSPIRE].
[1117] D. Mohler et al., PoS **LATTICE2014**, 085 (2015) [arXiv:1412.1057 [hep-lat]] [Search INSPIRE].
[1118] K. Cichy et al., arXiv:1603.06467 [hep-lat] [Search INSPIRE].
[1119] L. Liu et al., J. High Energy Phys. **1207**, 126 (2012) [arXiv:1204.5425 [hep-ph]] [Search INSPIRE].
[1120] F.-K. Guo and U.-G. Meißner, Phys. Rev. Lett. **109**, 062001 (2012) [arXiv:1203.1116 [hep-ph]] [Search INSPIRE].
[1121] C. Hughes et al., Phys. Rev. D **92**, 094501 (2015) [arXiv:1508.01694 [hep-lat]] [Search INSPIRE].
[1122] R. Lewis and R. M. Woloshyn, Phys. Rev. D **84**, 094501 (2011) [arXiv:1108.1137 [hep-lat]] [Search INSPIRE].
[1123] R. Lewis and R. M. Woloshyn, Phys. Rev. D **86**, 057501 (2012) [arXiv:1207.3825 [hep-lat]] [Search INSPIRE].
[1124] J. J. Dudek et al., Phys. Rev. D **79**, 094504 (2009) [arXiv:0902.2241 [hep-ph]] [Search INSPIRE].
[1125] D. Becirevic and F. Sanfilippo, J. High Energy Phys. **01**, 028 (2013) [arXiv:1206.1445 [hep-lat]] [Search INSPIRE].
[1126] D. Becirevic et al., J. High Energy Phys. **05**, 014 (2015) [arXiv:1411.6426 [hep-lat]] [Search INSPIRE].
[1127] Y. Chen et al., Phys. Rev. D **84**, 034503 (2011) [arXiv:1104.2655 [hep-lat]] [Search INSPIRE].
[1128] K. J. Juge et al., Phys. Rev. Lett. **90**, 161601 (2003) [arXiv:hep-lat/0207004] [Search INSPIRE].
[1129] G. S. Bali and A. Pineda, Phys. Rev. D **69**, 094001 (2004) [arXiv:hep-ph/0310130] [Search INSPIRE].
[1130] E. Braaten and M. Kusunoki, Phys. Rev. D **69**, 074005 (2004) [arXiv:hep-ph/0311147] [Search INSPIRE].
[1131] S. Fleming et al., Phys. Rev. D **76**, 034006 (2007) [arXiv:hep-ph/0703168] [Search INSPIRE].
[1132] V. Baru et al., Phys. Rev. D **84**, 074029 (2011) [arXiv:1108.5644 [hep-ph]] [Search INSPIRE].
[1133] E. Epelbaum et al., Rev. Mod. Phys. **81**, 1773 (2009) [arXiv:0811.1338 [nucl-th]] [Search INSPIRE].
[1134] P. Bicudo et al., arXiv:1612.02758 [hep-lat] [Search INSPIRE].
[1135] A. Peters et al., arXiv:1609.00181 [hep-lat] [Search INSPIRE].
[1136] M. Berwein et al., Phys. Rev. D **92**, 114019 (2015) [arXiv:1510.04299 [hep-ph]] [Search INSPIRE].
[1137] S. K. Choi et al., Phys. Rev. D **84**, 052004 (2011) [arXiv:1107.0163 [hep-ex]] [Search INSPIRE].
[1138] B. Aubert et al., Phys. Rev. D **77**, 111101 (2008) [arXiv:0803.2838 [hep-ex]] [Search INSPIRE].
[1139] D. Acosta et al., Phys. Rev. Lett. **93**, 072001 (2004) [arXiv:hep-ex/0312021] [Search INSPIRE].
[1140] A. Abulencia et al., Phys. Rev. Lett. **98**, 132002 (2007) [arXiv:hep-ex/0612053] [Search INSPIRE].
[1141] T. Aaltonen et al., Phys. Rev. Lett. **103**, 152001 (2009) [arXiv:0906.5218 [hep-ex]] [Search INSPIRE].
[1142] V. M. Abazov et al., Phys. Rev. Lett. **93**, 162002 (2004) [arXiv:hep-ex/0405004] [Search INSPIRE].
[1143] R. Aaij et al., Eur. Phys. J. C **72**, 1972 (2012) [arXiv:1112.5310 [hep-ex]] [Search INSPIRE].
[1144] R. Aaij et al., Phys. Rev. Lett. **110**, 222001 (2013) [arXiv:1302.6269 [hep-ex]] [Search INSPIRE].
[1145] R. Aaij et al., Phys. Rev. D **92**(1), 011102 (2015) [arXiv:1504.06339 [hep-ex]] [Search INSPIRE].
[1146] S. Chatrchyan et al., J. High Energy Phys. **04**, 154 (2013) [arXiv:1302.3968 [hep-ex]] [Search INSPIRE].
[1147] M. Ablikim et al., Phys. Rev. Lett. **112**, 092001 (2014) [arXiv:1310.4101 [hep-ex]] [Search INSPIRE].
[1148] K. Abe et al., arXiv:hep-ex/0505037 [Search INSPIRE].
[1149] P. del Amo Sanchez et al., Phys. Rev. D **82**, 011101 (2010) [arXiv:1005.5190 [hep-ex]] [Search INSPIRE].
[1150] V. Bhardwaj et al., Phys. Rev. Lett. **107**, 091803 (2011) [arXiv:1105.0177 [hep-ex]] [Search INSPIRE].
[1151] B. Aubert et al., Phys. Rev. D **74**, 071101 (2006) [arXiv:hep-ex/0607050] [Search INSPIRE].
[1152] B. Aubert et al., Phys. Rev. Lett. **102**, 132001 (2009) [arXiv:0809.0042 [hep-ex]] [Search INSPIRE].
[1153] R. Aaij et al., Nucl. Phys. B **886**, 665 (2014) [arXiv:1404.0275 [hep-ex]] [Search INSPIRE].
[1154] G. Gokhroo et al., Phys. Rev. Lett. **97**, 162002 (2006) [arXiv:hep-ex/0606055] [Search INSPIRE].
[1155] T. Aushev et al., Phys. Rev. D **81**, 031103 (2010) [arXiv:0810.0358 [hep-ex]] [Search INSPIRE].
[1156] B. Aubert et al., Phys. Rev. D **77**, 011102 (2008) [arXiv:0708.1565 [hep-ex]] [Search INSPIRE].
[1157] M. Ablikim et al., Phys. Rev. Lett. **110**, 252001 (2013) [arXiv:1303.5949 [hep-ex]] [Search INSPIRE].

[1158] Z. Q. Liu et al., Phys. Rev. Lett. **110**, 252002 (2013) [arXiv:1304.0121 [hep-ex]] [Search INSPIRE].
[1159] T. Xiao et al., Phys. Lett. B **727**, 366–370 (2013) [arXiv:1304.3036 [hep-ex]] [Search INSPIRE].
[1160] M. Ablikim et al., Phys. Rev. Lett. **115**, 112003 (2015) [arXiv:1506.06018 [hep-ex]] [Search INSPIRE].
[1161] M. Ablikim et al., Phys. Rev. Lett. **111**, 242001 (2013) [arXiv:1309.1896 [hep-ex]] [Search INSPIRE].
[1162] M. Ablikim et al., Phys. Rev. Lett. **112**, 022001 (2014) [arXiv:1310.1163 [hep-ex]] [Search INSPIRE].
[1163] M. Ablikim et al., Phys. Rev. D **92**, 092006 (2015) [arXiv:1509.01398 [hep-ex]] [Search INSPIRE].
[1164] M. Ablikim et al., Phys. Rev. Lett. **115**, 222002 (2015) [arXiv:1509.05620 [hep-ex]] [Search INSPIRE].
[1165] M. Ablikim et al., Phys. Rev. Lett. **113**, 212002 (2014) [arXiv:1409.6577 [hep-ex]] [Search INSPIRE].
[1166] X. L. Wang et al., Phys. Rev. D **91**, 112007 (2015) [arXiv:1410.7641 [hep-ex]] [Search INSPIRE].
[1167] M. Ablikim et al., arXiv:1703.08787 [hep-ex] [Search INSPIRE.
[1168] M. Ablikim et al., Phys. Rev. Lett. **112**, 132001 (2014) [arXiv:1308.2760 [hep-ex]] [Search INSPIRE].
[1169] M. Ablikim et al., Phys. Rev. Lett. **115**, 182002 (2015) [arXiv:1507.02404 [hep-ex]] [Search INSPIRE].
[1170] I. Adachi, arXiv:1105.4583 [hep-ex] [Search INSPIRE].
[1171] A. Bondar et al., Phys. Rev. Lett. **108**, 122001 (2012) [arXiv:1110.2251 [hep-ex]] [Search INSPIRE].
[1172] A. Garmash et al., Phys. Rev. D **91**, 072003 (2015) [arXiv:1403.0992 [hep-ex]] [Search INSPIRE].
[1173] P. Krokovny et al., Phys. Rev. D **88**, 052016 (2013) [arXiv:1308.2646 [hep-ex]] [Search INSPIRE].
[1174] I. Adachi et al., arXiv:1209.6450 [hep-ex] [Search INSPIRE].
[1175] A. Garmash et al., Phys. Rev. Lett. **116**, 212001 (2016) [arXiv:1512.07419 [hep-ex]] [Search INSPIRE].
[1176] A. Abdesselam et al., Phys. Rev. Lett. **117**, 142001 (2016) [arXiv:1508.06562 [hep-ex]] [Search INSPIRE].
[1177] K. Abe et al., Phys. Rev. Lett. **93**, 051803 (2004) [arXiv:hep-ex/0307061] [Search INSPIRE].
[1178] J. Brodzicka et al., Phys. Rev. Lett. **100**, 092001 (2008) [arXiv:0707.3491 [hep-ex]] [Search INSPIRE].
[1179] J. Z. Bai et al., Phys. Lett. B **605**, 63 (2005) [arXiv:hep-ex/0307028] [Search INSPIRE].
[1180] N. E. Adam et al., Phys. Rev. Lett. **96**, 082004 (2006) [arXiv:hep-ex/0508023] [Search INSPIRE].
[1181] G. S. Adams et al., Phys. Rev. D **73**, 012002 (2006) [arXiv:hep-ex/0509011] [Search INSPIRE].
[1182] V. Bhardwaj et al., Phys. Rev. Lett. **111**, 032001 (2013) [arXiv:1304.3975 [hep-ex]] [Search INSPIRE].
[1183] M. Ablikim et al., Phys. Rev. Lett. **115**, 011803 (2015) [arXiv:1503.08203 [hep-ex]] [Search INSPIRE].
[1184] K. Chilikin et al., arXiv:1704.01872 [hep-ex] [Search INSPIRE].
[1185] K. Abe et al., Phys. Rev. Lett. **94**, 182002 (2005) [arXiv:hep-ex/0408126] [Search INSPIRE].
[1186] B. Aubert et al., Phys. Rev. Lett. **101**, 082001 (2008) [arXiv:0711.2047 [hep-ex]] [Search INSPIRE].
[1187] S. Uehara et al., Phys. Rev. Lett. **104**, 092001 (2010) [arXiv:0912.4451 [hep-ex]] [Search INSPIRE].
[1188] J. P. Lees et al., Phys. Rev. D **86**, 072002 (2012) [arXiv:1207.2651 [hep-ex]] [Search INSPIRE].
[1189] S. Uehara et al., Phys. Rev. Lett. **96**, 082003 (2006) [arXiv:hep-ex/0512035] [Search INSPIRE].
[1190] B. Aubert et al., Phys. Rev. D **81**, 092003 (2010) [arXiv:1002.0281 [hep-ex]] [Search INSPIRE].
[1191] K. Abe et al., Phys. Rev. Lett. **98**, 082001 (2007) [arXiv:hep-ex/0507019] [Search INSPIRE].
[1192] P. Pakhlov et al., Phys. Rev. Lett. **100**, 202001 (2008) [arXiv:0708.3812 [hep-ex]] [Search INSPIRE].
[1193] M. Ablikim et al., Phys. Rev. D **86**, 071101 (2012) [arXiv:1208.1857 [hep-ex]] [Search INSPIRE].
[1194] X. L. Wang et al., Phys. Rev. D **87**, 051101 (2013) [arXiv:1210.7550 [hep-ex]] [Search INSPIRE].
[1195] R. Mizuk et al., Phys. Rev. D **78**, 072004 (2008) [arXiv:0806.4098 [hep-ex]] [Search INSPIRE].
[1196] J. P. Lees et al., Phys. Rev. D **85**, 052003 (2012) [arXiv:1111.5919 [hep-ex]] [Search INSPIRE].
[1197] T. Aaltonen et al., Phys. Rev. Lett. **102**, 242002 (2009) [arXiv:0903.2229 [hep-ex]] [Search INSPIRE].
[1198] T. Aaltonen et al., Mod. Phys. Lett. A **32**, 1750139 (2017) [arXiv:1101.6058 [hep-ex]] [Search INSPIRE].

[1199] J. Brodzicka, Heavy flavor spectroscopy, in Proc. 24th Int. Symp. on Lepton–Photon Interactions at High Energy (LP09) (2009).
[1200] R. Aaij et al., Phys. Rev. D **85**, 091103 (2012) [arXiv:1202.5087 [hep-ex]] [Search INSPIRE].
[1201] S. Chatrchyan et al., Phys. Lett. B **734**, 261 (2014) [arXiv:1309.6920 [hep-ex]] [Search INSPIRE].
[1202] V. M. Abazov et al., Phys. Rev. D **89**, 012004 (2014) [arXiv:1309.6580 [hep-ex]] [Search INSPIRE].
[1203] J. P. Lees et al., Phys. Rev. D **91**, 012003 (2015) [arXiv:1407.7244 [hep-ex]] [Search INSPIRE].
[1204] R. Aaij et al., arXiv:1606.07895 [hep-ex] [Search INSPIRE].
[1205] R. Aaij et al., arXiv:1606.07898 [hep-ex] [Search INSPIRE].
[1206] V. M. Abazov et al., Phys. Rev. Lett. **115**, 232001 (2015) [arXiv:1508.07846 [hep-ex]] [Search INSPIRE].
[1207] M. Ablikim et al., Phys. Rev. D **91**, 112005 (2015) [arXiv:1503.06644 [hep-ex]] [Search INSPIRE].
[1208] K. Chilikin et al., Phys. Rev. D **90**, 112009 (2014) [arXiv:1408.6457 [hep-ex]] [Search INSPIRE].
[1209] B. Aubert et al., Phys. Rev. Lett. **95**, 142001 (2005) [arXiv:hep-ex/0506081] [Search INSPIRE].
[1210] J. P. Lees et al., Phys. Rev. D **86**, 051102 (2012) [arXiv:1204.2158 [hep-ex]] [Search INSPIRE].
[1211] T. E. Coan et al., Phys. Rev. Lett. **96**, 162003 (2006) [arXiv:hep-ex/0602034] [Search INSPIRE].
[1212] Q. He et al., Phys. Rev. D **74**, 091104 (2006) [arXiv:hep-ex/0611021] [Search INSPIRE].
[1213] C. Z. Yuan et al., Phys. Rev. Lett. **99**, 182004 (2007) [arXiv:0707.2541 [hep-ex]] [Search INSPIRE].
[1214] M. Ablikim et al., arXiv:1611.01317 [hep-ex] [Search INSPIRE].
[1215] M. Ablikim et al., arXiv:1610.07044 [hep-ex] [Search INSPIRE].
[1216] M. Ablikim et al., Phys. Rev. Lett. **114**, 092003 (2015) [arXiv:1410.6538 [hep-ex]] [Search INSPIRE].
[1217] C. P. Shen et al., Phys. Rev. Lett. **104**, 112004 (2010) [arXiv:0912.2383 [hep-ex]] [Search INSPIRE].
[1218] X. L. Wang et al., Phys. Rev. Lett. **99**, 142002 (2007) [arXiv:0707.3699 [hep-ex]] [Search INSPIRE].
[1219] J. P. Lees et al., Phys. Rev. D **89**, 111103 (2014) [arXiv:1211.6271 [hep-ex]] [Search INSPIRE].
[1220] M. Ablikim et al., Phys. Rev. D **93**, 011102 (2016) [arXiv:1511.08564 [hep-ex]] [Search INSPIRE].
[1221] G. Pakhlova et al., Phys. Rev. Lett. **100**, 062001 (2008) [arXiv:0708.3313 [hep-ex]] [Search INSPIRE].
[1222] S. K. Choi et al., Phys. Rev. Lett. **100**, 142001 (2008) [arXiv:0708.1790 [hep-ex]] [Search INSPIRE].
[1223] R. Mizuk et al., Phys. Rev. D **80**, 031104 (2009) [arXiv:0905.2869 [hep-ex]] [Search INSPIRE].
[1224] K. Chilikin et al., Phys. Rev. D **88**, 074026 (2013) [arXiv:1306.4894 [hep-ex]] [Search INSPIRE].
[1225] B. Aubert et al., Phys. Rev. D **79**, 112001 (2009) [arXiv:0811.0564 [hep-ex]] [Search INSPIRE].
[1226] R. Aaij et al., Phys. Rev. Lett. **112**, 222002 (2014) [arXiv:1404.1903 [hep-ex]] [Search INSPIRE].
[1227] R. Aaij et al., Phys. Rev. D **92**, 112009 (2015) [arXiv:1510.01951 [hep-ex]] [Search INSPIRE].
[1228] G. Pakhlova et al., Phys. Rev. Lett. **101**, 172001 (2008) [arXiv:0807.4458 [hep-ex]] [Search INSPIRE].
[1229] B. Aubert et al., Phys. Rev. Lett. **96**, 232001 (2006) [arXiv:hep-ex/0604031] [Search INSPIRE].
[1230] B. Aubert et al., Phys. Rev. D **78**, 112002 (2008) [arXiv:0807.2014 [hep-ex]] [Search INSPIRE].
[1231] A. Sokolov et al., Phys. Rev. D **75**, 071103 (2007) [arXiv:hep-ex/0611026] [Search INSPIRE].
[1232] A. Sokolov et al., Phys. Rev. D **79**, 051103 (2009) [arXiv:0901.1431 [hep-ex]] [Search INSPIRE].
[1233] K. F. Chen et al., Phys. Rev. Lett. **100**, 112001 (2008) [arXiv:0710.2577 [hep-ex]] [Search INSPIRE].
[1234] X. H. He et al., Phys. Rev. Lett. **113**, 142001 (2014) [arXiv:1408.0504 [hep-ex]] [Search INSPIRE].
[1235] A. Abdesselam et al., arXiv:1609.08749 [hep-ex] [Search INSPIRE].
[1236] D. Santel et al., Phys. Rev. D **93**, 011101 (2016) [arXiv:1501.01137 [hep-ex]] [Search INSPIRE].
[1237] L. Maiani et al., Phys. Rev. D **89**, 114010 (2014) [arXiv:1405.1551 [hep-ph]] [Search INSPIRE].
[1238] A. E. Bondar et al., Phys. Rev. D **84**, 054010 (2011) [arXiv:1105.4473 [hep-ph]] [Search INSPIRE].
[1239] M. B. Voloshin, Phys. Rev. D **71**, 114003 (2005) [arXiv:hep-ph/0504197] [Search INSPIRE].
[1240] F.-K. Guo and U. Meißner, Phys. Rev. D **86**, 091501 (2012) [arXiv:1208.1134 [hep-ph]] [Search INSPIRE].
[1241] S. Olsen, Phys. Rev. D **91**, 057501 (2015) [arXiv:1410.6534 [hep-ex]] [Search INSPIRE].
[1242] Z.-Y. Zhou et al., Phys. Rev. Lett. **115**, 022001 (2015) [arXiv:1501.00879 [hep-ph]] [Search INSPIRE].
[1243] V. Baru et al., arXiv:1703.01230 [hep-ph] [Search INSPIRE].
[1244] G. Cotugno et al., Phys. Rev. Lett. **104**, 132005 (2010) [arXiv:0911.2178 [hep-ph]] [Search INSPIRE].
[1245] F.-K. Guo et al., Phys. Rev. D **82**, 094008 (2010) [arXiv:1005.2055 [hep-ph]] [Search INSPIRE].

[1246] S. Godfrey and K. Moats, Phys. Rev. D **92**, 054034 (2015) [arXiv:1507.00024 [hep-ph]] [Search INSPIRE].
[1247] A. G. Drutskoy et al., Eur. Phys. J. A **49**, 7 (2013) [arXiv:1210.6623 [hep-ph]] [Search INSPIRE].
[1248] T. Mehen and J. Powell, Phys. Rev. D **88**, 034017 (2013) [arXiv:1306.5459 [hep-ph]] [Search INSPIRE].
[1249] L. Maiani et al., Phys. Lett. B **749**, 289 (2015) [arXiv:1507.04980 [hep-ph]] [Search INSPIRE].
[1250] L. Roca et al., Phys. Rev. D **92**, 094003 (2015) [arXiv:1507.04249 [hep-ph]] [Search INSPIRE].
[1251] U. Meißner and J. A. Oller, Phys. Lett. B **751**, 59 (2015) [arXiv:1507.07478 [hep-ph]] [Search INSPIRE].
[1252] F.-K. Guo et al., Phys. Rev. D **92**, 071502 (2015) [arXiv:1507.04950 [hep-ph]] [Search INSPIRE].
[1253] C. J. Morningstar and M. J. Peardon, Phys. Rev. D **60**, 034509 (1999) [arXiv:hep-lat/9901004] [Search INSPIRE].
[1254] T. Barnes et al., Phys. Rev. D **52**, 5242 (1995) [arXiv:hep-ph/9501405] [Search INSPIRE].
[1255] D. V. Bugg, Phys. Lett. B **598**, 8 (2004) [arXiv:hep-ph/0406293] [Search INSPIRE].
[1256] D. V. Bugg, Europhys. Lett. **96**, 11002 (2011) [arXiv:1105.5492 [hep-ph]] [Search INSPIRE].
[1257] D.-Y. Chen and X. Liu, Phys. Rev. D **84**, 094003 (2011) [arXiv:1106.3798 [hep-ph]] [Search INSPIRE].
[1258] D.-Y. Chen and X. Liu, Phys. Rev. D **84**, 034032 (2011) [arXiv:1106.5290 [hep-ph]] [Search INSPIRE].
[1259] C.-Y. Chen et al., Phys. Rev. D **84**, 074032 (2011) [arXiv:1108.4458 [hep-ph]] [Search INSPIRE].
[1260] D.-Y. Chen et al., Phys. Rev. D **88**, 036008 (2013) [arXiv:1304.5845 [hep-ph]] [Search INSPIRE].
[1261] D.-Y. Chen et al., Phys. Rev. Lett. **110**, 232001 (2013) [arXiv:1303.6842 [hep-ph]] [Search INSPIRE].
[1262] E. S. Swanson, Phys. Rev. D **91**, 034009 (2015) [arXiv:1409.3291 [hep-ph]] [Search INSPIRE].
[1263] F.-K. Guo et al., Phys. Rev. D **91**, 051504 (2015) [arXiv:1411.5584 [hep-ph]] [Search INSPIRE].
[1264] E. S. Swanson, arXiv:1504.07952 [hep-ph] [Search INSPIRE].
[1265] V. Baru et al., Eur. Phys. J. A **44**, 93 (2010) [arXiv:1001.0369 [hep-ph]] [Search INSPIRE].
[1266] C. Hanhart et al., Eur. Phys. J. A **47**, 101 (2011) [arXiv:1106.1185 [hep-ph]] [Search INSPIRE].
[1267] P. G. Ortega et al., Phys. Rev. D **81**, 054023 (2010) [arXiv:1001.3948 [hep-ph]] [Search INSPIRE].
[1268] P. G. Ortega et al., Phys. Rev. D **81**, 0054023 (2010) [arXiv:0907.3997 [hep-ph]] [Search INSPIRE].
[1269] Z.-Y. Zhou and Z. Xiao, Eur. Phys. J. A **50**, 165 (2014) [arXiv:1309.1949 [hep-ph]] [Search INSPIRE].
[1270] E. Cincioglu et al., arXiv:1606.03239 [hep-ph] [Search INSPIRE].
[1271] M. Gell-Mann, Phys. Lett. **8**, 214 (1964).
[1272] C. Alexandrou et al., Phys. Rev. Lett. **97**, 222002 (2006) [arXiv:hep-lat/0609004] [Search INSPIRE].
[1273] R. L. Jaffe and F. Wilczek, Phys. Rev. Lett. **91**, 232003 (2003) [arXiv:hep-ph/0307341] [Search INSPIRE].
[1274] L. Maiani et al., Phys. Rev. Lett. **93**, 212002 (2004) [arXiv:hep-ph/0407017] [Search INSPIRE].
[1275] G. 't Hooft et al., Phys. Lett. B **662**, 424 (2008) [arXiv:0801.2288 [hep-ph]] [Search INSPIRE].
[1276] R. L. Jaffe, Phys. Rept. **409**, 1 (2005) [arXiv:hep-ph/0409065] [Search INSPIRE].
[1277] L. Maiani et al., Phys. Rev. D **71**, 014028 (2005) [arXiv:hep-ph/0412098] [Search INSPIRE].
[1278] L. Maiani et al., arXiv:1712.05296 [hep-ph] [Search INSPIRE].
[1279] A. Ali et al., Eur. Phys. J. C **78**, 29 (2018) [arXiv:1708.04650 [hep-ph]] [Search INSPIRE].
[1280] S. J. Brodsky et al., Phys. Rev. Lett. **113**, 112001 (2014) [arXiv:1406.7281 [hep-ph]] [Search INSPIRE].
[1281] A. Ali et al., Phys. Rev. D **91**, 017502 (2015) [arXiv:1412.2049 [hep-ph]] [Search INSPIRE].
[1282] G. C. Rossi and G. Veneziano, Nucl. Phys. B **123**, 507 (1977).
[1283] G. C. Rossi and G. Veneziano, Phys. Lett. B **70**, 255 (1977).
[1284] L. Montanet et al., Phys. Rept. **63**, 149 (1980).
[1285] L. Maiani et al., Phys. Rev. D **94**, 054026 (2016) [arXiv:1607.02405 [hep-ph]] [Search INSPIRE].
[1286] A. Ali et al., Phys. Rev. D **85**, 054011 (2012) [arXiv:1110.1333 [hep-ph]] [Search INSPIRE].
[1287] A. Esposito et al., Phys. Lett. B **758**, 292 (2016) [arXiv:1603.07667 [hep-ph]] [Search INSPIRE].
[1288] M. Papinutto et al., arXiv:1311.7374 [hep-ph] [Search INSPIRE].
[1289] A. L. Guerrieri et al., Phys. Rev. D **90**, 034003 (2014) [arXiv:1405.7929 [hep-ph]] [Search INSPIRE].
[1290] C. Bignamini et al., Phys. Rev. Lett. **103**, 162001 (2009) [arXiv:0906.0882 [hep-ph]] [Search INSPIRE].

[1291] A. Esposito et al., Phys. Rev. D **92**, 034028 (2015) [arXiv:1508.00295 [hep-ph]] [Search INSPIRE].
[1292] P. Artoisenet and E. Braaten, Phys. Rev. D **81**, 114018 (2010) [arXiv:0911.2016 [hep-ph]] [Search INSPIRE].
[1293] C. Bignamini et al., Phys. Lett. B **684**, 228 (2010) [arXiv:0912.5064 [hep-ph]] [Search INSPIRE].
[1294] F.-K. Guo et al., Eur. Phys. J. C **74**, 3063 (2014) [arXiv:1402.6236 [hep-ph]] [Search INSPIRE].
[1295] M. Albaladejo et al., Chin. Phys. C **41**, 121001 (2017) [arXiv:1709.09101 [hep-ph]] [Search INSPIRE].
[1296] M. S. Chanowitz and S. R. Sharpe, Nucl. Phys. B **222**, 211 (1983); **228**, 588 (1983) [erratum].
[1297] T. Barnes et al., Nucl. Phys. B **224**, 241 (1983).
[1298] S. R. Cotanch and F. J. Llanes-Estrada, Nucl. Phys. A **689**, 481 (2001).
[1299] I. J. General et al., Eur. Phys. J. C **51**, 347 (2007) [arXiv:hep-ph/0609115] [Search INSPIRE].
[1300] F. J. Llanes-Estrada and S. R. Cotanch, Phys. Lett. B **504**, 15 (2001) [arXiv:hep-ph/0008337] [Search INSPIRE].
[1301] E. Abreu and P. Bicudo, J. Phys. G **34**, 195207 (2007) [arXiv:hep-ph/0508281] [Search INSPIRE].
[1302] D. Horn and J. Mandula, Phys. Rev. D **17**, 898 (1978).
[1303] A. Le Yaouanc et al., Z. Phys. C **28**, 309 (1985).
[1304] F. Iddir et al., Phys. Lett. B **433**, 125 (1998) [arXiv:hep-ph/9803470] [Search INSPIRE].
[1305] Y. A. Simonov, QCD and topics in hadron physics, in QCD: Perturbative or nonperturbative? Proc. 17th Autumn School, Lisbon, Portugal, September 29–October 4, p. 60 (1999) [arXiv:hep-ph/9911237] [Search INSPIRE].
[1306] Y. A. Simonov, Phys. Atom. Nucl. **64**, 1876 (2001), [arXiv:hep-ph/0110033] [Search INSPIRE].
[1307] Y. S. Kalashnikova and Y. B. Yufryakov, Phys. Lett. B **359**, 175 (1995) [arXiv:hep-ph/9506269] [Search INSPIRE].
[1308] Y. A. Simonov, Phys. Atom. Nucl. **68**, 1294 (2005) [arXiv:hep-ph/0406290] [Search INSPIRE].
[1309] Y. S. Kalashnikova and D. S. Kuzmenko, Phys. Atom. Nucl. **66**, 955 (2003), [arXiv:hep-ph/0203128] [Search INSPIRE].
[1310] F. Buisseret and C. Semay, Phys. Rev. D **74**, 114018 (2006) [arXiv:hep-ph/0610132] [Search INSPIRE].
[1311] F. Buisseret et al., Eur. Phys. J. A **32**, 123 (2007) [arXiv:hep-ph/0703020] [Search INSPIRE].
[1312] Y. S. Kalashnikova and A. V. Nefediev, Phys. Rev. D **77**, 054025 (2008) [arXiv:0801.2036 [hep-ph]] [Search INSPIRE].
[1313] Y. Kalashnikova et al., Phys. Rev. D **94**, 114007 (2016) [arXiv:1611.10066 [hep-ph]] [Search INSPIRE].
[1314] N. Isgur and J. E. Paton, Phys. Rev. D **31**, 2910 (1985).
[1315] F. Buisseret and V. Mathieu, Eur. Phys. J. A **29**, 343 (2006) [arXiv:hep-ph/0607083] [Search INSPIRE].
[1316] J. Merlin and J. E. Paton, Phys. Rev. D **35**, 1668 (1987).
[1317] E. Braaten et al., Phys. Rev. Lett. **112**, 222001 (2014) [arXiv:1401.7351 [hep-ph]] [Search INSPIRE].
[1318] Y. S. Kalashnikova, Z. Phys. C **62**, 323 (1994).
[1319] E. Kou and O. Pene, Phys. Lett. B **631**, 164 (2005) [arXiv:hep-ph/0507119] [Search INSPIRE].
[1320] N. Isgur, R. Kokoski, and J. Paton, Phys. Rev. Lett. **54**, 869 (1985).
[1321] Y. S. Kalashnikova, Phys. Rev. D **72**, 034010 (2005) [arXiv:hep-ph/0506270] [Search INSPIRE].
[1322] E. Eichten et al., Phys. Rev. D **17**, 3090 (1978); **21**, 313 (1980) [erratum].
[1323] X. Li and M. B. Voloshin, Phys. Rev. D **88**, 034012 (2013) [arXiv:1307.1072 [hep-ph]] [Search INSPIRE].
[1324] J. M. Torres-Rincon and F. J. Llanes-Estrada, Phys. Rev. Lett. **105**, 022003 (2010) [arXiv:1003.5989 [hep-ph]] [Search INSPIRE].
[1325] F. E. Close, Phys. Lett. B **342**, 369 (1995) [arXiv:hep-ph/9409203] [Search INSPIRE].
[1326] I. Dunietz et al., Eur. Phys. J. C **1**, 211 (1998) [arXiv:hep-ph/9612421] [Search INSPIRE].
[1327] F. E. Close et al., Phys. Rev. D **57**, 5653 (1998) [arXiv:hep-ph/9708265] [Search INSPIRE].
[1328] G. Chiladze et al., Phys. Rev. D **58**, 034013 (1998) [arXiv:hep-ph/9804248] [Search INSPIRE].
[1329] F. E. Close and P. R. Page, Phys. Lett. B **628**, 215 (2005) [arXiv:hep-ph/0507199] [Search INSPIRE].
[1330] G. Pakhlova et al., Phys. Rev. D **80**, 091101 (2009) [arXiv:0908.0231 [hep-ex]] [Search INSPIRE].
[1331] M. B. Voloshin, Prog. Part. Nucl. Phys. **61**, 455 (2008) [arXiv:0711.4556 [hep-ph]] [Search INSPIRE].

[1332] S. Dubynskiy and M. B. Voloshin, Phys. Lett. B **666**, 344 (2008) [arXiv:0803.2224 [hep-ph]] [Search INSPIRE].
[1333] X. Li and M. B. Voloshin, Mod. Phys. Lett. A **29**, 1450060 (2014) [arXiv:1309.1681 [hep-ph]] [Search INSPIRE].
[1334] M. Cleven et al., Phys. Rev. D **92**, 014005 (2015) [arXiv:1505.01771 [hep-ph]] [Search INSPIRE].
[1335] F.-K. Guo et al., Rev. Mod. Phys. **90**, 015004 (2018) [arXiv:1705.00141 [hep-ph]] [Search INSPIRE].
[1336] S. Weinberg, Phys. Rev. **130**, 776 (1963).
[1337] E. Braaten and H. W. Hammer, Phys. Rept. **428**, 259 (2006) [arXiv:cond-mat/0410417] [Search INSPIRE].
[1338] T. Hyodo, Int. J. Mod. Phys. A **28**, 1330045 (2013) [arXiv:1310.1176 [hep-ph]] [Search INSPIRE].
[1339] T. Sekihara et al., Prog. Theor. Exp. Phys. **2015**, 063D04 (2015) [arXiv:1411.2308 [hep-ph]] [Search INSPIRE].
[1340] F. Aceti et al., Int. J. Mod. Phys. Conf. Ser. **26**, 1460077 (2014) [arXiv:1301.2554 [hep-ph]] [Search INSPIRE].
[1341] Z.-H. Guo and J. A. Oller, Phys. Rev. D **93**, 096001 (2016) [arXiv:1508.06400 [hep-ph]] [Search INSPIRE].
[1342] M. Cleven et al., Phys. Rev. D **90**, 074039 (2014) [arXiv:1310.2190 [hep-ph]] [Search INSPIRE].
[1343] W. Qin et al., Phys. Rev. D **94**, 054035 (2016) [arXiv:1605.02407 [hep-ph]] [Search INSPIRE].
[1344] C. Hanhart, arXiv:1712.01136 [hep-ph] [Search INSPIRE].
[1345] A. A. Filin et al., Phys. Rev. Lett. **105**, 019101 (2010) [arXiv:1004.4789 [hep-ph]] [Search INSPIRE].
[1346] F.-K. Guo and U. Meißner, Phys. Rev. D **84**, 014013 (2011) [arXiv:1102.3536 [hep-ph]] [Search INSPIRE].
[1347] N. A. Törnqvist, Z. Phys. C **61**, 525 (1994) [arXiv:hep-ph/9310247] [Search INSPIRE].
[1348] J. Nieves and M. P. Valderrama, Phys. Rev. D **86**, 056004 (2012), [arXiv:1204.2790 [hep-ph]] [Search INSPIRE].
[1349] F.-K. Guo et al., Phys. Rev. Lett. **102**, 242004 (2009) [arXiv:0904.3338 [hep-ph]] [Search INSPIRE].
[1350] C. Hidalgo-Duque et al., Phys. Lett. B **727**, 432 (2013) [arXiv:1305.4487 [hep-ph]] [Search INSPIRE].
[1351] M. B. Voloshin, Phys. Rev. D **84**, 031502 (2011) [arXiv:1105.5829 [hep-ph]] [Search INSPIRE].
[1352] T. Mehen and J. W. Powell, Phys. Rev. D **84**, 114013 (2011) [arXiv:1109.3479 [hep-ph]] [Search INSPIRE].
[1353] F.-K. Guo et al., Phys. Rev. D **88**, 054007 (2013) [arXiv:1303.6608 [hep-ph]] [Search INSPIRE].
[1354] V. Baru et al., Phys. Lett. B **763**, 20 (2016) [arXiv:1605.09649 [hep-ph]] [Search INSPIRE].
[1355] V. Baru et al., J. High Energy Phys. **06**, 158 (2017) [arXiv:1704.07332 [hep-ph]] [Search INSPIRE].
[1356] M. Albaladejo et al., Eur. Phys. J. C **75**, 547 (2015) [arXiv:1504.00861 [hep-ph]] [Search INSPIRE].
[1357] Q. Wang, V. Baru, A. A. Filin, C. Hanhart, A. V. Nefediev, and J. L Wynen, Phys. Rev. D **98**, 074023 (2018) [arXiv:1805.07453 [hep-ph]] [Search INSPIRE].
[1358] T. Barnes et al., Phys. Rev. D **68**, 054006 (2003) [arXiv:hep-ph/0305025] [Search INSPIRE].
[1359] E. van Beveren and G. Rupp, Phys. Rev. Lett. **91**, 012003 (2003) [arXiv:hep-ph/0305035] [Search INSPIRE].
[1360] E. E. Kolomeitsev and M. F. M. Lutz, Phys. Lett. B **582**, 39 (2004) [arXiv:hep-ph/0307133] [Search INSPIRE].
[1361] F.-K. Guo et al., Phys. Lett. B **641**, 278 (2006) [arXiv:hep-ph/0603072] [Search INSPIRE].
[1362] Y.-J. Zhang et al., Phys. Rev. D **74**, 014013 (2006) [arXiv:hep-ph/0604271] [Search INSPIRE].
[1363] M. Cleven et al., Eur. Phys. J. A **50**, 149 (2014) [arXiv:1405.2242 [hep-ph]] [Search INSPIRE].
[1364] S. Fajfer and A. Prapotnik Brdnik, Phys. Rev. D **92**, 074047 (2015) [arXiv:1506.02716 [hep-ph]] [Search INSPIRE].
[1365] S. Fajfer and A. Prapotnik Brdnik, Eur. Phys. J. C **76**, 537 (2016) [arXiv:1606.06943 [hep-ph]] [Search INSPIRE].
[1366] L. Liu et al., Phys. Rev. D **87**, 014508 (2013) [arXiv:1208.4535 [hep-lat]] [Search INSPIRE].
[1367] M. Albaladejo, Phys. Lett. B **767**, 465 (2017) [arXiv:1610.06727 [hep-ph]] [Search INSPIRE].
[1368] M.-L. Du et al., Phys. Rev. D **98**, 094018 (2018) [arXiv:1712.07957 [hep-ph]] [Search INSPIRE].
[1369] R. Aaij et al., Phys. Rev. D **90**, 072003 (2014) [arXiv:1407.7712 [hep-ex]] [Search INSPIRE].
[1370] N. A. Tornqvist, Phys. Lett. B **590**, 209 (2004) [arXiv:hep-ph/0402237] [Search INSPIRE].
[1371] E. S. Swanson, Phys. Lett. B **588**, 189 (2004) [arXiv:hep-ph/0311229] [Search INSPIRE].

[1372] D. Gamermann and E. Oset, Phys. Rev. D **80**, 014003 (2009) [arXiv:0905.0402 [hep-ph]] [Search INSPIRE].
[1373] T. Mehen, Phys. Rev. D **92**, 034019 (2015) [arXiv:1503.02719 [hep-ph]] [Search INSPIRE].
[1374] Q. Wang et al., Phys. Rev. Lett. **111**, 132003 (2013) [arXiv:1303.6355 [hep-ph]] [Search INSPIRE].
[1375] M. Cleven et al., Eur. Phys. J. A **47**, 120 (2011) [arXiv:1107.0254 [hep-ph]] [Search INSPIRE].
[1376] M. Albaladejo et al., Phys. Lett. B **755**, 337 (2016) [arXiv:1512.03638 [hep-ph]] [Search INSPIRE].
[1377] C. Hanhart et al., Phys. Lett. B **739**, 375 (2014) [arXiv:1407.7452 [hep-ph]] [Search INSPIRE].
[1378] A. Esposito et al., Phys. Lett. B **746**, 194 (2015) [arXiv:1409.3551 [hep-ph]] [Search INSPIRE].
[1379] F-K. Guo et al., Phys. Lett. B **725**, 127 (2013) [arXiv:1306.3096 [hep-ph]] [Search INSPIRE].
[1380] G.-J. Ding, Phys. Rev. D **79**, 014001 (2009) [arXiv:0809.4818 [hep-ph]] [Search INSPIRE].
[1381] Q. Wang et al., Phys. Rev. D **89**, 034001 (2014) [arXiv:1309.4303 [hep-ph]] [Search INSPIRE].
[1382] L. Ma et al., Phys. Rev. D **91**, 034032 (2015) [arXiv:1406.6879 [hep-ph]] [Search INSPIRE].
[1383] A. E. Bondar and M. B. Voloshin, Phys. Rev. D **93**, 094008 (2016) [arXiv:1603.08436 [hep-ph]] [Search INSPIRE].
[1384] F.-K. Guo et al., Phys. Rev. Lett. **103**, 082003 (2009); **104**, 109901 (2010) [erratum] [arXiv:0907.0521 [hep-ph]] [Search INSPIRE].
[1385] F.-K. Guo and U.-G. Meißner, Phys. Rev. Lett. **108**, 112002 (2012) [arXiv:1111.1151 [hep-ph]] [Search INSPIRE].
[1386] F.-K. Guo et al., Phys. Lett. B **760**, 417 (2016) [arXiv:1604.00770 [hep-ph]] [Search INSPIRE].
[1387] F.-K. Guo et al., Phys. Rev. D **83**, 034013 (2011) [arXiv:1008.3632 [hep-ph]] [Search INSPIRE].
[1388] F.-K. Guo et al., Phys. Rev. Lett. **105**, 162001 (2010) [arXiv:1007.4682 [hep-ph]] [Search INSPIRE].
[1389] D. M. J. Lovelock et al., Phys. Rev. Lett. **54**, 377 (1985).
[1390] D. Besson et al., Phys. Rev. Lett. **54**, 381 (1985).
[1391] N. A. Tornqvist, Phys. Rev. Lett. **53**, 878 (1984).
[1392] C. Meng and K.-T. Chao, Phys. Rev. D **77**, 074003 (2008) [arXiv:0712.3595 [hep-ph]] [Search INSPIRE].
[1393] Y. A. Simonov and A. I. Veselov, Phys. Lett. B **671**, 55 (2009) [arXiv:0805.4499 [hep-ph]] [Search INSPIRE].
[1394] R. Kaiser et al., Phys. Rev. Lett. **90**, 142001 (2003) [arXiv:hep-ph/0208194] [Search INSPIRE].
[1395] M. B. Voloshin, Phys. Rev. D **85**, 034024 (2012) [arXiv:1201.1222 [hep-ph]] [Search INSPIRE].
[1396] A. E. Bondar et al., Mod. Phys. Lett. A **32**, 1750025 (2017) [arXiv:1610.01102 [hep-ph]] [Search INSPIRE].
[1397] Y. Lu et al., Phys. Rev. D **95**, 034018 (2017) [arXiv:1701.00692 [hep-ph]] [Search INSPIRE].
[1398] V. Bernard et al., J. High Energy Phys. **01**, 019 (2011) [arXiv:1010.6018 [hep-lat]] [Search INSPIRE].
[1399] M. Göckeler et al., Phys. Rev. D **86**, 094513 (2012) [arXiv:1206.4141 [hep-lat]] [Search INSPIRE].
[1400] M. Döring et al., Eur. Phys. J. A **47**, 139 (2011) [arXiv:1107.3988 [hep-lat]] [Search INSPIRE].
[1401] M. Döring et al., Eur. Phys. J. A **47**, 163 (2011) [arXiv:1108.0676 [hep-lat]] [Search INSPIRE].
[1402] M. Döring et al., Eur. Phys. J. A **48**, 114 (2012) [arXiv:1205.4838 [hep-lat]] [Search INSPIRE].
[1403] Z.-H. Guo et al., Phys. Rev. D **95**, 054004 (2017) [arXiv:1609.08096 [hep-ph]] [Search INSPIRE].
[1404] D. Agadjanov et al., J. High Energy Phys. **06**, 043 (2016) [arXiv:1603.07205 [hep-lat]] [Search INSPIRE].
[1405] G. S. Bali et al., Phys. Rev. D **84**, 094506 (2011) [arXiv:1110.2381 [hep-lat]] [Search INSPIRE].
[1406] S. Sasaki and T. Yamazaki, Phys. Rev. D **74**, 114507 (2006) [arXiv:hep-lat/0610081] [Search INSPIRE].
[1407] V. Baru et al., Phys. Lett. B **726**, 537 (2013) [arXiv:1306.4108 [hep-ph]] [Search INSPIRE].
[1408] M. Jansen et al., Phys. Rev. D **89**, 014033 (2014) [arXiv:1310.6937 [hep-ph]] [Search INSPIRE].
[1409] M. Padmanath et al., Phys. Rev. D **92**, 034501 (2015) [arXiv:1503.03257 [hep-lat]] [Search INSPIRE].
[1410] E. J. Garzon et al., Phys. Rev. D **89**, 014504 (2014) [arXiv:1310.0972 [hep-lat]] [Search INSPIRE].
[1411] S. Ozaki and S. Sasaki, Phys. Rev. D **87**, 014506 (2013) [arXiv:1211.5512 [hep-lat]] [Search INSPIRE].
[1412] S. Aoki et al., Phys. Rev. D **87**, 034512 (2013) [arXiv:1212.4896 [hep-lat]] [Search INSPIRE].
[1413] Y. Chen et al., Phys. Rev. D **89**, 094506 (2014) [arXiv:1403.1318 [hep-lat]] [Search INSPIRE].
[1414] S. Prelovsek et al., Phys. Rev. D **91**, 014504 (2015) [arXiv:1405.7623 [hep-lat]] [Search INSPIRE].
[1415] M. Albaladejo et al., Eur. Phys. J. C **76**, 573 (2016) [arXiv:1606.03008 [hep-ph]] [Search INSPIRE].

[1416] G. Bali and M. Hetzenegger, PoS **LATTICE2010**, 142 (2010) [arXiv:1011.0571 [hep-lat]] [Search INSPIRE].
[1417] G. Bali and M. Hetzenegger, PoS **LATTICE2011**, 123 (2011) [arXiv:1111.2222 [hep-lat]] [Search INSPIRE].
[1418] G. S. Bali et al., Phys. Rev. D **71**, 114513 (2005) [arXiv:hep-lat/0505012] [Search INSPIRE].
[1419] Z. S. Brown and K. Orginos, Phys. Rev. D **86**, 114506 (2012) [arXiv:1210.1953 [hep-lat]] [Search INSPIRE].
[1420] P. Bicudo et al., Phys. Rev. D **92**, 014507 (2015) [arXiv:1505.00613 [hep-lat]] [Search INSPIRE].
[1421] P. Bicudo et al., Phys. Rev. D **93**, 034501 (2016) [arXiv:1510.03441 [hep-lat]] [Search INSPIRE].
[1422] Y. Ikeda et al., Phys. Lett. B **729**, 85 (2014) [arXiv:1311.6214 [hep-lat]] [Search INSPIRE].
[1423] A. L. Guerrieri et al., PoS **LATTICE2014**, 106 (2015) [arXiv:1411.2247 [hep-lat]] [Search INSPIRE].
[1424] A. Francis et al., Phys. Rev. Lett. **118**, 142001 (2017) [arXiv:1607.05214 [hep-lat]] [Search INSPIRE].
[1425] D. Janc and M. Rosina, Few Body Syst. **35**, 175 (2004) [arXiv:hep-ph/0405208] [Search INSPIRE].
[1426] A. Del Fabbro et al., Phys. Rev. D **71**, 014008 (2005) [arXiv:hep-ph/0408258] [Search INSPIRE].
[1427] M. Alberti et al., Phys. Rev. D **95**, 074501 (2017) [arXiv:1608.06537 [hep-lat]] [Search INSPIRE].
[1428] X. Liao and T. Manke, Phys. Rev. D **65**, 074508 (2002) [arXiv:hep-lat/0111049] [Search INSPIRE].
[1429] C. Michael, [arXiv:hep-ph/0308293] [Search INSPIRE].
[1430] Y. Liu and X.-Q. Luo, Phys. Rev. D **73**, 054510 (2006) [arXiv:hep-lat/0511015] [Search INSPIRE].
[1431] X.-Q. Luo and Y. Liu, Phys. Rev. D **74**, 034502 (2006); **74**, 039902 (2006) [erratum] [arXiv:hep-lat/0512044] [Search INSPIRE].
[1432] T. Burch and C. Ehmann, Nucl. Phys. A **797**, 33 (2007) [arXiv:hep-lat/0701001] [Search INSPIRE].
[1433] J. J. Dudek et al., Phys. Rev. D **77**, 034501 (2008) [arXiv:0707.4162 [hep-lat]] [Search INSPIRE].
[1434] J. J. Dudek and E. Rrapaj, Phys. Rev. D **78**, 094504 (2008) [arXiv:0809.2582 [hep-ph]] [Search INSPIRE].
[1435] M. Foster and C. Michael, Phys. Rev. D **59**, 094509 (1999) [arXiv:hep-lat/9811010] [Search INSPIRE].
[1436] S. R. Beane, E. Chang, S. D. Cohen, W. Detmold, H.-W. Lin, K. Orginos, A. Parreño, and M. J. Savage, Phys. Rev. D **91**, 114503 (2015) [arXiv:1410.7069 [hep-lat]] [Search INSPIRE].
[1437] J. J. Dudek et al., Phys. Rev. D **93**, 094506 (2016) [arXiv:1602.05122 [hep-ph]] [Search INSPIRE].
[1438] R. A. Briceno et al., Chin. Phys. C **40**, 042001 (2016) [arXiv:1511.06779 [hep-ph]] [Search INSPIRE].
[1439] A. Esposito et al., Int. J. Mod. Phys. A **30**, 1530002 (2015) [arXiv:1411.5997 [hep-ph]] [Search INSPIRE].
[1440] R. Oncala and J. Soto, Phys. Rev. D **96**, 014004 (2017) [arXiv:1702.03900 [hep-ph]] [Search INSPIRE].
[1441] N. Brambilla et al., Phys. Rev. D **93**, 054002 (2016) [arXiv:1510.05895 [hep-ph]] [Search INSPIRE].
[1442] S. K. Choi et al., Phys. Rev. Lett. **89**, 102001 (2002); **89**, 129901 (2002) [erratum] [arXiv:hep-ex/0206002] [Search INSPIRE].
[1443] E. J. Eichten et al., Phys. Rev. Lett. **89**, 162002 (2002) [arXiv:hep-ph/0206018] [Search INSPIRE].
[1444] T. Barnes et al., Phys. Rev. D **72**, 054026 (2005) [arXiv:hep-ph/0505002] [Search INSPIRE].
[1445] A. Vinokurova et al., J. High Energy Phys. **06**, 132 (2015) [arXiv:1501.06351 [hep-ex]] [Search INSPIRE].
[1446] T. Iwashita et al., Prog. Theor. Exp. Phys. **2014**, 043C01 (2014) [arXiv:1310.2704 [hep-ex]] [Search INSPIRE].
[1447] V. Bhardwaj et al., Phys. Rev. D **93**, 052016 (2016) [arXiv:1512.02672 [hep-ex]] [Search INSPIRE].
[1448] D.-Y. Chen, Eur. Phys. J. C **76**, 671 (2016) [arXiv:1611.00109 [hep-ph]] [Search INSPIRE].
[1449] A. Bala et al., Phys. Rev. D **91**, 051101 (2015) [arXiv:1501.06867 [hep-ex]] [Search INSPIRE].
[1450] B. Aubert et al., Phys. Rev. Lett. **96**, 052002 (2006) [arXiv:hep-ex/0510070] [Search INSPIRE].
[1451] V. N. Baier and V. S. Fadin, Phys. Lett. B **27**, 223 (1968).
[1452] A. B. Arbuzov et al., J. High Energy Phys. **12**, 009 (1998) [arXiv:hep-ph/9804430] [Search INSPIRE].
[1453] S. Binner et al., Phys. Lett. B **459**, 279 (1999) [arXiv:hep-ph/9902399] [Search INSPIRE].
[1454] M. Benayoun et al., Mod. Phys. Lett. A **14**, 2605 (1999) [arXiv:hep-ph/9910523] [Search INSPIRE].
[1455] F.-K. Guo et al., Phys. Lett. B **665**, 26 (2008) [arXiv:0803.1392 [hep-ph]] [Search INSPIRE].

[1456] K. Abe et al., arXiv:hep-ex/0612006 [Search INSPIRE].
[1457] B. Aubert et al., Phys. Rev. Lett. **98**, 212001 (2007) [arXiv:hep-ex/0610057] [Search INSPIRE].
[1458] C. P. Shen et al., Phys. Rev. D **89**, 072015 (2014) [arXiv:1402.6578 [hep-ex]] [Search INSPIRE].
[1459] C.-Z. Yuan, Chin. Phys. C **38**, 043001 (2014) [arXiv:1312.6399 [hep-ex]] [Search INSPIRE].
[1460] H. Czyz, J. H. Kuhn, and S. Tracz, Phys. Rev. D **90**, 114021 (2014) [arXiv:1407.7995 [hep-ph]] [Search INSPIRE].
[1461] V. M. Budnev et al., Phys. Rept. **15**, 181 (1975).
[1462] C.-N. Yang, Phys. Rev. **77**, 242 (1950).
[1463] K. Abe et al., Phys. Rev. Lett. **89**, 142001 (2002) [arXiv:hep-ex/0205104] [Search INSPIRE].
[1464] E. Braaten and J. Lee, Phys. Rev. D **67**, 054007 (2003); **72**, 099901 (2005) [erratum] [arXiv:hep-ph/0211085] [Search INSPIRE].
[1465] J. P. Ma and Z. G. Si, Phys. Rev. D **70**, 074007 (2004) [arXiv:hep-ph/0405111] [Search INSPIRE].
[1466] A. E. Bondar and V. L. Chernyak, Phys. Lett. B **612**, 215 (2005) [arXiv:hep-ph/0412335] [Search INSPIRE].
[1467] Y.-J. Zhang et al., Phys. Rev. Lett. **96**, 092001 (2006) [arXiv:hep-ph/0506076] [Search INSPIRE].
[1468] H.-M. Choi and C.-R. Ji, Phys. Rev. D **76**, 094010 (2007) [arXiv:0707.1173 [hep-ph]] [Search INSPIRE].
[1469] K. Abe et al., Phys. Rev. D **70**, 071102 (2004) [arXiv:hep-ex/0407009] [Search INSPIRE].
[1470] B. Aubert et al., Phys. Rev. D **72**, 031101 (2005) [arXiv:hep-ex/0506062] [Search INSPIRE].
[1471] P. Pakhlov et al., Phys. Rev. D **79**, 071101 (2009) [arXiv:0901.2775 [hep-ex]] [Search INSPIRE].
[1472] A. V. Berezhnoy and A. K. Likhoded, Phys. Atom. Nucl. **67**, 757 (2004) [arXiv:hep-ph/0303145] [Search INSPIRE].
[1473] A. V. Berezhnoy and A. K. Likhoded, Phys. Atom. Nucl. **70**, 478 (2007) [arXiv:hep-ph/0602041] [Search INSPIRE].
[1474] Y. Kato et al., Phys. Rev. D **89**, 052003 (2014) [arXiv:1312.1026 [hep-ex]] [Search INSPIRE].
[1475] B. Aubert et al., Phys. Rev. Lett. **101**, 071801 (2008) [arXiv:0807.1086 [hep-ex]] [Search INSPIRE].
[1476] B. Aubert et al., Phys. Rev. Lett. **103**, 161801 (2009) [arXiv:0903.1124 [hep-ex]] [Search INSPIRE].
[1477] G. Bonvicini et al., Phys. Rev. D **81**, 031104 (2010) [arXiv:0909.5474 [hep-ex]] [Search INSPIRE].
[1478] P. Krokovny, talk at ICHEP 2014 (2014).
[1479] S. Sandilya et al., Phys. Rev. Lett. **111**, 112001 (2013) [arXiv:1306.6212 [hep-ex]] [Search INSPIRE].
[1480] S. Dobbs et al., Phys. Rev. Lett. **109**, 082001 (2012) [arXiv:1204.4205 [hep-ex]] [Search INSPIRE].
[1481] M. Artuso et al., Phys. Rev. Lett. **94**, 032001 (2005) [arXiv:hep-ex/0411068] [Search INSPIRE].
[1482] H. S. Chung et al., Phys. Lett. B **697**, 48 (2011) [arXiv:1011.1554 [hep-ph]] [Search INSPIRE].
[1483] M. B. Voloshin, Mod. Phys. Lett. A **19**, 2895 (2004) [arXiv:hep-ph/0410368] [Search INSPIRE].
[1484] S. E. Csorna et al., arXiv:hep-ex/0207060 [Search INSPIRE].
[1485] G. Bonvicini et al., Phys. Rev. D **70**, 032001 (2004) [arXiv:hep-ex/0404021] [Search INSPIRE].
[1486] P. del Amo Sanchez et al., Phys. Rev. D **82**, 111102 (2010) [arXiv:1004.0175 [hep-ex]] [Search INSPIRE].
[1487] E. Rice et al., Phys. Rev. Lett. **48**, 906 (1982).
[1488] P. Moxhay and J. L. Rosner, Phys. Rev. D **28**, 1132 (1983).
[1489] A. M. Badalian et al., Phys. Atom. Nucl. **73**, 138 (2010) [arXiv:0903.3643 [hep-ph]] [Search INSPIRE].
[1490] J. P. Lees et al., Phys. Rev. D **84**, 091101 (2011) [arXiv:1102.4565 [hep-ex]] [Search INSPIRE].
[1491] J. P. Lees et al., Phys. Rev. D **84**, 011104 (2011) [arXiv:1105.4234 [hep-ex]] [Search INSPIRE].
[1492] M. B. Voloshin, Sov. J. Nucl. Phys. **43**, 1011 (1986).
[1493] Y.-P. Kuang and T.-M. Yan, Phys. Rev. D **41**, 155 (1990).
[1494] S. F. Tuan, Mod. Phys. Lett. A **7**, 3527 (1992).
[1495] D. M. Asner et al., Phys. Rev. D **78**, 091103 (2008) [arXiv:0808.0933 [hep-ex]] [Search INSPIRE].
[1496] S. Dobbs et al., Phys. Rev. D **86**, 052003 (2012) [arXiv:1205.5070 [hep-ex]] [Search INSPIRE].
[1497] C. P. Shen et al., Phys. Rev. D **88**, 011102 (2013) [arXiv:1305.5887 [hep-ex]] [Search INSPIRE].
[1498] D. Cronin-Hennessy et al., Phys. Rev. D **76**, 072001 (2007) [arXiv:0706.2317 [hep-ex]] [Search INSPIRE].
[1499] C. Cawlfield et al., Phys. Rev. D **73**, 012003 (2006) [arXiv:hep-ex/0511019] [Search INSPIRE].
[1500] X.-H. Liu et al., Eur. Phys. J. C **73**, 2284 (2013) [arXiv:1212.4066 [hep-ph]] [Search INSPIRE].
[1501] F.-K. Guo et al., Phys. Lett. B **658**, 27 (2007) [arXiv:hep-ph/0601120] [Search INSPIRE].

[1502] Y.-H. Chen et al., Phys. Rev. D **95**, 034022 (2017) [arXiv:1611.00913 [hep-ph]] [Search INSPIRE].
[1503] J. P. Lees et al., Phys. Rev. D **84**, 072002 (2011) [arXiv:1104.5254 [hep-ex]] [Search INSPIRE].
[1504] J. P. Lees et al., Phys. Rev. D **90**, 112010 (2014) [arXiv:1410.3902 [hep-ex]] [Search INSPIRE].
[1505] U. Heintz et al., Phys. Rev. D **46**, 1928 (1992).
[1506] M. Kornicer et al., Phys. Rev. D **83**, 054003 (2011) [arXiv:1012.0589 [hep-ex]] [Search INSPIRE].
[1507] Y.-J. Gao et al., arXiv:hep-ph/0701009 [Search INSPIRE].
[1508] B. Aubert et al., Phys. Rev. Lett. **102**, 012001 (2009) [arXiv:0809.4120 [hep-ex]] [Search INSPIRE].
[1509] S. Ono, A. I. Sanda, and N. A. Tornqvist, Phys. Rev. D **34**, 186 (1986).
[1510] I. Adachi et al., Phys. Rev. Lett. **108**, 032001 (2012) [arXiv:1103.3419 [hep-ex]] [Search INSPIRE].
[1511] C. B. Lang et al., Phys. Lett. B **750**, 17 (2015) [arXiv:1501.01646 [hep-lat]] [Search INSPIRE].
[1512] M. B. Voloshin, Phys. Rev. D **95**, 054017 (2017) [arXiv:1701.03064 [hep-ph]] [Search INSPIRE].
[1513] C. B. Lang et al., Phys. Rev. D **90**, 034510 (2014) [arXiv:1403.8103 [hep-lat]] [Search INSPIRE].
[1514] D. Mohler et al., Phys. Rev. Lett. **111**, 222001 (2013) [arXiv:1308.3175 [hep-lat]] [Search INSPIRE].
[1515] T.-P. Cheng and L.-F. Li, Phys. Rev. D **16**, 1425 (1977).
[1516] B. W. Lee and R. E. Shrock, Phys. Rev. D **16**, 1444 (1977).
[1517] J. R. Ellis et al., Eur. Phys. J. C **14**, 319 (2000) [arXiv:hep-ph/9911459] [Search INSPIRE].
[1518] A. Dedes et al., Phys. Lett. B **549**, 159 (2002) [arXiv:hep-ph/0209207] [Search INSPIRE].
[1519] A. Brignole and A. Rossi, Phys. Lett. B **566**, 217 (2003) [arXiv:hep-ph/0304081] [Search INSPIRE].
[1520] A. Masiero et al., Nucl. Phys. B **649**, 189 (2003) [arXiv:hep-ph/0209303] [Search INSPIRE].
[1521] J. Hisano et al., J. High Energy Phys. **12**, 030 (2009) [arXiv:0904.2080 [hep-ph]] [Search INSPIRE].
[1522] S. R. Choudhury et al., Phys. Rev. D **75**, 055011 (2007) [arXiv:hep-ph/0612327] [Search INSPIRE].
[1523] G. Cvetic et al., Phys. Rev. D **66**, 034008 (2002); **68**, 059901 (2003) [erratum] [arXiv:hep-ph/0202212] [Search INSPIRE].
[1524] S. Davidson et al., Z. Phys. C **61**, 613 (1994) [arXiv:hep-ph/9309310] [Search INSPIRE].
[1525] C.-X. Yue et al., Phys. Lett. B **547**, 252 (2002) [arXiv:hep-ph/0209291] [Search INSPIRE].
[1526] A. G. Akeroyd et al., Phys. Rev. D **79**, 113010 (2009) [arXiv:0904.3640 [hep-ph]] [Search INSPIRE].
[1527] R. Harnik et al., J. High Energy Phys. **03**, 026 (2013) [arXiv:1209.1397 [hep-ph]] [Search INSPIRE].
[1528] A. Celis et al., Phys. Rev. D **89**, 013008 (2014) [arXiv:1309.3564 [hep-ph]] [Search INSPIRE].
[1529] Y. Omura, J. High Energy Phys. **05**, 028 (2015) [arXiv:1502.07824 [hep-ph]] [Search INSPIRE].
[1530] A. Goudelis, O. Lebedev, and J.-H. Park, Phys. Lett. B **707**, 369 (2012) [arXiv:1111.1715 [hep-ph]] [Search INSPIRE].
[1531] A. M. Baldini et al., Eur. Phys. J. C **76**, 434 (2016) [arXiv:1605.05081 [hep-ex]] [Search INSPIRE].
[1532] V. Khachatryan et al., Phys. Lett. B **749**, 337 (2015) [arXiv:1502.07400 [hep-ex]] [Search INSPIRE].
[1533] CMS Collaboration, Search for lepton flavour violating decays of the Higgs boson in the mu–tau final state at 13 TeV, CMS report CMS-PAS-HIG-16-005 (2016).
[1534] G. Aad et al., Eur. Phys. J. C **77**, 70 (2017) [arXiv:1604.07730 [hep-ex]] [Search INSPIRE].
[1535] J. R. Ellis et al., Phys. Rev. D **66**, 115013 (2002) [arXiv:hep-ph/0206110] [Search INSPIRE].
[1536] K. Hayasaka et al., Phys. Lett. B **666**, 16 (2008) [arXiv:0705.0650 [hep-ex]] [Search INSPIRE].
[1537] K. Hayasaka et al., Phys. Lett. B **687**, 139 (2010) [arXiv:1001.3221 [hep-ex]] [Search INSPIRE].
[1538] Y. Miyazaki et al., Phys. Lett. B **648**, 341 (2007) [arXiv:hep-ex/0703009] [Search INSPIRE].
[1539] I. I. Bigi and A. I. Sanda, Phys. Lett. B **625**, 47 (2005) [arXiv:hep-ph/0506037] [Search INSPIRE].
[1540] G. Calderon et al., Phys. Rev. D **75**, 076001 (2007) [arXiv:hep-ph/0702282] [Search INSPIRE].
[1541] Y. Grossman and Y. Nir, J. High Energy Phys. **04**, 002 (2012) [arXiv:1110.3790 [hep-ph]] [Search INSPIRE].
[1542] J. P. Lees et al., Phys. Rev. D **85**, 031102 (2012); **85**, 099904 (2012) [erratum] [arXiv:1109.1527 [hep-ex]] [Search INSPIRE].
[1543] H. Zeen Devi et al., Phys. Rev. D **90**, 013016 (2014) [arXiv:1308.4383 [hep-ph]] [Search INSPIRE].
[1544] V. Cirigliano et al., Phys. Rev. Lett. **120**, 141803 (2018) [arXiv:1712.06595 [hep-ph]] [Search INSPIRE].
[1545] F.-S. Yu et al., Phys. Rev. Lett. **119**, 181802 (2017) [arXiv:1707.09297 [hep-ph]] [Search INSPIRE].
[1546] J. H. Kuhn and E. Mirkes, Z. Phys. C **56**, 661 (1992).
[1547] J. H. Kuhn and E. Mirkes, Phys. Lett. B **398**, 407 (1997) [arXiv:hep-ph/9609502] [Search INSPIRE].
[1548] Y. S. Tsai, Phys. Rev. D **51**, 3172 (1995) [arXiv:hep-ph/9410265] [Search INSPIRE].
[1549] C. A. Nelson et al., Phys. Rev. D **50**, 4544 (1994).
[1550] S. Y. Choi et al., Phys. Rev. D **52**, 1614 (1995) [arXiv:hep-ph/9412203] [Search INSPIRE].
[1551] U. Kilian et al., Z. Phys. C **62**, 413 (1994).

[1552] K. Kiers et al., Phys. Rev. D **78**, 113008 (2008) [arXiv:0808.1707 [hep-ph]] [Search INSPIRE].
[1553] N. Mileo et al., Phys. Rev. D **91**, 073006 (2015) [arXiv:1410.1909 [hep-ph]] [Search INSPIRE].
[1554] L. Beldjoudi and T. N. Truong, Phys. Lett. B **351**, 357 (1995) [arXiv:hep-ph/9411423] [Search INSPIRE].
[1555] D. Kimura et al., arXiv:0905.1802 [hep-ph] [Search INSPIRE].
[1556] D. Kimura et al., Prog. Theor. Exp. Phys. **2013**, 053B03 (2013); **2014**, 089202 (2014) [erratum] [arXiv:1201.1794 [hep-ph]] [Search INSPIRE].
[1557] M. Jamin et al., Phys. Lett. B **640**, 176 (2006) [arXiv:hep-ph/0605096] [Search INSPIRE].
[1558] M. Antonelli et al., Eur. Phys. J. C, **69**, 399 (2010) [arXiv:1005.2323 [hep-ph]] [Search INSPIRE].
[1559] M. Gourdin, Phys. Rept. **11**, 29 (1974).
[1560] H. Leutwyler, Electromagnetic form-factor of the pion, in Proc. Conf. on continuous advances in QCD, Minneapolis, USA, May 17–23, p. 23 (2002) [arXiv:hep-ph/0212324] [Search INSPIRE].
[1561] G. Colangelo, Nucl. Phys. Proc. Suppl. **162**, 256 (2006).
[1562] V. Bernard, J. High Energy Phys. **06**, 082 (2014) [arXiv:1311.2569 [hep-ph]] [Search INSPIRE].
[1563] H. Neufeld and H. Rupertsberger, Z. Phys. C **68**, 91 (1995).
[1564] S. Nussinov and A. Soffer, Phys. Rev. D **78**, 033006 (2008) [arXiv:0806.3922 [hep-ph]] [Search INSPIRE].
[1565] S. Descotes-Genon and B. Moussallam, Eur. Phys. J. C **74**, 2946 (2014) [arXiv:1404.0251 [hep-ph]] [Search INSPIRE].
[1566] P. Avery et al., Phys. Rev. D **64**, 092005 (2001) [arXiv:hep-ex/0104009] [Search INSPIRE].
[1567] D. Aston et al., Nucl. Phys. B **296**, 493 (1988).
[1568] R. F. Dashen and M. Weinstein, Phys. Rev. Lett. **22**, 1337 (1969).
[1569] J. Gasser and H. Leutwyler, Nucl. Phys. B **250**, 517 (1985).
[1570] M. Jamin et al., Nucl. Phys. B **622**, 279 (2002) [arXiv:hep-ph/0110193] [Search INSPIRE].
[1571] D. Epifanov et al., Phys. Lett. B **654**, 65 (2007) [arXiv:0706.2231 [hep-ex]] [Search INSPIRE].
[1572] V. Baru et al., Eur. Phys. J. A **23**, 523 (2005) [arXiv:nucl-th/0410099] [Search INSPIRE].
[1573] V. Bernard et al., Phys. Rev. D **44**, 3698 (1991).
[1574] M. Bischofberger et al., Phys. Rev. Lett. **107**, 131801 (2011) [arXiv:1101.0349 [hep-ex]] [Search INSPIRE].
[1575] W. Fetscher et al., Phys. Lett. B **173**, 102 (1986).
[1576] W. Fetscher and H. J. Gerber, Adv. Ser. Direct. High Energy Phys. **14**, 657 (1995).
[1577] A. B. Arbuzov and T. V. Kopylova, J. High Energy Phys. **09**, 109 (2016) [arXiv:1605.06612 [hep-ph]] [Search INSPIRE].
[1578] A. Flores-Tlalpa et al., J. High Energy Phys. **04**, 185 (2016) [arXiv:1508.01822 [hep-ph]] [Search INSPIRE].
[1579] Y.-S. Tsai, Phys. Rev. D **4**, 2821 (1971); **13**, 771 (1976) [erratum].
[1580] W. Fetscher, Phys. Rev. D **42**, 1544 (1990).
[1581] K. Tamai, Nucl. Phys. B **668**, 385 (2003).
[1582] S. Jadach and Z. Was, Acta Phys. Polon. B **15**, 1151 (1984); **16**, 483 (1985) [erratum].
[1583] A. B. Arbuzov et al., J. High Energy Phys. **10**, 001 (1997) [arXiv:hep-ph/9702262] [Search INSPIRE].
[1584] D. A. Epifanov, Nucl. Part. Phys. Proc. **287–288**, 7 (2017).
[1585] N. Shimizu et al., Prog. Theor. Exp. Phys. **2018**, 023C01 (2018) [arXiv:1709.08833 [hep-ex]] [Search INSPIRE].
[1586] S. Weinberg, Phys. Rev. **112**, 1375 (1958).
[1587] N. Severijns et al., Rev. Mod. Phys. **78**, 991 (2006) [arXiv:nucl-ex/0605029] [Search INSPIRE].
[1588] M. Bourquin et al., Z. Phys. C **12**, 307 (1982).
[1589] C. Leroy and J. Pestieau, Phys. Lett. B **72**, 398 (1978).
[1590] B. Aubert et al., Phys. Rev. Lett. **103**, 041802 (2009) [arXiv:0904.3080 [hep-ex]] [Search INSPIRE].
[1591] N. Paver and Riazuddin, Phys. Rev. D **86**, 037302 (2012) [arXiv:1205.6636 [hep-ph]] [Search INSPIRE].
[1592] A. Pich, Phys. Lett. B **196**, 561 (1987).
[1593] R. Escribano et al., Phys. Rev. D **94**, 034008 (2016) [arXiv:1601.03989 [hep-ph]] [Search INSPIRE].
[1594] M. Fujikawa et al., Phys. Rev. D **78**, 072006 (2008) [arXiv:0805.3773 [hep-ex]] [Search INSPIRE].
[1595] Z.-H. Guo and J. A. Oller, Phys. Rev. D **84**, 034005 (2011) [arXiv:1104.2849 [hep-ph]] [Search INSPIRE].

[1596] C. Adolph et al., Phys. Lett. B **740**, 303 (2015) [arXiv:1408.4286 [hep-ex]] [Search INSPIRE].
[1597] S. Nussinov and A. Soffer, Phys. Rev. D **80**, 033010 (2009) [arXiv:0907.3628 [hep-ph]] [Search INSPIRE].
[1598] P. del Amo Sanchez et al., Phys. Rev. D **83**, 032002 (2011) [arXiv:1011.3917 [hep-ex]] [Search INSPIRE].
[1599] K. Hayasaka, PoS **EPS-HEP2009**, 374 (2009).
[1600] E. A. GarcÈs et al., J. High Energy Phys. **12**, 027 (2017) [arXiv:1708.07802 [hep-ph]] [Search INSPIRE].
[1601] K. Inami et al., Phys. Lett. B **672**, 209 (2009) [arXiv:0811.0088 [hep-ex]] [Search INSPIRE].
[1602] J. E. Bartelt et al., Phys. Rev. Lett. **76**, 4119 (1996).
[1603] B. Aubert et al., Phys. Rev. D **77**, 112002 (2008) [arXiv:0803.0772 [hep-ex]] [Search INSPIRE].
[1604] T. Bergfeld et al., Phys. Rev. Lett. **79**, 2406 (1997) [arXiv:hep-ex/9706020] [Search INSPIRE].
[1605] S. U. Chung et al., Phys. Rev. **165**, 1491 (1968).
[1606] A. Pich, Prog. Part. Nucl. Phys. **75**, 41 (2014) [arXiv:1310.7922 [hep-ph]] [Search INSPIRE].
[1607] M. Ablikim et al., Phys. Rev. D **90**, 012001 (2014) [arXiv:1405.1076 [hep-ex]] [Search INSPIRE].
[1608] H. Albrecht et al., Phys. Lett. B **292**, 221 (1992).
[1609] G. Abbiendi et al., Phys. Lett. B **492**, 23 (2000) [arXiv:hep-ex/0005009] [Search INSPIRE].
[1610] K. Abe et al., Phys. Rev. Lett. **99**, 011801 (2007) [arXiv:hep-ex/0608046] [Search INSPIRE].
[1611] D. Atwood and A. Soni, Phys. Rev. D **45**, 2405 (1992).
[1612] K. Inami et al., Phys. Lett. B **551**, 16 (2003), [arXiv:hep-ex/0210066] [Search INSPIRE].
[1613] S. Schael et al., Phys. Rept. **421**, 191 (2005) [arXiv:hep-ex/0506072] [Search INSPIRE].
[1614] M. Davier et al., Rev. Mod. Phys. **78**, 1043 (2006) [arXiv:hep-ph/0507078] [Search INSPIRE].
[1615] M. Davier et al., Eur. Phys. J. C **74**, 2803 (2014) [arXiv:1312.1501 [hep-ex]] [Search INSPIRE].
[1616] R. Barate et al., Eur. Phys. J. C **11**, 599 (1999) [arXiv:hep-ex/9903015] [Search INSPIRE].
[1617] K. Ackerstaff et al., Eur. Phys. J. C **7**, 571 (1999) [arXiv:hep-ex/9808019] [Search INSPIRE].
[1618] G. Abbiendi et al., Eur. Phys. J. C **35**, 437 (2004) [arXiv:hep-ex/0406007] [Search INSPIRE].
[1619] A. Pich, Talk at 3rd Belle II Theory Interface Platform (B2TiP) Workshop, Tokyo, 26–29 October (available at: https://kds.kek.jp/indico/event/19103/session/15/contribution/19/material/slides/0.pdf) (KEK, Tokyo, 2015).
[1620] J. Erler, Rev. Mex. Fis. **50**, 200 (2004) [arXiv:hep-ph/0211345] [Search INSPIRE].
[1621] S. Narison and A. Pich, Phys. Lett. B **211**, 183 (1988).
[1622] E. Braaten, Phys. Rev. D **39**, 1458 (1989).
[1623] E. Braaten et al., Nucl. Phys. B **373**, 581 (1992).
[1624] MITP, Workshop on the determination of the fundamental parameters in QCD, in Proc. Mainz Institute for Theoretical Physics workshop, Johannes Gutenberg University, Mainz, Germany (2016).
[1625] M. A. Shifman et al., Nucl. Phys. B **147**, 385 (1979).
[1626] P. A. Baikov et al., Phys. Rev. Lett. **101**, 012002 (2008) [arXiv:0801.1821 [hep-ph]] [Search INSPIRE].
[1627] A. A. Pivovarov, Z. Phys. C **53**, 461 (1992) [arXiv:hep-ph/0302003] [Search INSPIRE].
[1628] F. Le Diberder and A. Pich, Phys. Lett. B **286**, 147 (1992).
[1629] M. Beneke and M. Jamin, J. High Energy Phys. **09**, 044 (2008) [arXiv:0806.3156 [hep-ph]] [Search INSPIRE].
[1630] S. Menke, arXiv:0904.1796 [hep-ph] [Search INSPIRE].
[1631] K. G. Chetyrkin and A. Kwiatkowski, Z. Phys. C **59**, 525 (1993) [arXiv:hep-ph/9805232] [Search INSPIRE].
[1632] A. Pich and A. Rodriguez-Sanchez, Phys. Rev. D **94**, 034027 (2016) [arXiv:1605.06830 [hep-ph]] [Search INSPIRE].
[1633] D. Boito et al., Phys. Rev. D **95**, 034024 (2017) [arXiv:1611.03457 [hep-ph]] [Search INSPIRE].
[1634] G. P. Lepage et al., arXiv:1404.0319 [hep-ph] [Search INSPIRE].
[1635] D. Boito et al., Phys. Rev. D **91**, 034003 (2015) [arXiv:1410.3528 [hep-ph]] [Search INSPIRE].
[1636] M. N. Achasov et al., J. Exp. Theor. Phys. **109**, 379 (2009).
[1637] J. P. Lees et al., Phys. Rev. D **96**, 092009 (2017) [arXiv:1709.01171 [hep-ex]] [Search INSPIRE].
[1638] G. Ciezarek et al., Nature **546**, 227 (2017) [arXiv:1703.01766 [hep-ex]] [Search INSPIRE].
[1639] E. Gamiz et al., J. High Energy Phys. **01**, 060 (2003) [arXiv:hep-ph/0212230] [Search INSPIRE].
[1640] E. Gamiz et al., Phys. Rev. Lett. **94**, 011803 (2005) [arXiv:hep-ph/0408044] [Search INSPIRE].

[1641] J. C. Hardy and I. S. Towner, Phys. Rev. C **91**, 025501 (2015) [arXiv:1411.5987 [nucl-ex]] [Search INSPIRE].
[1642] A. Pich and J. Prades, J. High Energy Phys. **06**, 013 (1998) [arXiv:hep-ph/9804462] [Search INSPIRE].
[1643] A. Pich and J. Prades, J. High Energy Phys. **10**, 004 (1999) [arXiv:hep-ph/9909244] [Search INSPIRE].
[1644] P. A. Baikov et al., Phys. Rev. Lett. **95**, 012003 (2005) [arXiv:hep-ph/0412350] [Search INSPIRE].
[1645] E. Gamiz et al., PoS **KAON**, 008 (2008) [arXiv:0709.0282 [hep-ph]] [Search INSPIRE].
[1646] S. Chen et al., Eur. Phys. J. C **22**, 31 (2001) [arXiv:hep-ph/0105253] [Search INSPIRE].
[1647] K. G. Chetyrkin et al., Nucl. Phys. B **533**, 473 (1998) [arXiv:hep-ph/9805335] [Search INSPIRE].
[1648] J. G. Korner et al., Eur. Phys. J. C **20**, 259 (2001) [arXiv:hep-ph/0003165] [Search INSPIRE].
[1649] K. Maltman, Phys. Rev. D **58**, 093015 (1998) [arXiv:hep-ph/9804298] [Search INSPIRE].
[1650] J. Kambor and K. Maltman, Phys. Rev. D **62**, 093023 (2000) [arXiv:hep-ph/0005156] [Search INSPIRE].
[1651] K. Maltman and J. Kambor, Phys. Rev. D **64**, 093014 (2001) [arXiv:hep-ph/0107187] [Search INSPIRE].
[1652] K. Maltman and C. E. Wolfe, Phys. Lett. B **639**, 283 (2006) [arXiv:hep-ph/0603215] [Search INSPIRE].
[1653] M. Antonelli et al., J. High Energy Phys. **10**, 070 (2013) [arXiv:1304.8134 [hep-ph]] [Search INSPIRE].
[1654] K. Maltman et al., Nucl. Phys. Proc. Suppl. **189**, 175 (2009) [arXiv:0906.1386 [hep-ph]] [Search INSPIRE].
[1655] K. Maltman, Nucl. Phys. Proc. Suppl. **218**, 146 (2011) [arXiv:1011.6391 [hep-ph]] [Search INSPIRE].
[1656] K. Maltman et al., Mod. Phys. Lett. A **31**, 1630030 (2016).
[1657] R. Hudspith et al., Phys. Lett. B **781**, 206 (2018) [arXiv:1702.01767 [hep-ph]] [Search INSPIRE].
[1658] I. M. Nugent, Nucl. Phys. Proc. Suppl. **253–255**, 38 (2014) [arXiv:1301.7105 [hep-ex]] [Search INSPIRE].
[1659] S. Jadach et al., Eur. Phys. J. C **22**, 423 (2001) [arXiv:hep-ph/9905452] [Search INSPIRE].
[1660] S. Jadach et al., Phys. Rev. D **94**, 074006 (2016) [arXiv:1608.01260 [hep-ph]] [Search INSPIRE].
[1661] Stanislaw J. et al., Comput. Phys. Commun. **64**, 275 (1990).
[1662] M. Jezabek et al., Comput. Phys. Commun. **70**, 69 (1992).
[1663] S. Jadach et al., Comput. Phys. Commun. **76**, 361 (1993).
[1664] P. Golonka et al., Comput. Phys. Commun. **174**, 818 (2006), [arXiv:hep-ph/0312240] [Search INSPIRE].
[1665] E. Barberio et al., Comput. Phys. Commun. **66**, 115 (1991).
[1666] E. Barberio and Z. W*c*as, Comput. Phys. Commun. **79**, 291 (1994).
[1667] P. Golonka and Z. W*c* as, Eur. Phys. J. C **45**, 97 (2006), [arXiv:hep-ph/0506026] [Search INSPIRE].
[1668] S. Jadach et al., Comput. Phys. Commun. **140**, 475 (2001) [arXiv:hep-ph/0104049] [Search INSPIRE].
[1669] O. Shekhovtsova, EPJ Web Conf. **80**, 00054 (2014) [arXiv:1410.2428 [hep-ph]] [Search INSPIRE].
[1670] P. Roig, Nucl. Part. Phys. Proc. **260**, 41 (2015) [arXiv:1410.8559 [hep-ph]] [Search INSPIRE].
[1671] D. M. Asner et al., Phys. Rev. D **61**, 012002 (2000) [arXiv:hep-ex/9902022] [Search INSPIRE].
[1672] T. E. Browder et al., Phys. Rev. D **61**, 052004 (2000) [arXiv:hep-ex/9908030] [Search INSPIRE].
[1673] S. Actis et al., Eur. Phys. J. C **66**, 585 (2010) [arXiv:0912.0749 [hep-ph]] [Search INSPIRE].
[1674] O. Shekhovtsova et al., Phys. Rev. D **86**, 113008 (2012) [arXiv:1203.3955 [hep-ph]] [Search INSPIRE].
[1675] I. M. Nugent et al., Phys. Rev. D **88**, 093012 (2013) [arXiv:1310.1053 [hep-ph]] [Search INSPIRE].
[1676] Z. Was and J. Zaremba, Eur. Phys. J. C **75**, 566 (2015); **76**, 465 (2016) [erratum] [arXiv:1508.06424 [hep-ph]] [Search INSPIRE].
[1677] M. Chrzaszcz et al., arXiv:1609.04617 [hep-ph] [Search INSPIRE].
[1678] A. E. Bondar et al., Comput. Phys. Commun. **146**, 139 (2002) [arXiv:hep-ph/0201149] [Search INSPIRE].
[1679] J. H. Kuhn and Z. W*c* as, Acta Phys. Polon. B **39**, 147 (2008) [arXiv:hep-ph/0602162] [Search INSPIRE].
[1680] M. Fael et al., Phys. Rev. D **88**, 093011 (2013) [arXiv:1310.1081 [hep-ph]] [Search INSPIRE].

[1681] M. Fael et al., J. High Energy Phys. **07**, 153 (2015) [arXiv:1506.03416 [hep-ph]] [Search INSPIRE].
[1682] J. Sasaki, Nucl. Part. Phys. Proc. **287–288**, 212 (2017).
[1683] A. B. Arbuzov et al., Eur. Phys. J. C **73**, 2625 (2013) [arXiv:1212.6783 [hep-ph]] [Search INSPIRE].
[1684] T. Doan et al., Phys. Lett. B **725**, 92 (2013) [arXiv:1303.2220 [hep-ph]] [Search INSPIRE].
[1685] S. Jadach et al., Phys. Rev. D **88**, 114022 (2013) [arXiv:1307.4037 [hep-ph]] [Search INSPIRE].
[1686] G. Nanava et al., Eur. Phys. J. C **70**, 673 (2010) [arXiv:0906.4052 [hep-ph]] [Search INSPIRE].
[1687] F. Gray, arXiv:1510.00346 [physics.ins-det] [Search INSPIRE].
[1688] N. Saito, AIP Conf. Proc. **1467**, 45 (2012).
[1689] G. W. Bennett et al., Phys. Rev. D **73**, 072003 (2006) [arXiv:hep-ex/0602035] [Search INSPIRE].
[1690] D. Nomura, Acta Phys. Polon. B **46**, 2251 (2015).
[1691] F. Jegerlehner, EPJ Web Conf. **118**, 01016 (2016) [arXiv:1511.04473 [hep-ph]] [Search INSPIRE].
[1692] F. Jegerlehner, Acta Phys. Polon. B **49**, 1157 (2018) [arXiv:1804.07409 [hep-ph]] [Search INSPIRE].
[1693] A. Keshavarzi et al., Phys. Rev. D **97**, 114025 (2018) [arXiv:1802.02995 [hep-ph]] [Search INSPIRE].
[1694] J. P. Lees et al., Phys. Rev. D **86**, 032013 (2012) [arXiv:1205.2228 [hep-ex]] [Search INSPIRE].
[1695] M. Ablikim et al., Phys. Lett. B **753**, 629 (2016) [arXiv:1507.08188 [hep-ex]] [Search INSPIRE].
[1696] D. Babusci et al., Phys. Lett. B **720**, 336 (2013) [arXiv:1212.4524 [hep-ex]] [Search INSPIRE].
[1697] F. Ambrosino et al., Phys. Lett. B **700**, 102 (2011) [arXiv:1006.5313 [hep-ex]] [Search INSPIRE].
[1698] F. Ambrosino et al., Phys. Lett. B **670**, 285 (2009) [arXiv:0809.3950 [hep-ex]] [Search INSPIRE].
[1699] R. R. Akhmetshin et al., Phys. Lett. B **648**, 28 (2007) [arXiv:hep-ex/0610021] [Search INSPIRE].
[1700] M. N. Achasov et al., J. Exp. Theor. Phys. **103**, 380 (2006) [arXiv:hep-ex/0605013] [Search INSPIRE].
[1701] K. Hagiwara et al., J. Phys. G **38**, 085003 (2011) [arXiv:1105.3149 [hep-ph]] [Search INSPIRE].
[1702] S. J. Brodsky and E. De Rafael, Phys. Rev. **168**, 1620 (1968).
[1703] H. Czyz and J. H. Kuhn, Eur. Phys. J. C **18**, 497 (2001) [arXiv:hep-ph/0008262] [Search INSPIRE].
[1704] M. Davier, Talk at $g-2$ Theory Initiative FermiLab, 3–6 June 2017 (available at: https://indico.fnal.gov/event/13795/session/10/contribution/47/material/slides/0.pdf) (2017).
[1705] H. Czyz et al., Eur. Phys. J. C **27**, 563 (2003) [arXiv:hep-ph/0212225] [Search INSPIRE].
[1706] F. Campanario et al., J. High Energy Phys. **1402**, 114 (2014) [arXiv:1312.3610 [hep-ph]] [Search INSPIRE].
[1707] V. L. Chernyak and A. R. Zhitnitsky, JETP Lett. **25**, 510 (1977).
[1708] A. V. Efremov and A. V. Radyushkin, Theor. Math. Phys. **42**, 97 (1980).
[1709] G. P. Lepage and S. J. Brodsky, Phys. Lett. B **87**, 359 (1979).
[1710] I. I. Balitsky et al., Nucl. Phys. B **312**, 509 (1989).
[1711] V. L. Chernyak and I. R. Zhitnitsky, Nucl. Phys. B **345**, 137 (1990).
[1712] A. Khodjamirian, Eur. Phys. J. C **6**, 477 (1999) [arXiv:hep-ph/9712451] [Search INSPIRE].
[1713] S. S. Agaev et al., Phys. Rev. D **83**, 054020 (2011) [arXiv:1012.4671 [hep-ph]] [Search INSPIRE].
[1714] S. S. Agaev et al., Phys. Rev. D **86**, 077504 (2012) [arXiv:1206.3968 [hep-ph]] [Search INSPIRE].
[1715] A. P. Bakulev et al., Phys. Rev. D **86**, 031501 (2012) [arXiv:1205.3770 [hep-ph]] [Search INSPIRE].
[1716] S. S. Agaev et al., Phys. Rev. D **90**, 074019 (2014) [arXiv:1409.4311 [hep-ph]] [Search INSPIRE].
[1717] S. V. Mikhailov et al., Phys. Rev. D **93**, 114018 (2016) [arXiv:1604.06391 [hep-ph]] [Search INSPIRE].
[1718] H.-N. Li and G. F. Sterman, Nucl. Phys. B **381**, 129 (1992).
[1719] H.-C. Hu and H.-N. Li, Phys. Lett. B **718**, 1351 (2013) [arXiv:1204.6708 [hep-ph]] [Search INSPIRE].
[1720] H.-N. Li et al., J. High Energy Phys. **01**, 004 (2014) [arXiv:1310.3672 [hep-ph]] [Search INSPIRE].
[1721] B. Aubert et al., Phys. Rev. D **80**, 052002 (2009) [arXiv:0905.4778 [hep-ex]] [Search INSPIRE].
[1722] S. Uehara et al., Phys. Rev. D **86**, 092007 (2012) [arXiv:1205.3249 [hep-ex]] [Search INSPIRE].
[1723] J. Gronberg et al., Phys. Rev. D **57**, 33 (1998) [arXiv:hep-ex/9707031] [Search INSPIRE].
[1724] V. M. Braun et al., Phys. Rev. D **74**, 074501 (2006) [arXiv:hep-lat/0606012] [Search INSPIRE].
[1725] R. Arthur et al., Phys. Rev. D **83**, 074505 (2011) [arXiv:1011.5906 [hep-lat]] [Search INSPIRE].
[1726] V. M. Braun, S. Collins, M. Göckeler, P. Pérez-Rubio, A. Schäfer, R. W. Schiel, and A. Sternbeck, Phys. Rev. D **92**, 014504 (2015) [arXiv:1503.03656 [hep-lat]] [Search INSPIRE].
[1727] B. Melic et al., Phys. Rev. D **68**, 014013 (2003) [arXiv:hep-ph/0212346] [Search INSPIRE].
[1728] V. M. Braun et al., J. High Energy Phys. **03**, 142 (2016) [arXiv:1601.05937 [hep-ph]] [Search INSPIRE].

[1729] A. E. Blechman et al., Phys. Lett. B **608**, 77 (2005) [arXiv:hep-ph/0410312] [Search INSPIRE].
[1730] L. A. Harland-Lang et al., Eur. Phys. J. C **73**, 2429 (2013) [arXiv:1302.2004 [hep-ph]] [Search INSPIRE].
[1731] P. Ball and G. W. Jones, J. High Energy Phys. **0708**, 025 (2007) [arXiv:0706.3628 [hep-ph]] [Search INSPIRE].
[1732] N. Offen, F. A. Pokert, and A. Schafer, Phys. Rev. D **88**, 034023 (2013) [arXiv:1307.2797 [hep-ph]] [Search INSPIRE].
[1733] Y.-Y. Charng et al., Phys. Rev. D **74**, 074024 (2006); **78**, 059901 (2008) [erratum] [arXiv:hep-ph/0609165] [Search INSPIRE].
[1734] X. Liu et al., Phys. Rev. D **86**, 011501 (2012) [arXiv:1205.1214 [hep-ph]] [Search INSPIRE].
[1735] J.-F. Hsu et al., Phys. Rev. D **78**, 014020 (2008) [arXiv:0711.4987 [hep-ph]] [Search INSPIRE].
[1736] P. del Amo Sanchez et al., Phys. Rev. D **84**, 052001 (2011) [arXiv:1101.1142 [hep-ex]] [Search INSPIRE].
[1737] B. Aubert et al., Phys. Rev. D **74**, 012002 (2006) [arXiv:hep-ex/0605018] [Search INSPIRE].
[1738] Y. Grossmann, J. High Energy Phys. **04**, 101 (2015) [arXiv:1501.06569 [hep-ph]] [Search INSPIRE].
[1739] S. Alte et al., J. High Energy Phys. **02**, 162 (2016) [arXiv:1512.09135 [hep-ph]] [Search INSPIRE].
[1740] M. Masuda et al., Phys. Rev. D **93**, 032003 (2016) [arXiv:1508.06757 [hep-ex]] [Search INSPIRE].
[1741] V. M. Braun et al., J. High Energy Phys. **06**, 039 (2016) [arXiv:1603.09154 [hep-ph]] [Search INSPIRE].
[1742] G. P. Lepage and S. J. Brodsky, Phys. Rev. D **22**, 2157 (1980).
[1743] G. Colangelo et al., J. High Energy Phys. **09**, 091 (2014) [arXiv:1402.7081 [hep-ph]] [Search INSPIRE].
[1744] G. Colangelo et al., Phys. Lett. B **738**, 6 (2014) [arXiv:1408.2517 [hep-ph]] [Search INSPIRE].
[1745] G. Colangelo et al., J. High Energy Phys. **09**, 074 (2015) [arXiv:1506.01386 [hep-ph]] [Search INSPIRE].
[1746] G. Colangelo et al., Phys. Rev. Lett. **118**, 232001 (2017) [arXiv:1701.06554 [hep-ph]] [Search INSPIRE].
[1747] G. Colangelo et al., J. High Energy Phys. **04**, 161 (2017) [arXiv:1702.07347 [hep-ph]] [Search INSPIRE].
[1748] M. Hoferichter et al., Phys. Rev. D **86**, 116009 (2012) [arXiv:1210.6793 [hep-ph]] [Search INSPIRE].
[1749] M. Hoferichter et al., Phys. Rev. D **96**, 114016 (2017) [arXiv:1710.00824 [hep-ph]] [Search INSPIRE].
[1750] M. Hoferichter et al., Eur. Phys. J. C **74**, 3180 (2014) [arXiv:1410.4691 [hep-ph]] [Search INSPIRE].
[1751] C. Hanhart et al., Eur. Phys. J. C **73**, 2668 (2013); **75**, 242 (2015) [erratum] [arXiv:1307.5654 [hep-ph]] [Search INSPIRE].
[1752] C. W. Xiao et al., arXiv:1509.02194 [hep-ph] [Search INSPIRE].
[1753] M. Hoferichter et al., Phys. Rev. Lett. **121**, 112002 (2018) [arXiv:1805.01471 [hep-ph]] [Search INSPIRE].
[1754] M. Hoferichter et al., J. High Energy Phys. **10**, 141 (2018) [arXiv:1808.04823 [hep-ph]] [Search INSPIRE].
[1755] R. García-Martín and B. Moussallam, Eur. Phys. J. C **70**, 155 (2010) [arXiv:1006.5373 [hep-ph]] [Search INSPIRE].
[1756] M. Hoferichter et al., Eur. Phys. J. C **71**, 1743 (2011) [arXiv:1106.4147 [hep-ph]] [Search INSPIRE].
[1757] L.-Y. Dai and M. R. Pennington, Phys. Rev. D **90**, 036004 (2014) [arXiv:1404.7524 [hep-ph]] [Search INSPIRE].
[1758] B. Moussallam, Eur. Phys. J. C **73**, 2539 (2013) [arXiv:1305.3143 [hep-ph]] [Search INSPIRE].
[1759] M. Hoferichter et al., Int. J. Mod. Phys. Conf. Ser. **35**, 1460400 (2014) [arXiv:1309.6877 [hep-ph]] [Search INSPIRE].
[1760] V. Pauk and M. Vanderhaeghen, Eur. Phys. J. C **74**, 3008 (2014) [arXiv:1401.0832 [hep-ph]] [Search INSPIRE].
[1761] V. Pascalutsa, V. Pauk, and M. Vanderhaeghen, Phys. Rev. D **85**, 116001 (2012) [arXiv:1204.0740 [hep-ph]] [Search INSPIRE].
[1762] I. Danilkin and M. Vanderhaeghen, Phys. Rev. D **95**, 014019 (2017) [arXiv:1611.04646 [hep-ph]] [Search INSPIRE].
[1763] R. Essig et al., arXiv:1311.0029 [hep-ph] [Search INSPIRE].
[1764] C. Boehm et al., J. Phys. G **30**, 279 (2004) [arXiv:astro-ph/0208458] [Search INSPIRE].

[1765] C. Boehm and P. Fayet, Nucl. Phys. B **683**, 219 (2004) [arXiv:hep-ph/0305261] [Search INSPIRE].
[1766] P. Fayet, Phys. Rev. D **74**, 054034 (2006) [arXiv:hep-ph/0607318] [Search INSPIRE].
[1767] P. Fayet, Phys. Rev. D **75**, 115017 (2007) [arXiv:hep-ph/0702176] [Search INSPIRE].
[1768] O. Adriani et al., Nature **458**, 607 (2009) [arXiv:0810.4995 [astro-ph]] [Search INSPIRE].
[1769] A. A. Abdo et al., Phys. Rev. Lett. **102**, 181101 (2009) [arXiv:0905.0025 [astro-ph.HE]] [Search INSPIRE].
[1770] M. Aguilar et al., Phys. Rev. Lett. **110**, 141102 (2013).
[1771] N. Arkani-Hamed et al., Phys. Rev. D **79**, 015014 (2009) [arXiv:0810.0713 [hep-ph]] [Search INSPIRE].
[1772] M. Pospelov and A. Ritz, Phys. Lett. B **671**, 391 (2009) [arXiv:0810.1502 [hep-ph]] [Search INSPIRE].
[1773] Y. Nomura and J. Thaler, Phys. Rev. D **79**, 075008 (2009) [arXiv:0810.5397 [hep-ph]] [Search INSPIRE].
[1774] P. J. Fox and E. Poppitz, Phys. Rev. D **79**, 083528 (2009) [arXiv:0811.0399 [hep-ph]] [Search INSPIRE].
[1775] D. N. Spergel et al., Phys. Rev. Lett. **84**, 3760 (2000) [arXiv:astro-ph/9909386] [Search INSPIRE].
[1776] M. R. Buckley and P. J. Fox, Phys. Rev. D **81**, 083522 (2010) [arXiv:0911.3898 [hep-ph]] [Search INSPIRE].
[1777] A. Loeb and N. Weiner, Phys. Rev. Lett. **106**, 171302 (2011) [arXiv:1011.6374 [astro-ph.CO]] [Search INSPIRE].
[1778] S. Tulin et al., Phys. Rev. D **87**, 115007 (2013) [arXiv:1302.3898 [hep-ph]] [Search INSPIRE].
[1779] M. Vogelsberger et al., Mon. Not. Roy. Astron. Soc. **423**, 3740 (2012) [arXiv:1201.5892 [astro-ph.CO]] [Search INSPIRE].
[1780] M. Duerr et al., J. High Energy Phys. **09**, 042 (2016) [arXiv:1606.07609 [hep-ph]] [Search INSPIRE].
[1781] M. Pospelov and J. Pradler, Ann. Rev. Nucl. Part. Sci. **60**, 539 (2010) [arXiv:1011.1054 [hep-ph]] [Search INSPIRE].
[1782] R. Essig et al., Phys. Rev. Lett. **109**, 021301 (2012) [arXiv:1206.2644 [astro-ph.CO]] [Search INSPIRE].
[1783] C. Kouvaris and J. Pradler, Phys. Rev. Lett. **118**, 031803 (2017) [arXiv:1607.01789 [hep-ph]] [Search INSPIRE].
[1784] B. Aubert et al., arXiv:0808.0017 [hep-ex] [Search INSPIRE].
[1785] P. del Amo Sanchez et al., Phys. Rev. Lett. **107**, 021804 (2011) [arXiv:1007.4646 [hep-ex]] [Search INSPIRE].
[1786] R. Essig et al., J. High Energy Phys. **11**, 167 (2013) [arXiv:1309.5084 [hep-ph]] [Search INSPIRE].
[1787] E. Izaguirre et al., Phys. Rev. D **88**, 114015 (2013) [arXiv:1307.6554 [hep-ph]] [Search INSPIRE].
[1788] B. Batell et al., Phys. Rev. D **90**, 115014 (2014) [arXiv:1405.7049 [hep-ph]] [Search INSPIRE].
[1789] P. Coloma et al., J. High Energy Phys. **04**, 047 (2016) [arXiv:1512.03852 [hep-ph]] [Search INSPIRE].
[1790] B. Batell et al., Phys. Rev. Lett. **113**, 171802 (2014) [arXiv:1406.2698 [hep-ph]] [Search INSPIRE].
[1791] S. Alekhin et al., Rept. Prog. Phys. **79**, 124201 (2016) [arXiv:1504.04855 [hep-ph]] [Search INSPIRE].
[1792] M. Battaglieri et al., arXiv:1607.01390 [hep-ex] [Search INSPIRE].
[1793] B. Batell et al., Phys. Rev. D **80**, 095024 (2009) [arXiv:0906.5614 [hep-ph]] [Search INSPIRE].
[1794] B. Holdom, Phys. Lett. B **166**, 196 (1986).
[1795] M. Freytsis et al., Phys. Rev. D **81**, 034001 (2010) [arXiv:0911.5355 [hep-ph]] [Search INSPIRE].
[1796] M. Cicoli et al., J. High Energy Phys. **10**, 146 (2012) [arXiv:1206.0819 [hep-th]] [Search INSPIRE].
[1797] M. Millea et al., Phys. Rev. D **92**, 023010 (2015) [arXiv:1501.04097 [astro-ph.CO]] [Search INSPIRE].
[1798] W. J. Marciano et al., Phys. Rev. D **94**, 115033 (2016) [arXiv:1607.01022 [hep-ph]] [Search INSPIRE].
[1799] J. Jaeckel and M. Spannowsky, Phys. Lett. B **753**, 482 (2016) [arXiv:1509.00476 [hep-ph]] [Search INSPIRE].
[1800] I. Brivio et al., Eur. Phys. J. C **77**, 572 (2017) [arXiv:1701.05379 [hep-ph]] [Search INSPIRE].
[1801] S. Knapen et al., Phys. Rev. Lett. **118**, 171801 (2017) [arXiv:1607.06083 [hep-ph]] [Search INSPIRE].

[1802] B. Doebrich et al., J. High Energy Phys. **02**, 018 (2016) [arXiv:1512.03069 [hep-ph]] [Search INSPIRE].
[1803] E. Izaguirre et al., Phys. Rev. Lett. **118**, 111802 (2017) [arXiv:1611.09355 [hep-ph]] [Search INSPIRE].
[1804] M. Reece and L.-T. Wang, J. High Energy Phys. **07**, 051 (2009) [arXiv:0904.1743 [hep-ph]] [Search INSPIRE].
[1805] R. Essig et al., Phys. Rev. D **80**, 015003 (2009) [arXiv:0903.3941 [hep-ph]] [Search INSPIRE].
[1806] B. Batell et al., Phys. Rev. D **79**, 115008 (2009) [arXiv:0903.0363 [hep-ph]] [Search INSPIRE].
[1807] J. D. Clarke et al., J. High Energy Phys. **02**, 123 (2014) [arXiv:1310.8042 [hep-ph]] [Search INSPIRE].
[1808] M. J. Dolan et al., J. High Energy Phys. **03**, 171 (2015); **07**, 103 (2015) [erratum] [arXiv:1412.5174 [hep-ph]] [Search INSPIRE].
[1809] B. Batell et al., Phys. Rev. D **95**, 075003 (2017) [arXiv:1606.04943 [hep-ph]] [Search INSPIRE].
[1810] J. P. Lees et al., Phys. Rev. D **87**, 031102 (2013); **87**, 059903 (2013) [erratum] [arXiv:1210.0287 [hep-ex]] [Search INSPIRE].
[1811] J. P. Lees et al., Phys. Rev. D **88**, 071102 (2013) [arXiv:1210.5669 [hep-ex]] [Search INSPIRE].
[1812] J. P. Lees et al., Phys. Rev. Lett. **107**, 221803 (2011) [arXiv:1108.3549 [hep-ex]] [Search INSPIRE].
[1813] J. P. Lees et al., Phys. Rev. D **88**, 031701 (2013) [arXiv:1307.5306 [hep-ex]] [Search INSPIRE].
[1814] B. Batell et al., Phys. Rev. D **83**, 054005 (2011) [arXiv:0911.4938 [hep-ph]] [Search INSPIRE].
[1815] K. Schmidt-Hoberg et al., Phys. Lett. B **727**, 506 (2013) [arXiv:1310.6752 [hep-ph]] [Search INSPIRE].
[1816] G. Krnjaic, Phys. Rev. D **94**, 073009 (2016) [arXiv:1512.04119 [hep-ph]] [Search INSPIRE].
[1817] R. Aaij et al., Phys. Rev. Lett. **115**, 161802 (2015) [arXiv:1508.04094 [hep-ex]] [Search INSPIRE].
[1818] N. Fernandez et al., Phys. Rev. D **90**, 015029 (2014) [arXiv:1404.6599 [hep-ph]] [Search INSPIRE].
[1819] G. K. Yeghiyan, Phys. Rev. D **80**, 115019 (2009) [arXiv:0909.4919 [hep-ph]] [Search INSPIRE].
[1820] N. Fernandez et al., Phys. Rev. D **93**, 054023 (2016) [arXiv:1511.03728 [hep-ph]] [Search INSPIRE].
[1821] S. Godfrey and H. E. Logan, Phys. Rev. D **93**, 055014 (2016) [arXiv:1510.04659 [hep-ph]] [Search INSPIRE].
[1822] J. P. Lees et al., Phys. Rev. Lett. **108**, 211801 (2012) [arXiv:1202.1313 [hep-ex]] [Search INSPIRE].
[1823] I. Jaegle, Phys. Rev. Lett. **114**, 211801 (2015) [arXiv:1502.00084 [hep-ex]] [Search INSPIRE].
[1824] J. Alexander et al., arXiv:1608.08632 [hep-ph] [Search INSPIRE].
[1825] J. P. Lees et al., Phys. Rev. Lett. **119**, 131804 (2017) [arXiv:1702.03327 [hep-ex]] [Search INSPIRE].
[1826] Y. Hochberg et al., Phys. Rev. D **97**, 055030 (2018) [arXiv:1706.05008 [hep-ph]] [Search INSPIRE].
[1827] C. Boehm et al., J. Cosmol. Astropart. Phys. **1405**, 009 (2014) [arXiv:1401.6458 [hep-ph]] [Search INSPIRE].
[1828] M. Ackermann et al., Phys. Rev. Lett. **115**, 231301 (2015) [arXiv:1503.02641 [astro-ph.HE]] [Search INSPIRE].
[1829] J. P. Lees et al., Phys. Rev. Lett. **113**, 201801 (2014) [arXiv:1406.2980 [hep-ex]] [Search INSPIRE].
[1830] J. Alwall et al., J. High Energy Phys. **07**, 079 (2014) [arXiv:1405.0301 [hep-ph]] [Search INSPIRE].
[1831] R. Essig et al., Phys. Rev. D **82**, 113008 (2010) [arXiv:1008.0636 [hep-ph]] [Search INSPIRE].
[1832] S. Jadach et al., Phys. Lett. B **390**, 298 (1997) [arXiv:hep-ph/9608412] [Search INSPIRE].
[1833] D. Karlen, Nucl. Phys. B **289**, 23 (1987).
[1834] H. Ikeda et al., Nucl. Instrum. Meth. A **441**, 401 (2000).
[1835] K. Mimasu and V. Sanz, J. High Energy Phys. **06**, 173 (2015) [arXiv:1409.4792 [hep-ph]] [Search INSPIRE].
[1836] M. J. Dolan et al., J. High Energy Phys. **12**, 094 (2017) [arXiv:1709.00009 [hep-ph]] [Search INSPIRE].
[1837] B. Aubert et al., Phys. Rev. D **76**, 091102 (2007) [arXiv:0707.2798 [hep-ex]] [Search INSPIRE].
[1838] T. Ferber, Acta Phys. Polon. B **46**, 2067 (2015).
[1839] X. G. He et al., Phys. Rev. D **43**, R22 (1991).
[1840] X.-G. He et al., Phys. Rev. D **44**, 2118 (1991).
[1841] J. P. Lees et al., Phys. Rev. D **94**, 011102 (2016) [arXiv:1606.03501 [hep-ex]] [Search INSPIRE].
[1842] P. Fayet, Phys. Rev. D **81**, 054025 (2010) [arXiv:0910.2587 [hep-ph]] [Search INSPIRE].
[1843] H. Albrecht et al., Phys. Lett. B **179**, 403 (1986).
[1844] D. Besson et al., Phys. Rev. D **30**, 1433 (1984).
[1845] O. Tajima et al., Phys. Rev. Lett. **98**, 132001 (2007) [arXiv:hep-ex/0611041] [Search INSPIRE].

[1846] B. Aubert et al., Phys. Rev. Lett. **103**, 251801 (2009) [arXiv:0908.2840 [hep-ex]] [Search INSPIRE].
[1847] F. Wilczek, Phys. Rev. Lett. **39**, 1304 (1977).
[1848] R. E. Shrock and M. Suzuki, Phys. Lett. B **110**, 250 (1982).
[1849] G. Bonneau and F. Martin, Nucl. Phys. B **27**, 381 (1971).
[1850] V. N. Baier et al., Nucl. Phys. B **65**, 381 (1973).
[1851] G. Rodrigo et al., Eur. Phys. J. C **22**, 81 (2001) [arXiv:hep-ph/0106132] [Search INSPIRE].
[1852] B. McElrath, Phys. Rev. D **72**, 103508 (2005) [arXiv:hep-ph/0506151] [Search INSPIRE].
[1853] A. David et al., arXiv:1209.0040 [hep-ph] [Search INSPIRE].
[1854] A. Rashed et al., Phys. Rev. D **82**, 054031 (2010) [arXiv:1004.5419 [hep-ph]] [Search INSPIRE].
[1855] J. F. Gunion and H. E. Haber, Phys. Rev. D **67**, 075019 (2003) [arXiv:hep-ph/0207010] [Search INSPIRE].
[1856] P. Bechtle et al., Eur. Phys. J. C **75**, 421 (2015) [arXiv:1507.06706 [hep-ph]] [Search INSPIRE].
[1857] P. Franzini et al., Phys. Rev. D **35**, 2883 (1987).
[1858] B. Aubert et al., arXiv:0902.2176 [hep-ex] [Search INSPIRE].
[1859] B. Aubert et al., Phys. Rev. Lett. **103**, 181801 (2009) [arXiv:0906.2219 [hep-ex]] [Search INSPIRE].
[1860] M. A. Sanchis-Lozano, Mod. Phys. Lett. A **17**, 2265 (2002) [arXiv:hep-ph/0206156] [Search INSPIRE].
[1861] M.-A. Sanchis-Lozano, J. Phys. Soc. Jap. **76**, 044101 (2007) [arXiv:hep-ph/0610046] [Search INSPIRE].
[1862] J. P. Alexander et al., Phys. Rev. D **58**, 052004 (1998) [arXiv:hep-ex/9802024] [Search INSPIRE].
[1863] G. S. Adams et al., Phys. Rev. Lett. **94**, 012001 (2005) [arXiv:hep-ex/0409027] [Search INSPIRE].
[1864] D. Besson et al., Phys. Rev. Lett. **98**, 052002 (2007) [arXiv:hep-ex/0607019] [Search INSPIRE].
[1865] R. S. Chivukula and H. Georgi, Phys. Lett. B **188**, 99 (1987).
[1866] B. Grinstein and M. B. Wise, Phys. Lett. B **201**, 274 (1988).
[1867] M. Misiak and M. Steinhauser, Eur. Phys. J. C **77** 201 (2017) [arXiv:1702.04571 [hep-ph]] [Search INSPIRE].
[1868] S. L. Glashow and S. Weinberg, Phys. Rev. D **15**, 1958 (1977).
[1869] W.-S. Hou, Phys. Lett. B **296**, 179 (1992).
[1870] F. Mahmoudi and O. Stal, Phys. Rev. D **81**, 035016 (2010) [arXiv:0907.1791 [hep-ph]] [Search INSPIRE].
[1871] G. Aad et al., J. High Energy Phys. **08**, 045 (2016) [arXiv:1606.02266 [hep-ex]] [Search INSPIRE].
[1872] T. P. Cheng and M. Sher, Phys. Rev. D **35**, 3484 (1987).
[1873] D. Chang et al., Phys. Rev. D **48**, 217 (1993) [arXiv:hep-ph/9302267] [Search INSPIRE].
[1874] F. Mahmoudi, Comput. Phys. Commun. **180**, 1579 (2009) [arXiv:0808.3144 [hep-ph]] [Search INSPIRE].
[1875] M. Aaboud et al., Phys. Lett. B **759**, 555 (2016) [arXiv:1603.09203 [hep-ex]] [Search INSPIRE].
[1876] A. J. Buras, Weak Hamiltonian, CP violation and rare decays, in Probing the standard model of particle interactions. Proc. Summer School in Theoretical Physics, NATO Advanced Study Institute, 68th session, Les Houches, France, July 28–September 5 p. 281 (1998) [arXiv:hep-ph/9806471] [Search INSPIRE].
[1877] L. Mercolli and C. Smith, Nucl. Phys. B **817**, 1 (2009) [arXiv:0902.1949 [hep-ph]] [Search INSPIRE].
[1878] C. Smith, Acta Phys. Polon. Supp. **3**, 53 (2010) [arXiv:0909.4444 [hep-ph]] [Search INSPIRE].
[1879] C. Smith, Minimal flavor violation, Habilitation à diriger des recherches, Université Grenoble Alpes (2015).
[1880] J. M. Gerard, Z. Phys. C **18**, 145 (1983).
[1881] G. Colangelo et al., Eur. Phys. J. C **59**, 75 (2009) [arXiv:0807.0801 [hep-ph]] [Search INSPIRE].
[1882] P. Paradisi et al., Phys. Lett. B **668**, 202 (2008) [arXiv:0805.3989 [hep-ph]] [Search INSPIRE].
[1883] J. Bernon and C. Smith, J. High Energy Phys. **07**, 038 (2014) [arXiv:1404.5496 [hep-ph]] [Search INSPIRE].
[1884] P. Mertens and C. Smith, J. High Energy Phys. **08**, 069 (2011) [arXiv:1103.5992 [hep-ph]] [Search INSPIRE].
[1885] L. J. Hall and L. Randall, Phys. Rev. Lett. **65**, 2939 (1990).
[1886] R. Brommer et al., Eur. Phys. J. C **74**, 3059 (2014) [arXiv:1402.4024 [hep-ph]] [Search INSPIRE].
[1887] G. Colangelo and G. Isidori, J. High Energy Phys. **09**, 009 (1998) [arXiv:hep-ph/9808487] [Search INSPIRE].

[1888] A. J. Buras et al., Nucl. Phys. B **566**, 3 (2000) [arXiv:hep-ph/9908371] [Search INSPIRE].
[1889] G. Isidori et al., J. High Energy Phys. **08**, 064 (2006) [arXiv:hep-ph/0604074] [Search INSPIRE].
[1890] E. Nikolidakis and C. Smith, Phys. Rev. D **77**, 015021 (2008) [arXiv:0710.3129 [hep-ph]] [Search INSPIRE].
[1891] C. Smith, arXiv:0809.3152 [hep-ph] [Search INSPIRE].
[1892] C. Csaki et al., Phys. Rev. D **85**, 095009 (2012) [arXiv:1111.1239 [hep-ph]] [Search INSPIRE].
[1893] C. Smith, Phys. Rev. D **85**, 036005 (2012) [arXiv:1105.1723 [hep-ph]] [Search INSPIRE].
[1894] G. Durieux and C. Smith, J. High Energy Phys. **10**, 068 (2013) [arXiv:1307.1355 [hep-ph]] [Search INSPIRE].
[1895] V. Cirigliano et al., Nucl. Phys. B **728**, 121 (2005) [arXiv:hep-ph/0507001] [Search INSPIRE].
[1896] J. A. Casas and A. Ibarra, Nucl. Phys. B **618**, 171 (2001) [arXiv:hep-ph/0103065] [Search INSPIRE].
[1897] A. de Gouvea and P. Vogel, Prog. Part. Nucl. Phys. **71**, 75 (2013) [arXiv:1303.4097 [hep-ph]] [Search INSPIRE].
[1898] R. Alonso et al., J. High Energy Phys. **04**, 159 (2014) [arXiv:1312.2014 [hep-ph]] [Search INSPIRE].
[1899] F. Feruglio et al., Phys. Rev. Lett. **118**, 011801 (2017) [arXiv:1606.00524 [hep-ph]] [Search INSPIRE].
[1900] M. Carpentier and S. Davidson, Eur. Phys. J. C **70**, 1071 (2010) [arXiv:1008.0280 [hep-ph]] [Search INSPIRE].
[1901] A. Abada et al., Phys. Rev. D **91**, 113013 (2015) [arXiv:1503.04159 [hep-ph]] [Search INSPIRE].
[1902] Y. Kuno and Y. Okada, Rev. Mod. Phys. **73**, 151 (2001) [arXiv:hep-ph/9909265] [Search INSPIRE].
[1903] B. M. Dassinger et al., J. High Energy Phys. **10**, 039 (2007) [arXiv:0707.0988 [hep-ph]] [Search INSPIRE].
[1904] R. Brüser et al., J. High Energy Phys. **10**, 082 (2015) [arXiv:1506.07786 [hep-ph]] [Search INSPIRE].
[1905] A. A. Petrov and D. V. Zhuridov, Phys. Rev. D **89**, 033005 (2014) [arXiv:1308.6561 [hep-ph]] [Search INSPIRE].
[1906] A. Brignole and A. Rossi, Nucl. Phys. B **701**, 3 (2004) [arXiv:hep-ph/0404211] [Search INSPIRE].
[1907] R. Mohanta, Eur. Phys. J. C **71**, 1625 (2011) [arXiv:1011.4184 [hep-ph]] [Search INSPIRE].
[1908] P. Langacker and M. Plumacher, Phys. Rev. D **62**, 013006 (2000) [arXiv:hep-ph/0001204] [Search INSPIRE].
[1909] A. Crivellin et al., Phys. Rev. D **92**, 054013 (2015) [arXiv:1504.07928 [hep-ph]] [Search INSPIRE].
[1910] W. Altmannshofer et al., Phys. Lett. B **762**, 389 (2016) [arXiv:1607.06832 [hep-ph]] [Search INSPIRE].
[1911] I. Doršner et al., Phys. Rept. **641**, 1 (2016) [arXiv:1603.04993 [hep-ph]] [Search INSPIRE].
[1912] E. Bečirević et al., arXiv:1608.07583 [hep-ph] [Search INSPIRE].
[1913] I. Doršner et al., J. High Energy Phys. **06**, 108 (2015) [arXiv:1502.07784 [hep-ph]] [Search INSPIRE].
[1914] A. Abada et al., J. High Energy Phys. **12**, 061 (2007) [arXiv:0707.4058 [hep-ph]] [Search INSPIRE].
[1915] A. Abada et al., Phys. Rev. D **78**, 033007 (2008) [arXiv:0803.0481 [hep-ph]] [Search INSPIRE].
[1916] J. F. Kamenik and M. Nemevsek, J. High Energy Phys. **11**, 023 (2009); **03**, 033 (2014) [erratum] [arXiv:0908.3451 [hep-ph]] [Search INSPIRE].
[1917] J. Hisano et al., Phys. Rev. D **53**, 2442 (1996) [arXiv:hep-ph/9510309] [Search INSPIRE].
[1918] T. Feldmann et al., J. High Energy Phys. **11**, 078 (2016) [arXiv:1608.04124 [hep-ph]] [Search INSPIRE].
[1919] M. Beneke et al., Nucl. Phys. B **906**, 561 (2016) [arXiv:1508.01705 [hep-ph]] [Search INSPIRE].
[1920] A. Atre et al., J. High Energy Phys. **05**, 030 (2009) [arXiv:0901.3589 [hep-ph]] [Search INSPIRE].
[1921] W. Altmannshofer et al., J. High Energy Phys. **11**, 202 (2013) [arXiv:1308.3653 [hep-ph]] [Search INSPIRE].
[1922] E. Lunghi and A. Soni, Phys. Lett. B **666**, 162 (2008) [arXiv:0803.4340 [hep-ph]] [Search INSPIRE].
[1923] A. J. Buras and D. Guadagnoli, Phys. Rev. D **78**, 033005 (2008) [arXiv:0805.3887 [hep-ph]] [Search INSPIRE].
[1924] W. Altmannshofer et al., Nucl. Phys. B **830**, 17 (2010) [arXiv:0909.1333 [hep-ph]] [Search INSPIRE].
[1925] M. Blanke and A. J. Buras, Eur. Phys. J. C **76**, 197 (2016) [arXiv:1602.04020 [hep-ph]] [Search INSPIRE].
[1926] R. Barbieri et al., Eur. Phys. J. C **71**, 1725 (2011) [arXiv:1105.2296 [hep-ph]] [Search INSPIRE].
[1927] R. Barbieri et al., Phys. Lett. B **377**, 76 (1996) [arXiv:hep-ph/9512388] [Search INSPIRE].

[1928] A. Pomarol and D. Tommasini, Nucl. Phys. B **466**, 3 (1996) [arXiv:hep-ph/9507462] [Search INSPIRE].
[1929] LHCb Collaboration, Measurement of the CKM angle γ from a combination of $B \to DK$ analyses, LHCb-CONF-2016-001 (2016).
[1930] R. Barbieri et al., Eur. Phys. J. C **71**, 1812 (2011) [arXiv:1108.5125 [hep-ph]] [Search INSPIRE].
[1931] R. Barbieri et al., J. High Energy Phys. **07**, 181 (2012) [arXiv:1203.4218 [hep-ph]] [Search INSPIRE].
[1932] R. Barbieri et al., J. High Energy Phys. **10**, 040 (2012) [arXiv:1206.1327 [hep-ph]] [Search INSPIRE].
[1933] A. J. Buras and J. Girrbach, J. High Energy Phys. **01**, 007 (2013) [arXiv:1206.3878 [hep-ph]] [Search INSPIRE].
[1934] S. Dimopoulos and G. F. Giudice, Phys. Lett. B **357**, 573 (1995) [arXiv:hep-ph/9507282] [Search INSPIRE].
[1935] A. G. Cohen et al., Phys. Lett. B **388**, 588 (1996) [arXiv:hep-ph/9607394] [Search INSPIRE].
[1936] G. Blankenburg and J. Jones-Pérez, Eur. Phys. J. C **73**, 2289 (2013) [arXiv:1210.4561 [hep-ph]] [Search INSPIRE].
[1937] R. Barbieri et al., J. High Energy Phys. **05**, 105 (2014) [arXiv:1402.6677 [hep-ph]] [Search INSPIRE].
[1938] W. Porod, Comput. Phys. Commun. **153**, 275 (2003) [arXiv:hep-ph/0301101] [Search INSPIRE].
[1939] W. Porod and F. Staub, Comput. Phys. Commun. **183**, 2458 (2012) [arXiv:1104.1573 [hep-ph]] [Search INSPIRE].
[1940] F. Staub, Comput. Phys. Commun. **185**, 1773 (2014) [arXiv:1309.7223 [hep-ph]] [Search INSPIRE].
[1941] W. Porod et al., Eur. Phys. J. C **74**, 2992 (2014) [arXiv:1405.1434 [hep-ph]] [Search INSPIRE].
[1942] F. Staub et al., Comput. Phys. Commun. **183**, 2165 (2012) [arXiv:1109.5147 [hep-ph]] [Search INSPIRE].
[1943] B. Blankenburg et al., Eur. Phys. J. C **72**, 2126 (2012) [arXiv:1204.0688 [hep-ph]] [Search INSPIRE].
[1944] J. Jones-Pérez, Eur. Phys. J. C **74**, 2772 (2014); **74**, 2886 (2014) [erratum] [arXiv:1311.1837 [hep-ph]] [Search INSPIRE].
[1945] B. Aubert et al., Phys. Rev. Lett. **104**, 021802 (2010) [arXiv:0908.2381 [hep-ex]] [Search INSPIRE].
[1946] A. M. Baldini et al., arXiv:1301.7225 [physics.ins-det] [Search INSPIRE].
[1947] A. Crivellin et al., Phys. Rev. D **91**, 075006 (2015) [arXiv:1503.03477 [hep-ph]] [Search INSPIRE].
[1948] A. Celis et al., Phys. Rev. D **92**, 015007 (2015) [arXiv:1505.03079 [hep-ph]] [Search INSPIRE].
[1949] A. Crivellin et al., Phys. Rev. Lett. **114**, 151801 (2015) [arXiv:1501.00993 [hep-ph]] [Search INSPIRE].
[1950] C. Bobeth et al., J. High Energy Phys. **04**, 079 (2017) [arXiv:1609.04783 [hep-ph]] [Search INSPIRE].
[1951] W. Altmannshofer et al., Phys. Rev. D **94**, 095026 (2016) [arXiv:1604.08221 [hep-ph]] [Search INSPIRE].
[1952] X. G. He et al., Phys. Rev. D **43**, 22 (1991).
[1953] R. Foot, Mod. Phys. Lett. A **6**, 527 (1991).
[1954] X.-G. He et al., Phys. Rev. D **44**, 2118 (1991).
[1955] P. Binetruy et al., Nucl. Phys. B **496**, 3 (1997) [arXiv:hep-ph/9610481] [Search INSPIRE].
[1956] N. F. Bell and R. R. Volkas, Phys. Rev. D **63**, 013006 (2001) [arXiv:hep-ph/0008177] [Search INSPIRE].
[1957] S. Choubey and W. Rodejohann, Eur. Phys. J. C **40**, 259 (2005) [arXiv:hep-ph/0411190] [Search INSPIRE].
[1958] A. J. Buras and J. Girrbach, J. High Energy Phys. **12**, 009 (2013) [arXiv:1309.2466 [hep-ph]] [Search INSPIRE].
[1959] A. J. Buras et al., J. High Energy Phys. **02**, 116 (2013) [arXiv:1211.1896 [hep-ph]] [Search INSPIRE].
[1960] T. Hurth et al., J. High Energy Phys. **12**, 053 (2014) [arXiv:1410.4545 [hep-ph]] [Search INSPIRE].
[1961] R. Aaij et al., J. High Energy Phys. **06**, 115 (2015) [arXiv:1503.07138 [hep-ex]] [Search INSPIRE].
[1962] S. Meinel and D. van Dyk, Phys. Rev. D **94**, 013007 (2016) [arXiv:1603.02974 [hep-ph]] [Search INSPIRE].
[1963] D. Becirevic et al., Eur. Phys. J. C **76**, 134 (2016) [arXiv:1602.00881 [hep-ph]] [Search INSPIRE].

[1964] M. Gronau and J. L. Rosner, Phys. Rev. D **59**, 113002 (1999) [arXiv:hep-ph/9809384] [Search INSPIRE].
[1965] A. J. Buras et al., Nucl. Phys. B **697**, 133 (2004) [arXiv:hep-ph/0402112] [Search INSPIRE].
[1966] S. Baek and D. London, Phys. Lett. B **653**, 249 (2007) [arXiv:hep-ph/0701181] [Search INSPIRE].
[1967] R. Fleischer et al., Eur. Phys. J. C **51**, 55 (2007) [arXiv:hep-ph/0702275] [Search INSPIRE].
[1968] L. Hofer and L. Vernazza, arXiv:1212.4785 [hep-ph] [Search INSPIRE].
[1969] N. Arkani-Hamed et al., Phys. Rev. D **61**, 116003 (2000) [arXiv:hep-ph/9909326] [Search INSPIRE].
[1970] B. Grinstein et al., J. High Energy Phys. **11**, 067 (2010) [arXiv:1009.2049 [hep-ph]] [Search INSPIRE].
[1971] R. T. D'Agnolo and D. M. Straub, J. High Energy Phys. **05**, 034 (2012) [arXiv:1202.4759 [hep-ph]] [Search INSPIRE].
[1972] A. J. Buras et al., J. High Energy Phys. **03**, 088 (2012) [arXiv:1112.4477 [hep-ph]] [Search INSPIRE].
[1973] R. Alonso et al., J. High Energy Phys. **12**, 119 (2016) [arXiv:1609.05902 [hep-ph]] [Search INSPIRE].
[1974] F. Pisano and V. Pleitez, Phys. Rev. D **46**, 410 (1992) [arXiv:hep-ph/9206242] [Search INSPIRE].
[1975] P. H. Frampton, Phys. Rev. Lett. **69**, 2889 (1992).
[1976] A. J. Buras et al., J. High Energy Phys. **1302**, 023 (2013) [arXiv:1211.1237 [hep-ph]] [Search INSPIRE].
[1977] A. J. Buras et al., J. High Energy Phys. **1408**, 039 (2014) [arXiv:1405.3850 [hep-ph]] [Search INSPIRE].
[1978] A. J. Buras et al., J. High Energy Phys. **1402**, 112 (2014) [arXiv:1311.6729 [hep-ph]] [Search INSPIRE].
[1979] A. J. Buras and F. De Fazio, J. High Energy Phys. **03**, 010 (2016) [arXiv:1512.02869 [hep-ph]] [Search INSPIRE].
[1980] A. J. Buras and F. De Fazio, J. High Energy Phys. **08**, 115 (2016) [arXiv:1604.02344 [hep-ph]] [Search INSPIRE].
[1981] R. A. Diaz et al., Phys. Rev. D **72**, 035018 (2005) [arXiv:hep-ph/0411263] [Search INSPIRE].
[1982] A. E. Carcamo Hernandez et al., Phys. Rev. D **73**, 035007 (2006) [arXiv:hep-ph/0510421] [Search INSPIRE].
[1983] A. J. Buras and J.-M. Gerard, J. High Energy Phys. **12**, 008 (2015) [arXiv:1507.06326 [hep-ph]] [Search INSPIRE].
[1984] J. M. Cabarcas et al., Int. J. Mod. Phys. A **29**, 1450015 (2014) [arXiv:1310.1407 [hep-ph]] [Search INSPIRE].
[1985] S. M. Boucenna et al., Phys. Rev. D **92**, 053001 (2015) [arXiv:1502.07546 [hep-ph]] [Search INSPIRE].
[1986] J. C. Pati and A. Salam, Phys. Rev. D **10**, 275 (1974); **11**, 703 (1975) [erratum].
[1987] R. N. Mohapatra and J. C. Pati, Phys. Rev. D **11**, 566 (1975).
[1988] R. N. Mohapatra and J. C. Pati, Phys. Rev. D **11**, 2558 (1975).
[1989] G. Senjanovic and R. N. Mohapatra, Phys. Rev. D **12**, 1502 (1975).
[1990] S. Patra et al., Phys. Lett. B **752**, 186 (2016) [arXiv:1506.03456 [hep-ph]] [Search INSPIRE].
[1991] G. Aad et al., Phys. Lett. B **754**, 302 (2016) [arXiv:1512.01530 [hep-ex]] [Search INSPIRE].
[1992] V. Khachatryan et al., Phys. Rev. Lett. **116**(7), 071801 (2016) [arXiv:1512.01224 [hep-ex]] [Search INSPIRE].
[1993] K. Hsieh et al., Phys. Rev. D **82**, 035011 (2010) [arXiv:1003.3482 [hep-ph]] [Search INSPIRE].
[1994] P. Langacker and S. U. Sankar, Phys. Rev. D **40**, 1569 (1989).
[1995] G. Barenboim et al., Phys. Rev. D **55**, 4213 (1997) [arXiv:hep-ph/9611347] [Search INSPIRE].
[1996] K. Kiers et al., Phys. Rev. D **66**, 095002 (2002) [arXiv:hep-ph/0205082] [Search INSPIRE].
[1997] M. Blanke et al., J. High Energy Phys. **03**, 024 (2012) [arXiv:1111.5014 [hep-ph]] [Search INSPIRE].
[1998] A. Crivellin, Phys. Rev. D **81**, 031301 (2010) [arXiv:0907.2461 [hep-ph]] [Search INSPIRE].
[1999] C.-H. Chen and S.-H. Nam, Phys. Lett. B **666**, 462 (2008) [arXiv:0807.0896 [hep-ph]] [Search INSPIRE].
[2000] R. Feger et al., Phys. Rev. D **82**, 073002 (2010) [arXiv:1003.4022 [hep-ph]] [Search INSPIRE].
[2001] A. J. Buras et al., Nucl. Phys. B **843**, 107 (2011) [arXiv:1007.1993 [hep-ph]] [Search INSPIRE].
[2002] A. Crivellin and S. Pokorski, Phys. Rev. Lett. **114**, 011802 (2015) [arXiv:1407.1320 [hep-ph]] [Search INSPIRE].

[2003] G. Senjanovic, Nucl. Phys. B **153**, 334 (1979).
[2004] R. N. Mohapatra et al., Phys. Rev. D **17**, 2462 (1978).
[2005] D. Chang, Nucl. Phys. B **214**, 435 (1983).
[2006] G. C. Branco et al., Nucl. Phys. B **221**, 317 (1983).
[2007] H. Harari and M. Leurer, Nucl. Phys. B **233**, 221 (1984).
[2008] G. Beall et al., Phys. Rev. Lett. **48**, 848 (1982).
[2009] G. Ecker and W. Grimus, Phys. Lett. B **153**, 279 (1985).
[2010] J. M. Frere et al., Phys. Rev. D **46**, 337 (1992).
[2011] G. Barenboim et al., Nucl. Phys. B **478**, 527 (1996) [arXiv:hep-ph/9608450] [Search INSPIRE].
[2012] W. Dekens and D. Boer, Nucl. Phys. B **889**, 727 (2014) [arXiv:1409.4052 [hep-ph]] [Search INSPIRE].
[2013] T. Heidsieck, PhD thesis, Munich, Tech. U. (2012).
[2014] S. Bertolini et al., Phys. Rev. D **89**, 095028 (2014) [arXiv:1403.7112 [hep-ph]] [Search INSPIRE].
[2015] W. Noll, PhD thesis, Karlsruher Institut fur Technologie (2016).
[2016] D. Guadagnoli and R. N. Mohapatra, Phys. Lett. B **694**, 386 (2011) [arXiv:1008.1074 [hep-ph]] [Search INSPIRE].
[2017] G. M. Asatrian and A. N. Ionnisian, Mod. Phys. Lett. A **5**, 1089 (1990).
[2018] G. M. Asatryan and A. N. Ioannisyan, Sov. J. Nucl. Phys. **51**, 858 (1990).
[2019] D. Cocolicchio et al., Phys. Rev. D **40**, 1477 (1989).
[2020] E. Guadagnoli et al., J. High Energy Phys. **04**, 093 (2011) [arXiv:1103.4170 [hep-ph]] [Search INSPIRE].
[2021] R. N. Mohapatra, Phys. Rev. D **46**, 2990 (1992).
[2022] A. G. Akeroyd et al., Phys. Rev. D **76**, 013004 (2007) [arXiv:hep-ph/0610344] [Search INSPIRE].
[2023] F. Gursey et al., Phys. Lett. B **60**, 177 (1976).
[2024] Q. Shafi, Phys. Lett. B **79**, 301 (1978).
[2025] Y. Achiman and B. Stech, Phys. Lett. B **77**, 389 (1978).
[2026] K. S. Babu et al., J. High Energy Phys. **05**, 108 (2015) [arXiv:1504.00904 [hep-ph]] [Search INSPIRE].
[2027] J. L. Rosner, Comments Nucl. Part. Phys. **15**, 195 (1986).
[2028] J. L. Hewett and T. G. Rizzo, Phys. Rept. **183**, 193 (1989).
[2029] P. Athron et al., J. High Energy Phys. **01**, 153 (2015) [arXiv:1410.6288 [hep-ph]] [Search INSPIRE].
[2030] J. L. Rosner, Phys. Rev. D **90**, 035005 (2014) [arXiv:1404.5198 [hep-ph]] [Search INSPIRE].
[2031] O. Eberhardt et al., Phys. Rev. Lett. **109**, 241802 (2012) [arXiv:1209.1101 [hep-ph]] [Search INSPIRE].
[2032] E. Kuflik et al., Phys. Rev. Lett. **110**, 091801 (2013) [arXiv:1204.1975 [hep-ph]] [Search INSPIRE].
[2033] R. Barbieri and D. V. Nanopoulos, Phys. Lett. B **91**, 369 (1980).
[2034] H. Georgi, Nucl. Phys. B **156**, 126 (1979).
[2035] R. Barbieri et al., Phys. Lett. B **90**, 91 (1980).
[2036] S. Bertolini et al., Phys. Rev. D **80**, 015013 (2009) [arXiv:0903.4049 [hep-ph]] [Search INSPIRE].
[2037] N. G. Deshpande et al., Phys. Rev. D **47**, 2892 (1993) [arXiv:hep-ph/9211232] [Search INSPIRE].
[2038] V. V. Dixit and M. Sher, Phys. Rev. D **40**, 3765 (1989).
[2039] B. Stech and Z. Tavartkiladze, Phys. Rev. D **70**, 035002 (2004) [arXiv:hep-ph/0311161] [Search INSPIRE].
[2040] K. Ishiwata, Z. Ligeti, and M. B. Wise, J. High Energy Phys. **10**, 027 (2015) [arXiv:1506.03484 [hep-ph]] [Search INSPIRE].
[2041] E. Abouzaid et al., Phys. Rev. D **83**, 092001 (2011) [arXiv:1011.0127 [hep-ex]] [Search INSPIRE].
[2042] J. Kang et al., Phys. Rev. D **77**, 035003 (2008) [arXiv:0708.2701 [hep-ph]] [Search INSPIRE].
[2043] F. F. Deppisch et al., Phys. Rev. D **94**, 013003 (2016) [arXiv:1603.07672 [hep-ph]] [Search INSPIRE].
[2044] F. F. Deppisch et al., Phys. Lett. B **762**, 432 (2016) [arXiv:1608.05334 [hep-ph]] [Search INSPIRE].
[2045] D. B. Kaplan, Nucl. Phys. B **365**, 259 (1991).
[2046] Y. Grossman and M. Neubert, Phys. Lett. B **474**, 361 (2000) [arXiv:hep-ph/9912408] [Search INSPIRE].
[2047] T. Gherghetta and A. Pomarol, Nucl. Phys. B **586**, 141 (2000) [arXiv:hep-ph/0003129] [Search INSPIRE].
[2048] S. J. Huber and Q. Shafi, Phys. Lett. B **498**, 256 (2001) [arXiv:hep-ph/0010195] [Search INSPIRE].

[2049] C. Csaki et al., Phys. Rev. D **70**, 015012 (2004) [arXiv:hep-ph/0310355] [Search INSPIRE].
[2050] K. Agashe et al., Phys. Rev. D **71**, 016002 (2005) [arXiv:hep-ph/0408134] [Search INSPIRE].
[2051] M. Blanke et al., J. High Energy Phys. **03**, 001 (2009) [arXiv:0809.1073 [hep-ph]] [Search INSPIRE].
[2052] M. Bauer et al., J. High Energy Phys. **09**, 017 (2010) [arXiv:0912.1625 [hep-ph]] [Search INSPIRE].
[2053] R. Barbieri et al., J. High Energy Phys. **05**, 069 (2013) [arXiv:1211.5085 [hep-ph]] [Search INSPIRE].
[2054] K. Agashe et al., Phys. Lett. B **641**, 62 (2006) [arXiv:hep-ph/0605341] [Search INSPIRE].
[2055] A. J. Buras et al., J. High Energy Phys. **09**, 076 (2009) [arXiv:0905.2318 [hep-ph]] [Search INSPIRE].
[2056] David M. Straub, J. High Energy Phys. **08**, 108 (2013) [arXiv:1302.4651 [hep-ph]] [Search INSPIRE].
[2057] C. Csaki et al., J. High Energy Phys. **09**, 008 (2008) [arXiv:0804.1954 [hep-ph]] [Search INSPIRE].
[2058] A. L. Fitzpatrick et al., Phys. Rev. Lett. **100**, 171604 (2008) [arXiv:0710.1869 [hep-ph]] [Search INSPIRE].
[2059] C. Csaki et al., Phys. Rev. D **80**, 016001 (2009) [arXiv:0806.3757 [hep-ph]] [Search INSPIRE].
[2060] J. Santiago, J. High Energy Phys. **12**, 046 (2008) [arXiv:0806.1230 [hep-ph]] [Search INSPIRE].
[2061] C. Csaki et al., Phys. Rev. D **81**, 075025 (2010) [arXiv:0907.0474 [hep-ph]] [Search INSPIRE].
[2062] C. Delaunay et al., Phys. Rev. D **83**, 115003 (2011) [arXiv:1007.0243 [hep-ph]] [Search INSPIRE].
[2063] M. Bauer et al., Phys. Rev. Lett. **108**, 081603 (2012) [arXiv:1110.0471 [hep-ph]] [Search INSPIRE].
[2064] M. Redi, Eur. Phys. J. C **72**, 2030 (2012) [arXiv:1203.4220 [hep-ph]] [Search INSPIRE].
[2065] O. Matsedonskyi, J. High Energy Phys. **02**, 154 (2015) [arXiv:1411.4638 [hep-ph]] [Search INSPIRE].
[2066] G. Cacciapaglia et al., J. High Energy Phys. **06**, 085 (2015) [arXiv:1501.03818 [hep-ph]] [Search INSPIRE].
[2067] G. Cacciapaglia et al., J. High Energy Phys. **04**, 006 (2008) [arXiv:0709.1714 [hep-ph]] [Search INSPIRE].
[2068] M. Redi and A. Weiler, J. High Energy Phys. **11**, 108 (2011) [arXiv:1106.6357 [hep-ph]] [Search INSPIRE].
[2069] M. Ciuchini et al., J. High Energy Phys. **07**, 013 (2001) [arXiv:hep-ph/0012308] [Search INSPIRE].
[2070] M. Bona et al., J. High Energy Phys. **07**, 028 (2005) [arXiv:hep-ph/0501199] [Search INSPIRE].
[2071] M. Bona et al., J. High Energy Phys. **03**, 080 (2006) [arXiv:hep-ph/0509219] [Search INSPIRE].
[2072] M. Bona et al., J. High Energy Phys. **03**, 049 (2008) [arXiv:0707.0636 [hep-ph]] [Search INSPIRE].
[2073] A. Andreazza et al., Frascati Phys. Ser. **60**, 1 (2015).
[2074] Y. Sakaki and H. Tanaka, Phys. Rev. D **87**, 054002 (2013) [arXiv:1205.4908 [hep-ph]] [Search INSPIRE].
[2075] A. Datta et al., Phys. Rev. D **86**, 034027 (2012) [arXiv:1206.3760 [hep-ph]] [Search INSPIRE].
[2076] P. Biancofiore et al., Phys. Rev. D **87**, 074010 (2013) [arXiv:1302.1042 [hep-ph]] [Search INSPIRE].
[2077] K. Hagiwara et al., Phys. Rev. D **89**, 094009 (2014) [arXiv:1403.5892 [hep-ph]] [Search INSPIRE].
[2078] S. Bhattacharya et al., Phys. Rev. D **93**, 034011 (2016) [arXiv:1509.07259 [hep-ph]] [Search INSPIRE].
[2079] D. Becirevic et al., arXiv:1602.03030 [hep-ph] [Search INSPIRE].
[2080] R. Alonso et al., Phys. Rev. D **94**, 094021 (2016) [arXiv:1602.07671 [hep-ph]] [Search INSPIRE].
[2081] B. Dumont et al., Phys. Rev. D **94**, 034001 (2016) [arXiv:1603.05248 [hep-ph]] [Search INSPIRE].
[2082] G. Aad et al., J. High Energy Phys. **10**, 189 (2013) [arXiv:1308.2631 [hep-ex]] [Search INSPIRE].
[2083] V. Khachatryan et al., J. High Energy Phys. **06**, 116 (2015) [arXiv:1503.08037 [hep-ex]] [Search INSPIRE].
[2084] G. Aad et al., Eur. Phys. J. C **76**, 5 (2016) [arXiv:1508.04735 [hep-ph]] [Search INSPIRE].
[2085] V. Khachatryan et al., Phys. Lett. B **739**, 229 (2014) [arXiv:1408.0806 [hep-ex]] [Search INSPIRE].
[2086] G. Aad et al., , Phys. Rev. Lett. **114**, 161801 (2015) [arXiv:1501.01325 [hep-ex]] [Search INSPIRE].
[2087] T. Blake et al., Prog. Part. Nucl. Phys. **92**, 50 (2017) [arXiv:1606.00916 [hep-ph]] [Search INSPIRE].
[2088] C. Bobeth et al., J. High Energy Phys. **07**, 098 (2010) [arXiv:1006.5013 [hep-ph]] [Search INSPIRE].
[2089] S. Descotes-Genon et al., J. High Energy Phys. **06**, 099 (2011) [arXiv:1104.3342 [hep-ph]] [Search INSPIRE].
[2090] C. Bobeth et al., J. High Energy Phys. **07**, 067 (2011) [arXiv:1105.0376 [hep-ph]] [Search INSPIRE].
[2091] W. Altmannshofer et al., J. High Energy Phys. **04**, 008 (2012) [arXiv:1111.1257 [hep-ph]] [Search INSPIRE].

[2092] C. Bobeth et al., J. High Energy Phys. **01**, 107 (2012) [arXiv:1111.2558 [hep-ph]] [Search INSPIRE].
[2093] F. Beaujean et al., J. High Energy Phys. **08**, 030 (2012) [arXiv:1205.1838 [hep-ph]] [Search INSPIRE].
[2094] W. Altmannshofer and D. M. Straub, J. High Energy Phys. **08**, 121 (2012) [arXiv:1206.0273 [hep-ph]] [Search INSPIRE].
[2095] F. Beaujean et al., Eur. Phys. J. C **74**, 2897 (2014); **74**, 3179 (2014) [erratum] [arXiv:1310.2478 [hep-ph]] [Search INSPIRE].
[2096] R. R. Horgan et al., Phys. Rev. Lett. **112**, 212003 (2014) [arXiv:1310.3887 [hep-ph]] [Search INSPIRE].
[2097] T. Hurth and F. Mahmoudi, J. High Energy Phys. **04**, 097 (2014) [arXiv:1312.5267 [hep-ph]] [Search INSPIRE].
[2098] D. Ghosh et al., J. High Energy Phys. **12**, 131 (2014) [arXiv:1408.4097 [hep-ph]] [Search INSPIRE].
[2099] F. Beaujean et al., Eur. Phys. J. C **75**, 456 (2015) [arXiv:1508.01526 [hep-ph]] [Search INSPIRE].
[2100] T. Hurth et al., Nucl. Phys. B **909**, 737 (2016) [arXiv:1603.00865 [hep-ph]] [Search INSPIRE].
[2101] A. Karan et al., Phys. Rev. D **95**, 114006 (2017) [arXiv:1603.04355 [hep-ph]] [Search INSPIRE].
[2102] A. J. Buras et al., J. High Energy Phys. **11**, 121 (2014) [arXiv:1408.0728 [hep-ph]] [Search INSPIRE].
[2103] O. Cata and M. Jung, Phys. Rev. D **92**, 055018 (2015) [arXiv:1505.05804 [hep-ph]] [Search INSPIRE].
[2104] D. Becirevic et al., Phys. Rev. D **86**, 034034 (2012) [arXiv:1205.5811 [hep-ph]] [Search INSPIRE].
[2105] C. Bobeth et al., J. High Energy Phys. **07**, 106 (2008) [arXiv:0805.2525 [hep-ph]] [Search INSPIRE].
[2106] S. Descotes-Genon and J. Virto, J. High Energy Phys. **04**, 045 (2015); 07, 049 (2015) [erratum] [arXiv:1502.05509 [hep-ph]] [Search INSPIRE].
[2107] M. Ciuchini et al., J. High Energy Phys. **06**, 116 (2016) [arXiv:1512.07157 [hep-ph]] [Search INSPIRE].
[2108] G. Hiller and F. Kruger, Phys. Rev. D **69**, 074020 (2004) [arXiv:hep-ph/0310219] [Search INSPIRE].
[2109] C. Niehoff et al., Phys. Lett. B **747**, 182 (2015) [arXiv:1503.03865 [hep-ph]] [Search INSPIRE].
[2110] D. Becirevic et al., Phys. Rev. D **92**, 014016 (2015) [arXiv:1503.09024 [hep-ph]] [Search INSPIRE].
[2111] B. Aubert et al., Phys. Rev. D **73**, 092001 (2006) [arXiv:hep-ex/0604007] [Search INSPIRE].
[2112] J. P. Lees et al., Phys. Rev. D **86**, 012004 (2012) [arXiv:1204.2852 [hep-ex]] [Search INSPIRE].
[2113] W. Altmannshofer et al., Phys. Rev. D **93**, 031301 (2016) [arXiv:1507.07927 [hep-ph]] [Search INSPIRE].
[2114] D. Melikhov et al., Phys. Lett. B **428**, 171 (1998) [arXiv:hep-ph/9803269] [Search INSPIRE].
[2115] J. Albrecht et al., arXiv:1709.10308 [hep-ph] [Search INSPIRE].
[2116] B. Capdevila et al., J. High Energy Phys. **01**, 093 (2018) [arXiv:1704.05340 [hep-ph]] [Search INSPIRE].
[2117] F. Mahmoudi, Comput. Phys. Commun. **178**, 745 (2008) [arXiv:0710.2067 [hep-ph]] [Search INSPIRE].
[2118] F. Mahmoudi, Comput. Phys. Commun. **180**, 1718 (2009).
[2119] P. Z. Skands et al., J. High Energy Phys. **07**, 036 (2004) [arXiv:hep-ph/0311123] [Search INSPIRE].
[2120] B. C. Allanach et al., Comput. Phys. Commun. **180**, 8 (2009) [arXiv:0801.0045 [hep-ph]] [Search INSPIRE].
[2121] F. Mahmoudi et al., Comput. Phys. Commun. **183**, 285 (2012) [arXiv:1008.0762 [hep-ph]] [Search INSPIRE].
[2122] V. G. Chobanova et al., J. High Energy Phys. **07**, 025 (2017) [arXiv:1702.02234 [hep-ph]] [Search INSPIRE].
[2123] T. Hurth et al., Phys. Rev. D **96**, 095034 (2017) [arXiv:1705.06274 [hep-ph]] [Search INSPIRE].
[2124] T. Hurth et al., J. High Energy Phys. **11**, 176 (2017) [arXiv:1708.04474 [hep-ph]] [Search INSPIRE].
[2125] F. U. Bernlochner et al., Eur. Phys. J. C **77**, 786 (2017) [arXiv:1705.07933 [hep-ph]] [Search INSPIRE].
[2126] P. Athron et al., Eur. Phys. J. C **77**, 784 (2017); **78**, 98 (2018) [addendum] [arXiv:1705.07908 [hep-ph]] [Search INSPIRE].
[2127] A. Arbey and F. Mahmoudi, Comput. Phys. Commun. **181**, 1277 (2010) [arXiv:0906.0369 [hep-ph]] [Search INSPIRE].
[2128] A. Arbey and F. Mahmoudi, Comput. Phys. Commun. **182**, 1582 (2011).
[2129] J. A. Evans and D. Shih, arXiv:1606.00003 [hep-ph] [Search INSPIRE].

[2130] J. Aebischer et al., Comput. Phys. Commun. **232**, 71 (2018) [arXiv:1712.05298 [hep-ph]] [Search INSPIRE].
[2131] D. Foreman-Mackey et al., Publ. Astron. Soc. Pac. **125**, 306 (2013) [arXiv:1202.3665 [astro-ph.IM]] [Search INSPIRE].
[2132] W. Altmannshofer et al., Phys. Rev. D **96**, 055008 (2017) [arXiv:1704.05435 [hep-ph]] [Search INSPIRE].
[2133] M. Ciuchini et al., PoS **ICHEP2016**, 584 (2016) [arXiv:1611.04338 [hep-ph]] [Search INSPIRE].
[2134] V. Cacchio et al., J. High Energy Phys. **11**, 026 (2016) [arXiv:1609.01290 [hep-ph]] [Search INSPIRE].
[2135] F. Beaujean et al., J. Phys. Conf. Ser. **664**, 072003 (2015).
[2136] J. Rosiek et al., Comput. Phys. Commun. **181**, 2180 (2010) [arXiv:1003.4260 [hep-ph]] [Search INSPIRE].
[2137] A. Crivellin et al., Comput. Phys. Commun. **184**, 1004 (2013) [arXiv:1203.5023 [hep-ph]] [Search INSPIRE].
[2138] J. Rosiek, Comput. Phys. Commun. **188**, 208 (2015) [arXiv:1410.0606 [hep-ph]] [Search INSPIRE].
[2139] S. Pokorski et al., Nucl. Phys. B **570**, 81 (2000) [arXiv:hep-ph/9906206] [Search INSPIRE].
[2140] A. J. Buras et al., Nucl. Phys. B **714**, 103 (2005) [arXiv:hep-ph/0408142] [Search INSPIRE].
[2141] A. Dedes et al., Phys. Rev. D **79**, 055006 (2009) [arXiv:0812.4320 [hep-ph]] [Search INSPIRE].
[2142] M. Misiak et al., Adv. Ser. Direct. High Energy Phys. **15**, 795 (1998) [arXiv:hep-ph/9703442] [Search INSPIRE].
[2143] A. Dedes et al., J. High Energy Phys. **11**, 137 (2014) [arXiv:1409.6546 [hep-ph]] [Search INSPIRE].
[2144] A. J. Buras et al., Nucl. Phys. B **619**, 434 (2001) [arXiv:hep-ph/0107048] [Search INSPIRE].
[2145] A. J. Buras et al., Nucl. Phys. B **659**, 3 (2003) [arXiv:hep-ph/0210145] [Search INSPIRE].
[2146] J. Rosiek, Phys. Rev. D **41**, 3464 (1990).
[2147] J. Rosiek, arXiv:hep-ph/9511250 [Search INSPIRE].
[2148] A. Crivellin et al., J. High Energy Phys. **07**, 017 (2011) [arXiv:1103.4272 [hep-ph]] [Search INSPIRE].
[2149] D. van Dyk et al., EOS ("btoplxnu" release) Zenodo, doi:10.5281/zenodo.50968 (2016).
[2150] T. Feldmann et al., Phys. Rev. D **92**, 034013 (2015) [arXiv:1503.09063 [hep-ph]] [Search INSPIRE].
[2151] M. Bordone et al., Eur. Phys. J. C **76**, 360 (2016) [arXiv:1602.06143 [hep-ph]] [Search INSPIRE].
[2152] R. Fleischer, Nucl. Phys. Proc. Suppl. **241–242**, 135 (2013) [arXiv:1208.2843 [hep-ph]] [Search INSPIRE].
[2153] A. J. Buras et al., Nucl. Phys. B **631**, 219 (2002) [arXiv:hep-ph/0203135] [Search INSPIRE].
[2154] B. Grinstein and D. Pirjol, Phys. Rev. D **70**, 114005 (2004) [arXiv:hep-ph/0404250] [Search INSPIRE].
[2155] C. Bobeth et al., Phys. Rev. D **87**, 034016 (2013) [arXiv:1212.2321 [hep-ph]] [Search INSPIRE].
[2156] P. Boer et al., J. High Energy Phys. **01**, 155 (2015) [arXiv:1410.2115 [hep-ph]] [Search INSPIRE].